

WOODHEAD PUBLISHING SERIES IN MATERIALS



ADVANCES IN STRUCTURAL ADHESIVE BONDING

SECOND EDITION



Edited by
DAVID A. DILLARD

Advances in Structural Adhesive Bonding

This page intentionally left blank

Woodhead Publishing Series in Materials

Advances in Structural Adhesive Bonding

Second Edition

Edited by

David A. Dillard

**Department of Biomedical Engineering and
Mechanics, Virginia Tech, Blacksburg, VA,
United States**



ELSEVIER

WP

WOODHEAD
PUBLISHING

An imprint of Elsevier

Woodhead Publishing is an imprint of Elsevier
50 Hampshire Street, 5th Floor, Cambridge, MA 02139, United States
The Boulevard, Langford Lane, Kidlington, OX5 1GB, United Kingdom

Copyright © 2023 Elsevier Ltd. All rights reserved.

No part of this publication may be reproduced or transmitted in any form or by any means, electronic or mechanical, including photocopying, recording, or any information storage and retrieval system, without permission in writing from the publisher. Details on how to seek permission, further information about the Publisher's permissions policies and our arrangements with organizations such as the Copyright Clearance Center and the Copyright Licensing Agency, can be found at our website: www.elsevier.com/permissions.

This book and the individual contributions contained in it are protected under copyright by the Publisher (other than as may be noted herein).

Notices

Knowledge and best practice in this field are constantly changing. As new research and experience broaden our understanding, changes in research methods, professional practices, or medical treatment may become necessary.

Practitioners and researchers must always rely on their own experience and knowledge in evaluating and using any information, methods, compounds, or experiments described herein. In using such information or methods they should be mindful of their own safety and the safety of others, including parties for whom they have a professional responsibility.

To the fullest extent of the law, neither the Publisher nor the authors, contributors, or editors, assume any liability for any injury and/or damage to persons or property as a matter of products liability, negligence or otherwise, or from any use or operation of any methods, products, instructions, or ideas contained in the material herein.

ISBN: 978-0-323-91214-3 (print)

ISBN: 978-0-323-98437-9 (online)

For information on all Woodhead publications
visit our website at <https://www.elsevier.com/books-and-journals>

Publisher: Matthew Deans
Acquisitions Editor: Ana Claudia A. Garcia
Editorial Project Manager: Rafael Guilherme Trombaco
Production Project Manager: Kamesh R
Cover Designer: Victoria Pearson Esser

Typeset by STRAIVE, India



Contents

Contributors	xvii
Preface	xxiii
Part One Adhesive chemistries and formulations	1
1 Advances in epoxy adhesives	3
<i>Jay S. Schlechte</i>	
1.1 Introduction and history of epoxy adhesives	3
1.2 Major uses and important minor uses	3
1.3 Epoxy resins and epoxy functional raw materials, processes, and suppliers	4
1.4 Curatives for epoxy resins and epoxy functional raw materials, processes, and suppliers	13
1.5 Accelerators and catalysts	30
1.6 Tougheners and flexibilizers	37
1.7 General property specifications and certificate of analysis	37
1.8 Environmental, health, and safety considerations	38
1.9 Typical form factors and packaging of epoxy adhesives	38
1.10 Formulation and design	39
1.11 Adhesive production	41
1.12 Use and properties of epoxy adhesives	42
1.13 Recent advances in epoxy adhesives	46
1.14 Additional resources	56
Acknowledgments	56
References	56
2 Advances in acrylic structural adhesives	69
<i>Jian-ping (JP) Huang and John Lean</i>	
2.1 Introduction	69
2.2 Basics of acrylic structural adhesives	73
2.3 Interfacial adhesion	87
2.4 Trends in acrylic structural adhesives	92
2.5 Applications	93
2.6 Futures trends	97
Acknowledgments	98
References	98

3	Advances in polyurethane structural adhesives	103
	<i>Fabien Choffat, Antonio Corsaro, Claudio Di Fratta, and Steffen Kelch</i>	
3.1	Introduction	103
3.2	Characterization of PUR adhesives	106
3.3	Chemical overview and PUR structure to property relationships	111
3.4	Formulation and raw materials of PUR adhesives	117
3.5	Selected applications of structural polyurethane adhesives	124
3.6	Recent advances in PUR adhesives	127
	References	132
4	Advances in cyanoacrylate structural adhesives	137
	<i>Barry Burns</i>	
4.1	Introduction	137
4.2	Chemistry of α -cyanoacrylates	138
4.3	Industrial synthesis/manufacture of α -cyanoacrylate esters	139
4.4	Typical performance characteristics of α -cyanoacrylates—Strengths, weaknesses, and recent developments	143
4.5	Two-component (2K) cyanoacrylate adhesives	146
4.6	Photocuring cyanoacrylates	149
4.7	Biomedical cyanoacrylate adhesives	150
4.8	Cyanoacrylates and sustainability	151
4.9	Summary	152
	Acknowledgments	153
	References	153
5	Advances in anaerobic adhesives	159
	<i>David Condron</i>	
5.1	Anaerobic adhesives	159
5.2	Recent advances in anaerobic technology	167
5.3	Summary	175
	Acknowledgments	176
	References	176
6	Advances in structural silicone adhesives	179
	<i>F. de Buyl, V. Hayez, B. Harkness, J. Kimberlain, and N. Shephard</i>	
6.1	Introduction	179
6.2	Properties of silicone structural adhesives	179
6.3	Product forms and cure chemistry	181
6.4	Silicone adhesive formulations	190

6.5	Applications of structural silicone adhesives	196
6.6	Design techniques	206
6.7	Conclusions	211
6.8	Future trends	211
6.9	Sources of further information and advice	212
	References	212
7	Emerging structural adhesive chemistries and innovations	221
	<i>Erich Bain, Marvin Pollum, David Fortman, Martin E. Losada, Christopher M. Jackson, and Robert Jensen</i>	
7.1	Introduction	221
7.2	Structural adhesives innovations	225
7.3	Functionality beyond structural reinforcement	239
7.4	Using digital tools to advance the adhesives industry	242
7.5	Conclusions	244
	Acknowledgments	245
	References	245
8	Advances in toughening strategies for structural adhesives	251
	<i>Declan Carolan, Sammy He, and Ambrose C. Taylor</i>	
8.1	Introduction: What is toughness and why is it important?	251
8.2	Toughening of bulk epoxy polymers	252
8.3	Prediction of effectiveness of toughening	260
8.4	Toughness of an adhesive joint	274
8.5	Future trends	276
8.6	Conclusions	277
	Acknowledgment	278
	References	278
	Part Two Adherends and surfaces: Addressing and troubleshooting bonding challenges	287
9	What went wrong? Solving bonding challenges through surface science	289
	<i>Giles Dillingham and Rose Roberts</i>	
9.1	Prologue: Example of a bonding process suffering from “unexplainable” failures	289
9.2	Introduction	290
9.3	Adhesion: Resistance of an interface to failure	292
9.4	Adhesion failure in bonded and coated structures	304
9.5	Failure analysis	304
9.6	Critical concepts for surface preparation	305

9.7	Surface cleaning and treatment technologies	306
9.8	Processes out of control	308
9.9	Summary	322
	References	322
10	Advances in bonding plastics	327
	<i>Grace Wan, Colin Li Pi Shan, and Shaoguang Feng</i>	
10.1	Introduction	327
10.2	Principles governing plastics bonding	328
10.3	Challenge and surface characteristic in bonding plastics	332
10.4	Advanced surface treatment to improve plastic bonding	334
10.5	Chemical treatment to improve plastic bonding	337
10.6	Aging effect of plastic treatment	343
10.7	Advances in polyolefin adhesion	345
10.8	Summary and future trends in plastic bonding	352
	References	353
11	Structural bonds without an adhesive: Understanding adhesion of semicrystalline thermoplastic interfaces	359
	<i>Vinayak Khatavkar, Markus Bulters, and Michelle Elizabeth Seitz</i>	
11.1	Challenges in obtaining high adhesion at semicrystalline polymer interfaces	359
11.2	Overview of overmolding experiments and thermal modeling	362
11.3	Adhesion of overmolded polyamide 6 interfaces	364
11.4	Requirements for strong polymer interfaces	370
11.5	Summary of overmolding experiments and insights from quantifying crystallization and diffusion timescales	379
11.6	Exploiting geometry to achieve adhesion	380
11.7	Outlook and conclusions	381
	Acknowledgments	384
	References	384
12	Adhesive joining of thermoplastic composites	389
	<i>Dong Quan, Gennaro Scarselli, Neal Murphy, and Alojz Ivankovic</i>	
12.1	Introduction	389
12.2	Brief summary of surface treatment techniques for TPCs	390
12.3	UV irradiation of the TPCs	391
12.4	Joining TPCs to TPCs	394
12.5	Joining TPCs to metals	399
12.6	Joining TPCs to TSCs	406
12.7	Conclusions and future work	411
	References	412

13 Advances in structural wood products adhesive bonding	417
<i>Frederick A. Kamke and John A. Nairn</i>	
13.1 Overview	417
13.2 Substrate considerations	418
13.3 Structural wood composite products	420
13.4 New developments of wood adhesives	425
13.5 Adhesive/wood interactions	434
13.6 Wood-adhesive bondline characterization	436
13.7 Strength characterization—Quality control methods	437
13.8 Fracture testing	438
13.9 Adhesive bond durability	442
13.10 Characterizing bondline stiffness	445
References	446
Part Three Joint design, testing and modeling for performance & durability	457
14 Standard test methods and their need to evolve	459
<i>Aaron M. Forster, Christopher C. White, and David A. Dillard</i>	
14.1 Expanding roles in structural bonding	459
14.2 Infrastructure of standard test methods and measurements	460
14.3 Strength and fracture: An evolution in adhesive joint measurements	463
14.4 The evolution of strength and fracture energy in adhesive design	466
14.5 Future opportunities: The interface between standards and advances in structural adhesives	481
14.6 Conclusions	484
References	484
15 Predicting adhesive bond performance	493
<i>Alireza Akhavan-Safar, E.A.S. Marques, R.J.C. Carbas, and Lucas F.M. da Silva</i>	
15.1 Introduction	493
15.2 Stress and strain concepts	494
15.3 Stress types in bonded joints	495
15.4 Sources of adhesive joint stresses	496
15.5 Analytical approaches	498
15.6 Numerical methods	501
15.7 Hybrid analytical/numerical methods	508
15.8 Effects of joint geometry	509
15.9 Effects of strain rate	512
15.10 Effects of aging	512

15.11	Effects of temperature	514
15.12	Conclusions	514
	References	515
16	Innovations in fracture testing of structural adhesive bonds	525
	<i>Stephan Marzi</i>	
16.1	Introduction	525
16.2	Data reduction techniques	526
16.3	Advances in quasistatic single-mode testing	535
16.4	Novel developments in mixed-mode testing	542
16.5	Extending experimental methods to fatigue, aging, and creep	555
16.6	Experimental challenges in impact and high-rate testing	560
16.7	Conclusions and future trends	566
	References	567
17	Understanding fracture mode-mixity and its effects on bond performance	579
	<i>Bamber Blackman, Fengzhen Sun, Sofia Teixeira de Freitas, Silvio de Barros, Marcio Moreira Arouche, and Alojz Ivankovic</i>	
17.1	Introduction	579
17.2	Brief summary of test methods to introduce mixed-mode loading	580
17.3	Mixed-mode partitioning schemes	582
17.4	Application of global partitioning to mixed-mode bi-material interface joints	586
17.5	Mixed-mode fracture behavior	598
17.6	Conclusions and outlook	609
	References	610
18	Bondline thickness: Fracture mechanics perspective	615
	<i>Sofia Teixeira de Freitas and Michal K. Budzik</i>	
18.1	Introduction	615
18.2	From thin to thick adhesive layers	616
18.3	Adhesive thickness analysis using double cantilever beam (DCB) configuration	624
18.4	Effect of adhesive thickness on failure modes and fracture properties	627
18.5	Summary and future directions	638
	References	638
19	Evaluating and predicting fatigue behavior in adhesively bonded joints	643
	<i>Ian Ashcroft and John-Alan Pascoe</i>	
19.1	Introduction	643
19.2	General considerations for fatigue of adhesives	644

19.3	Experimental techniques	645
19.4	Stress/strain-life approaches	647
19.5	Strength/stiffness wearout	651
19.6	Fracture mechanics	653
19.7	Effect of joint features	660
19.8	Environmental and loading effects	661
19.9	Damage mechanics	662
19.10	Summary	666
	References	666
20	Durability and accelerated characterization of adhesive bonds	675
	<i>Scott W. Case, Arit Das, Michael J. Bortner, David A. Dillard, and Christopher C. White</i>	
20.1	Introduction	675
20.2	Correlating environmental exposure to mechanistic changes in polymer structure	676
20.3	Test methods for characterizing durability	683
20.4	TTSP and accelerated characterization	695
20.5	Examples and a case study	699
20.6	Summary: Status and future needs	702
	References	703
21	High-rate testing of structural adhesives	711
	<i>Evan L. Breedlove, Chaodi Li, Chao Chen, and Luis Trimiño</i>	
21.1	Introduction	711
21.2	The physics of high-rate testing	711
21.3	Rate-dependent properties in structural adhesives	715
21.4	DMA methods	718
21.5	Servohydraulic methods	719
21.6	Drop weight, falling striker, and pendulum impact tests	723
21.7	Kolsky bar/split-Hopkinson bar	734
21.8	Advancements and gaps in high-speed testing	743
	References	744
22	Application of high-throughput methodologies and artificial intelligence for adhesion testing	751
	<i>Kshitish A. Patankar, Tom Kalantar, Simon Cook, Edoardo Nicoli, Brad Tuft, and Matthew Crimmins</i>	
22.1	Introduction	751
22.2	Background	752
22.3	Considerations in HT workflow and screen development	754
22.4	Previous instances of HT in adhesion science	755
22.5	Workflow concept overview	756
22.6	Shear test: From workflow concept to integration	757
22.7	Durability: From workflow concept to integration	763

22.8	Supporting the adhesion HT workflow	768
22.9	Role of machine learning/artificial intelligence in adhesion science	770
22.10	Summary	772
	Acknowledgments	772
	References	772
Part Four Adhesive specification, quality control, & risk mitigation		777
23	Aerospace structural bonding: Qualification, quality control, substantiation, and risk mitigation	779
	<i>Cindy Ashforth, Guilherme Garcia Momm, Waruna Seneviratne, Ashley Trace, and Larry Ilcewicz</i>	
23.1	Introduction	779
23.2	Certification regulations and guidance	780
23.3	Bonding systems for both metal and composite bonds	783
23.4	Bonded joint certification	790
23.5	Bonded joint applications	796
23.6	Conclusion	802
	Acknowledgments	802
	References	802
24	Automotive adhesives: Specification, qualification, and quality control	807
	<i>John Hill and Ahmad Rezaei Mojdehi</i>	
24.1	Introduction	807
24.2	Specifications	810
24.3	Qualification	814
24.4	Quality control	818
24.5	Future trends	824
	References	824
25	Construction adhesives: Qualification, specification, quality control, and risk mitigation	827
	<i>Till Vallée, Marvin Kaufmann, and Morten Voß</i>	
25.1	Scope and structure of this chapter	827
25.2	Adhesive bonding for typical civil engineering materials	828
25.3	Structural verification	833
25.4	Manufacturing, quality control and risk mitigation	835
25.5	Conclusions	837
	References	839

26	General industrial adhesive applications: Qualification, specification, quality control, and risk mitigation	849
	<i>Mario Madrid, Jani Turunen, and Wolfgang Seitz</i>	
26.1	Use of adhesives in general industry	849
26.2	Capital goods end-user sector	856
26.3	Durable goods end-user sector	863
26.4	Consumable goods end-user sector	871
	Acknowledgments	873
	References	873
27	Biomedical adhesives: Qualification, specification, quality control, and risk mitigation	877
	<i>Juan Carlos del Real, Sara Lopez de Armentia, Eva Paz, Hermann Handwerker, and Felix Debor</i>	
27.1	Introduction	877
27.2	Biomedical adhesives	878
27.3	Clinical application of adhesives: Tissue adhesives	888
27.4	Adhesives in medical device industry	893
27.5	Certification, safety, quality, and specifications	898
	References	904
28	Structural monitoring of adhesive joints using machine learning	909
	<i>A. Francisco G. Tenreiro, Gabriel M.F. Ramalho, António Mendes Lopes, and Lucas F.M. da Silva</i>	
28.1	Introduction	909
28.2	Nondestructive testing and evaluation	910
28.3	Structural health monitoring	914
28.4	Weak adhesion detection using Lamb wave signals	924
28.5	Void detection using EMIS signals	930
28.6	Conclusion	942
	References	944
Part Five Emerging technologies for structural bonding		951
29	Sustainable adhesives: Bioadhesives, chemistries, recyclability, and reversibility	953
	<i>Yuanqiao Rao and Grace Wan</i>	
29.1	Introduction	953
29.2	Controlled adhesion in biological systems; multifunctional materials in nature	953

29.3	Sustainable materials for adhesives	958
29.4	Smart adhesives for recyclability: Reversible adhesion and adhesion on demand	967
29.5	Self-healing adhesives	974
29.6	Conclusions and outlook	978
	References	979
30	Accelerated curing of bonded joints	987
	<i>Morten Voß and Till Vallée</i>	
30.1	Introduction	987
30.2	Influence of accelerated curing on the adhesive	991
30.3	Accelerated curing of large-scale joints	996
30.4	Modeling accelerated curing processes	998
30.5	Conclusions	1003
	References	1005
31	Residual stress development in curing processes: Material characterization and modeling	1011
	<i>David Lindeman, Aaron Hedegaard, Chaodi Li, and Samuel Carpenter</i>	
31.1	Introduction	1011
31.2	Adhesive curing processes and material property evolution	1011
31.3	Experimental methods	1013
31.4	Modeling methods	1025
31.5	Additional notes	1030
	References	1031
32	Digital image correlation: Advancing mechanical property characterization of adhesive joints	1035
	<i>Christopher M. Jackson, Jeffrey A. McGuire, Martin E. Losada, Raffaella De Vita, and David A. Dillard</i>	
32.1	Introduction	1035
32.2	Digital image correlation background	1037
32.3	DIC applications in adhesive and bonded joint testing	1040
32.4	Augmenting traditional fracture analysis with DIC	1050
32.5	DIC utilization for traction-separation laws and finite element modeling	1059
32.6	Case study: Using DIC with FEA to develop a mixed-mode fracture envelope	1063
32.7	Conclusions	1068
	Acknowledgments	1069
	References	1069

33	Improving joint performance through graded materials and geometries	1077
	<i>E.A.S. Marques, R.J.C. Carbas, Alireza Akhavan-Safar, and Lucas F.M. da Silva</i>	
33.1	Introduction	1077
33.2	Mixed adhesive joints	1085
33.3	Functionally graded adhesives	1089
33.4	Functionally graded adherends	1093
33.5	Conclusions	1098
	References	1099
34	Architected adhesive joints with improved fracture toughness	1105
	<i>Thomas Pardoën, Kevin T. Turner, and Michal K. Budzik</i>	
34.1	Introduction	1105
34.2	Overview of working principles for extrinsic joint toughening	1106
34.3	Embodiments of toughening principles through architecture	1111
34.4	Summary and possible future trends	1120
	References	1121
35	Sensing stresses and damage in adhesive bonds using mechanophores	1123
	<i>Jared A. Gohl, Nazmul Haque, and Chelsea S. Davis</i>	
35.1	Introduction	1123
35.2	Introduction to mechanoresponsive materials	1124
35.3	Mechanochemistry for sensing stress in bulk adhesives	1125
35.4	Mechanochemistry for sensing interfacial damage	1131
35.5	Challenges to implementation	1133
35.6	Conclusions and future trends	1135
	References	1137
	Index	1141

This page intentionally left blank

Contributors

Alireza Akhavan-Safar Institute of Science and Innovation in Mechanical and Industrial Engineering (INEGI), Porto, Portugal

Ian Ashcroft University of Nottingham, Nottingham, United Kingdom

Cindy Ashforth Federal Aviation Administration, Des Moines, WA, United States

Erich Bain Engineering Systems, Inc., Dallas, TX, United States

Bamber Blackman Department of Mechanical Engineering, Imperial College London, South Kensington Campus, London, United Kingdom

Michael J. Bortner Macromolecules Innovation Institute; Department of Chemical Engineering, Virginia Tech, Blacksburg, VA, United States

Evan L. Breedlove 3M Company, Corporate Research Laboratory, Maplewood, MN, United States

Michal K. Budzik Department of Mechanical and Production Engineering, Aarhus University, Aarhus, Denmark

Markus Bulters Idésol BV, Sittard, The Netherlands

Barry Burns Henkel Ireland Operations and Research, Dublin, Ireland

R.J.C. Carbas Institute of Science and Innovation in Mechanical and Industrial Engineering (INEGI), Porto, Portugal

Declan Carolan FAC Technology, London, United Kingdom

Samuel Carpenter 3M Company, Saint Paul, MN, United States

Scott W. Case Via Department of Civil and Environmental Engineering; Macromolecules Innovation Institute, Virginia Tech, Blacksburg, VA, United States

Chao Chen 3M Company, Corporate Research Laboratory, Maplewood, MN, United States

Fabien Choffat Sika Technology AG, Zürich, Switzerland

David Condrón Henkel Ireland Operations and Research, Dublin, Ireland

Simon Cook Core Research and Development, The Dow Chemical Company, Midland, MI, United States

Antonio Corsaro Sika Technology AG, Zürich, Switzerland

Matthew Crimmins Core Research and Development, The Dow Chemical Company, Midland, MI, United States

Lucas F.M. da Silva Advanced Joining Processes Unit, Institute of Science and Innovation in Mechanical and Industrial Engineering (INEGI); Department of Mechanical Engineering, Faculty of Engineering (FEUP), University of Porto, Porto, Portugal

Arit Das Macromolecules Innovation Institute; Department of Chemical Engineering, Virginia Tech, Blacksburg, VA, United States

Chelsea S. Davis School of Materials Engineering, Purdue University, West Lafayette, IN, United States

Sara Lopez de Armentia Institute for Research in Technology, ICAI School of Engineering, Universidad Pontificia Comillas, Madrid, Spain

Silvio de Barros LINEACT CESI Engineering School, Paris, France

F. de Buyl Dow Chemical, Seneffe, Belgium

Sofia Teixeira de Freitas Aerospace Structures and Materials Department, Faculty of Aerospace Engineering, Delft University of Technology, Delft, Netherlands

Felix Debor Henkel Technologies Industrial & Infrastructure, Henkel AG & Co. KGaA, Düsseldorf, Germany

Juan Carlos del Real Institute for Research in Technology, ICAI School of Engineering, Universidad Pontificia Comillas, Madrid, Spain

Claudio Di Fratta Sika Services AG, Zürich, Switzerland

David A. Dillard Department of Biomedical Engineering and Mechanics; Macromolecules Innovation Institute, Virginia Tech, Blacksburg, VA, United States

Giles Dillingham Brighton Science, Cincinnati, OH, United States

Shaoguang Feng The Dow Chemical Company, Midland, MI, United States

Aaron M. Forster Materials Measurement Laboratory, National Institute of Standards and Technology, Gaithersburg, MD, United States

David Fortman Coatings Innovation Center, PPG Industries, Inc., Allison Park, PA, United States

A. Francisco G. Tenreiro Advanced Joining Processes Unit, Institute of Science and Innovation in Mechanical and Industrial Engineering (INEGI), Porto, Portugal

Jared A. Gohl School of Materials Engineering, Purdue University, West Lafayette, IN, United States

Hermann Handwerker Henkel Technologies Industrial & Infrastructure, Henkel AG & Co. KGaA, Düsseldorf, Germany

Nazmul Haque School of Materials Engineering, Purdue University, West Lafayette, IN, United States

B. Harkness Dow USA, Midland, MI, United States

V. Hayez Dow Chemical, Seneffe, Belgium

Sammy He FAC Technology, London, United Kingdom

Aaron Hedegaard 3M Company, Saint Paul, MN, United States

John Hill Ford Motor Co., Dearborn, MI, United States

Jian-ping (JP) Huang Parker Lord Corporation, Engineered Materials Group, Assembly & Protection Solutions Division, Cary, NC, United States

Larry Ilcewicz Federal Aviation Administration, Des Moines, WA, United States

Alojz Ivankovic University College Dublin, Dublin, Ireland

Christopher M. Jackson Civil and Environmental Engineering Department, Virginia Tech, Blacksburg, VA, United States

Robert Jensen U.S. Army Combat Capabilities Development Command, Army Research Laboratory, Aberdeen Proving Ground, MD, United States

Tom Kalantar Core Research and Development, The Dow Chemical Company, Midland, MI, United States

Frederick A. Kamke Oregon State University, Corvallis, OR, United States

Marvin Kaufmann Fraunhofer Institute for Manufacturing Technology and Advanced Materials IFAM, Adhesive Bonding Technology and Surfaces, Bremen, Germany

Steffen Kelch Sika Technology AG, Zürich, Switzerland

Vinayak Khatavkar DSM Materials Science Center; DSM Engineering Materials, Geleen, The Netherlands

J. Kimberlain Dow USA, Midland, MI, United States

John Lean Parker Lord Corporation, Engineered Materials Group, Assembly & Protection Solutions Division, Cary, NC, United States

Chaodi Li 3M Company, Corporate Research Laboratory, Maplewood, MN, United States

David Lindeman 3M Company, Saint Paul, MN, United States

António Mendes Lopes Advanced Joining Processes Unit, Institute of Science and Innovation in Mechanical and Industrial Engineering (INEGI); Department of Mechanical Engineering, Faculty of Engineering (FEUP), University of Porto, Porto, Portugal

Martin E. Losada Coatings Innovation Center, PPG Industries, Inc., Allison Park, PA, United States

Mario Madrid Henkel AG & Co. KGaA, Düsseldorf, Germany

E.A.S. Marques Department of Mechanical Engineering, Faculty of Engineering (FEUP), University of Porto, Porto, Portugal

Stephan Marzi University of Applied Sciences Mittelhessen, Institute of Mechanics and Materials, Gießen, Germany

Jeffrey A. McGuire Department of Biomedical Engineering and Mechanics, Virginia Tech, Blacksburg, VA, United States

Ahmad Rezaei Mojdehi Ford Motor Co., Dearborn, MI, United States

Guilherme Garcia Momm National Civil Aviation Agency, São José dos Campos, Brazil

Marcio Moreira Arouche Aerospace Structures and Materials Department, Faculty of Aerospace Engineering, Delft University of Technology, Delft, Netherlands

Neal Murphy University College Dublin, Dublin, Ireland

John A. Nairn Oregon State University, Corvallis, OR, United States

Edoardo Nicoli Core Research and Development, The Dow Chemical Company, Midland, MI, United States

Thomas Pardoën Institute of Mechanics, Materials and Civil Engineering Ecole Polytechnique de Louvain-Louvain School of Engineering, Université Catholique de Louvain, Ottignies-Louvain-la-Neuve, Belgium

John-Alan Pascoe Delft University of Technology, Delft, The Netherlands

Kshitish A. Patankar Core Research and Development, The Dow Chemical Company, Midland, MI, United States

Eva Paz Institute for Research in Technology, ICAI School of Engineering, Universidad Pontificia Comillas, Madrid, Spain

Marvin Pollum Coatings Innovation Center, PPG Industries, Inc., Allison Park, PA, United States

Dong Quan Shandong University, Jinan, China

Gabriel M.F. Ramalho Department of Mechanical Engineering, Faculty of Engineering (FEUP), University of Porto, Porto, Portugal

Yuanqiao Rao The Dow Chemical Company, Midland, MI, United States

Rose Roberts Brighton Science, Cincinnati, OH, United States

Gennaro Scarselli University of Salento, Lecce, Italy

Jay S. Schlechte 3M Company, Saint Paul, MN, United States

Michelle Elizabeth Seitz DSM Materials Science Center, Geleen, The Netherlands

Wolfgang Seitz Aurora Lichtwerke GmbH, Eichstätt, Germany

Waruna Seneviratne National Institute for Aviation Research, Wichita State University, Wichita, KS, United States

Colin Li Pi Shan The Dow Chemical Company, Midland, MI, United States

N. Shephard Dow USA, Midland, MI, United States

Fengzhen Sun Tongji University, Shanghai, China

Ambrose C. Taylor Imperial College London, London, United Kingdom

Ashley Trace The Boeing Company, Seattle, WA, United States

Luis Trimiño 3M Company, Corporate Research Laboratory, Maplewood, MN, United States

Brad Tuft Dow Performance Silicones, Product Development, The Dow Chemical Company, Midland, MI, United States

Kevin T. Turner Department of Mechanical Engineering and Applied Mechanics, University of Pennsylvania, Philadelphia, PA, United States

Jani Turunen Valmet Technologies, Inc., Espoo, Finland

Till Vallée Fraunhofer Institute for Manufacturing Technology and Advanced Materials IFAM, Adhesive Bonding Technology and Surfaces, Bremen, Germany

Raffaella De Vita Department of Biomedical Engineering and Mechanics, Virginia Tech, Blacksburg, VA, United States

Morten Voß Fraunhofer Institute for Manufacturing Technology and Advanced Materials IFAM, Adhesive Bonding Technology and Surfaces, Bremen, Germany

Grace Wan The Dow Chemical Company, Midland, MI, United States

Christopher C. White Exponent, Inc., Bowie, MD, United States

Preface

Technological advances in an expanding realm of applications increasingly rely on adhesive bonding, which has matured from being one joining method alternative to an enabling technology for many modern designs and products. Driven by the need for lighter, stronger, more cost-effective, and more robust system performance, adhesive technology has come of age in successfully meeting demands in many industrial sectors. This includes improvements in fields ranging from safety, health, and medical care to progress in engineering a more sustainable future — all enabling components, devices, and structures that would not be possible without these materials. Significant strides made by scientists, engineers, and designers who develop and make use of these products in their industries have grown the global annual market value of structural adhesives to more than \$20 billion. As an “*Advances in...*” book, the emphasis of this second edition focuses on recent developments in the field, while reminding readers along the way of the fundamentals of adhesion science that have served us well in our progress on this journey.

Adhesives are used in so many ways that we often take them for granted. They are usually hidden from view yet perform critical functions for many of the consumer goods, transportation vehicles, infrastructure, and electronic devices we encounter on a daily basis. The increased reliance on adhesive bonding for these demanding applications has come about through improved understanding of the chemistries, physics, and mechanics of surfaces, polymers, and bond configurations. Adhesive developers, suppliers, and users have often recognized the underlying liabilities of inadequate bond performance for the industry as a whole. This is a risk factor that has motivated significant multidisciplinary advances to improve products, processes, designs, and monitoring. After all, success stories do not make news but consequential failures do.

An individual bond failure might represent an inconvenient nuisance, a product malfunction, or a serious risk to life, limb, and property. Some might associate this latter category with *structural adhesive bonding*, which takes on different connotations in different contexts, and indeed the consequences of failure could be a factor in defining *structural adhesive bonding*. The aircraft industry has for decades used failure consequences to distinguish assemblage bonding as flight-critical primary bonding from secondary bonding, where failures would be much less likely to result in devastating outcomes. A more general definition of structural adhesive bonding, however, simply focuses on the bond’s load-bearing capabilities. In some circles, structural adhesives are defined by their quantitative load-bearing capabilities. Although I am reluctant to state specific values lest this implies endorsement, a quick web search reveals definitions of minimum single-lap shear joint strengths ranging from 1 to 18 MPa (145 to 2600 psi) as examples of criteria that have been suggested

and used by their respective advocates. Some definitions might also include a durability aspect, meaning the joint's ability to maintain structural integrity for the life of the product under anticipated mechanical, thermal, and environmental challenges. We should not forget that product quality, loading scenarios, and ultimately the joint's performance are all statistical quantities, so the likelihood of failures might be considered in some applications due in part to imperfectly made bonds, uncertainties of loading, or the possibility of particularly deleterious exposure conditions.

While definitions such as these may be useful in the context of the industry in which they are employed, they may not fully capture the growing opportunities and applications open to adhesive bonding. In this book, we take a broad view of structural adhesives and bonding by including many of the key chemical families that all would consider structural adhesives as well as some materials that might not meet specific—though rather arbitrary—metrics such as mentioned above. For all these products, the consequences of failure will often depend on the application, ranging from inconvenience remedied by inexpensive repairs to the potential for significant and consequential failures. Herein, we consider structural adhesive bonding to include those adhesive systems, along with their assessment and design methods, that function by transmitting forces from one adherend to another.

However, in the rapidly expanding field of adhesive joining, we cannot be comprehensive in a book of this length. Instead, the book represents a further installment in the Woodhead Publishing Series in Welding and Other Joining Technologies, which includes first and second editions of *Structural Adhesive Bonding*, edited by Prof. Robert Adams, and the first edition of our *Advances in Structural Adhesive Bonding*. Readers of this second edition of the latter will find a very different book than the first version, including a number of new authors, chapter topics, and themes. As the book includes contributions from many leading groups around the world, we feel it makes a significant contribution to the literature in the field of adhesion science, and hope readers will find a number of new insights and perspectives.

Although there are numerous instances of natural and, more recently, synthetic adhesives being used for a range of applications throughout recorded history, most of these involved rather modest load-bearing requirements and capabilities, at least compared to modern adhesive bonding. Significant advances for structural adhesive bonding can perhaps be traced to nearly 90 years ago. Phenol-formaldehyde resins and the redux process, the first successful adhesive for metal-to-metal bonding, began with a £1000 consultancy provided to Norman de Bruyne (1904–97) in 1936 by de Havilland, as described in a fascinating history by John Bishopp [1]. On the engineering front, Olaf Volkersen (1907–2007) wanted to model stresses in long riveted joints, but chose to smear the discrete row of rivets into an elastic continuum. This effectively defined an adhesive layer, though not explicitly stated, leading to the well-known shear lag model published in 1938.

Having started my own career in the structural adhesive bonding field in the days of the Primary Adhesively Bonded Structure Technology (PABST) program funded by the US Air Force, I found it interesting to reflect on the progress that has been made and the remaining needs in our field. One outcome of this extensive, multiyear

research effort conducted by the McDonnell Douglas Corporation was that company's 1979 report titled *Design Handbook for Adhesive Bonding*. Noting that aircraft bonding was mostly limited to secondary structures at the time, this program sought to understand the roles of surface preparation, adhesives, processing, bond designs, loading situations, and environmental exposures, as well as how joint performance, durability, and reliability could be improved [2–5]. Their introduction contained the schematic (shown in Fig. 1) of what was advocated as the interdisciplinary process required for the “proper design of (a) bonded structure.” Seeing this reminds us of the complexity of choosing to use adhesives for primary structural bonding applications—a challenge we have partially met in the nearly 45 years that have elapsed since this seminal study in our field. Indeed, the various components required for the successful design and implementation of structural bonding still ring true with us as we look at the significant inroads structural adhesive bonding has made in joining applications in transportation vehicles, infrastructure, and the industrial and consumer

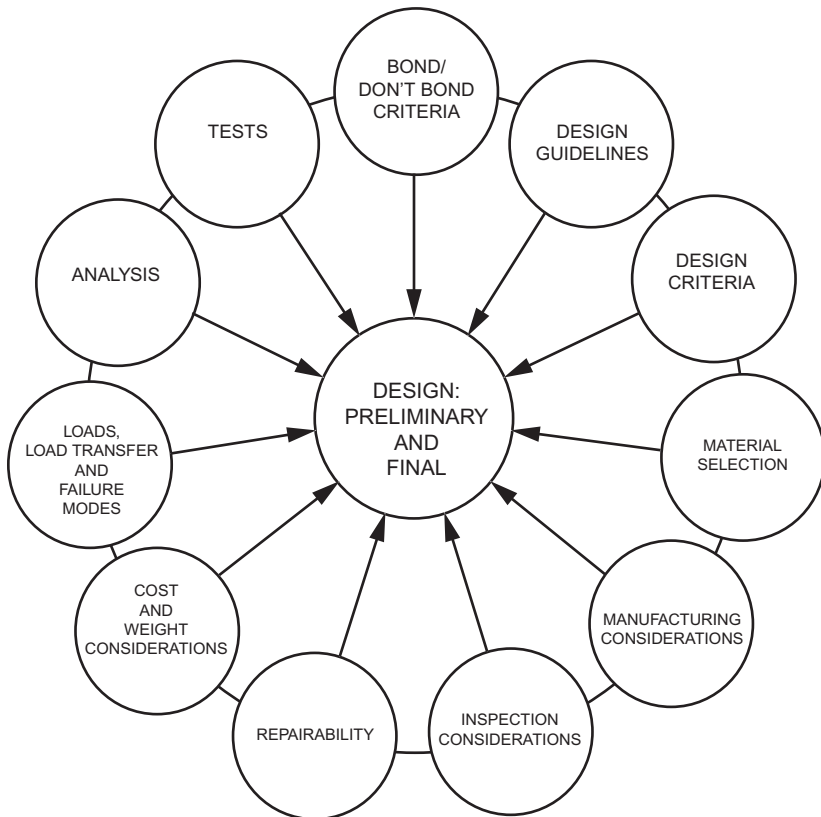


Fig. 1 The interdisciplinary design process recommended by the PABST Design Handbook for Adhesive Bonding [6].

products we regularly encounter. Issues of material selection, surface preparation, testing and analysis, robustness and durability, cost and weight, repairability, and manufacturing continue to dominate our decisions for using structural adhesives in products we design, build, and use. Clearly, there remain enduring challenges in the field that will continue to inspire insights, innovations, and improvements in the years ahead as we seek to make adhesive joining safe, effective, durable, reliable, and sustainable.

The book is divided into five parts. The first part is focused on major structural adhesive chemistry families. These include traditional polymers that have excelled in their ability to not only form strong bonds with a variety of substrates, but also provide the desired strength, flexibility, and energy absorption capabilities that vary from one application to another. In addition to describing the chemical components and reactions involved in making and using these materials, recent progress in improving these chemical families, sourcing relevant raw materials, and reducing health, safety, and environmental consequences are also provided. Chapters include epoxies, acrylics, polyurethanes, cyanoacrylates, anaerobics, and structural silicones as well as a chapter on emerging systems that are meeting the evolving needs for strength, information capabilities, and overall toughness. Part One closes with a chapter on toughening strategies used to improve the mechanical performance of adhesives.

Part Two of the book is focused on surfaces and the challenges faced in robust bonding to several substrate classes. This section opens with a troubleshooting chapter addressing surface bonding problems that are encountered. Other chapters address the challenges of bonding to plastic substrates, forming structural bonds in thermoplastic overmolding processes without the use of separate adhesives, and bonding thermoplastic composite materials with structural adhesives. Wrapping up this section is a chapter on structural bonding involved in producing sustainable wood products.

The focus of Part Three is on evolving joint considerations, modeling approaches, and testing methods—topics directly related to characterizing and improving performance, durability, and reliability. This section starts off with the role of standards in characterizing and communicating adhesive behavior as well as their need to evolve as improved adhesives and application demands arise. This is followed by a chapter on modeling options, conveying various failure criteria and analysis methods. Chapters follow that involve a review of fracture mechanics testing methods and innovations, our evolving understanding of fracture mode mixity and its effect on bond performance, and bond thickness effects. These are followed by chapters related to the time scales of loading, including discussions of fatigue behavior, characterization, and modeling; accelerated characterization and durability of adhesive bonds; and high-speed and impact testing. This section closes with a chapter on recent developments in high-throughput methodologies and artificial intelligence for adhesive characterization and development.

A particularly interesting addition to this second edition is provided in Part Four, which addresses the adhesive specification, quality control, and risk mitigation

strategies one must take in deciding to use adhesives in respective industrial sectors. Chapters are provided for the aerospace, automotive, and construction industries as well as for industrial products and biomedical adhesive applications. Clearly, a given industry's decision to incorporate adhesive bonding in its devices and structures requires careful consideration of the adhesive properties, design and processing considerations, risk mitigation, and adhesive specification and quality control. Hopefully, these chapters will promote continued discussion as we learn from the various sectors about effective adhesive implementation.

Our final section, Part Five, includes a number of new topics dealing with several emerging technologies for structural bonding. Some of these are already becoming useful tools in adhesive processing, characterization, and design, and others represent intriguing technologies that, with further development, may lead to new products, new applications, and new technologies for monitoring structural integrity. This section begins with a chapter on nondestructive and machine learning for process control and structural integrity, followed by a chapter on developing greener adhesives for sustainability, recyclability, reversibility, and repairability. A chapter on accelerated curing of bonded connections offers insights into improved methods for manufacturing. Innovations in characterizing modeling cure evolution and residual stress development are presented, followed by a chapter exploring inroads digital image correlation has been making in adhesive characterization and joint design. The final three chapters address functionally graded bonding offering opportunities to improve joint performance metrics through the use of multiple or graded adhesive products, novel architected interfaces that suggest promising directions for improving joint behavior, and the use of mechanically responsive materials for sensing stresses and damage in adhesive bonds.

I am very excited by the chapters we have brought together in this edition, and anticipate they will foster continued discussions, hopefully across many disciplines and industrial sectors, on evolving chemistries; addressing environmental and sustainability issues; improving characterization, design, robustness, and durability; and ensuring structural integrity. As the editor of this book, I would like to acknowledge the extraordinary efforts of the authors and coauthors in collaborating on this work. It has been truly delightful to interact with these respected individuals, whose contributions make this book possible. I extend sincere thanks to them for the efforts they made in organizing their writing teams, collecting information and assembling it into condensed summaries of the important topics they address, citing numerous published works where readers can find additional information, and working through the editing and proofreading processes to finalize the book. In addition, I would like to extend a special thanks to Elaine M. Yorkgitis (3M Division Scientist, retired) for many helpful discussions that led up to this volume, including topics, specific content, potential authors, and encouragement as this book has proceeded from concept to a published volume.

David A. Dillard

References

- [1] J.A. Bishopp, The history of Redux[®] and the Redux bonding process, *Int. J. Adhes. Adhes.* 4 (1997) 287–301.
- [2] L. Hart-Smith, *Adhesive Layer Thickness and Porosity Criteria for Bonded Joints*, McDonnell Douglas Corp Long Beach CA Douglas Aircraft Div, 1982.
- [3] R. Crane, G. Dillingham, B. Oakley, Progress in the reliability of bonded composite structures, *Appl. Compos. Mater.* 24 (2017) 221–233.
- [4] E.W. Thrall Jr., Primary adhesively bonded structure technology (PABST), *J. Aircr.* 14 (1977) 588–594.
- [5] L.J. Hart-Smith, *Handbook of Adhesion Technology*, Springer, 2020.
- [6] D. Potter, *Primary Adhesively Bonded Structure Technology (PABST). Design Handbook for Adhesive Bonding*, Douglas Aircraft co, Long Beach, CA, 1979.

Part One

Adhesive chemistries and formulations

This page intentionally left blank

Advances in epoxy adhesives



Jay S. Schlechte

3M Company, Saint Paul, MN, United States

1.1 Introduction and history of epoxy adhesives

The new Olympic motto fits well as a descriptor of adhesive bonding and epoxies, as “Citius, Altius, Fortius—Communiter” translates to “Faster, Higher, Stronger—Together,” where the boundaries of adhesive performance are being pushed for faster on-demand curing, higher toughness, and stronger, more durable bonding of substrates. The diversity of epoxy resins, curatives, and curing methods as shown in Fig. 1.1 gives them their nature as a jack of all trades and a master of several for metal and composite bonding.

The rich history of epoxy chemistry starts in 1909 with the discovery and methodology to make the epoxide ring by Prileschajew through reacting peroxybenzoic acid with olefins [1]. Then, Schlack reported the reaction of amines with multifunctional epoxides for the preparation of high molecular weight amines [2]. A few years later, Castan filed a patent exemplifying the preparation of bisphenol A diglycidyl ether (BADGE) from bisphenol A (BPA) and epichlorohydrin (ECH) for thermosetting resins with anhydrides used in cast and molded products, and solvent-based varnishes. The compositions were noted to have good adhesion to glass, porcelain, and metals [3]. Greenlee’s first patent demonstrates how to make higher molecular weight epoxy resins using the same reactants. These were esterified with unsaturated fatty acids [4] for drying compounds used in varnishes. Greenlee built on Schlack’s work with polyethylene amine reactions with the higher molecular weight epoxy resins. The resulting epoxy-amine reacted materials were for solvent-based coatings, but he and others quickly recognized the potential of epoxy resins in adhesives [5–7]. By the late 1940s, continuous processes were developed [8] and several grades of epoxy resins had been commercialized by Ciba and Shell under the Araldite and Epon trade names in a licensing agreement with Devoe Reynolds [9].

1.2 Major uses and important minor uses

The excellent adhesion, low shrinkage, and chemical resistance properties of cured epoxy resins have led to significant uses in paints and protective coatings as well as a wide variety of composites and adhesives. Epoxy adhesives are used in transportation, electronics, recreational equipment, and building and commercial applications from small wearable electronic devices to wind blade bonding. Market size estimates for epoxy resins range into several billion dollars, with growth over the last decade

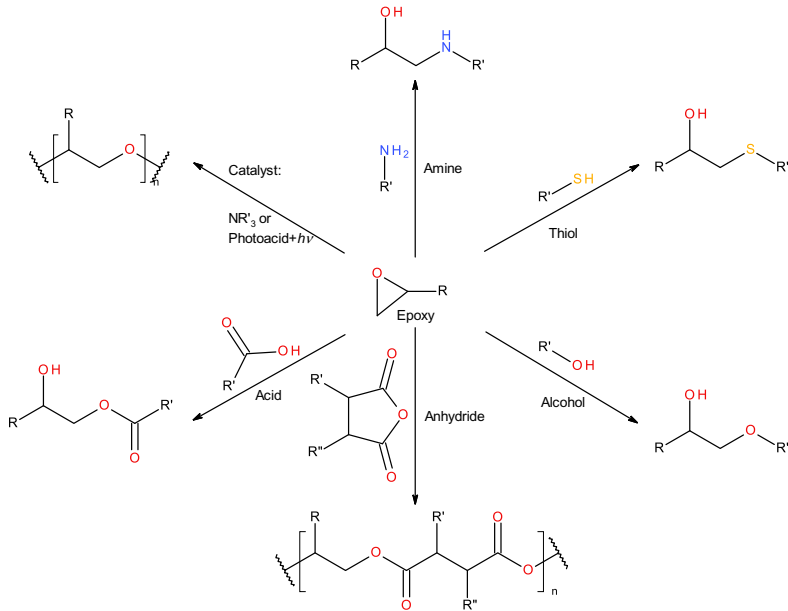


Fig. 1.1 Epoxy reactions.

being 5%–7% annually while similar growth rates are expected well into the 2020s. Bio-based materials used in epoxies comprise a small portion at about 1% of the overall epoxy market. However, they have about double the expected growth rates of the overall market at 12% annually. The transportation and automotive applications constitute a large share of the adhesives market due to light-weighting and changes in manufacturing processes.

1.3 Epoxy resins and epoxy functional raw materials, processes, and suppliers

1.3.1 Bisphenol glycidyl ether resins

The bisphenol A-based epoxy resins continue to be manufactured based on the processes described by Castan and Greenlee in reacting bisphenol A and epichlorohydrin with a basic catalyst in Fig. 1.2. A wide range of viscosities are available for these liquid epoxy resins with only slightly different epoxy equivalent weights (EEW) where the number of repeat units is less than 0.5 and often about 0.15 for the standard resins. Higher molecular weight solid epoxy resins are produced with either a lower ratio of epichlorohydrin to BPA (taffy process) or by extending the polymer through the reaction of low molecular weight epoxy resins with BPA (fusion process) [10]. The upstream chemistry of bisphenol A is the reaction of acetone with phenol while

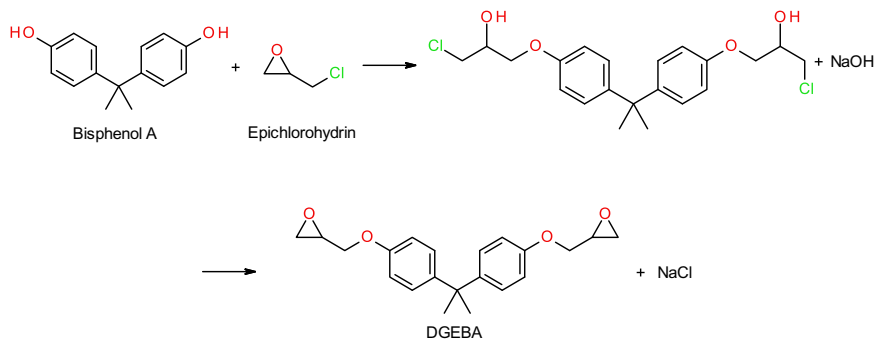


Fig. 1.2 Standard bisphenol A diglycidyl ether resin from ECH and BPA reaction steps.

epichlorohydrin is prepared by chlorinating propylene to allyl chloride, which is then chlorohydrated with hypochlorous acid followed by dehydrohalogenation under basic conditions in the same manner as epoxy resin production. Epichlorohydrin is also produced from glycerol driven by economics or bio-based carbon content goals. Other phenols can also be used such as bisphenol F or halogenated bisphenols, which give different properties to the resins. The residual chlorine present in standard epoxy resins compromises color, reactivity, and physical and electrical properties. Processes were developed starting in 1968 with incremental progress over the decades to reduce and remove chlorine for low halogen content resins, which are used extensively in the electronics industry to minimize corrosion and improve electrical properties [11–18].

1.3.2 Epoxy novolac resins

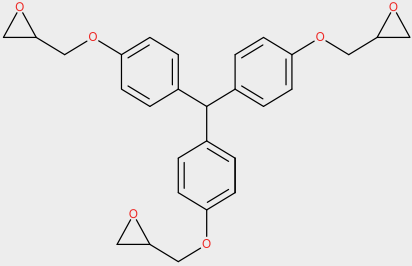
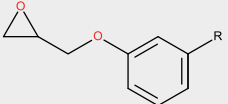
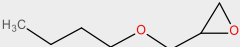
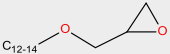
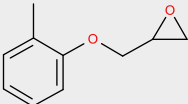

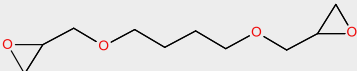
Cresol and phenol novolac resins prepared from phenol formaldehyde condensation can be epoxidized with ECH, resulting in resins with a wide range of molecular weight and functionality [19]. Additional novolac resins include dicyclopentadiene incorporated into the backbone with phenol or *o*-cresol, available as Tactix 556 and Epiclon HP-7200L. The improved thermal stability and higher glass transition temperature (T_g) of the novolac resins make them useful in adhesives in high-temperature applications. The dicyclopentadiene novolac is well suited for electrical applications due to low water absorption. The higher functionality may lead to decreased toughness depending on the curative used.

1.3.3 Glycidyl ether resins and diluents

Following bisphenol-based resins, other glycidyl ether epoxies made from alcohols and ECH include hydrogenated versions of bisphenol A (Epalloy 5000, Eponex 1510, DENACOL EX-252), which are lower in viscosity than their aromatic counterparts but maintain good mechanical properties. Tables 1.1, 1.3 and 1.4 show several glycidyl ethers of mono, di, tri, and tetrafunctional alcohols such as butanol and longer alkane alcohols; butane diol; neopentyl glycol; cyclohexanedimethanol; trimethylolpropane; various phenols including cashew nut shell liquid; cresol;

Table 1.1 Common glycidyl epoxy resins and diluents.

Chemical name	Structure	EEW (g/eq)	Viscosity ^a (mPa·s)	Tradenames
Bisphenol A diglycidyl ether (BADGE, DGEBA)		182–195 170–196 500–560	10,000–15,000 4000–6000 Solid, low melting point	Epon 828, DER 331, Araldite GY6010 Epon 825, DER 332 Epon 1001F, DER 661, Epotuf 37-001
Bisphenol F diglycidyl ether		156–172	2000–7000	Araldite GY 281, Araldite GY 285, DER 354
Epoxy phenol and cresol novolac (EPN, ECN)		172–179 176–181 171–185 217–233	Solid Solid Solid Solid	DEN 431, DEN 438, EPN 9880, ECN 1273
Hydrogenated bisphenol A resin		205–230	1300–2500	Epalloy 5000, Eponex 1510, Denacol EX-252

1,1,1-Tris(4-hydroxyphenyl) methane		150–170	Solid	Tactix 742, Epotec YDM-460
Cashew nut oil glycidyl ether	 R = C ₁₅ H ₃₁ , C ₁₅ H ₂₉ , C ₁₅ H ₂₇ , or C ₁₅ H ₂₅	425–575	40–70	Cardolite NC-513
<i>n</i> -Butyl glycidyl ether		145–155	1–2	Heloxy 61, Epotec RD-106
Aliphatic C12–14 glycidyl ether		280–315	6–15	Heloxy 8, Araldite DY-E, Epotec RD 108
<i>o</i> -Cresol glycidyl ether		167–195	5–25	Heloxy 62, Araldite DY-K, Denacol EX-141
Neopentylglycol diglycidyl ether		125–145	10–25	Heloxy 68, Araldite DY-N, Denacol EX-211
Butanediol diglycidyl ether		117–137	10–25	Heloxy 67, Araldite DY-D, Denacol EX-214L

^a Viscosity reported at 25°C unless otherwise noted.

1,1,1-tris(4-hydroxyphenyl)methane (Tactix 742); and 1,1,2,2-tetrakis(*p*-hydroxyphenyl)ethane (Epon 1031) [20]. The glycidyl etherification of the alcohols leads to reactive diluents, flexible resins and even high performance solid resins. These may supplement a formulation or even be the major resin to provide the desired properties.

1.3.4 Glycidyl amine resins

The aromatic amine epoxy resins are made by reacting epichlorohydrin with the amine and phenol. Examples of this are glycidyl ethers of *m*- or *p*-aminophenol (Araldite MY500, MY600) [21], which gives a trifunctional resin, and methylene dianiline [22] (Araldite MY720), which gives a tetrafunctional resin. Both reactions are done with an excess of epichlorohydrin to minimize unwanted polymerization. The higher crosslink density with aromatic backbones gives cured materials with high T_g s. However, due to the presence of tertiary amine in these resins, their shelf life is significantly less than other resins (Table 1.2).

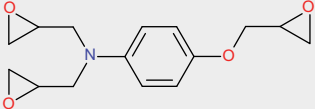
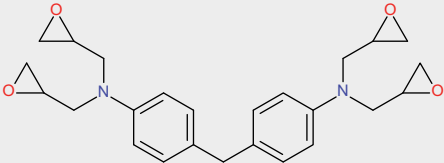
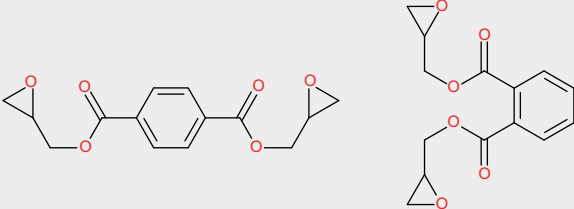
1.3.5 Glycidyl ester resins

While significant work was done on glycidyl epoxy esters in the 1940s and 1950s, the materials suffered from cost and ease of preparation versus the phenolic glycidyl ether resins due to hydrolysis of the ester, byproducts during production, and overall poorer stability. Production of the glycidyl esters can be done through transesterification, epoxidation of allyl esters with peracids, reaction of epichlorohydrin with carboxylic acids, or acid chloride condensation with glycidol [23–29]. Transesterification of aromatic methyl esters with glycidol using alkali salts of pseudohalogen hydrides such as sodium azide enabled production at mild temperatures [28]. Aromatic glycidyl esters include terephthalate-based Denacol EX-711. Low viscosity glycidyl ester resins include ones based on hexahydrophthalic and tetrahydrophthalic, sometimes also referred to as cycloaliphatic epoxies, which have good outdoor exposure characteristics. Carboxylic acid-based resins include neodecanoic acid (Cardura 10) and epoxidized dimerized fatty acid with bisphenol A (Epon 872). Glycidyl ester resins can be readily cured with anhydrides and a catalyst.

1.3.6 Cycloaliphatic epoxy resins

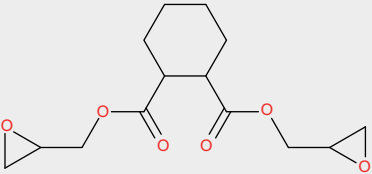
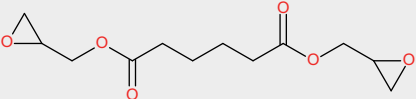
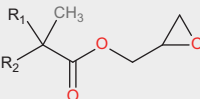
More often, cycloaliphatic epoxy resins shown in Table 1.3 refer to nonglycidyl epoxy functionality such as the epoxies produced from oxidation of cyclic alkenes via peroxyacid described in 1953 [30]. One example is the oxidation of 3'-cyclohexenylmethyl 3-cyclohexencarboxylate to 3,4-epoxycyclohexylmethyl 3,4-epoxycyclohexanecarboxylate, which is commercially available. Cycloaliphatic epoxies can be used in radiation or thermal curing systems. Resins produced by the peracid method are chlorine free and low viscosity. The cyclic aliphatic backbone adds stiffness and gives good thermal strength. Bis(3,4-epoxycyclohexylmethyl) adipate is another standard cycloaliphatic epoxide resin with more flexibility due to the adipate backbone. Several other mono- and di-functional resins are

Table 1.2 Glycidyl amine and glycidyl ester epoxy resins.

Chemical name	Structure	EEW (g/eq)	Viscosity ^a (mPa · s)	Tradenames
Triglycidyl- <i>p</i> -aminophenol		105–115	2000–5000	Araldite MY 0500
		95–107	550–850	Araldite MY 0510 Epotec YDM 451
<i>N,N,N',N'</i> -Tetraglycidyl-4,4'-diaminophenylmethane		117–134	7000–19,000	Araldite MY 720, Epotec YDM 441
		111–117	3000–6000	Araldite MY 721
Diglycidyl phthalate		147	Solid	Denacol EX-711 (terephthalate—DGT)
		154	980	Denacol EX-721 (<i>o</i> -phthalate)

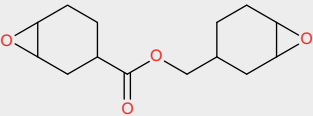
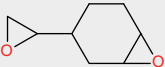
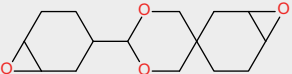
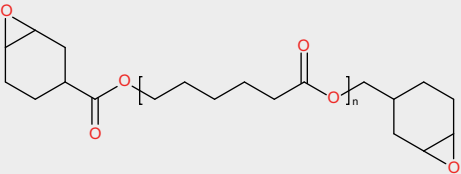
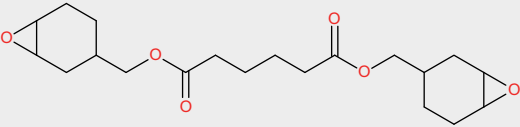
Continued

Table 1.2 Continued

Chemical name	Structure	EEW (g/eq)	Viscosity (mPa·s)	Tradenames
Diglycidyl hexahydrophthalate		164–177	450–900	Denacol FCA-640, Epotec YDH-184
Diglycidyl adipate		153–181	50–150	
Glycidyl ester of C10 branched alkyl acid		235–244	7	Cardura E10P, ShiGENA

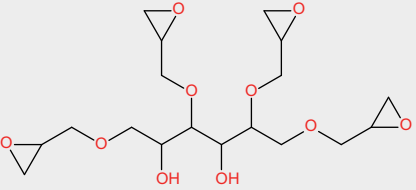
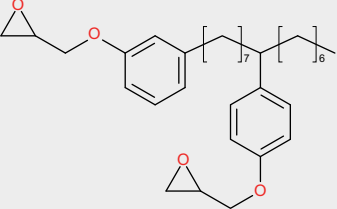
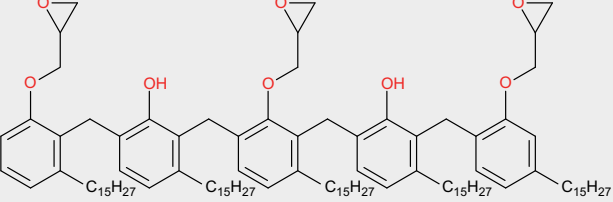
^aViscosity reported at 25°C unless otherwise noted.

Table 1.3 Cycloaliphatic and additional bio-based epoxy resins.

Chemical name	Structure	EEW (g/eq)	Viscosity ^a (mPa·s)	Tradenames
3,4-Epoxy cyclohexylmethyl 3,4-epoxycyclohexanecarboxylate (CAE)		128–133	220–270	Celloxide 2021P, ERL-4221, GPE-221, UviCure S105
Vinyl cyclohexene dioxide		70–80	15–30	TTA22, ERL4206
2-(3,4-Epoxy cyclohexyl)-5,5'-spiro-(3,4-epoxy)cyclohexane- <i>m</i> -dioxane		133–154	7000–17,000 @ 38°C	Araldite CY 175, ERL-4234
3,4-Epoxy cyclohexylmethyl 3',4'-epoxycyclohexanecarboxylate modified capralactone		200	96	Celloxide 2081
Bis[(3,4-epoxycyclohexyl)methyl] adipate		190–210	400–750	TTA26, UVR6128, GPE-228, UviCure S128

Continued

Table 1.3 Continued

Chemical name	Structure	EEW (g/eq)	Viscosity (mPa·s)	Tradenames
Sorbitol glycidyl ether		160–195	8000–18,000	Erysis GE 60, Denacol EX-622
Diglycidyl cardanol ether		350–500	10,000–35,000	Cardolite NC-514
Cardanol novolac epoxy		550–850	20,000–50,000	Cardolite NC-547

^a Viscosity reported at 25°C unless otherwise noted.

commercially available and find applications in exterior and electronics markets due to the aliphatic nature and minimal chlorine content from the peroxyacid epoxidation method.

Epoxidized vegetable oils (Vikoflex 7190, ChemFlexx ESO, Epoxol 9–5) are also produced by the peroxyacid route to convert the alkenes along the fatty acid chain to the epoxide. While these have been used more as plasticizers in PVC, they are also used as reactive diluents in epoxy formulations. A cyclic siloxane functionalized with cycloaliphatic epoxies is available from Shin-Etsu (KR-470).

1.3.7 Bio-based epoxy resins

The most prevalent bio-based epoxy raw materials used in adhesives are probably those based on cashew nutshell liquid (CNSL) (Table 1.3). The monofunctional epoxy was developed in 1954 by 3M as NC-513, but is now also available from other suppliers. A diglycidyl version, NC-514, imparts flexibility with less mechanical property loss. Higher functionality is obtained through novolac resins derived from cardanol (NC-547). Sorbitol polyglycidyl ether is a multifunctional resin available as Erysis GE-60 and Denacol EX-622, and it has good weathering resistance as it is fully aliphatic.

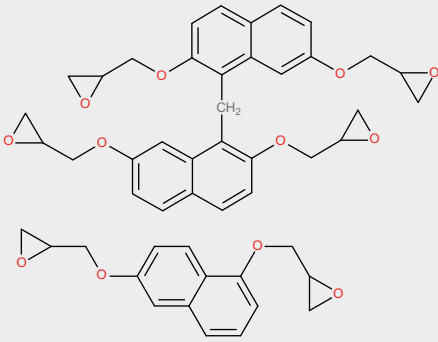
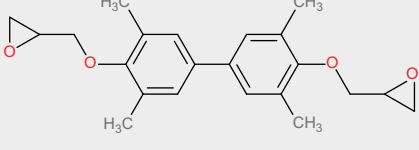
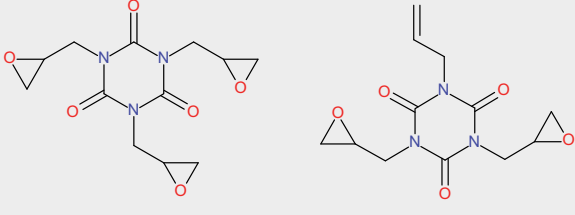
1.3.8 Specialty epoxy resins

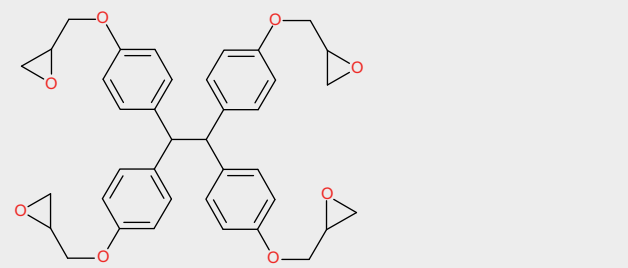
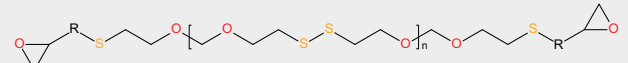
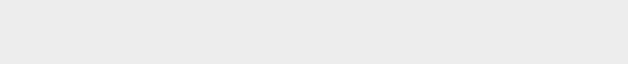
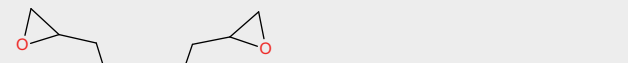
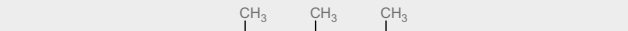
Additional commercially available specialty resins are shown in Table 1.4. Resins with rigid backbone structures include glycidyl resins based on tetramethyl biphenol (YX-4000) [31] and dihydroxynaphthalene (Araldite MY 0816) (DIC HP 4000 series), which are used in high-performance applications. Nonaromatic tri- and diglycidyl isocyanurate (Huntsman PT 810, Shikoku MA-DGIC) and hydantoin resins have excellent outdoor weathering properties. Highly flexible backbones include glycidyl functionalized polybutadienes, nitrile rubbers, urethanes, silicones, polyalkylene oxides, and polysulfides from several companies. Silicone resins available from Genesee Polymers have terminal epoxy groups (GP-682) or have pendant epoxy groups along the backbone that are glycidyl (GP-607) or cycloaliphatic (GP-712). Resins such as Struktol Polyphlox, Exolit EP 360, and Adeka's EP-49-10P incorporate phosphorus and are used to improve adhesion and fire retardancy similar to halogenated epoxy resins. A polyhedral oligomeric silsesquioxane (POSS) with epoxy functionality from Hybrid Plastics (EP0409) has been used as an additive to improve properties of underfill adhesives for printed circuit boards with improved modulus above the adhesive's T_g [32].

1.4 Curatives for epoxy resins and epoxy functional raw materials, processes, and suppliers

Epoxies can be cured under a wide range of environmental conditions with the right choice of curative for ambient, heat, or light cure. Primary and secondary amines provide the largest selection of curatives including linear and branched aliphatic,

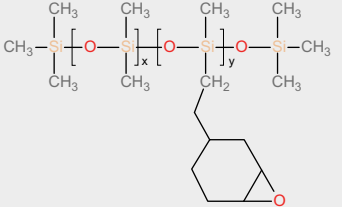
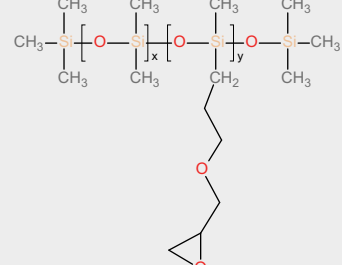
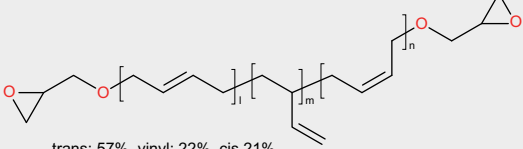
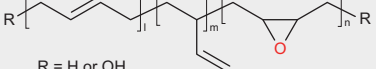
Table 1.4 Specialty epoxy resins.

Chemical name	Structure	EEW (g/eq)	Viscosity ^a (mPa·s)	Tradenames
Hydroxynaphthalene glycidyl ethers		144–151 143 204	1500–2500 @ 50°C Solid	Araldite MY 0816, DIC HP 4032 DIC HP 4770
3,3',5,5'-Tetramethyl-4,4'-diglycidylxybiphenyl		185	Solid	jER YX4000
Triglycidyl isocyanurate, Monoallyl diglycidyl isocyanurate		100–108 ~150	Solid Solid	Huntsman PT 810 Shikoku MA-DGIC

1,1,2,2-Tetrakis(<i>p</i> -hydroxyphenyl)ethane		180–220 195–230	Solid Solid	jER 1031 Epon 1031
Polysulfide glycidyl ether R = CH ₂ or BADGE		400–800	2000–4000	Aliphatic type (Thioplast EPS 25, EPS 35)
Tetraglycidyl Glycoluril		280–350	5000–10,000	Aromatic type (Thioplast EPS 70, EPS 80)
Silicone epoxy terminated resins		92	Liquid	Shikoku TG-G
Silicone epoxy terminated resins		1100 3100	38 140	GP-682 GP-504

Continued

Table 1.4 Continued

Chemical name	Structure	EEW (g/eq)	Viscosity (mPa·s)	Tradenames
Silicone epoxy pendant resins	 <p>The structure shows a linear silicone chain with four methyl groups on each silicon atom. The chain is represented as $\text{CH}_3\text{-Si}(\text{CH}_3)_2\text{-O-Si}(\text{CH}_3)_2\text{-O-Si}(\text{CH}_3)_2\text{-O-Si}(\text{CH}_3)_2\text{-CH}_3$. The third silicon atom from the left is substituted with a $\text{-CH}_2\text{-}$ group, which is further connected to a cyclohexane ring. One of the carbons in the cyclohexane ring is part of an epoxide group.</p>	4575	1000	GP-712
	 <p>The structure is similar to the first one, but the $\text{-CH}_2\text{-}$ group on the third silicon atom is part of a polyether chain: $\text{-CH}_2\text{-CH}_2\text{-O-CH}_2\text{-CH}_2\text{-O-CH}_2\text{-CH}_2\text{-O-}$, which is terminated by an epoxide group.</p>	210	450	GP-607
Polybutadiene epoxy terminated resin	 <p>The structure shows a polybutadiene chain with three different units: $\text{-[CH}_2\text{-CH=CH-CH}_2\text{]-}_n\text{-[CH}_2\text{-CH=CH-CH}_2\text{]-}_m\text{-[CH}_2\text{-CH=CH-CH}_2\text{]-}_n\text{-}$. The first and third units are trans-1,4 polybutadiene, and the middle unit is vinyl-terminated. The chain is terminated with an epoxide group. Below the structure, it is noted: trans: 57%, vinyl: 22%, cis 21%.</p>	1400	10,000 @ 20°C	Polyvest EP ET
Epoxidized polybutadiene resin	 <p>The structure shows a polybutadiene chain with units $\text{-[CH}_2\text{-CH=CH-CH}_2\text{]-}_m\text{-[CH}_2\text{-CH=CH-CH}_2\text{]-}_n\text{-}$. The chain is terminated with an epoxide group. Below the structure, it is noted: R = H or OH.</p>	193	29,000 @ 45°C	Epolead PB3600

^a Viscosity reported at 25°C unless otherwise noted.

cycloaliphatic, polyether, aromatic, amidoamines, and polyamides. Thiol curatives, while slow to cure on their own with epoxy resins, can be extremely fast curing with the addition of a tertiary amine. Less commonly used in adhesive applications are carboxylic anhydrides, which give high-temperature performance and slightly better electrical properties than aromatic amines. Tertiary amines, boron trifluoride complexes, and cationic photo initiators are all capable of promoting homopolymerization of epoxy resins.

1.4.1 Aliphatic amines

While amines are extensively used in curing epoxy resins, low molecular weight primary aliphatic ethylene amines such as diethylenetriamine (DETA), triethylenetetramine (TETA), tetraethylenepentamine (TEPA), and aminoethylpiperazine (AEP) are among the most common aliphatic amines used and are readily produced by a reaction of ethylene dichloride with excess ammonia, followed by hydrolysis of the salt with sodium hydroxide (Table 1.5). This results in a complex mixture of ethylene amines where a high ammonia ratio to chloride will result in ethylene diamine being the major product. Alternatively, ethylene amines can be produced through the reductive amination of monoethanolamine with ammonia over a heterogeneous catalyst [33]. Improvements in processes and raw material choices have been developed to produce DETA with higher selectivity with few nonusable byproducts [34–36].

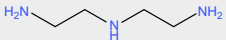
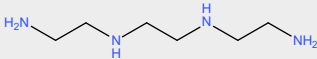
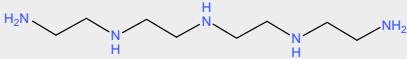
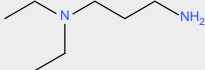
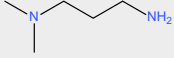
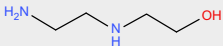
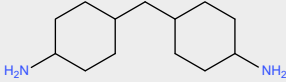
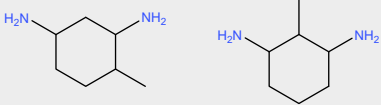
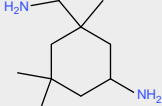
Substituted aliphatic amines diethylaminopropylamine and dimethylamino-propylamine can also be prepared from dimethyl or diethyl substituted amines reacting with acrylonitrile followed by the hydrogenation of nitriles to primary amines [37,38]. Alkanolamines are typically manufactured from the corresponding olefin oxide with a large excess of ammonia to obtain the monoamine [39].

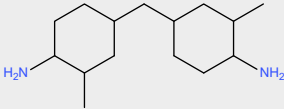
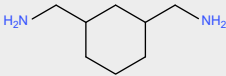
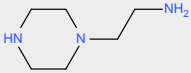
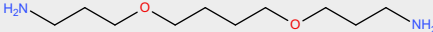
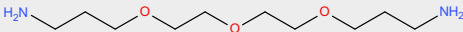
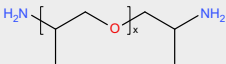
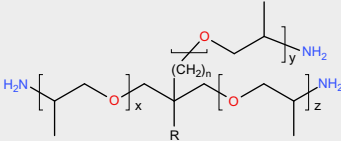
Challenges in using low molecular weight ethylene amines include safety concerns, short pot life, sensitivity to ratio due to the low amine hydrogen equivalent weight (AHEW) relative to the epoxy resins, carbamate formation with carbon dioxide and water, blooming or blushing to the surface due to incompatibility with the resin, and relatively brittle cured materials. These disadvantages have led to curatives based on modified amines such as alkanol amines or adduction of the amines with epoxies.

1.4.2 Cycloaliphatic amines

The ring structure of cycloaliphatic amines gives higher temperature resistance and T_g s to the cured resins than the ethylene diamine-based aliphatic amines while the toughness and elongation typically improve due to the higher equivalent weight of the amine. While the reactivity of cycloaliphatic amines is slower, the rate of carbamate formation is also reduced. Isophorone diamine (IPDA) is the most commonly used cycloaliphatic (Table 1.5). It is derived from acetone by alkaline condensation to form isophorone, which undergoes hydrocyanation followed by reductive amination. Many other cycloaliphatic amines are produced through the hydrogenation of the precursor aromatic diamines. Toluene diamine and aniline are derived from the hydrogenation of the corresponding nitrated aromatic compounds. Aniline can

Table 1.5 Aliphatic, cycloaliphatic, and polyether amines.

Chemical name	Structure	AHEW (g/eq)	Viscosity ^a (mPa·s)
Diethylene triamine (DETA)		21	5
Triethylenetetramine (TETA)		24	19
Tetraethylenepentamine (TEPA)		27	52
3-(Diethylamino)propylamine (DEAPA)		65	1.2
3-Dimethylaminopropylamine (DMAPA)		51	1
<i>N</i> -(2-Hydroxyethyl)ethylenediamine		34	141 @ 20°C
4,4'-Methylenedicyclohexanamine (PACM)		55, 52.5	19
Methyl-diaminocyclohexane (MCDA), 4-Methylcyclohexane-1,3-diamine and 2-Methylcyclohexane-1,3-diamine		31	7
Isophorone diamine (IPDA)		41	19

Bis(4-amino-3-methylcyclohexyl)methane (DMDC)		61	110
1,3-Bis(aminomethyl)cyclohexane (BAC)		36	9
<i>N</i> -(2-Aminoethyl)piperazine (AEP)		43	15 @ 20°C
4,9-Dioxa-1,12-dodecanediamine (DODA)		52	10
4,7,10-Trioxa-1,13-tridecanediamine (TTD)		56	13
Polyetheramines, diamines		61	10
D230		111	25
D400		501	273
D2000			
Polyetheramines, triamines		81	102
T403, R = C ₂ H ₅ , n = 1		530	367
T3000, R = H, n = 0		967	870
T5000, R = H, n = 0			

^a Viscosity reported at 25°C unless otherwise noted.

then be condensed with formaldehyde to give methylene dianiline (MDA). Commercial products include hydrogenated MDA, 4,4'-diaminodicyclohexylmethane (PACM), methyl substituted mono or dicycloaliphatic rings (3,3'-Dimethyl-4,4'-diamino-dicyclo-hexyl-methane (Baxxodur EC 331), Methyl-diaminocyclohexane (Baxxodur EC 210)), and IPDA Isophorone diamine (Baxxodur EC 201). Cycloaliphatic amines are also often provided in a modified or formulated composition from curative suppliers, including Mannich bases. Substitution of the primary amines [40,41] to give secondary amines was developed for polyureas and greatly extends the pot life or work time of the epoxy adhesive.

1.4.3 Aliphatic polyetheramines

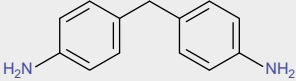
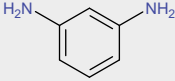
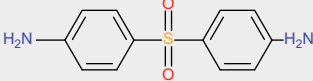
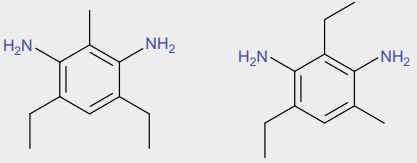
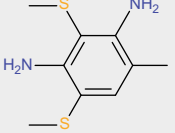
A wide range of polyetheramines are available in varying chain length and functionality, giving great latitude in the properties cured compositions. They are generally prepared from the respective polyols with reductive amination using ammonia and a metal catalyst [42,43]. Moderate to higher molecular weight monoamines, diamines, and triamines are all commercially available (Jeffamine M series, D series and T series from Huntsman). Shorter chain polyether diamines include trioxa-1,13-tridecanediamine (TTD) and 4,9-dioxadodecane-1,12-diamine (DODA). Polyether amines are generally primary, and the nitrogen is attached to terminal primary carbons as in TTD, DODA, and polyTHF amines or to a secondary carbon when derived from polypropylene glycols. The steric effect of the secondary carbon significantly slows the rate of reaction with epoxy. Polyether amines have good flexibility and toughness, and T_g generally decreases with chain length. High molecular weight amines based on tetramethylene oxide or propylene oxide are often used to improve toughness and peel strength.

1.4.4 Aromatic amines

The aromatic amines provide exceptional chemical resistance but require higher-temperature curing than their cycloaliphatic counterparts as the aromatic amine is a poorer nucleophile; however, they are even less prone to carbamate formation. The major drawback to using aromatic amines is their toxicity. The main route to production is discussed in the prior section on cycloaliphatic amines. Common aromatic curatives shown in Table 1.6 include diaminodiphenyl sulfone (DDS), 3,5-diethyltoluenediamine (DETDA, Ethacure 100), and dimethylthiotoluenediamine DMTA (Ethacure 300). The aromatic *m*-phenylenediamine (MPDA) is produced by hydrogenation of 1,3-dinitrobenzene [44], which is prepared by dinitration of benzene [45]. Modified aromatic amines help alleviate the carbamate issues of cycloaliphatic amines with reduced toxicity and faster cure rates relative to their unmodified counterparts [46].

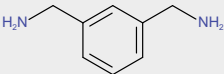
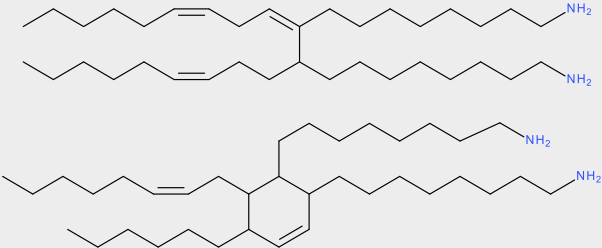
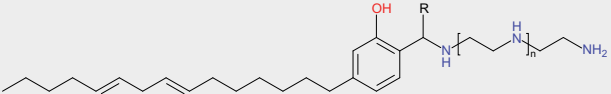
While meta-xylene diamine (MXDA) is aromatic, the amine is benzylic. It cures faster at low temperatures than aromatic and cycloaliphatic amines and has better chemical resistance than cycloaliphatic amines, but not quite as high a T_g when compared to IPDA or MPDA.

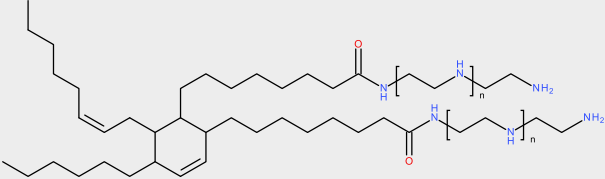
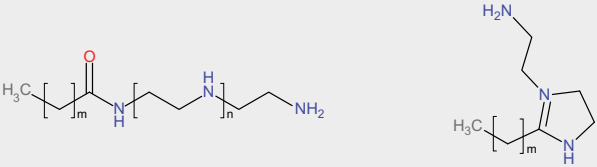
Table 1.6 Aromatic and bio-based amine curatives.

Chemical name	Structure	AHEW (g/eq)	Viscosity ^a (mPa·s)	Tradenames
4,4'-Methylenedianiline (MDA)		50	Solid	
Metaphenylenediamine (MPDA)		27	Solid	
4,4'-Diaminodiphenyl sulfone (DDS)		62	Solid	Aradur 976-1
Diethyltoluenediamine (DETDA)		45	155	Ethacure 100
Dimethylthiotoluenediamine (DMTA)		54	690	Ethacure 300

Continued

Table 1.6 Continued

Chemical name	Structure	AHEW (g/eq)	Viscosity (mPa·s)	Tradenames
<i>m</i> -Xylene diamine (MXDA)		34	7	Aradur 22
Dimer fatty acid-based amines	 <p data-bbox="545 709 899 726">two possible isomers, may also have aromatic isomers</p>	140 139 135 205	250 250 200 210	Priamine 1071 Priamine 1073 Priamine 1074 Priamine 1074
Phenalkamines		81	2000	Cardolite NC-540, 541, Epotec TH7940

<p>Polyamides</p>	 <p>n = 1, 2 or 3 typically ratio of amine to dimer acid determines extent of oligomerization and viscosity</p>	<p>100–250</p>	<p>Typically 1000–50,000; some higher and solid</p>	<p>Ancamide, Versamid, Aradur</p>
<p>Amidoamines</p>	 <p>generic amidoamine dehydration to form imidazoline</p>	<p>65–115</p>	<p>Typically liquid 30–1200</p>	<p>Ancamide, Aradur, Epotec TH7560</p>

^a Viscosity reported at 25°C unless otherwise noted.

1.4.5 Bio-based amines

Dimer and trimer fatty acid reaction products with lower molecular weight multifunctional amines such as ethylene diamine or diethylene triamine form amine terminated polyamides [47]. Priamine 1071 is a fatty acid dimer-based diamine with 100% renewable carbon content. It is a low-viscosity curative with good adhesion and imparts flexibility and hydrophobicity. Additional examples of polyetheramine reaction products with dimer acids soon followed [48].

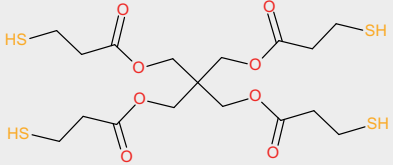
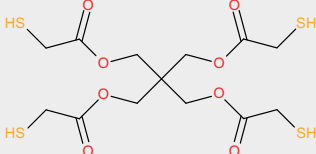
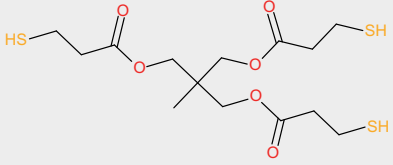
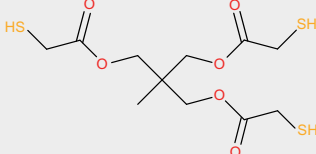
Amidoamines are quite like polyamides except that monofunctional acids are used to make the amide along with a multifunctional amine such as ethylene diamine or diethylene diamine. This helps alleviate the extreme sensitivity to stoichiometry of the low molecular weight aliphatic amine, improves compatibility, and imparts toughness and flexibility when compared to the unmodified aliphatic amines [6,49]. Both polyamide and amidoamine curatives may include imidazolines, which are lighter in color and extend the cure time along with improving surface wetting, interlayer adhesion, and compatibility with epoxy resins [50].

In the 1970s, amine functional curing agents based on CNSL were developed and given the generic name “phenalkamines.” These products are synthesized via Mannich reaction of cardanol, formaldehyde, and typically low molecular weight amines such as DETA, TETA, TEPA, or mixtures thereof (NC-540 and NC-541) [51]. Phenalkamides are similarly produced from cardanol, formaldehyde, and polyamides such as in the Cardolite Lite 3000 series [52]. Additional CNSL variations with cycloaliphatic, aromatic, and other aliphatic amines have also been explored [53–55] (Table 1.6).

1.4.6 Thiols

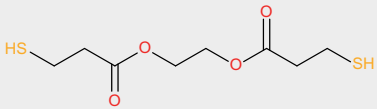
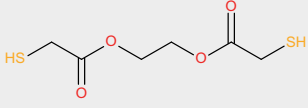
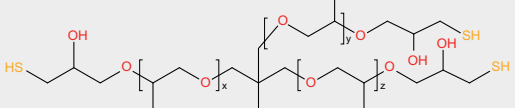
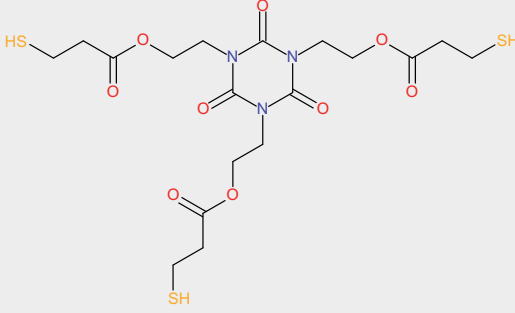
Thiols on their own react very slowly with epoxy resins, but in the presence of a catalyst such as a tertiary amine or phosphonium salt, they can react quickly even at sub-ambient temperatures. The functionality and types of thiols are similar to polyols and multifunctional alcohols are common starting materials (Table 1.7). Thiol terminated polyoxyalkylene glycols can be derived from the polyol reaction with epichlorohydrin, but the halogen is substituted with a thiol and an alpha hydroxyl group remains as in Capcure 3–800 [56]. Esterification of polyoxoalkylene glycols using thiolglycolic acid and 3-mercaptopropionic acids, or transesterification of the thiol esters, gives an ester instead of the hydroxyl functionality as found in Bruno Bock’s Thiocure product line [57]. Polyether polythiols were developed from the allyl ethers of pentaerythritol, trimethylolpropane, glycerin, and others using a diazo catalyst and hydrogen sulfide to improve moisture resistivity and susceptibility to decreased performance due to the presence of alpha hydroxyl groups [58]. Longer chain polyether thiols include the disulfide containing Thiokol LP and Thioplast G product families. Longer pot life thiols with excellent water resistance that have the thiol attached to a secondary carbon were more recently developed by Showa Denko [59,60]. A thiol based on glycoluril by Shikoku (TS-G) has a T_g of 112°C as compared to 63°C with PETMP when cured with a bisphenol A type resin along with a faster cure [61,62].

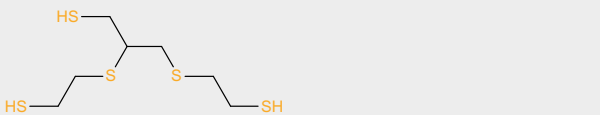
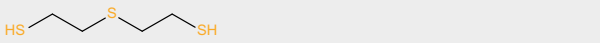
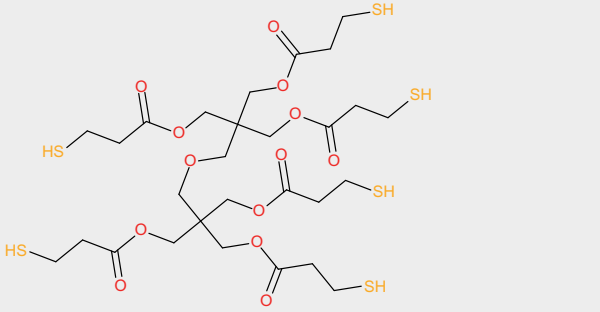
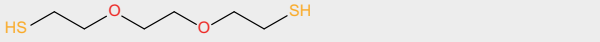
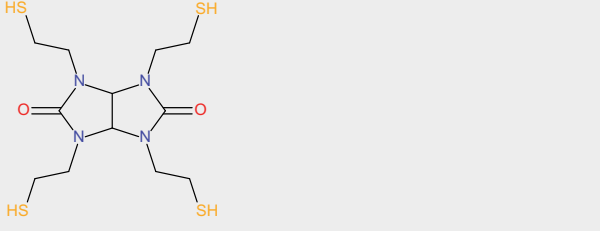
Table 1.7 Thiol curatives available from Arkema, Bruno Bock, Huntsman, Nouryon, Shikoku, Showa Denko, and Toray.

Chemical name	Structure	Active hydrogen equivalent weight (g/eq)	Viscosity ^a (mPa·s)	Tradenames
Pentaerythritol tetra(3-mercaptopropionate) (PETMP)		125–128	500	Thiocure 340
Pentaerythritol tetra(3-mercптоacetate) (PETMA)		111–114	400	Thiocure 140
Trimethylolpropane tris(3-mercaptopropionate) (TMPMP)		136–140	150	Thiocure 330
Trimethylolpropane Tris(thioglycolate) (TMPMA)		122–125	120	Thiocure TMPMA

Continued

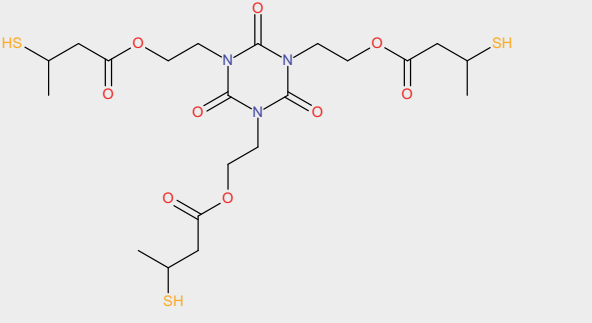
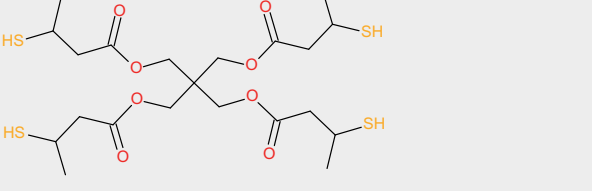
Table 1.7 Continued

Chemical name	Structure	Active hydrogen equivalent weight (g/eq)	Viscosity (mPa·s)	Tradenames
Glycol dimercaptopropionate (GDMP)		122–125	10	Thiocure 320
Glycol dimercaptoacetate (GDMA)		107	10	Thiocure 120
Poly[oxy(methyl-1,2-ethanediyl)], α -hydro- ω -(2-hydroxy-3-mercaptopropoxy)-, $\alpha, \alpha', \alpha''$ -triether with 2-(hydroxymethyl)-2-methyl-1,3-propanediol		270–280	10,000–15,000	Capcure 3-800, GPM 800
Tris[2-(3-mercaptopropionyloxy)ethyl]isocyanurate (TEMPIC)		175–184	8000–10,000	Thiocure 331

2,3-Bis((2-mercaptoethyl)thio)-1-propanethiol (DMPT)		87	Liquid	
Dimercaptodiethylsulfide (DMDS)		77	Liquid	
Di-pentaerythritolhexakis (3-mercaptopropionate) (Di-PETMP)		135–140	2500	Thiocure 360
3,6-Dioxa-1,8-octanedithiol (DMDO)		91	3.7	
1,3,4,6-Tetrakis (2-mercaptoethyl) glycoluril		108	Oil	TS-G

Continued

Table 1.7 Continued

Chemical name	Structure	Active hydrogen equivalent weight (g/eq)	Viscosity (mPa·s)	Tradenames
1,3,5-Tris(2-(3-sulfanyl butanoyloxy)ethyl)-1,3,5-triazinan-2,4,6-trion		183–195	7500	Karenc MT NR1
Pentaerythritol tetrakis(3-mercaptobutylate)		131–141	1100	Karenc MT PE1

1,4-Bis(3-mercaptobutyryloxy)butane		142–152	21	Karenc MT BD1
Polysulfide polymer with thiol end groups			1000–140,000	Thiokol LP series, Thioplast G series

^a Viscosity reported at 25°C unless otherwise noted.

Thiol curatives can give improvements in low-temperature curing, flexibility, elongation, low-temperature properties, hydrolytic stability, and low color compared to amine-cured systems. These characteristics contribute to their use in consumer products as well as construction and outdoor environments. One drawback is many thiol curatives have distinct to strong odors, but low-odor options are provided in a few cases.

1.4.7 Anhydrides

While anhydrides are used extensively in composites and casting, their adhesive applications are more limited due to the long, elevated temperature curing need for achieving full properties. The low curing exotherm, low cure shrinkage, good moisture resistance, and good electrical properties work well for potting and encapsulation adhesives. The reaction is often accelerated with Lewis bases or acids such as tertiary amines, metal oxides, or boron trifluoride complexes. The accelerator type and concentration along with the anhydride to epoxy stoichiometry affects polymerization as esterification is favored by amines while etherification is promoted by acids. The amount of acid impurity, alcohol functionality, and water are also contributing factors when optimizing the curing composition. Several common anhydrides shown in Table 1.8 are prepared via Diels Alder reactions of dienes with maleic anhydride [63–66] and subsequent hydrogenation for the saturated analogs. Other important anhydrides including phthalic anhydride [67,68], maleic anhydride, and benzo-phenonetetracarboxylic dianhydride [69–71] are produced via catalytic oxidation. Maleic anhydride is not typically used by itself but in conjunction with other anhydrides. Eutectic mixtures of anhydrides for liquid and lower melting point curative systems are used to balance curing and performance properties.

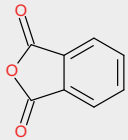
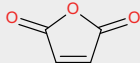
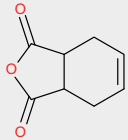
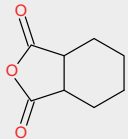
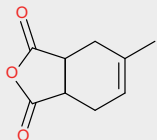
1.4.8 Latent curatives

Many latent curatives are simply solid, powdered amines that are insoluble in the epoxy resins. Dicyandiamide (Dicy) is a common latent curative [72] and is used with imidazole or urea accelerators to decrease the onset and curing temperatures. Other solid modified polyamines have been developed as latent curatives such as proprietary Ancamine 2014, 2441, and 2442 as well as the Adeka Hardener Series (EH-3615, EH-43375, and EH-4342S), which can also act as accelerators for dicyandiamide [73]. Additional latent curatives for 1K epoxy adhesives include dihydrazides [74–76] and similar to Dicy, accelerators can be used to increase reactivity at lower temperatures (Table 1.8).

1.5 Accelerators and catalysts

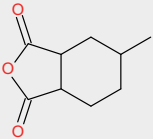
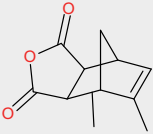

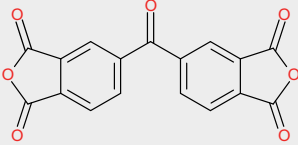
Both acceleration of the polyaddition reactions of epoxides with epoxy reactive groups and catalysis of their homopolymerization are incredibly rich areas with complex mechanisms, including some that are still not well understood or proceed in a

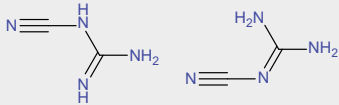
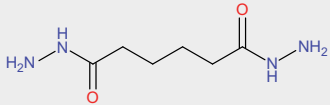
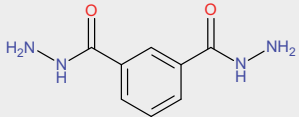
Table 1.8 Anhydride and latent amine curatives.

Chemical name	Structure	Anhydride or active hydrogen equivalent weight (g/eq)	Melting point or viscosity ^a	Trade names
Phthalic anhydride (PA)		148	131°C	
Maleic anhydride (MA)		98	53°C	
Tetrahydrophthalic anhydride (THPA)		152	~100°C	Rikacid TH
Hexahydrophthalic anhydride (HHPA)		154	<100 mPa·s @ 40°C	Rikacid HH, Aradur HT 907
Methyltetrahydrophthalic anhydride (MTHPA)		166	50–80 mPa·s	Epiclon B-570, Aradur HT 917

Continued

Table 1.8 Continued

Chemical name	Structure	Anhydride or active hydrogen equivalent weight (g/eq)	Melting point or viscosity	Trade names
Methyl hexahydrophthalic anhydride (MHHPA)		168	50–80 mPa·s	Epiclon B-650, Rikacid MH-700, Aradur HT 1102
Nadic methyl anhydride or methyl himic anhydride (NMA, MHA)		178	175–275 mPa·s	Aradur HY 906, Kayahard MCD
Dodecylsuccinic anhydride (DDSA)		266	300–800 mPa·s	
Benzophenonetetracarboxylic dianhydride (BTDA)		171	220–225°C	

Dicyandiamide			207–211°C	DyHard 100, Dicyanex series
Adipic dihydrazide		43	176–185°C	
Isophthalic dihydrazide		49	220–230°C	

^a Viscosity reported at 25°C unless otherwise noted.

manner dependent on reaction conditions. Homopolymerization of epoxies can be thermally initiated or photoinitiated with Lewis acids or bases and a variety of complexed salts (Table 1.9). Regardless of catalyst, homopolymerization results in a poly-ether network dependent on the epoxy resin and not the catalyst. While not discussed here as a category of accelerators, alcohols and water can both accelerate epoxy reactions.

1.5.1 Amine accelerators

Tertiary amines by themselves such as benzyldimethylamine (BDMA) or present in multifunctional amine curatives such as AEP or DMAPA and tertiary amine phenols such as 2,4,6-tris(dimethylaminomethyl)phenol (Ancamine K54, DMP-30) are among the most common accelerators. Imidazoles and substituted ureas are often used in 1 K epoxy systems with latent amines for faster thermal curing. Acid blocked or encapsulated tertiary amines [77] can also be used as latent accelerators to promote amine, thiol, or anhydride reactions in addition to homopolymerization of glycidyl epoxy. However, amine accelerators are not very effective in accelerating the reaction of cycloaliphatic epoxy resins.

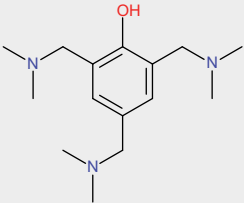
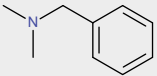
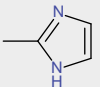
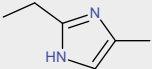
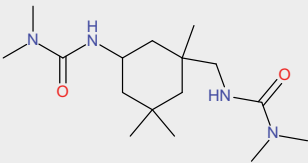
1.5.2 Boron trifluoride catalysts

Boron trifluoride is such an effective Lewis acid catalyst for polymerization that it is typically complexed with an amine or ether. Several BF_3 -amine complexes are available with reactivities dependent on the amine. Both aliphatic and aromatic as well as primary and secondary amines are used to complex BF_3 .

1.5.3 Photoinitiation catalysts

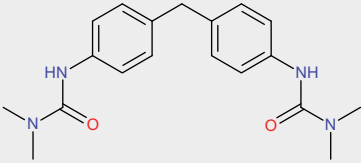
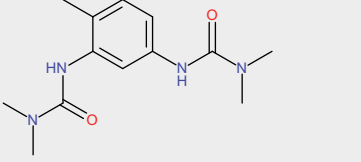
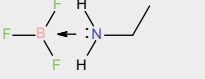
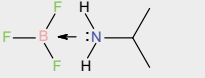
Photoinitiators have been known for curing epoxides since the 1960s, in which alpha and beta unsaturated nitrosamines were used to cure coating compositions [78]. Since then, preferred photoinitiators include those that generate acids, such as onium salts for cationic polymerization of the epoxy resins [79–81]. Diazonium salts are capable of both photoinitiation and thermal initiation for cationic curing. Cure rates can be increased by the addition of a photosensitizer for increased absorption of light, and continuation of curing after exposure to light has ended with aromatic iodonium salts of halogenides [82]. Light curing requires a joint design that is transparent or a polymerization process that can be initiated and will continue after the bond is closed or once the light source is removed. Photoinitiators in combination with sensitizing dyes to improve efficiency can be incorporated into the various form factors to initiate cationic curing upon exposure to the triggering radiation. Cycloaliphatic epoxy resins are often preferred for cationic curing due to their curing faster than the glycidyl ether resins.

Table 1.9 Accelerators and catalysts.

Chemical name	Structure	Typical use levels (PHR)	Melting point or viscosity ^a	Trade names
2,4,6-Tris(dimethylaminomethyl) phenol		1–15	200 mPa·s	Ancamine K54, Versamine EH-30, Accelerator DY 960-1
Benzyl dimethylamine		1–10	25 mPa·s	Accelerator DY 062, Ancamine BDMA
2-Methyl imidazole		0.5–5	140–145°C	Imicure AMI-2
2-Ethyl-4-methylimidazole EMI-24		0.5–5	1000–9600 mPa·s	Imicure EMI-24
<i>N</i> -3-(Dimethylamino) carbonylamino-methyl- 3,5,5-trimethylcyclohexyl- <i>N</i> , <i>N</i> -dimethyl-urea		0.5–3	190–210°C	Omicure 35M

Continued

Table 1.9 Continued

Chemical name	Structure	Typical use levels (PHR)	Melting point or viscosity	Trade names
[4,4'-(Methylene bis(phenyl dimethyl)] urea (MDI-urone)		0.5–3	220–230°C	Omicure 52
[1,1'-(4-Methyl-mphenylene)bis-(3,3-dimethyl)] urea		0.5–3	182–195°C	Dyhard UR 500, Amicure UR2T
BF ₃ Ethylamine complex		1–15	85–95°C	
BF ₃ Isopropylamine complex		1–15	106–110°C	

^aViscosity reported at 25°C unless otherwise noted.

1.5.4 Ionic liquids

Both solid and ionic liquid phosphonium-based salts have been developed for curing epoxy systems both for homopolymerization and with other curative (anhydride, dicyandiamide, phenols, and carboxylic acids) systems. These include electronic bonding applications [83] and composites [84,85].

1.5.5 Metal salts

Halide, nitrate, and phosphate metal salts have been demonstrated to decrease gel time in epoxy amine compositions. As the metal compounds can be challenging to incorporate into an adhesive system, the rate of reaction was improved further by increasing the solubility of the salt in the amine with the addition of a small amount of water, triethylene glycol, or dimethyl formamide as a cosolvent [86]. Additional metal salts have been found to accelerate amine epoxy reactions and have been used in combination with amine accelerators [87,88].

1.6 Tougheners and flexibilizers

Several previously mentioned epoxy resins and curatives are utilized as tougheners or to add flexibility to the adhesive. Common functionalized curatives and resins include polymer backbones with polyglycol ethers, silicones, polyurethane, butadiene rubber, and butyl nitrile rubber. Reactive terminal and side chain functionalities include epoxy, amine, thiol, and carboxylic acid. Core-shell rubber products from Kaneka, Arkema, Dow, Wacker, Mitsubishi, and Shandong Rike Chemical are available with different sizes as well as core and shell chemistries for a range of performance and reactivity with the polymer matrix of the adhesive.

1.7 General property specifications and certificate of analysis

Epoxy functional resins and reactive diluents will typically list a relevant selection of properties and suggested uses on a technical data sheet (TDS) with a smaller selection of properties on a certificate of analysis (COA) including, but not limited to, epoxy equivalent weight or epoxy content, viscosity, hydrolysable chlorine, total chlorine, color, acid number, hydroxyl content, percent of volatiles, density, flash point, boiling point, melting point, shelf life, storage conditions, and process for melting crystallized liquid resins.

Curative technical data sheets and COAs contain much of the same type of information and will list reactive equivalent weight or percent content such as amine hydrogen equivalent weight, thiol equivalent weight, or anhydride equivalent weight to enable the stoichiometric calculations for the quantity of curative to epoxy. Other properties listed may include primary, secondary, and tertiary amine content; particle

size for solid or latent curatives along with use level for 1:1 stoichiometry; gel time; glass transition temperature; and recommended cure schedule with a standard liquid epoxy resin.

1.8 Environmental, health, and safety considerations

Epoxies are known skin irritants and sensitizers. The terminal epoxy groups are the most chemically and biologically reactive with the toxicity being dependent on the epoxy equivalent weight. The most common starting materials, bisphenol A and epichlorohydrin, have several category 1 GHS warnings. The status of bisphenol A as an endocrine disrupter has brought a use limit as a substance on its own and in mixtures intended for consumer use. The European Union has had two calls for evidence relating to BPA and structurally related bisphenols in 2021 as it looks to reduce release into the environment. In addition, any free epichlorohydrin present in the epoxy resin increases the toxicity of the system.

The toxicity of amines is highly dependent on structure and often depends on the molecular weight. Several low molecular weight aliphatic amines have warnings for acute toxicity for skin contact or inhalation. Many amines are regarded as corrosive as they can cause burns to both skin and eyes. Those that are less toxic often fall into the warning category for irritation. Aromatic amines can be carcinogenic, mutagenic, or reproductive toxins. A few amines present a hazard to aquatic environments. The general functionalization of the amines used in polyamides, polyamidoamines, and phenalkamines results in a lower level of toxicity and irritation.

While potentially high in odor, thiol curatives are generally less toxic than comparative amine curatives but will still carry warnings for skin, eye, and respiratory irritation. Anhydrides can cause eye and skin irritation and potentially burns. Higher molecular weight anhydrides tend to have lower toxicity. Inhalation of dust is a risk with solid anhydrides. The chemistry of catalysts and accelerators is highly varied and requires a careful safety review.

1.9 Typical form factors and packaging of epoxy adhesives

Epoxy adhesives are generally packaged and supplied in one-component (1K) or two-component (2K) formulations that can include different form factors such as liquid, paste, or film based. Solvent and water-based epoxy will not be addressed as these are much more frequently used as coatings. Depending on the application, 2K adhesives may be supplied in cartridges with a set ratio of curative to resin or in separate containers where the ratio is set by dispensing the appropriate amount for mixing as directed by the adhesive manufacturer. Manufacturing facilities with high volume adhesive application use dispensing systems designed for bulk containers such as 5-gal and 20–30L pails or 55-gal drums to dispense 1K or by metering each part of 2K adhesives to control the mix ratio and mix quality.

Smaller consumers of adhesives may use cartridges from roughly 5–600 mL. A dispenser with a mixing nozzle attached to the cartridge controls the mix ratio and mix quality of the applied adhesives. Products are also supplied in manual cartridges with a plunger incorporated or smaller bulk packaging for applications requiring a limited amount of adhesive. Hand mixing or manual bulk mixing is also an option for small quantities or when pot life is not a concern.

Epoxy film adhesives are often a partially cured B-staged product, or a mixture of high molecular weight resins with a latent curative that behaves somewhat like a PSA or tape in dispensing and application. The film may be supported on a liner or by a scrim within the adhesive. Shelf life is typically prolonged with cold storage, as ambient conditions may shorten the useful life to a matter of days.

1.10 Formulation and design

Adhesive formulation is highly dependent on adhesive form factor and the product requirements from both end-use application process and product performance requirements. The adhesive also must be able to be manufactured and delivered to the customer with enough shelf life for the customer to be able use the adhesive in the expected manner. The same basic tenets apply to epoxy adhesive formulations in that the choices of resin, curative, accelerator, reactive and nonreactive diluents, fillers, adhesion promoters, and rheology modifiers can be incorporated as needed to fit 1 K, 2 K, or film adhesives.

1.10.1 Epoxy resins

For all epoxy adhesives, whether a film or paste that needs to hold a shape as dispensed or a liquid that flows, the epoxy resins are a major component of the adhesive and play a key role in the dispensing of the adhesive and the cured properties. The resin choices from standard liquid to solid BPA backbones to epoxy novolac to epoxy modified resins of various types can be used to optimize properties such as stiffness, toughness, flame retardancy, adhesion, glass transition temperature, tensile strength, elongation, reactivity, and viscosity. Reactive diluents are often used to help lower the viscosity but may impact the cured properties depending on the functionality and structure of the diluent. Monofunctional and nonreactive diluents plasticize the cured adhesive but can help improve surface wet-out on the substrate.

1.10.2 Curatives

The choice of curative or hardener is typically determined by two key factors: curing conditions and the mechanical properties of the cured adhesive. Ambient temperature curatives for 2K standard epoxy resin adhesives are most often polyamines and then mercaptans. While heat may be used to accelerate the cure, it is not required. Full cure or complete consumption of the epoxy groups may not occur without additional heat, depending on the stoichiometry of the active hydrogens and the accelerator used.

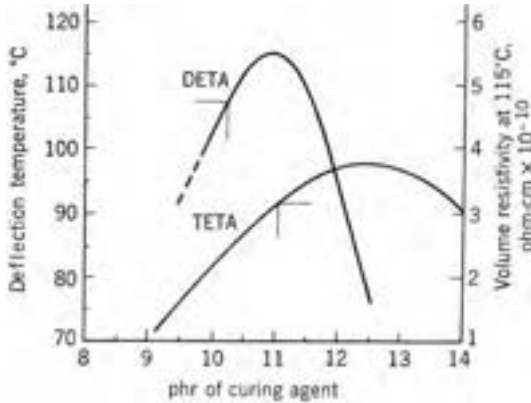


Fig. 1.3 Effect of curative concentration on deflection temperature of DGEBA [89].

Heat may further develop or enhance properties if applied as a second curing step or “postcure” such as an increase in T_g . The effect of stoichiometry on a fully cured system is well illustrated by Lee and Neville in Fig. 1.3, with the inverted parabolas of DETA and TETA cured DGEBA with maximum heat deflection temperatures at essentially 1:1 active hydrogen to epoxy [89]. Primary and secondary amines are nucleophilic and will preferentially add to the less hindered carbon of the epoxide ring, followed by formation of the secondary alcohol. The reactivity of mercaptans without an accelerator is quite slow. When the thiol is deprotonated with a tertiary amine accelerator, it is a much more efficient nucleophile and the ring opens the epoxy again at the less hindered carbon. Tertiary amines promote the homopolymerization of the epoxy groups by the reaction with secondary alcohol when the amine or thiol is stoichiometrically deficient. The glass transition temperature and heat resistance of mercaptan-cured epoxies are lower than those of similar amine-cured adhesives due to the lower degree of functionality and higher equivalent weights. Many of these curatives work well down to 10°C while certain amines and mercaptans will still cure relatively quickly at 5°C, 0°C, and even lower temperatures, including phenalkamines, polyamides, or amine epoxy adducts (Aradur 3441, Ancamide 2424, 2444, 2445, Ancamines 2489, MCA, 2423, 2641, 1856, Cardolite series, Kukdo KH500).

Latent, blocked, or slow curatives such as dicyandiamide and other solid amines, aromatic amines, BF_3 -amine complexes, photoinitiators, and anhydrides need externally applied heat or light to initiate or fully cure the adhesive to achieve final properties. Often, these curatives are coupled with accelerators such as tertiary amines, imidazoles, metal salts, acids, or ureas to reduce the curing temperature or time. While other curatives with active hydrogens react with the epoxy resins similarly to that discussed with amine and thiols, the reaction of dicyandiamide and its active hydrogens is quite complex. Dicy can behave as a crosslinker and chain extender as the reaction progresses [90].

1.10.3 Tougheners

In 1K adhesive systems, toughening can be incorporated through functional and nonreactive resins such as previously discussed polyethers, urethanes, butylnitrile rubbers, block copolymers, thermoplastics, and core-shell rubber particles. Toughening resins that contain epoxy reactive functional chemistry can easily be added to the curative side of a two-part adhesive or incorporated into a film adhesive as part of the B-stage manufacturing process. The liquid rubber, block copolymer, and thermoplastic toughening mechanisms require a phase separation during the curing process but not before to be effective. The phase separation and domain size may be influenced by curing conditions such as temperature, humidity, and rate of cure. Core-shell rubber particles eliminate the need for a cure-induced phase separation with the self-contained rubber inside the shell. Powder grades of core-shell particles need to be dispersed into the resins with shear and temperature; however, relatively newer grades disperse much more readily such as Clearstrength XT100, Kane Ace M731, and M734. Predispersed core-shell rubbers in a variety of resins are also available with a wide range of core-shell rubber content, rubber type, and core-shell size for improving toughness over different temperature ranges.

1.10.4 Fillers and rheology modifiers

Several additional components may be added to an adhesive to modify properties for the application process, curing, or cured state. Rheology can be modified with fumed silicas, clays, or waxes. Inexpensive fillers such as talcs and calcium carbonates can be added to lower cost, reduce shrinkage, change rheology, reduce flammability, increase modulus, increase impact strength, reduce corrosion, and change thermal or electrical conductivity. Highly filled epoxy adhesives may also be machined, abraded, or polished after curing to impart esthetic features not easily achieved by other means. Specific fillers known for corrosion inhibition, fire or flame retardancy, thermal conductivity, and electrical conductivity can improve those properties in the adhesive.

1.10.5 Adhesion promoters

Alkoxysilanes are among the most common adhesion promoters. The alkoxysilanes with a secondary functionality reactive to an epoxy adhesive system are commonly used and can be put in 1K or 2K systems. Metal chelating epoxies, phosphorus compounds, dithiooxamides, titanates, zirconates, and carboxylic acids are among the many compounds that can be used to improve adhesion, either as part of the adhesive or with a direct application to the substrate [91–93].

1.11 Adhesive production

Epoxy adhesives are typically manufactured in batch kettles, on a continuous line, or a combination of both depending on the manufacturing volumes and adhesive type. New facilities and new equipment with “smart” factory design are modernizing the

industry with better feedback and control of equipment regardless of the type of manufacturing process. Reactive chemistry, whether in the production of one-part systems with latent catalysts or epoxy adduct reactions, needs to be closely monitored and controlled with temperature and raw material charging to prevent runaway reactions. Similarly, light-activated or thermally sensitive catalysts and curatives must be properly handled in the manufacturing process to not cause premature activation.

In two-part adhesive production, where both parts are mixed on the same equipment, proper cleaning must be done to ensure cross-contamination does not cause reactions in the epoxy resin component. Batch kettles with dispersion capability do well for liquid and paste adhesives up to a certain viscosity if fillers such as fumed silica need to be incorporated. Planetary mixers and extruders can handle higher viscosity pastes. Environmental, health, and safety considerations are significant as bulk quantities are typically being handled during manufacturing processes, and hazards are specific to each raw material.

General adhesive product properties may be measured during manufacturing as an in-process test or as part of quality release specifications after manufacturing and prior to packaging or shipment to a customer. These may be properties based on uncured components, the mixed adhesive, and the cured adhesive. Internal specification tests may include density, viscosity, color, appearance, spectral measurements, strength measurements, and cure and open times. Typical values for a selection of properties the manufacturers have deemed valuable to customers are provided on technical data sheets.

1.12 Use and properties of epoxy adhesives

1.12.1 Common applications

Epoxy adhesives have broad applications due to their overall versatility and excellent adhesion to many substrates. They are capable of functioning in extreme environments while maintaining high strength and toughness. Epoxy adhesives can be chemically and heat resistant, electrically insulating, thermally conductive, and can be cured under adverse cold, damp, and wet conditions. Most epoxy adhesives are essentially solvent free.

Guidance on adhesive use, substrate preparation, curing conditions, and storage can vary widely and is dependent on the specific adhesive and application. For optimal adhesion, substrates need to be clean. Automotive body-in-white adhesives are an exception as the steels and aluminums used in the production process have oils or lubes present that the adhesive must penetrate or absorb to wet out the metal substrate. The high-temperature curing step does facilitate the displacement of the oils and lubes.

Typical properties for T_g as well as tensile and flexural strengths and modulus are highly dependent on the curative system, even with a standard bisphenol A resin. By using other epoxy resins and diluents along with tougheners and fillers, the range of properties attainable is even broader. The T_g of cured epoxy adhesives can be slightly above ambient temperatures to more than 200°C while tensile strength and modulus are often in the range of 50–100 MPa and 2500–3500 MPa, respectively.

1.12.2 *Applicable substrates and preparation*

Epoxy adhesives can be used on metals, glass, plastics, composites, ceramics, cement, stone, wood, and more. Epoxies benefit from surface cleaning with degreasers, alcohol, or soap and water to remove oils, lubes, water soluble residues, mold release compounds, dirt, corrosion, dust, or other contaminants. Surface abrasion can improve interfacial adhesion by removing weakly bound coatings or oxide layers while also increasing the surface area between the substrate and adhesive. This can help to promote higher strengths and cohesive failure mode, which is typically preferable over adhesive or substrate failure. Additional details on surface preparation can be found in [Chapter 9](#).

1.12.3 *Mixing and dispensing*

Large volume dispensing of an adhesive in a manufacturing line process is done with commercial dispensing and mixing equipment capable of pumping the one- or two-part adhesive in the correct ratios while mixing and dispensing the adhesive manually or robotically in a preset pattern and time frame for efficiency. For highly viscous adhesives, the materials may be preheated to ease dispensing or mixing. Manual, electric, or pneumatic dispensers are commonly used for the different types of two component cartridges that typically require equalization of the two parts by initially dispensing adhesive until both parts are extruded from the cartridge prior to attaching the mix nozzle to the cartridge. Adhesive manufacturers may recommend dispensing speeds or settings for optimized mixing and the initial few grams of dispensed adhesive, typically equivalent to the volume of the mix nozzle, are often recommended to be discarded.

Bulk material provided by the adhesive manufacturer for hand mixing of two-part adhesives can present challenges including uniform mixing, entrainment of air, viscosity changes over time, excess adhesive mixed, proper mix ratio, mass exotherm, shorter work time or pot life, and health and safety issues with handling bulk materials for mixing. Smaller packages and premeasured single-use packages with self-contained mixing help alleviate some of these challenges.

1.12.4 *Aerospace*

Aerospace applications of epoxy adhesives are in original construction and repair for both primary structures and interior components including engine nacelles, flaps, aileron bonding, helicopter blades, landing gear doors, floor and ceiling panels, sidewalls, overhead bins, and partitioning. The adhesives help distribute stress along joints, allow bonding of mixed materials and construction of laminates, absorb vibrations, reduce weight, are often flame resistant or fire retardant, and can be resistant to degradation by fuel. Film adhesives are used for bonding composites as well as metal and honeycomb structures. Syntactic materials for sandwich panels, core filling, and splicing products provide low-density bonding solutions. Expanding film adhesives and foaming epoxy adhesives expand while curing with heat to bond, fill, and seal

structures. Service temperatures for aerospace go as low as -55°C and as high as 177°C . Unlike automotive applications, aerospace applications may use primers to improve adhesion and corrosion resistance. Two-component paste adhesives can be used in a similar manner to film adhesives but with ambient or heat curing. Liquid shim adhesives act as both a gap filler and an adhesive for thick bond lines up to a few millimeters while providing high compressive strength. Potting, sealant, and edge filling compounds are used to seal, fill voids, and reinforce and protect parts, especially electrical components, from environmental exposures including thermal shock and stress, corrosion, vibration, chemicals and fluids, and moisture. [Chapter 23](#) is dedicated to aerospace bonding applications and requirements.

1.12.5 Automotive

Automotive utilization of adhesives has been driven by light-weighting to meet fuel efficiency standards, increase safety with crash energy management, improve vehicle handling, allow the use of new materials, and reduce noise, vibration, and harshness. Structural adhesives have reduced the number of welds, rivets, or other mechanical fastening and the full bond-line has been stiffened by adhesive along the length of joined parts rather than just by the individual weld or rivet points. Tape, 1K, and 2K adhesives have been developed for bonding primary structures and hang-on parts such as doors, tailgates, and hoods. The adhesives may be cured at room temperature with induction, lower-level heat curing such as 80°C , or standard body-in-white bake processes of more than 130°C . They can withstand the metal stamping and drawing lubricants, be fully cured weeks after application, and be induction spot cured for handling strength of bonded parts.

While first developed for production, similar 2K ambient curing adhesives are used in vehicle repair. Quarter panels, door skins, roof panels, pillars, and frame structures now incorporate adhesives when these parts are replaced or repaired. Often, the adhesive replaces a production adhesive or other type of joining that cannot be replicated in aftermarket repair at a body shop. The previously bonded surfaces and replacement part surfaces need to be cleaned and may also need to have coatings or residual adhesive removed down to bare metal, as directed by the original equipment manufacturer (OEM) repair process and adhesive directions. See also [Chapter 24](#) on automotive adhesive applications.

1.12.6 Building, industrial, construction, civil engineering, and general manufacturing

Epoxy adhesives can be found underground, underwater, and all over buildings and structures above ground. Concrete is a common substrate for bonding, crack repair, and patches in buildings, roads, and bridges. Bridges, tunnels, and buildings use steel anchors bonded into concrete or rock. Concrete beams are reinforced with epoxy laminated composites or steel panels. Road lane markers are bonded to highways and dividers. Repair and rehabilitation of aging structures is done by reinforcing and

repairing weakened structures with adhesive lamination of stiffening metal rails or composite panels to the original structure. Prefabricated building and container sandwich panels, wood laminates, tile, insulated glass, and even railway joints are bonded with epoxy adhesives. Adhesives used in applications exposed to the elements are able to withstand environmental conditions ranging from wet and humid to arid with large variations in daily temperatures while providing the benefit of sealing components from the environment. The assembly of products such as golf clubs, bicycles, tools, electric motors, fuel cells, and appliances uses a variety of epoxy adhesives specific to the application requirements. Additional information related to construction adhesives can be found in [Chapter 25](#) while [Chapter 26](#) relates to general industrial and consumer goods.

1.12.7 Energy

Wind turbines and solar panels both use adhesives in assembly and maintenance. Epoxy adhesives enable assembly processes and give long-term durability in thermally and mechanically stressful environments. As the wind blades increase in size, the scale challenges include the increasing mechanical stresses the blades experience and the assembly time for adhesive application and curing. Hydrogen for fuel cells uses epoxy composites in the storage tanks.

1.12.8 Electronics and communications

The electronics use of adhesives has dramatically changed design and assembly by reducing or eliminating mechanical fastening. Applications include potting, underfill, electrical insulation, adhesive solder, and lamination. Conductivity can be achieved with a high loading of silver particles or other conductive fillers and can replace traditional solder joints while improving durability. Thermally conductive adhesives enable heat dissipation through bond lines and into heat sinks with high filler loadings of materials such as aluminum oxide and boron nitride. Optical applications include light-emitting diode encapsulation and attachment, lens bonding, and display lamination and bonding. See also [Chapter 26](#).

1.12.9 Marine

Boat, watercraft, and ship building applications use laminate bonding resins and structural bonding of metal and composites where epoxy adhesives have good resistance to the temperature variations and corrosive conditions of marine environments. Highly filled epoxy adhesives are used in the repair of metal parts damaged from corrosion, wear and tear, or accidents. Again see [Chapter 26](#) for more marine adhesive information.

1.12.10 Medical

Medical applications where the epoxy adhesives come into contact with human tissue or fluids include disposable as well as reusable and durable products ranging from syringes and needle assemblies to catheters to bonding and potting applications for

medical and dental devices and surgical instruments. Biocompatibility to ISO-10993 or USP Class VI Standard along with heat and chemical stability for resistance to autoclave sterilization and other sterilization processes are common attributes. These adhesives can be heat cured or light cured depending on the limitations of the application and device. Substrates used in the medical field can be metal, composite, or a variety of plastics. [Chapter 27](#) also provides additional details.

1.12.11 Specialty vehicles and transportation

Epoxy adhesives are used in the bonding of honeycomb sheets and composites as well as insulated panels for refrigerated containers, trucks, recreational vehicles, emergency vehicles, and passenger rail. Battery pack assemblies for electric vehicles utilize epoxy adhesives for sealing, encapsulation, environmental intrusion, thermal management, coolant barrier, structural integrity, and crash resistance when incorporated into the vehicle frame. For more information, see [Chapter 26](#).

1.13 Recent advances in epoxy adhesives

1.13.1 Mixing and dispensing advances

Innovations in applicators and dispensing cross adhesive technology boundaries. New cartridge designs utilizing foil packaging with MIXPAC ecopaCC Collapsible from Medmix and 2K Film-Pak Cartridges from Nordson tout sustainability and high-performance two-component packaging where the waste is significantly reduced from standard side-by-side cartridges. New coaxial cartridge designs for 2K adhesives in UTAH by Nordson and Mixpeel by Medmix allow dispensing with standard caulk guns for a variety of mix ratios by volume. Dynamic mixing of high-viscosity materials and new static mix nozzle designs provide more efficient mixing and less adhesive waste.

One method of addressing the challenge of bulk mixing for epoxy amine compositions was done by Warnsdorfer back in the 1950s by adding a triarylmethane dye to the epoxy resin. The color change gave confirmation of complete mixing and served to indicate that the system was approaching the end of its pot life [94]. New advances in this area apply to 2K mercaptan-curing epoxy adhesives in which a dye added to the adhesive allows for monitoring of the cure with a color change down to temperatures as low as 0°C [95]. Latent 1K epoxy resin systems have also been developed utilizing dyes that indicate the adhesive is still sufficiently fresh for use and give a color change as the resin system is cured [96]. A two-component epoxy amine with dyes in both the amine and epoxy give a mixed color distinct from the colors of the two components, followed by a different distinct cured color [97]. In construction, a flooring adhesive indicated the degree of strength with a change in color or hue [98]. A 2K adhesive has a two-stage color change for curing at a first temperature followed by a second color change at a second, higher temperature [99]. Polymeric colorants have also been developed for easier incorporation into the adhesive to show the degree of cure as a visual color change [100]. Color change has also been used as an indicator of

activation for epoxy paste or film adhesives to verify the adhesive will cure as the ultraviolet (UV) activation step causes the photo initiator to release the acid that interacts with the dye [101,102]. As the reaction proceeds, the color changes again dependent on the level of cure that is incorporated into Lohmann UV-LUX adhesive tapes [102].

1.13.2 Raw material advances

1.13.2.1 Bio-based raw materials, bisphenol alternative resins, and adhesives

Sustainability has become a corporate pillar as companies have forward net-zero carbon emission or bio-based content targets. Whether polysaccharides, plant oils, or lignins, plant biomass is a major source of chemical feedstock. The Renewable Carbon Initiative comprising 11 companies includes key players in adhesives and is focused on speeding up the transition to renewable carbon for organic chemicals and materials. Health and safety concerns especially focused on toxicity and life cycle management are being driven by regulators, consumers, and manufacturers.

The challenge beyond already commercialized products is twofold: matching the performance of current adhesives and cost. The exploration of renewable bio-based or BPA-free resins, diluents, and curatives is an active area as energy, climate change, sustainability, and health and safety are driving regulators, manufacturers, and consumers to explore alternatives to fossil fuel-based raw materials as well as increasing scrutiny of bisphenol-containing materials.

Two main approaches have been taken for incorporating bio-based content into epoxy resins. The first approach to increasing carbon content of epoxy resins is simply to utilize bio-based ECH derived from fatty acid triglycerides. The second approach is to start with a bio-based derived polyol that can be reacted with ECH, giving potentially a fully bio-based resin if combined with the first approach.

Epichlorohydrin (ECH) has been primarily industrially produced starting with propylene. However, Epicerol has been developed by Solvay and commercialized by Advanced Biochemical Thailand (ABT) using glycerol from plant oil triglycerides. Hexion, now Westlake Chemical, has plans for the expansion of ECH production at their plant in the Netherlands with glycerin as part of the sustainability commitment.

1.13.2.2 Furans

A variety of mono- and difunctional furan epoxy resins and amine curatives has been reported in the literature and patents with good adhesion but typically lower T_g s than corresponding thermosets based on DGEBA [103–109]. These are readily synthesized from sugars or cellulose, which makes them ideal building blocks (Fig. 1.4) compared to other less-refined cellulosic raw materials that are often complex mixtures. One of the first examples in patent literature describes the preparation and use for low shrink UV curing application for electronic materials [104]. Several paths to producing the furan epoxy resins have been put forth in the patent literature, with the most recent

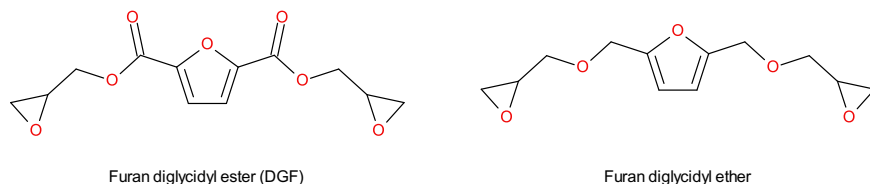


Fig. 1.4 Furan-based epoxy resins.

being a fully bio-based synthesis using a two-step process starting with furfuryl alcohol, formaldehyde, propionic acid, and sodium propionate. These materials were reacted for 5 h at 125°C, at which point sodium hydroxide was added and residual furfuryl alcohol was removed under vacuum. The resulting solid was reacted at a molar ratio of 1:5 hydroxyl content in the solid to ECH in propylene glycol methyl ether as the solvent. The resulting epoxy resin was cured with both IPDA and MXDA, which gave excellent adhesion to the iron substrate with a crosshatch peel test; it was better than YD-128, an all-purpose liquid bisphenol A resin from Kukdo. The cure speed was also significantly faster by nearly a factor of four when comparing gel time at 15 to 55 min for IPDA, but the T_g of the IPDA-cured furan epoxy was 60.9°C compared to 152.5°C for the IPDA-cured YD-128 [107]. A slightly higher purity monomeric diglycidyl furan has a reported T_g of 69°C, showing the effect of chain extension on the T_g [105].

One exception to the decrease in comparative property performance is the bio-based diglycidyl ester of 2,5-furandicarboxylic acid (DGF) compared to diglycidyl ester of terephthalic acid (DGT, in Table 1.2) or a standard BADGE resin cured with the D230 amine (Table 1.5) or MHPHA, shown in Table 1.8. The tensile strengths and modulus were quite similar to slightly lower for the BADGE resin, but its flexural strength and modulus were slightly higher. Both DGF compositions cured with MPHHA and D230 have higher T_g s of 152°C and 101°C, respectively, by DMA to the BADGE composition T_g s of 125°C and 97°C, respectively. The reactivity of DGF was also faster than that of DGT [109].

1.13.2.3 Isosorbides

Isosorbides are sugar-derived difunctional dicyclic alcohols prepared from starch via hydrogenation of glucose and dehydration of the resulting sorbitol. Diglycidyl ethers, amines, and thiols prepared from isosorbide have chirality and rigidity in the ring structure (Fig. 1.5).

Isosorbide diglycidyl ether resin as a reactive diluent compares favorably to trimethylolpropane triol, butane diol, and C12–C14 alcohol glycidyl ethers with less effect on T_g when cured with IPDA than the other diluents used at 40 wt% in DGEBA. The T_g dropped from 150°C to 138°C as compared to 126°C, 33°C, and 45°C for the other diluents, respectively. At the high level of loading, elongation, tensile strength, and toughness were improved while modulus was slightly lower. The isosorbide epoxy was less effective at viscosity reduction of the resin [110].

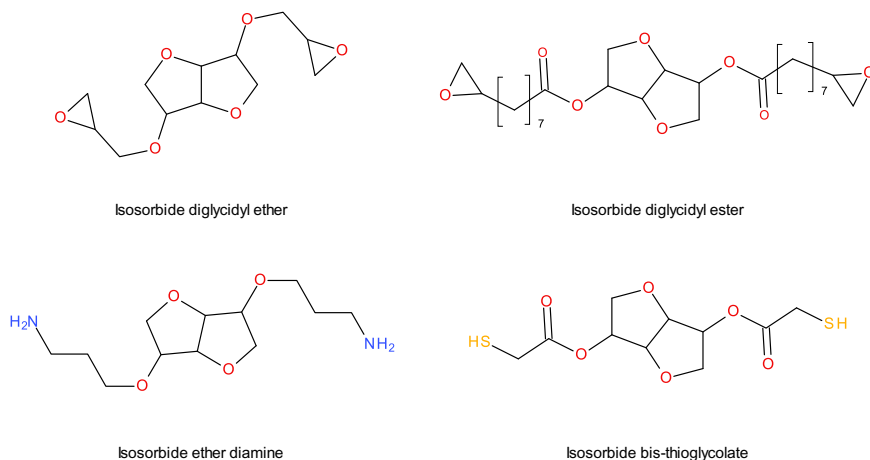


Fig. 1.5 Isosorbide-based epoxy resins and curatives.

A 100% possible biomass carbon content adhesive utilizes the hydrophilic nature of isosorbide resins. The adhesive was cured with a polyamide and compared to a standard bisphenol A epoxy resin, YD-128 from Kukdo. The resulting T_g s as measured by DSC were quite similar with 64.5°C and 66.7°C, respectively. The isosorbide adhesive quickly absorbed water, which as they note as a debonding method [111]. By utilizing polymeric isosorbide resins to replace BADGE along with mono- and tri-functional nonbisphenol epoxy glycidyl ethers, water uptake over a period of 4 days was significantly reduced with only modest differences in T_g for several amine curatives [112].

Isosorbide esterified with 9-decenoic acid and then epoxidized with peracid gave a diepoxy compound that when cured with a bio-based diamine, ethylenedibisfurylamine, gave lap shear strength of over 20 MPa on steel [113].

Another high bio-based content adhesive composition using thiol ether and esters of isosorbide developed as curatives for epoxy resins showed a wide range of lap shear strength from not quite 3 MPa to more than 20 MPa when cured with Erisys GE-60, a sorbitol glycidyl ether epoxy resin, depending on the structure of the thiol substituent. Combinations with amine curatives improved the cure speed. A mixture of ethylene glycol dithioglycolate (EGDTG) and GE-60 cured with 2-aminomethylfuran that took more than 30 min to harden went down in less than 1 min when the EGDTG was replaced with the isosorbide bis-thioglycolate [114].

1.13.2.4 Fatty acids and sugars

Epoxy resins of fatty acid sugar esters via epoxidation of internal alkenes were investigated for coatings cured by UV. Sefose sucrose fatty acid esters were epoxidized using peracetic acid generated in situ. The functionality of these relative to ESO is significantly higher with 10–15 epoxy groups per molecule. This leads to good substrate adhesion as well as higher T_g and hardness when cured under cationic UV

conditions and also when cured with anhydrides relative to the comparative epoxidized soybean oil [115].

1.13.2.5 Fatty acids and lignins

Lignin is a diverse source for epoxy resins from depolymerized lignans and phenolic monomers such as vanillin and guaiacols [116–124]. Pilot plant-scale production of depolymerized lignin gave oils that were subsequently epoxidized with ECH. The resulting resins were blended with a BADGE resin at varying ratios. The resins cured with DETA showed a decrease in T_g as the lignin resin content increased. By DSC, the T_g went from 114°C for pure BADGE to 66–72°C for the 67% lignin-containing epoxy resin with the depolymerized lignins. Mechanical measurements showed similar or better flexural strength and stiffness for all compositions with up to half the BADGE resin being replaced with the lignin-based epoxy resin [118].

Two types of bio-based epoxy resins, one being epoxy functionalized dimer acids and the other based on the reaction product of vanillin and guaiacol, when cured with DETA and optionally a hyperbranched epoxy oligomer gave a range of peel strengths from 2 to 9 N/mm and T_g s from 23°C to 74°C. A cured composition using DETA with a mixture of the three resins was compared to a BPA-based epoxy. The T_g , hardness, adhesion, and solvent resistance by rub test of the three were similar to the BPA epoxy after curing at room temperature for 3 days [125].

Another potential fully bio-based epoxy resin is diglycidyl ethers of diphenolic esters (DGEDP-ester) shown in Fig. 1.6 [126]. The starting materials can be derived from biomass [127] and when cured with IPDA have comparable properties to pure DGEBA for the DGEDP-methyl and ethyl ester resins. Toughness was improved by mixing DGEDP-methyl resin with the NC-514, a cardanol-based epoxy resin. The system was optimized with a 60:40 ratio of DGEDP-methyl to NC-514, which gave a K1c of 2.6 times that of the neat DGEDP-methyl composition. The rheology of the mixed adhesive was modified by dispersing TEMPO-modified cellulose nanocrystals into

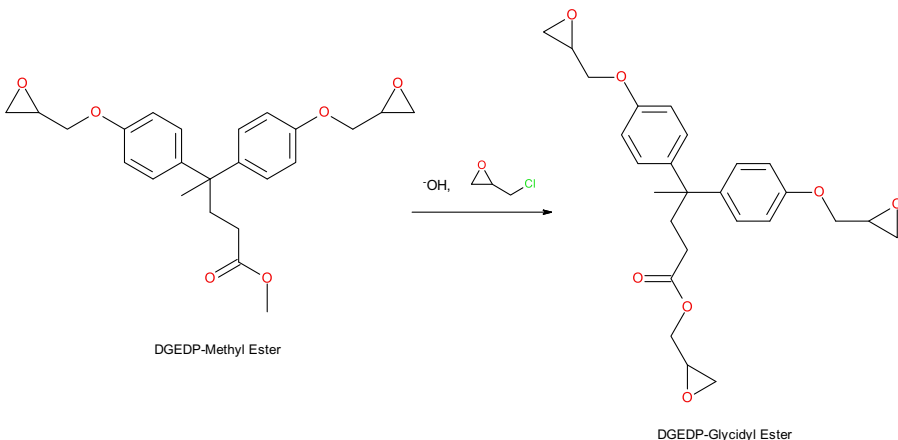


Fig. 1.6 Potential lignin-based epoxy resins.

the 60:40 epoxy resin mixture. This improved sag resistance and cure speed was due to the presence of hydroxyl groups on the CNCs. Using bis-furfurylamine in place of IPDA with 1.0% CNC in the mixed cardanol and diphenolic ester epoxy resins led to an increase in lap shear strength to 20 MPa on 1.5 mm thick 6063-T6 aluminum from about 10 MPa for the IPDA-cured system for what could be produced as a fully bio-based carbon content adhesive.

1.13.2.6 Bisphenol A resin alternatives

The coatings industry, mainly food and beverages along with water infrastructure and marine, is driving the BPA-free resin development due to previously discussed EHS concerns regarding bisphenols, and adhesive compositions can utilize the same resins (Fig. 1.7). One example is 2-methyl-2-phenyl-1,3-propanediol, MPPD, which places an aromatic ring pendant to the resin backbone. These resins have much lower viscosity, a slightly lower EEW, a slower gel time, and a reduced T_g when cured with the same amines as a standard BADGE resin. At 23°C, a stoichiometric amount of IPDA-cured MPPD resin has a gel time of nearly 34 h and a T_g of 86°C versus a gel time of 7.5 h and a T_g of 169°C for Epilox A19-03. As a reactive diluent, the MPPD resin compares favorably to hexanediol diglycidyl ether and alkyl monoglycidyl ether with similar mechanical properties, less of a reduction in T_g , and faster gel times when used at 10% by weight in the BADGE resin cured with MXDA [128]. To increase mechanical properties and thermal stability, resins incorporating multiring structures

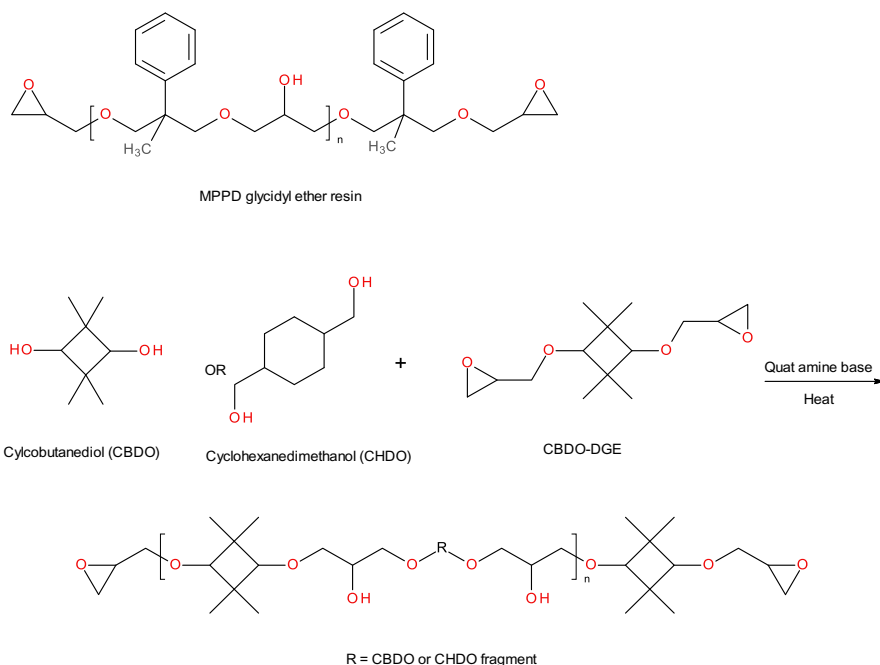


Fig. 1.7 Bisphenol A free epoxy resins.

were developed by Khullar et al. that contain a mix of aromatic, aliphatic, and cycloaliphatic components exclusive of the bisphenol moieties with EEWs ranging from 500 to 25,000 g/equivalent and similar performance to type 7 and type 9 BPA-based resins used in can coatings [129].

Another BPA-free resin based on cycloaliphatic diols exemplifies the diglycidyl ethers of a tetramethyl substituted 1,3-cyclobutanediol (CBDO-DGE) alone and then chain extended with cyclohexanedimethanol. The CBDO-DGE resin when cured with TETA has slightly better lap shear strength and similar hardness compared to a BADGE resin, but a lower T_g and modulus [130,131]. New high-functionality resins based on polyphenols of cyclododecane have $T_{g,s}$ of more than 300°C, rapid onset to cure, and reduced cure enthalpy compared to the diglycidyl ether of diphenol of cyclododecanone resins used in powder coatings, composites, and laminates [132].

1.13.2.7 Curatives

Aditya Birla has the Recyclamine product line of polyamine curing agents that undergo cleavage at specific sites via heat and pH to allow the crosslinked epoxy to convert from a thermoset to a thermoplastic for product recycling [133]. They have also filed a patent application for reworkable and recyclable epoxy resins [134]. The Recyclamine curatives when used with conventional BPA resins have a pot life range of 70 min to more than a day at 23°C with $T_{g,s}$ from 100°C to 130°C.

Faster, more robust curing with secondary amines based on MXDA for epoxy coating applications has been developed primarily due to environmental regulations of VOCs [135,136]. Similar challenges for robust curing with a long open time and highly variable environmental conditions in the wind blade industry have been approached with the addition of *N*-(3-aminopropyl)cyclohexylamine (APCHA) to the curative package [137] and blends of amine curatives that gave the unexpected combination of higher exotherms for faster curing with longer open times [138].

1.13.2.8 Tougheners

As previously discussed, new core-shell rubber powders that disperse more readily into resins and predispersed core-shell rubbers are commercially available in Bisphenol A, F, Novolac, glycidyl amine resins, and cycloaliphatic resins. Predispersed and powdered core-shell rubbers have also been incorporated into the amine curative portion of a two-part adhesive to increase the overall toughener content [139,140]. Polyurethane tougheners such as DY 965 in conjunction with block copolymers such as Fortegra 202 have been shown to give high impact peel resistance of more than 30 N/mm at -40°C [141]. Academic research has explored modifying thermoplastic resin hydroxyl terminated poly(ether ether ketone), PEEK, with urethane linkages to epoxy resins at loadings of 5%–15% in the epoxy resin. The PEEK toughener accelerated the reaction with TETA and the lap shear strength increased from 9 to 16 MPa at 25°C at a 5% loading level due to the increased toughness. Higher loading reduced the lap shear strength due to poor wetting and lower cohesive strength

of the cured adhesive. The increase in lap shear strength over the untoughened composition was also observed at -196°C and 100°C [142]. Chitin nanowhiskers with surface functionality have been incorporated into composites and improve the strength and toughness of the composites [143].

Epoxy adhesives incorporating Arkema's SBM E21, a polystyrene, 1,4-polybutadiene, and syndiotactic poly(methyl methacrylate) block copolymer combined with graphene nanoplatelets functionalized by ozonolysis have shown an increase of 129% in lap shear strength over the pure epoxy on aluminum 2024-T3 [144,145]. Fracture surfaces showed the SBM had worm-like micelles with fracture energies (G_{Ic}) of 300% and 1000% higher than the neat adhesive measurement of $\sim 230\text{J/m}^2$ when used alone and combined with the graphene nanoplatelets, respectively. The spherical micelles formed by MAM M51, a symmetric block copolymer of PMMA, on either side of a poly(butyl acrylate) gave G_{Ic} values of about 100% and 300% higher than the neat adhesive. Epoxy modified with a diblock copolymer, poly(ethylene-*alt*-propylene)-*b*-poly(ethylene oxide) (PEP-PEO), and nanosilica enhanced fracture toughness individually at 25% and 400% of G_{Ic} over the neat epoxy-amine value of 230J/m^2 . Combining the PEP-PEO and nanosilica gave a G_{Ic} increase of 500% [146].

1.13.3 General manufacturing

Sustainability and economics are providing incentives for faster and more energy-efficient curing of composites and adhesives. Induction curing is one approach that can be done with conductive substrates or by incorporating susceptor particles within the adhesive. Temperature control in the bondline was improved by utilizing Curie temperature tuned magnetic nanoparticles (CNP) that switch off heating above the Curie temperature, as discussed in detail in Chapter 30. The CNPs were stabilized with oleic acid and BADGE to prevent agglomeration of the nanoparticles in the formulation [147]. The type and weight of CNP in the adhesive along with the alternating magnetic frequency allowed for a range of temperature control up to 160°C . Light-triggered curing via radical-induced cationic frontal polymerization uses a traditional photoacid generator in conjunction with a radical thermal initiator. The thermal initiator is triggered by the heat of reaction from the light curing, which then drives a thermal front to cure through the bondline. A $500\mu\text{m}$ bondline with a ratio of 60:40 CAE:BADGE resins with a 7–8 s light exposure and less than 10 s total cure time gave equivalent lap shear strength to a thermal cure at 110°C for 60 min on aluminum substrates. The thermal conductivity of the aluminum necessitated heating to 80°C to allow the thermal front to propagate for a full cure. The onset temperature for thermal-only curing was shown by DSC to be about 100°C and conversion at 80°C over 40 min was only 10%–20% depending on the ratio of CAE to BADGE [148]. Light curing of both epoxy amine and epoxy anhydride adhesives incorporating a photosensitizer and photoacid catalyst gave an increase in rate of cure with 405, 785, and 1064 nm light and a range of cure depths for both systems [149,150]. Light-curing and light-activated adhesive films provide application versatility and long shelf life without the need for cold temperature storage [151,152].

Longer shelf life at room temperature, lower temperature curing, and faster curing are common themes in the 1 K paste and film adhesive patent literature. Several film adhesive applications utilize latent amines such as dihydrazides with a variety of accelerators ranging from a clathrate with imidazoles, substituted urones, and combinations thereof that reduce cure time at 150°C, still maintained high T_g s, and have increased the out life at 23°C [153–155]. Two new products from Hexcel, HexPly M77 and HexMC, demonstrate the above attributes which allow for demolding of composites while hot for faster cycle times while the new HexBond 679 is a low thermal curing film for sandwich structures and faster cycle time due to curing at 70°C to 80°C.

1.13.3.1 Automotive

Many of these same sustainability attributes along with toughness and durability are present in automotive adhesive development. Crash-durable adhesives have improved impact resistance as measured by the ISO 11343 wedge impact method down to temperatures of –35°C to –40°C. Newer production 1 K, 2 K, and film adhesives have improved bonding to oily metals, faster curing, lower temperature curing, improved corrosion resistance, and longer shelf life at room temperature. Examples include new hydrophobic tougheners that also help improve dwell time and humidity resistance prior to the bake cycle curing [156], new adducts of monoamines with alcohol functionality combined with a polyurethane toughener [157], combinations of tougheners with block copolymers and polyurethanes [141], lower temperature, and faster curing with room temperature storage stability with latent, encapsulated, or blocked amines [77, 158–160]. Formulations incorporating zinc nanoparticles, amino-salicylic acids, or phosphorus-modified resins have been shown to help the cured adhesive maintain strength over long-term corrosion tests [161–163]. More recently, adhesives can include blowing or expansion agents that activate during the curing cycle and help fill gaps or provide structural strength as a foam [164].

New products SikaPower 550-G, Dupont Betamate 1640, and 3M SAT1010 reflect the improvements in adhesive performance by enabling longer dwell prior to cure with humidity resistance, increased corrosion resistance, or better stress durability performance, a static load with APGE cycling [165–167]. Impact-resistant adhesives have spread to the aftermarket in the form of 2 K adhesives that cure under ambient conditions with the introductions of Fusor 2098 from DuPont, PN07333 from 3M, Teroson EP 5065 from Henkel, Pliogrip 5770R from Ashland, and SEM 39757 over the last decade to help meet the bonding needs when replacing production adhesives in the vehicle repair process.

1.13.3.2 Aerospace

The changes and advances in epoxy adhesives for aerospace include previous areas as well as the bonding of composite structures; lightweight bonding, potting, and shimming; and fire, smoke and toxicity (FST). Antimony and halogens for FST properties are notably being replaced in new products such as Henkel's Loctite EA 9365FST AERO for aircraft interior bonding. Patent literature shows nonhalogen options such

as alumina trihydrate, magnesium hydroxide, molybdate-coated fillers, and expandable graphite, phosphorus, or phosphorus-containing compounds being used for FST properties in void fillers and honeycomb splicing materials [168–172]. Reduced density products for void filling and FST compliant are Huntsman EPOCAST 1648 and 1649 and 3M EC-3550 or flame retardant 3M EC-3542 for potting, edge close-out, and honeycomb bonding. Solvay launched Aeropaste 1006, 1009, and 1100 adhesives with film-like performance in paste form for rapid assembly and tolerance for variable bondline thickness.

Epoxy films are also used to protect the surface of aerospace composites by improving resistance to microcracking from thermal cycling, adding UV and moisture protection as well as protection from lightning, and resistance to paint strippers for refinishing as found in Solvay's SURFACE MASTER 905, 3M's AF 536, and Toray's TC235SF [173,174].

1.13.3.3 Energy, construction, and infrastructure

Adhesives used in construction of large structures need to have long open times, be able to withstand adverse environments, and be able to cure under a wide variety of conditions. Incorporation of waste materials into epoxy mortar was studied where fly ash, slag, and glass could be incorporated at levels greater than 50% without severely comprising adhesion or flexural or compressive strengths [175]. Using peroxide in a two-part tertiary amine accelerated thiol epoxy adhesive, the gel time could range from a matter of 4 min to beyond a full day without negatively affecting the lap shear strength [176].

Bonding underwater and maintaining good adhesion are challenging, but have been improved with a DETA-epoxy system with a catechol-based Mannich base. The DETA functionalized catechol shows better underwater bonding strength similar to dry strength even down to 4°C [177]. The Nanjing Hitech Lica 600 series and Gurit's Spabond series of epoxy adhesives are new products for wind blades and other industrial applications that give faster cycle times and enable the production of larger blades.

1.13.3.4 Electronics and communication

Electronics assembly has been facilitated and advanced by adhesives [178–181]. Adhesive advancements include the development of one-part epoxy adhesives that can be stored for longer times at room temperature, do not suffer waste from mixing two parts, have longer open times at ambient conditions, and cure with lower heating temperature thresholds utilizing thiols with stabilized accelerators or with light where plastics and electronic components will not be damaged [182–187]. The advantages of using a liquid adhesive in electronics include joint design flexibility and sealing components against environmental exposures such as water, sweat, and sunscreen for phones and wearable devices or salty road spray for vehicle cameras. Newer adhesives exhibit rheology characteristics that allow them to be screen-printed, jetted, or stenciled for precise placement and quantity of the adhesive for minimizing bond areas

while maximizing displays. Improved flexibility and toughness help to reduce damage from both thermal and mechanical shocks, especially for mixed material bonding. New products in this area include 3M's Scotch-Weld 6101, a low thermal cure 1K adhesive, and Delo's dual-initiator Katiobond FA light-triggered adhesives.

1.14 Additional resources

As a supplement to the representative information in the tables from technical and supplier literature, reading recommendations for adhesive and raw material information are the books *Epoxy Resins Chemistry and Technology*, May 1988, and *Handbook of Epoxy Resins*, Lee and Neville, 1967. Also included are the chapter Epoxy Resins in *Ullman's Encyclopedia of Industrial Chemistry*, and technical literature from supplier websites of epoxy resins, epoxy functional diluents and modifiers, and curatives including Albemarle, Adeka, Aditya Birla, Alzchem, Arkema, BASF, Bitrez, Bruno Bock, Cardolite, Chang Chun Group, Croda, Daicel, DIC, Evonik, Genesee Polymers Corporation, Huntsman, Kukdo, Mitsubishi, Nagase, Nan Ya Plastics, Nouryon, Olin, Reichold, Rikacid, Shikoku, Shin Etsu, Showa Denko, Solvay, and Westlake Chemical. Major suppliers of adhesives in addition to those companies listed as raw material suppliers are also a useful source of adhesive information and include Delo, DuPont, Gurit, Henkel, Hexcel, Masterbond, PPG, Sika, ThreeBond, and 3M.

Acknowledgments

I am incredibly grateful to my wife, Sheila, for her support, encouragement, and expanded parenting role during the writing of this chapter. Thank you to my teenage sons who also gave me encouragement along with some peace and quiet to write. Thank you to the many colleagues here at 3M, especially Zachary Thompson for thoughtful conversation about epoxy trends; Lianzhou Chen, Yangbin Chen, Mary Caruso Dailey, Sohaib Elgimiabi, Christian Heering, Matthew Kryger, Eike Klünker, and Dmitriy Salnikov for current technology discussions; Jennifer Nelson for help in navigating literature and patent art; Victor Ho for content review; Scarlett Godinez for editing; and the many members of our structural adhesives community from whom I keep learning. Finally, thank you to Elaine Yorkgitis for reaching out with the opportunity and the vision for the chapter.

References

- [1] N. Prileschajew, "Oxydation ungesättigter Verbindungen mittels organischer Superoxyde," *Ber. Dtsch. Chem. Ges.*, vol. 42, no. 4, pp. 4811–4815, 1909, <https://doi.org/10.1002/cber.190904204100>.
- [2] S. Paul, "Manufacture of Amines of High Molecular Weight, Which are Rich in Nitrogen," US2136928A, 1938. Available from: <https://patents.google.com/patent/US2136928A>.
- [3] C. Pierre, "Process of Preparing Synthetic Resins," US2324483A, 1943 Available from: <https://patents.google.com/patent/US2324483A>.
- [4] G.S. Owen, "Synthetic Drying Compositions," US2456408A, 1948. Available from: <https://patents.google.com/patent/US2456408A>.

- [5] G.S. Owen, "Amine-Epoxy Compositions," US2585115A, 1952. Available from: <https://patents.google.com/patent/US2585115A>.
- [6] G.S. Owen, "Amide-Epoxy Compositions, Etc.," US2589245A, 1952. Available from: <https://patents.google.com/patent/US2589245A>.
- [7] G. Alphonse, K. Wilhelm, P. Eduard, W. Gustav, and W. Werner, "Adhesives and Articles United Therewith," US2682490A, 1954. Available from: <https://patents.google.com/patent/US2682490A>.
- [8] P. Philip, "Process for Manufacture of Glycidyl Ethers of Polyhydric Phenols," US2840541A, 1958. Available from: <https://patents.google.com/patent/US2840541A>.
- [9] "Celebrating 75 Years of Epoxy Resins." <https://www.hexion.com/en-us/catalyst/catalyst-blog/2018/05/21/celebrating-75-years-of-epoxy-resins> (Accessed 29 January 2022).
- [10] J.E. Masters, "Manufacture of Epoxy Resins," US2767157A, 1956. Available from: <https://patents.google.com/patent/US2767157A>.
- [11] H.P. Price and D.A. Shimp, "Epoxy Resin Process," US3417050A, 1968. Available from: <https://patents.google.com/patent/US3417050A>.
- [12] J.B. William, "Low Chlorine Content Diglycidyl Ethers," CA802231A, 1968. Available from: <https://patents.google.com/patent/CA802231A>.
- [13] T.L. Caskey, T.L. Parker, and P.H. Martin, "Method of Preparing Epoxy Resins Having Low Hydrolyzable Chloride Contents," US4447598A, 1984. Available from: <https://patents.google.com/patent/US4447598A>.
- [14] J.M. Hunter, "Process for Preparing Epoxy Resins Having Low Hydrolyzable Chlorine Contents," US4535150A, 1985. Available from: <https://patents.google.com/patent/US4535150A>.
- [15] C.S. Wang, R.L. Bowden, and W.N. Chen, "Method for Preparing Advanced Epoxy or Phenoxy Resins with Low Aliphatic Halide Content," US4684701A, 1987. Available from: <https://patents.google.com/patent/US4684701A>.
- [16] C.S. Wang and Z. Liao, "Preparation of Epoxy Resins Having Low Undesirable Halogen Content," US4778863A, 1988. Available from: <https://patents.google.com/patent/US4778863A>.
- [17] A.T. Au and J.L. Nafziger, "Process for Preparation of Epoxy Compounds Essentially Free of Organic Halides," US5578740A, 1996. Available from: <https://patents.google.com/patent/US5578740A>.
- [18] P. Gröppel, "Low Chlorine Content Epoxy Resin," US7582706B2, 2009. Available from: <https://patents.google.com/patent/US7582706B2>.
- [19] G.S. Owen, "Phenol Aldehyde Polyepoxide Compositions and Reaction Products," US2521912A, 1950. Available from: <https://patents.google.com/patent/US2521912A>.
- [20] C.G. Schwarzer, "Polyglycidyl Ethers of Tetraphenols," US2806016A, 1957. Available from: <https://patents.google.com/patent/US2806016A>.
- [21] N.H. Reinking, B.P. Barth, and F.J. Castner, "Glycidyl Derivatives of Amino Phenols," US2951825A, 1960. Available from: <https://patents.google.com/patent/US2951825A>.
- [22] S. Leon, W. John, and N.H. Reinking, "Hardener for Epoxy Resin Composition," US2897179A, 1959. Available from: <https://patents.google.com/patent/US2897179A>.
- [23] E. Phyllis, "Method of Producing a Glycidyl Ester," US2537981A, 1951. Available from: <https://patents.google.com/patent/US2537981A>.
- [24] A.C. Mueller, "Process for Preparing Epoxy Esters," US2772296A, 1956. Available from: <https://patents.google.com/patent/US2772296A>.
- [25] I.H. Updegraff, "Polymerizable Compositions Containing Polyglycidyl Esters of Polycarboxylic Acids," US2781333A, 1957. Available from: <https://patents.google.com/patent/US2781333A>.

- [26] D.R. Smith, "Process for the Preparation of Glycidyl Esters," US3335156A, 1967. Available from: <https://patents.google.com/patent/US3335156A>.
- [27] R. Ackermann, H. Kolb, G. Morlock, and G. Schreyer, "Process for the Production of Glycidyl Methacrylate," US4228084A, 1980. Available from: <https://patents.google.com/patent/US4228084A>.
- [28] F. Nees, P. Werle, G. Reissmann, and W. Merk, "Process for the Production of Aromatic Glycidyl Esters," US4667044A, 1987. Available from: <https://patents.google.com/patent/US4667044A>.
- [29] A.T. Au, "Preparation of Glycidyl Esters," US5036154A, 1991. Available from: <https://patents.google.com/patent/US5036154A>.
- [30] F. Frostick Jr. and B. Phillips, "Diepoxides of Cycloaliphatic Esters," US2716123A, 1955. Available from: <https://patents.google.com/patent/US2716123A>.
- [31] Y. Murata, Y. Nakanishi, and M. Yoshimura, "Process for Producing Biphenol Skeleton-Containing Epoxy Resins," JP3315436B2, 2002. Available from: <https://patents.google.com/patent/JP3315436B2>.
- [32] P. Czubarow, O. Suzuki, and T. Sato, "Underfill for High Density Interconnect Flip Chips," US20120172495A1, 2012. Available from: <https://patents.google.com/patent/US20120172495A1>.
- [33] M. Lichtenwalter and T. Howard, "Production of Linear Polyethylene Polyamines," US3714259A, 1973. Available from: <https://patents.google.com/patent/US3714259A>.
- [34] R.M. Harnden and D.W. Calvin, "Process for the Manufacture of Diethylenetriamine," US4387249A, 1983. Available from: <https://patents.google.com/patent/US4387249A>.
- [35] M. Frauenkron *et al.*, "Method for Producing Ethylene-Amines," US7393978B2, 2008. Available from: <https://patents.google.com/patent/US7393978B2>.
- [36] D.M. Petraitis, S.W. King, and T.Z. Srnak, "Method of Manufacturing Ethyleneamines," US8188318B2, 2012. Available from: <https://patents.google.com/patent/US8188318B2>.
- [37] J.K. Dixon and E.W. Cook, "Production of Aminopropionitriles," US2439359A, 1948. Available from: <https://patents.google.com/patent/US2439359A>.
- [38] M.F. Zuckerman, "Process for the Hydrogenation of Nitriles to Primary Amines," US4739120A, 1988. Available from: <https://patents.google.com/patent/US4739120A>.
- [39] C.T. Kautter, "Production of Monoalkylolamines," US2051486A, 1936. Available from: <https://patents.google.com/patent/US2051486A>.
- [40] D.W. House, R.V. Scott, Jr, and M.J. Gattuso, "Bis(N-Alkylaminocyclohexyl)Methanes as Curing Agents for Polyurethanes and Polyureas," US5312886A, 1994. Available from: <https://patents.google.com/patent/US5312886A>.
- [41] W. Hanson, D. Primeaux, and R. Scott, "Methods of Preparing and Using Polyurea Elastomers," US20070066786A1, 2007. Available from: <https://patents.google.com/patent/US20070066786A1>.
- [42] P.H. Moss, "Nickel-Copper-Chromia Catalyst and the Preparation Thereof," US3152998A, 1964. Available from: <https://patents.google.com/patent/US3152998A>.
- [43] E.L. Yeakey, "Process for Preparing Polyoxyalkylene Polyamines," US3654370A, 1972. Available from: <https://patents.google.com/patent/US3654370A>.
- [44] D.E. Graham, "Catalytic Reduction of Aromatic Polynitro Compounds," US2894036A, 1959. Available from: <https://patents.google.com/patent/US2894036A>.
- [45] R.M. Robinson and R.G. Sundberg, "Catalytic Hydrogenation of Nitroaromatic Compounds to Aromatic Amines," US3194839A, 1965. Available from: <https://patents.google.com/patent/US3194839A>.
- [46] D.A. Dubowik, P.A. Lucas, and A.K. Smith, "Epoxy Resins Cured With Mixed Methylenylene Bridged Poly(Cyclohexyl-Aromatic)Amine Curing Agents," US5280091A, 1994. Available from: <https://patents.google.com/patent/US5280091A>.

- [47] M.M. Renfrew and W. Harold, Thermosetting Resinous Compositions From Epoxy Resins and Polyamides Derived From Polymeric Fat Acids. US2705223A, 1955 Available from: <https://patents.google.com/patent/US2705223A>.
- [48] J.N.S. Kwong, Epoxy Resins Cured With Polyaminopoly-Amides From Diaminopolyethers and Dicarboxylicacids. US3257342A, 1966. Available from: <https://patents.google.com/patent/US3257342A>.
- [49] G.S. Owen, Amide-Epoxy-Phenol Compositions, US2510886A, 1950. Available from: <https://patents.google.com/patent/US2510886A>.
- [50] P. Lowell, Curing Epoxy Resin With an Amino-Poly-Imidazoline, US3002941A, 1961. Available from: <https://patents.google.com/patent/US3002941A>.
- [51] R.A. Gardiner, Polyaminophenol Epoxy Resin Curing Agent, CA1082229A, 1980. Available from: <https://patents.google.com/patent/CA1082229A>.
- [52] Dai Z., Zhang K., and Fu S., A Kind of Modified by Alkyl Phenol Phenolic Aldehyde Amide Hardener and Preparation Method Thereof, CN102633991B, 2016. Available from: <https://patents.google.com/patent/CN102633991B>.
- [53] G.S. Lal and M. Cook, Phenalkamine Epoxy Curing Agents From Methylene Bridged Poly(Cyclohexyl-Aromatic) Amines and Epoxy Resin Compositions Containing the Same, US20210139642A1, 2021. Available from: <https://patents.google.com/patent/US20210139642A1>.
- [54] G.S. Lal, M. Cook, G.A. Vedage, and E. Roumpelakis, Phenalkamine Epoxy Curing Agents and Epoxy Resin Compositions Containing the Same, US20210355270A9, 2021. Available from: <https://patents.google.com/patent/US20210355270A9>.
- [55] G.S. Lal, M. Cook, E. Roumpelakis, and G.A. Vedage, Process for Producing Phenalkamines, US20210188762A1, 2021. Available from: <https://patents.google.com/patent/US20210188762A1>.
- [56] F.G.M. Le, F.Y. Hayashi, and A.W. Fradkin, Thiol Terminated Polyoxyalkylene Glycols, US3258495A, 1966. Available from: <https://patents.google.com/patent/US3258495A>.
- [57] F.G.M. Le and F.Y. Hayashi, Thiol Terminated Liquid Polymers, US3278496A, 1966. Available from: <https://patents.google.com/patent/US3278496A>.
- [58] R.L. Harris and P.H. Goble, Polymercaptans for Curing Epoxy Resins and Method of Preparation Thereof, US4092293A, 1978. Available from: <https://patents.google.com/patent/US4092293A>.
- [59] T. Katoh, H. Kamata, and M. Onishi, Thiol Compound, Photopolymerization Initiator Composition and Photosensitive Composition, US7341828B2, 2008. Available from: <https://patents.google.com/patent/US7341828B2>.
- [60] Y. Urakawa, H. Miyata, I. Yamagami, and K. Murofushi, Epoxy Resin Curing Agent, Process for Preparing the Same, and Epoxy Resin Composition, US8242217B2, 2012. Available from: <https://patents.google.com/patent/US8242217B2>.
- [61] T. Kumano, T. Takeda, and N. Mizobe, Mercaptoalkylglycolurils and Use of Same, US10030023B2, 2018. Available from: <https://patents.google.com/patent/US10030023B2>.
- [62] A. Matsuda, N. Okumura, and T. Kumano, Mercaptoethylglycol Uril Compound and Utilization Thereof, US10550131B2, 2020. Available from: <https://patents.google.com/patent/US10550131B2>.
- [63] D. Otto and A. Kurt, Organic Compound Having Hydrogenated Ring Systems and Process Of Preparing It, US1944731A, 1934. Available from: <https://patents.google.com/patent/US1944731A>.
- [64] R.L. Wear, Aromatic Epoxidized Polyester and Method of Making, US2944035A, 1960. Available from: <https://patents.google.com/patent/US2944035A>.

- [65] P.G. Irwin and C.M. Selwitz, Process for Reacting an Olefin with Maleic Anhydride to Obtain an Alkenyl Succinic Anhydride, US3412111A, 1968. Available from: <https://patents.google.com/patent/US3412111A>.
- [66] E. Yax and M. Zander, Mixture of Homologue Anhydrides of Tetra-Hydrophthalic Anhydride and the Process for Obtaining Same, US3976590A, 1976. Available from: <https://patents.google.com/patent/US3976590A>.
- [67] K. Hideo, K. Inaho, and A. Yasuo, Oxidation Catalysts of Orthoxylene and Naphthalene and the Preparation Thereof, US3215644A, 1965. Available from: <https://patents.google.com/patent/US3215644A>.
- [68] W. Friedrichsen and O. Goehre, Supported Catalysts Containing Vanadium Pentoxide and Titanium Dioxide, US3565829A, 1971. Available from: <https://patents.google.com/patent/US3565829A>.
- [69] J.H. Mccracken and S.J.G. David, Benzophenone-Tetracarboxylic Dianhydrides, US3078279A, 1963. Available from: <https://patents.google.com/patent/US3078279A>.
- [70] J.G.D. Schulz and A. Onopchenko, Process for Preparing 3,4,3,4-Benzophenone-Tetracarboxylic Dianhydride, US4173573A, 1979. Available from: <https://patents.google.com/patent/US4173573A>.
- [71] H. Rögl, Method for Oxidizing a 1,1,-bis-(3,4-Dimethylphenyl)-Alkane to 3,3',4,4'-Benzophenone Tetracarboxylic Acid, US20210179527A1, 2021. Available from: <https://patents.google.com/patent/US20210179527A1>.
- [72] M.M. Bagga and C.H. Bull, Solid Solution of Amine and Polymerized Phenol as Epoxy Resin Cure Accelerator, US4659779A, 1987. Available from: <https://patents.google.com/patent/US4659779A>.
- [73] K. Frick, A. Lutz, and I. Wipf, Two-Component Adhesive of Epoxy Resins and Amine Compound, US7511097B2, 2009. Available from: <https://patents.google.com/patent/US7511097B2>.
- [74] R.L. Wear, Stable Heat-Curing Epoxy Resin Compositions, US2847395A, 1958. Available from: <https://patents.google.com/patent/US2847395A>.
- [75] R.D. Hermansen and S.E. Lau, Adhesive of Flexible Epoxy Resin and Latent Dihydrazide, US6723803B1, 2004. Available from: <https://patents.google.com/patent/US6723803B1>.
- [76] M. Agrawal, S.M. Fisher, and N.K.E. Verghese, Curing Composition for High Heat Adhesive Epoxy Resin, WO2021096654A1, 2021. Available from: <https://patents.google.com/patent/WO2021096654A1>.
- [77] M. Ming et al., Storage-Stable Heat-Activated Tertiary Amine Catalysts for Epoxy Resins, US9951256B2, 2018. Available from: <https://patents.google.com/patent/US9951256B2>.
- [78] W.R. Workman, Photo-Sensitive Compositions and Articles Therefrom, US3074869A, 1963. Available from: <https://patents.google.com/patent/US3074869A>.
- [79] J.V. Crivello and S.H. Schroeter, Photocurable compositions and methods, US4026705A, 1977. Available from: <https://patents.google.com/patent/US4026705A>.
- [80] J.V. Crivello, Photocurable Compositions Containing Group via Aromatic Onium Salts, US4058401A, 1977. Available from: <https://patents.google.com/patent/US4058401A>.
- [81] D.E. Albrecht, Photocurable Epoxy Composition Having Improved Flexibility Comprising Vinyl Terminated Acrylonitrile-Butadiene Polymer, US4219377A, 1980. Available from: <https://patents.google.com/patent/US4219377A>.
- [82] J.V. Crivello and B.A. Ashby, Method of Adhesive Bonding Using Visible Light Cured Epoxies, US4356050A, 1982. Available from: <https://patents.google.com/patent/US4356050A>.

- [83] J. Smith, Latent Organic Phosphonium Salt Catalysts for Curing Glycidyl Ether Epoxy Resins, US3784583A, 1974. Available from: <https://patents.google.com/patent/US3784583A>.
- [84] J.D.B. Smith, Quaternary phosphonium compound latent accelerators for anhydride-cured epoxy resins, in *Epoxy Resin Chemistry*, vol. 114, American Chemical Society, 1979, pp. 47–56. <https://doi.org/10.1021/bk-1979-0114.ch003>.
- [85] S. Livi, Epoxy/Reinforcing Polymer Composite Material and Its Method of Preparation, US11034833B2, 2021. Available from: <https://patents.google.com/patent/US11034833B2>.
- [86] P. Janssen, W. Vogt, and H. Richtzenhain, Epoxy Resin Hardening Process Using Inorganic Metal Salt Accelerators, US3492269A, 1970. Available from: <https://patents.google.com/patent/US3492269A>.
- [87] J.M. Baldwin and J. Robins, Epoxy Adhesive Composition Comprising a Calcium Salt and Mannich Base, US5629380A, 1997. Available from: <https://patents.google.com/patent/US5629380A>.
- [88] J. Robins and C.D. Wright, Fast Curing Epoxy Resin Compositions, US4668736A, 1987. Available from: <https://patents.google.com/patent/US4668736A>.
- [89] H. Lee and K. Neville, *Handbook of Epoxy Resins*. New York: McGraw-Hill, 1967.
- [90] M.D. Gilbert, N.S. Schneider, and W.J. MacKnight, Mechanism of the dicyandiamide/epoxide reaction, *Macromolecules*, vol. 24, no. 2, pp. 360–369, 1991, <https://doi.org/10.1021/ma00002a004>.
- [91] C.R. Costin, G.W. Ceska, and M.A. Bailey, Coating Composition of Epoxy Resin, Metal Di(Meth)Acrylate and Poly(Meth)Acrylate, US5656703A, 1997. Available from: <https://patents.google.com/patent/US5656703A>.
- [92] V.C. Marhevka, A.L. Griggs, and K.S. Tarbuton, Epoxy Adhesives with Dithioamide Adhesion Promoters, US5712039A, 1998. Available from: <https://patents.google.com/patent/US5712039A>.
- [93] K.J. Abbey and M.W. Pressley, Thiol-Cured Epoxy Composition, US6153719A, 2000. Available from: <https://patents.google.com/patent/US6153719A>.
- [94] J.C.J. Warnsdorfer, Method for Indicating Complete Mixing of Epoxy Resin and Amine Hardener and Compositions Resulting Therefrom, US3030329A, 1962. Available from: <https://patents.google.com/patent/US3030329A>.
- [95] G. Zaffaroni, A. Talamini, and M. Nosedà, Indicator for Cure of Two-Component-Epoxy Adhesives, US9315698B2, 2016. Available from: <https://patents.google.com/patent/US9315698B2>.
- [96] A. Lühning, Epoxy Resin System with Visual Control of the State of Curing, WO2012123403A1, 2012. Available from: <https://patents.google.com/patent/WO2012123403A1>.
- [97] A.T. Jung, Color Indicating Epoxy Resins and Methods Thereof, US8975312B2, 2015. Available from: <https://patents.google.com/patent/US8975312B2>.
- [98] R.K. Ddamulira, Cure signaling Adhesive, US10160887B1, 2018. Available from: <https://patents.google.com/patent/US10160887B1>.
- [99] A.T. Jung, M. Bardts, and D. Hasenberg, Two-Part Adhesive Composition That Undergoes a Visual Change When Cured, US11198802B1, 2021. Available from: <https://patents.google.com/patent/US11198802B1>.
- [100] K.W. Lienert, M. Busi, N. Colombi, A. Pederzani, and P. Gherardi, Epoxy Resin Curing Indicator Composition, US8809422B2, 2014. Available from: <https://patents.google.com/patent/US8809422B2>.
- [101] H.-J. Weippert, Amine-Catalyzed Thiol-Curing of Epoxide Resins, US10179831B2, 2019. Available from: <https://patents.google.com/patent/US10179831B2>.

- [102] R. Friedland, V. Ritter, and J. Stahl, Compressible, UV or Thermally Activated (Semi) Structural Adhesive Film with Color Change After Activation and Curing, DE102019004662A1, 2021. Available from: <https://patents.google.com/patent/DE102019004662A1>.
- [103] F. Hu, S.K. Yadav, J.J.L. Scala, J.M. Sadler, and G.R. Palmese, Preparation and characterization of fully furan-based renewable thermosetting epoxy-amine systems, *Macromol. Chem. Phys.*, vol. 216, no. 13, pp. 1441–1446, 2015.
- [104] J.K. Cho et al., Furan-Based Curable Compound Derived From Biomass, Solvent-Free Curable Composition, and Method for Preparing Same, US9035018B2, 2015. Available from: <https://patents.google.com/patent/US9035018B2>.
- [105] C. Buffe and M. Ibert, Process for Manufacturing Furanic Glycidyl Ethers Compositions, Compositions Obtained and Uses Thereof, FR3021656B1, 2017. Available from: <https://patents.google.com/patent/FR3021656B1>.
- [106] D.C. Webster, M.P. Sibi, C.A. Sutton, D.J. Kalita, and E.M. Serum, Novel bio-Based Diols From Sustainable Raw Materials, Uses Thereof to Make Diglycidyl Ethers, and Their Coatings, WO2021007171A1, 2021. Available from: <https://patents.google.com/patent/WO2021007171A1>.
- [107] S.Y. Lee and H.S. Lee, Furfuryl Alcohol-Derived Bifunctional Furan Epoxy and Method for Producing Same, US20210355267A1, 2021. Available from: <https://patents.google.com/patent/US20210355267A1>.
- [108] C. Urban and N. Schäffeler, Furan-Based Amines as Curing Agents for Epoxy Resins in Low VOC Applications, US10287389B2, 2019. Available from: <https://patents.google.com/patent/US10287389B2>.
- [109] J. Deng, X. Liu, C. Li, Y. Jiang, and J. Zhu, Synthesis and properties of a bio-based epoxy resin from 2,5-furandicarboxylic acid (FDCA), *RSC Adv.*, vol. 5, no. 21, pp. 15930–15939, 2015, <https://doi.org/10.1039/C5RA00242G>.
- [110] C. Buffe, J.-P. Pascault, L.R. Meizoso, P.P. Gonzales, and S.P. Abuin, Use of a Composition of Low-Viscosity Bis-Anhydrohexitol Ethers as a Reactive Diluent for Crosslinkable Resin, Adhesive, Coating and Matrix Compositions for Composites, US10913817B2, 2021. Available from: <https://patents.google.com/patent/US10913817B2>.
- [111] H.S. Lee and J.I. Kim, Highly Functional Natural Material-Derived Epoxy Resin, Preparation Method Thereof, and Epoxy Resin Curing Composition Using Same, US10392468B2, 2019. Available from: <https://patents.google.com/patent/US10392468B2>.
- [112] R. Saint-Loup and A. Sahut, Epoxy Resin Comprising Isosorbide Epoxy, FR3102987A1, 2021. Available from: <https://patents.google.com/patent/FR3102987A1>.
- [113] K. Owusu-Adom, K.M. Lewandowski, J.E. Janoski, and M.A. Kropp, Oxirane-Containing Bisanhydrohexitol Derivatives and Uses Thereof, US9932438B2, 2018. Available from: <https://patents.google.com/patent/US9932438B2>.
- [114] K. Owusu-Adom, K.M. Lewandowski, and J.E. Janoski, Mercapto-Containing Bisanhydrohexitol Derivatives and Uses Thereof, US9388274B2, 2016. Available from: <https://patents.google.com/patent/US9388274B2>.
- [115] D.C. Webster, P.P. Sengupta, Z. Chen, X. Pan, and A. Paramarta, Highly Functional Epoxidized Resins and Coatings, US10907008B2, 2021. Available from: <https://patents.google.com/patent/US10907008B2>.
- [116] E.D. Hernandez, A.W. Bassett, J.M. Sadler, J.J. La Scala, and J.F. Stanzione, Synthesis and characterization of bio-based epoxy resins derived from vanillyl alcohol, *ACS Sustainable Chem. Eng.*, vol. 4, no. 8, pp. 4328–4339, 2016, <https://doi.org/10.1021/acssuschemeng.6b00835>.

- [117] S. Nikafshar et al., A renewable bio-based epoxy resin with improved mechanical performance that can compete with DGEBA, RSC Adv., vol. 7, no. 14, pp. 8694–8701, 2017, <https://doi.org/10.1039/C6RA27283E>.
- [118] E. Feghali, D.J. van de Pas, and K.M. Torr, Toward bio-based epoxy thermoset polymers from depolymerized native lignins produced at the pilot scale, Biomacromolecules, vol. 21, no. 4, pp. 1548–1559, 2020, <https://doi.org/10.1021/acs.biomac.0c00108>.
- [119] N. Van de Velde et al., Bio-based epoxy adhesives with lignin-based aromatic monophenols replacing bisphenol A, Polymers (Basel), vol. 13, no. 22, p. 3879, 2021, <https://doi.org/10.3390/polym13223879>.
- [120] E. Savonnet, E. Grau, S. Grelier, B. Defoort, and H. Cramail, Divanillin-based epoxy precursors as DGEBA substitutes for biobased epoxy thermosets, ACS Sustain. Chem. Eng., vol. 6, no. 8, pp. 11008–11017, 2018, <https://doi.org/10.1021/acssuschemeng.8b02419>.
- [121] F. Ng, G. Couture, C. Philippe, B. Boutevin, and S. Caillol, Bio-based aromatic epoxy monomers for thermoset materials, Molecules, vol. 22, no. 1, p. E149, 2017, <https://doi.org/10.3390/molecules22010149>.
- [122] M. Fache, R. Auvergne, B. Boutevin, and S. Caillol, New vanillin-derived diepoxy monomers for the synthesis of biobased thermosets, Eur. Polym. J., vol. 67, pp. 527–538, 2015, <https://doi.org/10.1016/j.eurpolymj.2014.10.011>.
- [123] M. Fache, A. Viola, R. Auvergne, B. Boutevin, and S. Caillol, Biobased epoxy thermosets from vanillin-derived oligomers, Eur. Polym. J., vol. 68, pp. 526–535, 2015, <https://doi.org/10.1016/j.eurpolymj.2015.03.048>.
- [124] K.H. Reno, J.F.S. Iii, R.P. Wool, J.M. Sadler, J.J. LaScala, and E.D. Hernandez, Bisphenol Alternative Derived From Renewable Substituted Phenolics and Their Industrial Application, US10723684B2, 2020. Available from: <https://patents.google.com/patent/US10723684B2>.
- [125] J. Zhang and T. Liu, Vegetable Oil-Derived Epoxy Compositions Having Improved Performance, US20210371579A1, 2021. Available from: <https://patents.google.com/patent/US20210371579A1>.
- [126] A. Patel et al., Design and formulation of a completely biobased epoxy structural adhesive, ACS Sustain. Chem. Eng., vol. 7, no. 19, pp. 16382–16391, 2019, <https://doi.org/10.1021/acssuschemeng.9b03489>.
- [127] A. Maiorana, S. Spinella, and R.A. Gross, Bio-based alternative to the diglycidyl ether of bisphenol A with controlled materials properties, Biomacromolecules, vol. 16, no. 3, pp. 1021–1031, 2015, <https://doi.org/10.1021/acs.biomac.5b00014>.
- [128] U. Karl, M. Charrak, H.-J. Thomas, and N. Marion, Diglycidyl Ethers of 2-Phenyl-1,3-Propanediol Derivatives and Oligomers Thereof as Curable Epoxy Resins, US9150685B2, 2015. Available from: <https://patents.google.com/patent/US9150685B2>.
- [129] A. Khullar et al., A Modified Epoxy Resin, WO2021024033A1, 2021. Available from: <https://patents.google.com/patent/WO2021024033A1>.
- [130] D. Schmidt, Bisphenol A (BPA) Free Epoxy Resins, US9139690B2, 2015. Available from: <https://patents.google.com/patent/US9139690B2>.
- [131] D. Schmidt, Bisphenol A (BPA) Free Epoxy Resins, US9434867B2, 2016. Available from: <https://patents.google.com/patent/US9434867B2>.
- [132] R.E. Hefner, Jr and E.J. Molitor, Preparation and Uses of Epoxy Resins of Cyclododecane Polyphenols, US9487617B2, 2016. Available from: <https://patents.google.com/patent/US9487617B2>.
- [133] Recyclamine. <https://www.adityabirlachemicals.com/brand/recyclamine> (Accessed 01 May 2022).

- [134] C.K. Singh, P.K. Dubey, W. Sripet, and K. Sittipumpongkol, Recyclable and Reworkable Epoxy Resins, US20210363287A1, 2021. Available from: <https://patents.google.com/patent/US20210363287A1>.
- [135] F.H. Walker, R.M.T. Rasing, G.A. Vedage, M.I. Cook, and P.A. Lucas, Curing Agent of N,N'-Dimethyl-Meta-Xylylenediamine and Multifunctional Amin(s), US8512594B2, 2013. Available from: <https://patents.google.com/patent/US8512594B2>.
- [136] E. Kasemi, A. Kramer, U. Stadelmann, and U. Burckhardt, Amine for Low-Emission Epoxy Resin Products, US9580381B2, 2017. Available from: <https://patents.google.com/patent/US9580381B2>.
- [137] M.T.A. van Gorkom and E.J. Tjisma, APCHA as a Building Block in Curing Agent Formulations for Structural Adhesives, US10253225B2, 2019. Available from: <https://patents.google.com/patent/US10253225B2>.
- [138] F. Sharp and T. Bonser, Epoxy Resin Adhesives, WO2021048282A1, 2021. Available from: <https://patents.google.com/patent/WO2021048282A1>.
- [139] L. Chen, J.S. Schlechte, G.S. Stout, and R.J. Squires, Two-Part Adhesive Including Toughened Curative, US10329464B2, 2019. Available from: <https://patents.google.com/patent/US10329464B2>.
- [140] L. Chen, S. Elgimiabi, D. Salnikov, J.S. Schlechte, and Y. Chen, Curable Composition, WO2021220090A1, 2021. Available from: <https://patents.google.com/patent/WO2021220090A1>.
- [141] G.L. Jialanella, A. Lutz, E.E. Cole, G.G. Eagle, R.H. Turakhia, and Y. Feng, Crash Durable Epoxy Adhesive Compositions Having Improved Low-Temperature Impact Resistance and Wash Off Resistance, US10392539B2, 2019. Available from: <https://patents.google.com/patent/US10392539B2>.
- [142] L. Karthikeyan, T.M. Robert, D. Desakumaran, N. Balachandran, and D. Mathew, Epoxy terminated, urethane-bridged poly (ether ether ketone) as a reactive toughening agent for epoxy resins, *Int. J. Adhes. Adhes.*, vol. 112, p. 102983, 2022, <https://doi.org/10.1016/j.ijadhadh.2021.102983>.
- [143] M. Wang, H. Xue, Z. Feng, B. Cheng, and H. Yang, Increase of tensile strength and toughness of bio-based diglycidyl ether of bisphenol A with chitin nanowhiskers, *PLoS ONE*, vol. 12, no. 6, p. e0177673, 2017, <https://doi.org/10.1371/journal.pone.0177673>.
- [144] J. Panta, Y.X. Zhang, A.N. Rider, J. Wang, R. Wuhrer, and B.G. Prusty, High-performance epoxy-based adhesives modified with functionalized graphene nanoplatelets and triblock copolymers, *Int. J. Adhes. Adhes.*, vol. 98, p. 102521, 2020, <https://doi.org/10.1016/j.ijadhadh.2019.102521>.
- [145] J. Panta, Y.X. Zhang, A.N. Rider, and J. Wang, Ozone functionalized graphene nanoplatelets and triblock copolymer hybrids as nanoscale modifiers to enhance the mechanical performance of epoxy adhesives, *Int. J. Adhes. Adhes.*, vol. 116, p. 103135, 2022, <https://doi.org/10.1016/j.ijadhadh.2022.103135>.
- [146] V. Pang, Z.J. Thompson, G.D. Joly, L.F. Francis, and F.S. Bates, Block copolymer and nanosilica-modified epoxy nanocomposites, *ACS Appl. Polym. Mater.*, vol. 3, no. 8, pp. 4156–4167, 2021, <https://doi.org/10.1021/acsapm.1c00619>.
- [147] R. Chaudhary, V. Chaudhary, R.V. Ramanujan, and T.W.J. Steele, Magnetocuring of temperature failsafe epoxy adhesives, *Appl. Mater. Today*, vol. 21, p. 100824, 2020, <https://doi.org/10.1016/j.apmt.2020.100824>.
- [148] M. Turani, A. Baggio, V. Casalegno, M. Salvo, and M. Sangermano, An epoxy adhesive crosslinked through radical-induced cationic frontal polymerization, *Macromol. Mater. Eng.*, vol. 306, no. 12, p. 2100495, 2021, <https://doi.org/10.1002/mame.202100495>.

- [149] P. Garra et al., Ultrafast epoxy–amine photopolyaddition, *Macromolecules*, vol. 51, no. 24, pp. 10230–10236, 2018, doi: <https://doi.org/10.1021/acs.macromol.8b02340>.
- [150] H. Mokbel, F. Dumur, and J. Lalevée, On demand NIR activated photopolyaddition reactions, *Polym. Chem.*, vol. 11, no. 26, pp. 4250–4259, 2020, doi: <https://doi.org/10.1039/D0PY00639D>.
- [151] C.A. Anderson, T.Q. Chastek, X. Gao, K.S. Shafer, and S. Ye, Methods of Bonding Hardware to Vehicular Glass, US10927276B2, 2021. Available from: <https://patents.google.com/patent/US10927276B2>.
- [152] P. Kopf and O. Kuehl, Adhesive Film That can be Wound and Stamped, US20200040237A1, 2020. Available from: <https://patents.google.com/patent/US20200040237A1>.
- [153] C. Harrington and V. Burton, Adhesive Compositions, US9932503B2, 2018. Available from: <https://patents.google.com/patent/US9932503B2>.
- [154] N. Verge and T. Ganglberger, Improved Curative Composition, EP3794053A1, 2021. Available from: <https://patents.google.com/patent/EP3794053A1>.
- [155] C.R. Mason and N. Verge, Improvements in or Relating to Curing Agents, US20210198420A1, 2021. Available from: <https://patents.google.com/patent/US20210198420A1>.
- [156] A. Lutz, D. Schneider, J. Flueckiger, and F. Koch, One-Component Toughened Epoxy Adhesives with Improved Humidity Resistance, WO2020256902A1, 2020. Available from: <https://patents.google.com/patent/WO2020256902A1>.
- [157] T. Auvil, G.L. Jialanella, B. Krishnan, F. Koch, and E.E. Cole, Epoxy Adhesive Having Improved Low-Temperature Impact Resistance, WO2018081032A1, 2018. Available from: <https://patents.google.com/patent/WO2018081032A1>.
- [158] I. Miller, M. Czaplicki, and M. Awkal, Relating to Thermosetting Adhesive Films, US10577523B2, 2020. Available from: <https://patents.google.com/patent/US10577523B2>.
- [159] C. Holtgrewe, P. Walter, T. Bachon, and R. Schoenfeld, Storage Stable Heat Activated Quaternary Ammonium Catalysts for Epoxy Cure, US10179832B2, 2019. Available from: <https://patents.google.com/patent/US10179832B2>.
- [160] U. Schumann, N. Buggy, S. Dietze, and K. Elsenbach, Thermally Curing Adhesive and Adhesive Tape Produced Therefrom, US20210002521A1, 2021. Available from: <https://patents.google.com/patent/US20210002521A1/en/>.
- [161] F. Koch, A. Lutz, C. Grossnickel, and J. Flueckiger, One-Component Toughened Epoxy Adhesives, US20210130663A1, 2021. Available from: <https://patents.google.com/patent/US20210130663A1>.
- [162] F. Koch, A. Lutz, B. Steiner, C. Grossnickel, and J. Flueckiger, Epoxy Resin Adhesive Compositions, US20210062054A1, 2021. Available from: <https://patents.google.com/patent/US20210062054A1>.
- [163] H. Wu, T. Bachon, R. Schonfeld, X. Lin, and Z. Cao, One-Part Curable Adhesive Composition and the Use Thereof, US10280346B2, 2019. Available from: <https://patents.google.com/patent/US10280346B2>.
- [164] K. Frick, U. Gerber, and J. Finter, Polyester Prepolymers as Impact Modifiers in Epoxy Formulations, US10273326B2, 2019. Available from: <https://patents.google.com/patent/US10273326B2>.
- [165] T. Davidson, *Advanced structural adhesives keep pace with vehicle bodies of the future*, *Automot. Ind.*, vol. 199, no. 2, pp. 50–51, 2020.
- [166] BETAMATE™ 1640. <https://dupont.materialdatacenter.com/products/datasheet/SI/BETAMATE%E2%84%A2%201640> (Accessed 01 February 2022).

- [167] 3M™ Structural Adhesive Tape SAT1010. https://www.3m.com/3M/en_US/p/d/b40063157/ (Accessed 01 May 2022).
- [168] S. Elgimiabi and F. Neuroth, Hot/Wet Resistant Low Density Epoxy Compositions, US11091629B2, 2021. Available from: <https://patents.google.com/patent/US11091629B2>.
- [169] S. Elgimiabi, Thermal Cycling Resistant Low Density Composition, US20200347260A1, 2020. Available from: <https://patents.google.com/patent/US20200347260A1>.
- [170] E.H. Ebersohl and M. Awkal, Honeycomb Core Splice Adhesive with Improved Fire Retardancy, US20210054239A1, 2021. Available from: <https://patents.google.com/patent/US20210054239A1>.
- [171] O. Lemoine, M. Winkler, N. Parent, and M. Awkal, Low Density Flame Retardant Two-Component Composition for Structural Void Filling, WO2021165304A1, 2021. Available from: <https://patents.google.com/patent/WO2021165304A1>.
- [172] S. Elgimiabi and F. Neuroth, Room Temperature Stable One-Part Void Filler, US20220017684A1, 2022. Available from: <https://patents.google.com/patent/US20220017684A1>.
- [173] S.A. Boyd, D. Salnikov, and D.T. Amos, Epoxy Compositions and Surfacing Films Therefrom, US10865271B2, 2020. Available from: <https://patents.google.com/patent/US10865271B2>.
- [174] J.J. Sang and D.K. Kohli, Surfacing film for Composite Structures and Method of Making the Same, US9676961B2, 2017. Available from: <https://patents.google.com/patent/US9676961B2>.
- [175] R. Hermann, P. Figala, L. Mészárosová, and R. Drochytka, Study of polymer-based adhesive mortar with higher durability, IOP Conf. Ser. Mater. Sci. Eng., vol. 1209, no. 1, p. 012038, 2021, doi: <https://doi.org/10.1088/1757-899x/1209/1/012038>.
- [176] H. Wu, R. Schoenfeld, N. Fay, and J. Zhang, Gel Time Controllable Two Part Epoxy Adhesive, US9371475B2, 2016. Available from: <https://patents.google.com/patent/US9371475B2>.
- [177] G. Li et al., Biomimetic epoxy adhesive capable of large-scale preparation: from structural underwater bonding to hydrothermal durability, Chem. Eng. J., vol. 431, p. 134011, 2022, doi: <https://doi.org/10.1016/j.cej.2021.134011>.
- [178] M.C. Sesti, R.A. Devota, Y. Lu, S.V. Byrne, and J.S. Gibson, Vehicular Camera and Lens Assembly and Method of Manufacturing Same, US10917548B2, 2021. Available from: <https://patents.google.com/patent/US10917548B2>.
- [179] S.R. McClure, J.D. Banko, K.D. Gibbs, B.M. Rappoport, and J.P. Ternus, Component Assembly, US10642316B2, 2020. Available from: <https://patents.google.com/patent/US10642316B2>.
- [180] J.S. Steckel et al., Light Emitting Structure to Aid LED Light Extraction, US11217567B2, 2022. Available from: <https://patents.google.com/patent/US11217567B2>.
- [181] F.W. Ow, P.C. Hrudehy, Y.-C. Hsu, A.D. Minervini, J.K. Queeney, and T.Q. Ashcroft, Sensor Assembly for Electronic Device, US11228846B2, 2022. Available from: <https://patents.google.com/patent/US11228846B2>.
- [182] A. Zillessen, S. Roediger, B. Sueveges, and R. Born, Light-Fixable and Heat-Curing Compounds Based on Epoxy Resins and Thiols, US20200385513A1, 2020. Available from: <https://patents.google.com/patent/US20200385513A1>.
- [183] K. Iwaya and F. Arai, Resin Composition, US9926405B2, 2018. Available from: <https://patents.google.com/patent/US9926405B2>.

-
- [184] B. Burns and J. Wigham, Epoxy-Thiol Compositions With Improved Stability, KR101898742B1, 2018. Available from: <https://patents.google.com/patent/KR101898742B1>.
- [185] Y. Lin, H. Sahouani, and G.D. Joly, Epoxy Stabilization Using Metal Nanoparticles and Nitrogen-Containing Catalysts, and Methods, US11053348B2, 2021. Available from: <https://patents.google.com/patent/US11053348B2>.
- [186] M.A. Kropp and M.J. Kryger, Epoxy Stabilization Using Substituted Barbituric Acids, WO2018109617A1, 2018. Available from: <https://patents.google.com/patent/WO2018109617A1>.
- [187] R. Deisling, S. Rödiger, M. Ehret, and A. Zillessen, Light-Fixation and Moisture-Cured Masses Based on Epoxy Resins and Thiols, WO2021115881A1, 2021. Available from: <https://patents.google.com/patent/WO2021115881A1>.

This page intentionally left blank

Advances in acrylic structural adhesives*

2

Jian-ping (JP) Huang[#] and John Lean

Parker Lord Corporation, Engineered Materials Group, Assembly & Protection Solutions Division, Cary, NC, United States

2.1 Introduction

Structural adhesives are adhesives that join two substrates together, and once cured, they become a structural element of the composite part. Acrylic structural adhesives are two-component adhesives based on acrylate and methacrylate monomers, often toughened with a rubber additive to improve flexibility and impact resistance. One component of the adhesive contains the accelerator, and the other component contains the initiator. When the two components are mixed, free radicals are formed, initiating the polymerization of the acrylic monomers. Traditionally, methyl methacrylate (MMA) has been the monomer of choice for acrylic structural adhesives because of its cost, reaction speed, solvation properties, and excellent adhesive performance. This chapter will discuss the basic chemistry, types, physical properties, and applications of acrylic structural adhesives specifically related to two-component, 100% solid methacrylate-based adhesives. The authors will not discuss anaerobic acrylic adhesives, cyanoacrylate adhesives, solution acrylic adhesives, or water-based acrylic adhesives. The first two of these are addressed in [Chapter 4](#) and [Chapter 5](#), respectively.

2.1.1 Historical perspective

Acrylic structural adhesives were initially developed in the 1950s, and their history has been well documented in previous publications [1,2]. After 70 years of use in industry, acrylic structural adhesives may be considered a mature technology. However, trends in industrial assembly such as bonding dissimilar substrates, elimination of fasteners, and higher corrosion resistance standards have led to acrylic structural adhesives being an excellent fit for many applications. Acrylic structural adhesives are attractive because of their ability to bond unprepared substrates and dissimilar substrates as well as cure rapidly at room temperature. They also offer cost advantages, multiple suppliers, and proven performance. Current major global suppliers of acrylic structural adhesives are ITW Plexus, Henkel, 3M, Sika, and Parker LORD. From 2020 to 2030, acrylic structural adhesives are expected to grow at an annual rate of 7.6%

* Both contributors are no longer affiliated with LORD Corporation.

[#] Retired.

globally, with the highest expected use in North America, Europe, and Asia based on current industrial output [3]. The Asia-Pacific region has the highest use of acrylic structural adhesives, followed by North America and Europe. In 2020, the Asia-Pacific, North America, and European regions were expected to use approximately 226.7 kilotonnes, 127.5 kilotonnes, and 120.0 kilotonnes, respectively, of acrylic structural adhesives. The total amount of acrylic structural adhesives used is expected to grow to 981.7 kilotonnes by 2030.

2.1.2 Acrylic structural adhesive types [4]

2.1.2.1 Untoughened MMA-based acrylic adhesive

First-generation acrylic adhesives were invented in the 1950s, and initially, MMA was the primary component of the formulation. Some higher molecular weight polymers such as polymethyl methacrylate (PMMA) and polystyrene (PST) were dissolved in the monomer and carried into the adhesive for performance enhancement. A redox initiation system was used for convenient ambient temperature cure. Given the high T_g of PMMA homopolymer (105°C), the cured adhesive matrix was hard but brittle; it tended to shatter in low-temperature applications. Its lack of toughness and flexibility led to second-generation acrylic adhesives.

2.1.2.2 Toughened MMA-based acrylic adhesive

In the 1970s, second-generation acrylic adhesives emerged, overcoming the shortcomings of the first generation by incorporating toughening agents. The types of tougheners included:

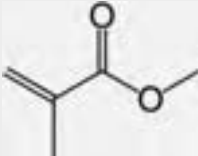
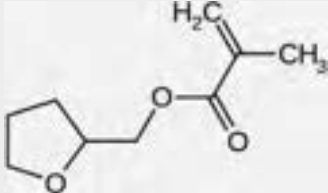
- Powdery rubbers (crosslinked polybutadiene, acrylonitrile-butadiene rubber).
- Core-shell impact modifiers (rubber particles having a PMMA shell with a polybutadiene core).
- Methacrylate-functionalized liquid rubbers.
- Random copolymers of acrylonitrile-butadiene-styrene (ABS) elastomers.

A common feature of these tougheners is that they have rubber segments with low glass transition temperatures, ranging from -50°C to -80°C . As these rubbery components stay flexible and resilient at low temperatures, they are capable of absorbing impact energy by retaining the matrix's compressibility. Toughening mechanisms will be addressed in [Chapter 8](#) of this book.

2.1.2.3 Toughened THFMA-based acrylic adhesive

Through the 1970s and early 1990s, second-generation acrylic adhesives successfully extended their applications to industries such as metal furniture, recreational marine, recreational vehicles, and other truck and trailer assemblies as well as automotive aftermarket repair. However, the flammability, high vapor pressure, and pungent odor of MMAs prevented them from being used in the automotive assembly setting, where MMA vapor could potentially catch fire from welding sparks. There was a strong need for a nonflammable acrylic adhesive.

Table 2.1 Physical properties of MMA vs THFMA.

Property	MMA	THFMA
CAS #	80-62-6	2455-24-5
Structure		
Molecular weight	100.12	170.21
Boiling point (°C)	100.5/760 mmHg	59–62/0.6 mmHg
Flashpoint (°C)	10	91
Vapor pressure	38.5 mmHg	0.16100 mmHg
Tg homopolymer (°C)	100–105	65–70

Tetrahydrofurfuryl methacrylate (THFMA) (Table 2.1) fits the bill. THFMA is a high boiling point, high flash point, nonflammable, low vapor pressure, and low odor methacrylate monomer. THFMA readily polymerizes and is reactive with multiple other methacrylate monomers. When toughened, this acrylic adhesive possesses robust initial properties and good environmental properties. In comparison, THFMA-based adhesives have a lower Tg and are thus generally tougher than MMA-based systems. Their disadvantages compared to MMA are lower solvency power on plastics, and less desirable air inhibition layers on the cured adhesive surface.

The LORD Corporation introduced successful, THFMA-based, toughened acrylic adhesives with the Versilok line (4:1 by volume ratio) of acrylic structural adhesives to various automotive original equipment manufacturers (OEM) and stamping plants around 1994–95 [5,6]. Around 2000, this technology was adopted by some European automakers for its outstanding dimensional accuracy and stability when going through the e-coat and paint bake processes. LORD Versilok acrylic structural adhesive line has since become a major metal bonder alongside 1 K- and 2 K-epoxy adhesives, having served the automotive industry for nearly three decades. In addition, 3M's Scotch Weld DP 810 has found utilizations in the HVAC industry, assembling industrial and residential air handling units. In addition to liquid rubber tougheners, the triblock copolymers of styrene-butadiene/isoprene-styrene have begun to play an effective role as auxiliary tougheners in acrylic structural adhesive systems.

2.1.2.4 Environmental, health, and safety-friendlier acrylic structural adhesives

In the past couple of decades, adhesive operators have gained more awareness of environmental, health, and safety (EH&S) compliance while using chemical supplies [7,8]. Major complaints included the offensive odor of MMA and methyl acrylic acid (MAA) as well as the flammability of MMA. In the mid-2010s, tetrahydrofurfuryl methacrylate

(THFMA) was classified as a reproductive toxin. This has generated a demand for THFMA-free counterparts. Formulators have searched for and tested numerous low toxicity, low odor, and high flashpoint methacrylates as potential THFMA replacements.

2.1.3 Major application categories

2.1.3.1 Automotive

Automotive applications for acrylic structural adhesives tend to be in parts that either do not go through a bake cycle in the process and need quick room temperature curing or have reduced impact requirements. The decision by an automotive engineer to utilize an acrylic structural adhesive usually is the result of the need or benefit of room temperature curing. In hem-flange bonding applications, where adhesives are used to bond the inner and outer panels of a closure panel, acrylic structural adhesives offer a clear advantage in the dimensional stability of the part. Room temperature curing locks the panel in a low stress state, allowing the panel to return to this state after bake cycles for e-coat curing and paint curing, resulting in less distortion of the closure panel compared to one-part epoxy adhesives also used in this type of application. Acrylic structural adhesives are often chosen for bonding composite parts due to good adhesion and room temperature curing. Spoilers and composite body panels are some applications utilizing acrylic structural adhesives. Acrylic structural adhesives find significant use in electric vehicle battery packs. Due to the nature of the lithium ion battery cells, these packs cannot be heated to a significant temperature, making the room temperature curing of acrylic structural adhesives valuable. Electric vehicle battery packs are also designed with multiple materials, resulting in the need to bond bare metal to various coatings and to plastics. Acrylic structural adhesives provide the ability to make these assemblies at room temperature and at the speed needed for rapid mass production.

2.1.3.2 Transportation other than automotive

Acrylic structural adhesives find many applications in the bus, boat, aerospace, trailer, and service truck markets. Once again, the abilities of acrylic structural adhesives to bond dissimilar materials, composites, and plastics at room temperature make them ideal for these large assemblies where it is difficult to apply heat effectively. In these applications, the adhesive is often used in conjunction with mechanical fasteners, especially in locations where peel forces may be applied such as corners and ends of panels in trailers. In the aerospace industry, acrylic structural adhesives are used in gap filler applications and to attach fasteners to composite substrates that would be weakened by the penetration of a mechanical fastener.

2.1.3.3 Industrial assembly

Acrylic structural adhesives are used in applications ranging from horse hoof bonding to sign assembly. Rapid, room temperature curing to unprepared surfaces, along with excellent environmental performance, often makes acrylic structural adhesives an

excellent choice. Acrylic structural adhesives find use in large assemblies such as wind turbine blades, where long open times and gap filling are required. Architectural cladding is another application where acrylic structural adhesives are ideally suited because of the ability to bond dissimilar materials such as metal to a composite as well as environmental performance and room temperature curing. The range of open times, rapid cure profile, and ability to bond unprepared surfaces make acrylic structural adhesives applicable to a diverse set of applications.

2.2 Basics of acrylic structural adhesives

2.2.1 Formulation components

The acrylic structural adhesive is a two-part, reactive toughened system, consisting of a resin component and a curative component [9–11]. In a typical redox initiation system, the main constituents on the resin side are methacrylate monomer(s), toughener(s), and functional additives such as those shown in Table 2.2. On the curative side, the key ingredients include an initiator and functional additives. In general, both resin and curative exist in paste form. Upon mixing, the initiator and coinitiator go through a redox reaction to form a flux of free radicals, which in turn initiates the polymerization of the methacrylate monomer. The mixed adhesive paste is then applied to and sandwiched between the designated substrates (adherends). The adhesive paste wets the adherend surface to ensure intimate contact and a strong adhesion to substrates. Meanwhile, the adhesive bulk cures into a three-dimensional network via free radical polymerization. The adhesive is designed to provide necessary structural strength, toughness, and service durability to the assembled articles. The two-part acrylic system is also referred to as two-component, two-pack, or 2K-acrylics. In some adhesive literature such as technical data sheets (TDS) or material safety data sheets (SDS), the resin side may be referred to as Part A while the curative side is Part B. Per application needs, the resin and curative can be designed to different mix ratios of resin (Part A) to curative (Part B). Adhesives display optimal performance at the designed mix ratios. Some commonly used mix ratios are 1:1, 2:1, 4:1, and 10:1.

Table 2.2 Two-part acrylic adhesive components in general.

Resin component (Part A)	Curative component (Part B)
Methacrylate monomers	Initiator (diacyl peroxide)
Toughener(s)	Pigment
Adhesion promotor(s)	Rheology modifier
Crosslinker	Plasticizer
Coinitiator [tertiary amine(s)]	Filler
Pigment	
Rheology modifier	
Stabilizer	
Filler	

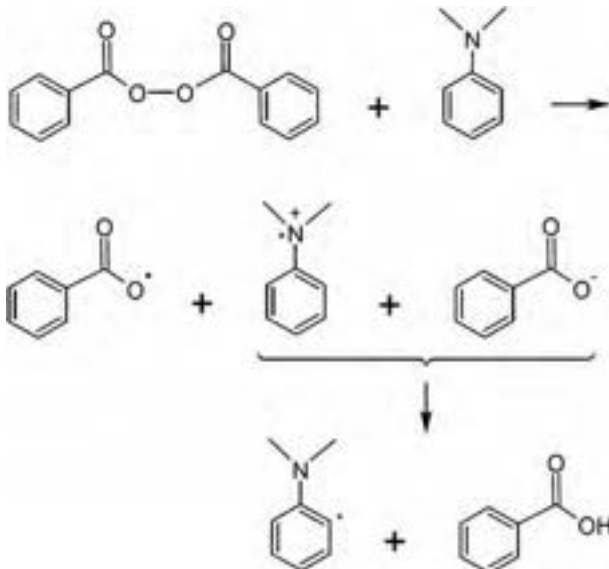
2.2.2 Initiation and polymerization

2.2.2.1 Redox initiation

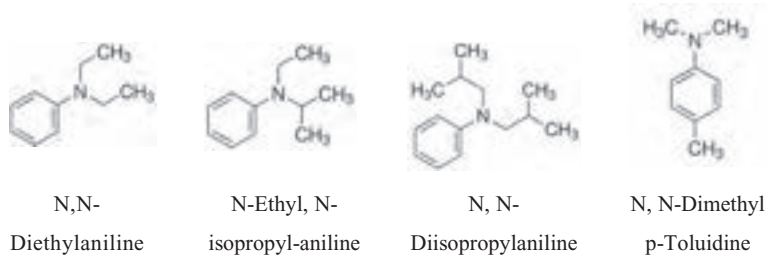
For two-part acrylic structural adhesives, the redox initiation system is the most popular [12,13]. The biggest advantage of this initiation method is that free radicals can be generated from the peroxide at ambient conditions. In contrast to the thermal decomposition of peroxide, where the R-O-O-R peroxide bond is thermally homo-cleaved, producing two free radicals per molecule, the peroxide in the curative is reduced by the tertiary amine in the resin, producing one free radical per molecule plus a byproduct that is not capable of initiating. The free radicals in turn initiate the polymerization of methacrylate monomers. This ambient initiation and cure process provide significant benefits in adhesive assembly factories. For instance, a one-component epoxy adhesive requires gel ovens to fully cure while the ambient cure provides savings on gel ovens, cycle times, and manufacturing space.

Scheme 2.1 shows the redox initiation process [14]. *N,N*-Diethylaniline is the most well-known tertiary amine used in the redox initiation process. It is known for its unwelcome odor and toxicity. In the past half century, some less-hazardous variants of aromatic tertiary amines have become commercially available (Scheme 2.2). Research in finding more effective aromatic tertiary amines is ongoing [15].

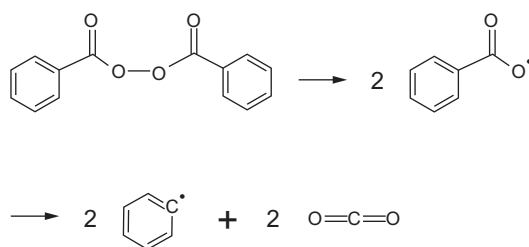
It is important to note that benzoyl peroxide (BPO) naturally decays even at ambient conditions, shown by the thermal decomposition in Scheme 2.3 [16]. As a result, the cure speed and conversion may be negatively impacted by its shelf life. To preserve the freshness of the curative, it is recommended to store the curative in a cold environment. For the very same reason, BPO cannot be formulated with the



Scheme 2.1 Benzoyl peroxide (BPO) decomposition in the redox initiation process.



Scheme 2.2 Aromatic tertiary amines for redox initiation.



Scheme 2.3 The thermal decomposition and decay of BPO.

methacrylates, where the natural decay of BPO would cause a gelation of unsaturated methacrylates, limiting shelf life.

In the mid-1970s, a new initiation system was developed by Briggs and Muschiatti [17]. The initiation package contains cumene hydroperoxide (CHP) and chlorosulfonated polyethylene (CSPE) dissolved in methacrylates in Part A and the activator, *N*-phenyl-3,5-diethyl-2,3-dihydropyridine (PDHP), dispersed in methacrylates in Part B (Table 2.3). In contrast to benzoyl peroxide (BPO), which slowly releases free radicals at ambient conditions (10h half-life is 70°C), the cumene hydroperoxide

Table 2.3 The initiation package of CSPE/CHP/PDHP system.

Part A	Part B
<p style="text-align: center;">Chlorosulfonated polyethylene</p>	<p style="text-align: center;"><i>N</i>-phenyl-3,5-diethyl-2,3-dihydropyridine</p>
<p style="text-align: center;">Cumene hydroperoxide</p>	

(CHP, 10 h half-life is 135°C) does not decompose in ambient conditions. Therefore, it is safe to formulate CHP with methacrylates without gelation concerns. One can formulate a 1:1 equal mix acrylic structural adhesive with this initiation system that has good shelf stability [18,19].

2.2.2.2 Polymerization of methacrylates [12,20]

MMA is the most common acrylic adhesive monomer, having served product assembly markets for more than seven decades. MMA (R=CH₃) is the smallest molecule among methacrylic acid (MAA) esters; it has desirable attributes as a reactive monomer:

- High mobility and reactivity for effective cure and high conversion.
- Copolymerizes well with other methacrylates.
- High homopolymer T_g of 105°C for good adhesive strength.

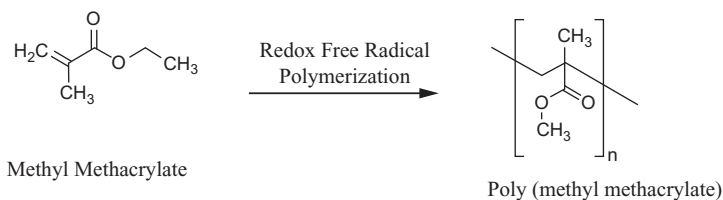
Some downsides of MMA include its volatility, odor, and flammability. The EH&S aspect of the acrylic structural adhesive will be discussed in a later section.

MMA has been the workhorse of the acrylic adhesive market since the 1960s (Scheme 2.4). In the earliest acrylic formulations, solid poly (methyl methacrylate) (PMMA) or polystyrene (PST) was dissolved in MMA and cured into the adhesive matrix to reduce its brittleness. However, the adhesive still lacked flexibility and toughness, shown by poor impact resistance, especially at low temperature.

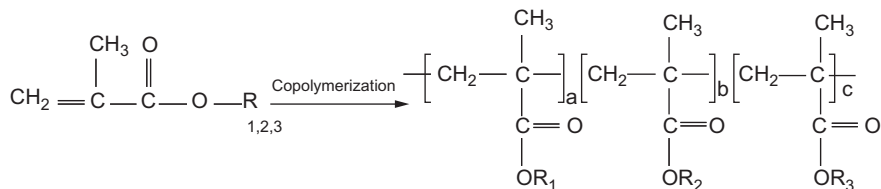
With application demands, the acrylic structural adhesive technology has advanced tremendously in the past decades [21,22]. Formulators have engineered polymer networks and adhesive matrices by:

- Introducing toughening agents, allowing cured parts to better withstand mechanical shocks, especially at low temperature [23].
- Using effective adhesion promoters so that they couple the adhesive matrix and the substrate at the interface [24].
- Incorporating comonomers, crosslinkers, and/or oligomeric di-methacrylate so that the adhesive properties are tailored per application needs [14].
- Adding rheology modifiers for proper dispensing, fillers for cost reduction, pigments for esthetics, and stabilizers for shelf life [25].

One can visualize the cured adhesive matrix as a crosslinked, randomly copolymerized three-dimensional (3D) network of methacrylate monomers, oligomeric methacrylates, coupling adhesion promoters (with one end attached to the substrate



Scheme 2.4 MMA homo-polymerization.



Scheme 2.5 Copolymerization of methacrylate monomers.

surface), and a multifunctional crosslinker (Scheme 2.5). Within this organic moiety, the inorganic ingredients such as rheology modifiers, fillers, and pigments are evenly dispersed and “frozen” throughout the polymeric environment.

2.2.3 Attributes of acrylic structural adhesives

2.2.3.1 Mix ratio

Most two-part acrylic structural adhesives are designed to integer mix ratios by volume. When used at the designed mix ratios, the adhesive demonstrates optimal performance in terms of adhesion, strength, cure profile, and durability. For small applications, the side-by-side or coaxial cylindrical cartridges are ideal to ensure an accurate mix ratio. Zulser/Medmix in Switzerland (Mixpac brand) [26] and Nordson in the United States (Ratio-Pak brand) [27] are two well-known suppliers of two-part adhesive cartridges (Image 2.1). Most commercial cartridges have 1:1, 2:1, 4:1, or 10:1 by volume mix ratios. It is worth mentioning that the cartridge barrels and pistons are made of different polymeric materials such as polypropylene, polyester, or polyamide. Adhesive formulators and engineers should always examine the compatibility of the cartridge material with the resin and curative in advance. This will prevent the adhesive from permeating through the barrel, plastic swelling, and leakage at the pistons.

In large-scale applications, both resin and curative are dispensed from individual pails, drums, or totes by using meter-mix dispensing (MMD) equipment (Image 2.2). In principle, MMD equipment can continuously dial in a range of mix ratios between



Image 2.1 Side-by-side cylindrical cartridges with various mix ratios.



Image 2.2 The MMD equipment made by Rook Metering Equipment.

1:1 and 10:1. The equipment is commonly used in automotive, recreational marine, and industrial assembly settings.

2.2.3.2 *Open time*

Open time is also referred to as work time. It is defined as a time interval from the moment when a fresh adhesive bead is put down on the substrate to the moment when the adhesive bead loses bondability, demonstrated by diminished liquidity, compromised failure mode, and inadequate bond strength. Within the open time, the adhesive mixture remains a creamy paste capable of wetting the substrate; the operator can position, align, and fixture the parts. A typical open time of commercial acrylic structural adhesives ranges from 3 to 90 min, measured at a defined temperature and bead dimension, targeting relevant applications. For acrylic or any adhesive chemistry, the bonding environment and adhesive bead dimension strongly affect the open time. In high temperatures such as summer conditions, open times are typically reduced while lower temperatures in winter tend to extend them by delaying the cure. By the same token, a larger adhesive mass would have a shorter open time while a narrow adhesive bead would have a longer open time. Because this property is critical to process

efficiency, it is desirable to formulate a family of products with varying open times to meet the needs of manufacturers in cold and hot seasons.

2.2.3.3 Handling strength development

Handling strength is the specific bond strength (force per unit area by shear or force per linear length by peel) at which the bonded object can be securely picked up and moved around without dimensional shift or delamination. For industrial applications, 100psi in shear force is an acceptable handling strength. Most two-part acrylic products on the market could reach 100psi anywhere between a few minutes to a few hours at ambient conditions at a given adhesive bead dimension. In the automotive industry, hem flange bonding calls for a handling strength of greater than 500psi after a 1 h cure at 25°C with a 3–4 mm adhesive bead.

Handling strength development embodies the cure rate, often shown by a cure profile of bond strength vs time. It is also known as the rate of bond strength development (ROBSD). While a typical ROBSD curve of epoxy or urethane adhesive presents a step-wise increase in polymerization conversion (Fig. 2.1, dotted line), the acrylic adhesive demonstrates an exponential increase in strength after passing the induction period (Fig. 2.1, solid line). The ROBSD curve could be shifted left or right depending on the cure conditions.

Ideally, the adhesive user wants an adhesive to have an infinite open time, then to develop handling strength immediately after parts are mated. This feature is referred to as snap cure [28]. Adhesive formulators strive to dial in a delicate balance of adhesive composition to reach such a cure state.

However, open time and handling strength development are opposing features; for instance, while it may chemically be feasible to extend the open time by reducing the initiator/coinitiator levels in the mixed formulation, this tends to result in a sluggish cure that is not conducive to rapid strength build. Sometimes compromises are required to ensure bonded joints perform adequately in their final assembly.

In the mid-1990s, a family of styrenic monomers was identified as acrylic cure retardants, which allowed formulators to extend the induction period yet still obtain a rather snap cure. This technique adds another wrench to the toolbox for acrylic cure control [29].

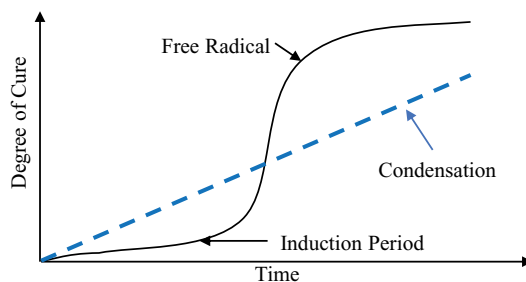


Fig. 2.1 Typical cure profile (Rate of Bond Strength Development) for an acrylic adhesive (solid line) and epoxy/urethane adhesive (dotted line).

2.2.3.4 Purge time

Purge time (minutes) is a time duration timed right after adhesive dispensing is stopped. During this time, the adhesive mass in the static mixer transforms from a fluid paste to a soft gel, which cannot be expelled readily out of the static mixer by compressed air. In a normal operation, the suspension of adhesive dispensing happens from time to time. The adhesive's purge time helps alert the operator to empty the mixer, so that the operation could be resumed without having to replace a clogged mixer. The purge time is temperature-sensitive as well and is only meaningful for a specific dispensing set-up (mixer geometry, air pressure, etc.).

2.2.4 Bond strength and failure mode

The adhesive strength is commonly determined by destructive tests, where standard testing coupons are bonded in specific geometries. After parts are cured, bond joints are subject to external force in the form of tension, compression, shear, cleavage, or peel stress [30]. Among these forces, cleavage and peel are the most destructive, as they concentrate stress at a fine line in the adhesive matrix. While lab tests try to isolate these stress modes, a practical bonded structure may experience a mix of stress modes. For optimal load-bearing capacity, the design of the bond joint should try to avoid major cleavage and peel loading.

The outcome of destructive tests is force at break, expressed by force per unit area for shear, tension, and compression tests (lbs/in.^2 aka psi or MPa), or force per unit length for peel and cleavage tests (lbs/in. aka pli or N/mm). Typical traces of impact force vs displacement in the impact wedge peel (IWP, ISO 11343) test are shown below (Fig. 2.2). The peak force is required to initiate the crack; the force at the flat portion of the curve is needed to propagate the crack. The integrated area underneath

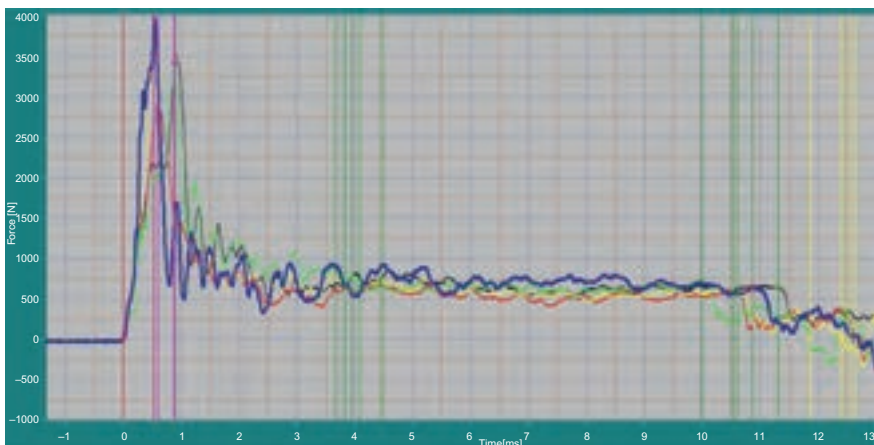


Fig. 2.2 High-speed impact wedge peel test output and specimen geometry.

the curve is the energy required to destroy the bonds. The same is true for both overlap shear (ASTM D3163, ASTM D5868) and peel (ASTM D1876) tests.

It is necessary to point out that the energy needed to break a bondline is more important than the force at break. That is because a stiff but brittle adhesive could display a high strength at break but not be able to endure the stress, potentially causing sudden and catastrophic failure in structural application. Several chapters herein will address strength and fracture energy concepts and distinctions, starting with [Chapter 14](#).

Another outcome from the destructive test is the bond joint's failure mode. It tells how the bond joint fails so that adhesive developers will be aware of the interfacial interaction while adhesive users would know if the adhesive is a good fit for their applications. Some common failure modes are shown in [Image 2.3](#), and more details on the locus of failure can be found in [Chapter 9](#).

- Cohesive failure, where the bond destruction is through the adhesive matrix; there are adhesive residuals deposited evenly on both substrates.
- Adhesive failure, where the adhesive matrix is cleanly peeled off the substrate; there is no adhesive residual on one or both substrates.
- Thin layer cohesive failure is a type of cohesive failure but the bond joint is split unevenly; a thin layer of adhesive residue sticks to one side while a thicker layer is on the other side.
- Stock break, where the substrate either breaks or yields/elongates.
- Fiber tear, commonly observed in fiber reinforced plastic (FRP) and sheet molded compound (SMC), is the structural damage of composites by pulling glass fibers.
- There may be more failure types that could be substrate- or application-specific.

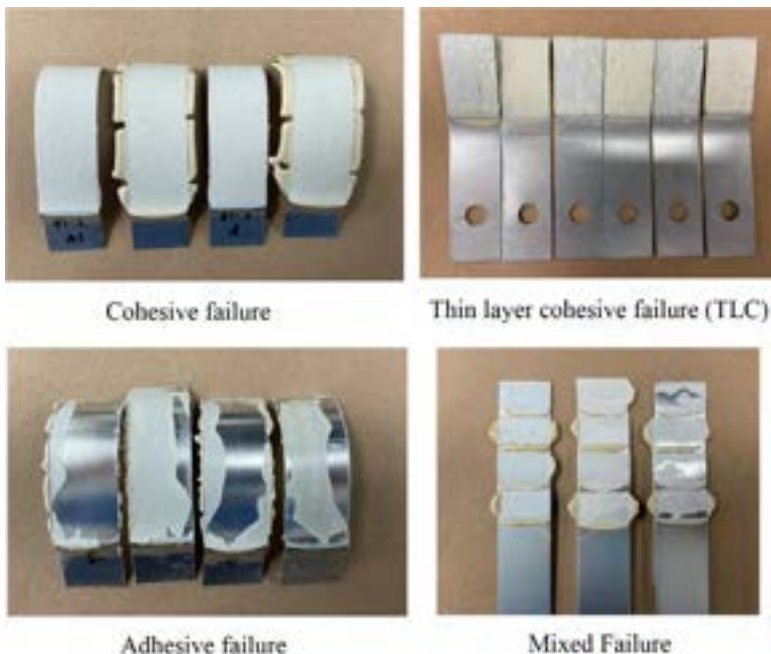


Image 2.3 Metal specimen failure mode illustration.

For automotive structural and semistructural metal bonding, both cohesive and thin layer cohesive failures are desirable failures while adhesive failure is unacceptable, as users do not want an adhesive that does not adhere. In most cases, the failure at a destroyed bond joint is not one type, but mixed. An adhesive's failure mode is quantified by the area percentile of each type of failure.

In situations where an adhesive is stronger than the substrate on which it is applied, adhesive developers may observe the substrate breaking before the joint. This failure mode is referred to as stock break, and it results in a nontested joint and a lack of true adhesive strength data. It is recommended to either use the same but thicker substrate or to reduce the bonding area so that the failure could be directed to the bondline.

The bond joint strength can be affected by bondline thickness, as discussed in more detail in [Chapter 18](#). When the bondline thickness is next to zero, the bonded substrates are not sufficiently connected by the adhesive mass and are typically low in strength. As bondline thicknesses increase, the strength will peak, then gradually decrease. The optimal bondline thickness is in the range of 10–30 mils or 0.20–0.80 mm. This correlation is nicely displayed in Huntsman's Adhesives Technology User Guide [\[31\]](#).

In typical applications, substrates such as metals, especially as large sheets, are not completely flat. The bondline gap could vary in thickness as the metal sheet warps. Another example is the wet lay-up FRP; its bonding side could be uneven and bumpy. Keeping this correlation in mind will help one understand performance limits.

2.2.4.1 Rheological behavior

The resin, curative, and their mixture freshly out of the mixer all exist in the form of fluid/paste; they can be categorized as Newtonian or non-Newtonian fluids. While the viscosity of a Newtonian fluid is not a function of shear rate, the non-Newtonian fluid's viscosity is dependent on the shear rate it encounters during application [\[32\]](#). A Newtonian type of mixed adhesive can be encountered when an application calls for a self-leveling feature, where the resin and/or curative have a relatively low viscosity to begin with (8000–10,000 cps). After the adhesive is dispensed (high shear), the adhesive mass will flow outward due to its gravity (low shear) ([Image 2.4](#)). This feature is necessary when the adhesive is required to fill gaps or spread out on a surface.

In contrast, some applications call for a non-sag feature, in which case a non-Newtonian adhesive fits the bill. In this circumstance, the resin and/or curative have a relatively high viscosity to begin with (150,000–500,000 cps). The mixture is sheared thin out of the dispensing nozzle (high shear) but sets up immediately with a well-defined bead shape after the external shear force is removed. The adhesive beads should not sag on a flat surface or slide down on a vertical surface. This feature is also known as sag resistance; it is sought in many applications.

2.2.4.2 Environmental durability

During their service lives, adhesively assembled structures are exposed to a wide spread of environmental conditions: indoor vs outdoor, humid and hot summers vs dry and cold winters, subzero to more than 100°F daily temperature shifts in the desert



Image 2.4 Acrylic adhesive rheological types.

vs humid salt mist along the coastlines. The adhesive joint must be designed to survive these fluctuating service conditions for years or decades after assembly. To help ensure robust performance, ASTM and ISO have published a good collection of accelerated aging tests to estimate the service duration of adhesive-joined objects [33]. Additional details on fatigue and environmental durability can be found in Chapters 19 and 20, respectively.

When reporting results from these tests, the bond strength and failure mode before and after the environmental treatment are compared, then averaged over the total number of parts. Five replicates are typically required for qualitative information while quantitative comparisons require upward of 30 replicates. Should significant losses be seen, formulators should identify root causes and optimize the interfacial adhesion, bulk properties, or cure conditions.

High temperature endurance [ASTM D5824-98 (2017)]

Adhered joints have much lower heat resistance than mechanically fastened joints. To validate an adhesive's service capacity under high temperatures, bonded parts can be exposed to continuous, intermittent, or cyclic dry heat. The temperature range can be selected amid the upper and lower limits of service conditions to ensure that the adhesive performs properly at all stages of the assembly process, such as paint baking [34,35].

High humidity exposure [ASTM D1776, ASTM D1776M-15, ISO 16701]

For automotive hem flange adhesives, high humidity testing is often run at 35°C/85% RH for as long as 1 month. These conditions are chosen to mimic the transit of room temperature (RT) assembled structures (car doors, lift gates, trunks, and hoods) from stamping plant to final assembly site, where a bake following the e-coating process will fully cure the adhesive. This period is also called humidity layover. The allowed loss in strength and failure is around 20%–30% depending on specific auto manufacturers [36].

For electronic assembly, a typical testing condition is 85% RH at 85°C. This hot, humid environment can be held for as long as 1000 h to simulate 20 years of moisture ingress into a given product.

Corrosive environment [DIN 50 021-SS, ASTM B117]

The salt spray, also known as the salt mist, is a standard environmental test called for by automotive and boat manufacturers. The salt spray chamber generates a salt mist and holds at 35°C. A typical duration for a quick screen is 500 h on steels and 3000 h on various aluminums. It is beneficial to prepare more than one set of sample specimens so that they can be pulled at different time intervals. One will look for strength loss as well as failure mode decay. One may visually detect moisture and corrosive ingress around the edges of the bonding area. Adhesive user requirements are often seen as acceptable loss of strength and failure mode over a given duration.

Environmental cycling [DIN 50 021-SS, DIN 50 017-KFW & DIN 50 014]

This is a more stringent test that exposes the bonded parts to temperature/humidity/salt mist cycles. A commonly used procedure required by European automakers is VDA 621-415. Recently, the requirement changed from 10 cycles to 20, with an allowed loss of less than 30% in both strength and failure. The resulting adhesive improvements will assist the automaker in extending a vehicle's anticorrosion warranty.

Thermal shock

This test generates a steep temperature gradient by cycling the sample specimens between two extreme temperatures. The temperature gradient creates vigorous thermal expansion and shrinkage that stress the bondline adversely. This type of temperature cycling may be seen in deserts, which often have wide daily temperature fluctuations. Adhesives for this type of application need to have a coefficient of thermal expansion (CTE) that matches that of the substrates or enough elongation to withstand the stress caused by the expansion and contraction of the substrates.

Chemical resistance [ASTM G44]

Depending on the application environments, adhesively bonded parts, such as lap shear or T-peel samples, can also be evaluated via soaking tests in different media, such as sea water, diluted acids, gasoline, boiling water, etc. This quick and simple test helps to determine the compatibility of adhesive bondlines with the media they will most commonly encounter throughout their service lives. [Chapter 20](#) will contain more information on the exposure of loaded joints to environmental factors.

2.2.5 Composition-property relationship

2.2.5.1 Mechanical properties of adhesive matrix

The adhesive's polymer matrix (adhesive bulk) is a significant component of the adhered joint. Its physical properties contribute substantially to the overall performance of the adhesive joint [37]. Not only is the adhesive matrix required to deliver

good adhesion to the designated adherend, but also good strength and toughness when the bonded structure bears a dynamic load over its service life.

Tensile testing (ASTM D648, DIN ISO 527)

In this test, the adhesive is cast and cured into an even sheet with a controlled thickness. Dog bone-shaped specimens are punched out using the standard die cutter per ASTM D648 or DIN ISO 527. The specimens can be tested as room condition cured, or after being thermally treated to mimic application processes. The measurement generates a stress-strain curve, from which one can obtain tensile strength and elongation as well as calculate the Young's or elastic modulus and the energy at failure. As pointed out earlier, a rigid material may have high tensile strength at break but only deform or elongate to a limited extent before it breaks (Material 1, Fig. 2.3). The energy needed to break this material is significantly lower than the other material that breaks at a similar tensile strength, but with a higher elongation (Material 2). The energy at break is a representation of a material's toughness, though it is distinct from fracture toughness, as will be discussed in Chapter 14.

Dynamic mechanical analysis (ASTM D4065, D4440, D5279)

Dynamic mechanical analysis (DMA) is an indispensable tool for determining the viscoelastic properties of a cured adhesive. A typical DMA diagram is shown in Fig. 2.4. The test measures a material's complex modulus, a combination of the storage modulus, E' , and the loss modulus, E'' , a quantity related to damping characteristics, as a function of time and temperature by applying a sinusoidal stress onto a specimen. The DMA test also yields the glass transition temperature/range, at which the tan delta value peaks. At this transition region, the adhesive displays the highest capacity of energy dissipation [38–41].

The DMA specimen of the mixed adhesive can be cast into a preshaped mold or can be die cut from a precast sheet. The test can be run under a chosen atmosphere (e.g.,

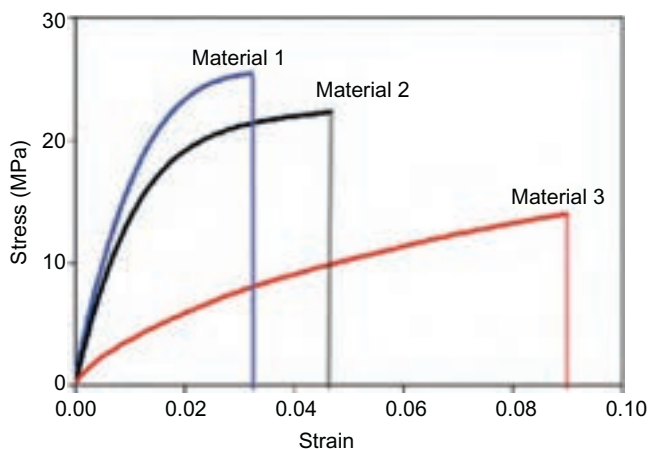
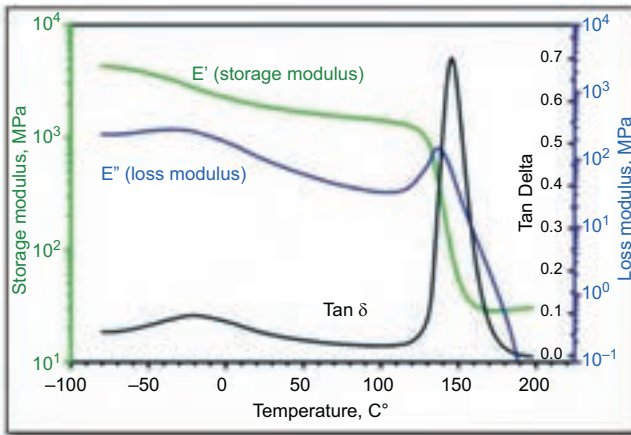


Fig. 2.3 Stress/strain curves of two materials in the tensile testing.



- Loss modulus (E'') measures the energy dissipated as heat, representing the *viscous* portion
- Storage Modulus (E') measures the stored energy, representing the *elastic* portion
- Tan Delta ($\text{Tan } \delta$) is simply a ratio between the two, loss/storage, or E''/E'

Fig. 2.4 The DMA traces of cured adhesive as function of temperature at fixed frequency.

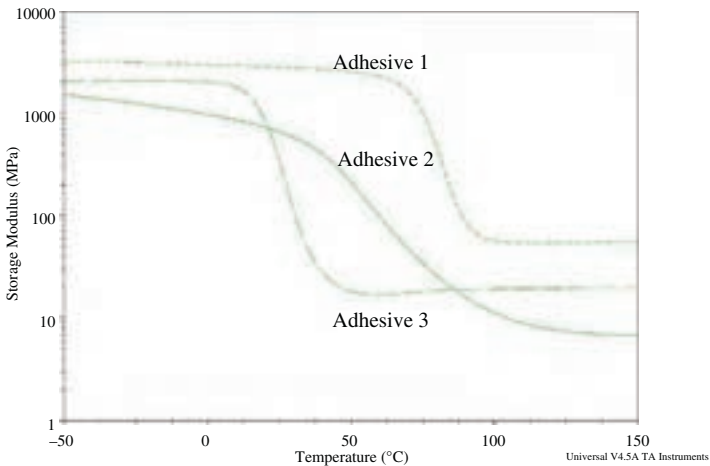


Fig. 2.5 Storage Moduli traces of three distinctive adhesives.

nitrogen vs air) and oscillation stress. The test temperature range can be set to bracket the assembly environments such as automotive bake cycles, auto aftermarket paint oven, and service condition through the seasons.

Fig. 2.5 details storage modulus vs temperature (1 Hz) correlations of three adhesives, where Adhesives 1 and 3 have a sharp transition while Adhesive 2 has a gradual and broader transition. In addition, the three adhesives possess different moduli after the glass transitions, an indication of strength at the high-temperature region.

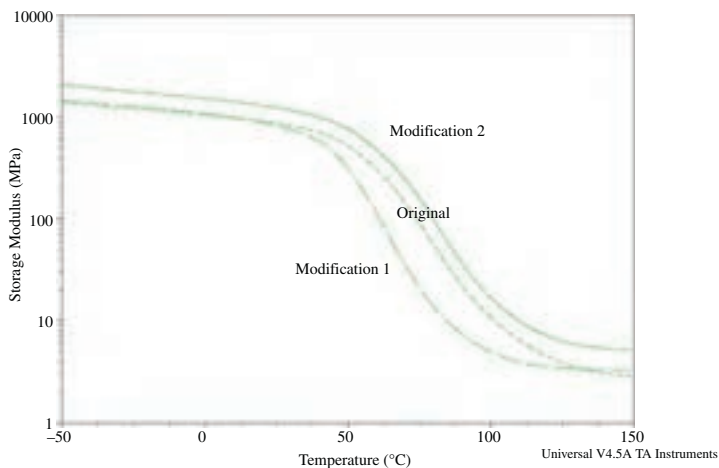


Fig. 2.6 Effect of formulation variation on glass transition and storage modulus.

$$T_g = w_1 \times T_{g1} + w_2 \times T_{g2} + w_3 \times T_{g3} + \dots \text{ etc.}$$

Scheme 2.6 The Fox equation of copolymer glass transition temperature.

$$T_g = (w_1 T_{g1} + k w_2 T_{g2}) / (w_1 + k w_2) + q w_1 w_2$$

Scheme 2.7 The Gordon-Taylor-Kwei equation of polymer blend T_g .

DMA behavior is also used as a response to formulation modifications. In Fig. 2.6, Modification 1 shifted the T_g lower while Modification 2 raised the glass transition temperature and storage modulus. Per the Fox equation (Scheme 2.6) [42], the T_g of a copolymer is determined by the homopolymer T_g s of the participating monomers and oligomers as well as their weight percentages in the copolymer.

For the case of incorporating nonreactive polymers in the resin, the Gordon-Taylor-Kwei equation [43] describes the T_g for polymer blends (Scheme 2.7). These theories have been used to guide the design adhesive matrices.

Other bulk property tests include thermogravimetric analysis (TGA) for thermal stability [44], thermomechanical analysis (TMA) for dimensional expansion, differential scanning calorimetry (DSC) for glass transition, and the Charpy impact test, also known as the Charpy V-notch test, for fracture energy.

2.3 Interfacial adhesion

The interfacial interaction between the substrate and adhesive is known as adhesion. This interaction can be mechanical, ionic, covalent, or an interpenetrating polymer network (IPN) [45–47]. The good bulk adhesive properties are only significant while the adhesion at the interface is sufficient.

In general, the two-part acrylic adhesives bond a broad category of substrates, but for specific applications, adhesive products need to be tailored to deliver exact adhesions.

2.3.1 Metals

Traditionally, aluminum, steel and other metal parts are joined together by mechanical or thermal methods, such as rivets or resistance welding. Now structural adhesive is an alternative. In the automotive industry, commonly encountered metal panels include galvanized steels, painted/e-coated steels, various aluminums, and their alloys. In the past decade, the trend of weight savings and emission reduction has made aluminum alloys a key player over the traditional zinc-treated steels (a.k.a. galvanized and galvaneal steels). To achieve good adhesion and then robust environmental resistance, several metal-to-adhesive coupling agents, a.k.a. adhesion promoters, have played a key role. Among them, methacrylic acid (MAA) and the monoester of phosphoric acid with 2-hydroxyethylmethacrylate (mono-HEMA-phosphate) are most popular [6]. The adhesion promoters form ionic bonds on the metal surface at the acidic end and cure into adhesive matrix at the methacrylate end. This method only suits the bare metals, would not work on coated metals, for instance, painted or e-coated steels. In addition to the automotive industry, sheet metals are also heavily used in selected industrial markets, including but not limited to school bus, bus fleet, office furniture, metal boxes, fire truck, truck and trailer businesses.

2.3.2 Thermoplastics and polymer composites

Acrylic adhesives bond thermoplastics other than thermoplastic olefins (TPO) quite well; for instance, acrylonitrile-butadiene-styrene (ABS) random copolymer, polycarbonate, polymethyl methacrylate (PMMA), more than 100 manufactures globally, poly terephthalic ester (PTE), and polyamides are all bondable by specialized acrylic structural adhesives.

MMA-based acrylic adhesives tend to show the best plastic bonding characteristics by solvating the top layer of the plastic's polymer network, where MMA molecules thread through the swollen surface of the substrates and form a covalent, interpenetrating polymer network (IPN) after curing. In contrast, some higher molecular weight, higher boiling point methacrylate monomers can't achieve the same solvating effect.

Fiber-reinforced plastics (FRPs) and sheet molding compound (SMCs) are heavily used in building water jets, sailboats, vehicle panels and bumpers, household bathtubs and shower stalls, horse trailers, etc. [48,49]. On these substrates, MMA-based adhesives utilize the same solvating effect to penetrate into the resin layer and achieve covalent IPN interlocking. As part of the surface preparation, the loose contaminations on FRP and SMC surfaces (such as mold release agents, antioxidants, or antiozonants), along with poorly cured top layers due to air inhibition, should be removed by solvent wiping, scuffing, or sanding prior to adhesive application and bonding. The two-part Plexus Acrylics of ITW are used by the recreational marine industry.

2.3.3 Low surface energy thermoplastics

TPOs represent a group of hydrocarbon polymers including many grades of high- and low-density polyethylene (PE), amorphous/crystalline polypropylene (PP), ethylene-propylene-diene elastomers (EPDM), etc. They are light weight, chemically inert, and easy to mold to shapes. But their low surface energy (LSE) nature makes adhesive bonding inconvenient and unreliable.

A conventional method to bond these LSE materials is to apply a primer prior to dispensing the adhesive. The primer solution mainly consists of chlorinated polymer and organic solvents, which strengthen the interfacial interactions between the LSE substrate and adhesive. Both 3M and Parker Lord Corporation supply such TPO bonding primers.

In the late 1990s and early 2000s, a new brand of acrylic structural adhesive, 3M's Scotch-Weld 800/8000 series, was introduced to the marketplace. These adhesives specifically target the LSE polyolefin bonding through a unique organo-borane/oxygen initiation mechanism. This breakthrough simplifies the assembly processes by eliminating priming, chemical etching, or surface treatments [50,51].

In recent years, surface treatment on LSE polyolefins has become more accepted by adhesive users. Open-air plasma and flame treatment are among the best options. In both situations, oxidative ozone is generated by an electric arc or at the flame tip, which in turn activates the inert surface and raises the surface energy from <30 to 55–70 dyne/cm, making adhesive bonding feasible [52,53]. These methods will be discussed in more detail in [Chapter 9](#).

2.3.4 Acrylic cure profile

Different from the stepwise polymerization of two-part epoxy or urethane adhesives, two-part acrylic adhesive is based on free radical polymerization so as to have a different cure profile ([Fig. 2.7](#)). The cure process is divided into three regions:

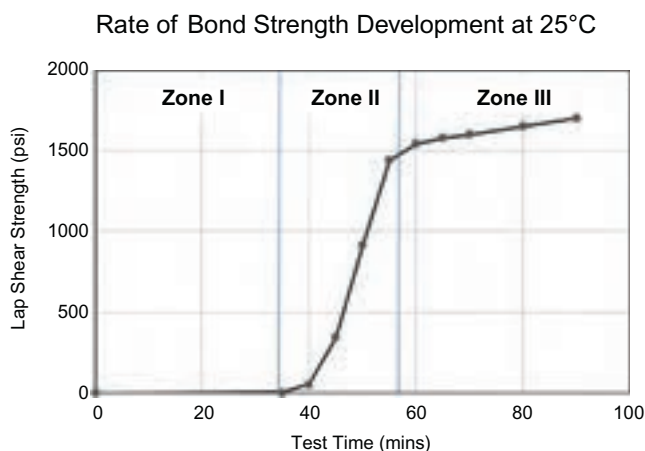


Fig. 2.7 A typical acrylic bond strength development curve.

Zone I is the induction period, where there is little reaction or viscosity change. In Zone II, a rapid chain polymerization takes off, shown by an instant viscosity increase, exothermic emission of heat, and gaining of bond strength. Once in Zone III, the adhesive has hardened, its bond strength starts to level, and methacrylate conversion reaches a plateau.

2.3.5 Toughening of acrylic structural adhesives

Toughening of the adhesive matrix is essential for acrylic structural adhesives to endure static or dynamic loads throughout their prolonged service durations; car doors must support repeated opening and closing especially in cold winters; outdoor commercial signs survive wind pounding; boat hulls must withstand slamming by high-speed waves; and car frames must safely dissipate collision energy. In the past half century, the toughening technology for two-part acrylic adhesives has significantly advanced both in formulation and measurement [54,55].

2.3.5.1 Advancement in testing

While conventional peel tests measure the resistance of adhesive joints to low-speed peel forces (1–4 in./min), they cannot replicate the high-speed impact encountered, for instance, in a car collision. The impact wedge peel method (IWP), ISO 11343, was introduced in the mid-2000s in Europe. The equipment can deliver an impact speed of 2–5 m/s. Since then, its utilization has extended to the automotive industries globally. The high-speed impact force can be delivered by dropping a weight [56] or swinging a pendulum [57] with calculated weight and potential energy on a specimen bonded to a particular geometry, as discussed in Chapter 21. In both cases, the wedge is driven through the bond joint. An adhesive that demonstrates an impact resistance of 30–45 N/mm can be certified as a crash-worthiness adhesive. In a test, the impact speed and potential energy are often set according to specific applications/specifications for adhesive developers as a measure of passenger safety protection [58].

2.3.5.2 Particulate rubbers as toughener

In this category, tougheners are powdery rubbers or core-shell impact modifiers. The former can be obtained from recycling of tires or freshly made from crosslinked polybutadiene and its copolymers. Core-shell impact modifiers are synthesized via advanced emulsion polymerization technology. They consist of an inner core of rubber and an outer shell of a rigid polymer. They typically have dimensions ranging from submicrons to several dozen microns. Often, their shells are made of glassy PMMA or polystyrene (PST) while the core is made of rubbery polymers such as polybutadiene, its copolymers, or polybutyl-acrylate. Elasticity imparted by the rubbery core enables core-shell particles to quickly absorb impact energy while retaining their overall structure reinforced by the glassy outer shell [59,60].

Both types of tougheners initially found application in 1K epoxy adhesives. However, a large number of core-shell products swell by absorbing methacrylate

monomers, especially MMA, while they typically remain intact in 1K epoxies. The absorbed methacrylates partially solvate rubber particles in the core, changing their rubbery nature and reducing their spring-like elasticity. Core shell particles also make the adhesive drier by absorbing monomers that are critical for wetting the substrate and ensuring dispensability. In general, the amount of rubber particles in the resin part is 15–30 wt%.

2.3.5.3 Block copolymer elastomers

Triblock copolymers in pellet form have been extensively used in making hot-melt adhesives ($MW > 100,000$) (Fig. 2.8). Polystyrene blocks at both ends provide strength while the rubbery segment of polybutadiene or polyisoprene at the center provides flexibility and toughness. The polystyrene content is usually between 25 and 30 wt%. They are made via anionic polymerization [61,62].

In late 1990s, triblock copolymers were introduced in the acrylic adhesive as an auxiliary toughener at low levels [63–65]. The rubbery block in the middle contributes to the matrix toughness while the hard polystyrene blocks and the chain entanglement throughout the adhesive matrix add strength. This contributes to improved peel strength and failure mode as well as to the overall integrity throughout its service life. They are designed in linear, branched, or star-shaped configurations. These high MW polymers come in pellet form and need to be dissolved in monomers to be carried into the adhesive formulation. Kraton Polymer and ZEON are two top suppliers of these triblock tougheners.

The primary disadvantage is that the block copolymers need monomers as a carrier, leaving the formulators less flexibility in formulating.

2.3.5.4 Other elastomers [66]

While polybutadiene provides the best low-temperature properties, nonfunctionalized polybutadiene is insoluble in MMA and thus cannot be incorporated in the acrylic matrix. Instead, polychloroprene possesses polar chlorine pendant groups on each repeating unit, which increase its solubility in MMA and allows it to disperse into MMA-based formulations. Similarly, randomly copolymerized butadiene-acrylonitrile

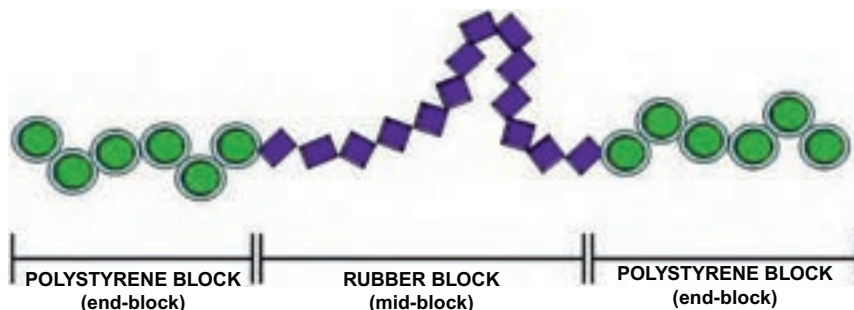


Fig. 2.8 Styrene-butadiene of isoprene-styrene triblock copolymer.

rubber has acrylonitrile pendant groups throughout the polymer chain and is also MMA-soluble. Both polychloroprene and butadiene-acrylonitrile rubber meet toughening requirements well in MMA-based acrylic structural adhesives.

Polybutyl(meth)acrylate and its methacrylate copolymers have good solubility in and compatibility with methacrylates, and as such also find use as tougheners. Similarly, elastomer pellets need methacrylate monomers to dissolve. These high MW elastomers may impact adhesive viscosity and its dispensing as well as formulation flexibility.

2.4 Trends in acrylic structural adhesives

2.4.1 Odor

Scientifically, one may quantify odor with modern analytical instruments such as gas chromatography (GC), mass spectrometry (MS), or infrared spectrum (IR) by analyzing an enriched gaseous phase in the headspace of the sealed adhesive container. These analyses can chemically identify what volatile compounds make up the gas mixture that produces the odor in question.

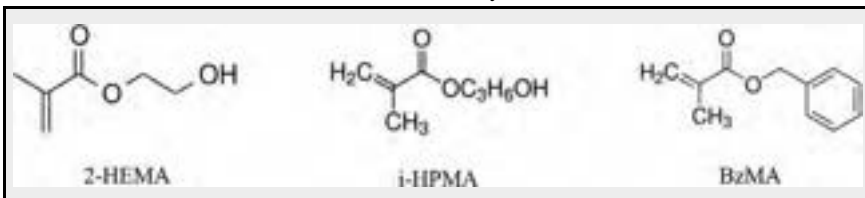
However, the most adapted method by adhesive users/formulators is via human olfactory senses, utilizing human noses as the primary odor detector. To be more specific, an odor panel of 8–10 trained panelists sniff and evaluate the odor source. Based on the test procedure, the odor will be ranked numerically per its offensiveness and/or intensity. A pass/fail line is drawn based on particular applications. Low-odor adhesives mainly benefit two groups of people—adhesive users such as manufacturing operators at assembly stations, and end users such as drivers and passengers in motor vehicles and rail carts made with these adhesives.

Methods that couple the human sensory approach with analytical instruments such as GC/MS have become popular [67,68].

2.4.1.1 Low toxicity, low odor, and nonflammable methacrylates

Both 2-hydroxyethyl methacrylate (HEMA) and 2-hydroxypropyl methacrylate (HPMA) are low-odor and nonflammable methacrylates (Table 2.4). However, both HEMA and HPMA are hydroxy-containing and are thus hydrophilic. They were only used partially in some products in to not negatively impact humidity resistance.

Table 2.4 Some low odor nonflammable methacrylates.



In addition, their high polarity made them less compatible with traditional rubber tougheners such as polybutadiene-based liquid rubber and hydrocarbon triblock copolymers. Another low-odor, nonflammable monomer is benzyl methacrylate (BzMA), which is also used as a modifier in formulations when low odor is called for.

Formulators identified another collection of high boiling point, less volatile, non-flammable, and less humanly toxic methacrylates, including norbornyl methacrylate (NBMA), isobornyl methacrylate (IBOMA), cyclohexyl methacrylate (CHMA), 3,3,5-tri-methyl cyclohexyl methacrylate (t-MCHMA), and so on. After being evaluated in acrylic formulations, these methacrylates showed inferior performance to MMA or THFMA. Plus, they showed some common disadvantages:

- Due to the bulky pendant groups, they are sluggish in (co)polymerization.
- Their high boiling point and low volatility result in thicker air inhibition layers on the cured adhesive beads; this tacky surface may carry residual odor.
- They may lack sufficient EH&S/GHS information due to their more limited usage.
- Some of them are low in production volume, driving raw material costs up.

2.4.2 Additive impact on EH&S profile

In addition to methacrylate monomers, which represent the biggest portion of the formulation, additives in the adhesive can also negatively impact an adhesive's EH&S profile.

In acrylic resins, MAA has been commonplace since the early introduction of two-part acrylic adhesive. MAA is an effective adhesion promotor on metals. Even though it is used at a relatively low level, its pungent odor is noticeable. *N,N*-Dimethyl Aniline (DMA) is a powerful reducing agent for the redox initiation. However, its high toxicity has prevented its use in adhesives sold in Europe.

In acrylic curatives, dialkyl phthalates have been used as plasticizers for decades. They are known as human reproductivity toxins and environmental hazards. Dialkyl phthalates have been banned in Europe.

Developing EH&S-compliant products is now a top priority for adhesive formulators, who have teamed up with regulatory experts to assess the EH&S profiles of raw materials at the formulation design stage. Eliminating the use or reducing the levels of problematic components allows adhesive formulators and engineers to proactively mitigate EH&S risks.

2.5 Applications

2.5.1 Hem-flange bonding

Under hem-flange bonding of automotive closure panels is an application where the room temperature curing property of acrylic structural adhesives, the ability to bond unprepared substrates, and the ability to bond through common metal lubricants give acrylic structural adhesives advantages over other adhesives such as epoxy structural adhesives. For decades, LORD Versilok adhesives have been successfully used as an



Image 2.5 Typical hem flange cross-section with LORD Versilok adhesive.

underhem adhesive in automotive closure panels ([Image 2.5](#)) bonding hot-dip galvanized, electro-galvanized, bare aluminum, and cold rolled steel. The main property resulting in a number of significant benefits over other solutions is the room temperature curing chemistry used in LORD Versilok adhesives. LORD Versilok adhesives cure at room temperature, locking in the dimensions of a hemmed closure panel before going into the e-coat process, allowing the panel to be handled without a loss in quality. In contrast, 1K-epoxy chemistries cure and adhere to the closure panel during the e-coat process while the panel is hot and expanded, locking the panel in a stressed state. The latest generation of LORD Versilok adhesives has been designed with improved room temperature adhesion to all common substrates, especially aluminum. LORD Versilok adhesives offer improved performance over previous generations on almost all substrates, allowing automotive manufacturers to use thinner panels, more aluminum, and expanded design space for closure panels.

2.5.1.1 Room temperature adhesion versus high temperature adhesion

Room temperature adhesion with LORD Versilok adhesives improves dimensional stability by reducing stress in the hem flange joint, as illustrated in [Fig. 2.9](#). Because the adhesive is cured before entering the e-coat bake process, the closure panel is fixed. As the panel heats and expands, the adhesive modulus decreases, allowing for the expansion. Upon cooling, the closure panel returns to its original size as the adhesive modulus increases, resulting in less stress in the hem flange. A 1K epoxy adhesive does not cure until the panel is heated and in the expanded state. The 1K epoxy adhesive modulus increases with heat and the adhesive begins to have adhesion to the closure panel, locking the panel in the expanded state. Upon cooling, the fixed panel attempts to return to the original shape but is locked by the adhesive, resulting in stress in the hem flange. Closure panel dimensions suffer as the panel twists and flexes to reduce the stress.

Room temperature curing LORD Versilok adhesives simplify the hemming process and reduce the need for induction curing and welding. LORD Versilok adhesives eliminate induction cure stations and welding stations and reduce the handling of panels, which can cause dimensional issues from movement. LORD Versilok adhesives also give the manufacturer the option to build closure panels in one facility and transport to another with reduced concern of dimensional issues because the adhesive is cured, locking the closure panel in place.

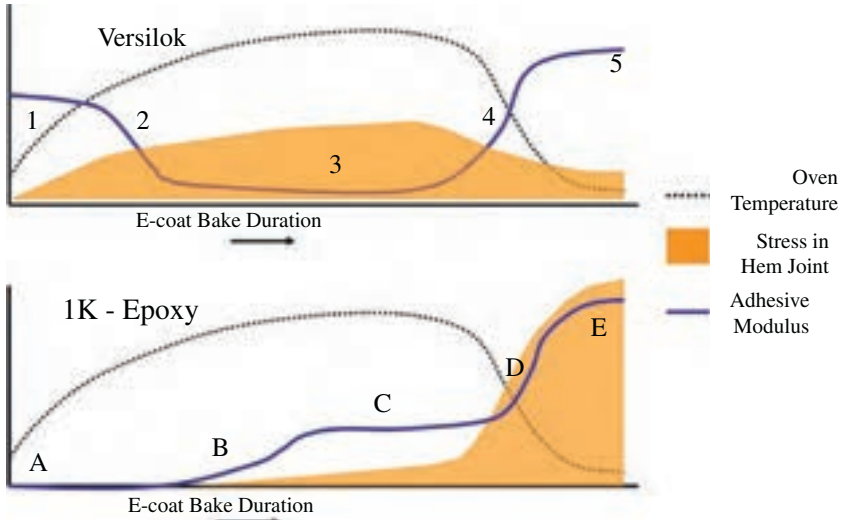


Fig. 2.9 Adhesive modulus during the e-coat bake cycle.

2.5.2 Rail/bus/trailer/recreation marine

2.5.2.1 Composite to composite

Polymer composites are one big class of industrial substrates. Fiber-reinforced plastic (FRP) is widely used in recreational marine [45] (water jets, fishing boats, sail boats, and yachts), bus (panels and gates), trailer (recreational vehicles, horse trailer panels), and rail (platforms, interior panels, and racks) industries; they also find use in residential construction (bath tubes and shower stalls). SMC is another type of composite, often found as large parts for automotive applications that require higher mechanical strength [46]. Acrylic adhesives have been used in many of the above applications.

The resin matrices used in FRP and SMC are mainly polystyrene and/or polyesters. The keys to successfully bonding FRP and SMC are good wetting, swelling, and loosening up the top layer of resins by methacrylate monomers. An MMA-based adhesive is most effective to do so, and capable of delivering desirable fiber tear failure.

It is important to pay attention to the surface contamination of the composite plaque, which was often found full of dust, mold release agents such as wax, air inhibition layers, and other impurities such as antioxidants and/or antiozonants. These impurities will negatively affect the polymerization and form a weak bonding layer between the adhesive and the resin. Scuffing or sanding is sometimes needed so that the impurities are removed and strong bonds between the adhesive and resin can form.

2.5.2.2 Composite to metals

Both FRP and SMC parts often need to be attached to metal structures when they are used as outer panels or bumpers on cars and buses. FRP and SMC to metal cross-bonding has become popular for weight saving. The acrylic adhesive here is required to have good adhesion to metal and solvating power to composites.

Carbon fiber-reinforced plastics (CFRP) are advanced composite and structural materials. Their uses can be found in aerospace, sport and leisure goods, and automotive and industrial parts. Their merit is a combination of high strength and modulus, light weight, anticorrosion, and high fatigue resistance [48,49]. In recent literature, research in CFRP-to-metal cross-bonding is active and in depth, which suggests a growing need for CFRP-to-metal cross-bonding adhesives [69–71].

2.5.3 Electric vehicle battery pack assembly

Electric vehicle battery packs are assembled from multiple types of materials, often with multiple interfaces between dissimilar substrates. A typical battery pack contains bare metal, coated metal, and plastic parts, making acrylic structural adhesives ideal candidates for rapid assembly of the packs. Again, room temperature curing is also an advantage due to the nature of typical lithium (Li) ion battery cells used in electric vehicle battery packs and the need to avoid exposure to excessive temperatures. Acrylic structural adhesives have been designed to provide not only structural bonding but also thermal conductivity, electrical resistivity, environmental resistance, and nonflammability. The main limitations for using acrylic structural adhesives in electric vehicle battery pack assembly are odor during application and the inability to be reworked after assembly.

2.5.3.1 Cell to cooling plate

Thermally conductive and electrically insulating acrylic structural adhesives find significant use in the assembly of Li ion battery cells to the cooling plate, providing the structural strength needed and a path for thermal transfer to cool and heat the battery cell (Image 2.6). Typically, the cooling plate portion of the assembly is coated with some sort of dielectric coating while the battery cell is Ni-plated steel. A thermally



Image 2.6 Thermally conductive acrylic structural adhesive bonding battery cells to cooling plate.

conductive acrylic adhesive does well in bonding these two dissimilar substrates while having the necessary open time and cure profile for rapid mass production. Thermal conductivity is provided by a specially designed filler package that allows the high filler loading necessary for thermal conductivity while keeping the rheology of the adhesive sufficient for dispensing. In the application, a bead of adhesive is dispensed and then the cells are applied to the bead to affix. Glass beads in the adhesive are used to maintain a minimum bondline thickness and consistent thermal conductivity.

2.6 Futures trends

While two-part acrylic adhesives enjoy their successes in fast strength development, ambient cure, robust performance, formulation flexibility, substrate versatility, and environmental duration, they continue to face challenges in various areas:

2.6.1.1 *EH&S compliance*

EH&S requirements will continue to tighten in the future to the betterment of people and the environment. Chemicals continue to be added to restricted lists and formulators need to stay abreast of this constantly changing situation. To be successful, EH&S requirements need to be factored into adhesive design from the start and be continually evaluated over the life cycle of the product.

2.6.1.2 *Vehicle crash worthiness*

Enhanced crash performance requires an improvement in the energy-dissipation capability of acrylic adhesives. Currently, Dow Chemical's Betamate 1 K epoxy adhesive is the state of the art in dissipating collision impact energy. Its acrylic counterparts still have a long way to go to match its crashworthiness.

2.6.1.3 *Bonding carbon-fiber composite*

CFRPs differentiate themselves from glass fiber-reinforced plastics by providing lighter weights and higher strengths. In previous decades, CFRPs could be found on wind turbine blades, vehicle structures, airplanes, and electronics. When CFRP materials replace metals, car manufacturers will be able to reduce weight and improve fuel efficiency without compromising performance or safety. CFRPs often have smooth, shiny resin surfaces to which acrylic adhesives have trouble adhering. Certain surface treatments, such as open-air plasma treating, will be needed to achieve reliable adhesion.

2.6.1.4 *Bonding through dry lubricants*

In the past decade, more metal suppliers have switched from liquid metal lubricants to semisolid metal lubricants. This is because the dry lubricants (Dry Lube) deliver better stamping results on aluminum panels, which in turn facilitates the use of aluminum for vehicle weight saving. In addition, metal sheets coated with Dry Lube are easier and cleaner to handle.

The current workhorse methacrylates such as MMA and THFMA bond through liquid lubricants very well, but they are not capable of displacing the Dry Lube without heat.

2.6.1.5 Supply-chain uncertainty

In the past decade, it has become a norm for chemical supply industries to deal with raw material supply issues; the acrylic structural adhesive manufacturers are being affected as well. Some raw materials became unusable due to EH&S concerns; some were discontinued for various reasons, and some couldn't meet the ever-growing demand. Formulators are working hard to find replacements that can deliver equivalent performance; that often requires reengineering of a polymer network. Furthermore, issues such as cost, logistics, and supply reliability are also critical in the long run. It takes a cross-functional team of adhesive developers, raw material suppliers, business developers, and so on to bring in sustainable solutions.

The adhesive industry is always innovating and evolving. Formulators and engineers are working to address the above issues so that future acrylic adhesives will be cleaner, tougher, and more adaptable to new lubricants and lighter substrates.

In the past few years, adhesive manufacturers have steadily increased their efforts to reduce their carbon footprint, setting goals to achieve carbon neutral operations within the next 20–30 years. To reach carbon neutrality, formulators have strived to eliminate unreactive volatile organic compounds (VOC) in resins and curatives and ensure that the resin and curative are 100% reactive. Additional efforts include incorporating renewable raw materials, reducing energy consumption in production, minimizing waste generation, and optimizing delivery routes to customers.

Acknowledgments

This chapter is an update of the previous version written by P.C. Briggs of IPS Corporation and G.L. Villanella of Dow Chemical Company in the first edition of *Advances in Structural Adhesive Bonding*. The authors acknowledge their initiation and contribution.

The authors also acknowledge the contribution of Jacob Nelson, scientist in structural adhesives technology at Parker Lord Corporation for contributing ideas and creating drawings.

References

- [1] D.J. Damico, Reactive acrylic adhesives, in: *Engineered Materials Handbook Volume 3: Adhesives and Sealants*, ASM International, 1990.
- [2] P.C. Briggs, G.L. Jialanella, Advances in acrylic structural adhesives, in: D.A. Dillard (Ed.), *Advances in Structural Adhesive Bonding*, Woodhead Publishing, 2010 (Chapter 6).
- [3] N. Mittal, E. Prasad, *Structural Adhesives Market*, Allied Market Research, 2021.
- [4] A.G. Bianchi, *Advances in Acrylic Adhesive Technology*, Adhesives & Sealants Industry, 1996.
- [5] B. Zwang, Adhesives aid truck and trailer assembly, *Assem. Mag.* (2017).
- [6] H.D. Dawday, Epoxy Modified Structural Adhesives Having Improved Heat Resistance, US 4,467,071, 1984.

- [7] EH&S. <https://www.ehs.com/resources/ghs-answer-center/10-ghs-facts-in-60-seconds/>. (Accessed 24 February 2022).
- [8] Chemical safety. <https://www.oecd.org/chemicalsafety/risk-management/50500627.pdf>. (Accessed 24 February 2022).
- [9] D.J. Stampfer, Toughened acrylic and epoxy adhesives, in: W.C. Wake (Ed.), *Synthetic Adhesives and Sealants*, John Wiley and Sons, New York, 1987.
- [10] E.M. Petrie, Structural Thermosetting Acrylic Adhesives - Basics & Formulation Practices; SpecialChem The Material Selection Platform. <https://adhesives.specialchem.com/>. (Accessed 6 January 2022).
- [11] G.W. Ritter, Bonding lines: acrylic adhesives forte-versatility, *Assem. Mag.* (2008).
- [12] G. Odian, Radical chain polymerization, in: *Principles of Polymerization*, second ed., John Wiley & Sons, 2004, pp. 201–205 (Chapter 3).
- [13] Redox Free Radical Polymerization, <https://polymerdatabase.com/polymer%20chemistry/Redox.html/> (Revised July 28, 2020) (Accessed 2022-1-6).
- [14] A.S. Sarac, Redox polymerization, *progress polymer*, *Science* 24 (1999) 1149–1204.
- [15] K. Kangmin, et al., Rational design of efficient amine reductant initiators for amine–peroxide redox polymerization, *J. Am. Chem. Soc.* 141 (15) (2019) 6279.
- [16] Initiation by Diacyl Peroxides. <http://polymerdatabase.com/polymer%20chemistry/Diaroyl%20Peroxides.html>. (Accessed 6 January 2022).
- [17] P.C. Brigg, N. Muschiatti, Novel Adhesive Compositions, US 3,890,407, 1975.
- [18] A.S. Toback, Process for Bonding with Acrylate Polymerized by a Peroxide and a Condensation Product of Aldehyde and Primary or Secondary Amine, US 3,616,040, 1971.
- [19] D.P. Melody, S.M. Grant, F.R. Martin, Two-Part Composition with Activator Enriched with Dihydropyridone, US 4,430,480s, 1984.
- [20] Polymethylmethacrylate. <https://pslc.ws/macrog/pmma.htm>. (Accessed 6 January 2022).
- [21] S.D. Anderson, Structural adhesive is being used for more and more assembly applications. *Adhesives for structural metal bonding*, *Assem. Mag.* (2006).
- [22] J. Sprovieri, 50 years of assembly: assemblers stick with adhesives, *Assem. Mag.* (2007).
- [23] D. Dunn, Reactive, Toughened Acrylic Adhesives – Poised for Growth, *Adhesive & Sealant Industry*, 2003.
- [24] E.M. Petrie, Adhesion Promoters: Adhesion Basics & Material Selection Tips for Adhesives. <https://adhesives.specialchem.com/>. (Accessed 6 January 2022).
- [25] V. Joseph, et al., *Additives Handbook, PAINT & COATINGS INDUSTRY*, 2011, 2011. www.pcimag.com.
- [26] Cartridges, Mixers, and Dispensers. <https://www.medmix.swiss/en/Products/Industry>. (Accessed 28 February 2022).
- [27] Syringe Barrels & Cartridges. <https://www.nordson.com/en/divisions/efd/products/syringe-barrels-and-cartridges>. (Accessed 28 February 2022).
- [28] E. Pitia, J. Hill, Reactive acrylic adhesives, in: A. Pizzi, K.L. Mittal (Eds.), *Handbook of Adhesive Technology*, CRC Press, 2018.
- [29] R. Righettini, et al., US Patent 7,019,075 B2, 2006.
- [30] D. Kopeliovich, Adhesive Joints. https://www.substech.com/dokuwiki/doku.php?id=adhesive_joints. (Accessed 17 January 2022).
- [31] ARALDITE Adhesives Technology User Guide, Araldite Industrial Adhesives, Adhesive Technology, 2017. <https://huntsman-pimcore.equisolve-dev.com/>. (Accessed 28 February 2022).
- [32] G. Ianniruberto, Introduction on polymer rheology, in: *Chemistry, Molecular Sciences and Chemical Engineering*, Elsevier Inc, 2015.
- [33] L.F.M. Da Silva, D.A. Dillard, B. Blackman, R.D. Adams (Eds.), *Testing Adhesive Joints: Best Practices*, Wiley-VCH Verlag GmbH & Co. KGaA, 2012.

- [34] EDN, Specialized Adhesives Withstand Thermal Cycling, September 25 2012. <https://www.edn.com/specialized-adhesives-withstand-thermal-cycling/>. (Accessed 21 February 2022).
- [35] Electronics Cooling, Choosing Adhesives for Withstanding Thermal Cycling Stresses. <https://www.electronics-cooling.com/2012/11/choosing-adhesive-for-withstanding-thermal-cycling-stresses/>. (Accessed 21 February 2022).
- [36] Testing of Corrosion Protection of Vehicle Paint by Alternating Cycles Test, Standard: VDA 621–415. <https://www.ascott-analytical.com/>.
- [37] J.P. Huang, Mechanical properties of adhesive matrix and their influence on adhesive performance, in: Proceedings, 2011 Annual Meeting, Thermoset Resin Formulators Association, Niagara-Falls, Ontario, Canada, 2011.
- [38] F. Rodriguez, et al., Mechanical properties at small deformations, in: Principles of Polymer Systems, fifth ed., CRC Press, 2003 (Chapter 8).
- [39] A. Hayashi, et al., Effect of temperature and loading rate on the mode I fracture energy of structural acrylic adhesives, *J. Adv. Join. Process* 5 (2022), 100079.
- [40] W.M. Groenewoud, Dynamic Mechanical Analysis, in: Characterization of Polymers by Thermal Analysis, Plastics Design Library, William Andrew Applied Science Publisher, 2018.
- [41] B.E. Read, G.D. Dean, The Determination of Dynamic Properties of Polymers and Composites, A Halsted Press Book, John Wiley & Sons, New York, 1978.
- [42] F. Rodriguez, et al., Physical states and transitions, in: Principles of Polymer Systems, fifth ed., CRC Press, 2003 (Chapter 3).
- [43] A. Lin, T.K. Kwei, A. Reiser, On the physical meaning of the Kwei equation for the glass transition temperature of polymer blends, *Macromolecules* 22 (1989) 4112–4119.
- [44] J. Vohlidal, Polymer degradation: a short review, *Chem. Teach. Int.* 3 (2) (2021) 213–220.
- [45] L.-H. Lee (Ed.), Adhesives, Sealants, and Coatings for Space and Harsh Environments, Polymer Science and Technology, vol. 37, Plenum Press, 1987.
- [46] G. Wypych, Handbook of Adhesion Promoters, ChemTech Publishing, 2018.
- [47] A.J. Kinloch, Adhesion and Adhesives, Science and Technology, Chapman and Hall, 1987.
- [48] M. Inagaki, Carbon composites, in: New Carbon – Control of Structure and Functions, Elsevier Science, 2000, pp. 177–211.
- [49] E.G. Melby, J.M. Castro, Glass-reinforced thermosetting polyester molding: materials and processing, *Compr. Polym. Sci. Suppl.* 7 (1989) 51–109.
- [50] J. Sprovieri, Bonding breakthrough for polyolefins, *Assem. Mag.* (2012).
- [51] Bonding and Assembly/Categorizing Surface Energy, https://www.3m.com/3M/en_US/bonding-and-assembly-us/resources/science-of-adhesion/categorizing-surface-energy.
- [52] S. Ebnesaïjad, Surface Treatment of Materials for Adhesive Bonding, second ed., William Andrew, 2014.
- [53] R.F. Wegman, J.V. Twisk, Surface Preparation Techniques for Adhesive Bonding, second ed., William Andrew, 2013.
- [54] Adhesive Bonding, in: R. Adams (Ed.), Science, Technology and Applications, second ed., Elsevier, 2021 (Chapter 9).
- [55] E.M. Petrie, Test Methods to Measure Impact Strength of Adhesive Joints. <https://adhesives.specialchem.com/selection-guide/test-methods-to-measure-impact-strength-of-adhesive-joints#iwt>. (Accessed 6 January 2022).
- [56] Instron Application Report, Impact Performance of Adhesive Bonds Under Impact – ISO 11343, 2007. www.instron.com.
- [57] Pendulum Impact Testers for Tests on Metals. <https://www.zwickroell.com/products/products-for-impact-testing/pendulum-impact-testers-for-tests-on-metals/>. (Accessed 1 March 2022).

- [58] C. Sato, S. Marzi, High-rate loading and impact in adhesively bonding joints, in: R. Adams (Ed.), *Adhesive Bonding, Science, Technology and Applications*, second ed., Elsevier, 2021 (Chapter 9).
- [59] D. Gosiewski, et al., *Structural Adhesive*, 2002. US 6,462,126, (core shell).
- [60] J.-M. Boutillier, M. Havel, et al., Self-Assembling Acrylic Block Copolymers for Enhanced Adhesives Properties, May 1 2013. <https://www.adhesivesmag.com/articles/91909-self-assembling-acrylic-block-copolymers-for-enhanced-adhesives-properties>.
- [61] A Complete Guide on Styrene Butadiene Copolymer Resins. <https://adhesives.specialchem.com/>. (Accessed 6 January 2022).
- [62] J.T. Harlan, L.A. Petershagen, E.E. Ewins Jr., G.A. Davies, Thermoplastic rubber (A-B-A block copolymers) in adhesives, in: I. Skeist (Ed.), *Handbook of Adhesives*, third ed., van Nostrand Reinhold, New York, 1991 (Chapter 13).
- [63] J. Huang, R.F. Righettini, F.G. Dennis, *Adhesive Formulations*, US 6,225,408 B1, 2001.
- [64] M.A. Kropp, Z.J. Thompson, *Structural Acrylic Adhesive*, 2016. US 9,416,299 B2, (like Versilok).
- [65] S. Tsuno, R.D. Cooman, (Meth)acrylic Adhesive with Low Odor and High Impact Resistance, US 8,070,908 B2s, 2011.
- [66] Hoffmann Minerals, Solvent Borne Neoprene Contact Adhesives with Functional Fillers (A, B, C). <https://adhesives.specialchem.com/>. (Accessed 6 January 2022).
- [67] P. Denk, A. Buettner, Sensory characterization and identification of odorous constituents in acrylic adhesives, *Int. J. Adhes. Adhes.* 78 (2017) 182–188.
- [68] ASTM, E3261–21, Standard Guide for Odor Evaluation of Products and Materials Under Controlled Conditions with Trained Panel, 29 Oct 2021.
- [69] B. Tan, et al., Optimizing adhesive bonding between CFRP and Al alloy substrate through resin pre-coating by filling micro-cavities from sandblasting, *Int. J. Adhes. Adhes.* 110 (2021).
- [70] M. Jabbari, et al., Environmental durability of epoxy-bonded CFRP-to-steel joints in mode I fracture, *Int. J. Adhes. Adhes.* 112 (2022).
- [71] G. Qin, et al., Failure prediction of adhesively bonded CFRP-Aluminum alloy joints using cohesive zone model with consideration of temperature effect, *J. Adhes.* 95 (10) (2018) 1–24 (CFRP-Al).

This page intentionally left blank

Advances in polyurethane structural adhesives

3

Fabien Choffat^a, Antonio Corsaro^a, Claudio Di Fratta^b, and Steffen Kelch^a
^aSika Technology AG, Zürich, Switzerland, ^bSika Services AG, Zürich, Switzerland

3.1 Introduction

3.1.1 Basic concepts

Structural adhesives are nowadays key elements for the production of industrial goods, consumer devices, and vehicles of all kinds. They are also used in the construction industry when using modular assembly methods or during the completion and renovation of buildings. This chapter describes design aspects of organic structural adhesives that are based on polyurethane (PUR) chemistry using chemical reaction (curing) mechanisms; PUR adhesives that are mainly based on physical hardening such as hotmelt adhesives or PUR dispersion-based (i.e., water-based) adhesives are not discussed in detail. In reactive systems, the covalent crosslinking of monomers and prepolymers forms a three-dimensional (3D) polymer network, which represents a prerequisite for structural performance. The well-balanced combination of adhesion to a given substrate and the resulting cohesive strength determine the suitability of an adhesive for the intended application. Conventional structural adhesives are typically two-component (2C) reaction adhesives while for elastic bonding or in sealant applications, mainly reactive (humidity curing, oxidative, or ultraviolet (UV) curing) one-component (1C) adhesives play the predominant role (Fig. 3.1). 1C adhesives can also contain an encapsulated hardener component that is activated and set free upon heating the adhesive. In the latter case, a chemical reaction as in 2C adhesives takes place [1].

This chapter gives an overview of the ingredients of reactive PUR adhesives, the used raw materials, reactive intermediates, and the formulation of the same in components. The aim of the adhesive development efforts is the adjustment of adhesion and mechanical properties to technical design aspects and requirement profiles. In chemically curing PUR adhesive systems, the choice of reactive groups and the properties of molecular building blocks allow us to define the formation of a crosslinked polymer network structure directly at the site of production or construction. The interesting aspect about PUR networks is the well-orchestrated formation of covalent chemical bonds and consequently physical or secondary bonds based on (inter)molecular interactions and as a consequence of possible demixing of polymer segments such as phase separation processes. Besides the well-controllable crosslink density determining mechanical strength, the resulting miscibility or thermodynamic incompatibility of the formed polymer segments can be used to generate different types of polymer morphologies and consequently different performance profiles. In this way, adhesion,

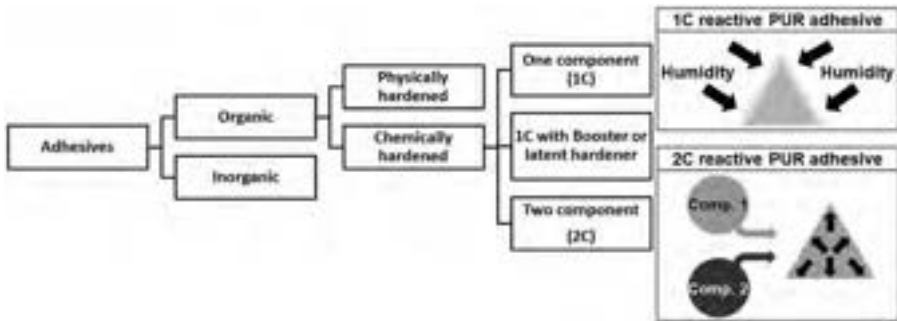


Fig. 3.1 Polyurethane adhesive classification and differences in curing from the outside on reaction with moisture or homogeneously in the adhesive for 2C adhesives. Courtesy of Sika Technology AG.

cohesive strength, thermo-mechanical behavior, and chemical (environmental) stability can be tailored.

Structural adhesives with significant load-bearing capabilities, which are resistant to creep and have sufficient durability at the required working temperature, are usually produced by 2C reaction adhesives. Adhesives must have a liquid stage during application to guarantee good surface wetting, which is a prerequisite for building up adhesion [2]. Typical properties of 2C PUR reaction adhesives are fast curing within a time span of several minutes to 1 h and a fast build-up of green strength, whereas 1C reactive PUR adhesives have curing times between 1 h and 1 day. In 1C adhesives, the curing rate is defined by the gradual diffusion of water or oxygen or the achievement of the necessary UV radiation level. Instead of a strict differentiation between 1C and 2C adhesives with diverse characteristics, which are linked to the respective mixing, dosing, and application techniques, this chapter introduces an alternative, more differentiated modular approach as shown schematically in Fig. 3.2. For example, humidity-curing 1C PUR systems are often accelerated by combining with a water-containing booster component or a second curing mechanism is introduced by doping the adhesive with an additional (latent) hardener, which helps increase the number of formed urea bonds and thus increases physical crosslinking and consequently the final strength. In this way, the formation of carbon dioxide produced by the direct reaction of isocyanate and water can be controlled efficiently or even be avoided, which decreases the risk of bubble formation on the substrate-adhesive interface and increases adhesion forces [3]. In addition, 2C PUR can also be modified by using latent hardeners, which can be employed to increase green and final strength and—through the incorporation of additional urea bonds—to support the formation of a more pronounced hard segment phase (Fig. 3.2, middle part).

Due to the great variability of chemical building blocks and the formation of urethane and possibly urea bonds, polyurethane adhesives represent a modular approach, allowing the systematic realization of manifold structure-to-property relationships by adjusting the mechanical strength and consequently adhesive strength. In this sense, PUR adhesive applications in different fields, ranging from soft-elastic sealants to structural-stiff adhesives, are technically feasible (Fig. 3.3).

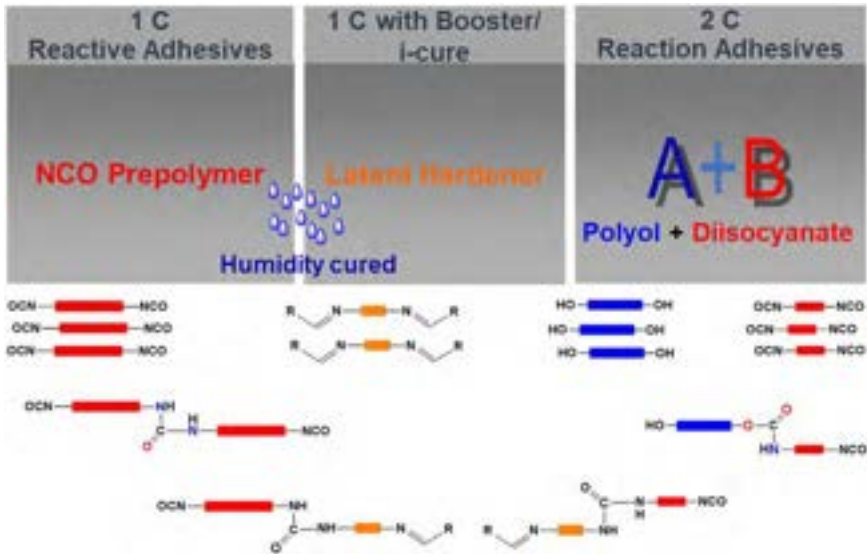


Fig. 3.2 Spectrum of adhesive curing reactions from 1C to 2C PUR.
 Courtesy of Sika Technology AG.

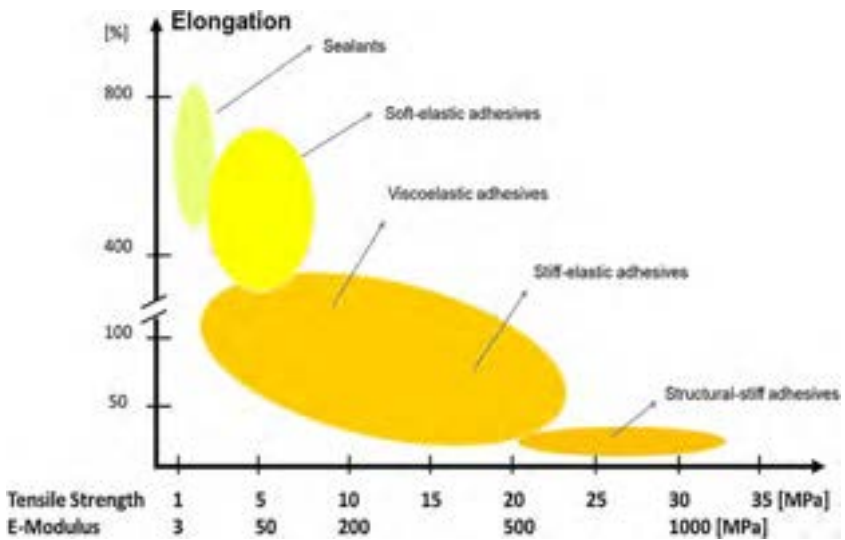


Fig. 3.3 Mechanical performance spectrum of PUR adhesives recorded at room temperature and strain rates between 10 and 200mm/min.
 Courtesy of Sika Technology AG.

Table 3.1 Surface pretreatments to support adhesion build-up.

Pretreatment	Mechanical	Physical	Chemical
Procedure	Roughening Grinding (Sand) blasting Wet/dry cleaning	Flaming Irradiation (UV, infrared, electrons, laser) Plasma treatment (atmospheric or low pressure) Corona discharge	Activators Primers Coating, lacquer
Purpose	Removal of contaminants Support build- up of adhesion	Increase in surface energy Generation of unsaturated bonds/free radicals/polar groups	Surface activation, stabilization

In practical bonding applications where PUR adhesives are involved, it is often necessary to support the build-up of adhesion by appropriate surface activation to increase surface energy by generating unsaturated bonds or free radicals and thus reach an enrichment of polar chemical groups on the substrate. Besides the cleaning of surfaces with washing agents or solvents, additional chemical and/or mechanical pretreatments such as grinding or sand blasting with different abrasive materials and tools as well as physical treatment (irradiation, flame or plasma surface treatments, etc.) may be necessary. Such pretreatment removes possible contamination and increases wetting, consequently improving the stability of the formed interfacial layers of PUR adhesive to the diverse substrates such as metals, glass, ceramics, plastics, polymer blends, or fiber-reinforced composite materials. Surface preparation and pretreatment represent an important and wide field, especially when elastic PUR adhesives are involved. Table 3.1 gives a schematic overview of the various pretreatments used in combination with PUR adhesives. A valuable overview can be found in the relevant literature [4,5].

3.2 Characterization of PUR adhesives

3.2.1 Mechanical properties

Several types of PUR adhesives were developed over the past years, including solvent-borne, waterborne, hot-melt, and one- or two-component reactive adhesives [1]. As mentioned in the introduction, this chapter focuses on reactive adhesives and, in particular, on 2C reaction systems because they are most often employed for structural bonding applications in industry. A wide range of chemical formulations is possible, resulting in adhesives with different mixing ratios and curing kinetics as well as mechanical properties. PUR structural adhesives are nowadays commercially available in rigid, semirigid, or even flexible products. As an example, the elastic modulus—between 0.05% and 0.25% elongation—range can extend from about 5–10 MPa

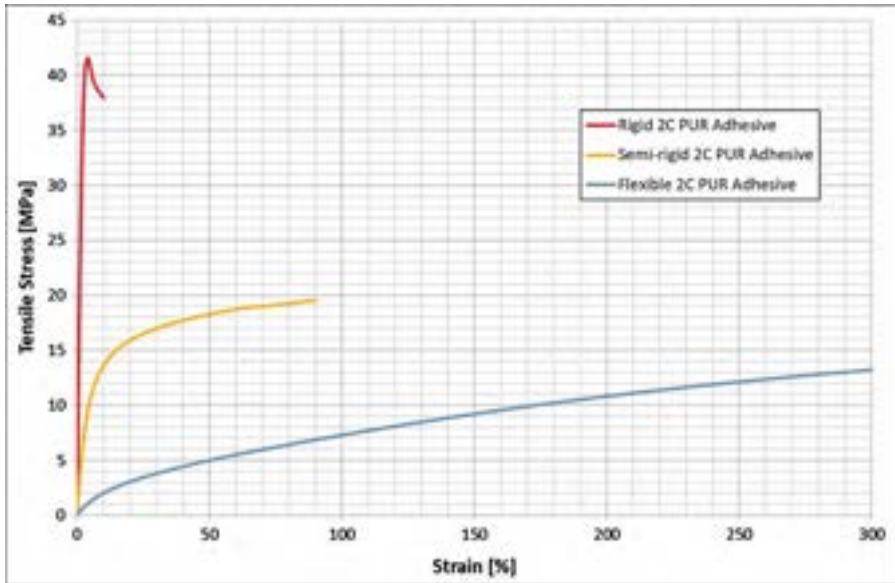


Fig. 3.4 Exemplary tensile stress-strain curves of 2C PUR adhesives with different mechanical strength profiles.

Data courtesy of Sika AG.

to more than 2000 MPa. [Fig. 3.4](#) compares three tensile stress-strain curves of representative 2C PUR adhesives, showing the diversity of mechanical behavior within the same class of chemicals.

When compared to other structural adhesive technologies such as epoxies and acrylics, most PUR adhesives exhibit reasonably good levels of mechanical strength and stiffness—albeit typically lower than epoxies—together with high elasticity and the ability to accommodate peel stress. Hence, polyurethanes are found in several industrial applications, ranging from thin layer bonding to large gap filling, and are frequently employed to bond dissimilar materials. Their inherent flexibility usually enables use in applications demanding elevated toughness and crash resistance. [Fig. 3.5](#) presents the results of T-joint impact tests [6,7] using toughened epoxy and structural 2C PUR—whose basic mechanical properties are summarized in [Table 3.2](#)—to bond the T-joints. Noticeably, higher crash forces and greater energy absorption—namely, the areas underneath the experimental load-deflection curves—are obtained using the PUR adhesive. It is, however, worth mentioning that unlike most epoxies and acrylics, industrial applications of PUR adhesives are generally limited by the substrates to be bonded, whose surfaces may require specific chemical or physical pretreatment. Therefore, industrial researchers [8,9] developed hybrid PUR-epoxy adhesive systems, which combine the high strength and broad adhesion range of epoxies with the ductility and crash resistance given by PUR compounds, in the form of organic toughening agents [10,11].

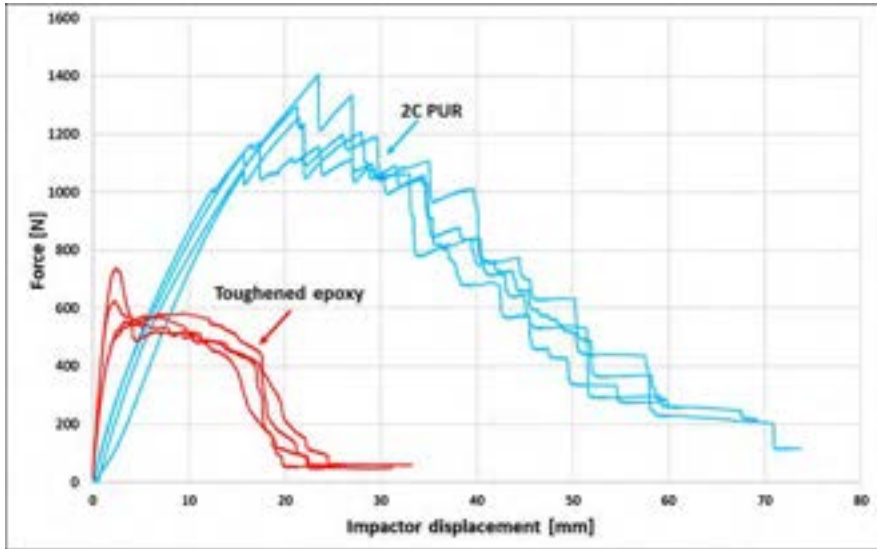


Fig. 3.5 Impact test results of a T-joint bonded with a toughened epoxy (*red curves*) in comparison to a 2C PUR (*blue curves*) adhesive. Data courtesy of IWK, OST Rapperswil.

Table 3.2 Basic properties of the adhesives used for the T-joint.

Material property	Toughened epoxy adhesive	Structural 2C PUR adhesive
Tensile strength	30 MPa	10 MPa
Lap-shear strength	20 MPa	10 MPa
Young's modulus	2000 MPa	25 MPa
Elongation at break	10%	300%

Data courtesy of IWK, OST Rapperswil.

The durability of PUR-bonded joints is regularly tested by fatiguing lap-shear samples under cyclic loads [12]. Testing the fatigue behavior is essential to identify the maximal allowable strength, which enables designing bondlines that will survive the entire service life of the bonded structures [10]. Fig. 3.6 shows an exemplary cyclic stress (S) as a function of the number of cycles (N), a so called S-N curve—also named the Wöhler curve—of structural 2C PUR-bonded samples, highlighting a limit of endurance greater than 5 MPa at 10 million load cycles. Such a limit—approximately a fourth of the static lap-shear strength—is adhesive/application-specific and can vary largely due to the broad spectrum of possible PUR adhesive formulations. The above-mentioned mechanical properties are measured from tests at room temperature. While flexible polyurethanes show quite stable properties over a large temperature range, traditional structural 2C PUR may exhibit remarkably temperature-dependent

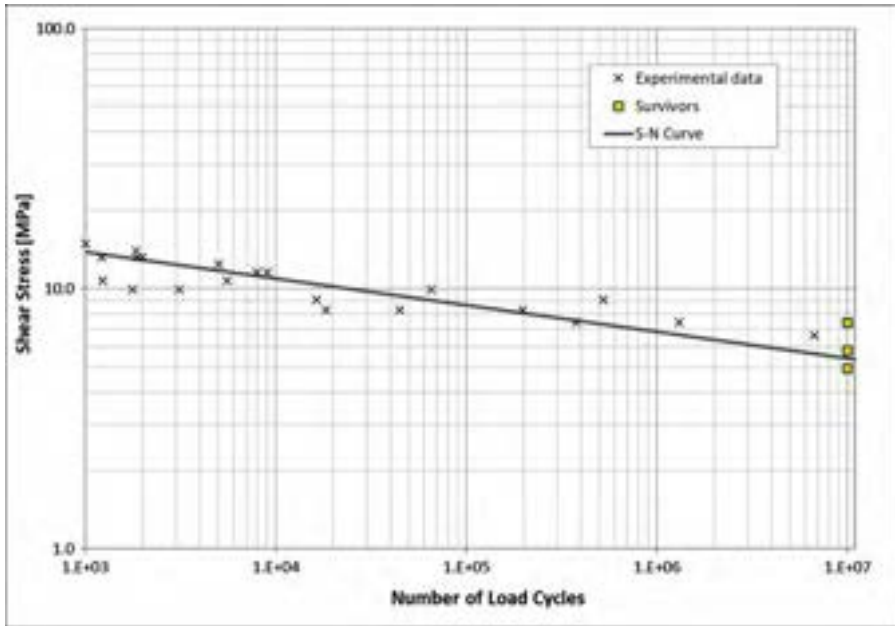


Fig. 3.6 Representative fatigue test results for lap-shear samples bonded by 2C PUR adhesive, according to Ref. [12].

Data courtesy of Sika AG.

behavior. The latter often tend to be brittle at low temperatures, whereas they lose mechanical strength and stiffness at high temperatures; such behavior is the consequence of a glass transition occurring within the service temperature range [13]. This typical limitation of standard structural 2C PUR has, however, been overcome by recent advancements, which are illustrated in the following sections.

3.2.2 Thermomechanical properties

Knowledge of the frequency and temperature dependence of dynamically stressed components (e.g., elastic adhesives) is essential for application development. The mechanical properties of polymeric materials, including PUR adhesives, are dependent on temperature and, in the case of a dynamically applied mechanical load, on the frequency used for stimulation. Mechanical properties change significantly in the range of transition temperatures that characterizes glass transition or melting processes. Dynamic mechanical thermal analysis (DMTA or DMA) is a versatile method to determine thermal transitions within a multiphase material such as PUR adhesives. The viscoelastic properties of the sample materials can be evaluated from the time intervals between the mechanical stimulus and the sample response. Various test methods are used. Most commonly, samples of solid material (ranging from soft-elastic to stiff) are supplied to tension, torsion, or bending tests. The DMTA is an

off-resonance method. The process works with forced vibrations. The test specimens are exposed to sinusoidal mechanical excitations at test frequencies of typically 0.1 to 100 Hz—either free of preload or statically loaded. The measurement modes used most frequently are a temperature sweep at a constant frequency or a frequency sweep while holding a constant temperature [14]. The application of sinusoidal stress to a material produces a strain with the same frequency. For purely elastic materials, the applied stress (force) and the strain (deformation) are in phase. The phase angle δ is 0 degrees. A purely elastic sample oscillates without loss of energy. Purely viscous materials have a phase angle of 90 degrees. In a purely viscous sample, deformational energy is fully converted into heat. In viscoelastic materials such as PUR adhesives, the deformation of the sample follows with some delay with respect to the applied stress. The phase angle δ is therefore between 0 and 90 degrees. The larger the phase angle, the stronger the damping effect [15]. The frequency-dependent dynamic modulus can be expressed as a complex number resulting in complex dynamic modulus $E^*(\omega)$, which is composed of two frequency-dependent terms, $E'(\omega)$ the storage modulus and $E''(\omega)$ the loss modulus. While $E'(\omega)$ measures the amount of stored mechanical energy, $E''(\omega)$ although expressed as an imaginary part represents the energy dissipated by the sample being a real quantity (Formula 3.1).

$$E^*(\omega) = E'(\omega) + iE''(\omega) \quad (3.1)$$

For not perfectly elastic materials, the mechanical answer is out of phase with the stimulation. This shift is also referred to as a phase angle or loss angle δ . In a geometrical representation the equation given in Formula (3.2) becomes obvious (Fig. 3.7).

$$\tan \delta = \frac{E''(\omega)}{E'(\omega)} \quad (3.2)$$

In the case of multiphase polymers such as PURs, various glass transition temperatures (T_g) can, for example, be seen by a local maximum in the $\tan \delta$ curve. Alternatively, the maximum for the $E''(\omega)$ is often taken as the dynamic T_g . The above-

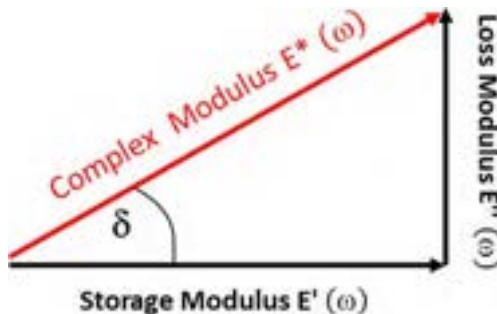


Fig. 3.7 Schematic representation of the complex modulus E^* defined by storage modulus E' , loss modulus E'' , and the loss angle δ (Formula 3.2).

mentioned considerations are valid for bulk materials [16]. The viscoelastic mechanical behavior of adhesives in technical joints depends on the rate of deformation and on temperature in a more complex way. Any adhesive bonding mechanism immobilizes polymer molecules at the contact layer to the substrate. This interaction may trigger the demixing of polymer domains and cause orientation of polymer segments along the interface layers. As a result, the mechanical properties of the interface region can differ from the mechanical properties in bulk. The effective mechanical properties of the adhesive joint are found to be dependent on the bondline thickness. As a consequence, higher values for dynamic T_g and a narrower T_g region are found. The storage modulus of the rubbery plateau rises with decreasing bondline thickness [17].

3.3 Chemical overview and PUR structure to property relationships

3.3.1 Chemistry of PUR adhesives

Four chemical reactions shown in Fig. 3.8 dominate the curing chemistry of PUR adhesives. Besides the formation of urethane bonds by the reaction of isocyanate and alcohol groups, the formation of urea bonds by the reaction of isocyanate with amines takes place. In the case of the reaction of isocyanates with water, the intermediately formed carbamic acid decays into a primary amine releasing carbon dioxide [18].



Fig. 3.8 Set of basic isocyanate-related chemical reactions including possible transition states used in 1C and 2C PUR adhesives. Courtesy of Sika Technology AG.

The mentioned transformation of isocyanate functionalities into amines on reacting with water molecules as a preliminary step is a prerequisite for the curing of 1C PUR adhesives. The amount of water necessary for curing is either provided by humidity from the ambient air or by a separate water-containing component, the so-called “booster” paste. Fig. 3.9 shows schematically the curing reaction of a 1C PUR composition, resulting in a crosslinked polyurethane-urea. As a side product, one molecule of carbon dioxide is released for every urea bond that is formed. Here, the diffusion of humidity from the environment into the adhesive bondline controls the curing behavior and defines the through-hardening behavior. As curing proceeds, the water diffusivity through already hardened layers decreases and the curing rate slows down. The formed carbon dioxide escapes from the system as soon as solubility in the matrix is exceeded. If this process proceeds too fast, bubble formation can occur, which may compromise the proper adhesion to the surface and weaken the PUR matrix by the formation of voids [19]. In contrast, curing in 2C reaction adhesives proceeds homogeneously throughout the whole volume of the bondline. The difference in curing is illustrated in Fig. 3.1.

A way to avoid bubble formation and reduce the water sensitivity of freshly produced 1C PUR adhesives is through the use of latent amine hardeners. Instead of the isocyanate-water reaction, this approach uses, in concurrence to the isocyanate-water reaction, the back reaction of the latent hardener with water, setting free a reactive amine species. As soon as the reactive species is formed, the preferred reaction of isocyanate and amine groups can proceed. By partly using this additional curing pathway, the stability of the 1C PUR formulation during storage can be increased and the carbon dioxide bubble formation can be reduced effectively (Fig. 3.10).

The classic way to produce structural adhesives, which are completely linked via urethane bonds, is the 2C PUR approach, where a polyol resin component is cured with an isocyanate hardener component (Fig. 3.11). The hardener is based on a

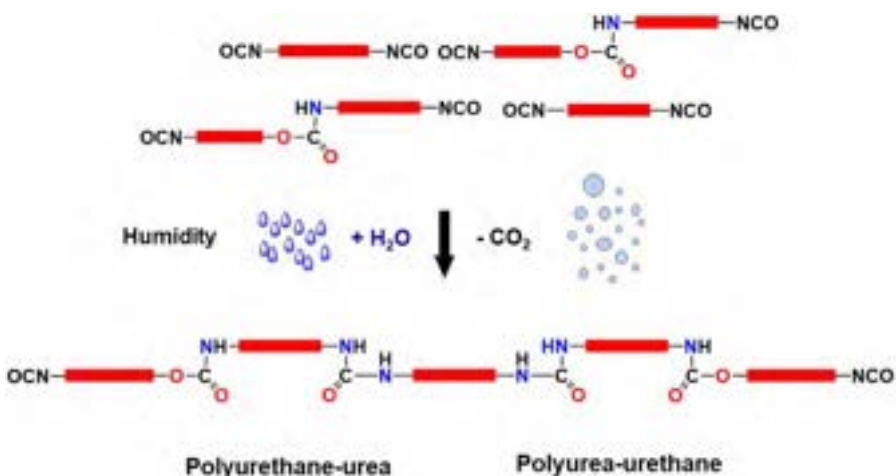


Fig. 3.9 Schematic representation of humidity-triggered curing of 1C PUR. Courtesy of Sika Technology AG.

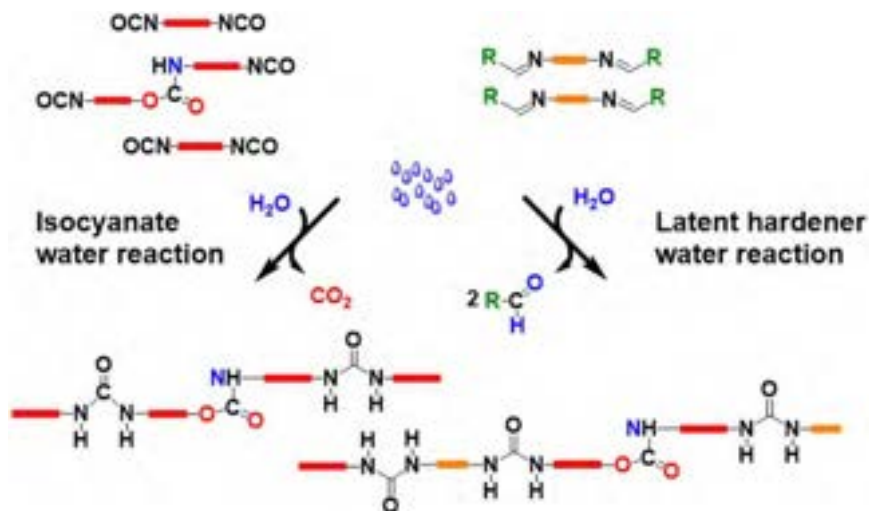


Fig. 3.10 Schematic representation of humidity-triggered curing of 1C PUR directly humidity triggered or via latent hardener approach.
Courtesy of Sika Technology AG.

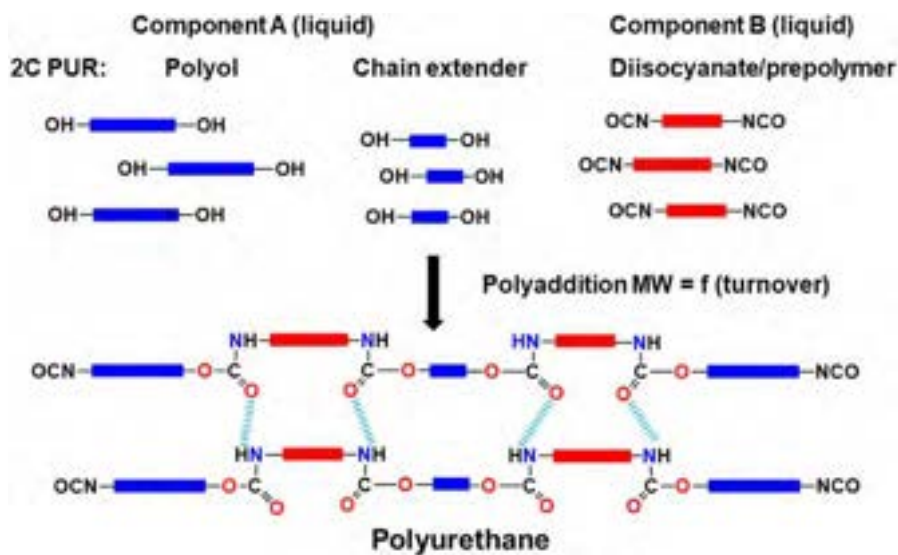


Fig. 3.11 Schematic representation of reactive curing 2C PUR.
Courtesy of Sika Technology AG.

mixture of mainly aromatic monomeric diisocyanates and higher molar mass polyisocyanates. Structural PUR adhesives with high variability in performance and a good price-performance ratio are easily accessible from polyether- or polyester-based polyols and aromatic isocyanate hardeners mostly based on 4,4'-methylene diphenyl diisocyanate (MDI). Unfortunately, 2C PUR adhesives have a tendency to show foaming, due to the high reactivity of MDI toward humidity coming from the environment or adsorbed on the substrates as well as humidity from the resin component, which is contained in the polyols and/or the fillers. Attempts to reduce foaming and increase the selectivity for the isocyanate-polyol reaction by adding a specific catalyst are only successful when humidity is adequately controlled [19]. Depending on the crosslink density introduced via the functionality and molar mass of the reactive components and the miscibility of the formed urethane bond-rich (hard segments) and polyol segment-rich (soft segments), either amorphous phase-mixed or, in the case of incompatibility, microphase-separated polymer networks are formed [20,21].

3.3.2 PUR structure to property relationships

Fig. 3.12 shows the course of E^* as a function of temperature measured at a constant frequency for a mixed-phase PUR adhesive. Due to a lack of phase separation, highly crosslinked PUR form amorphous, mixed-phase materials showing one broad glass transition temperature range (T_g mix) in a temperature window between 0°C and 100°C.

The mechanical properties of a structural adhesive are the key parameters for secure bonding. Amazingly, most conventional 2C PUR adhesives dominating the market represent highly crosslinked PUR adhesives. In most cases, they represent

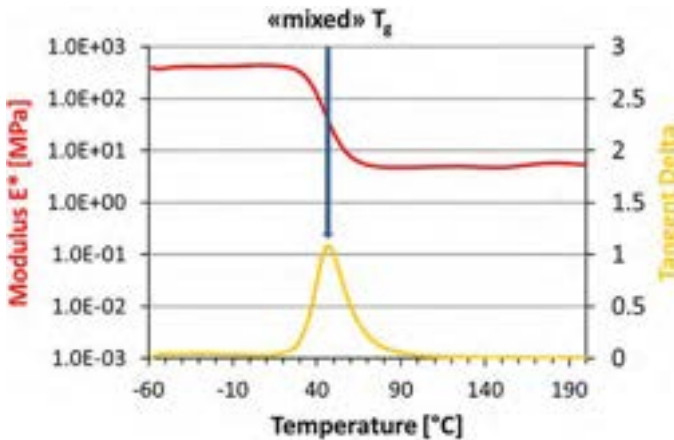


Fig. 3.12 Schematic representation of E^* and $\tan \delta$ of a mixed phase PUR adhesive measured as temperature sweep at a constant frequency.

Courtesy of Sika Technology AG.

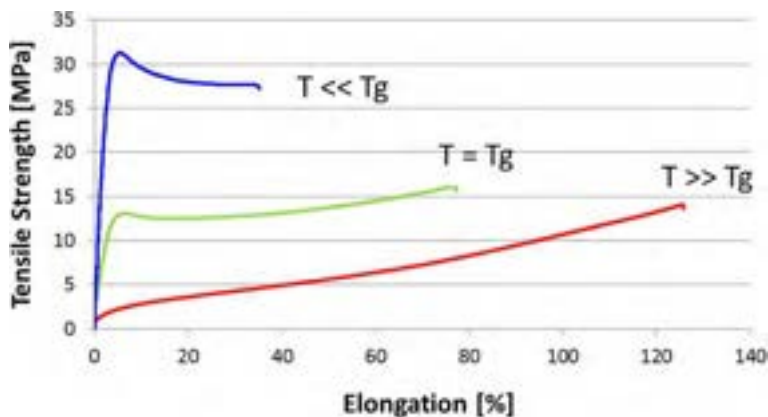


Fig. 3.13 Dependency of mechanical properties of a PUR adhesive on temperature in relation to the glass transition temperature (T_g) recorded at room temperature and strain rates between 10 and 200 mm/min.

Courtesy of Sika Technology AG.

amorphous phase-mixed materials, which exhibit only one dominant T_g in a temperature range between 10°C and 90°C. Consequently, these materials cannot be considered stiff-elastic, highly structural adhesives when the operation temperature is close to the T_g . The mechanical properties of such PUR are strongly dependent on the relationship of the measurement temperature and T_g , as shown schematically in Fig. 3.13 for tensile curves recorded below ($T \ll T_g$), around ($T = T_g$), and above T_g ($T \gg T_g$). Concepts developed to overcome the temperature dependence of mechanical properties are discussed in the following paragraph.

Phase separation in PUR adhesives can occur as a consequence of more selective crosslinking followed by microphase separation. Fig. 3.14 shows the course of E^* as a function of temperature measured at a constant frequency for a phase-separated PUR adhesive. Microphase separation is evident when characteristic softening of the material at cold temperatures upon heating above the first glass transition temperature determined by the polyol-segment phase (T_g low) occurs. Above the lower T_g , the material enters the rubbery plateau and is in a rubber-like visco-elastic state. Depending on the weight ratio of the hard segment as well as the reaction product of low molecular weight diols and especially aromatic isocyanate hardeners, the first drop in modulus between the glassy state and the viscoelastic state can be up to three orders of magnitude. A further significant drop of the modulus is observed at temperatures above the second T_g defined by the loosening of intermolecular interactions and aggregates within the hard segment phase (T_g high). Above this higher T_g , the material is in a plastic state characterized by a rubbery flow and, upon further heating, decomposition by chemical degradation due to oxidation or other depolymerization processes that result in irreversible liquidation of the PUR. Controlled thermal degradation can be used for heat-triggered debonding. A structural polyurethane

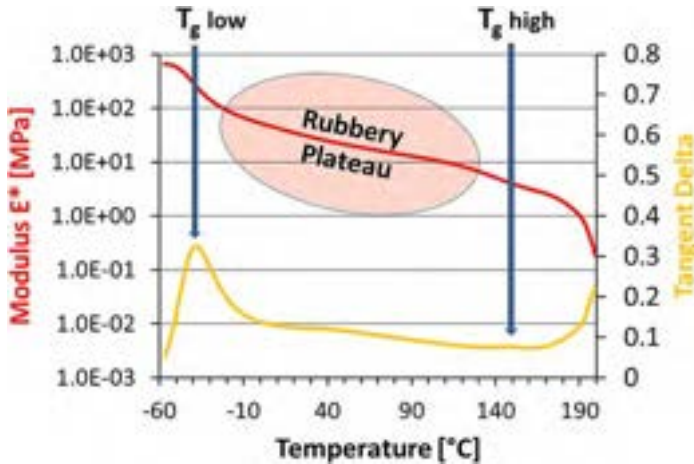


Fig. 3.14 Schematic representation of E^* and $\tan \delta$ of a soft elastic, phase-separated PUR adhesive measured as temperature sweep at a constant frequency. Courtesy of Sika Technology AG.

adhesive with optimal toughness and less dependency of the mechanical properties on temperature presents a major but highly rewarding challenge. This could be solved by promoting the microphase separation tendency between hard and soft segments and by the combination of two nonmixable polyols such as polybutadiene-based polyol and higher functional polyether polyols. Such products form phase-separated polymer matrixes, each of them having its own T_g , one at lower and one at higher temperatures. In this way, structural elastic adhesives with a variable elastic modulus in the operation temperature window can be obtained [22–25]. An alternative way to achieve a temperature-insensitive structural adhesive that can be cured at room temperature is an approach of producing an adhesive with only one low T_g , comparable to 1C PUR adhesives [13]. The soft segment-defining polymer phase is based on prepolymers obtained from the combination of low T_g polyols that are chain terminated with (mainly) difunctional isocyanates ($f > 2$ and < 2.3 preferably). 2C PUR formed in this way exhibits highly elastic properties and one low T_g in the range of -40°C to -60°C . To guarantee mechanical stability, physical crosslinking by short chain hard segments is chosen. Therefore, the isocyanate-terminated prepolymers are chain elongated with low molar mass diols forming hard segments for physical crosslinking. Fig. 3.14 shows a schematic DMTA diagram of such an adhesive that was cured at room temperature, showing a dominant T_g at -55°C . At temperatures above 150°C , the gradual softening of the formed hard segments can be observed. Within a common service temperature range of -30°C to 80°C , no phase transition occurs, and a PUR adhesive with stable modulus is achieved. Depending on the weight ratio of soft segment to hard segment, the resulting multiphase materials are either soft segment-dominated soft elastic (Fig. 3.14) or hard segment-dominated stiff elastic in the temperature range of the rubbery plateau (Fig. 3.15).

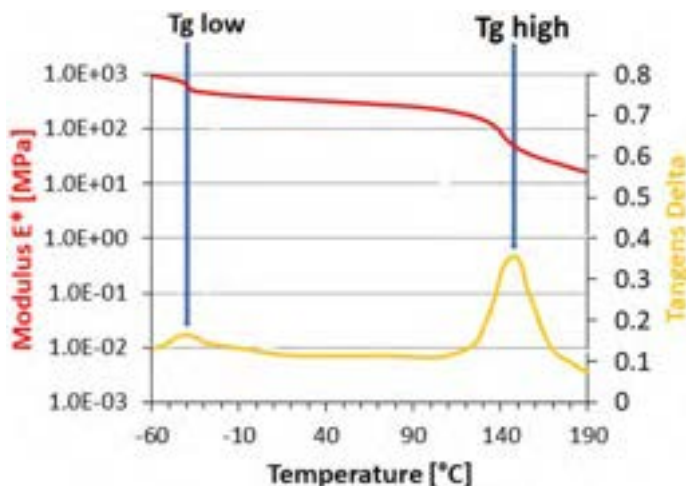


Fig. 3.15 Schematic representation of E^* and $\tan \delta$ of a hard elastic PUR adhesive measured as temperature sweep at a constant frequency. Courtesy of Sika Technology AG.

3.4 Formulation and raw materials of PUR adhesives

As discussed in detail in [Section 3.1](#), the properties of PUR adhesives can vary greatly. Different properties can be reached by adjustments in the formed network architecture such as crosslink density, the nature of polymer chains, and further raw materials used, which influence the kinetics, adhesion, mechanics, rheologic behavior, workability, and storage stability of the adhesive. This chapter will deal with chemical aspects and will present some selected tactics to adjust properties of 2C PUR adhesives. Taking a closer look at the formulation of a 2C PUR adhesive, in addition to the polymer matrix consisting of isocyanates and polyols, there are additional compounds necessary to adjust workability and mechanical properties as well as other adhesive specific properties such as color, UV stability, or thermal stability. It is the formulator's task to make the right choice of raw materials to achieve the desired product properties with respect to the uncured material, such as rheological behavior or application behavior, mixing ratio, and mixing properties, but also with respect to the cured material, such as working time or open time, curing speed, handling strength, final mechanical properties, and aging resistance. The properties of the cured adhesive are strongly dependent on the formed polymer, its chemical base, and crosslink density (either physical crosslinking by segregation driven by intermolecular interaction or covalent crosslinking by polyols, isocyanates, and crosslinkers with a functionality higher than 2). The following section introduces classes of raw materials used to formulate structural PUR adhesives. A summary is given in [Table 3.3](#).

Table 3.3 Overview of selected raw materials, trade names, and suppliers.

Class	Type	Examples	Impact	Supplier
Isocyanate	Aromatic Aliphatic	4,4'-MDI, 2,4-TDI HDI-biuret, HDI-isocyanurate, IPDI-Isocyanurate	Reactivity Crosslinking, weathering stability Elongation, softening	Borsodchem, BASF, Covestro, DOW, Lanxess, Huntsman
	Prepolymers	Adiprene LFH 2840: HDI-based polycaprolactone prepolymer Desmodur E 22: MDI-based prepolymer		
Polyol	High M_w	$f=2$: PPG 2000, PPG 4000, PPG 8000 $f=3$: PPG/EO 5000, PPG/EO 6000	Softening, low T_g , elongation Mechanical strength Chemical crosslinking	BASF, Covestro, DOW, Evonik, Kuraray, Shell, Repsol
	Low M_w	$f=2$: Castor oil, PPG 400 $f=3$: PPG 300, PPG 450		
	Chain extenders	1,4-Butanediol, 2-ethyl-1,3-hexanediol		
Polyamine	Crosslinkers	Trimethylolpropane (TMP)	Chemical crosslinking Reactivity, mechanical strength, physical crosslinking	Evonik, Albemarle
	Low M_w diamines	Dimethylthiotoluenediamine, 3,5-Diethyltoluene-2,4-diamine, 4,4'-Methylenebis(<i>N-sec</i> -butylaniline)		
	High M_w diamines	Poly(oxy-1,4-butanediyl), α -(4-aminobenzoyl)- ω -[(4-aminobenzoyl)oxy] VERSALINK P 650 Propane-1,3-diyl bis(4-aminobenzoate) VERSALINK 740 M		
Plasticizer	Aromatic esters	Diisononylphthalate (DINP) Diisodecylphthalate (DIDP)	Diluent, pricing, softening	Evonik, Lanxess, Exxonmobile Chem.
	Aliphatic esters	Diocyladipate (DOA) Diisononyladipate (DINA)		
	Others	Tris(2-ethylhexyl) phosphate, Tris(methylphenyl) phosphate Biodiesel/fatty acid esters	Flame retardant Renewable	

Structural filler	Carbon black	Printex 60, Printex 25	Reinforcing,	Orion
	Pyrogenic silica	Monarch 570, Regal 330R	mechanical strength,	Cabot
Filler	Minerals	AEROSIL R 972	nonsag properties,	Evonik
	Light weight	CAB-O-SIL TS-720	thixotropy	Cabot
	Organic polymers	CaCO ₃ ground or precipitated	Rheology, mechanical strength	Omya, BASF
Pigments	Iron oxides	Calcined China clay	Density reduction	Imerys
	Titanium dioxide	Expancel types	Rheology, density	Nouryon
	Organic pigments	PVC powder	Coloring	Inovyn (INEOS)
Catalyst	Metal	Bayferrox types	Base white pigment	Lanxess
	Amine	KRONOS types	Coloring	KRONOS
		Hostaperm types	Reactivity, pot life, handling strength	Clariant
Additives [23]	Stabilizers UV/heat	Dibutyl[bis(dodecanoyloxy)]stannan		Borchers, Reaxis, Evonik, Varistor, TIB Chemicals
		Bismuth-neodecanoate	Stabilization	BASF, BYK
		1,4-Diazabicyclo[2.2.2]octan		
		1,8-Diazabicyclo[5.4.0]undec-7-en		
		HALS: mixture of bis (1, 2, 2, 6, 6-pentamethyl-4-piperidyl) sebacate and methyl 1, 2, 2, 6, 6-pentamethyl-4-piperidyl sebacate Tinuvin 765		
		Antioxidant: benzenepropanoic acid, 3,5-bis (1,1-dimethyl-ethyl)-4-hydroxy-, C7-C9 branched alkyl esters Irganox 1135		
	Rheology control	PA waxes, hydrogenated castor oil	Rheology	
	Defoamer/degassing	Modified PDMS	Defoaming/degassing	

3.4.1 Raw materials

3.4.1.1 Isocyanates

Isocyanate-containing molecules undergo a reaction with alcohol-containing molecules to form a urethane bond (see Section 3.3, Fig. 3.8). Commonly used building blocks are aromatic and aliphatic isocyanates. The main aromatic ones are 4,4'-diphenylmethane diisocyanate (MDI) and toluene diisocyanate (TDI). Regarding the aliphatic hardeners, three main chemicals must be mentioned: 1,6-hexamethylene diisocyanate (HDI), isophorone diisocyanate (IPDI), and the hydrogenated MDI 4,4'-dicyclohexane diisocyanate (H12-MDI). Products based on aliphatic isocyanates result in adhesives with higher light stability or better nonyellowing properties. Nevertheless, MDI is the preferred diisocyanate due to an attractive cost-to-performance ratio and the low vapor pressure of the monomer, which allows safe handling. In recent years, diisocyanates have been considered “substances of great concern” for safety. PUR adhesive manufacturers are therefore investigating new routes to reduce or even completely replace the monomeric diisocyanates in adhesives. One easy and straightforward approach is to use polymeric isocyanates instead. Polymeric isocyanates are higher molar mass (M_w) oligomers or polymers and therefore contain lower levels of monomeric diisocyanates, which reduces the risks in handling such adhesives. As mentioned earlier, MDI and its polymeric versions (crude MDI) as well as di- or trimeric HDI are among the most widely used isocyanates for structural adhesives. Other types of isocyanates (TDI, HDI, H12-MDI, IPDI) are usually introduced via prepolymers due to the toxicity of the free monomer. This toxicity issue is nowadays overcome by the use of stripped prepolymers, where the free monomers are removed by distillation. Finally, the stoichiometric ratio of NCO to OH groups, the so-called isocyanate index, is important for the curing and the final properties of the PUR adhesive. As a rule of thumb, an excess of 10% of NCO groups is commonly applied, such as an isocyanate index of 1.1. In the case of crude MDI, a higher index (up to around 1.3) is recommended because some NCO groups are lower in reactivity due to steric hindrance [26–28].

3.4.1.2 Polyols

Regarding the polyols, a huge variety of raw materials is available. Besides the chemical nature of the polymer backbone (polyethers, polyesters, polycarbonates, sugar alcohols, or hydrocarbon polyols), chain length (molar mass) and functionality (mono-, di-, tri-, or higher) also have a huge impact on the PUR network formed upon curing, that is, polyesters are used to enhance adhesion performance. Polyethers typically provide low viscosity to the uncured adhesive and introduce flexibility of the cured adhesive at a low temperature. To improve chemical resistance, hydrophobic polyols such as hydroxy-terminated polybutadiene (ht-polyBD) or polyesters obtained from oleochemical processes are used. Other advantages of the nature of the polyol will be discussed in more detail in Section 3.6. Besides the polymeric polyols, low molar mass diols (called chain extenders) or low M_w polyols (crosslinkers) play a key role in PUR adhesives. Such crosslinkers or chain-extender molecules are

important to adjust gelation (curing speed) and the mechanical properties of the final adhesive. In addition, the use of a catalyst has a strong impact on the curing behavior of the adhesive. In the polyol component, polyether polyols based on polypropylene glycol (PPG) but also polyester polyols, polycarbonate polyols, polyacrylic polyols, and OH-functional polyolefins such as ht-polyBD are common. Polyols with a high M_w and low functionality will soften the products and enhance elastic or plastic properties. Short chained and bi- or higher functional PPG polyols as well as castor oil are among the most common polyols for structural adhesives, leading to high crosslinking and therefore high mechanical properties at moderate elongation. Some PPGs are also offered with ethylene oxide (EO) polymer chain termination, so called endcapping, to enhance the reactivity of the system because the OH-group in pure PPG polyols is on a secondary carbon atom neighbored by a methyl group, causing steric hindrance and therefore reducing the reactivity. Low molar mass linear as well as asymmetric diols are used as chain extenders to increase the mechanical properties and to support hard segment segregation. Low M_w polyols with an OH-functionality $f > 3$ (ethoxylated or propoxylated sugar types for example) are used as a crosslinker to increase the crosslinking density and accordingly the mechanical properties in general except for elongation, which naturally decreases with a higher crosslinking degree.

3.4.1.3 Amines as copolymers

A more specific ingredient are the amine functional reaction partners. Due to their high reactivity with isocyanates, polyamines that are used as reactive additives in PUR adhesives to generate additional polyurea (PUA) segments are usually sterically hindered or electronically passivated to control their high reactivity with isocyanates. While the reaction of polyol and isocyanate can be controlled by a catalyst, polyamines are too reactive and must be designed accordingly. Additionally, polyamines are usually used with less reactive isocyanates than MDI or in a suitable application process (reactive injection molding, for example). Due to the nature of the urea bond and its ability to form strong hard segments, such adhesives exhibit high mechanical strength and have superior heat stability compared to pure PUR. Substituted toluenediamines or methylene-bis-anilines as well as adducts of amines and maleic acid ester are among the commonly used polyamines and should also be mentioned here.

3.4.1.4 Structural fillers

To improve the mechanical properties on the one hand and the rheological properties on the other hand, structural fillers play an important part. The most commonly used types are carbon black and silica (pyrogenic, surface coated). The structure of such fillers is defined by surface area and particle size. These fillers have a direct impact on rheological properties such as yield stress and viscosity as well as on the resulting mechanical properties such as elongation, tear resistance, tensile and lap-shear strength. There are many different types of fillers to choose from (particle size, surface area, oil absorption) and it is the formulator's task to find the most suitable reinforcing filler for the intended properties and application. Aside from the structural fillers,

there is also a variety of other fillers available. These will also impact the mechanical and rheological properties of the adhesive but to a lesser degree [29–31]. Particle size and shape depend on the kind of mineral used and how processed. The most common and important mineral fillers are limestone or marble (calcium carbonate) available as spherical-shaped, ground types (GCC), and precipitated types (PCC) with different particle size distribution (either surface coated with mainly fatty acids (e.g., stearic acid) for better chemical resistance or uncoated) as well as sheet silicates (Kaolin, Talcum) or silicate fibers (Wollastonite) [32]. Among the specialty fillers are aluminum trihydroxide (ATH), a main filler for flame-retardant adhesives but also for thermally conductive adhesives, and Barite, a high-density, chemically very stable filler. Many inorganic minerals have limited suitability as fillers due to the high Mohs hardness, causing abrasion and damage to production and application equipment.

3.4.1.5 Lightweight fillers, rheology modifiers, pigments, and surface-active agents

Lightweight fillers or hollow spheres are used to reduce the density of adhesives in applications where weight reduction is important. Heat expandable or already expanded microspheres, often based on polystyrene nitrile (SAN), are very common but also glass beads with different shell thicknesses and diameters, for promoting shear and pressure resistance, as well as silica-based hollow spheres from fly ash are available. There are also organic fillers such as polyvinyl chloride (PVC), polyethylene (PE), polypropylene (PP), and polyamide (PA) all available as powders or fibers. The most common one is PVC powder, which is important for plastisol applications. It can be used in plasticizer-containing formulations where controlled swelling is done at an elevated temperature to achieve thixotropic behavior of the adhesive component. While PVC powder can be produced directly by suspension polymerization processes, other plastic powders must be manufactured using a cryo-mill process. For rheology control (application properties, surface wetting), cost optimization, and adjustment of physical properties, many kinds of plasticizers can be used. They can also help achieve better segregation of hard segments but will decrease the mechanical strength of the final product. Among the most important are the phthalate esters, the most common plasticizers in 1C and 2C PUR adhesives. Moreover, phosphates, particularly phosphoric acid esters, are mainly used in flame-retardant adhesives, and adipic acid esters are used as an alternative to phthalates with the advantage of lower viscosity but at the cost of decreased hydrolysis stability. Citric acid esters are mainly used for adhesives that get in contact with food and living organisms. The use of carboxylic acid esters as plasticizers is very common, and with respect to renewable raw materials, esters of fatty acids (e.g., biodiesel) are used more and more, even though the hydrolysis stability is often insufficient. Of less importance are nonfunctional plasticizers such as mineral oil fractions with a high boiling point and low vapor pressure that can also be used, but compatibility with and possible demixing from other ingredients in the adhesive formula can be a crucial point. In the case of colored adhesives, special fillers or pigments are used to differentiate the components from each other, to

indicate the type of adhesive used in parts, or for decorative or stabilization reasons. Titanium dioxide (TiO_2), ground types and/or coated types with a very high white color index are mainly used as a white and base pigment, often combined with clay of a high purity to reduce costs for the pigments used. Moreover, TiO_2 is used as a UV stabilizer. Iron oxides are available in a variety of colors and used as pigments in adhesives because of their nontoxic nature due to their insolubility. Carbon black is also used as a common pigment for grayish and black-colored adhesives, and for very specific colors and effects organic pigments offer solutions for almost all requirements, even for fluorescence and phosphorescence effects. Hydrogenated fatty acids such as hydrogenated castor oil as well as low molar mass polyamides are among the most commonly used rheology control additives. After incorporation at elevated temperatures and cooling to room temperature, the adhesive will show the desired rheological properties. Especially for low viscosity formulations, coatings, and self-leveling applications, the use of degassing agents and defoamers is important to obtain the desired appearance of the cured product. Wetting agents help to overcome differences in surface tension between the adhesive matrix and substrate or filler surfaces [33].

3.4.1.6 Curing catalysts

There are a variety of catalysts available, and among the most often used are tertiary amines and metal carboxylates. Amines are suitable for aromatic isocyanates but can also be used in aliphatic systems in higher concentrations. Metal carboxylates can be used with any kind of isocyanate but should not be formulated into the isocyanate compound (except for di-organo-tin catalysts) because carboxylate ions can catalyze the homopolymerization of isocyanates to form uretdiones, isocyanurates, and other oligomers. Strong bases (tertiary amines) also catalyze these side reactions [18,19]. Here as well, the variety of available catalysts for polyurethane reaction includes many different substances. Finally, the choice of the right catalyst system is highly dependent on the intended use. Which curing speed is required? At which temperature will the adhesive be applied? What are the ambient conditions? Based on such requirements, the adhesive formulator will have to choose accordingly.

3.4.1.7 Stabilizers

Based on the required properties and applications, the use of special additives to improve the workability and storage stability of the adhesive formula is often helpful. A great variety of such additives is commercially available. Among the most important stabilizers (antioxidants and UV stabilizers) are sulfides, phosphonates, sterically hindered phenols, phosphite, benzotriazole, and sterically hindered amine light stabilizer (HALS). Further heat and UV stabilizers are available for all kinds of PUR formulations; suppliers are very helpful in making the right choice [34–36].

3.4.2 Regulatory aspects of PUR adhesives

The toxicity of isocyanates is the main concern with PUR adhesives. Isocyanates are highly reactive chemicals that undergo reactions with a variety of functional groups such as alcohols, amines, and thiols. Such functional groups are available in the human body as well. This is why the safety of users working with such chemicals is of high importance. From February 2022, all polyurethane adhesives containing more than 0.1 wt% of free monomeric diisocyanate must be labeled accordingly in the European Union [37]. End users working with such adhesives will have to undergo PUR training to be allowed to apply these products [38,39]. Additionally, most European countries, but also the United States and China, have established an occupational exposure limit (OEL) of isocyanates in the breathing air of a user of such products. Isocyanates are therefore closely observed chemicals with a lot of health-related information. With proper handling, the use of such adhesives should be safe. Nevertheless, more and more suppliers are investigating solutions to reduce the free monomeric diisocyanate content of the adhesive or are looking for alternative curing chemistries allowing the realization of similar property profiles.

3.5 Selected applications of structural polyurethane adhesives

3.5.1 Industrial use of structural PUR adhesives

The great variety of structural PUR formulations aids the designing of adhesives in several application fields. Most applications are found in vehicle manufacturing, ship-building, renewable energy production (e.g., bonding of wind turbine blades [10,40]), general manufacturing, and the construction industry [41–44]. Some examples are given in Figs. 3.16–3.20.

In the automotive and transportation industries, 2C PUR adhesives are frequently used in assembly lines and trim shops as well as for aftermarket repair work.



Fig. 3.16 Selected applications in vehicle manufacturing: 2C PUR is regularly employed for sandwich panel fabrication and the assembly of refrigerated trucks.

Photo courtesy of Sika AG.



Fig. 3.17 Selected applications in the marine industry: deck-to-hull and bulkhead bonding by 2C PUR adhesives.

Photo courtesy of Sika AG.



Fig. 3.18 Examples of CFRP components that are assembled using 2C PUR adhesives.

Photo courtesy of 1. BMW AG, 2. Narke Jet Ltd., 3. Sika AG.



Fig. 3.19 Example of modular assembly in bus manufacturing [13]: a prefabricated roof is bonded to the bus chassis by 2C PUR.

Photo courtesy of Van Hool NV.



Fig. 3.20 Vehicle assembly for the Peak Evolution project. Photo courtesy of Peak Evolution.

Both structural and nonstructural elements are bonded, including cabin/cockpit components, panels, floors, roofs, hoods, tailgates, spoilers, bumpers, hang-on parts, and so on. The main driver of the application of structural polyurethanes is their capability of fulfilling demanding requirements and the bonding of the diverse materials (metals, composites, polymer blends, etc.) now widely employed for vehicle parts. In particular, the assembly of lightweight components such as carbon fiber-reinforced plastics (CFRP), glass fiber-reinforced plastics (GFRP), sheet molding compounds (SMC), thermoplastics, and foams motivates the incremental use of versatile 2C PUR adhesives (Fig. 3.18), which can suit production needs well and allow joining structures that are stable under various driving conditions [13,44].

The rising manufacture of electric vehicles and the growing trend of modular assembly in production (see Fig. 3.19) also enlarge the application range of structural polyurethane adhesives. Referenced examples, therefore, are offered not only by several car models, but also by commercial and special vehicles [13]. In this context, a pioneering example is represented by the fully electric agricultural vehicle developed by the Peak Evolution team [45]. This vehicle, whose performance is tested off-road under extreme weather conditions over an altitude greater than 6000m, sees the utilization of 2C PUR adhesives for the assembly of the cabin, the transportation box, and the steel subframe for the solar panels (Fig. 3.20).

3.5.2 Application equipment

Depending on the amount of applied adhesive and the production size, structural 2C polyurethanes can be applied out of bulk packaging—that is, cans, pails, drums, etc.—or cartridges through static or dynamic mixers. Bulk applications are carried out by



Fig. 3.21 Examples of adhesive dosing equipment.
Photo courtesy of Sika AG.

appropriate pumping, mixing, and dispensing equipment (Fig. 3.21), which suits manufacturing and automation needs. Such equipment has become standard for industrial adhesive applications because it generally delivers the best mixing quality, largest extrusion amount, and fastest flow rate. On the other hand, cartridge applications are typically preferred for prototyping, although they are also frequently used in small- to medium-scale production. In this context, attention must be given when choosing the right dispenser and following the correct application procedure, which ensures optimal mixing. Just like professional users of dosing equipment for bulk applications, the users that apply adhesives out of cartridges must be properly instructed and trained.

3.6 Recent advances in PUR adhesives

3.6.1 *New concepts to fully develop the potential of PUR adhesives*

When screening PUR adhesive literature from the last 20 years, the most often mentioned topics deal with fracture mechanics, thermomechanical and stability testing, the use of renewable resource bio-based or recycled raw materials, special applications such as debonding on demand or thermo-reversible materials, and so-called non-isocyanate polyurethane (NIPU). Pretreatment of substrates and polyurethane dispersion adhesives are often highlighted fields, but are not further discussed in detail herein.

3.6.1.1 *Fracture mechanics*

The application of adhesively bonded joints in structural components for the automotive industry and the influences on these joints, such as the nature and surface roughness of bonded substrates, the geometry of the lap joint, and the type of PUR adhesive (viscoelastic and stiff) are highlighted [46,47]. In general, increasing fracture toughness with increasing joint thickness was found, though lap-shear strength decreases with increasing adhesive layer thickness. In contrast to structural adhesives with high stiffness, viscoelastic PUR adhesives provide advantages in applications where damping properties and impact energy dissipation are required [48]. An example of a fracture toughness-enhanced structural 2C PUR adhesive is obtained by adding thermally expanding thermoplastic particles. In this way, for low concentrations of such particles, fracture toughness is increased without compromising the elastic modulus. Here, a mechanism is discussed as to how far the incorporation of an additional soft phase can help to prevent crack formation upon application of mechanical stress in lap joints [49].

3.6.1.2 *Thermomechanical and stability testing*

The influence of layer thickness in the range of 50–200 μm on PUR morphology and molecular mobility on glass transition in very thin model adhesive layers was investigated. These investigations revealed a higher crosslink density and less molecular mobility within the PUR adhesive in thin adhesive joints compared to conditions found for the polymer bulk [17]. The investigation of the environmental durability of adhesive joints as well as the aging and corrosion of PUR adhesives in contact with technical metal surfaces is of great interest for industrial applications. To increase the relevance for practical applications, testing conditions should be close to industrial standard test cycles such as Cataplasma conditions combining the exposure to moisture and elevated temperatures (70°C and 100% relative humidity) as well as weathering tests including UV-A radiation in addition to storage at elevated temperatures and moisture [50,51]. In general, control of the diffusion of water within the lap joint and an anticorrosion treatment of the substrate surface help to stabilize the adhesively bonded joint and prevent corrosion. The weakening of the interface by degradation of the adhesive or corrosion of the surface causes adhesive failure. For most industrial applications, the preferred failure mode is cohesive failure, which can often be achieved by good adhesion and well-balanced cohesive strength within the bulk adhesive. The aging mechanism of a model polyurethane steel interface under the influence of humidity is shown in Ref. [52]. The two major factors—water transport and saturation in the adhesive joint and the simultaneous corrosion of the steel surface—led to a macroscopic deadhesion process of the joint.

3.6.1.3 *Bio-based PUR*

This field has gained interest over the past 20 years. The original motivation was a reduction in using limited resources when using petrol as a raw material base for the polyol part in the adhesive [53,54]. The focus was on using polyols from

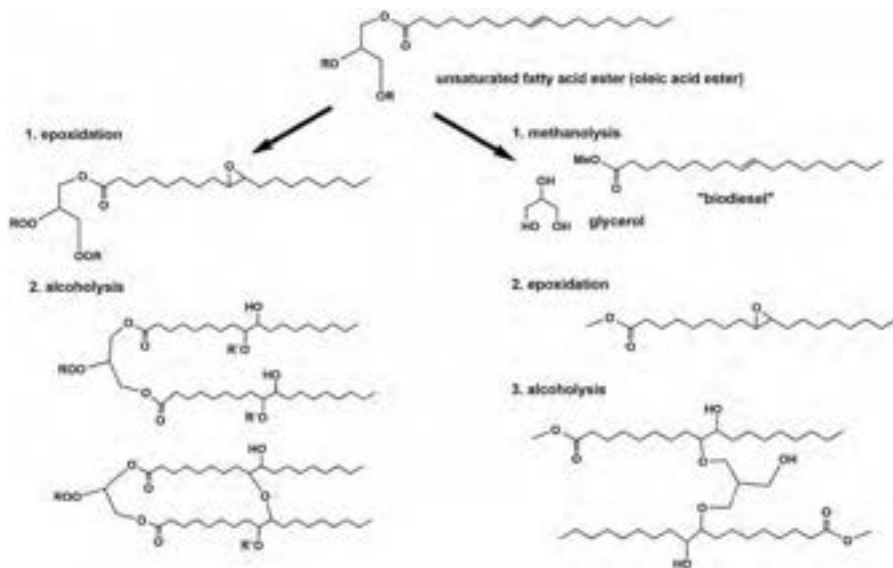


Fig. 3.22 Synthesis of polyols from oleochemical processes. Courtesy of Sika Technology AG.

oleochemical processes starting with canola, rapeseed, palm, or soybean oil. These bio-based, mostly polyester but also polyether-like polyols are synthesized by epoxidation of unsaturated double bonds in the fatty acid chains followed by transesterification or a ring-opening reaction with alcohols (Fig. 3.22). Moreover, the focus was on using nonedible castor oil in the production of structural PUR adhesives. To date, the discussion about the carbon footprint, life cycle considerations, and sustainability has become a strong driver for using biomass-derived raw materials (poly)saccharides and lignocellulose as a renewable resource as well as for the polyol and the isocyanate part. Under certain conditions, the materials can be designed to be very stable against the influence of chemicals and humidity or can be weather resistant [55]. An increasing number of projects is dealing with organic materials that do not compete with food production, such as polyols derived from lignin. A prominent example is the use of Kraft lignin, as a side product of cellulose production processes, which due to its inertness and insolubility, is often only considered to be useful for thermal recycling [56–59].

3.6.1.4 Thermo-reversible PUR/debonding effects

Stimuli-responsive adhesives, especially thermo-reversible PUR, are discussed in various concepts. For example, concepts based on polyesterurethane (hotmelt) adhesive doped with Diels-Alder functional groups are described as thermo-reversibly tunable adhesives. This functionality could be used to reverse crosslink or release bonds and therefore enable bonding and debonding with heat stimulus [60]. A comparable model concept uses the Diels-Alder functional groups for thermal switching of thermoplastic

PUR while the urethane bonds are produced by a NIPU approach, using the reaction of polyamines with cyclocarbonates to form urethane bonds [61]. For application as thermo-reversible adhesives, a certain degree of crosslinking could guarantee higher mechanical strength. A more recent approach showed how to incorporate chemo-sensitive moieties into the PUR backbone that allow a cleavage of the PUR on demand and consequently debonding by adding specific anions such as fluoride [62,63].

3.6.2 Recent advances—Designable open time followed by immediate curing

An additional challenge for the practical use of structural adhesives is the balance among pot life, open time, and curing rate. Using the conventional approach of adding a standard curing catalyst may not fully suit customer-specific application processes. In this case, an adjustment to customer needs is possible, allowing a tailor-made curing profile to be reached. Besides the presented approaches on stable mechanical properties over a broad temperature range, designable open time followed by immediate curing is a key feature, which simplifies any automatized bonding process. Currently, adhesive producers are working on solutions to propose such tailored curing behavior. Commonly used descriptors are “snapcure,” “smartcure,” “curing on demand,” or “curing by design” [13,64–66]. Usually, an additional external activation source providing heat, UV light, or microwaves is needed to initiate an accelerated curing reaction. A novel concept provides a designable open time followed by immediate curing without any additional external stimuli. The key component here is using an isocyanate reactive blocking agent for the metal catalyst. As mentioned in Section 3.3.1, the addition of a curing catalyst is a versatile tool to control the reactions necessary to reach the proper curing of a PUR adhesive. Metal catalysis in polyurethane curing relies on the ability of reactive compounds to coordinate with the metallic center of the catalyst. Two mechanisms are discussed here: the coordination of isocyanate groups at the metal center (activation of electrophiles) and the exchanging of ligands at the metal (activation of nucleophiles). The ability to coordinate with the metal and the ability to react with the isocyanate are specific for the used reactive blocking agent. To design a sequenced reaction scheme, this combination of catalyst and blocking agent can be used to control the pot life or working time of the adhesive by implementing a first, antecedent reaction that temporarily inhibits the reactive compounds responsible for chemical crosslinking (gelation) [64]. Once the first reaction stage is fully completed, the curing of the adhesive starts immediately due to a delayed action catalysis, promoting a fast gelation reaction. By using this technique, 2C PUR adhesives with a tailored delay period after mixing and application followed by a very fast curing reaction are obtained. This allows for separate adhesive working time and curing speed, thus reducing unproductive fixing or holding times until the assembled parts can be handled and further processed. By isothermal viscosity measurement at 20°C using a plate-plate system (25 mm diameter, 1 mm gap) and oscillation (radial frequency of 10rad/s and an amplitude γ of 1%), the curing behavior (Fig. 3.23) as well as the pot life (Fig. 3.24) of 2C PUR adhesives can be

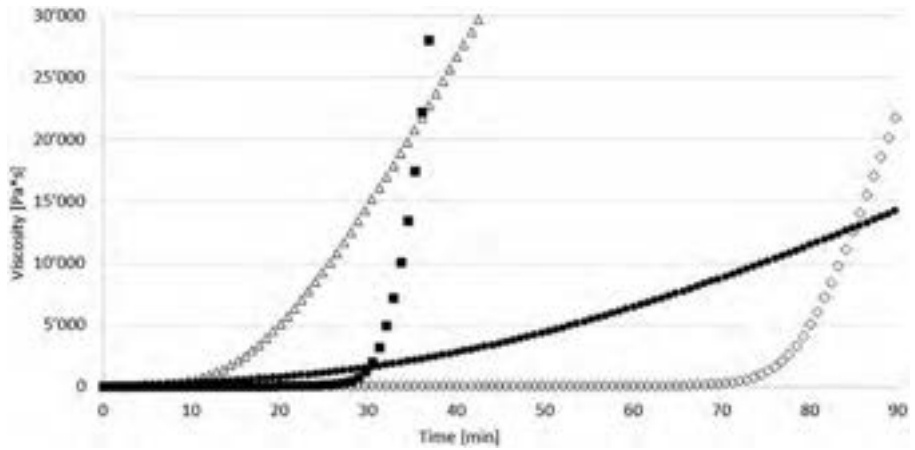


Fig. 3.23 Viscosity increase (gelation) depending on curing time for 2C PUR adhesives with a sequenced reaction scheme in comparison to a conventional fast curing and a slow curing 2C adhesive. Δ adhesive 1: fast curing and short pot life, \bullet adhesive 2: slow curing and long pot life, \blacksquare adhesive 3: extended pot life and fast curing, \diamond adhesive 4: long pot life and fast curing. Courtesy of Sika Technology AG.

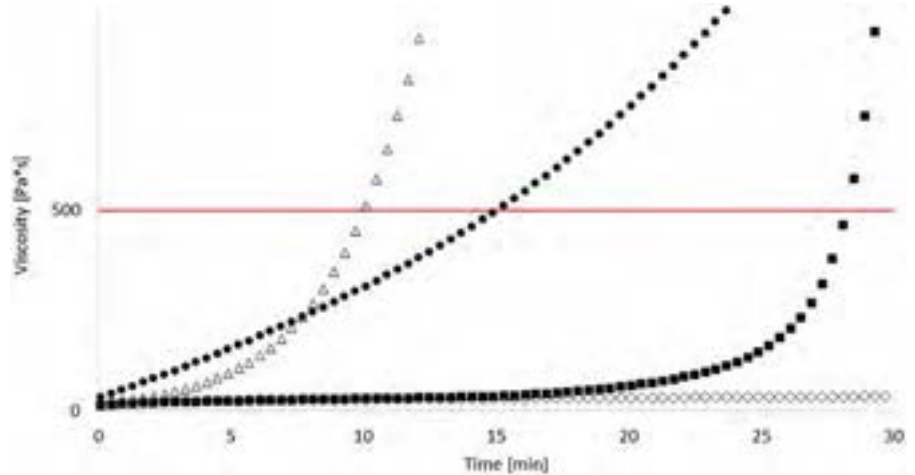


Fig. 3.24 Viscosity increase (gelation) with respect to the limit of workability for 2C PUR adhesives with a sequenced reaction scheme in comparison to a conventional fast curing and a slow curing 2C adhesive. Δ adhesive 1: fast curing and short pot life, \bullet adhesive 2: slow curing and long pot life, \blacksquare adhesive 3: extended pot life and fast curing, \diamond adhesive 4: long pot life and fast curing. Courtesy of Sika Technology AG.

determined easily and the sequenced reaction becomes visible. The curing behavior of an adhesive is important in a production process. On the one hand, the time until parts can be handled and undergo the next process step defines the possible cycle time and the handling strength, and on the other hand the time until the adhesive viscosity rises to a level where it cannot be processed anymore, the pot life, defines the workability time needed to mount the parts that are bonded together. Fig. 3.23 visualizes the curing behavior of two standard catalyzed adhesives as well as two adhesives using a sequenced pot life. A sequenced pot life greatly improves the workability and retains the fast-curing properties to shorten the gap between pot life and handling strength; handling strength is generally defined by the customer and its process and not by measured viscosity values. The curing speed is visualized by the slope of the curve, which causes adhesive 3 to cure faster than adhesive 1 even though the workability time span is greatly extended; the same is valid for adhesives 2 and 4.

In Fig. 3.24, the workability range is visualized using the same data as in Fig. 3.23. In many applications, a viscosity of approximately 500 Pa·s is defined as a limit of workability and therefore often used as a definition for reaching the end of the pot life of a 2C PUR adhesive. In conventionally catalyzed systems, the reaction of isocyanates and polyols starts right after mixing and steadily increasing viscosity can be observed. This so-called front reaction is important with respect to workability but also handling strength. The end cure, the time needed to reach the final product properties, is affected by the amount of catalyst used and therefore the present pot life will have an impact on the time needed to reach the final properties. A desirable way to eliminate this dependency is a sequenced reaction, a first sequence that has a minor impact on the viscosity during pot life and a second sequence that cures the adhesive rapidly. Such behavior can be clearly seen in Fig. 3.23. Moreover, the impact on the viscosity during pot life as well as the subsequent start of a fast-curing reaction is illustrated in Fig. 3.24: adhesives 1 and 2 show a steady rise in viscosity right from the beginning of the measurement and get to the defined limit of 500 Pa·s after 10 and 15 min, respectively. Adhesives 3 and 4 behave differently. After the components are mixed, there is no impact on the viscosity during most of the pot life; adhesive 3 starts to show an increase in viscosity after approximately 20 min and reaches the limit after 28 min while adhesive 4 starts to show increasing viscosity after approximately 65 min and reaches the limit after 72 min. Both adhesives then show a fast curing reaction. Being able to adjust the pot life and curing speed to customer-specific demands without the need to accelerate the curing speed by application of additional energy such as heat or radiation of any kind is a promising technology for tailoring bonding processes.

References

- [1] N. Adam, et al., Polyurethanes, Ullmann's Encyclopedia of Industrial Chemistry, vol. 29, Wiley-VCH Verlag, Weinheim, 2005, pp. 546–604, https://doi.org/10.1002/14356007.a21_665.pub2.
- [2] B. Burchardt, Advances in Polyurethane Structural Adhesives, Advances in Structural Adhesives, Woodhead Publishing Limited, Cambridge, 2010, <https://doi.org/10.1533/9781845698058.1.35> (Chapter 3).

- [3] J. Grimm, A. Zahn, High strength for multi-material bonding, *Adhes. Adhes. Sealants* 10 (2013) 32–35, <https://doi.org/10.1365/s35784-013-0235-9>.
- [4] S. Ebnesajjad, C.F. Ebnesajjad, *Surface Treatment of Materials for Adhesive Bonding*, second ed., Elsevier, Amsterdam, October 2013.
- [5] N. Encinas, J. Abenojar, M.A. Martinez, Development of improved polypropylene adhesive bonding by abrasion and atmospheric plasma surface modifications, *Int. J. Adhes. Adhes.* 33 (2012) 1–6, <https://doi.org/10.1016/j.ijadhadh.2011.10.002>.
- [6] P. Jousset, M. Rachik, Evaluation and comparison of two types of cohesive zone models for the finite element analysis of fracture propagation in industrial bonded structures, *Eng. Fract. Mech.* 132 (2014) 48–69.
- [7] P. Jousset, M. Henne, M. Niedermeier, Ein Leitfaden für Praxis—Fünf Schritte für eine erfolgreiche Anwendung der Klebtechnologie, *KunststoffXtra* 4 (2020) 34–37.
- [8] B. Burchardt, J.O. Schulenburg, M. Linnenbrink, The latest developments in hybrid joining: new building blocks for lightweight structures, *Adhes. Adhes. Sealants* 6 (2009) 22–27.
- [9] F. Koch, A. Lutz, High modulus structural body shop adhesives, *Adhes. Adhes. Sealants* 15 (2018) 17–19.
- [10] C. Di Fratta, D. Vogt, Key features of two-component adhesives for structural composite bonding, in: *SAMPE Europe Conference 2018*, Southampton (UK), 2018.
- [11] C. Di Fratta, D. Hofstetter, M. Zivaljic, B. Bosshard, Two-component epoxies with SmartCore technology for durable bonding of structural components in rail and commercial transportation industry, in: *Rapperswil International Bonding Forum 2018*, Rapperswil (Switzerland), 2018.
- [12] DIN 6701-3, Kleben von Schienenfahrzeugen und -fahrzeugteilen - Teil 3: Leitfaden zur Konstruktion und Nachweisführung von Klebverbindungen im Schienenfahrzeugbau, 2015–2012.
- [13] C. Di Fratta, M. Zivaljic, A. Corsaro, D. Hofstetter, M. Schlumpf, B. Bosshard, F. Choffat, Structural adhesives with customized fast curing, *Adhes. Adhes. Sealants* 17 (2020) 18–23.
- [14] M. Wagner, M. Toledo, *Collected Applications Handbook: Thermal Analysis*, (2009) 194–219. M. Wagner, *Collected Applications Handbook: Thermal Analysis*, Mettler-Toledo, 2009, pp. 194–219.
- [15] NETZSCH GABO Instruments, *Dynamic Mechanical Testing Systems*, 2016.
- [16] J.M.G. Cowie, *Polymers: Chemistry Physics of Modern Materials*, second ed., Nelson Thornes, Cheltenham, 2001, pp. 286–288.
- [17] L. Krogh, J. Schawe, W. Possart, Dynamic mechanical properties of very thin adhesive joints, *J. Appl. Polym. Sci.* 132 (24) (2015), <https://doi.org/10.1002/app.42058>.
- [18] J.H. Saunders, K.C. Frisch, *Polyurethanes: Chemistry and Technology (Part I: Chemistry)*, 1962, Interscience Publishers, New York, 1964.
- [19] A.L. Silva, J.C. Bordado, Recent developments in polyurethane catalysis: catalytic mechanisms review, *Catal. Rev.* 46 (2004) 31–51, <https://doi.org/10.1081/CR-120027049>.
- [20] T.K. Chen, J.Y. Chui, T.S. Shieh, *Macromolecules* 30 (1997) 5068–5074. T.K. Chen, J.Y. Chui, T.S. Shieh, Glass transition behaviour of a polyurethane hard segment and the calculation of microdomain composition, *Macromolecules* 30 (1997) 5068–5074.
- [21] I. Yilgör, E. Yilgör, G.L. Wilkes, *Polymer* 58 (2015) 1–36. I. Yilgör, E. Yilgör, G.L. Wilkes, Critical parameters in designing segmented polyurethanes and their effect on morphology and properties: a comprehensive review, *Polymer* 58 (2015) 1–36.
- [22] S. Kelch, Two-Component Polyurethane Composition, *Pat. Appl.* 2018, EP 3339 343 A1, Sika Technology AG, 2018.

- [23] S. Kelch, Two-Component Polyurethane Composition, Pat. Appl. 2018, EP 3339 345 A1, Sika Technology AG, 2018.
- [24] S. Kelch, M. Schlumpf, T. Voci, Hydrophobic and Highly Elastic Two Component Polyurethane Composition Having Mechanical Properties and Adhesive Properties Not Dependent on Temperature, Patent Appl. US 2018201815 (A1), Sika Technology AG, 2018.
- [25] S. Kelch, Two Component Polyurethane Composition, Patent Appl. US 2020199286 (A1), Sika Technology AG, 2020.
- [26] A. Pizzi, K.L. Mittal (Eds.), Handbook of Adhesive Technology, third ed., CRC Press, Boca Raton, 2020.
- [27] D.G. Lay, P. Cranley, Polyurethane adhesives, in: A. Pizzi, K.L. Mittal (Eds.), Handbook of Adhesive Technology, second ed., CRC Press, Boca Raton, 2003 (Chapter 34).
- [28] P. Cognard, Adhesives and sealants, basic concepts and high-tech bonding, in: P. Cognard (Ed.), Handbook of Adhesives and Sealants, vol. 1, Elsevier, Amsterdam, 2005.
- [29] D. Gysau, Fillers for Paints, Vincentz Network Hannover, 2017, <https://doi.org/10.1515/9783748600312>. third revised edition.
- [30] E.M. Petrie, Handbook of Adhesives & Sealants, McGraw-Hill Engineering Handbooks, McGraw Hill Professional, New York, 1999.
- [31] M.D. Kiran, H.K. Govindaraju, T. Jayaraju, N. Kumar, Review-effect of fillers on mechanical properties of polymer matrix composites, Mater. Today Proc. (2018), <https://doi.org/10.1016/j.matpr.2018.06.611>.
- [32] O.A. Jimoh, K.S. Ariffin, H.B. Hussin, A.E. Temitope, Synthesis of precipitated calcium carbonate: a review, Carbonates Evaporites (2018), <https://doi.org/10.1007/s13146-017-0341-x>.
- [33] B. Müller, U. Poth (Eds.), Lackformulierung und Lackrezeptur: Das Lehrbuch für Ausbildung und Praxis, Vincentz Network, Hannover, 2017.
- [34] N.J. Earhart, A. Patel, G. Knobloch, Thermal stabilization of adhesives, in: A. Pizzi, K.L. Mittal (Eds.), Handbook of Adhesive Technology, (second ed., Revised and Expanded), CRC Press, Boca Raton, 2003, pp. 441–455.
- [35] D. Horsey, Ultraviolet stabilization of adhesives, in: A. Pizzi, K.L. Mittal (Eds.), Handbook of Adhesive Technology, (second ed., Revised and Expanded), CRC Press, Boca Raton, 2003, pp. 429–439.
- [36] 2022. <https://adhesives.specialchem.com/selection-guide/uv-light-stabilizers-state-of-the-art>. (Accessed 24 February 2022).
- [37] ANNEX XVII TO REACH, Conditions of Restriction Restrictions on the Manufacture, Placing on the Market and Use of Certain Dangerous Substances, Mixtures and Article, ECHA European Chemical Agency. <https://echa.europa.eu/documents/10162/503ac424-3bc3-137b-9247-09e41eb6dd5a>.
- [38] 2021. <https://safeusediisocyanates.eu/diisocyanates-reach>. (Accessed 24 February 2022).
- [39] 2022. <https://www.feica.eu/our-priorities/safe-use-diisocyanates>. (Accessed 24 February 2022).
- [40] K.P. Subrahmanian, F. Dubouloz, Adhesives for bonding wind turbine blades, Reinf. Plast. 53 (2009) 26–29.
- [41] H.M.C.C. Somarathna, S.N. Raman, D. Mohotti, et al., The use of polyurethane for structural and infrastructural engineering applications: a state-of-the-art review, Construct. Build Mater. 190 (2020) 995–1014.
- [42] B. Burchardt, K. Diggelmann, S. Koch, B. Lanzendörfer, Elastic Bonding: The Basic Principles of Adhesive Technology and a Guide to Its Cost-Effective Use in Industry, Verlag Moderne Industrie, Landsberg am Lech, 1998.

- [43] W. Brockmann, P.L. Geiss, J. Klingen, K.B. Schröder, *Adhesive Bonding: Materials, Applications and Technology*, Wiley VCH, Weinheim, 2009.
- [44] C. Di Fratta, M. Zivaljic, New adhesive solutions for designing and bonding composite structures in commercial transportation, in: *In-Adhesives 2021*, Munich, 2021.
- [45] Press Release—Structural Adhesives Are Reaching New Heights With an Innovative Electric Vehicle, ASI Adhesives & Sealants Industry, 2021. October Issue.
- [46] Y. Boutar, Effect of adhesive thickness and surface roughness on the shear strength of aluminium one-component polyurethane adhesive single-lap joints for automotive applications, *J. Adhes. Sci. Technol.* 30 (17) (2016) 1913–1929, <https://doi.org/10.1080/01694243.2016.1170588>.
- [47] M.D. Banea, L.F.M. da Silva, R.D.S.G. Campilho, The effect of adhesive thickness on the mechanical behavior of a structural polyurethane adhesive, *J. Adhes.* 91 (5) (2015) 331–346, <https://doi.org/10.1080/00218464.2014.903802>.
- [48] A.L. Loureiro, L.F.M. da Silva, C. Sato, M.A.V. Figureido, Comparison of the mechanical behaviour between stiff and flexible adhesive joints for the automotive industry, *J. Adhes.* 86 (7) (2010) 765–787, <https://doi.org/10.1080/00218464.2010.482440>.
- [49] M.D. Banea, L.F.M. da Silva, R.J.C. Carbas, R.D.S.G. Campilho, Mechanical and thermal characterization of a structural polyurethane adhesive modified with thermally expandable particles, *Int. J. Adhes. Adhes.* 54 (2014) 191–199, <https://doi.org/10.1016/j.ijadhadh.2014.06.008>.
- [50] K. Ramani, J. Verhoff, G. Kumar, N. Blank, S. Rosenberg, Environmental durability of moisture-cured urethane adhesive joints, *Int. J. Adhes. Adhes.* 20 (5) (2000) 377–385, [https://doi.org/10.1016/S0143-7496\(00\)00005-1](https://doi.org/10.1016/S0143-7496(00)00005-1).
- [51] J. Verhoff, K. Ramani, N. Blank, S. Rosenberg, Moisture durability of four moisture cure urethane adhesives, *J. Adhes. Sci. Technol.* 16 (4) (2002) 373–393, <https://doi.org/10.1163/156856102760067172>.
- [52] J. Weiss, M. Voigt, C. Kunze, J.E. Huacuja Sanchez, W. Possart, G. Grundmeier, Ageing mechanisms of polyurethane adhesive/steel interfaces, *Int. J. Adhes. Adhes.* 70 (2016) 167–175, <https://doi.org/10.1016/j.ijadhadh.2016.06.009>.
- [53] S. Sahoo, S. Mohanty, S.K. Nayak, Biobased polyurethane adhesive over petroleum based adhesive: use of renewable resource, *J. Macromol. Sci. A* 55 (1) (2018) 36–48, <https://doi.org/10.1080/10601325.2017.1387486>.
- [54] A. Tenorio-Alfonso, M. Carmen Sanchez, J.M. Franco, A review of the sustainable approaches in the production of bio-based polyurethanes and their applications in the adhesive field, *J. Polym. Environ.* 28 (3) (2020) 749–774, <https://doi.org/10.1007/s10924-020-01659-1>.
- [55] G. Behnken, A. Hecking, B. Vega Sanchez, *Höchstleistung aus Biomasse, Farbe und Lack* 8 (2015) 42–47.
- [56] V. Ibrahim, G. Mamo, P.-J. Gustafsson, R. Hatti-Kaul, Production and properties of adhesives formulated from laccase modified Kraft lignin, *Ind. Crop Prod.* 45 (2013) 343–348, <https://doi.org/10.1016/j.indcrop.2012.12.051>.
- [57] A.M. Nacas, N.M. Ito, R.R. de Sousa, M.A. Spinacé, D.J. dos Santos, Effects of NCO:OH ratio on the mechanical properties and chemical structure of Kraft lignin-based polyurethane adhesive, *J. Adhes.* 93 (1–2) (2017) 18–29, <https://doi.org/10.1080/00218464.2016.1177793>.
- [58] J. Rocha Gouveia, R.R. de Sousa Junior, A.O. Ribeiro, S.A. Saraiva, D.J. dos Santos, Effect of soft segment molecular weight and NCO:OH ratio on thermomechanical properties of lignin-based thermoplastic polyurethane adhesive, *Eur. Polym. J.* 131 (2020) 109690, <https://doi.org/10.1016/j.eurpolymj.2020.109690>.

- [59] Y. Chen, H. Zhang, Z. Zhu, S. Fu, High-value utilization of hydroxymethylated lignin in polyurethane adhesives, *Int. J. Biol. Macromol.* 152 (2020) 775–785, <https://doi.org/10.1016/j.ijbiomac.2020.02.321>.
- [60] D.H. Turkenburg, H. van Bracht, B. Funke, M. Schmider, D. Janke, H.R. Fischer, Polyurethane adhesives containing Diels-Alder-based thermoreversible bonds, *J. Appl. Polym. Sci.* 134 (2017) 44972, <https://doi.org/10.1002/app.44972>.
- [61] E. Dolci, G. Michaud, F. Simon, B. Boutevin, S. Fouquay, S. Caillol, Remendable thermosetting polymers for isocyanate-free adhesives: a preliminary study, *Polym. Chem.* 6 (45) (2015) 7851–7861, <https://doi.org/10.1039/C5PY01213A>.
- [62] T. Singh Babra, A. Trivedi, C.N. Warriner, N. Bazin, D. Castiglione, C. Sivoir, W. Hayes, B.W. Greenland, Fluoride degradable and thermally debondable polyurethane based adhesive, *Polym. Chem.* 8 (2017) 7207–7216, <https://doi.org/10.1039/C7PY01653K>.
- [63] T.S. Babra, M. Wood, J.S. Godleman, S. Salimi, C.N. Warriner, N. Bazin, C. Sivoir, I.W. Hamley, W. Hayes, B.W. Greenland, Fluoride-responsive debond on demand adhesives: manipulating polymer crystallinity and hydrogen bonding to optimise adhesion strength at low bonding temperatures, *Eur. Polym. J.* 119 (2019) 260–271, <https://doi.org/10.1016/j.eurpolymj.2019.07.038>.
- [64] U. Burckhardt, A. Corsaro, M. Schlumpf, Zweikomponentige Polyurethanzusammensetzung mit einstellbarer Topfzeit, Patent Appl. WO 2019/002538, Sika Technology AG, 2018.
- [65] T. de Vries, G.L. Jialanella, A. Lutz, S. Schmatloch, Isocyanate-Blocked Amidines as Latent Polyurethane Catalysts, Patent Appl. WO 2018/102333, Dow Global Technologies LLC, 2018.
- [66] S. Grunder, S. Schmatloch, J. Kunz, Latent Two-Part Polyurethane Adhesives, WO 2019/182715, Dow Global Technologies LLC, 2019.

Advances in cyanoacrylate structural adhesives

4

Barry Burns

Henkel Ireland Operations and Research, Dublin, Ireland

4.1 Introduction

Cyanoacrylate (CA) instant adhesives, or “superglues” [1], are an important class of adhesive materials based on the alkyl α -cyanoacrylate ester monomer structure (Fig. 4.1). First synthesized in 1949 by Ardis at B.F. Goodrich [2], it was not until the 1950s that Coover at Eastman Kodak discovered and patented their utility as rapid curing adhesive compositions [3].

Such adhesives have found widespread use as both industrial and consumer instant adhesives, mainly because of their ease of use (no mixing, one component), rapid cure speed at ambient temperature, and versatile bonding performance on a range of commonly encountered substrate surfaces such as plastics, metals, ceramics, woods, leather, and rubbers [4]. Once these adhesives have been applied between two close-fitting substrate surfaces, the extremely high rate of polymerization permits them to cure rapidly to form high-strength bonds that can be handled within seconds to minutes. Since Coover’s original discovery, cyanoacrylate instant adhesives have grown to become a multibillion-dollar industry serving the general industrial assembly, engineering, electronic, consumer, and medical device/tissue adhesive markets globally.

Despite this success, there are several key challenges [5] facing cyanoacrylate instant adhesive technology that have restricted their penetration into the wider structural adhesive bonding market, namely,

- (a) Inability to cure through large bond gaps.
- (b) Limited thermal/humidity resistance performance in hot/wet environments.
- (c) Poor toughness/impact resistance.
- (d) Limited choice of cyanoacrylate monomers.

This chapter will focus on recent developments in cyanoacrylate adhesive technology aimed at addressing some of the above challenges, particularly in the following areas:

- Improvements in methods of manufacture extend the range of available monomers with a broader range of properties.
- Advancements in thermally stable cyanoacrylates with improved heat resistance and hot strength properties that extend the safe operating temperature window.
- New two-component (2K) and hybrid adhesives that enable cure through thick (larger gap) bondlines, with enhanced toughness and thermal resistance while maintaining the benefits of one-component (1K) instant adhesives.

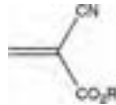


Fig. 4.1 Alkyl α -cyanoacrylate ester.

- Developments in photocuring cyanoacrylates with a dual cure mechanism that enables rapid cure through gaps/thick bondlines triggered by ultraviolet (UV)/visible light.

The final sections of this chapter will briefly address recent advances in biomedical cyanoacrylate adhesives as well as sustainability issues and future challenges facing cyanoacrylate adhesive technology.

4.2 Chemistry of α -cyanoacrylates

The chemistry of α -cyanoacrylates has been reviewed in several recent articles [6–8]. The high reactivity of the monomers is attributed to the presence of the strongly electron withdrawing nitrile and ester functional groups on the α -carbon of the carbon-carbon double bond (Fig. 4.2), which result in the polarization of the electron density in the double bond, thus activating the β -carbon toward attack by weak nucleophiles (such as moisture) present on the surface of the substrates to be bonded. The resulting propagating negative charge on the α -carbon arising from the addition of a nucleophile to the sterically unhindered β -carbon, is further stabilized through resonance delocalization of the negative charge across the nitrile and ester groups via the resonance stabilized tautomer structures I and II in Fig. 4.3 [5,7,9].

Polymerization can occur via three distinct mechanisms: anionic, zwitterionic, and free radical (Fig. 4.4), with the anionic and zwitterionic modes being the most predominant because of their rapid initiation at ambient temperature [5,9].

The combination of a highly electrophilic and sterically unhindered β -carbon with an α -carbanion stabilized by delocalization results in exceptionally high propagation rates during anionic and zwitterionic polymerization. When the initiating species is an anion (such as hydroxyl, chloride, acetate, etc.), polymerization proceeds via the

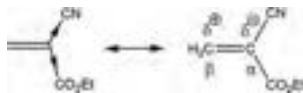


Fig. 4.2 β -Carbon activation through electron withdrawing effects of the CN and CO_2R groups.

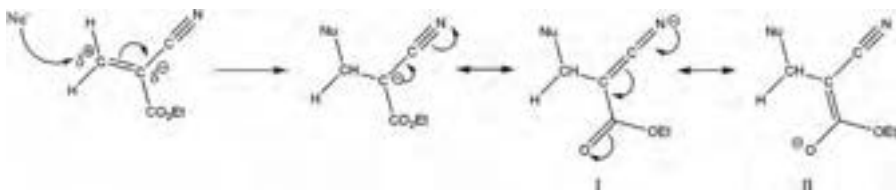


Fig. 4.3 Resonance stabilization of negative charge.

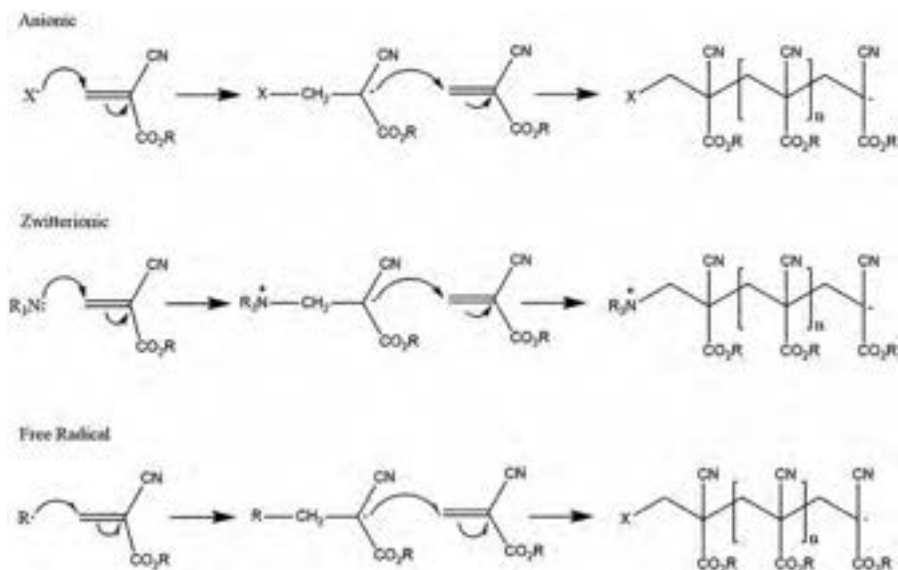


Fig. 4.4 Anionic, zwitterionic, and free radical polymerization modes.

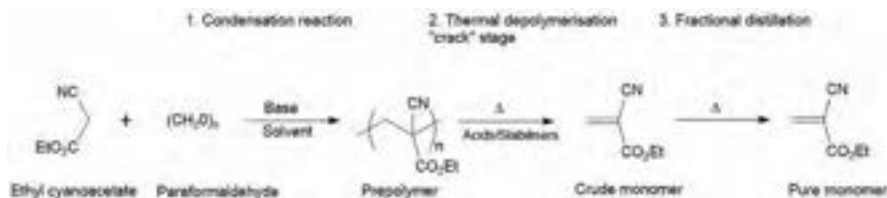
anionic mode. Nondissociated nucleophilic base species (neutral molecules) possessing a free electron pair, such as phosphine, alcohol, or amine functional groups, can also trigger rapid initiation, and polymerization proceeds via the zwitterionic polymerization mode [5,10–16]. In both anionic and zwitterionic modes, the polymerization is completely inhibited by the presence of strong acids [10]. The kinetics of base-catalyzed solution polymerization of cyanoacrylates have been thoroughly investigated [10–19] and the reported results show that in the absence of a strong acid, the polymerization has no intrinsic termination step, and the overall kinetics are dependent on the rates of initiation of different initiators.

Free radical polymerization of cyanoacrylates has recently been reviewed [6,20] and, while typically more difficult to achieve due to the relative ease of polymerization via the competing anionic and zwitterionic reaction pathways, it is synthetically more useful with both homo- and copolymerization modes possible [21–24]. The so-produced polymers/copolymers are reported to be more stable due to the suppression of degradation via the unzipping process [25].

Aronovich recently provided an overview of the different mechanisms of cyanoacrylate polymerization and typical fields of application where each mode is used [6].

4.3 Industrial synthesis/manufacture of α -cyanoacrylate esters

A number of synthetic methodologies exist for the synthesis of cyanoacrylate monomers and a review of the most common methods for preparing α -cyanoacrylate monomers was recently published by Aronovich [26]. Commercially, the most important



Scheme 4.1 Industrial manufacture of α -cyanoacrylate monomers via Knoevenagel condensation.

industrial manufacturing process is that based on the classical Knoevenagel base-catalyzed condensation of ethyl cyanoacetate with paraformaldehyde [27–33], as illustrated in Scheme 4.1. This process consists of three key steps:

- (1) The Knoevenagel condensation reaction step.
- (2) The thermal depolymerization “cracking” step.
- (3) The purification step via distillation.

The initial base-catalyzed (typically amine) condensation step of paraformaldehyde with α -cyanoacetate ester results in the formation of the α -cyanoacrylate monomer. However, because of the basic/aqueous reaction conditions, the monomer cannot be isolated as it polymerizes in situ to form a low molecular weight oligomer or prepolymer. Careful control of the condensation reaction conditions (ratio of cyanoacetate/paraformaldehyde, rate of addition, reaction temperature, etc.) is required to minimize competing side reactions and to control the molecular weight of the prepolymer, minimize viscosity build-up, and maintain ease of processing; this is critical to the overall process yield.

The second stage of the process involves a thermal depolymerization (“cracking”) step, which is carried out by heating the prepolymer at high temperature and reduced pressure. The residual base catalyst must first be neutralized by the addition of measured quantities of acidic compounds and free radical stabilizers added [23,34]. Under these carefully controlled reaction conditions, the prepolymer undergoes thermal depolymerization to afford the desired 2-alkyl- α -cyanoacrylate monomer in crude form [26–33]. The final stage of the process involves vacuum distillation of the crude monomer to yield the final pure adhesive-grade monomer. There has been considerable recent research into various process improvements (yield, purity, stability, etc.) such as catalyst optimization, azeotropic distillation, solvents with enhanced heat transfer properties, etc., to enhance the purity, yield, and stability of the α -cyanoacrylate monomers; these are well documented in recent reviews [26,34]. The use of activated carbon at the crude monomer distillation stage is reported to be effective at producing pure cyanoacrylate monomer with improved yellowing and shelf-life properties [35]. Also, a recent improved purification process involving the removal of low boiling point compounds such as ethanol and acrylonitrile that contribute to the irritating odor associated with ethyl cyanoacrylate monomer was also claimed [36].

From a commercial perspective, the most important 2-cyanoacrylate esters produced by the Knoevenagel condensation-depolymerization method include the

methyl, ethyl, *n*-butyl, β -methoxyethyl, allyl, and 2-octyl esters, with ethyl-2-cyanoacrylate being the most important for the global instant adhesive market. Other alkyl cyanoacrylate esters have been prepared and their physical properties studied and compared [28,37,38]. Krishnamurti synthesized and compared the monomer physical properties and cured mechanical properties of simple alkyl (methyl-octyl), branched alkyl, cycloalkyl, alkenyl, and substituted alkyl 2-cyanoacrylates [39]. More recently, Raja reviewed and compared the physical properties and performance of a range of different cyanoacrylate esters, such as simple alkyl esters for industrial and consumer instant adhesives, higher alkyl (butyl, heptyl, octyl, and ethoxyethyl) esters for medical applications, and unsaturated esters such as allyl cyanoacrylate for applications requiring thermal resistance [34]. The glass transition temperatures (T_g) of the most common cyanoacrylate polymers are listed in Table 4.1. The measured T_g values will vary depending on the method of preparation of the polymer and the method used for the measurement.

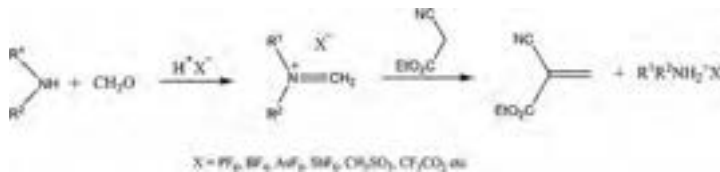
A significant limitation of the Knoevenagel process is that it is restricted to the lower alkyl esters. With the higher alkyl esters, the increased steric bulk associated with the prepolymer results in less-efficient depolymerization during the crack step due to competing degradation reactions, which lower the yield and make the process unviable from a commercial viewpoint. Additionally, monomers containing more than one cyanoacrylate (e.g., bis cyanoacrylates) or other reactive functional groups are difficult to produce via the traditional Knoevenagel route due to polymerization occurring during the condensation step, which leads to the formation of a crosslinked polymer that cannot be thermally depolymerized (“cracked”) to a monomer.

Several other synthetic approaches have been reported for the synthesis of cyanoacrylate monomers [2,40–48], but most of these are not commercially viable.

More recently, the use of activated iminium ionic liquids has been reported as a means of preparing simple or more complex cyanoacrylate esters [49–53]. In the reported process, an imine is prepared by the reaction of an amine with formaldehyde, followed by protonation with acid to form an active iminium ionic liquid. The iminium ionic liquid acts as a methylene transfer agent that reacts with the cyanoacetate to form the cyanoacrylate directly (Scheme 4.2). It is critical to use

Table 4.1 Glass transition temperature (T_g) values of common cyanoacrylate polymers.

Polycyanoacrylate ester	T_g (°C)
Methyl	160–165
Ethyl	140–150
Allyl	130
<i>n</i> -Butyl	90
β -Methoxyethyl	80–90
2-Octyl	10
<i>n</i> -Decyl	–70



Scheme 4.2 Activated iminium ionic liquid synthesis of cyanoacrylates.



Scheme 4.3 “Crackless” process for the direct synthesis of cyanoacrylate monomers.

the protonated imine species to reduce the nucleophilicity of the imine nitrogen and prevent polymerization of the cyanoacrylate as it forms.

A significant advancement in the above process is a so-called “crackless” process based on the reaction between a cyanoacetate and an active methylene compound such as methylene diacetate in the presence of catalytic quantities of an ammonium/iminium catalyst (Scheme 4.3).

In this process, the methylene diacetate behaves as the methylene transfer agent, which can be synthesized separately or generated in situ, and the reaction between the methylene diacetate and the cyanoacetate ester is catalyzed by an iminium reagent or ammonium salt. This process is reported to permit both the direct synthesis of simple alkyl CA esters in higher yield and purity as well as higher alkyl/more complex (labile) α -cyanoacrylate monomers that typically cannot be accessed via traditional Knoevenagel condensation depolymerization [54]. In this process, the cyanoacrylate monomer is formed directly from the cyanoacetate, and reaction conditions are such that the newly formed monomer does not polymerize to a prepolymer that requires the additional “crack” step to form a crude monomer. The absence of the crack step is claimed to widen the scope of cyanoacrylate manufacturing by allowing the synthesis of a broader range of multifunctional (labile) cyanoacrylate esters otherwise not accessible via the traditional Knoevenagel process. Monomer examples reported include trimethylsilylmethyl cyanoacrylate, 1,6-hexane diol-bis-cyanoacrylate, and 12-methacryloyloxy dodecyl cyanoacrylate (Fig. 4.5), although it appears to date none of these more “exotic” monomers have been commercialized beyond the research and development scale.

Other authors have reported similar direct synthesis of cyanoacrylate monomers using acid-catalyzed Knoevenagel condensation, or via a one-pot, two-stage esterification Knoevenagel condensation of cyanoacetic acid directly to α -cyanoacrylate monomers. The use of specific acid catalysts in place of the traditional basic catalysts in the condensation step prevents polymerization and thus avoids the formation of a prepolymer; it is claimed to afford a similar “crackless” process whereby the cyanoacrylate monomer is synthesized directly from the α -cyanoacetate ester or from α -cyanoacrylic acid [55,56].

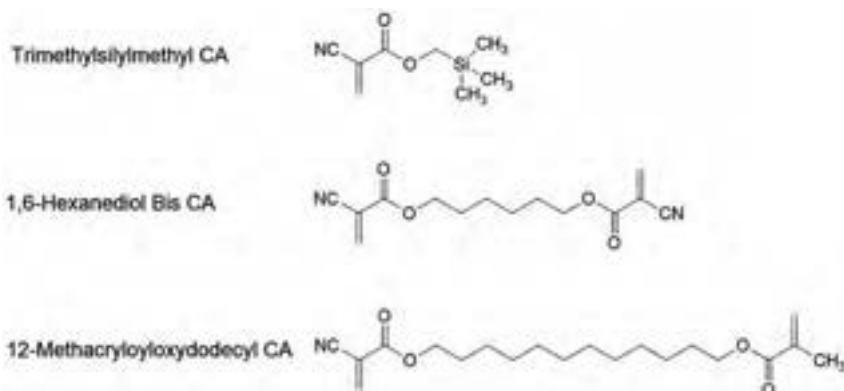


Fig. 4.5 Monomers produced via the “crackless” process.

4.4 Typical performance characteristics of α -cyanoacrylates—Strengths, weaknesses, and recent developments

As outlined previously in Section 4.1, cyanoacrylate instant adhesive technology faces several key technical challenges that have limited their penetration into a wider range of structural bonding markets and applications. These weaknesses have recently been further highlighted by several authors [9,57] and include

- Thermal resistance properties such as heat resistance and hot strength.
- Humidity resistance in hot/wet environments.
- Highly brittle polymers with poor toughness/impact resistance.
- Cure through larger bond gaps.

Such characteristics are critical for the successful use of an adhesive in the more demanding environments typically experienced by structural bonding adhesives. The poor thermal/humid aging properties of cyanoacrylate instant adhesives, coupled with their poor impact resistance and slow cure through larger bond gaps, has restricted their use to zero-gap, instant adhesive applications in typically more benign bonding environments.

In recent years, there has been intensive research into approaches aimed at improving such performance weaknesses. Aronovich in his recent review [57] highlighted numerous additives and formulation modifiers for the purpose of improving specific adhesive performance properties for different adhesive applications. Such additives and formulation modifiers include recent developments in stabilizers, accelerators, adhesion promoters, plasticizers, tougheners, additives to improve thermal and humidity performance, and viscosity modifiers.

4.4.1 Improvements in thermal resistance performance

The thermal resistance performance of cyanoacrylate adhesives has also been recently reviewed [7,9]. The intrinsic poor heat resistance of polycyanoacrylate polymers is attributed to the fact that cyanoacrylates are monofunctional monomers that

polymerize to form high molecular weight, linear homopolymers that, due to the absence of crosslinking, are thermoplastic in nature. Such polymers exhibit a strong tendency to readily undergo thermally induced depolymerization-repolymerization (so-called “unzipping”) upon exposure to hot or humid environments. The depolymerization is initiated by a deprotonation step involving removal of the proton located at the terminus of the dormant homopolymer chain. The deprotonation step is facilitated by the enhanced acidity of the terminal proton due to its position on the α -carbon with the adjacent electron-withdrawing nitrile and ester functional groups. Such depolymerization leads to rapid deterioration in bond strengths on metal and/or glass substrates (Fig. 4.6) [25,58,59].

The review by Burns [9] highlights various recent developments aimed at improving thermal resistance properties, including the use of various additive strategies that are believed to retard the depolymerization step. Reported additives include the use of various sulfur-containing compounds, acids, anhydrides, fluorinated materials, and maleimides or combinations of the aforementioned. Improved thermal properties are also reported through the use of materials that allow the introduction of crosslinking into the cured polycyanoacrylate polymer. Most commercially available cyanoacrylate monomers (methyl, ethyl, butyl, β -methoxyethyl, and octyl) are monofunctional, and they polymerize to form high molecular weight linear (non-crosslinked) homopolymers that can be dissolved in common solvents such as acetone. Crosslinkable monomers include materials such as bis cyanoacrylates, alkyl-2-cyanopentadienoates, or allyl cyanoacrylate.

Allyl cyanoacrylate polymerizes in the same manner as the commercially available monomers listed above, via anionic polymerization to form a linear polyallyl CA (PACA) homopolymer with thermoplastic properties. However, allyl cyanoacrylate also possesses a secondary cure mechanism involving thermally induced free radical

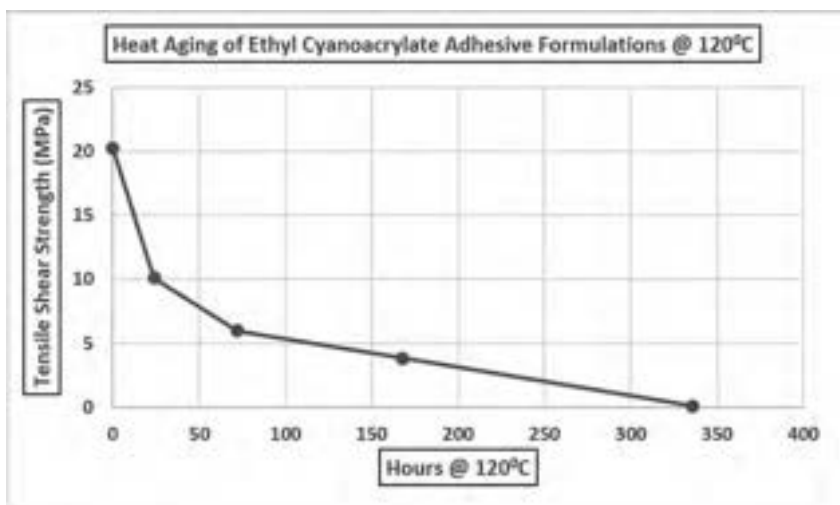
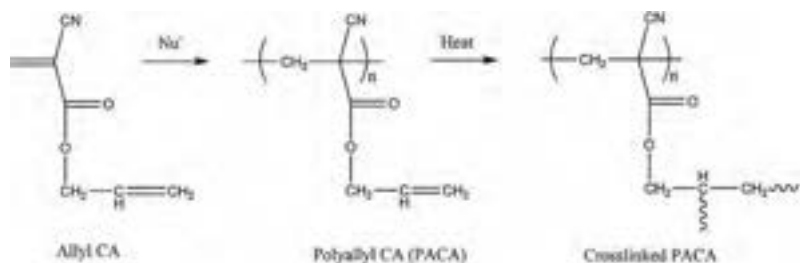


Fig. 4.6 Deterioration in tensile shear strength after aging at 120°C.



Scheme 4.4 Anionic polymerization of ACA and thermally induced crosslinking.

crosslinking via the unsaturated allyl functional groups (Scheme 4.4), which allows the formation of a crosslinked network with improved thermal properties.

Crosslinking of the allyl groups takes place upon exposure of the cured polyallyl CA (PACA) linear homopolymer to elevated temperatures approaching 150°C or higher, leading to improved thermal resistance at such temperatures. Crosslinking of the allyl groups compensates for the loss in tensile strength associated with degradation/depolymerization of the linear homopolymer, leading to improved heat resistance. This only occurs if the cured adhesive is given an elevated temperature postbake or is exposed to an elevated service temperature close to, or higher than 150°C. At temperatures below 150°C, the kinetics of the free radical crosslinking step are too slow, and the linear homopolymer proceeds to degrade via the usual unzipping degradation/depolymerization mechanism. Hot strength and heat resistance of the cured adhesive at temperatures between 100°C and 150°C is thus poor because polymer unzipping proceeds at a faster rate than allyl crosslinking. Many of the recent advancements in high temperature resistant cyanoacrylate adhesives focus on the use of allyl-2-cyanoacrylate (ACA)-based adhesives.

Recent patents claim improved heat resistance and hot strength performance through the use of specific combinations of a free radical inhibitor and a free radical initiator to drive crosslinking of the allyl groups between temperatures of 120–150°C [60]. A further recent patent claims the use of allyl/ethyl monomer blends in conjunction with a fluorobenzonitrile, a hydrogenated aromatic anhydride, and a toughening agent [61] to provide an adhesive with improved high temperature heat aging performance and improved hot strength at temperatures between 135°C and 150°C.

Thermal cycling performance is also reported to be improved through the use of onium salts such as methyltri-*n*-octylammonium bis(trifluoromethanesulfonyl)imide, leading to claims about improvements to thermal cycling performance between –40°C and +80°C with 40%–70% retention of initial bond strengths [62].

4.4.2 Adhesive curing through large bond gaps

Conventional single-component (1K) cyanoacrylate adhesives typically cure, or polymerize, very efficiently when used to assemble close-fitting substrates (often referred to as “zero gap” bonds), resulting in the formation of a very strong adhesive joint between the substrate surfaces. Polymerization is very effective because the initiation

process is triggered by the presence of an abundance of various nucleophilic or ionic species, present on most substrate surfaces (e.g., adsorbed water, oxides, salts, or basic materials) and a strong bond is formed within seconds. As the bond gap increases, the concentration of available nucleophilic species within the bulk adhesive decreases with increasing distance from the substrate surface. This results in lower rates of polymerization initiation and retardation in the rate of cure in thicker bondlines (poor cure through volume (CTV)). This limitation has restricted use of CAs to bonding close-fitting substrates with narrow (“zero”) bond gap thickness and has prevented their penetration into structural bonding applications involving more complex geometries and larger bond gaps. When cyanoacrylates are used to bond substrates with large bond gaps, the rate of cure slows down, and they no longer cure instantly. Raheem and coworkers recently reported the use of confocal Raman microscopy to characterize the depth of cure of ethyl cyanoacrylate at different gap sizes and confirmed the degree of cure decreases with increasing gap size [63].

In certain cases, it is possible to overcome this problem through the practice of using additional nucleophilic initiating moieties applied directly onto the substrate in a low boiling solvent as a surface primer or activator prior to adhesive application. The activating species should not cause instant polymerization but should have initial miscibility with the adhesive to allow the activator species to mix into the adhesive bulk and give cure through volume. The use of such activator/primers is well known within cyanoacrylate adhesive technology, particularly for modifying the surface properties and adhesion to difficult-to-bond substrates such as polyethylene or polypropylene; this has recently been discussed and reviewed [6,26]. Most recently, a polyethyleneimine initiator has been used as a surface activator for improved bonding performance of cyanoacrylates to low surface energy substrates [64].

While the use of activators for accelerating cure, improving adhesion to difficult-to-bond substrates, and providing cure through volume has been long known, most of the reported cases involve the addition of the activator to the substrate surface or directly to the cyanoacrylate adhesive at the time of use [65–68].

Several approaches have been reported with the specific aim of addressing poor cure through volume of cyanoacrylates in applications involving large gaps between substrates such as in the sealing, filling, and repair of depressions, cracks, or holes in a substrate. Most of the reported examples involve combining a cyanoacrylate formulation with, for example, a variety of particulate fillers at the point of application to both fill the hole and to polymerize the cyanoacrylate within the hole [69–72].

4.5 Two-component (2K) cyanoacrylate adhesives

4.5.1 Two-component cyanoacrylate adhesives

A significant recent trend in cyanoacrylate technology has been the introduction to the marketplace of two-component (2K or two-part) cyanoacrylate adhesives, whereby a polymerization initiator component is packaged separately to the cyanoacrylate component. The initiator is then mixed into the CA component via a static mixing nozzle



Fig. 4.7 Part A and Part B components in a 2K adhesive.

just before application to the substrate surface. This provides a sufficient concentration of initiator throughout the bulk adhesive, thus ensuring sufficient cure through volume of the bulk adhesive in thicker bond gaps. A 2K cyanoacrylate adhesive consists of a twin or dual chamber syringe with the cyanoacrylate composition packaged in one chamber (Part A) and an initiator solution packaged separately in the other chamber (Part B) (Fig. 4.7).

Recent developments include the development and introduction to the marketplace of a two-component CA adhesive comprising a dual barrel chamber syringe with a 10:1 mix ratio of Part A to Part B [73]. The authors report the use of specific 2-substituted benzothiazole compounds in an inert plasticizer as the Part B initiator component, and which are reported to give an optimum balance of longer gel time for improved nozzle life coupled with rapid fixturing and cure through volume when the bonded parts are mated together. The 2K composition is reported to afford a multipurpose adhesive with high gap-filling capabilities. Ward and coworkers reported a similar two-component 10:1 mix ratio adhesive with improved thermal and humidity resistance properties [74]. Part A contains the cyanoacrylate component plus a rubber toughening agent, with a polymerization initiator in the form of a 2-substituted benzothiazole compound in Part B. The formulation additionally contains a di-, tri-, or tetra functional (meth)acrylate, a benzonitrile, and an anhydride component. The adhesive composition is reported to offer excellent gap curing performance coupled with improved thermal and humidity aging performance.

A 4:1 mix ratio 2K flexible gel CA for the bonding, sealing, or repair of elastic substrates was reported by Jimenez and coworkers [75]. The two-part adhesive composition is based on a low-odor/bloom, flexible cyanoacrylate monomer such as 2-ethoxyethyl CA, 2-methoxyethyl CA, or 1-methoxypropyl CA and a Part B comprising the polymerization initiator in a plasticizer component containing a thixotropic agent. On mixing Parts A and B in a 4:1 mix ratio, a cured adhesive is obtained with flexible and elastic properties suitable for bonding substrates that are subject to

relative movement to each other, impact, or shock. McArdle et al. also reported a 4:1 2K cyanoacrylate adhesive useful for repairing and filling depressions, cracks, and holes in a substrate whereby a hydrated calcium silicate filler is used as the polymerization initiator, and which is present in Part B [76].

4.5.2 2K “hybrid” cyanoacrylate adhesives

The above two-component adhesive examples involve mix ratios where A to B is restricted to 10:1 or 4:1, with Part B always being the minor component. Limiting the amount of Part B avoids the introduction of high levels of inert, nonreacting carrier liquid present in Part B into the cured adhesive such as a plasticizer that, at higher mix ratios, would have a detrimental effect on the mechanical properties of the cured adhesive polymer. More recently, this problem has been circumvented by replacement of the inert plasticizer in Part B with reactive monomers such as epoxy resins, (meth)acrylates, hydrolysable silanes, etc., in 1:1 mix ratios. Such hybrid systems are reported to afford a cured adhesive that exhibits the beneficial properties of the two separate resin chemistries in one hybrid polymer, such as the fast speed of cure and multisubstrate bonding of cyanoacrylates combined with the durability of epoxies. These systems are formulated to contain an initiator for the cyanoacrylate in Part B and an initiator for the epoxy/(meth)acrylate/silane in Part A. There have been several such “hybrid” two-component adhesives reported in recent years, for example, a two-component hybrid 1:1 cyanoacrylate-epoxy adhesive system [77–79] (Fig. 4.8).

In this “hybrid” system, the CA formulation in Part A contains an epoxy cure initiator in the form of a lithium tetrafluoroborate salt, in addition to the usual

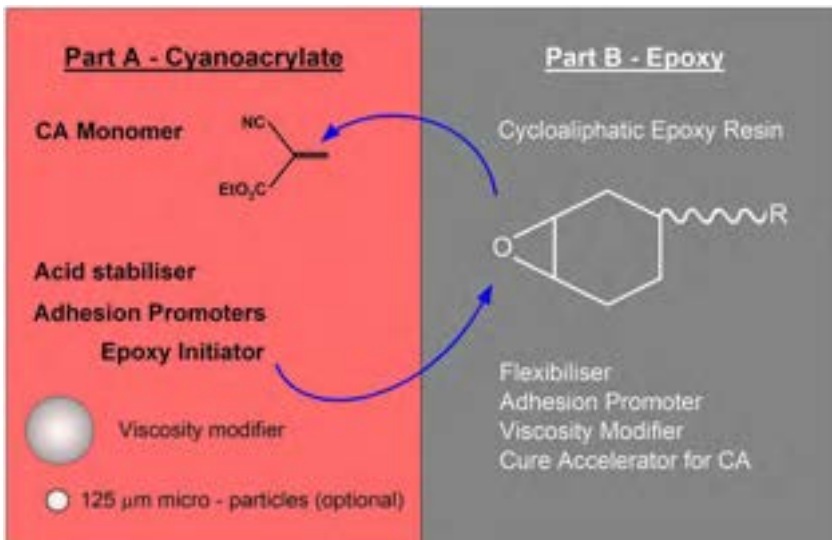


Fig. 4.8 2-Component 1:1 cyanoacrylate-epoxy hybrid system.

formulation additives (stabilizers, thixotropes, viscosity modifiers, accelerators, fillers, etc.). The epoxy formulation in Part B comprises various epoxy resins (diluent/flexibilizers/viscosity modifiers/adhesion promoters/thixotropes, etc.) in addition to a cyanoacrylate polymerization initiator component. On mixing the two parts via a static mixer, the two components rapidly polymerize together to form a cured polymer composite comprising an interpenetrating network of crosslinked epoxies and linear polycyanoacrylate chains. The cured network provides excellent adhesive strength to both metals and plastics while the crosslinked epoxy network provides thermal and moisture durability, hot strength, and chemical/solvent resistance.

Similar hybrid 2K cyanoacrylates based on cyanoacrylate/free radically polymerizable methacrylate adhesives are also reported [80]. Once again, a fast curing hybrid adhesive is obtained that offers the beneficial properties of an instant cyanoacrylate adhesive combined with the structural bonding performance of a structural acrylic (metal and plastics bonding, toughness). Such hybrid systems are claimed to afford adhesives with improved health and safety labeling and without the strong odor and flammability issues associated with the use of methyl methacrylate (MMA).

Highly flexible 2K cyanoacrylate adhesives have also been reported [81] that are based on a Part A containing a cyanoacrylate formulation with a Part B containing a hydrolysable alkoxy silane functional polymer. The A and B parts are mixed to give a cured adhesive polymer with good flexibility and adhesion durability such as cold/hot durability and warm water immersion resistance.

The development of such hybrid 2K adhesive technologies represents a significant technical advance in cyanoacrylate adhesive technology in that it helps to bridge the gap between 1K instant adhesives (fast curing at “zero” gap plus high performance on plastics) and more demanding structural bonding applications (high gap fill, structural performance, environmental durability, and high performance on metals). Such hybrid 2K adhesives now offer fast cure through thicker bondlines, universal adhesion (metals and plastics), excellent structural and environmental durability, and with additional health and safety benefits such as reduced strong odor and flammability.

4.6 Photocuring cyanoacrylates

Cyanoacrylate instant adhesives are unique with regard to cure speed and their ability to bond a broad range of substrate types without the need for an additional external energy stimulus such as heat or light. In certain applications, a disadvantage of CA relates to the presence of uncured excess adhesive outside the bonded joint area. Such uncured bulk adhesive material can result in contamination issues of the finished bonded goods, machine parts, operator hands, etc., or ultimately spoil the aesthetic appearance of the bonded part. To address such issues, dual-curing cyanoacrylate adhesives were developed whereby the adhesive would cure rapidly within close-fitting parts by the traditional anionic cure mechanism and any excess bulk adhesive on the bondline periphery could be cured using a photocuring mechanism. Such dual-curing UV CAs have been reported [82,83] whereby the adhesive comprises a cyanoacrylate component, a metallocene such as ferrocene, and a free radical photoinitiator

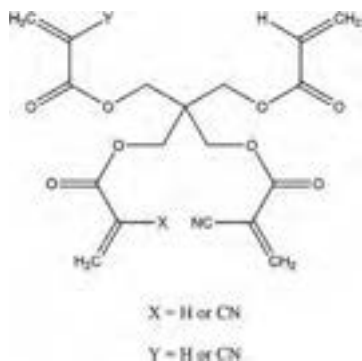


Fig. 4.9 Multifunctional acrylate-cyanoacrylate monomer.

such as an acyl phosphine oxide. Such UV-curing CA adhesives have found widespread utility in applications involving the assembly of electronic or medical devices, for example, for bonding hypodermic needles to syringe needle hubs in a fast production assembly line. The secondary UV curing mechanism enables the full and fast cure of any excess adhesive, which also helps to seal and strengthen the bond between the needle and the syringe hub.

Subsequent developments in UV photocuring CA adhesives have focused on the development of UV photocured adhesives that have lower odor and exhibit fewer blooming characteristics [84]. Less brittle, more flexible UV cured adhesives were attained through the addition of higher alkyl cyanoacrylate monomers plus a plasticizer component to either ethyl or β -methoxyethyl CA monomers [85], or by the use of a plasticizer component [86]. Stable, odorless, nonblooming, nonirritant, fast light curing adhesives based on alkoxyalkyl CAs have also recently been reported [87]. Such compositions are based on a specific ferrocene/acyl germane photoinitiator system that is sensitive to polymerization in either the UV or visible light wavelength range.

A multifunctional hybrid acrylate-cyanoacrylate monomer (Fig. 4.9) has been reported [88] for providing UV photocurable adhesive compositions with “dark cure” capability. The acrylate functionality is reported to react rapidly under photolysis conditions in the presence of a photoinitiator while the cyanoacrylate functionality undergoes anionic polymerization in the presence of weak bases.

The use of such specific acrylate-cyanoacrylate monomer materials enables the ability to control the viscosity of the adhesive formulation at the monomer level, without having to resort to the use of filler materials (e.g., fumed silica), which will deleteriously affect the depth of cure in thicker bondlines, allowing adequate filling of gaps between components during the assembly process.

4.7 Biomedical cyanoacrylate adhesives

The use of cyanoacrylate adhesives in surgical applications was recently reviewed [89–91] (see also Chapter 27). The articles by Petrie, Nian, and Xian present overviews of the adhesive requirements and the benefits and limitations of cyanoacrylates

for surgical applications. An overview of the chemistry, adhesive types, and recent progress in formulation modifications and clinical applications of medical-grade cyanoacrylate adhesives was also presented. The ease of use (no mix), rapid cure speed, high strength, excellent adhesion to moist human tissues or organs, biocompatibility, and availability of formulations that are compliant with relevant regulatory requirements make them ideal as adhesives for surgical applications. A study on the comparative properties of a range of cyanoacrylate esters and their suitability for medical adhesive applications was recently reported [92]. The majority of cyanoacrylate adhesives for surgical applications are based on either the *n*-butyl or 2-octyl cyanoacrylate monomers. 2-octyl CA cures to give a softer, more flexible polymer relative to *n*-butyl CA. However, 2-octyl CA cures more slowly and tends to be used in conjunction with an activator.

Critical considerations for biomedical adhesive applications are:

- Open time and cure speed of the adhesive.
- The cured adhesive must afford a polymer with high bond strength to the substrate with sufficient flexibility.
- Waterproofing and barrier properties to protect the sealed wound and provide good microbial barrier properties to prevent ingress of common pathogens.

Recent investigations have focused on the use of *n*-butyl, octyl, or butyl/octyl CA monomer blends for optimizing flexibility/barrier properties, and the use of activators to achieve the desired cure speed without the risk of generating too high an exothermic polymerization, which can cause damage to the tissues. Other formulation modifications include the addition of dyes to the adhesive formulation to allow better visualization for the surgeon, and the use of viscosity modifiers to allow better flow control during application on to the substrate. There have also been significant developments in device design to provide an extended shelf life of the adhesive formulation and to allow for improved ease of use during application of the adhesive to the substrate.

4.8 Cyanoacrylates and sustainability

From a sustainability perspective, cyanoacrylate instant adhesive technology offers several unique benefits. Their rapid cure at room temperature means that no external energy source such as energy-intensive thermal ovens is required, which can help to reduce the energy spend of industrial assembly processes and hence lower the CO₂ footprint. Adhesives with faster curing times enable faster, more efficient manufacturing processes. The enhanced bonding characteristics and performance of the latest generation of cyanoacrylate instant adhesives greatly help to minimize waste in the manufacturing assembly process by allowing the simplification of complex finished part design by reducing the number of parts required in a finished product (e.g., replacement of screws/rivets/solder with an effective adhesive). This in turn makes such goods lighter, requiring less energy to manufacture. Fewer parts also equate to better use of resources and less waste, which improves manufacturer sustainability goals.

Cyanoacrylate adhesives also offer benefits from a recycling and repair perspective. Products that are at the end of life, or in need of repair, can be dismantled or disassembled when subjected to specific processing conditions involving the application of heat cycles, allowing valuable components to be recycled or reused. Parts bonded with cyanoacrylate adhesives can often be separated by soaking in common solvents such as acetone, which can dissolve the cyanoacrylate polymer (due to its thermoplastic nature) and thus facilitate the recycling of valuable components. There have been recent reports of new water-soluble cyanoacrylate monomers that can be used for temporary bonding applications, which can easily be removed via aqueous treatment [93].

Adhesive manufacturers are also continually modifying the adhesive/monomer manufacturing process to reduce the amount of energy, waste, and emissions produced in the process. Continuous improvements are being made to improve the overall manufacturing process yield and to reuse/recycle byproducts, thereby reducing waste and creating a “cleaner” industrial process with fewer emissions and reduced waste to landfill. This can lower the overall CO₂ footprint of the adhesive/monomer manufacturing process.

Increasing regulation on health and chemical safety issues [94] as well as environmental concerns are becoming increasingly important and will increase pressure on the adhesive industry to minimize the impact of adhesives in these areas. It is likely that such regulatory pressures will focus future developments in the area of new resins, monomers, additives, and processes with reduced environmental and health and safety impacts.

4.9 Summary

Cyanoacrylates represent a class of adhesives that offer superior benefits to the end user in terms of rapid cure at ambient temperature, outstanding adhesion to a broad range of substrate types, and high tensile bond strengths. Their ease of use and ability to rapidly bond (fixture) assembled parts without the need for external energy sources to drive the cure process enable end users to reduce the complexity of design and minimize waste in their final assembly process. This represents a truly sustainable assembly and bonding process that helps to reduce the CO₂ footprint and achieve sustainability targets.

Recent technology developments are helping to extend the use of cyanoacrylates beyond the confines of traditional instant adhesives into the more demanding realm of structural bonding applications. Developments in additive technology, new crosslinking CAs such as allyl CA, and exciting developments with new two-component and hybrid CA adhesives have helped to address many of the traditional weaknesses associated with cyanoacrylates, such as curing through thicker bondlines and thermal/humidity resistance. Such new developments, coupled with the potential for the development of new monomers accessible via new, improved manufacturing processes, will open new markets and opportunities for cyanoacrylate adhesive technology.

Acknowledgments

Thanks to my colleague Dr. Emer Ward (Henkel Ireland Operations and Research) and to Eadaoin Ledwidge (Connexicon Medical) for the fruitful discussions, input, and support. In memory of my parents, Angie and Tommy.... thank you for everything you gave me.

References

- [1] H. Lee, *Cyanoacrylate Resins—The Instant Adhesives*, Pasadena Technology Press, Los Angeles, 1986.
- [2] A.E. Ardis, Preparation of Monomeric Alkyl Alpha-Cyanoacrylates, 1949. US Patent 2,467,927, assigned to B.F. Goodrich.
- [3] H.W. Coover, N.H. Shearer, Adhesive Compositions Containing Alkyl Esters of Cyanoacrylic Acid, 1957. US Patent 2,794,788, assigned to Eastman Kodak Co.
- [4] G.H. Millet, Cyanoacrylate adhesives, in: S.R. Hartshorn (Ed.), *Structural Adhesives: Chemistry and Technology*, Plenum Press, New York, 1986, pp. 249–307.
- [5] P. Klemarczyk, J. Guthrie, Advances in anaerobic and cyanoacrylate adhesives, in: D.A. Dillard (Ed.), *Advances in Structural Adhesive Bonding*, Woodhead Publishing Limited, Cambridge, UK, 2010, pp. 96–131.
- [6] D.A. Aronovich, Modern achievements in the field of cyanoacrylate adhesives. Mechanisms of polymerization of cyanoacrylates and their application value, *Polym. Sci., Ser. D* 12 (3) (2019) 290–295.
- [7] B. Burns, Polycyanoacrylates, in: *Encyclopedia of Polymer Science and Technology*, vol. 4, John Wiley & Sons, New Jersey, 2016, pp. 1–27.
- [8] J.M. Korde, B. Kandasubramanian, Biocompatible alkyl cyanoacrylates and their derivatives as bio-adhesives, *Biomater. Sci.* 6 (7) (2018) 1691–1711.
- [9] B. Burns, Cyanoacrylates: towards high temperature resistant instant adhesives, *Rev. Adhes. Adhes.* 5 (4) (2017) 361–390.
- [10] D.C. Pepper, B. Ryan, Initiation processes in polymerizations of alkyl cyanoacrylates by tertiary amines: inhibition by strong acids, *Makromol. Chem.* 184 (2) (1983) 383–394.
- [11] D.C. Pepper, Kinetics and mechanism of zwitterionic polymerizations of alkyl cyanoacrylates, *Polym. J.* 12 (1980) 629–637.
- [12] E.F. Donnelly, D.S. Johnston, D.C. Pepper, D.J. Dunn, Ionic and zwitterionic polymerization of n-alkyl 2-cyanoacrylates, *J. Polym. Sci., Polym. Lett. Ed.* 15 (1977) 399–405.
- [13] J.P. Cronin, D.C. Pepper, Zwitterionic polymerization of butyl cyanoacrylate by triphenylphosphine and pyridine, *Makromol. Chem.* 189 (1988) 85–102.
- [14] D.S. Johnston, D.C. Pepper, Polymerization by macrozwitterions, 1. Ethyl and butyl cyanoacrylates by triethyl and triphenylphosphines, *Makromol. Chem.* 182 (2) (1981) 393–406.
- [15] I.C. Ermoesele, D.C. Pepper, Anionic polymerizations of butyl cyanoacrylate by tetrabutylammonium salts, *Makromol. Chem.* 190 (12) (1989) 3095–3103.
- [16] D.C. Pepper, Zwitterionic chain polymerisations of cyanacrylate, *Makromol. Chem. Macromol. Symp.* 60 (1) (1992) 267–277.
- [17] D.C. Pepper, B. Ryan, Kinetics of polymerization of alkyl cyanoacrylates by tertiary amines and phosphines, *Makromol. Chem.* 184 (2) (1983) 395–410.
- [18] D.C. Pepper, Anionic and zwitterionic polymerization of α -cyanoacrylates, *J. Polym. Sci., Polym. Symp.* 62 (1978) 65–77.

- [19] D. Katti, N. Krishnamurti, Anionic polymerization of alkyl cyanoacrylates: in vitro model studies for in vivo applications, *J. Appl. Polym. Sci.* 74 (1999) 336–344.
- [20] C. Duffy, P.B. Zetterlund, F. Aldabbagh, Radical polymerization of alkyl cyanoacrylates, *Molecules* 23 (2) (2018) 465–485.
- [21] A.J. Canale, W.E. Goode, J.B. Kinsinger, J.R. Panchak, R.L. Kelso, R.K. Graham, Methyl α -cyanoacrylate. I. Free-radical homopolymerization, *J. Appl. Polym. Sci.* IV (11) (1960) 231–236.
- [22] J.C. Bevington, J.A.L. Jemmet, Polymerization of methyl α -cyanoacrylate. Part 1. Initiation by benzoyl peroxide, *J. Chem. Soc. Faraday Trans. 1* (69) (1973) 1866–1871.
- [23] J.C. Bevington, J.A.L. Jemmet, P.F. Onyon, Polymerization of methyl α -cyanoacrylate -I: conditions for radical polymerization, *Eur. Polym. J.* 12 (4) (1976) 255–257.
- [24] C. Duffy, M. Phelan, P.B. Zetterlund, F. Aldabbagh, Reversible addition-fragmentation chain transfer polymerization of alkyl-2-cyanoacrylates: an assessment of livingness, *J. Polym. Sci. A Polym. Chem.* 55 (8) (2017) 1397–1408.
- [25] D.R. Robello, T.D. Eldridge, M.T. Swanson, Degradation and stabilization of polycyanoacrylates, *J. Polym. Sci. A Polym. Chem.* 37 (24) (1999) 4570–4581.
- [26] D.A. Aronovich, Modern achievements in the field of cyanoacrylate adhesives: synthesis of cyanoacrylate monomers, *Polym. Sci., Ser. D* 12 (4) (2019) 401–409.
- [27] F.B. Joyner, G.F. Hawkins, *Methods of Making α -Cyanoacrylates*, 1955. US Patent 2,721,858, assigned to Eastman Kodak.
- [28] F. Leonard, R.K. Kulkarni, G. Brandes, J. Nelson, J.J. Cameron, Synthesis and degradation of poly (alkyl α -cyanoacrylates), *J. Appl. Polym. Sci.* 10 (2) (1966) 259–272.
- [29] H.W. Coover Jr., J.B. Dickey, *Stabilized Alpha-Cyanoacrylate Adhesive Compositions*, 1956. US Patent 2,765,332, assigned to Eastman Kodak.
- [30] C.G. Jeremias, *Process for Making Monomeric α -Cyanoacrylates*, 1956. US Patent 2,763,677, assigned to Eastman Kodak.
- [31] C.H. McKeever, *Preparation of Alkyl α -Cyanoacrylates*, 1959. US Patent 2,912,454, assigned to Rohm and Haas.
- [32] C.H. McKeever, H.R. Raterink, *Process for Preparing of α -Cyanoacrylates*, 1960. US Patent 2,926,188, assigned to Rohm and Haas.
- [33] H.W. Coover Jr., T.H. Wicker Jr., *Cyanoacrylate adhesives*, in: H.F. Mark, N.G. Gaylord, N.M. Bikales (Eds.), *Encyclopedia of Polymer Science and Technology*, vol. 1, Interscience Publishers, New York, 1964, pp. 337–342.
- [34] P.R. Raja, *Cyanoacrylate adhesives: a critical review*, *Rev. Adhes. Adhes.* 4 (4) (2016) 398–416.
- [35] W. Hong, et al., *Synthesis Method of α -Cyanoacrylate*, 2019. Chinese Patent CN109678758, assigned to Hebei Chengxin.
- [36] Y. Nishino, H. Yamamoto, C. Hata, *Method for Purifying Ethyl-2-Cyanoacrylate Adhesive Composition and Ethyl-2-Cyanoacrylate Adhesive Composition*, 2015. US Patent 8,945,299, assigned to Taoka Chemical Co., Ltd.
- [37] H.W. Coover Jr., J.M. McIntire, *Cyanoacrylate adhesives*, in: I. Skeist (Ed.), *Handbook of Adhesives*, second ed., Van Nostrand Reinhold, New York, 1977, pp. 569–580.
- [38] P. Klemarczyk, *Cyanoacrylate instant adhesives*, in: M. Chaudhury, A.V. Pocius (Eds.), *Adhesion Science and Engineering (The Mechanics of Adhesion)*, vol. 1, Elsevier Science, Amsterdam, 2002, pp. 847–867.
- [39] V. Vijayalakshmi, J.N.R. Vani, N. Krishnamurti, Alkyl and substituted alkyl 2-cyanoacrylates. Part I. Synthesis and properties, *J. Adhes. Sci. Technol.* 4 (9) (1990) 733–750.
- [40] P. Klemarczyk, *A general synthesis of 1,1-disubstituted electron deficient olefins and their polymer properties*, *Polymer* 39 (1) (1998) 173–181.

- [41] V.A. Dyatlov, G.A. Katz, Process for the Preparation of Esters of 2-Cyanoacrylic Acid and Use of the Esters so Prepared as Adhesives, 1994. PCT Pat. App. WO 9415907, assigned to Eurotax Ltd.
- [42] V.A. Dyatlov, I.R. Rustamov, T.A. Grebeneva, et al., Synthesis of 2-cyanoacryloyl chloride and its interaction with O- and S-nucleophiles, *Mendeleev Commun.* 23 (2013) 356–357.
- [43] J. Voitekunas, et al., Method of Preparing Cyanoacrylic Acid Esters, 1980. Russian Patent 726,086, assigned to USSR Academy of Sciences.
- [44] Y. Gololobov, W. Gruber, C. Nicolaisen, Process for the Production of Biscyanoacrylates, 2000. US Patent 6,096,848, assigned to Henkel.
- [45] C. Friese, L. Zander, Method for Preparing Cyanoacrylates Esters, 2010. PCT Pat. App. WO 2010/091975, assigned to Henkel.
- [46] C.J. Buck, Modified Cyanoacrylate Esters and Methods of Preparation, 1977. US Patent 4,012,402, assigned to Johnson and Johnson.
- [47] L. Giral, Synthesis of fluorinated alkyl alpha-cyanoacrylates: setting an experimental procedure, *Ann. Pharm. Fr.* 43 (1985) 439–449.
- [48] B. Malofsky, I.T. Badejo, Transesterification Method for Making Cyanoacrylates, 2001. US Patent 6,245,933, assigned to Ethicon Inc.
- [49] C. McArdle, L. Zhao, Imines and Methods of Preparing Electron Deficient Olefins Using Such Novel Imines, 2011. US Patent 8,053,589, assigned to Henkel.
- [50] C. McArdle, L. Zhao, Method of Preparing Electron Deficient Olefins, 2009. US Patent 7,569,719, assigned to Henkel.
- [51] F. Bigi, C. McArdle, L. Zhao, Method of Preparing Electron Deficient Olefins, 2010. US Patent 7,718,821, assigned to Henkel.
- [52] C. McArdle, L. Zhao, Iminium Salts and Methods of Producing Electron Deficient Olefins Using Such Novel Iminium Salts, 2011. US Patent 8,022,251, assigned to Henkel.
- [53] C. McArdle, et al., Electron Deficient Olefins, 2016. US Patent 9,481,640, assigned to Henkel.
- [54] V. Tchaplinski, S. Gherardi, V.D.L.F. Molina, Process for Preparing 1,1-Disubstituted Ethylene Monomers, 2017. US Patent 9,670,145, assigned to Afinitica Technologies, S.L.
- [55] C. Duffy, B. Burns, M. Phelan, Process for Preparing Electron Deficient Olefins, 2021. US Patent 10,913,707, assigned to Henkel.
- [56] C. Duffy, B. Burns, M. Phelan, Process for Preparing Electron Deficient Olefins, 2021. US Patent 10,927,071, assigned to Henkel.
- [57] D.A. Aronovich, Progress in cyanoacrylate adhesives. Studies of adhesive modification, *Polym. Sci., Ser. D* 13 (3) (2020) 297–305.
- [58] B. Ryan, G. McCann, Novel sub-ceiling temperature rapid depolymerisation repolymerization reactions of cyanoacrylate polymers, *Macromol. Rapid Commun.* 17 (1996) 217–227.
- [59] M.G. Han, S. Kim, S.X. Liu, Synthesis and degradation behaviour of poly(ethyl) cyanoacrylate, *Polym. Degrad. Stab.* 93 (7) (2008) 1243–1251.
- [60] G. Zaffaroni, A. Monesi, Cyanoacrylic Adhesive Compositions With Improved Resistance to High Temperatures, 2020. US Patent Application 2020/0407596, assigned to Permabond Engineering Adhesives.
- [61] T. Gernon, A. Mooney, M. Jordan, S. Reilly, M. Smyth, D. Moore, P. Hedderman, Cyanoacrylate Compositions, 2021. PCT application WO2021/260160, assigned to Henkel IP & Holding GmbH.
- [62] K. Ishizaki, Y. Ando, Adhesive Composition, 2016. US Patent 9,458,361, assigned to Toagosei.

- [63] K. Raheem, J. Cassidy, A. Betts, B. Ryan, Use of confocal Raman spectroscopy to characterize ethyl cyanoacrylate adhesive depth of curing, *Phys. Chem. Chem. Phys.* 22 (2020) 23899–23907.
- [64] R.V. Prabhu, P. Shetty, R. Jagtap, M. Digar, Polyethyleneimine as a surface activator for low surface energy substrates bonded with cyanoacrylate adhesives, *Int. J. Adhes. Adhes.* 107 (2021) 102840–102847.
- [65] H. Misiak, I. Scheffler, Activator for Cyanoacrylate Adhesives, 2003. US Patent 6,547,917, US, assigned to Henkel.
- [66] J. Delahunty, Cyanoacrylate Adhesive Composition, 1972. GB Patent 1,414,317, assigned to Loctite (Ireland) LTD.
- [67] O. Shigeru, Y. Yoshio, Method of Precisely Positioning and Fixing Parts, 1987. JP 62-022877, assigned to Janome Sewing Machine.
- [68] J.-C. Liu, Non-Volatile Adhesive Promoter Composition for Curing Adhesives, 2002. EP0785865, assigned to Henkel Loctite.
- [69] R.C. Jimenez, Sealant Composition, 1987. ES 556,348, assigned to Renbec International Corp.
- [70] P.F. McDonnell, B. Kneafsey, R.J. Lambert, Cyanoacrylate Composite Forming System, 2011. US Patent 8,071,675, assigned to Henkel.
- [71] A.J. Bennetts, C.E. Wilde, A.D. Wison, Hubs High Strength Universal Bonding and Filling System, 2005. GB 6,382,161, assigned to Bennett, Wilde and Wilson.
- [72] G.J. Mader, Method of Repairing Breaks in Sheet Material, 1985. US Patent 4,526,636, assigned to Mader.
- [73] W. Hally, E. Ward, P.A. Hedderman, D. Moore, D. Heatley, Activators for Two-Part Cyanoacrylate Adhesives, 2015. US Patent 8,933,168, assigned to Henkel.
- [74] E. Ward, D. Coleman, R. Tully, Two-Part Cyanoacrylate Curable Adhesive system, 2018. US Patent 10,100,235, assigned to Henkel.
- [75] A.P. Jimenez, V. De La Fuente Molina, C. McArdle, Fast and Elastic Adhesive, 2020. US Patent 10,626,299, assigned to Afinitica Technologies, S.L.
- [76] C. McArdle, A.P. Jimenez, J.A. Lopez-Maeso, S. Gherardi, Cyanoacrylate Composition, 2018. US Patent 10,144,851, assigned to Afinitica Technologies, S.L.
- [77] B.N. Burns, R.M. Hersee, M. Loane, R. Tully, E. Ward, Two-Part Cyanoacrylate/Cationically Curable Adhesive System, 2013. US Patent 8,580,888, assigned to Henkel.
- [78] B.N. Burns, R. Barnes, J. Guthrie, R.M. Hersee, R. Tully, Two-Part Cyanoacrylate/Cationically Curable Adhesive System, 2014. US Patent 8,742,048, assigned to Henkel.
- [79] P. Hedderman, R.M. Hersee, D.A. Moore, S. Reilly, E. Ward, Two-Part Cyanoacrylate/Cationically Curable Adhesive Systems, 2015. US Patent 8,981,027, assigned to Henkel.
- [80] B. Burns, R. Barnes, J.P. Wigham, E. Ward, Two-Part Cyanoacrylate/Free Radically Curable Adhesive Systems, 2016. US Patent 9,371,470, assigned to Henkel.
- [81] K. Ishizaki, Y. Ando, Two-Part Curable Composition, 2018. US Patent 9,994,662, assigned to Toagosei Co., Ltd.
- [82] S. Wojciak, S. Attarwala, Radiation-Curable, Cyanoacrylate-Containing Compositions, 2004. US Patent 6,726,795, assigned to Henkel Corporation.
- [83] Y. Nishiyama, H. Mikuni, Photocurable Composition Containing an α -Cyanoacrylate and a Metallocene Compound, 2003. US Patent 6,503,959, assigned to Three Bond Co., Ltd.
- [84] H. Misiak, Radiation-Curable, Cyanoacrylate-Containing Compositions, 2004. US Patent 6,734,221, assigned to Henkel.
- [85] H. Misiak, Cyanoacrylate Compositions Curable to Flexible Polymeric Materials, 2005. US Patent 6,977,278, assigned to Henkel.

-
- [86] L. Li, X. Wei, S.T. Attarwala, Flexible Photocurable Cyanoacrylate Compositions, 2022. US Patent application 2022/0033544A1, Henkel.
- [87] J.L.L. Maeso, C. McArdle, C.M. Fraga, V.D.L.F. Molina, A.P. Jimenez, V. Tchaplinski, Fast Light Curing Cyanoacrylate Compositions, 2020. US Patent 10,626,310, assigned to Afinitica Technologies, S.L.
- [88] S.K. Czaplewski-Campbell, J. Kuczynski, M.K. Miller, R. Morones, Acrylate-Cyanoacrylate Monomers, 2020. US Patent 11,028,294, assigned to International Business Machines Corporation.
- [89] E.M. Petrie, Cyanoacrylate adhesives in surgical applications: a critical review, *Rev. Adhes. Adhes.* 2 (3) (2014) 253–310.
- [90] R. Nian, M. Xian, et al., The recent progress of tissue adhesives in design strategies, adhesive mechanism and applications, *Mater. Sci. Eng. C* 111 (2020) 110796–110810.
- [91] S.N. Ayyildiz, A. Ayyildiz, Cyanoacrylic tissue glues: biochemical properties and their usage in urology, *Turk. J. Urol.* 43 (1) (2017) 14–24.
- [92] A.J. Domb, A. Basu, et al., Comparative evaluation of polycyanoacrylates, *Acta Biomater.* 48 (15) (2017) 390–400.
- [93] E. Isshiki, K. Ishizaki, Y. Horie, E. Okazaki, Adhesive Composition that Easily Disintegrates in Water, 2021. US Patent application 2021/0363393, Toagosei Co., LTD.
- [94] European Commission, 17th Adaptation to Technical Progress (ATP) to the Classification, Labeling and Packaging (CLP) Regulation, 2021 (28th May, 2021).

This page intentionally left blank

Advances in anaerobic adhesives

5

David Condon

Henkel Ireland Operations and Research, Dublin, Ireland

5.1 Anaerobic adhesives

5.1.1 Introduction

In 1953, American professor Vernon K. Kriebel developed the first commercial anaerobic threadlocking adhesives in his basement laboratory at Trinity College in Hartford, Connecticut. Kriebel's company, American Sealants, founded the Loctite brand, which was promoted as ushering in a new era of mechanical reliability by eliminating the vibrational loosening of mechanical fasteners, a frequent cause of machine failure [1]. American Sealants became Loctite Corporation in 1965 and developed another important class of adhesives known as cyanoacrylates or instant adhesives, which are discussed in [Chapter 4](#). Anaerobic and cyanoacrylate adhesives have some similarities as they are one-part, surface-activated adhesives that cure at room temperature; for this reason, they are often linked. However, their cure chemistry, properties, and applications differ, and it is appropriate to treat them separately. Recent research on anaerobic adhesives has focused on improving their sustainability characteristics, thermal resistance, and cure on inactive surfaces. Recent advances on these topics will be considered in this chapter.

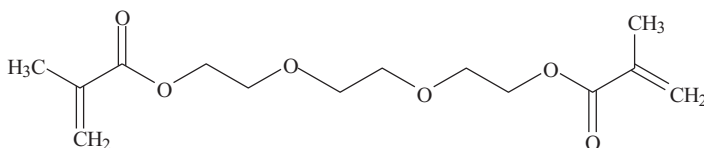
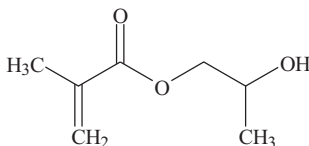
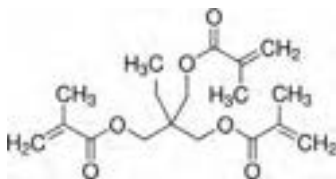
Anaerobic adhesives are one-part systems usually based on methacrylate monomers or oligomers, with methacrylate functionality. Anaerobic adhesives cure at room temperature, in bond lines in the absence of oxygen, and in the presence of redox active metal ions. The cure mechanism is complex but can be described as a redox-initiated free radical polymerization. The metal ions that promote the cure of the adhesive generally come from the substrate. For this reason, anaerobic adhesives are normally used for bonding metals and are sometimes referred to as machinery adhesives. Anaerobic adhesives are used in many machinery-related applications such as threadlocking, thread sealing, flange sealing, retaining, and impregnation sealing.

5.1.2 Formulation chemistry of anaerobic adhesives

Anaerobic adhesives are versatile adhesive systems, and there is ample scope for the formulation chemist to adjust the properties of the adhesive to meet the requirements of a given application. A simplified, generalized formulation is provided in [Table 5.1](#). Monomers are an essential part of the formulation, as they bond together to form chains and crosslinked networks as the adhesive cures. The main reactive functional unit used is methacrylate, although acrylates may sometimes be included. Di-functional

Table 5.1 Basic formulation components of an anaerobic adhesive.

Formulation component	Examples
Monomers Oligomers	Triethyleneglycol dimethacrylate (TRIEGMA) Polyurethane methacrylates
Curatives	
<ul style="list-style-type: none"> • Initiator • Accelerator • Metal substrate 	Cumene hydroperoxide 1-Acetyl-2-phenylhydrazine, saccharin Redox active metal such as Fe or Cu
Stabilizers	
<ul style="list-style-type: none"> • Free radical • Metal chelator 	Naphthoquinone Tetrasodium ethylenediaminetetraacetic acid
Plasticizers	Polyester adipates
Form modifiers	Silica, mica, talc

**Fig. 5.1** Triethylene glycol dimethacrylate.**Fig. 5.2** 2-Hydroxy propyl methacrylate.**Fig. 5.3** Trimethylol propane trimethacrylate.

methacrylates such as triethylene glycol dimethacrylate (Fig. 5.1) are commonly employed, although mono-functional methacrylates such as hydroxypropyl methacrylate (Fig. 5.2) and higher-functionality monomers such as trimethylolpropane trimethacrylate (Fig. 5.3) are often included to promote crosslinking of polymer chains. Oligomers with methacrylate functionality are often used in anaerobic adhesives to modify performance features such as thermal resistance and flexibility.

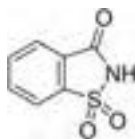


Fig. 5.4 Saccharin.

Plasticizers are used to moderate the strength of an adhesive where easy disassembly is a requirement.

Another key component of an anaerobic adhesive is the cure system, which can be complex but normally includes an oxidizing agent such as a peroxide or a hydroperoxide, a reducing agent such as an amine or hydrazine, and a weak acid such as saccharin (Fig. 5.4). The amine and saccharin exert a synergistic effect to increase the cure speed; they are commonly known as accelerators. A key component of the anaerobic cure system is the metal substrate, which provides redox active metal ions such as Fe and Cu that act as catalysts in the cure system.

Monomers, oligomers, plasticizers, and the cure system determine to a large extent the key properties of the cured adhesive such as strength, temperature resistance, and flexibility.

Stabilizers are also an essential part of the formulation and include free radical stabilizers such as naphthoquinone (Fig. 5.5) and metal chelators such as Na₄EDTA (Fig. 5.6). These stabilizers prevent premature polymerization of the adhesive.

Many other ingredients are used in anaerobic adhesive formulations to adjust properties such as appearance, color, and rheology. Examples include dyes, pigments, fluorescing agents, viscosity builders, and thixotropic agents. In general, the chemistry is tolerant to a wide variety of materials, making these adhesive systems quite versatile. The basic elements of an anaerobic formulation outlined in Table 5.1 provide some insight into the type of materials used along with their function. However, it should be emphasized that in practice, a typical anaerobic formulation would be more complex and include several types of these components to achieve the required product performance.

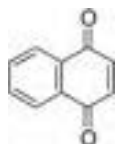


Fig. 5.5 1,4-Naphthoquinone.

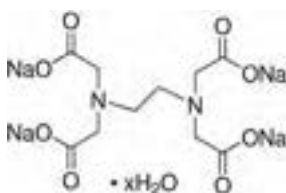
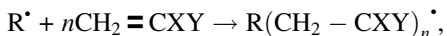


Fig. 5.6 Ethylenediaminetetraacetate tetrasodium salt.

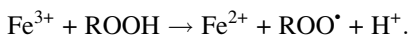
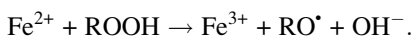
5.1.3 Anaerobic adhesive cure chemistry

Anaerobic adhesives cure by a free radical-initiated addition polymerization:



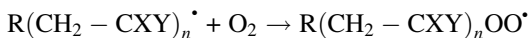
where R^{\bullet} is the initiating free radical (for a methacrylate monomer, X is $-\text{CH}_3$ and Y is $-\text{CO}_2R'$). Eventually, chain growth will terminate through radical recombination or disproportionation.

However, there are two important features that distinguish the anaerobic adhesive cure mechanism. The first is the pair of redox reactions between a transition metal ion and a hydroperoxide [2]:



Similar reactions apply to other transition metals that exist in different oxidation states such as Cu^{+} and Cu^{2+} . The peroxy radical generated by the higher oxidation state metal ion is a much less powerful initiator for polymerization than the alkoxy radical generated by the lower oxidation state metal ion. In the presence of oxygen, the higher oxidation state will predominate.

The second feature is that even if polymerization is initiated by an alkoxy radical, the oligomeric chain will eventually encounter an oxygen molecule if oxygen is present. This will convert an active tertiary alkyl radical into a much less active peroxy radical:



Hence, the polymerization is doubly inhibited by the presence of oxygen.

Commercial anaerobic adhesives also contain saccharin (benzoic sulfimide) (Fig. 5.4) and an amine (generally an aromatic amine) used as accelerators to speed the rate of cure under anaerobic conditions. Saccharin probably plays several roles. As a weak acid, it may help transport metal ions from the surface of the substrate into the bulk of the adhesive, and it may catalyze the decomposition of hydroperoxides [3]. The amine also probably plays several roles. The combination of amine and saccharin is much more effective, suggesting a degree of synergy, and it is probable that some sort of complex is involved. Both a charge transfer complex (Fig. 5.7) [4] and an aminoral (Fig. 5.8) have been proposed [5].

The amine most studied in the literature is dimethyl *p*-toluidine (Fig. 5.9), which was used in the 1980s in commercial products. However, it has now largely been replaced by several alternatives: a blend of dimethyl *o*-toluidine (Fig. 5.10) and diethyl *p*-toluidine (Fig. 5.11); 1,2,3,4-tetrahydroquinoline (THQ) (Fig. 5.12); and 1-acetyl-2-phenylhydrazine (APH) (Fig. 5.13). The reaction mechanisms associated with these accelerators are complex and likely differ in their details. The APH cure mechanism

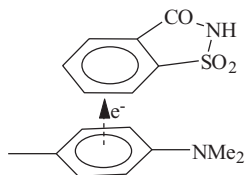


Fig. 5.7 Charge transfer complex.

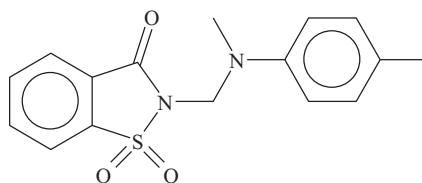


Fig. 5.8 Aminal.

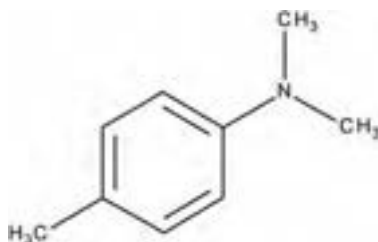


Fig. 5.9 *N,N*-Dimethyl-*p*-toluidine.

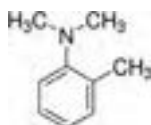


Fig. 5.10 *N,N*-Dimethyl-*o*-toluidine.

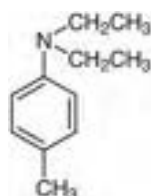


Fig. 5.11 *N,N*-Diethyl-*p*-toluidine.

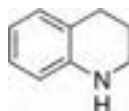


Fig. 5.12 1,2,3,4-Tetrahydroquinoline.

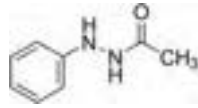


Fig. 5.13 1-Acetyl-2-phenylhydrazine.

has been extensively studied [6,7] and a general overview of anaerobic cure chemistry is provided in a recent paper published by Aronovich [8]. In general, it can be stated that the mechanism of anaerobic curing depends significantly on both the curing accelerators and the nature of the metal substrate. As the cure is surface activated, anaerobic adhesives achieve their highest strength when the gaps between metal surfaces are small (0.05–0.15 mm).

5.1.4 Anaerobic adhesive applications

5.1.4.1 Threadlocking

This was the earliest application for anaerobic products. Threadlocking products prevent self-loosening and secure threaded fasteners against vibration and shock loads. The introduction of chemical threadlocking products eliminated many of the design faults and shortcomings of threaded fasteners. Threadlockers are anaerobic adhesives that cure to a tough solid state when deprived of atmospheric oxygen (air). The cured product is a thermoset plastic that cannot be liquefied by heating and resists most solvents. These products are specifically designed to lock and seal threaded components.

If two plates are fastened together with a nut and bolt, then the plates are under compression and the bolt is under tension (Fig. 5.14). All that prevents the assembly from coming apart under vibration is the friction between the nut and the bolt. This, in turn, comes from the microscopic roughness of their surfaces—there are only a few



Fig. 5.14 Application of threadlocker on a through-hole.

points of true contact. Threadlockers fill the empty spaces with a solid material that dramatically increases adhesion to the metal substrate and secures the fastener against vibrational loosening. There are many different anaerobic threadlockers with varying strengths, speeds, and rheology characteristics.

It is also possible to coat threaded parts with threadlockers (and with thread sealants for that matter) in the form of dry-to-the touch films containing microcapsules. The *preapplied* products only polymerize on assembly, whereupon the capsules rupture and release a quick curing resin.

Testing standards and performance specifications for anaerobic adhesives and sealants have been established by government agencies and industrial organizations in several countries. For example, ASTM D5363-16 covers single-component adhesives suitable for locking, sealing, and retaining threaded or cylindrical assemblies. The specification also aims to be a means of classifying anaerobic adhesives.

5.1.4.2 Thread sealing

Anaerobic thread sealants, available in liquid or paste form, prevent leakage of gases and liquids from connections involving threaded pipe assemblies (Fig. 5.15). Designed for low- to high-pressure applications, they fill the space between threaded parts and provide an instant, low-pressure seal. When fully cured, they seal to the burst strength of most pipe systems. Threadlockers and thread sealants share many common components and can sometimes be used interchangeably. However, thread sealants usually require an optimized rheology for ease of use in the application.

Thread sealants for larger pipe fittings are usually highly filled, thixotropic adhesives but lower-viscosity thread sealants have also been developed for fittings with fine threads used in hydraulic and pneumatic sealing applications.

European standard EN 751-1:1996 specifies requirements and test methods for anaerobic jointing compounds to be used on threaded metallic joints in contact with first, second, and third family gases and hot water. This is the relevant standard for anaerobic adhesives and has been widely adopted by a number of European countries as a national standard such as BS EN 751-1 (Britain) and DIN EN 751-1 (Germany).



Fig. 5.15 Application of an anaerobic thread sealant to a threaded pipe fitting.

5.1.4.3 Retaining

Anaerobic retaining compounds are used to secure bearings, bushings, and cylindrical parts into housings or onto shafts. They are designed to achieve high load transmission and uniform stress distribution while eliminating fretting and corrosion. Applied as a liquid, retaining compounds fill the inner space between the components to be bonded and cure to form a strong precision assembly (Fig. 5.16). Retaining compounds are generally optimized for maximum strength, which is normally measured on steel pins and collars according to ISO 10123:2013.

Anaerobic retaining compounds offer advantages over mechanical retainers. Because there is 100% surface to surface contact, load and stress are distributed evenly over the joint. Corrosion and fretting of the joint are prevented by the presence of the adhesive, which fills any voids and eliminates frictional sliding. Anaerobic retaining compounds are often used in combination with interference fits, augmenting the strength of the assembly and facilitating the use of relaxed tolerances. A more detailed treatment of the retaining application is provided by Haviland [9].

5.1.4.4 Gasketing

Gaskets are used to prevent leakage of liquids and gases by forming impervious barriers. The seal should remain intact and leak-free over a long period of time. The gasket should be resistant to the liquids and/or gases and withstand the operating temperatures and pressures to which it is subjected. Anaerobic gasketing products are self-forming gaskets that provide an excellent seal between components, with maximum face-to-face contact (Fig. 5.17). They are also useful in eliminating flange face corrosion. A low-pressure seal is formed immediately upon assembly. Upon fully curing, the cured adhesive gives a joint that will not shrink, crack, or relax.

Gasketing compounds, also known as flange sealants, can be optimized to suit the requirements of the application. An important factor is flexibility control, which is achieved by the optimum use of bulk components in the formulation. Gasketing products can be designed to span the entire flexibility range from rigid to flexible as measured by elongation at break of the cured gasketing compound. Values in the range of 0%–200% can be achieved. A higher flexibility product is recommended for highly

Fig. 5.16 Application of an anaerobic retaining compound to a bearing.





Fig. 5.17 Application of an anaerobic product to a flange.

stressed flanges subjected to micromovements. It is also possible to lower the adhesion of anaerobic gasketing products to facilitate easy removal and repair. These lower adhesion products still exhibit good sealing properties, but the products should be carefully chosen to ensure adequate chemical resistance to circulating fluids.

The tensile lap shear strength of gasketing compounds is normally measured using lap shears according to ISO 4587:2003. Specialist seal testing may also be conducted to confirm sealing performance [9].

5.2 Recent advances in anaerobic technology

Anaerobic adhesives tolerate a diverse range of raw materials, provided the level of redox active metals is in the low ppm range. In recent years, researchers have focused on the enhancement of product performance and sustainability characteristics. A range of new curatives has been patented to enhance cure on inactive surfaces such as stainless steel and new materials have been incorporated to improve thermal performance. Considerable research has been conducted with the aim of improving the health and safety of anaerobic products and reducing their carbon dioxide footprint by incorporating raw materials from renewable resources.

5.2.1 *New curatives for anaerobic products*

Considerable research has been conducted in recent years to discover new curing agents for anaerobic adhesives. The main objectives are to identify curatives with reduced health and safety labeling, and to improve anaerobic cure performance on difficult to bond surfaces. Examples of these low activity metallic surfaces include anodized aluminum, stainless steel, galvanized steel, zinc, titanium, and Al/Zn flake anticorrosion coatings.

A comprehensive overview of the work conducted over the past 20 years is beyond the scope of this review. Interested readers are directed to more detailed reviews on this topic [8]. However, the following examples provide a short summary of the type of research being conducted in the field of anaerobic cure chemistry.

Birkett et al. synthesized derivatives of THQ (Fig. 5.12) and indoline (Fig. 5.18), which proved useful as accelerators for anaerobic adhesives. Examples include *N*-methyl tetrahydroquinoline (Fig. 5.19), *N*-butyl tetrahydroquinoline (Fig. 5.20), and adducts with glycidol (Fig. 5.21) [10].

Klemarczyk et al. provided additional examples of THQ and indolene derivatives such as *N*-ethyl acetate THQ (Fig. 5.22), *N*-acetonitrile indoline (Fig. 5.23), *N*-nitrobenzyl THQ (Fig. 5.24), and *N*-cyanobenzyl indoline (Fig. 5.25). It was demonstrated that these materials are useful accelerators in model anaerobic adhesives,



Fig. 5.18 Indoline.

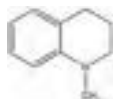


Fig. 5.19 *N*-Methyl tetrahydroquinoline.

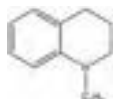


Fig. 5.20 *N*-Butyl tetrahydroquinoline.

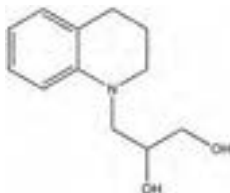


Fig. 5.21 THQ-glycidol adduct.

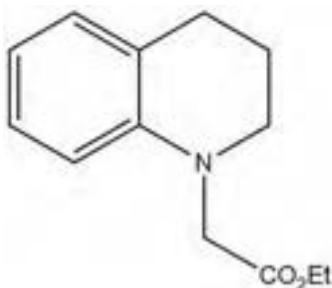


Fig. 5.22 *N*-Ethyl acetate THQ.

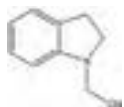


Fig. 5.23 *N*-Acetonitrile indoline.

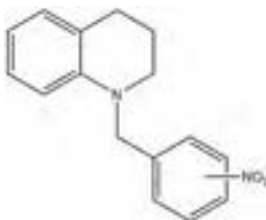


Fig. 5.24 *N*-Nitrobenzyl THQ.

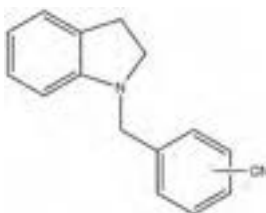


Fig. 5.25 *N*-Cyanobenzyl indoline.

promoting cure on inactive substrates such as stainless steel. The authors propose additional benefits for these accelerators related to odor reduction and reduced toxicity compared to standard amine accelerators [11].

Klemarczyk et al. investigated adducts of phenylhydrazine and cyclic and bicyclic anhydrides as accelerators for anaerobic adhesives [12]. Examples of materials investigated include tetrahydrophthalic phenyl hydrazine (Fig. 5.26) and hexahydrophthalic phenyl hydrazine (Fig. 5.27). These molecules combine hydrazine and acid functionality and when used in model anaerobic formulations, were shown to provide increased strength on stainless steel substrates as measured by the required torque to loosen the bolt.

Another approach investigated with the aim of reducing the toxicity potential of anaerobic curatives describes the development of polymeric materials with hydrazine, toluidine, and peroxide functional groups [13]. In one embodiment of the concept, a polystyrene maleic acid copolymer was reacted with phenylhydrazine to produce a polymeric adduct capable of accelerating the cure of a model anaerobic adhesive (Fig. 5.28).

Ionic liquids such as *N*-butylpyridinium saccharinate (Fig. 5.29) and *N*-butylpyridinium acesulfamate (Fig. 5.30) have been prepared and shown to work as accelerators in model anaerobic adhesives. These materials were demonstrated to have low cytotoxicity and antimicrobial activity [14].

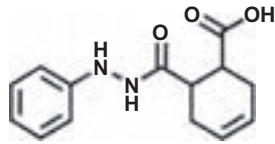


Fig. 5.26 Tetrahydrophthalic phenyl hydrazine.

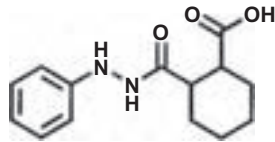


Fig. 5.27 Hexahydrophthalic phenyl hydrazine.

Fig. 5.28 Polystyrene maleic acid copolymer with phenylhydrazine.

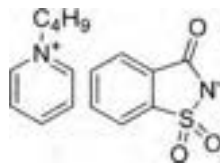
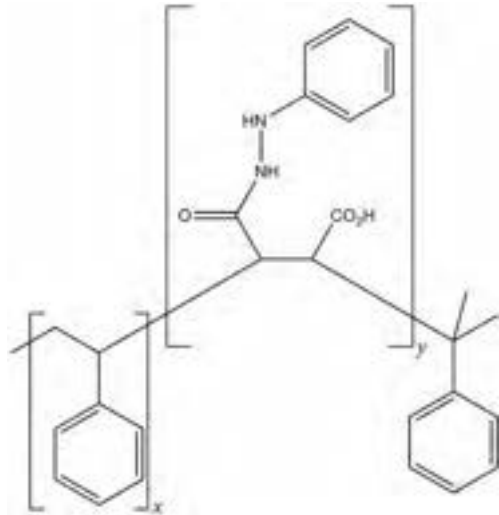


Fig. 5.29 *N*-butyl pyridinium saccharinate.

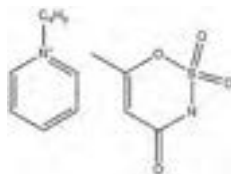


Fig. 5.30 *N*-butyl pyridinium acesulfamate.

5.2.2 Research to improve the sustainability credentials of anaerobic products

5.2.2.1 Overview

A key trend for anaerobic adhesives and adhesives in general is the drive to improve their sustainability credentials. A particular focus is to employ materials with improved health and safety labeling in an environment of ever more stringent regulations and to develop anaerobic adhesives with a lower carbon footprint and a reduced environmental impact.

The sustainability characteristics of standard anaerobic adhesives are already reasonably good as they have low volatile organic carbon content (VOC), are nonflammable, cure at room temperature and facilitate lightweighting of vehicle designs. Anaerobic adhesives also help to extend the lifetime of machinery and are frequently used to repair, maintain, and overhaul equipment. Medium-strength threadlockers are designed to facilitate the easy disassembly of fasteners and thereby aid the repair and recycling of machine parts.

Generally, the health and safety (H&S) labeling of anaerobic adhesives is low with typically just an irritant pictogram, but there is room for improvement. Curatives such as APH [13] and cumene hydroperoxide (Fig. 5.31), although used at low levels in anaerobic adhesives, have come under increased scrutiny; options to find alternatives have been investigated in recent years. These are considered under the section on new cure chemistry.

Another important sustainability topic for anaerobic adhesives and adhesives in general is the need to incorporate raw materials from nonfossil renewable sources to reduce the environmental impact caused by carbon dioxide and other greenhouse gas emissions. This has been an active area of research and the following sections provide a brief overview of recent activity.

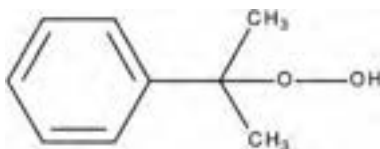


Fig. 5.31 Cumene hydroperoxide.

5.2.2.2 Monomers from renewable sources

Methyl methacrylate (MMA) (Fig. 5.32) can be reacted with bio-based alcohols to provide monomers with methacrylate functionality for use in adhesives [15].

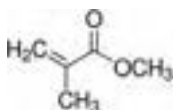


Fig. 5.32 Methyl methacrylate.

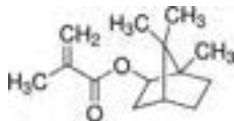


Fig. 5.33 Isobornyl methacrylate.

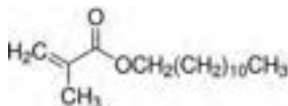


Fig. 5.34 Lauryl methacrylate.

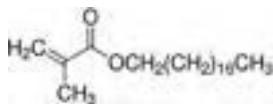


Fig. 5.35 Stearyl methacrylate.

Production of bio-based MMA is difficult, but bio-based alcohols are readily available. For example, *n*-butanol can be derived from the fermentation of sugarcane.

Certain commercially available monomers such as isobornyl methacrylate (Fig. 5.33), lauryl methacrylate (Fig. 5.34), and stearyl methacrylate (Fig. 5.35) already have a proportion of their carbon content coming from renewable sources. For example, Evonik has produced isobornyl methacrylate using camphene derived from pine tree resin.

Evonik markets biorenewable monomers as part of its VISIOMER Terra range [16]. Arkema also provides a range of biorenewable monomers as part of its Sarbio range.

There is scope to further increase the bio-based content of methacrylate monomers if the methacrylate functionality can also be made from bio-based sources. Significant progress has recently been made in this direction with the manufacture of methyl methacrylate in a one-pot synthesis from bio-based itaconic acid using a barium hexaluminate catalyst. The itaconic acid is derived from lignocellulosic biomass [17].

5.2.2.3 Oligomers from renewable sources

A number of researchers have established methods for the preparation of new monomers and oligomers with methacrylate functionality based on natural sugars such as isosorbide. Miske et al. described a method for the preparation of isosorbide dimethacrylates by transesterification of alkyl methacrylates [18]. Dworak et al. patented methods for the preparation of polyurethane isosorbide resins by reaction of isosorbide with various isocyanates followed by end-capping with methacrylate functional groups [19]. A typical reaction scheme is outlined in Fig. 5.36. These monomers and resin systems are capable of free radical polymerization with the potential to be used in adhesive systems such as anaerobic adhesives.

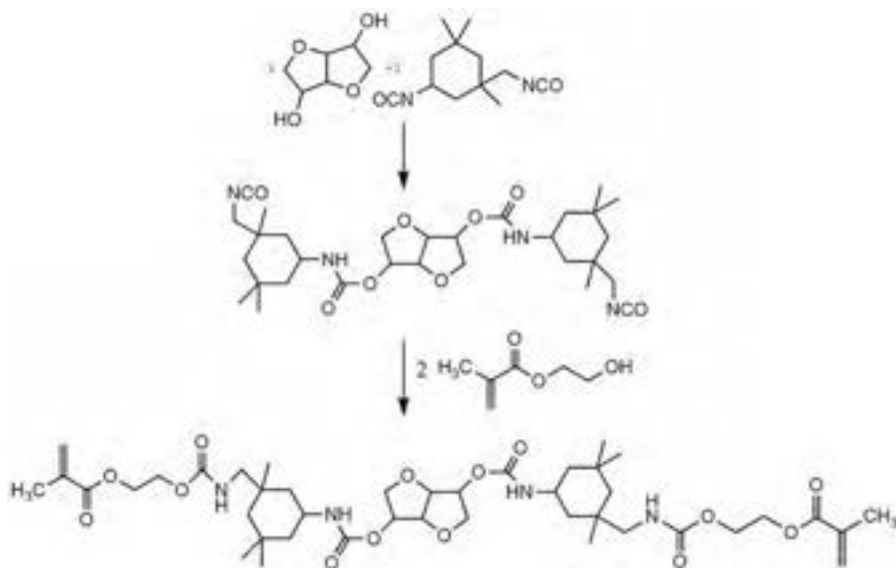


Fig. 5.36 Reaction scheme for synthesis of isosorbide urethane methacrylate oligomer.

The use of raw materials from bio-based sources also has the potential to deliver new advantages apart from CO₂ reduction. Plant-based materials can provide properties that were not previously possible due to their specific molecular architecture. Such materials with high molecular weights and high functionalities favor the formation of densely crosslinked networks and adhesion to a variety of substrates. Examples of interesting bio-based building blocks include vegetable oils, proteins, polysaccharides, and lignin [20].

Soybean oil is one of the most widely investigated platform chemicals to replace petroleum-based chemicals in the preparation of bio-based adhesives due to its abundant availability, sustainability, and relatively low cost. Messina et al. described a method for preparing a (meth)acrylate functionalized biorenewable oligomer that can be used as a component of an anaerobic adhesive [21]. Various oils including soybean oil or an alkyl ester of soybean oil were reacted with isocyanates (e.g., isophorone diisocyanate) in the presence of a catalyst and further reacted with a methacrylate monomer such as hydroxyethyl methacrylate to provide a biorenewable olefinous polyurethane polymer that can advantageously be employed in anaerobic adhesives. The cure performance of the bio-based anaerobic threadlocking adhesive so produced was compared to that of a control anaerobic product, based on a non-renewable plasticizer. The bio-based adhesives performed well and retained higher breakloose strength on oiled bolts (Table 5.2). The biorenewable content in the novel resins ranged from 30% to 70%.

Kabiri et al. synthesized star-shaped glycerol-lactic acid oligomers that can be used in anaerobic adhesives at a high level of 70%–95% [22]. The properties of the bio-based adhesives were found to match those of their petroleum-based counterparts.

Table 5.2 Strength retention of anaerobic adhesives on oiled surfaces.

		Degreased steel bolts and nuts		Lab. oil 72D on steel bolts and nuts		Elf evolution SXR (5W30) oil on steel bolts and nuts	
		Torque (in-lbs.)		Torque (in-lbs.)		Torque (in-lbs.)	
		Breakloose	Prevail	Breakloose	Prevail	Breakloose	Prevail
Loctite 242	1 h cure	98	18			58	3
Loctite 2400 NA		85	5	39	4	59	6
Loctite 2400 NA	No plasticizer	134	45	68	9	48	33
Loctite 2400 NA	With SoyGold 1000 biorenewable plasticizer	116	58	86	10	87	14
Loctite 242	24 h cure	148	38			88	23
Loctite 2400 NA		156	27	80	3	88	17
Loctite 2400 NA	No plasticizer	173	85	72	36	63	38
Loctite 2400 NA	With SoyGold 1000 biorenewable plasticizer	178	58	116	15	134	42

The structure of these bio-based star-shaped oligomers can be varied to control rheological and mechanical properties.

5.2.2.4 *Plasticizers from biorenewable sources*

Plasticizers are often used in anaerobic adhesive formulations for strength moderation. Many companies offer plasticizers with high biorenewable content. For example, Hallstar offers a range of renewable esters under the brand name HallGreen. Messana et al. describes a number of biorenewable plasticizers based on soybean oil and canola oil [21]. Examples of methyl esters based on soybean oil are SoyGold 1000, CanolaGold 1000, and SoyClear 1500, which are available commercially from Ag Environmental Products. Piedmont Chemical Industries produces Pomoflex 6156, which the manufacturer describes as a polyester polyol having a molecular weight of about 2000.

5.2.3 *Anaerobic products with higher temperature performance*

Anaerobic adhesives exhibit good resistance to thermal degradation due to the nature of the methacrylate monomers used and their ability to crosslink. A typical service temperature for an anaerobic adhesive is -50°C to 150°C . However, there are applications that require higher temperature resistance, and much research has focused on incorporating materials that can increase the service temperature beyond 200°C and in some cases even as high as 450°C .

Attarwala et al. incorporated materials such as bismaleimides, isocyanurates, and organosiloxanes with methacrylate functionality into anaerobic adhesives to improve thermal performance [23]. Aronovich provides an overview of many different types of material investigated with the objective of improving the thermal resistance of anaerobic adhesives [24]. Examples include polyimide compounds, various copolymers of *N*-maleimide, oligosiloxane methacrylates, borosiloxane oligomers, cyanate esters, and benzoxazines. In general, the strategy is to provide materials with functional groups that crosslink at higher temperature.

It is difficult to determine the practical service temperatures of the various high-temperature anaerobic adhesives described in the literature as it is somewhat dependent upon the specifics of the application and the methods used to determine strength retention. However, it is apparent that some technologies based on oligosiloxane methacrylates and borosiloxane oligomers could conceivably be used at temperatures as high as 450°C in threadlocking and thread sealing applications.

5.3 Summary

Anaerobic adhesives are widely used to bond and seal metal joints in a wide variety of engineering applications such as threadlocking, thread sealing, retaining, and flange sealing. These adhesives are easy to use, one-part systems that cure at room temperature.

The sustainability credentials of anaerobic adhesives are excellent as heat is not required to cure them. Anaerobic adhesives help to extend machinery lifetime, facilitate repair of equipment, and provide designers with options for lightweight machinery parts. In addition, anaerobic medium-strength threadlockers are designed for easy disassembly with hand tools and thereby facilitate the recycling of machine parts.

Recent developments in anaerobic adhesive technology have focused on enhancing performance and thereby expanding the range of applications where this adhesive technology can be used. For example, new cure systems have been developed to enable anaerobic adhesives to cure on highly inactive surfaces such as 316 stainless steel and new anticorrosion fastener coatings, with improved health and safety, such as Geomet and Dacromet. There has also been much research to increase the temperature resistance of anaerobic adhesives to meet new requirements in engine design and pipe sealing.

Notwithstanding the excellent sustainability credentials of anaerobic adhesives, there is room for further improvement. Considerable research has been conducted in recent years to improve the health and safety of anaerobic adhesives and reduce their CO₂ footprint. It is now possible to design high-performance anaerobic adhesives with a low CO₂ footprint that are made almost entirely from raw materials emanating from renewable sources. As anaerobic adhesives work best in bondlines with small gaps, a little goes a long way. The versatility and high performance of anaerobic adhesives coupled with their sustainability credentials will surely see new opportunities emerge in the future for this adhesive technology.

Acknowledgments

Thanks to my colleagues at Henkel who have contributed much over the years to the development of anaerobic adhesive technology.

References

- [1] Loctite Threadlocker Handbook, 2022. In press.
- [2] D. Birkett, D. Condron, Anaerobic adhesives, in: A. Pizzi, K.L. Mitta (Eds.), *Handbook of Adhesive Technology*, third ed., CRC Press, Boca Raton, Florida, 2017, pp. 367–382.
- [3] V. Kriebel, Accelerated Anaerobic Curing Compositions, US Patent 3,046,262, Assigned to American Sealants Co, 1962.
- [4] Y. Okamoto, Anaerobic adhesive cure mechanism, *J. Adhes.* 32 (1990) 227–235.
- [5] S. Wellmann, H. Brockmann, New aspects of the curing mechanism of anaerobic adhesives, *Int. J. Adhes. Adhes.* 14 (1994) 47–55.
- [6] D. Raftery, *Some Electroanalytical Investigations into the Cure Chemistry of Industrial Sealants* (PhD Thesis), Dublin City Univ, 1996.
- [7] D. Raftery, M. Smyth, R. Leonard, D. Heatley, Effect of copper(II) and iron(III) ions on reactions undergone by the accelerator 1-acetyl-2-phenylhydrazine commonly used in anaerobic adhesives, *Int. J. Adhes. Adhes.* 17 (1997) 151–153.
- [8] D.A. Aronovich, Achievements in the field of initiating systems of curing of anaerobic adhesives, *Polym. Sci., Ser. D* 14 (2021) 143–155.
- [9] G.S. Haviland, *Machinery Adhesives for Locking, Retaining, and Sealing*, first ed., Marcel Dekker, New York, 1986, pp. 220–272.

- [10] D. Birkett, M. Wyer, A. Messana, P. Klemarczyk, A.F. Jacobine, Cure Accelerators for Anaerobic Curable Compositions, US Patent 20120157641A1, Assigned to Henkel Corporation, 2012.
- [11] P.T. Klemarczyk, J. Liu, O. Hajatpour, D.P. Birkett, Cure Accelerators for Anaerobic Curable Compositions, US Patent 9969690B2, Assigned to Henkel Corporation, 2018.
- [12] P.T. Klemarczyk, D.P. Birkett, Phenylhydrazine/Anhydride Adducts and Anaerobic Curable Compositions using Same, WO Patent 2016064543A1, Assigned to Henkel IP & Holding GmbH, 2016.
- [13] A.D. Messana, A.F. Jacobine, Adducts Useful as Cure Components for Anaerobic Curable Compositions, US Patent 8598279B2, Assigned to Henkel IP & Holding GmbH, 2013.
- [14] A. Porter, Green Chemistry in the Design of Safer Anaerobic Adhesives (PhD Thesis), Dublin City Univ, 2015. <http://doras.dcu.ie/20829/>.
- [15] N. Sweeney, Anaerobic adhesives, in: A. Pizzi, K.L. Mitta (Eds.), Handbook of Adhesive Technology, third ed., CRC Press, Boca Raton, Florida, 2017, pp. 395–402.
- [16] Evonik: New Product Family Visiomer Terra, 2014. <http://Methyl-methacrylate-monomers.evonik.com/en/Evonik-new-product-family-visioner-terra-102845.html>.
- [17] A. Bohre, K. Avasthi, U. Novak, B. Likozar, Single-step production of bio-based methyl methacrylate from biomass-derived organic acids using solid catalyst material for cascade decarboxylation-esterification reactions, ACS Sustainable Chem. Eng. 9 (2021) 2902–2911.
- [18] A. Misske, F. Fleischhaker, C. Fleckenstein, M. Kaller, R. Nair, U. Stengel, M. Blanchot, Method for Producing Isosorbide Dimethacrylate, WO Patent 2016135191A1, Assigned to BASF Se, 2016.
- [19] D.P. Dworak, D. Gustafson, D. Mullen, A.D. Messana, A. Hynes, D. Ledwith, R. O’Kane, Methacrylate-Functionized Extended Isosorbide, US Patent 20180022848A1, Assigned to Henkel IP & Holding GmbH, 2018.
- [20] L.A. Heinrich, Future opportunities for bio-based adhesives – advantages beyond renewability, Green Chem. 21 (2019) 1866–1888.
- [21] A.D. Messana, D.P. Dworak, A. Messana, A.F. Jacobine, D. Gustafson, Anaerobic Curable Compositions, US Patent 9587151B2, Assigned to Henkel AG & Co KGaA, 2017.
- [22] N. Moini, M. Khaghanipour, K. Kabiri, A. Salimi, M.J. Zohuriaan-Mehr, A. Jahandideh, Engineered Green Adhesives based on demands: star-shaped glycerol-lactic acid oligomers in anaerobic adhesives, ACS Sustainable Chem. Eng. 7 (19) (2019) 16247–16256.
- [23] S. Attarwala, G.M. Mazzella, H.K. Chu, D.D. Luong, L.D. Bennington, M.M. Konarski, E. Maandi, R.D. Rich, N.R. Li, F.F. Newberth III, S.L. Levandoski, High Temperature, Controlled Strength Anaerobic Compositions Curable Under Ambient Environmental Conditions, 2002. US Patent 6391993B1. Assigned to Henkel IP and Holding GmbH, L’Air Liquide SA pour l’Etude et l’Exploitation des Procèdes George Claude.
- [24] D.A. Aronovich, Achievements in improving thermal properties of anaerobic adhesives. Review, Polym. Sci., Ser. D 14 (1) (2021) 52–68.

This page intentionally left blank

Advances in structural silicone adhesives

6

F. de Buyt^a, V. Hayez^a, B. Harkness^b, J. Kimberlain^b, and N. Shephard^b

^aDow Chemical, Seneffe, Belgium, ^bDow USA, Midland, MI, United States

6.1 Introduction

A **structural adhesive** is an adhesive that “hardens” or cures into a material capable of holding two or more substrates together, transmitting the load-bearing forces involved for the lifetime of the product. It is often termed a “load-bearing” adhesive. The product may undergo shock, vibration, chemical exposure, temperature deviations, or many other types of potentially weakening or destructive agents, and still be bonded. The substrates may be the same, or quite different, including metals, plastics, glass, rubbers, ceramics, or composites. The parts may be under constant load or intermittent loads and shocks. Silicone structural adhesives can be further classified as typically liquid-applied, curable, elastomeric materials. They behave like a liquid during their application, which is important to achieve good wetting of the substrate surfaces, and cure to form a high molecular weight, crosslinked, solid elastomer. By nature, silicones have lower cohesive strength than other structural adhesives such as epoxies; however, this property is an advantage in several applications. The lower strength and modulus mean that silicones are excellent for repair and rework applications and are ideally suited for applications that require a certain level of flexibility in the adhesive joint. The latter need typically arises when the adhesive joint must be capable of absorbing a certain amount of movement, such as resulting from differences in thermal expansion between the substrates, vibration of the components, exterior loads, and so on. Silicone structural adhesives provide excellent adhesion to a wide range of substrates, are capable of operating over a wide range of service temperatures, and have long service lives even in harsh environments. Furthermore, they can be formulated for either high or low electric and thermal conductivities. Because of these unique properties, they are used in a wide range of electric, electronic, automotive, domestic appliance, and construction applications.

6.2 Properties of silicone structural adhesives

Silicones occupy the regime between inorganic silicates and organic polymers and exhibit some of the properties of their extremes owing to the combination of the partially ionic siloxane (Si—O—Si) bond and the organic substituent groups. Because of these unique features of their polymeric backbone, silicone adhesives and sealants possess:

- Low toxicity.
- Good adhesion to a wide variety of substrates.
- Excellent elastomeric properties (high movement capability, high elastic recovery (85%–98%), low creep, good fatigue resistance).
- Environmental resistance to ultraviolet (UV) radiation, moisture, heat, ozone.
- High temperature resistance (up to 300°C).
- Flexibility, including cold temperature flexibility (down to –90°C or –115°C for one- and two-part formulations, respectively).
- Electrical properties ranging from high resistivity to high conductivity.
- Fire-resistant properties.
- High gas permeability.
- Chemical resistance.
- High optical clarity (adhesive can be formulated from opaque to optically clear).

These properties are discussed in greater detail below. Owing to their low modulus of elasticity (typically below 10 MPa), silicone adhesives have gained popularity in structural and semistructural applications requiring flexible bonding, resistance to environmental extremes, and high durability of the adhesive bond. Most silicone adhesives have a very low level of toxicity; this explains the use of certain silicone adhesive grades in biomedical applications, including class II and class III medical devices, as defined by the European Economic Community Medical Device Directive [1]. Special formulations are also available for applications involving food contact. A more detailed review can be found in [Chapter 27](#).

Cured silicone adhesives display extraordinary environmental resistance [2]. The lack of chromophores (light-absorbing groups) along the polymeric backbone and the high Si—O bond energy provide inherent resistance to sunlight. With proper selection of the organo substituents in the siloxane polymer (e.g., fluoro-organo, phenyl, etc.), silicone adhesives can meet the most demanding chemical resistance requirements, even in high-temperature applications. Silicone adhesives display good resistance to oxidation by ozone and oxygen. The oxidation of the hydrocarbon side groups results in the formation of carbonyl groups [3–6]. Because carbonyl groups do not interact strongly with other chemical groups in silicone polymers, the oxidation has little effect on the mechanical properties of the adhesive. Silicone adhesives display extreme low-temperature flexibility as standard formulations remain flexible down to –60°C, special one-part (condensation cure) formulations down to –90°C, and special two-part formulations down to –115°C. Cured silicone adhesives display excellent high-temperature stability. Certain products can be used in applications involving continuous exposure to 260–300°C or intermittent exposure up to 340–350°C. The excellent environmental resistance of silicones is consistent with the fact that, even after prolonged service periods in extreme climates, silicone adhesives show comparatively minor changes in physical properties [7].

Cured silicone adhesives display good elastomeric properties, such as $\pm 50\%$ joint movement capability, high elastic recovery (85%–98%), and low creep. These properties are also much less temperature dependent than those of other common organic adhesives. Their good fatigue resistance allows them to withstand repetitive movement in the adhesive joint caused by flexible flanges, equipment or component

vibration, and temperature cycling of joints with high differential thermal expansion of substrates. Their large gap-filling capability often allows the relaxation of surface flatness requirements and provides for ease of alignment and assembly. Because the rheology of silicone adhesives can be varied over a wide range and tailored to the specific requirements of the application, their application process can be easily automated.

In general, silicone adhesives are good insulators and are characterized by high dielectric strength, high volume resistivity, low dielectric constant, and a low dissipation factor. The low dissipation factor is a desirable property because it minimizes the waste of electrical energy as heat. However, by formulating with conductive fillers, flexible conductive adhesives can be achieved for charge dissipation and even solder replacement.

Cured silicones display favorable fire performance characteristics, for example a low heat release rate and an insensitivity of burn rate to fire severity. The key combustion products exhibit minimal toxicity to humans. Indeed, pyrolysis of silicones results in the formation of carbon dioxide, water, amorphous silica, and low yields of carbon monoxide. The combustion products demonstrate minimal potential for corrosive damage. A substantial portion of the amorphous silica generated during the combustion process is deposited on the fuel-generating, burning surface, resulting in the formation of a silica char. These surface silica deposits are believed to contribute to the unique burning characteristics of silicones.

6.3 Product forms and cure chemistry

Products are available in a variety of forms, from paste-like nonslump materials to flowable self-leveling adhesives and hot melt curable adhesives. Both single and multicomponent versions are available. Silicone adhesives can be formulated based on the different chemistry of the cure. Silicones can be formulated to cure at room temperature by reaction with moisture, room-temperature vulcanizing (RTV), or by addition cure reactions at room temperature or accelerated with heat. Radiation-cured silicones are also available. Combinations of multiple cure chemistries are more often used to provide fast cure, good shelf life, and robust adhesion.

6.3.1 Condensation cure chemistry (RTV)

6.3.1.1 Hydrolysis reactions

One-part condensation cure silicone adhesives are based on siloxane polymers with hydrolysable groups attached to the polymer chain ends combined with a hydrolysable silane crosslinker, which also acts as a water scavenger to maintain the shelf-stability of the unopened container. Once the one-part package is opened, atmospheric moisture reacts with the hydrolysable groups, resulting in the formation of silanol (Si—OH) groups. The terminal silanol groups formed initiate condensation reactions under acidic or mild basic conditions.



where OR is a hydrolysable organofunctional group. The OR groups are either available from a prefunctionalized polymer or as a result of the reaction between a silanol-terminated polymer and a multifunctional organosilane crosslinking agent. The latter occurs during the sealant manufacturing process, wherein the crosslinking agent is typically used in excess or other organosilanes may be incorporated to function as adhesion promoters and/or moisture scavengers, with the following stoichiometry.



Eq. (6.2) is also relevant for other silanol-functional fluids used as processing aids. Finally, the moisture content in the fillers and the OR content from the catalyst have to be considered according to the stoichiometry of Eq. (6.1). The original OR concentration is reduced from the moment the sealant is formulated during its manufacturing process and throughout its shelf life due to reactions with any silanol-functional components and moisture in the fillers or diffusing into the package.

Thus, one-part cure systems depend on atmospheric moisture to complete cure and cure proceeds from the outside into the interior of the material. The cure byproducts, HOR, which diffuse out of the RTV silicone and may cause a characteristic smell during cure, include alcohols [8–10], ketoximes [11], carboxylic acids [12–17], amides [18,19], hydroxylamines [20–23], ketones [24,25], and amines [26–28]. Alkoxy-, oximo-, and enoxysilane crosslinkers eliminate byproducts displaying a pH-neutral chemical reaction, that is, they are neither acidic nor basic and therefore are the key component of neutral, noncorrosive cure chemistry. The acetoxysilane-based cure system releases acetic acid. It is important to keep the acid curing materials away from cementitious and alkaline substrates to minimize acid-base reactions resulting in poor bonding. In many cases, the cure byproducts are sufficiently acidic or basic to act as condensation catalysts; these are referred to as self-catalytic cure systems. While these systems provide good depth of cure, an additional condensation catalyst generally is required to achieve a tack-free surface. This condensation catalyst may be a tin compound such as stannous octoate and dibutyltin dilaurate [29] or an organotitanate [10]. Titanates are employed primarily in neutral cure (alkoxy, amide) systems while tin catalysts are added to acetoxy-, oxime-, and amine-cure formulations. There is also the option of formulating alkoxy-cure systems with tin catalysts; however, to achieve good shelf stability, the system must be kept free of water and silanol [29–32].

6.3.1.2 *Physics of RTV cure*

While the properties of these condensation-curing sealant and adhesive materials have been well established and reviewed in the first edition of this work, the fundamental understanding of the physics of crosslinking (or curing) of one-part RTV (1-RTV) adhesives or sealants has greatly advanced over the last 20 years [33]. The growing demand to increase manufacturing productivity by using adhesive and sealant products, which allow assemblies to move faster through different production stages,

necessitates better understanding of cure physics under different processing and application conditions. The ability to do this will depend, in part, on the mechanical strength that the adhesive/sealant contributes to the integrity of the assembly. For one-part, moisture-reactive systems, this mechanical strength can be expected to reach an equilibrium value as the adhesive/sealant cures over time in the presence of atmospheric moisture, the rate of which will depend on chemical and physical factors as well as on the design of the assembly. A general rule of thumb reported in the prior edition of this book states that 1-RTV silicones typically cure at a rate of 3–4 mm per day.

Since 1998, Comyn et al. have advanced this rudimentary understanding to encompass Fickian diffusion kinetics, relative humidity, temperature, and joint shape [34–36]. A four-parameter permeation model that described the thickening of a cured layer in moisture-reactive silicones and polyurethane sealants was proposed. According to Comyn, the following assumptions can be made,

- (1) The crosslinking reaction is much faster than the rate of moisture diffusion as supported by observations that the sealants rapidly form a cured skin upon extrusion and exposure to humid air.
- (2) A cured layer will act as a barrier for the permeation of water molecules to the uncured sealant, but any water permeating through this barrier reacts quickly with the uncured sealant to increase the thickness of the cured layer, z (cm).
- (3) The equivalent material volume, V ($\text{m}^3 \text{mol}^{-1}$), reacting with 1 mol of water remains constant, that is, the water reactive species remains relatively stationary in the silicone matrix.

The depth z (cm) of unidirectional cure with time t (h) was derived to be a function of the vapor pressure p (cm Hg) of water in the atmosphere in the proximity of the material's surface, and two material properties: the permeability, P ($\text{mol s}^{-1} \text{m}^{-1} \text{Pa}^{-1}$), of moisture through the cured layer and the equivalent material volume, V ($\text{m}^3 \text{mol}^{-1}$), reacting with 1 mol of water.

Following the schematic below in Fig. 6.1, Comyn proposed the model described by Eq. (6.3) to determine the rate at which the number of moles of water n permeates a unit cross-section of a cured layer z of sealant with a permeability coefficient P based on the vapor pressure p of water in the atmosphere. For a unit (constant) cross-sectional area, the volume of sealant V that is cured can be described by

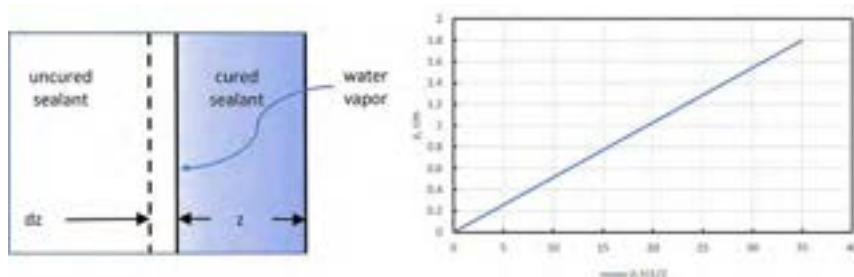


Fig. 6.1 Comyn's generalized model of diffusion-controlled cure on the left, with resulting cure in depth on the right.

Eq. (6.4). After substituting Eq. (6.4) into Eq. (6.3) in terms of dn , the resulting integration yields Eq. (6.5) with the initial condition that $z=0$ when $t=0$.

$$dn/dt = P p/z \quad (6.3)$$

$$V = dz/dn \quad (6.4)$$

$$z = (2V P p t)^{1/2} \quad (6.5)$$

Hence, the thickness of the cured layer should increase with $t^{1/2}$. That is, a plot of z vs $t^{1/2}$ should yield a straight line where, for a particular RTV material, the magnitude of its slope is a function of the temperature and relative humidity during cure. This was shown for organic hot-melt adhesives and silicone sealants; validation of the moisture-cure model was demonstrated using gravimetrically based measurements to determine V and P separately. However, deviation from a linear moisture-cure model was reported in more recent studies using an alkoxy silicone sealant in geometries requiring deep-section cure and therefore, longer cure times [37,38]. The effect of such deviation from a simple moisture-cure model on adhesion strength and mode of failure at the sealant/substrate (glass, aluminum) interface was also established. Results obtained on the mobility of water and alcohol molecules and the diffusion of adhesion promoter and crosslinking species in the 1-RTV Dow Corning 1358 clear silica filled alkoxy-functional dimethylsiloxane sealant were published [39,40]. These latter studies revealed the following additional information:

- (1) Weight loss during the cure process was initially controlled by the diffusion of methanol, which is not surprising because methoxy groups represented 76.5 mol% of the total amount of hydrolysable alkoxy groups in the sealant and methanol was the smallest molecule (largest diffusion coefficient, D) of the alcohols released during cure [40].
- (2) While the thickness of the cured layer z was proportional to the square root of time $t^{1/2}$ at a given temperature and relative humidity, the gradient of this plot $(2VPp)^{1/2}$ increased after a certain period. This characteristic time increased as the total sealant thickness, l (cm), increased but decreased with increasing temperature as reproduced in Fig. 6.2 (left plot) for $l=1.7$ cm. The result was two regions of cure with the outer, shallower region having a higher crosslink density ascribed to the migration of low molar mass crosslinking and coupling (adhesion promoters) agents toward the outer region—in the opposite direction of water permeation during the initial stage of the cure process. Therefore, the initial cure rate was influenced by the reaction of these migrating species with water, thus initially reducing the hydrolysis reaction rate of the silicone polymer. As the cured layer thickened over time, there would be a depleted concentration (or complete lack) of these species in the uncured portion of the sealant that would not interfere with the crosslinking process of the siloxane polymer. The change in cure rate was attributed to the migration of low molar mass crosslinkers and adhesion promoters toward the cure front and the eventual depletion of these species, which compete with the silicone polymer to react with the diffusing water. A method devised to measure the diffusion of two crosslinking agents revealed that while the coefficient of diffusion, D , was constant for the tetra-*t*-butyl titanate crosslinking catalyst, the diffusion of the isobutyltrimethoxysilane crosslinking agent decreased with time, possibly due to interaction with hydroxyl groups on the fumed silica filler [41].

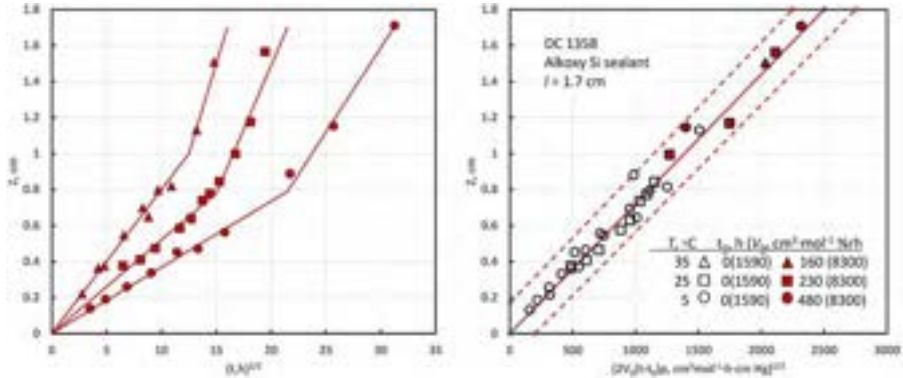


Fig. 6.2 Cure depth, z , versus square root of cure time, $t^{1/2}$ (left plot), and versus square root of volume, time, and water vapor pressure for Dow Corning 1358 alkoxy sealant as a function of temperature and relative humidity for a total sealant thickness $l = 1.7$ cm [38,39]. The regression (solid lines) and 95% confidence intervals (dotted lines) were based on data from the first cure stage corresponding to $t_0 = 0$ and $V_0 = 1590 \text{ cm}^3 \text{ mol}^{-1}$.

The study confirmed that at a given temperature, increasing the relative humidity increased the cure rate. According to Eq. (6.5), the slope of each line plotted in Fig. 6.1 should correspond to $(2VPp)^{1/2}$. To validate the permeation model, gravimetric experiments were conducted to estimate V and P . The water vapor permeability P was found, within experimental error, to be independent of relative humidity in agreement with reports for unfilled and filled silicone rubbers [41,42]. It was also noted that the final state of cure was independent of the relative humidity, except for the rate at which a complete vulcanization occurred within these 1-RTV sealants.

V could be estimated by noting 1 mol of water reacts with 2 mol of the hydrolysable group, -OR, according to Eq. (6.1). Based on 1 g silicone sealant of density ρ (g cm^{-3}), V can be calculated.

$$V = \frac{\frac{1 \text{ g}}{\text{mol(OR - OH)}} \cdot \frac{2 \text{ mol(OR - OH)}}{\text{molH}_2\text{O}}}{\rho, \text{ g cm}^{-3}} \tag{6.6}$$

For comparison to experimentally measured data of $1400 \text{ cm}^3 \text{ mol}^{-1}$ [39], the calculated V according to the above equation was $1590 \text{ cm}^3 \text{ mol}^{-1}$ for Dow Corning 1358 alkoxy (with a density of 1.02 g cm^{-3}).

The water permeability coefficient P is the fourth and last parameter in the Comyn permeation model. The permeation of water vapor through the cured layer of sealant can be described in terms of a solution-diffusion mechanism [43]. The permeability coefficient P is a product of the diffusion coefficient D and a function S related to the solubility of the water vapor in the cured layer.

$$P \equiv D \cdot S \tag{6.7}$$

However, it was measured that a significant reduction in moisture permeability occurred if the sealant thickness exceeded 1 cm. A plausible interpretation of this trend is that clustering of absorbed water molecules occurs. These water clusters are much less mobile and, therefore, have a negligible contribution to diffusion [44]. For sealant and adhesives based on poly(dimethylsiloxane) (PDMS) polymer, clustering is the most likely mechanism occurring because molecular interaction between water and the PDMS polymer is perceived to be weaker than that between water molecules.

In summary, the depth of cure starting from the outer surface of an RTV condensation curing sealant can be modeled as the square root of the product of four parameters (Eq. 6.8): water permeability coefficient P of the cured layer, the volume of material reacting with 1 mol of water V , the vapor pressure of the atmospheric moisture p , and cure time t .

$$z = [2V_0 Pp(t - t_0)]^{1/2} \quad (6.8)$$

V is a strong function of the concentration of silane used as a crosslinking, adhesion-promoting, or moisture-scavenging agent but interfered with the crosslinking process of the siloxane polymer. The permeation model is proposed to account for a two-stage curing process that occurs from the depletion of the silane in the sealant as it migrates toward the cure front, which increases V . V_0 is a function of the characteristic time t_0 . For the initial cure stage, $V_0 = V(t_0 = 0)$. From data obtained in Fig. 6.2 (left plot), and calculated volumes V_0 of $1590 \text{ cm}^3 \text{ mol}^{-1}$ and $8300 \text{ cm}^3 \text{ mol}^{-1}$, respectively, for the two-stage curing process, the right end-side plot of Fig. 6.2 was obtained by plotting z as a function of $(tp)^{1/2}$. Therefore, datasets for each material collected at different conditions of temperature and relative humidity merged into a single straight line with a very high coefficient of determination. For end users of 1-RTV silicone sealants and adhesives, this latter approach provides a material-specific reference line that demonstrates the correspondence between time and vapor pressure. For instance, a certain cure in depth can be reached at short cure times with a high relative humidity or at long times with a low relative humidity. The cure kinetics of 1-RTV condensation curing sealant can be fully characterized from cure in-depth measurements at one set of temperature and relative humidity conditions.

Formulators can refine the cure green strength of a formulation by adjusting the moles of water per unit volume needed to achieve crosslinking. For end users of 1-RTV silicone sealants and adhesives, this latter approach provides a material-specific reference line that can be used to control cure kinetics by manipulating vapor pressure as a function of temperature and relative humidity conditions, that is, a certain cure depth can be reached at short cure times with a high relative humidity or at long times with a low relative humidity. The extent and location of crosslinked rubber as a function of cure time can be modeled for various joint shapes to provide an estimate of green strength.

In two-part condensation cure systems, the silane crosslinker and catalyst are packaged together as one reactive component, with the mixture of polymer and filler as the unreactive component. The two components must be mixed shortly before

application. Once mixed, the crosslinking reaction proceeds without the need for external, atmospheric moisture. To achieve successful completion of cure and good heat stability of the cured material, it is important to ensure that the cure byproducts completely leave the curing adhesive. The key benefit of two-part condensation cure systems is their ability to achieve deep-section cure and high green strength within a few hours. For full development of physical properties, several days may be required to completely eliminate cure byproducts from the bulk.

As in one-part systems, the condensation cure involves a functional silicone chain end, typically silanol, and a polyfunctional silane. Suitable crosslinkers are tri-, tetra-, or multifunctional materials, such as alkyl orthosilicate esters, and esters of ortho- or metasilicic acid (polyalkylsilicates) [45,46]. *N*-Propyl orthosilicate and tetraethyl orthosilicate are the most commonly used crosslinkers in two-part systems. Generally, the same condensation cure catalysts that apply to one-part systems are also employed in two-part systems.

Hot-melt silicone adhesives are solventless thermoplastic compositions that are applied at elevated temperatures above the melting or softening point of the composition. This allows the heated hot melt to be transferred and applied in a flowable viscous liquid state. Upon cooling, the hot melt returns to a semisolid state. The compositions of hot-melt silicone adhesives are quite similar to those of pressure-sensitive adhesives. Silicone hot melts are based on high levels (commonly 60% and above) of a silicate resin and appropriate amounts of reactive and nonreactive silicone polymers to provide viscous, semisolid systems at room temperature. A refinement of this technology is the incorporation of reactive end groups on the polymer chains that postcure over time via regular RTV chemistry to a temperature-insensitive, crosslinked state that has enhanced performance characteristics [47–53]. Reactive hot melts combine the advantages of conventional liquid reactive adhesives, such as resistance to high temperature creep and solvents, with typical hot-melt attributes such as zero volatile content, easy dispensing, and high green strength.

6.3.2 Addition cure chemistry

Condensation cure chemistry is less suitable for applications requiring very fast cure, cure in confinement, or used near reactive chemistry-sensitive components. Additional cure systems can provide a more suitable cure chemistry.

Crosslinking is accomplished in the RTV or low-temperature vulcanization (LTV) thermal addition cure system via a hydrosilation reaction whereby a Si—H group in a low molecular weight siloxane is added to a vinyl group in a siloxane polymer. The vinyl group may also be located on the siloxane oligomer and the silicon hydride group on the polymer. Generally, however, a Si—H polyfunctional siloxane oligomer plays the role of the crosslinker and the siloxane polymer is blocked at the vinyl end. This reaction occurs readily at room temperature in the presence of a platinum catalyst and can be accelerated by heat to obtain a crosslinked network with a well-defined topology and mechanical properties depending on the formulation components used [54,55]. The platinum catalyst can exist in a variety of forms; the more commonly used ones are chloroplatinic acid, H_2PtCl_6 , and its complexes with vinyl-functional

cyclic siloxanes such as tetramethyltetra vinyl-cyclotetrasiloxane [56] or linear siloxanes such as divinyltetramethyldisiloxane [57]. The platinum-siloxane complexes have better compatibility with the siloxane medium and achieve similar cure rates at a lower addition level.

The addition cure has several advantages when compared with the condensation cure system. First, it does not produce cure byproducts and therefore does not give rise to any odor or shrinkage upon cure; second, it achieves almost instant homogeneous deep-section cure at elevated temperature; and third, it is not prone to aging in high service temperature. The hydrothermal stability of crosslinked liquid silicone rubber (LSR) has been monitored for a prolonged period of 2 years immersion in water at 100°C [58]. The study has shown that the extent of hydrothermal degradation leading to hydrolysis and oxidation at a prolonged time was limited to only 100 μm of the outer surface layer. Underneath, the LSR remains intact and the properties identical to control unexposed specimens. The plausible reaction mechanisms involve attack on Si—O—Si bonds, methyl side group in the side chains (—Si—CH₃) within the repeating units of the LSR, and unreacted vinyl side groups (—Si—CH=CH₂). These degradation pathways could then lead to the formation of hydroxyl groups as an intermediate step and upon further degradation (i.e., oxidation) into carbonyl groups. These reactions would ultimately result in oxidation and breakdown of the LSR (i.e., hydrolysis). In terms of physical properties, the exposed LSR sample exhibits a significant reduction in volume as a consequence of leaching the low molecular weight species (oligomers) into the exposure medium (water). On the other hand, the micro surface hardness increases due to the chemical modification of the surface (i.e., changing to silica-rich surfaces) as well as the formation of degradation products (e.g., formation of oxygenated species including OH groups) on the outer surface (100 μm).

The main disadvantages of addition-curing silicone elastomers are their easy inhibition by a number of electron-donating substances, such as amines and organosulfur compounds, and the fact that they require special proprietary adhesion promoters to achieve good adhesion [59–66]. Without the incorporation of adhesion promoters, the crosslinked siloxane structure does not contain substantial amounts of reactive groups after completion of an addition cure. Moreover, the Si—H and Si—CH=CH₂ groups are not particularly reactive toward many chemical groups found on surfaces of common substrates. It is therefore expected that no coupling between the polymeric network and the substrate will take place during application and cure, unless special adhesion promoters are added to the formulation.

Because the hydrosilation reaction in the presence of a platinum catalyst occurs readily at room temperature, one-part addition-cure RTV systems are not feasible. Still, one-part products can be formulated that are shelf stable at room temperature, but for which the cure is triggered by a slight increase in temperature, for example up to 60°C to 80°C. In this LTV cure system, the platinum is sequestered by chelation with an inhibitor, usually a conjugated polar species. Sequestered cure systems generally have a rather short shelf life, typically only a few days. Another interesting approach is based on the microencapsulation of the platinum [67]. Cure is then

activated either by heating the composition above the melt temperature of the encapsulating shell or by the addition of a suitable solvent.

For two-component compositions, the platinum catalyst as well as the fillers and a part of the vinyl functional siloxane polymer represent one package (part A) while the silicon hydride material and the remaining part of the vinyl functional siloxane polymer represent the other package (part B). The two components are mixed together in the proper ratio at the point of application. Cure of these “uninhibited” formulations initiates immediately upon mixing. Therefore, to extend the pot life and simplify application, two-part addition cure formulations often contain a “cure inhibitor” or “cure retarder.” These are chemicals containing carbon-carbon triple bonds capable of complexing the platinum catalyst. Ethynylcyclohexanol [68], 3-methyl-3-hydroxy-1-butyne [69], $(\text{HCCCH}_2\text{O})_3\text{SiMe}$ [70], and dialkyl acetylenedicarboxylates [58,71,72] are some of the cure retarders referred to in the patent literature. As in the above-described one-part systems, cure is triggered by a slight increase in temperature.

More recent developments have considered the benefits of combining hard and soft polymeric materials such as a rigid thermoplastic polymer and an elastomeric silicone elastomer. For that purpose, strategies for improving the adhesion strength of a self-adhesive silicone rubber on thermoplastic substrates need to be envisaged, such as surface treatment [73], or an adhesion promoter based on either phenyl-acrylates [74] or condensation-curing organosilane mixed within the addition-curing silicone elastomer, which upon migration to the interface between the silicone rubber and the substrate will help develop strong adherence [75,76].

6.3.3 Electron-beam and photo-cure induced addition chemistry

Other addition cure systems that have emerged in recent years are the UV and electron beam (eb) radiation cure systems. UV curing is initiated by the excitation of a photoinitiator through the absorption of photons of UV radiation while eb curing involves ionization of adhesives with high-energy electrons. The development of these systems has been prompted by the ever-increasing need for fast cure rates and low cure temperatures. The UV cure system is more common than the eb-based system for general applications in silicone adhesives. Although both UV radiation and thermal curing offer rapid cure rates, there are several advantages gained from using UV radiation instead of heat for curing silicone systems. The main benefit is that a low cure temperature allows deposition and cure of the adhesive on heat-sensitive substrates such as polyolefins and other plastic materials. Also, UV curing requires minimal energy, thus eliminating major energy losses typically encountered in thermal cure systems. The UV cure system contains an epoxy or a vinyl ether functionalized polydimethylsiloxane (PDMS) polymer and a photocatalyst [77]. The latter, a diaryliodonium salt, is photolytically decomposed to form an active acid that polymerizes the epoxy or vinyl ether groups and crosslinks the network. UV-curable compositions based on thiolene cure systems provide rapid cure and less yellowing compared to the epoxy cure chemistry.

6.4 Silicone adhesive formulations

Formulations of silicone adhesives are based on the following ingredients:

- Reactive and/or nonreactive siloxane polymer.
- Reactive and/or nonreactive silicone resin.
- Plasticizer.
- Crosslinker.
- Catalyst.
- Adhesion promoter.
- Reinforcing, semireinforcing, and/or nonreinforcing (extending) fillers.
- Special additives.

The functionalities of the reactive components (polymer, crosslinker, adhesion promoter) and the nature of the catalyst depend on the cure chemistry of the formulation. For example, the reactive polymer may have functionalities of silanol, oximosiloxy, alkoxyloxy, alkoxyethylsilyloxy, vinyltrimethylsiloxy, or other reactive groups, depending on the cure chemistry utilized. Tables 6.1 and 6.2 provide an overview of the different formulation ingredients and their functions in condensation and addition cure systems, respectively [78].

6.4.1 Polymers

6.4.1.1 Silanol-terminated PDMS polymer

RTV condensation cure adhesives are formulated from α,ω -silanol-terminated siloxane polymers with a molecular weight of about 20,000–200,000 Da, corresponding to a viscosity of about 1 to 300 Pa s.

6.4.1.2 Vinyltrimethylsiloxy-terminated PDMS polymer

RTV/LTV addition cure systems are formulated from vinyl-terminated PDMS polymers with a molecular weight of about 63,000–140,000 Da, corresponding to a viscosity of about 10–100 Pa s.

6.4.2 Plasticizer (trimethylsiloxy-terminated PDMS polymer)

Owing to its excellent compatibility with the liquid siloxane polymer and the cured network, trimethylsiloxy-terminated PDMS polymer, often referred to as “silicone fluid,” is widely used as a plasticizer in silicone adhesives. The plasticizer can be selected to lower the viscosity and/or to lower the modulus of the formulation. Most commercial silicone fluids have viscosities of 0.1–60 Pa s. These plasticizers have the same durability characteristics as the PDMS network. An interesting group of silicone fluids is the so-called “reactive” plasticizers, in which a substantial fraction of the PDMS molecules are trimethylsiloxy-terminated at one end and silanol-terminated at the other end. These reactive fluids tie in to the network during cure, forming loose

Table 6.1 Formulation ingredients and their functions (condensation cure chemistry).

Component	Typical chemical	Function
Polymer	Hydroxyl $\sim\text{SiOH}$	Backbone required to form the elastomeric network
Plasticizer	Trimethylsiloxy-endblocked-PDMS	Adjustment of mechanical properties such as hardness, viscoelasticity, rheology
Reinforcing fillers (active)	Fumed silica (SiO_2); precipitated calcium carbonate (CaCO_3); carbon black	Thixotropic reinforcing agents (non slump), adjustment of mechanical properties (cohesion); provide toughness for the elastomer as opposed to brittle materials
Nonreinforcing fillers (passive)	Ground calcium carbonate (CaCO_3)	Reduce formulation cost; adjust rheology and mechanical properties
Crosslinkers	Acetoxy $\sim\text{Si}(\text{OOCCH}_3)_3$ Alkoxy $\sim\text{Si}(\text{OR})_3$ Oxime $\sim\text{Si}(\text{ON}=\text{CRR}')_3$ Amine $\sim\text{Si}(\text{NHR})_3$	Crosslinking of the polymeric component; provide network structure
Specific additives	Catalysts: organo-Sn, -Ti, -Pt, -Zn, -Rh Adhesion promoter: $\text{X}-\text{CH}_2\text{CH}_2\text{CH}_2-\text{Si}(\text{OR})_3$; water scavenger; pigments; rheology additive	Control of the rate of the curing process Enhance the adhesive bonding properties against substrates Prolonging shelf life Offering wide range of colors Adjust ease-of-use characteristics and features

polymer ends. By doing so, they plasticize the network internally. The benefit of these plasticizers is that they cannot migrate (bleed) from the cured formulation.

6.4.3 Crosslinkers

6.4.3.1 RTV condensation-cure

Silane $\text{R}_{4-n}\text{SiX}_n$ crosslinkers ($n = 3$) are used with one-part silicone cure systems. The reactivity of these crosslinkers is influenced by several factors, such as the number of hydrolyzable groups (X) attached per silicon atom, the number and type of organo-functional groups (R) attached to silicon, and the substituents (R') on the hydrolyzable group itself. A variety of these crosslinkers with different organic substituent R-groups and hydrolysable leaving X-groups are commercially available. For instance, acetoxy crosslinkers are available with methyl, ethyl, and vinyl R groups. Oxime crosslinkers can be purchased with methyl or vinyl R groups and methylethylketoxime (MEKO) or methyl-iso-butylketoxime (MiBKO) leaving groups, X. Blends of some

Table 6.2 Formulation ingredients and their functions (addition cure chemistry).

Component	Polymer/additive	Function
Polymer	Alkenyl functionalized PDMS	Backbone of silicone cured network
Crosslinker	Si—H functionalized polymer	Crosslink alkenyl PDMS
Catalyst	Platinum-based complex	Fast cure at room or high temperature
Inhibitor	Various organic or organosilicone types	Delays cure at room temperature and increases pot life
Inorganic or organic filler	Silica, carbon black	Reinforces mechanical strength
Pigment	Various metallic oxides	Color/thermal stability
Adhesion promoter	Various silanes and proprietary complex compounds	Enhance adhesion of silicone to specific substrates; prolonged durability

of these crosslinkers are also commercially available. Standard blends are methyltriacetoxysilane (MTA) and ethyltriacetoxysilane (ETA), methyltrioximosilane (MTO) and vinyltrioximosilane (VTO), MTO and tetraoximosilane (TOS), and MTO, VTO, and TOS. These blends have tailored reaction rates, allowing an optimum balance of surface cure versus deep-section cure. The crosslinker is added at about 3.5%–7.5% by weight based on the total formulation. However, since 2017, industrial hygiene recommendations based on REACH regulation limit the exposure to MEKO down to 0.15 ppm. MEKO is classified as a probable human carcinogen (Category 1B). It is therefore recommended to avoid any new oxime sealants on the market.

6.4.3.2 RTV/LTV addition cure

Both cyclic and linear silicon hydride crosslinkers are available. Linear trimethylsiloxy-endblocked poly[(hydrogenmethyl)(dimethyl)] siloxane crosslinkers are commercially available with viscosities between 0.005 and 0.1 Pa s and molar hydrogen content between 0.7% and 1.5% by weight. The amount of crosslinker added to the formulation is adjusted based on its molar hydrogen content.

6.4.4 Catalysts

6.4.4.1 Condensation-cure catalysts

Commercially the most important condensation cure catalysts are dialkyl tin (IV) carboxylates, for example, dibutyltin dilaurate, dibutyltin dioctoate, and dibutyltin diacetate (commercially available, for example, as “t-series catalysts” from Air Products and Chemicals, Allentown, Pennsylvania, United States); tin (II) compounds, for example tin dioctoate, and alkyl titanates, for example tetraisobutylorthotitanate,

tetra-*n*-propyl titanate, tetra-*n*-butyl titanate, tetra-*tert*-butyl titanate, titanium acetylacetonate, and acetoacetic ester titanate (commercially available, for example, as Tyzor catalysts from Dorf Ketal Specialty Catalyst). The amount of catalyst added is typically in the range of 0.05%–0.2% for tin soaps and 0.5%–2.0% for titanates by weight based on the total formulation.

6.4.4.2 Addition-cure catalysts

A suitable catalyst for the hydrosilation addition-cure reaction is a metal of the platinum group in the periodic table, or a compound of such a metal. Platinum and palladium compounds are generally preferred based on their high activity. Platinum compounds are commercially the most important based on cost considerations. The platinum catalyst can exist in a variety of forms; the more commonly used ones are chloroplatinic acid, H_2PtCl_6 , and its complexes with vinyl-functional cyclic siloxanes, such as tetra (methylvinyl) cyclotetrasiloxane, or linear siloxanes, such as divinyltetramethyldisiloxane. The platinum-siloxane complexes have better compatibility with the siloxane medium and achieve similar cure rates at a lower addition level. The divinylsiloxane complexes in toluene are generally more active catalysts while cyclic vinylsiloxanes provide a more moderate rate of cure. The platinum catalyst is generally used at a concentration of about 5–150 ppm based on the total formulation.

6.4.5 Adhesion promoters

Adhesion promoters are a ubiquitous component in self-priming silicone adhesive formulations and are generally used at low levels, between 0.2 and 3 wt% of the total composition. They are designed to be compatible with silicones yet have the ability to migrate to the bonding interface when the adhesive is applied and cured. At the interface, the adhesion promoter enhances bonding between the adhesive matrix and the substrate by interacting with both constituents through combinations of covalent bonding, hydrogen bonding, physical adsorption, and molecular entanglements. Adhesion promoters are designed to integrate with the adhesive matrix composition, the cure system (primarily condensation and addition cure), and the substrate to realize optimal adhesion performance under the conditions of application, processing, and use. Adhesion promoters range from simple molecules with one active component to multicomponent geometrically complex molecules. The active components are chemical moieties independently capable of covalent or physical bonding interactions with the adhesive matrix and/or substrate. To adhere to inorganic substrates, adhesion promoters functionalized with alkoxysilane moieties ($-\text{Si}(\text{OR}')_3$ where R' is typically a methyl group) are preferred. At the interface, alkoxysilanes improve adhesion by hydrogen and/or covalent bonding with the silicone matrix and substrate. This occurs when the silane undergoes hydrolysis on contact with trace water at the interface to form silanol ($\text{Si}-\text{OH}$) groups that can hydrogen bond and/or form a covalent $\text{Si}-\text{O}$ -substrate and $\text{Si}-\text{O}$ -matrix bonds through condensation reactions.

Alkoxysilane groups are effective for promoting the adhesion of silicones to inorganic surfaces in general but are insufficient on other surfaces such as plastics. To overcome this, adhesion promoters are typically designed with additional active groups such as aminoalkyl, methacrylylalkyl, or epoxyalkyl groups as exemplified by the bi-functional coupling agents aminopropyltrimethoxysilane, methacryloyloxypropyltrimethoxysilane, and glycidoxypyltrimethoxysilane [79]. Other reactive groups include silyl hydride [80] (Si—H) and vinyl [81] (Si—Vi) functionality that enables the covalent bonding of adhesion promoters to addition cure silicones. Catalysts and other adjuvants can be added to facilitate the reaction of adhesion promoters with surfaces [82]. The choice of reactive groups will also depend on their chemical compatibility with the silicone cure system. Condensation cure systems tend to be compatible with a range of reactive functionality, but addition cure systems have chemical sensitivities that need to be addressed in adhesion promoter selection.

6.4.6 Fillers

Fillers are primarily added to adhesive formulations to improve their physical (viscoelastic) properties. The addition of fillers affects the rheological properties of the uncured material, such as extrusion rate, “body,” handling, and tooling as well as the elastomeric properties of the cured sealant, such as hardness, modulus, elongation at break, tensile strength, and abrasion resistance. The first type of filler is referred to as an “active” filler and the second as an “inactive” or “extending” filler. Generally, a sealant formulation contains a combination of two or more active and inactive fillers. Surface area and energy, structure, density, and availability of reactive surface groups influence the degree of interaction between fillers and the silicone rubber network [83].

Reinforcing fillers increase the tensile strength of the cured elastomer and reduce slump (sag) of the uncured material. Conventional reinforcing fillers are finely divided particulates that have a particle size of less than about 50 nm and include precipitated and fumed silicas (Brunauer, Emmett, and Teller (BET) surface area of 150–300 m² g⁻¹). Semireinforcing fillers have a primary particle size of between 50 and 500 nm, more typically between 70 and 150 nm; a BET surface area of about 20–80 m² g⁻¹; and include fatty acid-treated precipitated calcium carbonates and calcium silicates (talc). Nonreinforcing fillers have a primary particle size of greater than 500 nm.

Nonreinforcing fillers interact very weakly with the silicone network. Examples include ground calcium carbonate (chalk), ground quartz, diatomaceous earth, mica, kaolin and bentonite clays, barium sulfate, and aluminum hydroxide. To reduce the cost of the formulation on a per volume basis, low-density fillers such as ceramic microspheres (commercially available, for example, as Z light Spheres, Zecosphere, and Macrolite Ceramic Spheres from 3 M Corporation, Saint Paul, Minnesota, United States) and glass microbubbles may be added to the formulation. Filler content varies widely depending on the type of filler. Typical fumed silica content is in the 8%–15% range, for ground calcium carbonate in the 15%–45% range, and for precipitated

calcium carbonate in the 25%–45% range (all ranges given as weight percent of the total formulation).

6.4.7 Special additives

6.4.7.1 Heat stabilizers

Iron oxides and carbon blacks are widely used as heat stabilizers in silicone sealants and adhesives. Iron carboxylate salts [84], cerium hydrate, barium zirconate [85], cerium and zirconium octoates [86], and porphyrins [87] are presented in the literature.

6.4.7.2 Flame retardants

Carbon black [88], hydrated aluminum hydroxide [89], and wollastonite [90] have been described in the patent literature as additives that improve the fire-resistance or self-extinguishing property of silicone adhesives. Platinum and platinum compounds also are known to improve the fire resistance of silicone compounds.

6.4.7.3 Electrically conductive fillers

Silicone adhesives have excellent dielectric properties, which make them good insulators. However, for some applications such as electrically conductive adhesives, a substantial increase in electrical conductivity is highly desirable. This is achieved by adding electrically conductive fillers to the formulation. Conductivity is attained by the percolation of electricity through the silicone matrix via a network of conductive filler particles, where each conductive particle must be in contact with at least two other such particles for electricity to flow. This requires very high filler loadings; for instance, for metal particles up to 80% by weight of the formulation. Carbon black [91,92], silver particles [93–99], or silver-coated particles [100] such as ceramic spheres are the most frequently used electrically conductive fillers. Other electrically conductive metal fillers such as copper, aluminum, and nickel have been described in the patent literature; however, these readily can oxidize to form an insulating metal oxide layer on the filler surface, which has a strong negative impact on the electrical conductivity of the silicone adhesive. Use of metal oxides in conductive silicone adhesives has been described as well [101], although these oxides generally are not as suitable as metal particles, owing to their higher resistivity.

6.4.7.4 Thermally conductive fillers

Silicone adhesives have a very low thermal conductivity. However, for some applications such as thermally conductive adhesives (TCA), a substantial increase in thermal conductivity is strongly desired. This is achieved by adding thermally conductive fillers to the formulation. Thermal conductivity is attained both by direct heat transfer via a conductive filler network as well as by indirect transfer via filler/polymer interfaces and, therefore, is a function of the filler volume loading (for a more detailed

discussion of the mechanisms involved, see the comprehensive review of methods used to predict the thermal conductivity of a filled system by Rogelhof et al.) [102]. Filler volume loading can be increased substantially by the use of mixtures of different thermally conductive fillers with different particle sizes or shapes. Hence, formulations often include two or more thermally conductive fillers. The most commonly used thermally conductive filler, aluminum oxide (Al_2O_3), has a thermal conductivity of 35 W (mK)^{-1} , which is about 180 times the thermal conductivity of polydimethylsiloxane polymer. Other metal oxides have thermal conductivities similar to aluminum oxide. The exception to this rule is beryllium oxide, which has a substantially higher conductivity. However, this compound is highly toxic. Ceramic fillers, other than oxides, some of them with higher thermal conductivity than Al_2O_3 , have been disclosed [103]. Often an increase in thermal conductivity is desirable for electronic applications while low electrical conductivity is maintained. This is best achieved by the use of ceramic fillers. Aluminum trihydrate is used when low abrasion or density is desired. Other applications demand a simultaneous increase in thermal and electrical conductivity. These compositions containing metal particles such as silver flakes or metal-coated fillers have been described in the patent literature [104].

6.4.8 Dual cure chemistry

To fulfill the need for very fast cure while maintaining other important properties, dual cure systems are becoming more common, especially for high end applications in electronics and aerospace. Fast cure speed may be achieved using photo-initiated cure, hot-melt transition, peroxide cure, or common hydrosilation. A second cure chemistry for improved adhesion, delayed adhesion build, delayed modulus build, or cure in shadow areas is included with the fast cure chemistry. Condensation cure is commonly used for the second cure reaction because it can proceed at room temperature at a later time. The use of dual cure systems requires the careful selection of polymer chemistry, catalysts, and additives that are compatible. Occasionally, two-part formulations are needed to provide the desired combination of chemistries and achieve good shelf life.

6.5 Applications of structural silicone adhesives

Joining materials with structural silicone adhesives offers substantial benefits over mechanical methods of fixation. The silicone adhesive distributes the load over a larger area of the joint rather than concentrating it at one location, resulting in a more even distribution of stresses. The adhesively bonded joint is thus more resistant to flexural and vibrational movement than a mechanically fixed joint. A further important aspect is that the silicone adhesive forms a seal as well as a bond in a single processing step (dual functionality). Mechanically fixed (e.g., bolted or riveted) assemblies are often sealed in an additional process step. The hydrophobic silicone adhesive inhibits corrosion, which often occurs in a mechanically fastened joint. The capability to fill larger gaps with a structural silicone adhesive allows irregularly

shaped surfaces to be joined more easily than does a mechanical fastener or thin applied structural adhesives such as epoxy. Owing to the excellent self-adhesion of silicone adhesives, failed or serviced assemblies can be easily reassembled and resealed.

There is a wide range of silicone structural adhesive products available, including flame resistant, heat resistant, chemical resistant, and oil resistant as well as products specified by the US Food and Drug Administration (FDA) and aerospace. Therefore, it is impossible to produce a definitive list of applications of silicone structural adhesives, as the versatility of these materials enables their use in almost every industry. Below is a list of a few examples that will be discussed in greater detail in this section:

- Automotive—lamp bonding, “under the hood” bonding applications, mirror mount adhesives.
- Aerospace—high temperature bonding, vibration protection.
- Construction—structural glazing, bonded windows, multiple glass pane bonding, panel stiffeners, impact mitigation protection, mirror adhesives.
- Domestic appliances—attaching glass and door hinges to oven doors.
- Electronics—bonding electronic components and subassemblies.
- Solar/photovoltaic (PV) renewable energy industry—bonding PV modules into frames, attaching control boxes, bonding wind turbine rotor blades.

6.5.1 Automotive

Key requirements for the automotive industry in general include fast handling of components; rapid development of bond strength; adhesion to a wide range of materials including many metals and plastics, such as polyamide (PA), poly(methyl methacrylate) (PMMA), polycarbonate (PC), poly(butylene terephthalate) (PBT), poly(ethylene terephthalate) (PET), and acrylonitrilebutadiene-styrene terpolymer (ABS); and excellent resistance to weathering, salt spray, and heat. Silicone adhesives meet these key requirements, which fit them perfectly to automotive applications.

Structural silicone adhesives are used in the assembly of automotive head and fog lamps. One of the most important of these applications is the bonding of the lens, made either from glass or PC, to the reflector housing or body (Fig. 6.3). This application is

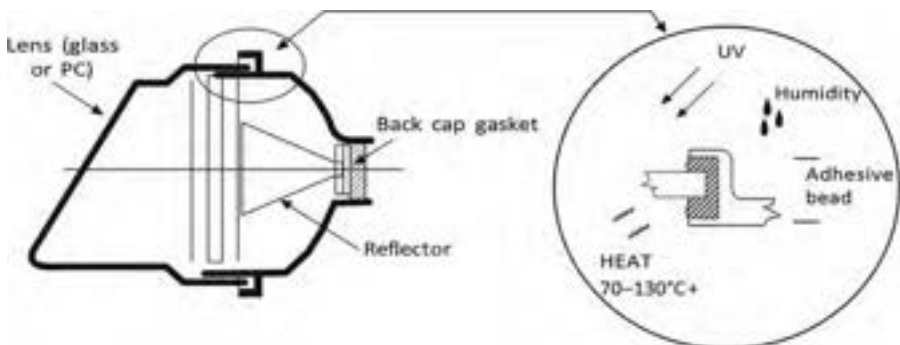


Fig. 6.3 Example of a car headlight module bonding application.

done today almost exclusively using silicone adhesives. One reason for this is that flange space is rather constrained, limiting the use of compression gaskets. However, the primary reason is that the lens/reflector bond needs to be hermetically sealed against moisture, dirt, and engine fluids such that they do not penetrate into the reflector and impair its optical function. Silicone adhesives have been used with great success in this application since at least the 1980s. Lamp operating conditions are harsh, with operating temperatures ranging at the high end between 70°C and 110°C for headlamps and 110–130°C for fog lamps. The inherent stability of silicones at high- and low-temperature extremes and their excellent adhesion characteristics make these materials well suited for this demanding application. The use of silicones in this application has an excellent track record of performance [105].

Most of the silicone adhesives used in this application are of the one- and two-component RTV condensation types (commonly alkoxy cures). Condensation cure silicone adhesives are preferred in this application over other silicone adhesives types, for example the addition cure types, because cure and especially adhesion can be tailored to proceed rapidly at room temperature. Durable adhesion is a key performance characteristic in this structural application [106]; adhesive failure of either the glass or the reflector body creates a path for moisture or other engine fluids into the lamp, leading to degradation of the optical performance. The lower shear modulus of a silicone structural adhesive results in lower stresses being induced at the interface by differential thermal expansion of the glass and the reflector housing. A further requirement for the silicone adhesive is low out-gassing at the high operational temperatures of the lamps. Proper functioning of automotive lamps demands that during operation, the lens and reflector be kept absolutely free of any surface imperfections or deposits that impair lighting efficiency. Through careful research and development, it is possible to formulate adhesives with reduced out-gassing and optimized joint design to reduce the fogging potential.

Furthermore, progress continues to be made in increasing the lighting power or brightness of (high brightness) light-emitting diodes (HB-LEDs) with resultant higher power ratings. LED headlamps are already a reality in automotive applications since the commercialization of adaptive driving beam LED headlights by Hella for Daimler cars in 2014 [107,108]. LED headlamp units will generate even more heat than conventional halogen and xenon lights and the resulting temperatures in the lamp are expected to range from 105°C to 160°C, depending on design and size. These operating conditions will continue to necessitate the use of silicone adhesives, which are able to function in this environment.

The most recent development in automotive lamp assembly is the use of silicone reactive hot-melt or warm-melt adhesives. Hot- or warm-melt adhesives are applied to the substrates at elevated temperatures and make use of a rapid increase in viscosity during cooling to achieve a high level of green strength or consistency. This green strength allows the adhesive to withstand moderate loads in the still-uncured state and permits handling and manipulation of bonded parts. Hot or warm melts, in general, allow an increase in manufacturing productivity, owing to their instant green strength and absence of adhesive squeeze-out. Silicone hot or warm melts further offer the following performance advantages: good adhesion durability, no cold flow

(creep), good elastic recovery, high joint movement capability, excellent temperature resistance, and excellent resistance to UV light and humidity. Silicone reactive hot-melt adhesives for automotive lamp assembly represent an exciting new development in adhesives. These products combine the processing advantage associated with hot-melt adhesives with the performance benefits of silicones.

Dual curing formulations utilizing condensation cure for corrosion resistance and a second cure for fast assembly have recently been introduced to the market. The second fast cure is hydrosilation, or peroxide cure. Peroxide cure provides facile adhesion to many plastics without the issues associated with platinum catalyst deactivation. The increasing use of flame retardants and thermal stabilizers in modern engineering plastic makes inhibition resistance an important factor.

Addition curing silicone structural adhesives frequently are used in automotive electronics that are placed “under the hood” and exposed to high operational temperatures. These materials develop a high strength bond after a short heat cure cycle with lap shear strengths of more than 6 MPa on unprimed surfaces and can be exposed to more than 10,000 temperature cycles in the engine compartment, with a maximum service temperature of 200°C. Typical successful applications include engine management units in which the thermoplastic casing is adhered to the metal heat sink and semiconductor power modules in which stick cases are bonded to metal base plates.

However, in spite of many studies, knowledge about the fundamental factors influencing adhesion between addition curing silicones and aluminum substrates was very limited until researchers from the Robert Bosh GmbH company issued a series of publications on their work that aimed to study the influence of the formulation and the surface state of the adherend on bond strength. For this purpose, the composition of an addition curing silicone was systematically varied and the effects on both material and bond properties were examined. The authors have shown that although high tensile strengths up to 9.2 MPa for the silicone material can be achieved by adjusting the formulation, lap-shear strengths remain moderate at approximately 3.5 MPa. It was proposed that interactions of the PDMS backbone with the aluminum adherend have the most important contribution to adhesion strength. Adhesion promoters must be incorporated or the surface needs further treatment, such as a primer finish, to improve bond strengths [109]. In a subsequent publication, the same authors studied the effect of various accelerated heat (85°C, 130°C, 150°C) and relative humidity (85°C/85% RH) aging conditions of the addition curing silicone adhesive on its lap-shear strength to an aluminum adherend. Overall, addition curing silicones are able to build up strong adhesion with aluminum adherends without the use of adhesion promoters or primers. The reason is the unique chemistry of siloxanes, which leads to chemisorption through reactions of excess hydrosiloxane groups and the siloxane backbone. High temperatures and dry conditions are beneficial for the build-up of adhesion through chemisorption and physisorption. In contrast, humid cure conditions are disadvantageous. These results are expected to be transferrable to the oxidic surfaces of metals other than aluminum as well as to glass surfaces [110].

From the perspective of material and lifetime modeling of silicone adhesives, another author from the Robert Bosh GmbH company has led a study on an

elastomeric silicone adhesive with different thermomechanical methods. The first stretch invariant at break is independent of strain rate and shows a reciprocal temperature dependency, that is, fracture energy can be provided by thermal and strain energy. Maximum principal strain is identified as a suitable failure criterion for different load cases and strain rates for static loading as well as for fatigue. Long-term stress relaxation behavior follows a power law with stretch-dependent preexponential factor and exponent. Using compressibility from a hydrostatic pressure experiment, a hyperelastic material model is used to describe the quasistatic stress-stretch curves for different load cases at 23°C with strain rates of 0.01 s^{-1} . Validation experiments show good agreement for two joint geometries with multiaxial load cases [111].

Addition curing, optically clear structural adhesives are used to attach rear view mirror mounts to windshields of automobiles. The heat cure of the adhesive assembly takes place in the autoclave, which is used to laminate the windshields. The silicone adhesive attaches a mounting plate to the glass so that a mirror can be fixed mechanically to the assembly. The UV resistance, heat resistance, and vibration resistance of the silicone adhesive make it suitable for this application. This type of adhesive is also used to attach and protect optical sensors used to initiate windshield wipers during the rain. The optically clear nature of these special automotive adhesives gives them excellent performance in such applications.

6.5.2 Aviation and aerospace

Silicones are fundamental in many of the components used in aviation and aerospace, which, by their nature, place extreme demands on materials. Silicone semistructural adhesives have been used in jet engines for more than 30 years where, for instance, they prevent bimetallic corrosion even at high temperatures. They are also used in electrical, micro- and optoelectronics [112], optical assemblies, and in the mounting of optics, resistors, connectors, and other components. Additional benefits stemming from the use of silicone adhesives are a wide operating temperature range; easy repairability; good physical and electrical stability over a range of frequencies, temperatures, and humidities; and the protection of components from temperature extremes, high humidity, radiation, thermal shock, and mechanical vibration. Adhesives for aviation and aerospace applications must adhere to a wide range of substrates, including some difficult-to-bond plastics, such as PC, polyetherimide (PEI), PMMA, and polyethersulfone (PES). In general, any material used in space must possess the following characteristics:

- Excellent resistance to temperature extremes and microcracking during thermal cycling.
- Resistance to radiation degradation.
- Outstanding atomic oxygen resistance.
- Low out-gassing characteristics.

The special grades of silicone structural adhesives used in aerospace applications maintain adhesion and a good degree of flexibility over a wide range of operating temperatures, typically from -45°C to 200°C , where other materials would stiffen and crack. PDMS has the lowest glass transition temperature (T_g), measured at

–127°C, and the lowest melting temperature of crystalline phase (T_m) measured at about –45°C, by DSC [58,113]. A typical temperature frequency sweep by dynamic mechanical analysis (DMA) of any silicone elastomer will show a drop in both storage and loss modulus of more than two orders of magnitude from –35°C to –60°C due to the first-order phase transition from the crystalline to the amorphous state at $T_m = -45^\circ\text{C}$ [114]. These special grades of silicone adhesives also possess excellent resistance to radiation. While silicone adhesives in space applications are not directly exposed to atomic oxygen, as they are encapsulated between two surfaces, the special aerospace grades show excellent resistance to this highly reactive form of oxygen that causes erosion of polymers [115,116].

Silicone adhesives can dampen the effects of launch vibrations to compensate for differential thermal expansion and to protect components from temperature extremes, high humidity, radiation, thermal shock, and atomic oxygen. Silicone structural adhesives in space applications are often near or directly adjacent to electronic optical devices where contamination would be of major concern. Silicone adhesives, made by special formulation and processing techniques, meet or exceed the requirements set by American and European space agencies for low thermal vacuum out-gassing. Silicone structural adhesives are used in aerospace applications for bonding solar cells to substrates, cover glasses to solar cells, and optical solar reflectors to substrates as well as for the assembly of electronic subcomponents and subassemblies, optical and other sensors, electronic components, modules, relays, and connectors.

6.5.3 Construction

The primary use of silicone structural adhesives in the construction industry is in structural sealant glazing (SSG) and in multiple glass pane bonding (insulating glass units, IGU). SSG is the method of bonding glass, ceramic, or metal to the frame of a building by utilizing the bond strength, movement capability, and durability of a silicone structural adhesive. The total vision system (TVS) developed during the 1960s was an early version of SSG, as in this design the glass panes were structurally bonded to glass mullions by a silicone adhesive.

The design of the 37 story, 23,000 m² two-sided structural glazing façade of New York City's Park Avenue Tower, completed in 1983, established the SSG technique as an architectural landmark. After the completion of this building, SSG rapidly became the fastest-growing form of curtain-wall construction in the United States because it allowed broader architectural flexibility and achieved dramatic design accents in new construction or the renovation of old buildings. Today, SSG is one of the most versatile forms of curtain-wall construction in the commercial façade business. The silicone structural adhesive in all SSG designs carries repetitive intermittent wind loads. In some super-tall buildings exposed to hurricane-strength winds, the structural bond must resist very high wind loads. In more advanced SSG designs, the silicone structural adhesive also permanently carries the weight (dead load) of the glazing panel. Other advanced SSG designs use the silicone to transfer shear loads to the glazing so that the glass reinforces the aluminum framing to resist deflections.

The SSG designs offer a number of performance benefits:

- Effective air and weather sealing of the façade.
- Improved thermal and sound insulation.
- Protection of the supporting structure from the elements by a durable glass skin.
- Increased rigidity and stability of the façade, resulting in the ability to withstand higher wind loads.
- Absorption of differential movements between glass and building frame, resulting in superior performance of SSG façades during seismic events.
- Esthetically pleasing smooth glass façade free of mechanical interruptions.
- Reduced deflection of glass under wind loads compared to conventional glazing because the flexible rubber anchor resists loads in both shear and tension.

The SSG technique utilizes both the adhesive and sealing properties of structural silicone adhesives. Medium modulus, elastomeric properties, and excellent, highly durable adhesion are needed to support the weight of glazed panels and to resist wind load while simultaneously being able to absorb differential movements between dissimilar materials induced by thermal fluctuations, seismic loading, or other forces. Because the interface between structural adhesive and glass can be directly exposed to sunlight, the adhesive must be developed to be UV-stable to achieve an expected service life up to 50 years or beyond. Because of this requirement, only silicone adhesives are allowed for use in structural glazing applications by international standards and building code bodies. In 2021, the first project using a structural silicone adhesive as the sole means of attachment for glass onto a building façade achieved a significant milestone, 50 years of performance without any known failures. This innovative design was utilized to renovate the decades old Cass Building at 455 West Fort Street in Detroit, Michigan (Fig. 6.4).

Structural silicones are also used successfully for the assembly of multipane units (double or triple insulating glass units) whereby the edge is not protected by a frame or



Fig. 6.4 Cass building at 455 West Fort Street, Detroit, Michigan.

coating and fully exposed to UV. Typically higher modulus silicones will be preferred from a performance point of view, as they ensure stiffness of the assembly and reduce the risk of leakage at the level of the primary seal. They are also preferred from an aesthetic point of view, as this allows reducing the sightline. Knowledge of SSG system performance has led naturally to the expanded use of silicone glazing in new high-performance façade systems, in particular for protective, safety, and security glazing systems for seismic-resistant, hurricane-glazing, or bomb blast-resistant façades. The unique characteristics of the continuous flexible rubber anchor resisting loads in both tension and shear, designed into a safety glazing system with proper frame design, have superior performance unequaled by any other design.

These types of applications are characterized by extremely high loads acting on the building over a short impact time. Silicone adhesives display a very low glass transition temperature (T_g) owing to the flexibility of their siloxane polymer backbone. The time-temperature equivalence principle developed by Williams, Landel, and Ferry [117] implies that a low T_g means high flexibility of the polymer chains at high temperatures within very short time scales. The theory thus predicts particularly good performance for silicone adhesives when submitted to a sudden load condition, typical for a bomb blast, hurricane, or earthquake [118–120]. Requirements for US government buildings that may be potential terrorist targets utilize a blast mitigation system for the glazing whereby bonding of laminated glass panes enhances the overall blast resistance. SSG has been used successfully since the 1980s in the typhoon-prone Pacific area as well as in the hurricane-prone Gulf and Atlantic areas in the United States, requiring special design according to building codes for structures. The effects of seismic activity on curtain wall façades are transmitted through the structure on which they are attached to. The more inflexible the exterior materials for the walls and cladding of a building, the more potential damage there is likely to be during a seismic event. Tying into the stable foundation characteristic, structural and nonstructural components should ideally be interconnected so inertial forces can dissipate. The serviceability and ultimate drift capacities of SSG systems are higher than their dry-glazed counterparts under seismic action. A remarkable extension of the structural glazing technology is the use of wet-applied RTV silicone structural adhesives in the manufacture of residential windows. This technology provides several key benefits for both window manufacturers and building owners. With the structural adhesive transferring loads between the frame and the insulating glass, the rigidity of the insulating glass unit contributes to the overall stability of the window. Obviously, the strength of the window then depends on the structural strength of the glass unit. However, glass has a good load-bearing capability (stiffness) and can contribute considerably to the overall strength of the system. Therefore, structural bonding of the glass panes to the frame and the resulting load transfer between frame and glass result in a number of benefits:

- Increased structural strength of window (load transfer between frame and glass, glass panes take on a role as a structural element).
- Increased window sizes with current standard frame cross-sections (steel inserts combined with bonding technology).

- Elimination or reduction of steel reinforcement inserts in PVC windows.
- Improved thermal insulation (U-value) of bonded window.
- Improved protective glazing properties (resistance to burglars, bomb blasts, hurricanes, earthquakes, avalanches, etc.).
- Improved esthetics (appearance of the window) through leaner and more slender frame designs (larger vision area—increased light transmission via window opening).
- Reduced maintenance.

The bonding technology results in substantial productivity gains and cost savings for the manufacturer. For the building owner, improved thermal performance, aesthetic benefits, and lower maintenance costs, all associated with this glazing technique, are important considerations.

Silicone adhesives also may be employed in the structural bonding of other façade components. Silicone adhesives have been used in adhering opaque panels of natural and man-made stones along vertical rails of ventilated rain screens. Newer materials beyond one and two-part RTV materials are being considered. Hot-melt materials based on a mixture of resin, polymer, and fillers have been explored in applications such as glazing and use in adhering all glass components together to form treads and support to create all glass stairways.

6.5.4 Domestic appliances

Silicone structural adhesives are used in domestic appliances where flexible bonding and resistance to harsh environments are important. For example, the metal base plate of a steam iron is bonded to the plastic water tank with silicone adhesives. In electric or gas ranges, silicone adhesives bond the glass pane to the metal door frame and often also the hinges to the door frame. Numerous other applications of silicone adhesives exist in domestic appliances where they function as durable dielectric insulation, barriers against environmental contaminants, and stress-relieving shock and vibration absorbers over wide temperature and humidity ranges. However, in these applications, silicones are used primarily as assembly adhesives and their application would not qualify as truly structural in nature.

6.5.5 Electronics

Silicone adhesives find extensive use in electrical and electronic applications where stable dielectric properties and resistance to harsh environments are important. The majority of these applications are not truly structural in nature; however, certain electric or electronic components in aerospace, automotive, or military applications may be exposed to large acceleration or deceleration forces. Therefore, the bonding must be capable of transferring considerable loads.

Silicone adhesives are used frequently in electronics as thermal and mechanical stress absorbers because of their flexibility, low ionic impurity, dielectric insulation properties, moisture resistance, and wide operation temperature range. Specially formulated grades are available as low volatile silicone adhesives as well as adhesives with high electrical and/or thermal conductivity. The trend in electronics product

development and design is toward ever-increasing density, complexity, and power dissipation. This results in higher local heat flux and higher temperatures inside the modules or packaging. Interconnection of substrates having a mismatch of coefficients of thermal expansion (CTE) can lead to failure upon thermal cycling owing to a build-up of mechanical stresses. In these applications, thermally conductive silicone adhesives are used in the bonding of sensitive electronic components and subassemblies.

Thermally conductive adhesives eliminate the need for mechanical fasteners and clips while providing an efficient method of thermal transfer between heat-generating electronics devices and their heat sinks. To improve the thermal conductivity even further, these adhesives must be able to be applied in very thin bond lines. Silicone thermally conductive adhesives can be used to form thermal pathways in applications where the distance between a component and a heat sink is highly variable. A typical application would be printed circuit board components of different heights that need to be brought into contact with a chassis or heat sink. Silicone thermally conductive adhesives are used, for example, in bonding large ceramic substrates to their heat sink in automobile microprocessor-controlled ignition and fuel injection.

Continuing improvements in silicone adhesive technology have enabled these adhesives to replace solder in many electronic assembly applications. Whereas solder and most other electrically conductive adhesives would be too rigid to hold up against vibrations or impact loads, highly flexible and resilient silver-filled conductive silicones easily survive high-impact applications. Electrically conductive silicones help to protect devices from environmental hazards such as moisture as well as shield electromagnetic and radio frequency interference (EMI/RFI) emissions.

6.5.6 Solar/photovoltaic renewable energy industry

In the early days of photovoltaic and solar panel design in the 1980s, silicone was mostly used as an encapsulant of the PV cells, which resulted in very durable and reliable modules. However, silicone encapsulation was replaced at the end of the 1980s by EVA for process and cost reasons. However, since the simultaneous emergence of a market for very robust and durable modules (long lifetime utility modules, sunbelt region modules, tropical region modules) and the development of specific silicones and encapsulation processes meeting the requirements of modern PV manufacturing, silicone-encapsulated panels have become again a feasible and attractive technology option in recent years. Double glass modules with silicone encapsulation have recently been launched and are now mass produced and globally commercialized by the BYD Shenzhen manufacturing plant in China, for instance (Fig. 6.5). The combination of the glass-glass structure and silicone is shown to lead to exceptional durability in accelerated aging tests [121].

On PV modules fabricated in the early 1980s, which were in operation outdoors in a semitropical climate for more than 20 years, an investigation was done to analyze the properties of the silicone elastomer used for their fabrication [122]. It was observed that the silicone materials have very similar properties to recent, freshly cured silicone. The information gathered gives evidence that silicone elastomers undergo only

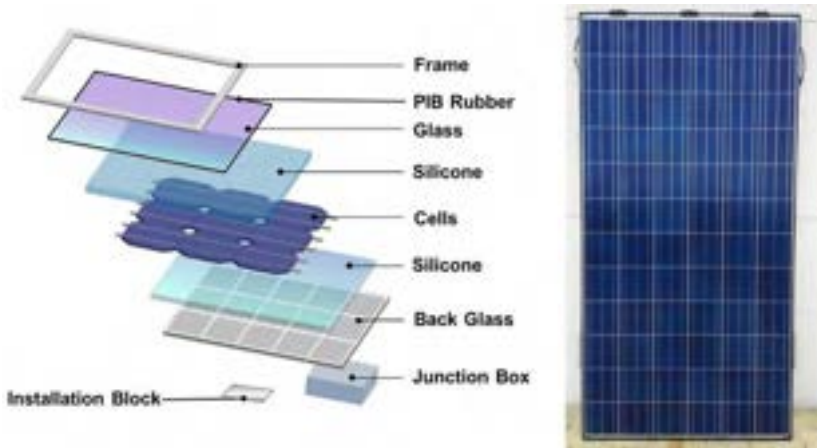


Fig. 6.5 Schematic structure of BYD's double glass module (left) and picture of the front side of the panel.

From K. Yarosh, A.T. Wolf, S. Sitte, Evaluation of silicone sealants at high movement rates relevant to bomb mitigating window and curtain wall design, *J. ASTM Int.* 6(2) (2009), <https://doi.org/10.1520/JAI101953>, with permission of authors.

very limited degradation after years of exposure in the field in operating PV modules. A moderate decrease in elastic modulus was observed, but further studies are needed to determine whether this effect is real. The very limited degradation of silicone encapsulant is consistent with the low performance decrease reported in several prior studies and discussed in this chapter to a large extent.

For assembly purpose, a silicone-reactive hot-melt structural adhesive is used to bond the photovoltaic modules into the frames and to attach the polypropylene junction and control boxes to the solar modules. The key benefits of using silicones are the increased production rate in the assembly operation owing to fast bonding, the use of substrates (plastics, glass, metals) without the need for priming or surface activation, and the ability of the material to accommodate thermally induced movements in the joint. Silicone structural adhesives are also used in the integration of photovoltaic modules into curtain-wall façades and in bonding the giant rotor blades of wind turbines.

6.6 Design techniques

Design techniques factor in the material behavior of the silicone adhesive and the impact of induced stresses or strains expected on the silicone adhesive with an assigned safety factor. Loads may be repetitive or permanent so understanding the impact of duration or frequency of load will be important. Similar to loads, adhesives may be required to withstand different strains either as a single event, over the long term, or with cyclical straining. Other design boundaries may also require thermal or

conductance performance in combination with the described resistance to stresses and strains.

Material behavior models are required to describe the performance of the structural adhesive and must be suitable for the design technique being used. Understanding the relationship of the specimen tested is important in comparison to the application. Using modulus from a uniaxial test focused on sealant behavior only in the tensile direction would not be suitable when designing for an application of a sealant functioning mostly in shear unless the software has the ability to convert between different elastic moduli for homogenous isotropic materials, the materials themselves are well described by the isotropic relationship, and sufficient moduli exist for the material for conversion. Behavior of silicone adhesives can differ due to geometry, temperature, rate of deformation, or even formulation type. For sealants formulated with a mostly PDMS polymer backbone, the stress-strain behavior of the resulting cured elastomer is considered to be hyperelastic. Key characteristics of these substances include the ability to exhibit large deformations prior to failure (on the order of 100%–700% of their initial, unloaded size) and the tendency to demonstrate stiffening behaviors in which the material will first soften and then become stiffer as applied loads are increased. In general, the relationship between applied loads and resulting deformations (or analogously, between stresses and strains within the material) tend to exhibit nonlinear relationships. This is in contrast to more traditional “engineering materials” like metals that follow more or less linear correlations between applied loadings and deformations. Consider the side-by-side comparison of stress-strain curves for a linearly elastic material and a hyperelastic material shown in Fig. 6.6.

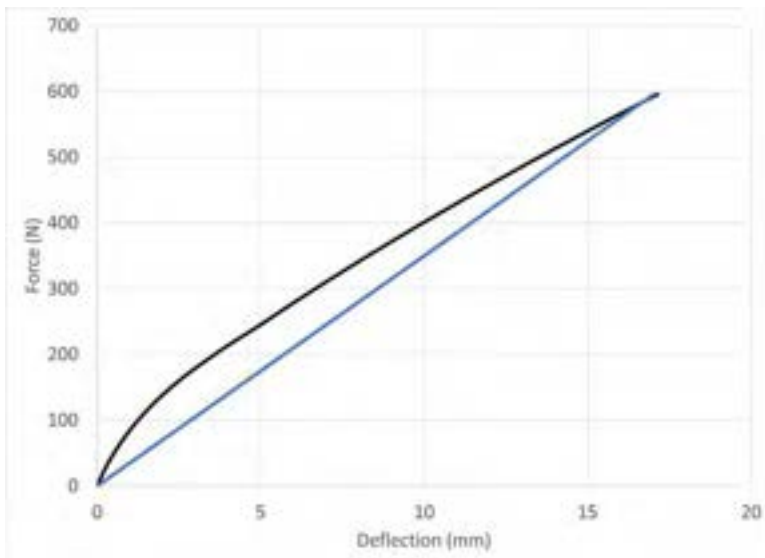


Fig. 6.6 Comparison of linear elastic (*blue*) and hyperelastic (*black*) mechanical response.

Conversely, formulations like hot-melt silicones contain bulkier molecules with more branching rather than larger lengths of polymer chains between crosslinks. These materials exhibit a more plastic behavior, slower recovery, and influence by the temperature, which may be best described using linear models. It is possible to adequately describe joints undergoing low levels of strain that are constrained into a specific section of the engineering stress-strain curve by using a linear assumption of the secant modulus up to the level of strain. The most important part of simplification is that the act of doing so does not eliminate potential interactions between materials that would be critical in understanding the application. This linearization of material properties is adopted successfully in ETAG or ASTM procedures whose scope of application is limited to simple load cases and shapes. Full constitutive models for hyperelastic materials can more accurately describe potential behavior for the sealant under complex conditions such as combined loads. The constitutive models are found based on a series of material testing to estimate the behavior of the cured elastomer representing pure states of tension, shear, and/or compression. The use of constitutive models usually is utilized in finite element analysis software to fully capture complex adhesive interactions. As part of the behavior development process, validation of the type of model can ensure accuracy in a predictive analysis. There are multiple models available and not all yield the same results. The validation process may be as simple as modeling experimental behavior of typical test specimens and comparing the results.

6.6.1 Analytical analysis

A simple summation of forces might adequately describe the potential stresses transferred to the structural adhesive. For structural silicone glazing, the material behavior is based on a prototypical structural joint using a tensile adhesion joint pulled to failure. An allowable stress is derived (typically 20 psi but can be higher) where potential for strain is reduced with a robust safety factor compared to strength at break. The allowable stress is then used in a simple mathematical relationship (ETAG, ASTM) between the size of the load applied and the dimension of the short length of the glazing unit to dimension the bite. The approach has been proven to be successful as the load used in the design is considered to be the maximum load in the life of the unit that will span decades where nominal loads are much less on a daily basis. However, this approach has limitations due to the made calculation assumptions and cannot be used for all designs or load cases.

6.6.2 Finite element analysis

Finite element analysis software packages can utilize more complex hyperelastic material models to better describe the actual reaction of stresses or strains on structural silicone adhesives within an application. This is especially important as some applications may generate complex interactions that are not easily described by mono-directional behaviors. As equally important, many software packages can generate visual depictions of the different distributions of stresses or strains within the

application elements. The visual depictions can provide more insight such as the potential for failure or unexpected interactions where stress may be accumulating unexpectedly.

The capability for using complex behavior models between software offerings can differ. Material behavior can be treated differently depending on the used software, including within the software. Some silicone manufacturers provide an array of data that can be used, including datasheets [123] for complex models such as Neo-Hookean, Mooney-Rivlin, or similar. Understanding the capability of the software is important as it will influence the type of input data needed to ensure better accuracy of the modeling effort.

For software packages with the most design utility, silicone adhesives are best modeled as a brick element using solid mechanics equations. Within the brick element, the mesh size selected must be sufficient to capture the interactions through the system of nodes defined by the mesh sizes. Mesh sizing that is too coarse may over- or underpredict the forces and displacements within the simulation. Mesh sensitivity should be analyzed to ensure accuracy [124,125].

6.6.2.1 *Model simplification*

Simplification of the modeling effort can be pursued and may be required if the software used does not support specific model types. Larger, more complex analysis will also increase the time needed to come to a solution, so simplified models may be used to more quickly understand proof of concept initially where more complex models will be used later to validate iterations in the design process. Descamps et al. illustrate the ability to use spring elements to simplify models for dynamic loading of structural silicone joints by relating the stiffness due to geometry as a function of an increased material modulus or rigidity modulus [126]. While the Young's modulus is a material property, the joint rigidity modulus is a quantity depending on the geometry of the joint and more precisely on the joint aspect ratio [127]. This value, determined by testing a specimen at the specific geometry, should be used for the spring axial stiffness while the shear modulus is used for the spring shear stiffness. Further simplifications describe the possibility to reduce the number of springs along the joint bite by adding the effect of the rotation of the pane through an adapted equation similar to the improved joint dimensioning calculation method proposed.

Joints undergoing low levels of strain that are constrained into a specific modulus section of the engineering stress-strain curve may be adequately described using a linear assumption of the secant modulus up to the level of strain or stress from testing a prototypical joint dimension. Behavior initiating from the origin during the stress development well before the yield in the curve related to strain could be suitable for use in software packages that have simplistic models for hyperelasticity or linear inputs. The most important part of simplification is that the act of doing so does not eliminate potential interactions between materials that would be critical in understanding the application.

6.6.2.2 Model validation

As part of the modeling effort, validation of the model parameters is also an important part of confirming the accuracy of information used in the simulation. The validation can be completed by simulating standardized test specimens and comparing to the actual results found from testing. Jobst illustrates this concept by testing an L-shaped sealing geometry and comparing the load required as the samples are pulled apart [115]. The joint represents a realistic challenge to assess sealant behavior where shear and tension occur in a constrained geometry. Replicates capture the inherent variation with the test method where the simulation indicates the relative accuracy predicted within the variability interjecting some reality as to what can be expected in simulation efforts. The variability is less likely due to mesh sensitivity and more about how stress or strain collects at the edges during the calculation or just differences in workmanship in the fabrication of the specimen (Fig. 6.7).

6.6.2.3 Durability/failure analysis

As part of the simulation, several different outputs can be calculated, related to the predicted forces and displacements within the elements of the application. Possible outputs include the maximum and minimum principal stresses, strains, or von Mises forces or strain-based outputs. Although structural denotes the need to evaluate the impact of load on a system, the determination of stretch displacement should also be considered. Significant research in determining what is the true measure of durability in silicone adhesives is performed [128]. A safe region, where the material can sustain complex loads indefinitely, can be described in stress, strain, or stretch space. Accordingly, a region where the material will fail exists in either space. Both regions are separated by a failure surface. A function representing all points on this surface is called failure criterion.

Early studies described failure surfaces of rubber polymers using stress-based failure criteria were not accurately describing experimental data. They are difficult to

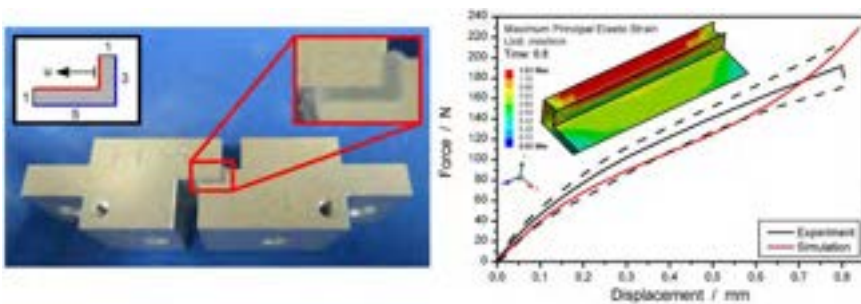


Fig. 6.7 Validation of FEA model by practical measurements.

From B.A. Banks, K.K. de Groh, S.K. Rutledge, F.J. DiFilippo, Prediction of In Space Durability of Protected Polymers Based on Ground Laboratory Thermal Energy Atomic Oxygen, NASA technical Memorandum 107209, NASA, Washington, DC, 1996, with permission.

determine experimentally, depend on the specific choice of strain energy density function in computational applications, and may become unphysical if polyconvexity is not strictly enforced. Fitting polynomial or exponential functions to experimental data in principal stretch and strain space gives a more satisfactory representation of experiments. Each measure has specific advantages and inconveniences. True strains allow for the separation of distortional and dilatational parts of deformation. Stretches can be measured readily and are used for the formulation of constitutive laws in continuum mechanics. Finally, other approaches assume energy-driven material failure and incorporate failure directly in the description of the constitutive behavior of hyperelastic materials.

6.7 Conclusions

Silicone structural adhesives are highly durable, have excellent adhesion to a wide range of substrates, are capable of operating over a wide range of service temperatures, and have long service lives even in very demanding environments. Silicone structural adhesives can join dissimilar substrates and fill gaps, therefore eliminating corrosion problems and vibration failures, and accommodate relative motion of adherends, including to compensate for a mismatch in the coefficients of CTE. The stable network structure and strong adhesion enable load-bearing joints proven to last multiple decades. Recent advances in FEA modeling and improved understanding of diffusion-controlled cure chemistry enable efficient and durable joint design. With a proven track record and better tools for joint design, silicone-based structural adhesives continue to be utilized in a wide range of electric, electronic, automotive, domestic appliance, and construction applications.

6.8 Future trends

The continued desire and regulatory need for adhesives and sealants with low toxicity will be the way of the future for applications in occupied spaces such as automotive and building construction. Each new generation will utilize more environmentally friendly catalysts and crosslinkers. The trend toward low volatile content or solventless adhesives will continue into the future, favoring silicone adhesives in general, but especially the reactive silicone hot melts and low volatile polymers. The need for primerless adhesion will also continue to exist. More recent material trends that are likely to become even more important in the future are reversible adhesion (to ease the recycling of bonded components) and command cure, that is, rapid cure initiated by external triggers. Silicone adhesives based on nanocomposite or hybrid copolymeric systems will provide novel or modified properties, such as lower gas permeability, higher strength, refractive index matching, and even higher service temperature performance. Life cycle cost analysis of components and systems will favor silicone adhesives because of their greater durability and easy serviceability, both of which contribute to low overall maintenance costs and lower overall carbon footprint.

The need for lower total applied costs will continue to exist, requiring improved productivity and a reduction in components. Changes in substrate type and surface modification as well as increased utilization of dissimilar substrates in designs will require silicone adhesives to adhere to an even broader range of substrate types, especially low surface energy substrates. Vehicle electrification and light weighting will be a strong driver for adhesives with the ability to control thermal, sound, and electrical energy. Adhesives with electrical conductivity for EMI shielding will be needed to replace solder in the growing list of Internet-connected devices, radar, lidar, and high-frequency communication devices utilized in autonomous driving and 5G applications.

6.9 Sources of further information and advice

Further information on silicone adhesives and their applications may be obtained from some recent publications listed below:

Huneau, B. Le Cam, J-B, Marco, Y; Verron, Erwan, *Constitutive Models for Rubber XI*, CRC Press, 2019, ISBN: 9780367342586, and prior editions.

Miyachi, H.; White, C. Durability of Building and Construction Sealants and Adhesives, 6th Volume – (STP 1604), ASTM International, 2018, and prior volumes.

Lee, V.Y. *Organosilicon Compounds, Two Vol Set*, Academic Press, 2017, ISBN:9780128143292.

ASTM (2008), *ASTM Standards and Technical Articles Relating to Structural Glazing*, available from www.aStM.org, viewed December 4, 2008.

Brockmann, W., Geiß, P.L., Klingen, J., Schröder, K.B. and Mikhail, B. (Translator) (2008), *Adhesive Bonding: Materials, Applications and Technology*, Wiley, New York.

Dunn, D.J. (2003), *Adhesives and Sealants – Technology, Applications and Markets*, RAPRA technology limited, Shawbury, Shropshire, United Kingdom.

De Buyl, F. (2001), ‘Silicone sealants and structural adhesives’, *International Journal of Adhesion and Adhesives*, **21**, 411–22.

L. Yan, D. A. Dillard, R. L. West, L. D. Lower and G. V. Gordon. “Mullins effect recovery of a nanoparticle-filled polymer.” *Journal of Polymer Science Part B: Polymer Physics*, **48** (21): 2207–2214 (2010).

David A. Dillard; Lei Yan; Robert L. West; Glenn V. Gordon; Loren D. Lower, “Estimating the Stresses in Linear Viscoelastic Sealants Subjected to Thermally-Driven Deformations,” *The Journal of Adhesion*, **87**(2):162–178, (2011).

Lei Yan, David A. Dillard, Robert L. West, Kenneth J. Rubis and Glenn V. Gordon, “Strain Rate and Temperature Dependence of a Nanoparticle-Filled Poly(dimethylsiloxane) Undergoing Shear Deformation”, *Journal of Polymer Science: B – Polymer Physics*, **50** (13), 2012, 929–937; ISSN: 0887–6266. DOI: <https://doi.org/10.1002/polb.23088>.

References

- [1] [The European Parliament and the Council of the European Union, Directive 2007/47/EC of The European Parliament and of the Council of 5 September 2007 amending Council Directive 90/385/EEC on the approximation of the laws of the Member States relating to active implantable medical devices, Council Directive 93/42/EEC concerning medical](#)

- devices and Directive 98/8/EC concerning the placing of biocidal products on the market, Off. J. Eur. Union L 247 (2007) 21–55.
- [2] A. Wolf, Durability of silicone sealants, in: A. Wolf (Ed.), *Durability of Building Sealants—RILEM Report 21*, RILEM Publications Sarl, Cachan, France, 1999, pp. 253–274.
 - [3] Y. Israeli, J.L. Phillipart, J. Cavezzan, J. Lacoste, J. Lemaire, Photooxidation of polydimethylsiloxane oils. Part I. Effect of silicon hydride groups, *Polym. Degrad. Stab.* 36 (1992) 179–185.
 - [4] Y. Israeli, J. Cavezzan, J. Lacoste, Photo-oxidation of polydimethylsiloxane oils. Part II. Effect of vinyl groups, *Polym. Degrad. Stab.* 37 (1992) 201–208.
 - [5] Y. Israeli, J. Cavezzan, J. Lacoste, J. Lemaire, Photo-oxidation of polydimethylsiloxane oils. Part III. Effects of dimethylene groups, *Polym. Degrad. Stab.* 42 (1993) 267–279.
 - [6] Y. Israeli, J. Lacoste, J. Cavezzan, J. Lemaire, Photo-oxidation of polydimethylsiloxane oils and resins. IV. effect of phenyl groups, *Polym. Degrad. Stab.* 47 (1995) 357–362.
 - [7] D. Oldfield, T. Symes, Long term natural aging of silicone elastomers, *Polym. Test.* 15 (1996) 115–128.
 - [8] P.L. Brown, J.F. Hyde, Polyfunctional alkoxy Endblocked Polysiloxanes and Their Cured Compositions, US Patent 3,161,614, 1964.
 - [9] D.R. Weyenberg, Method of Making One Component Room Temperature Curing Siloxane Rubbers, US Patent 3,334,067, 1967.
 - [10] S.D. Smith, S.B. Hamilton Jr., Curable Compositions, US Patent 3,689,454, 1972.
 - [11] E. Sweet, Organosilicon Intermediates Containing Silicon-Bonded Oxime Radicals, US Patent 3,189,576, 1965.
 - [12] L. Ceyzeriat, Room Temperature Curable Siloxane Compositions, US Patent 3,133,891, 1964.
 - [13] L.B. Bruner, Acyloxy-Endblocked Diorganopolysiloxane, US Patent 3,032,532, 1962.
 - [14] L.B. Bruner, Acyloxy Siloxanes and a Method of Using Them, US Patent 3,035,016, 1962.
 - [15] M.D. Beers, Curable Compositions and Process, US Patent 4,257,932, 1981.
 - [16] T.A. Kulpa, Curable Organopolysiloxane, US Patent 3,296,161, 1967.
 - [17] M.D. Beers, Composition Containing Silanol Chain-Stopped Polydimethyl-Siloxane, Organosilicon Process Aid, and Curing Agent, US Patent 3,382,205, 1968.
 - [18] H.D. Goelitz, K. Damm, W. Noll, Organopolysiloxane Composition Convertible at Room Temperature, US Patent 3,364,160, 1968.
 - [19] H. Sattlegger, W. Noll, K. Damm, H.D. Golitz, Organopolysiloxane Compositions Convertible into Elastomers, Bayer AG, US Patent 3,378,520, 1968.
 - [20] K.C. Pande, R.E. Ridenour, Aminoxysilanes, US Patent 3,448,136, 1969.
 - [21] J. Boissieras, L.F. Ceyzeriat, M.J.C. Lefort, Organosilicon Compounds and Their Use, US Patent 3,359,237, 1967.
 - [22] R.A. Murphy, Organopolysiloxane Compositions and a Method for Making Them, US Patent 3,341,486, 1967.
 - [23] J. Boissieras, L.F. Ceyzeriat, Organosilicon Compounds and Compositions Containing the Same, US Patent 3,429,847, 1969.
 - [24] T. Takago, T. Sato, H. Aoki, Room Temperature Vulcanizing Organopolysiloxane Compositions, US Patent 3,819,563, 1974.
 - [25] T. Takago, Room Temperature Curable Organosiloxane Compositions, US Patent 4,180,642, 1979.
 - [26] S. Nitzsche, M. Wick, Silicone Elastomers, US Patent 3,032,528, 1962.
 - [27] P. Hittmair, S. Nitzsche, M. Wick, E. Wohlfarth, Room Temperature Vulcanizable Organopolysiloxane Elastomers, US Patent 3,408,325, 1968.

- [28] S. Nitzsche, W. Kaiser, E. Wohlfarth, P. Hittmair, Room Temperature Vulcanizable Silicone Rubber Stocks, US Patent 3,674,738, 1972.
- [29] M.A. White, M.D. Beers, G.M. Lucas, R.A. Smith, R.T. Swiger, One Package, Stable, Moisture Curable, Polyalkoxy-Terminated Organopolysiloxane Compositions and Method for Making, US Patent 4,395,526, 1983.
- [30] J.J. Dziark, Scavengers for One-Component Alkoxy-Functional RTV Compositions and Processes, US Patent 4,417,042, 1983.
- [31] G.M. Lucas, J.J. Dziark, Adhesion Promoters for One-Component RTV Silicone Compositions, US Patent 4,483,973, 1984.
- [32] R.H. Chung, End-Capping Catalysts for Forming Alkoxy-Functional One Component RTV Compositions, US Patent 4,515,932, 1985.
- [33] C. White, K. Tan, A.T. Wolf, L.D. Carbary, in: D. Dillard (Ed.), *Advances in Structural Adhesive Bonding*, Woodhead Publishing Ltd., Cambridge, UK, 2010, pp. 66–95.
- [34] J. Comyn, J. Day, S.J. Shaw, Kinetics of moisture cure of silicone sealants, *J. Adhes.* 66 (1998) 289–301.
- [35] J. Comyn, F. Brady, R.A. Dust, M. Graham, A. Haward, Mechanism of moisture-cure of isocyanate reactive hot melt adhesives, *Int. J. Adhes. Adhes.* 18 (1998) 51–60.
- [36] J. Comyn, Moisture cure of adhesives and sealants, *Int. J. Adhes. Adhes.* 18 (1998) 247–253.
- [37] F. de Buyl, J. Comyn, N. Shephard, N. Subramaniam, Kinetics of cure, cross link density and adhesion of water-reactive alkoxy silicone sealants, *J. Adhes. Sci. Technol.* 16 (2002) 1055–1071.
- [38] F. de Buyl, J. Comyn, N. Shephard, N. Subramaniam, Kinetics of cure, crosslink density and adhesion of water-reactive alkoxy silicone sealants, *Int. J. Adhes. Adhes.* 22 (2002) 385–393.
- [39] J. Comyn, F. de Buyl, Mobility of water and alcohols in a silica reinforced siloxane network, *Eur. Polym. J.* 37 (2001) 2385–2391.
- [40] J. Comyn, F. de Buyl, T. Comyn, Diffusion of adhesion promoting and crosslinking additives in an uncured silicone sealant, *Int. J. Adhes. Adhes.* 23 (2003) 495–497.
- [41] J.A. Barrie, D. Machin, The sorption and diffusion of water in silicone rubbers: Part I. Unfilled rubbers, *J. Macromol. Sci. Phys.* B3 (1969) 645–672.
- [42] J.A. Barrie, D. Machin, The sorption and diffusion of water in silicone rubbers. Part II. Filled rubbers, *J. Macromol. Sci. Phys.* B3 (1969) 673–692.
- [43] S.A. Stern, B. Krishnakumar, S.M. Nadakatti, in: J.E. Mark (Ed.), *Physical Properties of Polymers Handbook*, American Institute of Physics Press, Woodbury, NY, 1996 (Chap. 50).
- [44] J.A. Barrie, B. Platt, The diffusion and clustering of water vapour in polymers, *Polymer* 4 (1963) 303–313.
- [45] H.G. Brod, O. Schweitzer, Verfahren zur Herstellung von Formkoerpem und Ueberzuegen aus Elastomeren Organopolysiloxanen (Process for the Manufacture of Moldings and Coatings Based on Elastomeric Organopolysiloxanes), German Patent 1,035,358, 1958.
- [46] K.E. Polmanteer, Siloxane Elastomers, US Patent 2,927,907, 1960.
- [47] M.E. Cifuentes, W.P. Brady, W.N. Fenton, R.G. Schmidt, M.R. Strong, D.L. Stickles, B. VanWert, Moisture-Curable Compositions Containing Aminoalkoxy Functional Silicone, US Patent 5,302,671, 1994.
- [48] M.E. Cifuentes, M.R. Strong, B. VanWert, M.A. Lutz, R.G. Schmidt, Moisture Curable Hot Melt Silicone Pressure-Sensitive Adhesives, US Patent 5,508,360, 1996.

- [49] M.E. Cifuentes, W.P. Brady, R.G. Schmidt, W.J. Schoenherr, M.R. Strong, B. VanWert, G.A. Vincent, Moisture-Curable Hot Melt Silicone Pressure-Sensitive Adhesives, US Patent 5,905,123, 1999.
- [50] M.E. Cifuentes, M.R. Strong, B. VanWert, M.A. Lutz, R.G. Schmidt, Moisture-Curable Hot Melt Silicone Pressure-Sensitive Adhesives, European Patent EP 0 735 103 b1, 2003.
- [51] G.A. Vincent, W.P. Brady, M.E. Cifuentes, W.J. Schoenherr, H.L. Vincent, Oxime-Functional Moisture-Curable Hot Melt Silicone Pressure-Sensitive Adhesives, US Patent 5,340,887, 1994.
- [52] M.R. Strong, M.E. Cifuentes, B. VanWert, W.J. Schoenherr, Moisture-Curable Hot Melt Silicone Pressure-Sensitive Adhesives, US Patent 5,473,026, 1995.
- [53] A. Be, Y. Cai, L.D. Lower, Continuous Process for Producing Hot Melt Adhesive Compositions, PCT Patent application Wo 2004/037941 a2, 2004.
- [54] E. Delebeck, F. Ganachaud, Looking over liquid silicone rubbers: (1) mechanical properties vs chemical formulations, ACS Appl. Mater. Interfaces 4 (2002) 3340–3352.
- [55] E. Delebeck, N. Hermeline, A. Flers, F. Ganachaud, Looking over liquid silicone rubbers: (2) mechanical properties vs network topology, ACS Appl. Mater. Interfaces 4 (2012) 3353–3363.
- [56] R.P. Eckberg, Vinyl Gum Cure Accelerators for Addition-Cure Silicone, US Patent 4,340,647, 1982.
- [57] R.P. Eckberg, Silicone Release Coatings and Inhibitors, US Patent 4,347,346, 1982.
- [58] A. Ghanbari-Siahkali, S. Mitra, P. Kingshott, A. Almdal, C. Bloch, H.K. Rehmeir, Investigation of the hydrothermal stability of cross-linked liquid silicone rubber (LSR), Polym. Degrad. Stab. 90 (2005) 471–480.
- [59] J. Stein, Addition-Curable Silicone Adhesive Compositions and N-Heterocyclic Silane Adhesion Promoters, US Patent 5,362,781, 1994.
- [60] J. Stein, B.E. Eichinger, T. Early, C.D. Wood, A new class of adhesion promoters for addition curable silicone adhesives, adhesive joints: formation, characteristics and testing, in: 2nd International Symposium on Adhesive Joints, Formation, Characteristics and Testing, Newark, NJ, May 22–24, 2000, pp. 89–100.
- [61] J. Stein, J.A. King Jr., A.J. Caruso, Addition-Curable Silicone Adhesive Compositions, and Bis(Trialkoxysilylalkyleneoxy-Carbonylalkylene) Amine Adhesion Promoters, US Patent 5,342,870, 1994.
- [62] J. Stein, Michael Addition Products as Adhesion Promoters for Addition-Curable Silicone Adhesive Compositions, US Patent 5,569,689, 1996.
- [63] J. Stein, M.W. Davis, Room Temperature Addition-Curable Silicone Adhesive Compositions and N-Heterocyclic Silane Adhesion Promoters, US Patent 5,380,788, 1995.
- [64] J. Stein, S. Rubinsztajn, Addition-Curable Silicone Adhesive Compositions and Bis(trialkoxysilylalkylene)urea Adhesion Promoters, US Patent 5,416,144, 1995.
- [65] H. Hara, Addition Curing-Type Silicone Compositions Containing an Adhesion Promoter for Heat-Resistant Adhesives, European Patent application 0,934,981 a2, 1999.
- [66] D. Ahn, M.A. Lutz, Silicone Composition and Cured Silicone Product, US Patent 6,512,037, 1998.
- [67] S.M. Evans, C.L. Lee, M.H. Yeh, Storage-Stable Heat-Curable Transparent Organosiloxane Compositions Containing a Microencapsulated Catalyst, US Patent 5,194,460, 1993.
- [68] M. Ikeno, H. Fujiki, Siloxane Compositions and Their Cured Products, 1992. Japan, Kokai tokkyo Koho 04,013,768 a2.
- [69] H. Fujiki, Addition-Curable Silicone Rubber Adhesive Compositions, Japan, Kokai tokkyo Koho 08,291,254 a2, 1996.

- [70] N. Nishiwaki, T. Urabe, Storage-Stable Siloxane Compositions Curable by Addition Reaction, Japan, Kokai Tokkyo Koho 06,345,969 A2, 1994.
- [71] K.C. Melancon, Latently-Curable Organosilicone Release Coating Compositions, US Patent 4,504,645, 1985.
- [72] O. Brummer, E.D. Carlson, T. Crevier, Y. Giraud, A.-M. la Pointe, S. Sterin, Catalytic PGM Mixture for Hydrosilylation, Wo/2003/050174, 2003.
- [73] V. Seitz, K. Arzt, S. Mahnel, C. Rapp, S. Schwaminger, M. Hoffstetter, Improvement of adhesion strength of self-adhesive silicone rubber on thermoplastic substrates—comparison of an atmospheric pressure plasma jet (APPJ) and a Pyrosil[®] flame, *Int. J. Adhes. Adhes.* 66 (2016) 65–72.
- [74] T. Otomo, T. Tasaki, Silicone Rubber Composition and Composite Made Therefrom, Dow Corning Toray Co., Ltd., 2021. US10968375B2.
- [75] P. Beyer, D. Ahn, F. de Buyl, I. Kaldewey, M. Tischendorf, J. Treharne, R. Vanecek, Trends and New Requirements for Silicone Elastomers in Mobility and Transportation, Silicone Elastomers World Summit, Berlin, Germany, 2021.
- [76] T. Lin, Y. Wu, E. Santos, X. Chen, D. Ahn, C. Mohler, Z. Chen, Molecular insights into adhesion at a buried silica-filled silicone/polyethylene terephthalate interface, *Langmuir* 36 (49) (2020) 15128–15140.
- [77] J. Stein, R.P. Eckberg, UV-curable silicone release coatings and controlled release additives, *J. Coat. Fabr.* 20 (1990) 24–42.
- [78] F. De Buyl, Silicone sealants and structural adhesives, *Int. J. Adhes. Adhes.* 21 (2001) 411–422.
- [79] E.P. Plueddemann, Silane Coupling Agents, Springer Science+Business Media, New York, 1982.
- [80] Y. Sato, H. Inomata, Curable Organosilicon Compositions, US3996195, 1974.
- [81] Y. Hamamoto, T. Kashiwagi, Silicone Resin Composition and an Optical Semiconductor Device, US9117985, 2014.
- [82] H. Hara, Addition Cure Silicone Rubber Adhesive Composition and Making Method, US7825177, 2007.
- [83] J.H. Wu, Y.K. Chen, Z. Shen, J.L. Huang, N.S. Chen, Surface energy of mineral powders and interaction between silicone, *J. Mater. Sci. Lett.* 18 (6) (1999) 461–462.
- [84] B.P. Bayly, One Component Room Temperature Vulcanizable (RTV) Silicone Sealant with Improved High Temperature Adhesion, US Patent 5,932,650, 1999.
- [85] B.W. Carlson, B.S. Glasbrenner, High Temperature Sealant Containing Phenyl Silicone, US Patent 5,310,588, 1994.
- [86] S.B. Lin, High-temperature stability of silicone polymers and related pressure sensitive adhesives, in: *High Temperature Properties and Applications of Polymeric Materials*, ACS Symposium Series, vol. 603, 1995, pp. 37–51.
- [87] F. Achenbach, W. Hechtel, G. Eberl, N. Egerter, S. Schreyer, Porphyrin Containing Silicones Having Increased Thermal Stability, US Patent 5,847,034, 1998.
- [88] P. Delatorre, M.D. Beers, Self-Extinguishing Room Temperature Vulcanizable Silicone Rubber Compositions, US Patent 4,102,852, 1978.
- [89] K. Mitsuhashi, H. Tabei, Fireproof, Fire-Retardant Silicone Rubber Composition, Japanese Laid Open Patent Application JP 9,012,888, 1997.
- [90] K.E. Alvarez, K.L. Shephard, Fire Resistant Sealant Composition, US Patent 6,271,299, 2001.
- [91] N. Kobayashi, Y. Mizuishi, Electrically Conductive Silicon Rubber Composition Prepared by Mixing Silicone Rubber Base Material Containing Carbon Black with Ground

- Vulcanised Silicone Rubber, Japanese Laid Open Patent Application JP 61,108,661, 1986.
- [92] K. Higuchi, A. Nakamura, Silicone Rubber Composition Containing Alkenyl Containing Polydiorganosiloxane, Including Carbon Black and Curing Agent, Having Stable and Narrow Variation of Volume Resistivity, European Patent EP 0,392,262-b1, 1990.
- [93] M.A. Lutz, R.L. Cole, Flexible silicone adhesive with high electrical conductivity, in: Proceedings of IEEE 39th Electronic Components Conference, Houston, TX, 1989, pp. 22–24.
- [94] R.L. Cole, M.A. Lutz, Electrically Conductive Silicone Compositions, US Patent 5,075,038, 1991.
- [95] R.L. Cole, J.E. Fiori, M.A. Lutz, Organosiloxane Composition Curable to Electro-Conductive Material, Contains Silver-Particles Coated with Fatty Acid Ester, European Patent EP 0,545,568-b1, 1993.
- [96] K. Mine, K. Nakayoshi, R. Tazawa, Electrically Conductive, Curable Organosiloxane Composition Containing Ag Particles Treated with Organo-Si Compounds Containing Si-Bonded Alkoxy Groups, European Patent EP 0,647,682b1, 1995.
- [97] D.L. Kleyer, M.A. Lutz, Silicone Composition and Electrically Conductive Silicone Adhesive Formed Therefrom, US Patent 6,361,716, 2002.
- [98] D.L. Kleyer, M.A. Lutz, Electrically Conductive Hot-Melt Silicone Adhesive Composition, US Patent 6,433,055, 2002.
- [99] D.L. Kleyer, M.A. Lutz, Silicone Composition and Electrically Conductive Silicone Adhesive Formed Therefrom, US Patent 6,534,581, 2003.
- [100] J.C. Getson, M.A. La Scola, Electrically Conductive, Cured Silicone Rubber Compounds, Made from Storage-Stable Compositions Based on Known Organopolysiloxane Composition Containing Silver-Coated Mica and Carbon Black Stabilizer, US Patent 4,777,205, 1988.
- [101] H. Adachi, N. Suganuma, Electrically Conductive, Moisture-Curable Silicone Rubber Sealants Obtained by Blending Polyorganosiloxane with Silane or Siloxane Curing Agent and Blending the Mixture with Light-Coloured Electrically Conductive Metal Oxide Filler, European Patent EP 0,558,044-b1, 1993.
- [102] R.C. Rogelhof, J.L. Throne, R.R. Ruetsch, Methods for predicting the thermal conductivity of composite systems: a review, *Polym. Eng. Sci.* 16 (9) (1976) 615–625.
- [103] J.C. Getson, M. Pate, Thermally Conductive Room Temperature Vulcanizable Silicone-Elastomer Containing Silicon Nitride Filler, US Patent 4,584,336, 1986.
- [104] L.N. Lewis, S.K. Gifford, S. Rubinsztajn, Curable Silicone Compositions, Methods and Articles made Therefrom, US Patent 6,639,008, 2003.
- [105] E.A. Joseph, The role of silicone adhesives and sealing materials in the assembly of automotive exterior lighting components, in: RAPRA Automotive Adhesives, Sealants and Coatings Conference, Stuttgart, Germany, 10–11 June, 2008, 2008.
- [106] General Motors (GM), Engineering Standards, Material Specification: Adhesives (GMN11280), Performance Requirements of an Exterior Lighting Structural Adhesive, General Motors Corporation, 2006.
- [107] M. Maier, J. Moisel, F. Herold, Multibeam headlights in the Mercedes-Benz CLS-class, *ATZ World* 117 (2015) 4–9, <https://doi.org/10.1007/s38311-015-0156-0>.
- [108] M. Maier, A.G. Daimler, Multibeam LED lights up the night. The future of illumination technology at Mercedes-Benz, in: IQPC 15th Intelligent Automotive Lighting conference, Dusseldorf, January 28, 2015.

- [109] A. Kochanke, J. Nagel, C. Ueffing, A. Hartwig, Influence of addition curing silicone formulation and surface aging of aluminum adherends on bond strength, *Int. J. Adhes. Adhes.* 95 (2019) 102424, <https://doi.org/10.1016/j.ijadhadh.2019.102424>.
- [110] A. Kochanke, K. Kraemer, C. Ueffing, A. Hartwig, Influence of high-temperature and high-humidity aging on the material and adhesive properties of addition curing silicone adhesives, *Int. J. Adhes. Adhes.* 111 (2021) 102980, <https://doi.org/10.1016/j.ijadhadh.2021.102980>.
- [111] S. Jobst, M. Stommel, Experimental and simulative characterization for material and lifetime modelling of a silicone adhesive, *Int. J. Adhes. Adhes.* 113 (2022) 103042, <https://doi.org/10.1016/j.ijadhadh.2021.103042>.
- [112] F. de Buyl, S. Yoshida, Degradation mechanisms of silicones, in: W.D. van Driel, M.Y. Mehr (Eds.), *Reliability of Organic Compounds in Microelectronics and Optoelectronics*, Springer publisher, 2022, ISBN: 978-3-030-81575-2, <https://doi.org/10.1007/978-3-030-81576-9> (Chapter 1).
- [113] A. Dupont, Characterization of silicones, in: R. De Jaeger, M. Gleria (Eds.), *Silicones in Industrial Applications, Inorganic Polymers*, Nova Sciences Publisher, 2008 (Chapter 2).
- [114] C.E. Weir, W.H. Leser, L.A. Wood, Crystallization and second-order transitions in silicone rubbers, *J. Res. Natl. Bur. Stand.* 44 (1950) 367–372.
- [115] B.A. Banks, K.K. de Groh, S.K. Rutledge, F.J. DiFilippo, *Prediction of In Space Durability of Protected Polymers Based on Ground Laboratory Thermal Energy Atomic Oxygen*, NASA technical Memorandum **107209**, NASA, Washington DC, 1996.
- [116] B.A. Banks, R. Demko, Atomic Oxygen Protection of Materials in Low Earth Orbit, NASA Technical MEMORANDUM 211360, NASA, Washington, DC, 2002.
- [117] J.D. Ferry, *Viscoelastic Properties of Polymers*, second ed., John Wiley & Sons, New York, 1970.
- [118] K. Yarosh, A.T. Wolf, S. Sitte, Evaluation of silicone sealants at high movement rates relevant to bomb mitigating window and curtain wall design, *J. ASTM Int.* 6 (2) (2009), <https://doi.org/10.1520/JAH101953>.
- [119] E. Wang, M. Yu, V. Hayez, M. Jiang, Technical considerations and performance of structural glazing glass façade of high-rise building in extreme climate (Proceedings of Glass Performance Days Conference), 2019.
- [120] K.A. Broker, S. Fisher, A.M. Memari, Seismic racking test evaluation of silicone used in a 4-sided structural sealant glazed curtain wall system, in: 4th Symposium on Durability of Building and Construction Sealants and Adhesives, 2011.
- [121] G. Beaucarne, S.C. Wang, X. Sun, Y. Wu, Y. Huang, N. Shephard, Back in the PV galaxy: the return of the silicone module, in: Proceedings of the 32nd European Photovoltaic Solar Energy Conference and Exhibition (EU PVSEC), Munich, Germany, 2016, pp. 89–93.
- [122] G. Beaucarne, A. Dupont, D. Puthenmadom, N. Shephard, T. Sample, Material study of photovoltaic modules with silicone encapsulation after long-term outdoor exposure, *Sol. Energy Mater. Sol. Cells* 230 (2021) 111298, <https://doi.org/10.1016/j.solmat.2021.111298>.
- [123] www.dow.com/documents/en-us/mark-prod-info/63/63-6668-01-dowsil-995-simulation-data-sheet.pdf. Consulted August 25th, 2022.
- [124] Technical Note FKG 01/2021, Structural Silicone Sealants in Structural Glass Systems, 2021. https://glas-fkg.org/v2/images/Merkblaetter/210921_Technical_Note_FKG_01-2021_Structural_silicone_sealant_en.pdf. (Accessed April 2022).
- [125] S. Sitte, V. Hayez, J. Kimberlain, M. Mirgon, J. Feng, Structural silicone joint behavior study for cold bent glass, *Glass Struct. Eng.* 6 (2021) 39–63, <https://doi.org/10.1007/s40940-020-00125-7>.

-
- [126] P. Descamps, G. Van Wassenhove, V. Hayez, Simulating structural silicone glazing joint deformation with spring models, *Glass Struct. Eng.* 5 (2020) 171–185.
- [127] P. Descamps, V. Hayez, M. Chabih, Next generation calculation method for structural silicone joint dimensioning, *Glass Struct. Eng.* (2017) 169–182.
- [128] P.L. Rosendahl, M. Drass, J. Felger, J. Schneider, W. Becker, Equivalent strain failure criterion for multiaxially loaded incompressible hyperelastic elastomers, *Int. J. Solids Struct.* 0020-7683, 166 (2019) 32–46, <https://doi.org/10.1016/j.ijsolstr.2019.01.030>.

This page intentionally left blank

Emerging structural adhesive chemistries and innovations

7

Erich Bain^a, Marvin Pollum^b, David Fortman^b, Martin E. Losada^b, Christopher M. Jackson^c, and Robert Jensen^d

^aEngineering Systems, Inc., Dallas, TX, United States, ^bCoatings Innovation Center, PPG Industries, Inc., Allison Park, PA, United States, ^cCivil and Environmental Engineering Department, Virginia Tech, Blacksburg, VA, United States, ^dU.S. Army Combat Capabilities Development Command, Army Research Laboratory, Aberdeen Proving Ground, MD, United States

7.1 Introduction

The modern range of available structural adhesive chemistries is very broad. Major chemical families include epoxies, polyurethanes, reactive acrylics, hybrid formulations, silicones, cyanoacrylates, and more specialized resins. In combination with innumerable additives, fillers, carriers, and processing methods, these chemistries offer a dizzying array of property and design options. Property ranges offered by today's chemistries encompass shear moduli (stiffness) ranging from a few MPa for semistructural elastomers to 10s of GPa for highly filled glassy thermosets; lap shear strengths in excess of 40 MPa; use temperature ranges below -50°C and in excess of 200°C (though few chemistries perform well across this entire range); flexibility, peel, and impact resistance; damping; durability; fatigue resistance; environmental and chemical resistance; esthetics; and much more. Structural adhesives are available as one or multiple component formulations in film, paste, or liquid forms with the ability to control a broad range of properties including viscosity, cure time, pot life, and cure shrinkage. They can be optimized for performance at different application thicknesses, and to bond to metals, plastics, composites, and other substrates with or without extensive surface preparation. This vast range of chemistry and formulation options enables engineers to continue pushing the boundaries of design, manufacturability, performance, and durability in industries as diverse as aerospace, automotive, marine, building construction, energy, and more.

Despite the wealth of options currently available, novel chemistries and adhesive innovations are continually developed to address emerging needs and enable next-generation systems with lighter weight and improved performance, manufacturability, sustainability, reliability, cost, and durability for extreme service challenges. In this chapter, we highlight select emerging developments in the areas of structural adhesives that push the boundaries of the process by which structural adhesives are currently developed, tested, and applied in the field. We begin with a discussion of novel strategies for bond strength retention during overload failure, an area with applications in military protective systems and crashworthy structural components where modeling

and prediction of performance are notoriously difficult. We further discuss novel chemistries with the potential to generate improved toughness adhesives or provide additional features, such as debondability, to structural adhesive joints. We close the chapter with a view of potential opportunities offered by standardized digital property databases, leveraging modern computational tools to enhance adhesive selection, design, and processing, which may ultimately help propel the adhesives industry into markets that have thus far resisted adoption of adhesive bonding as a viable design and manufacturing strategy. We hope this chapter will serve as an interesting and useful introduction to select emerging innovations in adhesives chemistry and application, which ideally will spark readers' interest to explore these topics more thoroughly.

7.1.1 Rethinking design rules

One motivation for leap-ahead innovations in structural adhesive chemistries will be in response to bonded joint designs requiring substantial strength retention beyond linear peak elastic stresses into nonlinear domains of plastic deformation. Such criteria are found where there is a high probability of catastrophic failure during the service lifetime of the article, such as bonded military armor or side-impact crashworthiness structures used for passenger compartment protection in automobiles [1]. This is in direct contrast to traditional aerospace applications, where high-strength but relatively brittle structural adhesives can trace a continuous use lineage dating back to the 1930s. Zero-failure adhesive bonding environments, such as flight, use joint designs based on linear-elastic loading with service strengths defined from partial safety factors [2], offsets from peak loads [3], or fracture mechanics [4].

Precedents for designing with high levels of postfailure strength retention have been established in civil engineering applications where the behavior of rock mass is critical for modeling ground reaction curves for tunnel excavation. Rock mass is rated using a geological strength index that can be high (brittle), low (perfectly plastic), or intermediate (strain softening), which mirrors the range of possible responses found in polymeric adhesives. Accurately modeling postfailure residual strength envelopes proves to be the most difficult for strain softening rock masses due to modulus and dilatancy characteristics that are confinement stress dependent [5]. Traditional analytical convergence confinement methods used by tunnel designers are challenged by strain softening loading behavior, which is problematic due to the high prevalence of this type of rock mass encountered in the natural environment. Similar concern for strain energy dissipated after the peak load is also crucial in retaining strength during floor heave events in longwall gate roads used in mining operations [6]. Strength retention after initial cracking of structural beams is a recurrent theme in civil engineering, where avoidance of sudden collapse is an essential design consideration [7].

To date, limited postfailure design methodologies have been adopted for adhesive bonding. Finite element (FE) analysis has been used to model postelastic response of adhesively bonded joints using failure criterion defined by singularity-free peak elastic stresses [8]. In this work, the overall load versus displacement curve to complete failure was considered, which included the postelastic yielding of the adherends. The FE model predicted a loading response of a perfectly plastic adhesive as higher than a brittle counterpart for the complete displacement domain due to its ability to

support load after yielding. Despite potentially enhanced bonding performance, experimental studies and further computational modeling of adhesive joints with significant nonlinear postpeak yielding and adherend deformation are exceptionally sparse in the academic literature.

Strength retention after peak loading, plastic strain energy dissipation, and yielding of the adherend are all considered for adhesive bonding in the recent US Army performance requirement MIL-PRF-32662 [9,10], which was derived using statistical correlations between single-lap joints and damage tolerance to ballistic events in bonded lightweight armor packages. A simple damage tolerance assessment of an adhesive can be made at low levels of effort by measuring maximum lap shear strength (S_{\max}) and crosshead displacement at complete failure (d_{failure}) using standard 1.6 mm thick Al 2024-T3 adherends under quasistatic loading conditions at room temperature. Adhesives with high strength retention beyond adherend yielding lead to significant adherend deformation and relatively high displacements, which permanently bends and stretches the single-lap joint specimen during loading. Fig. 7.1 shows the property assignment regions for adhesive group categories in MIL-PRF-32662, with the inclusion of experimental data points collected from multiple commercial adhesives.

The adhesives used to derive MIL-PRF-32662 can be partitioned into four groups:

- Group I—high ballistic damage tolerance.
- Group II—industrial-grade structural (including automotive/aerospace).

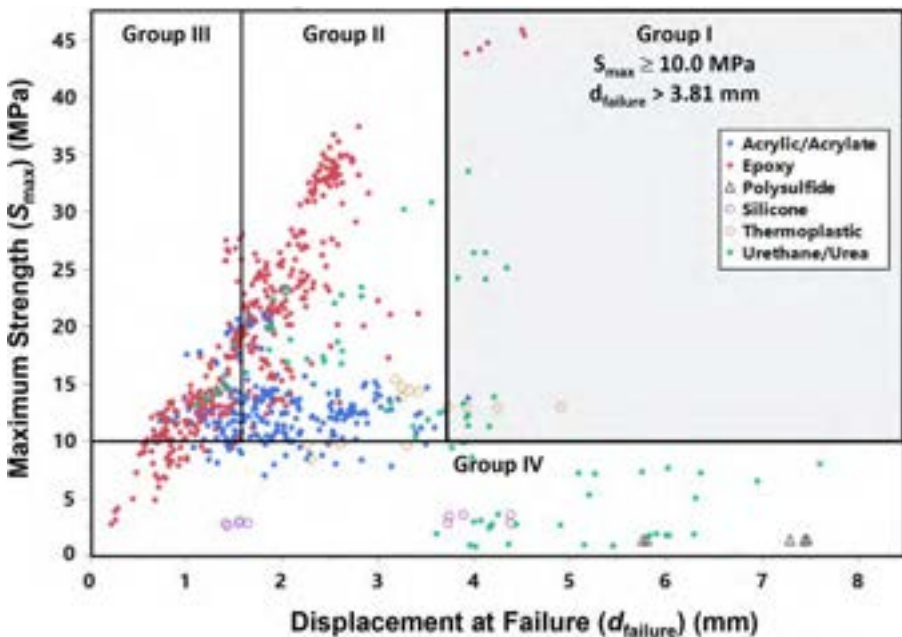


Fig. 7.1 Experimental population of adhesive groups based upon single-lap joint strength and failure displacement performance. Per MIL-PRF-32662 Tier I dry conditioning and room temperature testing. Substrate material is Al 2024-T3.

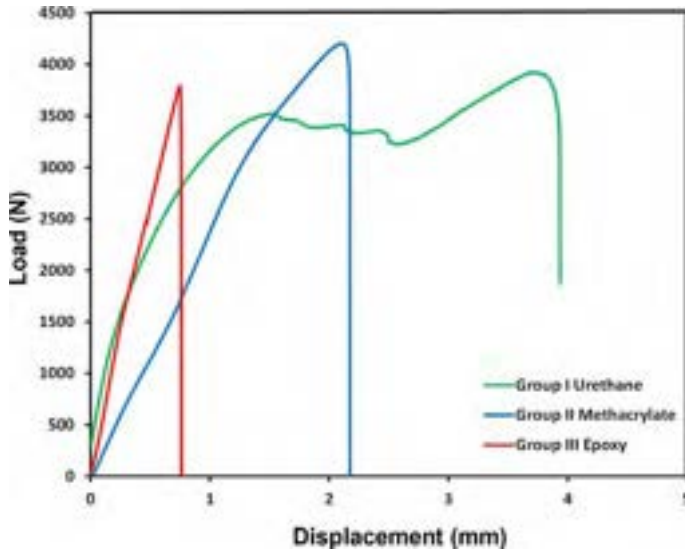


Fig. 7.2 Representative single-lap joint load vs displacement curves for MIL-PRF-32662 Group I, II, and III adhesives.

- Group III—consumer-grade structural.
- Group IV—low tensile strength (polysulfides, silicones, urethanes).

Fig. 7.2 shows the single-lap joint load versus displacement response for representative Group I urethane, Group II methacrylate, and Group III epoxy adhesives at room temperature. (See also [Chapter 3](#), [Chapter 2](#), and [Chapter 1](#), respectively, for more details on these adhesive chemistry families.)

A ballistic event near the protection limit of the bonded armor assembly will without exception result in complete failure of the adhesive. Any linear or nonlinear strain energy dissipation mechanism that the adhesive can engage during this inevitable total drop in loading capacity is beneficial to optimizing the protection ability of the armor package and localizing the damage area, which is crucial to surviving multiple battlefield engagements. Group I represents a challenging performance region that is not easily obtainable by a majority of existing commercial adhesive products, but offers enhanced ballistic damage tolerance in some bonded armor configurations. Epoxies have difficulty in obtaining Group I requirements due to relatively low strains to failure. Urethanes, with single-lap joint strengths above 10 MPa, offer excellent post-failure strength retention, but can be limited by poor elevated temperature tolerance. The performance requirements for Group I were written as a “window” ($S_{\max} > 10 \text{ MPa}$ and $d_{\text{failure}} > 3.81 \text{ mm}$) as armor evolution is constantly adapting to new battlefield threats and is unpredictable, with stronger adhesives not always offering the best solution. MIL-PRF-32662 Group I represents a difficult performance region regardless of location in the requirement window, which may provide unique opportunities for adhesives beyond armor intentions.

7.2 Structural adhesives innovations

7.2.1 Furthering mechanical performance attributes in applications with a high probability of overload failure

Recent work at PPG has focused on achieving Group I adhesive performance with a toughened epoxy system due to the benefits of typical structural epoxies, including high temperature tolerance, stiffness, strength, chemical stability, low cure shrinkage, and lack of volatile reaction products. Initially, the epoxy adhesives were modified in an attempt to sacrifice some of the high adhesive strength for improved displacement of the joint before failure. It was found that regardless of the chemical or physical methods used to flexibilize and/or toughen the epoxy materials, the ultimate adhesive failure exhibited a linear relationship with the gross lap shear deformation as measured by crosshead displacement. This trend is similar to previous observations by Jensen et al. [11] and highlights the need to significantly alter traditional epoxy resins, flexibilizers, and hardeners to shift the adhesive performance beyond this limitation.

The gross lap shear displacements reported in Fig. 7.3 are known to primarily capture the Al 2024-T3 adherend deformation and are therefore more indicative of the adhesive's ability to transmit loads to the adherends than anything else. Bondline displacement turns out to be relatively insignificant to the gross displacement due to a combination of shear lag, the small adhesive dimensions relative to those of the adherends, and machine compliance from the load train. Fig. 7.4 shows the partitioned displacements determined from a finite element model of a lap shear joint, where the vertical axis corresponds to the nominal bond shear stress (load divided by bond area). The crosshead displacement includes the displacements of both the lap shear specimen and a spring boundary condition used to model the effective machine and wedge grip

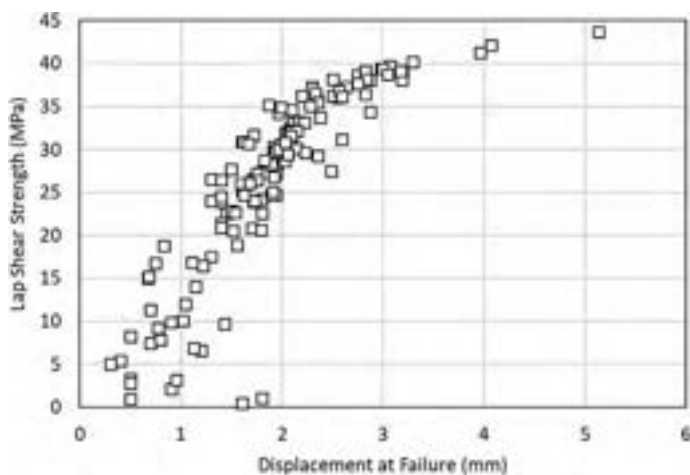


Fig. 7.3 Single-lap joint maximum load versus crosshead displacement at failure for modified epoxy adhesives bonding Al 2024-T3 substrates. Each data point represents the average performance of a unique epoxy adhesive formulation.

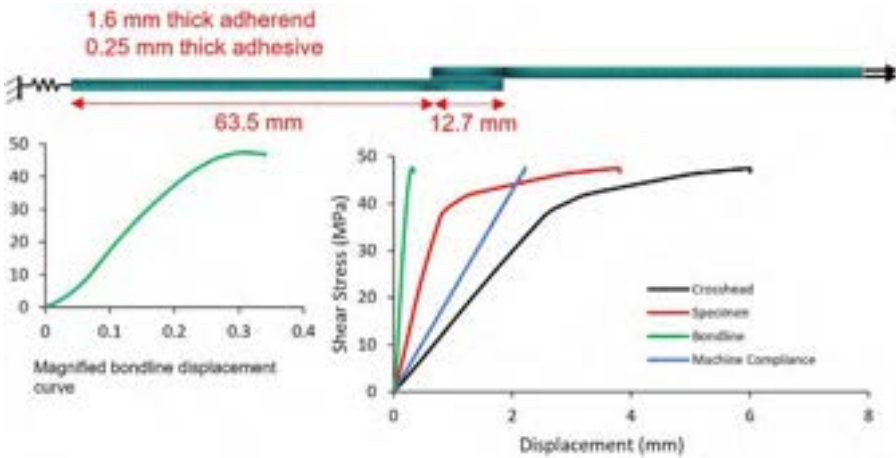


Fig. 7.4 Single-lap joint (A) model used in finite element analysis to partition (B) the different displacements as analyzed from different reference points. The machine compliance and adherend deformations can be seen to dominate the overall crosshead displacement, especially as the adherends plastically deform. The shear stress plotted on the y-axis refers to the shear stress in the bondline.

compliance. The specimen displacement was analyzed at the terminal ends of the adherends and bondline displacement was analyzed at the terminal ends of the bondline. The analysis of bondline displacement is similar to the method described in [Chapter 32](#), where digital image correlation (DIC) was used to measure the displacement of each adherend slightly beyond the ends of the bond. For a test that has about 6 mm of measured crosshead displacement, bondline displacement was found to contribute less than 10% of crosshead displacement. Viewing [Fig. 7.3](#) in light of this analysis, it is noteworthy how few adhesive formulations had sufficient integrity to transmit loads capable of plastically deforming the Al 2024-T3 adherends, which is what is required to achieve the large displacements desired. These large displacements seen after adherend yield are largely controlled by plastic tensile deformations of the adherends, with the ratio of adherend to adhesive deformations becoming much larger beyond this point. For more discussion on measuring and partitioning deformations in single-lap joints, see [Chapter 32](#).

Exploration of significantly softer epoxy resins compromised the strength and thermal robustness of the adhesives, so the researchers instead focused on maximizing the combined strength and toughness of the epoxy material. Group I adhesive performance was achieved with a one-component, high-temperature cure ($>160^{\circ}\text{C}$) epoxy structural adhesive. [Fig. 7.5](#) presents a TEM cross-section of the cured epoxy material. The high density of monodisperse, sub-100 nm toughening phases within an optimized epoxy matrix affords the material with high modulus and high yield stress yet a large amount of plastic deformation after yielding ([Fig. 7.6](#); for further discussion on toughening strategies for structural adhesives, see [Chapter 8](#)).

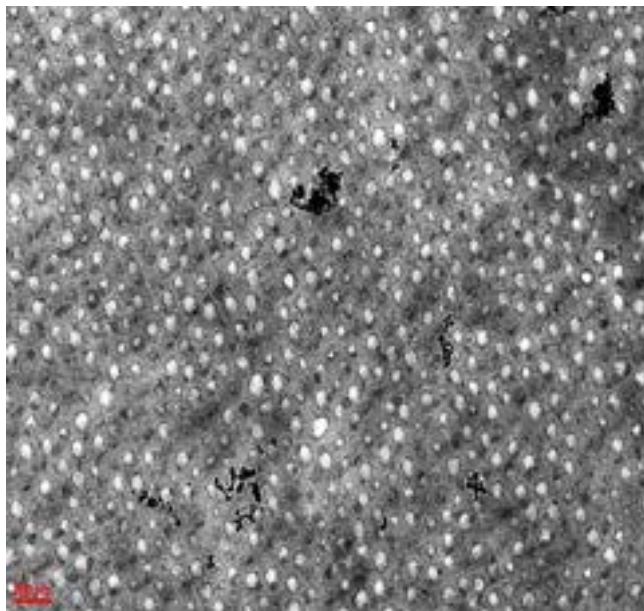


Fig. 7.5 TEM cross-section of cured toughened epoxy adhesive; the scale bar is 200nm.

The Group I toughened epoxy adhesive material exhibits a bulk shear stress of 65 ± 2 MPa and a shear strain before failure of $64 \pm 6\%$, resulting in a total strain energy density of 30 ± 3 MPa. This is nearly twofold higher than the maximum shear stress and strain measured for a state-of-the-art industrial epoxy structural adhesive material (34 ± 2 MPa and $35 \pm 5\%$). As demonstrated in Fig. 7.6, single-lap joints constructed in accordance with MIL-PRF-32662 exhibit significant bending modes and plastic deformation of the aluminum adherends when the joint approaches and exceeds a load of 40 MPa. Therefore, Group I performance of the epoxy adhesive material can only be realized with this combination of higher strength, higher ductility, and superior aluminum adhesion.

In addition to single-lap joint performance at room temperature, it is important that a structural adhesive exhibit high durability, with performance across a broad temperature range and after prolonged environmental exposure. Tiers II and III of MIL-PRF-32662 begin to address these exposure and lifetime concerns for structural adhesive technologies. The Group I epoxy structural adhesive developed maintains many of the inherent benefits of epoxy-based structural adhesives, wherein the robust adhesion, high glass transition temperature (T_g), and high crosslink density result in adhesive durability. The Group I epoxy structural adhesive maintains 78% of the initial shear strength after 2-week immersion in hot water (63°C), and 82% of the initial shear strength when tested at elevated temperature (71°C), in accordance with Tier II of MIL-PRF-32662. Overall, the Group I epoxy adhesive maintains structural performance from -50°C to $+100^\circ\text{C}$ (Fig. 7.7).

The long-term durability of the adhesive was also evaluated under both static and dynamic conditions. Static load performance was investigated on 12.7 mm thick

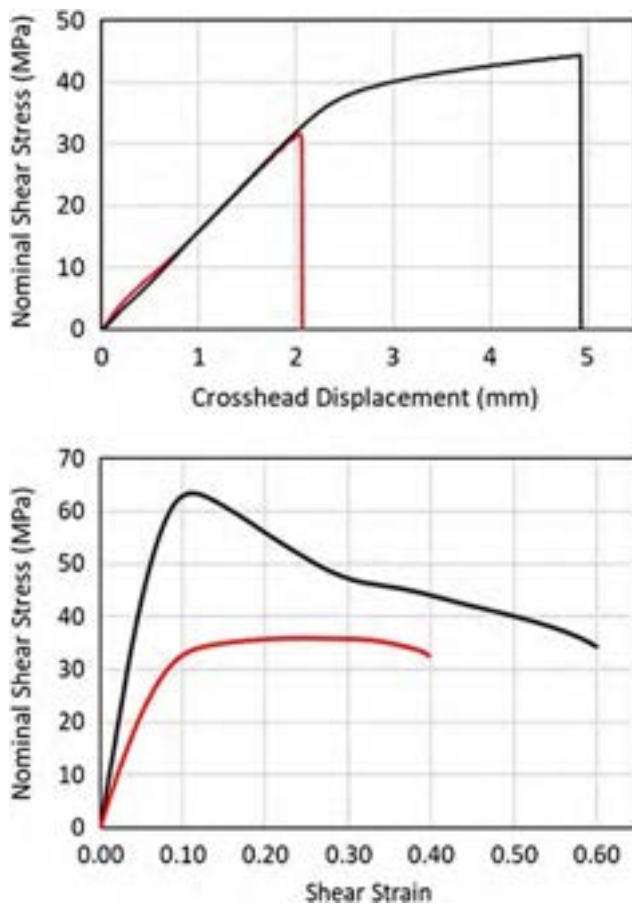


Fig. 7.6 Representative single-lap joint performance (top) and bulk shear properties (bottom) for the developed Group I epoxy structural adhesive (*black*) as compared to a state-of-the-art industrial epoxy structural adhesive (*red*). Single-lap joint measurements on T3-2024 aluminum, in accordance with MIL-PRF-32662. Bulk shear properties measured in accordance with the Thick Adherend Shear Test, ISO 11003-2.

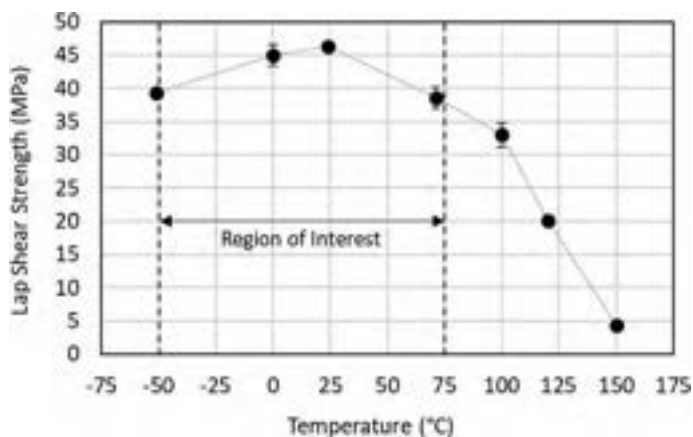


Fig. 7.7 Lap shear strength of Group I epoxy structural adhesive measured at temperatures from -50°C to 150°C . All samples prepared and measured in accordance with MIL-PRF-32662. The “Region of Interest” represents the standard service temperature range for many industrial applications.

T3-2024 aluminum with the bonding surface prepared via grit blasting and epoxy-silane treatment, as described in ARL-SR-0356 [12]. The adhesive bondline thickness was controlled at 250 μm and test specimens were held in an oven at 180°C until the bondline reached >170°C for at least 30 min to cure the adhesive. After cure and cooling, specimens were placed under static load and held at elevated temperature and humidity (60°C, 100% relative humidity) for 5 weeks, in accordance with Tier III of MIL-PRF-32662. Throughout this time, the initial crack only propagated through the adhesive an average of 73 mm from the loading point, corresponding to a Mode I fracture toughness (G_{ISCC}) of 4.5 kJ/m² and well above the Tier III specification of 0.61 kJ/m² in MIL-PRF-32662.

The dynamic fatigue resistance was investigated on 4.8 mm thick T3-2024 aluminum with the same surface preparation, bondline thickness, and cure conditions as described above. Single-lap joints were prepared with an overlap length of 9 mm and cyclically loaded at a rate of 20 Hz, in accordance with ASTM D3166-99. Fig. 7.8 compares the resulting performance against Wöhler fatigue curves reported in the literature for conventional and advanced epoxy adhesives. The combined high strength and ductility of the PPG Group 1 epoxy resulted in adhesive joints that withstood more than 1,000,000 cycles to failure when cycled at a dynamic maximum load of 27.5 MPa. It is worth noting that this load is sufficient to fail many structural adhesive joints in a single cycle.

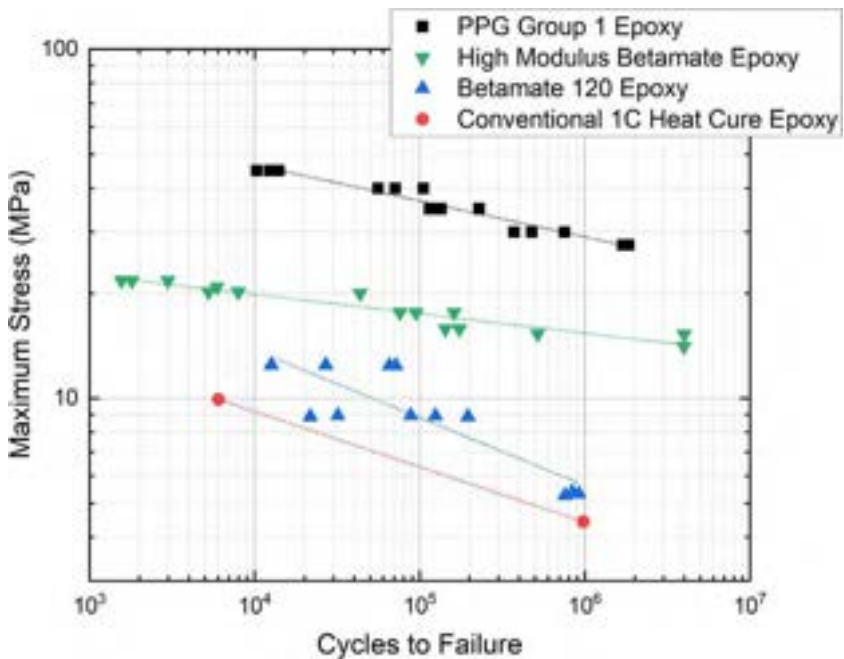


Fig. 7.8 Fatigue properties of PPG Group 1 epoxy adhesive (*black square symbols*) measured on 4.8 mm thick T3-2024 aluminum (ASTM D3166-99) with an overlap length of 9 mm and cyclically loaded at a rate of 20 Hz. Results for other epoxy structural adhesives are reproduced from the literature for comparison: high modulus Betamate [13], Betamate 120 [14], and conventional one-component heat cure epoxy [15].

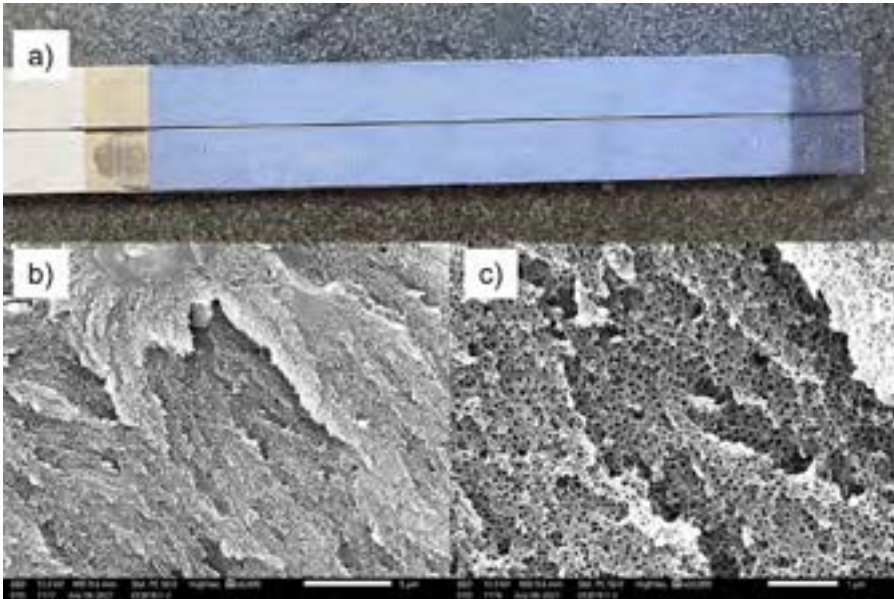


Fig. 7.9 Photograph (a) and scanning electron micrographs (b and c) of adhesive fracture surface from double cantilever beam specimens after Mode I testing of PPG Group 1 epoxy adhesive. The scale bars in (b) and (c) are 5 μm and 1 μm , respectively.

The complete fracture envelope of this adhesive has recently been characterized. Analysis of the adhesive fracture surface in double cantilever beam (DCB) specimens after Mode I testing (Fig. 7.9) shows stress whitening along the adhesive layer. A more detailed analysis of these failure surfaces using scanning electron microscopy reveals voids from the cavitation of toughening domains, one of the mechanisms that allows for ductility to be achieved. The material properties of this adhesive, including fracture energies under tensile (Mode I) and shear (Mode II) loadings, are compiled in Table 7.1. The Mode I fracture energy, G_{Ic} , of the Group 1 epoxy adhesive was measured to be 3200 J/m² on average, but as high as 4600 J/m² in DCB tests. The toughness

Table 7.1 Material properties of PPG Group 1 epoxy adhesive.

Property	Value
Young's modulus ^a	2890 MPa
Shear modulus ^b	980 MPa
Tensile strength ^{c, d}	80 MPa
Shear strength ^c	65 \pm 2 MPa
Mode I fracture energy (G_{Ic}) ^c	3200 \pm 450 J/m ²
Mode II fracture energy (G_{IIc}) ^c	14,000 J/m ²

^a Value from bulk adhesive tensile test.

^b Value from thick adherend shear test data.

^c Value from butt joint test.

^d Measured from DCB and ENF fracture tests.

of the adhesive caused significant plastic deformations of substrates during end-notched flexure (ENF) tests. This does not allow for a simplified calculation of the Mode II fracture energy, G_{IIc} , with closed-form solutions. To solve this problem, finite element analysis with cohesive zone modeling was used. Simulations of the ENF test found that a G_{IIc} of 14,000 J/m² resulted in a good fit between numerical and experimental results. Cohesive zone models of the DCB, single-leg bend (SLB), and single-lap joint geometries were also simulated to provide validation of the properties given in Table 7.1.

While the Group 1 epoxy structural adhesive shows outstanding toughness and durability that should enable application in a wide range of markets, a high-temperature cure (160–200°C) is currently required to achieve these levels of performance. Achieving these properties with a lower cure temperature is an ongoing challenge to expand the use of this class of adhesive to further applications and large-scale manufacturing.

7.2.2 Fundamental structure-property-performance tradeoffs for structural adhesives

In their cured state, the major components of most structural adhesive formulations are crosslinked polymers, commonly referred to as thermosets. Mechanics of polymers are intimately related to their dynamics, which arise from combined effects of chemistry (e.g., monomer stiffness, hydrogen bonding) and structure (e.g., crosslink density). For amorphous polymers, these attributes result in a relaxation spectrum that is dominated by the glass transition temperature, T_g , corresponding to a drop in dynamic modulus typically of several orders of magnitude as temperature is increased from below to above T_g . In practice, T_g often governs the range of operating conditions, with maximum use temperatures for many structural adhesives limited to 20–30°C below T_g . Adhesives operating above their T_g can be favored in applications where relatively large deformations are expected, but for rigid, high-strength bonding, glassy (well below T_g) structural adhesives are commonly used. Fig. 7.10 shows the relaxation spectra of a series of polymers measured by dynamic mechanical analysis (DMA). The T_g is easily identified by a sharp drop in storage modulus (Fig. 7.10a) and primary peak in the loss tangent $\tan \delta$ (Fig. 7.10b), which for this series of polymers occurs over a range from 50°C to more than 150°C.

Epoxy adhesives are widely used in structural bonding due to their many material advantages discussed above; however, structural epoxies with high T_g are typically brittle, with failure strains on the order of 1% or lower. Polyurethanes (PU) offer a widely tunable range of properties, making them well-suited to applications requiring flexibility, ductility, and toughness. However, polyurethanes typically have glass transition temperatures well below 100°C, limiting their use in applications requiring high temperatures or high stiffness and strength. Reactive acrylics tend to cover the middle of the range of properties offered by other chemistries without offering as much flexibility as the lowest T_g polyurethanes, nor as much strength as the highest T_g epoxies, but with particular advantages in manufacturability and bonding to challenging

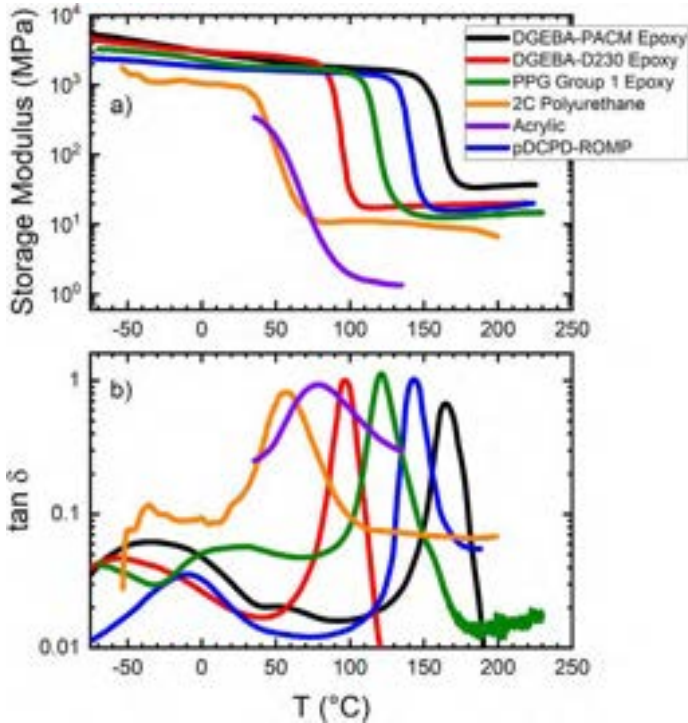


Fig. 7.10 Dynamic mechanical analysis of structural adhesive polymers: Diglycidyl ether of bisphenol A (DGEBA) epoxy cured with 4,4'-methylenebis(cyclohexylamine) (PACM), and DGEBA cured with polypropylene oxide-based Jeffamine diamine D230 (reproduced from Ref. [16]), PPG Group 1 epoxy adhesive (cured at 180°C for 30 min), high-strength two-component polyurethane (reproduced from Ref. [15]), reactive acrylic (reproduced from Ref. [17]), and poly(dicyclopentadiene) (pDCPD) cured by ring opening metathesis polymerization (reproduced from Ref. [16]).

substrates owing to their chain-growth polymerization mechanism and other unique chemical properties.

To improve toughness and ductility for adhesives in high-temperature applications, rubber-toughened epoxy and acrylic formulations have been developed over the past 50 years, providing greatly improved toughness while retaining many of the favorable properties of glassy thermosets. However, for structural adhesives, the returns are limited by the fact that toughening performance decreases as crosslink density increases, that is, as T_g , stiffness, and strength all increase, the toughening ability of rubbery inclusions becomes more modest [18].

Typical mechanical property ranges for epoxy, toughened epoxy, PU, and acrylic adhesive chemistries are illustrated by black squares, red circles, orange left-facing triangles, and purple right-facing triangles, respectively, in Fig. 7.11. Properties were taken from a combination of commercial product data sheets and peer-reviewed research reports [17,19–23]. Mode I fracture energy G_{IC} (Fig. 7.11c) was measured

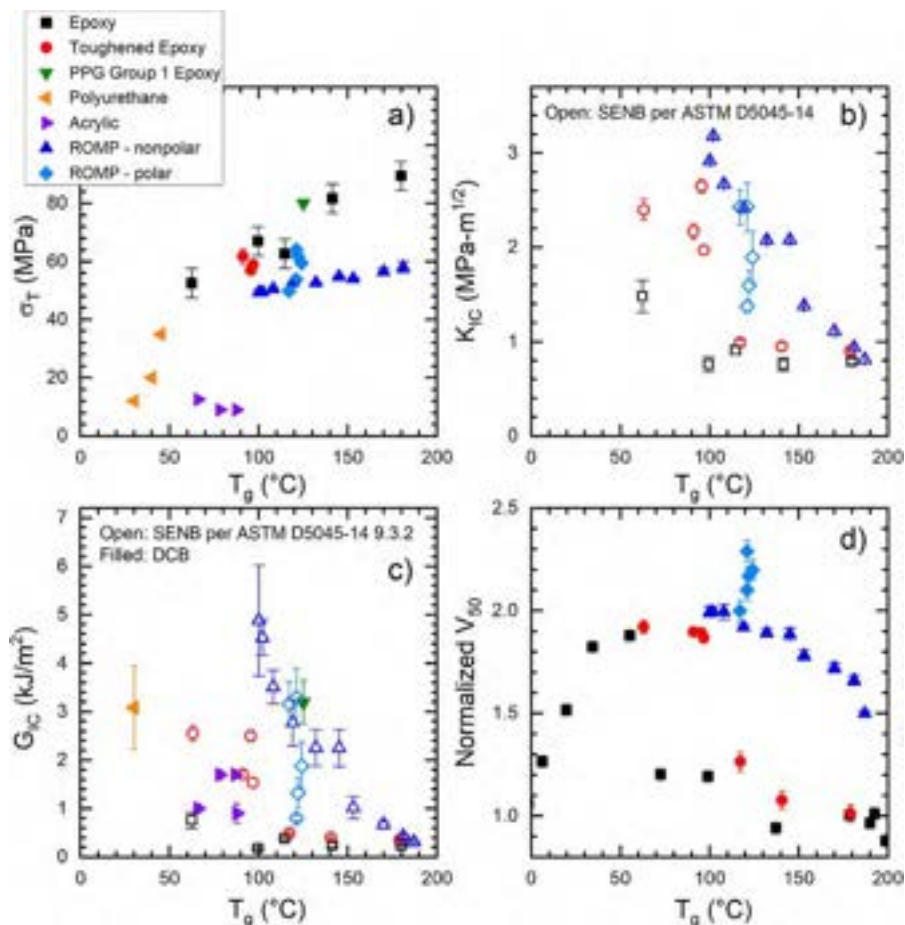


Fig. 7.11 Mechanical property comparison of structural adhesive chemistry families, plotted as a function of glass transition temperature T_g . (a) Tensile (yield) strength, (b) quasistatic mode I critical stress intensity factor K_{IC} measured using single edge-notched beam (SENB) specimens of cured plaques according to ASTM D5045, (c) Mode I fracture energy G_{IC} , including measurements from SENB specimens according to ASTM D5045 (*open symbols*) as well as double cantilever beam specimens (*closed symbols*), (d) normalized velocity at 50% probability of penetration (V_{50}) determined according to MIL-STD-662F using a 0.22 caliber gas gun with 5.56mm diameter stainless steel ball bearings.

Data reproduced from D.B. Knorr, J.H. Yu, A.D. Richardson, M.D. Hindenlang, I.M. McAninch, J.J. La Scala, J.L. Lenhart, Glass transition dependence of ultrahigh strain rate response in amine cured epoxy resins, *Polymer* 53(25) (2012) 5917–5923. <https://doi.org/10.1016/j.polymer.2012.09.058>; E.D. Bain, D.B. Knorr, A.D. Richardson, J.H. Yu, K.A. Masser, J. L. Lenhart, Failure processes governing high rate impact resistance of epoxy resins filled with core shell rubber nanoparticles, *J. Mater. Sci.* 51(5) 2016 2347–2370. <https://doi.org/10.1007/s10853-015-9544-5>; P. Gálvez, R.J.C. Carbas, R.D.S.G. Campilho, J. Abenojar, M.A. Martínez, L.F.M. da Silva, Fracture toughness in mode I (GIC) for ductile adhesives, *J. Phys. Conf. Ser.* 843 (2017) 012008. <https://doi.org/10.1088/1742-6596/843/1/012008> (6th International Conference on

(Continued)

using double cantilever beam specimens for polyurethane and acrylic adhesive specimens, whereas for the epoxy and toughened epoxy materials reported here, K_{IC} and G_{IC} were measured using single edge-notched beam (SENB) specimens of cured polymer plaques, using integration of load-displacement curves to determine G_{IC} according to ASTM D5045-14 part 9.3.2. Values of G_{IC} determined by different methods may not be quantitatively comparable; for example G_{IC} of a commercial epoxy structural adhesive was reported as $1 \pm 0.2 \text{ kJ/m}^2$ when measured using DCB specimens having bondline thickness much greater than the plastic zone size, whereas the same material exhibited G_{IC} of approximately 0.5 kJ/m^2 when tested using appropriately sized SENB specimens [24].

A series of cured solid epoxy plaques was formulated having systematically varying crosslink density and backbone chemistry [19,21]. Glass transition temperatures T_g were found to increase with increasing crosslink density and increasing monomer stiffness, as expected. Tensile yield strength was found to increase systematically with T_g (black squares in Fig. 7.11a) while fracture toughness K_{IC} and G_{IC} tended to decrease with increasing T_g (Fig. 7.11b and c), as had been previously observed [25].

Ballistic impact resistance V_{50} , the ballistic limit impact velocity as defined in MIL-STD-662F, was studied for unmodified epoxies [21] and found to exhibit a sharp peak for formulations with T_g of about $50 \pm 15^\circ\text{C}$ (black squares in Fig. 7.11d). On either side of this peak (e.g., for epoxies with T_g higher or lower than 50°C by about 15°C), V_{50} tended to drop off rapidly. Further testing across a range of measurement temperatures found peak impact resistance of a series of unmodified epoxies occurred approximately $25 \pm 15^\circ\text{C}$ below their T_g [26]. Based on these results, molecular relaxations, specifically the alpha relaxation associated with the glass transition, were hypothesized to play a primary role in high-rate energy dissipation and fracture resistance of amorphous thermosets.

Upon incorporating 1%–10% core-shell rubber toughening nanoparticles (KaneAce, Kaneka Americas) into a similar series of epoxies, ballistic impact resistance nearly doubled for epoxies within a narrow range of T_g from 60°C to 100°C (red circles in Fig. 7.11d). However, for epoxies with $T_g > 110^\circ\text{C}$, the effect of core shell

Fig. 7.11—Cont'd Fracture Fatigue and Wear, IOP Conf. Series); Sika, Structural Bonding Solutions. High Performance Adhesives. SikaFast, SikaPower, SikaForce. Technical Brochure, April 2018; Y. Sekiguchi, Y. Yamagata, C. Sata, Mode I fracture energy of adhesive joints bonded with adhesives with different characteristics under quasi-static and impact loading, *J. Adhes. Soc. Jpn.* 53(10) (2017) 330–337; A. Hayashi, Y. Sekiguchi, C. Sato, Effect of temperature and loading rate on the mode I fracture energy of structural acrylic adhesives, *J. Adv. Join. Process*, 5 (2022), 100079. <https://doi.org/10.1016/j.jajp.2021.100079>; T.R. Long, R.M. Elder, E.D. Bain, K.A. Masser, T.W. Sirk, D.B. Knorr, J.L. Lenhart, Influence of molecular weight between crosslinks on the rate dependent brittle-to-ductile transition in polymers formed via ring-opening metathesis, *Soft Matter* 14 (2018) 3344–3360, <https://doi.org/10.1016/j.polymer.2016.09.076>; J.M. Dennis, T.R. Long, A. Krishnamurthy, N.T. Tran, B. A. Patterson, C.E. Busch, K.A. Masser, J.L. Lenhart, D.B. Knorr, Influence of hydroxyl group concentration on mechanical properties and impact resistance of ROMP copolymers, *ACS Appl. Polym. Mater.* 2(6) (2020) 2414–2425. <https://doi.org/10.1021/acsapm.0c00352>.

rubber toughener incorporation on K_{IC} , G_{IC} , and V_{50} was minimal (Fig. 7.11b–d). In addition, ballistic resistance at temperatures below 0°C sharply decreased, even for formulations in the 60°C < T_g < 100°C range that exhibited good performance at room temperature. Hence, rubber toughening of epoxies was found to be practically insufficient for protective applications subjected to high-rate impact loading at high or low temperatures (for further discussions of core-shell rubber toughening, see Chapter 8).

As discussed above, T_g , tensile strengths, and single-lap joint strengths of PU and acrylic adhesives tend to be lower than those offered by highly crosslinked (thermally cured) epoxies (Figs. 7.1 and 7.11a and c) while fracture energies G_{IC} are comparable to those that can be achieved with rubber-toughened epoxies over a comparable range of T_g . Highly flexible PUs with T_g s in the range of –50°C can have G_{IC} as high as 20 kJ/m² [20] but they are soft adhesives suited for a very different application space than high-strength (higher T_g) polyurethanes or epoxies.

Nanophase separated epoxies were studied by Masser et al. [27,28]. By mixing short and long chain propylene oxide diamine hardeners in various proportions, optically transparent formulations were obtained demonstrating a near doubling of V_{50} with primary T_g approaching 150°C. This performance was found to correlate with dispersed phase separated domains on the order of 2–5 nm, which was hypothesized to facilitate ductility at the microscale while maintaining relatively high stiffness under macroscopic loading. However, the dispersed rubbery phase contributed a secondary T_g of approximately –50°C, making mechanical behavior complex over the range of typical use temperatures.

7.2.3 Ring-opening metathesis polymerization (ROMP)

Dicyclopentadiene (DCPD) is a low-cost chemical produced in abundant quantities by steam cracking of common petroleum fractions. DCPD has been used for decades as an additive and comonomer in polyester resins, rubbers, and many other polymer products to improve processability and properties. DCPD is amenable to ring-opening metathesis polymerization (ROMP) in the presence of appropriate transition metal catalysts due to its strained tricyclic ring structure and carbon-carbon double bonds (Fig. 7.12). ROMP of DCPD has been exploited commercially for reaction injection molding (RIM) to produce large molded components such as body panels for heavy machinery with outstanding dimensional stability, impact resistance, low-temperature performance, and environmental and chemical resistance. The low viscosity of DCPD and rapid cure kinetics of ROMP enable very large parts with greater than 100 ft² (10 m²) surface area weighing hundreds of pounds to be formed extremely quickly, with typical cycle times as low as 60 s from injection to demolding, all near room temperature. Similar monomers such as norbornene and 5-ethylidene-2-norbornene (ENB) are also polymerized by ROMP to produce commercially important materials.

ROMP catalyst development has historically been a primary factor limiting wider application of these polyolefin thermosets. Catalysts based on titanium, tungsten, and other transition metal complexes have been in commercial use since the 1980s, but these tend to be highly intolerant of air and moisture, limiting the use of ROMP to enclosed chambers with carefully controlled environments [29]. This has made

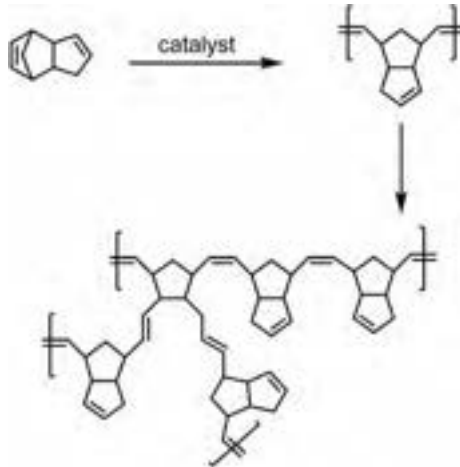


Fig. 7.12 Ring-opening metathesis polymerization of dicyclopentadiene followed by crosslinking of the secondary cyclopentene ring to form a thermoset.

ROMP suitable for RIM and resin transfer molding (RTM), but not for adhesives or other applications where curing must take place in ambient environments. Early catalysts were intolerant of most chemical functional groups, limiting the application to nonpolar hydrocarbons such as DCPD, and they offered poor control over molecular weight and its distribution. This situation has been changed over decades of painstaking work by many chemists, including Chauvin, Schrock, and Grubbs, to develop a wide library of ROMP catalysts that today offer improved tolerance of air, moisture, and polar functional groups as well as precisely controlled and versatile “living” polymerization capability. These efforts were recognized in 2005 with the Nobel Prize in chemistry, and are now finding their way into commercial applications including Materia, Inc., founded by Grubbs and recently acquired by ExxonMobil.

Thermosets formed by ROMP of DCPD using Grubbs’ catalyst tend to have T_g above 100°C (Fig. 7.10), and can be tuned over a T_g range similar to epoxies by incorporating additional crosslinking sites [30]. For a series of DCPD-based nonpolar ROMP resins studied at the US Army Research Laboratory (ARL), tensile yield stress σ_y was found to cover a range of 50–60 MPa (Fig. 7.11a, blue up-facing triangles). This is 25%–35% lower than epoxies at similar crosslink density and T_g , but higher than typical tensile strengths of PU and acrylic structural adhesives, which tend to have lower T_g s. Notably, fracture toughness K_{IC} and G_{IC} (Fig. 7.11b and c) of ROMP resins as high as $3\text{ MPa m}^{1/2}$ and 5 kJ/m^2 were measured (using SENB specimens per ASTM D5045 as described above), corresponding to as much as five times that of untoughened epoxies, and as much as double that of toughened epoxies at corresponding T_g . Fracture energies G_{IC} for ROMP resins in the range $100^\circ\text{C} < T_g < 125^\circ\text{C}$ ($3\text{--}5\text{ kJ/m}^2$) are comparable to that of the PPG Group 1 epoxy adhesive having similar T_g , and significantly higher than PU and acrylic adhesives with similar or lower T_g ($G_{IC} \leq 3\text{ kJ/m}^2$), bearing in mind that the latter values were measured using DCB specimens.

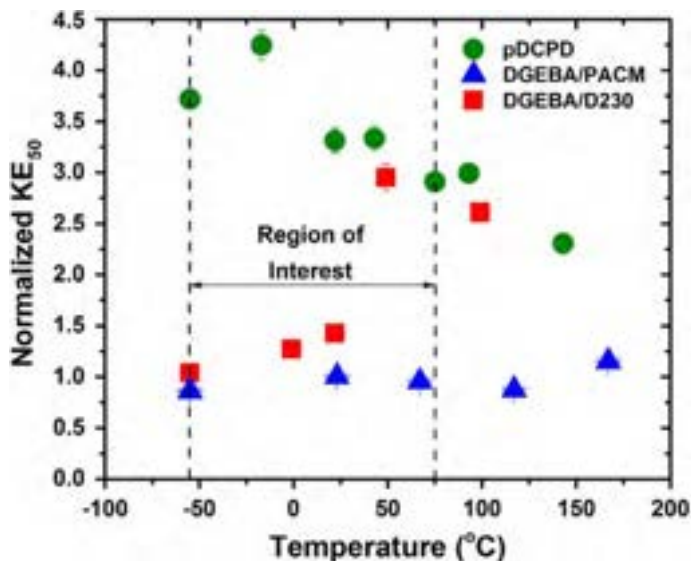


Fig. 7.13 Temperature dependence of normalized kinetic energy ballistic limit (KE_{50}) for ROMP-cured polydicyclopentadiene (pDCPD), DGEBA-PACM epoxy, and DGEBA-D230 epoxy. Formulations are the same as Fig. 7.10 and test conditions are the same as Fig. 7.11d. Samples were conditioned at the temperatures shown for 24h under inert gas and tested in a controlled environment chamber.

Reproduced with permission from D.B. Knorr, K.A. Masser, R.M. Elder, T.W. Sirk, M.D. Hindenlang, J.H. Yu, A.D. Richardson, S.E. Boyd, W.A. Spurgeon, J.L. Lenhart, Overcoming the structural versus energy dissipation trade-off in highly crosslinked polymer networks: Ultrahigh strain rate response in polydicyclopentadiene, *Compos. Sci. Technol.* 114 (2015), 17–25. <https://doi.org/10.1016/j.compscitech.2015.03.021>. Copyright 2015 Elsevier.

In ballistic testing, the series of nonpolar ROMP resins (blue up-facing triangles in Fig. 7.11d) exhibited 50%–100% higher V_{50} than untoughened epoxies for $T_g > 65^\circ\text{C}$, and exhibited similar improvement over toughened epoxies for $T_g > 110^\circ\text{C}$. Furthermore, pDCPD (T_g 120°C) was found to exhibit systematically increasing KE_{50} (kinetic energy ballistic limit) with decreasing temperature to as low as -50°C [16]. As shown in Fig. 7.13, the high rate impact toughness of pDCPD far exceeds that of epoxies at low temperatures. Overall, pDCPD demonstrates a remarkable combination of both toughness and strength that covers a service temperature range from at least -50°C to as high as $+150^\circ\text{C}$.

This highly unusual and technologically desirable set of performance properties, combined with the low cost and manufacturability of pDCPD-ROMP, makes it an attractive candidate for structural adhesive applications. This would appear to be particularly true in emerging markets such as automotive, where the ability of ROMP to cure in seconds at near-ambient temperatures and achieve remarkable toughness, strength, temperature tolerance, and chemical resistance could be a natural fit for bonding crashworthy structural components in high-volume production vehicles. The recent availability of air- and moisture-tolerant ROMP catalysts brings this vision closer to reality while necessarily increasing cost.

Published efforts toward adhesive bonding applications using ROMP have been relatively limited. Caster and coworkers developed “contact metathesis polymerization” (CMP) of polynorbornene for bonding rubber and tire cords in the early 2000s [31]. ROMP was widely publicized in the early 2010s as a possible route to self-healing materials by dispersing encapsulated DCPD monomer and Grubbs’ catalyst in an epoxy matrix, causing the materials to contact upon fracture of the epoxy and polymerize by ROMP to heal the crack [32]. More recently, ROMP of DCPD has been demonstrated to proceed by frontal polymerization, enabling relatively energy-efficient and scalable manufacturing that could apply to the adhesive bonding of large structures [33].

A major challenge for adhesive applications is that DCPD forms a highly nonpolar polymer with low surface energy, making surface bonding inherently difficult. For components produced by RIM, a surface oxide layer typically forms after a short environmental exposure, making the parts amenable to painting and adhesive bonding. However for cured-in-place adhesive formulations, it is difficult to envision that this would be effective. Thus, several routes to improve the surface bondability of ROMP polymers are currently being explored.

Silane coupling agents and other surface treatments have been found to improve the bonding of nonpolar ROMP polymers to a variety of substrates. Carbon nanotubes and particulate silica fillers functionalized with norbornene and vinyl surface groups [34–36] were demonstrated to covalently incorporate into the pDCPD network, resulting in tunable interfacial bonding and improved composite properties. Recently, Al 2024-T3 substrates were prepared with a series of silane coupling agents for bonding with pDCPD-ROMP [37]. PDCPD demonstrated lap shear strengths as high as 20 MPa and lap shear displacements as high as 2.5 mm on aluminum substrates treated with norbornene or vinyl functional silanes, compared to 11 MPa and 1.5 mm, respectively, on substrates without silane treatment. Although the properties achieved using silane treatment are within MIL-PRF-32662 Group II for industrial-grade structural adhesives (Fig. 7.1), they are not good enough to reach Group I, which might have been expected based on the outstanding toughness of high T_g ROMP polymers discussed above (Fig. 7.11). Furthermore, after immersion in 63°C water for 2 weeks, the lap shear strength of pDCPD on silane-treated aluminum decreased by 38%, falling short of the MIL-PRF-32662 Tier II requirement that 75% of dry strength be retained under hot/wet conditioning. Therefore, additional surface bonding improvements are needed.

An alternative strategy is to form ROMP polymers with polar functionality [38], which is enabled by the latest generations of Grubbs catalysts. In a recent study [39], the polar monomer 5-methanol-2-norbornene (NBOH) was copolymerized with 5-ethylidene-2-norbornene (ENB) in varying proportions by ROMP (Fig. 7.14). As NBOH content was increased, tensile strength and ballistic resistance tended to increase in approximately linear proportion (Fig. 7.11a and d, light blue diamond symbols) while T_g was relatively unaffected. Fracture toughness tended to decrease with increasing NBOH content (Fig. 7.11b and d) while still remaining higher than typical toughened epoxies at comparable T_g . These results provide an interesting set of options for tuning chemical polarity to optimize adhesion while maintaining good mechanical and chemical performance in future work.



Fig. 7.14 Copolymerization of 5-methanol-2-norbornene (NBOH) and 5-ethylidene-2-norbornene (ENB) by ROMP to study effects of polar functionality on mechanical response. Reproduced with permission from J.M. Dennis, T.R. Long, A. Krishnamurthy, N.T. Tran, B.A. Patterson, C.E. Busch, K.A. Masser, J.L. Lenhart, D.B. Knorr, Influence of hydroxyl group concentration on mechanical properties and impact resistance of ROMP copolymers, *ACS Appl. Polym. Mater.* 2(6) (2020) 2414–2425. <https://doi.org/10.1021/acsapm.0c00352>.

7.3 Functionality beyond structural reinforcement

7.3.1 Reversible or debondable structural adhesives

Continuing to push the boundaries of mechanical performance and durability is critical to enable adhesives as an efficient and differentiating technology applicable to a wide variety of end-use markets. However, in many envisioned and currently practiced applications, attributes beyond adhesive strength and robustness are required to enable more efficient and sustainable technologies. One application space that has seen growing interest in both the academic and industrial sectors is the development of reversible or debondable structural adhesives that match the performance of traditional high-end structural adhesives while offering facile debonding under a specific stimulus [40,41]. Adhesives that can debond on demand will improve the ability to maintain complicated systems by enabling the facile replacement of worn parts or efficient upgrading with new bonded components. Adhesives with these properties will also improve end-of-life options for complicated joint assemblies, enabling more efficient recycling of dissimilar bonded materials and the recovery of parts for second-hand markets. Furthermore, durable adhesives that can efficiently debond on demand can empower new technology spaces, such as release-on-command systems in the areas of robotics. Traditional structural adhesive technologies require aggressive conditions to debond, such as unselective thermal degradation, mechanical removal that is often incomplete and leaves significant adhesive residue, or reactive or hazardous chemical stripping methodologies that present environmental health and safety issues. Therefore, the paradoxical requirement of structural adhesives that provide sufficient structural integrity during service while allowing for simple debonding has led to the emergence of novel technologies to enable these applications in an efficient manner.

7.3.1.1 Formulation additives for debonding

A popular technical approach aimed to address this challenge is the development of specific functional additives that can impart easier debondability into traditional adhesive systems. For example, the incorporation of additives that undergo rapid physical expansion under thermal stimulus weakens the adhesive bond to a degree that it can be

easily removed from the substrate. This approach is attractive because, in theory, it can be applied to currently commercial adhesive technologies, so long as the additives are compatible with the adhesive matrix and curing profile. A variety of thermally expandable microspheres and chemical blowing agents have been reported for these applications; the additives can be tailored to enable expansion over a relatively broad temperature range, allowing for improved control over the precise debonding temperature. These additives are available from a variety of suppliers (Expancell from Nouryon, Advancell from Sekisui, etc.) and have been applied in some commercially available debondable structural adhesives. Rescoll has commercialized the INDAR series of structural adhesives that can be debonded by thermal exposure to temperatures $>100^{\circ}\text{C}$. However, the limitations of these current systems can include only partial delamination of the adhesive from the adherend and the inherent destruction of the adhesive by this technology.

Additional debondable adhesives have been designed to include additives responsive to stimuli other than heat, with one growing area being the addition of materials responding to the application of electrical voltage. Under the application of a voltage differential across the adhesive bondline, charged moieties will migrate to the adhesive-adherend interface, weakening the bond and enabling delamination of the adhesive. For example, the ElectRelease technology from EIC Labs Inc. is a commercially available debondable adhesive system that shows adhesive strengths of greater than 10 MPa under service conditions but debonds easily from metallic substrates under an applied voltage of 5–50 V.

7.3.1.2 *Intrinsically debondable structural adhesives*

An alternate technical approach to generate efficiently debondable structural adhesives that can theoretically be debonded and rebonded multiple times is the development of novel polymer resin technologies that incorporate functional groups that are intrinsically reversible under certain stimuli. If controlled properly, these linkages maintain sufficient stability under service conditions, but will reverse or exchange under appropriate conditions, weakening the adhesive bond such that the adhesive can easily be removed from the adherend. One attractive stimulus that has received significant attention for this approach is the use of ultraviolet light irradiation to enable depolymerization of light-sensitive functional groups [42]. Because the UV stimulus is orthogonal to the thermal conditions required for curing typical adhesives or during their service lifetime, it represents an ideal trigger for adhesive debonding in certain applications. The academic literature has reported the incorporation of functional groups capable of undergoing photo-reversible dimerization such as coumarins, anthracenes, and stilbenes, among others. Groups that trigger irreversible photodepolymerization, such as *o*-nitro benzyl esters [43], have also been leveraged to develop adhesives that debond under irradiation. Increasing patent activity is occurring in this area as well.

Thermal depolymerization or network rearrangement also offers a potential mechanism for debondable structural adhesives. Assuming the adhesive is not required to withstand elevated temperatures during its service lifetime, bonds can be incorporated

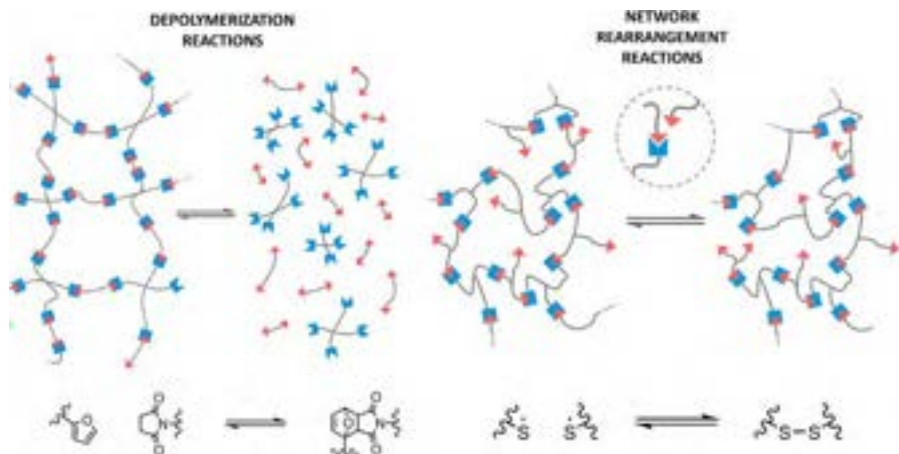


Fig. 7.15 Approaches to reworkable adhesive networks based on depolymerization or network rearrangement. Reversible Diels-Alder and disulfide linkages are illustrated as typical chemistries enabling the flow of chemically crosslinked networks at elevated temperatures. Reproduced with permission from D.J. Fortman, J.P. Brutman, G.X. De Hoe, R.L. Snyder, W.R. Dichtel, M.A. Hillmyer, Approaches to sustainable and continually recyclable cross-linked polymers, *ACS Sustain. Chem. Eng.* 6 (2018) 11145–11159 (<https://pubs.acs.org/doi/10.1021/acssuschemeng.8b02355>, further permission related to the material excerpted should be directed to the ACS).

into the polymer backbone that will depolymerize or undergo exchange reactions at mild elevated temperature, enabling polymers to display thermoset-like properties under service conditions while flowing more akin to thermoplastics at mild elevated temperatures. In the academic literature, these dynamic covalent networks, commonly referred to as vitrimers, have received immensely growing attention as a new technology area (Fig. 7.15) [44,45]. The incorporation of dynamic bonds such as furan-maleimide adducts, disulfides, imines, boronic esters, and many others could potentially yield thermally reprocessable adhesives with properties competitive to traditional structural adhesives. Specific examples have demonstrated that these technologies not only can enable efficient debonding or reworking of thermoset-like adhesives, but can also improve adhesive bond performance by facilitating the relaxation of stresses within the adhesive polymer network and potentially allowing for improved surface interaction during elevated temperature treatment [46]. Significant numbers of patent applications have been filed in this area in recent years; in many cases, reversible bonding applications in the electronics sector are specifically targeted, further exemplifying the growing technological investment in this emerging structural adhesive application space.

Development of these intrinsically debondable adhesive technologies will include the formulation of economically viable resin systems for widespread application, improved control of the precise temperatures at which materials can be debonded, and the creation of triggers that are extremely rapid and selective for depolymerization of the desired linkages.

7.4 Using digital tools to advance the adhesives industry

7.4.1 Industry standardization of digital performance datasets

Commercial adoption of next-generation adhesives will only transpire if the chemistry is accompanied by a full suite of modern data science tools, including standardized database formatting, free access to pedigreed testing results, and inclusion of computational models within the manufacturer's technical data package. Current adhesive implementation into engineered products involves selection, acquisition of data for design, validation, environmental durability assessment, and quality control [47,48]. The steps between selection and quality control are highly labor intensive and extremely expensive, resulting in a tall entry barrier for innovative technology advancements into the commercial market. The adhesives industry remains exceedingly disorganized and difficult for nonexperts to successfully navigate selection searches beyond Google, favoring incumbent product lock-in. Social introduction of new product is antiquated and costly, as the burden is placed on the potential end user to invest labor into generating their own validation test data, further reinforcing incumbent product lock-in. In 2023 and beyond, adhesive manufacturers should be augmenting their decades-old static product data sheets with a full complement of digital testing results and modeling parameters to lessen the cost burden of repetitive testing that is imposed on the end user.

MIL-PRF-32662 incorporates data-capable workflows used to derive correlations between DOD and commercial dual-use performance metrics. MIL-PRF-32662 assumes that if an adhesive manufacturer's product technical data package is sufficiently complete and robust to qualify for harsh DOD end-use applications, then the same vetted data could easily be leveraged to bolster their entry prospects to non-DOD customers. Qualified technical data should be provided on an open-access platform. Furthermore, qualification standards should also allow for the option of accepting test data directly from the manufacturer.

The digital data propositions embedded in the drafting of MIL-PRF-32662 were predicted in the late 1990s [49], but the acceptance of digital materials management was still in its infancy and lacked the necessary sophistication to overcome an adhesives industry-wide low projection of "measure of belief" for experimental properties claimed on technical data sheets. This is the primary factor in driving costly repetitive testing and the principal difficulty in implementing confident digital toolsets. Adhesives do not have well-behaved properties (in comparison to metal alloys) owing to a heavy reliance on processing conditions, surface pretreatments, and the expertise of the technician preparing the bonded joint, which results in deviations in measured fracture energies varying by 10%–15% [50]. Fig. 7.16 shows the single-lap joint performance of the PPG Group 1 epoxy adhesive measured at the US Army Research Laboratory, Virginia Tech, and PPG by experienced laboratory personnel working in ideal conditions. The data partition into both the Group I and Group II performance regions of MIL-PRF-32662, with the most variation in response occurring at high strength and failure displacement. Specifically for the datasets generated by ARL, the variation in the bonded joint response was caused by changing an intermediate

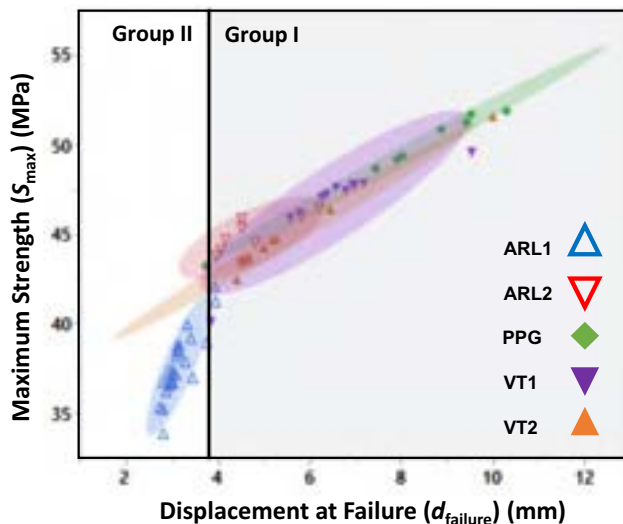


Fig. 7.16 Single-lap joint performance of PPG Group 1 epoxy adhesive for samples prepared by the US Army Research Laboratory (ARL 1 and 2), PPG, and Virginia Tech (VT 1 and 2). Sample set ARL1 shows the effects of removing a simple intermediate water-rinse step during the surface pretreatment process, thus highlighting the sensitivity of bonded adhesive properties. 90% confidence ellipses are used to represent the statistical variation.

water-rinse step during the surface pretreatment processing of the adherends. Troubleshooting the surface pretreatment sequence resulted in a 16% increase in strength and 33% increase in displacement at failure (for the ARL data), which steps the adhesive from MIL-PRF-32662 Group II into the preferred Group I performance. Adhesive performance variation is the norm, not the exception, but it is infrequently referenced in technical data packages. The current cultural acceptance of high-cost and low-throughput validation testing is reflective of the end user's low measure of belief in optimistic manufacturer data and the need to know by direct experience the adhesive's lower bounds of performance.

The adhesives industry would benefit by incorporating robust data management tools with the capability to capture domain expertise that is traditionally reserved for humans who are knowledgeable in "the art." The realistic projection of adhesive properties, showing ideal and nonideal testing results, is needed to bring about the next generation of novel chemistries. The absence of nonideal data for new adhesives leads to overly conservative engineering, which again favors incumbent product lock-in. Adhesive innovations will only move forward in earnest once the industry begins to embrace uncertainty as a formalized and quantifiable measurement for new product data [51–54]. Introducing disciplined data capture and management schemes will also have the benefit of bringing the power of artificial intelligence and machine learning to bear on the development of novel adhesives from complex formulation domains at reduced time and cost.

7.4.2 Incorporation into engineering modeling packages

Predictive computational techniques to evaluate structural adhesive performance have become essential given the important role played in automotive and aerospace manufacturing. Finite element analysis (FEA) is a capable tool for modeling structural adhesive behavior under a wide range of conditions. Complications with FEA arise primarily due to interfacial (or interphasial) effects and the presence of variations or defects within the bondline. Additionally, the application of linear elastic fracture mechanics to predicting the performance of this type of adhesives has challenges with stress concentration zones (e.g., sharp corners or bi-material interfaces), strongly depending on how well the stress field is modeled (i.e., mesh refinement). The implementation of cohesive zone modeling (CZM) [55] into FEA solves these limitations, simulating and analyzing damage initiation and propagation in bonded joints and laminates, but not without a cost. The new challenge is the identification of both an accurate traction separation law and a damage model that can properly capture the adhesive damage initiation and propagation for each fracture mode. Finally, this is further complicated by the increasingly complex, heterogeneous nature of many structural adhesive materials and interfaces.

Despite the rise in computing power and the increasingly efficient FEA solvers, predictions of joint performance at large strain values and close to joint failure tend to be unreliable. To improve this situation, there is increased interest in the development of material constitutive models with higher predictive accuracy, particularly for the performance prediction of bonded structures under impact loading so that the load and absorbed energy prior to failure can be accurately calculated. More accurate models require proper consideration of plasticity and its dependence on the stress state, applied strain rate, temperature, and other factors. The use of complex material models places greater demands on engineers to select the most realistic parameters while minimizing computational cost.

Structural adhesives that exhibit strength retention after peak loading, plastic strain energy dissipation, and significant yielding of the adherends before failure (e.g., Group I adhesives discussed above) present a particularly challenging case for predictive modeling. Numerous factors aside from the bulk adhesive material properties come into play under these severe loading conditions, such as substrate properties, substrate surface preparation, joint configuration, measurement conditions, and environmental factors. In consequence, no theoretical tools to date can precisely predict the real-life behavior of joints bonded with high-performance structural adhesives, particularly beyond the linear-elastic regime. Addressing these limitations will therefore be critical to enabling the further application of novel, high-performing adhesive technologies in a variety of industries.

7.5 Conclusions

Structural adhesives have fundamentally improved the design, manufacturing, and performance of products in many important industries over the past 100 years or so. Although chemistries including epoxy, polyurethane, acrylic, and others have

evolved to offer a seemingly endless range of properties, important gaps become apparent when considering certain challenging applications. Such applications include bonded structures subjected to a high probability of overload failure as well as assemblies in which components may need to be reversibly bonded and debonded for maintenance, upgrading, recycling, and recovery. To address the former case, the Group 1 window established in US Army performance requirement MIL-PRF-32662 provides a stiff challenge that has motivated the development of innovative epoxy-based adhesives offering exceptional strength and ductility across a broad range of parameters, ultimately delivering improved safety in critical protective applications. Similarly, ROMP offers an unusual combination of polymer strength and high-rate impact toughness across a broad temperature range as well as processing advantages that could prove valuable in future protective systems and other structural bonding applications. On-demand debonding has been demonstrated by a growing range of experimental additives and chemistries promising to expand the sustainability and versatility of structural adhesives in traditional applications and emerging technologies. Unfortunately, the promise of these and other innovations may not be realized without careful thought by industry leaders about the standardization of adhesive technical data, including ranges of property variability due to processing as well as model parameters for accurate performance prediction. Digitization of reliable product data can be harnessed in conjunction with modern computational tools to promote customer confidence in emerging adhesive innovations, reducing barriers to growth in both new and existing markets.

Acknowledgments

Research related to the development of Group I adhesives was sponsored by the Army Research Laboratory and was accomplished under Cooperative Agreement Number W911NF-13-2-0046 to Drexel University and subagreement to PPG Industries, Inc. The views and conclusions contained in this document are those of the authors and should not be interpreted as representing the official policies, either expressed or implied, of the Army Research Laboratory or the US government. The US government is authorized to reproduce and distribute reprints for government purposes notwithstanding and copyright notification herein.

The work reviewed in this chapter is the product of dedicated efforts by several large teams, much of it spanning more than a decade. Although it is impossible to list every individual by name, special acknowledgments are due to Joseph Lenhart, Dan Knorr, Randy Mrozek, Kevin Masser, Tyler Long, Adam Richardson, Mark Hindenlang, Tim Sirk, Rob Elder, Dan DeSchepper, Dave Flanagan, Chris Rinderspacher, Jian Yu, John La Scala, Ian McAninch, Eugene Napadensky, Ngon Tran, Brendan Patterson, Doug Harris, and Joe Dennis.

References

- [1] J.J.M. Machado, E.A.S. Marques, L.F.M. da Silva, Adhesives and adhesive joints under impact loadings: an overview, *J. Adhes.* 94 (6) (2018) 421–452, <https://doi.org/10.1080/00218464.2017.1282349>.
- [2] I.J.J. van Straalen, J. Wardenier, L.B. Voegesang, F. Soetens, Structural adhesive bonded joints in engineering - drafting design rules, *Int. J. Adhes. Adhes.* 18 (1998) 41–49, [https://doi.org/10.1016/S0143-7496\(97\)00068-7](https://doi.org/10.1016/S0143-7496(97)00068-7).

- [3] L. Goglio, M. Rossetto, E. Dragon, Design of adhesive joints based on peak elastic stresses, *Int. J. Adhes. Adhes.* 28 (2008) 427–435, <https://doi.org/10.1016/j.ijadhadh.2008.04.001>.
- [4] R. Haghani, M. Al-Emrani, A new design model for adhesive joints used to bond FRP laminates to steel beams – part a: background and theory, *Constr. Build. Mater.* 34 (2012) 486–493, <https://doi.org/10.1016/j.conbuildmat.2012.02.051>.
- [5] L.R. Alejano, A. Rodriguez-Dono, E. Alonso, G. Fdez-Manín, Ground reaction curves for tunnels excavated in different quality rock masses showing several types of post-failure behaviour, *Tunn. Undergr. Space Technol.* 24 (2009) 689–705, <https://doi.org/10.1016/j.tust.2009.07.004>.
- [6] M. Wang, D. Zheng, K. Wang, W. Li, Strain energy analysis of floor heave in longwall gateroads, *R. Soc. Open Sci.* 5 (2018), 180691, <https://doi.org/10.1098/rsos.180691>.
- [7] E. Speranzini, S. Agnetti, Strengthening of glass beams with steel reinforced polymer (SRP), *Compos. Part B* 67 (2014) 280–289, <https://doi.org/10.1016/j.compositesb.2014.06.035>.
- [8] D. Castagnetti, E. Dragoni, A. Spaggiari, Efficient post-elastic analysis of bonded joints by standard finite element techniques, *J. Adhes. Sci. Technol.* 23 (2009) 1459–1476, <https://doi.org/10.1163/156856109X433027>.
- [9] DOD, Adhesive, high-loading rate, for structural and armor applications, MIL-PRF-32662, CCDC Army Research Laboratory, Aberdeen Proving Ground, MD, US, 2020. https://quicksearch.dla.mil/qsDocDetails.aspx?ident_number=283919.
- [10] DOD, MIL-PRF-32662: Adhesive, High-Loading Rate, for Structural and Armor Applications – Frequently Asked Questions, ARL-TN-1035, CCDC Army Research Laboratory, Aberdeen Proving Ground, MD, US, 2020. <https://apps.dtic.mil/sti/citations/AD1110598>.
- [11] DOD, Adhesives: Test Method, Group Assignment, and Categorization Guide for High-Loading Rate Applications – History and Rationale, ARL-SR-0371, CCDC Army Research Laboratory, Aberdeen Proving Ground, MD, US, 2017. <https://apps.dtic.mil/sti/pdfs/AD1032445.pdf>.
- [12] DOD, Adhesives: Test Method, Group Assignment, and Categorization Guide for High-Loading-Rate Applications – Preparation and Testing of Single Lap Joints (Ver. 2.2, Unlimited), ARL-SR-0356, CCDC Army Research Laboratory, Aberdeen Proving Ground, MD, US, 2016. <https://materialsdata.nist.gov/bitstream/handle/11256/652/Joint%20bonding%20process?sequence=13&isAllowed=y>.
- [13] F. Koch, A. Lutz, High modulus structural body shop adhesives, *Adhes. Adhes. Sealants* 15 (2018) 17–19, <https://doi.org/10.1007/s35784-018-0008-6>.
- [14] C.E. Cruz Gonzalez, R.P. Mora, S.D. Santillan Gutierrez, J.J. Taha-Tijerina, B.V. Arista, A.B. Pingarron, Fatigue strength evaluation and fracture behavior of joined dual phase steel/AA6061-T6 aluminum alloy, *Frat. Integrità Strutt.* 48 (2019) 530–544, <https://doi.org/10.3221/IGF-ESIS.48.51>.
- [15] B. Burchardt, *Advances in polyurethane structural adhesives*, in: D.A. Dillard (Ed.), *Advances in Structural Adhesive Bonding*, first ed., Woodhead, Cambridge, UK, 2010 (Chapter 3).
- [16] D.B. Knorr, K.A. Masser, R.M. Elder, T.W. Sirk, M.D. Hindenlang, J.H. Yu, A.D. Richardson, S.E. Boyd, W.A. Spurgeon, J.L. Lenhart, Overcoming the structural versus energy dissipation trade-off in highly crosslinked polymer networks: Ultrahigh strain rate response in polydicyclopentadiene, *Compos. Sci. Technol.* 114 (2015) 17–25, <https://doi.org/10.1016/j.compscitech.2015.03.021>.
- [17] A. Hayashi, Y. Sekiguchi, C. Sato, Effect of temperature and loading rate on the mode I fracture energy of structural acrylic adhesives, *J. Adv. Join. Process.* 5 (2022), 100079, <https://doi.org/10.1016/j.jajp.2021.100079>.

- [18] R.A. Pearson, A.F. Yee, Toughening mechanisms in elastomer-modified epoxies. Part 3: the effect of cross-link density, *J. Mater. Sci.* 24 (1989) 2571–2580, <https://doi.org/10.1007/BF01174528>.
- [19] E.D. Bain, D.B. Knorr, A.D. Richardson, J.H. Yu, K.A. Masser, J.L. Lenhart, Failure processes governing high rate impact resistance of epoxy resins filled with core shell rubber nanoparticles, *J. Mater. Sci.* 51 (5) (2016) 2347–2370, <https://doi.org/10.1007/s10853-015-9544-5>.
- [20] P. Gálvez, R.J.C. Carbas, R.D.S.G. Campilho, J. Abenojar, M.A. Martínez, L.F.M. da Silva, Fracture toughness in mode I (G_{IC}) for ductile adhesives, *J. Phys. Conf. Ser.* 843 (2017), 012008, <https://doi.org/10.1088/1742-6596/843/1/012008> (6th International Conference on Fracture Fatigue and Wear, IOP Conf. Series).
- [21] D.B. Knorr, J.H. Yu, A.D. Richardson, M.D. Hindenlang, I.M. McAninch, J.J. La Scala, J.L. Lenhart, Glass transition dependence of ultrahigh strain rate response in amine cured epoxy resins, *Polymer* 53 (25) (2012) 5917–5923, <https://doi.org/10.1016/j.polymer.2012.09.058>.
- [22] Y. Sekiguchi, Y. Yamagata, C. Sata, Mode I fracture energy of adhesive joints bonded with adhesives with different characteristics under quasi-static and impact loading, *J. Adhes. Soc. Jpn.* 53 (10) (2017) 330–337.
- [23] Sika, Structural Bonding Solutions. High Performance Adhesives. SikaFast, SikaPower, SikaForce. Technical Brochure, April 2018.
- [24] S.R. Ranade, Y. Guan, D.C. Ohanehi, J.G. Dillard, R.C. Batra, D.A. Dillard, A tapered bondline thickness double cantilever beam (DCB) specimen geometry for combinatorial fracture studies of adhesive bonds, *Int. J. Adhes. Adhes.* 55 (2014) 155–160.
- [25] E. Crawford, A.J. Lesser, The effect of network architecture on the thermal and mechanical behavior of epoxy resins, *J. Polym. Sci. B Polym. Phys.* 36 (8) (1998) 1371–1382, [https://doi.org/10.1002/\(sici\)1099-0488\(199806\)36:8<1371::aid-polb11>3.0.co;2-4](https://doi.org/10.1002/(sici)1099-0488(199806)36:8<1371::aid-polb11>3.0.co;2-4).
- [26] K.A. Masser, T.R. Long, J.H. Yu, D.B. Knorr, M.D. Hindenlang, T. Taylor, D. Harris, J.L. Lenhart, The temperature-dependent ballistic performance and the ductile-to-brittle transition in polymer networks, *J. Polym. Sci. B Polym. Phys.* 57 (2019) 511–523, <https://doi.org/10.1002/polb.24807>.
- [27] K.A. Masser, D.B. Knorr, M.D. Hindenlang, J.H. Yu, A.D. Richardson, K.E. Strawhecker, F.L. Beyer, J.L. Lenhart, Relating structure and chain dynamics to ballistic performance in transparent epoxy networks exhibiting nanometer scale heterogeneity, *Polymer* 58 (2015) 96–106, <https://doi.org/10.1016/j.polymer.2014.12.027>.
- [28] K.A. Masser, E.D. Bain, F.L. Beyer, A.M. Savage, J.H. Yu, J.L. Lenhart, Influence of nano-scale morphology on impact toughness of epoxy blends, *Polymer* 103 (2016) 337–346, <https://doi.org/10.1016/j.polymer.2016.09.076>.
- [29] C.W. Bielawski, R.H. Grubbs, Living ring-opening metathesis polymerization, *Prog. Polym. Sci.* 32 (1) (2007) 1–29.
- [30] T.R. Long, R.M. Elder, E.D. Bain, K.A. Masser, T.W. Sirk, D.B. Knorr, J.L. Lenhart, Influence of molecular weight between crosslinks on the rate dependent brittle-to-ductile transition in polymers formed via ring-opening metathesis, *Soft Matter* 14 (2018) 3344–3360, <https://doi.org/10.1016/j.polymer.2016.09.076>.
- [31] K.C. Caster, E.F. Tokas, C.G. Keck, M.E. Hontz, Contact metathesis polymerization (CMP), *J. Mol. Catal. A Chem.* 190 (1–2) (2002) 65–77, [https://doi.org/10.1016/S1381-1169\(02\)00247-9](https://doi.org/10.1016/S1381-1169(02)00247-9).
- [32] H. Jin, G.M. Miller, N.R. Sottos, S.R. White, Fracture and fatigue response of a self-healing epoxy adhesive, *Polymer* 52 (2011) 1628–1634, <https://doi.org/10.1016/j.polymer.2011.02.011>.

- [33] I.D. Robertson, M. Yourdkhani, P.J. Centellas, J. En Aw, D.G. Ivanoff, E. Goli, E.M. Lloyd, L.M. Dean, N.R. Sottos, P.H. Geubelle, J.S. Moore, S.R. White, Rapid energy-efficient manufacturing of polymers and composites via frontal polymerization, *Nature* 557 (2018) 223–227.
- [34] W. Jeong, M.R. Kessler, Toughness enhancement in romp functionalized carbon nanotube/polydicyclopentadiene composites, *Chem. Mater.* 20 (22) (2008) 7060–7068.
- [35] N.T. Tran, B.A. Patterson, D.E. Harris, E. Napadensky, J.L. Lenhart, D.B. Knorr, E.D. Bain, Influence of interfacial bonding on the mechanical and impact properties of ring-opening metathesis polymer (ROMP) silica composites, *ACS Appl. Mater. Interfaces* 12 (2020) 53342–53355, <https://doi.org/10.1021/acsami.0c16280>.
- [36] G. Yang, S.C. Lee, J.K. Lee, Reinforcement of norbornene-based nanocomposites with norbornene functionalized multi-walled carbon nanotubes, *Chem. Eng. J.* 288 (2016) 9–18.
- [37] A.J. Boyer, N.T. Tran, D.B. Knorr, Ring-opening metathesis polymerization (ROMP) polymers as structural adhesives and the effects of silane coupling agents on their lap shear properties, *J. Adhes. Sci. Technol.* (2022), <https://doi.org/10.1080/01694243.2022.2095183>.
- [38] R.M. Elder, T.R. Long, E.D. Bain, J.L. Lenhart, T.W. Sirk, Mechanics and nanovoid nucleation dynamics: effects of polar functionality in glassy polymer networks, *Soft Matter* 14 (2018) 8895–8911, <https://doi.org/10.1039/C8SM01483C>.
- [39] J.M. Dennis, T.R. Long, A. Krishnamurthy, N.T. Tran, B.A. Patterson, C.E. Busch, K.A. Masser, J.L. Lenhart, D.B. Knorr, Influence of hydroxyl group concentration on mechanical properties and impact resistance of ROMP copolymers, *ACS Appl. Polym. Mater.* 2 (6) (2020) 2414–2425, <https://doi.org/10.1021/acsapm.0c00352>.
- [40] N. Blelloch, H. Yarbrough, K. Mirica, Stimuli-responsive temporary adhesives: enabling debonding on demand through strategic molecular design, *Chem. Sci.* 12 (2021) 15183.
- [41] K. Mulcahy, A. Kilpatrick, G. Harper, A. Walton, A. Abbott, Debondable adhesives and their use in recycling, *Green Chem.* 24 (2022) 36.
- [42] T. Hughes, G. Simon, K. Saito, Chemistries and capabilities of photo-formable and photoreversible crosslinked polymer networks, *Mater. Horiz.* 6 (2019) 1762–1773.
- [43] A. Romano, I. Roppolo, E. Rossegger, S. Schlogl, M. Sangermano, Recent trends in applying ortho-nitrobenzyl esters for the design of photo-responsive polymer networks, *Materials* 13 (2020) 2777.
- [44] N. Zheng, Y. Xu, Q. Zhao, T. Xie, Dynamic covalent polymer networks: a molecular platform for designing functions beyond chemical recycling and self-healing, *Chem. Rev.* 121 (2021) 1716–1745.
- [45] D.J. Fortman, J.P. Brutman, G.X. De Hoe, R.L. Snyder, W.R. Dichtel, M.A. Hillmyer, Approaches to sustainable and continually recyclable cross-linked polymers, *ACS Sustain. Chem. Eng.* 6 (2018) 11145–11159.
- [46] L. Li, X. Chen, J. Torkelson, Covalent adaptable networks for enhanced adhesion: exploiting disulfide dynamic chemistry and annealing during application, *ACS Appl. Polym. Mater.* 2 (2020) 4658–4665.
- [47] Duncan, B. (2009), ‘Developments in testing adhesive joints’ *Advances in Structural Adhesive Bonding*, Woodhead Publishing Limited. B. Duncan, Developments in testing adhesive joints, in: *Advances in Structural Adhesive Bonding*, Woodhead Publishing Limited, 2010.
- [48] J.C. Suárez, I. Diez de Ulzúrrun, M.V. Biezma, J.M. Ruiz Román, M.A. Martínez, J.C. del Real, F. López, Case studies in adhesives selection, *J. Mater. Process. Technol.* 143–144 (2003) 219–224, [https://doi.org/10.1016/S0924-0136\(03\)00428-X](https://doi.org/10.1016/S0924-0136(03)00428-X).

-
- [49] K.R. Trethewey, R.J.K. Wood, Y. Puget, P.R. Roberge, Development of a knowledge-based system for materials management, *Mater. Des.* 19 (1998) 39–56.
- [50] B.R.K. Blackman, A.J. Kinloch, M. Paraschi, W.S. Teo, Measuring the mode I adhesive fracture energy, GIC, of structural adhesive joints: the results of an international round-robin, *Int. J. Adhes. Adhes.* 23 (2003) 293–305, [https://doi.org/10.1016/S0143-7496\(03\)00047-2](https://doi.org/10.1016/S0143-7496(03)00047-2).
- [51] C.L. Chandler, *Certainty Factor Determination in a Rule-Based Expert System for a Factory Floor Testing System*, Texas Tech University, 1990.
- [52] H.J. Pasma, W.J. Rogers, How to treat expert judgment? With certainty it contains uncertainty! *J. Loss Prev. Process Ind.* 66 (2020), 104200, <https://doi.org/10.1016/j.jlp.2020.104200>.
- [53] J. Wang, Y. Hu, F. Xiao, X. Deng, Y. Deng, A novel method to use fuzzy soft sets in decision making based on ambiguity measure and Dempster–Shafer theory of evidence: an application in medical diagnosis, *Artif. Intell. Med.* 69 (2016) 1–11, <https://doi.org/10.1016/j.artmed.2016.04.004>.
- [54] R.R. Yager, Satisfying uncertain targets using measure generalized Dempster–Shafer belief structures, *Knowl.-Based Syst.* 142 (2018) 1–6, <https://doi.org/10.1016/j.knosys.2017.11.012>.
- [55] R.D.S.G. Campilho (Ed.), *Strength Prediction of Adhesively-Bonded Joints*, CRC Press, Boca Raton, 2017. <https://doi.org/10.1201/9781315370835>.

This page intentionally left blank

Advances in toughening strategies for structural adhesives

8

Declan Carolan^a, Sammy He^a, and Ambrose C. Taylor^b

^aFAC Technology, London, United Kingdom, ^bImperial College London, London, United Kingdom

8.1 Introduction: What is toughness and why is it important?

In the popular science paperback, “The New Science of Strong Materials—or Why You Don’t Fall Through the Floor,” J.E. Gordon [1] wrote that “the greatest sin of an engineering material is not a lack of strength or lack of stiffness, desirable as these properties are, but lack of toughness, that is to say, lack of resistance to propagation of cracks.” This is especially true in the context of structural adhesives, where the role of joining materials, often at critically stressed locations, means that they have to work particularly hard to achieve their intended function. The toughness of a material is properly quantified as either the fracture toughness, K_{Ic} , or the fracture energy, G_c , where the latter is generally preferred in the field of polymers, adhesives and composites. Toughness is a measure of a material’s resistance to crack propagation and this cannot be simply obtained from the area under a stress-strain curve. It must therefore be measured by an appropriately designed fracture mechanics test [2].

Adhesives have been used by mankind as a means of joining materials for centuries to build structures. The use of birch bark tar as a means of joining materials can be traced back to at least the Middle Stone Age and perhaps even further [3,4]. The emergence of metals as the structural materials of choice somewhat halted the development of adhesives. However, more recently, engineered structural adhesives have begun to replace traditional bolts and rivets as joining methods in the aerospace, automotive, and energy industries. Adhesively bonded joints have many advantages over conventional fasteners such as the elimination of the stress concentrations present in bolted joints, improved joint rigidity, and the possibility of joining dissimilar materials. Adhesive bonding is also the most suitable method in joining polymer matrix-reinforced composites. However, most thermoset structural adhesives are relatively brittle materials with poor resistance to crack initiation and propagation when compared to their metallic counterparts. It is no great surprise, then, that improving the toughness of these materials has been the subject of considerable research effort. In this chapter, we focus mainly on the toughening of epoxy-based adhesives and polymers. Epoxy has found itself to be the material of choice for most structural adhesives because it provides good adhesion and stiffness (see Chapter 1 for detailed discussion of epoxies). In general, the toughening strategies discussed here for

epoxy-based structural adhesives can be applied to other classes of polymeric structural adhesives with some modifications. In a brittle thermoset, the crack tip requires little energy to propagate. Therefore to toughen adhesives, the size of the energy dissipation zone at the crack tip needs to be increased to resist crack propagation. This is achieved by initiating toughening mechanisms that effect a delocalization of the high stresses at the crack tip, spreading these stresses out over a greater volume of material.

8.2 Toughening of bulk epoxy polymers

As unmodified thermosets are so brittle, considerable attention has been paid to their toughening. Ductile fracture behavior can be promoted over brittle fracture behavior by plasticization of the polymer. In general, this will have the effect of reducing both the glass transition temperature and modulus. This is undesirable in many applications as this reduces the maximum operating temperature and creep resistance. The introduction of a minority second phase that does not adversely affect either the glass transition temperature or the modulus of the thermoset matrix is an alternative and preferred method to improve fracture performance by promoting toughening mechanisms near the crack tip. In this section, the many types of modifiers and their associated toughening mechanisms to improve the fracture toughness of epoxy polymers will be discussed.

8.2.1 Chemical modification

Plasticization of the glassy epoxy polymer can promote ductile fracture mechanisms. However, as plasticization involves the use of chain extenders [5], which increase the molecular weight between crosslinks, the glass transition temperature and modulus are often adversely affected.

A second chemical modification is the creation of interpenetrating polymer networks (IPNs). Interpenetrating networks consist of two crosslinked networks that are not chemically bonded to each other but occupy the same physical volume. To completely fracture the resultant polymer, the chemical bonds of both networks within the IPN must be broken.

To form an IPN, the secondary polymer must be initially miscible with the epoxy polymer. Elastomers [6] and thermosets [7–9] have been reported to form IPNs with epoxy polymers. Lim et al. [10] reported the possible formation of a dual particle IPN morphology using carboxyl-terminated butadiene styrene rubber in diglycidyl ether of bisphenol A (DGEBA), although they do not comment further on the role of the IPN on the resultant fracture toughness. Masser et al. [11] reported a significant correlation between the existence of an IPN type morphology, which they term a “nanoscale morphology,” and the improved ballistic properties of the resultant epoxy polymer. Moreover, they demonstrated an ability to tune the morphology from nanoscale IPN to a macrophase separation with a resultant loss in optical clarity and ballistic performance, but maintained static fracture performance.

8.2.2 Rubber toughening

The most successful and widely used form of toughening epoxy polymers and adhesives is the use of a minority second phase of rubber. Generally, the rubber is distributed as spherical particles throughout the majority epoxy phase. This can be achieved either via reaction-induced phase separation (Section 8.2.2.1), or via the incorporation of preformed rubber particles (Section 8.2.2.2).

8.2.2.1 Reactive liquid rubbers

The use of reactive liquid rubbers, which are mostly butadiene-acrylonitrile based, is one of the earliest methods of toughening structural epoxies, as it originated in the 1960s. Carboxyl-terminated butadiene-acrylonitrile (CTBN) is the most widely used, and was first utilized by Sultan and McGarry [12]. Other types include amine-terminated (ATBN), epoxy-terminated (ETBN), and vinyl-terminated (VTBN) butadiene-acrylonitrile rubbers. These are usually prereacted to form an adduct and predissolved in epoxy because the rubber is initially miscible with the epoxy. The rubber is then able to phase separate during the curing process via reaction-induced phase separation to form micron-sized rubber particles.

The size and morphology of the phase-separated rubber particles are dependent on many factors, such as the rubber concentration, initial miscibility, and curing conditions [13–16], and therefore cannot be easily controlled. Possible morphologies include spherical particles, cocontinuous structures, and partial or full phase inversion between the rubber and the epoxy (see Fig. 8.1). Higher rubber concentrations promote the latter microstructures.

There are many studies that report significant increases in fracture energy with the addition of reactive liquid rubber in the epoxy polymer [18–21], with many reporting thousands of percentage increase. For example, Bascom et al. [20] reported an increase from 121 J/m² for an unmodified piperidine-DGEBA epoxy system, to 3500 J/m² with 15 wt% CTBN modification. Fracture energies are usually at their maximum around 10–15 wt% concentration, but they stagnate or even decrease when the concentration is increased further. Some studies attributed this behavior to the

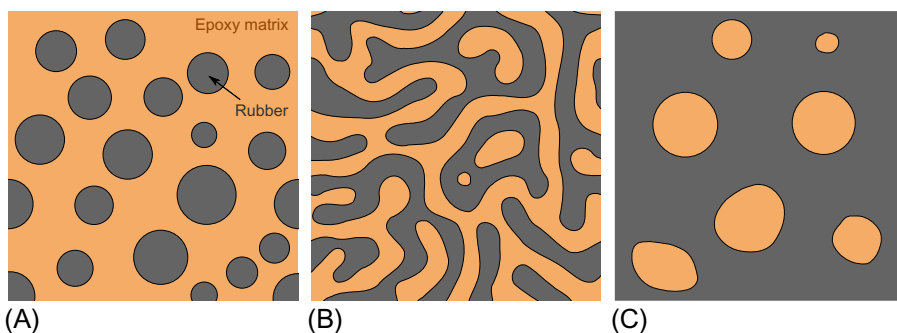


Fig. 8.1 Possible rubber morphologies of reactive liquid rubber-modified epoxies [17]. (A) Spherical particles; (B) Cocontinuous; (C) Phase inversion.

transition in morphology from spherical particles to cocontinuous and phase-inverted structures that occurs at high rubber concentrations [19,20,22]. The toughening mechanisms for rubber particles of spherical morphology are well understood [23], with shear band yielding and plastic void growth providing the majority of the toughening contribution. However, the toughening mechanisms for cocontinuous or phase-inverted structures are relatively less understood.

In addition to the inherent decrease in modulus that comes with the addition of rubber, most studies also report a decrease in the glass transition temperature, T_g , of the epoxy polymer. Lim et al. [10] reported a decrease in T_g from 143°C to 133°C with the addition of 9 wt% CTBN in their anhydride-cured DGEBA system. This is due to some CTBN not phase separating and remaining dissolved in the epoxy, which can compromise the elevated temperature performance but will increase the toughness of the epoxy matrix, which is beneficial [24].

8.2.2.2 Core-shell rubbers

Most of the limitations of using phase-separating liquid rubbers can be alleviated by using a newer class of rubber particle called core-shell rubbers (CSRs). These particles usually consist of a soft rubbery core (such as polybutadiene) within a harder shell, and are typically formed by emulsion polymerization, hence the particle size can be readily controlled and is usually in the nanoscale [25,26]. The polymer used for the outer shell is often chosen to be compatible with epoxy polymers, such as poly(methylmethacrylate) [21,27], which can also be functionalized to further improve compatibility [26].

Because the particles are preformed before being dispersed in the epoxy resin, the glass transition temperature of the epoxy polymer is unaffected by the presence of the CSR particles [28], and can provide similar magnitudes of toughening to reactive liquid rubbers [21,29–32]. Despite this, CSR particles can be prone to agglomeration [33,34], a common problem that is shared with other types of nanoparticles. This can decrease the efficiency of toughening because the shear band yielding and plastic void growth toughening mechanisms are limited by the volume of epoxy around the rubber particles. Some studies report a plateau in fracture energy at high concentrations of CSR particles [29,34], which was attributed to the lack of available epoxy around each particle that is able to deform plastically.

8.2.2.3 Rubber-like toughening via microvoid toughening

Inspired by the success of rubber particles in toughening epoxy polymers, a number of researchers explored the possibility of toughening via the direct inclusion of voids. Bureau and Kumar [35] investigated the fracture toughness of microcellular polycarbonate foam with a relative density between 0.7 and 0.9. They found that while the fracture toughness of the 0.7 relative density foam was reduced compared to the bulk polymer, the fracture energy was increased due to a reduction in modulus. Huang and Kinloch [36] tested epoxy with 17% volume of 0.7 μm voids. They found that the combination of an increase in K_c and a reduction in modulus gave rise to a significant

increase in fracture energy, G_c . Kim and Kim [37] achieved an improvement in fracture toughness by introducing voids through an aeration process. Bagheri and Pearson [38–40] studied epoxy containing a range of hollow latex particles acting as voids. The particles ranged in size from 0.2 to 40 μm . They found that conventional rubber modifiers and the hollow particles toughened the epoxy in the same manner. They showed that the materials go through a brittle-to-tough transition as the interparticle distance decreases, and that the critical distance is related to the particle size. The changing from a plane strain to a plane stress state is the major factor in this transition.

8.2.3 Thermoplastic toughening

Research into the rubber modification of epoxy polymers has typically shown significant increases in fracture toughness. However, it has also typically shown decreases in Young's modulus, yield strength, and creep resistance, which can be undesirable in some applications. The use of thermoplastic tougheners can mitigate the compromises typically seen in rubber toughening while also moderately increasing the fracture toughness [41,42]. Many types of thermoplastic modification have been studied since the technology originated in the early 1980s, such as the use of polysulfone [43], polyetherimide [44], poly(ether ether ketone) [45], etc. These thermoplastics usually come in a powdered form, and are dissolved into the epoxy at elevated temperature. Similarly to reactive liquid rubbers, the thermoplastic phase separates during the curing of the epoxy into spherical particles, cocontinuous structures, or phase-inverted structures, depending on the thermoplastic concentration (higher concentrations promote the latter morphologies).

While thermoplastics are able to toughen epoxies, the toughening mechanisms they provide are fundamentally different to those from rubbery particles [46]. Toughening mechanisms proposed include crack pinning, microcracking, and plastic deformation of the thermoplastic-rich phase [41,42,47]. Studies have found that the highest toughness is achieved at higher thermoplastic concentrations (15–30 wt%) where cocontinuous and phase-inverted morphologies occur, which is the opposite behavior for reactive liquid rubber-modified epoxies. Some observe a step change in fracture toughness [48,49] and therefore attribute the increase to the change in microstructure. However, some see a linear increase [41,44,50] and argue that the fracture toughness is simply a function of the thermoplastic concentration, and not due to any changes in thermoplastic morphology.

8.2.4 Block copolymers

The use of block copolymers (BCPs) is one of the latest and most highly promising strategies into toughening structural epoxies. BCPs comprise at least two different block-wise monomer units covalently bonded together, such as diblock (AB), triblock (ABA, ABC), etc. [51]. Monomer blocks can be selected such that some are epoxy-phobic (usually a rubbery phase) while others are epoxy-philic to create an amphiphilic BCP. These types of BCPs have been of particular interest in epoxy toughening because they are able to self-assemble into nanoscale structures, such as spherical

micelles, worm-like micelles, and vesicles [51–53], which are then fixed in place by the polymerization process of the epoxy polymer. Such structures can significantly increase the fracture toughness of epoxies while having a minimum impact on the modulus and glass transition temperature [54]. Yang et al. [55] investigated poly(ϵ -caprolactone)-block-poly(butadiene-co-acrylonitrile)-block-poly(ϵ -caprolactone)-modified epoxies and found that the nanostructures formed from the BCP provided a higher T_g and fracture toughness than the direct ternary blend of poly(butadiene-co-acrylonitrile) and poly(ϵ -caprolactone) into the epoxy. Understandably, the toughening mechanisms of such nanostructures are relatively difficult to observe. However, Chen and Taylor [56], using transmitted and cross-polarized light microscopy, proposed that crack branching and shear band yielding are the main mechanisms that contribute to the toughness improvements.

Furthermore, some BCPs are also able to microphase separate into spherical, cocontinuous, and phase-inverted morphologies, with the nanoscale structures contained within the BCP phase [56–58]. The toughening mechanisms are the same as with reactive liquid rubber-modified epoxies, with shear band yielding and plastic void growth being the main contributors to toughening. Interestingly, two separate studies [56,57] on poly(methyl methacrylate)-block-poly(butylacrylate)-block-poly(methyl methacrylate) (MAM)-modified epoxies have found a remarkable step increase in fracture toughness at 10 wt% concentration (e.g., from 300 to 1800 J/m² [56]), where a cocontinuous microstructure of MAM and epoxy domains was present. Chen and Taylor [56] proposed several mechanisms to explain the large improvements in toughness. In a cocontinuous structure, the hard and soft composite-like structure spans across the fracture surface. The soft phase deforms and absorbs energy more readily than the epoxy phase, due to the low yield stress and high ductility of the soft phase. The deformation and energy absorption occur before the epoxy ligaments spanning across the crack surfaces fracture, effectively blunting the crack tip and leading to large increases in fracture energy [58]. In addition, the connected structures can interact to greatly increase the size of the plastic deformation zone and thus increase toughness.

8.2.5 Inorganic rigid particles

Generally, the toughening from rigid particles is less effective than rubber particles. There are some advantages, these include improved modulus, reduced cure shrinkage, and minimal effect on glass transition temperature, compared to using rubber. Some of the toughening mechanisms provided by rigid particles are dependent on the particle-matrix adhesion, with moderate levels of adhesion providing the greatest amount of toughening [59,60]. Sprenger et al. [61] were the first to report improvements in the toughness of structural adhesives with the addition of silica nanoparticles. Sprenger [62] states that at a particle loading of 10%, the toughness of a core-shell rubber-modified epoxy polymer increases by a factor of two to four, whereas for the same loading of silica nanoparticles, the improvement is only 50%. Recently, the use of nanosilica in combination with rubber has shown great potential because the

nanosilica can recover the lost modulus as well as provide additional synergistic toughening effects, as discussed in [Section 8.2.7](#).

Kinloch and Taylor [63] investigated the effect of a range of inorganic particles such as mica and montmorillonites (“organoclays”). They noted that the high aspect ratio and relatively large particle size of the mica were beneficial for toughening. Crack deflection was noted as a potential toughening mechanism, although it did not account for all the observed increase in toughness. Debonding and plastic deformation of the matrix surrounding the particles were determined as the principal toughening mechanisms. Kothmann et al. also reported debonding and subsequent void growth as toughening mechanisms [64]. The use of mica and “organoclays” as an inclusion in structural adhesives appears to have fallen out of favor. Much of the research on high aspect ratio, platelet-type particles in structural adhesives and polymers is now focused on graphene and derivatives, which are discussed in [Section 8.2.6.2](#).

8.2.6 Organic rigid particles (carbon nanotubes, graphene, etc.)

Carbon-based fillers such as nanotubes and graphene have been the subject of much recent research. This is, in part, due to their potential to offer multifunctional performance improvements such as thermal and electrical conductivity, damage-sensing capabilities to a structural adhesive or nanocomposite, and a mechanical reinforcing effect.

8.2.6.1 Carbon nanotubes

First reported by Iijima [65], carbon nanotubes (CNTs) have also shown some promise as a nanomaterial which can be functionalized and used to enhance the toughness of epoxy adhesives. CNTs possess some exciting properties such as high electrical and thermal conductivity in addition to excellent mechanical properties. These make CNTs an attractive candidate as a potential toughening agent in multifunctional adhesives.

Early work by Sandler et al. [66] and Gojny et al. [67,68] studied the effect of CNTs on the mechanical, electrical, and fracture properties of epoxy composites. They observed that the addition of a small amount of CNTs resulted in an improvement in both the mechanical properties, that is, the strength, Young’s modulus, and strain to failure, and the fracture toughness of the resultant nanocomposite. Furthermore, the percolation threshold, defined as the filler content to achieve a conductivity of $c \geq 10^{-6}$ S/m, was reported to be very low, that is, below 0.1 wt% for single-walled CNTs.

Jakubinek et al. [69] reported that the incorporation of CNTs into epoxy polymers resulted in an enhancement of the peel strength and a decrease in the lap shear strength. They also reported a percolation threshold between 0.2 and 0.5 wt% to obtain electrical conductivity.

Burkholder et al. [70] demonstrated that the addition of multiwalled CNTs in the adhesive can improve the fracture properties of both steel-composite and composite-composite adhesive joints. It was shown that chemical functionalization of the

nanotubes as well as concentration and dispersion all play significant roles in determining whether the incorporation of nanotubes into an epoxy polymer adhesive strengthened or weakened the adhesive joint and increased or decreased the fracture toughness.

Hsieh et al. [71] reported an improvement of almost 100% in the quasistatic fracture performance of a model epoxy polymer modified with 0.5 wt% of multiwalled CNTs. They also reported a fatigue performance improvement of approximately 200%. The threshold strain energy release rate, G_{th} , improved from 24 J/m² to 73 J/m². They further noted that debonding of the nanotubes from the epoxy matrix and subsequent pull-out are the principal toughening mechanisms, and that the contribution of void growth around the debonded nanotubes was not a significant contributor to the toughening effect.

8.2.6.2 Graphene and derivatives

Since first reported by Geim, Novoselov, and coworkers [72,73], graphene has been hailed as a wonder material with a myriad of applications. As a potential additive to improve the performance of a structural adhesive, graphene has extremely high stiffness and strength, and when combined with polymers has shown similar promise to CNTs in terms of multifunctional properties, that is, a toughening effect and an enhancement of the conductivity of the adhesive [74,75]. However, as with CNTs, the effective transfer of stress between graphene and the surrounding polymer has proven difficult to achieve and has limited the utility of graphene as an additive in structural adhesives. These difficulties are mainly due to problems in effectively dispersing graphene and achieving strong platelet-matrix interfacial adhesion. Indeed, it is worth noting that many publications in the literature on graphene as a modifier in structural adhesives, such as [10,76], actually use graphene nanoplatelets (GNPs or multilayered graphene) rather than single-sheet graphene.

Early work on using graphene as a reinforcement in structural adhesives and polymers focused on graphene oxide, such as [77,78]. Graphene oxide can be relatively easily exfoliated and dispersed throughout the polymer due to the presence of the functional groups. However, the functional groups can cause wrinkling of the sheets, reducing the reinforcing effectiveness of the graphene oxide [79].

GNPs have emerged as a lower cost option relative to both CNTs and single-layer graphene, providing conductivity at a very low particle content while also providing reinforcement and toughening that cannot be achieved using carbon black. GNPs are small stacks of multiple graphene sheets, typically derived from bulk graphite compounds.

Rafiee et al. [80] considered the effect of 0.1 wt% GNPs on the mechanical properties of epoxy. Their work also compared the results with epoxy composite modified with CNTs at the same weight percentage. GNPs were dispersed into the epoxy matrix through sonication in an acetone solution, although they did not report on the quality of dispersion achieved. They reported that the mechanical properties of a graphene-modified epoxy composite were significantly better than those achieved using either single-walled or multiwalled CNT-modified composite at the same levels of loading.

The fracture toughness for the GNP-modified composite was reported to be 53% higher than for unmodified epoxy. Detailed analysis on the fracture surfaces suggested that the toughening mechanism responsible for the toughness enhancement was crack deflection. They dismissed the possibility of the GNP pull-out from the matrix as a significant contributor to the enhanced toughness, as they claimed that GNPs had a strong interfacial adhesion with the epoxy matrix.

Chong et al. [81] compared the effectiveness of various commercially available GNPs as well as the dispersion method in a systematic study. They found that the Young's modulus was highly dependent on the dispersion quality. However, the fracture energy appeared largely insensitive to dispersion quality. GNPs dispersed via sonication in tetrahydrofuran (THF) tended to form larger agglomerates and the associated toughening mechanism was identified as crack deflection. A second solvent, *n*-methyl pyrrolidone (NMP), was also used to disperse the GNPs. This generally resulted in smaller agglomerates than when dispersed in THF. The associated toughening mechanisms were identified as platelet debonding, platelet pull-out, and plastic void growth of the epoxy. This suggests that the effective toughening of epoxy adhesives via GNP inclusion can be achieved at low GNP loading if special care is taken in achieving a good dispersion of small agglomerates.

8.2.7 Hybrid toughening

The concept of hybrid toughening, that is, using more than one type of particle to toughen a system, has been around almost as long as the concept of toughening epoxy polymers. An early focus was on combining both soft and rigid particles together, the concept being that the soft rubber particles were effective tougheners, but the reduction in modulus and strength caused by using these particles could be ameliorated by the inclusion of a third, more-rigid phase. Kinloch and coworkers were among the first to report on this phenomenon [82–84]. They studied a combination of 50 μm -scale glass particles with phase-separating carboxyl-terminated butadiene nitrile rubber. They noted that the fracture energy of these materials in combination was substantially higher than the sum of the individual contributions from each particle type alone. Further, the loss in modulus due to the addition of the rubber particles was recovered by the addition of the stiff glass particles. Crack pinning by the relatively large glass particles was identified as a toughening mechanism while shear band yielding was proposed as the primary toughening mechanism induced by the presence of the rubber particles. The synergistic effect reported here has since been sought by several research groups, such as [30,85–89]. These groups mainly concentrated on investigating blends of rubber and silica nanoparticles. Of these studies, it is worth noting that only Hsieh et al. [89] and Liang and Pearson [88] reported a synergistic effect. In both cases, a phase-separating CTBN rubber was used. In the case of Hsieh et al., atomic force microscope (AFM) and transmission electron microscope (TEM) images of the microstructure revealed “necklace” type regions of silica nanoparticles. Liang and Pearson [88] speculate that the enhancement in toughness of the hybrid material involves an increase in shear band density between rubber particles in the plastic zone, thus increasing the plastic zone size. Carolan et al. [30] explored the existence of a

synergy using CSR particles and silica nanoparticles. They reported a negative synergy under certain conditions, that is, where the combination of CSR particles and silica nanoparticles resulted in almost no toughening effect. Scanning electron microscope (SEM) imaging of the fracture surface revealed that the silica nanoparticles tended to agglomerate around the larger CSR particles. This had the effect of (a) shielding the rubber particles from the stresses required to cavitate, (b) partially inhibiting the formation of effective shear bands, and (c) preventing void growth. The introduction of a reactive diluent to the epoxy polymer removed the effect of clustering, although no synergistic effect was subsequently observed. The measured toughness of the hybrid silica-rubber-epoxy polymers was statistically equivalent to the additive effect of the silica-epoxy and rubber-epoxy polymers on their own.

8.3 Prediction of effectiveness of toughening

Intrinsic toughening mechanisms develop resistance to damage and crack growth ahead of the crack tip, such as by debonding of particles, initiation of shear bands, and void growth. The principal factor providing resistance here is plastic deformation, and the presence of the minority particulate rubbery phases enhances the plastic deformation mechanisms ahead of the crack tip. As these mechanisms promote plasticity, they can be said to promote ductile fracture behaviors, although the bulk material may still be regarded as brittle.

Extrinsic toughening mechanisms, such as fiber bridging, take place in the wake of the crack tip and act to shield the crack tip from the globally applied loads causing the crack propagation. Quantitative prediction of these mechanisms is a useful tool to predict the effectiveness of toughening strategies for various materials.

8.3.1 Toughening mechanisms for soft secondary phases

8.3.1.1 Shear band yielding

Shear band yielding is identified as one of the major toughening mechanisms in rubber-modified epoxies [23]. A shear band is a narrow region of material subjected to intense plastic shear strains. In rubber-modified epoxies, the rubber particles act as stress concentrations that promote the formation of shear bands between the particles. A schematic of the shear band yielding toughening mechanism is shown in Fig. 8.2. This plastic deformation can absorb a significant amount of energy, thus increasing fracture toughness [23].

The localized shear bands between the rubber particles can be observed experimentally using transmission optical microscopy, such as in Fig. 8.3, which shows a CSR-modified epoxy polymer [31]. A thin, polished section of a subcritically loaded crack tip in the plane strain region was observed with transmitted light. The micrograph shows that a large feather-like deformation zone was formed at the crack tip. The localized shear bands between the CSR particles scatter the visible light and therefore

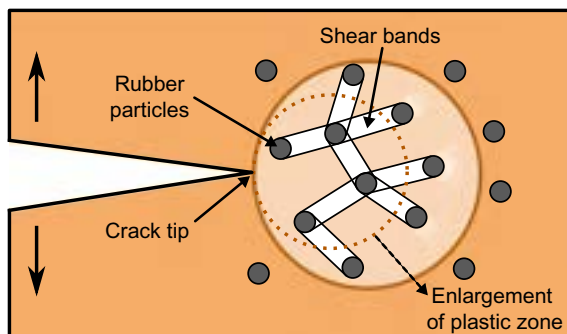


Fig. 8.2 Schematic showing the shear band yielding toughening mechanism.



Fig. 8.3 Transmission optical micrograph of a subcritically loaded crack tip in the plane strain region of a 10 wt% CSR-modified epoxy polymer [31].

appear dark using the optical microscope. The formation of shear bands was also successfully modeled using a two-dimensional (2D) finite element analysis method [23].

In the literature, a common approach to observe the evidence of the shear band yielding toughening mechanism is to view compression specimens using transmitted light microscopy [32,58]. An example is shown in Fig. 8.4, which shows plane strain compression specimens of CTBN rubber-modified epoxy polymers loaded past the yield point and into the strain softening region. The samples were observed using cross-polarized light.

The transmission optical micrograph for the unmodified epoxy in Fig. 8.4A clearly shows the macroscopic shear bands that were formed in the strain softening region as highly focused birefringence. Yielded regions of epoxy will have a different refractive index than the otherwise unrefractive nonyielded regions. Polarized light is therefore rotated after passing through the shear bands, which is why they appear bright when using cross-polarized light. As the concentration of CTBN increases, the compressed region appears more diffuse, the intensity of the shear bands is decreased, and the shear bands become less focused. This suggests that the CTBN particles have formed highly localized microscopic shear bands that initiate and terminate between adjacent particles due to the stress concentration effect around the particles. The formation of such highly localized microscopic shear bands between the rubber particles has thus suppressed the macroscopic inhomogeneous shear band deformation; it also confirms the presence of the shear band yielding toughening mechanism.

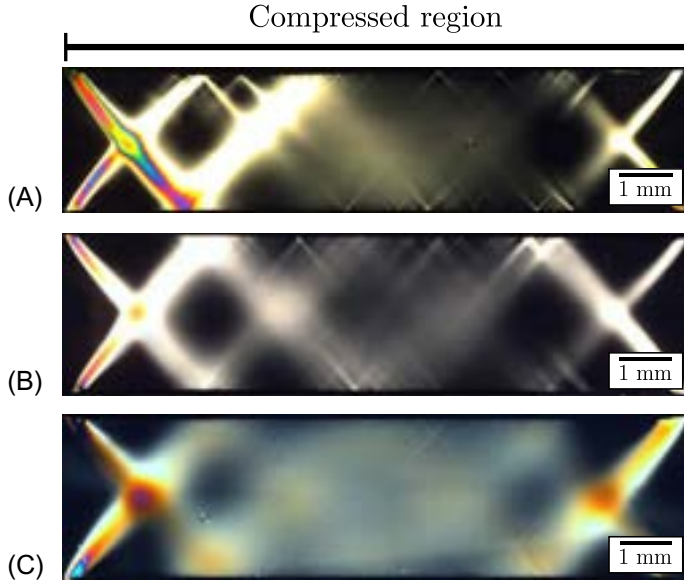
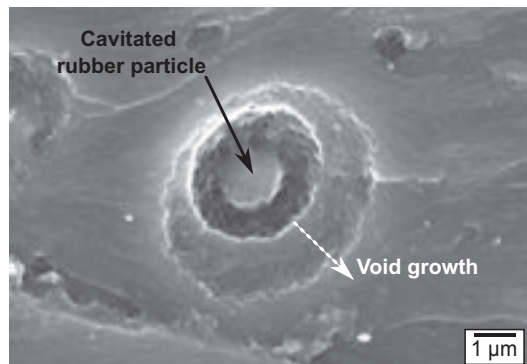


Fig. 8.4 Transmission optical microscopy images of plane strain compression specimens loaded to the strain softening region for (A) unmodified, (B) 6 wt% CTBN and (C) 12 wt% CTBN rubber-modified epoxies.

8.3.1.2 Plastic void growth

The large hydrostatic stresses ahead of the crack tip will cause cavitation of the rubber particles, such as that seen in Fig. 8.5, which leads to the formations of voids. Although the process of cavitation does not absorb a significant amount of energy [21], it is crucial in relieving the stress triaxiality ahead of the crack tip [90]. The rubber particles cavitate at a low stress. This was noted by Pearson and Yee [91] to precede localized shear yielding, although Huang and Kinloch [23] later demonstrated that cavitation can occur before or after shear banding. The high bulk modulus of

Fig. 8.5 Scanning electron micrograph of a cavitated rubber particle and subsequent void growth.



the rubber particles inhibits volumetric deformation of the surrounding polymer until the particles cavitate, after which the resultant void offers no further resistance to deformation. This cavitation relieves the triaxial stress state constraint ahead of the crack tip, inducing the surrounding matrix around the void to undergo plastic deformation, which absorbs a significant amount of energy, thus enhancing toughness.

8.3.1.3 Rubber bridging

The rubber bridging mechanism occurs when rubber particles are stretched between two crack surfaces behind the crack tip. Further advance of the crack requires the stretching and tearing of the rubber ligaments, which absorbs energy, thus resulting in an increase in toughness. The radius of the rubber particles must be of similar order to the crack tip radius to be able to bridge the crack. Pearson and Yee [92] showed evidence of rubber bridging for epoxies modified with 200 μm diameter rubber particles, but not with 0.2 μm diameter particles. Other works on epoxies that were modified with nanosized rubber particles (~ 40 nm diameter) [31] also showed no evidence of rubber bridging in the fractography. A schematic of the rubber bridging mechanism is shown in Fig. 8.6.

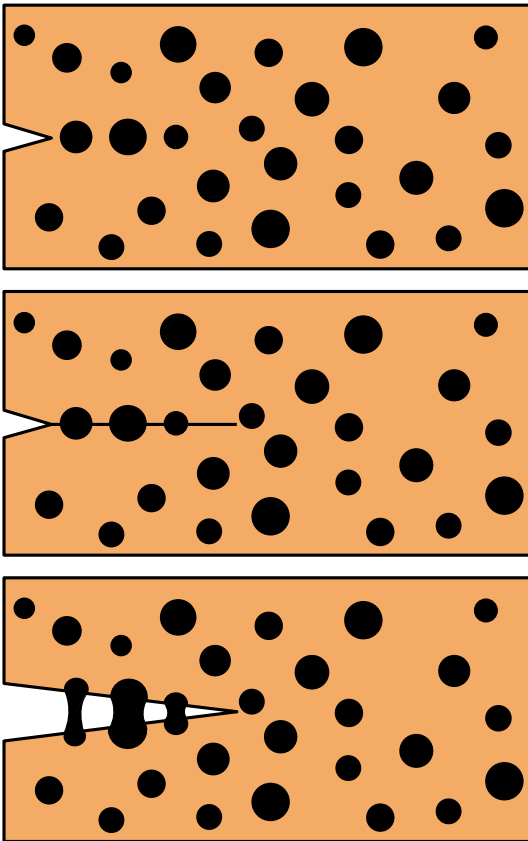


Fig. 8.6 Schematic showing the stages of the rubber bridging mechanism.

Redrawn from S. Kunz-Douglass, P.W.R. Beaumont, M.F. Ashby, A model for the toughness of epoxy-rubber particulate composites, *J. Mater. Sci.* 15 (1980) 1109–1123.

This mechanism was thought to have the major role in rubber-modified epoxies according to Kunz-Douglass et al. [93]. However, this was disputed by several authors who commented that this mechanism does not take into account the properties of the epoxy matrix, and that it cannot explain stress whitening effects nor can it accurately model fracture toughness at higher temperatures [23]. A model developed by Huang and Kinloch [23] found that only 8% of the overall toughening is due to rubber bridging at room temperature. It is now generally accepted that rubber bridging is a secondary toughening mechanism in rubber-toughened epoxies.

8.3.2 The Huang-Kinloch model

The Huang-Kinloch model [23] is a very powerful tool for predicting the fracture energy of modified epoxies. It can be a truly predictive model that depends solely on material properties and requires no fitting to experimental data. Published in 1992, the Huang-Kinloch model still has profound use at present. Although originally developed to predict the fracture energy of rubber-modified epoxies, the Huang-Kinloch model has been generalized to predict the toughening increments caused by many other types of modifiers such as nanosilica [30], CNTs [71], hollow glass microspheres [94], etc.

The Huang-Kinloch model in its original form is given by:

$$G_{Ic} = G_{Icu} + \psi \quad (8.1)$$

where the fracture energy in Mode I of the modified epoxy, G_{Ic} , is expressed as the sum of the fracture energy of the unmodified epoxy, G_{Icu} , and the overall toughening contributions from the toughening modifier, ψ . For the case of rubber-modified epoxies, the ψ term can be separated into the toughening contributions from each of the toughening mechanisms described previously, and can therefore be written as:

$$\psi = \Delta G_s + \Delta G_v + \Delta G_r \quad (8.2)$$

where ΔG_s , ΔG_v , and ΔG_r are the fracture energy contributions from shear band yielding, plastic void growth, and rubber bridging, respectively.

8.3.2.1 Plastic zone radius

For modeling of the shear band yielding and plastic void growth toughening mechanisms, the plastic zone radius of the modified material, r_y , is required in the calculations. This can be estimated using [23]:

$$r_y = K_{vm}^2 \left(1 + \frac{\mu_m}{\sqrt{3}} \right)^2 r_{yu} \quad (8.3)$$

where K_{vm} is the von Mises stress concentration factor, μ_m is the pressure-dependent material constant, and r_{yu} is the radius of the plastic zone for the unmodified epoxy

polymer under plane strain conditions. The value of K_{vm} is dependent on the particle volume fraction, V_f , and whether the particles are classed as soft or rigid. For the case of soft particles, such as CTBN rubber, the value of K_{vm} can be fitted to the data of Huang and Kinloch [95], who modeled a rubber-modified epoxy using finite element analysis. The fitting equation is:

$$K_{vm} = 3.9337V_f + 2.1126 \quad (8.4)$$

In the case of hard particles, K_{vm} was found to vary linearly with the particle volume fraction, using the data from Guild and Young [96]. The fitting equation for the data is:

$$K_{vm} = 0.59V_f + 1.65 \quad (8.5)$$

The radius of the plastic zone for the unmodified epoxy, r_{yu} , can be calculated using the equation proposed by Irwin [97]:

$$r_{yu} = \frac{1}{6\pi} \left(\frac{K_{Icu}^2}{\sigma_{yt}^2} \right) \quad (8.6)$$

where K_{Icu} and σ_{yt} are the fracture toughness and plane strain tensile yield stress of the unmodified epoxy, respectively.

8.3.2.2 Shear band yielding

The fracture energy contribution from the shear band yielding toughening mechanism, ΔG_s , was proposed by Huang and Kinloch [23] as a function of the radial distance from the crack tip, r , as:

$$\Delta G_s = 2 \int_0^{r_y} U_s(r) dr \quad (8.7)$$

where r_y is the radius of the plastic zone ahead of the crack tip, and $U_s(r)$ is the dissipated strain energy density for the shear yielding mechanism. However, a slightly modified version of this equation has now generally been accepted, where the lower limit of the integral has been changed to the radius of the particle, r_p , as suggested by Evans et al. [98], giving:

$$\Delta G_s = 2 \int_{r_p}^{r_y} U_s(r) dr \quad (8.8)$$

They proposed this lower limit as the minimum distance from the crack plane at which the epoxy polymer between the particles experiences shear yielding, which is in the order of the particle radius.

The dissipated strain energy density from shear band yielding, $U_s(r)$, is given by [23]:

$$U_s(r) = V_{sy}(r)W_d(r) \quad (8.9)$$

where $V_{sy}(r)$ is the volume fraction of shear yielded material and $W_d(r)$ is the shear plastic strain energy density of the matrix material. The former, $V_{sy}(r)$, can be expressed as [23]:

$$V_{sy}(r) = 0.5V_f \left[3 \left(\frac{4\pi}{3V_f} \right)^{\frac{1}{3}} \alpha(r) + 4[1 - \alpha(r)]^{\frac{3}{2}} - 4 \right] \quad (8.10)$$

where $\alpha(r)$ is a scaling factor, which was suggested by Kinloch [99] to be:

$$\alpha(r) = 1 - \frac{r}{r_y} \quad (8.11)$$

which allows for the degree of shear banding to be more intense as the radial distance approaches the crack tip, as $\alpha(r) \rightarrow 1$, and to diminish toward the outside of the plastic zone, as $\alpha(r) \rightarrow 0$.

The shear plastic strain energy density, $W_d(r)$, can be calculated using [23]:

$$W_d(r) = 0.5\sigma_{yc}\gamma_f\alpha(r) \quad (8.12)$$

where σ_{yc} and γ_f are the uniaxial compressive yield stress and compressive failure strain for the unmodified epoxy, respectively. Substitution of the terms into Eq. (8.8) and integrating then gives:

$$\Delta G_s = 0.5V_f\sigma_{yc}\gamma_f F'(r_y) \quad (8.13)$$

where [89,100]:

$$F'(r_y) = r_y \left[\left(\frac{4\pi}{3V_f} \right)^{\frac{1}{3}} \left(1 - \frac{r_p}{r_y} \right)^3 - \left(\frac{8}{5} \right) \left(1 - \frac{r_p}{r_y} \right) \left(\frac{r_p}{r_y} \right)^{\frac{5}{2}} - \left(\frac{16}{35} \right) \left(\frac{r_p}{r_y} \right)^{\frac{7}{2}} - 2 \left(1 - \frac{r_p}{r_y} \right)^2 + \left(\frac{16}{35} \right) \right] \quad (8.14)$$

8.3.2.3 Plastic void growth

The toughening contribution from plastic void growth, ΔG_v , was derived from Huang and Kinloch [23]:

$$\Delta G_v = 2 \int_0^{r_y} U_v(r) dr \quad (8.15)$$

where $U_v(r)$ is the dissipated strain energy density for the plastic void growth mechanism. Assuming that linear elastic fracture mechanics (LEFM) is valid, $U_v(r)$ can be expressed as [23]:

$$U_v(r) = 0.5\sigma_{yt}(V_v - V_f) \quad (8.16)$$

where V_v is the volume fraction of the voids. Substituting Eq. (8.16) into Eq. (8.15), and substituting for r_y from Eq. (8.3) in the integration, gives:

$$\Delta G_v = \left(1 + \frac{\mu_m}{\sqrt{3}}\right)^2 (V_v - V_f)\sigma_{yt}r_{yu}K_{vm}^2 \quad (8.17)$$

The volume fraction of the voids may be measured directly postfracture (such as measuring a scanning electron micrograph), or a purely predictive method can be used. Assuming that the extent to which a void can grow is limited by the failure strain of the epoxy polymer in plane strain compression [89], γ_f , then the circumferential strain of the void is equal to the failure strain, such that the radius of the void, r_v , can be predicted using:

$$r_v = (1 + \gamma_f)r_p \quad (8.18)$$

where r_p is the radius of the particle. The term $(V_v - V_f)$ in Eq. (8.17) can therefore be written as:

$$V_v - V_f = V_f \left[(1 + \gamma_f)^3 - 1 \right] \quad (8.19)$$

8.3.2.4 Rubber bridging

The fracture energy contribution from rubber bridging was given by Kunz-Douglass et al. [93], and is of the form:

$$\Delta G_r = 4\Gamma_t(T)V_f \quad (8.20)$$

where $\Gamma_t(T)$ is the tearing energy of the rubber particles. As mentioned previously, it is generally accepted that rubber bridging is a secondary toughening mechanism in rubber-toughened epoxies, and only has a minor contribution to the overall fracture energy. More recent studies on rubber-modified epoxies have even omitted this toughening contribution in their analytical modeling with no detriment to the predictions [29–32].

8.3.3 Finite element modeling of toughening

The Huang-Kinloch [23] model is very effective at predicting the toughening effect for modified epoxies. It is a statistical model in that the actual microstructure is not considered. To see the effects of changes in the microstructure requires finite element

or finite volume modeling. This is typically combined with a statistical analysis to predict the effect of differences in microstructure between regions or between samples of the same formulation, for example by averaging the results from many different arrangements of particles.

Guild and Young have considered the toughness of modified epoxies, initially by considering a unit cell of epoxy matrix containing a single hard [96] or soft [101] particle, and applying triaxial tension loading to simulate the boundary conditions within the plastic zone at a crack tip. By examination of the three-dimensional stress state ahead of a crack with finite element simulations, Guild et al. [102] showed that the triaxial loading should have relative magnitudes of 1.0:0.8:0.8. This work predicted that higher strains are required for the cavitation of rubber particles as the particle diameter decreases, so small particles may not cavitate and hence not initiate toughening mechanisms before the matrix yields, preventing cavitation occurring. Guild et al. [103] also modeled hard particles in epoxy, and predicted when debonding will occur. The unit cell approach has also been used to study the formation of shear bands between particles such as in [95,104] (see Fig. 8.7). It is, however, not straightforward

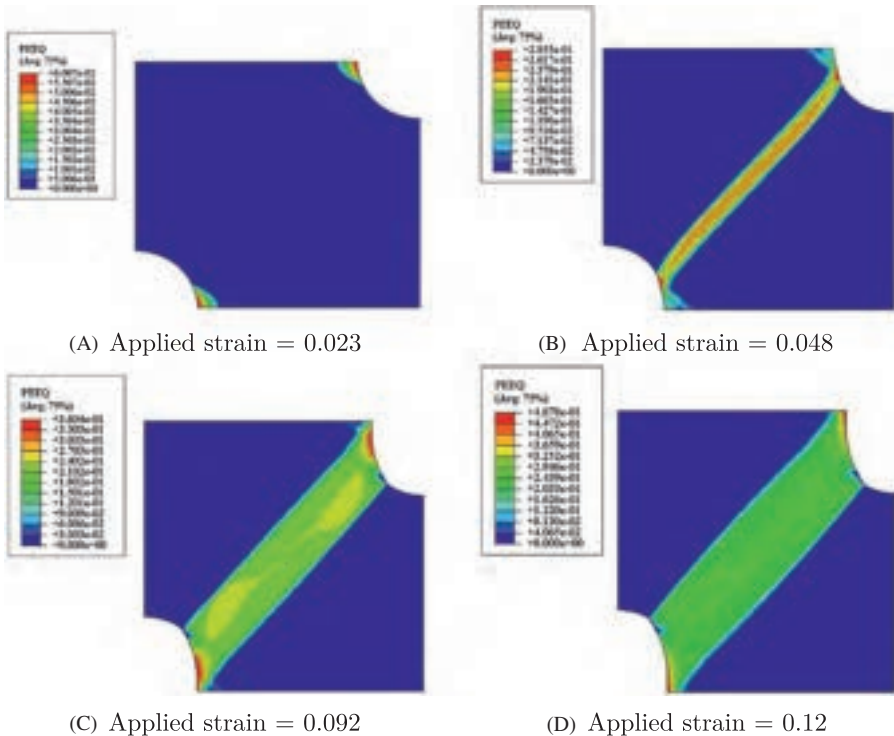


Fig. 8.7 Equivalent plastic strain showing development of shear bands between rubber particles in core-shell rubber-modified epoxy, at applied strains of (A) 0.023, (B) 0.048, (C) 0.092, and (D) 0.12 [105].

to predict the fracture energy from these toughening mechanisms using such finite element models.

The effects of hybrid toughening have also been considered. Khaleque [105] showed that the addition of silica nanoparticles to a CSR-modified epoxy increased the plastic energy dissipation density within the shear bands formed by rubber particles. The predictions showed no effect of the arrangement of the particles, but the energy increased with the volume fraction as was seen experimentally. No synergy was identified in the toughness values measured experimentally, and the modeling work also predicted an additive rather than a synergistic effect on toughening. However, Chong [106] used finite element analysis (FEA) to show that the presence of silica nanoparticles may increase the width of the shear bands that form between the larger rubber particles.

If it is important to consider the effect of the observed microstructure, then images obtained using optical, scanning electron, or atomic force microscopy can be meshed for use with finite element models. It can be a significant effort to convert from image to mesh, but suitable algorithms are available, such as in [107]. These models can be used to study the local effects of microstructure, for example if irregularly-shaped particles are present, and to predict the path that a crack will take [108].

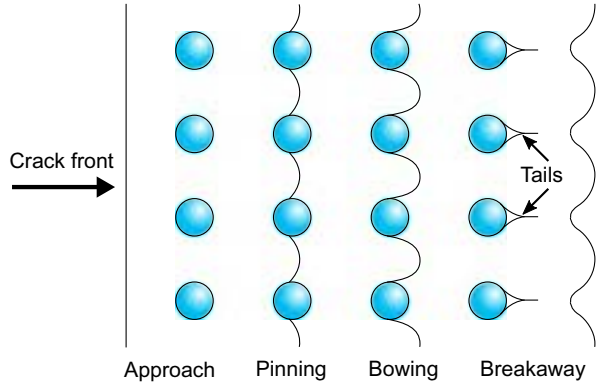
The quality of the dispersion of particles has also been considered, as clustering may affect the toughness if, for example, particles are locally located so close to each other such that there is insufficient matrix around them to maximize the toughening effect. Bray et al. [109] used a Delaunay tessellation method to quantify the dispersion, and showed that silica nanoparticles in epoxy were dispersed in an arrangement that was slightly more ordered than a random arrangement [110], but also that the silica clustered when CTBN rubber was added. Keller et al. [32] showed that CSR particles were distributed randomly in epoxy. Chong [111] showed that this method of analysis may be used successfully to identify changes in the quality of dispersion as the volume fraction of particles is increased. For an epoxy containing CTBN rubber and silica nanoparticles, Chong showed that the silica nanoparticles become more clustered as the volume fraction of rubber increases [111]. Recent modeling work has shown that slight clustering may increase the properties of the modified epoxy [103].

8.3.4 Toughening mechanisms for rigid secondary phases

8.3.4.1 Crack pinning

The crack pinning mechanism was first suggested by Lange [112]. A schematic of the crack pinning toughening mechanism is shown in Fig. 8.8. The crack front has a certain energy per unit length. The crack front approaches the rigid, impenetrable particles and becomes pinned, and can bow between the particles. The overall length of the crack front has increased, therefore increasing the energy and toughness. Authors such as Kinloch, Maxwell, and Young [83] have identified features on the fracture surfaces of glass particle-toughened epoxies that they associated with crack pinning.

Fig. 8.8 Schematic representation of the crack pinning mechanism showing successive crack fronts as they pass a row of particles.



8.3.4.2 Crack deflection

Crack deflection is a mechanism where the crack front is forced to deviate from its main plane when it encounters a rigid particle. The plane of the crack front can tilt or twist depending on the orientation and positioning of the rigid particles (see Fig. 8.9) as proposed by Faber and Evans [113,114].

The nominally Mode I crack is deflected and is then subjected to local mixed-mode loading. Mode II and Mode III crack propagation require more energy than Mode I, thus crack deflection imparts an increase in fracture energy [113]. The three modes of crack growth are shown in Fig. 8.10. A tilted crack will have Mode I and Mode II contributions while a twisted crack will have Mode I and Mode III contributions. However, in more complex systems, such as adhesive bonding of fiber-reinforced composites, the mode-mixity can be sufficient to drive the crack out of the tough adhesive and either into the underlying substrate or along the substrate adhesive interface, which is often less tough [115].

The crack pinning and crack deflection mechanisms can occur provided that the particles are larger than the crack tip opening displacement, which is shown schematically in Fig. 8.11. The crack opening displacement is defined as the distance between the opposite faces of the crack.

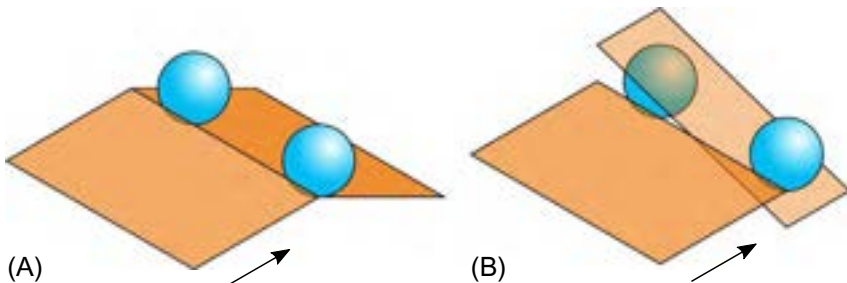


Fig. 8.9 Schematic representation of the crack deflection toughening mechanism. Arrows represent the direction of crack plane propagation. (A) Crack tilt; (B) Crack twist.

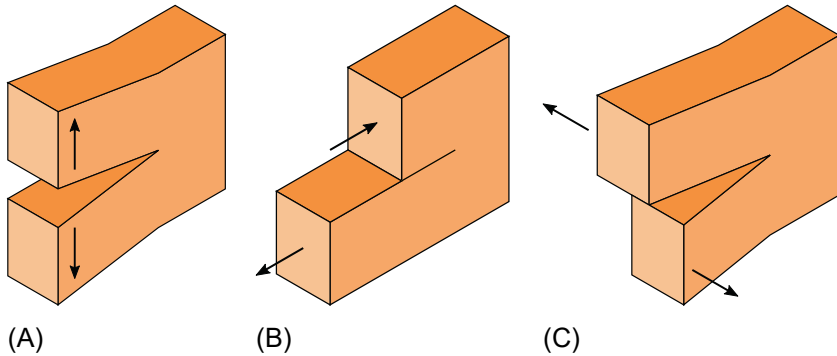


Fig. 8.10 The three modes of crack growth. (A) Mode I: Opening; (B) Mode II: In-plane shear; (C) Mode III: Out-of-plane shear.

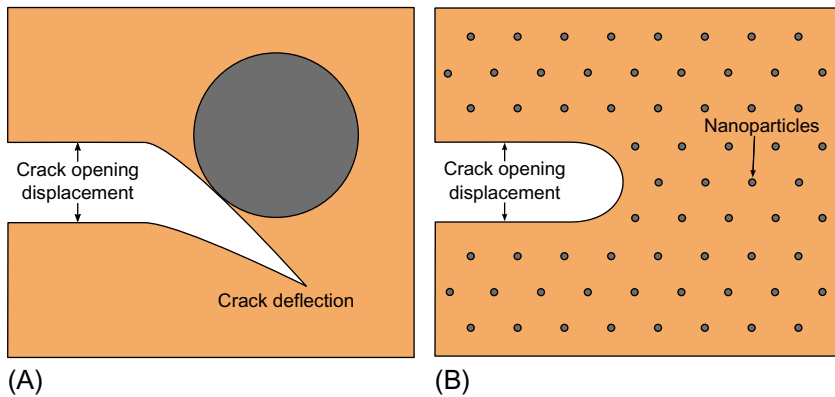


Fig. 8.11 Schematic representation of the crack deflection toughening mechanism for (A) micro- and (B) nanoparticle-modified epoxies.

Work on nanosilica-modified epoxies, where the particles have a diameter of 20 nm, has often neglected the activation of these mechanisms [116] as the particles are much smaller than the crack opening displacement, which is in the order of microns.

8.3.4.3 Debonding and plastic void growth

The triaxial stresses ahead of the crack tip cause the rigid particles within the plastic zone to debond from the epoxy matrix. The debonding process can absorb some energy. However, it is generally considered to be small compared to the energy absorbed by the subsequent plastic deformation of the matrix. Debonding is essential in relieving the stress triaxiality at the crack tip and hence allows the matrix to deform via plastic void growth [90]. Gent [117] describes the debonding process as being dependent on the particle diameter, the strength of the particle-to-matrix adhesion, and the elasticity of the matrix; Gent concluded that small particles are generally more

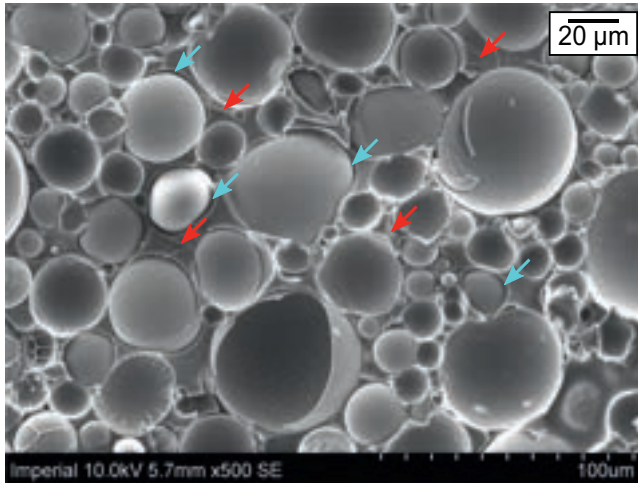


Fig. 8.12 Scanning electron micrograph of the fracture surface of a hollow glass microsphere-modified epoxy. Crack propagation is from *left to right*. Plastic void growth is indicated by *blue arrows*. Crack deflection is indicated by *red arrows*.

difficult to debond than larger particles. An example of the debonding and plastic void growth mechanism is shown in Fig. 8.12, where cavities can be seen around the hollow glass microspheres in an epoxy syntactic foam.

8.3.5 Fiber and platelet-type reinforcements

Fiber reinforcements (such as glass and carbon fibers, CNTs) and platelet-type reinforcements (such as GNPs and mica) can be added to an epoxy polymer to enhance the fracture properties. Because fibers and platelets themselves are rigid particles, they can also exhibit the toughening mechanisms listed in Section 8.3.4. However, there are toughening mechanisms that are unique to these types of modifiers, which will be described below.

8.3.5.1 Bridging

A common type of toughening mechanism in fiber-reinforced composites is fiber bridging, whereby fibers can bridge the two surfaces in the wake of the crack (see Fig. 8.13). This mechanism also applies to platelet-type reinforcements [10]. Provided that the interface region between the particle and the matrix is strong enough for stress transfer, yet weak enough for the partial debonding of the particle [118], bridging can occur. An interface that is too strong would otherwise cause direct fracture of the particle as the crack opens. Some stress is able to be transferred to the bridging particles, which can then deform elastically and store strain energy. The progression of the crack is resisted, thus leading to improvements in fracture toughness.

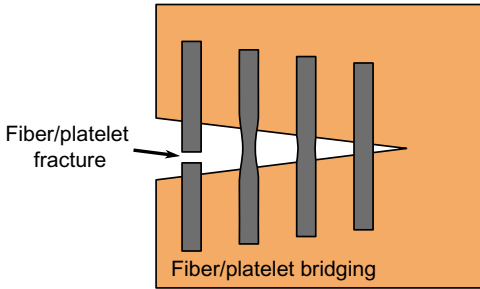


Fig. 8.13 Schematic representation of the fiber/platelet bridging and fracture mechanisms.

As the crack continues to extend, bridging particles furthest away from the crack tip may fracture and suddenly dissipate the stored strain energy (see Fig. 8.13), which can also contribute to increased fracture toughness. In carbon and glass fiber-reinforced composites, the contribution from fiber fracture is usually small, in the order of tens of J/m^2 , because these fibers are brittle in nature [119]. The use of more ductile fibers such as steel [120] or cellulose [121,122] has shown much higher contributions due to fiber fracture.

A steady-state toughness value is reached when a balance of the fiber bridging and fiber fracture mechanisms occurs as the crack advances, which is commonly taken as the propagation fracture energy, $G_{Ic,prop}$, in the fracture testing of fiber-reinforced composites [33].

8.3.5.2 Pull-out

In the case where the fibers/platelets are completely debonded from the matrix, the pull-out from their sockets in the matrix can absorb a significant amount of energy due to interfacial frictional sliding. A schematic of the pull-out mechanism is shown in Fig. 8.14.

Particles that are above a critical length (i.e., deeply embedded in the matrix) will have a probability of fracture before undergoing pull-out. The critical length, l_c , is

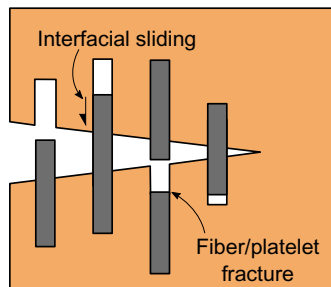


Fig. 8.14 Schematic representation of the pull-out mechanism.

derived from the shear-lag concept developed by Kelly and Tyson [123], and is given by:

$$l_c = \frac{\sigma_f d}{2\tau_y} \quad (8.21)$$

where σ_f is the failure strength of the fiber, d is the fiber diameter, and τ_y is the shear yield stress of the matrix. The stresses are highest at the locations where the particle is bridging the crack, in which case the particle is expected to fracture at the crack plane and hence pull-out should not occur [119]. However, the variability in strength along the length of the particle can allow fracture within the socket in the matrix [124].

8.4 Toughness of an adhesive joint

8.4.1 Effect of adhesive bond gap thickness

The thickness of an adhesive joint can have a significant impact on the Mode I fracture toughness, G_{Ic} , of an adhesive joint. Consistent bond thickness control is needed from an industrial perspective to obtain repeatable joint performance. Bond gap thicknesses are usually achieved by using shims or spacers, such as thin wires or glass beads of a known diameter or designed directly into the product. For very large engineering parts, such as wind turbine blades, and aircraft wings, maintaining a consistent bondline thickness is very difficult to achieve in practice. There is no simple functional relationship between the fracture energy of an adhesive bond and the bond gap thickness. A number of studies have been conducted to investigate the bond gap thickness effect in adhesive joints. Mostovoy et al. [125] were possibly the earliest to investigate this phenomenon on a commercially available-toughened epoxy between aluminum alloy adherends. They concluded that an increase in bond thickness led to an increase in toughness. Later, Bascom et al. [20] showed that the fracture energy of their rubber-toughened epoxy adhesive in a tapered double-cantilever beam was maximized when the bond gap thickness was equal in size to the diameter of the plastic zone ahead of the crack tip. Kinloch and Shaw [126] explained that the constraining effects of the adherends controlled the plastic zone size up to the point at which the plastic zone was fully developed (see Fig. 8.15). They proposed that the maximum value of fracture energy occurs when the bond gap was approximately equal to the plastic zone size. This maximum value was noted to be higher than that of the bulk adhesive fractured via single edge notch bend tests. Furthermore, with increasing bond gap thicknesses above the plastic zone size, they noted that the value fell toward that of bulk adhesive specimens. Martiny et al. [127] demonstrated that the combination of plastic zone constraint in the adhesive joint gives rise to several zones of plasticity in the joint, including additional plastic shear deformation at the adhesive/substrate interface.

Since 2010, a number of studies [128–131] have emerged that show the fracture energy at first increases with increasing bond gap thickness and then plateaus rather than returning to a lower bulk-like value as proposed by Kinloch and Shaw [126]. The

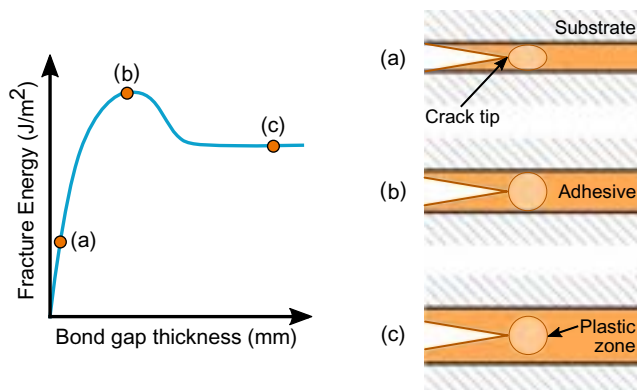


Fig. 8.15 The effect of adhesive bond gap thickness on the measured toughness and plastic zone size of an adhesive joint.

Redrawn from K. Khraponichev, D. Incerti, D. Carolan, A. Fergusson, Effect of rapid manufacturing on the performance of carbon fiber epoxy polymers, *J. Mater. Sci.* 56 (2021) 6188–6203.

adhesives in these studies can best be characterized as ductile when compared to those studies that report the behavior shown in Fig. 8.15.

To explain this behavior, Quan, Murphy, and Ivankovic [131,132] proposed the concept of an intrinsic fracture energy that is a material constant and not affected by the geometry of the adhesive bond. Further, they contend that differences in apparent fracture behavior are attributable to the variation in constraint ahead of the crack tip. Their work does not, however, address the fact that at very low bond gap thicknesses, a value less than their intrinsic fracture energy can be recorded, implying that there is still a bond gap dependency on the fracture toughness of the adhesive joint, that is, limited volume in which to dissipate energy. Khraponichev et al. later demonstrated that the same concept could be used to explain the limited toughness transfer from a bulk polymer to a fiber reinforced composite [133].

8.4.2 Cohesive and interfacial failure

The path taken by a crack is an important consideration when evaluating the performance of an adhesive joint [134]. For adhesive joints, the failure locus can be classified as either cohesive or interfacial failure. In cohesive failure, the crack propagates through the adhesive layer. This results in significant amounts of adhesive remaining on both faces of the separated joint after failure. In the case of interfacial failure, the crack travels at, or near, the interface. In these types of failures the majority of the adhesive is present on one of the substrates after failure. By the naked eye, the failure may appear to be interfacial but higher-resolution imaging or detailed surface analysis usually reveals traces of adhesive on the surface. It is important to note that many real joint failures may present aspects of both cohesive and interfacial failure. These three mechanisms are illustrated schematically in Fig. 8.16.

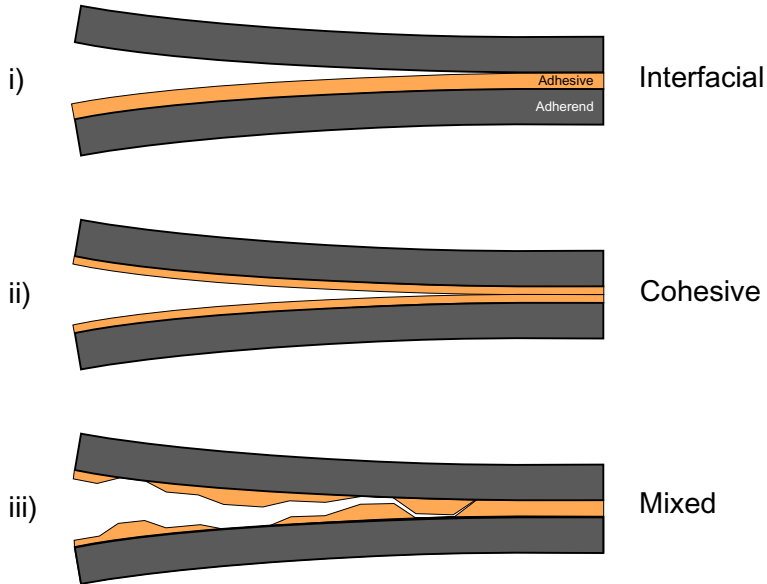


Fig. 8.16 Schematic representation of (i) interfacial, (ii) cohesive, and (iii) mixed failure of an adhesive joint.

8.5 Future trends

The future is green. Major consumers of adhesives, especially in the aerospace and automotive industries, have published detailed plans on reducing the environmental impact of their sectors.

Environmental concerns about fiber composites are leading manufacturers to consider biobased alternatives to petroleum-derived epoxies. Biobased resins can achieve a reduction in impact on the environment. They sequester carbon and their production can often have a smaller carbon footprint. According to the US Department of Agriculture, a biobased epoxy must contain a minimum of 25% biocontent [135]. The bio-based content is generally measured using radiocarbon dating, although it can be reasonably estimated by considering the stoichiometry of the reaction and knowing which precursors are bioderived [136]. There are a large number of groups reporting fully bio-based resin systems at laboratory scale [137–143]. However, these are typically achieved via intensive and commercially unattractive synthesis schemes, with much more difficult processing and inferior properties to petroleum-derived counterparts.

Some resin suppliers have replaced petroleum-based resins with biobased resins in their formulations. One of the most successful biobased systems is the production of partially biobased DGEBA epoxy resin. This is achieved by replacing epichlorohydrin, one of the key ingredients for synthesizing DGEBA epoxy, with the 100% bioderived epichlorohydrin, Epicerol, developed by Solvay [144]. Epicerol is manufactured from glycerol, itself a byproduct of biofuel production.

Terry and Taylor reported the engineering properties of several commercially available biobased epoxy systems and compared them to standard petroleum-derived chemistries [145]. They report that fully biobased systems are generally inferior, particularly in terms of glass transition temperature. However, partially biobased systems show significant promise, with reasonable combinations of strength, stiffness, toughness, and glass transition temperature comparable to petroleum-based alternatives.

A green future requires a multipronged engineering approach, so simply transitioning to the use of renewable feedstocks is not sufficient. The recyclability of adhesively bonded components at end of life is also a major issue that requires addressing. Early attempts at debonding have relied on heating the adhesive above its glass transition temperature, that is, thermal softening, or to its decomposition temperature window, such as thermal decomposition [146,147]. Several new technologies have recently emerged in this space. These involve the use of thermally expanding microparticles [148,149], chemical foaming agents [150], and reversible chemical adducts, such as, Diels-Alder adducts [151,152]. One of the most promising techniques that has emerged to date was developed by EIC laboratories and is sold commercially as ElectRelease [153–155]. The ElectRelease family of adhesives allows disbond of the adhesive from a metallic substrate by applying a small voltage across the adhesive bond. The debonding mechanism is achieved through ion conduction along the resin-substrate interface. Debond-on-demand adhesives represent a major step toward improving component disassembly and there is significant potential to explore the dual use of some of these technologies in conjunction with the toughening mechanisms discussed in this chapter. Indeed, debonding strategies explored to date have mainly focused on reclaiming the substrates, whereas little effort has yet been focused on the recovery and second-life use of the adhesive itself [156].

8.6 Conclusions

Most structural adhesives are made from thermosetting polymers, such as epoxy, and are therefore inherently brittle. Cracks can propagate through unmodified thermosets with little energy absorption, thus causing catastrophic failure. Considerable research has been conducted into improving the toughness of these materials, and this is well established and reasonably well understood.

Several toughening methods and their associated toughening mechanisms have been discussed in this chapter. The use of a soft secondary phase such as rubber is generally the most effective method in improving the fracture toughness. However, this method also reduces the modulus and glass transition temperature. More recent technologies such as core-shell rubbers, thermoplastics, and BCPs have been developed to alleviate these compromises. Structural adhesives can also be toughened by rigid particle reinforcements such as glass, graphene, and other carbon nanoparticles. Rigid particles do not offer the same level of toughening as rubber particles, but they come with several other advantages such as improved modulus, minimal effect on glass transition temperature, and multifunctionality. As the Huang-Kinloch model [23] continues to be generalized to include more modifiers other than rubber, the

fracture energy of modified epoxies can be modeled successfully in a truly predictive manner.

The emergence of biobased polymers and the myriad of different chemistries associated with these new systems presents opportunities to design new, tougher structural adhesives, with sustainability as a key driver. Research into the application of toughened bioderived epoxy resins as structural adhesives is very much in its infancy. The current social and political urgency to address climate change and the transition to net zero economics will ensure that green alternatives to currently deployed structural adhesive technologies will be increasingly demanded by customers and end users, driving research and development in the structural adhesives sector.

Acknowledgment

Declan Carolan acknowledges the support of the UKRI Future Leaders Fellowship under Grant No. [MR/T023406/1].

References

- [1] J.E. Gordon, *The New Science of Strong Materials—or Why You Don't Fall Through the Floor*, Penguin, Harmondsworth, UK, 1968.
- [2] D.R. Moore, A. Pavan, J.G. Williams, *Fracture Mechanics Testing Methods for Polymers, Adhesives and Composites*, first ed., Elsevier Science, Oxford, UK, 2001.
- [3] M. Regert, I. Rodet-Belarbi, A. Mazuy, G. Le Dantec, R.M. Dessì, S. Le Briz, A. Henry, M. Rageot, Birch-bark tar in the Roman world: the persistence of an ancient craft tradition? *Antiquity* 93 (372) (2019) 1553–1568.
- [4] P.R.B. Kozowyk, M. Soressi, D. Pomstra, G.H.J. Langejans, Experimental methods for the Palaeolithic dry distillation of birch bark: implications for the origin and development of Neandertal adhesive technology, *Sci. Rep.* 7 (2017) 8033.
- [5] M. Murali, D. Ratna, A.B. Samui, B.C. Chakraborty, Synthesis, characterization, and evaluation of carboxyl-terminated poly(ethylene glycol) adipate-modified epoxy networks: Effect of molecular weight, *J. Appl. Polym. Sci.* 103 (3) (2007) 1723–1730.
- [6] M.-S. Lin, C.-C. Liu, C.-T. Lee, Toughened interpenetrating polymer network materials based on unsaturated polyester and epoxy, *J. Appl. Polym. Sci.* 72 (4) (1999) 585–592.
- [7] K. Dinakaran, M. Alagar, Preparation and characterization of epoxy-cyanate ester interpenetrating network matrices/organoclay nanocomposites, *Polym. Adv. Technol.* 14 (8) (2003) 574–585.
- [8] Z.G. Shaker, R.M. Browne, H.A. Stretz, P.E. Cassidy, M.T. Blanda, Epoxy-toughened, unsaturated polyester interpenetrating networks, *J. Appl. Polym. Sci.* 84 (12) (2002) 2283–2286.
- [9] A.B. Cherian, L.A. Varghese, E.T. Thachil, Epoxy-modified, unsaturated polyester hybrid networks, *Eur. Polym. J.* 43 (4) (2007) 1460–1469.
- [10] Y.J. Lim, D. Carolan, A.C. Taylor, Simultaneously tough and conductive rubber-graphene-epoxy nanocomposites, *J. Mater. Sci.* 51 (18) (2016) 8631–8644.
- [11] K.A. Masser, E.D. Bain, F.L. Beyer, A.M. Savage, H.Y. Jian, J.L. Lenhart, Influence of nano-scale morphology on impact toughness of epoxy blends, *Polymer* 103 (2016) 337–346.
- [12] J.N. Sultan, F.J. McGarry, Effect of rubber particle size on deformation mechanisms in glassy epoxy, *Fatigue Fract. Eng. Mater. Struct.* 13 (1) (1973) 29–34.

- [13] K. Yamanaka, Y. Takagi, T. Inoue, Reaction-induced phase separation in rubber-modified epoxy resins, *Polymer* 30 (10) (1989) 1839–1844.
- [14] D. Verchère, H. Sautereau, J.P. Pascault, S.M. Moschiar, C.C. Riccardi, R.J.J. Williams, Miscibility of epoxy monomers with carboxyl-terminated butadiene-acrylonitrile random copolymers, *Polymer* 30 (1) (1989) 107–115.
- [15] S.-A. Xu, Miscibility and phase separation of epoxy/rubber blends, in: J. Parameswaranpillai, N. Hameed, J. Pionteck, E.M. Woo (Eds.), *Handbook of Epoxy Blends*, Springer, Cham, Switzerland, 2017, pp. 69–100.
- [16] D. Puglia, J.M. Kenny, Cure kinetics of epoxy/rubber polymer blends, in: J. Parameswaranpillai, N. Hameed, J. Pionteck, E.M. Woo (Eds.), *Handbook of Epoxy Blends*, Springer, Cham, Switzerland, 2017, pp. 211–237.
- [17] D. Carolan, H.M. Chong, A. Ivankovic, A.J. Kinloch, A.C. Taylor, Co-continuous polymer systems: a numerical investigation, *Comput. Mater. Sci.* 98 (2015) 24–33.
- [18] A.F. Yee, R.A. Pearson, Toughening mechanisms in elastomer-modified epoxies—Part 1. Mechanical studies, *J. Mater. Sci.* 21 (7) (1986) 2462–2474.
- [19] S.C. Kunz, J.A. Sayre, R.A. Assink, Morphology and toughness characterization of epoxy resins modified with amine and carboxyl terminated rubbers, *Polymer* 23 (13) (1982) 1897–1906.
- [20] W.D. Bascom, R.L. Cottingham, R.L. Jones, P. Peyser, The fracture of epoxy- and elastomer-modified epoxy polymers in bulk and as adhesives, *J. Appl. Polym. Sci.* 19 (1975) 2545–2562.
- [21] R. Bagheri, R.A. Pearson, Role of particle cavitation in rubber-toughened epoxies: 1. Microvoid toughening, *Polymer* 37 (20) (1996) 4529–4538.
- [22] V.V. Kozii, B.A. Rozenberg, Mechanisms of energy dissipation in elastomer-modified thermosetting polymer matrices and composites based on such polymers, *Polym. Sci.* 34 (1992) 919–951.
- [23] Y. Huang, A.J. Kinloch, Modelling of the toughening mechanisms in rubber-modified epoxy polymers—Part II. A quantitative description of the microstructure-fracture property relationships, *J. Mater. Sci.* 27 (10) (1992) 2763–2769.
- [24] G. Levita, Matrix ductility and toughening of epoxy resins, in: C.K. Riew (Ed.), *Rubber-Toughened Plastics*, American Chemical Society, Washington, DC, USA, 1989, pp. 93–118.
- [25] A. Maazouz, H. Sautereau, J.F. Gérard, Toughening of epoxy networks using pre-formed core-shell particles or reactive rubbers, *Polym. Bull.* 33 (1994) 67–74.
- [26] R.J. Day, P.A. Lovell, D. Pierre, Toughening of epoxy resins using particles prepared by emulsion polymerization: effects of particle surface functionality, size and morphology on impact fracture properties, *Polym. Int.* 44 (3) (1999) 288–299.
- [27] J.Y. Qian, R.A. Pearson, V.L. Dimonie, M.S. El-Aasser, Synthesis and application of core-shell particles as toughening agents for epoxies, *J. Appl. Polym. Sci.* 58 (2) (1995) 439–448.
- [28] H.-J. Sue, E.I.G. Meitin, D.M. Pickelman, C.J. Bott, Fracture mechanisms in rigid core-shell particle modified high performance epoxies, *Colloid Polym. Sci.* 274 (1996) 342–349.
- [29] G. Giannakopoulos, K. Masania, A.C. Taylor, Toughening of epoxy using core-shell particles, *J. Mater. Sci.* 46 (2) (2011) 327–338.
- [30] D. Carolan, A. Ivankovic, A.J. Kinloch, S. Sprenger, A.C. Taylor, Toughening of epoxy-based hybrid nanocomposites, *Polymer* 97 (2016) 179–190.
- [31] J. Chen, A.J. Kinloch, S. Sprenger, A.C. Taylor, The mechanical properties and toughening mechanisms of an epoxy polymer modified with polysiloxane-based core-shell particles, *Polymer* 54 (16) (2013) 4276–4289.

- [32] A. Keller, H.M. Chong, A.C. Taylor, C. Dransfield, K. Masania, Core-shell rubber nanoparticle reinforcement and processing of high toughness fast-curing epoxy composites, *Compos. Sci. Technol.* 147 (2017) 78–88.
- [33] D. Carolan, A. Ivankovic, A.J. Kinloch, S. Sprenger, A.C. Taylor, Toughened carbon fibre-reinforced polymer composites with nanoparticle-modified epoxy matrices, *J. Mater. Sci.* 52 (2017) 1767–1788.
- [34] A. Klinger, A. Bajpai, B. Wetzel, The effect of block copolymer and core-shell rubber hybrid toughening on morphology and fracture of epoxy-based fibre reinforced composites, *Eng. Fract. Mech.* 203 (2018) 81–101.
- [35] M.N. Bureau, V. Kumar, Fracture toughness of high density polycarbonate microcellular foams, *J. Cell. Plast.* 42 (3) (2006) 229–240.
- [36] Y. Huang, A.J. Kinloch, The toughness of epoxy polymers containing microvoids, *Polymer* 33 (6) (1992) 1330–1332.
- [37] N.H. Kim, H. Kim, Micro-void toughening of thermosets and its mechanism, *J. Appl. Polym. Sci.* 98 (2005) 1290–1295.
- [38] R. Bagheri, R.A. Pearson, The use of microvoids to toughen polymers, *Polymer* 36 (25) (1995) 4883–4885.
- [39] R. Bagheri, R.A. Pearson, Role of particle cavitation in rubber-toughened epoxies: I. Microvoid toughening, *Polymer* 37 (20) (1996) 4529–4538.
- [40] R. Bagheri, R.A. Pearson, Role of particle cavitation in rubber-toughened epoxies: II. Inter-particle distance, *Polymer* 41 (1) (2000) 269–276.
- [41] R.D. Brooker, A.J. Kinloch, A.C. Taylor, The morphology and fracture properties of thermoplastic-toughened epoxy polymers, *J. Adhes.* 86 (7) (2010) 726–741.
- [42] R.A. Pearson, A.F. Yee, Toughening mechanisms in thermoplastic-modified epoxies: I. Modification using poly(phenylene oxide), *Polymer* 34 (17) (1993) 3658–3670.
- [43] J.L. Hedrick, I. Yilgör, G.L. Wilkes, J.E. McGrath, Chemical modification of matrix Resin networks with engineering thermoplastics. I. Phenolic hydroxyl terminated poly(aryl ether sulfone)-epoxy systems, *Polym. Bull.* 13 (1985) 201–208.
- [44] C.B. Bucknall, A.H. Gilbert, Toughening tetrafunctional epoxy resins using polyetherimide, *Polymer* 30 (2) (1989) 213–217.
- [45] B. Francis, V.L. Rao, S. Jose, B.K. Catherine, R. Ramaswamy, J. Jose, S. Thomas, Poly(ether ether ketone) with pendent methyl groups as a toughening agent for amine cured DGEBA epoxy resin, *J. Mater. Sci.* 41 (17) (2006) 5467–5479.
- [46] J.H. Hodgkin, G.P. Simon, R.J. Varley, Thermoplastic toughening of epoxy resins: a critical review, *Polym. Adv. Technol.* 9 (1) (1998) 3–10.
- [47] B.B. Johnsen, A.J. Kinloch, A.C. Taylor, Toughness of syndiotactic polystyrene/epoxy polymer blends: microstructure and toughening mechanisms, *Polymer* 46 (18) (2005) 7352–7369.
- [48] D.J. Hourston, J.M. Lane, The toughening of epoxy resins with thermoplastics: I. Trifunctional epoxy resin-polyetherimide blends, *Polymer* 33 (7) (1992) 1379–1383.
- [49] J.B. Cho, J.W. Hwang, J.H. An, C.E. Park, Effects on morphology on toughening of tetrafunctional epoxy resins with poly(ether imide), *Polymer* 34 (23) (1993) 4832–4836.
- [50] A.J. Kinloch, M.L. Yuen, S.D. Jenkins, Thermoplastic-toughened epoxy polymers, *J. Mater. Sci.* 29 (14) (1994) 3781–3790.
- [51] Y. Mai, A. Eisenberg, Self-assembly of block copolymers, *Chem. Soc. Rev.* 41 (18) (2012) 5969–5985.
- [52] H. Kishi, Y. Kunimitsu, Y. Nakashima, T. Abe, J. Imade, S. Oshita, Y. Morishita, M. Asada, Control of nanostructures generated in epoxy matrices blended with PMMA-b-PnBA-b-PMMA triblock copolymers, *Express Polym. Lett.* 9 (1) (2015) 23–25.

- [53] R.B. Grubbs, J.M. Dean, M.E. Broz, F.S. Bates, Reactive block copolymers for modification of thermosetting epoxy, *Macromolecules* 33 (26) (2000) 9522–9534.
- [54] J.M. Dean, R.B. Grubbs, W. Saad, R.F. Cook, F.S. Bates, Mechanical properties of block copolymer vesicle and micelle modified epoxies, *J. Polym. Sci. Part B Polym. Phys.* 41 (20) (2003) 2444–2456.
- [55] X. Yang, F. Yi, Z. Xin, S. Zheng, Morphology and mechanical properties of nanostructured blends of epoxy resin with poly(ϵ -caprolactone)-block-poly(butadiene-co-acrylonitrile)-block-poly(ϵ -caprolactone) triblock copolymer, *Polymer* 50 (16) (2009) 4089–4100.
- [56] J. Chen, A.C. Taylor, Epoxy modified with triblock copolymers: morphology, mechanical properties and fracture mechanisms, *J. Mater. Sci.* 47 (11) (2012) 4546–4560.
- [57] A. Bajpai, B. Wetzel, Effect of different types of block copolymers on morphology, mechanical properties, and fracture mechanisms of bisphenol-F based epoxy system, *J. Compos. Sci.* 3 (3) (2019) 68.
- [58] H.M. Chong, A.C. Taylor, The microstructure and fracture performance of styrene-butadiene-methylmethacrylate block copolymer-modified epoxy polymers, *J. Mater. Sci.* 48 (19) (2013) 6762–6777.
- [59] J. Spanoudakis, R.J. Young, Crack propagation in a glass particle-filled epoxy resin—Part 2. Effect of particle-matrix adhesion, *J. Mater. Sci.* 19 (2) (1984) 487–496.
- [60] A.J. Kinloch, A.C. Taylor, The toughening of cyanate-ester polymers. Part I Physical modification using particles, fibres and woven-mats, *J. Mater. Sci.* 37 (2002) 433–460.
- [61] S. Sprenger, C. Eger, A.J. Kinloch, J.H. Lee, A.C. Taylor, D. Egan, Nanoadhesives: toughness and high strength, *Adhaes. Kleben Dichten* 03 (2003) 24–30.
- [62] S. Sprenger, Nanosilica-toughened epoxy resins, *Polymers* 12 (8) (2020) 1777.
- [63] A.J. Kinloch, A.C. Taylor, The mechanical properties and fracture behaviour of epoxy-inorganic micro- and nano-composites, *J. Mater. Sci.* 41 (2006) 3271–3297.
- [64] M.H. Kothmann, M. Ziadeh, G. Bakis, A. Rios de Anda, J. Breu, V. Altstadt, Analyzing the influence of particle size and stiffness state of the nanofiller on the mechanical properties of epoxy/clay nanocomposites using a novel shear-stiff nano-mica, *J. Mater. Sci.* 50 (14) (2015) 4845–4859.
- [65] S. Iijima, Helical microtubules of graphitic carbon, *Nature* 354 (6348) (1991) 56–58.
- [66] J.K.W. Sandler, J.E. Kirk, I.A. Kinloch, M.S.P. Shaffer, A.H. Windle, Ultra-low electrical percolation threshold in carbon-nanotube-epoxy composites, *Polymer* 44 (19) (2004) 5893–5899.
- [67] F.H. Gojny, M.H.G. Wichmann, U. Kopke, B. Fiedler, K. Schulte, Carbon nanotube-reinforced epoxy-composites: enhanced stiffness and fracture toughness at low nanotube content, *Compos. Sci. Technol.* 64 (15) (2004) 2363–2371.
- [68] F.H. Gojny, M.H.G. Wichmann, B. Fiedler, I.A. Kinloch, W. Bauhofer, A.H. Windle, K. Schulte, Evaluation and identification of electrical and thermal conduction mechanisms in carbon nanotube/epoxy composites, *Polymer* 47 (6) (2006) 2036–2045.
- [69] M.B. Jakubinek, B. Ashrafi, Y. Zhang, Y. Martinez-Rubi, C.T. Kingston, A. Johnston, B. Simard, Single-walled carbon nanotube epoxy composites for structural and conductive aerospace adhesives, *Compos. Part B Eng.* 69 (2015) 87–93.
- [70] G.L. Burkholder, Y.W. Kwon, R.D. Pollak, Effect of carbon nanotube reinforcement on fracture strength of composite adhesive joints, *J. Mater. Sci.* 46 (10) (2011) 3370–3377.
- [71] T.H. Hsieh, A.J. Kinloch, A.C. Taylor, I.A. Kinloch, The effect of carbon nanotubes on the fracture toughness and fatigue performance of a thermosetting epoxy polymer, *J. Mater. Sci.* 46 (12) (2011) 7525–7535.

- [72] K.S. Novoselov, A.K. Geim, S.V. Morozov, D. Jian, Y. Zhang, S.V. Dubonos, I.V. Grigorieva, A.A. Firsov, Electric field effects in atomically thin carbon films, *Science* 306 (5696) (2004) 666–669.
- [73] K.S. Novoselov, F. Schedin, T.J. Booth, V.V. Khotkevich, S.V. Morozov, A.K. Geim, D. Jiang, Two-dimensional atomic crystals, *Proc. Natl. Acad. Sci.* 102 (30) (2005) 10451–10453.
- [74] R.J. Young, I.A. Kinloch, L. Gong, K.S. Novoselov, The mechanics of graphene nanocomposites: a review, *Compos. Sci. Technol.* 72 (12) (2012) 1459–1476.
- [75] J.R. Potts, D.R. Dreyer, C.W. Bielawski, R.S. Ruoff, Graphene-based polymer nanocomposites, *Polymer* 52 (1) (2011) 5–25.
- [76] D. Quan, D. Carolan, C. Rouge, N. Murphy, A. Ivankovic, Mechanical and fracture properties of epoxy adhesives modified with graphene nanoplatelets and rubber particles, *Int. J. Adhes. Adhes.* 81 (2018) 21–29.
- [77] C. Bao, Y. Guo, L. Song, Y. Kan, X. Qian, Y. Hu, Insitu preparation of functionalized graphene oxide/epoxy nanocomposites with effective reinforcements, *J. Mater. Chem.* 21 (35) (2011) 13290.
- [78] D.R. Bortz, C. Merino, I. Martin-Gullon, Carbon nanofibers enhance the fracture toughness and fatigue performance of a structural epoxy system, *Compos. Sci. Technol.* 71 (1) (2011) 31–38.
- [79] H. Kim, A.A. Abdala, C.W. Macosko, Graphene/polymer nanocomposites, *Macromolecules* 43 (16) (2010) 6515–6530.
- [80] M.A. Rafiee, J. Rafiee, Z. Wang, H. Song, Z.-Z. Yu, K. Koratkor, Enhanced mechanical properties of nanocomposites at low graphene content, *ACS Nano* 3 (12) (2009) 3884–3890.
- [81] H.M. Chong, S.J. Hinder, A.C. Taylor, Graphene nanoplatelet-modified epoxy: effect of aspect ratio and surface functionality on mechanical properties and toughening mechanisms, *J. Mater. Sci.* 51 (19) (2016) 8764–8790.
- [82] A.J. Kinloch, D.L. Maxwell, R.J. Young, The fracture of hybrid-particulate composites, *J. Mater. Sci.* 20 (11) (1985) 4169–4184.
- [83] A.J. Kinloch, D.L. Maxwell, R.J. Young, Micromechanisms of crack-propagation in hybrid-particulate composites, *J. Mater. Sci. Lett.* 4 (10) (1985) 1276–1279.
- [84] R.J. Young, D.L. Maxwell, A.J. Kinloch, The deformation of hybrid-particulate composites, *J. Mater. Sci.* 21 (2) (1986) 380–388.
- [85] H.R. Azimi, R.A. Pearson, R.W. Hertzberg, Role of crack-tip shielding mechanisms in fatigue of hybrid epoxy composites containing rubber and solid glass spheres, *J. Appl. Polym. Sci.* 58 (2) (1995) 449–463.
- [86] A.J. Kinloch, J.H. Lee, A.C. Taylor, S. Sprenger, C. Eger, D. Egan, Toughening of structural adhesives via nano- and micro-phase inclusions, *J. Adhes.* 79 (2003) 867–873.
- [87] B.T. Marouf, R.A. Pearson, R. Bagheri, Anomalous fracture behavior in an epoxy-based hybrid composite, *Mater. Sci. Eng. A* 515 (1) (2009) 49–58.
- [88] Y.L. Liang, R.A. Pearson, The toughening mechanism in hybrid epoxy-silica-rubber nanocomposites (HESRNs), *Polymer* 51 (21) (2010) 4880–4890.
- [89] T.H. Hsieh, A.J. Kinloch, K. Masania, J. Sohn Lee, A.C. Taylor, S. Sprenger, The toughness of epoxy polymers and fibre composites modified with rubber microparticles and silica nanoparticles, *J. Mater. Sci.* 45 (5) (2010) 1193–1210.
- [90] A.F. Yee, D. Li, X. Li, The importance of constraint relief caused by rubber cavitation in the toughening of epoxy, *J. Mater. Sci.* 28 (1993) 6392–6398.
- [91] R.A. Pearson, A.F. Yee, Toughening mechanisms in elastomer-modified epoxies—Part 2. Microscopy studies, *J. Mater. Sci.* 21 (17) (1986) 2475–2488.

- [92] R.A. Pearson, A.F. Yee, Influence of particle size and particle size distribution on toughening mechanisms in rubber-modified epoxies, *J. Mater. Sci.* 26 (14) (1991) 3828–3844.
- [93] S. Kunz-Douglass, P.W.R. Beaumont, M.F. Ashby, A model for the toughness of epoxy-rubber particulate composites, *J. Mater. Sci.* 15 (5) (1980) 1109–1123.
- [94] S. He, D. Carolan, A. Fergusson, A.C. Taylor, Toughening epoxy syntactic foams with milled carbon fibres: mechanical properties and toughening mechanisms, *Mater. Des.* 169 (2019) 107654.
- [95] Y. Huang, A.J. Kinloch, Modelling of the toughening mechanisms in rubber-modified epoxy polymers—Part I. Finite element analysis studies, *J. Mater. Sci.* 27 (10) (1992) 2753–2762.
- [96] F.J. Guild, R.J. Young, A predictive model for particulate-filled composite materials—Part 1. Hard particles, *J. Mater. Sci.* 24 (1) (1989) 298–306.
- [97] G.R. Irwin, Plastic zone near a crack and fracture toughness, in: Meeting of the 7th Sagamore Ordnance Materials Research Conference, Racquette Lake, USA, 1960, pp. 63–78.
- [98] A.G. Evans, S. Williams, P.W.R. Beaumont, On the toughness of particulate filled polymers, *J. Mater. Sci.* 20 (10) (1985) 3668–3674.
- [99] A.J. Kinloch, Relationships between the microstructure and fracture behavior of rubber-toughened thermosetting polymers, in: C.K. Riew (Ed.), *Rubber-Toughened Plastics*, American Chemical Society, Washington, DC, USA, 1989, pp. 67–91.
- [100] T.H. Hsieh, A.J. Kinloch, K. Masania, J. Sohn Lee, A.C. Taylor, S. Sprenger, Erratum to: the toughness of epoxy polymers and fibre composites modified with rubber microparticles and silica nanoparticles, *J. Mater. Sci.* 46 (11) (2011) 4092.
- [101] F.J. Guild, R.J. Young, A predictive model for particulate-filled composite materials—Part 2. Soft particles, *J. Mater. Sci.* 24 (7) (1989) 2454–2460.
- [102] F.J. Guild, A.J. Kinloch, A.C. Taylor, Particle cavitation in rubber toughened epoxies: the role of particle size, *J. Mater. Sci.* 45 (14) (2010) 3882–3894.
- [103] F.J. Guild, W.L. Tsang, A.C. Taylor, Silica nano-particle filled polymers: debonding and microstructure, *Compos. Sci. Technol.* 218 (2022) 109202.
- [104] F.J. Guild, A.J. Kinloch, A.C. Taylor, The debonding of nanoparticles in toughened adhesives, in: 37th Annual Meeting of the Adhesion Society, San Diego, USA, 2014, pp. 63–78.
- [105] T. Khaleque, Modelling and Experimental Study of Toughening Mechanisms of Core-Shell Rubber Particle- and Nanosilica Particle-Modified Epoxy Polymers (Ph.D. Thesis), Department of Mechanical Engineering, Imperial College London, London, UK, 2018.
- [106] H.M. Chong, Personal Communication: Synergy FEA, Department of Mechanical Engineering, Imperial College London, London, UK, 2018.
- [107] E. Tarleton, M.N. Charalambides, C. Leppard, Image-based modelling of binary composites, *Comput. Mater. Sci.* 64 (2012) 183–186.
- [108] R. Zhang, J.Y.S. Li-Mayer, M.N. Charalambides, Development of an image-based numerical model for predicting the microstructure-property relationship in alumina trihydrate (ATH) filled poly(methyl methacrylate) (PMMA), *Int. J. Fract.* 211 (1) (2018) 125–148.
- [109] D.J. Bray, S.G. Gilmour, F.J. Guild, A.C. Taylor, Quantifying nanoparticle dispersion by using the area disorder of Delaunay triangulation, *J. R. Stat. Soc. Ser. C (Appl. Stat.)* 61 (2) (2012) 253–275.
- [110] D.J. Bray, S.G. Gilmour, F.J. Guild, T.H. Hsieh, K. Masania, A.C. Taylor, Quantifying nanoparticle dispersion: application of the Delaunay network for objective analysis of sample micrographs, *J. Mater. Sci.* 46 (19) (2011) 6437–6452.

- [111] H.M. Chong, Toughening Mechanisms of Block Copolymer and Graphene Nanoplatelet Modified Epoxy Polymers (Ph.D. Thesis), Department of Mechanical Engineering, Imperial College London, London, UK, 2015.
- [112] F.F. Lange, The interaction of a crack front with a second-phase dispersion, *Philos. Mag.* A 22 (179) (1970) 0983–0992.
- [113] K.T. Faber, A.G. Evans, Crack deflection processes—I. Theory, *Acta Metall.* 31 (4) (1983) 565–576.
- [114] K.T. Faber, A.G. Evans, Crack deflection processes—II. Experiment, *Acta Metall.* 31 (4) (1983) 577–584.
- [115] D.A. Dillard, H.K. Singh, D.J. Pohlit, J.M. Starbuck, Observations of decreased fracture toughness for mixed mode fracture testing of adhesively bonded joints, *J. Adhes. Sci. Technol.* 23 (10–11) (2009) 1515–1530.
- [116] B.B. Johnsen, A.J. Kinloch, R.D. Mohammed, A.C. Taylor, S. Sprenger, Toughening mechanisms of nanoparticle-modified epoxy polymers, *Polymer* 48 (2) (2007) 530–541.
- [117] A.N. Gent, Detachment of an elastic matrix from a rigid spherical inclusion, *J. Mater. Sci.* 15 (11) (1980) 2884–2888.
- [118] M. Sakai, T. Miyajima, M. Inagaki, Fracture toughness and fiber bridging of carbon fiber reinforced carbon composites, *Compos. Sci. Technol.* 40 (3) (1991) 231–250.
- [119] D. Hull, T.W. Clyne, *An Introduction to Composite Materials*, second ed., Cambridge University Press, Cambridge, UK, 1996.
- [120] M.G. Callens, L. Gorbatikh, I. Verpoest, Ductile steel fibre composites with brittle and ductile matrices, *Compos. A Appl. Sci. Manuf.* 2014 (61) (2014) 235–244.
- [121] R.B. Adusumali, M. Reifferscheid, H. Weber, T. Roeder, H. Sixta, W. Gindl, Mechanical properties of regenerated cellulose fibres for composites, *Marcomol. Symp.* 244 (1) (2006) 119–125.
- [122] J.-C. Zarges, D. Minkley, M. Feldmann, H.-P. Heim, Fracture toughness of injection molded, man-made cellulose fiber reinforced polypropylene, *Compos. A Appl. Sci. Manuf.* 2017 (98) (2017) 147–158.
- [123] A. Kelly, W.R. Tyson, Tensile properties of fibre-reinforced metals: Copper/tungsten and copper/molybdenum, *J. Mech. Phys. Solids* 13 (6) (1965) 329–338.
- [124] J.K. Wells, P.W.R. Beaumont, The toughness of a composite containing short brittle fibres, *J. Mater. Sci.* 1988 (23) (1988) 1274–1278.
- [125] S. Mostovoy, E.J. Ripling, C.F. Bersch, Fracture toughness of adhesive joints, *J. Adhes.* 3 (1971) 125–144.
- [126] A.J. Kinloch, S.J. Shaw, The fracture resistance of a toughened epoxy adhesive, *J. Adhes.* 12 (1981) 59–77.
- [127] P. Martiny, F. Lani, A.J. Kinloch, T. Pardoen, A multiscale parametric study of mode I fracture in metal-to-metal low-toughness adhesive joints, *Int. J. Fract.* 173 (2012) 105–133.
- [128] S. Azari, M. Papini, J.K. Spelt, Effect of adhesive thickness on fatigue and fracture of toughened epoxy joints—Part I: Experiments, *Eng. Fract. Mech.* 78 (1) (2011) 153–162.
- [129] V. Cooper, A. Ivankovic, A. Karac, D. McAuliffe, N. Murphy, Effects of bond gap thickness on the fracture of nano-toughened epoxy adhesive joints, *Polymer* 53 (4) (2017) 5540–5553.
- [130] S.R. Ranade, Y. Guan, D.C. Ohanehi, J.G. Dillard, R.C. Batra, D.A. Dillard, A tapered bondline thickness double cantilever beam (DCB) specimen geometry for combinatorial fracture studies of adhesive bonds, *Int. J. Adhes. Adhes.* 55 (2014) 155–160.
- [131] D. Quan, N. Murphy, A. Ivankovic, Fracture behaviour of epoxy adhesive joints modified with core-shell rubber nanoparticles, *Eng. Fract. Mech.* 182 (2017) 566–576.

- [132] D. Quan, N. Murphy, A. Ivankovic, Fracture behaviour of a rubber nano-modified structural epoxy adhesive: bond gap effects and fracture damage zone, *Int. J. Adhes. Adhes.* 77 (2017) 138–150.
- [133] K. Khraponichev, D. Incerti, D. Carolan, A. Fergusson, Effect of rapid manufacturing on the performance of carbon fibre epoxy polymers, *J. Mater. Sci.* 56 (2021) 6188–6203.
- [134] BS EN ISO 10365, Adhesives—Designation of Main Failure Patterns, British Standards Institution, London, UK, 1995.
- [135] S.S. Vickner, A USDA-certified biobased product introduction, *Am. J. Agric. Econ.* 95 (2) (2013) 512–518.
- [136] BS ISO 16620-5, Plastics—Biobased Content—Part 5: Declaration of Biobased Carbon Content, Biobased Synthetic Polymer Content and Biobased Mass Content, British Standards Institution, London, UK, 2017.
- [137] M. Chrysanthos, J. Galy, J.-P. Pascault, Preparation and properties of bio-based epoxy networks derived from isosorbide diglycidyl ether, *Polymer* 52 (16) (2011) 3611–3620.
- [138] E.D. Hernandez, A.W. Bassett, J.M. Sadler, J.J. La Scala, J.F. Stanzione III, Synthesis and characterization of bio-based epoxy resins derived from vanillyl alcohol, *ACS Sustain. Chem. Eng.* 4 (8) (2016) 4328–4339.
- [139] A.D. La Rosa, G. Recca, J. Summerscales, A. Latteri, G. Cozzo, G. Cicala, Bio-based versus traditional polymer composites. A life cycle assessment perspective, *J. Clean. Prod.* 74 (2014) 135–144.
- [140] H. Nabipour, X. Wang, L. Song, Y. Hu, A high performance fully bio-based epoxy thermoset from a syringaldehyde-derived epoxy monomer cured by furan-derived amine, *Green Chem.* 23 (1) (2021) 501–510.
- [141] C.H. Chen, S.H. Tung, R.J. Jeng, M.M. Abu-Omar, C.H. Lin, A facile strategy to achieve fully bio-based epoxy thermosets from eugenol, *Green Chem.* 21 (16) (2019) 4475–4488.
- [142] E. Savonnet, E. Grau, S. Grelier, B. Defoort, H. Cramail, Divanillin-based epoxy precursors as DGEBA substitutes for biobased epoxy thermosets, *ACS Sustain. Chem. Eng.* 6 (8) (2018) 11008–11017.
- [143] E. Feghali, D.J. van de Pas, K.M. Torr, Toward bio-based epoxy thermoset polymers from depolymerized native lignins produced at the pilot scale, *Biomacromolecules* 21 (4) (2020) 1548–1559.
- [144] S. Charati, C. Cochenec, M. Dahanayake, P. Gilbeau, M.P. Labeau, P. Lapersonne, P. Marion, S. Martins, F. Monnet, R. Nascimento, F. Speroni, Chemistry and chemicals from renewables resources within Solvay, in: F. Cavani, S. Albonetti, F. Basile, A. Gandhi (Eds.), *Chemicals and Fuels from Bio-Based Building Blocks*, Wiley-VCH, Weinheim, Germany, 2016, pp. 615–642.
- [145] J.S. Terry, A.C. Taylor, The properties and suitability of commercial bio-based epoxies for use in fiber-reinforced composites, *J. Appl. Polym. Sci.* 20 (2021) 50417.
- [146] F. Vigano, S. Consonni, M. Grosso, L. Rigamonti, Material and energy recovery from automotive shredded residues (ASR) via sequential gasification and combustion, *Waste Manag.* 30 (1) (2010) 145–153.
- [147] Y. Lu, J. Broughton, P. Winfield, A review of innovations in disbonding techniques for repair and recycling of automotive vehicles, *Int. J. Adhes. Adhes.* 50 (2014) 119–127.
- [148] Y. Nishiyama, N. Uto, C. Sato, H. Sakurai, Dismantlement behavior and strength of dismantlable adhesive including thermally expansive particles, *Int. J. Adhes. Adhes.* 23 (5) (2003) 377–382.
- [149] B. Lee, I. Son, J.H. Kim, C. Kim, J.Y. Yoo, B.W. Ahn, J. Hwang, J. Lee, J.H. Lee, Polymeric nanocapsules containing methylcyclohexane for improving thermally induced debonding of thin adhesive films, *J. Appl. Polym. Sci.* 135 (31) (2018) 46586.

-
- [150] M. Minnicino, J.M. Sands, Reactive nanocomposites for controllable adhesive debonding, Army Research Lab Aberdeen Proving Ground MD, Weapons and Materials Research, 2011 (Tech. rep.).
- [151] J.H. Aubert, Note: thermally removable epoxy adhesives incorporating thermally reversible Diels-Alder adducts, *J. Adhes.* 79 (6) (2003) 609–616.
- [152] M.D. Banea, L.F.M. da Silva, R.D.S.G. Campilho, C. Sato, Smart adhesive joints: an overview of recent developments, *J. Adhes.* 90 (1) (2014) 16–40.
- [153] D.W. Haydon, ElectRelease—Electrically disbonding adhesive, *Assem. Autom.* 22 (2002) 326–329.
- [154] S. Leijonmarck, A. Cornell, C.O. Danielsson, T. Åkermark, B.D. Brandner, G. Lindbergh, Electrolytically assisted debonding of adhesives: an experimental investigation, *Int. J. Adhes. Adhes.* 32 (2012) 39–45.
- [155] S. Leijonmarck, A. Cornell, C.O. Danielsson, G. Lindbergh, Electrochemical characterization of electrically induced adhesive debonding, *J. Electrochem. Soc.* 158 (2011) 109–114.
- [156] K.R. Mulcahy, A.F.R. Kilpatrick, G.D.J. Harper, A. Walton, A.P. Abbott, Debondable adhesives and their use in recycling, *Green Chem.* 24 (1) (2022) 36–61.

Part Two

Adherends and surfaces: Addressing and troubleshooting bonding challenges

This page intentionally left blank

What went wrong? Solving bonding challenges through surface science

9

Giles Dillingham and Rose Roberts
Brighton Science, Cincinnati, OH, United States

9.1 Prologue: Example of a bonding process suffering from “unexplainable” failures

A large automotive manufacturer offered painted hard tops as an option for a newly revamped line of vehicles. These painted tops passed all quality inspections during the prototyping phase, so few or no issues were expected during mass production.

Hard top production was outsourced to a second-tier manufacturer nearby. Large batches of the sheet molding compound (SMC) material were purchased, molded into the appropriate shape, washed, dried, and painted. But the paint was failing the quality test, a cycling process of flash freeze then heat. The parts were thoroughly washed before painting, so it couldn't be a contaminant issue. Was there something wrong with the paint? Did the SMC manufacturer change the composition without telling them?

After the manufacturer's own investigations led to no improvements, a surface inspection company was brought in to consult on the project. Several points in the manufacturing process were identified as potential sources of contamination: (1) A mold release was used on the side of the SMC that was not going to be painted. However, mold releases have been known to migrate. (2) The cleaning step used detergent that was being recycled for a variable number of times before being exchanged for fresh solution. (3) The forced air drying step used after washing may have induced outgassing or blooming from the SMC; this was recognized as a potential source of detrimental contamination if it resulted in contamination of the SMC surface. (4) The part handling between the drying process and paint application was not well controlled and could be resulting in contamination of the part surface.

At the manufacturing facility, water contact angle measurements were used as the primary tool for monitoring the changes in surface characteristics occurring with each step of the process to identify the potential source of the “random” paint adhesion issues. Water contact angles are sensitive to surface chemical composition and can help pinpoint a process step that results in a potentially detrimental change to a surface, such as contamination. A wettable surface (low contact angle) that shows uniform wetting properties across the surface is frequently a good predictor of how well a

coating or adhesive will spread and adhere to that surface, and in general a good indicator of bond quality.

Contact angle inspection showed the SMC surfaces to have an approximately 50–60 degrees contact angle after the molding step, with high point-to-point variability. This is typical for surfaces that have had relatively uncontrolled handling and storage and indicates that there were nonuniform contaminants on the surface, such as fingerprints or airborne hydrocarbons. The washing step resulted in a surface with an average contact angle of approximately 40 degrees that was much more uniform point to point. This showed that the washing process was successfully cleaning off a large amount of the contamination to create a more uniform high energy surface. However, the drying step increased the contact angle to about 70 degrees. A change this large between a washed surface and a dried one is often indicative of a contaminant being introduced to the surface. Was the drier somehow a source of contamination? Apparently not, because when this was tested by running a clean piece of aluminum through a drying cycle, the contact angle showed little change.

Plastics such as SMCs are highly formulated products containing various functional additives designed to adjust several material properties. These include plasticizers to adjust hardness and glass transition temperature, tougheners to improve impact resistance, reinforcing fillers to increase strength and modulus, and inert fillers to reduce cost. Other classes of functional additives are mold releases and lubricants. These can improve part release from a mold during processing or lubricate the surface and reduce the tendency of the polymer to deform or scratch during use. Some of these additives must be present on the part surface to work, and therefore are specifically designed to segregate to the surface during processing. This needs to happen during molding, of course, but if these compounds are not removed prior to painting or bonding, they can wreak havoc with adhesion. In this case, it turned out that although the washing step was removing enough internal mold release to create a paintable surface, the drying conditions were promoting a return of these compounds to the surface, causing paint adhesion failures on the hard tops.

Further investigation showed that there had been an increase in the drying temperature between prototyping and scale-up in an attempt to improve manufacturing efficiency by reducing cycle times. This seemingly subtle “improvement” had the unintended consequence of degrading a critical material property and disrupting the manufacturing process to the point of introducing a significant delay in product release. This is a story repeated over and over again in every industry, and provides the motivation for this chapter: obtaining reliable (i.e., predictable) adhesion requires the understanding and control of subtle and delicate material properties that do not always lend themselves to easy analysis by common tools.

9.2 Introduction

Bonding processes are found in almost every manufacturing industry today, and the volume of adhesives used was \$52.55 billion in 2017, a number that is expected to continue increasing at a compound annual growth rate of 5.6% from 2018 until

2025 [1]. The primary areas driving growth are the automotive, construction, packaging, furniture, footwear, and pressure-sensitive adhesive applications. The criticality of bonding processes to manufacturing is unquestionable. Yet as demonstrated by the actual example outlined in the prologue, even though adhesive bonding processes have been commercialized for well more than 100 years, unexpected failures in *properly designed* bonded structures continue to plague manufacturing (*properly designed* is italicized because if a bonded structure is not designed with careful consideration for the stress state that the bond will experience in use, no manner of manufacturing process control can ensure predictable performance. This chapter is predicated on the existence of a proper mechanical design of the bonded structure, which is the focus of other chapters within this volume).

The lack of quantifiable reliability of adhesive bond performance has been recognized for a long time and has significantly impeded the more widespread use of adhesive bonding in many applications. This lack of confidence means that, as discussed in more detail in [Chapter 23](#), the Federal Aviation Administration (FAA) will not currently certify bonded composite commercial aircraft for flight unless the structures can be demonstrated to remain airworthy with no intact bonds, that is, the bonds need to be made redundant by mechanical fasteners. These requirements can largely negate any advantage from using primary bonded structure in design. The criticality of bonding to the realization of high-performance aircraft designs has led to significant government and industry investment in both basic and applied research to understand the fundamentals of adhesion as well as develop measurement methods for the development and control of adhesive bonding processes, such as the Primary Aircraft Bonded Structures Technology (PABST) program of the 1970s [2] and the DARPA-funded TRUST program of the mid 2000s [3], the results of which have informed much of the work discussed in this chapter.

“Mysterious” bond reliability issues stem from a continued tendency of designers and manufacturing engineers to treat adhesive bonding processes as analogous to mechanical fastening processes with a few changes in the procedural details. Instead of “Drill holes to 0.502” (± 0.002 ”), lubricate threads, insert fastener, and torque to 50 ft lbs,” adhesive application instructions might typically read: “Ensure surfaces are clean and dry. Roughen surface with sandpaper for best results. Apply adhesive and cure overnight at room temperature.” Anyone who understands the basic mechanisms of adhesive bond formation, has worked in or around a typical manufacturing facility, and has faced the consequences of inconsistent adhesive bond performance shudders when reading this sort of simplistic instruction set. “Unanticipated” adhesion failures are common.

Why do these sorts of instructions result in unpredictable bond performance? They paint adhesive bonding as a sequence of physical steps, like those for installing a bolt or a rivet. This view ignores an important and underappreciated characteristic of adhesive bonding: it is a *chemical synthesis* process, wherein the bonding process consists of synthesizing two distinct chemical products, the bulk adhesive and the adhesive/substrate interface. Control of the structure of the bulk adhesive is primarily the domain of the formulator; control of the interface depends on the ability of the operator to repeatably control the chemical composition of the uppermost few molecular

layers of the bond surface. Many years of investigation of bond failures in manufacturing processes have shown us that variability in the adhesive properties is rarely to blame for poor performance of bonded structures; it is almost invariably the result of improper or inconsistent surface preparation. The success of these processes depends on establishing a bond surface of controlled and reproducible composition. When bonding processes are developed and executed with this in mind, they become controllable and therefore as reliable as other joining methods. This may benefit from the involvement of an interdisciplinary team that includes materials science and/or chemistry expertise along with structures and manufacturing engineers.

Reliable, repeatable mechanical fastening processes require measuring devices for the precise control of mechanical factors such as fastener torque and clamping force. Likewise, the control and reliability of adhesive bonding operations require measurement tools sensitive to the chemical composition of surfaces. An important part of this chapter will be a discussion of measurement tools appropriate for this purpose.

Some adhesive systems and pretreatment approaches are more robust than others, meaning less sensitive to inadvertent contamination or other process excursions. For example, the automotive industry's focus on rapid, simple processes has resulted in the development of adhesives that are effective at displacing/absorbing certain processing oils from steel surfaces, reducing the need for cleaning prior to bonding [4]. Elevated curing of room-temperature paste adhesives typically show more tolerance of contaminants, and at least some high-temperature epoxy film adhesives show remarkable tolerance to the presence of a wide range of nonsilicone contaminants on the prebond surface [3,5]. This is believed to be due to the increased solubility of contaminants in these adhesives at higher temperatures.

A useful definition of an adhesive bond is a structure that contains one or more load-bearing interfaces. The interfaces consist of the chemical bonds that were synthesized between the adhesive and substrate during application and curing of the adhesive. Creating a consistent and reliable interface is not the job of the structural engineer or the product design engineer; rather, it is the job of the manufacturing engineer who designs the process and the quality engineer to manages the process on a day-to-day basis. What is not so obvious to many designers of adhesive bonding processes is the nature of the chemical reactions that establish the interface, and the sensitivity of the interface properties to the seemingly insignificant details of the bonding process. A second goal of this chapter is to provide a basic understanding of and appreciation for these details. The careful reader of this chapter will be equipped with the tools to not only solve seemingly random adhesion problems but design adhesion processes in a manner that can help avoid the occurrence of these problems during production.

9.3 Adhesion: Resistance of an interface to failure

9.3.1 *Why bonds fail*

Obtaining consistent quality of an interface in manufacturing depends on generating a prepared surface of controlled chemical composition and structure time after time [6–12]. This can be more difficult than it may seem at first glance because the

properties of a surface are determined by the composition and structure of only the uppermost two to perhaps five or so molecular layers, which is readily disrupted by things as seemingly innocuous as a fingerprint, the lubricating oil vapor from an electric motor, or the exhaust from a nearby forklift. What might seem to be insignificant changes in incoming material, storage and handling, processing, or environment can actually result in large changes in the properties of a surface, and therefore the properties of an adhesive bond.

The most sensitive factor in the control of a bonding process is control of the structure and the composition of the interface between the adhesive and the substrate. It is also one of the most difficult factors to control because it is vanishingly thin (therefore delicate) and is often created by technicians using manual processes in an environment that typically has marginal controls over temperature, humidity, and airborne contaminants. As a point of reference, another industry whose product performance and quality depend equally heavily on the structure and composition of surfaces is semiconductor device manufacture. Because of this industry's appreciation of the delicate nature of surfaces and interfaces, semiconductor device manufacturing is performed by highly trained workers in stringently controlled clean rooms. Furthermore, manual processes are avoided as much as possible because of the difficulty in control.

The properties of an adhesive bond depend to a large extent on the properties of the interface that is established between the adhesive and the substrate. Therefore, control of the quality and consistency of the bond depends on control of this interface. The interface is established between an adhesive and a surface that has been prepared in some manner to receive the adhesive (i.e., surface treated). Surface treatment can be as simple (and often as ineffective) as a solvent wipe, it can consist of peel ply removal, or it may entail chemical and physical modification of the composite surface via abrasion (with or without solvent wiping) or perhaps a plasma treatment.

A properly prepared surface is chemically reactive and delicate. It is these reactive sites that provide stable and durable integrity to a bonded structure. A chemically reactive surface, however, is in a dynamic state: its properties are evolving (i.e., degrading) with time at a rate and to an extent that depend on handling and storage conditions. The degradation mechanisms include consumption of reactive sites via oxidation, occlusion of the reactive surface sites via contaminants, or (in the case of surface-treated polymers), reorientation and diffusion of reactive surface sites toward the polymer bulk. Contaminants are either extrinsic (originating in the environment) or intrinsic (migratory substances from within the material). For thermoplastics, contaminants are frequently intrinsic, coming from low molecular weight fractions or perhaps from functional additives such as plasticizers intentionally compounded into the material. In the case of composite materials, the primary route for deterioration of a properly prepared surface is frequently through extrinsic contamination originating from the storage/handling environment or perhaps through contact with substandard wipers, solvents, or abrasives. These contamination events result from a poor understanding of the nanometer-scale sensitivity and transient nature of a bond surface by both M&P engineers and manufacturing technicians. Bond environments need to be well controlled, formulations need to be monitored carefully, personal protective equipment

must be well utilized, and the critical details of preparation processes must be well controlled.

Materials systems differ in their sensitivity to specific classes of contaminants [13]. In general, room temperature-curing paste adhesive systems are more sensitive to a wider range of contaminant classes than high-temperature film adhesives. This is due to the ability of a modern high-temperature curing system to solubilize and absorb a wide range of contaminants. One class of contaminants that is highly detrimental to all known adhesive systems consists of organosilicones. This is due to several reasons. They present extremely low surface energies when present at even monomolecular layer coverage. They are only sparingly soluble in most resin systems, and are therefore difficult to displace from the interface. Due to their ubiquity as mold releases and lubricants, they are present in many bonding environments.

The ability of an organosilicone to interfere with bonding depends on the structural details, however. The basic repeat unit for an organosilicone is $(\text{SiO}(\text{CH}_3)_2)_n$, where n represents the degree of polymerization. Lack of polarity means that adhesion of silicones to typical adherends is very low (unless there is significant functionalization of the silicone with polar groups such as hydroxyls). Low surface tension means that these materials spread readily on most surfaces: a small amount of silicone oil on a workbench will quickly migrate to cover adjacent surfaces. The detrimental nature of silicones scales closely with the molecular weight. Silicones of low enough molecular weight to be volatile ($n \sim 2$ or 3) are of little concern; their low adhesion ensures that they do not remain on the surface. Silicones of slightly higher molecular weight that are not volatile are still not generally detrimental due to their relatively high solubility. However, as molecular weight increases to that of more common silicone oils, the solubility decreases significantly and these materials tend to stay at an interface rather than dissolve into an adhesive. This molecular weight regime represents materials that begin to function as mold releases. These materials are of great concern in manufacturing environments as they are low enough molecular weight to be very mobile on surfaces yet high enough to have low solubility in adhesives and coatings. The highest-performance silicone-based mold releases are designed to both crosslink and adhere to mold surfaces during drying through the addition of a small concentration of silanol groups. These are excellent mold releases and because of their ability to adhere to mold surfaces, they are not migratory when properly applied and cured. Problems do arise, however, when application of these release agents onto the molds introduces them as aerosols into the manufacturing environment. These aerosols have been known to be picked up by air handling systems and wreak havoc on adhesion processes in adjacent rooms.

Conceptually, there are three components to an adhesive bond or coated structure that must be controlled to obtain reproducible performance: (1) the adhesive or coating, (2) the surface to which it is applied, and (3) application and curing. Our experience over the past decades in analyzing and resolving failures in bonded and coated structures has shown that only a small fraction of these failures can be traced to poor adhesive quality or poor application and curing processes: More than 95% of these failures are due to a failure to control the composition and properties of the adherend

surface. This results in a lack of robustness due to failure at the interface or near the interface in an interphase of substandard properties [14].

There are good reasons for variations in surface properties to be the overriding source of adhesion inconsistencies. Adhesive resins are manufactured in large-volume chemical synthesis operations that are tightly controlled; it is well understood that extremely small excursions in reactant quantities, reaction temperatures and time, and mixing conditions can result in a “bad batch” of adhesive and generate large amounts of waste. Likewise, the consistent application and curing of adhesives are relatively straightforward engineering tasks that don’t usually present significant problems for repeatability. The performance of the interface in a bonded or coated structure, however, depends on the composition and structure of a vanishingly small volume of material comprised of the few molecular layers immediately adjacent to the free surface. For perspective, consider that a fingerprint is a film approximately 1000 molecular layers thick composed of both water-soluble salts and amino acids along with water-insoluble proteins and amino acids [15]. Such a film can totally prevent a carefully prepared surface from being able to establish contact with an adhesive or coating. Human breath exposes a surface to a complex mixture with large concentrations of isoprene, C16 hydrocarbon, and 4-methyl-octane [16]. Given that a properly prepared surface is chemically active by design to enable the strong sorption of organic adhesive or coating molecules, the sensitivity of the interface to seemingly trivial process excursions becomes obvious. Workers tasked with designing reliable bonding and coating processes as well as those carrying out these tasks are rarely aware of the dependence of the predictable success of these processes on the delicate composition of an invisible zone of the substrate (or in the words of the late Bob Hume of H.B. Fuller, “what the glue sees,” based on a personal communication with David Dillard).

9.3.2 Tools for understanding surfaces and interfaces

To understand “what the glue sees” for the purposes of adhesive bonding, the surface can be defined as the zone of the substrate whose properties differ from the bulk material. This zone can be anywhere from a few molecular layers (1–10 nm) to several microns in thickness. Because this critical zone is so thin, specialized tools are needed to measure and control its properties. Appropriate tools include surface chemical analysis via techniques such as X-ray photoelectron spectroscopy (XPS) and Fourier transform infrared spectroscopy (FTIR), and physical analysis via techniques such as water break tests, wetting tension measurements using dyne solutions, and contact angle measurements.

This section focuses on analytical techniques that are currently available for deployment in manufacturing processes. Other techniques for the detection of silicone contaminants on surfaces are under active development and may prove useful in the near future. These include laser-induced breakdown spectroscopy (LIBS) and X-ray fluorescence spectroscopy (XRF). LIBS in particular shows sensitivity to these compounds that is excellent and similar to XPS [17].

XPS is an ultrahigh vacuum analysis technique that is restricted to the analysis of small samples (such as witness coupons) that can be valuable for process development and failure analysis but is limited to laboratory use. FTIR instrumentation is available in both laboratory as well as hand-held versions, making it deployable in a manufacturing environment. It provides information about molecular structure and is therefore useful for establishing the cure state of a resin and the presence of thermo-oxidative damage from overcuring. It can also be useful for identifying contaminants. The most useful technique for obtaining infrared spectra from polymer surfaces is attenuated total reflectance (ATR). Current handheld instruments are generally equipped with a diamond ATR element that provides an effective sampling depth of several microns, weighted toward the surface. Contaminant layers that are around a micron or more thick can be readily detected. However, because detrimental levels of contaminants may be no more than a fraction of a micron thick, this limits the utility of FTIR for detecting their presence. If contamination is suspected, ATR-FTIR can be used to help identify a contaminant through solvent extraction and concentration of the contaminant.

Wetting tests can be particularly valuable for understanding and controlling adhesion processes. For a manufacturing environment, water break tests [5], wetting tension measurements using dyne solutions [18,19], and contact angle measurements [20] are more commonly used. All are sensitive to one degree or another to surface free energy, which is a measure of the chemical reactivity of a surface [14,21–23]. These wetting measurements all involve gauging the interaction of a test liquid with the surface in question. When a liquid is brought into contact with a surface, the outcome (for example, wetting and spreading vs beading up) is determined by the balance of the attractive forces between neighboring liquid molecules and those between the liquid molecules and the surface. Any change in surface composition from surface treatment or contamination will be reflected in the wetting behavior.

If the attraction of the liquid to the solid is weak compared to the attraction of the liquid molecules to each other, the liquid will tend to bead up. If the attraction is strong, the liquid will tend to spread on the surface to maximize interfacial area. The importance of wetting is shown in Fig. 9.1 where a conformal circuit board coating exhibits dewetting due to the low surface energy of the circuit board, in this case



Fig. 9.1 Dewetting of a substrate (in this case a circuit board) by a liquid (a conformal coating).

from failure to adequately remove solder flux. The low surface energy solder flux-contaminated surface had insufficient attraction to the coating to overcome its surface tension and cause it to spread.

Strong attraction of a test liquid to a surface is an indication that other liquids, such as adhesives, paints, or other coatings, will be attracted to the surface strongly enough to wet and spread, and establish good adhesion upon curing.

Many wetting tests are in common enough use to have been standardized. Water break tests are codified in ASTM F22, and a test where the surface is sprayed using an atomizer and visually evaluated is described in ASTM F21. These test methods are not quantitative and only provide a binary (and subjective) indicator of surface condition. For example, in ASTM F22 a stream of water is visually evaluated as it flows over a surface. If it spreads out into a continuous, unbroken sheet, it indicates that the surface is substantially free of hydrophobic contaminants. If the surface is contaminated with low surface energy substances, the flowing water will not sheet uniformly over the surface but rather will break into rivulets and tend to bead up (termed “water break”). Water break tests are not ideal as a quality control tool. They are messy: a relatively large amount of water is used that has to be removed, and the component must be dried before coating or bonding. Cases of water break tests contaminating sensitive surfaces because of impure water or transfer of contaminants during the drying process are not uncommon. Finally, because the result is only a binary “water break free/not water break free,” it is unknown whether it is too sensitive for some applications or not sensitive enough.

Another common tool in the printing and food packaging industries is the wetting tension measurement for polymeric sheeting (codified in ASTM D2578) [24]. This is accomplished via dyne solutions or dyne pens, which are mixtures of two miscible liquids in different proportions to obtain a range of surface tensions. Surface treatment level and readiness for printing or bonding are estimated as the surface tension of the lowest surface tension mixture that will remain spread on the surface for at least 2 s. This value is termed the wetting tension and is intended to approximate Zisman’s critical surface tension, γ_c [25]. The wetting tension is related to the surface energy and is affected by many of the same characteristics that control surface energy, such as level of surface treatment, but it is important to keep in mind that wetting tension and surface energy are not equivalent [26,27]. The approach generates numbers that quite often correlate well with surface treatment level for certain materials such as polymers as long as soluble contaminants or low molecular weight products of corona, flame, or plasma treatments are not present [23,28]. It is an inexpensive test but suffers from significant subjectivity [27,29]. Repeatability and reproducibility are affected by operator skill, changes in the solution composition that occur with time, and the presence of contaminants that may be soluble in the test fluids. Furthermore, the test results are hard to evaluate on typical industrial surfaces that may not be very smooth and are in fact frequently textured.

However, the value of these measurements in manufacturing for process control and for troubleshooting faulty processes lies not in the ability to predict if an interface will be strong, but rather in their sensitivity to changes in surface properties. If a surface treatment or surface preparation process is being performed in a manner that

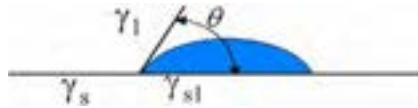


Fig. 9.2 Relationship of solid surface energy (γ_s), liquid surface tension (γ_l), and interfacial energy (γ_{sl}) to the contact angle θ .

creates a reproducible chemical composition, its wetting properties will be consistent. If the wetting properties change, this is an indication that something in the process has resulted in an unexpected change to the chemical composition of the surface. This sensitivity has been exploited in work ranging from fundamental studies of the structure of surfaces [21] to the resolution of “mysterious” bond failures in seemingly well-controlled manufacturing processes [30].

A more robust approach for quantifying important surface characteristics such as treatment level is through measuring the degree of spreading of a drop of liquid applied to the surface through determining the contact angle. This is the angle between a line tangent to the drop and the surface at the drop perimeter (Fig. 9.2).

Contact angles relate the surface tension of the liquid, the surface energy of the solid, and the strength of the interaction between them through the Young-Dupre equation [13]:

$$\gamma_s = \gamma_l \cos \theta + \gamma_{sl}$$

Measurement methods based on contact angle are shown in Test Methods C813, D5946, and D7490 as well as Practice D7334. Recent advances in contact angle instrumentation and methods have made this method quite practical for bond process development and process control in bonding and coating operations [6,10–12,31].

Because contact angles are sensitive to the composition of the uppermost few molecular layers of a surface, they can be extremely useful tools in adhesion science for studying fundamental adhesion mechanisms as well as for process development and troubleshooting. An example of how contact angles of water correlate directly to the level of oxidation of a flame-treated polypropylene surface is shown in Fig. 9.3. As the flame treatment level increases, the total amount of oxygen (incorporated as hydroxyls, ketones, carbonyls, and carboxylates) increases; these polar functional groups attract polar water molecules and cause the drop to spread, thereby decreasing the contact angle. This decreased contact angle generally predicts improved adhesion: the same attractive forces that exist between the surface and the water molecules function to cause adhesion of paints and adhesives.

As a rough guide, untreated polyolefins show contact angles around 80–90 degrees and wetting tension of about 32 dynes/cm.^a Immediately after flame treatment, these same materials typically show contact angles around 40 degrees and wetting tensions of 45–50 dynes/cm.

^a Surface energies (for solids) and surface tensions (for liquids) are historically presented in cm/cm, which are numerically equivalent to the corresponding MKS units of mJ/m².

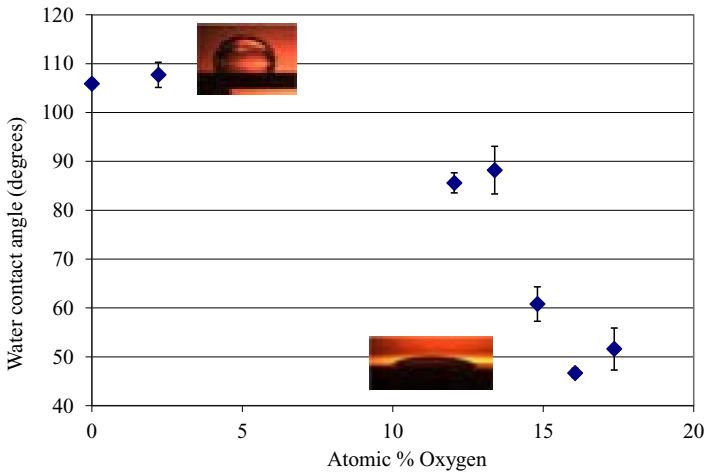


Fig. 9.3 Effect of increased oxygen content in a polypropylene surface (obtained by flame treatment) on water contact angle. >15% oxygen content is generally predictive of excellent adhesion.

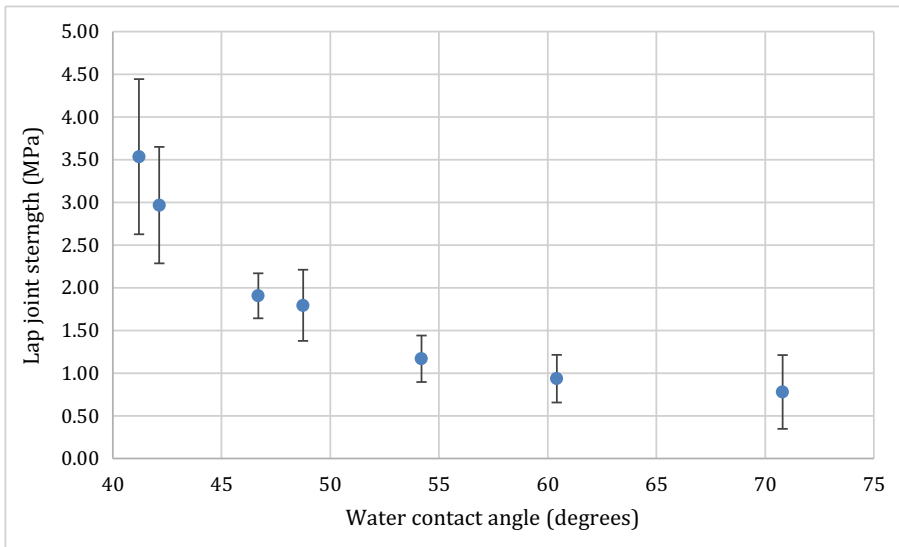


Fig. 9.4 Average lap joint strengths (ASTM D1002) for high-density polyethylene bonded with Henkel 9394 RT cure paste adhesive after various levels of plasma treatment. Error bars represent ± 1 standard deviation of five samples.

The relationship of water contact angles to adhesion (and by extension, adhesive bond performance) is well established for substrates ranging from metals to polymers and concrete [6,8,32–39]. Fig. 9.4 shows an example from our laboratory for lap joints of plasma-treated high-density polyethylene bonded with a room temperature cure paste adhesive. The failure modes ranged from interfacial (for untreated and lightly treated substrates) to cohesive within the polyethylene (for higher treatment levels).

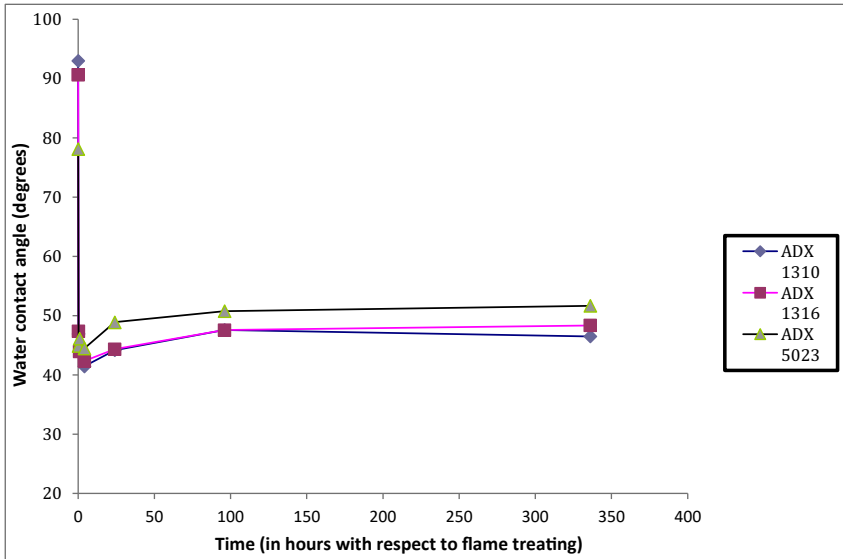


Fig. 9.5 Ballistic contact angle vs time for three flame-treated talc-filled polypropylene compounds. Time zero data is immediately prior to flame treatment.

Typical contact angle behavior for treated automotive polymers is shown in Fig. 9.5, from a study of the effect of aging after surface treatment for three talc-filled polypropylene compounds. 4" × 8" plaques were flame treated using a linear burner (FTS Technologies) under a fixed set of conditions. Water contact angles were determined immediately after treatment and after aging for various times using a Surface Analyst SA1001 (Brighton Science). Untreated values of 80–90 degrees dropped to the mid-40s immediately after flame treatment. Aging for >300 h under ambient conditions (about 23°C, 50% RH) resulted in a small amount of hydrophobic recovery for all three materials. Because values around 40–50 degrees are generally representative of highly paintable/bondable polypropylene surfaces, these surfaces do not appear to have significantly degraded during storage.

If active functional groups are "buried" by thin contaminant layers and prevented from interacting with a paint or adhesive, adhesion suffers. Contact angles on these surfaces reflect the occlusion of the active functional groups. Fig. 9.6 shows a correlation of a water contact angle to the areal density of a silicone oil contaminant on a carbon fiber-reinforced epoxy surface. The contact angle starts at a low value indicative of a high-energy surface; areal densities of this contaminant as small as 1–2 $\mu\text{g}/\text{cm}^2$ result in a readily detectable change in contact angle. This is well below the threshold level at which adhesion is adversely affected for many adhesive systems.

The sensitivity of contact angle measurements to surface chemical composition allows for rapid quantitative evaluation of cleaning processes, reducing reliance on spectroscopic methods. Fig. 9.7 shows the correlation of X-ray photoelectron spectroscopy to water contact angle measurements for a series of metal surfaces cleaned

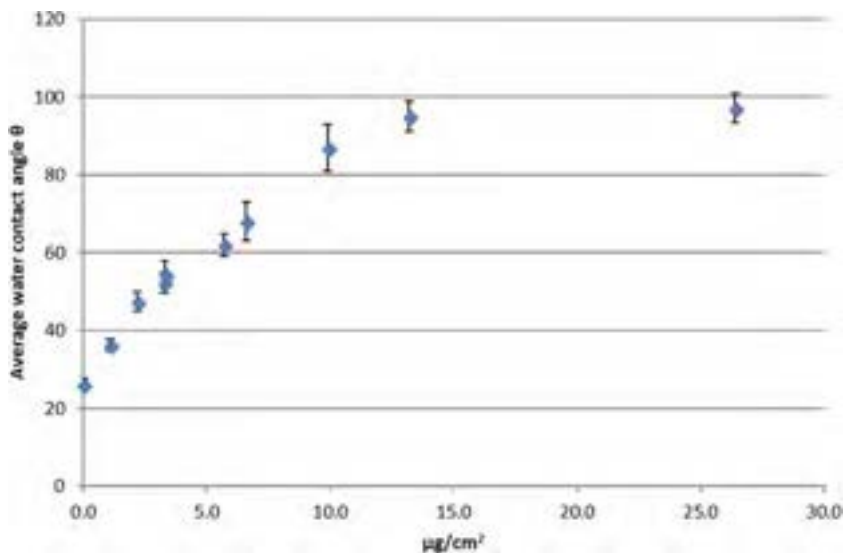


Fig. 9.6 Water contact angle vs areal density of silicone oil on a carbon fiber-reinforced epoxy surface. Contaminant amounts as small as 1–2 $\mu\text{g}/\text{cm}^2$ result in readily measurable changes in contact angle.

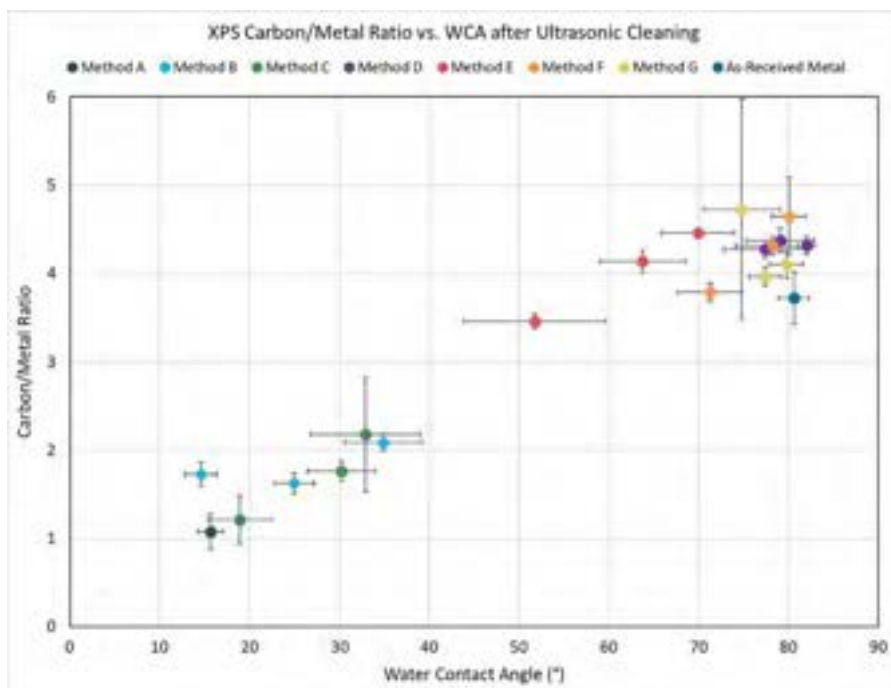


Fig. 9.7 Correlation of carbon/metal atomic ratios as determined by XPS with the water contact angle for a series of various metals cleaned via a variety of detergents. Low carbon/metal ratios indicate cleaner surfaces.

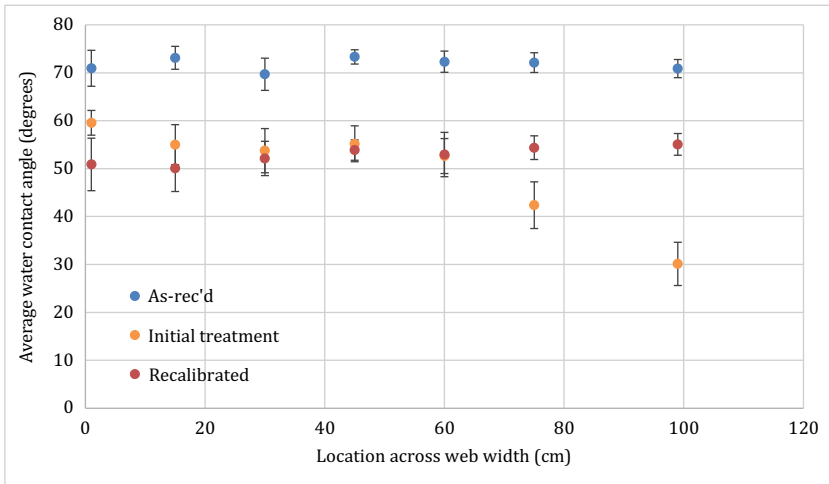


Fig. 9.8 Distribution of water contact angles across the width of polyester film prior to treatment (as received), after initial corona treatment (initial treatment), and after treatment with freshly adjusted corona equipment. Each data point represents the mean (± 1 standard deviation) of 16 measurements taken along about 200 cm in the machine direction.

with detergents of varying effectiveness. The carbon/metal ratio in XPS is a direct measure of the amount of contaminant overlayer; this measure correlates in an approximately linear fashion with the contact angle.

The simplicity and ease of water contact angle measurements combined with their sensitivity to minor changes in surface chemistry make them a practical method for monitoring spatial variation quickly and precisely in surface treatment or contamination. By way of example, Fig. 9.8 shows the distribution of water contact angles over the surface of a piece of polyester film intended for fabricating into a gas bag by adhesive bonding for a lighter-than-air ship. For the as-received (untreated) film, the contact angles had an average of 72 degrees and a standard deviation of about 2.8 degrees across the width of the web. This is a reasonably uniform and narrow distribution. However, it also represents a relatively low energy surface, and one that is difficult to bond with most adhesives. Corona treatment was being used to introduce oxidized functional groups into the surface and increase the surface energy; water contact angle measurement is recognized as an excellent way to quantify the treatment level [23,25,32,33]. The contact angle distribution after the initial treatment shows that the contact angles were lowered, but in a nonuniform manner. The right side of the film showed significantly lower contact angles than the rest of the web. This indicates a nonuniform treatment and would result in adhesion that would vary depending on which area was being bonded. This indicated that the corona treatment equipment was likely out of adjustment and service was performed. The treatment and measurements were then repeated; Fig. 9.6 shows that the treatment uniformity was greatly improved and adhesion was found to be extremely consistent across the entire width of the web.

These data serve to illustrate the utility of water contact angle measurements not just in process development and process control but in the solution of practical adhesion problems.

Not all wetting-based surface assessment techniques are equally useful. In particular, contact angle measurements are much more widely applicable than dyne solution measurements. For example, dyne solutions tend to be insensitive to small amounts of soluble contaminants. These solutions are of either ethanol and water or 2-ethoxy ethanol and formamide in different proportions. These solvents are effective at dissolving contaminants during application; as a result, the measurement process can function to clean the surface. This means that treated, contaminated surfaces can return the same wetting tension value as treated, uncontaminated surfaces. This may not be a problem for light corona and flame treatment of packaging films, which create little in the way of soluble contaminants, but can be a real problem for accurate sensing of heavier treatment levels (which create soluble byproducts) [28]. It can also be a significant issue for plasma treatment and cleaning processes of other polymers and metals (Note that the ASTM D2578 method specifically states that dyne solution measurements are only valid for polyethylene and polypropylene films). Because the pure water used for contact angle measurements is a poor solvent for most contaminants, contact angles are generally very sensitive to the presence of contaminants.

Nonetheless, contact angle measurements can correlate well to wetting tension measurements made with dyne solutions for well-behaved systems, that is, surfaces that are chemically very uniform point to point and have no contaminants soluble in the dyne solutions themselves. An example correlation is shown in Fig. 9.9 for a flame-treated polypropylene compound.

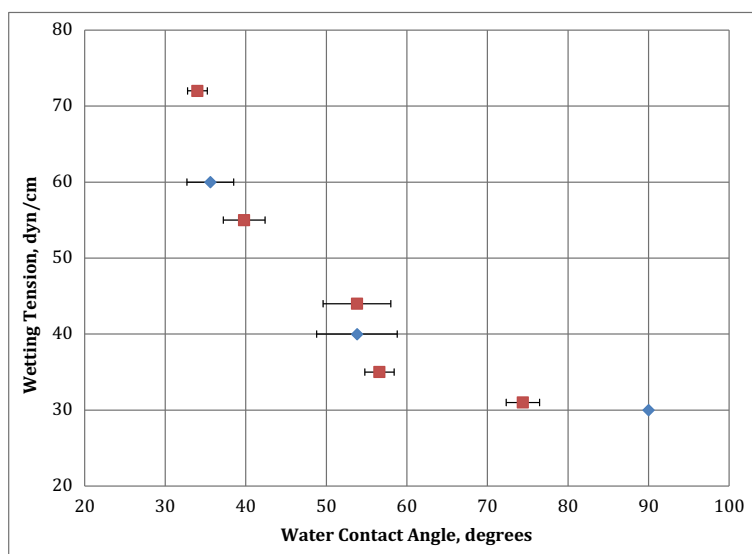


Fig. 9.9 Relationship of wetting tension as measured by dyne solutions to water contact angle for flame-treated polypropylene measured using a Surface Analyst 1001 (Brighton Science).

9.4 Adhesion failure in bonded and coated structures

Properties of a bonded or coated structure that define failure include an initial strength or toughness that is less than expected, or durability that is less than expected. Failures that show up during manufacturing quality inspections are generally initial strength or toughness; products that pass these inspections can show premature failure in the field due to instability of the interface to environmental stressors, generally related to heat and moisture. These are distinct properties in that they depend on very different characteristics of the bonded/coated structure. Both types of failure indicate that one or more factors are out of control in the manufacturing process; something has changed. The ultimate goal of failure analysis is to identify the factor(s) that have fallen out of control so that they can be rectified.

9.5 Failure analysis

Solving bonding challenges depends on accurate determination of the cause of failure, which is accomplished by analysis of failed specimens. This allows identification of the “weak link” in the structure. Determination as to *why* a particular component has failed is necessary to be able to fix the problem and thereby improve product performance.

At its simplest, there are only three structural (i.e., load-bearing) elements where failure could occur: the substrate, the adhesive or coating, or the interface between them. In practice, this number can be higher. For example, if there is a primer present, there are two more interfaces (substrate-primer and primer-adhesive). A further complication results if two of the components interact to form an interphase of distinct composition from either parent material. An example is failure in an amine-cured epoxy/aluminum bond that occurs in an interphase of undercured resin resulting from the consumption of amines to form amine salts by reaction with the aluminum oxide surface [40]. Another point to consider is that the locus of failure initiation can have a strong influence on the final crack path. When failure initiates and a crack begins to grow in a bonded structure, the stress state in the remaining intact structure can change in a manner that results in the cohesive failure mode of an intact (i.e., high-quality and nondegraded) material. It can be critical to pay close attention to failure initiation, which may represent a small fraction of the overall failure surface. This highlights the potential complexity of failure analysis.

Determination of the cause of failure in an interface-containing structure is complex, but like any complex problem it can be made easier by breaking it down into steps. One such approach is outlined here.

1. *Establish familiarity with the fundamental materials and process chemistry.* This is a fundamental background step required for the solution of most problems in materials science. This involves reviewing what is known about the factors affecting substrate chemistry as it relates to bond surface composition and properties, including:
 - Precleaning.
 - Surface treatments such as plasma treatment, anodization, primer.

- Substrate composition, including additives with potential for blooming such as internal mold release, antistats, scratch/mar packages, color concentrate masterbatch composition.
 - Adhesive composition, cure reactions, manufacturer-recommended procedures.
2. *Perform a careful analysis of failure mode* to establish the “weak link” in the structure; this is the crux of the failure analysis process. It consists of a determination of the molecular structure and composition of the two surfaces created by failure. This analysis starts with a careful visual and/or microscopic inspection of the failure surfaces. However, failure occurs in a zone of molecular dimensions, and the phase through which a crack propagates is frequently a thin (submicron) contaminant or adhesive layer. Because of this, optical or microscopic inspection by itself may not be sufficient to precisely identify the failure mode, except in clear cases of cohesive fracture in one of the bulk phases. Failure analysis should almost always be combined with some level of surface chemical analysis (i.e., XPS, FTIR, etc.).
 3. *Thorough “eyes open” analysis of the entire process from supply chain to final assembly.* Once the failure surface composition has been established, the next step in fixing the problem is to determine where in the entire process the formation of the desired bonded structure has been interrupted. This requires an appreciation for the steps in the manufacturing process that are capable of affecting the properties of the final bonded structure. These steps are not confined to the surface preparation and adhesive/coating application steps: There are many points in the manufacturing process from the upstream material suppliers to the final application and curing steps that affect adhesion. These steps are called critical control points (CCPs), and adhesion failure can originate at any of them. This phase in the solution of adhesion problems involves identification of the CCPs and correlating their potential effects on the bond surface to the results of the failure mode analysis.

9.6 Critical concepts for surface preparation

The goal of surface preparation and treatment is to convert an ill-defined surface into one with a precisely defined surface of controlled composition. The effects of not controlling and monitoring these bond surfaces can be expensive, both financially and reputationally. One statistic provided verbally by an employee of a large automotive manufacturer stated that one warranty claim on an oil pan cost seven new vehicle sales, which is a rather steep price for an ill-prepared oil pan surface.

Assuming the design engineers have properly chosen the materials and geometries of a joint, the most common issues observed with bond failures are surface contaminants, thick oxide layers, or an inherently low surface energy of the substrate prior to adhesion.

9.6.1 Surface contaminants

Surface contaminants are introduced from extrinsic and intrinsic sources. Extrinsic sources are often introduced at the CCPs in a manufacturing process leading up to the bond step. Intrinsic sources are ingredients in the substrate material that may

interfere with bonding, often becoming more concentrated at the surface with a change in temperature. Some common examples of these are listed below.

Extrinsic contaminant source examples:

- Processing aids: Mold releases, rust preventatives, rolling oils, die lubricants, cutting fluids.
- Cleaning residues: Leftover contaminants (poor cleaning step), leftover detergents (poor rinse step).
- Handling: Fingerprints, packaging used for transport (plastic bags, bubble wrap, etc.), some glove types.
- Aerosols: Dirty warehouse with uncovered bond surfaces, freshly waterproofed jackets for rain protection.

Intrinsic contaminant source examples:

- Blooming agents: Antistatic molecules, plasticizers, scratch/mar packages, slip agents/intrinsic mold releases.
- Composite layup materials: Peel ply.

9.6.2 Oxide layers

Oxide layers on most metallic surfaces are inevitable when preparing the surface in atmospheric conditions. Clean, freshly made oxides that are only a few molecular layers thick often exhibit extremely high surface energies and create a strong interface for a bonded joint. When these surfaces are exposed to oxygen for long periods of time, the oxide layer will grow. In a clean environment, the oxide can remain clean. However, a thick metal oxide (ceramic) layer is brittle and does not exhibit the strength or toughness required by a bond to a metal, often leading to substrate failure within the oxide layer. If the oxide surface is allowed to grow in an uncontrolled environment, such as a hot, humid warehouse with typically large amounts of grease and dirt, the oxide layer will incorporate more organics from the environment and create a low energy surface. These surfaces will often exhibit interfacially failed bonds.

9.6.3 Low energy surfaces

Materials with inherently low surfaces, such as polyolefins, often require some surface activation to achieve a robust bond. Chemical treatment such as plasma, flame, or corona (covered in a later section) or primers/adhesion promoters are common methods to increase the number of functional groups that will chemically react to an adhesive to form a covalent bond.

9.7 Surface cleaning and treatment technologies

As indicated above, metallic and polymeric surfaces express different chemical functionalities that change how each reacts with adhesives to form covalent bonds. If the right adhesive is chosen, a bond should break within the adhesive or within the substrate, which indicates that the bond between the adhesive and the substrate is not the

weakest link in the chain of the bonded joint. For metallics, old and thick oxide layers must be removed and a fresh, molecularly thin oxide layer should be formed. Polymers should be checked as to whether their surface energy is high enough to achieve the performance specifications required, as some may require chemical treatment to enhance the surface energy. For all surfaces, chemical cleanliness is critical to ensure good bond performance. Below is a brief review of various technologies that are commonly used in manufacturing.

9.7.1 Physical treatments

Cleaning methods and abrasion techniques are the most common way to clean and treat surfaces. Cleaning methods can be used for metallic and polymeric surfaces. Techniques can include simple, manual processes such as a solvent wipe or complex and tightly controlled processes such as an automated, highly tuned, machine-washing system. Manual solvent wipes are ideal for small areas (such as repair jobs) or parts where the geometries change often (such as the automotive industry) where investing in a parts washer may be difficult to adapt on a year-to-year basis. Common semiautomatic or fully automatic machine systems include aqueous methods, such as a spray or ultrasonic system, or solvent-based methods, such as vapor degreasing. Note that due to concerns around the environment, many regulatory agencies are encouraging companies to move away from solvent-based methods and invest in more environmentally friendly cleaning methods where possible.

Abrasive techniques are generally reserved for metallics, where the top oxide layers are removed with an abrasive process. Much like cleaning processes, manual and automatic techniques exist. Electric or pneumatic hand sanders and even sanding blocks are used for manual processes. Grit blasting and CO₂ blasting can be conducted using an automatic system.

9.7.2 Chemical treatments

Chemical treatments often assume that the surface is already clean before treating with chemical means. A clean surface will provide the most efficient and homogenous coverage of treatment for improving a bond surface.

Plasma, flame, and corona treatments use similar physics to introduce oxygenated groups on a surface. Corona is commonly used in polymer film industries, where a voltage can easily be passed through the substrate to administer treatment. Plasma and flame are generally used on thicker substrates. Flame treatment equipment is less expensive than plasma equipment generally; however, there is a cost to using natural gas, and the environmental footprint of using carbon materials should be taken into consideration during the decision-making process. Plasma treatment can use a variety of different gasses, such as argon, helium, nitrogen, and compressed air. The most commonly used gas is compressed air, which is easily fed with an air compressor and can be used for vacuum and open-air plasma systems. A large range of plasma systems is available, from very gentle plasma pens designed for dental applications to plasma blast systems designed for removing paint and oxides to prepare a metal

surface for welding. Each has its own advantages that we will not touch on here but should be carefully considered during the design process.

Primers and adhesion promoters can have multiple effects on a surface. An adhesion promoter is most often a solvent-based adhesive tailored to low surface energy materials. Adhesion promoters therefore can absorb some contaminants on a surface, making the system more tolerant to contamination while creating a higher energy material for the main adhesive to bond to. Primers are best used for increasing the durability of a bond. Primers can inhibit corrosion of a metallic surface, especially when laden with chrome or a chrome substitute. Primers can also be used as a conversion coating such as with silanization or a sol-gel, which can create a highly bondable surface that is more stable than the highly reactive, freshly oxidized surface of a metal.

Etching and anodization techniques can have similar effects on metallics to primers: stabilizing a fresh oxide layer and inhibiting corrosion. These processes tend to be conducted in large baths rather than applied manually, as many primers and adhesion promoters are. Baths introduce the potential for additional complications during the surface preparation process, so careful monitoring and control of these processes should be conducted to avoid the effects of bath contamination (from treatment of soiled parts or dragout) as well as changes in concentration or reactivity of active ingredients (through consumption or dilution).

9.7.3 Surface tolerant adhesive systems

For every surface preparation methodology, each adhesive system will provide more or less tolerance to the surface state of the substrate. Rubbery adhesives and adhesives with long curing times tend to be more tolerant to poor surface states due to the mobility of the chains, either initially or over time, allowing some absorption of the contaminant into the adhesive. Bonded joints for critical systems where safety is involved, such as structural joints of aircraft, may require much tighter tolerances to have the necessary confidence in the strength and longevity of a joint. For any process, monitoring the surfaces prior to adhesion is a best practice for ensuring that the bonds will perform as required.

9.8 Processes out of control

An adhesion failure in a process that has a history of acceptable adhesion is a clear indicator that some portion of the process has drifted, that is, it is not under sufficient control. Root cause analysis is a matter of identifying what part of the process has deviated by an unacceptable amount. This can be difficult if processes are being performed with few or no control measurements of the outcome of these process steps. Unfortunately, in bonding and coating processes, this is all too often the case. Here, root cause analysis will require open eyes and thoughtfulness in examining all environments a surface may experience before bonding.

Case study 1: Paint adhesion failure

An instructive example is from an automotive supplier manufacturing painted polyolefin components for an OEM. Flame treatment was being used for two purposes: to deflash the mold parting lines as well as to increase the polymer surface energy to provide acceptable paint adhesion. Flame treatment increases surface energy by oxidizing the uppermost few molecular layers of the polymer surface through conversion of C—C and C—H groups to C—O, C=O, and O—C=O groups. The increased polarity of these groups compared with C—C and C—H results in improved adhesion of paints and adhesives. One way to define treatment level is by the concentration of the various oxidized functional groups created on the surface. This concentration is determined by variables such as:

- Stoichiometry of the flame (determined by factors such as % excess oxygen and gas composition, such as natural gas or propane).
- Burner design.
- Gas velocity.
- Distance of part from burner.
- Traverse speed of flame over the surface.
- Chemical composition of the part surface prior to treatment.

All represent parameters that need to be controlled if consistent results are to be obtained. Whereas it is the chemical composition of the treated surface that determines paint adhesion, the control of manufacturing processes that determine adhesion is usually minimum or nonexistent. Surface chemical analysis is rarely used in manufacturing to determine treatment level; the most sophisticated control information available is usually the wetting tension of the surface as determined by dyne fluids.

In this particular example, the flame treatment process was being evaluated by the routine evaluation of treatment level via dyne solutions. However, an unacceptable level of paint adhesion failures was being experienced by the customer. Fig. 9.10 shows a sample received for analysis showing apparent paint adhesion failure.

Surface compositions were determined using XPS. Because of the surface sensitivity of XPS, analyzing the cause of failure requires a pristine failure surface, that is, one that has not been touched by a hand or other object. This sample had an unknown handling history, making it necessary to obtain fresh, uncompromised surfaces for analysis by debonding a small additional area of paint around the edge of the previously exposed surface. This was accomplished by teasing the edge with a needle then peeling back paint using a tweezer. The underside of the peeled paint was analyzed along with the matching substrate polymer surface. In this way, matching failure surfaces could be analyzed to precisely determine both the failure locus and its precise chemical composition. An additional sample was created by shaving off a thin slice of polymer with a razor blade to obtain a clean, untreated polymer surface.

Figs. 9.11–9.13 show the XPS survey spectra obtained from the three samples. The elements detected were carbon, oxygen, silicon, and in some instances a trace of either magnesium or lithium. This peak was so weak that its identity was uncertain without further analysis. Relative peak height is related to the atomic percentage of each element. These are summarized in Table 9.1 and represented graphically in Fig. 9.14.

The oxygen content of the untreated polymer was a few percent. This is typical of injection-molded polyolefins and in contrast to flame- or plasma-treated polyolefins, which typically show 12%–15% oxygen. Notice that the oxygen content of the failure surface of the polypropylene side was only 5.2%, very close to that of the untreated polymer and well below that of a typical treated polyolefin surface. This suggests that paint adhesion failure was interfacial

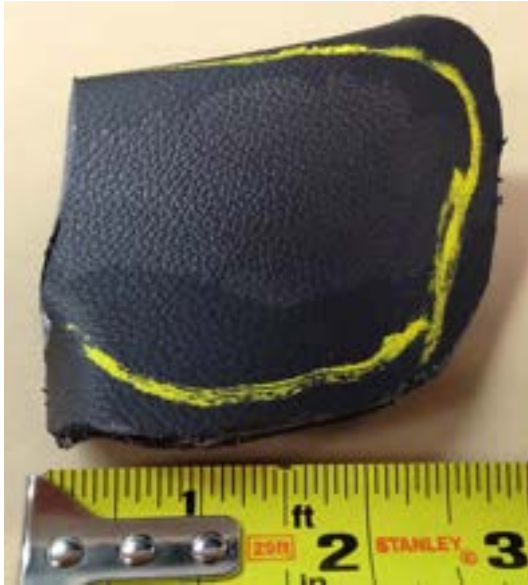


Fig. 9.10 Painted, flame-treated polypropylene showing apparent paint adhesion failure.

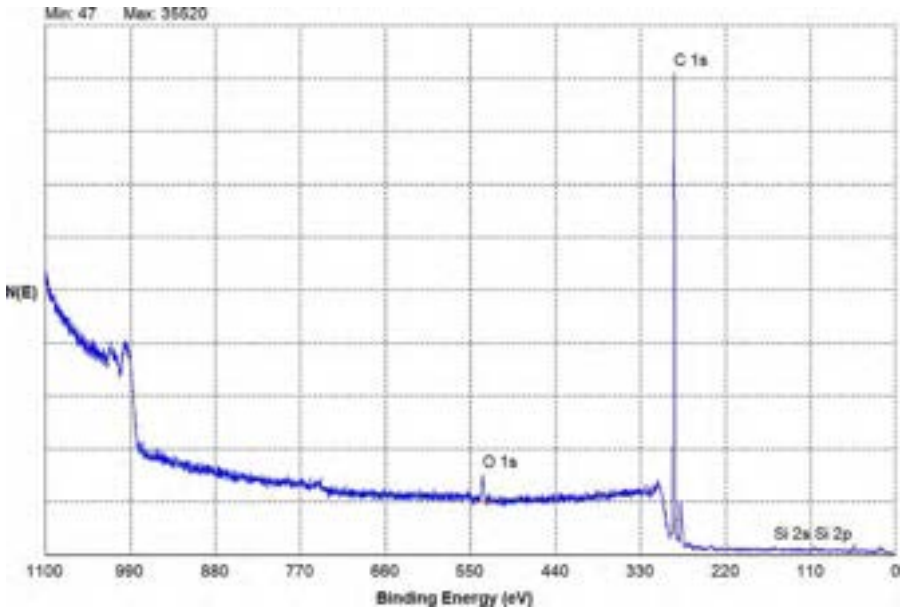


Fig. 9.11 XPS spectrum, untreated surface.

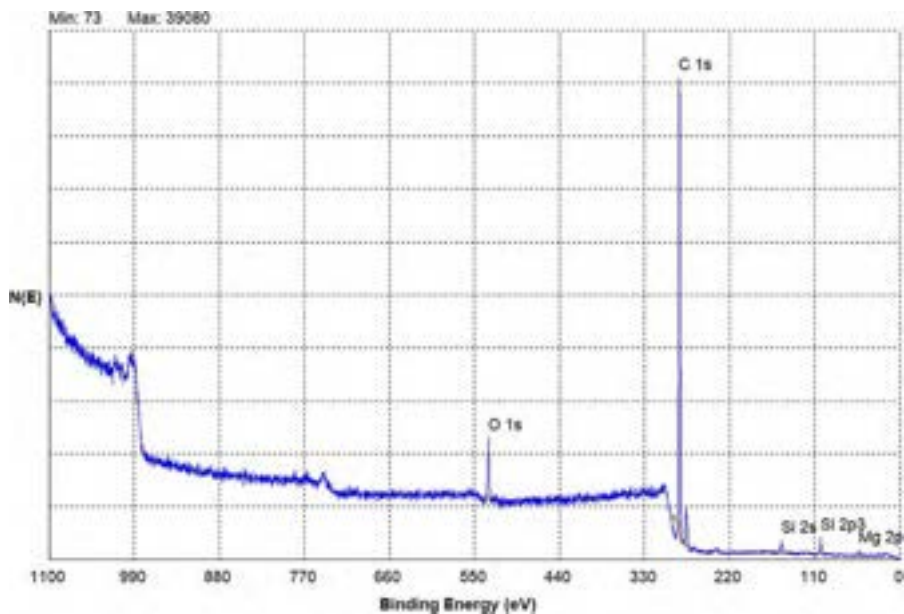


Fig. 9.12 XPS spectrum, TPO side of failure surface.

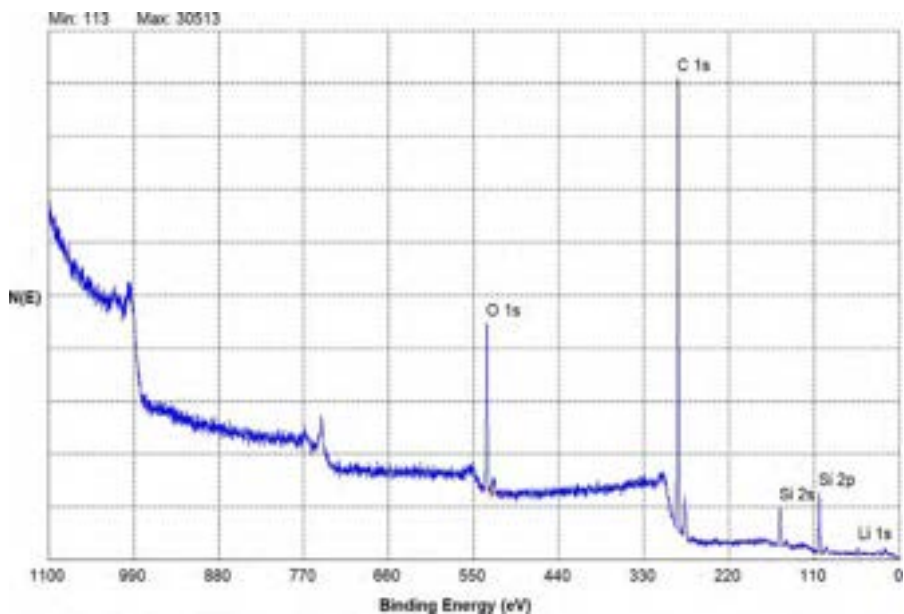
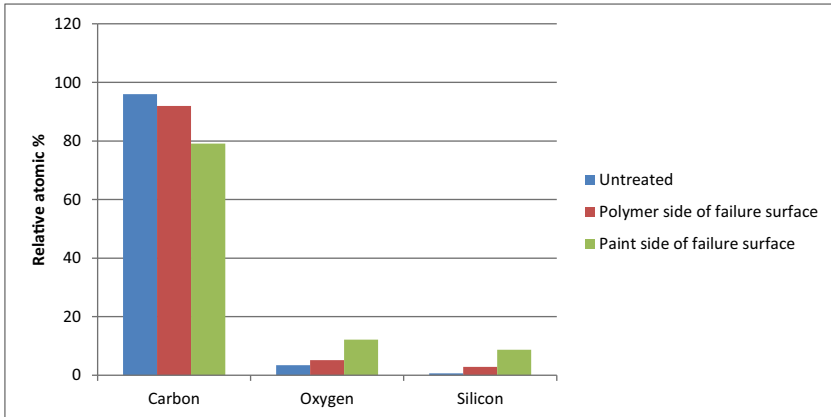


Fig. 9.13 XPS spectrum, paint side of failure surface.

Table 9.1 Atomic compositions.

	Carbon	Oxygen	Silicon	Li or Mg
Untreated	96.0	3.4	0.6	–
Polymer side of failure surface	91.9	5.2	2.9	Trace
Paint side of failure surface	79.1	12.2	8.7	Trace

**Fig. 9.14** Relative atomic compositions.

between the paint and the polymer, and likely due to insufficient treatment of the polymer surface.

Flame treatment can be deceptively complex. Because the level of oxidation depends so strongly on both the part of the flame in contact with the surface as well the length of time that the surface stays in contact with the flame, uniform flame treatment of three-dimensional part surfaces (e.g., automotive components) can be significantly more challenging than two-dimensional surfaces such as packaging film. Drifts in flame surface offset distance as small as a millimeter can have large effects in treatment level. Motion programs that don't maintain a consistent offset distance or traverse rate over surfaces with complex curvature will result in treatment nonuniformity. Furthermore, with formulated polymer systems that contain mobile and potentially surface active components, the preflame treatment surface can have significant variability across a part surface due to variable flow and cooling rates in different parts of the tooling. Contact angle maps over these surfaces both pre- and posttreatment can flag potential trouble areas that may require additional (or less) treatment to achieve uniformity of treatment and adhesion (see Fig. 9.8).

XPS is a particularly powerful surface analysis tool that provides unequivocal information regarding atomic composition along with significant information regarding molecular structure. However, there are situations where the more detailed level of structural analysis provided by techniques such as infrared spectroscopy can be very useful in determining the root cause of adhesion failure. The following example shows the utility in using FTIR for the solution of adhesion problems.

Table 9.2 Typical additive classes grouped by potential to migrate.

Generally nonmigrating	Compatibilizers Impact modifiers Reinforcing fillers; coupling agents Pigments Blowing agents Antioxidants/stabilizers
Frequently migratory	Plasticizers Lubricants and mold release agents Scratch and mar additives Antistats

Case study 2: TPO to polyurethane bond failures

Most polymers, both thermosets and thermoplastics, are highly formulated products. They typically contain many nonpolymeric components intended to stabilize, toughen, color, reinforce, and lubricate the final product. Certain classes of these additives are mobile and capable of migrating to the surface, driven by thermodynamics and enhanced by time and temperature. This additive migration can create a surface that has a composition and properties very different from the bulk of the polymer. If the manufacturing process includes the creation of an interface between the polymer and an adhesive or paint, or in the case of a medical device, contact with human tissues, additive migration to the surface (a process known as blooming) can have serious consequences. Blooming represents a form of contamination that can result in adhesive or paint failures or worse. [Table 9.2](#) lists typical additive classes grouped according to the tendency to migrate.

The function of lubricants, internal mold releases, antistats, and scratch and additives depend upon their ability to migrate to the surface. Plasticizers, however, function by remaining solubilized in the polymer bulk. Migration of these additives to the surface is problematic and can result in product failure.

The driving force for additive migration is the thermodynamic tendency of a system to evolve to a low energy state. When an object is molded from a thermoplastic, the surface is in a relatively high energy state. Migration of plasticizer to the surface creates a lower-energy, more thermodynamically favorable state. The rate and extent to which migration occurs depend on the concentration of the additive in polymer (high concentration favors blooming); the mobility of the additive (smaller, more mobile molecules migrate more readily); solubility (lower solubility favors blooming); temperature (high and low temperatures can facilitate migration to the surface, depending on the system); and finally surface energy (the higher surface energy of flame- or plasma-treated polymer surfaces favors blooming).

Useful tools for detecting and controlling the migration of surface active additives are those that are sensitive to the region of a material that determines properties such as adhesion. Because this zone is typically only a fraction of a micron in thickness, there are few analytical tools sufficiently surface sensitive to be useful. Surface energy measurements via dyne solutions have proven to be of limited usefulness in identifying and studying blooming phenomena based on the solution components' ability to dissolve and remove typical blooming additives. As a result, blooming additives tend to be essentially invisible to these measurements. Water contact angle measurements, on the other hand, are extremely sensitive to small variations in surface composition while not perturbing the surface as solvent-based probes do [22]. These measurements can

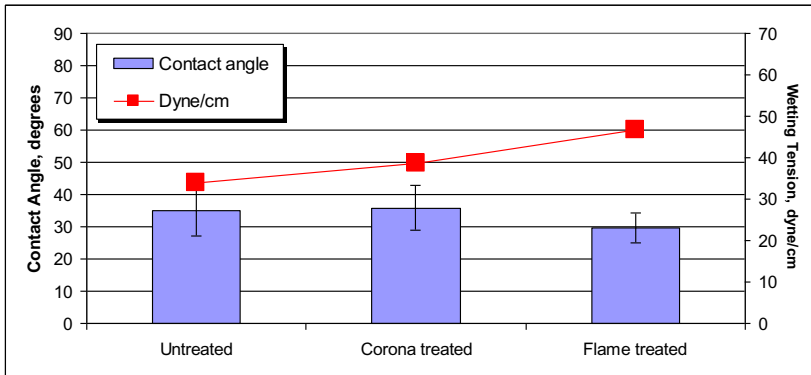


Fig. 9.15 Wetting tension (from dyne solutions) and water contact angles on injection-molded TPO airbag chutes as a function of treatment.

be extremely useful for detecting and controlling additive blooming. With appropriate handheld instrumentation, water contact angle measurements can be very useful in the hands of manufacturing and quality personnel for detecting and controlling additive blooming in the manufacturing environment.

This example outlines the results of work using a combination of ATR-IR and water contact angle measurements to detect and identify blooming in an injection-molded automotive airbag chute. This particular component was molded from thermoplastic olefin (TPO), a rubber-toughened polypropylene compound, and was oxidized through either a flame or corona treatment to provide sufficient adhesion to a urethane foam layer. However, seemingly random adhesion failures could not be correlated to any differences in treatment level as determined by wetting tension measurements. The surface appeared to be responding in a predictable manner to flame treatment when evaluated using dyne solutions. As seen in Fig. 9.10, treated surfaces could readily achieve 50–60 dyne/cm values, yet adhesion of urethane foam to these surfaces was unreliable and did not seem to correlate to treatment type or dyne level.

Fig. 9.15 also shows the results of water contact angle evaluation on these surfaces: although they showed different wetting tension values, the contact angles were not significantly different. It appeared that the changes occurring during flame and corona treatment were not affecting the uppermost few molecular layers of the surface, the region to which contact angle measurements is sensitive. At this point, FTIR spectroscopy with an attenuated total reflectance accessory was used to evaluate the molecular structure of the uppermost few microns of the surface in an attempt to determine the reason for the discrepancy.

Fig. 9.16 (top) shows the initial FTIR analysis of the TPO surface of an as-molded specimen. In addition to the expected CH, CH₂ and CH₃ peaks due to the polypropylene matrix, additional peaks were present near 1635 and 1660 cm⁻¹ as well as two peaks near 3190 and 3370 cm⁻¹ (arrows). These are characteristic of a long-chain amide, specifically oleic amide, which is a lubricant found in commercial scratch and mar additive packages. This additive is specifically intended to bloom to the surface of an injection-molded part to provide some protection against the cosmetic damage that can occur during part handling, storage, and use. The presence of a scratch and mar package in a compound intended to be encapsulated beneath a layer of urethane foam seemed unusual but the spectral evidence was strong.

The location within the molded part of the amide seen in the top spectrum of Fig. 9.11 was established by several experiments designed to determine if it was on the surface or distributed within the bulk sampling depth of the ATR-FTIR technique (perhaps 3 μm). Wiping with water

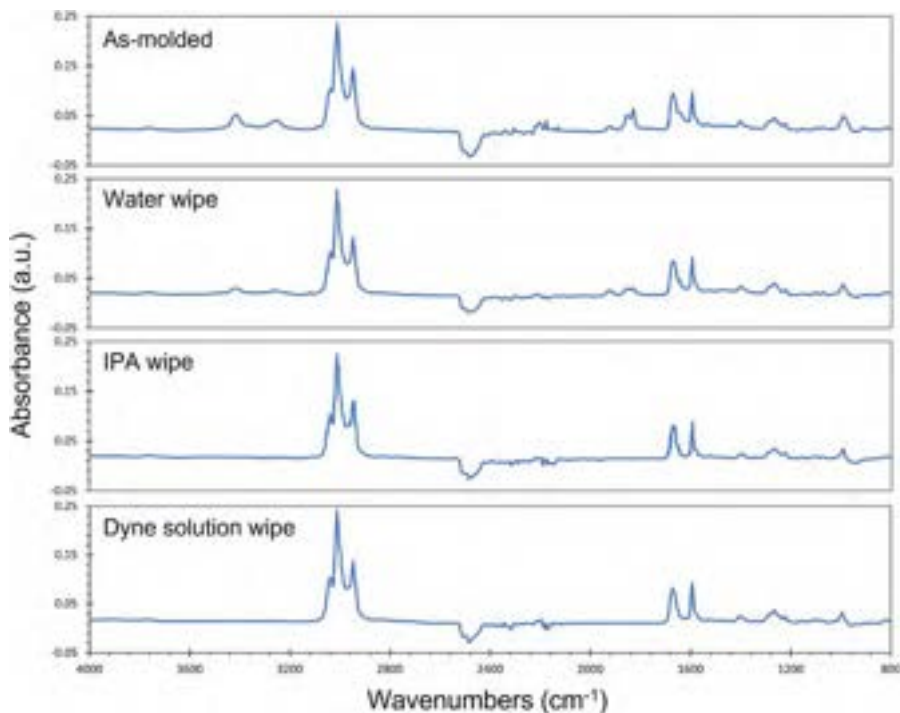


Fig. 9.16 ATR-IR spectra of injection-molded TPO airbag chutes as a function of treatment. *Arrows* indicate peaks characteristic of oleic amide scratch and mar additive.

resulted in little change in peak intensity. Wiping with isopropanol or with dyne solution completely eradicated the bands due to amide. This demonstrated that the amide was concentrated on the part surface. Furthermore, it showed significant solubility in both isopropanol and dyne solutions, but little or no solubility in water. These solubility results are consistent with the identification of the material as a long chain amide.

The amide showed significant mobility: Removal of the bloomed material via solvent wiping was only temporary. [Fig. 9.17](#) shows the effect of wiping followed with gentle overnight heating. The bands due to the amide reappear, indicating that this material will continue to bloom to the surface over time.

In this case, surface treatment of the freshly molded TPO components was effectively raising the surface energy. However, with variable storage time and temperatures after treatment but prior to bonding, additive blooming was contaminating the treated surface and interfering with adhesion of the urethane foam overlayer. Because the solvents used in the wetting tension measurements were dissolving the blooming oleic amide, they sensed the treatment state of the underlying surface without detecting the contaminant overlayer. This resulted in a “false positive” in terms of indicating a surface that was ready for adhesion to a coating or adhesive. Contact angle measurements, on the other hand, were sensitive to the actual uppermost surface being presented to the adhesive and were predictive of adhesion.

[Fig. 9.18](#) shows the effect on contact angle measurements of removing the blooming additive via a solvent wipe. Once the treated surface was exposed by removal of the blooming additive, the chemical state of the treated surface became accessible.

These results have significant implications for the control of processes intended to prepare surfaces for adhesion of paint or adhesives. Surfaces are dynamic systems whose properties

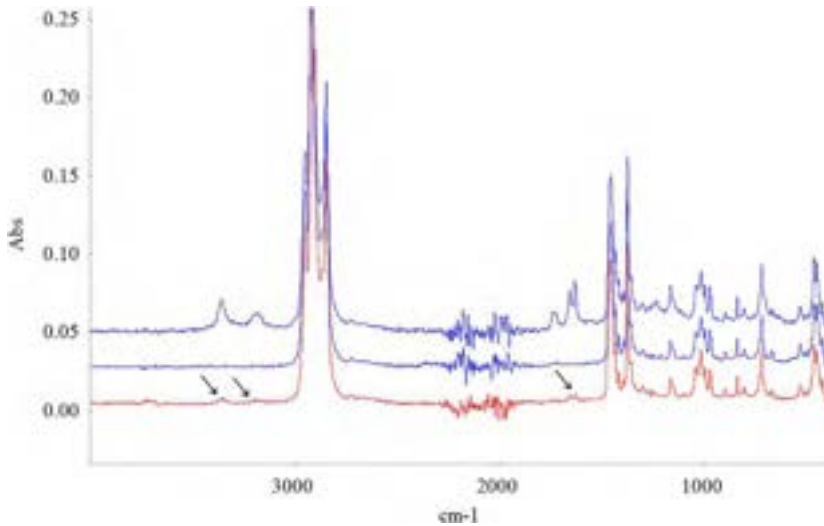


Fig. 9.17 ATR-IR spectra of injection-molded TPO airbag chutes. Top spectrum: as-molded. Middle spectrum: wiped with IPA. Bottom spectrum: after 20h at 70°C. Arrows indicate bands characteristic of long-chain amide additive.

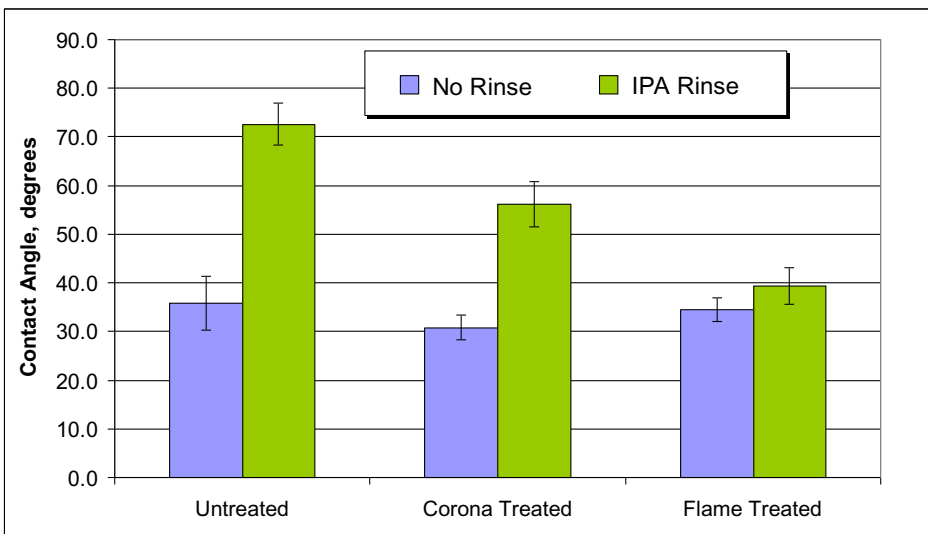


Fig. 9.18 Contact angle measurements on untreated and treated TPO surfaces before and after wiping with isopropanol.

evolve over time at rates dependent on factors such as time and temperature. Flame-treated parts that are initially bondable can decay and lose bondability with time after molding. Such surfaces will require inspection immediately prior to painting or bonding and may require removal of any surface active agents that have migrated to the surface.

Case study 3: In-mold adhesion of thermoplastic urethane to polycarbonate

Adhesion of one polymer to another (polymer-polymer adhesion) can be very challenging. Because most polymers are immiscible, there is usually little to no interdiffusion at the plane of contact and the structure will form a defined (two-dimensional) interface. The energy required to disrupt a discrete interface such as forms between two immiscible polymers scales with the work of adhesion (W_A) [29,31,41–43]:

$$W_A = \gamma_1 + \gamma_2 - \gamma_{1,2}$$

where γ_1 = surface energy of polymer 1, γ_2 = surface energy of polymer 2, and $\gamma_{1,2}$ = free energy remaining at the interface after the two polymers have interacted. W_A is a way to quantify the amount of chemical interaction that occurs at an interface. Because most polymer pairs are only capable of interacting through weak dispersion forces, $\gamma_1 + \gamma_2$ is almost equal to $\gamma_{1,2}$, and W_A is generally low for polymer-polymer interfaces.

Printing and sealing food packaging, painting or bonding automotive plastics, and bonding of fiber-reinforced composite materials are all examples of products that depend on polymer-polymer adhesion. The most common approaches for improving adhesion in these products involve increasing the surface energy (i.e., chemical reactivity) of the polymer surface through techniques such as wet chemical etching or gas-phase treatments such as plasma, corona, or flame treatments, which graft polar and/or reactive functional groups into the uppermost nanometer or so of the surface [44]. In terms of the equation for W_A , this approach increases W_A by increasing γ for the substrate polymer, and (in some cases) by providing mechanisms for specific chemical interactions between the two polymers that result in lower $\gamma_{1,2}$.

The situation is different for polymers that are at least partially miscible (i.e., mutually soluble) in each other. Miscibility of polymers implies that specific chemical interactions such as hydrogen bonding can occur among the component polymers [45]; dispersion force interactions are generally insufficient for structural bonds. Adhesion that results from a well-formed interphase between polymers that are at least partially miscible comes not just from the intermolecular interactions that determine W_A , but also from the energy necessary to disrupt these entanglements and/or fracture the entangled chains. Adhesion as measured by mechanical tests is not governed by W_A but rather by the mechanical properties and stress state of the individual polymer phases and the interphase. Polymer-polymer adhesion where there is some miscibility can be excellent. However, very few polymer pairs are miscible.

Polycarbonate and some polyurethanes represent one of the few pairs of miscible polymers. They form blends with properties useful enough to have resulted in commercial products. In polyester urethane-polycarbonate blends, this miscibility may be enhanced by the occurrence of ester interchange reactions between the carbonate and ester moieties that form compounds that function as in situ compatibilizers [46–48]. The same chemical compatibility that results in miscibility and blending can result in good adhesion between polycarbonate and polyurethanes when one is overmolded onto the other in an injection-molding process.

In-mold adhesion between a thermoplastic urethane and a polycarbonate was being exploited by a manufacturer to create a shaft seal for lubricant retention in a machine that consisted of a rigid fiberglass-reinforced polycarbonate shell with an overmolded elastomeric urethane sealing element. In general, the adhesion of these polymers directly out of the mold was sufficient to cause cohesive failure in one of the polymers during testing. However, intermittent cases of poor adhesion indicated that uncontrolled variables in materials or process were interfering with consistent product quality, which prompted this investigation.

In this case study, the materials of construction included glass-reinforced bisphenol A polycarbonate (PC) and a polyester-based polyurethane elastomer (TPU). The soft segment consisted of

the adipate ester of hydroquinone and butanediol while the hard segment was MDI (3,3'-dimethyl-4,4'-diphenylmethane diisocyanate). Polymer-polymer adhesion was quantified using a 90 degrees peel test according to ASTM D429-81 for measuring adhesion of elastomers to rigid substrates. A mold was constructed for injection of 1'' \times 2.38'' \times 0.125'' polycarbonate coupons followed by overmolding of the urethane. In addition to generating mechanical strength data as a function of material composition and processing conditions, these specimens provided ideal failure surfaces for chemical analysis of failure locus using XPS and ATR-IR spectroscopy.

C(1s) XPS spectra of the two bulk polymers along with the functional group assignments of the component peaks are shown in Figs. 9.19 and 9.20; they showed that the component polymers were readily distinguishable by their XPS spectra.

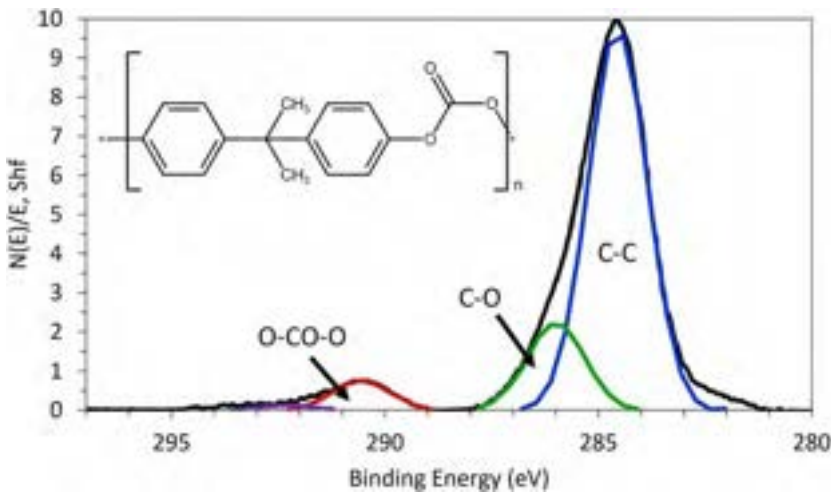


Fig. 9.19 C(1s) XPS spectrum of bulk bisphenol A polycarbonate.

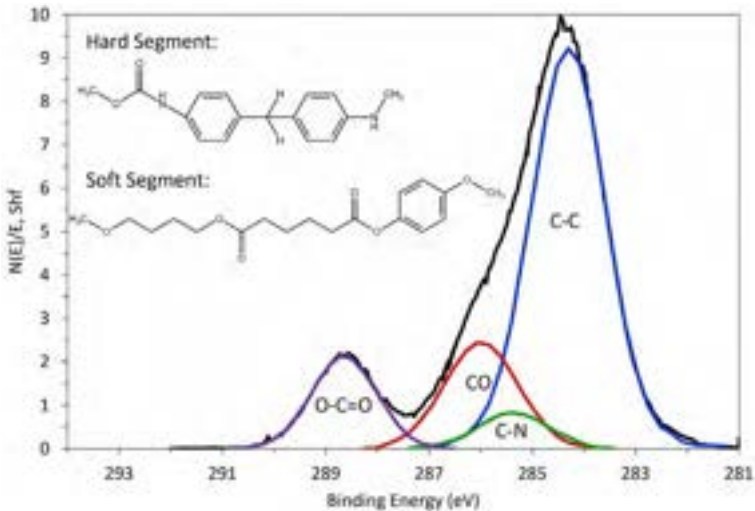


Fig. 9.20 C(1s) XPS spectrum of bulk polyester urethane.

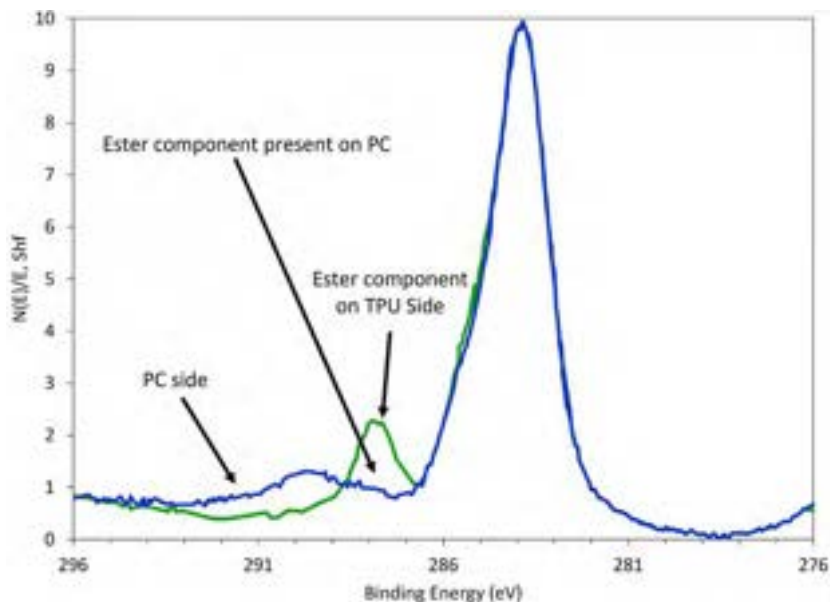


Fig. 9.21 C(1s) XPS spectra of failure surfaces, well-adhered sample. Presence of ester component on PC side is consistent with failure occurring in a thin zone containing TPU.

Production of parts consisting of polyurethane injection molded onto polycarbonate surfaces in general showed excellent adhesion. Peel tests produce rough failure surfaces with much cohesive tearing. Superimposed C(1s) XPS spectra of matching failure surfaces from these samples are shown in Fig. 9.21. Notice that the characteristic carbonate peak of the polycarbonate side is absent in the spectrum of the polyurethane side, but there is some ester evident on the polycarbonate side.

These spectra suggest that failure in well-adhered samples was within the TPU phase very close to a zone of interdiffusion of TPU and polycarbonate. Excellent peel strength showed that this interdiffused zone was perhaps stronger than the bulk TPU. This type of failure, which occurs in one of the bulk phases and not within the interphase zone, is characteristic of an excellent bond.

However, certain specific lots of urethane were associated with poor bond strengths. The failure surfaces were smooth in these cases, showing little polymer deformation. XPS spectra of failure surfaces corresponding to these samples (Fig. 9.22) clearly showed the carbonate moiety ($\Delta eV = 6.0$) on both failure surfaces. Failures in these cases were not occurring within one of the bulk phases but rather within an interphase consisting of interdiffused TPU and PC.

The weak interphase in this system appears to be created by diffusion into the polycarbonate of thermal degradation products from the urethane. Polyurethanes are known to be susceptible to thermal degradation with the regeneration of amines and isocyanates [49]. The appearance of these degradation products was confirmed in this study by investigating the stability of the polyester urethane to processing

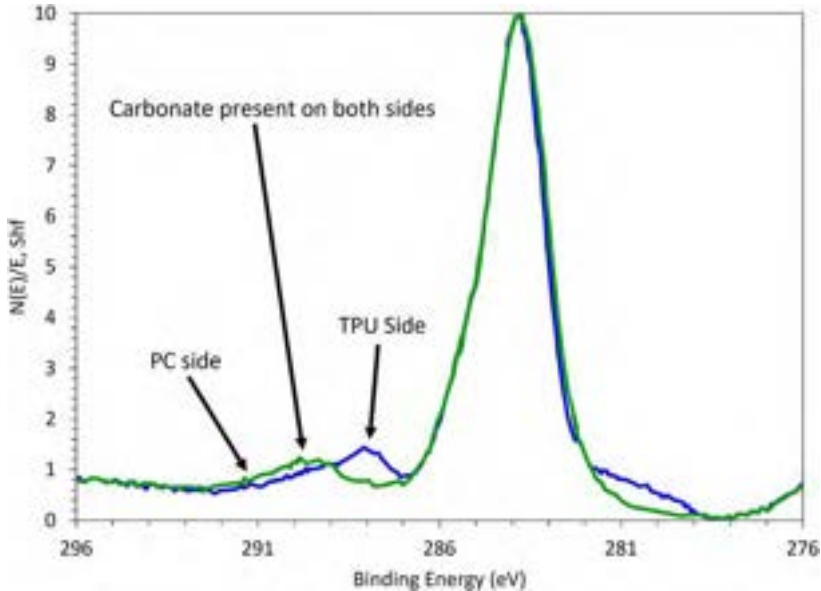


Fig. 9.22 C(1s) XPS spectra of failure surfaces, poorly adhering sample. Presence of carbonate component on both sides is consistent with failure occurring in the polycarbonate very close to the interface.

temperatures between 170°C and 210°C using thermogravimetric analysis-gas chromatography-mass spectroscopy (TGA-GC-MS). This work showed the evolution of readily detectable amounts of amines and isocyanates during heating to typical processing temperatures, and the relative amount correlated to the observed adhesion seen in production lots.

Both isocyanates and amines are potentially capable of diffusion into the polycarbonate phase and reacting through grafting (in the case of isocyanate) or hydrolysis (in the case of amines). Diffusion of amine into the polycarbonate phase was confirmed by attenuated total reflectance infrared spectroscopy (ATR-IR) mapping of a cross-section of the PC/TPU structure obtained by cutting with a sharp blade. [Fig. 9.23](#) shows an example of the collected spectra; [Fig. 9.24](#) shows both the peak height and peak area ratios of amine N-H band intensity to aliphatic C-H band intensity as a function of distance across the interface. These data clearly showed an increase in the amine concentration at the interface over the bulk.

Further experiments demonstrated that these amine products of thermal degradation of TPU were capable of severely degrading the strength of the TPU-PC interface. In one set of experiments, PC substrates were exposed to diethyl amine vapor at room temperature. In another set of experiments, PC substrates were suspended over a hot plate where TPU was heated to processing temperature. ATR-IR spectra of the PC substrates showed identical degradation products of PC in both cases. Similarly exposed PC substrates were then overmolded with TPU and the strength of the interface was found to be directly proportional to the exposure time.

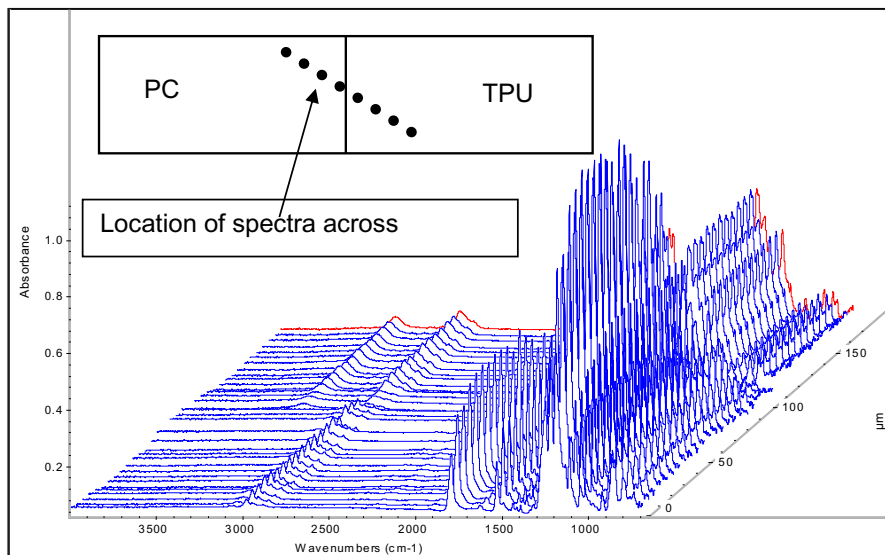


Fig. 9.23 ATR-IR spectra obtained as a function of location across the interface of a polycarbonate/overmolded thermoplastic urethane structure. Physical spacing between spectral acquisition points was 5 μm.

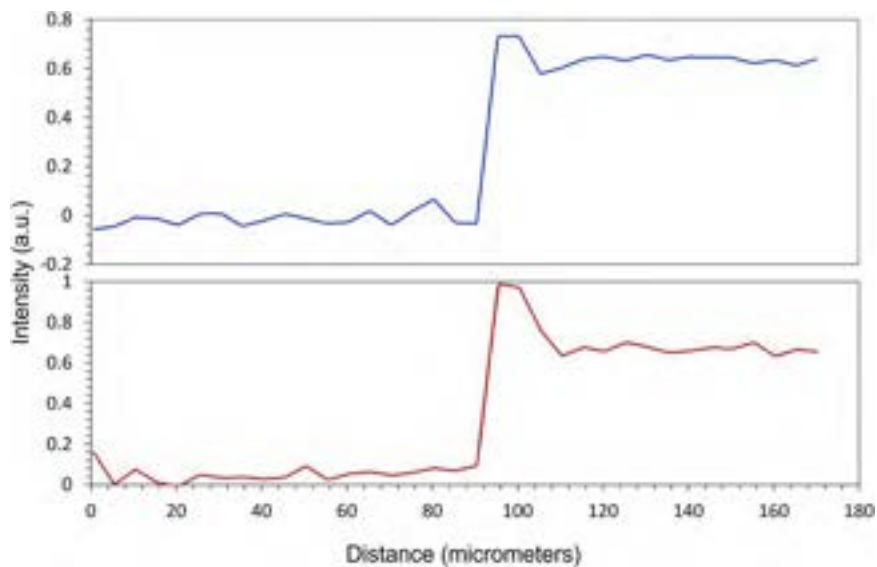


Fig. 9.24 N-H/C-H peak height ratios (top) and peak area ratios (bottom) from ATR-IR spectra obtained as a function of location across the interface of a polycarbonate/overmolded thermoplastic urethane structure.

In a final set of experiments, different TPU samples corresponding to suspected “good” and “bad” lots were held for varying lengths of time at processing temperature in the injection molding barrel prior to overmolding onto the PC substrates. The suspected “bad” lots produced poorly adhering samples immediately; the “good” lots initially produced samples with excellent adhesion but after approximately 10 min of holding time in the barrel prior to molding began to show poor adhesion and visually interfacial failures. Subsequent molecular weight evaluation of the “good” and “bad” lots showed broader molecular weight distributions and a markedly larger low molecular weight fraction in the “bad” lots.

In general, the adhesion of polyurethane to polycarbonate in an injection molding process is excellent. However, thermal stability of the urethane is critical. Thermal degradation products created during melt processing of a polyester urethane were shown to diffuse into the polycarbonate and degrade the molecular weight, resulting in a weak interphase and poor adhesion. Hence, it was shown that the thermal stability of the urethane controlled failure within the polycarbonate phase. The insight provided by this work into the failure mechanism permitted implementation of improved urethane specifications and resulted in significant improvement in production yields.

9.9 Summary

Successful processes that involve establishing interfaces between materials are *consistent* processes. Consistency requires control of the composition and properties of the bond surface, which is actually a volume of material that is perhaps a few tens of molecules thick at most. Control requires measurement; simply defining a set of process steps without accompanying quantitative feedback essentially guarantees failure will occur at some point. Measurement of bond surface properties requires analysis techniques sensitive to the small material volumes involved. Careful analysis of adhesion failures not only solves the acute problem, but when performed in a thoughtful manner paves the way for implementation of more reliable processes.

References

- [1] Adhesives and Sealants Market Size, Share & Trends Analysis Report By Technology, By Product, By Application, By Region (North America, Europe, Asia Pacific, CSA, MEA), And Segment Forecasts, 2019–2025, Grandview Research, February. Report ID: 978-1-68038-081-1, 2019.
- [2] L.J. Hart-Smith, Adhesive bonding of aircraft primary structures, SAE Trans. 89 (4) (1980) 801147–801431. (1980) pp. 3718–3732.
- [3] G. Gardiner, Building TRUST in bonded primary structures, Compos. World 1 (4) (2015) 38–43.
- [4] J.A. Graham, Adhesives that can live with oil, Mach. Des. 49 (28) (1977) 183–185.
- [5] ASTM F-22-02, Standard Test Method for Hydrophobic Surface Films by the Water Break Test, ASTM International.
- [6] R.G. Dillingham, B.R. Oakley, Surface energy and adhesion in composite-composite adhesive bonds, J. Adhes. 82 (4) (2006) 407–426.

- [7] F.J. Boerio, B. Roby, R.G. Dillingham, R.H. Bossi, R.L. Crane, Effect of grit-blasting on the surface energy of graphite/epoxy composites, *J. Adhes.* 82 (1) (2006) 19–37.
- [8] R.L. Crane, R.G. Dillingham, Composite bond inspection, *J. Mater. Sci.* 43 (20) (2008) 6682–6694.
- [9] F.J. Boerio, B. Roby, R.G. Dillingham, R.H. Bossi, Effect of surface engineering processes on the surface properties and adhesive bonding of graphite/epoxy composites, in: *Proceedings of the 39th International SAMPE Technical Conference*, Cincinnati, OH, Oct. 29–Nov. 1, 2007.
- [10] M.N. Charalambides, R. Hardouin, A.J. Kinloch, F.L. Matthews, Adhesively-bonded repairs to fibre-composite materials I: experimental, *Compos. A: Appl. Sci. Manuf.* 29 (11) (1998) 1371–1381.
- [11] J.W. Chin, J.P. Wightman, Surface characterization and adhesive bonding of toughened bismaleimide composites, *Compos. A: Appl. Sci. Manuf.* 27 (6) (1996) 419–428.
- [12] G. Dillingham, B.R. Oakley, Development of quantitative tools for the assessment of bond surface preparation quality, in: A. Jagota (Ed.), *Proceedings of the 30th Annual Meeting of the Adhesion Society*, The Adhesion Society, Blacksburg, VA, 2007.
- [13] M.E. Schrader, Young-Dupre revisited, *Langmuir* 11 (9) (1995) 3585–3589, <https://doi.org/10.1021/la00009a049>.
- [14] A.J. Kinloch, G.K.A. Kodokian, J.F. Watts, Relationships between the surface free energies and surface chemical compositions of thermoplastic fibre composites and adhesive joint strengths, *J. Mater. Sci. Lett.* 10 (1991) 815–818.
- [15] B. Scruton, B.W. Robins, B.H. Blott, The deposition of fingerprint films, *J. Phys. D: Appl. Phys.* 8 (6) (1975) 714–723.
- [16] D. Chen, W.A. Bryden, M. McLoughlin, A novel system for the comprehensive collection of nonvolatile molecules from human exhaled breath, *J. Breath Res.* 15 (1) (2020) 016001, <https://doi.org/10.1088/1752-7163/abba87.33084605>.
- [17] R. Ledesma, F. Palmieri, J. Connell, W. Yost, J. Fitz-Gerald, Surface characterization of carbon fiber reinforced polymers by picosecond laser induced breakdown spectroscopy, *Spectrochim. Acta B At. Spectrosc.* 140 (2018) 5–12.
- [18] J.F. Watts, A.M. Taylor, Interphase chemistry: the synergy of surface analysis, surface adsorption and adhesion, *J. Adhes.* 55 (1995) 99–107.
- [19] ASTM D2578-17, Standard Test Method for Wetting Tension of Polyethylene and Polypropylene Films, ASTM International.
- [20] ASTM D5946-17, Standard Test Method for Corona-Treated Polymer Films Using Water Contact Angle Measurements, ASTM International.
- [21] S.R. Holmes-Farley, R.H. Reamey, T.J. McCarthy, J. Deitch, G.M. Whitesides, Acid-base behavior of carboxylic acid groups covalently attached at the surface of polyethylene: the usefulness of contact angle in following the ionization of surface functionality, *Langmuir* 1 (1985) 725–740.
- [22] M. Strobel, C.S. Lyons, An essay on contact angle measurements, *Plasma Process. Polym.* 8 (2011) 8–13.
- [23] M. Strobel, S.M. Kirk, L. Heizen, E. Mischke, C.S. Lyons, J. Endle, D. Poirier, G. Dillingham, Contact angle measurements on oxidized polymer surfaces containing water soluble species, *J. Adhes. Sci. Technol.*, 29 (14) (2015) 1483–1508. M. Strobel, S.M. Kirk, L. Heizen, E. Mischke, C.S. Lyons, J. Endle, D. Poirier, G. Dillingham, Contact angle measurements on oxidized polymer surfaces containing water soluble species, *J. Adhes. Sci. Technol.* 29 (14) (2015) 1483–1507.
- [24] L.H. Sharpe, *Adhesion International*, first ed., CRC Press, London, England, 1993.
- [25] W.A. Zisman, Influence of constitution on adhesion, *Ind. Eng. Chem.* 55 (10) (1963) 19–38.

- [26] M. Jin, F. Thomsen, T. Skrivaneck, T. Willers, Why test inks cannot tell the whole truth about surface free energy of solids, in: K.L. Mittal (Ed.), *Advances in Contact Angle, Wettability and Adhesion*, vol. 2, Scrivener Publishing, 2015, pp. 419–438.
- [27] M. Blitshteyn, Wetting tension measurements on corona-treated polypropylene films, *TAPPI J.* 78 (3) (1995) 138–143.
- [28] M. Strobel, M.J. Walzak, J.M. Hill, A. Lin, E. Karbasheski, C.S. Lyons, A comparison of gas-phase methods of modifying polymer surfaces, *J. Adhes. Sci. Technol.* 9 (1995) 365.
- [29] R.J. Caimi, L.K. Derr, T.J. Dunn, Precision of the surface energy test, *Convert. Mag.* 10 (6) (1992) 62.
- [30] G. Dillingham, B. Oakley, P.J. Van Voast, P.H. Shelley, R.L. Blakley, C.B. Smith, Quantitative detection of peel ply derived contaminants via wettability measurements, *J. Adhes. Sci. Technol.* 26 (2012) 1563–1571.
- [31] B. Oakley, B. Bichon, S. Clarkson, G. Dillingham, B. Hanson, J. McFarland, M.J. Palmer, C. Popelar, M. Weatherston, TRUST—a novel approach to determining effects of archetypic contaminant compounds on adhesion of structural composites, in: *Proceedings of SAMPE*, Baltimore, Maryland, May 19–20, 2015.
- [32] A.N. Gent, J. Schultz, Effect of wetting liquids on the strength of adhesion of viscoelastic material, *J. Adhes.* 3 (1972) 281–294.
- [33] E.H. Andrews, A generalized theory of fracture mechanics, *J. Mater. Sci. Lett.* 9 (1974) 887–894.
- [34] A. Carré, J. Schultz, Polymer-aluminium adhesion II. Role of the adhesive and cohesive properties of the polymer, *J. Adhes.* 17 (2) (1984) 135–156.
- [35] R. Houwink, G. Salomon (Eds.), *Adhesion and Adhesives*, vol. 1, Elsevier, NY, 1965.
- [36] M.S. Islam, L. Tong, P.J. Falzon, Influence of metal surface preparation on its surface profile, contact angle, surface energy and adhesion with glass fibre prepreg, *Int. J. Adhes. Adhes.* 51 (2014) 32–41.
- [37] Q. Bénard, M. Fois, M. Grisel, Peel ply surface treatment for composite assemblies: chemistry and morphology effects, *Compos. Part A* 36 (2005) 1562–1568.
- [38] F.S. Gelfant, Cleaning oil-contaminated concrete for coating, *J. Prot. Coat. Linings* (December) (1996) 44–58.
- [39] T.S. Williams, H. Yu, R.F. Hicks, Atmospheric pressure plasma activation as a surface pre-treatment for the adhesive bonding of aluminum 2024, *J. Adhes. Sci. Technol.* 28 (7) (2014) 653–674.
- [40] R.G. Dillingham, F.J. Boerio, Interphase composition in aluminum/epoxy adhesive joints, *J. Adhes.* 24 (2–4) (1987) 315–335.
- [41] A.N. Gent, A.J. Kinloch, Adhesion of viscoelastic materials to rigid substrates III energy criterion for failure, *J. Polym. Sci.* 9 (A2) (1971) 659.
- [42] E.H. Andrews, A.J. Kinloch, Mechanics of adhesive failure I, *Proc. R. Soc. A* 332 (1973) 385–399.
- [43] E.H. Andrews, A.J. Kinloch, Mechanics of adhesive failure II, *Proc. R. Soc. A* 332 (1973) 401–414.
- [44] A.W. Adamson, A.P. Gast, *Physical Chemistry of Surfaces*, sixth ed., Wiley Interscience, New York, NY, 1997.
- [45] M. Doi, *Soft Matter Physics*, Oxford University Press, Oxford, UK, 2013, ISBN: 9780199652952.
- [46] L.H. Wang, Z. Huang, T. Hong, R.S. Porter, The compatibility and transesterification for blends of poly(ethylene terephthalate)/poly(bisphenol-A carbonate), *J. Macromol. Sci. B* 29 (1990) 155.

-
- [47] T.O. Ahn, S. Jung, J. Lee, H.M. Jeong, Influence of interchange reactions on the miscibility of polyesterurethanes/polycarbonate binary blends, *J. Appl. Polym. Sci.* 64 (12) (1997) 2363–2369.
 - [48] C. Hepburn, *Polyurethane Elastomers*, Elsevier Applied Science, Barking, Essex, 1992.
 - [49] J.J.B.N. Van Berkel, J.W. Dallinga, G.M. Möller, E.J. Moonen, E.F.M. Wouters, F.J. Van Schooten, A profile of volatile organic compounds in breath discriminates COPD patients from controls, *Respir. Med.* 104 (4) (2010) 557–563.

This page intentionally left blank

Advances in bonding plastics

10

Grace Wan, Colin Li Pi Shan, and Shaoguang Feng
The Dow Chemical Company, Midland, MI, United States

10.1 Introduction

Plastics comprise a growing and robust market segment with a value of ~\$600 billion in 2019, driven by increasing demand from key industry sectors including packaging, construction, fast-moving consumer goods, electronics, and automotive. Polyethylene (PE), consisting of low-density PE (LDPE), high-density PE (HDPE), and linear low-density PE (LLDPE), account for about 34% of the market share by volume, followed by polypropylene (PP, 23%), polyvinyl chloride (PVC, 18%), polystyrene (PS, 11%), polyethylene terephthalate (PET, 6%), and other engineered polymers (8%). These plastics belong to a class of polymers called thermoplastics and can be molded, extruded, or pressed into various shapes when heated, and this shape is retained upon cooling to room temperature. Thermoplastic polyolefins (TPO) are an indispensable class of materials with applications in both industrial- and consumer-oriented applications. Besides this adaptability, plastics are usually lightweight, durable, flexible, and inexpensive to produce, leading to their widespread use. They have varied origins including synthetic, semisynthetic, or natural occurring. Most modern plastics are derived from chemicals obtained from fossil fuels such as natural gas and petroleum. However, recent industrial methods use variants made from renewable materials, such as corn and cotton derivatives [1]. A more detailed discussion on renewable and sustainable adhesives can be found in [Chapter 29](#) of this book.

Over the last decade, a strong drive to understand adhesion to common plastics has emerged due to the adoption of lightweight thermoplastics in the automotive and aerospace industries for resultant energy savings. The basic principles governing adhesion of plastics with other plastics, glass, or metals are analogous to concepts prevalent in metal and glass bonding [2]. First, the adhesive must form intimate contact with or wet the plastic substrate. Second, there is covalent or noncovalent bond formation between the adhesive and the substrate. The adhesion strength depends on many aspects such as adhesive compositions, types of substrates, joint design, processes, and intended applications. Inherent differences between TPO and other solid materials have led to numerous technical challenges. Commonly used adhesives such as epoxy, acrylate, polyurethane, or silicone can be used to bond plastics, albeit with additional surface modification due to low surface energy and low surface interaction of most industrially relevant thermoplastic resins and composites [3]. Additional details on these adhesive families may be found in [Chapters 1, 2, 3, and 6](#), respectively.

This chapter will focus primarily on plastic surface characteristics, chemistry, and modification to achieve good joint bonding, with an aside on new adhesive

development. Additionally, fundamental adhesion mechanisms, especially pertaining to plastics, are briefly reviewed. Finally, we summarize novel approaches to achieve strong adhesion for polyolefins using primer technology with commercially successful examples. Adhesion of TPO specifically in automobile applications has been extensively reviewed in Chapter 9 with the primary focus on surface preparation using flame treatment and solvent removal of surface contaminants.

10.2 Principles governing plastics bonding

Although adhesion and adhesives have been used and studied for many years, no unifying theory exists relating basic material properties and surface properties to adhesion strength [4–6]. However, researchers have gained tremendous knowledge to achieve good adhesion such as through intimate contact and good bond formation. Detailed rationalizations of adhesion phenomena and associated theories can be found in the chapter by Kinloch [7]. In this section, we will briefly discuss the basic principles to achieve good bonding strength, with specific emphasis on plastic bonding.

10.2.1 Surface contact-wetting/spreading

It has been recognized that wetting a surface by adhesives is a prerequisite for strong bonding [8]. Additionally, a completely wet substrate can also reduce or eliminate any interfacial defects such as voids caused by poor wetting. Over the years, researchers have been able to predict the wettability of an adhesive on a given surface and have shown its dependence on the characteristics of the adhesive and substrate. The surface energy of a solid, the surface tension and rheology of an adhesive, and the interfacial tension between the substrate and adhesive determine the extent of wetting or spreading at equilibrium. The spreading parameter S is used to mathematically determine the wettability. If $S > 0$, the liquid completely wets the substrate, that is, high surface energy solids are easily wetted by low surface energy liquids.

$$S = \gamma_{sv} - (\gamma_{lv} + \gamma_{sl})$$

where γ_{sv} is the interfacial energy between the solid and gas phases, γ_{sl} is the interfacial energy between the substrate and the liquid, and γ_{lv} is the interfacial energy between the liquid and gas phases.

Surface free energy measures the energy required to create a new surface. The most common way to estimate surface energy is through contact angle measurement using Young's equation, which relates the contact angle (θ) to interfacial tension:

$$\gamma_{sv} = \gamma_{ls} + \gamma_{lv} \cos \theta$$

In theory, if the surface tension of a liquid, the interfacial energy between the solid and the liquid, and the contact angle of the liquid on the surface are known, the surface

energy of the solid can be calculated using the above equation. However, only the surface tension of the liquid and the contact angles are readily determined by experiments. To predict the polymer (solid) surface energy, several useful approaches have been suggested [9]. In practice, the contact angles measured for two or more liquids are used to estimate the surface energy of a solid. For example, Owens and Wendt demonstrated the surface energy estimation of various polymers using contact angles of water and methylene iodide. The surface energy can be expressed as the sum of contributions from the different intermolecular forces such as dispersion and dipole-hydrogen bonding interactions [10]. Owens and coworkers developed the Owens-Wendt-Rabel-Kaelble model [11,12] to calculate contributions from dispersion (γ^d) and dipole-hydrogen bonding (γ^p) forces to the surface energy. Table 10.1 lists surface energy data and the respective force contributions for common polymers estimated by contact angle measurements of water and methylene iodide. Reasonable agreement was obtained between the γ^{Total} from the model and direct experimental measurements.

Note that the contact angle measurement and adhesion performance depend on many other factors such as surface uniformity, roughness, and contamination [13]. Packham reviewed some fundamental principles that are relevant to understanding the effect of interfacial roughness on adhesion and developed corrections to existing models [14]. Roughness over a range of length scales ranging from microns to nanometers may strengthen an interface and increase fracture energy by allowing bulk energy dissipation when an adhesive bond is stressed. More details on other surface issues such as surface enrichment of low molecular weight species (weak boundaries) and contaminants on contact angle and adhesion can be found in Chapter 9.

Table 10.1 Surface energies in mJ m^{-2} for some common plastics estimated by contact angles at 20°C.

Surfaces	Water	Methylene iodide	γ^d	γ^p	γ^{Total}	γ^{Reported}
Water	–	–	21.8 ± 0.7	51.0	72.8	–
Methylene iodide	–	–	49.5	1.3	50.8	–
Polyethylene (low density)	104	53	33.2	0	33.2	31
Polyvinyl chloride	87	36	40	1.5	41.5	39
Polymethyl methacrylate	80	41	35.9	4.3	40.2	39
Poly(vinylidene fluoride)	82	63	23.2	7.1	30.3	25
Poly (tetrafluoroethylene)	108	77	18.6	0.5	19.1	18.5

10.2.2 Bonding formation between substrates and adhesives

Once the adhesives can wet the substrate well, the bond formation is essential in attaining good joint adhesion. Ideally, the bonds between the adhesive and substrate are stronger than the cohesive strength of the adhesive or substrates alone, resulting in the cohesive failure within adhesives and substrates while testing the adhesion of the monolith. This type of cohesive failure is highly desired in all adhesion properties. The primary adhesion challenge is to develop approaches that yield strong bonds at the interfaces [15,16].

The major types of intermolecular forces involved in adhesion between substrates include covalent bonding, acid-base interactions, electrostatic and van der Waals forces, mechanical interlocking, and molecular interdiffusion [3,4,17]. The applicability of these four mechanisms in understanding plastic bonding is discussed below.

10.2.2.1 Covalent bonding

A common approach to obtain strong adhesion for plastic bonding is to generate covalent bonds at the interfaces during the bonding process because the energy needed to break a mole of covalent bond is higher than other surface interaction forces. For example, the carbon-carbon bond energy is ~ 120 kcal/mol as compared to 1 kcal/mol for van der Waals interactions. Forming covalent bonds at the interfaces has been used in numerous adhesive bonding systems, even between substrates of dissimilar chemical compositions [18].

Laing et al. studied the reactive wetting and bonding of polyethylene (PE) on ethylene-propylene-diene terpolymer (EPDM) at the melting point [19]. The authors developed a high-temperature contact angle measurement method to study the interface of PE and EPDM. The spreading of PE was limited to vulcanizing peroxide-based EPDM due to covulcanization between two surfaces. This covalent bond formation led to 57% higher interfacial adhesion strength between EPDM and PE as compared to prevulcanized EPDM and PE. Increasing loading of dicumyl peroxide up to 6 phr led to greater adhesion strength [20].

Additionally, the interfacial covalent bond formation was found to impact the wettability, especially when one of the phases involves a melting polymer. Kumar and Prabhu reviewed nonreactive and reactive wetting of liquids on surfaces [16]. Reactive wetting refers to a wetting process that is influenced by a chemical reaction between the spreading liquid and substrate material.

10.2.2.2 Acid-base interaction

Acid-base interactions describe the interactions between an electronic donor (base) and an electronic acceptor (acid), which have been used to explain some observed adhesion phenomena. Siboni and Della reviewed the acid-base theory, especially on models and methods to determine and compare the acid-base behavior of varied materials [21]. Chehimi et al. also reviewed the theory of Lewis acid-base (AB) interactions and their relevance in adhesion, adsorption, and wetting [17]. The adhesion of phosphoric acid-treated glass-ionomer to a resin composite is increased significantly,

owing to the high acid-base interactions [22]. Dilsiz and Wightman studied the effect of acid-base properties of unsized and sized carbon fibers on fiber/epoxy matrix adhesion [23]. Arefi-Khonsari et al. studied the adhesion and wettability of ammonia- and helium plasma-treated polypropylene. PP surfaces became basic after treated with ammonia and helium plasma [24]. Fowkes confirms the role of acid-base interactions in polymer adhesion to inorganic surfaces and the polymer adhesion to iron surfaces was increased by acid-base interaction [25,26].

10.2.2.3 *Electrostatic theory*

If two adherends possess opposite electric charges, they will experience a mutual attractive force leading to adhesion of the two species. The energy required to break an ionic bond is large, usually about 10 kcal/mol or more [27]. However, except for a few types of plastic made from conductive polymers, this approach has limited applicability due to the lack of charged moieties on most used plastics.

Physical bond formation typically stems from van der Waals forces, which originate due to the attraction between localized polarization of neighboring molecules. These forces can be classified into three types of interactions based on the strength and longevity of the polarization of the associated molecules: (1) dipole-dipole interactions, (2) hydrogen-bonding interactions, and (3) molecule-molecule interactions (London dispersion forces) [28].

For adhesion primarily stabilized by physical bonds, the experimentally measured strengths have been consistently lower than those calculated from secondary interfacial forces. This discrepancy has been attributed to the presence of voids, defects, or other geometric irregularities on the interfaces [29].

10.2.2.4 *Mechanical interlocking*

Mechanical interlocking refers to the penetration of adhesives into pockets or valleys of a porous or rough substrate. When debonding, the adhesion strength may be greater for substrates with a rough surface as crack propagation during failure has to adopt a tortuous path as compared to a substrate with a smooth interface. The adhesives may be mechanically “locked” into the substrates within micro- or macrochannels to significantly increase bonding strength. Additionally, the increased contact area between adhesive and substrate further enhances the effective intermolecular forces and the resulting adhesion strength [30,31].

Mechanical interlocking is most applicable to porous materials such as wood, textiles, and metals. Alternatively, mechanical or chemical surface treatments are utilized to increase the surface roughness or create surface pores in nonporous plastics to enhance interlocking. Common practices include chemical etching using chromate or other strong acids or mechanical abrasion using sandpapers or sandblasting [32].

Larsson and Ahmad reported introducing means for mechanical interlocking to improve adhesion between dissimilar materials in microelectromechanical systems (MEMS) [33]. Interlocking features with an overhanging profile were generated on glass substrates using electroplating and wet etching. Peel tests on cured strips confirm

an increase in average peel strength by 3.5 times, compared to strips peeled from smooth substrates. This method provides a low-cost route to increase adhesion.

10.2.2.5 Diffusion theory

The diffusion theory states that the intermixing of the two materials at the interface results in good adhesion due to the formation of interfacial diffusion layers. For diffusion to occur, the adherends must be mobile at the interface, have similar solubility parameters, and sufficient chemical compatibility. Several diffusion models for polymer interfaces have been proposed, including entanglement, coupling, cooperativity, and reptation [30].

The diffusion theory has applicability for plastic adhesion when the adhesive and adherend exhibit mutual solubility or miscibility and readily diffuse to the interface to form entanglements at a molecular level. Appreciable diffusion occurs at temperatures greater than the respective glass transition (T_g) or melting (T_m) temperatures.

The strategies to increase plastic adhesion in accordance with the diffusion theory are: (1) improve the compatibility of adherends with the adhesives; (2) modify the polymer properties to enhance the polymer chain movement such as reducing the crosslinking density, lowering the molecular weight, or decreasing the polymer transition temperatures (T_g/T_m); and (3) change the process conditions such as increasing the temperature or using solvent to enhance polymer chain mobility.

Shcherbina studied the transient zones of several polymer-polymer systems including polyvinyl chloride-poly(ethylene-co-vinyl acetate) (EVA), PET-EVA, and steel-EVA adhesion [34]. The adhesion in these systems was affected by the diffusion of EVA into the phase. The depth of penetration of copolymer macromolecules into PVC was determined experimentally and the kinetics of adhesive-joint formation were studied.

Asseko et al. studied the effects of welding on the adhesion properties of reinforced glass fiber with unreinforced polycarbonate [35]. Self-diffusion was suggested to occur at $T > T_g$ of polycarbonate (140°C).

In summary, optimal adhesion can be achieved through the diligent selection of wetting adhesives that generate adequate bonding strength through the mechanisms of intermolecular interactions.

10.3 Challenge and surface characteristic in bonding plastics

10.3.1 Surface energy and solubility parameters of diverse types of plastics

To achieve a good bonding to plastics, it is necessary to understand the surface characteristics such as surface energy, polarity, and functionality of plastics.

Plastics can be homopolymers or copolymers, and adopt amorphous, semicrystalline, or crystalline morphologies. Plastics can incorporate a variety of chemistries such

as polyamide (nylon), polyvinyl chloride (PVC), polymethyl methacrylate (PMMA), polyethylene terephthalate (PET), acrylonitrile-butadiene-styrene copolymers (ABS), poly(ether ether ketone) (PEEK), polycarbonate (PC), polyethylene (PE), polypropylene (PP), polystyrene (PSt), and polytetrafluoroethylene (Teflon).

Although the chemistry, structures, and properties are different for various plastics, they share some common features relevant to adhesion. Typically, the polymer substrates are solids with the associated T_g or T_m being greater than room temperature. Analogous to small molecules, polymers thermo-reversibly transition between a solid phase and a flowable liquid phase above the transition temperatures. Depending on the chemical compositions, plastics have a broad range of surface energies ranging from 20 to 80 mJ m^{-2} , which is significantly lower than those of metals, inorganic oxides, or ceramics ($> 100 \text{ mJ m}^{-2}$). Table 10.2 lists the surface free energy of some common plastics.

Table 10.2 Surface free energy of some common plastics.

Polymer	Surface free energy (mJ/m^2)	Polymer	Surface free energy (mJ/m^2)
Polyacetylene	51.5	Poly(vinyl chloride) (PVC)	40.1
Poly(<i>p</i> -phenylene sulfide) (PPS)	46.8	Poly(<i>p</i> -methylstyrene) (PMS)	38.7
Polyacrylonitrile (PAN)	46.8	Poly(vinyl acetate) (PVAc)	38.5
Poly(butylene terephthalate) (PBT)	46.3–47.8	Polystyrene (PSt)	38.3
Poly(<i>p</i> -phenylene terephthalamide), aramid, Kevlar	45.7	Poly(acrylonitrile- <i>co</i> -butadiene- <i>co</i> -styrene) (ABS)	35–42
Nylon 6; polyamide-6; PA-6 (polyamide 6)	45.4	Polyurethane (PU, PUR)	37.5
Epoxy resin	45.3	Polyethylene (PE)	33.5
Polysulfone (PSF)	44.9	Ethylene-propylene diene terpolymer (EPDM)	32.5
Nylon-6,6; polyamide-6,6, PA-6,6	44.3	Poly(vinylidene chloride) (PVDC)	31.5
Poly(vinyl alcohol) (PVOH)	44.2	Ethyl cellulose	30.3
Poly(ethylene terephthalate) (PET)	44	Polypropylene (PP)	30.2
Poly(pyromellitimide-1,4-diphenyl ether) (PI)	43.8	Polydimethylsiloxane (PDMS)	20.4
Polycarbonate (PC)	42.3	Fluorinated ethylene-propylene copolymer (FEP)	18.5
Polymethylmethacrylate (PMMA)	41.8		

It can be seen from [Table 10.2](#) that several plastics such as nylon, PVC, PMMA, PET, and ABS with polar monomers have surface energies above 40mJm^{-2} while the hydrocarbon, fluorocarbon, and silicone such as PE, PP, and polydimethylsiloxane (PDMS) have low surface energy (below 30mJm^{-2}). The low surface energy of PP or PE usually leads to poor adhesion, low wettability and printability, and inferior dye uptake.

The surface tension of typical water-based adhesives is $\sim 44\text{--}50\text{mN/m}$ and that of waterborne inks is $\sim 54\text{--}56\text{mN/m}$. If the surface energy of the plastic substrate is above 40mJm^{-2} , the water-based adhesive can partially wet the plastic surface. However, if the surface energy of the plastics is lower than 40mJm^{-2} , wetting agents such as surfactants are needed within the formulation to increase the wettability on plastics with low surface energy [\[36\]](#).

10.3.2 Effect of temperature on surface energy and wetting

Note that surface energy is a strong function of temperature. A series of studies has been reported on molten polymer spreading and wetting [\[37–41\]](#). Fuentes et al. found that molten polymers exhibited different surface energies and complex polymer/substrate interactions due to increased polymer chain mobility at elevated temperature [\[42\]](#). For example, the wetting behavior of molten maleic anhydride modified polypropylene (MAPP) was observed to be significantly different from that at room temperature. The researchers presented a model to predict polymer/substrate compatibility between several molten thermoplastics on smooth glass fibers and plates. The value of the total surface energy of thermoplastics at elevated temperature (260°C) was 57% lower than that measured at room temperature, which strongly influences the wetting. In addition to surface energies of both the polymer and the substrate, particular intrinsic characteristics of the polymer melt controlled the wetting and adhesion. The authors speculated that the formation of covalent bonds between maleic anhydride and the glass surface enhanced the interfacial bonding strength.

Bex et al. studied the wettability of two molten polymers using contact angle measurements at elevated temperatures [\[39\]](#). They found that PP and PE best wet ethylene propylene diene monomer rubber while nitrile rubber was wet by polycarbonate. Excellent adhesion was observed in two-component injection molding of the polymers, which was attributed to the good wettability and compatibility of the polymers in the molten state.

10.4 Advanced surface treatment to improve plastic bonding

To improve plastic adhesion, there are typically two approaches used to increase the surface energy and functionality: bulk blending and surface treatments [\[43–45\]](#). Bulk blending is less favorable due to its limited effectiveness in increasing the surface

energy of the substrate, necessitating greater loadings of functional materials. Additionally, bulk blending typically changes the material properties and increases the total cost.

Many surface treatment methods have been developed. These methods can be classified into three major categories: (1) mechanical treatments involve roughening the surface of plastics, thereby enhancing the adhesion by potential mechanical interlocking. This method is cheap and easy to carry out, but it is labor intensive and is limited to use on flat surfaces; (2) chemical etching involves the use of strong acids such as chromic or sulfuric acid. In addition to long treatment times, the environmental and safety concerns make this strategy less desirable; and (3) physical/chemical treatments are the most preferred. This strategy involves the use of flame, corona, plasma, ultraviolet (UV)-ozone, gamma ray, electron beam, ion beam, and laser treatments. Among them, flame, corona, and plasma are the most widespread in industry. A brief description of these different approaches is provided below, and more details can be found in Chapter 9.

10.4.1 Surface degreasing by solvents and detergents

Both organic and aqueous cleaning agents are used to degrease and remove any surface contaminants. Additionally, appropriate solvents can also be used to rough or swell the plastic surface to improve molecular interdiffusion. Environmental concern regarding the use of solvents is a limiting factor for adoption of this method.

Schuman and Thames studied the solvent impact on plastic adhesion [46]. They found that when the topography of a plastic surface is modified due to the diffusion of the solvent through the interface, the adhesion was significantly enhanced.

10.4.2 Flame treatment

Flame treatment has been commercially used in plastic bumper coating in automotive assembly. Exposure to elevated temperature found in flames (1000–2000°C) leads to oxidation of the plastic surface, yielding polar functional groups. The new functionalities increase the surface energy and, therefore, the adhesion. For example, flame treatment on polyethylene generates hydroxyl, carbonyl, and carboxyl groups on the surface as detected by X-ray photoelectron spectroscopy (XPS) and contact angle measurements [47,48]. Many factors such as air-to-gas ratio, flow rate, distance from the inner core of the flame, and the contact time of the flame impact the effectiveness of the treatment and consequently improvements in adhesion [49]. Carefully controlling the flame treatment conditions is critical to obtain consistency in adhesion performance.

The main drawback of flame treatment is the hazard associated with the handling of open flames in an industrial setting. Furthermore, the uptake of environmental contaminants, the reorientation of surface groups, and the cascading chemical reactions at the surface with time, in many cases, result in an “aging” effect.

10.4.3 Corona treatment

Corona treatment produces plasma by ionizing air with a high electric field under atmospheric pressure. The electrons, ions, excited neutrals, and photons can react with the polymer surface, resulting in surface oxidation and functional group formation analogous to flame treatment [50]. The adhesion enhancement resulting from corona discharge treatment for various polymers such as PP, PE ethylene-vinyl acetate copolymers (EVA), and PEEK has been studied [51–53].

Green et al. showed that corona discharge treatment significantly improved the adhesion between polypropylene and BETASEAL 1780 polyurethane adhesive (trademark of The Dow Chemical Company) [47]. Shear stress increased from 0.07 MPa for untreated specimens to 2.72 MPa for the pretreated specimens. Comyn et al. studied the effects of corona treatment on the surface of PEEK [53]. For treated PEEK, the lap shear strengths significantly increased from 17 to 28–29 MPa.

Corona treatment may also increase surface roughness, which favors adhesion. Alternatively, it also leads to the formation of some low molecular weight oxidized molecules, which can negatively impact adhesion due to poor entanglement with the matrix. The conditions for corona treatment need to be optimized to balance these opposing factors and maximize adhesion. Corona treatment is the most popular method for treating flat surfaces such as films. The primary limitation of corona treatment is the difficulty in uniformly treating irregularly shaped objects. Corona treatment also suffers from the same “aging” effect pertinent to polymers that undergo flame treatment.

10.4.4 Plasma treatment and polymerization

Plasma treatment is suitable for increasing the surface energy and adhesion strength through irreversible reactions among dangling bonds on surfaces exposed to plasma [54,55]. Plasma treatment can be done with a range of gases, yielding tailor-made surfaces of varied functionalities for various applications. For example, oxygen plasma can be used to increase surface energy by oxidation of the surface, whereas fluorine plasma can be used to decrease surface energy and increase surface inertness. Inert gas plasma can be used to crosslink the surface. Plasma treatment has been used on various plastics such as PE, PP, PET, polybutylene terephthalate (PBT), polyamide 6, (PA6), PC, and PEEK [56–60]. Sundriyal et al. reviewed the plasma modification of polymeric surfaces and corresponding changes to their adhesion properties [61]. Noeske et al. studied the impact of plasma treatment on contact angle, surface functionality, and adhesion of various plastics. There were significant increases in lap shear strength and surface energy after plasma treatment for all the plastics (HDPE, PP, PET, and PA6) that were studied. Additionally, the failure modes for the plasma-treated substrate were either substrate breakage or cohesive failure as compared to adhesion failure that was observed for untreated substrates.

The main drawback of plasma treatment is that it is not a continuous process and requires high vacuum, which can be expensive.

10.4.5 UV treatment

UV treatment involves the generation of ozone by exposure to UV light, which is subsequently used to oxidize the surface. The oxidation reaction generates similar species to flame or corona treatment. Because ozone can diffuse easily, it is possible to treat irregularly shaped objects with this method.

Scarselli et al. studied the adhesion improvement on several plastic composites, including polyphenylene sulfide (PPS), polyetherimide (PEI), and PEEK carbon fiber by atmospheric plasma and UV radiation [62]. The performances of the PEEK and PPS joints were improved. Quan et al. used UV irradiation of varying durations to transform the failure mode of the PPS and PEEK composite specimens from adhesion failure to substrate damage [63]. The lap shear strength increased from 11.8 MPa to 31.7 MPa after irradiation of the PPS composites for 3 s, and from 8.3 to 37.3 MPa after longer irradiation for 5 s of PEEK composites with common epoxy adhesives.

The main drawback of UV radiation is that prolonged exposure times (up to several minutes) are required to effect significant increases in surface energy. In addition to negatively impacting the processing times, exposure to high-energy UV radiation for extended periods of time also causes scission of the molecules on the surface. Similar to corona treatment, the low molecular weight species formed due to this process can cause poor adhesion due to less entanglement with the matrix.

10.5 Chemical treatment to improve plastic bonding

Chemical treatments, including etching using acids and solvent-based primers, have been used extensively to enhance adhesion [64]. Chemical etching agents convert smooth hydrophobic polymeric surfaces to rough hydrophilic surfaces by a combination of the dissolution of amorphous regions and surface oxidation. Chromic and sulfuric acids are the most prevalent acid etch primers. The efficacy of these primers is dependent on the type of plastic, adhesive, and paint. Briggs et al. [65] obtained excellent joint bonding after acid-treated PE or PP [66]. Martinez-Garcia reported significant improvement in the adhesion of ethylene-vinyl acetate (EVA) by immersion in highly concentrated sulfuric acid (96 wt%) for 1 min [67].

Chemical treatments are used to treat irregularly shaped objects that are difficult to treat by corona or flame. However, environmental restrictions on the use of chromium-containing compounds are compelling industry to find alternatives. One alternative proposed in the literature for polyolefin modification is based on aziridine group-containing reactants.

Another type of chemical treatment is to create grafting functionalities onto the plastic surface, thus increasing the bonding formations between the plastics and adhesives. Two examples of this chemical grafting are briefly discussed below.

10.5.1 Grafting of organoboron chemistry

Alkyl boranes are known as adhesion promoters of acrylic adhesives to low surface energy substrates due to the ability of alkylboranes to generate radicals via autoxidation. Subsequently, the free radicals initiate vinyl polymerization to cure the resin and concurrently abstract H from the substrate surface to enable the formation of covalent bonds with acrylic adhesive yielding a strong joint. The oxidation of organoborane-based systems with molecular oxygen forms energetic peroxides, which is an exothermic process, and the resulting species themselves can be pyrophoric if not carefully controlled (Fig. 10.1).

Due to the pyrophoric nature of the alkyl boranes, they need to be stabilized or protected by anions or amine donors. The protecting group renders the organoborane center less susceptible to oxygen insertion and radical generation before the adhesive is applied. The blocking groups are removed using a two-part adhesive formulation to achieve the desired cure speed. The hardener consists of a catalyst (borane and blocker) and the resin side contains an acid to decomplex and release boranes (Fig. 10.2).

In 1996, Zharov and Krasnov discovered the use of organoborane-amine complexes to initiate a two-part acrylic adhesive system for bonding low-energy substrates with excellent adhesion [68]. The block of the borane initiator has been investigated extensively thereafter to achieve formulation stability. The blocking agent must be removed prior to curing the adhesive and balance for adhesive cure rate. During 1997–2000, Pocius et al. investigated amine-susceptible agents such as acids, acid chlorides, aldehyde, anhydrides, epoxies, polyisocyanate, and sulfonyl chloride as deblockers to generate free boranes for radical reactions [69]. Acrylic acid monomer will be the most convenient choice as it is already present in the formulation.

A variety of donors that act as blocking agents by forming borane-amine adducts or borates have been studied including hydrides, phenyl anion, mono and polyamines, imidazole, or pyridine derivatives. Kneafsey et al. reported a family of metal alkyl borohydrides, such as lithium tri-*sec*-butyl borohydride (L-selectride) [70]. This family of compounds has been used very effectively as initiators in methacrylate adhesives to bond low-energy substrates. In 2003, Kendall and coworkers described internally blocked borates, which are useful for curing acrylic adhesives, where boron is part of a ring structure bridging across at least two boron coordinates [71]. It was

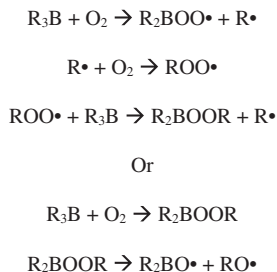


Fig. 10.1 Mechanism of alkylborane autoxidation.

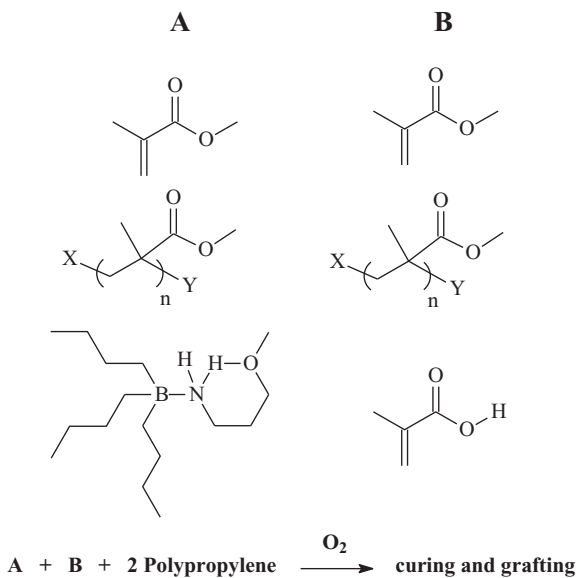


Fig. 10.2 Examples of two-part adhesive formulation.

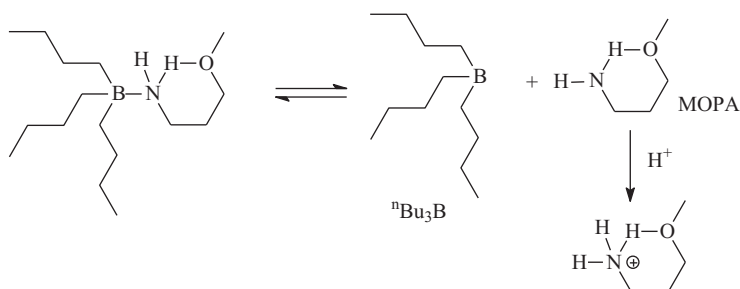
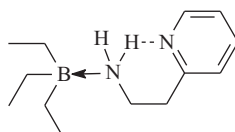


Fig. 10.3 Borane deactivation and reactivation.

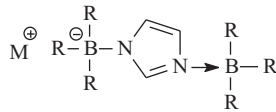
claimed that this catalyst exhibits good air stability and promotes adhesion to low-energy substrates when unblocked in an acrylic adhesive.

Sonnenschein et al. developed a series of organoborane/amine complexes, TnBB-MOPA complexes, that exhibit superior air stability (Fig. 10.3) [72].

Jialanella and Feng developed a blocking agent comprising a bifunctional Lewis base, based on amino alkyl pyridines that provide H-bonding and enhanced boron complex stability [73].



Feng and coworkers developed a family of amido-borate initiators with an imidazole anion bridging two alkyl boranes to form a hyper charge delocalization, thus providing excellent stability of the borane complex and adhesive formulation and faster cure rate of the adhesive [74].



In addition to the development of alkyl borane blocking agents, other advancements have been made based on this technology. Webb and Sonnenschein showed that high-temperature strength can be obtained when isocyanates are used as deblockers [75]. Sonnenschein et al. also disclosed the use of a two-phase (heterophase) system in which one phase is cured by free radical polymerization using alkyl boranes and the second phase is cured by ring-opening polymerization [76]. Additionally, a dual cure system comprising a cured organoborane and olefinic monomers and monomers/oligomers with a siloxane backbone, which are capable of polycondensation polymerization, has also been reported [76]. Lastly, an example pertinent to coating applications has also been reported. In all cases, excellent adhesion to most plastics has been reported including substrates with low-energy surfaces such as PE and PP. Jialanella et al. reported that the commercial product using the above catalyst structure exhibited excellent adhesion to glass-filled PP even after environmental aging [77]. Lutz and Feng reported a method to join plastic pipes using a curable two-part adhesive composition containing a boronic initiator [78].

In 2018, Zhu and coworkers described a curable composition suitable for adhesive and/or coating applications containing a poly(methacrylate) clustered functional polyorganosiloxane. The curable composition has a dual (radical and condensation) cure system and can cure at room temperature [79]. Zhu also developed a primer useful for adhering cured silicones to low-energy plastic substrates [80]. The primer is prepared from starting materials including an organoboron compound capable of forming a free radical generating species. Borane-initiated acrylic systems have shown promise for bonding low surface energy plastics, and continued advancement is being made for broad practical applications.

10.5.2 Uses of bio-inspired dopamine and catechol grafting

Dopamine and catechol have been widely known to contribute to the excellent adhesion of various marine organisms under water. For example, mussels secrete water-resistant adhesive proteins containing a significant amount of the catechol-containing amino acid 3,4-dihydroxyphenylalanine (DOPA), which has been identified as the key component allowing these organisms to stick to diverse types of surfaces including hard-to-bind plastics [36,81–84]. Although the role catechol plays in adhesion is not fully understood, there has been a great deal of progress in unveiling possible

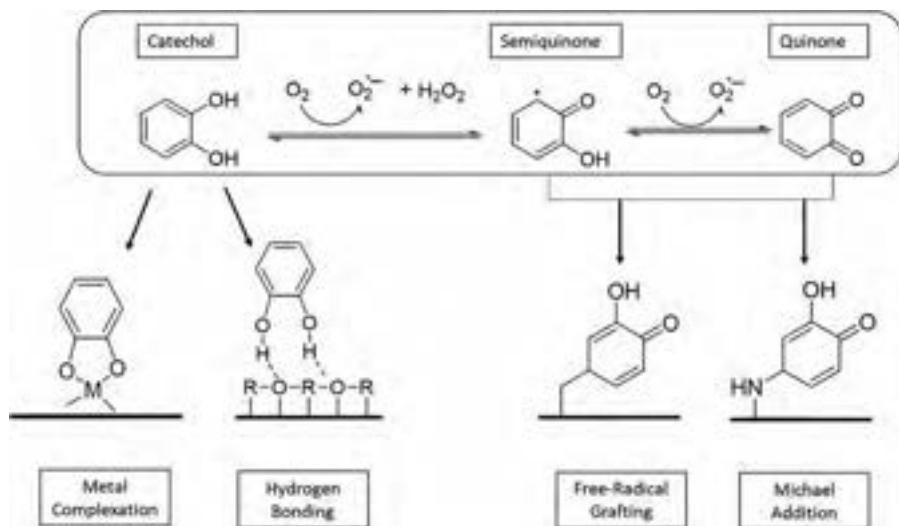


Fig. 10.4 Possible adhesion mechanisms with catechol functionality.

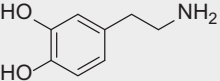
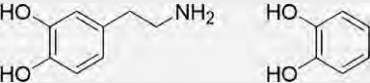
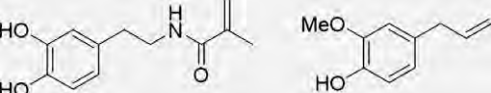
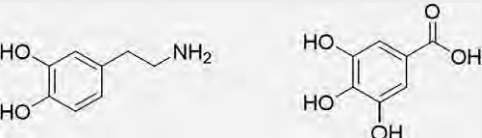
mechanisms, as shown in Fig. 10.4. For instance, the catechol functional group is a bidentate ligand that is capable of coordinating to metal ions and has been proposed to aid in the adhesion of catechol-containing polymers to metal surfaces. Hydrogen bonding has also been suggested to play a role in the adhesion to polar surfaces. Catechol is known to undergo redox chemistry, forming semiquinones and ultimately quinones through oxidation by O_2 . These oxidized species are excellent Michael acceptors and may permit covalent attachment to polar surfaces containing nucleophilic atoms. Furthermore, the radical species generated can lead to free-radical grafting, which is believed to contribute to adhesion to nonpolar surfaces such as polyolefins [85].

Inspired by the unique properties of these catechol-containing species, researchers have incorporated them into a variety of different polymers, including polyethylene glycols, polyvinyl alcohols, polyacrylic acids, polyallyl amines, polyacrylamides, polyethyleneimines, polystyrenes, and chitosan. We propose the use of catechol analogs to improve the adhesion of coatings to low-energy plastics as a means of prolonging durability as well as improving antifouling and optical properties.

There are several strategies to utilize catechol chemistry to improve adhesion, as outlined in Table 10.3. One strategy is to modify the plastic surface by immersing in catechol solution. Catechol or polyphenol induces free-radical oxidation and increases the surface energy of the plastics.

A similar approach of modifying the surface could be applied by simply adding a catechol analog directly to a paint formulation. In this case, migration of the low molecular weight species to the plastic surface could initiate grafting to the polymer resin. This strategy can be attractive because it does not require any additional treatment. However, the stability of these additives in the formulation can be problematic.

Table 10.3 Proposed four strategies for catechol to improve coating adhesion on plastics.

Approaches	Pros	Cons
<p>1. Primer to directly treat substrates</p> 	<ul style="list-style-type: none"> • Surface modification • Does not impact polymer composition 	<ul style="list-style-type: none"> • Requires pretreatment
<p>1. Additives into formulations</p> 	<ul style="list-style-type: none"> • Simple, no extra steps 	<ul style="list-style-type: none"> • Concerns on formulation stability
<p>2. Functional monomers to polymer backbone</p> 	<ul style="list-style-type: none"> • Covalent bond to polymer 	<ul style="list-style-type: none"> • Free-radical inhibition • Cost
<p>3. Postgrafting to polymer</p> 	<ul style="list-style-type: none"> • Covalent bond to polymer • Potential lower cost than functional monomers 	<ul style="list-style-type: none"> • Require postpolymerization step

10.5.2.1 Catechol functionalization of latex

Another approach to address plastic adhesion would be to covalently attach catechol functionality to a polymer resin. One way of generating these functional polymers is to copolymerize the catechol-containing monomers into the polymer backbone. The main advantage of this approach is the possibility of forming covalent bonds between the polymer resin and the surface. The potential drawback is the feasibility of copolymerizing the catechol-containing monomers due to the radical inhibition of hydroquinone to retard or prevent free-radical polymerization. The incorporation of aromatic functionality could also impart color.

Another way to incorporate catechol functionality into the polymer backbone is through postgrafting. When polymers contain some functional groups, including (i) epoxides (e.g., glycidyl methacrylate), (ii) carboxylic acids (MAA/AA/itaconic acid), (iii) amines (*t*-butyl aminoethyl methacrylate), (iv) ketones (diacetone acrylamide), (v) acetoacetates (acetoacetoxyethyl methacrylate, AAEM), and (vi) urea, these polymers could be reacted further to attach catechol functionalities to improve adhesion. Zhang et al. reported a postpolymerization modification scheme to attach catechol-functionalized side chains to butyl acrylate/methyl methacrylate/acetoacetoxyethyl methacrylate (BA/MMA/AAEM) copolymers with dopamine [86]. Crosshatch adhesion tests (according to ASTM D3359) were used to determine the adhesion of the catechol-containing latexes on corona-treated TPO substrates. Catechol-functionalized latexes showed significantly higher adhesion to TPO (5B level), when compared to nonfunctionalized controls (0B level), as shown in Fig. 10.5. This postpolymerization modification approach presents opportunities to improve the adhesion of waterborne coatings to a variety of low surface energy plastics.

Dopamine is expensive, which would limit the amount of functional monomer in a polymer and hence widespread industrial applicability. However, there are some economical alternatives including catechol, hydroquinone, tannic acid, pyrogallol, gallic acid, and eugenol, that could be modified or used directly.

10.6 Aging effect of plastic treatment

It is known that the surface properties of treated plastics revert to the original hydrophobic nature as a function of time, temperature, and other environmental conditions [87]. This hydrophobic recovery, also called the aging effect, can be detected by measurements of water contact angle and surface oxygen concentration using XPS [88]. A brief description of hydrophobic recovery is provided below, and more information on the impact of surface changes on adhesion can be found in Chapter 9.

The water contact angle measurements on several plastics before treatment, after plasma treatment, and after aging are listed in Table 10.4. The contact angles on cleaned control samples are all above 88, suggesting the hydrophobic nature of typical plastics. After plasma treatment, the fresh-treated samples show significantly lower

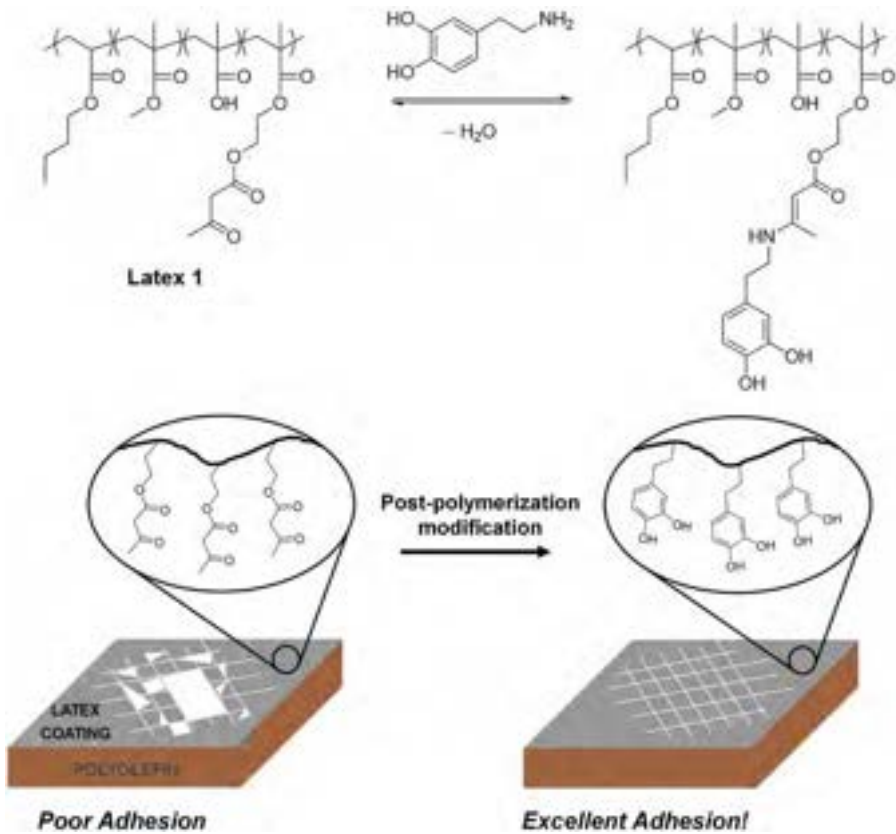


Fig. 10.5 Top: Postpolymerization functionalization of latex 1 with the primary amine-containing small-molecule dopamine via the AAEM group. Bottom: Schematic shows the excellent adhesion onto polyolefin achieved by catechol postpolymerization. Reprinted/adapted with permission from X. Zhang, M.C.D. Carter, M.E. Belowich, G. Wan, M. Crimmins, K.B. Laughlin, R.C. Even, T.H. Kalantar, Catechol-functionalized latex polymers display improved adhesion to low-surface-energy thermoplastic polyolefin substrates, *ACS Appl. Polym. Mater.* 1(6) (2019) 1317–1325.

contact angles with increased wettability. For example, the treated HDPE has a contact angle of 18 degrees, an 82% reduction to the untreated control. With aging, the contact angles gradually increase due to the surface molecular chain rearrangements. Different plastics demonstrate different aging dependence. Polypropylene and polystyrene exhibit nearly complete hydrophobic recovery as polar groups are subsumed as samples age. High-density polyethylene and polycarbonate exhibit minimal hydrophobic recovery, probably owing to plasma-induced crosslinking and intrinsic thermal stability.

Table 10.4 Water contact angles of untreated, freshly treated, and aged water plasma-modified plastics [89].

Samples	Contact angle (degrees) ^a	Samples	Contact angle (degrees) ^a
HDPE		Polystyrene	
Untreated ^b	101 ± 4	Untreated ^b	93 ± 4
Freshly treated	18 ± 3	Freshly treated	21 ± 4
1 week	38 ± 4	1 week	53 ± 2
1 month	49 ± 4	1 month	70 ± 1
LDPE		Polycarbonate	
Untreated ^b	100 ± 1	Untreated ^b	88 ± 4
Freshly treated	50 ± 1	Freshly treated	25 ± 2
1 week	66 ± 1	1 week	41 ± 1
1 month	71 ± 1	1 month	47 ± 1
PP			
Untreated ^b	105 ± 2		
Freshly treated	71 ± 2		
1 week	89 ± 2		
1 month	108 ± 4		

^a Reported error is one standard deviation.

^b Reported untreated elemental composition is from the fresh cleaned control analysis, performed in conjunction with the freshly treated sample time point.

Contact angle data adapted from B.D. Tompkins, E.R. Fisher, Evaluation of polymer hydrophobic recovery behavior following H₂O plasma processing, *J. Appl. Polym. Sci.* 132(20) (2015) 41978/1, Wiley Periodicals, Inc.

10.7 Advances in polyolefin adhesion

The adhesion of polyolefin to polar substrates is still an ongoing challenge for the use of materials in many consumer and industrial applications. Polyolefins are versatile materials with a market that constitute more than 300 billion pounds worldwide and is growing at a 7% compound annual growth rate. The manufacturing of polyethylene, polypropylene, LLDPE, and LDPE is well established and has expanded to polyolefin elastomers and olefin block copolymers. Polyolefins are known for their easy handling, processability, and lower densities compared to engineering plastics. Their light weight, crystallinity ranging from amorphous to highly crystalline, and saturated and nonpolar nature make polyolefins ideal for applications that require weathering resistance and durability such as photovoltaic films, automotive bumpers, roofing membranes, etc. Additionally, much attention has been given to sustainability in the manufacture of monomaterials for the recycling of polyolefins and the availability of bio-derived options, leaving a low carbon footprint. However, in many consumer and industrial applications, mixed and composite solutions are required to

meet the application performance targets, and other “polar materials” are needed for structural reinforcement, texturing, and abrasion resistance. Due to the differences in polarity and surface energy, the bonding of polyolefin thermoplastic elastomers to engineering plastics such as PET, polyamide (PA), PU, and other polar materials is largely unresolved [90].

A common approach to resolve the adhesion issues of polyolefins to polar polymers is via bulk modification, which involves the addition of a polar component such as a tie copolymer or a polar compatibilizer; however, as the substrate thickness increases, the bulk approach becomes less effective due to the lack of concentration at the surface. Instead, surface treatments such as corona, plasma, or flame treatments have been used effectively to charge the surface to promote adhesion. Presently, surface treatments are the most common and economical methods to promote adhesion between dissimilar substrates if it can fit in manufacturing.

A second approach to increase the surface concentration of polar groups is by means of primer approaches to target delivery for substrate bonding [91]. Bonding examples can include the lamination of dissimilar substrates and/or functional coatings. In these cases, a combination of a surface primer and the application method can be an effective solution to provide the needed bonding.

This approach will be the focus of the remainder of this chapter, as recent work has shown that specific bonding solutions can be developed. With a detailed understanding of the material requirements and processing, such bonding challenges can be resolved, shifting the focus away from surface treatment and more to the material solution.

10.7.1 Polyolefin specific adhesion

The mechanism of a primer to promote the adhesion of polyolefins to other substrates can usually be explained by one or a combination of the following strategies:

- (a) Mechanical interlocking (surface roughness, locking).
- (b) Interdiffusion at the interfaces.
- (c) Polar-polar interactions (like-like interactions and compatibility).
- (d) Reactive bonding (covalent or ionic bonding).

These methods are like the ones mentioned in the previous section about general mechanisms that govern adhesion.

Interfacial diffusion can be promoted by the physical melting and mixing of the polymer layers by controlling process parameters such as time, temperature, and pressure. Like polymer molecules in the molten or semimolten state during a lamination process, molten molecules on the surface can interdiffuse and entangle upon cooling and crystallization. This approach is effective if the polymer materials have similar melting temperatures and similar surface energy or affinities. Some extent of low molecular weight polymers can penetrate deeper into the substrates due to their higher mobility, thus enhancing the adhesion further.

Another approach to promote molecular interdiffusion is to use solvents. A solvent can be applied to clean the surface and remove surface contaminants but also functions

to solvate and swell the surface, increasing molecular mobility. This allows the penetration of the polymer chains deeper into the surface; once the solvent dries, the polymer chains are locked inside the matrix.

Next, the compatibility or polarity of interfaces is important. Polyolefins typically have low surface energy, low reactivity, and are semicrystalline. These characteristics are significantly different from those of other common polar materials such as polyurethane, acrylate, or epoxy. Put simply, their surfaces are different and have little to no surface affinity.

Initiating or promoting a reaction to resolve a covalent bond is the most effective approach to bonding. Due to the intolerance of polar monomers in the polyolefin production process using coordinated metal catalysts (Ziegler-Natta or metallocene or chrome-based catalysts), manufacturers look to postreactor means to modification. An exception is polymers made in the high-pressure free radical process in which polar monomers such as vinyl acetate, methacrylate, and primary acids, can be copolymerized. Very few manufacturers in the world have maintained investments in this capability, and such materials are positioned as specialty copolymers. Some of these materials function as excellent compatibilizers as polymeric tie layers, binders, and adhesion modifiers.

Grafted functionalities that are available include maleic anhydride (MAH) while oxidized versions of polymers can include OH, and further steps could include NH₂ or glycidyl methacrylate (GMA, epoxy). As shown in Table 10.5, bonding interactions can be promoted with thermoplastic polyurethanes (TPU), ABS, nylon, PET, and PC, which cover the major chemistries of engineering plastics. Specifically, amine-grafted polyolefin has excellent adhesion with studied TPU and fluoropolymers while MAH-grafted polyolefins show great adhesion with nylon and PET.

Incorporating these functionalities and coextruding or overmolding to promote entanglement and reaction to the substrate are effective. However, due to cost constraints, the addition of these materials is limited to a few weight percent in the bulk, and this does not often provide sufficient surface concentration to enable high-performance bonding. In contrast, we have shown that using the primer approach to deliver functionalities directly onto the surface is an effective way to improve bonding via a combination of the mechanisms discussed above: mechanical, polarity, and reactive [92,93].

Table 10.5 Several functionalized polyolefins to improve bonding with other polar substrates.

Materials	TPU	ABS	Nylon	PET	PC	Fluoropolymers
TPU/PO blends (50/50)	1	2	1	NT	NT	1
OH-grafted PO	1	3	3	2	3	1
MAH-grafted PO	5	0	10	9	4	1
Amine-grafted PO	10	3	1	4	4	10

NT, not tested; 0–4, poor adhesion; 5–8, acceptable adhesion; 9–10, excellent adhesion.

10.7.2 Case study #1—Adhesion of PET and PC to a polyolefin thermo-elastomer

Surface treatment solutions based on functionalized polyolefins improve the adhesion of a PET fabric and a PC coating to thermoplastic elastomer compounds based on polyolefin elastomers in lamination and coating processes. Results indicate that blends with monofunctional or bifunctional MAH and chlorine can be effective.

Polymer film-coated fabrics can be used to improve the durability and haptics of laminates for many consumer and industrial applications. To expand the use of polyolefin sheets, the lamination of PET fabrics on the top or within the sheet can improve the tensile strength and creep resistance in addition to modifying the appearance and surface characteristics of the sheet.

To improve the adhesion of a PET fabric to a polyolefin elastomer, an adhesion primer was coated onto the surface of the PET fabric using a draw-down procedure. The primer solution was prepared by dissolving 10% of an MAH-modified polymer. The primer solution was then applied to the PET fabric and subsequently dried. The modified fabric was then heat laminated to the polyolefin sheet for further testing. In this study, four adhesion primers were prepared with polymers containing various levels of MAH functionality (see Table 10.6). These primers were coated onto the fabric to achieve a target coating weight of 10 g/m² and then laminated on the POE sheet.

Primers A, B, C, and D contain random ethylene-octene copolymers with various levels of MAH functionality. The nominal density of the copolymer is 0.87 g/cc.

Fig. 10.6 shows the effect of having MAH functionality in the adhesion primer on the peel strength between the PET fabric and POE substrate. Primer A, having no MAH functionality, resulted in a peel strength similar to having no primer added. However, as the level of MAH functionality increased (from Primer B, low level to Primer D, high level), the peel strength increased. The highest peel strength achieved was 2.7 kgf/3 cm at the highest MAH level, which is acceptable for limited coated fabric applications.

To further improve the bonding strength, an additional two-component approach was attempted with the addition of an isocyanate crosslinker to the existing primer solutions. Fig. 10.7 shows the effect of adding 5 wt% of the isocyanate crosslinker to the same primer formulations based on its solids. The addition of a crosslinker resulted in increased peel strength. The addition of the crosslinker to primer A that contained no MAH showed an increase to 3 kgf/3 cm. However, in combination with

Table 10.6 MAH-functionalized adhesion primers.

Primer	% Solids concentration	MAH functionality level (wt%)
A	10	None
B	10	Low, 0.5–1
C	10	Medium, 1–2
D	10	High, > 2

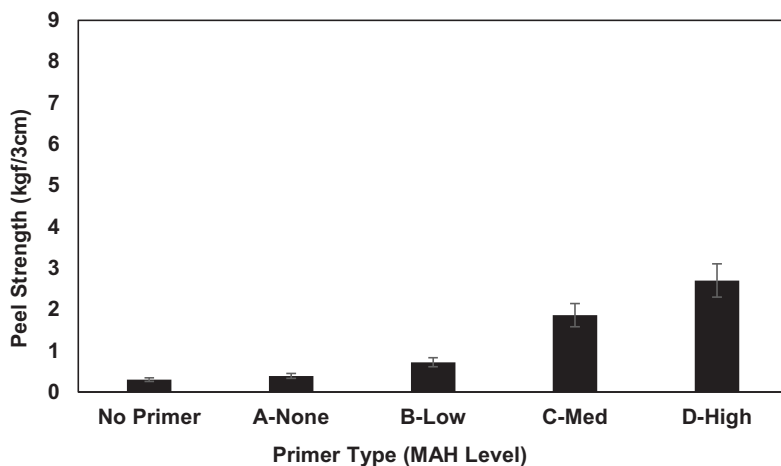


Fig. 10.6 PET-POE adhesion: effect of MAH functionality.

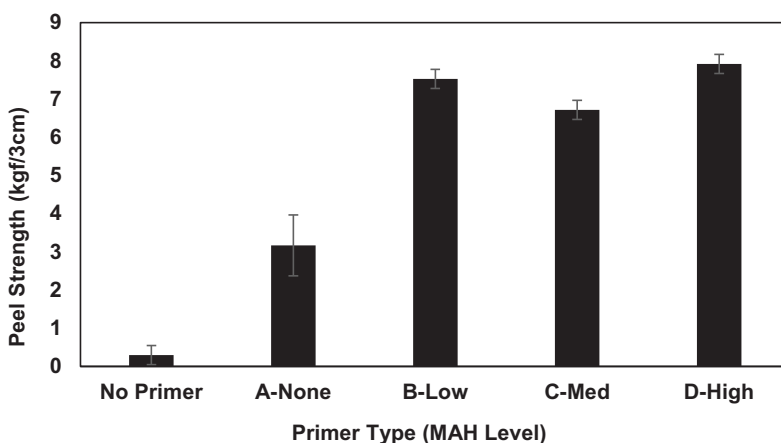


Fig. 10.7 PET-POE adhesion: effect of MAH functionality with isocyanate crosslinker.

MAH functionality, the bonding increased to a peel strength of greater than 6 kgf/3 cm, with the highest level close to 8 kgf/3 cm with Primer D.

To further understand the failure mechanism, visual inspection and attenuated total reflectance-Fourier transform infrared (ATR-FTIR) spectroscopy was used. Inspection of the samples coated with Primers B, C, and D without an isocyanate crosslinker showed cohesive failure with residual adhesive on both the POE and PET sides. Fig. 10.8 shows the ATR-FTIR composition of the surfaces of the failed substrates. The scans of the peeled POE and PET surfaces are almost identical, similar to the spectrum of the adhesive used. They have the characteristic C=O stretching (from the anhydride groups) and C—H stretches of polyolefins. However, samples coated with Primers B, C, and D with the isocyanate crosslinker displayed film breakage of the POE.

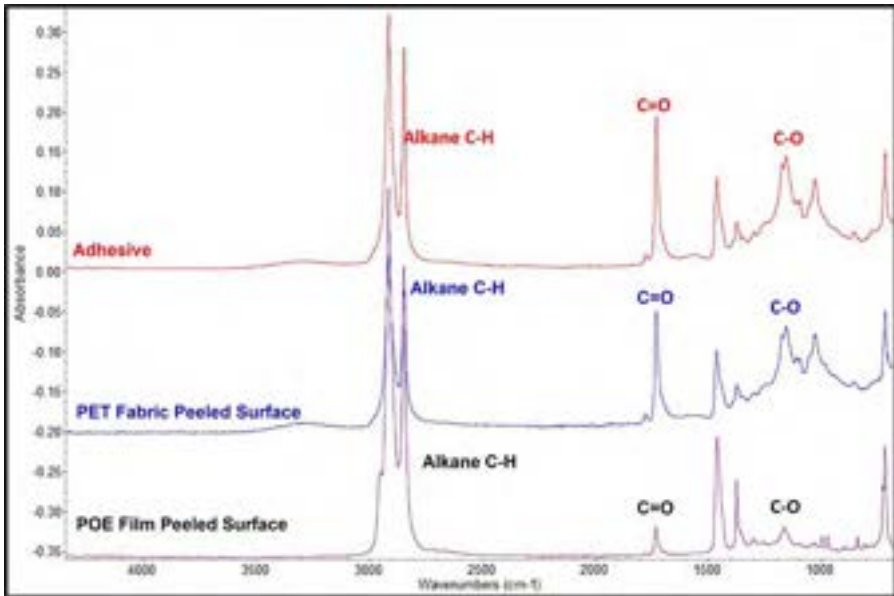


Fig. 10.8 ATR-FTIR spectra of the adhesive (without isocyanate crosslinker) and two peeled surfaces.

10.7.3 Case study #2—Polyolefin foam adhesion to polyurethane adhesive

The above information on the adhesion of nonpolar polyolefin to polar polymer substrates was leveraged to soft foams. Ethylene vinyl acetate (EVA) foams are commonly used as a midsole for athletic footwear to provide comfort. Recently, there has been a trend to incorporate polyolefin elastomers (POE) and olefin block copolymers (OBC) to replace EVA to enhance the cushioning and resilience, thus providing better comfort and longer durability. The chemistry of these three polymers is shown in Fig. 10.9. EVA is more polar than POE and OBC. One challenge of using OBC foam is the poor adhesion by using conventional PU adhesives and primers that were previously developed for EVA.

Fig. 10.10 shows the adhesion performance for the assembly of a foamed OBC using the typical EVA primers and a PU adhesive. The peel strengths are well below the requirements of 2 N/mm after 1 h and 3 N/mm after 24 h for assembly specifications. Additionally, the failure was at the interface of the OBC foam with the PU adhesive. There is a strong need to develop a primer onto OBC foam to improve adhesion with the existing PU adhesive.

Fig. 10.11 summarizes the final bonding performance achieved of the OBC foam and the targeted shoe structure. As indicated, the developed adhesion solution met the overall adhesion target after 1 h and 24 h, which was sufficient for the customer application requirements.

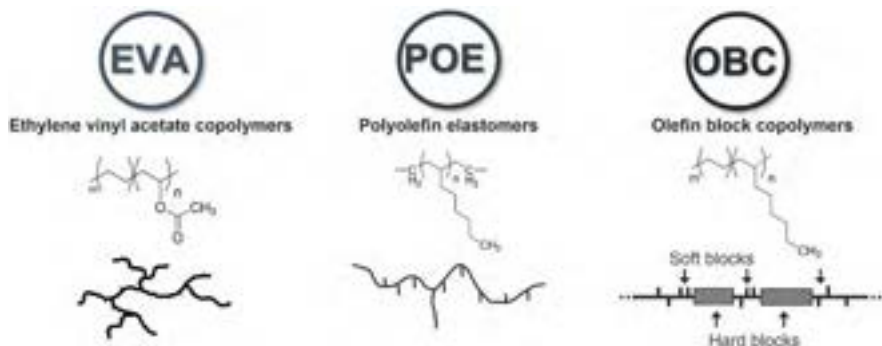


Fig. 10.9 Common polyolefins for foamed midsoles of shoes.

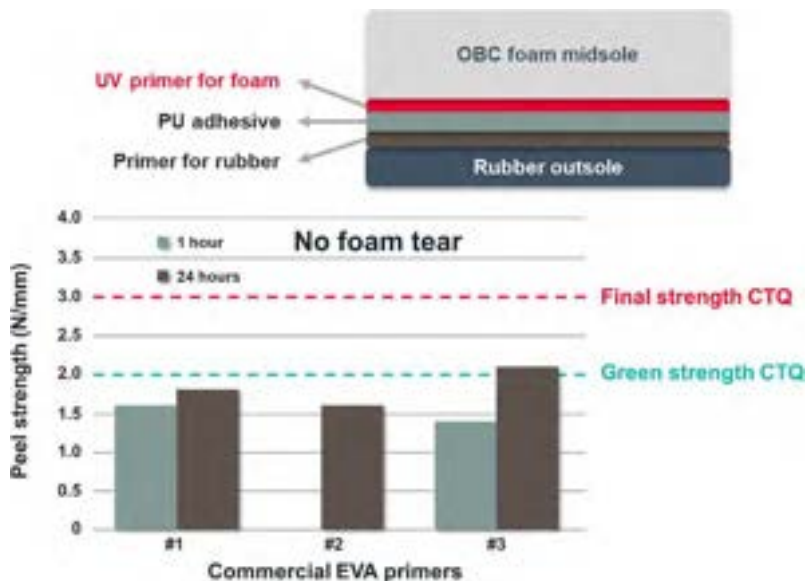


Fig. 10.10 Adhesion of a foamed olefin block copolymer using the typical EVA primers and a PU adhesive (top: illustration of shoe soles assembling, focusing on UV primer layer adhesion; bottom: peel strength of conventional EVA primers on OBC foam with a PU adhesive).

Besides the bonding strength, the key customer requirements were to observe the cohesive failure of the white foam layer to the black outsole, as shown in Fig. 10.11 (left) for the developed OBC primer.

The super bonding for this developed adhesion primer was achieved by the controlled phase separation of the components, the solvent selection and UV initiation for the wetting of the substrates. It is believed that the bonding mechanism is a combination of mechanical interlocks and chemical bonding to the OBC & PU, and UV crosslinking of the adhesive to achieve the high cohesive strength.

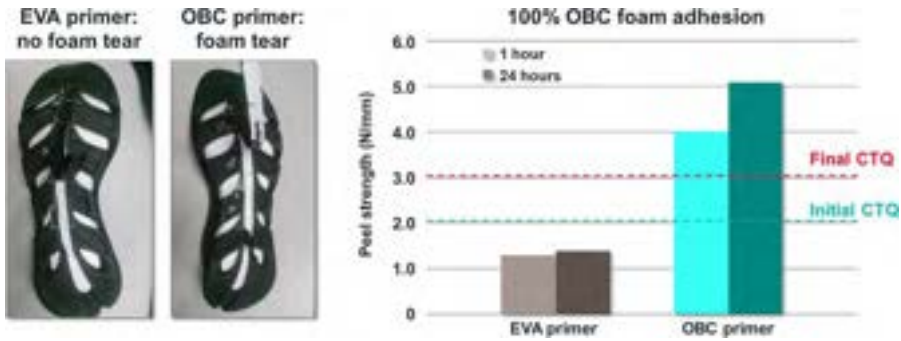


Fig. 10.11 The final bonding performance achieved of the OBC foam and the shoe structure (left: images of peel testing; right: average peel strength).

10.8 Summary and future trends in plastic bonding

The fundamentals to achieve strong adhesion include intimate surface wetting and strong bond formation at the interfaces. Surfaces with high surface energy can be easily wetted by the adhesives or second surface. The formation of covalent bonds, electrostatic attraction, and acid-base interactions at the interface is desired to achieve strong bonding. In the absence of these strong bonds, hydrogen bonding, polar-polar interaction, and van der Waals forces are also important to provide adhesion.

Bonding plastics is more challenging than other materials such as ceramics, wood, or metals due to the low surface energy of plastics, although there are many diverse types of plastics with varying degrees of polarity, composition, and crystallinity. Among common plastics, adhesion to polyolefins is one of the most challenging due to their nonpolar nature and semicrystal surface, preventing wetting and interfacial diffusion, which limits the use of polyolefins in many applications where adhesion is required.

Various technologies to improve adhesion to plastics including polar bulk modification as well as surface treatments such as flame, plasma, and corona were discussed. Chemically grafting of alkylborane and newly developed dopamine onto the plastic surface to improve adhesion was also presented. Case studies of solvent-borne systems that can bond polyolefins using polyurethane adhesives that eliminate the requirements for surface pretreatment are highlighted. It is the authors' opinion that effective adhesion solutions to polyolefins or plastics exist and can be tailored for specific process and application requirements. By understanding the adhesion mechanisms and applying the design principles of adhesion, we can develop adhesion solutions for the substrates of interest by solvent/additive selection for wetting, compatibility of the oligomer or polymeric components, and the balance of mechanical and chemical interaction.

With the sustainability trend of recycling and reuse of materials, simpler combinations of plastics will be needed. Although single polymers can meet many of the criteria, mixed and composite materials will continue to require bonding solutions. In the case of polyolefins, specific attention should be given to surface modification, primer, and adhesive developments.

References

- [1] S.M. Amaraweera, C. Gunathilake, O.H.P. Gunawardene, N.M.L. Fernando, D.B. Wanninayaka, R.S. Dassanayake, S.M. Rajapaksha, A. Manamperi, C.A.N. Fernando, A.K. Kulatunga, A. Manipura, Development of starch-based materials using current modification techniques and their applications: a review, *Molecules* 26 (22) (2021) 6880.
- [2] X. Jin, L. Heepe, J. Strueben, R. Adelung, S.N. Gorb, A. Staubitz, Challenges and solutions for joining polymer materials, *Macromol. Rapid Commun.* 35 (18) (2014) 1551–1570.
- [3] F. Awaja, M. Gilbert, G. Kelly, B. Fox, P.J. Pigram, Adhesion of polymers, *Prog. Polym. Sci.* 34 (9) (2009) 948–968.
- [4] A.J. Kinloch, *Adhesion and Adhesives*, Chapman and Hall, 1987.
- [5] A. Baldan, Adhesion phenomena in bonded joints, *Int. J. Adhes. Adhes.* 38 (2012) 95–116.
- [6] S.R. Sabreen, Solving the problems of plastics adhesion, *Plast. Eng.* 67 (4) (2011) 6–8.
- [7] A.V. Pocius, 6.2 Rationalizations of adhesion phenomena, in: *Adhesion and Adhesives Technology—An Introduction*, fourth ed., Hanser Publishers, 2021.
- [8] W.A. Zisman, Influence of constitution on adhesion, *Ind. Eng. Chem.* 55 (10) (1963) 18–38.
- [9] F.M. Fowkes, Attractive forces at interfaces, *Ind. Eng. Chem.* 56 (12) (1964) 40–52.
- [10] Fowkes, F.M., Determination of intermolecular forces by surface chemical techniques. ASTM Spec. Tech. Publ. No. 360, 1964 20;(a) F.M. Fowkes, Determination of intermolecular forces by surface chemical techniques, ASTM Spec. Tech. Publ. No. 360, 1964, p. 20. (b) F.M. Fowkes, Dispersion force contributions to surface and interfacial tensions, contact angles, and heats of immersion, *Adv. Chem. Ser.* 43 (1964) 99–111.
- [11] D.K. Owens, R.C. Wendt, Estimation of the surface free energy of polymers, *J. Appl. Polym. Sci.* 13 (8) (1969) 1741.
- [12] D.H. Kaelble, Dispersion-polar surface tension properties of organic solid, *J. Adhes.* 2 (April) (1970) 66–81.
- [13] K.L. Mittal, *Advances in Contact Angle, Wettability and Adhesion*, vol. 1, Scrivener Publishing LLC, 2013.
- [14] D.E. Packham, Surface energy, surface topography and adhesion, *Int. J. Adhes. Adhes.* 23 (6) (2003) 437–448.
- [15] L. Gong, L. Xiang, J. Zhang, J. Chen, H. Zeng, Fundamentals and advances in the adhesion of polymer surfaces and thin films, *Langmuir* 35 (48) (2019) 15914–15936.
- [16] K.D. Kumar, M.S. Satyanarayana, G.C. Basak, A.K. Bhowmick, Adhesion between compounded elastomers: a critical review, *Rev. Adhes. Adhes.* 6 (2) (2018) 105–201.
- [17] (a) M.M. Chehimi, A. Azioune, E. Cabet-Deliry, *Acid-Base Interactions. Relevance to Adhesion and Adhesive Bonding*, Marcel Dekker, 2003, p. 95. (b) M.M. Chehimi, E. Cabet-Deliry, A. Azioune, M.-L. Abel, Characterization of acid-base properties of polymers and other materials: relevance to adhesion science and technology, *Macromol. Symp.* 178 (2002) 169–181.
- [18] (a) R.J. Chang, A.N. Gent, Effect of interfacial bonding on the strength of adhesion of elastomers. II. Dissimilar adherends, *J. Polym. Sci. Polym. Phys. Ed.* 19 (10) (1981) 1635. (b) R.J. Chang, A.N. Gent, Effect of interfacial bonding on the strength of adhesion of elastomers. I. Self-adhesion, *J. Polym. Sci. Polym. Phys. Ed.* 19 (10) (1981) 1619. (c) A.N. Gent, R.H. Tobias, Effect of interfacial bonding on the strength of adhesion of elastomers. III. Interlinking by molecular entanglements, *J. Polym. Sci. Polym. Phys. Ed.* 22 (8) (1984) 1483.

- [19] B. Laing, D. Seveno, J. De Keyzer, A. Van Bael, Reactive wetting of polyethylene on ethylene-propylene-diene terpolymer, *Colloid Interface Sci. Commun.* 40 (2021) 100343.
- [20] B. Laing, J. De Keyzer, D. Seveno, A. Van Bael, Adhesion between ethylene-propylene-diene monomer and thermoplastics in two-component injection molding: effect of dicumylperoxide as curing agent, *J. Appl. Polym. Sci.* 137 (41) (2020) 49233.
- [21] S. Siboni, C. Della Volpe, Acid-base theory of adhesion: a critical review, *Rev. Adhes. Adhes.* 3 (3) (2015) 253–310.
- [22] E. Otsuka, A. Tsujimoto, T. Takamizawa, T. Furuichi, M. Yokokawa, K. Tsubota, M. Miyazaki, Influence of surface treatment of glass-ionomers on surface free energy and bond strength of resin composite, *Dent. Mater. J.* 32 (5) (2013) 702–708.
- [23] N. Dilsiz, J.P. Wightman, Effect of acid-base properties of unsized and sized carbon fibers on fiber/epoxy matrix adhesion, *Colloids Surf. A* 164 (2–3) (2000) 325–336.
- [24] F. Arefi-Khonsari, M. Tatoulian, N. Shahidzadeh, M. Chehimi, J. Amouroux, D. Leonard, P. Bertrand, Adhesion, Wettability and Mechanical Properties of Ammonia- and Helium-Plasma-Treated Polypropylene, *VSP*, 1998, p. 329.
- [25] F.M. Fowkes, *Acid-Base Interactions in Polymer Adhesion*, Plenum, 1983, p. 583.
- [26] F.M. Fowkes, C.Y. Sun, S.T. Joslin, *Enhancing Polymer Adhesion to Iron Surfaces by Acid-Base Interaction*, NACE, 1981, p. 1.
- [27] A.V. Pocius, 4.1 Introduction, in: *Adhesion and Adhesives Technology—An Introduction*, fourth ed., Hanser Publishers, 2021.
- [28] D.F. Eggers, *Physical Chemistry*, Wiley, 1964.
- [29] Kinloch, A.J., Review. The science of adhesion. Part 1. Surface and interfacial aspects. *J. Mater. Sci.* 1980, 15 (9), 2141; (a) A.J. Kinloch, Review. The science of adhesion. Part 1. Surface and interfacial aspects, *J. Mater. Sci.* 15 (9) (1980) 2141. (b) A.J. Kinloch, The science of adhesion. Part 2. Mechanics and mechanisms of failure, *J. Mater. Sci.* 17 (3) (1982) 617.
- [30] A.V. Pocius, *Adhesion and Adhesives Technology—An Introduction*, fourth ed., Hanser Publishers, 2021.
- [31] M. Shahmardani, R. Mohammadi, The role of interfacial adhesion on the mechanical behavior of thin metal/polymer laminate with surface roughness, *Polymers (Basel)* 14 (15) (2022).
- [32] L. Jian, Effect of surface treatment on enhancing interfacial strength of carbon fiber/polyimide composites, *J. Thermoplast. Compos. Mater.* 35 (5) (2022) 708–719.
- [33] (a) M.P. Larsson, M.M. Ahmad, Improved polymer-glass adhesion through micro-mechanical interlocking, *J. Micromech. Microeng.* 16 (6) (2006) S161. (b) M.P. Larsson, R.R.A. Syms, A.G. Wojcik, Improved adhesion in hybrid Si-polymer MEMS via micro-mechanical interlocking, *J. Micromech. Microeng.* 15 (11) (2005) 2074–2082.
- [34] A.A. Shcherbina, Y.Y. Gladkikh, A.E. Chalykh, Kinetics and mechanism of formation of adhesive joints based on ethylene-vinyl acetate copolymers, *Polym. Sci. Ser. A* 54 (5) (2012) 375–384.
- [35] A.C. Akue Asseko, B. Cosson, E. Lafranche, F. Schmidt, Y. Le Maoult, Effect of the developed temperature field on the molecular interdiffusion at the interface in infrared welding of polycarbonate composites, *Compos. Part B* 97 (2016) 53–61.
- [36] J.H. Ryu, P.B. Messersmith, H. Lee, Polydopamine surface chemistry: a decade of discovery, *ACS Appl. Mater. Interfaces* 10 (9) (2018) 7523–7540.
- [37] K. Grundke, S. Michel, K.-J. Eichhorn, D. Beyerlein, T. Bayer, Influence of chemical interactions on the macroscopic spreading of a maleic anhydride copolymer melt, *Macromol. Chem. Phys.* 203 (7) (2002) 937–946.

- [38] G. Zitzenbacher, Z. Huang, M. Laengauer, C. Forsich, C. Holzer, Wetting behavior of polymer melts on coated and uncoated tool steel surfaces, *J. Appl. Polym. Sci.* 133 (21) (2016) 43469.
- [39] G.-J. Bex, D. Seveno, J. De Keyzer, F. Desplentere, A. Van Bael, Wetting measurements as a tool to predict the thermoplastic/thermoset rubber compatibility in two-component injection molding, *J. Appl. Polym. Sci.* 135 (13) (2018) 46046.
- [40] Y. Zhang, C.A. Fuentes, R. Koekoekx, C. Clasen, A.W. Van Vuure, J. De Coninck, D. Seveno, Spreading dynamics of molten polymer drops on glass substrates, *Langmuir* 33 (34) (2017) 8447–8454.
- [41] W. Six, G.-J. Bex, A. Van Bael, J. De Keyzer, F. Desplentere, Prediction of interfacial strength of HDPE overmolded with EPDM, *Polym. Eng. Sci.* 59 (7) (2019) 1489–1498.
- [42] C.A. Fuentes, Y. Zhang, H. Guo, W. Woigk, K. Masania, C. Dransfeld, J. De Coninck, C. Dupont-Gillain, D. Seveno, A.W. Van Vuure, Predicting the adhesion strength of thermoplastic/glass interfaces from wetting measurements, *Colloids Surf., A* 558 (2018) 280–290.
- [43] T. Farajpour, Y. Bayat, M. Abdollahi, M.H. Keshavarz, Surface and bulk modification of ethylene-propylene-diene terpolymer elastomer: adhesion to polyurethane and mechanical properties, *Polym. Sci. Ser. A* 58 (2) (2016) 186–195.
- [44] M. Ginic-Markovic, N.R. Choudhury, M. Dimopoulos, J. Matison, Adhesion between polyurethane coating and EPDM rubber compound, *J. Adhes. Sci. Technol.* 18 (5) (2004) 575–596.
- [45] I. Novak, Adhesive properties of poly(propylene) modified in bulk, *Angew. Makromol. Chem.* 236 (1996) 35–41.
- [46] T. Schuman, S.F. Thames, Coating solvent effects producing adhesion to molded plastic parts, *J. Adhes. Sci. Technol.* 19 (13–14) (2005) 1207–1235.
- [47] M.D. Green, F.J. Guild, R.D. Adams, Characterisation and comparison of industrially pretreated homopolymer polypropylene, HF 135M, *Int. J. Adhes. Adhes.* 22 (1) (2002) 81–90.
- [48] I. Sutherland, E. Sheng, D.M. Brewis, R.J. Heath, Flame treatment and surface characterization of rubber-modified polypropylene, *J. Adhes.* 44 (1–2) (1994) 17–27.
- [49] I. Sutherland, D.M. Brewis, R.J. Heath, E. Sheng, Modification of polypropylene surfaces by flame treatment, *Surf. Interface Anal.* 17 (7) (1991) 507.
- [50] D. Zhang, Q. Sun, L.C. Wadsworth, Mechanism of corona treatment on polyolefin films, *Polym. Eng. Sci.* 38 (6) (1998) 965–970.
- [51] (a) B. Das, D. Chakrabarty, C. Guha, S. Bose, Effects of corona treatment on surface properties of co-extruded transparent polyethylene film, *Polym. Eng. Sci.* 61 (5) (2021) 1449–1462. (b) I. Sutherland, R.P. Popat, D.M. Brewis, R. Calder, Corona discharge treatment of polyolefins, *J. Adhes.* 46 (1–4) (1994) 79–88.
- [52] A. Martinez-Garcia, A. Sanchez-Reche, S. Gisbert-Soler, C.M. Cepeda-Jimenez, R. Torregrosa-Macia, J.M. Martin-Martinez, Corona discharge treatment of EVA with different vinyl acetate contents, *J. Adhes. Sci. Technol.* 21 (5–6) (2007) 441–463.
- [53] J. Comyn, L. Mascia, G. Xiao, B.M. Parker, Corona-discharge treatment of polyetheretherketone (PEEK) for adhesive bonding, *Int. J. Adhes. Adhes.* 16 (4) (1996) 301–304.
- [54] Atmospheric Pressure Plasma Treatment of Polymers: Relevance to Adhesion. John Wiley & Sons, Inc.: 2013. M. Thomas, K.L. Mittal, Atmospheric Pressure Plasma Treatment of Polymers: Relevance to Adhesion, John Wiley & Sons, Inc, 2013.
- [55] T.S. Williams, H. Yu, R.F. Hicks, Review of atmospheric pressure plasma effect on the activation of plastics for improved adhesion, *Annu. Tech. Conf. Soc. Plast. Eng.* 3 (2012) 1721–1726. 70th.

- [56] M. Noeske, J. Degenhardt, S. Strudthoff, U. Lommatzsch, Plasma jet treatment of five polymers at atmospheric pressure: surface modifications and the relevance for adhesion, *Int. J. Adhes. Adhes.* 24 (2) (2004) 171–177.
- [57] R.S. Bisht, R. Kumar, N. Thakur, Change in surface free energy and surface resistivity of polycarbonate and polypropylene sheets after plasma exposure, *Optoelectron. Adv. Mater. Rapid Commun.* 4 (2) (2010) 144–147.
- [58] R. Stewart, V. Goodship, F. Guild, M. Green, J. Farrow, Investigation and demonstration of the durability of air plasma pre-treatment on polypropylene automotive bumpers, *Int. J. Adhes. Adhes.* 25 (2) (2004) 93–99.
- [59] N. Anagreh, L. Dorn, Influence of low-pressure plasma treatment on adhesive bonding between polybutylene terephthalate (PBT) and aluminum, *Int. J. Adhes. Adhes.* 25 (2) (2004) 165–172.
- [60] J. Comyn, L. Mascia, G. Xiao, B.M. Parker, Plasma-treatment of polyetheretherketone (PEEK) for adhesive bonding, *Int. J. Adhes. Adhes.* 16 (2) (1996) 97–104.
- [61] P. Sundriyal, M. Pandey, S. Bhattacharya, Plasma-assisted surface alteration of industrial polymers for improved adhesive bonding, *Int. J. Adhes. Adhes.* 101 (2020) 102626.
- [62] G. Scarselli, D. Quan, N. Murphy, B. Deegan, D. Dowling, A. Ivankovic, Adhesion improvement of thermoplastics-based composites by atmospheric plasma and UV treatments, *Appl. Compos. Mater.* 28 (1) (2021) 71–89.
- [63] D. Quan, R. Alderliesten, C. Dransfeld, I. Tsakoniatis, S. Teixeira De Freitas, G. Scarselli, N. Murphy, A. Ivankovic, R. Benedictus, Significantly enhanced structural integrity of adhesively bonded PPS and PEEK composite joints by rapidly UV-irradiating the substrates, *Compos. Sci. Technol.* 199 (2020) 108358.
- [64] A. Santidrian, O. Sanahuja, B. Villacampa, J.L. Diez, A.M. Benito, W.K. Maser, E. Munoz, A. Anson-Casaos, Chemical postdeposition treatments to improve the adhesion of carbon nanotube films on plastic substrates, *ACS Omega* 4 (2) (2019) 2804–2811.
- [65] C.M. Cepeda-Jimenez, M. Mercedes Pastor-Blas, T.P. Ferrandiz-Gomez, J.M. Martin-Martinez, Influence of the styrene content of thermoplastic styrene-butadiene rubbers in the effectiveness of the treatment with sulfuric acid, *Int. J. Adhes. Adhes.* 21 (2) (2001) 161–172.
- [66] (a) D. Briggs, D.M. Brewis, M.B. Konieczko, X-ray photoelectron spectroscopy studies of polymer surfaces. Part 1. Chromic acid etching of polyolefins, *J. Mater. Sci.* 11 (7) (1976) 1270. (b) D. Briggs, V.J.I. Zichy, D.M. Brewis, J. Comyn, R.H. Dahm, M.A. Green, M.B. Konieczko, X-ray photoelectron spectroscopy studies of polymer surfaces. 4. Further studies of the chromic acid etching of low-density polyethylene, *SIA, Surf. Interface Anal.* 2 (3) (1980) 107.
- [67] A. Martinez-Garcia, A. Sanchez-Reche, J.M. Martin-Martinez, Surface modifications on EVA treated with sulphuric acid, *J. Adhes.* 79 (6) (2003) 525–547.
- [68] J.V. Zharov, J.N. Krasnov, Polymerizable Acrylic Compositions With Initiator Systems Based on Organoborane Amine Complexes, and Their Use as Adhesives, WO9522567, 1995.
- [69] Pocius, A.V. Organoborane Polyamine Complex Initiator Systems for Adhesives for Low Surface Energy Substrates. WO9707151, 1997; (a) A.V. Pocius, Organoborane Polyamine Complex Initiator Systems for Adhesives for Low Surface Energy Substrates, WO9707151, 1997. (b) A.V. Pocius, T.G. Nigatu, Organoborane-Polyamine Complexes and Adhesive Compositions Made Therewith, WO9632397, 1996.
- [70] B.J. Kneafsey, G. Coughlan, T.B. Harty, Polymerization Initiators and Polymerizable Compositions for Bonding Low Surface Energy Substrates, US7371466, 2008.
- [71] J.L. Kendall, K.J. Abbey, R.F. Righettini, Internally Blocked Organoborate Initiators for Adhesives, WO2003040151, 2003.

- [72] M.F. Sonnenschein, S.P. Webb, P.E. Kastl, D.J. Arriola, B.L. Wendt, D.R. Harrington, N. G. Rondan, Mechanism of trialkylborane promoted adhesion to low surface energy plastics, *Macromolecules* 37 (21) (2004) 7974–7978.
- [73] L. Jialanella Gary, M.U. Oxford, S. Feng, C.N. Shanghai, N. Nickias Peter, M.U. Midland, T. Ristoski, M.U. Rochester Hills, Blocking Agents for Organoborane Compounds Blocking Agents for Organoborane Compounds Blocking Agents for Organoborane Compounds, US8304543B2, 2012.
- [74] (a) S. Feng, M.U. Midland, L. Jialanella Gary, M.U. Oxford, P. Nickias, M.U. Midland, T. Ristoski, M.U. Rochester Hills, Amido-Organoborate Initiator Systems Amido-Organoborate Initiator Systems Amido-Organoborate Initiator Systems, US7816562B2, 2010. (b) S. Feng, M.U. Midland, L. Jialanella Gary, M.U. Oxford, P. Nickias, M.U. Midland, T. Ristoski, M.U. Rochester Hills, Amido-Organoborate Initiator Systems Amido-Organoborate Initiator Systems Amido-Organoborate Initiator Systems, US7737241B2, 2010.
- [75] S.P. Webb, M.F. Sonnenschein, Organoborane Amine Complex Polymerization Initiators and Polymerizable Compositions, WO2003038006, 2003.
- [76] M.F. Sonnenschein, S.P. Webb, R.C. Cieslinski, B.L. Wendt, Poly(acrylate/epoxy) hybrid adhesives for low-surface-energy plastic adhesion, *J. Polym. Sci. A Polym. Chem.* 45 (6) (2007) 989–998.
- [77] G.L. Jialanella, T. Ristoski, A.C. Cawley, Recent developments in novel stabilization chemistry for low energy surface adhesive (LESA) cured with alkyl boranes, in: Adhesion Society Meeting, 2007, pp. 1–5.
- [78] G. Lutz William, M.U. Linwood, S. Feng, C.N. Shanghai, C. Nickless Brian, M.U. Bay City, J. Spaulding Wesley, M.U. Freeland, L. Jialanella Gary, M.U. Oxford, Method for Joining Piping Systems and Piping Equipment, fixtures, Devies, Structures, and Appliances, US20090090454A1, 2009.
- [79] B. Zhu, D. Ahn, G. Lu, J. Quast, N.E. Shephard, Dual Cure Polyorganosiloxane Composition and Methods for Its Preparation and Use, WO2018160373, 2018.
- [80] B. Zhu, Method for Adhering Cured Silicones to Low Energy Plastics and Composites Prepared by the Method, WO2018182950, 2018.
- [81] H. Lee, S.M. Dellatore, W.M. Miller, P.B. Messersmith, Mussel-inspired surface chemistry for multifunctional coatings, *Science (Washington, DC, US)* 318 (5849) (2007) 426–430.
- [82] J. Waite, N. Andersen, S. Jewhurst, C. Sun, Mussel adhesion: finding the tricks worth mimicking, *J. Adhes.* 81 (3–4) (2005) 297–317.
- [83] B.P. Lee, P.B. Messersmith, J.N. Israelachvili, J.H. Waite, Mussel-inspired adhesives and coatings, *Annu. Rev. Mat. Res.* 41 (2011) 99–132.
- [84] Q. Ye, F. Zhou, W. Liu, Bioinspired catecholic chemistry for surface modification, *Chem. Soc. Rev.* 40 (7) (2011) 4244–4258.
- [85] S.M. Kang, N.S. Hwang, J. Yeom, S.Y. Park, P.B. Messersmith, I.S. Choi, R. Langer, D.G. Anderson, H. Lee, One-step multipurpose surface functionalization by adhesive catecholamine, *Adv. Funct. Mater.* 22 (14) (2012) 2949.
- [86] X. Zhang, M.C.D. Carter, M.E. Belowich, G. Wan, M. Crimmins, K.B. Laughlin, R.C. Even, T.H. Kalantar, Catechol-functionalized latex polymers display improved adhesion to low-surface-energy thermoplastic polyolefin substrates, *ACS Appl. Polym. Mater.* 1 (6) (2019) 1317–1325.
- [87] M. Morra, E. Occhiello, L. Gila, F. Garbassi, Surface dynamics vs. adhesion in oxygen plasma treated polyolefins, *J. Adhes.* 33 (1–2) (1990) 77–88.

-
- [88] B. Huennekens, A. Krause, H. Militz, W. Viöl, Hydrophobic recovery of atmospheric pressure plasma treated surfaces of wood-polymer composites (WPC), *Eur. J. Wood Wood Prod.* 75 (5) (2017) 761–766.
- [89] B.D. Tompkins, E.R. Fisher, Evaluation of polymer hydrophobic recovery behavior following H₂O plasma processing, *J. Appl. Polym. Sci.* 132 (20) (2015) 41978/1.
- [90] B. Goss, *Practical Guide to Adhesive Bonding of Small Engineering Plastic and Rubbers Parts*, Smithers Rapra Technology Ltd, 2010.
- [91] K. Anderson, Q. Wan, S. Anderson, J. Harris, Y. Li, V. Thakur, S. Ultsch, P.S.C. Li, *Surface Treatment to Enhance Adhesion of Polyolefin to Woven Fabric*, American Chemical Society, 2016.
- [92] (a) C.A. Kondos, J.T. Martz, M. Nakajima, Adhesion Promoting Agent and Coating Compositions for Polymeric Substrates, WO2001083628, 2001. (b) C.A. Kondos, J.T. Martz, M. Nakajima, Adhesion Promoting Agent and Coating Compositions for Polymeric Substrates, US20030212209, 2003.
- [93] R.L. Laakso Jr., R.G. Varathungarajan, A. Batra, P. Ansems, Chlorinated Polyethylene Composition With Improved Adhesion Properties, Method of Producing the Same, and Articles Made Therefrom, US20110305859, 2011.

Structural bonds without an adhesive: Understanding adhesion of semicrystalline thermoplastic interfaces

11

Vinayak Khataavkar^{a,b}, Markus Bulters^{c,*}, and Michelle Elizabeth Seitz^{a,*}

^aDSM Materials Science Center, Geleen, The Netherlands, ^bDSM Engineering Materials, Geleen, The Netherlands, ^cIdésol BV, Sittard, The Netherlands

11.1 Challenges in obtaining high adhesion at semicrystalline polymer interfaces

There is an excellent understanding of the factors that control the strength of glassy polymer interfaces [1–4]. Despite semicrystalline polymers being two-thirds of global production [5], an equivalent understanding for semicrystalline interfaces is lacking. This makes predicting whether sufficient adhesion can be obtained for different polymer combinations under a variety of processing conditions difficult. In recent years, more work on semicrystalline interfaces has been published, but the literature remains fairly limited [6–9].

This gap is understandable given the additional complexity introduced by the kinetics of crystallization and the difficulty in mimicking the thermal histories relevant to common industrial processes. Most processes result in microstructures far from equilibrium with the extent of crystallization and crystal stability strongly dependent on the thermal and flow history, especially at surfaces [10,11]. Adhesion is governed by the surface properties, which can vary significantly from those of the bulk, especially in semicrystalline polymers. The decoupling of the surface and bulk can result in adhesion being obtained, or lost, at surprising combinations of processing conditions, which we will demonstrate and explain in this chapter. To elucidate the key requirements for obtaining strong adhesion at semicrystalline polymer interfaces, it is necessary to understand the thermal history during interface formation as well as the crystallization and flow behavior of the material, and to have a well-defined sample geometry.

In this chapter, we use model overmolding experiments with unfilled polyamide 6 (PA6) to elucidate the critical conditions for obtaining adhesion at semicrystalline polymer interfaces. The approach laid out here can also be applied to many other

* Authors were employed at DSM when this work was performed, but are no longer affiliated with DSM.

industrial processes where adhesion of semicrystalline interfaces is critical such as inlay decoration [12], three-dimensional (3D) printing [13,14], heat sealing of film [15], blow molding of tanks around injection-molded inlets, continuous fiber thermoplastic composite tape lamination [16,17], and overmolding [8,18–20]. We focus on understanding systems with high rigidity—such as tested below the glass transition temperature (T_g) or with substantial crystallinity—rather than more elastomeric systems with lower modulus and yield stress, and therefore more substantial contributions from deformation away from the interface.

Overmolding is a process where one layer of material is molded over an already solidified part, resulting in multiple material layers being integrated in a single part [21,22]. It is widely used for soft touch applications where a thermoplastic elastomer surface layer covers a more rigid substrate to impart desired haptics, two-color aesthetics, and ergonomics. Familiar examples may be toothbrushes or tool handles [23]. Combinations of more rigid materials are also useful; for example, as shown in Fig. 11.1, integrating a low friction surface layer onto a reinforced gear body, combining a thermally conductive layer to a structural layer for light-emitting diode (LED) bulb housings, or integrating an impact resistant layer over a carbon fiber-reinforced outsole in a cycling shoe. With increasing interest in weight reduction in automotive applications, overmolding of ribs or attachments with short fiber-reinforced thermoplastics onto consolidated continuous fiber thermoplastic composites is an active area of development [8,18–20].

In direct overmolding of thermoplastics, an injection molding machine is equipped with two or more barrels, allowing multiple materials to be injected into one mold. This requires that the mold geometry be adapted during the process. In insert overmolding, the first piece is molded or machined separately and then overmolded in a new mold. Insert overmolding is often used for smaller part runs because the tooling costs are lower while direct overmolding provides shorter cycle times, lower labor costs, and often superior adhesion [23]. While direct and insert overmolding differ in terms of the thermal history of the interface, the essence of the processes is the same. In direct overmolding, as summarized schematically in Fig. 11.2, the first shot melt is injected into the first cavity followed by holding, where the part cools and solidifies.

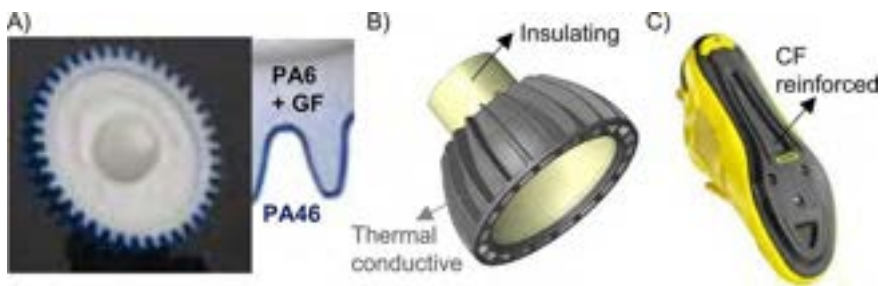


Fig. 11.1 Examples of applications using overmolding. (A) Gear with low friction surface; (B) LED bulb housing combining insulating and thermal conductive materials; (C) cycling shoe with carbon fiber-reinforced sole overmolded with impact resistant material.

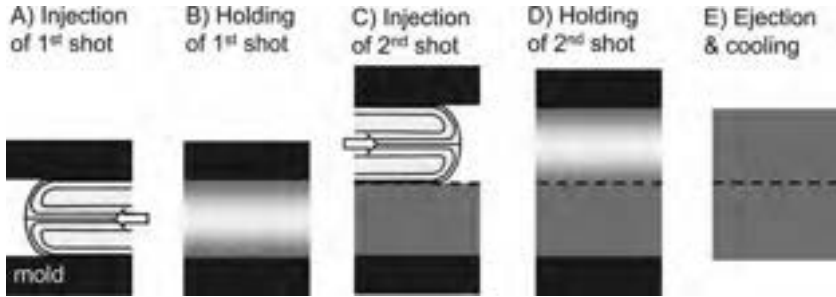


Fig. 11.2 Schematic of steps in direct overmolding process.

Next, the mold opens and the second cavity is brought into place and closes, thus forming a new larger cavity in which the second shot is injected on top of the first. After holding, the mold opens and the complete part is ejected. Usually for this purpose, a rotating mold is used allowing increased throughput by forming the first shot of a new part simultaneously with the second shot of the previous part.

In any overmolding application, adhesion is a critical requirement. The general wisdom is “hotter is better” at the interface for adhesion, and many studies have observed improved adhesion up to a plateau value with increased contact temperatures [24–33]. The contact temperature ($T_{contact}$) for the interface is an important parameter and can be estimated using standard heat transfer equations for two semiinfinite bodies brought in sudden, perfect contact knowing the temperature (T) and thermal effusivity ($b = \sqrt{\lambda\rho C_p}$ where λ is the thermal conductivity, ρ is the density, and C_p is the specific heat) of each component [34]. For direct overmolding, the temperature of the first shot surface is dictated by the mold temperature (T_{mold}) and the second shot temperature is the melt temperature (T_{melt}). A reasonable estimate of the contact temperature is given in Eq. (11.1).

$$T_{contact} = \frac{T_1 b_1 + T_2 b_2}{b_1 + b_2} \quad (11.1)$$

For a symmetric interface in overmolding $b_1 = b_2$ yielding $T_{contact} = \frac{T_{mold} + T_{melt}}{2}$.

Many studies looking at semicrystalline polymer interfaces report poor bonding for contact temperatures below the melting temperature (T_m) [6,24,35–39]. Therefore, it is often assumed that melt-to-melt contact is necessary for a minimum time to form a strong bond. Thus, we should compare the expected contact temperature with T_m to gauge whether overmolding a particular polymer will give high adhesion. This is shown in Fig. 11.3 for a range of industrially relevant semicrystalline polymers based on recommended injection molding conditions for unfilled materials. For most common semicrystalline polymers, the expected contact temperatures are 20–100°C lower than the T_m . Lower melting polyolefins are the exception where the contact temperature exceeds T_m . Trivially, the contact temperature can be increased by raising the mold or melt temperature (or both). However, there are practical limitations to how hot the melt (degradation) and mold temperatures (extremely long cycle times)

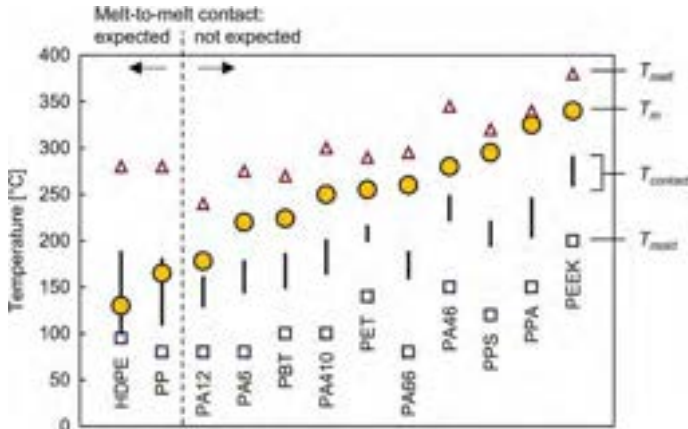


Fig. 11.3 Comparison of melting temperature (T_m) with a range of contact temperatures ($T_{contact}$) expected based on recommended processing conditions for various semicrystalline polymers. The highest recommended mold (T_{mold}) and melt (T_{melt}) temperatures are also included. The melting temperature is based on DSC at 10°C/min. Polymers included high-density polyethylene (HDPE); polypropylene (PP); polyamide 12 (PA12); polyamide 6 (PA6); polybutylene terephthalate (PBT); polyamide 4,10 (PA410); polyethylene terephthalate (PET); polyamide 6,6 (PA66); polyphenylene sulfide (PPS); polyamide 4,6 (PA46); polyphthalamide (PPA); and polyether ketone (PEEK).

can be. Thus, for most high melting thermoplastics, including PA6, melt-to-melt contact during overmolding is not expected and, consequently, poor adhesion is anticipated.

Contrary to the expectation set above, we find relevant conditions where excellent adhesion is observed for PA6 during direct overmolding [40,41]. The goal of this work is to understand the surprising result that excellent adhesion is possible in a non-isothermal process with limited contact time at contact temperatures below T_m . We address how the molecular and morphological features control adhesion for overmolded, nonreactive, semicrystalline polymer interfaces and how they are influenced by processing conditions.

11.2 Overview of overmolding experiments and thermal modeling

We begin by briefly summarizing the materials, set-up, and methods used for our experiments and modeling followed by the results obtained.

Overmolding experimental details: An Arburg 50 2 K injection molding machine with two injection units and a clamp force of 50 tons was used. Both horizontal and vertical injection units consist of a standard three-zone screw with a diameter of 25 mm. A schematic of the rotating mold used for the direct overmolding process is shown in Fig. 11.4 along with images of the samples. The first shot is slightly wider

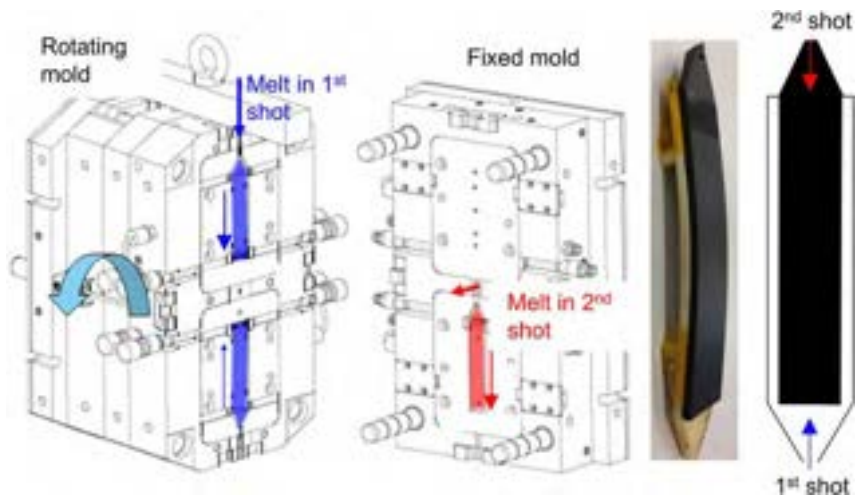


Fig. 11.4 Schematic of rotating mold showing flow direction for first and second shot. Photograph of sample with white first shot and black second shot showing slight warping. Schematic top view of overmolded samples with flow direction marked by *arrows*.

(30 mm) than the second shot (26 mm) and the overmolded length is 120 mm. Each shot was 2 mm thick. The mold temperature was varied between ~ 20 – 140°C and the melt temperature between ~ 230 – 310°C to achieve contact temperatures ranging from ~ 125 – 220°C . The injection time was kept constant at ~ 0.25 s and the holding time for each shot was ~ 50 s. To create a precrack for adhesion evaluation, polyimide tape was placed over the first shot at the end of the flow path.

Materials: Unfilled PA6 with weight average M_w varying between 34 and 66 kg/mol and a polydispersity index of 2 determined via SEC were used. All samples had a peak melting temperature (T_m) of 220°C determined via DSC at $10^\circ\text{C}/\text{min}$ on the second heating (following ISO 11357-3). Care was taken to ensure polymers were sufficiently dry to avoid degradation during molding and characterization. The linear viscoelastic response was determined using melt rheology experiments following the protocol in reference [42]. For details on rheology and M_w characterization of PA6, readers are directed to the references of Steeman and van Ruymbeke [42–44].

Adhesion evaluation: The difficulty with which the samples can be separated at room temperature is ranked on a qualitative 0–10 scale. Functionally no adhesion is indicated by 0 with samples separating on mold opening or with no effort by hand, 4–6 indicates it is moderately difficult to separate the parts, and 10 indicates we were unable to separate the interface even using a chisel, and failure occurred through the part bulk. While interface strength evaluation via double cantilevered beam (DCB) testing was performed for some samples, it was not used as the main evaluation method due to difficulty in assessing high adhesion levels, slight warping of the samples, and for the pragmatic reason that it requires more time and effort. Our focus is on understanding which conditions the samples go from functionally nonadhering to showing moderate to high adhesion rather than on determining the absolute strength

level of the interface. We consider an adhesion ranking of 4–5 to indicate the beginnings of adequate adhesion for many applications. From DCB evaluation, an adhesion ranking of 0–1 corresponds to $\sim 40 \text{ J/m}^2$, a ranking between 4 and 8 is $\sim 400 \text{ J/m}^2$, and a ranking above 8 was not measurable via DCB.

Thermal modeling: The heat transfer occurring during the overmolding process is modeled by unsteady heat conduction in a standard approach. Perfect thermal contact between all surfaces is assumed. In general, the effects of flow and heat of crystallization are neglected. Under these assumptions, the heat balance equation for each layer (j) is

$$\rho_j C_{pj} \frac{\partial T}{\partial t} = \nabla \cdot (k_j \nabla T) \quad (11.2)$$

where t is time and k is the thermal conductivity (treated as T independent along with specific heat, C_p). The resulting set of equations is solved numerically using a Galerkin finite element method (GFEM) for spatial discretization, whereas for temporal discretization, a first-order Euler implicit scheme is used using SEPRAN software [45,46]. In some cases, coupled heat and flow simulations using Polyflow software were used to capture the effects of viscous heat dissipation on contact temperature.

FLASH DSC experiments: Experiments were performed on a Flash DSC 1 from Mettler-Toledo controlled using StarE software, Version 12, of Mettler-Toledo. Sample preparation followed reference [47]. Helium was used as an inert purge gas at a flow rate of 20 mL/min.

11.3 Adhesion of overmolded polyamide 6 interfaces

11.3.1 Influence of contact temperature, mold temperature, and molecular weight

Overmolding experiments exploring the influence of processing conditions (mold and contact temperature) and M_w on adhesion for unfilled PA6 are summarized in Fig. 11.5.

The key observations from these experiments are summarized below:

- **Influence of contact temperature:** For a given mold temperature, increasing the contact temperature always improves adhesion. However, depending on how the contact temperature is achieved, very different levels of adhesion can be observed for the same system. Clearly, contact temperature is not the only variable influencing adhesion.
- **Influence of mold temperature:** Looking at our data for a contact temperature of 190°C, we observe no adhesion if the mold temperature is 135°C, moderate adhesion if the mold temperature is 100°C, and high adhesion if the mold temperature is 20°C. Thus, the mold temperature has a dramatic influence on the adhesion obtained. For cold molds, high adhesion is achieved even at a contact temperature 80°C below T_m . The contact temperature needed for adequate adhesion varies significantly whether the mold was below or above T_g . Obtaining adhesion using hot molds is *more* challenging than when using cold molds, contradicting the general wisdom that “hotter is better” for adhesion.

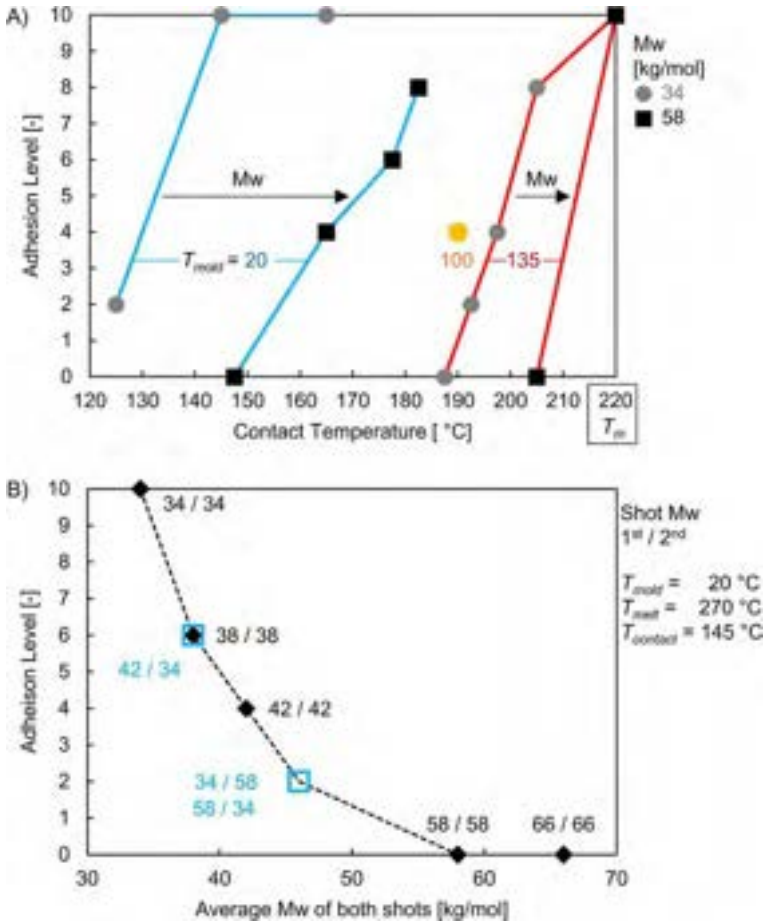


Fig. 11.5 (A) Adhesion level versus contact temperature for varied M_w and mold temperature. (B) Adhesion level versus average M_w of both shots. Lines are guides to the eye.

- **Influence of M_w :** Furthermore, we find a large difference in contact temperatures needed for low and high M_w samples to reach the same adhesion level. The contact temperature required for adequate adhesion is higher for high M_w samples for both hot and cold molds; however, the difference is less for hot molds (Fig. 11.5A). At fixed processing parameters (mold and melt temperatures), we see a gradual decrease in adhesion with increased M_w (Fig. 11.5B). Surprisingly, we observe the same adhesion level if the average M_w of both shots is the same—such as, 58/34 and 34/58 give the same result as do 42/34 and 38/38.

Our observations are consistent with other reported unfilled PA6 overmolding studies. Using insert overmolding of PA6 with a fixed mold temperature of 80 °C and a contact temperature ranging from 160 °C to 190 °C, Qui et al. observed a large increase in adhesion when the contact temperature increased from 160 °C to 170 °C to 180–190 °C and a lower sensitivity to other parameters at the higher contact

temperatures [28]. Pompe et al. observed that increasing the contact temperature from 165°C to 180°C in a direct overmolding of PA6 with mold temperature of 60°C led to a large increase in adhesion [48].

11.3.2 Thermal history of the interface

As we observe substantial adhesion for contact temperatures well below the melting point of PA6, a question naturally arises: Is our contact temperature estimate from Eq. (11.1) correct? The temperatures of the melt entering the mold and of the mold surface can be measured directly. However, if viscous heating occurs, this will underestimate the actual melt temperature and it will vary along the flow path. Fig. 11.6 shows the time evolution of the contact temperature calculated from flow simulations. Viscous heating is negligible for the 34 kg/mol sample and is maximum $\sim 10\text{--}15^\circ\text{C}$ for 58 kg/mol. Using contact temperatures based on Eq. (11.1) may slightly underestimate the temperature for higher M_w samples; however, it is insufficient to lead to contact temperatures higher than T_m for all cases where high adhesion is observed. Another important observation is the interface remains nearly isothermal for $\sim 2\text{ s}$ before cooling.

Thermal modeling also allows us to estimate the cooling and heating rates experienced by the interface. In the near surface region controlling adhesion, the cooling

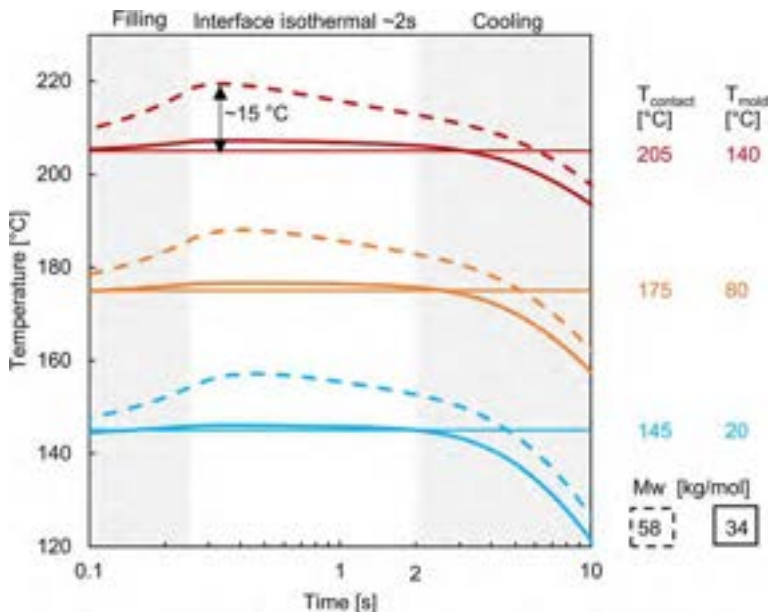


Fig. 11.6 Interface temperature versus time at the end of the flow path during the injection and holding of the second shot with lines indicating $M_w = 34$ (bold line) versus 58 (dashed). Estimated contact temperature from Eq. (11.1) (light line) along with mold temperatures are indicated.

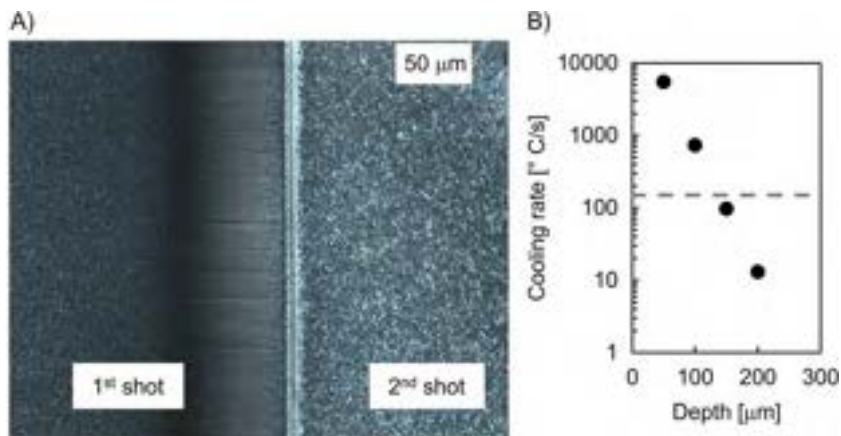


Fig. 11.7 (A) Optical micrograph showing variation in microstructure in the near interface region for a 34 kg/mol sample molded with $T_{\text{mold}}=20^{\circ}\text{C}$ and $T_{\text{melt}}=263^{\circ}\text{C}$. (B) Estimated cooling rate as a function of distance from the mold wall for the first shot surface with a $T_{\text{mold}}=20^{\circ}\text{C}$. Horizontal line indicates 150°C/s , the cooling rate above which amorphization is expected.

rates are $>1000^{\circ}\text{C/s}$ for the surface of the first shot, which contacts the mold. The heating rate when the second shot melt makes contact will be slightly lower due to the lower effusivity of polymers vs metals; however, it will still be extremely rapid. Of course, the cooling rate varies significantly with depth resulting in substantial differences in microstructure, as illustrated in Fig. 11.7A. While the chemical composition of the part does not vary with location, its temperature history and thus microstructure and properties do.

11.3.3 Influence of mold temperature on surface properties

Next, we turn our attention to understanding how the mold temperature affects the material at the first shot surface. As the heating and cooling rates experienced by the interface are extremely high, we use FLASH DSC experiments.

Using FLASH DSC to understand semicrystalline polymers under relevant processing conditions: If a polymer is cooled sufficiently quickly to below T_g , the chains will not have time to organize into crystals and the sample can be quenched in an amorphous glass. If the sample is cooled rapidly but remains above T_g , the polymer chains will eventually crystallize. Industrially relevant processing conditions are almost always in between and result in semicrystalline polymers being metastable materials with microstructures far from equilibrium. The thermal transitions typically reported on data sheets reflect slow cooled samples while the relevant values may be significantly different depending on the thermal and flow history at a given location.

Utilizing FLASH DSC helps here. This technique analyzes very small samples using extremely high heating and cooling rates. Significant strides in the last decade resulted in a versatile tool for studying polymers at industrially relevant cooling rates [49].

It can be used to follow the crystallization kinetics for rapidly crystallizing systems coming either from the melt or from a quenched glass [10]. Note that due to the extremely small sample mass, absolute values of crystallinity cannot be determined but relative crystallinity can be.

The cooling rates experienced when a polymer melt contacts the metal mold surface can easily exceed 1000°C/s . If the mold temperature is below the T_g , the high cooling rates result in an amorphous surface. The amorphization rates for different polyamides have been determined by FLASH DSC: PA6 $\sim 150^{\circ}\text{C/s}$, PA66 $\sim 1800^{\circ}\text{C/s}$, and PA46 $\sim 8000^{\circ}\text{C/s}$ [10]. Thus, PA6 surfaces may be easily quenched during molding with a cold mold while the much more rapidly crystallizing PA46 is unlikely to be fully amorphous. Not only can FLASH DSC mimic the relevant cooling rates experienced during injection molding, but fast heating also avoids reorganizing during analysis (e.g., cold crystallization), which often complicates interpretation [10]. Therefore, we use 1000°C/s for the analysis.

By mimicking the thermal history of the first shot surface, we can determine both the extent of crystallization as well as the thermal stability. Powerfully, we can also use FLASH DSC to study the change in crystallinity at any point during the overmolding process. This allows a snapshot of the structure at different points in time during the process, which is not possible by analyzing samples after molding. Three possible scenarios for the evolution of crystallinity at the surface are illustrated in Fig. 11.8. For a semicrystalline polymer surface, the cooling history determines the extent of crystallization as well as the crystal size and perfection (and hence melting temperature). Therefore, it is important to be able to estimate the melting and crystallization times under the relevant processing conditions.

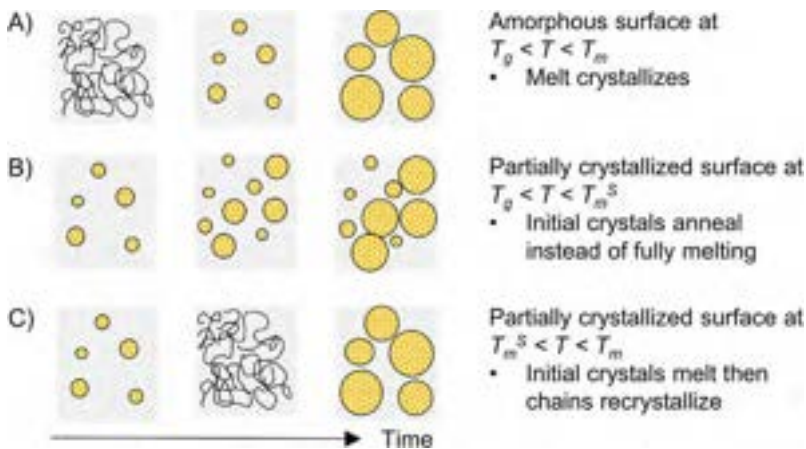


Fig. 11.8 Schematic illustration of different scenarios for semicrystalline interface evolution with time. (A) Initially amorphous system at temperature between the glass transition (T_g) and melting temperature (T_m). Partially crystallized surface at temperature (B) below the melting temperature of the surface crystals (T_m^S) or (C) above the melting temperature of the surface crystals (T_m^S) but below T_m .

Cold molds lead to amorphous surface. Consistent with the estimation from FLASH DSC that a cooling rate of $>150^{\circ}\text{C}/\text{s}$ is sufficient to prevent crystallization of PA6 [10], X-ray experiments (data not shown) confirm that the surface is quenched amorphous to a depth of $>25\ \mu\text{m}$ when the mold temperature is 20°C . It is worth noting that we found that if PA6 samples were stored at ambient conditions, the initially amorphous surface would crystallize over time due to moisture absorption and the associated increase in mobility. This resulted in higher contact temperatures needed to obtain the same level of adhesion for insert overmolding than for direct overmolding when care was not taken to keep the first shots from absorbing moisture. Thus, for insert overmolding, attention should be given to the storage conditions of the samples.

Hot molds lead to partially crystallized surface. FLASH DSC mimicking the first shot surface thermal history for a mold temperature of 140°C is shown in Fig. 11.9A. This mold temperature leads to a partially crystallized surface but whose crystals are imperfect and melt at temperatures well below T_m . To understand how this

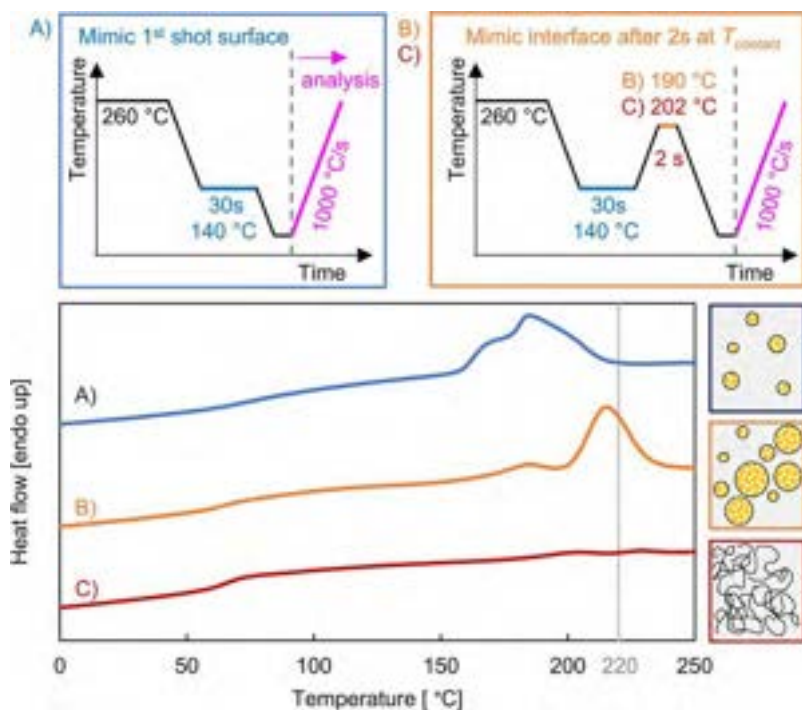


Fig. 11.9 (Top) FLASH DSC thermal histories mimicking (A) the first shot surface for mold temperature of 140°C and the interface after 2 s at contact temperature of (B) 190°C or (C) 202°C . Heating and cooling rates were $1000^{\circ}\text{C}/\text{s}$. *Dashed lines* separate thermal history from final heating segment used for analysis. (Bottom) Corresponding heat flow from the final heating for each thermal history. Cartoons represent resulting microstructure (A) Partially crystallization with crystals that melt $<220^{\circ}\text{C}$; (B) initial crystallinity anneals and increases thermal stability at contact temperature of 190°C ; (C) initial crystallinity fully melts at contact temperature of 202°C . The nominal melting temperature is denoted by the *vertical line* at 220°C .

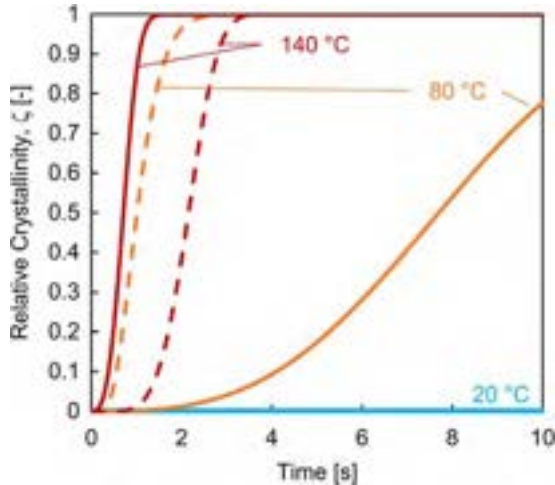


Fig. 11.10 Relative crystallinity versus time for mold temperatures of 20°C, 80°C, and 140°C. *Solid lines* indicate the surface while *dashed lines* represent a depth of 100 μm from the surface.

surface evolves when contacted by the melt, a 2 s isothermal hold at either 190°C or 202°C is added to the thermal history, denoted as B and C in Fig. 11.9. When the second shot melt makes contact, the initial crystals may either anneal, leading to increased crystal perfection and thermal stability, or they may melt, as illustrated in Fig. 11.8. This is what we observe for contact temperatures of 190°C and 202°C, respectively. This change in behavior coincides with the transition from non-adhering to high adhesion between contact temperature of 190–200°C when the mold temperatures is 135°C (see Fig. 11.5).

Impact of mold temperature on extent of crystallization. Fig. 11.10 shows the relative crystallinity of the surface versus time for different mold temperatures modeled using an approach based on Schneider rate equations and FLASH DSC data [50–53]. A 20°C mold results in an amorphous surface where hotter molds result in highly crystallized surfaces. While this modeling estimates the relative crystallinity, it is important to remember that the absolute extent of crystallization and the crystal perfection will be influenced by the thermal history determined by the mold and melt temperatures. Hence, the temperatures at which the crystals melt will differ for mold temperatures of 80°C and 140°C and can be evaluated with FLASH DSC. Also included in Fig. 11.10 is the relative crystallinity at a depth of 100 μm from the mold. While the surface crystallizes faster than the bulk for a mold temperature of 140°C, it crystallizes slower when the mold temperature is 80°C. This highlights the non-triviality of the impact of mold temperature on crystallization behavior.

11.4 Requirements for strong polymer interfaces

The development of adhesion for polymer/polymer interfaces has been extensively studied and excellent reviews of the topic are available [1,2,7,8,54,55]. Here, we will review key insights into the factors governing adhesion for linear nonreactive

thermoplastics. We focus on rigid, high-yield stress systems where there is limited deformation away from the interface, as the interfacial strength is more critical for these systems than for softer systems where substantial bulk deformation can be achieved with low interface strength. We begin by considering amorphous interfaces because there is a greater understanding of the molecular mechanisms governing interface strength.

Amorphous Polymer Interfaces. To obtain a reasonably tough polymer interface, stress must be transferred across the interface, preferably up to the level of the yield stress. For nonreactive systems, this requires that chains are mobile. Intimate contact is a prerequisite for chains to cross the interface.

For polymer systems, long range diffusion requires reptation as rouse-like motion cannot provide entanglement across the interface and will be ineffective at generating high-strength interfaces [1,56]. The timescale for the broadening of the interface can be estimated using reptation theory [54] where chain ends progressively escape from their initial tubes to cross the interface [57]. The memory of the interface will be erased when the entire chain has escaped its initial tube, that is, a diffusion distance equal to the end-to-end distance of the chain (R_g).

The interface toughness grows with the square root of time and is proportional to the areal density of interfacial entanglements; it plateaus when the interface entanglement density equals that of the bulk. Experimental and molecular dynamics studies have shown the interface reaches the bulk strength and toughness at times less than the time required for chains to move a distance of R_g [55]. If the interface width is less than the order of magnitude of an entanglement length, chains are not effectively anchored, and strengths are low due to pull-out. As the interface width increases, chains form entanglements that are effective at transferring stress across the interface, and interface strength increases until it reaches the bulk value. With increasing M_w , the bulk toughness increases until a plateau is reached. While we focus on the simpler case of symmetric interfaces, for asymmetric interfaces the same argument holds where the compatibility of the materials must be considered, and the interfacial width can be predicted using the Flory-Huggins theory.

Semicrystalline Polymer Interfaces. Entanglement across the interface is also critical for semicrystalline polymer interfaces, as it results in stress transfer among chains across the interface. While some welding experiments have observed adhesion at semicrystalline interfaces in contact below their melting point, the interfacial strengths are low and the times required long [8]. Without entanglement and anchoring of chains at the interface, adhesion is low [57]. Additionally, cocrystallization across the interface without entanglement does not produce robust interfaces [58,59]. Entanglement must occur followed by formation of crystallinity sufficient that the entanglements are trapped between crystals so they can't just slip out under stress [60].

In addition to the same challenges for understanding adhesion of amorphous polymer interfaces, semicrystalline interfaces pose at least three additional challenges.

The first challenge is understanding the initial conditions of the interface. As the amount and stability of crystals will depend on the thermal history, it is not surprising that the adhesion development is strongly influenced by whether the surface is amorphous or partly crystallized when contact is made [7,8,36].

The second challenge is to determine how the level of crystallinity retards interdiffusion. This is still a matter of debate; however, there is general agreement that any model must account for crystallinity hampering amorphous chain segment mobility [8,61]. Under conditions where crystallinity is absent, the same reptation theory may be used to estimate interdiffusion times as for amorphous systems [8,18,62,63].

The third challenge is to understand the evolution of crystallinity at the interface. As the amount of crystallinity can change due to melting or crystallization, the rate of interdiffusion will also change [27]. If at least one of the surfaces is partly crystallized when contact is made, then reptation will initially be hampered. However, if the temperature is sufficient to cause crystal melting, then the interdiffusion rate will increase to that of the melt. But the system may then recrystallize, reducing the interdiffusion rate again. If the temperature is too low, the initial crystals will simply anneal rather than melt hindering any interdiffusion.

11.4.1 Conditions needed for strong semicrystalline polymer interfaces

Based on insights from the literature, the following criteria must be satisfied to obtain reasonable adhesion for semicrystalline polymer interfaces:

- Surfaces must be brought into intimate contact.
- Chains must be mobile enough to diffuse across the interface.
- Sufficient entanglement must occur before crystallization or cooling retards chain mobility.
- Chains must be anchored after crossing the interface.

If samples are solidified when brought into contact, such as for hot pressing, the time to form contact can be rate limiting [16,64]. In contrast, during overmolding, a melt is brought in direct contact with the solidified surface and the pressurized flow means intimate contact is established almost instantaneously. Whether the other conditions are met for a given set of processing conditions will depend on the kinetics of crystallization and the nature of the first shot surface, as illustrated schematically in Fig. 11.11.

11.4.2 Quantifying competition between interdiffusion and crystallization

To quantitatively evaluate if our proposed mechanism for adhesion is consistent with our experimental observations, we must be able to determine the following:

- How far do chains need to move?
- How much time does it take for the chains to move that far?
- How much crystallinity is sufficient to greatly retard or stop interdiffusion?
- How much time does it take to reach that level of crystallinity?

In the next sections, we walk through the details of our approach.

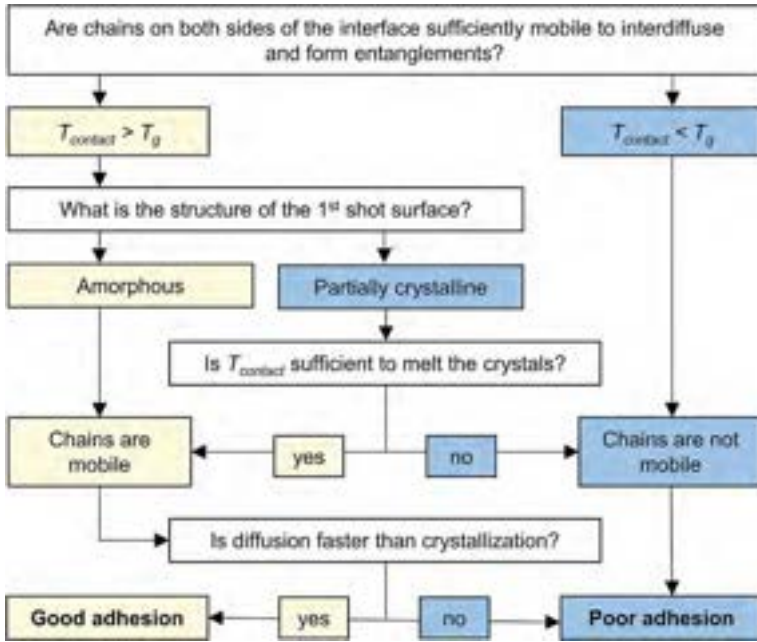


Fig. 11.11 Flow chart illustrating conditions where chains on both sides of the interface have sufficient mobility to interdiffuse and form entanglements resulting in good adhesion.

Time required to obtain an entangled interface: The time (t) required for chains to diffuse across the interface and form sufficient entanglements to give adequate strength is given by

$$t = \frac{d^2}{D} \quad (11.3)$$

where D is the self-diffusion coefficient and d is the distance chains need to move to form effective crossing at the interface.

How far do chains need to diffuse? At minimum, d should be equal to the distance between entanglements (R_e) and at maximum equal to R_g (full erasure of the interface memory). Based on work for glassy systems both experimentally [56,65] and from molecular dynamics [55], we select a minimum distance equal to $2R_e$.

How fast do chains move? For a chain to cross the interface and form entanglements, segmental relaxation is not sufficient [66,67] and the center of mass of the chain has to move via reptation [68]. The diffusion rate will depend on the contact temperature. Following the approach of Graessley [69], we estimate D for different temperatures and M_w , as shown in Fig. 11.12. At a given temperature, diffusion is ~ 2.9 times faster for M_w of 34 than for 58 kg/mol.

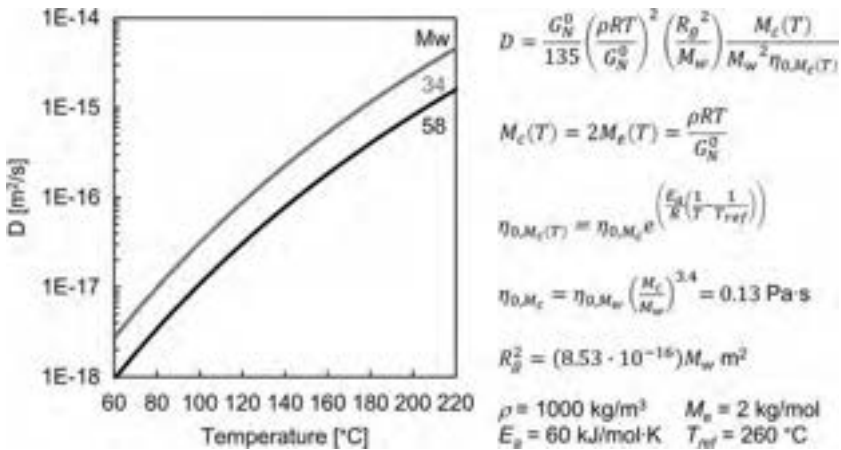


Fig. 11.12 Self-diffusion coefficient versus temperature for PA6 with $M_w = 34$ or 58 kg/mol calculated using expressions and values shown on the right. (R is the ideal gas constant, T is the absolute temperature, R_g^2 is the mean square end-to-end distance of the chain, $M_c(T)$ is the critical M_w weight at temperature T , M_e is the entanglement M_w , and η_0 is the zero-shear viscosity for M_c at temperature T . We use the values determined by Fetters [70] for PA6, $M_e = 2$ kg/mol, $R_g^2 = M_w \times 8.53 \times 10^{-16}$ m² and a constant $\rho = 1000$ kg/m³. The value for η_{0, M_c} is derived from the measured zero shear viscosity of 1139 Pa·s for a sample with $M_w = 57.7$ kg/mol at 260°C. From melt rheology, we estimate the flow activation energy (E_a) at 60 kJ/mol·K. Consistency of relaxation times predicted with these parameters and the measured melt rheology for different M_w are excellent (data not shown).)

Time available before crystallization stops diffusion: As chain diffusion will be retarded or stopped by crystallization, the next questions are how much crystallinity is sufficient to effectively stop interdiffusion and how long does it take to develop?

How much crystallinity is sufficient to retard interdiffusion of chains across the interface? There is little information available to guide the estimation of how much crystallinity is sufficient to retard interdiffusion. Once sufficient crystallinity has developed to form a gel, there could be an entropic swelling penalty for chains entering. Alternatively, if a chain is anchored in a crystal, it may be prevented from long range diffusion as it cannot drag the crystal along.

Pogodina and Winter combined rheology measurements with crystallization models to estimate that a critical gel (e.g., $\tan \delta = G''/G' < 1$ equivalent to phase angle, δ , < 45 degrees) was formed at absolute crystallinity level $< 2\%$ for iPP and speculated that this may be similar for other thermoplastics [61]. The same group found that the time required to form a critical gel was independent of M_w [71]. They draw an analogy between the behavior of the critical gel at low levels of crystallinity with a melt of multiarm polymer stars, which would dramatically increase the relaxation time of the system relative to a linear melt.

Using combined rheo-DSC experiments allows the extent of crystallization and resulting changes in rheology to be measured simultaneously [72,73]. Rheo-DSC results for PA6 at 205°C are presented in Fig. 11.13 showing the phase angle δ at

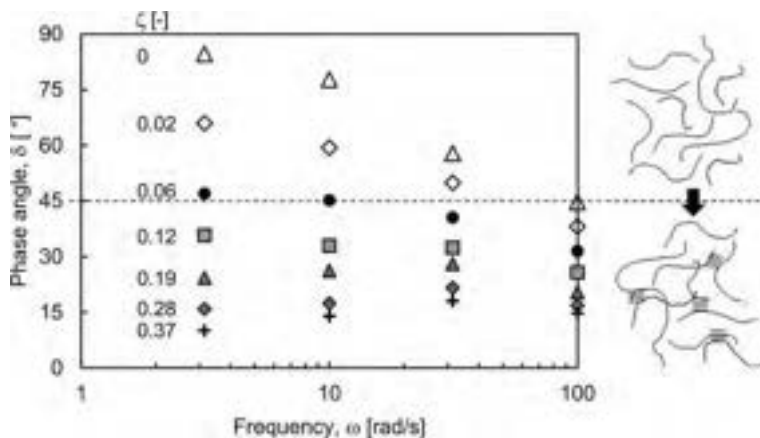


Fig. 11.13 Phase angle versus frequency for PA6 at 205°C at different levels of relative crystallinity (ζ) determined from Rheo-DSC experiments [73]. We appreciate the permission to include this unpublished data. Cartoons illustrate transition from melt to critical gel at crystallinity of 1.8 wt% ($\zeta=0.06$).

low frequencies is <45 degrees when the relative crystallinity is 0.06. This yields an estimate of the critical crystallinity for gel formation of 1.8 wt% by assuming a final crystallinity of 30 wt%. Given the surprisingly good agreement between these estimates of the critical crystallinity despite the difficulty in accurately determining low amounts of crystallinity, we will use 1.5 wt% as an estimate for when the interdiffusion would be substantially retarded.

How much time does it take to reach the critical crystallinity? Using the direct methodology for following polyamide crystallization with FLASH DSC as described by vanden Poel et al. [10], the development of the relative crystallinity versus time was determined at different temperatures coming either directly from the melt or from a quenched glassy state, as illustrated in Fig. 11.14. Clock-curves of time required to reach a specific crystallinity versus isothermal crystallization temperature can then be constructed. Typically, crystallization half-times are reported (time to reach 50% relative crystallinity). However, based on the rheological estimation that only a small level of crystallinity is sufficient to form a critical gel and retard interdiffusion, the time to reach 1.5 wt% crystallinity is the relevant threshold for our problem.

A few features are worth noting in Fig. 11.14. First, crystallization rates coming from the melt are significantly slower than coming from a quenched glass. Quenching leads to a higher number of nuclei being formed, leading to the increased crystallization rate [74]. Second, the influence of M_w is negligible when crystallizing from a glass. Third, the difference in time needed to reach 1.5 wt% crystallinity does not vary significantly between 34 and 58 kg/mol. This makes sense if at very low levels of crystallinity, nucleation rather than growth dominates the timescale. Based on these observations, we assume the critical timescale for crystallization is insensitive to M_w .

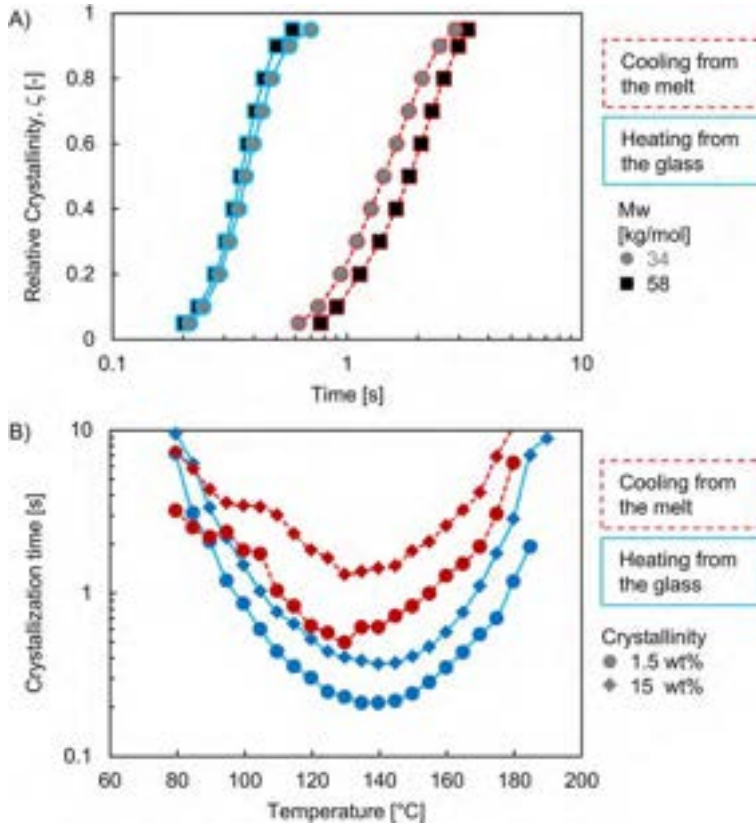


Fig. 11.14 (A) Relative crystallinity conversion versus time at 140°C either coming from the melt or from a quenched glass. (B) Time to reach either 1.5 or 15 wt% crystallinity (equivalent to crystallization half-time) for $M_w = 34$ kg/mol for different isothermal crystallization temperatures.

Now that we have criteria that allow for the quantitative estimation of the critical time for interdiffusion and crystallization, they can be compared to map out contact temperatures at which adhesion is or is not expected. The approach is summarized qualitatively in Fig. 11.15.

11.4.3 Comparing interdiffusion and crystallization timescales for PA6

Fig. 11.16 shows the estimated time required for interdiffusion length of $2R_c$ and for crystallinity to reach 1.5 wt% at different temperatures for PA6. From this model, the contact temperatures at which diffusion becomes faster than crystallization are estimated as 130°C and 152°C for $M_w = 34$ and 58 kg/mol, respectively. This is in good agreement with data in Fig. 11.5 for $T_{mold} = 20^\circ\text{C}$ where an adhesion level of ~ 4 –5 is observed at $\sim 135^\circ\text{C}$ and $\sim 165^\circ\text{C}$, respectively.

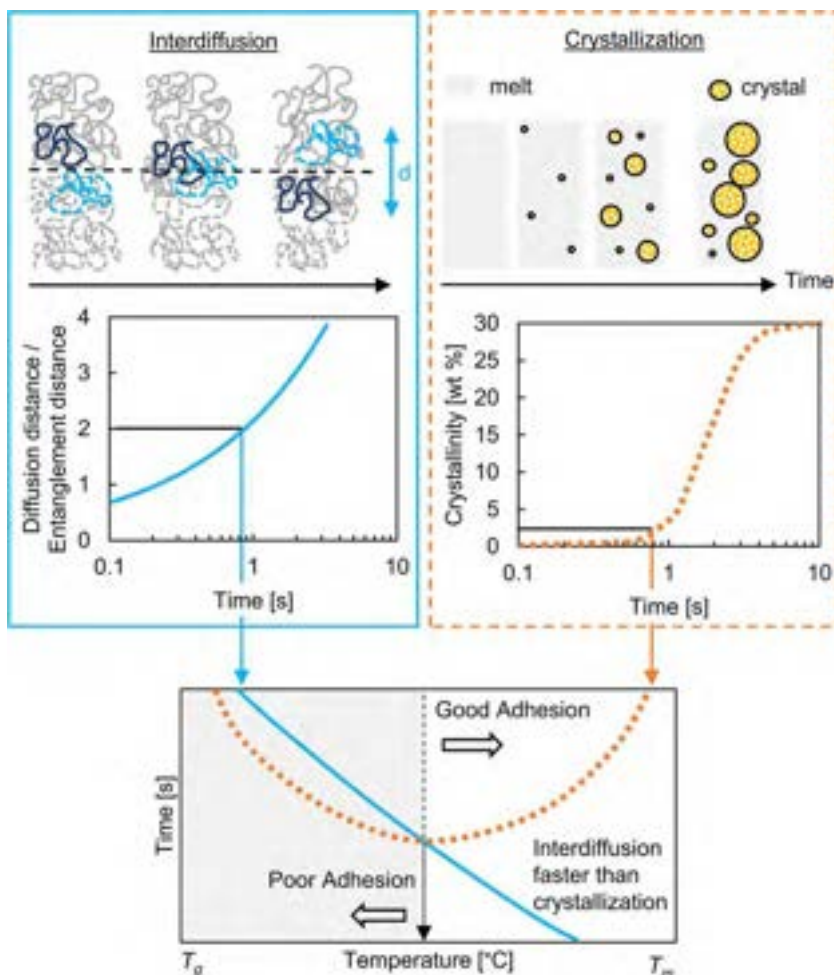


Fig. 11.15 Schematic illustrating the competing timescales governing interfacial strength for semicrystalline polymers. The first is the time required for chain diffusion such that sufficient entanglements are formed at the interface to give high strength. The second is the time required for sufficient crystallization to retard long-range diffusion. By comparing these timescales at each temperature, the range of contact temperatures where good adhesion is expected can be estimated.

As the calculated timescales for diffusion and crystallization are below the 2 s over which the interface remains at a constant temperature, as shown in Fig. 11.6, our assumption of isothermal interface formation is valid. This is also consistent with the assumptions we made with our overmolding experiments where the first shot surfaces were quenched amorphous due to cold molds.^a If complete erasure of the

^a Additional experiments with a 20°C mold and a contact temperature of ~155–163°C with a second shot thickness of 5 mm substantially increased the time the interface remained isothermal but had no impact on the interface strength determined by DCB, as would be expected from the model.

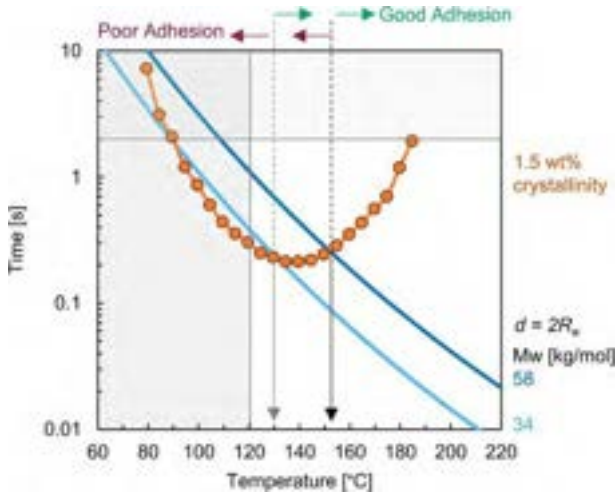


Fig. 11.16 Comparison of time required for chains to interdiffuse a distance of two entanglements and for 1.5 wt% crystallinity to be reached coming from a quenched glass. *Arrows* indicate the contact temperature above which good adhesion is expected because diffusion is faster than crystallization for $M_w = 34$ and 58 kg/mol. *Gray regions* indicate limits of experiments: *horizontal line* at 2s indicates time interface remains isothermal, *vertical line* is lowest contact temperature explored. Note diffusion time estimates become unreliable as the temperature approaches T_g (60°C).

interface was necessary (e.g., $d = R_g$), then the contact temperatures required for adhesion would be much higher than what we observe experimentally. If rouse-like motion was sufficient, then no crossover between low and high adhesion would be observed, as these timescales would always be much faster than crystallization.

For the cases when the first shot surface is partially crystallized due to higher mold temperatures, we do not predict the contact temperatures required for achieving adhesion. In this situation, the melting of the initial crystallinity must occur before interdiffusion can proceed, and this is expected to be the limiting step. Once sufficient melting has occurred to allow chains to diffuse across the interface, diffusion is much more rapid than recrystallization. Thus, the key criterion for hot molds is that the contact temperature be sufficiently high to melt the initial crystallinity. Due to initial rapid cooling, these crystals will melt at temperatures below the nominal T_m . The thermal stability of the crystals at the first shot surface is not very sensitive to M_w , which may explain why we observe less sensitivity to M_w when the first shot surface is partly crystallized.

Note that at low temperatures ($<90^\circ\text{C}$), the model predicts that crystallization becomes slower than diffusion for the low M_w , suggesting that there may be a second region where good adhesion could be expected if the interface remains isothermal sufficiently long. These contact temperatures are outside the range accessible with overmolding. The self-diffusion coefficients (and hence diffusion times) are likely

overpredicted in this temperature region close to T_g as we have extrapolated using the flow activation energy in the melt region. Further experiments exploring this region would be interesting.

The modeling approach here makes some strong assumptions. First, it assumes monodisperse chains to determine the interdiffusion time. Given that PA6 is a condensation polymer with $M_w/M_n \sim 2$, we expect limited impact of this assumption; however, for systems with broad M_w distribution, it becomes nontrivial to estimate reptation times as short chains can accelerate the mobility of long chains. Additionally, all chains are assumed to be linear. Second, potential impacts of flow or pressure on crystallization or diffusion rate are ignored. Third, the model presented above neglects viscous heating and assumes that the contact temperature is well described by Eq. (11.1). As shown in Fig. 11.6, this is a very good description for $M_w = 34$ kg/mol but seemingly underestimates the contact temperature for $M_w = 58$ kg/mol by ~ 10 – 15°C . Viscous dissipation creates regions of higher temperature in the second shot that are located not directly at the interface but slightly deeper as the shear rate is maximum slightly below the surface. This heat will reach the interface via conduction, which takes time (as seen in Fig. 11.6 where the maximum contact temperature is reached slightly after the filling stage is complete). In contrast, interdiffusion and crystallization at the interface begin as soon as contact is made, and the temperature is above T_g —conditions fulfilled during the filling stage. The contact temperature for the higher M_w , 58 kg/mol during the filling stage is only about $\sim 5^\circ\text{C}$ higher than estimated from Eq. (11.1). Because most of the interdiffusion and crystallization occurs during filling, it is this contact temperature that is relevant for determining the higher M_w sample behavior. As the impact of viscous heating is small, it does not alter the prediction that the 34 kg/mol will have good adhesion at lower nominal contact temperatures than the 58 kg/mol.

The model does a surprisingly good job of describing the onset of adhesion with increasing contact temperature when the first shot surface is initially amorphous. We further validated these predictions using film sealing experiments (data not shown) and again saw excellent agreement between the conditions predicted from the model and the experimental observations. We note that the model is appropriate for understanding the transition between no and high adhesion, which is particularly helpful for steering processing conditions rather than predicting the absolute interfacial strength.

11.5 Summary of overmolding experiments and insights from quantifying crystallization and diffusion timescales

The key observations from the PA6 overmolding experiments are:

- It is not necessary to have a contact temperature higher than T_m to obtain high adhesion.
- For a given mold temperature, adhesion increases with increased contact temperature.
- The large difference in adhesion observed at the same contact temperature for cold and hot molds is related to whether the first shot surface was quenched amorphous or partly crystallized.

- Increasing M_w requires increased contact temperatures to obtain adhesion; however, the influence is larger when the first shot is quenched amorphous than when it is partly crystallized.
- FLASH DSC is a powerful tool for understanding the influence of thermal history on the extent and stability of the crystallinity at the first shot surface as well as the isothermal crystallization rates.
- The melting temperature of crystals formed at the surface during molding of the first shot depends on the mold temperature used and can be significantly lower than the nominal T_m .

From the experimental observations and model comparing interdiffusion and crystallization times, we offer guidelines for the formation of strong, semicrystalline polymer interfaces:

- The contact temperature required for the onset of significant adhesion when the surface is amorphous is well described by the crossover between the time required for chains to form two entanglements at the interface and that needed to reach 1.5 wt% crystallinity.
 - M_w strongly influences the interdiffusion time but has little impact on the critical crystallization time.
- To obtain high adhesion, any initial surface crystallinity must sufficiently melt to allow interdiffusion.
 - At low contact temperatures, insufficient melting occurs to allow interdiffusion. Instead, crystallinity anneals, resulting in low adhesion.
 - At higher contact temperatures, interdiffusion will be very rapid. However, the initial crystallinity requires time to melt sufficiently to enable chain diffusion. This is likely the limiting timescale as recrystallization will be slow.
- All things being equal, it is easier to form a high-strength interface when:
 - Diffusion is rapid: lower M_w , linear chains, higher melt temperatures.
 - Crystallization is slow: A long induction time is beneficial.
 - The surface is quenched amorphous (mold temperature $< T_g$) or has limited crystallinity with low thermal stability (colder molds).

These results demonstrate that it is possible to obtain good adhesion for semicrystalline polymer interfaces at contact temperatures well below T_m as long as the first shot surface is quenched amorphous or any crystallinity can melt. However, for high-performance fast-crystallizing polymer systems such as PA46, satisfying these conditions for flat interfaces is extremely difficult. In the next section, we demonstrate that adjusting the geometry of the interface can enable local melting, resulting in high adhesion for such systems.

11.6 Exploiting geometry to achieve adhesion

The concept of using interfacial geometry (IFG) to promote adhesion relies on the use of surface protrusions to obtain a favorable ratio of the solid surface area to melt volume. If the heat available to flow into a protrusion is sufficient to cause local melting, it will result in a type of spotwelding [40,41]. The question is then what surface structures (size, spacing, geometry) are best? Additionally, the mold structuring should be easy and cheap, and the part must be able to be demolded without defects, which limits

the possible structures (no undercuts). IFGs in overmolding have some conceptual similarities with using protrusions as energy directors in ultrasonic welding of thermoplastic composites [75].

We simulated the effect of IFGs on the thermal history using the modeling approach described previously with boundary conditions allowing the simulation of periodic structures. To model the behavior of a single IFG, we chose the distance between two IFGs equal to 20 times the width of the IFG, which is sufficient to mimic an isolated IFG. Overmolding experiments were performed using PA46 and mold insert surfaces were textured via ion beam etching.

Fig. 11.17A shows the temperature at the tip of a triangular rib and a flat area of the interface versus time. At the tip of the rib, the temperature exceeds the melting point for more than 1 s. In contrast, the flat interface does not exceed the nominal contact temperature estimated from Eq. (11.1). To validate the predictions from thermal modeling, overmolding experiments were performed using PA46. A large increase in adhesion was obtained relative to a flat surface at the same settings (Fig. 11.17B), and optical micrographs confirm that local melting of the rib tip was achieved (Fig. 11.17C). By varying process conditions or rib height, we were able to change the amount of melting that occurred and found excellent agreement with the predictions of thermal modeling (Fig. 11.17D). Heat flux simulations not only give insight into whether a given geometry, molding conditions, and material parameters are sufficient to achieve melting, but also into how long the material will remain molten and allow for interdiffusion.

The use of IFGs can lead to melt-to-melt contact in overmolding at conditions where no melting occurs for flat interfaces. By promoting melting, IFG results in improved adhesion for material combinations where the adhesion is created by either interdiffusion or chemical reaction. Thermal modeling allows the IFG to be optimized for a particular situation. For example, density of features, aspect ratio, tip angle, etc., can be easily simulated to determine the structure that is the best compromise between enabling melt-to-melt contact and manufacturability. With appropriate knowledge of the materials and processing, overmolding conditions can be chosen to obtain good adhesion for a variety of applications. Flow can lead to deformation of molten IFG, so orientation of ribs with respect to both flow path and loading path is important. To attempt to control these orientation effects, the IFG orientation can be rotated at different locations along the surface. In some cases, deformation can result in hook-like geometries that may further enhance the interfacial strength.

11.7 Outlook and conclusions

The development of adhesion for semicrystalline polymer interfaces can be understood as a competition between interdiffusion to form entanglements and crystallization. We show that hotter is not always better for obtaining adhesion in overmolding. The initial morphology of the interface as well as the contact temperature and M_w have large influences on the conditions at which adhesion will be achieved. Contact temperatures do not need to exceed the nominal melting point if the surface can be

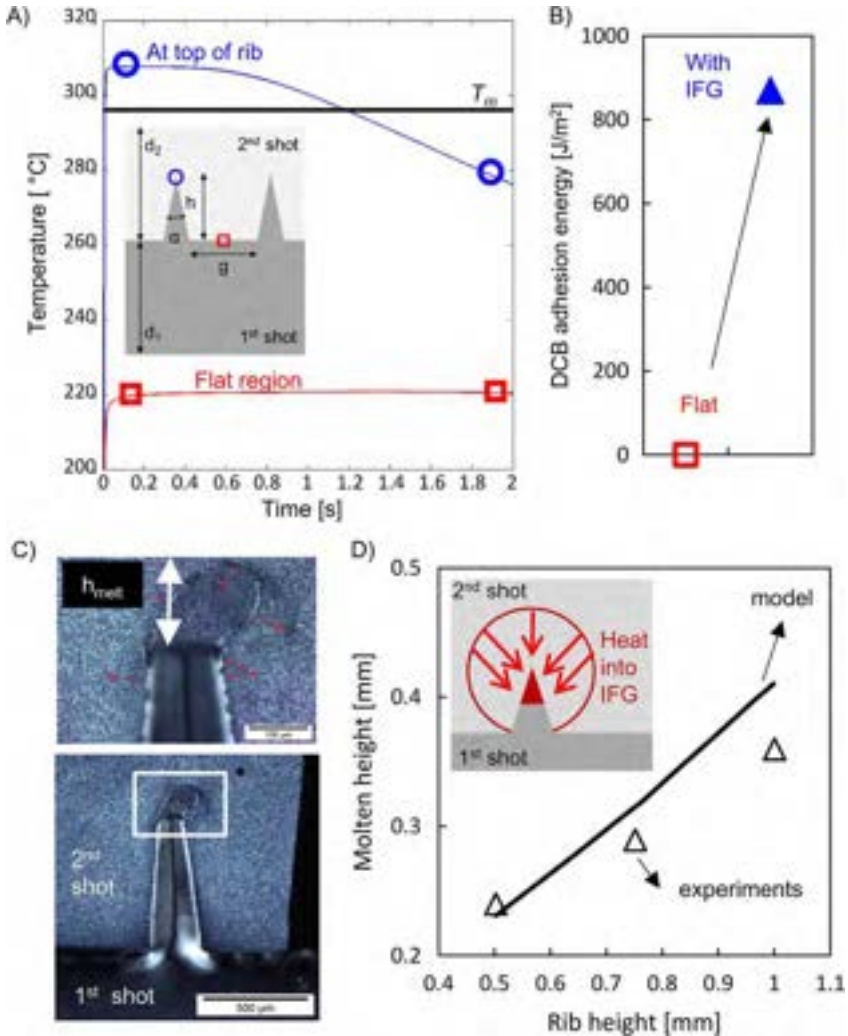


Fig. 11.17 (A) Temperature versus time for tip of the rib and flat surface for PA46 for triangular ribs with dimensions $h = g = 1$ mm, $d_1 = d_2 = 2$ mm, $\alpha = 15$ degrees when $T_{mold} = 120^\circ\text{C}$ and $T_{melt} = 315^\circ\text{C}$ and $T_m = 295^\circ\text{C}$. (B) Increase in adhesion observed when these IFGs are used instead of a flat interface. (C) Optical micrographs showing local melting at rib tip. (D) Comparison of maximum molten height from experiments and modeling for different rib heights.

quenched amorphous; we observed very high adhesion at contact temperatures 80°C below the melting point of PA6. The general ideas in the approach and model can be applied to other polymer materials and processes, provided the relevant timescales can be estimated from rheology and FLASH DSC experiments and the thermal history of the interface is understood.

While overmolding experiments with unfilled polymers offer an excellent approach to study the competition between interdiffusion and crystallization on interface strength, many applications will present additional challenges. For filled systems, the influence of filler orientation will impact the mechanics significantly and, obviously, fillers will not bridge the interface, leading to an intrinsically weaker layer even if full molecular healing is achieved. Additionally, shear may result in highly oriented layers near the interface whose properties may differ significantly from the bulk. As interfaces are far from equilibrium during processing, postmolding thermal history can potentially cause reorganizations that can influence adhesion. Annealing after bond formation may strengthen the interface due to increased crystallinity.

There is potential for tuning interface strength via manipulation of either diffusion or crystallization timescales. As we observe that the critical level of crystallinity is very low for reducing interdiffusion, approaches that would lead to a long induction time followed by rapid crystallization would be attractive, as they would allow for interface adhesion to develop without sacrificing short cycle times. Likewise, as adhesion is dominated by distances of $< R_g$, additives that increase bulk crystallization rates may not be present or effective at the interface. In this case, the bulk crystallization rate can be increased for faster cycle times without affecting overmolding adhesion. Another exciting possibility arising from control of the interface entanglement and crystallinity is to gain potential control over debonding to facilitate design for recycling [30]. Systems with initially low M_w allow for rapid interdiffusion and strong interfaces could undergo post treatment such as postcondensation to increase the final M_w and impart favorable properties, an approach that could be utilized in 3D printing. Polyamide powder reuse in selective laser sintering (SLS) is hampered by postcondensation occurring in the print bed, resulting in increased M_w that reduces diffusion and adhesion [76]. As pointed out by Vaes and Puyvelde in their extensive overview of semicrystalline polymer filament-based 3D printing [14], the limited number of systematic studies related to interlayer adhesion in those cases relates to crystallization complicating the welding time analysis. The conceptual approach laid out here could be of use in rationalizing the experimental observations as well as extending models to predict the weld strength of semicrystalline polymers more accurately for filament-based printing applications.

This work demonstrates that overmolding experiments are an excellent tool for understanding the fundamentals of semicrystalline interfaces because they access timescales well matched to the relevant molecular processes. A key contribution of this work is that both the interdiffusion and crystallization timescales are quantified at processing relevant conditions for PA6. Similar studies using other polymer systems or exploring a broader range of conditions would be interesting. Coupling the refined thermal modeling approach of Adhikari et al. [9] with crystallization rate and interfacial strength measurements would further refine insights into the controlling physical processes. We focused on the short-term strength of semicrystalline interfaces; however, long-term fatigue performance can be critical and future work exploring whether the same criteria in terms of number of interfacial entanglements also holds for fatigue would be valuable.

Acknowledgments

We dedicate this work to the late, inspiring Dr. Arnaud Chiche, who was a joy to work with and instrumental in the authors' understanding of adhesion phenomena. The authors are grateful to DSM Engineering Materials for supporting and enabling this work. All authors were employed at DSM at the time the work was performed. Substantial contributions from many DSM colleagues are included: Jos Kersemakers, Niels Stijnen, Daniel Istrate, Geert van den Poel, Wim Zoetelief, Peter Roozmond, and Patrick van Soelen were instrumental. We also thank Hugh Brown, Ed Kramer, and Costantino Creton for feedback as well as Peter van Puyvelde for permission to include the Rheo-DSC measurements.

References

- [1] H.R. Brown, The adhesion between polymers, *Annu. Rev. Mater. Sci.* 21 (1) (1991) 463–489, <https://doi.org/10.1146/annurev.ms.21.080191.002335>.
- [2] C. Creton, E.J. Kramer, H.R. Brown, C.Y. Hui, Adhesion and fracture of interfaces between immiscible polymers: from the molecular to the continuum scale, in: *Molecular Simulation Fracture Gel Theory*. Advances in Polymer Science, vol. 156, Springer, Berlin, Heidelberg, 2001, pp. 53–136, https://doi.org/10.1007/3-540-45141-2_2.
- [3] R.P. Wool, *Polymer Interfaces: Structure and Strength*, Hanser Publishers, 1995.
- [4] R.P. Wool, D.M. Bailey, A.D. Friend, The nail solution: adhesion at interfaces, *J. Adhes. Sci. Technol.* 10 (4) (1996) 305–325, <https://doi.org/10.1163/156856196X00724>.
- [5] Y. Men, Critical strains determine the tensile deformation mechanism in semicrystalline polymers, *Macromolecules* 53 (21) (2020) 9155–9157, <https://doi.org/10.1021/acs.macromol.0c02076>.
- [6] G. Jousse, *Self Adhesion of Semi-Crystalline Polymers Between Their Glass Transition Temperature and Their Melting Temperature (PhD thesis)*, L'Université Paris VI, 2004.
- [7] F. Awaja, Autohesion of polymers, *Polymer* 97 (2016) 387–407, <https://doi.org/10.1016/j.polymer.2016.05.043>.
- [8] R. Akkerman, S. Wijskamp, M. Bouwman, Analysis of the thermoplastic composite overmolding process: interface strength, *Front. Mater.* 7 (2020) 27, <https://doi.org/10.3389/fmats.2020.00027>.
- [9] S. Adhikari, C.J. Durning, J. Fish, J.W. Simon, S.K. Kumar, Modeling thermal welding of semicrystalline polymers, *Macromolecules* (2022), <https://doi.org/10.1021/acs.macromol.1c02612>.
- [10] G. vanden Poel, D. Istrate, V. Mathot, Full-temperature-range crystallization rates of polyamides by fast scanning calorimetry as key to processing, in: C. Schick, V. Mathot (Eds.), *Fast Scanning Calorimetry*, Springer International Publishing, New York, 2016, pp. 611–632, https://doi.org/10.1007/978-3-319-31329-0_1.
- [11] R. Massaro, P. Roozmond, P. Van Puyvelde, Flow-induced crystallization of polyamide-6, *Int. Polym. Process.* 33 (3) (2018) 327–335, <https://doi.org/10.3139/217.3524>.
- [12] L. Turng, Special and emerging injection molding processes, *J. Inject. Mold. Technol.* 5 (3) (2001) 160–179.
- [13] A. Das, C.A. Chatham, J.J. Fallon, C.E. Zawaski, E.L. Gilmer, C.B. Williams, M.J. Bortner, Current understanding and challenges in high temperature additive manufacturing of engineering thermoplastic polymers, *Addit. Manuf.* 34 (2020), 101218, <https://doi.org/10.1016/j.addma.2020.101218>.

- [14] D. Vaes, P. Van Puyvelde, Semi-crystalline feedstock for filament-based 3D printing of polymers, *Prog. Polym. Sci.* 118 (2021), 101411, <https://doi.org/10.1016/j.progpolymsci.2021.101411>.
- [15] P. Meka, F.C. Stehling, Heat sealing of semicrystalline polymer films. I. Calculation and measurement of interfacial temperatures: effect of process variables on seal properties, *J. Appl. Polym. Sci.* 51 (1) (1994) 89–103, <https://doi.org/10.1002/app.1994.070510111>.
- [16] W.J.B. Groupe, L.L. Warnet, B. Rietman, H.A. Visser, R. Akkerman, Optimization of the tape placement process parameters for carbon–PPS composites, *Compos. A: Appl. Sci. Manuf.* 50 (2013) 44–53, <https://doi.org/10.1016/j.compositesa.2013.03.003>.
- [17] C.M. Stokes-Griffin, P. Compston, Investigation of sub-melt temperature bonding of carbon-fibre/PEEK in an automated laser tape placement process, *Compos. A: Appl. Sci. Manuf.* 84 (2016) 17–25, <https://doi.org/10.1016/j.compositesa.2015.12.019>.
- [18] E. Lafranche, T. Renault, P. Krawczak, Effect of the interdiffusion at the polymer/polymer interface on the flexural properties of over-moulded short glass fibre/glass fabric reinforced PA6 composites, *Key Eng. Mater.* 611 (2014) 821–828, <https://doi.org/10.4028/www.scientific.net/KEM.611-612.821>.
- [19] R. Giusti, G. Lucchetta, Analysis of the welding strength in hybrid polypropylene composites as a function of the forming and overmolding parameters, *Polym. Eng. Sci.* 58 (4) (2018) 592–600, <https://doi.org/10.1002/pen.24786>.
- [20] T. Donderwinkel, M. van Drongelen, S. Wijskamp, Strength development in overmolded structures, in: C. Hopmann, R. Dahlmann (Eds.), *Advances in Polymer Processing 2020*, Springer Vieweg, Germany, 2020, pp. 291–300, https://doi.org/10.1007/978-3-662-60809-8_24.
- [21] G.-J. Bex, *Development of 2K Injection Moulding Products and Processes of Rubbers with Thermoplastics* (PhD thesis), KU Leuven, 2019.
- [22] V. Goodship, J.C. Love, *Multi-Material Injection Moulding*, vol. 13, iSmithers Rapra Publishing, 2002.
- [23] J. Markarian, Overmolding continues to grow & find creative new applications, *Plast. Eng.* 73 (2017) 24–27, <https://doi.org/10.1002/j.1941-9635.2017.tb01709.x>.
- [24] K. Dijkstra, G. Vlogman, A. Magelhaes, Softtouch-oberflächen: verbesserung der haftung bei hart-weich-verbindungen, *Kunststoffe* 88 (3) (1998) 348–350.
- [25] A.R. Carella, C. Alonso, J.C. Merino, J.M. Pastor, Sequential injection molding of thermoplastic polymers. analysis of processing parameters for optimal bonding conditions, *Polym. Eng. Sci.* 42 (11) (2002) 2172–2181, <https://doi.org/10.1002/pen.11107>.
- [26] L.M. Arzondo, N. Pino, J.M. Carella, J.M. Pastor, J.C. Merino, J. Póveda, C. Alonso, Sequential injection overmolding of an elastomeric ethylene-octene copolymer on a polypropylene homopolymer core, *Polym. Eng. Sci.* 44 (11) (2004) 2110–2116, <https://doi.org/10.1002/pen.20216>.
- [27] C. Lo, F.C. Laabs, B. Narasimhan, Interfacial adhesion mechanisms in incompatible semi-crystalline polymer systems, *J. Polym. Sci. B Polym. Phys.* 42 (14) (2004) 2667–2679, <https://doi.org/10.1002/polb.20148>.
- [28] J. Qiu, A. Tsuboi, K. Izumi, H. Wu, S. Guo, Y. Huang, Effects of interfacial morphology on the welding strength of injection-molded polyamide, *Polym. Eng. Sci.* 47 (12) (2007) 2164–2171, <https://doi.org/10.1002/pen.20950>.
- [29] G. Jiang, H. Wu, B. Yan, S. Guo, J. Huang, Reinforcement of solid-melt interfaces for semicrystalline polymers in a sequential two-staged injection molding process, *J. Polym. Sci. B Polym. Phys.* 47 (11) (2009) 1112–1124, <https://doi.org/10.1002/polb.21719>.

- [30] M. Dondero, J.M. Pastor, J.M. Carella, C.J. Perez, Adhesion control for injection overmolding of polypropylene with elastomeric ethylene copolymers, *Polym. Eng. Sci.* 49 (10) (2009) 1886–1893, <https://doi.org/10.1002/pen.21415>.
- [31] B. Yan, H. Wu, G. Jiang, S. Guo, J. Huang, Interfacial crystalline structures in injection over-molded polypropylene and bond strength, *ACS Appl. Mater. Interfaces* 2 (11) (2010) 3023–3036, <https://doi.org/10.1021/am1003574>.
- [32] Z. Hu, A. Zhang, Z. Wang, Y. Li, Study on the influence of process parameters on interface strength of film-insert molding, *IOP Conf. Ser. Mater. Sci. Eng.* 436 (1) (2018), <https://doi.org/10.1088/1757-899x/436/1/012023>.
- [33] R. Chandran, C.J.G. Plummer, P. Bourban, J.E. Månson, Morphology and interfacial strength of nonisothermally fusion bonded hard and soft thermoplastics, *Polym. Eng. Sci.* 58 (S1) (2018) E82–E92, <https://doi.org/10.1002/pen.24662>.
- [34] T.L. Bergman, F.P. Incropera, D.P. DeWitt, A.S. Lavine, *Fundamentals of Heat and Mass Transfer*, John Wiley & Sons, 2011.
- [35] Y.Q. Xue, T.A. Tervort, P.J. Lemstra, Welding behavior of semicrystalline polymers. 1. The effect of nonequilibrium chain conformations on autoadhesion of UHMWPE, *Macromolecules* 31 (9) (1998) 3075–3080, <https://doi.org/10.1021/ma000754y>.
- [36] Y.M. Boiko, G. Guérin, V.A. Marikhin, Prud'homme, R. E., Healing of interfaces of amorphous and semi-crystalline poly(ethylene terephthalate) in the vicinity of the glass transition temperature, *Polymer* 42 (21) (2001) 8695–8702, [https://doi.org/10.1016/S0032-3861\(01\)00406-2](https://doi.org/10.1016/S0032-3861(01)00406-2).
- [37] G.D. Smith, C.J. Plummer, P.E. Bourban, J.A.E. Månson, Non-isothermal fusion bonding of polypropylene, *Polymer* 42 (14) (2001) 6247–6257, [https://doi.org/10.1016/S0032-3861\(01\)00060-X](https://doi.org/10.1016/S0032-3861(01)00060-X).
- [38] A. Islam, H.N. Hansen, M. Bondo, Experimental investigation of the factors influencing the polymer–polymer bond strength during two-component injection moulding, *Int. J. Adv. Manuf. Technol.* 50 (2010) 101–111, <https://doi.org/10.1007/s00170-009-2507-8>.
- [39] Y. Xu, M. Huang, A.K. Schlarb, Print path-dependent contact temperature dependency for 3D printing using fused filament fabrication, *J. Appl. Polym. Sci.* 139 (24) (2022) 52337, <https://doi.org/10.1002/app.52337>.
- [40] V. Khatavkar, M.E. Seitz, M. Bulters, Adhesion in overmolding applications, in: Presented at the 32nd International Conference of the Polymer Processing Society, 2016.
- [41] V. Khatavkar, M.E. Seitz, J. Kersemakers, N. Stijnen, D. Istrate, M. Bulters, Adhesion in overmolding applications, in: Presented at the 39th Annual Adhesion Society Meeting, 2016.
- [42] E. van Ruymbeke, J.J.M. Slot, M. Kapnistos, P.A.M. Steeman, Structure and rheology of branched polyamide 6 polymers from their reaction recipe, *Soft Matter* 9 (29) (2013) 6921–6935, <https://doi.org/10.1039/c3sm50226k>.
- [43] P. Steeman, A. Nijenhuis, The effect of random branching on the balance between flow and mechanical properties of polyamide-6, *Polymer* 51 (12) (2010) 2700–2707, <https://doi.org/10.1016/j.polymer.2010.04.017>.
- [44] E. van Ruymbeke, H. Lee, T. Chang, A. Nikopoulou, N. Hadjichristidis, F. Snijkers, D. Vlassopoulos, Molecular rheology of branched polymers: decoding and exploring the role of architectural dispersity through a synergy of anionic synthesis, interaction chromatography, rheometry and modeling, *Soft Matter* 10 (27) (2014) 4762–4777, <https://doi.org/10.1039/c4sm00105b>.
- [45] F.J. Custódio, R.J. Steenbakkers, P.D. Anderson, G.W. Peters, H.E. Meijer, Model development and validation of crystallization behavior in injection molding prototype flows, *Macromol. Theory Simul.* 18 (9) (2009) 469–494, <https://doi.org/10.1002/mats.200900016>.

- [46] F.J.M.F. Custódio, Structure Development and Properties in Advanced Injection Molding Processes: Development of a Versatile Numerical Tool (PhD thesis), Technische Universiteit Eindhoven, 2009, <https://doi.org/10.6100/IR641679>.
- [47] G. vanden Poel, D. Istrate, A. Magon, V. Mathot, Performance and calibration of the Flash DSC 1, a new, MEMS-based fast scanning calorimeter, *J. Therm. Anal. Calorim.* 110 (3) (2012) 1533–1546, <https://doi.org/10.1007/s10973-012-2722-7>.
- [48] G. Pompe, M. Bräuer, D. Schweikle, J. Nagel, B. Hupfer, D. Lehmann, Influence of the temperature profile in the interface on the bond strength of polyamide-polyurethane two-component tensile bars, *J. Appl. Polym. Sci.* 100 (6) (2006) 4297–4305, <https://doi.org/10.1002/app.23842>.
- [49] J.E.K. Schawe, S. Pogatscher, Material characterization by fast scanning calorimetry: practice and applications, in: C. Schick, V. Mathot (Eds.), *Fast Scanning Calorimetry*, Springer International Publishing, New York, 2016, pp. 611–632, https://doi.org/10.1007/978-3-319-31329-0_18.
- [50] W. Schneider, A. Koppl, J. Berger, Non-isothermal crystallization of polymers. System of rate equations, *Int. Polym. Process.* 2 (3) (1988) 151–154.
- [51] M. van Drongelen, T.B. Van Erp, G.W.M. Peters, Quantification of non-isothermal, multi-phase crystallization of isotactic polypropylene: the influence of cooling rate and pressure, *Polymer* 53 (21) (2012) 4758–4769, <https://doi.org/10.1016/j.polymer.2012.08.003>.
- [52] P.C. Roozmond, T.B. van Erp, G.W. Peters, Flow-induced crystallization of isotactic polypropylene: modeling formation of multiple crystal phases and morphologies, *Polymer* 89 (2016) 69–80, <https://doi.org/10.1016/j.polymer.2016.01.032>.
- [53] N. Yaghini, G.W.M. Peters, Modeling crystallization kinetics and resulting properties of polyamide 6, *Macromolecules* 54 (4) (2021) 1894–1904, <https://doi.org/10.1021/acs.macromol.0c02588>.
- [54] H.H. Kausch, M. Tirrell, Polymer interdiffusion, *Annu. Rev. Mater. Sci.* 19 (1) (1989) 341–377, <https://doi.org/10.1146/annurev.ms.19.080189.002013>.
- [55] T. Ge, G.S. Grest, M.O. Robbins, Tensile fracture of welded polymer interfaces: miscibility, entanglements, and crazing, *Macromolecules* 47 (19) (2014) 6982–6989, <https://doi.org/10.1021/ma501473q>.
- [56] R. Schnell, M. Stamm, C. Creton, Direct correlation between interfacial width and adhesion in glassy polymers, *Macromolecules* 31 (7) (1998) 2284–2292, <https://doi.org/10.1021/ma971020x>.
- [57] F. Yang, R. Pitchumani, Healing of thermoplastic polymers at an interface under non-isothermal conditions, *Macromolecules* 35 (8) (2002) 3213–3224, <https://doi.org/10.1021/ma010858o>.
- [58] J.J. Benkoski, P. Flores, E.J. Kramer, Diblock copolymer reinforced interfaces between amorphous polystyrene and semicrystalline polyethylene, *Macromolecules* 36 (9) (2003) 3289–3302, <https://doi.org/10.1021/ma034013j>.
- [59] L. Martineau, F. Chabert, B. Boniface, G. Bernhart, Effect of interfacial crystalline growth on autohesion of PEEK, *Int. J. Adhes. Adhes.* 89 (2019) 82–87, <https://doi.org/10.1016/j.ijadhadh.2018.11.013>.
- [60] K.A. Chaffin, J.S. Knutsen, P. Brant, F.S. Bates, High-strength welds in metallocene polypropylene/polyethylene laminates, *Science* 288 (5474) (2000) 2187–2190, <https://doi.org/10.1126/science.288.5474.2187>.
- [61] N.V. Pogodina, H.H. Winter, Polypropylene crystallization as a physical gelation process, *Macromolecules* 31 (23) (1998) 8164–8172, <https://doi.org/10.1021/ma980134i>.
- [62] J. Lamethe, P. Beauchene, L. Leger, Polymer dynamics applied to PEEK matrix composite welding, *Aerosp. Sci. Technol.* 9 (3) (2005) 233–240, <https://doi.org/10.1016/j.ast.2005.01.008>.

- [63] E. Lafranche, S. Macedo, P. Ferreira, C.I. Martins, Thin wall injection-overmoulding of polyamide 6/polypropylene multilayer parts: PA6/PP-g-ma interfacial adhesion investigations, *J. Appl. Polym. Sci.* 138 (17) (2021) 50294, <https://doi.org/10.1002/app.50294>.
- [64] C.J.G. Plummer, P. Bourban, J. Zanetto, G.D. Smith, J.E. Månson, Nonisothermal fusion bonding in semicrystalline thermoplastics, *J. Appl. Polym. Sci.* 87 (8) (2003) 1267–1276, <https://doi.org/10.1002/app.11528>.
- [65] H.R. Brown, Relation between the width of an interface between two polymers and its toughness, *Macromolecules* 34 (11) (2001) 3720–3724, <https://doi.org/10.1021/ma991821v>.
- [66] G. Agrawal, R.P. Wool, W.D. Dozier, G.P. Felcher, J. Zhou, S. Pispas, J.W. Mays, T.P. Russell, Interdiffusion of polymers across interfaces, *J. Polym. Sci. B Polym. Phys.* 34 (17) (1996) 2919–2940.
- [67] K. Kunz, M. Stamm, Initial stages of interdiffusion of PMMA across an interface, *Macromolecules* 29 (7) (1996) 2548–2554, <https://doi.org/10.1021/ma950187s>.
- [68] M. Doi, S.F. Edwards, S.F. Edwards, *The Theory of Polymer Dynamics*, vol. 73, Oxford University Press, 1986.
- [69] W.W. Graessley, Some phenomenological consequences of the Doi–Edwards theory of viscoelasticity, *J. Polym. Sci. B Polym. Phys.* 18 (1) (1980) 27–34, <https://doi.org/10.1002/pol.1980.180180103>.
- [70] L.J. Fetters, D.J. Lohse, D. Richter, T.A. Witten, A. Zirkel, Connection between polymer molecular weight, density, chain dimensions, and melt viscoelastic properties, *Macromolecules* 27 (17) (1994) 4639–4647, <https://doi.org/10.1021/ma00095a001>.
- [71] S. Acierno, N. Grizzuti, H.H. Winter, Effects of molecular weight on the isothermal crystallization of poly (1-butene), *Macromolecules* 35 (13) (2002) 5043–5048, <https://doi.org/10.1021/ma0200423>.
- [72] V. Janssens, C. Block, G. Van Assche, B. Van Mele, P. Van Puyvelde, RheoDSC: design and validation of a new hybrid measurement technique, *J. Therm. Anal. Calorim.* 98 (3) (2009) 675–681, <https://doi.org/10.1007/s10973-009-0518-1>.
- [73] L. Verbelen, *Viscosity Build-Up During Crystallization of Nylon* (unpublished Masters thesis), KU Leuven, 2001.
- [74] P. Supaphol, J.E. Spruiell, Isothermal melt-and cold-crystallization kinetics and subsequent melting behavior in syndiotactic polypropylene: a differential scanning calorimetry study, *Polymer* 42 (2) (2001) 699–712, [https://doi.org/10.1016/S0032-3861\(00\)00399-2](https://doi.org/10.1016/S0032-3861(00)00399-2).
- [75] I.F. Villegas, G. Palardy, Ultrasonic welding of CF/PPS composites with integrated triangular energy directors: melting, flow and weld strength development, *Compos. Interfaces* 24 (5) (2017) 515–528, <https://doi.org/10.1080/09276440.2017.1236626>.
- [76] F. Paolucci, M.J.H. van Mook, L.E. Govaert, G.W.M. Peters, Influence of post-condensation on the crystallization kinetics of PA12: from virgin to reused powder, *Polymer* 175 (2019) 161–170, <https://doi.org/10.1016/j.polymer.2019.05.009>.

Adhesive joining of thermoplastic composites

12

Dong Quan^a, Gennaro Scarselli^b, Neal Murphy^c, and Alojz Ivankovic^c

^aShandong University, Jinan, China, ^bUniversity of Salento, Lecce, Italy, ^cUniversity College Dublin, Dublin, Ireland

12.1 Introduction

The use of fiber-reinforced thermoplastic composites (TPCs) has been extensively expanded over the last decade, with a more rapid growth foreseen in the near future. This is mainly attributed to their ability to offer significant advantages over thermoset composites (TSCs), including a high resistance to impact and fracture damage, the ability to be remelted and reshaped, and a low storage cost as a result of an infinite shelf life at ambient temperature. Consequently, a combination use of components based on TPCs, TSCs, and metal alloys has become a major development trend in a wide variety of industries, including the automotive, aerospace, construction, and marine sectors. Inevitably, the different material characteristics of TPCs, TSCs, and metal alloys introduce the challenge of developing appropriate joining methods for cost-effective assemblies.

To date, mechanical fastening [1–3], adhesive bonding [4–7], and welding (infusion bonding) [8, 9] are the major methods for joining thermoplastics and their composite materials. While each of these methods has its own strengths and weaknesses, adhesive bonding is unique for joining thin-walled sections or elements with a significant difference in thickness [10]. Moreover, it presents many advantages over its counterparts for the structural joining of FRPs, such as the possibility of joining any pair of dissimilar materials, reducing weight, and sealing the entire bonding area, thereby potentially providing high joint strength and durability [11]. As a result, the adhesive joining technique is extensively used in a wide variety of industrial assembly processes. There are also disadvantages of adhesive joining, the foremost being the requirement to perform an appropriate surface treatment before bonding, particularly for substrates with relatively low surface energies such as TPCs and aluminum (Al) [12,13]. Kinloch et al. [14–18] were the first to perform systematic investigations on the joining of TPCs using structural adhesives, and reported that obtaining high-strength adhesive joints for TPCs was far more difficult than for TSCs. This was due to the inherently low reactivities, low surface energies, and weak polarities of the majority of thermoplastics that led to poor compatibility between the TPCs and the typically epoxy-based adhesives [19]. In general, to ensure a sufficiently good adhesive/composite interfacial strength, a simple abrasion/solvent-wiping treatment is all that is needed for the TSCs while more intensive surface treatments are necessary

in the case of TPCs [15–17]. This limitation also applies to the most widely used advanced TPCs based on polyether ether ketone (PEEK) and polyphenylene sulfide (PPS) polymers, which possess inherently weak surface polarities. Accordingly, the development of an effective surface treatment method for the PEEK and PPS composites becomes critical for the adhesive joining of these TPCs to themselves and to other dissimilar materials. This chapter will focus on a high-power ultraviolet (UV)-irradiation technique that was recently proposed to activate the surfaces of the PEEK and PPS composites [20–23] prior to adhesive bonding. The structural performance of TPC-to-TPC, TPC-to-TSC, and TPC-to-Al joints bonded by aerospace-grade adhesives is presented.

12.2 Brief summary of surface treatment techniques for TPCs

In general, as also discussed in [Chapter 9](#), the application of surface treatments prior to adhesive bonding aims to improve the quality of the joint through a variety of mechanisms, from simply removing contaminants and increasing the surface roughness to increasing the free surface energy and/or modifying the surface chemistry of the adherends. The surface treatment of TSCs for adhesive bonding has been extensively studied, with many mechanical and chemical surface treatment techniques being used such as sanding [24], grit-blasting [25], etching [26], laser [27], plasma [28], flame, and peel-ply treatments [29]. However, the number of studies on the surface treatment of TPCs for adhesive bonding is relatively limited.

Kinloch et al. [16] used an acid etching method and a corona discharge method to treat the surfaces of TPCs for adhesive bonding. Five different adhesives were used for bonding carbon fiber-reinforced PEEK, PPS, PEI, PA, and PI composites. Overall, it was observed that the TPCs required more harsh surface treatments to obtain cohesive failure of the adhesive joints when compared to epoxy composites. For example, with the PEEK composites, it was found that cohesive failure was only achieved for the FM73M adhesively bonded joints following a prolonged acid etching time of 10 min while all the other acid etched joints exhibited interfacial failure. For the corona discharge method, cohesive failure took place only if the intensities of the corona discharge treatment were above 10 J/m^2 . It was reported that the corona discharge treatment increased the types and concentrations of oxygen-containing groups on the surface of the PEEK composites. The experimental results also clearly revealed that the corona discharge method was more effective than acid etching for the surface activation of TPCs.

Wade and Cantwell [30] treated the surfaces of a glass fiber-reinforced PA-66 composite using a plasma treatment method. The treatments were carried out in an inductively coupled RF quartz barrel reactor (24 V DC, 0.14 A at resonant frequency 13.56 MHz), using four different feed gases—Ar, O₂, N₂, and NH₃—for times between 5 s and 5 min. Pure cohesive failure was observed for the adhesive joints that were treated by O₂ plasma lasting for longer than 1 min. However, pure or partially interfacial failure of the adhesive joints took place when the other feed gases were used for the plasma treatment, even with a treatment time lasting for 5 min. More encouraging

results were observed by Iqbal et al. [31], who treated the surfaces of bulk PEEK and carbon fiber-reinforced PPS composites using atmospheric pressure plasma treatment for adhesive bonding. It was reported that applying a 60 s plasma treatment to the PEEK and PPS composites transited the failure locus of their adhesive joints from the adhesive-substrate interface to within the adhesive or substrate material.

Ramaswamy et al. [32] used a grit-blasting method to prepare the surfaces of PA-12 composites for adhesive bonding with Al. The composite adherends were grit-blasted for different durations using an aluminum oxide (Al_2O_3) blast medium having an angular grain shape and a mean particle size of 220 μm . As expected, posttreatment analysis of the composite surfaces revealed significantly increased surface roughness (R_a), that is, R_a increased from 0.5 μm for the nontreated composite to 3.0 μm for the composite that was grit-blasted for 40 s. However, no significant increases in the amount of functional groups, such as alkoxy (C–O), amide (N–C=O), carbonyl (C=O), and carboxyl (O–C=O) bonds, were observed after applying the grit-blast treatment to the PA-12 composites. Consequently, the grit-blast process failed to improve the lap shear strengths of the adhesively bonded PA-12 composite joints. This clearly demonstrated that enhancing the chemical activities of TPC surfaces is critical for adhesive bonding. The same conclusion can also be drawn from the work by Genna et al. [33], in which a laser surface treatment was applied to the surfaces of PPS composites. Similar to the grit-blast treatment, the laser treatment process increased the surface roughness of the PPS composites by burning off the matrix resin on the bonding surfaces. However, this process hardly resulted in any enhancement in the surface polarity of the PPS composites, and hence failed to achieve good bonding strengths.

The UV irradiation technique was initially used for treating the surfaces of wool fibers by Bradley et al. [34]. In the 1990s, Mathieson and Bradley [35] extended this technique for the surface treatment of poly-ethylene (PE) and PEEK polymers for adhesive bonding. It was observed that applying UV irradiation to the polymer surfaces significantly increased the lap shear strength (LSS) from approximately 0 to 10 MPa for the PE adhesive joints, and from 2.3 to 13 MPa for the PEEK adhesive joints. Shi et al. [36] also proved significantly enhanced adhesion between PEEK films and carbon fiber/epoxy composite upon irradiating the PEEK films with a UV light source for 15 min. More recently, Quan et al. [20–23] used UV irradiation to treat the surfaces of PPS and PEEK composites for adhesive bonding. In these works [20–23], high-powered UV light sources were used to shorten the duration of the irradiation for high-efficiency manufacturing. It has been demonstrated that the high-power UV irradiation process can significantly increase the amount of oxygen-containing functional groups on the surfaces of the PPS and PEEK composites in a very short time, and subsequently obtain adhesive joints with enhanced structural integrity.

12.3 UV irradiation of the TPCs

A UV irradiation chamber equipped with a Light Hammer 6 UV source (from Heraeus Noblelight, United Kingdom) was used to treat the PEEK and PPS composite substrates. The intensity of the UV spectral ranges can be controlled by placing the

Table 12.1 The intensities of the UV spectral ranges applied onto the PEEK and PPS composite surfaces.

Items	Wavelength (nm)	Intensity (mW/cm ²)
UVA	320–390	1546
UVB	280–320	343
UVC	250–260	51
UVV	395–445	1979

substrates at different distances to the UV lamp. The intensities of the UV spectral ranges that were applied on the surfaces of the TPCs are shown in Table 12.1. The bonding surfaces of the composite adherends were placed in the UV chamber and irradiated for different durations. After UV treatment, the surface free energies and water contact angles of the composite substrates were investigated using a mobile surface analyzer from KRÜSS, GmbH. The chemical composition and functional groups on the treated surfaces were analyzed using an x-ray photoelectron spectrometer (XPS, Kratos Axis Ultra DLD), equipped with an Al K α (1486.7 eV) x-ray source.

The results of the surface characterizations of the TPC surfaces are summarized in Table 12.2. It was found that applying short duration UV irradiation to the TPC surfaces notably increased their oxygen content and decreased their carbon content for both the PPS and PEEK composites. Consequently, the O/C ratio gradually increased from 0.15 to 0.28 for the PPS composites, and from 0.18 to 0.36 for the PEEK

Table 12.2 Results of the surface characterizations of the TPC surfaces, including carbon and oxygen content, O/C ratio, surface free energy (γ) and its polar component (γ^p), dispersive component (γ^d) and γ^p/γ^d ratio, and water contact angles (θ).

	UV irradiation	0 s	2 s	3 s	4 s	5 s	10 s	20 s	30 s
PPS	O (%)	11.51	12.29	13.11	13.84	14.52	16.38	17.33	18.25
	C (%)	76.35	73.96	72.03	71.05	70.06	67.60	66.98	66.01
	O/C (%/%)	0.15	0.17	0.18	0.19	0.21	0.24	0.26	0.28
	γ^d (mN/m)	46.84	45.39	45.99	45.09	45.66	44.54	42.48	43.36
	γ^p (mN/m)	1.26	2.56	3.09	3.68	4.00	4.94	5.78	6.19
	γ (mN/m)	48.10	47.95	49.08	48.77	49.66	49.48	48.26	49.55
	γ^p/γ^d	0.03	0.06	0.07	0.08	0.09	0.11	0.14	0.14
	θ (°)	85.21	78.49	76.23	72.47	72.44	68.13	66.67	66.40
	PEEK	O (%)	14.93	15.68	16.49	18.05	20.04	22.97	24.04
C (%)		82.67	80.18	79.23	77.91	76.75	73.89	70.39	69.49
O/C (%/%)		0.18	0.20	0.21	0.23	0.26	0.31	0.34	0.36
γ^d (mN/m)		46.92	48.11	46.48	47.25	47.81	46.95	45.14	46.76
γ^p (mN/m)		3.64	4.76	4.98	5.13	5.87	6.14	6.31	6.50
γ (mN/m)		50.56	52.87	51.46	52.38	53.68	53.09	51.45	53.26
γ^p/γ^d		0.08	0.10	0.11	0.11	0.12	0.13	0.14	0.14
θ (°)		80.22	78.77	75.09	73.22	69.84	67.49	68.37	67.68

composites as the duration of the UV irradiation increased to 30 s. This was because the high-power UV irradiation provided sufficient energy to break the C–C/C–H species, which were associated with the development of C–O, C=O, and O–C=O species along their molecular chains [35,37]. The increased amount of oxygen functional groups on the TPC surfaces subsequently affected their surface free energies. As shown in Table 12.2, the application of the UV irradiation to the TPC surfaces had no obvious effects on the dispersive component (γ^d) of the surface energy, but notably increased its polar component (γ^p), that is, γ^p increased from 1.26 to 6.19 mN/m (by 391%) for the PPS composite, and from 3.64 to 6.50 mN/m (by 79%) for the PEEK composite upon 30 s UV irradiation.

It should be noted that interactions at the interface of two phases only occur between the same type of forces, that is, dispersive-dispersive or polar-polar. Accordingly, a closer match between the γ^p/γ^d ratios of the TPCs and the epoxy adhesive is favored to achieve a higher level of interactions at their interface. γ^p and γ^d of epoxy adhesives were given by Kinloch [38] to be about 5–8 and 40 mN/m, respectively, corresponding to a γ^p/γ^d ratio of between 0.125 and 0.2. Clearly, applying the UV irradiation to the TPCs resulted in a better match of the γ^p/γ^d ratios between the TPCs and the epoxy adhesive; see Table 12.2.

The thermodynamic work of adhesion (W) is defined as the reversible work that is needed to separate the interface from the equilibrium state of a liquid-liquid or liquid-solid phase boundary to a separation distance of infinity [39]. W between the noncured adhesive and the TPCs can be calculated as:

$$W = W^p + W^d = 2(\gamma_a^p \gamma_s^p)^{1/2} + 2(\gamma_a^d \gamma_s^d)^{1/2} \quad (12.1)$$

where W^p and W^d are the contributions of the polar interactions and the dispersive interactions, respectively. The subscripts a and s denote the noncured adhesive and the TPC substrates, respectively. The results of the calculations are presented in Table 12.3. Clearly, the values of W^p at the adhesive/TPC interfaces significantly increased upon UV irradiating the TPC surfaces, with W^d exhibiting no obvious changes. It is noteworthy that, at the cured adhesive/TPC interfaces, the dispersive force is responsible for the temporary fluctuations of the charge distribution in the atoms/molecules, such as the van der Waals interactions, and the polar force generates

Table 12.3 Thermodynamic work of adhesion of the UV irradiated TPC surfaces.

	UV irradiation	0 s	2 s	3 s	4 s	5 s	10 s	20 s	30 s
PPS	W^p (mN/m)	5.72	8.16	8.96	9.78	10.19	11.33	12.26	12.69
	W^d (mN/m)	86.57	85.22	85.78	84.94	85.47	84.42	82.44	83.29
	W (mN/m)	92.29	93.38	94.74	94.72	95.66	95.75	94.70	95.97
PEEK	W^p (mN/m)	9.73	11.12	11.38	11.55	12.35	12.63	12.81	13.00
	W^d (mN/m)	86.65	87.74	86.24	86.95	87.46	86.67	84.98	86.50
	W (mN/m)	96.38	98.86	97.62	98.50	99.81	99.31	97.79	99.50

Coulomb interactions between permanent dipoles and between permanent and induced dipoles, and subsequently generates hydrogen bonds and covalent bonds. Because hydrogen bonds and covalent bonds are much stronger than van der Waals forces, the increased values of W^p results in significantly improved adhesive/TPC adhesion. As expected, the increased γ^p of the treated TPC surfaces significantly improved their wettability. As shown in Table 12.2, the water contact angles of the TPCs gradually decreased from 85.21 to 66.40 degrees for the PPS composites and from 80.22 to 67.68 degrees for the PEEK composites by UV irradiating the TPCs for 30 s.

12.4 Joining TPCs to TPCs

12.4.1 Surface treatment and joint preparation

The PEEK and PPS composites were surface treated in the UV irradiation chamber using the same UV intensity as in Table 12.1. After UV irradiation, the TPCs were bonded using an epoxy film adhesive, Scotch-Weld AF 163-2K from 3M Netherlands B.V. (See also Chapter 1, which focuses on epoxy adhesive chemistries.) The curing cycle of the adhesive joints was a single dwell step at 121°C for 90 min. The cured composite joints were then machined into required dimensions for characterizing the lap shear strength, Mode I fracture toughness, and Mode II fracture toughness, as schematically shown in Fig. 12.1.

12.4.2 The lap shear strength

Table 12.4 presents the LSSs of the PPS-PPS and PEEK-PEEK composite joints from the single lap shear joint tests. It was found that the application of a short-time UV irradiation to the PPS and PEEK composite substrates significantly increased the

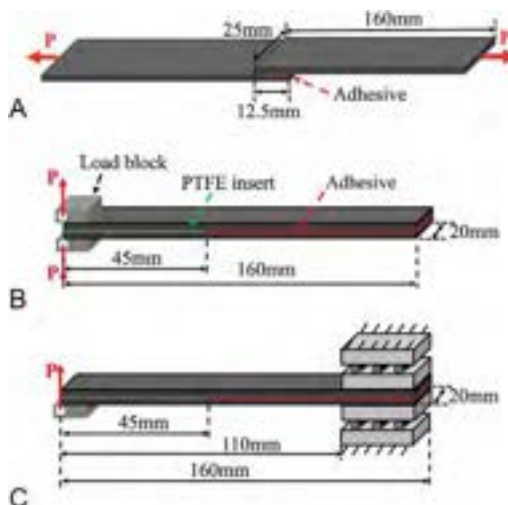


Fig. 12.1 Schematics of the (A) single lap shear joint test, (B) DCB test, and (C) ELS test.

Table 12.4 LSSs and joint stiffnesses of the PPS-PPS and PEEK-PEEK composite joints with the substrates UV irradiated for different times.

	UV irradiation	0 s	2 s	3 s	4 s	5 s	10 s	20 s	30 s
PPS-PPS	LSS (MPa)	11.8 ±0.3	22.4 ±0.6	31.7 ±1.5	31.2 ±0.3	30.7 ±1.3	31.4 ±1.8	32.3 ±2.2	28.9 ±0.2
PEEK-PEEK	LSS (MPa)	8.3 ±0.7	22.9 ±0.7	26.9 ±0.8	34.1 ±0.7	37.3 ±0.6	39.0 ±1.8	37.1 ±0.6	36.9 ±0.8

LSS of the adhesive joints. For the adhesive bonded PPS-PPS composite joints, the LSS increased from 11.8 MPa for the nontreated joints to 22.4 MPa by UV irradiating the substrates for 2 s, and then to a plateau value of approximately 32 MPa following a UV irradiation of 3 s and above. Similarly, the LSS of the PEEK-PEEK composite joints gradually increased from 8.3 MPa for the nontreated joints to 37.3 MPa as the duration of the UV irradiation increased to 5 s, and then remained more or less the same for a longer UV irradiation of up to 30 s.

Fig. 12.2A and B shows photographs of the failure surfaces of the lap shear specimens for the PPS-PPS and PEEK-PEEK composite joints, respectively. An adhesion failure between the adhesive layer and the substrate was observed for the nontreated PPS-PPS composite joints, leaving a clear surface on one side of the substrates and almost the entire adhesive layer on the opposite side. The failure behavior of the PPS-PPS composite joints transformed from an adhesion mode to a combination of adhesion and cohesion failure by applying a 2 s UV irradiation to the substrates. As the duration of the UV irradiation increased to 3 s and above, obvious damage to the PPS composites took place, evidenced by the presence of damaged PPS polymers on one side of the substrates and bare carbon fibers on the opposite side. Similarly to the PPS-PPS composite joints, applying UV irradiation to the substrates significantly affected the failure behavior of the PEEK-PEEK composite joints, that is, the failure mode changed from an adhesion failure of the nontreated joints to a combination of adhesion and cohesion failure by applying UV irradiation of between 2 and 3 s, and further to obvious substrate damage as the duration of the UV irradiation increased to 4 s and above. Overall, it is clear that applying a rapid UV irradiation, that is, 3 s for the PPS composites and 5 s for the PEEK composites, significantly improved the adhesion between the epoxy adhesive and the TPC substrates to a level that was sufficiently high to cause significant damage to the TPC substrates during the lap shear tests.

12.4.3 The Mode I and Mode II fracture behavior

Representative load versus displacement curves from the DCB tests are shown in Fig. 12.3A. It was found that the fracture loads of the DCB specimens for the nontreated TPC joints were very low, that is, below 20 N in all cases. This was typical for the adhesively bonded PEEK-PEEK and PPS-PPS joints, owing to the inherent

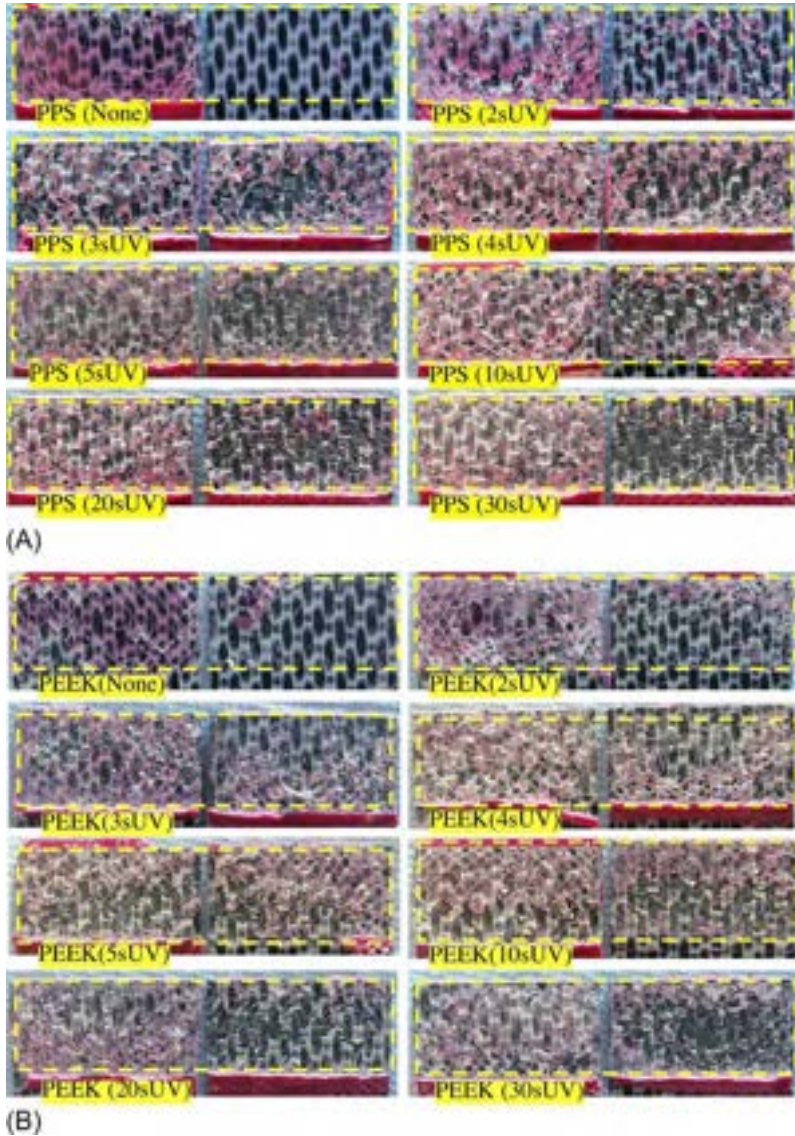


Fig. 12.2 Representative photographs of the failure surfaces of the lap shear specimens of the TPC adhesive joints. (A) PPS-PPS joints; (B) PEEK-PEEK joints.

low surface activities of the thermoplastic matrix [18,36]. The crack propagated in a stick-slip manner for all the UV-treated adhesive joints, indicated by the zigzag shape of the load versus displacement curves in Fig. 12.3A. In this case, only the peak loads on the load versus displacement curves were used to calculate the Mode I fracture energies, G_{Ic} . Clearly, the application of UV irradiation to the TPCs significantly increased the fracture propagation load of the adhesive joints, which corresponded to remarkable increases in G_{Ic} , as shown in Fig. 12.3B. One can see that the application

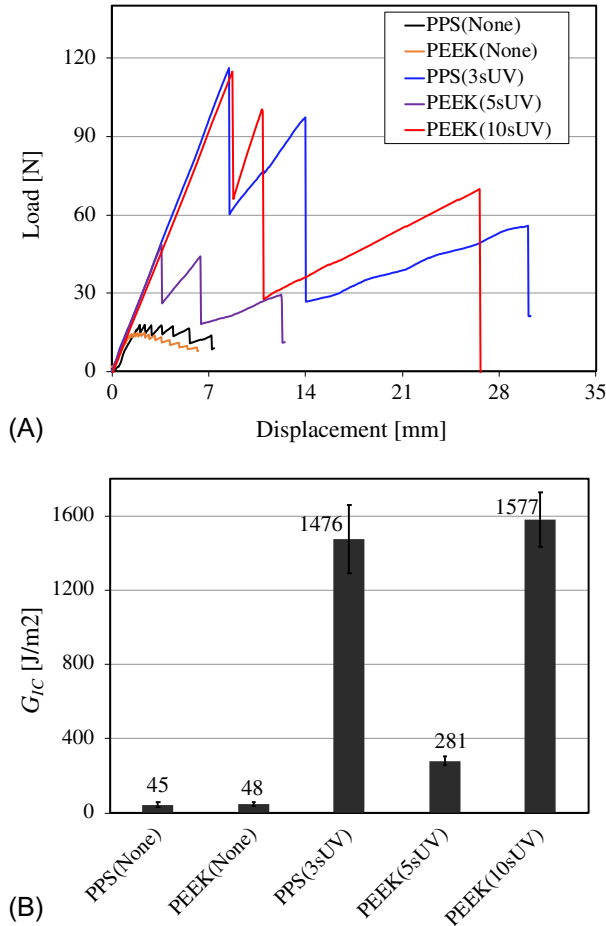


Fig. 12.3 Representative load versus displacement curves and corresponding Mode I fracture energies from the DCB tests of the TPC-TPC adhesive joints. (A) Load versus displacement curves; (B) Mode I fracture energies.

of 3 s UV irradiation to the PPS composite substrates remarkably increased G_{Ic} from 45 J/m² of the PPS(None) joints to 1476 J/m² of the PPS(3sUV) joints. However, the G_{Ic} of the PEEK(5sUV) joints was measured to be 281 J/m², which was relatively low when compared to the PPS(3sUV) joints. Fortunately, this value significantly increased to 1577 J/m² as the duration of the UV irradiation increased to 10 s.

The fracture surfaces of the DCB specimens were analyzed to investigate the fracture mechanisms of the adhesive joints, as shown in Fig. 12.4. As expected, both of the PPS(None) and PEEK(None) joints exhibited a pure adhesion failure without causing any damage to the adhesives and the TPC substrates. For the PPS(3sUV) and PEEK(10sUV) joints, the entire adhesive layer attached on to one side of the fracture surfaces, on which extensive thermoplastic polymers and numerous broken carbon fibers were observed. Consequently, only a small amount of thermoplastic polymers remained on the surfaces of the opposite-side substrates, and the majority of the

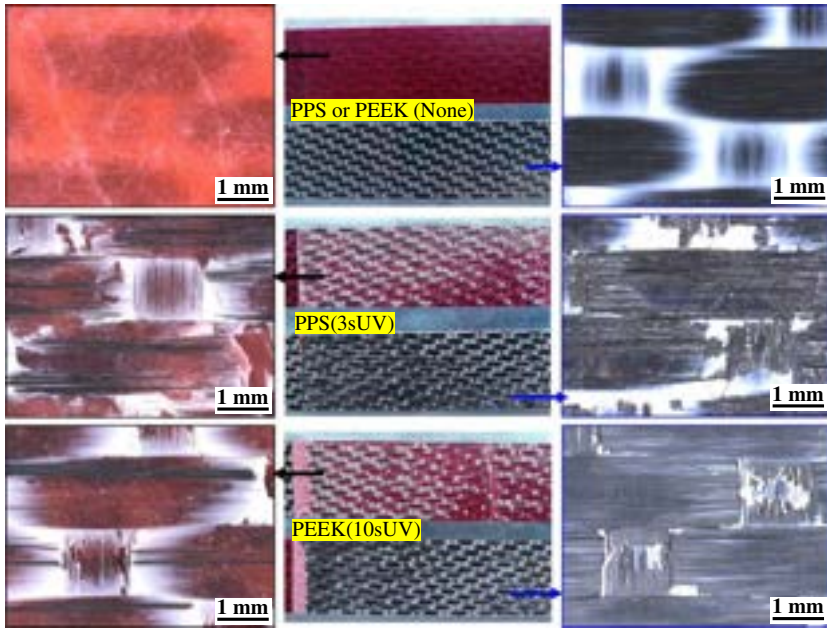


Fig. 12.4 Fracture surfaces of the DCB specimens for showing significant damage of the UV-treated TPC substrates.

surfaces were featured with bare and damaged carbon fibers; see Fig. 12.4. This means the crack propagation took place in the TPC substrates, that is, mainly at the interface between the TPC polymers and the carbon fibers. These phenomena contributed to the energy dissipation during the fracture process, and led to significant improvements in the Mode I fracture performance of the adhesive joints.

Fig. 12.5 shows the load versus displacement curves and Mode II fracture energies from the ELS tests of the adhesive joints. It was found that the maximum fracture propagation load increased from below 100 N to above 400 N in both cases upon applying rapid UV irradiation to the PPS and PEEK composite substrates, as shown in Fig. 12.5A. Consequently, G_{IIc} increased from below 300 J/m^2 for the nontreated adhesive joints to 7814 J/m^2 for the PPS(3sUV) joints and 6939 J/m^2 for the PEEK(5sUV) joints; see Fig. 12.5B. The significantly improved Mode II fracture performance upon applying UV irradiation to the TPC substrates could be correlated to the fracture mechanisms of the adhesive joints.

Fig. 12.6 presents photographs and microscopy images of the fracture surfaces of the ELS specimens. It was observed that the Mode II fracture mode of the adhesive joints transformed from pure adhesion failure of the nontreated joints to significant substrate damage upon application of UV irradiation to the TPC substrates in both cases. Interply delamination was observed for the PPS(3sUV) joints, that is, the crack propagation path diverted from the mid-plane into the adjacent material during the fracture process, causing severe damage to both sides of the substrates, as shown in Fig. 12.6. For the PEEK(5sUV) joints, the entire adhesive layer together with extensive regions of fractured PEEK matrix and associated carbon fibers were observed on

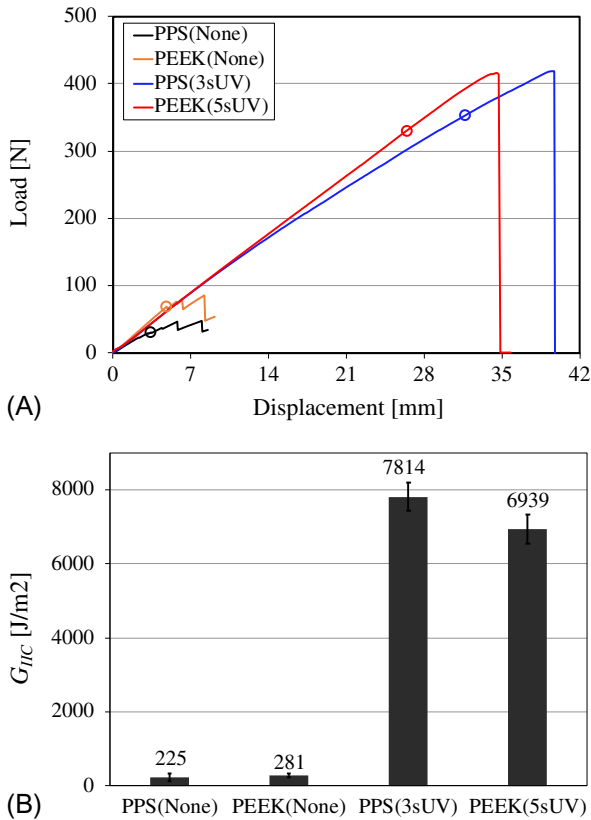


Fig. 12.5 Representative load versus displacement curves and Mode II fracture energies of the TPC adhesive joints. The points in (A) are where crack initiation took place. (A) Load versus displacement curves; (B) Mode II fracture energies.

one side of the substrates, leaving an obviously damaged PEEK layer and bare carbon fibers on the opposite side. Obviously, more severe damage to the substrates took place for the PPS(3sUV) joints than the PEEK(5sUV) joints, resulting in a higher associated G_{IIc} for the PPS(3sUV) joints, as shown in Fig. 12.5B.

12.5 Joining TPCs to metals

12.5.1 Surface treatment and joint preparation

In this section, the surfaces of the PEEK and PPS composites were UV irradiated in the UV chamber for between 5 and 10 s. The Al substrates were alloy 2024-T3. The bonding surfaces of the Al substrates were either treated using a CoBlast technique developed by ENBIO, Ireland [40], or a Stuart-Bengough chromic acid anodizing process. Both these treatment methods ensured good adhesion between the Al substrates and the adhesives, as will be shown later on.

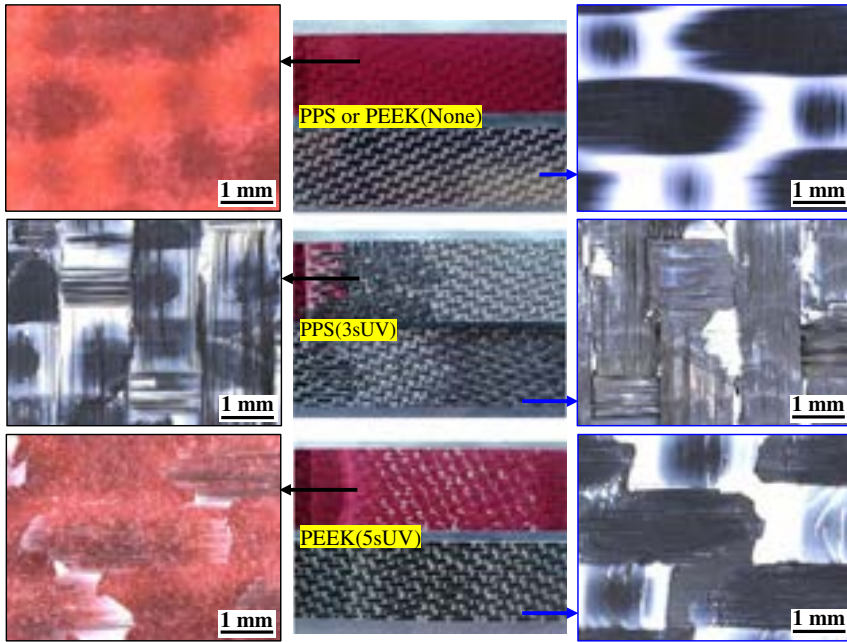


Fig. 12.6 Fracture surfaces of the ELS specimens for showing significant damage of the UV-treated TPC substrates.

After both the bonding surfaces of the Al and TPC adherends were prepared, aerospace-grade epoxy film adhesives, that is, either Scotch-Weld AF163-2 (from 3M) or Hysol EA9696 (from Henkel), were used to bond them together. The single lap shear joint, DCB, and ELS specimens were prepared to study the LSS and Mode I and Mode II fracture energies of the hybrid TPC-Al joints, as schematically shown in Fig. 12.7. The single lap shear joint specimens were bonded with the EA9696 adhesive and cured in an air-circulated oven. The DCB and ELS specimens were bonded with the Scotch-Weld AF163-2K and AF163-2OST adhesives and cured in an autoclave. The Scotch-Weld AF163-2K and AF163-2OST adhesives possessed the same adhesive matrix but different supporting carriers, that is, the supporting carrier was nonwoven thermoplastic fibers for the AF163-2OST, and thermoplastic fiber knit for the AF163-2K. The curing cycle for all the joints consisted of a 0.5-h ramp from room temperature to 120°C followed by a 1.5-h hold, or dwell, at 120°C. After the curing schedule, the specimens were allowed to cool naturally to room temperature inside the oven for approximately 4 h. The thicknesses of the Al 2024-T3 alloy and the PEEK composite were 1.6 and 2.0 mm, respectively. This configuration of the adhesive joints was determined by applying the criterion of matching the flexural stiffnesses of the two adherends, so as to ensure essentially pure Mode I and Mode II fracture mode in the DCB and ELS tests, respectively. While it is well known that the thermal curing process induces residual stresses in the adhesive joints of dissimilar materials, the magnitude of the residual stresses has not been calculated in this study.

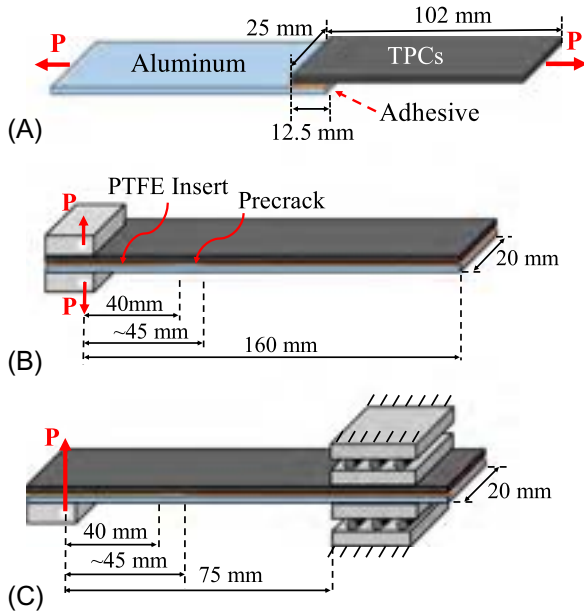


Fig. 12.7 Schematics of the (A) single lap shear joint test, (B) DCB test and (C) ELS test.

Interested readers are referred to a recent paper by Agha and Abu-Farha [41], who developed a suite of material models that works in conjunction to predict the effects of heat curing on adhesive joints. A curing kinetics model predicts the degree of cure, which is then fed into a viscoelastic mechanical model that defines the stiffness of the adhesive depending on the cure level, temperature, and relaxation in time. The calibrated material models were implemented into finite element models of the experimental setup for different combinations of substrates.

12.5.2 The lap shear strength

The LSSs of the TPC-Al joints are summarized in Table 12.5. A value of 16.0 MPa was measured for the LSS of the reference PEEK-Al joints, that is, without UV treatment on the PEEK composite substrates. This value significantly increased to around 35 MPa in all cases after the surfaces of the PEEK composites were UV treated. The LSS of the reference PPS-Al joints was measured to be 11.1 MPa, which remarkably increased to approximately 39 MPa after UV irradiation was applied to the PPS

Table 12.5 LSSs of the TPC-Al joints with the TPC substrates UV irradiated for different times.

UV irradiation	0 s	5 s	10 s	20 s
PPS-Al Joints	11.1 ± 0.9	37.5 ± 1.2	38.9 ± 0.6	38.6 ± 0.9
PEEK-Al Joints	16 ± 2.4	33.6 ± 3.1	35.0 ± 1.5	36.0 ± 0.7

composite surface. The LSS slightly increased as the duration of UV treatment increased, for example, the LSS of the PEEK-Al joints increased from 33.6 MPa for a 5 s treatment to 35.0 MPa for a 10 s treatment. Overall, the duration of the UV treatment had no significant effect on the LSS for both the PEEK-Al and PPS-Al joints. This means that a treatment of as brief as 5 s was sufficient to achieve a strong bond between the adhesive and the PEEK and PPS composite substrates.

Fig. 12.8A presents typical microscopy images of the failure surfaces of the single lap shear joints. It was found that the failure of the nontreated adhesive joints mainly occurred at the TPC/adhesive interface, which generated a large number of crack lines inside the thermoplastic matrix on the surface of the nontreated PEEK and PPS substrates. Applying UV irradiation to the TPCs resulted in more obvious damage to the TPC substrates. The layer of thermoplastic matrix on the surfaces of the UV-treated PEEK and PPS substrates was completely destroyed, with a number of regions on the surface showing bare carbon fibers. The observations demonstrated that UV irradiation successfully increased the adhesion at the TPC-adhesive interface to a level that was sufficient to transform the failure mode from TPC-adhesive interfacial failure to substrate failure in the TPC substrates. This phenomenon resulted in the significantly increased LSS of the TPC-Al joints. It is worth noting that the humidity resistance of the TPC-Al joints was also investigated in another study [20]. The results

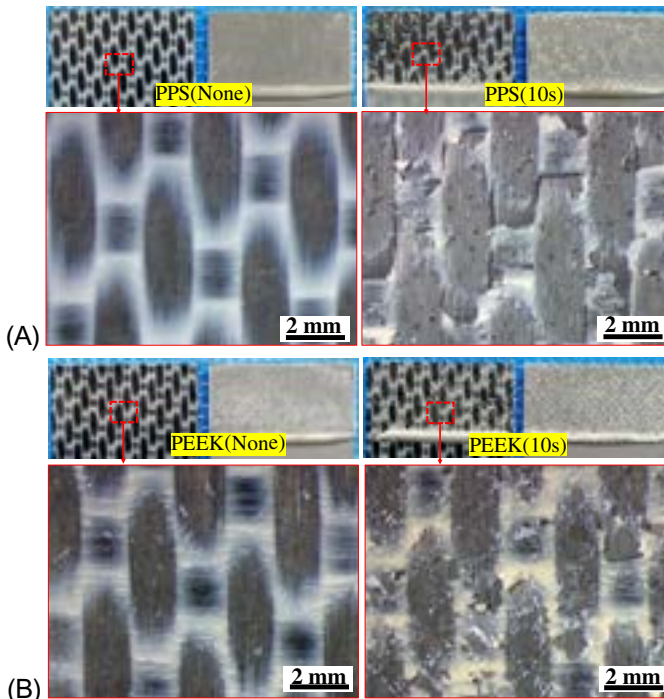


Fig. 12.8 Typical photographs and microscopy images of the failure surfaces of the lap shear specimens of the TPC-Al joints. (A) PPS-Al Joints; (B) PEEK-Al Joints.

demonstrated good performance of the UV-treated substrate/adhesive interface upon exposure of the adhesive joints to high humidity and temperature.

12.5.3 The Mode I and Mode II fracture behavior

It should be noted that only the adhesive joints between PEEK composites and Al substrates were investigated in this section. The PEEK composite substrates were UV irradiated for 7 s prior to adhesive bonding. Additionally, the DCB and ELS specimens of the nontreated PEEK-Al joints failed during the machining process, and hence no result for the nontreated adhesive joints is presented in this section.

12.5.3.1 Failure mode of the adhesive joints

Fig. 12.9 shows photographs and microscopy images of the fracture surfaces of the AF163-2OST adhesive joints. The color of the adhesive layer was green for the AF163-2OST adhesive and red for the AF163-2K adhesive. From the photographs of the Mode I and Mode II fracture surfaces, it was observed that both sides of the fractured specimens were attached with a layer of green color adhesive. Additionally, the representative SEM images showed that there were a large number of broken and debonded fibers on the fracture surfaces of the AF163-2OST adhesive joints in all cases. These fibers were the thermoplastic fibers that made up the nonwoven supporting carriers of the AF163-2OST adhesives. This indicates that the crack propagated cohesively inside the adhesive layers during the fracture processes of the AF163-2OST adhesive joints in both cases. The joints bonded by the AF163-2K adhesives exhibited significantly different types of failure mode to the AF163-2OST adhesive joints. As can be seen from the photographs of the fracture surfaces in Fig. 12.9,

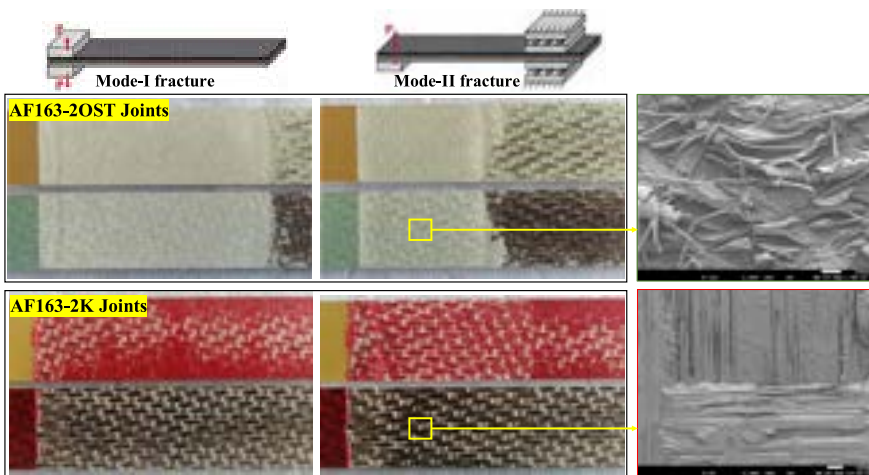


Fig. 12.9 Representative photographs and microscopy images of the fracture surfaces of the PEEK-Al joints. The images to the left refer to Mode I while those to the right refer to Mode II fracture tests. The insert SEM images are representative for both Mode I and Mode II fracture.

the entire red color adhesive layers were left on the Al sides of the Mode I and Mode II fracture surfaces. Additionally, the adhesive layers were all decorated with a large amount of PEEK debris. These phenomena indicate that substrate damage to the PEEK substrates occurred during the fracture process of the AF163-2K adhesive joints. This was associated with the peeling off of the PEEK resin from the composite substrates and associated carbon fiber breakage during the fracture process.

The above observations clearly demonstrate that excellent adhesion at the interface between the adhesives and the PEEK composites was obtained upon applying a rapid UV treatment (lasting for only 7 s) to the composite substrates. More importantly, the level of the adhesion was sufficient to prevent a failure at the adhesive/composite interfaces in all cases. However, the question that arises was why the AF163-2OST adhesive joints and the AF163-2K adhesive joints exhibited significantly different failure modes? As mentioned in [Section 12.5.1](#), the only difference between the two adhesives was the supporting carrier, that is, thermoplastic nonwoven for the AF163-2OST adhesive and thermoplastic fiber knit for the AF163-2K adhesive. During the fracture processes, the crack always propagated along the weakest path in the vicinity of the adhesive joints in both cases. For the AF163-2K adhesive, the thermoplastic fibers of the knit carrier were in a continuous and well-structured form, which formed a strong structure within the adhesive layer and prevented a cohesive failure. Accordingly, the crack migrated into the PEEK composite substrates. In contrast, the supporting carrier of the AF163-2OST adhesive consisted of randomly distributed thermoplastic discontinuous fibers, and hence it possessed relatively low failure strength. In this case, the crack was easily diverted into the adhesive layers, and remained within it while propagating forward in a stable manner.

12.5.3.2 Fracture energies of the adhesive joints

The load versus displacement curves of the fracture tests are shown in [Fig. 12.10](#). In general, a steady crack propagation failure mode was observed during the Mode I and Mode II fracture processes of the AF163-2OST adhesive joints. This corresponded to the relatively smooth load versus displacement curves. In contrast, typical nonsteady crack propagation behavior was observed for the AF163-2K joints in all cases. Specifically, a stick-slip fracture behavior was observed for the DCB tests, resulting in “saw-tooth” shaped load versus displacement curves. The ELS specimens failed dynamically (the crack suddenly jumped to the end of the specimens) after the crack had propagated for approximately 3 mm, resulting in a sharp drop of the load versus displacement curves at the peak. The different mechanical responses of the fracture specimens between the AF163-2OST joints and the AF163-2K joints were attributed to the different architectures of the crack paths. For the AF163-2OST joints, the crack propagated within the adhesive layer, in which the debonding, pulling out, and bridging mechanisms of the numerous thermoplastic fibers (as observed in [Fig. 12.9](#)) prevented obvious jumping of the crack. However, the dominating failure mechanism of the AF163-2K joints was the removal of PEEK resin from extensive regions on the surface of the composite substrate, as shown in [Fig. 12.9](#). In this case, the local nonuniformity caused by the woven style of the carbon fibers led to nonstable crack propagation in the adhesive

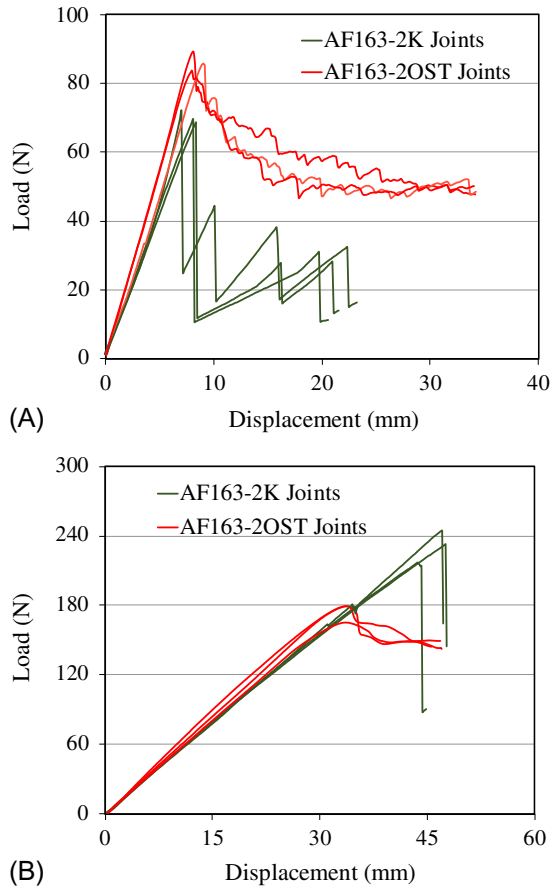


Fig. 12.10 The load versus displacement curves of the DCB and ELS tests of the PEEK-Al joints. (A) DCB; (B) ELS.

joints. Additionally, a dynamic failure of the Mode II fracture specimens was typically associated with significant extension in the length of the fracture process zone ahead of the crack tip and an associated increase in the value of G_{IIc} [42,43].

The Mode I and Mode II fracture energies of the adhesive joints are shown in Table 12.6. It should be noted that the G_{IIc} of the AF163-2K joints were taken as the values prior to the dynamic failure, that is, the maximum values on the corresponding R curves. It was observed that the AF163-2OST joints possessed a much higher G_{Ic} than the AF163-2K joints. This was because the debonding, breakage, and bridging mechanisms of the thermoplastic fibers noted above were highly effective for energy dissipation during a Mode I opening fracture [44,45], and subsequently increased the fracture energies of the adhesive joints. However, the typical low surface energy of the thermoplastic fibers caused a relatively weak adhesion at the interface between the individual thermoplastic fibers and the epoxy adhesive matrix. This negatively affected the shearing properties of the AF163-2OST adhesive

Table 12.6 Fracture energy value of each specimen (indicated by S1–S3) and the corresponding average values from the DCB and ELS tests of the PEEK-Al adhesive joints.

Items		G_{Ic} (J/m ²)	G_{IIIc} (J/m ²)
AF163-2OST	S1	1235	3522
	S2	1120	3352
	S3	1156	3406
	Mean	1170 ± 59	3427 ± 87
AF163-2K	S1	667	5794
	S2	796	6626
	S3	680	6862
	Mean	715 ± 71	6428 ± 561

layers. This explains why the mean value of G_{IIIc} of the AF163-2K joints is 88% higher than that of the AF163-2OST joints. Overall, the different crack propagation modes (in turn determined by the different scrim architectures of the adhesives) had a significant effect on the fracture energies of the adhesive joints.

12.6 Joining TPCs to TSCs

12.6.1 Surface treatment and joint preparation

The PPS and PEEK composites were placed in the UV irradiation chamber for a rapid surface treatment lasting 6 s. The TPC-TSC adhesive joints were prepared using a cobonding process. The carbon fiber-reinforced epoxy composite, that is, TSC, was unidirectional prepreg, HexPly 8552-IM7-35%-134 from Hexcel. The epoxy adhesive was an aerospace-grade film adhesive, FM300M from Solvay. A lay-up consisting of eight plies of carbon fiber/epoxy prepreg and one layer of film adhesive was prepared by a hand lay-up process, and then placed onto the consolidated and surface-irradiated TPC laminates. The assemblies were cured in an autoclave using a single dwell step at 180°C for 90 min. Hybrid joints without film adhesives between the epoxy composite and the TPCs were also prepared by following the same curing procedure. As in the case of the TPC-Al joints, the configurations of the TPC-TSC joints were defined to ensure that the flexural moduli of the TPC and TSC adherends were approximately equal, thereby ensuring an essentially pure Mode I fracture in the following DCB tests. After curing, specimens with the desired dimensions were cut from the bonded panels for subsequent lap shear and Mode I fracture testing; see Fig. 12.11. It should be noted that all the hybrid joints consisting of nontreated TPCs failed during the cutting process. This was due to the typically poor adhesion at the PPS-epoxy and PEEK-epoxy interfaces.

12.6.2 The lap shear strength

The LSSs of the hybrid TPC-TSC joints from the single lap shear joint tests are summarized in Fig. 12.12. In this figure, PPS(UV)/epoxy means the joints between the epoxy composites and the UV-treated PPS composite without a layer of adhesive

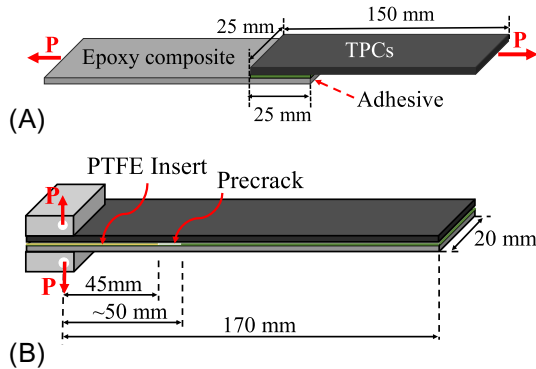


Fig. 12.11 Schematics of the (A) single lap shear joint test and (B) DCB test.

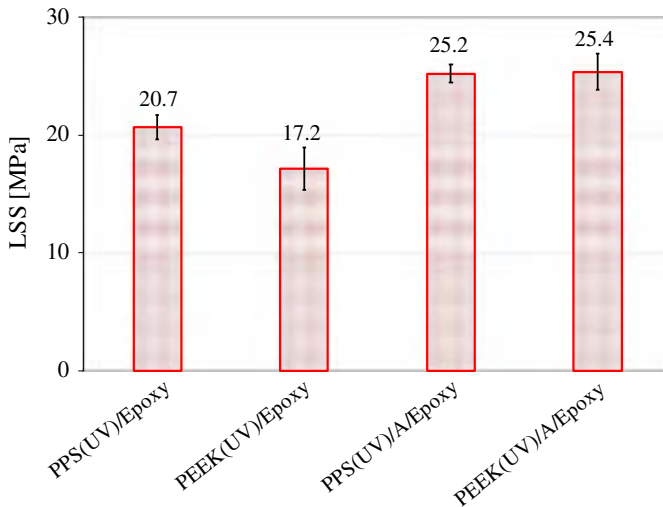


Fig. 12.12 The lap shear strengths of the hybrid TPC-TSC joints.

in between, and PPS(UV)/A/epoxy indicates the joints bonded with adhesives. As noted above, the LSSs were not measurable for the nontreated hybrid joints as they failed prior to test in all cases. It is clear that the application of 6 s UV treatment to the surfaces of the PEEK and PPS composites significantly increased the LSSs of the hybrid joints. In particular, the LSSs of the hybrid joints increased from essentially zero to a value of between 20.7 and 17.2 MPa for the PPS(UV)/Epoxy joints and the PEEK(UV)/Epoxy joints, respectively. More prominent increases in the LSSs were achieved for the adhesive bonded joints in conjunction with the UV treatment, that is, LSSs of 25.2 and 25.4 MPa were observed for the PPS(UV)/A/epoxy joints and the PEEK(UV)/A/epoxy joints, respectively.

The fracture surfaces of the lap shear specimens were analyzed to correlate the significantly enhanced lap shear strength with the failure locus and mechanisms of the

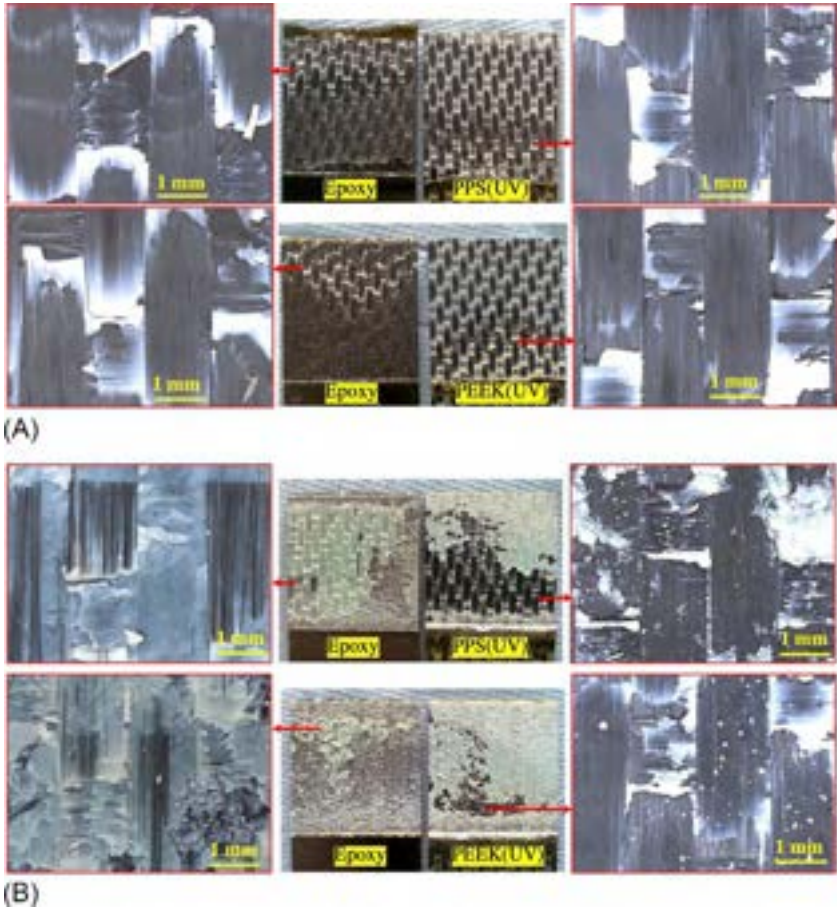


Fig. 12.13 Typical images of the fracture surfaces of the lap shear specimens of the co-cure bonded TPC-TSC joints. (A) Joints without adhesives; (B) Joints with adhesives.

hybrid joints. Fig. 12.13 shows typical images of the fracture surfaces of the lap shear specimens joined without and with film adhesives. For the hybrid joints without film adhesives, a large amount of white color PPS or PEEK polymers appeared on the surfaces of the epoxy composite substrates, leaving bare carbon fibers on the corresponding location of the opposite TPC sides, as shown in Fig. 12.13A. This indicates that substrate damage to the TPCs occurred during the lap shear test, that is, the thermoplastic polymer matrices on the surfaces of the UV-treated PPS and PEEK composite substrates were damaged and peeled off from the carbon fibers. An alternation of cohesive failure in the adhesive layer and substrate damage to the TPC substrates was observed for the hybrid joints bonded with adhesives, as shown in Fig. 12.13B. The damage to the TPCs was more severe when compared to their counterparts without film adhesives, that is, apart from damage and debonding of the

thermoplastic polymers, extensive carbon fiber delamination and breakage also took place. All these observations demonstrated that applying UV treatment to the TPCs significantly improved the adhesion with epoxies to a level that was sufficient to cause substrate damage to the PEEK and PPS composite substrates during the lap shear test. This resulted in remarkable increases in the LSSs of the adhesive joints, that is, from essentially zero to a value of between 17.2 and 25.4 MPa, as shown in Fig. 12.12.

12.6.3 The Mode I fracture behavior

The load versus displacement curves and the corresponding R curves from the DCB tests of the UV-treated hybrid TPC-TSC joints are shown in Fig. 12.14. A stick-slip fracture behavior was exhibited for the PEEK(UV)/epoxy joints, evidenced by the zigzag shape of the corresponding load versus displacement curve in Fig. 12.14A. In this case,

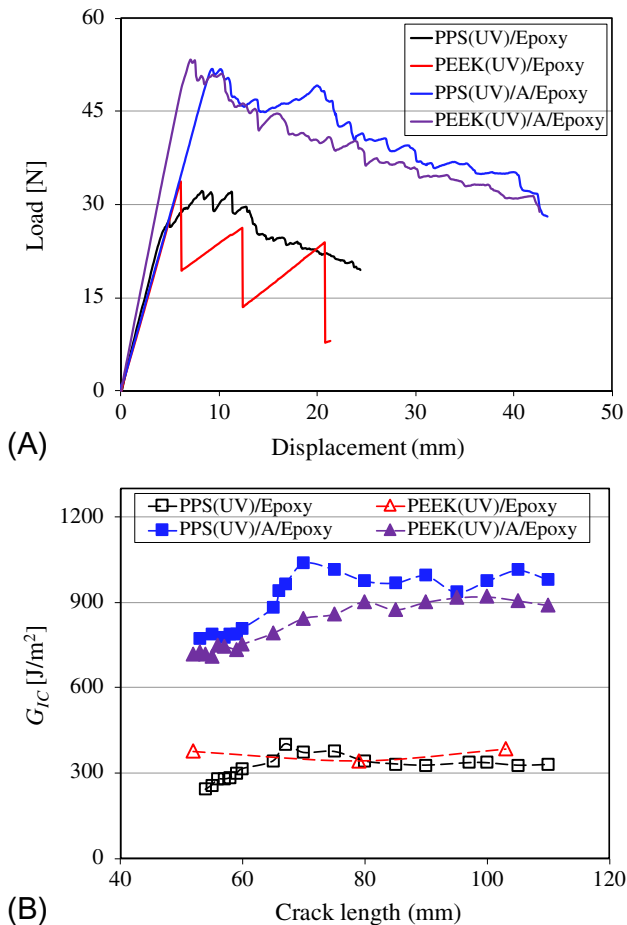
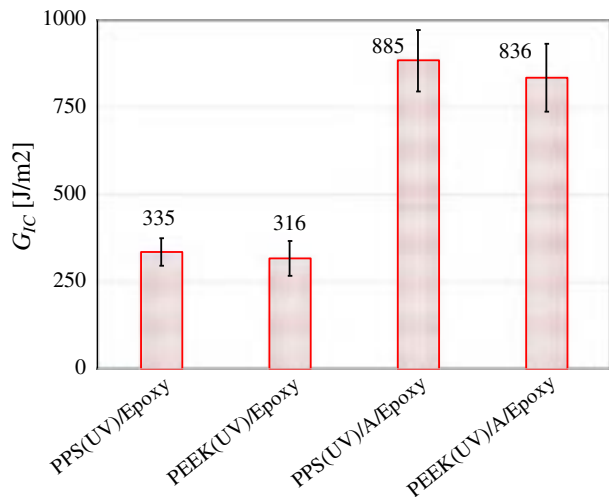


Fig. 12.14 Representative load versus displacement curves and corresponding R curves from the DCB tests of the TPC-TSC joints. (A) Load versus displacement curves; (B) R curves.

the values of the load at the peak points were used for the calculation of the fracture energy. Apart from the PEEK(UV)/epoxy joints, all other hybrid joints exhibited stable fracture propagation behavior. It is clear that the failure loads of the DCB specimens were much higher for the joints bonded with adhesives than their counterparts without adhesives. This corresponded to higher fracture energies of the adhesive bonded joints, as shown in Fig. 12.14B. Moreover, the R curves of the adhesive bonded joints exhibited an obviously “rising” trend for both the PPS(UV)/A/epoxy and PEEK(UV)/A/epoxy joints, indicating the presence of extensive fiber bridging during the fracture process. The Mode I fracture propagation energies, G_{Ic} , of the hybrid TPC/TSC joints are summarized in Fig. 12.15. The fracture energies of the hybrid joints without adhesives were measured to be 335 and 316 J/m² for the PPS(UV)/epoxy and PEEK(UV)/epoxy joints, respectively. These values were slightly lower than the interlaminar fracture energy of the epoxy composite, which was reported to be 380 J/m² in [36]. The fracture energies of the UV-treated PPS(UV)/A/epoxy and PEEK(UV)/A/epoxy joints were more or less equal, that is, 885 and 836 J/m², respectively.

An analysis of the fracture surfaces of the DCB specimens was carried out to understand the energy dissipation mechanisms during the fracture process. Typical images of the fracture surfaces of the DCB specimens bonded without and with adhesives are shown in Fig. 12.16. Some damage to the TPC substrates took place for the hybrid joints without adhesives, evidenced by the presence of many spots of white color PEEK or PPS polymers on the epoxy composite sides and signs of polymer damage on the TPC surfaces; see Fig. 12.16A. While this phenomenon indicates relatively good adhesion at the TPC/epoxy interfaces, the lack of resin at the fracture plane resulted in the relatively low Mode I fracture energies, as shown in Fig. 12.15. For the adhesive bonded joints, the majority of the adhesive together with a large amount of broken carbon fibers were observed to be well-attached to the TPC sides, leaving a small amount of adhesive on the severely damaged epoxy composite substrates. The presence of the delaminated and broken carbon fibers on the TPC surfaces, together

Fig. 12.15 Mode I fracture energies of the UV-treated hybrid joints.



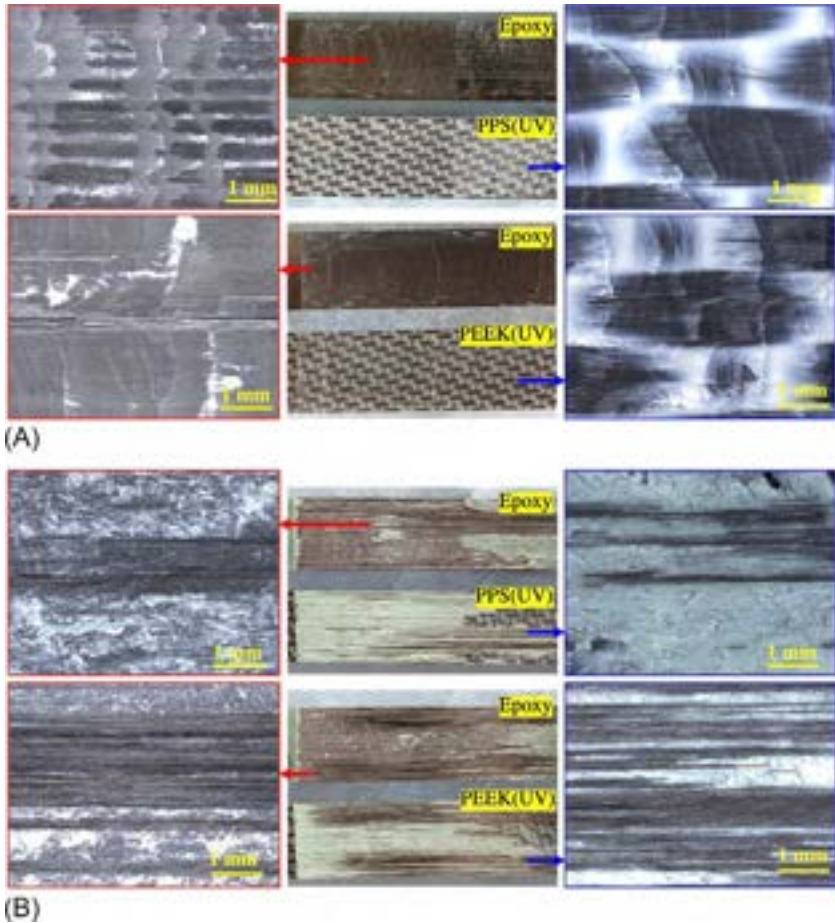


Fig. 12.16 Typical images of the fracture surfaces of the DCB specimens of the TPC-TSC joints: (A) without film adhesive and (B) with film adhesive.

with the “rising” trend of the R curves in Fig. 12.14B typically indicate extensive carbon fiber bridging during the fracture process. Overall, the significantly enhanced adhesive/TPC interface adhesion upon UV treatment resulted in severe damage to the adhesive layers and the epoxy composite substrates during the fracture process, and subsequently resulted in the high fracture energies of the adhesive bonded hybrid joints, as shown in Fig. 12.15.

12.7 Conclusions and future work

These experimental observations proved that high-power UV irradiation is a very promising method for surface preparation of TPCs for adhesive joining. It has been demonstrated that short duration (between 5 and 10 s) UV irradiation notably

increased the amount of oxygen elements on the PEEK and PPS composite surfaces, and decreased their water contact angles. This significantly improved the adhesion between the adhesives and the TPCs to a level that was sufficient to transform the failure from interfacial failure of the nontreated joints to substrate damage or cohesive failure of the UV-treated joints. Consequently, adhesive joints with high structural integrity between TPCs and themselves and other dissimilar materials, such as TSCs and Al, have been developed. Overall, high-power UV irradiation proved a highly efficient, rapid, and low-cost method to treat TPCs for adhesive bonding, and hence it demonstrated significant promise for industrial mass production. However, the long-term durability and hydrothermal resistance of the UV-treated TPC/epoxy interface still require further investigation. Additionally, the mechanical properties and fracture resistance of the adhesive joints under fatigue loading conditions should also be studied.

References

- [1] T. Zhao, G. Palardy, I. Fernandez Villegas, C. Rans, M. Martinez, R. Benedictus, Mechanical behaviour of thermoplastic composites spot-welded and mechanically fastened joints: a preliminary comparison, *Compos. Part B Eng.* 1359-8368, 112 (2017) 224–234, <https://doi.org/10.1016/j.compositesb.2016.12.028>.
- [2] S.D. Thoppul, J. Finegan, R.F. Gibson, Mechanics of mechanically fastened joints in polymer-matrix composite structure—a review, *Compos. Sci. Technol.* 0266-3538, 69 (3) (2009) 301–329, <https://doi.org/10.1016/j.compscitech.2008.09.037>.
- [3] A. Mehboob, S.-H. Chang, Effect of composite bone plates on callus generation and healing of fractured tibia with different screw configurations, *Compos. Sci. Technol.* 0266-3538, 167 (2018) 96–105, <https://doi.org/10.1016/j.compscitech.2018.07.039>.
- [4] D. Quan, J.L. Urdaniz, C. Rouge, A. Ivankovic, The enhancement of adhesively-bonded aerospace-grade composite joints using steel fibres, *Compos. Struct.* 0263-8223, 198 (2018) 11–18, <https://doi.org/10.1016/j.compstruct.2018.04.071>.
- [5] C. Barile, C. Casavola, G. Pappalettera, P.K. Vimalathithan, Characterization of adhesive bonded CFRP laminates using full-field digital image stereo-correlation and finite element analysis, *Compos. Sci. Technol.* 0266-3538, 169 (2019) 16–25, <https://doi.org/10.1016/j.compscitech.2018.10.032>.
- [6] D. Quan, N. Murphy, A. Ivankovic, Fracture behaviour of a rubber nano-modified structural epoxy adhesive: bond gap effects and fracture damage zone, *Int. J. Adhes. Adhes.* 0143-7496, 77 (2017) 138–150, <https://doi.org/10.1016/j.ijadhadh.2017.05.001>.
- [7] R. Tao, X. Li, A. Yudhanto, M. Alfano, G. Lubineau, On controlling interfacial heterogeneity to trigger bridging in secondary bonded composite joints: an efficient strategy to introduce crack-arrest features, *Compos. Sci. Technol.* 0266-3538, 188 (2020) 107964, <https://doi.org/10.1016/j.compscitech.2019.107964>.
- [8] C. Ageorges, L. Ye, M. Hou, Advances in fusion bonding techniques for joining thermoplastic matrix composites: a review, *Compos. A Appl. Sci. Manuf.* 1359-835X, 32 (6) (2001) 839–857, [https://doi.org/10.1016/S1359-835X\(00\)00166-4](https://doi.org/10.1016/S1359-835X(00)00166-4).
- [9] E. Tsiangou, S. Teixeira de Freitas, I. Fernandez Villegas, R. Benedictus, Investigation on energy director-less ultrasonic welding of polyetherimide (PEI)- to epoxy-based composites, *Compos. Part B Eng.* 1359-8368, 173 (2019) 107014, <https://doi.org/10.1016/j.compositesb.2019.107014>.

- [10] A. Pramanik, A.K. Basak, Y. Dong, P.K. Sarker, M.S. Uddin, G. Littlefair, A.R. Dixit, S. Chattopadhyaya, Joining of carbon fibre reinforced polymer (CFRP) composites and aluminium alloys—a review, *Compos. A Appl. Sci. Manuf.* 1359-835X, 101 (2017) 1–29, <https://doi.org/10.1016/j.compositesa.2017.06.007>.
- [11] A.J. Kinloch, *Adhesion and Adhesives: Science and Technology*, Chapman and Hall, 1987.
- [12] S.M. Goushegir, J.F. dos Santos, S.T. Amancio-Filho, Friction spot joining of aluminum AA2024/carbon-fiber reinforced poly(phenylene sulfide) composite single lap joints: microstructure and mechanical performance, *Mater. Des.* (1980-2015) 0261-3069, 54 (2014) 196–206, <https://doi.org/10.1016/j.matdes.2013.08.034>.
- [13] E. Arikan, J. Holtmannspötter, F. Zimmer, T. Hofmann, H.-J. Gudladt, The role of chemical surface modification for structural adhesive bonding on polymers—washability of chemical functionalization without reducing adhesion, *Int. J. Adhes. Adhes.* 0143-7496, 95 (2019) 102409, <https://doi.org/10.1016/j.ijadhadh.2019.102409>.
- [14] A.J. Kinloch, G.K.A. Kodokian, J.F. Watts, Relationships between the surface free energies and surface chemical compositions of thermoplastic fibre composites and adhesive joint strengths, *J. Mater. Sci. Lett.* 1573-4811, 10 (14) (1991) 815–818, <https://doi.org/10.1007/BF00724747>.
- [15] A.J. Kinloch, C.M. Taig, The adhesive bonding of thermoplastic composites, *J. Adhes.* 21 (3–4) (1987) 291–302, <https://doi.org/10.1080/00218468708074976>.
- [16] G.K.A. Kodokian, A.J. Kinloch, Surface pretreatment and adhesion of thermoplastic fibre-composites, *J. Mater. Sci. Lett.* 1573-4811, 7 (6) (1988) 625–627, <https://doi.org/10.1007/BF01730315>.
- [17] G.K.A. Kodokian, A.J. Kinloch, The adhesive fracture energy of bonded thermoplastic fibre-composites, *J. Adhes.* 29 (1–4) (1989) 193–218, <https://doi.org/10.1080/00218468908026487>.
- [18] A.J. Kinloch, G.K.A. Kodokian, J.F. Watts, The adhesion of thermoplastic fibre composites, *Philos. Trans. R. Soc. Lond. A Phys. Eng. Sci.* 338 (1649) (1992) 83–112, <https://doi.org/10.1098/rsta.1992.0004>.
- [19] S. Deng, L. Djukic, R. Paton, L. Ye, Thermoplastic/epoxy interactions and their potential applications in joining composite structures—a review, *Compos. A: Appl. Sci. Manuf.* 1359-835X, 68 (2015) 121–132, <https://doi.org/10.1016/j.compositesa.2014.09.027>.
- [20] D. Quan, B. Deegan, L. Byrne, G. Scarselli, A. Ivanković, N. Murphy, Rapid surface activation of carbon fibre reinforced PEEK and PPS composites by high-power UV-irradiation for the adhesive joining of dissimilar materials, *Compos. A Appl. Sci. Manuf.* 1359-835X, 137 (2020) 105976, <https://doi.org/10.1016/j.compositesa.2020.105976>.
- [21] D. Quan, R. Alderliesten, C. Dransfeld, I. Tsakoniatis, R. Benedictus, Co-cure joining of epoxy composites with rapidly UV-irradiated PEEK and PPS composites to achieve high structural integrity, *Compos. Struct.* 0263-8223, 251 (2020) 112595, <https://doi.org/10.1016/j.compstruct.2020.112595>.
- [22] D. Quan, N. Murphy, B. Deegan, D. Dowling, A. Ivankovic, Adhesion improvement of thermoplastics-based composites by atmospheric plasma and UV treatments, *Appl. Compos. Mater.* 1573-4897, 28 (1) (2021) 71–89, <https://doi.org/10.1007/s10443-020-09854-y>.
- [23] D. Quan, R. Alderliesten, C. Dransfeld, I. Tsakoniatis, S. Teixeira De Freitas, G. Scarselli, N. Murphy, A. Ivanković, R. Benedictus, Significantly enhanced structural integrity of adhesively bonded PPS and PEEK composite joints by rapidly UV-irradiating the substrates, *Compos. Sci. Technol.* 0266-3538, 199 (2020) 108358, <https://doi.org/10.1016/j.compscitech.2020.108358>.
- [24] G. Yang, T. Yang, W. Yuan, Y. Du, The influence of surface treatment on the tensile properties of carbon fiber-reinforced epoxy composites-bonded joints, *Compos. Part B Eng.* 160 (2019) 446–456, <https://doi.org/10.1016/j.compositesb.2018.12.095>.

- [25] M.R. Gude, S.G. Prolongo, A. Urea, Adhesive bonding of carbon fibre/epoxy laminates: correlation between surface and mechanical properties, *Surf. Coat. Technol.* 0257-8972, 207 (2012) 602–607, <https://doi.org/10.1016/j.surfcoat.2012.07.085>.
- [26] V.H. Martínez-Landeros, S.Y. Vargas-Islas, C.E. Cruz-González, S. Barrera, K. Mourtazov, R. Ramírez-Bon, Studies on the influence of surface treatment type, in the effectiveness of structural adhesive bonding, for carbon fiber reinforced composites, *J. Manuf. Process.* 1526-6125, 39 (2019) 160–166, <https://doi.org/10.1016/j.jmapro.2019.02.014>.
- [27] R. Tao, M. Alfano, G. Lubineau, In situ analysis of interfacial damage in adhesively bonded composite joints subjected to various surface pretreatments, *Compos. A: Appl. Sci. Manuf.* 1359-835X, 116 (2019) 216–223, <https://doi.org/10.1016/j.compositesa.2018.10.033>.
- [28] C.-Q. Li, H.-B. Dong, W.-W. Zhang, Low-temperature plasma treatment of carbon fibre/epoxy resin composite, *Surf. Eng.* 34 (11) (2018) 870–876, <https://doi.org/10.1080/02670844.2017.1420417>.
- [29] J. Mohan, A. Ivanković, N. Murphy, Mixed-mode fracture toughness of co-cured and secondary bonded composite joints, *Eng. Fract. Mech.* 0013-7944, 134 (2015) 148–167, <https://doi.org/10.1016/j.engfracmech.2014.12.005>.
- [30] G.A. Wade, W.J. Cantwell, Adhesive bonding and wettability of plasma treated, glass fiber-reinforced nylon-6,6 composites, *J. Mater. Sci. Lett.* 19 (2000) 1829–1832, <https://doi.org/10.1023/A:1006706826209>.
- [31] H.M.S. Iqbal, S. Bhowmik, R. Benedictus, Surface modification of high performance polymers by atmospheric pressure plasma and failure mechanism of adhesive bonded joints, *Int. J. Adhes. Adhes.* 0143-7496, 30 (6) (2010) 418–424, <https://doi.org/10.1016/j.ijadhadh.2010.02.007>.
- [32] K. Ramaswamy, R.M. O’Higgins, A.K. Kadiyala, M.A. McCarthy, C.T. McCarthy, Evaluation of grit-blasting as a pre-treatment for carbon-fibre thermoplastic composite to aluminium bonded joints tested at static and dynamic loading rates, *Compos. Part B Eng.* 1359-8368, 185 (2020) 107765, <https://doi.org/10.1016/j.compositesb.2020.107765>.
- [33] S. Genna, C. Leone, N. Ucciardello, M. Giuliani, Increasing adhesive bonding of carbon fiber reinforced thermoplastic matrix by laser surface treatment, *Polym. Eng. Sci.* 57 (2017) 685–692, <https://doi.org/10.1002/pen.24577>.
- [34] R. Bradley, I. Clackson, D. Sykes, UV ozone modification of wool fibre surfaces, *Appl. Surf. Sci.* 0169-4332, 72 (2) (1993) 143–147, [https://doi.org/10.1016/0169-4332\(93\)90005-V](https://doi.org/10.1016/0169-4332(93)90005-V).
- [35] I. Mathieson, R.H. Bradley, Improved adhesion to polymers by UV/ozone surface oxidation, *Int. J. Adhes. Adhes.* 0143-7496, 16 (1) (1996) 29–31, [https://doi.org/10.1016/0143-7496\(96\)88482-X](https://doi.org/10.1016/0143-7496(96)88482-X).
- [36] H. Shi, J. Sinke, R. Benedictus, Surface modification of PEEK by UV irradiation for direct co-curing with carbon fibre reinforced epoxy prepregs, *Int. J. Adhes. Adhes.* 0143-7496, 73 (2017) 51–57, <https://doi.org/10.1016/j.ijadhadh.2016.07.017>.
- [37] D. Quan, B. Deegan, L. Binsfeld, X. Li, J. Atkinson, A. Ivankovic, N. Murphy, Effect of interlaying UV-irradiated PEEK fibres on the mechanical, impact and fracture response of aerospace-grade carbon fibre/epoxy composites, *Compos. Part B Eng.* 1359-8368, 191 (2020) 107923, <https://doi.org/10.1016/j.compositesb.2020.107923>.
- [38] A.J. Kinloch, *Durability of Structural Adhesives*, Applied Science Publishers Ltd, 1983.
- [39] S. Ebnesajjad, Surface tension and its measurement, in: S. Ebnesajjad (Ed.), *Handbook of Adhesives and Surface Preparation*, Plastics Design Library, William Andrew Publishing, Oxford, 2011, pp. 21–30, ISBN: 978-1-4377-4461-3, <https://doi.org/10.1016/B978-1-4377-4461-3.10003-3>.

- [40] J. Flanagan, P. Schutze, C. Dunne, B. Twomey, K.T. Stanton, Use of a blast coating process to promote adhesion between aluminium surfaces for the automotive industry, *J. Adhes.* (2018) 1–22, <https://doi.org/10.1080/00218464.2018.1486713>.
- [41] A. Agha, F. Abu-Farha, Viscoelastic model to capture residual stresses in heat cured dissimilar adhesive bonded joints, *Int. J. Adhes. Adhes.* 0143-7496, 107 (2021) 102844, <https://doi.org/10.1016/j.ijadhadh.2021.102844>.
- [42] B. Blackman, A. Kinloch, M. Paraschi, The determination of the mode II adhesive fracture resistance, $G_{II}C$, of structural adhesive joints: an effective crack length approach, *Eng. Fract. Mech.* 0013-7944, 72 (6) (2005) 877–897, <https://doi.org/10.1016/j.engfracmech.2004.08.007>.
- [43] D. Quan, J.L. Urdaniz, A. Ivankovic, Enhancing mode-I and mode-II fracture toughness of epoxy and carbon fibre reinforced epoxy composites using multi-walled carbon nanotubes, *Mater. Des.* 0264-1275, 143 (2018) 81–92, <https://doi.org/10.1016/j.matdes.2018.01.051>.
- [44] D. Quan, F. Bologna, G. Scarselli, A. Ivankovic, N. Murphy, Interlaminar fracture toughness of aerospace-grade carbon fibre reinforced plastics interleaved with thermoplastic veils, *Compos. A: Appl. Sci. Manuf.* 128 (2020) 105642, <https://doi.org/10.1016/j.compositesa.2019.105642>.
- [45] V.A. Ramirez, P.J. Hogg, W.W. Sampson, The influence of the nonwoven veil architectures on interlaminar fracture toughness of interleaved composites, *Compos. Sci. Technol.* 0266-3538, 110 (2015) 103–110, <https://doi.org/10.1016/j.compscitech.2015.01.016>.

This page intentionally left blank

Advances in structural wood products adhesive bonding

13

Frederick A. Kamke and John A. Nairn
Oregon State University, Corvallis, OR, United States

13.1 Overview

Adhesives used for bonding wood are many and varied. Industrial wood adhesives are the subject of this review, with a focus on structural adhesives. Structural adhesives are intended for applications where the strength and stiffness of the adhesive should meet or exceed the wood properties. Structural adhesives must perform in long-term load applications, such as structural wood panels, composite wood beams, and cross-laminated timber. The structural adhesives included in this review are incorporated into structural wood composites. There are other adhesives used to bond wood in the furniture and cabinet industries as well as those adhesives used by craftsmen and do-it-yourselfers (DIY). For example, a common DIY adhesive is polyvinyl acetate (PVAc)—a thermoplastic with many nonstructural applications. There are also elastomeric construction adhesives (mastics) that are used extensively in wood building construction and typically in combination with mechanical fastener systems. Non-structural adhesives and mastics are not included in this review.

Structural wood adhesives are thermosets that are formulated for specific product applications as well as proprietary formulations for specific customers. Due to the customization of specific adhesive products, only general characterizations of the selected adhesive types are possible. Often, the speed of cure is critical. Thus, two-component (2K) adhesive systems are available, such as some polyurethanes (PUR), melamine-formaldehyde (MF), and phenol-resorcinol-formaldehyde (PRF) systems. The components of the 2K systems are stored separately and then mixed just before they are needed. Fluid characteristics of structural adhesives are also important due to issues of storage, flow, atomization, penetration, tack, and wetting of the wood surface. Some thermoset adhesives are applied to wood as 100% solid oligomers, such as diphenyl-methane-diisocyanate (often designated as pMDI to indicate a prepolymer). Other thermosets, such as phenol-formaldehyde (PF) and MF, are prepolymerized and dispersed in water. Some of the aqueous thermoset adhesive systems may be partially polymerized and spray dried to produce a powder, thus reducing weight for transportation and extending shelf life. The powdered adhesives may be rehydrated before use or applied as a powder and heated to initiate flow onto and into the wood substrate.

Increasingly, adhesive formulators, composite manufacturers, and customers are striving for adhesives with lower environmental impact, lower human toxicity, and

less dependence on petrochemicals. Toward this end, plant-based feedstocks have been extensively investigated over the past decade, in addition to alternatives to formaldehyde chemistry. Some bio-based adhesive products have found success in the wood-based composites industry. However, most commercial applications have been nonstructural and applications where water resistance is not critical. Partial substitution of petrochemicals by lignin and certain plant proteins has been commercially realized.

This chapter focuses on the developments of structural adhesives used for wood and their performance in structural wood-based composites over the past 10 years. Some background is provided for context. Topics include substrate characteristics, introduction to structural wood products, standards and test methods, new developments for wood adhesives, wood and adhesive interactions, bond strength characterization, toughness, bond stiffness, and durability.

13.2 Substrate considerations

Adhesive bonding of wood must consider the hygroscopic and porous nature of wood surfaces as well as significant differences among wood species in density, porosity, and liquid permeability. Wood is anisotropic, with unique surface anatomy on a microscale depicted as tangential, radial, and transverse surfaces (Fig. 13.1). Microstructural features will influence the depth of adhesive penetration into wood and subsequently impact the distribution of stress at the bond. The size and orientation of the pores (lumens) and the nature of the pits between cells affect the flow of liquids and gases in wood.

Pore structure orientation greatly affects liquid penetration. The permeability in the longitudinal direction (also called grain direction) may be 10,000 times greater than either the tangential or radial directions, thus promoting deep penetration of adhesives in the longitudinal direction. Wood cells created in a tree stem growing in temperate climates often exhibit greater porosity (large cell lumens) in the spring and summer seasons, when growth is rapid, compared to the fall. The former is referred to as earlywood and the latter as latewood (also called springwood and summer wood). Fig. 13.1a shows earlywood cells at the top and bottom, with latewood in the central region. The white areas are the cell lumens. Fig. 13.2 shows circular bands of earlywood/latewood on a cross-section view of a log, where the low-porosity (high-density) latewood appears darker than the high-porosity (low-density) earlywood. Sawn lumber cuts across earlywood/latewood bands (growth rings) while rotary-peeled veneer tends to follow growth rings. The potential for adhesive penetration into earlywood is much greater than into latewood, which may lead to bonding problems associated with overpenetration in earlywood or insufficient penetration in latewood. Porosity is also affected by silviculture and genetic improvement practices that accelerate growth rate. Fast-grown softwood species typically have wide earlywood bands. Organic extenders, or inorganic and organic fillers, are used to manipulate adhesive flow characteristics to compensate for porosity differences between species. Polymeric adhesives may also be formulated to adjust viscosity through molecular weight or water content for optimum adhesive flow.

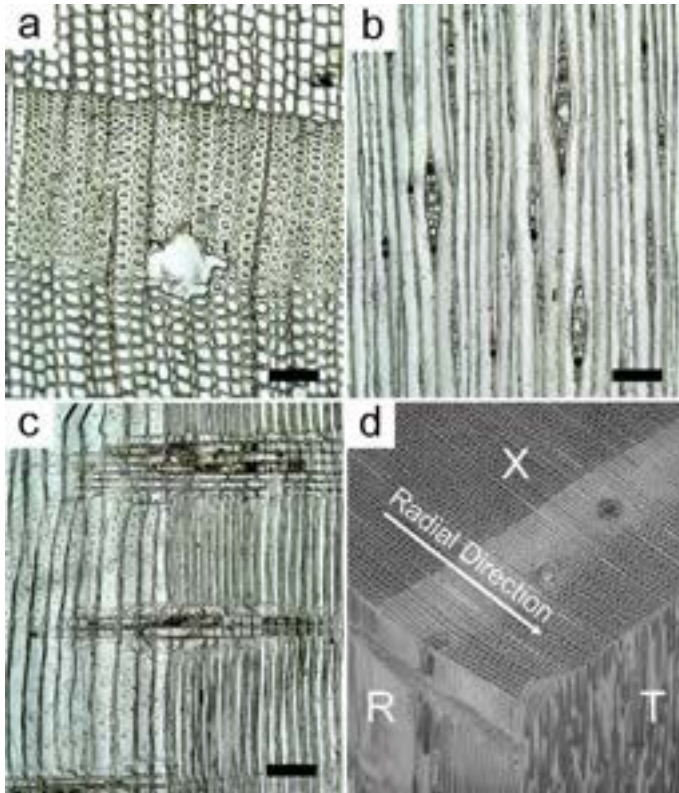


Fig. 13.1 Photomicrographs of Scotch pine (*Pinus sylvestris*); (a) transverse surface (X), (b) tangential surface (T), (c) radial surface (R), and (d) scanning electron micrograph illustrating cellular orientation; scale bars = 100 μm [1–3].



Fig. 13.2 Transverse view of Douglas fir log (*Pseudotsuga menziesii*) showing sapwood, heartwood, earlywood, and latewood.

Wood is further complicated by the natural presence of polar and nonpolar extractive chemicals, and their character and content vary by species and origin of the wood within the tree stem. While extractives are present throughout the tree stem, there is a difference between these complex organic compounds in the heartwood and sapwood (Fig. 13.2). Sapwood is differentiated from heartwood in a living tree stem due to the presence of living axial parenchyma and ray cells in sapwood, which contain various starches and lipids. Heartwood formation is characterized by the death of these cells and the breakdown of metabolic compounds into secondary metabolites, such as terpenes, phenols, fats, fatty acids, fatty alcohols, steroids, resin acids, rosin, and waxes. The chemical make-up and quantity of extractives depend on the wood species and various growth factors [4]. Loblolly pine (*Pinus taeda*), an example of one of the Southern pines, contains about 3% extractives by dry weight [5]. These extractives are primarily terpenes such as α -pinene, which is nonpolar [6]. Drying of loblolly pine in preparation for adhesive bonding causes an accumulation of nonpolar extractives at the surface, which inhibits wetting by aqueous adhesives. The addition of a surfactant to the adhesive formulation may be used to optimize wetting.

Heartwood formation is also associated with pit aspiration in some softwood (gymnosperm) species (e.g., Douglas fir, *Pseudotsuga menziesii*), which significantly reduces permeability. Some hardwood (angiosperm) species (e.g., white oak, *Quercus alba*) may form tyloses in the vessel cells of heartwood, thus blocking a critical liquid pathway and reducing permeability.

13.3 Structural wood composite products

Structural wood composite products are derived from lumber, scrim, veneer, and strands. The resulting structural wood-based composites are finger-jointed lumber, glue-laminated timber (glulam), cross-laminated timber (CLT), scrimber, plywood, laminated veneer lumber (LVL), mass plywood panels (MPP), parallel strand lumber (PSL), oriented strand board (OSB), laminated strand lumber (LSL), and I-joist (Table 13.1). Selected products and their applications are illustrated here (Figs. 13.3 and 13.4).

Sawn lumber, primarily softwood species, is used to manufacture glulam, CLT, and structural finger-jointed lumber. Finger-jointed lumber is made by cutting out critical defects (e.g., knots) and joining short lumber stock end to end using finger joints. Common adhesives used for finger joints are polyurethane (PUR), melamine-formaldehyde (MF), melamine-urea-formaldehyde (MUF), and emulsion polymer isocyanate (EPI). Glulam is composed of parallel-laminated, finger-jointed lumber and bonded with cold-setting adhesives, including PUR, MF, MUF, and melamine-phenol-formaldehyde (MPF). CLT is made by 90-degree cross lamination of alternating layers of finger-jointed lumber. The common cold-setting adhesives used for laminating CLT are PUR, MF, and MUF. Radio-frequency energy is sometimes used to accelerate cure for glulam and CLT. Many wood species of various grade classifications may be used in structural lumber composites, but all must possess minimum mechanical properties as specified in the applicable product standards. A few common species are listed in Table 13.1.

Table 13.1 Common wood species and adhesives used to manufacture structural wood-based composites in North America and Europe.

Product	Elements	Some common species	Adhesive
Finger-joint lumber	Sawn lumber	Douglas fir, Loblolly pine, Scots pine, White spruce	PUR, MF, MUF, EPI
Glue-laminated timber (Glulam)	Sawn lumber	Douglas fir, Loblolly pine, Scots pine, White spruce, Black spruce	PRF, MF, MPF, MUF
Cross-laminated timber (CLT)	Sawn lumber	Douglas fir, Loblolly pine, Scots pine, White spruce	MF, MUF, PUR
Mass plywood panels (MPP)	Veneer	Douglas fir	PF, MF
Plywood	Veneer	Douglas fir, Western hemlock, Loblolly pine, birch	PF, MF, MUF
Laminated veneer lumber (LVL)	Veneer	Douglas fir, Loblolly pine, Norway spruce	PF, MF
Parallel strand lumber (PSL)	Veneer	Yellow poplar, Douglas fir	PRF
Oriented strand board (OSB)	Strands	Aspen, Southern pines	PF, pMDI, MUF
Laminated strand lumber (LSL)	Strands	Aspen	pMDI
Scrimber	Scrim	Aspen, Southern pines, bamboo	PF, MF, pMDI
I-joist	Sawn lumber, veneer, strands	See finger-jointed lumber, LVL, plywood, and OSB	MF, EPI (flange to web)

The list is not exhaustive.

Veneer is the wood element used to make plywood, LVL, MPP, and PSL. Structural veneer is rotary peeled from logs to a typical thickness of 2.5–5 mm. Therefore, the thickness direction of rotary-peeled veneer is the radial direction, and length and width are the longitudinal and tangential directions, respectively. Most structural veneer-based products are made from softwood species (Table 13.1). However, hardwood species may be used, such as yellow poplar (*Liriodendron tulipifera*) from the Mid-South and Southeastern United States.

Plywood is assembled with alternating grain orientation in adjacent layers of veneer to provide dimensional stability and some minimum mechanical performance in both flatwise directions. LVL is produced with a greater thickness than plywood and all veneer is unidirectionally oriented. Structural plywood and LVL are produced in a heated press using PF, MF, or MUF adhesives. Although PSL contains the word “strand” in its name, it is produced from rotary-peeled veneer that has been clipped

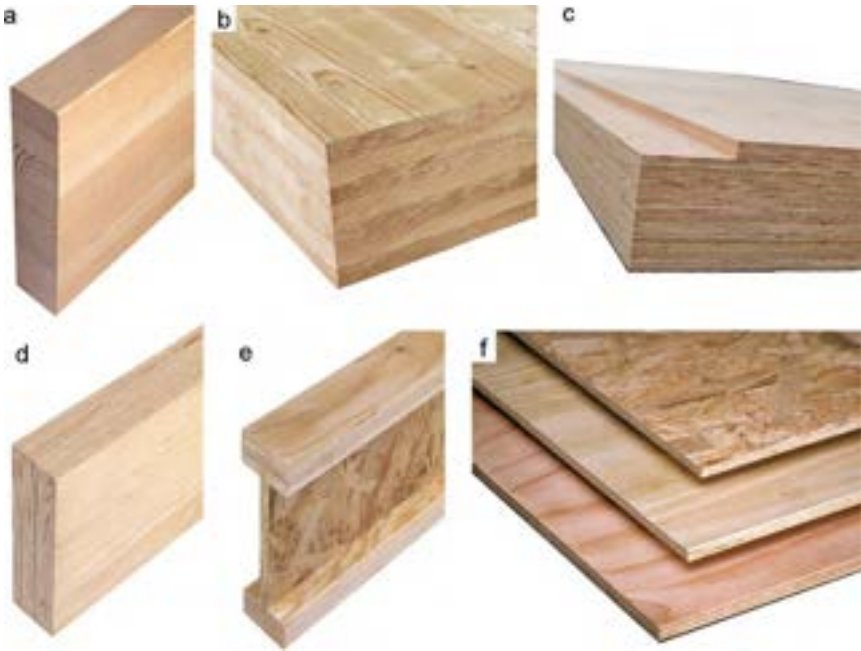


Fig. 13.3 Common structural wood-based composites: (a) glue laminated timber (glulam), (b) cross-laminated timber (CLT), (c) mass plywood panel (MPP), (d) laminated veneer lumber (LVL), (e) composite I-joist composed of LVL flange and OSB web, and (f) plywood and oriented strand board sheathing [7].



Fig. 13.4 Examples of structural wood-based composites in building construction, (a) CLT and floor panels, (b) MPP roof and wall panels, (c) curved glulam beams with plywood sheathing, and (d) LVL beam supporting composite I-joist and OSB floor sheathing [7].

parallel to grain to create elements of wood with a length of approximately 60–250 cm and a width of about 2 cm. PRF is used to make PSL, with the “strands” parallel aligned and extruded through a continuous press and, due to its large cross-section, cured using microwave energy.

MPP is manufactured in three steps. First, plywood containing mostly parallel-laminated veneer, with 25 mm thickness, is produced using PF. Some cross-ply veneer is used to enhance the strength and stiffness across the panel width and resist warping. Then, the specialty plywood panels are assembled lengthwise using scarf joints and MF to produce long lamellae (currently up to 14.6 m). The lamellae are then assembled into billets (currently up to 3.6 m × 14.6 m) using MF, and cold-pressed with a thickness up to 61 cm [8].

Structural strand products, such as OSB and LSL, are produced from wood elements (strands) that are sliced from whole logs or bolts. The length, width, and thickness of OSB strands are approximately 100 mm, 20 mm, and 0.6 mm, respectively. LSL strands are somewhat longer, perhaps 150–250 mm to facilitate a greater degree of strand orientation during manufacture. The common adhesives are pMDI and PF. The consolidation and cure of thick LSL billets are facilitated by steam-injection pressing. LSL with a thickness greater than 40 mm is typically produced using pMDI exclusively because of its rapid cure and tolerance to steam.

Scrim is crushed wood from bark-free tree stems or bamboo culms [9]. The stem or culm is processed through a roller press to cause fractures parallel to grain, resulting in long elements (scrim) that are loosely interconnected by the plant fibers. The scrim mats are dried and then adhesive is applied by either dipping in an adhesive bath or spray application. PF, MF, or pMDI are used. Hot pressing is accomplished via radio frequency, steam injection, or a conventional platen press.

Technically, wood particles and fibers could be used to manufacture structural panels and achieve certification under the requirements of a product standard or evaluation report based on performance rating and third-party verification. However, currently there are no such commercial products. There are examples of other wood-based composite products that have been investigated or achieved some level of commercialization for structural applications, but these products are rare.

The testing requirements for structural wood composite products include mechanical properties, dimensional stability, fastener holding capacity, resistance to heat, and resistance to water. Resistance to water is mostly due to the character of the thermosetting adhesive. Product standards may include mechanical testing after the product has been subjected to some form of water exposure, often a 24 h soak in room temperature water, vacuum-pressure soaking, cyclic wetting and drying, exposure to steam, or even soaking in boiling water. Some product standards for lumber-based or veneer-based composites evaluate the adhesive bond by assessing delamination after exposure to water and some standards assess the percentage of wood failure at the bond after shear testing (the premise is the adhesive should be stronger than the wood). The major North American product standards for structural wood-based composites are listed in [Table 13.2](#). For structural wood-based composites not included in a product standard, and intended for use in building construction,

Table 13.2 Major North American product standards for structural wood-based composites.

North American Product Standards	Reference
Voluntary Product Standard PS 2-18 Performance Standard for Wood Structural Panels	[10]
Voluntary Product Standard PS 1-19 Structural Plywood	[11]
ANSI/APA PRR 410-2021 Standard for Performance-Rated Engineered Wood Rim Boards	[12]
ANSI 117-2020 Specification for Structural Glued Laminated Timber of Softwood Species	[13]
ANSI A190.1-2017 Standard for Wood Products—Structural Glued Laminated Timber	[14]
ANSI/APA PRG 320-2019 Standard for Performance-Rated Cross-Laminated Timber	[15]
ANSI/APA PRS 610.1-2018 Standard for Performance-Rated Structural Insulated Panels in Wall Applications	[16]
APA PRI-405 Performance Standard for Commercial I-Joists	[17]
CSA O121-17 Douglas Fir Plywood	[18]
CSA O151-17 Canadian Softwood Plywood	[19]
CAN/CSA O122-16 (R2021) Structural Glued Laminated Timber	[20]
CSA O325:21 Construction Sheathing	[21]
CSA O177-06 (R2020) Qualification Code for Manufacturers of Structural Glued Laminated Timber	[22]

manufacturers must develop an evaluation report (also called a “code report”) in cooperation with a third-party certification organization, such as the International Code Council Evaluation Service (Brea, California, United States) or APA—The Engineered Wood Association (Tacoma, Washington, United States).

Structural adhesives are also tested independent of specific product applications. Some test standards for structural adhesives in North America and Europe are presented in [Table 13.3](#).

Table 13.3 Selected North American and European standard test procedures for adhesive bonded wood assemblies.

North American Test Standards	Reference
ANSI 405-2018. Standard for Adhesives for Use in Structural Glued Laminated Timber	[23]
ASTM D905-08(2021) Standard test Method for Strength Properties of Adhesive Bonds in Shear by Compression Loading	[24]
ASTM D906-20 Standard Test Method for Strength Properties of Adhesives in Plywood Type Construction in Shear by Tension Loading	[25]
ASTM D5266-13(2020) Standard Practice for Estimating the Percentage of Wood Failure in Adhesive Bonded Joints	[26]

Table 13.3 Continued

North American Test Standards	Reference
ASTM D7247-17 Standard Test Method for Evaluating the Shear Strength of Adhesive Bonds in Laminated Wood Products at Elevated Temperatures	[27]
CSA O112.10-08 (R2017) Evaluation of Adhesives for Structural Wood Products (Limited Moisture Exposure)	[28]
CSA 112.9:21 Evaluation of Adhesives for Structural Wood Products (Exterior Exposure)	[29]
European Test Standards	
CSN EN 301. 2017. Adhesives, Phenolic and Aminoplastic, For Load-Bearing Timber Structures—Classification and Performance Requirements	[30]
CSN EN 15425 Adhesives—One-Component Polyurethane for Load-Bearing Timber Structures—Classification and Performance Requirements	[31]
CSN EN 16254+A1 Adhesives—Emulsion Polymerized Isocyanate (EPI) for Load-Bearing Timber Structures—Classification and Performance Requirements	[32]

13.4 New developments of wood adhesives

13.4.1 Phenolics

The most important commercial phenolic adhesives include phenol-formaldehyde (PF), resorcinol-formaldehyde (RF), and phenol-resorcinol-formaldehyde (PRF). Phenolic adhesives are thermosets with excellent bond strength to wood. They are also extremely stiff, highly resistant to water, more thermally stable than wood, and possess long-term durability.

Due to their high resistance to hydrolysis when cured, phenolic adhesives have no significant release of formaldehyde once the product is placed in service. Formaldehyde release during manufacture, or short-term release of unreacted formaldehyde in the final product, will occur. These emissions of formaldehyde are very low. Therefore, the US Environmental Protection Agency (EPA) Formaldehyde Emission Standards for Composite Wood Products Act, which was added as Title VI to the Toxic Substances Control Act in 2016, exempts PF-bonded wood products. The resole PF adhesives are the second most common adhesive system used for wood products worldwide (urea-formaldehyde is first).

Common structural applications of PF are plywood, LVL, and OSB. PF-bonded products require elevated temperature (160–210°C typical) to cure in a heated press. Consequently, the product applications are usually limited to 40 mm thickness or less. However, radio-frequency energy and microwave energy have been adapted to press technology for the manufacture of CLT, glulam, and PSL. In addition, steam-injection platen presses have been available for decades to accelerate heat transfer to the core of thick billets during the manufacture of LSL, although PF is not typically used for this application due to steam incompatibility [33,34].

Resorcinol-formaldehyde is approximately 10 times more reactive than PF due to an extra hydroxyl group on the phenyl ring [35]. The high reactivity of RF allows for cure at room temperature, and thus the feasibility of bonding thick wood products. High reactivity shortens the shelf life. Therefore, RF is typically manufactured as a two-component system. RF is relatively expensive compared to PF. To reduce overall cost, a common practice is to copolymerize PF and RF, resulting in a PF chain with resorcinol end groups in a so-called PRF system. Common applications for PRF are glulam, PSL, and finger jointing.

Organic and inorganic fillers have long been used in PF formulations to assist with the control of viscosity, penetration, and cost reduction for plywood and LVL manufacture. Common organic fillers are lignocellulosic materials derived from nutshells, furfural digester residue, and bark. A comprehensive analysis was performed on commercially produced fillers derived from alder (*Alnus rubra*) bark, walnut shell, and corn cob residue [36–38]. The average particle sizes were 30, 50, and 80 μm , respectively. Corn cob residue was reported to be high in glucan content and low in xylan content, whereas alder bark and walnut shell each had significant xylan content as well as glucan. All these fillers contained about 30% acid-insoluble lignin. The fillers reduced the surface tension of PF resin by 17%–25%, and all fillers influenced rheological behavior. The addition of any of the fillers accelerated cure rate, with corn cob residue revealing the largest effect. When fillers were separated into three size classifications and mixed with PF, the fracture energy of double-cantilever bonded wood assemblies was found to be greatest for the largest size classification of corn cob residue and alder bark, but no effect was noted for walnut shell.

Recently, fillers have been tasked to enhance bond performance and improve dispersion of the particulates in PF resin. Cellulose nanofibers (CNF), with the addition of 1% by weight, improved PF bond performance in single-lap joints tested under tension load. Beyond 1% addition, the viscosity increased markedly, thus limiting application levels [39]. The authors suggested that a high pH system, as found in PF resins, causes carboxylic and hydroxyl groups of cellulose to separate into negatively charged ions, thus increasing viscosity. Liu et al. [40] studied the cure kinetics of PF with 3% CNF addition and revealed slower cure time, greater crosslinking, and lower activation energy. Kawalerczyk et al. [41] reported a 9% increase of viscosity with 3% addition of CNF to PF, along with a 20% increase of the glue-line shear strength of plywood. In contrast, the decreased viscosity of PF with less than 0.1% CNF addition has been reported [42]. The authors noted the reduction of bending properties of plywood bonded with CNF-PF adhesive and inconclusive results for glue-line shear strength in comparison to control samples.

Inorganic nanoparticles have been evaluated as fillers in PF, including alumina [43] and montmorillonite clay [44]. The viscosity increased 49% with 2% nanoalumina addition and the cure rate was accelerated. The wet shear strength of plywood made with 2% nanoalumina in PF improved by 20% [43]. The addition of 2% montmorillonite nanoclay particles in PF was proposed to reduce the modulus of the cured PF to more closely match the modulus of wood, thus reducing stress concentration at the bonded interface [44]. The dry shear strength of plywood was not notably different due to the nanoclay. However, the wet strength increased by 57%.

The biological decay resistance of plywood and OSB has been addressed by the addition of cupric oxide nanoparticles into PF [45–48]. Improved resistance to termites and fungi of the composite has been realized. Guo et al. [47] showed the addition of 1% nano-CuO to PF accelerated polymerization. Yi et al. [48] demonstrated that while a 1%–12% addition of nano-CuO had no significant impact on bending properties or thickness swelling of OSB, a reduction of internal bond strength was noted. Gao and Du [45] showed that the shear strength of plywood made with CuO-PF improved by about 14% after a 4 h hot water soak.

Lignin, from wood and other sources, has long been pursued as a partial or complete replacement of phenol in PF formulations. The use of lignin may significantly reduce the cost of materials to produce PF resin. In addition, phenol substitution by lignin reduces reliance on crude oil in favor of a renewable material [49]. Karthäuser et al. [50] reviewed the state of the art of lignin substitution for phenol in PF adhesives. Methylolated lignins have shown promise for the complete replacement of phenol. Because lignin appears in several natural forms, the source of the lignin impacts the degree of methylation and the subsequent bond performance. The method of lignin extraction also impacts the chemistry. Organosolv, soda, Kraft, and lignosulfonate processes result in different lignin compounds. There is considerable variation in the effectiveness of phenol substitution by lignin. Some studies reported the comparable performance of a lignin-phenol-formaldehyde (LPF) adhesive in plywood with 90% substitution while other studies could not exceed 50% replacement. Furthermore, the press temperature and time used to bond plywood were not consistently applied across the studies. In general, a longer press time or a greater temperature were needed to achieve favorable results. Phenolation is another approach to lignin modification in the preparation of an LPF adhesive.

Zhang et al. [51] formulated an LPF using Kraft lignin with 50% replacement of phenol. In addition, 15% furfural was added, which improved water resistance. Furfural was proposed to act as a crosslinking agent. There was no difference of shear strength between the LPF and the control PF. Without furfural, the shear strength of the LPF was 26% less than the control PF.

Younesi-Kordkheili and Pizzi [52] reported a 50% replacement of phenol by a soda bagasse lignin in a phenol-glyoxal (PLG) adhesive, which was then fortified with 7% epoxy (diglycidyl ether of bisphenol-A). (Epoxyes are discussed in detail in Chapter 1.) The PLG epoxy adhesive was compared to a conventional PF to manufacture plywood. The authors claim lignin is cheaper than phenol and glyoxal is less toxic than formaldehyde. The dry and wet shear strengths were identical.

Lignin has long been added to PF formulations used for wood bonding. Often the adhesive supplier does not specifically identify the lignin content, but rather groups this information under the category “resin solids content” or “nonvolatile content.” The PF adhesive system still meets the requirements for a structural wood adhesive. Whether the addition of lignin serves as a filler or extender or a direct replacement for phenol in the polymer is proprietary information. Commercial applications in Europe for up to 80% replacement of phenol by lignin in plywood PF adhesives have been reported [50].

13.4.2 Amino resins

Melamine-formaldehyde has long been used to manufacture structural wood-based composites, such as glulam and CLT. In Europe MF has been used for OSB and structural plywood, but not in North America where the availability, cost, and customer preference influence adhesive selection. MF is used to manufacture MPP in North America. The advantages for MF over PF are a light-colored bondline and the ability for cold pressing with a sufficient catalyst. However, PF is less expensive compared to MF while also having better moisture durability and greater thermal resistance than MF. The other major amino resin used with wood is urea-formaldehyde (UF). UF has relatively poor water resistance compared to PF or MF, and has an issue with off-gassing formaldehyde after polymerization, although modern technology can reduce formaldehyde emissions from UF resin systems to below existing government regulations. Sometimes MF and UF blends, so-called MUF, are formulated to impart greater water resistance and/or reduce formaldehyde emission. Depending on the melamine/urea ratio, suitable moisture resistance can be achieved for structural applications of MUF [53].

The substitution of formaldehyde in MF with glyoxal-glutaraldehyde (MGG) has been demonstrated for the manufacture of plywood [54]. Cure conditions for MGG were comparable to MF. Shear strength after 24 h immersion in water was approximately 50% greater than dry specimens. Some specimens subjected to 2 h boiling showed no reduction of shear strength.

13.4.3 Polymeric isocyanate

4,4'-Diphenyl-methane-diisocyanate (pMDI) has long been a major adhesive for bonding OSB and LSL—either as a single system or in combination with PF. This adhesive has excellent water resistance while being 100% solids. It also reacts rapidly and is extremely efficient for use with OSB. When PF and pMDI are both used in OSB manufacture, pMDI is used in the core layer and PF is used in the face layer. Because pMDI tends to stick to metal and has a fast reaction rate, location in the OSB core layer is beneficial. Recent formaldehyde emission concerns have prompted the use of pMDI as a replacement for UF in particleboard (PB) and medium-density fiberboard (MDF) manufacture. Because pMDI qualifies as a structural adhesive, some PB and MDF could qualify as a structural panel if the mechanical properties could meet the applicable product standard.

PF and pMDI may be copolymerized via the PF hydroxyl group and isocyanate group (-NCO). Liu et al. [55] characterized several PF/pMDI blends, at 1:1 mass ratio, with novolac PF at various molecular weights. The lower number average molecular weight ($M_n = 277$) PF resulted in residual isocyanate functional groups in the copolymer while the most advanced PF in the study ($M_n = 505$) showed no residual NCO. In a related study, Li et al. [56] copolymerized pMDI with novolac PF to create an adhesive suitable for bonding birch (*Betula* sp.) veneer. The pMDI mass content ranged from 15% to 75% in the copolymers tested. While the pMDI had viscosity of 278 mPas, the copolymer viscosities range from 1940 to 9820 mPas depending on

the mass ratio. Increasing the pMDI content from 15% to 75% improved the dry strength and wet strength of plywood, and a mass ratio of 50% and greater resulted in 100% wood failure when tested for shear by tension loading.

Polymeric MDI is not used in laminated wood composites such as plywood, LVL, and CLT because it wets and excessively penetrates into the wood, thus depleting needed adhesive at the interface. In addition, pMDI is significantly more expensive than PF or MF. There have been studies as well as proprietary commercial efforts to develop extenders and fillers to facilitate the use of pMDI for veneer-based structural composites [57,58]. Lignin has been copolymerized with pMDI, as reported by Ang et al. [59]. The resulting adhesives have gap-filling capabilities for use in veneer composites.

Emulsion polymer isocyanate (EPI) is a water-based emulsion adhesive. EPI is extensively used for finger-joints and the assembly of flange to web in wood I-joists. Other uses include CLT, glulam, window frames, and engineered veneer flooring. The common applications benefit from the ability for cold-setting, but cure may be accelerated with elevated temperature or radio-frequency energy. EPI consists of two components—an emulsion polymer and an isocyanate crosslinker. EPI adhesives used for wood bonding contain emulsions, including polyvinyl acetate (PVAc), ethylene vinyl acetate (EVAc), vinyl acetate-acrylate copolymerized (VAAC), acrylic-styrene (AcSt), or styrene-butadiene rubber (SBR). Polymeric MDI is the preferred crosslinker due to its high reactivity and low vapor pressure [60]. EPI cure depends on the coalescence of the emulsion particles due to water sorption into the wood, followed by the reaction of -NCO with water, other -NCO groups, and hydroxyl groups in the PVAc. As with pMDI, some reaction with hydroxyl groups in wood may also occur. Advantages of EPI include light color, room temperature cure, good water resistance, long storage life, and good gap-filling capability. Disadvantages are high cost, short assembly time, and foaming (due to CO₂ generation). The successful bonding of high moisture content finger-joint stock (37%–61%) has been demonstrated using EPI; some cases exceeded the mechanical performance of dry control specimens [61].

13.4.4 Polyurethane

Polyurethane (PUR) adhesives (discussed in detail in [Chapter 3](#)) offer advantages over phenolic adhesives, such as low cure temperature, no color, no formaldehyde, and equal or better bond strength. Disadvantages include high cost, low resistance to delamination, and poor gap filling. PUR is commonly used for CLT manufacture in Europe. PUR has numerous formulations depending on the application, desired working properties, and polymer performance in service [62]. Structural adhesive application for wood products requires a crosslinked system with greater strength and approximately equivalent stiffness as the wood substrate consistent with the direction of the applied stress.

PUR adhesive chemistry has many possibilities for raw materials and reaction pathways. The formulation of PUR as a wood adhesive consists of a diisocyanate-polyol reaction followed by chain extension and crosslinking using a diamine or diol.

Traditionally, the polyol is derived from petroleum and initiates from glycerol, ethylene glycol, propylene glycol, or trimethylol propane [62]. Bio-based polyols are being used, including compounds derived from plant-based glycerol, sorbitol, glucose, and triglycerides. Alinejad et al. [63] reviewed the challenges and opportunities of using lignin as the polyol in PUR synthesis. Challenges include sulfur content, low solubility, low reactivity, high glass transition temperature, dark color, and UV instability. Lignin polyols have been found to improve gap filling and reduce the potential for delamination [64]. The replacement of isocyanate in PUR formulations was reviewed by Aristi et al. [65], who suggested that starting materials, such as oleic acid, have demonstrated feasibility to produce diisocyanates. They concluded that a completely bio-based PUR is possible using lignin, tannin, and fatty acids as raw materials.

Bonding hardwood lumber for glulam manufacture has been problematic when using PUR [66]. When using PUR, a primer is required to manufacture glue-laminated timber from European beech (*Fagus sylvatica*) and European ash (*Fraxinus excelsior*) to pass the European product standard. A primer has also been demonstrated to be effective for PUR bonding of Douglas-fir and Southern pine when subjected to a vacuum pressure soak delamination test [67].

Bonding high moisture content wood, so called “green” wood, has been a subject of investigation for several decades. González Prieto et al. [68] demonstrated finger-joint bonding of green (average MC = 80%) blue gum (*Eucalypt globulus*) using a one-part PUR. Bending tests on the finger-joints revealed no statistical difference between the green- and dry-bonded specimens or the nonfinger-joint lumber.

13.4.5 Bio-based adhesives

Bio-based adhesives are derived in part or in totality from raw materials other than petrochemicals or minerals—so-called “natural resources.” Dunky [69–71] reviewed the state of the art of adhesives derived from natural resources, including proteins, carbohydrates, and plant-based poly-hydroxyphenols (lignins and tannins). The author points out that bio-based adhesives were the precursor to modern synthetic chemistries that dominate the structural wood adhesive industry today. Bio-based adhesives may include some synthetic compounds to assist with crosslinking or other modification, but the natural materials are in the majority. Synthetic adhesives may be partially replaced by bio-based materials, therefore facilitating the adoption of alternative materials. The primary ingredients for bio-based adhesives include lignins, tannins, plant and animal proteins (blood, soy, etc.), carbohydrates, unsaturated oils, and dissolved wood. The motivations for replacing synthetic polymers with bio-based materials include concern for the environment and human health as well as the cost of raw materials. The replacement of petrochemicals with natural resources improves the global carbon balance. The use of toxic compounds, such as formaldehyde and isocyanate, may be reduced by replacement with bioproducts. Some natural resources, such as lignin in the wastestream, offer the potential for substantial cost savings as a

replacement for petrochemicals. Other recent reviews of protein-based wood adhesives [72] as well as protein-based and poly-hydroxyphenols [73] and protein-based, carbohydrate-based, and poly-hydroxyphenols [74] are available.

Protein sources for adhesive polymers are many and varied [69,72]. The most common plant proteins studied, or in commercial production as adhesive products, are soybean protein, wheat gluten, and rapeseed (canola). The most common animal proteins are blood, keratin, and casein. Raydan et al. [72] summarized the advantages and disadvantage of these common adhesive protein sources (Table 13.4).

Table 13.4 Advantages and disadvantages of some common plant and animal proteins used for bio-based adhesives [72].

Protein	Advantages	Disadvantages	Reference
Wheat gluten	Abundant Low cost High protein Dispersible in alkali or acid Abundant hydrophobic amino acids	Insoluble in water High viscosity Poor shear strength	[75–77]
Soy	Abundant Low cost High protein content Good dry strength Low temperature cure Good thermal resistance	Low water resistance Poor wettability High viscosity Slow cure time Microbial degradation Food crop	[74,76,78,79]
Rapeseed	Abundant Good water resistance	Chemical modification required	[80–82]
Blood	Very rapid cure and cold cure Moderate to high dry strength Moderate to high wet strength with crosslinking Low viscosity	Dark bondlines Energy intensive Blood meal agglomerates	[76,83,84]
Keratin	Most abundant animal proteins Hydrophobic Broad structural variation Water resistant Fungal decay protection	Nonhomogeneous Poor solubility Disinfecting process needed	[85,86]
Casein	Moderate to high dry strength Moderate water resistance Safe handling Good thermal resistance	Slow cure time Short pot life Fungal degradation Moderately expensive	[87,88]

Carbohydrate-based adhesives are derived from polysaccharides, gums, sugar oligomers, and monomeric sugars [70]. No entirely carbohydrate-based wood adhesive is currently on the market due to poor water and thermal resistance. Isocyanate or epoxide crosslinkers [74], or coreaction with PF [89], are needed. Some success with starch-based adhesives crosslinked with sodium borate, epoxy chloropropane, hexamethoxymethylmelamine, formaldehyde, and some isocyanates have been reported [74].

Lignins and tannins have received the greatest attention as precursors for polymeric adhesives and drop-in chemistries for substituted phenolic and isocyanate adhesive systems [71,74]. Tannins may be extracted from bark, wood, nut shells, fruits, and other plant sources. A few of these plant sources have a high enough tannin yield for commercialization. Black wattle (*Acacia mearnsii*) is one example of a high yield tannin bark that has been used for adhesive manufacture [90]. Tannins are suitable for wood adhesives due to their high reactivity and ease of crosslinking with hexamine, glyoxal, and tris(hydroxymethyl)nitromethane [74,91]. Tannin will also polymerize with formaldehyde and has been commercially available for decades to produce exterior-grade plywood [92]. Recently, a tannin-based adhesive was crosslinked with a bacteria-derived ϵ -poly-L-lysine (EPL) to produce an EN 314-2 class 1 plywood bond quality [93]. Hydrolysable tannins can replace up to 50% of phenol in PF formulations, but their chemical structure somewhat inhibits reactivity and global production is limited [90]. Condensed (polyflavonoid) tannins make up more than 90% of world production and have greater reactivity than hydrolysable tannins. The reactivity of condensed tannins is closer to resorcinol than phenol [90]. Consequently, condensed tannins are more suitable for adhesives. Nevertheless, condensed tannins contain 20%–30% carbohydrates that are detrimental to adhesion, thus requiring the fortification of tannin-formaldehyde adhesives with phenol to meet requirements for structural applications.

Lignin is the second most abundant polymer (cellulose is first) and has long been the subject of extraction, fractionation, and use as a chemical feedstock. The primary source of lignin is spent pulping liquor from the manufacture of paper. Consequently, lignins are characterized by the chemical pulping method such as Kraft (most common), sulfite, and soda as well as the plant source (hardwood, softwood, nonwood). Lignin must be extracted from Kraft and sulfite pulping liquor, yet retain an undesirable sulfur content. Soda lignins have no sulfur content, which makes them preferable for thermoset adhesive applications [94]. However, soda pulping is limited to nonwood resources and has a very limited global supply. Organosolv lignin is also sulfur-free, but the process is independent of a pulping operation [95]. Organosolv lignin has drawn interest for the comanufacture of ethanol, or other chemical feedstocks, from lignocellulosics such as wood. There are no major sources of organosolv lignin currently. Organosolv lignin has potential in future structural adhesive applications based on laboratory studies and pending favorable economics [96]. At present, the only large industrial-scale supply of lignin is from Kraft and sulfite pulping, yielding approximately 50 million tons annually, of which 95% is burned onsite for energy [50]. The copolymerization of lignin with PF has been demonstrated as a structural adhesive, but the cost and performance are not favorable in comparison to PF [71,97,98], and the reactivity, without modification, is lower than phenol [71].

Very few of the bio-based wood adhesive systems have significant commercial production compared to synthetic wood adhesives (PF, PRF, MF, MUF, pMDI), and none are currently commercially used for structural wood adhesives [69]. The challenges for protein-based adhesives are costly modifications required to achieve acceptable water resistance and the need for synthetic crosslinking agents, thus negating some of the environmental incentives for bio-based systems [72,73]. The challenges for carbohydrate-based adhesives are similar to the proteins, and perhaps less promising. Carbohydrates and proteins may be broken down into monomers or oligomers to obtain basic building blocks for polymeric adhesives, but at great cost and loss of environmental advantages. Lignin in the form of spent pulping liquor is abundant throughout the world, but very little has been available on the open market. The sulfur content in Kraft and sulfite lignins is a hindrance. Partial substitution for phenol will continue to be the best option for lignins in structural adhesives in the near future.

13.4.6 Formaldehyde emissions

Formaldehyde is designated by the World Health Organization (WHO) as a carcinogenic hazard to humans [99]. While formaldehyde is naturally present in the environment, anthropogenic sources include resins containing formaldehyde. Potential human exposure to formaldehyde from adhesives used for wood products occurs during the synthesis of the adhesive, adhesive application, and hot pressing during composite manufacture, as well as off-gassing from the finished product. The US EPA and other world government organizations have recognized that the emission of formaldehyde from wood composites manufactured using phenol-formaldehyde adhesive is below critical threshold levels and is exempt from testing and certification requirements [100]. UF resins are known to off-gas formaldehyde after composite manufacture due to long-term hydrolysis. Consequently, formaldehyde emission testing and regulation are required for UF-bonded wood products. Modern UF formulations using formaldehyde scavengers can be designated as ultralow emitting formaldehyde (ULEF) resins. Melamine is also added to UF to reduce formaldehyde emissions as well as improve water resistance. No added formaldehyde (NAF) resins include soy protein, polyvinyl acetate, PUR, and pMDI. The NAF resins are not subject to formaldehyde testing.

Regulations for indoor formaldehyde concentration have become stricter over time throughout the world. The WHO suggests a maximum indoor air concentration of free formaldehyde of 0.1 mg/m^3 [101]. Occupational exposure limits (OEL) have been established by many countries and range from 0.3 to 2.0 ppm [102]. Each country sets its own emission limits and test protocols. The EPA has established formaldehyde emission limits for wood composite products made using UF, MF, and MUF adhesives. However, structural panels and composite lumber as well as many mass timber products in the United States are effectively exempt from the EPA rule because PF, PRF, PUR, EPI, and pMDI are currently used in these products. MF, although a much lower formaldehyde emitter than UF, is not exempt from testing [100]. In Europe, formaldehyde emissions from structural panels are addressed by the unified European Standard EN 13986, with a class E1 limit of 0.124 mg/m^3 [103].

Biogenic formaldehyde from wood may affect formaldehyde emission testing for government regulation, particularly with wood that has been heated [104]. Structural wood composite panels and structural composite lumber manufacturing subjects wood to high temperature during drying and hot pressing, thus increasing the potential for biogenic formaldehyde generation. The drying temperature for wood strands and veneer routinely exceeds 200°C, and hot-press temperature is typically in the range of 160–210°C. Samples of Virginia pine (*Pinus virginiana*) and yellow poplar (*Liriodendron tulipifera*) that were never heated produced biogenic formaldehyde in the range of 0.6–2.7 µg/g dry wood and 3–10 µg/g dry wood, respectively. After they were heated at 200°C for 10 min, the biogenic formaldehyde generation range was 17–38 and 34–45 µg/g dry wood, respectively [104]. When subjected to the same heating conditions, radiata pine (*Pinus radiata*) exhibited 2–3 times more formaldehyde generation than Virginia pine and yellow poplar. The three wood species studied showed different levels of biogenic formaldehyde generation, which could impact the formaldehyde emission level of wood-based composites regardless of the type of adhesive used.

13.5 Adhesive/wood interactions

The anisotropic, porous, lignocellulose nature of wood presents many challenges to successful adhesive bonding. Past success for adhesive bonding in commercial products has mostly been due to the careful synthesis and evaluation of adhesive formulations, followed by mechanical testing of bonded assemblies. For structural adhesives, the testing protocol includes an assessment of water resistance. Success is usually defined by whether the bond is as strong or as stiff as the wood. In some cases, the percent of wood failure at the bond is a critical criterion for acceptance for structural applications. In addition, delamination after some type of water exposure is an important test of water resistance. The interaction between wood and adhesive at the interface ultimately controls the performance of the bond [105]. Upon application, adhesive wets the wood surface and may penetrate into the exposed cell lumens if wetting is favorable. When the bond is assembled and mechanical force applied, the liquid adhesive is further driven by hydrodynamic force into the cell lumens and perhaps through pits interconnecting the cells [106–108]. Some low molecular weight adhesives have the ability to diffuse into the cell wall [55,109,110].

Penetration into wood creates an interphase region comprised of wood cell lumens filled with adhesive and the adjacent cell walls. The interphase exists on both sides of the bonded interface. Some adhesives, notably PVAc, PUR, and EPI, form a discernable adhesive layer at the interface while others have no measurable thickness of the adhesive layer. Examples of micro-X-ray tomographs of adhesive bonds in loblolly pine (*Pinus taeda*) are shown in Fig. 13.5 [111]. The three-dimensional (3D) datasets were segmented to show adhesive in cell lumens and adhesive in cell walls, revealing distinct differences of penetration depending on the adhesive used. Polymeric MDI typically has deep penetration, even before consolidation pressure is applied. Fig. 13.5b1 shows extensive penetration in the lumens of longitudinal tracheids

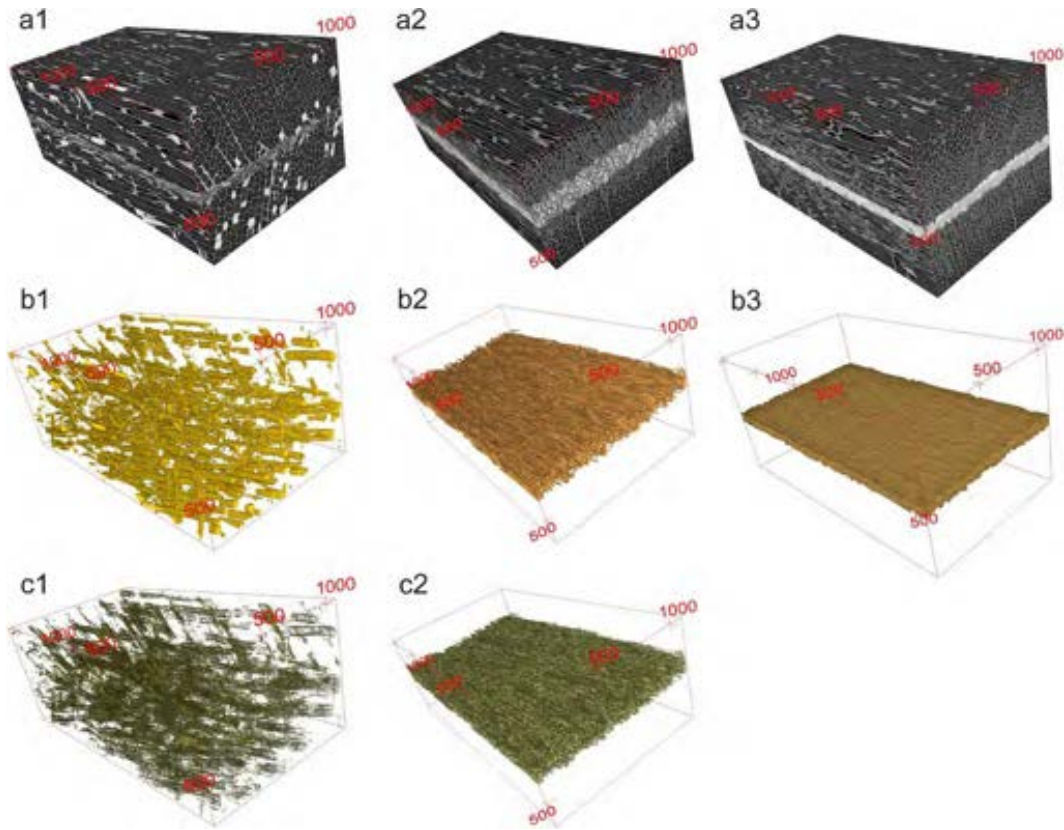


Fig. 13.5 Micro-X-ray tomographs of adhesive penetration in loblolly pine (*Pinus taeda*) bond; (a1–a3) gray-scale corresponds to *white* = adhesive, *gray* = cell wall, *black* = void (dimensions in microns); (a1–c1) pMDI bond, (b1) segmented pMDI in lumens, (c1) segmented pMDI in cell walls; (a2–c2) PF bond, (b2) segmented PF in lumens, (c2) segmented PF in cell walls; (a3–b3) PVAc bond, (b3) segmented PVAc at interface showing no penetration [111].

and ray cells while Fig. 13.5c1 reveals penetration into cell walls by pMDI. The neat PF resin used in the example depicted in Fig. 13.5a2–c2 shows no measurable thickness of an adhesive layer at the interface, but does reveal several rows of collapsed cells. Segmentation of the dataset shows PF in cell lumens (Fig. 13.5b2) and in the cell wall (Fig. 13.5c2). PVAc is a thermoplastic emulsion with very limited ability to penetrate wood, as shown in Fig. 13.5a3. The segmented PVAc in Fig. 13.5b3 reveals penetration only into lumens exposed at the surface. These examples of adhesive penetration are specific to the adhesive products used in the experiment. Modifications to formulations will affect the extent of penetration. Nevertheless, pMDI, PF, and PVAc adhesive types generally follow the trends depicted in Fig. 13.5.

The penetration of aqueous adhesive systems, such as PF and MF, is aided by the hydrophilic nature of wood. The water carrier is adsorbed by the cell wall, thus allowing coalescence of the polymer prior to final polymerization. Penetration into lumens and cell walls is proposed to improve bond strength by reducing stress concentration at the bonded interface and distributing stress throughout the interphase [112,113]. This distribution of stress is believed to be caused by the increased homogeneity of the modulus across the interphase that gradually transitioned into the wood substrate. Voids in cell lumens are either filled or coated with a rigid polymer, and in some cases, cell walls are swelled and penetrated by oligomers that either form secondary chemical bonds or covalent bonds with cell wall polymers, or perhaps self-polymerize to form an interpenetrating network (IPN). It is the cell wall penetration that likely has the largest impact on the water resistance of wood-adhesive bonds [114].

13.6 Wood-adhesive bondline characterization

Wood-adhesive bonds, as is common for natural materials, are complex and variable. One conceptual model of wood-adhesive bonds divides them into nine sublayers [115,116]: bulk wood, a penetration zone where adhesive penetrates into the wood cells, an interface between the penetration zone and adhesive, an interphase zone where adhesive properties are affected by interaction with wood, and bulk adhesive sufficiently far from the interface. The first four layers then repeat in reverse order on the other side of the bond, but may differ if bonding different wood species. Although bulk wood and bulk adhesive properties can be measured, neither the thickness nor the properties of the other zones are available. As a result, a nine-layer model is best viewed as a conceptual model of wood-adhesive bonds while methods to characterize bondline properties rely on more practical models.

The preferred characterization methods should recognize that adhesive bonds in wood products have two functions—to bond together two pieces of wood without failing and to transfer stress between the bonded elements. The first role can be described as bondline “strength.” If a bondline fails, the wood elements will cease to share load and the wood product will have reduced properties or might fail. The second role can be described as bondline “stiffness.” A stiff bondline transfers stress between bonded elements over a shorter distance and results in wood products with improved stiffness

properties. In contrast, a “soft” interface may remain intact but could result in reduced wood composite properties. Most bondline characterization methods focus on strength. The following sections cover both strength and stiffness characterization methods. Despite typically receiving much less emphasis, stiffness characterization can be the more important property. Consider designing a wood product for shelving. Typical wood composites have sufficient strength to support a row of books. But, if the wood composite stiffness is too low, the shelf might sag an unacceptable amount. Evaluating a wood adhesive to optimize a wood composite for shelving should focus more on the bondline stiffness than on the bondline strength. Shelf sag as well as many other adhesive properties can also change over time due to viscoelastic effects that can be enhanced by elevated temperature or moisture content. This chapter focuses on short-term testing methods; additional methods would be needed for viscoelastic characterization.

13.7 Strength characterization—Quality control methods

Tests described here as “quality control (QC) methods” seek to measure adhesive strength, which are also discussed in [Chapters 14 and 15](#). [Fig. 13.6](#) shows typical strength specimens from ASTM standards for wood-adhesive bonds. The two-ply, wood composite specimen [117] with notches cut to the bondline is a variant of the common single-lap shear configuration used in other adhesive testing [118]. The shear block specimen [24] is a variant of specimens used for shear strength of solid wood where the adhesive bondline is located at the specimen’s midplane. These two specimens are loaded until failure (in tension for two-ply composite or compression for shear block). The adhesive bond shear strength is reported by dividing the

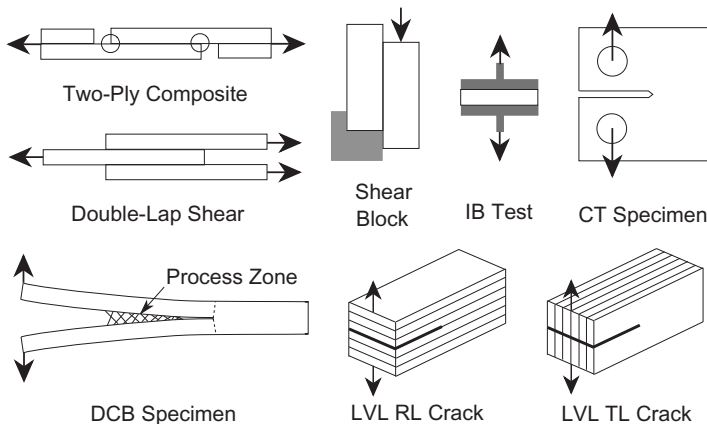


Fig. 13.6 Various specimens used to measure the properties of wood-adhesive bonds. The circles in the “two-ply composite” show the location where cracks initiate in testing. The process zone in the DCB specimen shows fiber bridging in the wake of the crack tip. The dashed lines in the DCB specimen show crack-root rotation of the arms.

failure force by the area of the bonded region. Sometimes the failure plane is inspected for wood or adhesive failure with the concept that maximizing wood failure implies that the adhesive is not the limiting factor in the bond strength. Alternative test methods used on bonds with other materials can also be used on wood-adhesive bonds (e.g., double-lap shear specimens [119]).

Some wood composites rely on adhesives for their properties, but do not provide a clear bondline that can be loaded in shear. Examples include PB, MDF, and OSB. One QC method for such materials is the internal bond (IB) test [120] (see Fig. 13.6). This specimen is loaded in tension. The internal bond strength (IB strength) is failure force divided by specimen cross-sectional area. The interpretation is that IB strength is influenced by the quality of the wood-adhesive bonds in the composite.

QC methods are often sufficient for product development, but are unacceptable for a detailed understanding of wood-adhesive bonds or for designing structures that include wood-adhesive bonds. Two limitations of QC methods are the meaning of “strength” and the influence of “size.” QC methods report the “average” stress in the bonded area at the point of failure. While force balance means this reported stress is an “exact” calculation of average stress, bond failure is not controlled by average stress. Rather, adhesive bonds fail by stress concentrations. For example, lap-shear specimens typically fail by a crack starting at the circled notches in Fig. 13.6, followed by propagation along the bondline. Such failure is not well characterized by average stress values.

Regarding size effects, detailed stress analysis (e.g., by finite element analysis) shows that the magnitude of the stresses in any of the specimens in Fig. 13.6 is independent of specimen size (provided all dimensions are scaled proportionally). Nevertheless, many experiments confirm that adhesive bond failure depends on specimen size. In other words, “adhesive bond strength” is not a material property. It is a specimen property. QC methods are adequate only if all comparisons are done for specimens of the same size. Similarly, without suitable modeling based on the fracture methods below, the strengths measured in one QC specimen cannot predict failure in other specimen types. Because the design of structures involving adhesive bonds requires methods to predict failures, measured QC adhesive strengths are not suitable for design tasks [121].

13.8 Fracture testing

13.8.1 Modified fracture mechanics methods

The alternative to QC methods is to turn to fracture mechanics, which are also discussed in Chapters 14, 16, 17, and 32. Fracture mechanics is an engineering discipline that seeks to predict the conditions that a stress concentration (at a crack tip or a notch) starts to propagate [122]. It is based on the energy available for crack growth rather than average stresses in QC methods. As a consequence, it can predict size effects and is therefore useful in designing structures with wood-adhesive bonds.

This section describes fracture methods for characterizing wood adhesive bonds. Although no ASTM standard for wood fracture mechanics is available, numerous standards for other materials are available (e.g., Ref. [123]). The challenge of adopting methods for other materials is dealing with different issues that arise when testing wood adhesive bonds. The foremost challenge is that crack propagation in both solid wood and in wood-adhesive bonds results in “messy” cracks that are characterized by large damage zones forming in the wake of propagating cracks. In contrast, crack propagation in ceramics and most metals result in “clean” stress-free cracks. Because the analysis methods for measuring toughness in standards such as ASTM E399-20a [123] assume such clean cracks, those methods must be changed when adopted for experiments on wood-adhesive bonds.

Another issue in wood-adhesive bonds, which is not seen in metallic bonds, is that the wood and adhesive fracture toughnesses are similar. As a consequence, attempts to measure adhesive toughness by propagating a crack along an adhesive bondline might be thwarted by that crack diverting into the wood adherends. If that diverted crack remains near the wood adhesive interface (perhaps within the penetration zone mentioned above), it would measure a useful structure toughness that could be used in design. But, if it diverts fully into the wood, it is measuring bulk wood toughness and not characterizing the wood-adhesive bond.

One choice for wood fracture experiments is to use fracture experiments developed for man-made, fiber-reinforced composites. A common experiment in aerospace composites is to measure delamination toughness using double cantilever beam (DCB) specimens (see Fig. 13.6) [124–127]. This specimen has been developed with numerous correction terms to account for such effects as end loading, large deformations, and crack-root rotation [126,127]. The most important correction is for crack-root rotation. In brief, because the bonded material ahead of the crack tip in DCB specimens is not rigid, the base of each arm (i.e., the crack root) displaces (i.e., rotates) a slight amount (see dashed lines in Fig. 13.6). This crack-root rotation can be analyzed with a beam-on-elastic foundation model [122] that results in defining an effective crack length that depends on adherend stiffness. Because the correction determined in modeling was ambiguous, standard delamination tests find an effective crack length by extra experiments rather than by a theoretical model. Both composite delamination and wood-adhesive bonds have nonnegligible amounts of crack-root rotation. That rotation is caused more by the fiber-bridging process zone than adherend stiffness [127]. Because standard DCB tests use experimental methods to find effective crack length, however, those correction methods can approximately account for fiber-bridging effects. The corrected crack length can be viewed as a measure of the damage zone length in the crack tip region.

This DCB geometry was used by Frazier and Dillard and coworkers [128–130] to measure the toughness of wood-adhesive bonds. A challenge in wood, however, is a need to avoid the crack propagation following wood grain into the adherends. This issue can be solved by cutting the adherends with a small grain angle pointing down along the propagation direction [128]. With that modification, standard DCB tests with crack-root rotation corrections can stably propagate cracks along a wood adhesive bond and determine the adhesive bond toughness or critical energy release rate,

G_c , as the amount of energy per unit crack area to propagate a crack. Most DCB experiments measure Mode I, or opening mode, fracture toughness, G_{Ic} . Similar modification of other composite specimens [131] can be used to measure Mode II fracture toughness, G_{IIc} , of wood-adhesive bonds [132], or mixed-mode toughness [130,133].

Typical composite delamination, wood fracture, or wood-adhesive bond experiments show that the toughness increases as the crack propagates. This measured curve is known as the adhesive bond's R curve or crack-resistance curve. The crack resistance increases as the crack grows because the fiber-bridging process zone in the wake of the crack inhibits further growth. If the process zone reaches a steady-state length, the R curve will plateau at a constant toughness. If the process zone is very large, the R curve may increase over the entire length of laboratory-scale specimens. Importantly, the fracture properties of wood-adhesive bonds are a curve and not a single value. Measuring these full properties requires crack propagation experiments. QC "strength" methods are incomplete characterization methods.

Fracture mechanics methods can also be used for wood composites without clear wood-adhesive bonds (e.g., PB, MDF, OSB, LSL, etc.), but getting useful toughness results must solve some new challenges. One approach was to try unmodified fracture methods in ASTM E399-20a [123]. For example, Niemz et al. [134] and Niemz and Diener [135] used compact tension (CT) specimens (see Fig. 13.6) to measure the critical plain-strain stress intensity factor, K_{Ic} , for PB, MDF, and OSB. Such experiments, which are common in fracture mechanics methods, are "hybrid" methods. The experiments measure load to initiate crack growth while the toughness is calculated by a fracture theory specific for each specimen type. The problem when applying such hybrid methods to wood fracture is that the assumptions used in the fracture theories do not apply to crack growth in materials that develop large process zones. In other words, those equations do not give the actual material toughness. Furthermore, ASTM E399-20a [123] does not monitor crack propagation and therefore cannot measure an R curve. The next section describes an alternate approach to determining toughness and R curves for a wider range of wood-adhesive specimen types.

13.8.2 Direct fracture energy methods

An alternative approach to measuring fracture toughness R curves is to directly measure the energy required to propagate a crack by a measured amount. This approach has been used in composite delamination experiments [127]. The process is to load until a small amount of delamination and then unload. The hysteresis area between loading and unloading curves (e.g., the gray area in Fig. 13.7A) is the energy released by crack growth. Dividing such areas by the observed increase in fracture area gives the material toughness. This process can be repeated with small increments in crack growth to measure a material's R curve or toughness as a function of crack length.

This "direct" method measures released energy and therefore determines toughness without any need for fracture theory modeling of cracks with process zones. It therefore works for any specimen that exhibits stable crack growth and for which specimen compliance increases a sufficient amount with crack growth (i.e., force stably drops during crack growth and resembles the force-displacement curve in Fig. 13.7A).

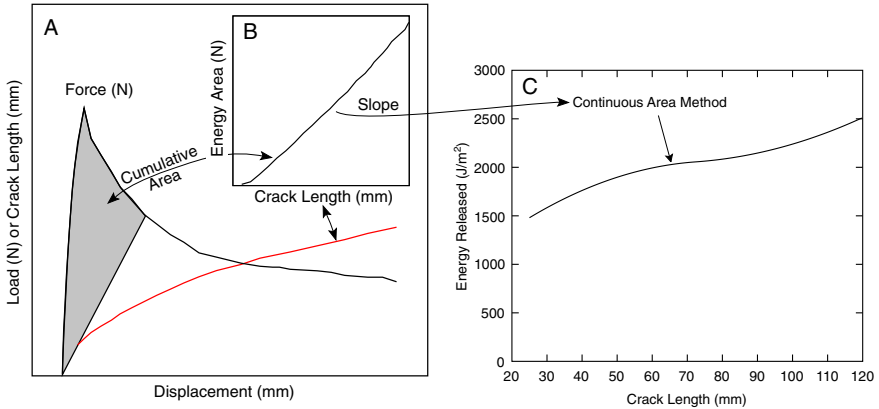


Fig. 13.7 Experimental methods to directly measure R curves during crack propagation. (A) Force displacement curve; (B) integrate area under the force-displacement curve up to each displacement, then cross-plotted as a function of crack length; (C) slope for the curve in B per unit thickness is the R curve for the material.

The first challenge for wood composites is that the large process zones in materials such as MDF or PB mean that unloading cannot be used. The process zone causes crack-plane interference such that unloading would crush that zone [136]. The effects of crushing would be that the load would not return to the origin and the crushing would change the process zone, thereby altering subsequent toughness results. The best (and perhaps only) alternative is to assume that if unloading could be done without interference, the loading would then return to the origin. Experimental results suggest this assumption is acceptable for fracture experiments in typical wood products [137]. Assuming linear unloading to the origin, the fracture toughness of any suitable wood-adhesive specimen can be measured by the method outlined in Fig. 13.7 [138]:

1. Conduct monotonic loading experiments to measure both force and crack length as a function of displacement (accurate displacement results are needed to get accurate energies that depend on both force and displacement).
2. For each force after crack initiation, find the hysteresis area under the force-displacement curve assuming unloading would return to the origin. Cross-plot that energy (U) as a function of crack length (a) to define $U(a)$ (see Fig. 13.7A).
3. The material's R curve toughness is found from the slope of $U(a)$ or $R(a) = (1/t)dU(a)/da$ where t is specimen thickness.

The second challenge in wood composites is accurately measuring the crack length needed in step 1 above. The corresponding experiment in aerospace composites is mostly able to measure crack length by visual inspection. But in wood composites, especially PB, MDF, and OSB, visual observation is insufficient. A good alternative is to map strain fields on the specimen surface using digital image correlation (DIC) methods [139]. This approach adds another task to step 1 to synchronize force and displacement experiments with DIC imaging. Postanalysis of DIC images can evaluate strain ahead of the crack tip. Although determining the precise location of the crack

tip is impractical by DIC methods, one can monitor crack growth increments by shifts in the strain field. Fortunately, $R(a)$ is determined by the slope of $U(a)$ and only needs crack growth increments.

This direct energy approach has successfully been applied to measuring in-plane and out-of-plane R curves for PB and MDF [137,140,141], out-of-plane R curves of OSB [142], and R curves for crack propagation parallel to veneer layers in plywood and LVL [142]. All R curves have an initiation value followed by increasing toughness caused by process zones in these materials. Matsumoto and Nairn [141] used this fracture toughness method with extended CT specimens to compare PB with UF or a soy-flour adhesive [143]. Mirzaei et al. [144–146] used it with DCB specimens to compare LVL made with PF, PRF, PVAc, or EPI adhesives. These fracture methods were able to differentiate between these adhesives. Fracture testing of LVL only works when the crack runs parallel to the fibers in the veneers, but that direction has two orthogonal options. As seen in Fig. 13.6, an RL crack in LVL has a crack plane normal to the veneers while a TL crack crosses all veneer layers. Experiments show that an RL crack can divert into the veneer, meaning the experiments are measuring wood properties rather than adhesive properties. In contrast, a TL crack is forced to break wood-adhesive bonds and is therefore the preferred fracture experiment for accessing wood-adhesive properties in LVL materials [144,147–149].

Out-of-plane fracture tests on PB, MDF, and OSB involve pulling perpendicular to the plane of the panel and therefore provide a fracture mechanics alternative to the quality-control IB test. Because typical panels are relatively thin, when loaded as a DCB specimen to induce crack growth down a panel's midplane, the arms typically break before a crack propagates. This issue can be solved by sandwiching the panel between thicker adherends [137,140]. Both the direct method and the alternative finite element methods [150,151] remain valid for such nonstandard specimen geometries. Comparison of fracture methods to IB testing suggests the fracture methods offer better characterization of wood-adhesive effects and a more accurate assessment of the role of adhesives in panel properties [147–149]. It is usually possible to get reliable fracture results with fewer specimens than needed to deal with the notorious variability of IB tests. Furthermore, fracture methods provide more information in the form of complete R curves from each specimen.

13.9 Adhesive bond durability

The most common reason that wood-adhesive bonds fail is because they are exposed to long-term changes in moisture or temperature—in other words, adhesive bond durability is often the limiting factor in wood composite development. The basic approach to assessing durability is to expose specimens to variations in moisture content or temperature and then measure wood-adhesive properties. Several ASTM standards specify procedures for varying moisture and temperature [152–155]. Some methods include boiling water (e.g., Ref. [154]). Because wood composites in actual use are not exposed to boiling water, such tests are qualified as “accelerated aging” tests. Once the exposure is completed, these standards typically recommend characterizing

the specimen using various QC methods. In some standards (e.g., Ref. [152]) the evaluation is pass/fail based on observation of total delamination length.

The use of QC or pass/fail methods in common durability standard tests limits their effectiveness at characterizing wood-adhesive bond durability. First, any strength method typically requires a large number of specimens to get reliable results. When that number is multiplied by periodic testing as a function of exposure cycles, the numbers increase further. Second, adhesive bond strength is an incomplete measure of adhesive bond properties and therefore may provide incomplete or misleading characterization of durability.

The characterization of wood-adhesive durability can be improved by replacing postexposure characterization methods with fracture mechanics methods. The goal becomes to measure wood-adhesive R curves as a function of exposure conditions. This approach has been adopted to assess the thermal stability of plywood, LVL, and OSB [142]; the moisture durability of LVL using four different adhesives [144–146]; and the moisture and thermal durability of PB, MDF, and OSB using two different adhesives [148,149]. One moisture study [149] supports the benefits of fracture testing over strength testing. The main effect of moisture immersion on PB, MDF, and OSB was to reduce the enhancement of toughness due to fiber bridging. Because fiber bridging-enhanced toughness bestows a “natural” ability on wood and wood products to resist extensive crack growth, whenever moisture exposure reduces that enhancement, those products will be susceptible to long crack propagation. Compared to fiber-bridging effects, the crack initiation is much less affected by moisture. Because strength tests only monitor initiation, they cannot monitor changes in fiber-bridging properties. Indeed, side-by-side testing showed that IB tests provide incomplete characterization of observed moisture effects compared to fracture R curves [149].

13.9.1 Adhesive effects in cross-laminated wood products

Degradation of adhesive bond properties observed in durability experiments can be caused by two processes—degradation of the adhesive itself or the formation of internal stresses that cause wood or adhesive bond failures. These two effects are often combined such that internal stresses that might not initially cause failure do cause failure after some adhesive degradation. Internal stress effects are most prevalent in cross-laminated products such as plywood, CLT, or OSB. Because wood is anisotropic with low moisture or thermal shrinkage parallel to the wood grain but high shrinkage in transverse directions [156], changes in moisture content or temperature cause disparate shrinkage between cross-laminated layers that induces internal stresses. This section considers structural and adhesive effects for durability in the presence of internal stresses.

Fig. 13.8 shows an edge view of a five-layer CLT panel with some locations indicated where adhesive bond properties affect durability. First, CLT panels are typically made by gluing faces between layers but not gluing the edges between timber elements within each layer. These nonglued edges act as precracks that terminate at a wood-adhesive bond. CLT is also prone to the formation of “drying cracks” whenever a reduction in moisture content induces sufficient tensile stress in the transverse

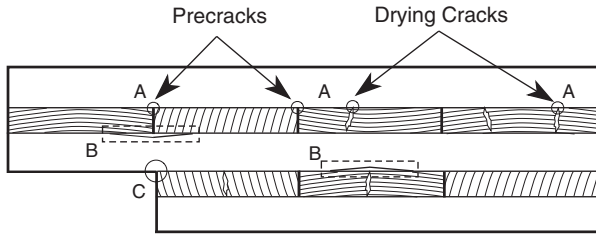


Fig. 13.8 Edge of a five-layer CLT panel with axial layers in white and transverse layers show wood end-grain patterns. The nonglued edges are precracks; the drying cracks form when moisture content decreases in the panels. The “A” circles show some intersections of cracks with adhesive bondlines. The dash rectangles “B” show delaminations emanating from those cracks. The “C” circle shows a notch tip prone to delamination.

layers [157,158]. These cracks typically span the thickness of the transverse layers and also terminate at a wood adhesive bond. Although precracks and drying cracks have relatively minor effects on in-plane tensile properties, the intersections of these cracks with wood-adhesive bonds (see “A” circles in Fig. 13.8) are stress concentrations that can promote delaminations (see dashed boxes “B” in Fig. 13.8). When a CLT structure includes notches in panels near a wood-adhesive bond (see “C” circle in Fig. 13.8), internal stresses may induce notch tip delamination [159]. If the CLT panel design and its adhesives are not chosen with attention to these effects, internal stress-induced delaminations will likely be the limiting factor in CLT durability.

How should one characterize adhesive bonds for use in CLT? A durability test for delamination in glulam exposes specimens to moisture and inspects for delaminations [152]. This test is inadequate for CLT. The timber layers in glulam are all in the same direction, which means it is much less prone to internal stresses seen in CLT. The observation that an adhesive inhibits delamination in glulam, which would have minimal internal stresses, does not imply it can inhibit delamination in CLT. A better way to choose adhesives for CLT is to use fracture mechanics tests such as DCB characterization of toughness [130]. Unlike in CLT, however, DCB tests use wood adherends with the same grain direction and tailor the adherend grain angle [128] or use auxiliary adherends [160] to keep crack propagation along the wood-adhesive bond. Attempts to revise DCB tests for a cross-grained adhesive bond would likely be thwarted by the crack diverting into the transverse layer, as it does for a CLT notch at an adhesive bondline [161,162]. Nevertheless, differences in adhesive bond toughness determined in DCB tests would likely correlate with the ability of CLT bonds made with that adhesive to resist delamination.

Both drying cracks and delaminations are promoted by the energy available in the internal stresses, and that energy scales with layer thickness [157,158,163,164]. In other words, the thicker the layers, the more likely the panels are to crack and delaminate. Similarly, thicker layers promote delaminations at notch tips [159]. This layer thickness problem cannot be solved with better adhesives. Even a “perfect” interface with an infinite toughness that eliminates delamination within the adhesive bond could not prevent layers causing cracks to divert into adjacent wood layers instead.

The practical consequences would be the same as adhesive bond failure. The only viable solution for durable CLT panels is to use thinner layers. Experiments in glass-epoxy composites confirm that thinner layers can suppress cracks [165]. A century of experience with plywood suggests that veneer layers in plywood are thin enough to suppress most cracks. It is therefore possible that MPP panels, provided they do not orient too many adjacent layers in the same direction, might offer a more durable mass timber product than thick-layer CLT.

In summary, internal stresses that develop in cross-laminated wood products place a higher burden on the adhesive than seen in other wood products. If the layers are too thick, the burden would be too high for any adhesive. The development of durable CLT panels will likely require a combination of thinner layers and adhesives with adequate toughness to resist delamination between layers. Fracture tests [130] emerge as a fundamental method for qualifying the adhesive for such products.

13.10 Characterizing bondline stiffness

The second role of wood-adhesive bonds is to transfer stress between the wood adherends. This role is best assessed by characterizing the stiffness of the wood-adhesive bond layer. Compared to methods proposed to measure strength or toughness, few if any methods are available for characterizing bondline stress transfer properties. Two ASTM standards [166,167] are aimed at measuring adhesive stiffness, but their intent is to measure bulk adhesive stiffness and not the stiffness of an adhesive bondline. They focus on adhesive properties by using thick adhesive layers and standardizing adherends to hard maple. Such a standard could not, for example, characterize the adhesive stress transfer properties of one adhesive when used with different wood species.

Because the stress transfer properties of wood-adhesive bonds influence the overall mechanical properties of the panel products, one option is to vary the adhesive type and look for changes in panel properties (e.g., by ASTM D1037-12 [120]). Although acceptable to product development, this approach does not provide clear adhesive bond properties. An alternative is to return to the bondline specimens in Fig. 13.6. Typical strength tests only measure load at failure, but if one records force vs displacement prior to failure, that information can, in principle, be related to bondline stiffness. The question remains, how can adhesive bond stiffness be deduced from the measured stiffness of any adhesive bondline specimen?

One experimental protocol for measuring bond stiffness properties is given in Le and Nairn [168]. This test method uses standard double-lap shear (DLS, see Fig. 13.6) specimens, but focuses on specimen stiffness prior to failure. Specifically, the experiments measure the global stiffness of DLS specimens. To interpret these results, a shear lag model [169,170] was developed that can calculate bond stiffness from the global stiffness, assuming the mechanical properties and thicknesses of all layers are known. The adhesive bondline was modeled as an imperfect interface [171] that defines an adhesive bond interface parameter, D_r , that is a proportionality constant between shear stress on the interface and bondline slippage. D_r varies from zero,

for a bond that transfers no stress, to infinite, for a “perfect” bond with zero slippage between the adherends. All other values characterize an “imperfect” bond.

The experiments measured D_t for bondlines between wood strands using either PVAc or PF adhesive [168]. The results identified PF bonds as much stiffer than PVAc bonds. An issue with OSB products is the effect of incomplete adhesive coverage on wood strands. DLS experiments showed that bondline stiffness can decrease by an order of magnitude for strands with reduced adhesive coverage. A debatable issue in wood-adhesive bonds is the role of adhesive penetration into the wood cells of the adherends. To study the role of penetration on adhesive bondline stiffness, Le and Nairn [168] compared D_t for bonding ordinary wood strands to D_t for bonding densified strands [172]. The densified strands compressed the wood cells and effectively eliminated adhesive penetration into the strands [168]. Nevertheless, D_t was unaffected by the lack of penetration. In fact, bonds with no penetration were less variable and slightly stiffer. Clearly, adhesive bond stiffness testing is a worthwhile addition to wood-adhesive bond characterization with the potential to provide results not revealed by any strength or fracture mechanics tests.

References

- [1] Anonymous, N.C. Brown Center for Ultrastructure Studies, College of Environmental Science and Forestry, State University of New York, 2021. <https://ncbrownultrastructure.wordpress.com/2021/02/16/wood-anatomy-digital-image-library-film-to-digital-project>. (Accessed 14 October 2021).
- [2] InsideWood, InsideWood, 2021. <http://insidewood.lib.ncsu.edu/search>. (Accessed 2 December 2021).
- [3] E.A. Wheeler, InsideWood—a web resource for hardwood anatomy, *IAWA J.* 32 (2) (2011) 199–211.
- [4] S. Bockel, I. Mayer, J. Konnerth, S. Harling, P. Niemz, C. Swaboda, M. Beyer, N. Bieri, G. Weiland, F. Pichelin, The role of wood extractives in structural hardwood bonding and their influence on different adhesive systems, *Int. J. Adhes. Adhes.* 91 (2019) 43–53.
- [5] G.E. Acquah, B.K. Via, B. Gallagher, N. Billor, O.O. Fasina, L.G. Eckhardt, High throughput screening of elite loblolly pine families for chemical and bioenergy traits with near infrared spectroscopy, *Forests* (2018), <https://doi.org/10.3390/f9070418>.
- [6] A. Thompson, J. Cooper, I. Ingram Jr., Distribution of terpenes in heartwood and sapwood of loblolly pine, *For. Prod. J.* 56 (7/8) (2006) 46–48.
- [7] APA, APA Photo Gallery, 2022. <https://www.apawood.org/photography>. (Accessed 12 January 2022).
- [8] D. Shell, Freres Lumber pioneers new mass plywood product with high-tech plant, *Panel World*, 2018, pp. 14–19.
- [9] V. Çavus, A.C. Konukcu, Innovative approach for engineered wood products: scrimber, in: A. Atik (Ed.), *Academic Research and Reviews in Agriculture, Forestry, and Aquacultural Sciences*, Duvar Publishing, Izmir, Turkey, 2021, pp. 5–18. https://www.researchgate.net/publication/352030133_Innovative_Approach_For_Engineered_Wood_Products_Scrimber#fullTextFileContent. (Accessed 20 January 2022).
- [10] APA, Voluntary Product Standard PS 2-18 Performance Standard for Wood Structural Panels, APA—The Engineered Wood Association, Tacoma, Washington, 2019.
- [11] APA, Voluntary Product Standard PS 1-19 Structural Plywood, APA—The Engineered Wood Association, Tacoma, Washington, 2019.

- [12] ANSI/APA, ANSI/APA PRR 410-2021 Standard for Performance-Rated Engineered Wood Rim Boards, APA—The Engineered Wood Association, Tacoma, Washington, 2021.
- [13] ANSI, ANSI 117-2020 Specification for Structural Glued Laminated Timber of Softwood Species, American National Standards Institute, New York, NY, 2020.
- [14] ANSI, ANSI A190.1-2017 Standard for Wood Products—Structural Glued Laminated Timber, American National Standards Institute, New York, NY, 2017.
- [15] ANSI, ANSI/APA PRG 320-2019 Standard for Performance-Rated Cross-Laminated Timber, American National Standards Institute, New York, NY, 2020.
- [16] ANSI, ANSI/APA PRS 610.1-2018 Standard for Performance-Rated Structural Insulated Panels in Wall Applications, American National Standards Institute, New York, NY, 2018.
- [17] APA, APA PRI-405 Performance Standard for Commercial I-Joists, APA—The Engineered Wood Association, Tacoma, Washington, 2021.
- [18] CSA, CSA O121-17 Douglas Fir Plywood, CSA Group Testing & Certification Inc, Toronto, ON, 2017.
- [19] CSA, CSA O151-17 Canadian Softwood Plywood, CSA Group Testing & Certification Inc, Toronto, ON, 2014.
- [20] CSA, CAN/CSA O122-16 (R2021) Structural Glued Laminated Timber, CSA Group Testing & Certification Inc, Toronto, ON, 2021.
- [21] CSA, CSA O325:21 Construction Sheathing, CSA Group Testing & Certification Inc, Toronto, ON, 2021.
- [22] CSA, CSA O177-06 (R2020) Qualification Code for Manufacturers of Structural Glued-Laminated Timber, CSA Group Testing & Certification Inc, Toronto, ON, 2020.
- [23] ANSI, ANSI 405-2018. Standard for Adhesives for Use in Structural Glued Laminated Timber, American National Standards Institute, New York, NY, 2018.
- [24] ASTM, ASTM D905-08 Standard Test Method for Strength Properties of Adhesive Bonds in Shear by Compression Loading, ASTM International, West Conshohocken, PA, 2021.
- [25] ASTM, ASTM D906-20 Standard Test Method for Strength Properties of Adhesives in Plywood Type Construction in Shear by Tension Loading, ASTM International, West Conshohocken, PA, 2020.
- [26] ASTM, ASTM D5266-13(2020) Standard Practice for Estimating the Percentage of Wood Failure in Adhesive Bonded Joints, ASTM International, West Conshohocken, PA, 2020.
- [27] ASTM, ASTM D7247-17 Standard Test Method for Evaluating the Shear Strength of Adhesive Bonds in Laminated Wood Products at Elevated Temperatures, ASTM International, West Conshohocken, PA, 2017.
- [28] CSA, CSA O112.10-08 (R2017) Evaluation of Adhesives for Structural Wood Products (Limited Moisture Exposure), CSA Group Testing & Certification Inc., Toronto, ON, 2017.
- [29] CSA, CSA 112.9:21 Evaluation of Adhesives for Structural Wood Products (Exterior Exposure), CSA Group Testing & Certification Inc., Toronto, ON, 2021.
- [30] CSN, CSN EN 301. 2017. Adhesives, Phenolic and Aminoplastic, for Load-Bearing Timber Structures—Classification and Performance Requirements, European Committee for Standardization, Brussels, 2017.
- [31] CSN, CSN EN 15425 Adhesives—One Component Polyurethane (PUR) for Loadbearing Timber Structures—Classification and Performance Requirements, European Committee for Standardization, Brussels, 2017.
- [32] CSN, CSN EN 16254+A1 Adhesives—Emulsion Polymerized Isocyanate (EPI) for Load-Bearing Timber Structures—Classification and Performance Requirements, European Committee for Standardization, Brussels, Belgium, 2016.

- [33] C.-Y. Hse, R.L. Geimer, W.E. Hsu, R.C. Tang, Effect of resin type on properties of steam-press-cured flakeboards, *For. Prod. J.* (1995) 57–62.
- [34] K. Umemura, S. Kawai, H. Sasaki, R. Hamada, Y. Mizuno, Curing behavior of wood adhesives under high steam pressure, *J. Adhes.* (1996) 87–100.
- [35] C.G. Frihart, C.R. Hunt, Wood adhesives—bond formation and performance, in: *Wood Handbook: Wood as an Engineering Material*, USDA Forest Service Forest Products Laboratory, Madison, WI, 2021. Gen. Tech. Rep. FPL-GTR-282. (Chapter 10).
- [36] X. Yang, Organic fillers in phenol-formaldehyde wood adhesives (PhD dissertation), Virginia Polytechnic Institute and State University, Blacksburg, VA, 2014. 182p.
- [37] X. Yang, C.E. Frazier, Influence of organic fillers on rheological behavior in phenol-formaldehyde adhesives, *Int. J. Adhes. Adhes.* 66 (2016) 93–98, <https://doi.org/10.1016/j.ijadhadh.2015.12.035>.
- [38] X. Yang, C.E. Frazier, Influence of organic fillers on surface tension of phenol-formaldehyde adhesives, *Int. J. Adhes. Adhes.* 66 (2016) 160–166, <https://doi.org/10.1016/j.ijadhadh.2016.01.004>.
- [39] S. Nader, F. Guzman, R. Becar, C. Segovia, C. Fuentealba, M. Peirera, E. Mauret, N. Brosse, Lignocellulosic micro and nanofibrillated cellulose produced by steam explosion for wood adhesive formulations, *J. Renew. Mater.* (2022), <https://doi.org/10.32604/jrm.2022.017923>.
- [40] C. Liu, S. Wang, Y. Zhang, Effects of cellulose nanofibrils on the cure kinetics of the phenol-formaldehyde resin, *Mater. Res. Express* 7 (6) (2020), 065009.
- [41] J. Kawalerczyk, D. Dziurka, R. Mirski, J. Siuda, K. Szentner, The effect of nanocellulose addition to phenol-formaldehyde adhesive in water resistant plywood manufacturing, *Bioresources* 15 (3) (2020) 5388–5401.
- [42] E.C. Lengowski, E.A. Bonfatti Jr., R. Dallo, S. Nisgoski, J.L. Monteiro de Mattos, J.G. Prata, Nanocellulose-reinforced phenol-formaldehyde resin for plywood panel production, *Maderas: Cienc. Tecnol.* 23 (5) (2021) 1–10.
- [43] R. Zhang, X. Jin Xiaobei, Q.C. Wen, D. Qin, Alumina nanoparticle modified phenol-formaldehyde resin as a wood adhesive, *Int. J. Adhes. Adhes.* 81 (2018) 79–82.
- [44] X. Wang, S. Wang, X. Xie, L. Zhao, Y. Deng, Y. Li, Multi-scale evaluation of the effects of nanoclay on the mechanical properties of wood/phenol formaldehyde bondlines, *Int. J. Adhes. Adhes.* 74 (2017) 92–99.
- [45] W. Gao, G. Du, Curing kinetics of nano cupric oxide (CuO)-modified PF resin as a wood adhesive: effect of surfactant, *J. Adhes. Sci. Technol.* 27 (22) (2013) 2421–2432.
- [46] W. Gao, G. Du, Physico-mechanical properties of plywood bonded by nano cupric oxide (CuO) modified PF resins against subterranean termites, *Maderas: Cienc. Tecnol.* 17 (1) (2015) 129–138.
- [47] C. Guo, T. Yi, J.J. Morrell, W. Gao, S. Zhao, K. Zhan, L. Yang, G. Du, Incorporation of a nano/micro CuO formulation into phenol formaldehyde (PF) resin: curing kinetics, morphological analysis, and application, *J. Wood Chem. Technol.* 39 (5) (2019) 372–383.
- [48] T. Yi, C. Guo, K. Zhan, L. Yanf, G. Du, The simultaneous preparation of nano cupric oxide (CuO) and phenol formaldehyde (PF) resin in one system: aimed to apply as wood adhesives, *Eur. J. Wood Wood Prod.* 78 (2020) 471–482.
- [49] M. Ghorbani, F. Liebner, H.W.G. van Herwijnen, L. Pfungen, M. Krahofer, E. Budjav, J. Konnerth, Lignin phenol formaldehyde resoles: the impact of lignin type on adhesive properties, *Bioresources* 11 (3) (2016) 6727–6741.
- [50] J. Karthäuser, V. Biziks, C. Mai, H. Militz, Lignin and lignin-derived compounds for wood—a review, *Molecules* 26 (9) (2021) 2533.

- [51] Y. Zhang, N. Li, Z. Chen, C. Ding, Q. Zheng, J. Xu, Q. Meng, Synthesis of high-water-resistance lignin-phenol resin adhesive with furfural as a crosslinking agent, *Polymers* 12 (2020) 2805.
- [52] H. Younesi-Kordkheili, A. Pizzi, Improving properties of phenol lignin glyoxal resin as a wood adhesive by an epoxy resin, *Eur. J. Wood Wood Prod.* 79 (2021) 199–205.
- [53] B. Jeong, B.-D. Park, V. Causin, Influence of synthesis method and melamine content of urea-melamine-formaldehyde resins to their features in cohesion, interphase, and adhesion performance, *J. Ind. Eng. Chem.* 79 (2019) 87–96.
- [54] X. Xi, A. Pizzi, S. Amirou, Melamine-glyoxal-glutaraldehyde wood panel adhesives without formaldehyde, *Polymers* 10 (1) (2018) 22, <https://doi.org/10.3390/polym10010022>.
- [55] X. Liu, Y. Wu, R. Shmulsky, Y. Luo, X. Chu, I. Wang, H. Wan, Developing a renewable hybrid resin system. Part 1: characterization of co-polymers of isocyanate with different molecular weights of phenolic resins, *Bioresources* 11 (2) (2016) 5299–5311.
- [56] Q. Li, X. Liu, H. Su, A. Mao, H. Wan, Development of a renewable hybrid resin system by blending isocyanate with novolac phenolic resins, *For. Prod. J.* 70 (3) (2020) 268–274.
- [57] H.Y. Chen, N. Yan, Application of Western red cedar (*Thuja plicata*) tree bark as a functional filler in pMDI wood adhesives, *Ind. Crop. Prod.* 113 (2018) 1–9.
- [58] H.Y. Chen, S.S. Nair, P. Chauhan, N. Yan, Lignin containing cellulose nanofibril application in pMDI wood adhesives for drastically improved gap-filling properties with robust bondline interfaces, *Chem. Eng. J.* 360 (2019) 393–401.
- [59] A.F. Ang, Z. Ashaari, S.H. Lee, P.M. Tahir, R. Halis, Lignin-based co-polymer adhesives for composite wood panels—a review, *Int. J. Adhes. Adhes.* 102408 (2019), <https://doi.org/10.1016/j.ijadhadh.2019.102408>.
- [60] K. Grøstad, A. Pedersen, Emulsion polymer isocyanates as wood adhesive: a review, *J. Adhes. Sci. Technol.* 24 (2010) 1357–1381.
- [61] S. Srivaro, Z. Börcsök, Z. Pásztoru, S. Jantawee, Finger joint performance of green-glued rubberwood (*Hevea brasiliensis*) lumber, *Bioresources* 14 (4) (2019) 9110–9116.
- [62] A. Das, P. Mahanwar, A brief discussion on advances in polyurethane applications, *Adv. Ind. Eng. Polym. Res.* 3 (2020) 93–101.
- [63] M. Alinejad, C. Henry, S. Nikafshar, A. Gondaliya, S. Bagheri, N. Chen, S.K. Singh, D.B. Hodge, M. Nejad, Lignin-based polyurethanes: opportunities for bio-based foams, elastomers, coatings and adhesives, *Polymers* 11 (2019) 1202, <https://doi.org/10.3390/polym11071202>.
- [64] J. Lima Garcia, G. Pans, C. Phanopoulos, Use of lignin in polyurethane-based structural wood adhesives, *J. Adhes.* 94 (2018) 814–828.
- [65] M.A. Aristi, M.A.R. Lubis, S.M. Yadav, P. Antov, A.N. Papadopoulos, A. Pizzi, W. Fatriasari, M. Ismayati, A.H. Iswanto, Recent developments in lignin- and tannin-based non-isocyanate polyurethane resins for wood adhesives—a review, *Appl. Sci.* 11 (2021) 4242, <https://doi.org/10.3390/app11094242>.
- [66] G. Clerc, M. Lehmann, J. Gabriel, D. Salzgeber, F. Pichelin, T. Strahm, P. Niemi, Improvement of ash (*Fraxinus excelsior* L.) bonding quality with one-component polyurethane adhesive and hydrophilic primer for load-bearing application, *Int. J. Adhes. Adhes.* 85 (2018) 303–307.
- [67] C. Amen-Chen, J. Gabriel, Wet adhesion durability improvement of polyurethane wood adhesives with primer, *Eur. J. Wood Wood Prod.* 73 (2015) 697–700.
- [68] O. González Prieto, J.M.C. Mirás, L.O. Torres, Finger jointing of green *Eucalyptus globulus* L. wood with one-component polyurethane adhesives, *Eur. J. Wood Wood Prod.* (2021), <https://doi.org/10.1007/s00107-021-01770-7>.

- [69] M. Dunky, Wood adhesives based on natural resources: a critical review, Part I. Protein-based adhesives, *Rev. Adhes. Adhes.* 8 (3) (2020) 199–332.
- [70] M. Dunky, Wood adhesives based on natural resources: a critical review, Part II. Carbohydrate-based adhesives, *Rev. Adhes. Adhes.* 8 (3) (2020) 333–378.
- [71] M. Dunky, Wood adhesives based on natural resources: a critical review, Part III. Tannin- and lignin-based adhesives, *Rev. Adhes. Adhes.* 8 (4) (2020) 379–525.
- [72] N.D. Raydan, L. Leroyer, B. Charrier, E. Robles, Recent advances on the development of protein-based adhesives for wood composite materials—a review, *Molecules* 26 (24) (2021) 7617, <https://doi.org/10.3390/molecules26247617>.
- [73] D. Gonçalves, J.M. Bordado, A.C. Marques, Non-formaldehyde, bio-based adhesives for use in wood-based panel manufacturing industry—a review, *Polymers* 13 (2021) 4086, <https://doi.org/10.3390/polym13234086>.
- [74] V. Hemmilä, S. Adamopoulos, O. Karlsson, A. Kumar, Development of sustainable bio-adhesives for engineered wood panels - a review, *RSC Adv.* 7 (2017) 38604–38630.
- [75] S. D'Amico, U. Müller, E. Berghofer, Effect of hydrolysis and denaturation of wheat gluten on adhesive bond strength of wood joints, *J. Appl. Polym.* 129 (2013) 2429–2434.
- [76] Z. He, in: Z. He (Ed.), *Bio-Based Wood Adhesives*, first ed., CRC Press, Boca Raton, FL, 2017.
- [77] P. Nordqvist, M. Lawther, E. Malmström, F. Khabbaz, Adhesive properties of wheat gluten after enzymatic hydrolysis or heat treatment—a comprehensive study, *Ind. Crop. Prod.* 38 (2012) 139–145.
- [78] F. Ferdosian, Z. Pan, G. Gao, B. Zhao, Bio-based adhesives and evaluation for wood composites application, *Polymers* 9 (2) (2017) 70, <https://doi.org/10.3390/polym9020070>.
- [79] Y. Lui, K. Li, Development and characterization of adhesives from soy protein for bonding wood, *Int. J. Adhes. Adhes.* 27 (2007) 59–67.
- [80] N. Bandara, A. Akbari, Y. Esparza, J. Wu, Canola protein: a promising protein source for delivery, adhesive, and material applications, *J. Am. Oil Chem. Soc.* 95 (2018) 1075–1090.
- [81] K. Hale, *The Potential of Canola Protein for Bio-Based Wood Adhesives* (MS thesis), Kansas State University, Manhattan, KS, 2013.
- [82] L.A. Heinrich, Future opportunities for biobased adhesives, *Green Chem.* 21 (2019) 1866–1888.
- [83] X. Li, J. Li, J. Luo, K. Li, Q. Gao, J. Li, A novel eco-friendly blood meal-based bio-adhesive: preparation and performance, *J. Polym. Environ.* 26 (2017) 607–615.
- [84] K. Ostendorf, P. Reuter, M. Euring, Manufacturing medium-density fiberboards and wood fiber insulation boards using a blood albumin adhesive on a pilot scale, *Bio-resources* 15 (2020) 1531–1546.
- [85] B.B. Adhikari, M. Chae, D.C. Bressler, Utilization of slaughterhouse waste in value-added applications: recent advances in the development of wood adhesives, *Polymers* 10 (2) (2018) 176, <https://doi.org/10.3390/polym10020176>.
- [86] R.K. Donato, A. Mija, Keratin associations with synthetic, biosynthetic and natural polymers: an extensive review, *Polymers* 12 (1) (2020) 32, <https://doi.org/10.3390/polym12010032>.
- [87] C.A. Eckelman, *Brief Survey of Wood Adhesives*, Purdue University Cooperative Extension Service, West Lafayette, IN, 1999.
- [88] D. Vnučec, M. Šernek, A. Kutnar, A. Goršek, Past and present protein adhesives based on soy, blood and casein, *Acta Silvae Ligni* 112 (2017) 35–47.

- [89] A.W. Christiansen, Durable wood adhesives based on carbohydrates, in: Proceedings of the International Conference on Wood Adhesives 1985: Status and Needs, Forest Products Society, Madison, WI, 1986, pp. 211–226.
- [90] A. Pizzi, Tannins: major sources, properties and applications, in: M.N. Belgacem, A. Gandini (Eds.), *Monomers, Polymers and Composites from Renewable Resources*, Elsevier, Amsterdam, 2008, pp. 179–200.
- [91] A. Pizzi, Polyflavonoid tannins self-condensation adhesives for wood particleboard, *J. Adhes.* 85 (2–3) (2009) 57–68.
- [92] X. Zhou, G. Du, Applications of tannin resin adhesives in the wood industry, in: A. Aires (Ed.), *Tannins—Structural Properties, Biological Properties and Current Knowledge*, IntechOpen, London, 2019, <https://doi.org/10.5772/intechopen.80170>.
- [93] S. Omura, Y. Kawazoe, D. Uemura, Analysis of the structural aspects of tannin-based adhesives by 2D-NMR, *Materials* 14 (19) (2021) 5479, <https://doi.org/10.3390/ma14195479>.
- [94] J. Lora, Industrial commercial lignins: sources, properties and applications, in: M.N. Belgacem, A. Gandini (Eds.), *Monomers, Polymers and Composites from Renewable Resources*, Elsevier, Amsterdam, 2008, pp. 225–242.
- [95] L.B. Dornelles, R.M. Filho, A.P. Mariano, Organosolv fractionation of eucalyptus: economics of cellulosic ethanol and chemicals versus lignin valorization to phenols and polyols, *Ind. Crop. Prod.* 173 (2021), 114097, <https://doi.org/10.1016/j.indcrop.2021.114097>.
- [96] G. Koumba-Yoya, T. Stevanovic, Study of organosolv lignins as adhesives in wood panel production, *Polymers* 9 (2017) 46, <https://doi.org/10.3390/polym9020046>.
- [97] M. Ghorbani, F. Liebner, H.W.G. van Herwijnen, P. Solt, J. Konnerth, Ligneous resole adhesives for exterior-grade plywood, *Eur. J. Wood Wood Prod.* 76 (1) (2018) 251–258.
- [98] P. Solt, A.-S. Jääskeläinen, P. Lingenfelter, J. Konnerth, H.W.G. van Herwijnen, Impact of molecular weight of kraft lignin on adhesive performance of lignin-based phenol-formaldehyde resins, *For. Prod. J.* 68 (4) (2018) 365–371.
- [99] WHO, Formaldehyde, Concise International Chemical Assessment Document 40, World Health Organization, Geneva, 2002. <https://www.who.int/ipcs/publications/cicad/en/cicad40.pdf>.
- [100] EPA, Formaldehyde Standards for Composite Wood Products Act, Title VI, Toxic Substances Control Act, Environmental Protection Agency, 2018. Federal Register, 2018-02144, 40 CFR Part 770.
- [101] WHO, WHO Guidelines for Indoor Air Quality: Selected Pollutants, World Health Organization, 2010. <https://www.euro.who.int/en/health-topics/environment-and-health/air-quality/publications/2010/who-guidelines-for-indoor-air-quality-selected-pollutants>. (Accessed 22 February 2022).
- [102] E. Athanassiadou, S. Tsiantzi, C. Markessini, Producing Panels with Formaldehyde Emission at Wood Levels, CHIMAR HELLAS S.A, Thessaloniki, Greece, 2014. https://www.researchgate.net/publication/242310214_Producing_Panels_with_Formaldehyde_Emission_at_Wood_Levels/figures?lo=1.
- [103] CEN, European Standard EN 13986:2004 +A1:2015 Wood-Based Panels for Use in Construction—Characteristics, Evaluation of Conformity and Marking, European Committee for Standardization, Brussels, 2015.
- [104] M. Tasooji, G. Wan, G. Lewis, H. Wise, C.E. Frazier, Biogenic formaldehyde: content and heat generation in the wood of three tree species, *ACS Sustainable Chemistry & Engineering*, 2017, pp. 4243–4348.

- [105] F.A. Kamke, J.N. Lee, Adhesive penetration in wood—a review, *Wood Fiber Sci.* 39 (2) (2007) 205–220.
- [106] J.E. Jakes, C.R. Frihart, C.G. Hunt, D.J. Yelle, N.Z. Plaza, L.F. Lorenz, D.J. Ching, Integrating multiscale studies of adhesive penetration into wood, *For. Prod. J.* 68 (4) (2018) 340–348.
- [107] P. McKinley, F.A. Kamke, A. Sinha, V. DeAndrade, J.E. Jakes, Analysis of adhesive penetration into wood using nano-X-ray computer tomography, *Wood Fiber Sci.* 50 (1) (2018) 66–76.
- [108] J.L. Paris, F.A. Kamke, Quantitative wood-adhesive penetration with X-ray computer tomography, *Int. J. Adhes. Adhes.* 61 (2015) 71–80.
- [109] J. Konnerth, D. Harper, S.-H. Lee, T.G. Rials, W. Gindl, Adhesive penetration of wood cell walls investigated by scanning thermal microscopy (SThM), *Holzforschung* 62 (2007) 91–98.
- [110] J.L. Paris, F.A. Kamke, X. Xiao, X-ray computer tomography of wood-adhesive bondlines: attenuation and phase contrast effects, *Wood Sci. Technol.* 49 (2015) 1185–1208.
- [111] J.L. Paris, *Wood-Adhesive Bondline Analyses with Micro X-ray Computed Tomography* (PhD dissertation), Oregon State University, Corvallis, OR, 2014.
- [112] D.J. Ching, F.A. Kamke, B.K. Bay, Methodology for comparing wood adhesive bond load transfer using digital volume correlation, *Wood Sci. Technol.* 52 (6) (2018) 1569–1587.
- [113] W. Gindl, A. Sretenovic, A. Vincenti, U. Müller, Direct measurement of strain distribution along a wood bond line. Part 2: effects of adhesive penetration on strain distribution, *Holzforschung* 59 (3) (2005) 307–310.
- [114] P. McKinley, A. Sinha, F.A. Kamke, Understanding the effect of weathering on adhesive bonds for wood composites using digital image correlation (DIC), *Holzforschung* 73 (2) (2019) 155–164.
- [115] C.R. Frihart, *Wood structure and adhesive bond strength. Characterization of the cellulosic cell wall*, Blackwell Pub, Ames, IA, 2000.
- [116] A.A. Marra, Applications of wood bonding, in: R.F. Bloomquist, A.W. Christiansen, R. H. Gillespie, G.E. Myers (Eds.), *Adhesive Bonding of Wood and Other Structural Materials*, EMMSE Project, the Pennsylvania State University, University Park, PA, 1980, pp. 365–418 (Chapter IX).
- [117] ASTM D2339-20, Standard Test Method for Strength Properties of Adhesives in Two-Ply Wood Construction in Shear by Tension Loading, ASTM International, West Conshohocken, PA, 2020.
- [118] A.J. Kinloch, *Adhesion and Adhesives: Science and Technology*, Oxford University Press, New York, London, 1987.
- [119] ASTM D3528–96, Standard Test Method for Strength Properties of Double Lap Shear Adhesive Joints by Tension Loading, ASTM International, West Conshohocken, PA, 2016.
- [120] ASTM D1037-12, Standard Test Methods for Evaluating Properties of Wood-Base Fiber and Particle Panel Materials, ASTM International, West Conshohocken, PA, 2020.
- [121] ASTM D4896–01, Standard Guide for Use of Adhesive-Bonded Single Lap-Joint Specimen Test Results, ASTM International, West Conshohocken, PA, 2016.
- [122] M. Kanninen, C.H. Popelar, *Advanced Fracture Mechanics*, Oxford University Press, New York, 1985.
- [123] ASTM E399–20a Standard Test Method for Linear-Elastic Plane-Strain Fracture Toughness of Metallic Materials, ASTM International, West Conshohocken, PA, 2020.
- [124] D.L. Hunston, Composite interlaminar fracture: effect of matrix fracture energy, *J. Compos. Technol. Res.* 6 (1984) 176–180.

- [125] W.S. Johnson, P.D. Mangalgi, Influence of the Resin on Interlaminar Mixed-Mode Fracture, Toughened Composites, 1987. ASTM STP 937, 295–215.
- [126] J.G. Williams, Large displacement and end-block effects in the DCB test in modes I and II, *J. Compos. Mater.* 21 (1987) 330–347.
- [127] S. Hashemi, A.J. Kinloch, J.G. Williams, The effects of geometry, rate and temperature on the mode-I, mode-II, and mixed-mode I/II interlaminar fracture of carbon-fibre/poly (ether ether-ketone) composites, *J. Compos. Mater.* (1990) 918–956.
- [128] E. Nicoli, D.A. Dillard, C.E. Frazier, A. Zink-Sharp, Characterization of mixed-mode I/II fracture properties of adhesively bonded yellow-poplar by a dual actuator test frame instrument, *Holzforschung* 66 (5) (2012) 623–631.
- [129] E. Nicoli, D.A. Dillard, C.E. Frazier, Effects of systematic variation of wood adherend bending stiffness on fracture properties: part 1. Influence of grain angle, *Holzforschung* 66 (6) (2012) 765–770.
- [130] H. Singh, A. Chakraborty, C.E. Frazier, D.A. Dillard, Mixed mode fracture testing of adhesively bonded wood specimens using a dual actuator load frame, *Holzforschung* 64 (3) (2010) 353–361.
- [131] J.G. Williams, On the calculation of energy release rates for cracked laminates, *Int. J. Fract.* 36 (1988) 101–119.
- [132] A. Kutnar, F.A. Kamke, J.A. Nairn, M. Sernek, Mode II fracture behavior of bonded viscoelastic thermal compressed wood, *Wood Fiber Sci.* 40 (2008) 362–373.
- [133] E. Nicoli, D.A. Dillard, C.E. Frazier, Effects of systematic variation of wood adherend bending stiffness on fracture properties. Part 2. Revisiting traditional DCB analysis methods, *Holzforschung* 66 (6) (2012) 771–779.
- [134] P. Niemz, M. Diener, E. Pöhler, Untersuchung zur ermittlung der bruchzähigkeit an MDF platten, *Holz Roh Werkst.* 55 (1997) 327–330.
- [135] P. Niemz, M. Diener, Vergleichende Untersuchung zur Ermittlung der Bruchzähigkeit an Holzwerkstoffen, *Holz Roh Werkst.* 57 (1999) 222–224.
- [136] A.G. Atkins, Y.-W. Mai, *Elastic and Plastic Fracture Mechanics: Metals Polymers, Composites, Biological Materials*, John Wiley and Sons, Ellis Horwood Limited, Market Cross House, Chichester, 1988, pp. 108–113.
- [137] N. Matsumoto, J.A. Nairn, Fracture toughness of MDF and other materials with fiber bridging, in: *Proc. 22nd Ann. Tech. Conf. of the Amer. Soc. of Composites*, Sept 17–19, 2007, Seattle, WA, 2007.
- [138] J.A. Nairn, Analytical and numerical modeling of R curves for cracks with bridging zones, *Int. J. Fract.* 155 (2009) 167–181.
- [139] M.A. Sutton, W.J. Wolters, W.H. Peters, W.F. Rawson, S.R. McNeil, Determination of displacement using an improved digital image correlation method, *Image Vis. Comput.* 1 (3) (1983) 133–139.
- [140] N. Matsumoto, J.A. Nairn, The fracture toughness of medium density fiberboard (MDF) including the effects of fiber bridging and crack-plane interference, *Eng. Fract. Mech.* 76 (2009) 2748–2757.
- [141] N. Matsumoto, J.A. Nairn, Fracture toughness of wood and wood composites during crack propagation, *Wood Fiber Sci.* 44 (2) (2012) 121–133.
- [142] A. Sinha, J.A. Nairn, R. Gupta, The effect of elevated temperature exposure on the fracture toughness of solid wood and structural wood composites, *Wood Sci. Technol.* 44 (2012) 1127–1149.
- [143] K. Li, S. Peshkova, X. Geng, Investigation of soy protein-Kymene adhesive systems for wood composites, *J. Am. Oil Chem. Soc.* 81 (5) (2004) 487–491.
- [144] B. Mirzaei, A. Sinha, J.A. Nairn, Using crack propagation fracture toughness to characterize the durability of wood and wood composites, *Mater. Des.* 87 (2015) 586–592.

- [145] B. Mirzaei, A. Sinha, J.A. Nairn, Assessing the role of adhesives in durability of wood-based composites using fracture mechanics, *Holzforschung* 70 (8) (2016) 763–772.
- [146] B. Mirzaei, A. Sinha, J.A. Nairn, Measuring and modeling fiber bridging: application to wood and wood composites exposed to moisture cycling, *Compos. Sci. Technol.* 128 (2016) 65–74.
- [147] G. Sinn, U. Müller, J. Konnerth, J. Rathke, Strain measurements within fibre boards. Part II: strain concentrations at the crack tip of MDF specimens tested by the wedge splitting method, *Materials* 5 (2012) 1495–1507.
- [148] S. Mahapatra, A. Sinha, J.A. Nairn, Understanding moisture durability of wood-based composites using crack propagation fracture toughness, *Wood Mater. Sci. Eng.* 17 (6) (2022) 598–606.
- [149] S. Mahapatra, A. Sinha, J.A. Nairn, Understanding the thermal durability of wood-based composites using crack propagation fracture toughness, *Holzforshung* 75 (11) (2021) 1032–1041.
- [150] J. Rathke, U. Müller, J. Konnerth, G. Sinn, Strain measurements within fibreboard. Part III: analyzing the process zone at the crack tip of medium density fiberboards (MDF) double cantilever I-beam specimens, *Materials* 5 (2012) 2190–2204.
- [151] J. Rathke, G. Sinn, M. Harm, A. Teischinger, M. Weigl, U. Müller, Fracture energy vs. internal bond strength—mechanical characterization of wood-based panels, *Wood Mater. Sci. Eng.* 7 (4) (2012) 176–185.
- [152] ASTM, ASTM D1101–97a(2018) Standard Test Methods for Integrity of Adhesive Joints in Structural Laminated Wood Products for Exterior Use, ASTM International, West Conshohocken, PA, 2018.
- [153] ASTM, D2559–12a(2018) Standard Specification for Adhesives for Bonded Structural Wood Products for Use Under Exterior Exposure Conditions, ASTM International, West Conshohocken, PA, 2018.
- [154] ASTM, D3434–00(2018) Standard Test Method for Multiple-Cycle Accelerated Aging Test (Automatic Boil Test) for Exterior Wet Use Wood Adhesives, ASTM International, West Conshohocken, PA, 2018.
- [155] ASTM, D4502–92(2019) Standard Test Method for Heat and Moisture Resistance of Wood-Adhesive Joints, ASTM International, West Conshohocken, PA, 2019.
- [156] Forest Products Laboratory, Wood handbook—wood as an engineering material, General Technical Report FPL–GTR–282., U.S. Department of Agriculture, Forest Service, Forest Products Laboratory, Madison, WI, 2021. 543 p.
- [157] J.A. Nairn, Cross-laminated timber properties including effects of non-glued edges and additional cracks, *Eur. J. Wood Wood Prod.* 75 (6) (2017) 973–983.
- [158] J.A. Nairn, Predicting layer cracks in cross-laminated timber with evaluations of strategies for suppressing them, *Eur. J. Wood Wood Prod.* 77 (3) (2019) 405–419.
- [159] J.A. Nairn, Predicting failure of notched cross-laminated timber plates including the effect of environmental stresses, *Wood Mater. Sci. Eng.* 16 (5) (2021) 299–311.
- [160] Y. Li, K. Howes, D.A. Dillard, C.E. Frazier, S.W. Case, Using auxiliary adherends to eliminate need for grain control in fracture testing of adhesively bonded wood, *Int. J. Adhes. Adhes.* 110 (2021), 102917.
- [161] E. Serrano, Cross laminated timber plates with notches—analyses based on fracture mechanics, in: G. Dill-Langer (Ed.), *Timber: Bonds, Connections, Structures. Commemorative Publication Honoring Simon Aicher on the Occasion of his 65th Birthday*, Material Testing Institute, University of Stuttgart, Germany, 2018, pp. 111–126.

-
- [162] E. Serrano, P.J. Gustafsson, H. Danielsson, Prediction of load-bearing capacity of notched cross laminated timber plates, in: 6th Meeting of International Network on Timber Engineering Research (INTER). Tacoma, WA, USA, 26–29 August, 2019.
- [163] J.A. Nairn, Comprehensive composite materials, in: R. Talreja, J.-A.E. Månson (Eds.), *Matrix Microcracking in Composites*, vol. 2, Elsevier Science, 2000, pp. 403–432.
- [164] J.A. Nairn, S. Hu, The initiation and growth of delaminations induced by matrix microcracks in laminated composites, *Int. J. Fract.* 57 (1992) 1–24.
- [165] A. Parvizi, J.E. Bailey, On multiple transverse cracking in glass-fiber epoxy cross-ply laminates, *J. Mater. Sci.* 13 (1978) 2131–2136.
- [166] ASTM, D3983-98(2019) Standard Test Method for Measuring Strength and Shear Modulus of Nonrigid Adhesives by the Thick-Adherend Tensile-Lap Specimen, 2019.
- [167] ASTM, D4027–98(2019) Standard Test Method for Measuring Shear Properties of Structural Adhesives by the Modified-Rail Test, ASTM International, West Conshohocken, PA, 2019.
- [168] E. Le, J.A. Nairn, Measuring interfacial stiffness of adhesively-bonded wood, *Wood Sci. Technol.* 48 (6) (2014) 1109–1121.
- [169] J.A. Nairn, Generalized shear-lag analysis including imperfect interfaces, *Adv. Compos. Lett.* 13 (2004) 263–274.
- [170] J.A. Nairn, Numerical implementation of imperfect interfaces, *Comput. Mater. Sci.* 40 (2007) 525–536.
- [171] Z. Hashin, Thermoelastic properties of fiber composites with imperfect interface, *Mech. Mater.* 8 (1990) 333–348.
- [172] A. Kutnar, F.A. Kamke, M. Sernek, Density profile and morphology of viscoelastic thermal compressed wood, *Wood Sci. Technol.* 43 (2008) 57–68.

This page intentionally left blank

Part Three

Joint design, testing and modeling for performance & durability

This page intentionally left blank

Standard test methods and their need to evolve

14

Aaron M. Forster^a, Christopher C. White^b, and David A. Dillard^c

^aMaterials Measurement Laboratory, National Institute of Standards and Technology, Gaithersburg, MD, United States, ^bExponent, Inc., Bowie, MD, United States, ^cDepartment of Biomedical Engineering and Mechanics, Virginia Tech, Blacksburg, VA, United States

14.1 Expanding roles in structural bonding

Adhesives have made remarkable inroads into many industries and engineered products in the last 50 years. In 2000, *The Adhesives and Sealants Industry Magazine* highlighted the growth opportunities and advantages for adhesives to meet increasing manufacturing and environmental demands in the next century [1]. Advances in chemistries rather than completely new chemistry platforms were expected to fuel growth in new markets, such as automotive [1]. Structural joining using adhesives can eliminate heavy components or allow lighter weight materials such as composites. Adhesives are expected to grow from 5% of the vehicle curb weight in 2025 to 15% of the vehicle curb weight in 2030 as a multifaceted approach to meeting lightweighting goals [2]. Globally, construction adhesives represent a \$9.65 billion market in 2021 with acrylic adhesives representing 45% of that market [3]. Challenges for adhesive bonding include joining dissimilar substrates, reducing the requirements for bond surface preparation, replacement/enhancement of mechanical joining methods, and the ability to meet short manufacturing cycle times [4].

Addressed in more detail in [Chapter 24](#), adhesive applications in the automotive industry include body structural components, semistructural components (e.g., roof, hood, panels), and sealing or elastic bonds (e.g., flange joints). The adhesive properties required for these applications span a broad range including high-modulus and high-strength structural adhesives as well as moderate elongation and low-modulus adhesives for vibration damping.

Adhesives have already reduced vehicle weight and increased stiffness, as shown by the following examples: From 2015 to 2020, the average bead length of structural adhesives per vehicle grew from 69 to 90 m [5,6]. In 2016, a single model of US-made luxury car lost 113 kg (7%) using adhesives and advanced joining technology. Similarly, a 2019 foreign-manufacturer employed 37 m of adhesive to augment structural welds, leading to a weight savings of 9 kg and an increase in body stiffness of 38% [7]. A report from the Center for Automotive Research expects that adhesive bonding of dissimilar materials will represent close to 50% of the bonds within a vehicle by 2030 [2]. The transition to battery electric vehicles will require new classes of adhesives to support cell-to-plate construction for weight reduction, increased energy

density, increased thermal transport, and increased battery pack rigidity [8]. These examples show that adhesives have become an *enabling* technology for the products of today and are expected to remain important for the innovations of tomorrow.

14.2 Infrastructure of standard test methods and measurements

Advanced manufacturing of complex machines relies on a global supply of parts, sub-components, and electronics. Manufacturers, suppliers, and customers need to know that parts and subcomponents are interoperable, meet minimum performance or compliance specifications, and offer predictable reliability. The global system of metrology standards and standard test methods has evolved over time to meet these economic needs. A brief overview of this system should help the reader understand the importance of documentary standards to the case studies.

14.2.1 Metrology standards

In order to measure anything, agreement is needed on the units of measurements. The International Bureau of Weights and Measures (BIPM) is composed of 59 member countries, whose charter is to work together on international measurement standards for chemistry, ionizing radiation, physical metrology, and coordinated universal time. BIPM members representing national metrology institutes (NMIs) are responsible for maintaining national measurements standards and represent their national interests in the development of international standards. National measurement standards are composed of primary standards (universal measurement constants or artifacts for mass, length, time, and other derived units) and secondary standards (a device directly calibrated by the primary standard). Each country supports a single NMI to maintain national standards and traceability to the International System of Units (SI) at a specified level of uncertainty [9]. Primary standards provide traceability for secondary standards. Secondary standards are used to calibrate measurement systems used in documentary standards.

The most recent example is the redefinition of the kilogram in 2019 from an artifact-based standard to a constant of nature, the Planck constant, which was archived in “*The Last Artifact*” documentary [10].

The NMI for the United States is the National Institute of Standards and Technology (NIST), originally the National Bureau of Standards (NBS). NBS was chartered by the US Congress on March 3, 1901 [11,12], and its role in national standards was recognized in Article 1, Section 8, of the US Constitution providing Congress the power to “...coin money, regulate the value thereof, and of foreign coins, and fix the standards of weights and measures” [13]. NBS was changed to NIST in a reorganization defined in the Omnibus Trade and Competitiveness Act of 1988. The name was changed to reflect the institute’s expanded participation in developing industry standards, precise instruments, and new measurement standards [11,12]. Prior to

1901, there were few authoritative national standards for measurement quantity or product quality in the United States. The country lagged behind other industrialized nations that had well-established standards laboratories. The industrial revolution required interoperability, traceability, calibrations, and legal measurement standards. This hampered commerce and competitiveness because many products were governed by regional or locally approved measurement standards. In addition, instruments required calibrations overseas that increased cost and time. The nation had established an office of weights and measures, but the office had limited ability to impose a national legal standard [11,12].

After Congress chartered NBS, the institute began work developing much needed national industry standards for the electrical industry. From there, NBS established national measurement standards for length and mass as well as new standards for temperature, light, and time [11,12]. The history of NBS and now NIST illustrates the importance of NMIs to the national and global economy through the development of rigorous metrology standards and standard test methods to support new or novel technologies.

14.2.2 Standard development organizations

Any regulation, specification, or code body needs to communicate and validate the interoperability or performance of a material or product. Standard test methods are a useful, though sometimes incomplete or imperfect, key for building trust in complex systems, assemblies, and markets. They are generally prescriptive or performance based. Prescriptive standards specify the equipment, test procedure, materials, and analysis method to meet the requirement while a performance standard states the level of performance along with the accepted methods to demonstrate whether a product meets the specified goal. The largest conduit for the development, acceptance, and publication of standard test methods (“standard”) is through standards development organizations (SDOs), for example ASTM, ANSI, IEEE, ISO, and ASHTO [14]. These organizations develop, publish, and maintain standards that include test methods, specifications or classifications, guides, and terminology.

SDO membership is composed of a variety of volunteer stakeholders (manufacturers, suppliers, regulators, NMI members, inspectors, academic researchers) that work together to identify needs, develop new standards, or perform standards maintenance. When a task is identified, the SDO assigns it to a working group to define the details and implementation path for the standards task. Periodically, feedback is obtained from the SDO membership by balloting the standard. This process provides an opportunity for members and nonmembers to provide feedback and vote on the acceptance of the working group draft. The SDO working group responds to this feedback to reach a consensus. There may be considerable resistance to substantial changes due to extensive legacy databases involving earlier methods and versions. Standards thus evolve slowly as the community of stakeholders encompasses a broad range of interests.

14.2.3 Industry-specific standards

In addition to SDO standards, industry-specific standard test methods may be adopted quickly and formalize measurement methods for specific applications or use environments. Drivers and enablers for industry-specific standards are often a lack of a stakeholder community to support the SDO-driven process, lack of a developed theoretical framework, or difficulty translating the use environment into a standard laboratory test. These standards often arise to fill a narrowly defined measurement need such as high-speed rock impacts into a coating or a translating haptic response for human-machine interactions.

14.2.4 Strengths, weakness, and opportunities

Adhesive developers, vendors, and users commonly employ both SDO and industry-specific standards. Manufacturing research and development groups rely on SDO standards for creating, refining, and modifying their adhesive products, as these application agnostic methods, provide data using common, consensus-approved methods for both internal and external product comparisons. Adhesive manufacturers rely on SDO standards for screening purposes, vendor acceptance, and quality control on a lot-by-lot basis, as well as to obtain common material properties used in engineering design. Design validation and risk mitigation often require the use of industry-specific test methods for finalizing designs, examining fielded systems, and monitoring manufacturing consistency.

Industry-specific standard test methods provide manufacturers a sense of continuity to maintain an established product reputation, reliability, or corporate image. Vendors or industry groups may employ both SDO and industry-specific methods to validate performance or gain access to new markets.

As adhesive bonding technology progresses and novel applications emerge, or as new metrologies and instrumentation develop and improve, test methods may need to evolve, and standards should reflect this change. There can be considerable resistance to change for both SDO and industry-specific standards. Working through the SDO process is one source of resistance, as this may take considerable time and effort on the part of the champion, whose role often includes proposing, refining, managing round robin tests, building consensus, and securing widespread acceptance and implementation of new standards development. Another source of resistance may be a history of “always doing it this way” that brings inherent bias toward internal expertise or extensive historical data. Over years, the resistance to change serves as its own justification, whether it is driven by manufacturers, suppliers, or customers. Unfortunately, reluctance to change potentially limits the acceptance of a new measurement standard derived from a rigorous theoretical foundation or evolving needs and practicalities.

To summarize, despite their limitations, standards serve an essential, though not always sufficient, role as a platform for adhesive development, screening, quality control, and acceptance purposes. SDO standards are particularly useful for comparison purposes, though caution is warranted when extending to design purposes, especially

for adhesively bonded joints where stress distributions are not uniform and are influenced by bonded assembly configuration.

SDO documentary standards for adhesively bonded joints provide:

- (1) A communication framework for the community to establish standards such as terminology and test methods.
- (2) Guidance or a protocol for material property characterization and error analysis that is useful for quantitative comparisons of new materials, process optimization, and vendors.
- (3) A consensus authoritative document that changes on a predictable time scale and in a predictable way.

In addition, and to partially address gaps in SDO documentary standards, industry-specific standards (including subcomponent assemblies or sections), if properly developed and applied, should and in some cases do probe performance relevant to their designs, processes, and service environment in a meaningful way. It is important for the stewards of industry-specific standards to quantify and report factors such as accuracy, repeatability, or round-robin tests. The accuracy, repeatability, relevance, necessity, and sufficiency, however, likely vary widely across industries and specific applications.

14.3 Strength and fracture: An evolution in adhesive joint measurements

In thinking of the evolution of test standards, one need look no further than the shift in focus from strength tests to fracture tests to assess adhesive bonds. *Strength* and *fracture energy or toughness* are often the starting points to quantify adhesive bond performance. Although both remain critical components of adhesive development and acceptance criteria, the last 20 years have led to an expansion of fracture characterization methods to support higher-performing bonded systems. One may ask *Who cares whether the adhesive joint is evaluated using a strength or fracture energy framework? Doesn't the joint just need to be strong enough?* The following mine accident example does not involve adhesives directly, but it starkly contrasts strength and energy approaches to design, where failure to consider the latter led to a loss of life. This example was inspired by a fatal mine accident and presented as an opportunity for learning [15–18].

In this mine, roof bolts were drilled into the rock ceiling to anchor a messenger steel cable (6.35 mm (0.25 in)) shown as the small blue circle in Fig. 14.1a. Electrical power or utilities could be attached to the messenger cable via spring wire clips, Fig. 14.1a. In this case, spring wire clips were attached approximately every 48 cm (19 in) to support a heavy 6.35 cm (2.5 in) diameter power cable (larger red circle, inset Fig. 14.1a). The power cable was over 1.6 km (1 mile) long and the spring clips facilitated an easy process to detach the power cable from the messenger cable where needed in the mine. The inset of Fig. 14.1a shows schematic representations of strength (magnitude of peak force) and toughness (integrated area) obtained from load-displacement tests on a clip pulled until it detached from its mounting. In a

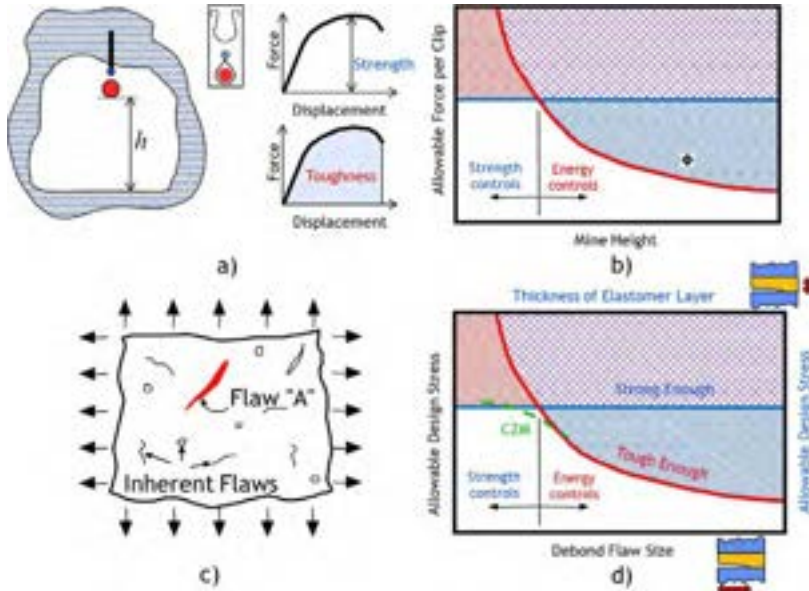


Fig. 14.1 Schematic illustration of the mine cable example: (a) the mine shaft cross section with an inset of the spring clip, along with diagrams of strength and toughness (area under load-displacement curve) for pull-out of the clip; (b) Resulting design envelope for mine clips showing strength and energy envelopes as well as the operating point of the mine as a function of mine height; (c) Illustration of dominant “flaw A” along with inherent flaws within a material; and (d) extension of the mine cable example to adhesive bonds, along with the cohesive zone model approach that bridges the transition between strength and fracture dominated regions. © DA Dillard, 2022, CC-BY-SA 4.0. Available at <http://hdl.handle.net/10919/113401>.

strength-based approach, the design envelope for the wire clips was independent of mine height (h), as a fixed number of clips per kilometer was required to support a cable of certain linear weight, shown by the horizontal line in Fig. 14.1b. The vertical line represents the design limit specified by the clip manufacturer. To the left, the force on each clip remains constant and does not exceed the strength value, the power cable remains attached to the messenger cable.

What happens if several adjacent clips catastrophically fail due to an unexpected event? Kinetic energy is transferred from the falling cable section into the clips that hold adjacent cable sections to the roof. In this case, an energy approach is required to predict whether adjacent clips release from the ceiling. This is called the dynamic load and is represented to the right of the vertical line in Fig. 14.1b. The design envelope becomes a function of the mine height, that is, mine tunnels with taller ceilings require more or higher strength clips to arrest the kinetic energy release as a cable falls through a height, h . In this unfortunate accident, the operating point of the mine was below the strength envelope, but above the dynamic load limit (energy limit), shown by the data point in Fig. 14.1b [17,18]. On the night of the accident a worker was approximately

91 m (300 ft) in the mine moving coal between conveyer belts. Further down the mine a group of workers were unloading 272 kg, 10 m (600 lb, 33 ft) long rails from a flat car. The rails were edged off the car and allowed to fall onto the ground. As one of the rails fell, the end rebounded and struck the power cable. This dislodged the cable from its clip and initiated a progressive failure. Within seconds a 134 m (439 ft) length of power cable detached from the roof and fell to the ground. Unfortunately, the cable struck and fatally injured the worker moving coal far away from the rail-cable impact. In the subsequent investigation and court case, it was discovered that the clip literature indicated safe static loads of 45 kg (100 lbs) or 2.3 kg (5.1 lb) per clip (spacing 0.46 m (1.5 ft)) was a safe application. There was not a consideration for dynamic loads [15,18]. The strength-based design approach alone was insufficient and failed to consider the possibility of a propagating failure mode that could easily have been addressed with a simple energy-based design.

The energy approach may be thought of as a method to address an event that causes a local failure. Fracture mechanics casts the fractured material as a new equilibrium state, where the fracture process represents a transfer in the material potential energy [19]. Extending this mine analogy to fracture mechanics, we consider that the relevant length scale in the mine was the height—the distance through which the cable could fall. In fracture mechanics, the relevant length scale is often the length or size of the dominant or most severely loaded flaw, as shown in Fig. 14.1d. If existing or anticipated imperfections are of a similar size to the inherent flaws, then a strength-type approach may be sufficient, recognizing that the strength of actual products is weakened by inherent flaws, accounted for by so-called knock down factors. If flaw A initiates growth because of an externally applied load or environmental degradation, the energy approach may be used to predict the material response. The extension of the design envelope (Fig. 14.1c) to fracture mechanics is shown in Fig. 14.1d, where the mine height is analogous to flaw A length for a structural bond (lower abscissa-axis), or elastomeric adhesive thickness (upper abscissa-axis). Thus, acceptable adhesive designs not only focus on strength but also on ensuring that the bond will be tough enough to survive “*when something goes wrong.*” Strength and fracture approaches have traditionally represented two distinct design philosophies, though as will be shown in Chapters 15–17 and 32, the cohesive zone model (CZM) offers a bridge between these two design approaches that has improved understanding and led to new innovations in joint design.

Strength and fracture energy considerations are needed for many practical bonding scenarios, as Gordon has stated: “The worst sin in an engineering material is not lack of strength or lack of stiffness, desirable as these properties are, but lack of toughness, that is to say, lack of resistance to the propagation of cracks” [20].

Evaluating the strength and fracture toughness measurements for an adhesive bond are more complex compared to test methods for monolithic materials. In contrast, a loaded structural joint exhibits complex, multiaxial, nonuniform stress states that are unique to the test method and often the material system. Stress distributions are typically functions of the mechanical properties of the materials, the geometry of the bonded joint, and the manner of loading, and these multiaxial stresses often vary widely across the bond area [21]. Several books [22–33] and reviews [34–37]

document progress in predicting stresses and strains within adhesive joints. The reader is encouraged to utilize these in addition to this book as resources.

14.4 The evolution of strength and fracture energy in adhesive design

In the consideration of strength and fracture perspectives for adhesive joint characterization and design approaches, we note that strength-based design is often attributed to Galileo [38]. Extending this method to adhesive joints might suggest that a bond will fail when the applied stress exceeds a maximum or critical stress. Fig. 14.2 shows some of the simpler joint geometries for evaluating the strength of structural adhesive bonds. Hybrid joining techniques incorporate spot welds (weld-bonding) or mechanical fasteners to provide structural rigidity to the joint while the adhesive cures (not shown) [39]. The single-lap joint (SLJ), shown in Fig. 14.2a, remains a widely used geometry for assessing the strength of an adhesive joint.

14.4.1 Strength approaches

Strength metrics, also reviewed in Chapter 15, are often defined in terms of the maximum applied stress prior to failure in a particular loading direction and test geometry. Other variations include a stress maximum, the stress at a particular strain, or some averaged stress value for a given joint configuration. Each class of overlap joint shown above potentially induces artifacts into the measurement, thus complicating the ability to link joint strength to the mechanics of the failure.

Historically, strength-based approaches utilized elastic or elastic-plastic mechanics to develop analytical models, usually two-dimensional (2D) closed form solutions, for

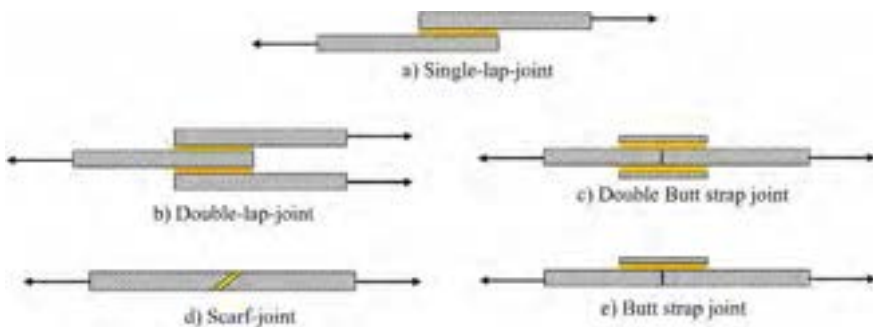


Fig. 14.2 Examples of structural adhesive overlap joints encountered in the construction, automotive, and aerospace industries.

Modified from R.D. Adams, W.C. Wake, *Structural Adhesive Joints in Engineering*, first ed., Springer, Dordrecht, 1984, doi:10.1007/978-94-009-5616-2.

the stresses in an adhesive joint [40,41]. These models remain useful as they provide insight into nonuniformities in the stress distribution, the onset of joint deformation, and the edge effects during loading. Examples of analytical models include the classic shear lag analysis of Volkersen [42] and Goland and Reissner's inclusion of geometric nonlinearity to account for eccentric loading and their adaptation of Winkler's [37] beam on elastic foundation to model peel stresses [34,37,43]. Hart-Smith [44] considered shear lag and peel stresses in an SLJ geometry, but also addressed the possibility of failure resulting from load eccentricity initiating adherend yielding, a common occurrence in bonded joints. The classic and more refined analytical models mentioned above are available for the preliminary analysis of simple geometries, such as single-lap, double-lap, and butt joint tests. Engineers with access to modern computing technology may use analytical models to extend their understanding of stresses in engineered joints; employ finite element or related models to simulate complex geometries and loading scenarios, material properties, and constitutive property relationships; or a variety of failure or fracture metrics in a relatively short amount of time without the use of a supercomputer.

Despite the availability of these analytical models, current SLJ standards report the strength as the breaking load divided by the nominal bond area. ASTM D1002-10 [45], for example, is a specific configuration for thin metal adherends joined with an adhesive. The standard hints at some controversy by referring to this quantity as the "apparent shear strength" and noting that "this test method is primarily comparative." Glimpses of the concerns are presented in ASTM D4896-01 [46], where we find:

Single-lap tests, like those described in ASTM test methods D906, D1002, D2339, D3163, D3164, D3165, and D3528, are not suitable for determining the true shear strength of an adhesive. The apparent shear strength measured with a single-lap specimen is not suitable for determining allowable design stresses, nor is it suitable for designing structural joints that differ in any manner from the joints tested without thorough analysis and understanding of the joint and adhesive behaviors.

Just as no competent engineer would base a design on the average stress of a component experiencing a nonuniform stress state, one should not think that the "apparent shear strength" translates to failure predictions for a different joint geometry.

Even within the production of SLJ joints for standardized testing, the details remain important as adherend and adhesive terminations and thicknesses, surface treatment, flaws, and specimen asymmetry can significantly affect the strength of bonded lap joints [47–50]. Villegas et al. [51] used ASTM D5868-01 [52] to investigate welded composite SLJ joints. They highlight a recurrent theme for structural adhesive joints that reporting only the "apparent shear strength" may not provide a complete picture of performance. A full understanding of the joint behavior requires information on the geometry/microstructure, adherend materials, surface preparation and cleanliness, adhesive, and other nonuniformities to make a proper evaluation of adhesive performance.

14.4.2 Cautions on production-level testing

Standard test methods evolve to meet a practical need to compare or verify performance claims. Research and quality control groups produce and test multitudes of SLJ specimens each year, but without careful oversight, these specimens risk becoming commodity items. In this case, microscopic irregularities, such as insufficient adhesive (starved joints), excess adhesive and varied spew at joint edges, voids, misalignment, and other issues, may not be conveyed or may be missed entirely due to the pressures of meeting schedules. As the number or significance of these errors or irregularities increases, within a sampled population, the scatter within strength data increases, resulting in difficulties interpreting the results. Programs that rely heavily on strength tests should keep this in mind. Even a perfectly manufactured adhesively bonded specimen, evaluated only by strength, exhibits a highly nonuniform stress state within the adhesive. This limits the ability of an engineer to infer performance of the SLJ to other joints [23,53].

The SLJ remains an important geometry and the community continues to work to improve our understanding. Joining a long list of others, Kendall [54] recently argued that standard test methods for lap joints rely on a failure stress criterion for strength that is inherently dependent on the geometry. SLJ specimens pulled in tension, for example, often result in a low-angle peel fracture, not a shear failure. He reframed the analytical model of the lap joint using the *Griffith energy principle* approach to arrive at a geometry-independent prediction of the peeling force, as previously reported in his works and that of others [55–58]. Chapter 15 addresses strength and predictive methods in detail.

14.4.3 Fracture mechanics and adhesive bonding

The modern framework for fracture mechanics dates to the 1921 publication of Griffith's seminal experiments on the failure of glass and his energy model of crack propagation from an elliptical hole in a brittle solid [19]. The fracture energy approach often utilizes simple geometries where the global loading is related to the local stress field, or more generally the energy release rate, at the crack tip. The Griffith fracture theory used a thermodynamic analysis to relate material strength to the crack or flaw size and the surface energy penalty to propagate the crack. This approach works well for brittle materials, but requires modifications for applications to more ductile metals [59].

Standard test methods for monolithic materials rely on simple specimen geometries, a sharp precrack, and a defined loading path to quantify a *material* parameter that is believed to be independent of sample geometry [59]. Fracture energy or critical energy release rate (G_c) is a measure of the material's resistance to crack propagation, measured independent of test geometry. Once known, the extension of a crack under other geometries and applied loading situations may be predicted. The energy release rate is a material property in idealized homogeneous materials, but in polymeric adhesive bonds it has been shown to be a function of temperature [21,60], test rate [60,61], the thickness of the bond [21] (see Chapter 18), the manner

of loading (see Chapter 17) for mode mixity, fatigue (see Chapter 19), high strain rate loading (see Chapter 21), and environmental exposure (see Chapter 20).

14.4.4 Addressing plasticity in joint failure

The maturation of fracture mechanics began in the 1950s with the development of linear elastic fracture mechanics (LEFM), which connects the applied stress on the specimen to the stress at the crack tip, the crack geometry, and the bulk material properties. This method assumes that the monolithic material obeys linear-elastic behavior yet allows for small amounts of plasticity *local* to the crack tip. Irwin extended LEFM for materials that exhibit a high degree of plasticity. Irwin separated the elastic strain energy released by crack growth and the plastically dissipated energy around the crack tip. He defined a stress intensity factor (K) that reflects the severity of the singular stress field surrounding the crack tip and the corresponding *material* property, the critical stress intensity factor or fracture toughness (K_c), that is proportional to the square root of the fracture energy (G_c) [59,62,63]. Rivlin and Thomas [64] modified Griffith's failure criterion to characterize the tearing of rubber. Polymeric adhesives dissipate energy through viscoelastic or viscoplastic processes that exhibit test rate and temperature [21,65–67] dependent fracture energies. The double cantilever beam test geometry [56,68–70] was proposed in 1960 to measure Mode I (crack opening) fracture energy for bonded joints and laminated materials. It remains widely used in the fracture mechanics community for the evaluation of adhesive joints and composites. The development of fracture mechanics to accommodate different material behaviors has fostered new approaches to understand elastic-plastic, dynamic, viscoelastic, and viscoplastic fracture phenomena [59]. Crack tip opening displacement (CTOD) [71] and the J-integral [72] were developed to quantify the fracture energy for increasing degrees of yielding and nonlinearity observed experimentally.

The cohesive zone model (CZM) is a powerful analysis tool that bridges the gap between strength and fracture concepts. The origins of CZM can be traced to the 1950s through the efforts of Barenblatt [73] and Dugdale [74] to understand cracks in brittle materials and the yielding of ductile steels. The numerical implementation of CZM involves a localized method in which each cohesive element obeys a specific traction-separation law (TSL); CZMs and TSLs are covered in more detail in Chapters 15–17 and 32. In essence, altering the cohesive law in relationship to the fracture energy, cohesive strength, and displacement at peak traction allows this technique to combine aspects of damage mechanics and continuum mechanics within the behavior of each CZM element [75]. Commercial finite element packages have supported the development of CZMs to predict stresses at a more granular level for complicated joint geometries and complex, nonlinear material properties.

Case Study 1: Strong and tough adhesives for automotive bonding

The automotive industry requires adhesives that are sufficiently strong but also tough enough to survive and dissipate energy in an extreme event such as a collision. In this case study, a U.S.-based auto manufacturer was evaluating the performance of a series of adhesives. The strength of the candidate adhesives was measured using an SLJ geometry at quasistatic rates;

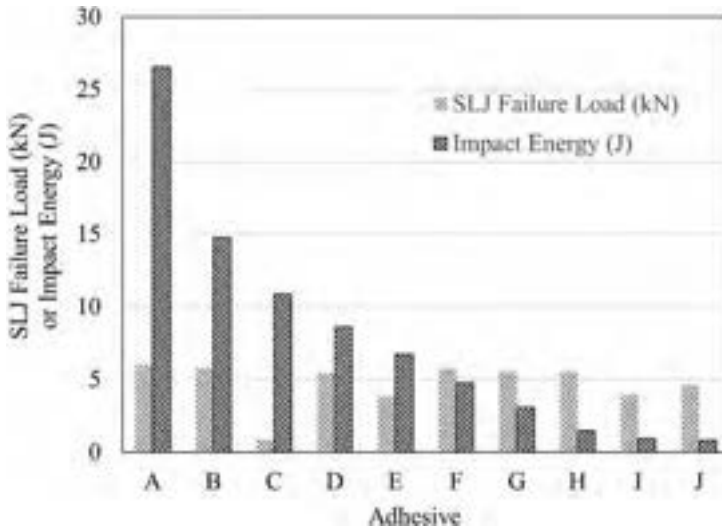


Fig. 14.3 Illustration of the stark differences in quasistatic SLJ failure load and impact energy absorption of a series of automotive adhesives. Most adhesives are strong when tested using quasistatic SLJ tests, but high-rate loading during a proposed high-rate wedge test illustrates the importance of toughness in absorbing impact energy. Courtesy of private communication, ca. 2000.

see Fig. 14.3. There were few adhesive impact tests available in the 1990s to quantify the adhesive fracture energy and energy absorption at rates typical of an automotive impact. Thouless et al. developed a new method to quantify the energy absorbed by the adhesive during impact [76]. His method involved driving a wedge into the adhesive joint at a high velocity. The analysis partitioned the impact energy into the work to fracture the adhesive and the work to plastically deform the thin adherends. This approach only required measurements of the residual curvature of the adherends post-impact and the nonlinear constitutive properties of the adherend to extract the adhesive energy [76]. Fig. 14.3 shows that most of the adhesives exhibited similar apparent lap shear strengths at quasi-static rates, but only a few of the candidate adhesives were perhaps tough enough for this application. Thouless noted that the technique underpredicted the published toughness values for the adhesives. Kinloch and Williams conducted a secondary analysis of the Thouless test method and showed that the inclusion of root rotation at the point of adhesion brought the toughness measurement in line with expected values [77]. While this innovative methodology highlighted the need for a quantitative measure of adhesive energy at impact rates, it did not transition to a standard test method.

Around the same time, two European-based manufacturing companies worked with Imperial College to develop the impact wedge test (IWT) that would eventually transition into the standard test method ISO 11343 [78,79]. (The reader is encouraged to read more on high-rate characterization in Chapter 21.)

Case 2: Time-dependent failure of roofing membrane seams

In the early 1980s, ethylene-propylene-diene terpolymer (EPDM) roofing membranes represented a revolution in low-sloped roofing system construction in the United States. As a new

material, EPDM membranes entered the market without a clear service life history. This inert, single-ply membrane replaced neoprene and chlorosulphonated polyethylene (CSME) membranes, rapidly capturing 50% of the roofing market. The US National Roofing Contractors Association (NCRA) had a survey program to track quality issues across the roofing industry [80]. The survey was part of a program to identify early problems in low-sloped roofs and develop a baseline of roof performance [81] for new materials. NCRA found that EPDM seams were failing and causing roof leaks much sooner than the roof design life. More than 85% of the losses occurred within the first 3 years after installation, with the majority of failures (60%) occurring within the first year. This problem was significant for the industry due to the rapid adoption of EPDM membranes, the number of failures, and the cost to repair failures.

During installation, the membrane was rolled out onto the roof, seams were created by overlapping adjacent membranes by 75–100 mm, and the seam was sealed using a liquid adhesive or preformed tape of neoprene rubber (prior to 1986) or butyl-rubber (after 1986). The NCRA investigation identified some failures attributed to poor installation practices, such as inadequate surface preparation or excessively thin adhesive layers, but NCRA concluded these were not enough to account for the number of reported failures [80]. It was noted that many of the failed roofs exhibited wrinkles along the seams, as shown in Fig. 14.4a.

The NCRA approached NIST to help identify the source of failures and propose solutions. NIST conducted an investigation and initially identified 24 different variables that could affect seam durability. Postmortem inspection of properly installed joints exhibiting early failures indicated a highly deformed adhesive with cohesive failure [82]. NIST began to identify the controlling variables for the reduced durability in the EPDM joints. One challenge was deciding how to measure the strength of the seam. For engineers, it is important to select test methodologies that are representative of the phenomena under investigation.

At the time, there was a debate in the scientific community as to whether a short-time, quasistatic SLJ test or a creep rupture peel test would be appropriate to quantify early failures, see Fig. 14.4b and c [83].

Short-time or quasistatic SLJ strength measurements exhibited larger tensile loads, higher strain rates, and higher extensions than are found in the in-service roof seam environment. In addition, SLJ tests using compliant adherends and tough adhesives exhibited large scatter in the strength data that made it difficult to identify trends within the data. On the other hand, long time creep-rupture T-peel joint measurements were more comparable to the in-service environment because the tensile loads and strain rates better matched the roofing application [82–86].

NIST compared short-time SLJ tests and creep-rupture in T-peel joints as a function of adhesive thickness, cure time, surface contamination, tensile load, and adhesive type [85]. It was shown that the maximum design stress a joint may sustain in peel is only a small fraction (roughly 5%) of the short-time SLJ strength. Creep-rupture on peel specimens indicated that the maximum load, adhesive thickness, and to a lesser extent contamination were important for durable joints. To the contrary, short-time SLJ indicated surface contamination was more important than adhesive thickness [85]. The importance of adhesive thickness identified via creep-rupture tests was consistent with established research on the peel and tensile failure of elastomeric adhesives [87–90]. Adhesive thickness was also shown to be important for facilitating toughening mechanisms [22,91].

Fig. 14.5 shows the results from a creep-rupture study of clean and dirty surfaces with different adhesive thicknesses. Thin adhesive layers on dirty or clean surfaces failed within weeks while a thick adhesive on a clean surface was predicted to last years. This research convinced the NCRA that creep-rupture testing was required to measure long-term seam joint strength despite

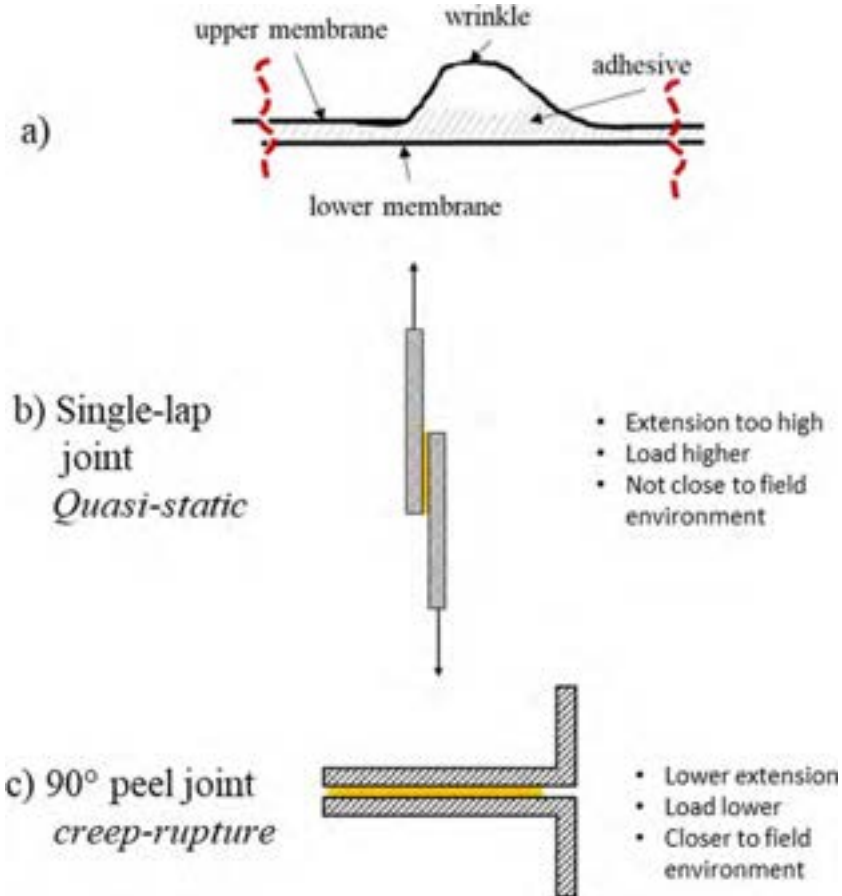


Fig. 14.4 (a) Image of the overlap seam for a low-slope EPDM roof. The wrinkle in the seams is circled in white chalk, and a knife handle is seen protruding to show the wrinkle scale. These wrinkles occurred during the installation of the membranes. (b) Illustration of single lap joint tested under quasi-static conditions. (c) Illustration of the peel test geometry tested under creep-rupture.

Modified from W.J. Rossiter, M.G. Vangel, E. Embree, K.M. Kraft, J.F.J. Seiler, Performance of Tape-Bonded Seams of EPDM Membranes: Factors Affecting the Creep-Rupture Response of Tape-Bonded and Liquid-Adhesive-Bonded Seams, Natl. Inst. Stand. Technol. Build. Sci. Ser. 175, 1996.

an initial bias for quasistatic testing. The partnership between NIST and the NCRA was critical to educating practitioners and for this method to gain acceptance in the community. In this case, it took failures in the EPDM roofing materials to drive the industry to change in order to find a solution to the problem. In 1993, ASTM published the Standard Test Method D5405, called the "Standard Test Method for Conducting Time-to-Failure (Creep-Rupture) Tests of Joints Fabricated from Nonbituminous Organic Roof Membrane Material," which standardized creep-rupture tests for both T-peel and SLJ geometries to evaluate the performance of roofing

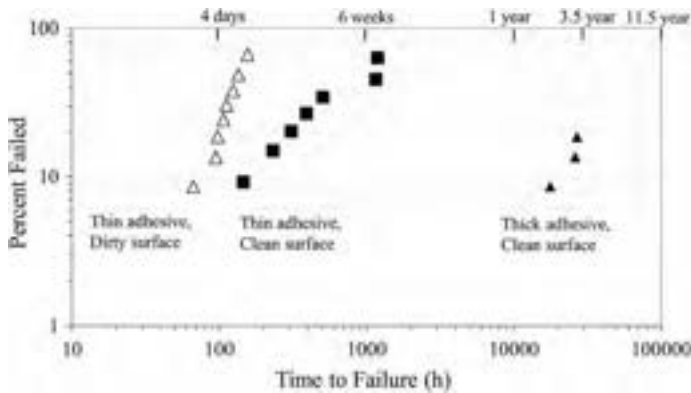


Fig. 14.5 Cumulative percent of T-peel specimens that failed in creep vs the time to failure. These tests were conducted at 23°C and 97% RH.

Modified from W.J. Rossiter, J.W. Martin, J.A. Lechner, E. Embree, J.F.J. Seiler, Effect of adhesive thickness and surface cleanness on creep-rupture performance of EPDM peel and lap-shear joints, in: T.J. Wallace, W.J. Rossiter (Eds.), *Roofing Research and Standards Development ASTM Special Technical Publication 1224*, vol. 3, ASTM International, West Conshohocken, 1994, pp. 123–138.

membrane seams. The installation guidance provided to the installers after publication of the ASTM standard was to minimize mechanical loads on the roofing membrane, in particular to reduce peel stresses, maintain a critical thickness of adhesive, and maintain the cleanliness of seams prior to bonding.

Case 3: Missing a standard specification leads to a catastrophic failure

As discussed in the previous example, adhesive design focused on short-term properties leaves designers blind to the long-term loading effects. The importance of creep was revealed again in Boston on July 2006. A passenger car, occupied by a husband and wife, was headed to Logan airport on the I-90 connector tunnel. The couple was about to exit the D street portal, which was constructed as part of Boston’s Central Artery/Tunnel (CA/T) project, or “Big Dig.” As the car approached the tunnel exit, concrete panels detached from the roof and fell onto the vehicle. The result was significant damage to the vehicle and one fatality [92].

The National Transportation Safety Board [93] (NTSB) took the lead in the accident investigation. The roof of the D Street portal was composed of a series of concrete panels suspended from the tunnel roof; see Fig. 14.6a. Above the ceiling were various facility services such as electrical and intake/exhaust air handling. The suspended ceiling construction within the D Street portal was composed of 15 panels—10 large panels and five smaller panels; a simplified drawing (six panels) is shown in Fig. 14.6a. The larger panel masses were approximately 2132 kg (21 kN) and the smaller panel masses were about 1134 kg (11 kN). The concrete panels were attached to steel support beams. The support beams were fixed to the concrete roof through a series of hanger plates joined by clevis connections. The steel support framework was attached via anchor rods. Holes were drilled into the concrete tunnel roof, and anchor rods were affixed with an epoxy adhesive; see Fig. 14.6b. After the epoxy was cured, the approved practice was to proof test each anchor by loading it in tension to 125% of the maximum design service load ($1.25 \times 1180 \text{ kg}$) equal to 1475 kg (14 kN). Failed anchors were replaced.

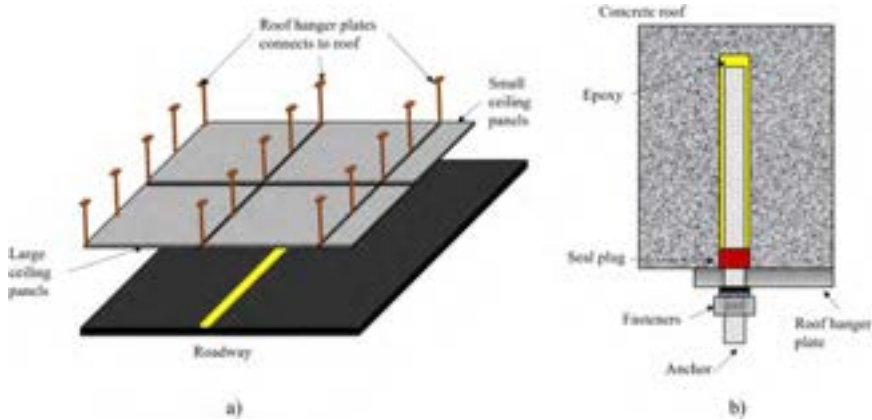


Fig. 14.6 (a) Illustration of D Street portal ceiling construction adhesive anchors. The total mass of material that fell from the roof was approximately 23,500 kg (235 kN), each anchor holding approximately 1000 kg (10 kN). (b) Schematic of the concrete anchors used to mount each panel to the tunnel roof. The anchors attached a steel plate hanger to the roof and were held in place with a construction adhesive.

During the postaccident investigation, NTSB noted that a number of the anchor rods in the roof had either fully detached or were pulled away from the roof with displacements ranging from approximately 0.25 to 2.5 cm. The number of displaced anchors in relationship to the total number of anchors was 78 of 198 in the westbound tunnel, 57 of 248 in the eastbound tunnel, and 26 of 188 in the high-occupancy vehicle (HOV) tunnel. The static loads were well below the maximum design load for the anchor system (1752 kg or 17 kN). The evidence of pull-out failures led NTSB investigators to focus on the epoxy adhesive used to affix the anchor bolts into the roof.

NTSB investigation

A review of the specification and procurement documents revealed that many of the construction details were unique for the D Street portal tunnel. The adhesive used for the anchors was packaged by an adhesives distribution company, but this company obtained the raw materials from a second company (adhesive manufacturer) while a third organization acted as the supplier for the D street portal. Two different versions of the adhesive, a fast set and a slow or standard set were sold at the time of the accident. Both used the same basic epoxy formulation and had very similar short-term loading properties such as strength and stiffness. The main reported difference between these versions was the fast set curing system was modified to accelerate the cure process to finish in a much shorter time than the standard set. In the discussion here, the fast set version is designated Epoxy A while the standard set material is designated Epoxy B. Early in the NTSB investigation, there was some uncertainty about which version was used in the D street portal, and as a result, most studies initiated in the NTSB program examined both versions of the adhesive. At the time of design approvals, the adhesive supply sold only one adhesive formulation, Epoxy A. They did not start distributing Epoxy B until the start of construction of the D Street portal in late 1999. At the time of construction of the D Street portal (1999), NTSB found that there was no distinction in the product literature between the two adhesive formulations. Through chemical analysis of samples from the tunnel, NTSB was able to determine that all the anchors in the D Street portal used the Epoxy A adhesive.

The NTSB investigation uncovered evidence that the adhesive company was aware, prior to the accident, that Epoxy A was sensitive to long-term loading. In 1997, the adhesive company proceeded to certify the fast-set adhesive for construction applications. As part of this process, an optional creep test may be conducted but it was not required. The fast-set adhesive failed the creep test and the standard set passed the creep test. As a result, the allowable loads for the fast set were reduced and the safety factor increased from 4 to 5.33. The allowable loads were also restricted to short term loading, which means only against external loading such as wind and not a sustained static load. For this application, the allowable tension load for Epoxy B was 2336 kg (23 kN) and the ultimate load capacity was 9344 kg (93 kN). The allowable short-term load for Epoxy A was 1750 kg (17 kN) and the ultimate load capacity was 9344 kg (93 kN). The adhesives were certified in 2000, but no distinction was made in the product literature between the fast-set Epoxy A and the standard-set Epoxy B materials. It would not be until May 2007 that the product literature was updated to indicate the differences between the two adhesives, and still the restriction to short-term loads for Epoxy A was not clear.

The HOV section of the D Street tunnel ceiling was completed in August 1999 and anchors began showing displacements by December 1999. An investigation by the contractors and the adhesive supplier indicated that these failures were likely due to improper installation and anchor bolt overtorque. The true locus of failure was not identified. An agreement was made to replace the anchors and rather than proof test to 125% of the maximum design service load, the anchors would be proof tested to the ultimate load (2880 kg (28 kN)) and the anchor bolt torque specification was reduced. Proof testing is a short-term maximum load test designed to identify early failures related to installation problems. An inspection of the tunnel in 2001 again found problems with anchor bolt displacement, but a deficiency report was not issued, and the bolts were replaced. The contribution of long-term creep was missed and installation was identified as a potential source of failure indicated a lack of understanding of the viscoelastic nature of epoxy adhesives by the construction community.

NIST and Federal Highway Administration roles

NTSB requested that the Federal Highway Administration (FHWA) conduct research into both epoxy anchor systems by replicating the installation procedures at the Turner-Fairbank Highway Research Center. Replicating the installation conditions and loading anchors with dead loads was a challenging and slow process. The size of the operation meant that not all the installation conditions (temperature, moisture, time) that might affect the epoxy chemistry could be easily explored. NTSB turned to NIST to help identify the material and performance differences between Epoxy A and Epoxy B. They were particularly interested in the possibility that time-temperature superposition might be used to provide insight into the long-term behavior of the adhesives. NIST conducted a thorough study of the thermo-viscoelastic, water absorption, and thermo-degradative properties of the epoxies [94,95]. The laboratory measurements were quicker than the live load experiments which provided valuable information on the differences between the two epoxies in a short amount of time. Epoxy adhesives, discussed in more detail in Chapter 1, start as a two-component liquid where one chemical (an epoxide) reacts with a second chemical (an amine in this case). As the reaction progresses, the epoxy and amine polymerize into long molecules that releases heat. The reacting molecules form a crosslinked network indicated by the transformation from liquid reactants to a glassy polymer. If the temperature is not high enough, the polymer network may vitrify prior to complete reaction as the glass transition temperature approaches the cure temperature. Often, structural adhesives require an elevated posture to complete the reaction to achieve their maximum properties. For this class of construction adhesives, the heat of reaction provides the thermal energy to cure the epoxy by increasing the temperature above the ambient to reach the final degree of cure, and further post-curing would be impractical.

NIST developed a plan to fully characterize Epoxy A and Epoxy B using differential scanning calorimetry (DSC), thermogravimetric analysis (TGA), dynamic mechanical thermal spectroscopy (DMTA), and infrared spectroscopy (IR). These techniques measured the structure of the epoxy network formed by each adhesive formulation, and the extent of reaction during cure at ambient conditions. DSC measures the thermal transitions of a polymer to measure quantities such as crystallization, melting, and the glass transition temperature (T_g). For epoxy networks, the measurement of interest is T_g , which is defined as the temperature at which the onset of long-range, cooperative motion of the polymer backbone occurs. DMTA measures the effect of frequency and temperature on the modulus and T_g . It imposes a sinusoidally varying small strain oscillation within the linear viscoelastic region of the material and measures the resulting oscillation in stress. This method quantifies the elastic (E' , *storage modulus*) and viscous (E'' , *loss modulus*) properties and their ratio ($\tan \delta = (E''/E')$). Tracking these parameters as a function of temperature and frequency allows one to quantify the dependence of the polymer motion on temperature and frequency [96].

DSC and DMTA measurements are powerful tools for probing the structure of a polymer network. Table 14.1 shows the measurements of the T_g from both techniques. Epoxy A had a lower T_g than Epoxy B. A postcure of the samples to 60°C was conducted to evaluate whether the epoxies completely cured. The T_g of Epoxy B did not change appreciably, indicating that it completely reacted. Surprisingly, Epoxy A exhibited a decrease in the T_g on the second heat, but there was no corresponding exothermic or endothermic transition measured in the DSC to indicate another thermal transition. This is unusual for epoxy materials, as further curing or polymer aging tends to increase T_g .

Moreover, since the DSC scan was performed immediately after the first scan, there is minimal time for any physical aging of the polymer so that would also tend to increase the T_g . One possible explanation was the thermal degradation of Epoxy A at low temperature in the DSC. TGA measurements of both epoxies indicated that the degradation temperature for Epoxy A ($T_{\text{onset}} = 75^\circ\text{C} \pm 2^\circ\text{C}$) was much lower than Epoxy B ($T_{\text{onset}} = 115^\circ\text{C} \pm 1^\circ\text{C}$) by more than 40°C. The reason for the significant differences between Epoxy A and Epoxy B was not apparent given the limited knowledge of the underlying formulation chemistry, but the polymer networks formed in each epoxy were significantly different.

Fig. 14.7 is a representative temperature sweep for Epoxy A (Fig. 14.7a) and Epoxy B (Fig. 14.7b) measured using DMTA. Both adhesives have similar glassy storage moduli, exhibit broad transition regions (distance from maximum E' to the minimum E'), and have distinct rubbery plateaus. The $\tan \delta$ peak is close to 1, which indicates the loss modulus (E'') becomes almost equal in magnitude to the storage modulus (E') through the transition region. Perhaps the most unexpected result is the difference in the storage modulus rubbery plateau (E'_{rubbery}) defined as the plateau in E' at high temperatures. E'_{rubbery} for Epoxy B is approximately 46 MPa and for Epoxy A it is about 10 MPa. This nearly fivefold difference is quite

Table 14.1 Summary of thermal analysis data for Epoxy A and Epoxy B, obtained from DSC and DMTA.

Temperature (°C)	Epoxy A	Epoxy B
DSC		
First heat T_g	48 ± 1	55 ± 1
Second heat T_g	44 ± 3	54 ± 2
DMTA T_g (E'' peak)	50 ± 1	52 ± 1

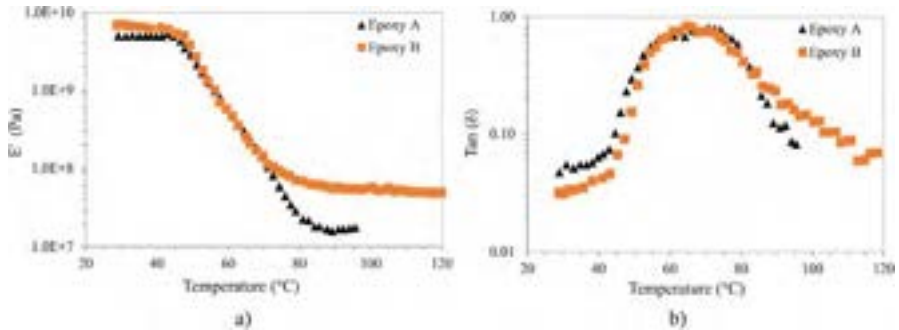


Fig. 14.7 Representative Epoxy A and Epoxy B results for (a) E' and E'' , and (b) $\tan \delta$; obtained at 5 Hz and strains $\leq 0.04\%$.

Modified from J. Chin, A. Forster, J. Ocel, J. Hartmann, P. Fuchs, D. Hunston, Thermoviscoelastic analysis and creep testing of ambient temperature cure epoxies used in adhesive anchor applications, *J. Mater. Civ. Eng.* 22(10) (2010) 1039–1046, doi:10.1061/(ASCE)MT.1943-5533.0000108.

unexpected for adhesives where the only reported difference was the cure rate. This suggests substantial differences in the crosslink densities between the polymer networks. The lower T_g and thermal degradation temperature reported earlier support this conclusion [97]. Given that investigators found evidence that the bolts pulled out from the roof and the epoxy failure was cohesive, determination of the creep response for each epoxy formulation was important. As reported in the NTSB report, the recertification process indicated the fast-set adhesive failed the optional creep test.

Creep behavior for the adhesives was determined by two different approaches that both involve generating master curves using time-temperature superposition (TTS). The first method used direct measurement of isothermal creep curves which were shifted to generate creep master curves. In the second approach, isothermal DMTA frequency response curves were generated and shifted to create master curves. The data were then converted to a reduced creep compliance using the Ninomiya and Ferry methodology [98,99], as shown in Fig. 14.8. It is important to note that these epoxy adhesives are not thermo-rheologically simple systems (i.e., exhibiting a single relaxation time). This was indicated by the fact that several of the isothermal curves showed some deviation from full overlap in the superposition process. Nevertheless, there was sufficient overlap that the master curves provided a reliable indication of general trends in the long-term creep behavior. Consequently, it was possible to use the time-temperature superposition principle (see Chapter 20) to shift the curves to obtain insight into their short- and long-term behavior. In both methods, a reference temperature (T_{ref}) of approximately 51.25 °C was used to shift the data [94,100].

Results from both techniques were comparable and showed that Epoxy A, the fast set adhesive, exhibited a much higher creep rate than Epoxy B, the standard-set adhesive. While it was not possible to predict anchor displacement and failure times in the tunnel using TTS, the failure times reported by NTSB indicate visible anchor displacement was found within 3 months of anchor installation. This fundamental characterization of these adhesives in the lab provided significant insight into performance differences with short-term measurements and without conducting a single adhesion test.

The NIST DMTA and creep tests were conducted on thin samples of adhesive in an ideal laboratory setting. FHWA was tasked with determining whether the creep behavior was

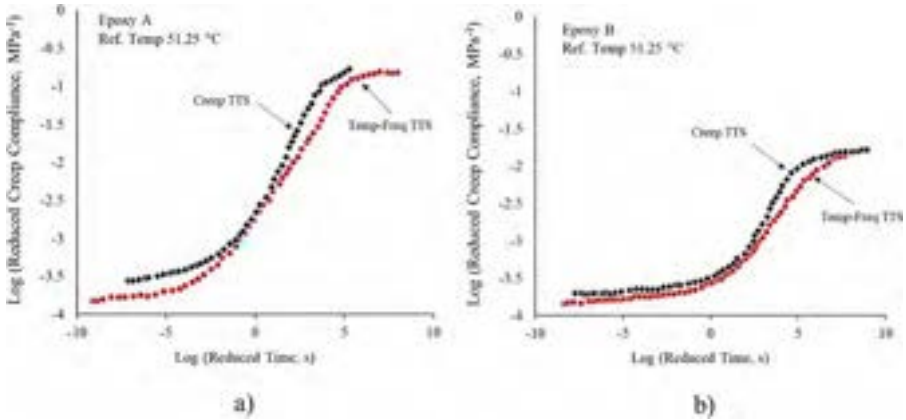


Fig. 14.8 Similar viscoelastic trends for Epoxy A (a) and Epoxy B (b) for comparison of creep compliance curves obtained from converting frequency-temperature sweeps at strains $\leq 0.04\%$ to creep compliance; comparison of creep compliance curves obtained from the superposition of creep curves at the temperature range of 20–80°C. T_{ref} is 51.25°C in both data sets. Modified from J. Chin, A. Forster, C. Clerici, D. Hunston, Characterization of ambient temperature cure epoxies used in adhesive anchor applications, *J. Adhes.* 86(10) (2010) 1041–1067, doi:10.1080/00218464.2010.515494.

observed under conditions more representative of the actual loading condition. Ocel et al. replicated the installation methods in the D Street portal and installed anchors with Epoxy A or Epoxy B into the strong floor of the Turner-Fairbank Highway Research Center [101]. Their test setup was as close as possible to the actual tunnel installation except that the anchors were instrumented with linear variable differential transformer (LVDT) displacement sensors, such that any displacements associated with creep of the adhesive were quantitatively monitored. Different dead masses (454 kg (4.5N) to 1814 kg (18kN)) were suspended from the anchors, and the anchor displacement was measured over 82 days. Fig. 14.9 shows the displacement vs. time results for a mass of approximately 900 kg (9 kN) suspended from the ceiling at FHWA. Epoxy A rapidly creeps extending more than 0.02 cm (0.010 in) in less than 10 days. Over the course of FHWA's measurements, it was found that Epoxy A exhibited significant anchor displacement between 7 to 384 h depending on the mass suspended from the anchors. For the highest loads tested, anchor failures were observed in less than 3 months for Epoxy A.

NTSB reported that ASTM Standard E1512 was specified for the recertification of the adhesives in 2000, but the creep test was optional and not required to receive certification. ASTM Standard D2990-09 [102] was available to measure viscoelastic material properties over time, temperature, and loading rate. The NTSB investigation report [93] identified four safety issues: insufficient understanding of adhesive anchors among designers and builders, lack of standards for sustained loading of adhesive anchors, inadequate regulatory requirements for tunnel inspections, and a lack of national standards for the design of tunnel finishes. The lack of standards played a critical role in the inability to communicate the dangers of creep in the fast-set epoxy and the lack of national standards meant every stakeholder failed to recognize anchor displacement as a sign of creep failure rather than incorrect installation. Standard polymer characterization equipment such as the DSC, DMA, TGA, and creep testing were powerful tools that identified the deficiencies in Epoxy A in a short amount of time. Since the accident, the regulatory and standards environment surrounding adhesive anchors has improved significantly.

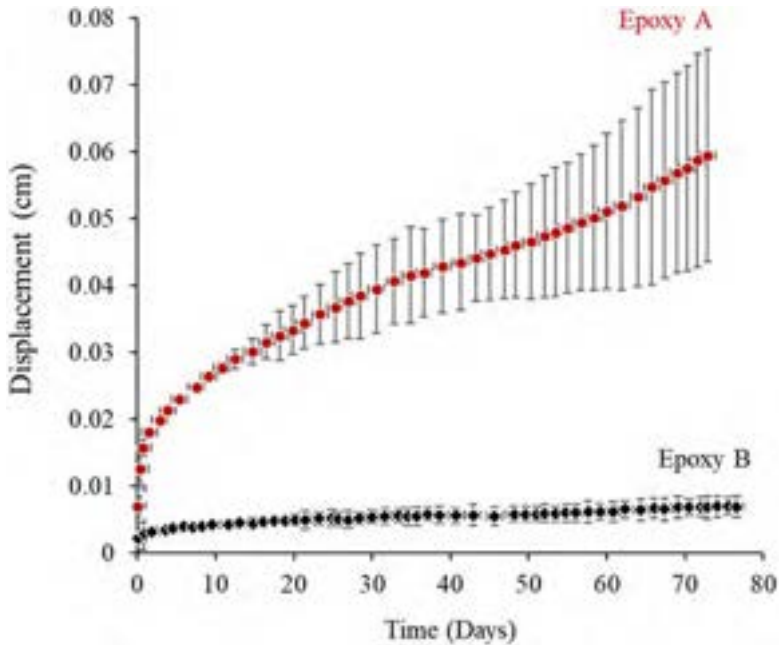


Fig. 14.9 Comparison of creep displacement curves for Epoxy A and Epoxy B obtained from a suspended dead load with a mass of approximately 900 kg (9 kN). Epoxy A creeps much faster than Epoxy B over the 82-day duration of the study.

Modified from J.M. Ocel, J. Hartmann, P. Fuchs, I-90 seaport portal tunnel partial ceiling collapse investigation: sustained load behavior of powers fasteners power-past+adhesive anchors, Fed. Highw. Adm. Turner-Fairbank Highw. Res. Cent. Rep., July 2007.

Case 4: Innovation in building technology and architectural adhesives

Standards to address environmental strains

In this case study, improvements in material performance facilitated novel construction methods that met design influences desired by architects for modern buildings. Glazing and sealants are used in construction to bond two surfaces, accommodate seasonal strains, and provide a barrier to environmental intrusion. Silicone sealants have been widely used to secure glazing in high-rise buildings for many years, and the liabilities involved in these applications have encouraged the related stakeholders to be diligent in their products, robustness, application guidance, and test standards [103]. As the guardian of the building envelope, these materials experience fluctuating and nonuniform stress states. Seasonal and daily temperature swings induce significant strains because glazing applications experience temperatures that are well above the elastomer's glass transition temperature, where the coefficient of thermal expansion is roughly threefold higher than that of a glassy (below T_g) polymer. In addition, glazing supports static loads induced by architectural elements such as windows, signs, and decorations. The expense to replace glazing or sealant is significant and building owners depend on long service lives to recover installation costs.

Daily temperature fluctuations may induce engineering strains as large as 7% in a glazing or sealant and standard test methods utilize cyclic temperature testing to replicate this environment. What about an installation that occurs in the winter or summer? In this case, the building

response to the change in seasons induces much larger strains on the glazing or sealant. Seasonal strains have been estimated to be approximately 25% strain, and this type of movement was not addressed by standard test methods until recently. NIST developed novel measurements to assess the durability of silicone sealants when the joint is allowed to move in response to both in-field and accelerated weathering [104–106] that are also discussed in Chapter 20. The new test methods incorporated mechanical strain to replicate both the daily and seasonal exposure for accelerated testing. This approach facilitated the development of new predictive models for service life [107,108].

Penetration of new materials into a market

In these demanding construction applications, the perceived risk of early failure may inadvertently preclude alternative material designs from gaining a foothold in the market. Premature failures expose companies to unexpected warranty costs and legal risks that are not insignificant, as shown in the low-sloped roof applications. The reluctance to adopt new materials was seen for structural glazing foams around 2010. Acrylic foam tapes were used for more than 20 years in glazing applications, purportedly with success. It was not until the material acceptance was established by the European Organization for Technical Approval (EOTA) and the development of the ETAG 002 Guideline for European Technical Approval for Structural Sealant Glazing Kits (SSGK) [109] that acrylic foam tapes became more accepted. This facilitated design guides [110] and third-party acrylic foam tape material studies using the standards environment for silicone sealants. The performance of acrylic foam tapes compared to silicone sealants led to the development of test methods for durability [111,112] and performance estimates under hurricane wind scenarios [113].

Construction technology drives standards needs

A continual challenge is the comparatively slow pace of documentary standards development compared to the pace of new technology and materials. In the 2000s, architects began to adopt modeling software to innovate building design, which led to rapidly conceptualizing highly complex, curved building geometries. The building envelope community developed a process for cold bending of insulating glass units (IGUs) to accommodate these dynamic designs. This method allows designers to achieve a continuously smooth reflective surface with double curvature cladding, rather than remaining confined to planar glass forms. Cold-bending IGUs produces a static strain on the structural glazing adhesive [114]. For example, strains up to 12.5% for 290 mm of deflection across a 3.5 m by 1.5 m (11.5 ft by 5 ft) single bent IGU would be common [115]. One of the first appearances of cold-bent glass in the architectural facade industry was insulating glass strip windows featured in the City Hall project in Alphen aan den Rijn, Netherlands, in 2001, as shown in Fig. 14.10 [116]. Another high-profile project is the Victoria and Albert Museum's renovation in London [117].

While this can be eye catching, there is a risk to adopting new technology similar to the rapid adoption of EPDM membranes for low-sloped roofs. There was little guidance on allowable warping limits for the glass panels, or additional performance required from the polymeric adhesive components. Manufacturers, fabricators, installers, designers, insurers, and physical asset owners were left to establish personal comfort levels regarding the cold bending of IGUs [114]. Similar to the previous examples, the additional strain imposed by the bent IGU potentially increases the risk of failure for a sealant or glazing susceptible to creep. In addition, standards that focus only on short-time static load tests may miss the long-term loading effect vulnerability.



Fig. 14.10 Cold-warped IGU featured in City Hall project in Alphen aan den Rijn, Netherlands. Courtesy E. Van Egeraat, City Hall, Alphen aan den Rijn <https://erickvanegeraat.com/project/city-hall-alphen-aan-den-rijn/> (Accessed 3 September 2022).

14.5 Future opportunities: The interface between standards and advances in structural adhesives

14.5.1 Material improvements exceed standard assumptions

Some tests, such as ASTM D905 [118], developed to measure the shear strength of adhesive bonds between wood blocks loaded in compression have been a valuable tool in evaluating and improving wood adhesives. And yet, despite their usefulness in the past, current wood adhesives have sufficient integrity that the failures of as-produced specimens frequently occur within the wood blocks themselves. When the failure occurs within the wood, the measured strength will be controlled by wood properties, which can vary considerably in natural materials. Test results from specimens that exhibit failure initiating and proceeding within the wood are likely to result in lower bounds on the adhesive performance rather than meaningful comparative results. Although this shear test was useful for discriminating between fair and good adhesives in the past, adhesive performance gains render this method less useful for evaluating the as-prepared bond strength of modern wood adhesives.^a The test now appears inadequate to discriminate between the better and best modern adhesives, unless they are weakened by environmental exposure or other challenges. A key lesson is that as

^a ASTM D905 remains useful for environmentally exposed specimens, where the adhesive is degraded from exposure, and the failures are more likely to depend on adhesive durability.

adhesives, processes, and designs improve, adhesive test methods may need to evolve to continue providing meaningful quantification of advanced systems.

14.5.2 *Driving performance gains with anticipatory standards*

The Army Research Laboratory (ARL) requires adhesives for high loading rate applications that exhibit strength, toughness, and durability in hot/wet environments. Like the automotive case study, high loading rate events often require extensive energy dissipation in both the adhesive and the adherends. In this study, researchers developed a methodology to leverage data from a quasistatic test to facilitate a qualitative understanding of an adhesive's damage tolerance in a high-rate applications. This represented a shift to a global view of bonded joint performance (adherend and adhesive) that differed from the traditional adhesive-focused documentary standard test method. The result was a framework that allowed ARL to drive adhesive suppliers toward an unrealized performance target area.

Discussed in more detail in [Chapter 7](#), the ARL program applied a tiered experimental approach [119] to develop a material's pedigree based on technical data sheets (TDS), materials safety data sheets (MSDS), and quasistatic testing of SLJs [45] and optional double cantilever beam specimens, in what is now the MIL-PRF-32662 standard [120]. The figures of merit for the SLJ were the maximum tensile strength (S_{\max}) and the displacement at failure (d_{failure}), measured by crosshead displacement. Material pedigrees were established for historical adhesive datasets (894 adhesives) and any new adhesive formulations were required to submit a similar materials pedigree. [Fig. 14.11](#) is a representative plot of maximum strength vs. crosshead displacement at failure under dry testing for the historical datasets. The majority of commercially available adhesives met either the strength or the elongation requirements, but there was a lack of adhesives that met both and fell within Group I. Based on experience to date, these Group I adhesives appear to have performed well in high-rate applications. ARL identified Group I as a goal for the SLJ-measured properties of any new adhesive.

The strength and displacement specifications of Group I were expected to induce adhesive failure and adherend yielding. The contribution of these two mechanisms to energy dissipation was recently quantified using digital image correlation (DIC). DIC is a technology to measure the displacements across a patterned surface. The information from DIC measurements provided additional insights into the underlying mechanics involved in the ARL approach, as found in [Chapters 7](#) and [32](#). DIC measurements of the SLJ bond region indicate that the majority of the displacement, at least for an initial material meeting Group I requirements, involves extensive plastic tensile deformations of the adherend. Furthermore, the lower strength bound of Group I (10 MPa) results in nominal tensile adherend stresses that are well below the yield strength of the specified aluminum alloy. Thus, the displacement criterion for Group IV adhesives is only met via adhesive flexibility and/or yielding. MIL-PRF-32662 requires 1.62 mm thick 2024T-3 aluminum adherends and a 12.7 mm bond length. On the other hand, if the SLJ apparent shear strength of the adhesive exceeds 35 MPa, then the aluminum adherends yield in tension to effectively

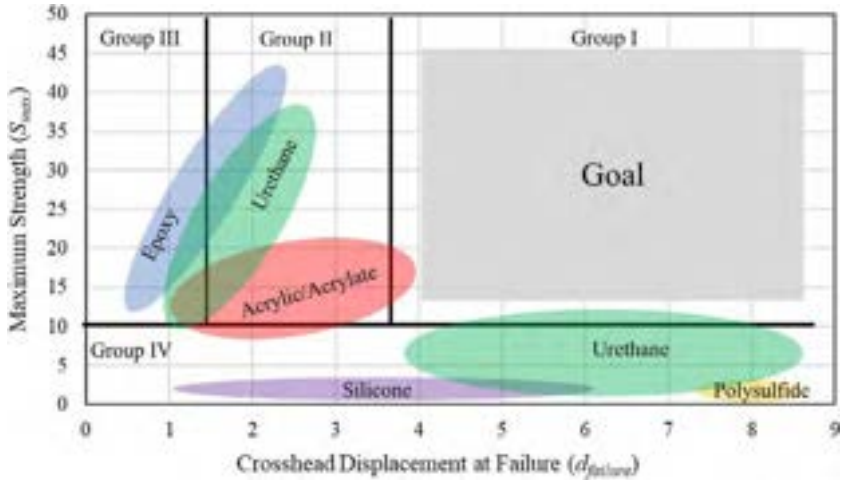


Fig. 14.11 Historical data on HRL adhesives of single-lap joint performance at ambient conditions compiled by ARL. Four different classifications based on the combination of S_{max} and $d_{failure}$ were identified.

Modified from R. Jensen, D. Deschepper, D. Flanagan, W.K. Chaney, J. Robinette, G. Chaney, C. Pergantis, Adhesives: test method, group assignment, and categorization guide for high-loading-rate applications, 2014, June.

achieve the displacement criteria. Thus, adhesive systems that are tough enough to resist fracture initiation and propagation and strong enough to induce and sustain extensive tensile plastic deformation in elastic-plastic adherends will likely achieve the large crosshead displacement values required for Group I. Further work is required to fully understand how meeting Group I targets with the specified adherend material and dimensions may apply to other adherend materials and joint configurations for testing product designs.

14.5.3 Large datasets, open data, and the advent of machine learning

The accessibility of finite element models and machine learning techniques relies on the democratization of large datasets. Guidelines for the curation of open datasets, called the Findable, Accessible, Interoperable, and Reusable (FAIR [121]) data principles, mean the stewardship of research data does not stop at the lab notebook or the journal paper. As discussed in Chapter 32, the routine access to DIC methods for adhesive bond measurements provides larger amounts of data and high-resolution measurements of strain fields around the crack tip. When coupled with sophisticated finite element software, adhesive joint analysis may be analyzed and validated, leading to enhanced confidence in our understanding and to joint optimization to achieve higher performance levels. Buehler et al. utilized machine learning on material datasets to predict a novel material's mechanical and fracture properties. These

methods have been used to predict the elastic behavior of composites and crack propagation in crystalline materials or composites [122,123] with computational advantages over finite element simulations. Unfortunately, standard test methods have only begun to address traceability, calibration, and error reporting for DIC [124].

14.6 Conclusions

Standards are an essential component for the development and engineering of structural adhesives. Despite the challenges with the ubiquitous SLJ and analysis, it remains an important baseline method to communicate structural adhesive performance. Toughness is also essential, and this requires an understanding of fracture mechanics to quantify the resistance of the material to fracture. Short-term properties often help identify candidate materials, but a structural adhesive's application and use environment may be very different. Long-term properties such as creep and environmental durability tend to expose weaknesses that short-term property characterization often overlooks. As materials and performance requirements change, standards may need to evolve to address these changes. A vigorous community interaction facilitated in SDOs is required. Finally, the availability of increasingly powerful computational tools to incorporate historical datasets or experiments that generate large datasets, such as DIC, are changing how structural adhesives are designed and qualified. The push for environmental stewardship and meeting cost/supply restraints means that these new tools will become more critical in the future. A rigorous, dynamic, and evolving standards development environment is healthy and increases the chances for success.

References

- [1] K. Kramer. <http://www.adhesivesmag.com/articles/83846-the-new-century-of-adhesives>. (Accessed 12 May 2021).
- [2] B. Smith, A. Spulber, S. Modi, T. Fiorelli, *Technology Roadmaps: Intelligent Mobility Technology, Materials and Manufacturing Processes, and Light Duty Vehicle Population*, Ann Arbor, 2017.
- [3] Report ID: GVR-1-68038-684-4, *Construction Adhesive Market Size, Share & Trends Analysis Report by Resin Type (Acrylic, Polyurethanes, Epoxy), By Technology, By Application, By Region, And Segment Forecasts, 2022-2030*, 2022.
- [4] Hindsight in 2020: How Automotive Adhesive Products Have Changed. <http://blog.lin-tecauto.com/automotive-adhesive-products-have-changed>. (Accessed 12 March 2021).
- [5] Part II: Adhesive Opportunities & Outlook in Light Vehicles. <https://www.adhesives.org/docs/pdfs/adhesives-sealants-org-white-paper-adhesive-opportunity-and-outlook-in-light-vehicles.pdf?sfvrsn=0>. (Accessed 12 January 2021).
- [6] Gary Vasilash S, *Increasing Use of Structural Adhesives in Automotive*. Gardner Business Media, Inc., 2020. [http://www.gardnerweb.com/articles/can-you-glue-a-car-together\(2\)](http://www.gardnerweb.com/articles/can-you-glue-a-car-together(2)). (Accessed 12 January 2021).
- [7] B. Visnic, *Stuck on Structural Adhesives*. <http://www.sae.org/news/2019/08/automotive-structural-adhesives-overview>. (Accessed 12 March 2021).

- [8] D. LaChance, Researchers: New Class of Adhesives Driving Increased EV Battery Pack Efficiency. <http://www.repairerdrivenews.com/2021/12/28/researchers-new-class-of-adhesives-driving-increased-ev-battery-pack-efficiency/>.
- [9] National Metrology Laboratories. <https://www.nist.gov/iaao/national-metrology-laboratories-page-4>. (Accessed 8 October 2022).
- [10] J. Jacobsen, E. Watkins, *The Last Artifact*, Montana PBS, USA, 2019.
- [11] Rexmond Cochrane C., Measures for Progress: A History of the National Bureau of Standards. NBS MP 275, National Bureau of Standards Miscellaneous Publication (1966), <https://doi.org/10.6028/NIST.MP.275>.
- [12] J.F. Schooley, Responding to National Needs: The National Bureau of Standards Becomes the National Institute of Standards and Technology, 1969-1993, Special Publication (NIST SP) 955 (2000).
- [13] U.S. Const. Art. I, § 8.
- [14] S.B. Madden, Why is service life prediction of polymers and plastics exposed to outdoor weathering important? An industrial perspective, in: M.T.F. Reitman, M.D. Dimitriou, J. R. Vargas, S. Ebnesajjad (Eds.), *Service Life Prediction of Polymers: Enhanced Methods*, Elsevier, Chadds Ford, 2020, pp. 19–32, <https://doi.org/10.1016/B978-0-12-818367-0.00002-3>.
- [15] *Lolie v. Ohio Brass Co.*, 502 F.2d 741 (7th Circuit 1974).
- [16] *Lolie v. Ohio Brass Co.*, 13 Ill. App. 3d 84 (4th District 1973).
- [17] *Lolie v. Ohio Brass Co.*, Dkt. No. 71-343, Circuit Court of Macoupin County, Ill (7th Circuit 1971).
- [18] *Lolie v. Ohio Brass Co.* United States Court of Appeals for the Seventh Circuit, United States (1973).
- [19] A.A. Griffith, The phenomena of rupture and flow in solids, *Philos. Trans. R. Soc. Lond. A* 221 (1921) 163–198.
- [20] J.E. Gordon, *Structures or Why Things Don't Fall Down*, 2003rd ed., Da Capo Press, Cambridge, 1978.
- [21] D.L. Hunston, A.J. Kinloch, S.S. Wang, Micromechanics of fracture in structural adhesive bonds, *J. Adhes.* 28 (2–3) (1989) 103–114, <https://doi.org/10.1080/00218468908030877>.
- [22] A.J. Kinloch, *Adhesion and Adhesives: Science and Technology*, first ed., Springer, Dordrecht, 1987, <https://doi.org/10.1007/978-94-015-7764-9>.
- [23] R.D. Adams, W.C. Wake, *Structural Adhesive Joints in Engineering*, first ed., Springer, Dordrecht, 1984, <https://doi.org/10.1007/978-94-009-5616-2>.
- [24] A.J. Kinloch (Ed.), *Durability of Structural Adhesives*, Springer, Dordrecht, 1983, p. first ed.
- [25] T. Liyong, G.P. Steven, *Analysis and Design of Structural Bonded Joints*, first ed., Springer, New York, 1999.
- [26] R.D. Adams, J. Comyn, W.C. Wake, *Structural Adhesive Joints in Engineering*, second ed., Springer, Dordrecht, 1997.
- [27] G.P. Anderson, J. Bennetts, S.J. Bennett, K.L. DeVries, *Analysis and Testing of Adhesive Bonds*, Materials Science and Technology Series, Academic Press, 1977.
- [28] A.V. Pocius, *Adhesion and Adhesives Technology*, third ed., Carl Hanser Verlag GmbH & Co. KG, 2012, <https://doi.org/10.3139/9783446431775.fm>.
- [29] D.A. Dillard, A.V. Pocius (Eds.), *Adhesion Science and Engineering I: The Mechanics of Adhesion*, Elsevier, Amsterdam, 2002.
- [30] L.F.M. da Silva, A. Öchsner, R.D. Adams, *Handbook of Adhesion Technology*, second ed., 1–2, 2018, <https://doi.org/10.1007/978-3-319-55411-2>.

- [31] L.F.M. da Silva, D.A. Dillard, B.R.K. Blackman, R.D. Adams (Eds.), *Testing Adhesive Joints: Best Practices*, Wiley-VCH, Weinheim, 2012.
- [32] D.A. Dillard (Ed.), *Advances in Structural Adhesive Bonding*, first ed., Woodhead, 2010.
- [33] H.F. Brinson (Ed.), *Engineering Materials Handbook Volume 3: Adhesives and Sealants*, ASM International, 1990.
- [34] L.F.M. da Silva, P.J.C. das Neves, R.D. Adams, J.K. Spelt, Analytical models of adhesively bonded joints—part I: literature survey, *Int. J. Adhes. Adhes.* 29 (3) (2009) 319–330, <https://doi.org/10.1016/j.ijadhadh.2008.06.005>.
- [35] L.F.M. da Silva, P.J.C. das Neves, R.D. Adams, A. Wang, J.K. Spelt, Analytical models of adhesively bonded joints—part II: comparative study, *Int. J. Adhes. Adhes.* 29 (3) (2009) 331–341, <https://doi.org/10.1016/j.ijadhadh.2008.06.007>.
- [36] X. Shang, E.A.S. Marques, J.J.M. Machado, R.J.C. Carbas, D. Jiang, L.F.M. da Silva, Review on techniques to improve the strength of adhesive joints with composite adherends, *Compos. Part B Eng.* 177 (July) (2019) 107363, <https://doi.org/10.1016/j.compositesb.2019.107363>.
- [37] D.A. Dillard, B. Mukherjee, P. Karnal, R.C. Batra, J. Frechette, A review of Winkler's foundation and its profound influence on adhesion and soft matter applications, *Soft Matter* 14 (19) (2018) 3669–3683, <https://doi.org/10.1039/c7sm02062g>.
- [38] S.P. Timoshenko, *History of Strength of Materials: With a Brief Account of the History of Theory of Elasticity and Theory of Structures*, Courier Corporation, 1983.
- [39] M. Benevento, Part I Adhesives and Joining Methods in Land Transportation. https://www.adhesives.org/docs/pdfs/adhesives-sealants-org-white-paper-adhesives-and-joining-in-land-transportation3.pdf?sfvrsn=1f86bd9f_0. (Accessed 12 March 2021).
- [40] L.J. Hart-Smith, Design of adhesively bonded joints, in: F.L. Mathews (Ed.), *Joining Fibre-Reinforced Plastics*, Elsevier, Amsterdam, 1987, pp. 271–311.
- [41] L.J. Hart-Smith, The design of adhesively bonded joints, in: D.A. Dillard, A.V. Pocius (Eds.), *Adhesion Science and Engineering I: The Mechanics of Adhesion*, 2002, pp. 725–777, <https://doi.org/10.1016/b978-0-444-51140-9.50046-9>. Amsterdam.
- [42] O. Volkersen, Die Niekraftverteilung in Zugbeanspruchten Mit Konstanten Laschenquerschnitten, *Luftfahrt Forschungen* 15 (1938) 41–47.
- [43] M. Goland, E. Reissner, The stresses in cemented joints, *J. Appl. Mech.* 11 (1) (1944) A17–A27, <https://doi.org/10.1115/1.4009336>.
- [44] L.J. Hart-Smith, *Adhesive-Bonded Single Lap Joints (No. NASA-CR-112236)*, 1973.
- [45] ASTM D1002-10(2019), Standard Test Method for Apparent Shear Strength of Single-Lap-Joint Adhesively Bonded Metal Specimens by Tension Loading (Metal-to-Metal), ASTM International, 2019, pp. 1–5, <https://doi.org/10.1520/D1002-10R19.1.2>. 01 (Reapproved).
- [46] ASTM D4896-01, Standard Guide for Use of Adhesive-Bonded Single Lap-Joint Specimen Test, ASTM International, 2016, pp. 1–6, <https://doi.org/10.1520/D4896-01R16.2>. i (Reapproved 2016).
- [47] R.D. Adams, J.A. Harris, The influence of local geometry on the strength of adhesive joints, *Int. J. Adhes. Adhes.* 7 (2) (1987) 69–80, [https://doi.org/10.1016/0143-7496\(87\)90092-3](https://doi.org/10.1016/0143-7496(87)90092-3).
- [48] E.D. Reedy, Strength of butt and sharp-cornered joints, in: D.A. Dillard, A.V. Pocius (Eds.), *Mechanics of Adhesion*, vol. 1, Elsevier Science B.V., Amsterdam, 2002, pp. 145–192, <https://doi.org/10.1016/B978-0-444-51140-9.50032-9>.
- [49] A.D. Crocombe, R.D. Adams, Influence of the spew fillet and other parameters on the stress distribution in the single lap joint, *J. Adhes.* 13 (2) (1981) 141–155, <https://doi.org/10.1080/00218468108073182>.

- [50] R.E. Jensen, D.C. DeSchepper, D.P. Flanagan, Multivariate analysis of high through-put adhesively bonded single lap joints, *Int. J. Adhes. Adhes.* 2019 (89) (2018) 1–10, <https://doi.org/10.1016/j.ijadhadh.2018.11.004>.
- [51] I.F. Villegas, C. Rans, The dangers of single-lap shear testing in understanding polymer composite welded joints, *Philos. Trans. R. Soc. A Math. Phys. Eng. Sci.* 379 (2203) (2021), <https://doi.org/10.1098/rsta.2020.0296>.
- [52] ASTM D5868-01, Standard Test Method for Lap Shear Adhesion for Fiber Reinforced Plastic (FRP), ASTM International, 2005, pp. 4–5, <https://doi.org/10.1520/D5868-01R14.2.01> (Reapproved 2014).
- [53] D.A. Dillard, Fundamentals of stress transfer in bonded systems, in: D.A. Dillard, A.V. Pocius (Eds.), *The Mechanics of Adhesion*, Elsevier, Amsterdam, 2002, pp. 1–44, <https://doi.org/10.1016/B978-0-444-51140-9.50028-7>.
- [54] K. Kendall, Energizing ASTM lap joint fracture standards, *Philos. Trans. R. Soc. A Math. Phys. Eng. Sci.* 379 (2203) (2021) 20200287, <https://doi.org/10.1098/rsta.2020.0296>.
- [55] K. Kendall, Crack propagation in lap shear joints, *J. Phys. D. Appl. Phys.* 8 (5) (1975) 512–522, <https://doi.org/10.1088/0022-3727/8/5/010>.
- [56] K. Kendall, Thin-film peeling—the elastic term, *J. Phys. D. Appl. Phys.* 8 (1975) 1449–1452.
- [57] M. Ciavarella, S. Zhang, H. Gao, G. Cricri, A linear cohesive model of zero degree peeling of a viscoelastic tape from a substrate, *J. Adhes. Sci. Technol.* (2022) 1–15, <https://doi.org/10.1080/01694243.2022.2099785>.
- [58] A.R. Mojdehi, D.P. Holmes, D.A. Dillard, Revisiting the generalized scaling law for adhesion: role of compliance and extension to progressive failure, 2017, pp. 7529–7536, <https://doi.org/10.1039/c7sm01098b>.
- [59] T.L. Anderson, *Fracture Mechanics Fundamentals and Applications*, Taylor & Francis, Boca Raton, 2005.
- [60] B.J. Cardwell, A.F. Yee, Rate and temperature effects on the fracture toughness of a rubber-modified epoxy, *Polymer (Guildf.)* 34 (8) (1993) 1695–1701, [https://doi.org/10.1016/0032-3861\(93\)90329-9](https://doi.org/10.1016/0032-3861(93)90329-9).
- [61] B.R.K. Blackman, A.J. Kinloch, F.S. Rodriguez-Sanchez, W.S. Teo, The fracture behaviour of adhesively-bonded composite joints: effects of rate of test and mode of loading, *Int. J. Solids Struct.* 49 (13) (2012) 1434–1452, <https://doi.org/10.1016/j.ijsolstr.2012.02.022>.
- [62] J.G. Williams, Introduction to linear elastic fracture mechanics, in: D.R. Moore, A. Pavan, J.G. Williams (Eds.), *Fracture Mechanics Testing Methods for Polymers, Adhesives and Composites*, vol. 28, Elsevier, 2001, pp. 3–10, [https://doi.org/10.1016/S1566-1369\(01\)80024-8](https://doi.org/10.1016/S1566-1369(01)80024-8).
- [63] G. Irwin, Analysis of stresses and strains near the end of a crack traversing a plate, *J. Appl. Mech.* 24 (1957) 361–364.
- [64] R.S. Rivlin, A.G. Thomas, Rupture of Rubber, I. Characteristic energy for tearing, *J. Polym. Sci.* 10 (3) (1953) 291–318, <https://doi.org/10.1002/pol.1953.120100303>.
- [65] A. Kinloch, Introduction to adhesion and adhesives, in: D.R. Moore, A. Pavan, J.G. Williams (Eds.), *Fracture Mechanics Testing Methods for Polymers, Adhesives and Composites*, vol. 28, Elsevier, 2001, pp. 199–202, [https://doi.org/10.1016/S1566-1369\(01\)80034-0](https://doi.org/10.1016/S1566-1369(01)80034-0).
- [66] A.J. Kinloch, S.J. Shaw, D.A. Tod, D.L. Hunston, Deformation and fracture behaviour of a rubber-toughened epoxy: 1. Microstructure and fracture studies, *Polymer (Guildf.)* 24 (10) (1983) 1341–1354, [https://doi.org/10.1016/0032-3861\(83\)90070-8](https://doi.org/10.1016/0032-3861(83)90070-8).
- [67] A.J. Kinloch, S.J. Shaw, D.L. Hunston, Deformation and fracture behaviour of a rubber-toughened epoxy: 2. Failure criteria, *Polymer (Guildf.)* 24 (10) (1983) 1355–1363, [https://doi.org/10.1016/0032-3861\(83\)90071-X](https://doi.org/10.1016/0032-3861(83)90071-X).

- [68] E.J. Ripling, S. Mostovoy, R.L. Patrick, ASTM STP360-EB: adhesion, in: *Adhesion*, ASTM International, Philadelphia, 1964, pp. 5–19.
- [69] S. Mostovoy, E.J. Ripling, Fracture toughness of an epoxy system, *J. Appl. Polym. Sci.* 10 (1966) 1351–1371.
- [70] S. Mostovoy, P.B. Crosley, E.J. Ripling, Use of crack-line-loaded specimens for measuring plane-strain fracture toughness, *J. Mater.* 2 (3) (1967) 661–681.
- [71] A.A. Wells, Application of fracture mechanics at and beyond general yielding, *Br. Weld. J.* 10 (1963) 563–570.
- [72] J.R. Rice, A path independent integral and the approximate analysis of strain concentration by notches and cracks, *J. Appl. Mech. Trans. ASME* 35 (2) (1968) 379–386, <https://doi.org/10.1115/1.3601206>.
- [73] G.I. Barenblatt, The mathematical theory of equilibrium cracks in brittle fracture, *Adv. Appl. Mech.* 7 (1962) 55–129, [https://doi.org/10.1016/S0065-2156\(08\)70121-2](https://doi.org/10.1016/S0065-2156(08)70121-2).
- [74] D.S. Dugdale, Yielding of steel, *J. Mech. Phys. Solids* 8 (1960) 100–104.
- [75] L.D.C. Ramalho, R.D.S.G. Campilho, J. Belinha, L.F.M. da Silva, Static strength prediction of adhesive joints: a review, *Int. J. Adhes. Adhes.* 2020 (96) (2019) 102451, <https://doi.org/10.1016/j.ijadhadh.2019.102451>.
- [76] M.D. Thouless, J.L. Adams, M.S. Kafkalidis, S.M. Ward, R.A. Dickie, G.L. Westerbeek, Determining the toughness of plastically deforming joints, *J. Mater. Sci.* 33 (1) (1998) 189–197, <https://doi.org/10.1023/A:1004370318709>.
- [77] A.J. Kinloch, J.G. Williams, Comments on “determining the toughness of plastically deforming joints”, *J. Mater. Sci. Lett.* 17 (10) (1998) 813–814.
- [78] B.R.K. Blackman, A.J. Kinloch, Y. Wang, The impact wedge-peel performance of structural adhesives, *J. Mater. Sci.* 35 (8) (2000) 1867–1884.
- [79] ISO-11343:1993 modified, Structural Adhesives—Determination of Dynamic Resistance to Cleavage of High Strength Adhesive Bonds Under Impact Conditions—Wedge Impact Method, 2002.
- [80] *Suvey Compares Practices to Problems*, The Roofing Spec., Rosemont, 1984, pp. 37–40. October.
- [81] *Project Pinpoint: The First Returns*, The Roofing Spec., Rosemont, 1975, pp. 12–13. March.
- [82] W.J. Rossiter, J.W. Martin, Factors affecting the service life of seams of EPDM roof membranes, in: 10th DBMC International Conference on Durability of Building Materials and Components, Lyon, 2005, pp. TT4–250.
- [83] W.J. Rossiter, Tests of Adhesive-Bonded Seams of Single-Ply Rubber Membranes, ASTM Special Technical Publication 959, ASTM International, 1986, 1986, pp. 53–62.
- [84] W.J. Rossiter, M.G. Vangel, E. Embree, K.M. Kraft, J.F.J. Seiler, Performance of Tape-Bonded Seams of EPDM Membranes: Factors Affecting the Creep-Rupture Response of Tape-Bonded and Liquid-Adhesive-Bonded Seams, *Natl. Inst. Stand. Technol. Build. Sci. Ser.*, NIST Building Science Series 175, 1996.
- [85] J.W. Martin, E. Embree, P.E. Stutzman, J.A. Lechner, Strength and creep-rupture properties of adhesive-bonded EPDM joints stressed in Peel, *Natl. Inst. Stand. Technol. Build. Sci. Ser.* 169 (1990) 59.
- [86] W.J. Rossiter, J.W. Martin, J.A. Lechner, E. Embree, J.F.J. Seiler, Effect of adhesive thickness and surface cleanliness on creep-rupture performance of EPDM peel and lap-shear joints, in: T.J. Wallace, W.J. Rossiter (Eds.), *Roofing Research and Standards Development ASTM Special Technical Publication 1224*, vol. 3, ASTM International, West Conshohocken, 1994, pp. 123–138.

- [87] D.H. Kaelble, Theory and analysis of peel adhesion: rate-temperature dependence of viscoelastic interlayers, *J. Colloid Sci.* 19 (5) (1964) 413–424, [https://doi.org/10.1016/0095-8522\(64\)90041-8](https://doi.org/10.1016/0095-8522(64)90041-8).
- [88] D.H. Kaelble, Peel adhesion: micro-fracture mechanics of interfacial unbonding of polymers, *Trans. Soc. Rheol.* 9 (2) (1965) 135–163, <https://doi.org/10.1122/1.549022>.
- [89] D.H. Kaelble, Theory and analysis of peel adhesion: bond stresses and distributions, *Trans. Soc. Rheol.* 4 (1) (1960) 45–73, <https://doi.org/10.1122/1.548868>.
- [90] A.N. Gent, R.P. Petrich, Adhesion of viscoelastic materials to rigid substrates, *Proc. R. Soc. Lond. A* 310 (1969) 433–448, <https://doi.org/10.1098/rspa.1969.0085>.
- [91] Y. Huang, D.L. Hunston, A.J. Kinloch, C.K. Riew, Mechanisms of toughening thermoset resins, *Advances in Chemistry*, American Chemical Society, Washington, DC, 1993, pp. 1–35.
- [92] Boston Tunnel Collapse Kills Newlywed, CBS News (2006). <https://www.cbsnews.com/news/boston-tunnel-collapse-kills-newlywed/>. (Accessed 10 March 2022).
- [93] NTSB, Ceiling Collapse in the Interstate 90 Connector Tunnel Boston Massachusetts July 10, 2006, 2007. Washington.
- [94] J. Chin, A. Forster, C. Clerici, D. Hunston, Characterization of ambient temperature cure epoxies used in adhesive anchor applications, *J. Adhes.* 86 (10) (2010) 1041–1067, <https://doi.org/10.1080/00218464.2010.515494>.
- [95] J. Chin, A. Forster, J. Ocel, J. Hartmann, P. Fuchs, D. Hunston, Thermoviscoelastic analysis and creep testing of ambient temperature cure epoxies used in adhesive anchor applications, *J. Mater. Civ. Eng.* 22 (10) (2010) 1039–1046, [https://doi.org/10.1061/\(ASCE\)MT.1943-5533.0000108](https://doi.org/10.1061/(ASCE)MT.1943-5533.0000108).
- [96] J.D. Ferry, *Viscoelastic Properties of Polymers*, third ed., John Wiley and Sons, New York, 1980.
- [97] T. Murayama, *Dynamic Mechanical Analysis of Polymer Material*, Elsevier Scientific Publishing Company, Amsterdam, 1978.
- [98] K. Ninomiya, J.D. Ferry, Some approximation equations useful in the phenomenological treatment of linear viscoelastic data, *J. Colloid Sci.* 14 (1959) 36–48, <https://doi.org/10.2324/gomu.40.4>.
- [99] I.M. Ward, D.W. Hadley, *An Introduction to the Mechanical Properties of Solid Polymers*, John Wiley and Sons, New York, 1993.
- [100] J. Chin, D.L. Hunston, A. Forster, Thermo-viscoelastic analysis of ambient cure epoxy adhesives used in construction applications, 2008, pp. 1–37. Nistir No. 7429.
- [101] J.M. Ocel, J. Hartmann, P. Fuchs, I-90 seaport portal tunnel partial ceiling collapse investigation: sustained load behavior of powers fasteners power-past+adhesive anchors, *Fed. Highw. Adm. Turner-Fairbank Highw. Res. Cent. Rep.*, July, 2007.
- [102] ASTM Standard D2990-09, Standard Test Methods for Tensile, Compressive, and Flexural Creep and Creep-Rupture of Plastics, 2011, pp. 1–20, <https://doi.org/10.1520/D2990-17.2>. *Annu. B. ASTM Stand.*, 200 (37 2).
- [103] ASTM C24 Committee on Building Seals and Sealants. <https://www.astm.org/get-involved/technical-committees/committee-c24>. (Accessed 3 August 2020).
- [104] C.C. White, D.L. Hunston, K.T. Tan, G.T. Schuenema, A test method for monitoring modulus changes during durability tests on building joint sealants, *ASTM Spec. Tech. Publ.*, 1545 STP (2), 2012, pp. 432–444, <https://doi.org/10.1520/stp154520120020>.
- [105] C.C. White, K.T. Tan, E.P. O'Brien, D.L. Hunston, J.W. Chin, R.S. Williams, Design, fabrication, and implementation of thermally driven outdoor testing devices for building joint sealants, *Rev. Sci. Instrum.* 82 (2) (2011), <https://doi.org/10.1063/1.3543817>.

- [106] C.C. White, D.L. Hunston, K.T. Tan, J. Hettenhouser, J.D. Garver, An accelerated exposure and testing apparatus for building joint sealants, *Rev. Sci. Instrum.* 84 (9) (2013), <https://doi.org/10.1063/1.4821880>.
- [107] C.C. White, D.L. Hunston, A. Pintar, J. Filliben, Designing an accelerated test method to determine the design life of building joint sealant using the ASTM C1850 procedure, 2018, pp. 74–93, <https://doi.org/10.1520/stp160420170141>. ASTM Spec. Tech. Publ. STP 1604 (37 2).
- [108] C.C. White, K.T. Tan, D.L. Hunston, R. Sam Williams, Durability of building joint sealants, in: *Service Life Prediction of Polymeric Materials Global Perspectives*, Springer, 2009, pp. 115–128.
- [109] EOTA, ETAG 002:2012 Structural Sealant Glazing Kits (SSGK)—Part-Supported and Unsupported Systems, IsmailBeyeStandartlar, No. October 2001, 2012.
- [110] T. Kremer, Useful Design Criteria for Acrylic Foam Tapes in Demanding Industrial Applications, 3M Industrial Adhesives and Tapes Division, St. Paul, 2005.
- [111] B.W. Townsend, D.C. Ohanehi, D.A. Dillard, S.R. Austin, F. Salmon, D.R. Gagnon, Characterizing acrylic foam pressure sensitive adhesive tapes for structural glazing applications—part II: creep rupture results, *Int. J. Adhes. Adhes.* 31 (7) (2011) 650–659, <https://doi.org/10.1016/J.IJADHADH.2011.06.018>.
- [112] B.W. Townsend, D.C. Ohanehi, D.A. Dillard, S.R. Austin, F. Salmon, D.R. Gagnon, Characterizing acrylic foam pressure sensitive adhesive tapes for structural glazing applications—part I: DMA and ramp-to-fail results, *Int. J. Adhes. Adhes.* 31 (7) (2011) 639–649, <https://doi.org/10.1016/J.IJADHADH.2011.06.017>.
- [113] B.W. Townsend, D.C. Ohanehi, D.A. Dillard, S.R. Austin, F. Salmon, D.R. Gagnon, Developing a simple damage model for the long-term durability of acrylic foam structural glazing tape subject to sustained wind loading, *J. Archit. Eng.* 18 (3) (2011) 214–222, [https://doi.org/10.1061/\(ASCE\)AE.1943-5568.0000070](https://doi.org/10.1061/(ASCE)AE.1943-5568.0000070).
- [114] K. Besserud, M. Bergers, A.J. Black, C.L. Donald, A. Mazurek, D. Mission, K. Rubis, Durability of cold-bent insulating-glass units, in: *Fourth International Symposium on Durability of Building and Construction Sealants and Adhesives*, vol. 9, ASTM International, Anaheim, 2011.
- [115] Pözl, F. N., *Mechanical Behavior of Cold-Bent Insulating Glass Units Numerical Investigations and Parameter Studies*, AV Akademikerverlag, 2017.
- [116] E. Van Egeraat. <http://architizer.com/projects/city-hall-grave/>. (Accessed 3 September 2022).
- [117] M. Eekhout, S. Niderehe, The cold bent glass roof of the Victoria & Albert Museum, London, in: *Challenging Glas. 2—Conf. Archit. Struct. Appl. Glas. CGC 2010*, May, 2010, pp. 139–148.
- [118] ASTM D905-08, Standard Test Method for Strength Properties of Adhesive Bonds in Shear by Compression Loading, ASTM Int. Inc, 2021, pp. 6–9. <https://doi.org/10.1520/D0905-08R21.1>.
- [119] R. Jensen, D. Deschepper, D. Flanagan, W.K. Chaney, J. Robinette, G. Chaney, C. Pergantis, Adhesives: test method, group assignment, and categorization guide for high-loading-rate applications, 2014. June.
- [120] B. Rinderspacher, B. Placzankis, W. Lum, R. Jensen, MIL-PRF-32662: adhesive, high-loading rate, for structural and armor applications-frequently asked questions, 2020. 33.
- [121] M.D. Wilkinson, M. Dumontier, I.J. Aalbersberg, G. Appleton, M. Axton, A. Baak, N. Blomberg, J.W. Boiten, L.B. da Silva Santos, P.E. Bourne, J. Bouwman, A.J. Brookes, T. Clark, M. Crosas, I. Dillo, O. Dumon, S. Edmunds, C.T. Evelo, R. Finkers, A. Gonzalez-Beltran, A.J.G. Gray, P. Groth, C. Goble, J.S. Grethe, J. Heringa, P.A.C. Hoen,

- R. Hooft, T. Kuhn, R. Kok, J. Kok, S.J. Lusher, M.E. Martone, A. Mons, A.L. Packer, B. Persson, P. Rocca-Serra, M. Roos, R. van Schaik, S.A. Sansone, E. Schultes, T. Sengstag, T. Slater, G. Strawn, M.A. Swertz, M. Thompson, J. Van Der Lei, E. Van Mulligen, J. Velterop, A. Waagmeester, P. Wittenburg, K. Wolstencroft, J. Zhao, B. Mons, Comment: the FAIR guiding principles for scientific data management and stewardship, *Sci. Data* 3 (2016) 1–9, <https://doi.org/10.1038/sdata.2016.18>.
- [122] G.X. Gu, M. Takaffoli, M.J. Buehler, Hierarchically enhanced impact resistance of bioinspired composites, *Adv. Mater.* 29 (28) (2017) 1–7, <https://doi.org/10.1002/adma.201700060>.
- [123] K. Guo, M.J. Buehler, A semi-supervised approach to architected materials design using graph neural networks, *Extrem. Mech. Lett.* 41 (2020) 101029, <https://doi.org/10.1016/j.eml.2020.101029>.
- [124] E.M.C. Jones, M.A. Iadicola (Eds.), *A Good Practices Guide for Digital Image Correlation*, International Digital Image Correlation Society, 2018, <https://doi.org/10.32720/idics/gpg.ed1>.

This page intentionally left blank

Predicting adhesive bond performance

15

Alireza Akhavan-Safar^a, E.A.S. Marques^b, R.J.C. Carbas^a, and Lucas F.M. da Silva^b

^aInstitute of Science and Innovation in Mechanical and Industrial Engineering (INEGI), Porto, Portugal, ^bDepartment of Mechanical Engineering, Faculty of Engineering (FEUP), University of Porto, Porto, Portugal

15.1 Introduction

The combination of a precise stress analysis with an appropriate failure model can lead to accurate predictions of adhesive bond performance. Accordingly, the first step in performance analysis of bonded joints is to obtain an accurate stress/strain distribution within the bonded area. Several approaches have been proposed by researchers to analyze the stress state in bonded joints subjected to a variety of loading conditions. The proposed methods are mainly analytical or are based on numerical techniques. However, in a few studies, a combination of both numerical and analytical methods has been proposed.

Since an initial attempt for stress analysis in bonded joints in 1938 [1], several analytical methods have been developed for the stress assessment of bonded joints, including many for single-lap joints (SLJ). Although low cost and simplicity are known advantages of the analytical approaches, they are limited in terms of the material type, joint geometry, loading conditions, and the inclusion of complicating factors such as environmental effects. Nonetheless, these models often provide useful insights, at least qualitatively, into stress distributions in classic joint geometries.

Considering these limitations and the increasing complexity of bond geometries and materials utilized, numerical methods appear as the most appropriate method for predicting the bond performance in adhesive joints. The first authors who considered finite element methods (FEM) in the stress analysis of bonded joints were Wooley and Carver [2] in 1971. However, due to the unique capabilities of FEM for solving complex problems, this method has been extensively considered by other researchers and now is a powerful approach for the performance analysis of bonded structures.

Continuum-based numerical methods are simple techniques that can analyze the stress state within the adhesive joint and predict the bond performance, assuming a perfect material with no initial defects or flaws. However, they can significantly overestimate the performance of adhesive joints, especially where the material contains defects or cracks. In this case, to predict the behavior of adhesive joints, fracture mechanics-based methods should be employed. The main shortcoming of fracture mechanics methods is their dependency on the presence of a predefect within the material. These approaches only

study the crack propagation phenomenon where the performance of the bonded joints before the crack initiation is ignored. To overcome this issue, damage mechanics-based methods were developed and are now considered extensively in the numerical assessment of the mechanical behavior of adhesive materials. Several damage modeling approaches have been developed and embedded in commercial finite element software. Recently, some authors have combined analytical methods with fracture mechanics-based approaches to predict the performance of single-lap bonded joints.

The mechanical performance of adhesive bonds is significantly influenced by the joint geometry, loading mode, and environmental conditions. To accurately predict the mechanical response of adhesive bonds, the selected method should be appropriate for the considered geometry and must be able to consider the effects of loading and environmental conditions. The effects of these parameters on the performance of adhesive joints are briefly discussed in the last part of this chapter.

15.2 Stress and strain concepts

The linear elastic constitutive law is defined as follows:

$$[\sigma] = [D] [\varepsilon] \quad (15.1)$$

where D is the stiffness matrix, and ε and σ are the strain and stress tensors, respectively.

Fig. 15.1 shows the scheme of the stress states for two-dimensional (2D) and three-dimensional (3D) conditions. To simplify the problem, analytical methods and numerical simulations are mostly based on 2D assumptions. Considering 2D analysis, one of the plane-based concepts (plane stress or plane strain) should be employed, but this introduces some errors in the numerical calculations. On the other hand, because one dimension of the joints is not simulated in 2D models, the stress components involving this direction are not considered in this type of analysis.

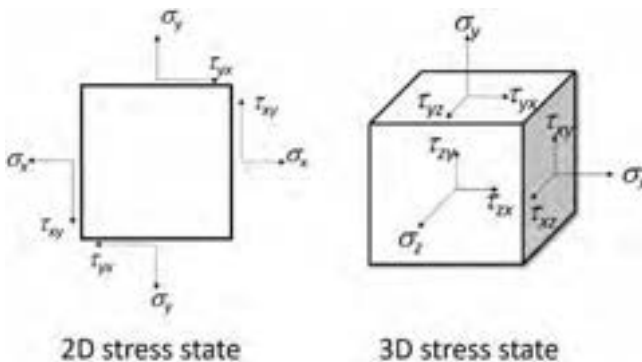


Fig. 15.1 Stress state in 2D vs 3D conditions.

Considering the geometry of the adhesive layer in adhesive joints, the stress state within the adhesive layer is assumed by some authors to be plane strain in the 2D analysis. However, in some studies, plane stress conditions have been considered [3,4]. Li et al. [5] discussed the differences between the mentioned assumptions. They found similar results based on both techniques for single-lap adhesive joints.

For simple joint geometries, a 2D analysis can precisely determine the most critical regions in a bonded joint, but for many conditions, in simplified 2D models the stress distribution is not precise enough and a correction factor must be applied to the obtained results [6,7]. To reduce the computational costs and time spent in a 3D analysis, a submodeling technique can be employed where only the critical parts of the model use fine elements. It should be noted that the above discussions regarding plane stress and plane strain are valid for linear elastic analysis where no plastic deformation is assumed during the loading. In the case of plastic deformation, plane stress and plane strain can lead to very different results because the plastic zone size is significantly influenced by the type of plane assumption. In this case, performing a 3D analysis is the best choice.

15.3 Stress types in bonded joints

Depending on the adhesive type, loading conditions, and joint geometry, different stress components can be considered as the failure parameter in analytical or numerical models. Among them, peel stress is the most critical one that can significantly reduce the performance of the bonded joints. In the current section, different stress types are briefly discussed.

Tensile stress: As shown in Fig. 15.2a, tensile stress is caused by uniformly loading a joint, where the load is perpendicularly applied to the bondline. Due to the uniform load distribution, no bending moment is generated in this type of stress.

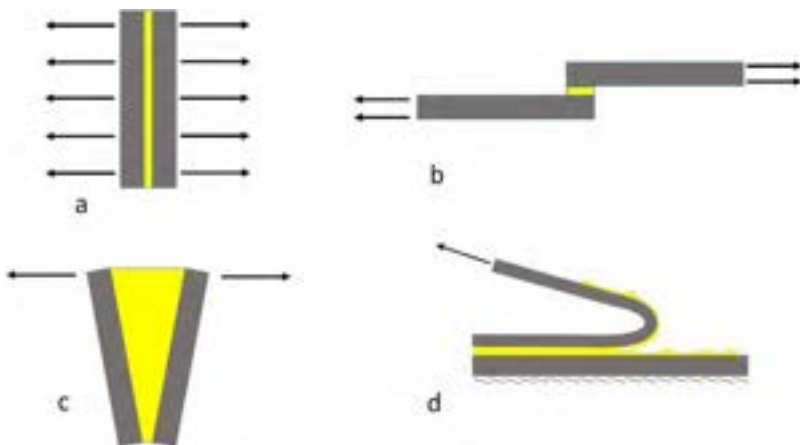


Fig. 15.2 Different stress types, (a) tensile, (b) shear, (c) cleavage, and (d) peel.

Shear stress: In plane stress conditions, and in the case of the absence of normal stress components, a pure shear stress state is generated within the adhesive layers. In practice, the adhesive layer experiences a nonuniform loading distribution through the bondline. In this condition, nonuniform tensile loads will generate peel stresses that can significantly reduce the load-bearing capacity of the joint. Accordingly, bonded joints must be ideally designed to be loaded mainly in shear loading conditions.

However, the complexity of the joint geometries and loading conditions makes it difficult to obtain such an ideal condition. Fig. 15.2b schematically shows the shear loading condition in a bonded joint.

Cleavage stress: Cleavage stress is a specific type of stress state generated by a nonuniform tensile loading distribution or by concentrated loads applied closer to one end of the joint. To generate a cleavage stress, the substrates should be thick enough. The double cantilever beam (DCB) test that is used for the fracture energy analysis of adhesives is an example of an adhesive joint where the adhesive layer experiences cleavage stresses during the test. In this type of loading, the stress is concentrated at one end of the joint. Stress concentration significantly increases the stress level in some regions of the bond layer and reduces the load-bearing capacity of the joint. Consequently, joints should often be designed in a way to minimize cleavage stresses in service. Fig. 15.2c schematically shows the cleavage stress in a bonded joint.

Peel stress: One of the most harmful stress conditions that joints can experience is peel stress. Peel stress can dramatically reduce the loading capacity of the bonded structures. Similar to the cleavage condition, the peel stress is generated by tensile loads where the load is mainly concentrated at one bonding end. However, in contrast to the cleavage, the substrates are sufficiently flexible to generate very high, localized peel stresses. Although the peel test is a common test method, any design in which the bondline undergoes significant peel stresses should be avoided. Fig. 15.2d shows a schematic view of the peel stress in a bonded joint.

15.4 Sources of adhesive joint stresses

Stresses in adhesive joints are often generated by the applied mechanical loads, but even in the absence of any external mechanical load, joints may still experience high stress levels within the adhesive layer. Thermal stresses caused by the ambient temperature and the swelling stresses generated in humid (or other diluent) environments are two nonmechanical loads that bonded joints may experience. This section discusses different sources of stresses in adhesive joints.

15.4.1 Mechanical loading

Mechanical loads in the form of force, pressure, bending, and moments are the main stress sources that an adhesive bondline may experience in service. These loads can be applied in a variety of types such as creep, fatigue, impact, or a combination of these. Experimental results show that the performance of joints is often time-dependent

when subjected to creep [8] and fatigue [9]. The mechanical performance of bonded joints subjected to fatigue (addressed in more detail in Chapter 19) is often complex because the variation in mechanical properties of the adhesive as a function of loading time must be taken into account in the stress analysis of the adhesive [10–12]. The material model should also take into account the strain rate effects (see Section 15.9 and Chapters 16 and 21 for further details).

15.4.2 Thermal stresses

At high service temperatures or during the heat curing process, both adhesives and adherends tend to expand. However, their thermal expansion coefficients are often very different [13–15]. This difference in the thermal expansion coefficient can induce considerable thermal stresses within the adhesive layer. These thermal stresses are more significant for joints with a stiff adhesive [16], such as those generated during curing, as discussed in Chapter 31. Daghyani et al. [14] showed that residual stresses can change the failure mode by changing the crack path in double cantilever beam (DCB) and compact tension (CT) adhesive joints. Following an optimized curing cycle, Lee and Lee [17] could minimize the residual thermal stresses in composite bonded joints. Not only the heat curing process but also the elevated temperature during service can induce thermal stresses within the adhesive layer. Thermal stresses are more significant if the adhesive bonds adherends with different materials. Results show that cyclic thermal loads may cause failure if the joint is subjected to a temperature close to the glass transition temperature (T_g) of the adhesive [18]. Effects of cyclic thermal service loads on joints with dissimilar adherends and with different adhesive thicknesses were analyzed by Safaei et al. [15] using the digital image correlation (DIC) technique. They showed that the thermal stresses increase by thermal cycles, leading to a reduction in the mechanical performance of the tested joints. da Silva and Adams [19] determined a stress-free temperature in joints with multiple adhesives and dissimilar substrates. They showed that the cure temperature for the high-temperature adhesive and the T_g for the low-temperature adhesive are the stress-free temperature of the considered bonded joints.

15.4.3 Swelling stresses

Exposure to a wet environment causes an adhesive layer to absorb water and consequently experience a volume expansion called swelling. Because the adhesive layer is constrained between two substrates, the swelling phenomenon will introduce stresses in the adhesive layer. Adhesives absorb water through two different mechanisms. Part of the water will occupy free spaces (of the molecule size or microscale defects) within the adhesive material while the rest will become bound to the adhesive polymer chains. Free water doesn't cause swelling in the adhesive while the bound water expands the adhesive volume. Swelling generates stresses mainly at bonding edges. Even after a long exposure time, the center region of the overlaps, especially for joints with large bonded areas, can remain dry with no swelling. A nonuniform swelling process causes a nonuniform stress distribution in bonded joints, which makes analysis of

the joints complex. Although the swelling process has a negative effect on the bond performance, water absorption can make the adhesive more flexible at bonding ends, reducing the peel stresses and consequently increasing the mechanical performance of the joint.

15.5 Analytical approaches

Analytical approaches were first considered in the late 1930s and early 1940s by considering the governing differential equations of specific joint geometries [1,20]. However, to simplify the problem, they were based on a one-dimensional assumption where only the linear response of the materials was considered. These models were adopted by other authors and extended to analyze joints with a nonlinear material behavior. The current section summarizes these analytical methods.

15.5.1 Lap shear joints

Among the shear-based approaches, the average shear stress model is the simplest failure analysis method. Based on this model, the average shear stress is obtained by dividing the applied load to the bonded area (see Eq. 15.2); when it reaches the maximum shear strain of the adhesive, the joint will fail.

$$\tau = \frac{P}{bl} \quad (15.2)$$

where P is the applied load, b is the joint's width, and l is the overlap length.

This model may be appropriate for more ductile adhesives where an almost uniform shear stress distribution along the overlap is assumed. In the late 1930s, Volkersen [21] developed a closed-form stress analysis model where he could show how the shear stress varies along the overlap in an SLJ. In his model, the substrates were considered as elastic that only experiences tensile deformations and the adhesive was assumed to only carry shear stresses. Volkersen did not take the bending effects into account. These assumptions make the model more appropriate for joints where the substrate stiffness is much higher than the adhesive and for double-lap joints. A few years later in 1944, Goland and Reissner [22] improved the Volkersen model by considering the effects of the bending moment induced due to the loading eccentricity. Accordingly, Goland and Reissner obtained higher shear stresses at the bond ends in SLJs, taking into account the bending effects. Fig. 15.3 shows a typical peel and shear stress state along an overlap in an SLJ.

The Goland and Reissner model was later improved by Hart-Smith in 1973 [23]. At higher loads, the stress level predicted by Hart-Smith is somewhat below that predicted by Goland and Reissner. Adhesive thickness effects and plastic deformation of the adhesive are considered in this model. Renton and Vinson [24] considered the Goland and Reissner technique with balanced composite substrates and assumed a linear elastic response and a constant stress level along the thickness.

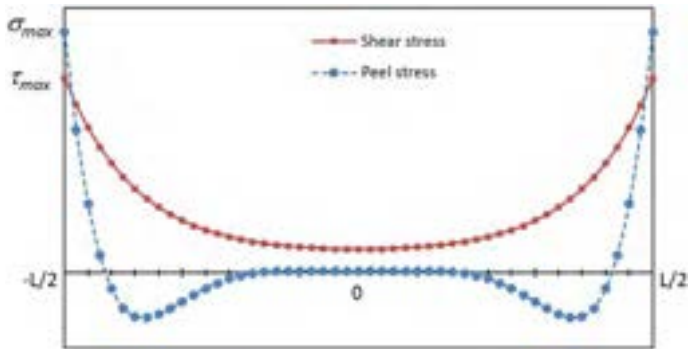


Fig. 15.3 Peel and shear stresses along an overlap in an SLJ using the Goland and Reissner approach.

While the already described models show that the shear stress reaches its maximum value at the bond ends, the maximum stress along the overlap is actually observed at a distance from the overlap ends. This effect was considered by Renton and Vinson [24]. Their model also takes the thermal effects into account. In this model the maximum shear and peel stresses were lower than the Goland and Reissner model. In 1977, Allman [25] suggested a new analytical approach where he assumed that the shear stress along the adhesive thickness is constant while the peel stress varies along the bondline thickness. One of the major differences between the Allman approach and the early analytical models is the edge effects that are considered by Allman. Accordingly, based on the Allman method, the maximum stress points are not found at the free surfaces at the ends of the overlap, which is in agreement with the finite element results.

Ojalvo and Eidinoff's [26] approach was also established based on the Goland and Reissner concepts. In contrast to the Allman model, Ojalvo and Eidinoff considered the variation of the shear stress component through the adhesive thickness. However, they considered the longitudinal stress along the overlap as negligible. This parameter was later studied by Delale et al. in 1981 [27].

To consider the effects of substrates with different thicknesses and lengths, Cheng et al. [28] extended their model based on the same energy and elasticity concepts. Drawing inspiration from the Goland and Reissner model, Bigwood and Crocombe [29–31] proposed a method to assess the peel stress and shear stresses. They later extended their method [32] to include the plasticity in the adhesives and the substrates. Comparing the Bigwood and Crocombe model with the finite element analysis results, good agreement was found between the two stress analysis methods.

Adams and Mallick in 1992 [33] produced an analytical model for both similar and dissimilar SLJs. In their model, the plastic deformation of the adhesive was also taken into account. They evaluated their model using both numerical methods [33] and experimental approaches. Composite lap shear joints were also studied by Yang and Pang [34]. They considered both balanced and unbalanced geometries. The Goland and Reissner method presents a quite accurate stress distribution along the

bondline; however, their model is limited to joints where the substrate thickness is much larger than the bondline thickness. To solve this issue, Oplinger in 1994 [35] suggested an extension to the Goland and Reissner method by considering the bending deflections of the central part of the joint.

The model developed by Tsai et al. [36] is one of the few studies in which the effect of shear deformation of the substrate has been taken into account. Effects of spew fillets on the adhesive stress state were considered by Frostig et al. [37] for both metal and composite materials as the substrate. They could also take into account the stress-free condition of the overlap ends and the variation of the peel stress along the adhesive thickness. One of the latest analytical methods was developed by Mortensen and Thomsen [38]. Similar to Yang and Pang [34], Mortensen and Thomsen [38] considered composite laminates for both balanced and unbalanced SLJ geometries. In their analysis, the effects of moments induced by the asymmetry of the substrates and both linear and nonlinear behavior of the adhesives have been considered. Interfacial stress has been less considered in the analytical methods. Sawa et al. [39] derived some analytical methods for the interfacial stress analysis in bonded lap shear joints. The effects of the overlap length, bondline thickness, and the stiffness of the substrates were all taken into account in their model.

Although most of the reviewed analytical approaches have been developed for lap shear joints (SLJs and DLJs), there are some studies for which other types of joints have been considered. The next section briefly reviews the analytical approaches that have been developed for stress analysis in other joint geometries.

15.5.2 Other joint configurations

15.5.2.1 Peel joints

In peel tests, one of the substrates should be relatively thin and flexible (see Fig. 15.2). Thin substrates often show an inelastic behavior during the test. This nonlinearity makes the stress analysis difficult. Spies in 1953 [40] and Kaelble in 1960 [41] proposed the first analytical stress models for peel joints. However, the Kaelble model was limited to the linear elastic response of the flexible substrate. Kim and Aravas [42] and later Kinloch et al. [43] extended the Kaelble model by considering the plastic deformation of the flexible substrate. In 1995, Moidu et al. [44] also presented an analytical approach for predicting the plastic deformation of bonded parts in metal bond peel tests, allowing for a more accurate measurement of fracture energy.

15.5.2.2 Scarf and stepped joints

Step joints are a kind of lap shear joint where the substrates are bonded through multiple overlaps. The scarf joint is a special configuration of the stepped joint in which the number of steps has been greatly increased. The Hart-Smith model [45] provided the first analytical solutions for stress analysis in stepped joints. A few years later in 1976, Grant [46] proposed his model based on the concepts of Goland and Reissner [22]. He considered the effects of unbalanced joints on the stress distribution in

stepped adhesive joints. Mortensen and Thomsen [47] also considered the unbalanced joints but with composite laminates as substrates, where the nonlinear stress-strain response of the adhesive was also taken into account. Helms et al. [48] considered composite substrates in scarf joints. Gleich et al. [49] developed a model for the peel and shear stress analysis in scarf joints for balanced configurations.

15.5.2.3 Butt joints

Stress analysis in butt joints is simpler than that for other joint types reviewed in these sections if an axial load is applied to the joints. However, the process is more challenging if the loading condition is different and dissimilar substrates are used. The analysis would be even more complex if the interfacial stress is considered. Several authors have investigated the stress distribution in butt joints. Nakano et al. [50] analyzed the stress state in a solid shaft butt joint subjected to torsional loading. Sawa et al. [51] proposed a solution for this problem. They introduced an analytical technique to analyze the stress distribution in a T-butt joint subjected to bending. You et al. [52] numerically studied the effects of adhesive thickness in steel/steel butt adhesive joints subjected to impact. They showed the interaction of the adhesive thickness and the interfacial stresses in butt joints.

Researchers have developed a wide range of analytical models and based on the overview presented, it is evident that none of them is a comprehensive analytical model that fits all conditions. Each model has its own advantages and limitations. The most appropriate model should be selected depending on the adhesive behavior (ductile vs brittle and linear vs nonlinear), the materials of the adherends (isotropic and orthotropic), the loading conditions, and the joint geometry. For example, the Volkersen model presents itself as one of the simplest approaches to single-lap joints with a brittle adhesive, where the substrate does not exhibit significant bending and remains in its elastic state.

It should be noted that most models are developed for 2D conditions while neglecting the stress along the width of the joints. Although the assumption of linear elasticity makes some models very easy to use, in the case of ductile materials, these models are not able to accurately estimate stress levels. On the other hand, implementing models that account for material nonlinearities would be time consuming and offer no advantages over finite element methods. Accordingly, the use of FEM is recommended for 3D analysis and for materials with complex behavior. A comparative study of analytical models conducted by da Silva et al. can be found in [53].

15.6 Numerical methods

Despite the simplicity and low costs, analytical models are unable to analyze complex joint geometries and also are unable to take the complex mechanical behavior of adhesives into account. For such conditions, using numerical tools is recommended. There are different approaches in strength and damage analysis of adhesively bonded structures using FEM. In this section, these methods are briefly discussed.

15.6.1 Continuum mechanics models

Stress-based criteria can be considered for brittle or quasibrittle adhesives in a simple continuum-based analysis. However, stress (strain) concentration at singular points, sensitivity to mesh size, and being less suitable for complex material behaviors are the most important drawbacks of the continuum elements in the performance analysis of adhesive joints. However, there are still several stress- and strain-based models developed for the performance analysis of adhesive joints, as discussed in the following sections.

15.6.1.1 Stress-based models

Peel stress, shear stress, von Mises stress, and maximum principal stress are the most important stress components considered in stress-based failure analysis models. Peel stress in T-shaped bonded joints was studied by Crocombe et al. [54], where they used a simple linear analysis that examined only the peeling stress in the joints. The peel stress was also introduced as a damage parameter by Rahman et al. [55]. They used their model for both brittle and ductile adhesives. They eventually proposed the crack tip opening angle method for ductile adhesive joints. For more brittle materials, results show that the crack propagates along a path perpendicular to the maximum principle stress direction [56]. Although the stress-based models are mainly recommended for brittle materials, Harris et al. [56] showed that there is not necessarily a relationship between the stress parameter as a measure of damage and the degree of ductility of the adhesive. The von Mises stress approach was also considered in some studies. This criterion was used by Ikegami [57] to estimate the bond strength of scarf composite to metal joints. But one of the weaknesses of this criterion is the lack of considering the effect of hydrostatic stresses. Goglio et al. [58] proposed a model according to which adhesion failure occurs when the combination of peel and shear stresses exceeds the safe range. Stress-based methods are mainly employed for joints where adhesive plasticity is negligible. But for adhesives with a ductile response, strain-based models are more recommended. These models are discussed in the following section.

15.6.1.2 Strain-based models

Similar to stress, different strain components have been considered in failure prediction models. Hart-Smith [59] proposed one of the first strain-based methods for the performance analysis of bonded joints. Lee et al. [60] proposed a criterion for joining circular edges under torsion and used strain parameters to estimate joint strength. Chai [61] also studied the maximum shear strain parameter in the adhesive. Results shows that the critical shear strain decreases with increasing adhesive thickness. However, there is no specific value for the critical shear strain as a material constant, which is why the application of the Chai criterion is limited. Tang [62] used the Goland and Reissner approach [63] and proposed a failure criterion considering the nonlinear response of the adhesive and the joint. They used shear strain and strain energy in their analysis. The maximum principal strain was used by Harris and Adams [56], but the disadvantage of their method lies in its dependence on the dimensions of the elements.

Adam and Wick [64] also used this criterion to estimate the strength of the adhesive bond. Plastic axial strain is another strain parameter proposed by Crocombe and Adams [65]. However, this approach is also sensitive to the size of the elements.

15.6.1.3 Critical distance-based models

Distance-based approaches have been proposed to solve the drawbacks of the stress- and strain-based models related to the sensitivity to mesh size and the singularity at corners and bonding ends. The critical distance is the distance from the singularity of the stress and strain at which the damage parameter is evaluated. According to these criteria, when the failure parameter reaches a critical value at the critical distance, the joint will fail. The main advantage of these criteria is moving away from the singular point to eliminate the effects of extreme fluctuations and singularity in stress and strain at this point. The critical parameter and the critical distance are assumed to be properties of the material and the geometry of the joint, which can be obtained by performing at least two calibration tests. Distance-based models developed for bonded joints showed that the model constants are functions of the joint type and geometry. These limitations make the application of the distance-based models very limited. On the other hand, because the proposed models are based on a linear elastic assumption for the behavior of the adhesive, they are also limited in terms of the material type. To overcome these issues, a critical distance-based approach was recently proposed, based on the critical longitudinal strain (CLS) measured along the adhesive mid-plane [66]. The model is based on a simple linear elastic analysis of the bonded joints that makes it very simple compared to other, more complex failure analysis methods. The results showed that the CLS model can precisely predict the strength of bonded single-lap joints. Another advantage of the CLS model is the independence of the model constants (the critical distance and critical strain) on the joint geometry. Results showed that the same critical distances and critical strains can be used to predict the strength of SLJs with different overlap lengths or substrate thicknesses. One of the main challenges in numerical analysis of the bonded joints using continuum approaches is taking the effects of adhesive thickness into account [67]. The CLS model is also able to take the effects of the bondline thickness on the strength of SLJs into account [68]. It was later shown that the CLS approach can also predict the strength of SLJs bonded with ductile adhesives and with a wide range of joint geometries and also substrate materials [69]; it also works for joints with dissimilar substrates [70]. Based on the CLS method, only one calibration experiment is needed to define the model constants [69].

15.6.2 Fracture mechanics methods

The presence of a macrocrack in the adhesive is essential for the application of the fracture mechanics method. Macrocracks in polymers will be about a few millimeters in size. However, the crack size necessary for a fracture analysis is a function of the adhesive thickness (see Chapter 18 for further details). Maximum tangential stress (MTS) is one of the well-known fracture mechanics-based methods used for the

strength analysis of materials. This approach has been also considered for the fracture assessment of bonded joints. Based on the MTS, fracture occurs in a direction where the tangential stress reaches its maximum value. Strain energy density (SED) is another fracture mechanics-based method that has been employed for the strength analysis of bonded joints [71]. Sih and Macdonald [72] also used the concepts of strain energy density for the fracture analysis of materials. According to the SED, a crack propagates when the SED value along a specific direction reaches a critical value at a specific critical distance. A combination of MTS and SED called maximum tangential strain energy density (MTSED) was also considered by Akhavan-Safar et al. [71] for the fracture assessment of single-lap adhesive joints. The MTSED uses a kinking angle, a critical distance, and a critical tangential strain energy density value to predict the failure loads of the precracked materials. Kinking angle (crack initiation and propagation path) analysis is part of the fracture analysis of bonded joints using fracture mechanics-based approaches. The crack path determines the resulting failure location and associated fracture resistance in adhesive joints. An improved understanding of crack path selection, especially in the presence of localized interfacial defects, might lead to adhesive joints with tunable failure locus and resistance to fracture [73]. Crack path is a function of the adhesive and adherend properties, joint configurations, and loading conditions. Based on MTSED, the crack propagates along a direction at which the tangential SED reaches its maximum value. Based on these results, for mode mixities close to mode I, the SED method can predict the crack kinking angle very well, though it is not that accurate when mode II loading conditions are predominant. The MTS method can be a good choice if the loading conditions are dominated by shear loads. However, for the intermediate mode ratios, none of the above-mentioned methods can predict the crack path precisely. Several authors have studied the crack initiation or propagation path in bonded joints [74,75]. The effect of T-stress on crack path was analyzed by Chen and Dillard [75,76]. Cracks tend to be directionally stable when the T-stress is negative, but they become unstable for a positive T-stress [77]. Chen and Dillard [75] experimentally showed this behavior in DCB joints. Using the same joint type, Chen et al. [78] analyzed the effect of loading conditions and joint geometry on the crack path. Changing the loading conditions and joint geometry led to a different T stress that influenced the crack path. The role of the T stress combined with stress triaxiality at the crack tip was also investigated by Akhavan-Safar et al. [79] to propose a new method for the fracture energy analysis of DCB adhesive joints.

The classical fracture mechanics-based approach is limited to specimens containing a crack. To cover this limitation, finite fracture mechanics (FFM) methods were developed that can also predict crack initiation. This approach has been also used for the strength analysis of adhesive joints [80]. Leguillon et al. [81] proposed an FFM model for the strength analysis of adhesive joints. However, the results showed that the model is too conservative and that it underestimates the experimental results. Other authors, such as Moradi et al. [82], also considered this approach for the analysis of the mechanical performance of bonded joints.

Fracture mechanics-based methods were also employed for interfacial strength analysis of adhesive joints. In this case, the generalized stress intensity factor (GSIF)

is used. GSIF has been considered by some authors [83,84] to analyze the adhesive stress field around the singular points in SLJs. According to the GSIF, the stress at the singular points at the interface of the adhesive and adherend is defined as a function of a singularity exponent, a distance, and a nondimensional function. The singularity exponent is also defined as a function of the geometry of the interface. In some studies, such as Groth [85], GSIF has been considered a material constant. Dundurs [86] investigated the stress state around the singular points in bonded joints using a new parameter named the mismatch factor. Ayatollahi et al. [87] studied the effect of the bi-material notch angle on the GSIF. Based on the results obtained for single-lap joints, the overlap length has a significant influence on the GSIF [83]. It has been also found that the effects of the substrate stiffness on the GSIF are more pronounced for thinner adhesive thickness. A combination of an analytical model and GSIF has been also considered for the strength analysis of SLJs. Not only for static loading conditions, GSIF has also been considered for the crack initiation analysis of adhesive joints subjected to cyclic loads [88,89]. Although the crack usually propagates away from the adhesive-adherend interface in a joint with good adhesion, fatigue initiation usually takes place in the region of the interface and close to the joint corners where the stress field experiences a singularity. Lefebvre et al. [88,90] theoretically and experimentally analyzed the fatigue performance of bonded joints using the GSIF method. They defined a 3D fatigue initiation surface using the GSIF and by considering a single singular eigenvalue for joints with a modulus ratio (adhesive to adherend) of 0.1 or smaller, and the interface apex angle of 90 degrees or less. Chapter 19 addresses fatigue experiments, results, and modeling in additional detail.

Despite the extensive studies carried out on the application of fracture mechanics-based methods for the performance assessment of adhesive joints, it should be noted that these methods are applicable mostly for brittle adhesives or where the small-scale yielding criterion is met.

15.6.3 *Damage mechanics methods*

Two main approaches for the damage analysis of adhesive joints are the continuum damage models (CDM) and cohesive zone modeling (CZM). These two techniques as well as the extended FEM (XFEM) are briefly discussed in the following sections. All three approaches use fracture energy as a key parameter for failure to characterize the crack propagation behavior of adhesive joints. Accordingly, adhesives should be characterized in terms of fracture energy as a function of loading mode. For pure Mode I loading conditions, the DCB test is often used as the standard approach. While there is no standard method for Mode II, end notched flexure (ENF) is a routine technique for measuring the fracture energy of adhesives under pure shear conditions (Mode II). However, for both DCB and ENF tests, the results are influenced by the joint geometry, loading rate, and even the data reduction approach [79,91–99]. In addition to these routine techniques, other methods such as semicircular bend (SCB) tests have been also proposed by some authors [100]. In some studies, Mode III (out-of-plane shear) fracture energy [101] has been also analyzed, where its value is often considered to be equal to Mode II (in-plane shear) in numerical damage analysis.

15.6.3.1 Continuum damage models

CDM proposes a damage model within the continuum mechanics framework. The first damage mechanics model was introduced by Kasyanov [102], who defined a damage parameter to characterize the degradation of the properties of materials. Based on the CDM, the stiffness degradation and the reduction of the effective cross-sectional area of the material due to the nucleation and propagation of voids decreases the load-bearing capacity of the specimen. Using CDM, the crack can propagate in an arbitrary path. CDM has been also considered for the strength analysis of adhesive joints [103,104]. The Drucker-Prager model, the linear traction separation law, or any type of nonlinear response can be employed to simulate the undamaged zone in CDMs. The damaged zone can be also considered as linear, or other softening shapes can be used. Accordingly, different CDMs have been proposed by authors. A linear softening behavior was considered by Riccio et al. [105] and Zhang et al. [106], and the effects of mode mixity were considered in CDM by Kim and Hong [107].

15.6.3.2 Cohesive zone modeling

CZM is widely used for the damage analysis of adhesive joints due to its advantages such as less sensitivity to the mesh size and the ability to simulate both damage initiation and its propagation. Similar to CDM, CZM defines a damage parameter to control the traction separation response of the adhesive. However, unlike CDM, CZM employs cohesive elements. In CZM, a traction separation law (TSL) relates the applied stress to the material separation at each material point. A variety of TSLs have been proposed that are customized for different material types (linear/nonlinear, ductile/brittle) and loading conditions (quasistatic and impact [95,108], fatigue [109–111], and creep [112]). However, one of the simplest and most widely used CZM shapes is the triangle. Fig. 15.4 shows a typical triangular traction separation law that

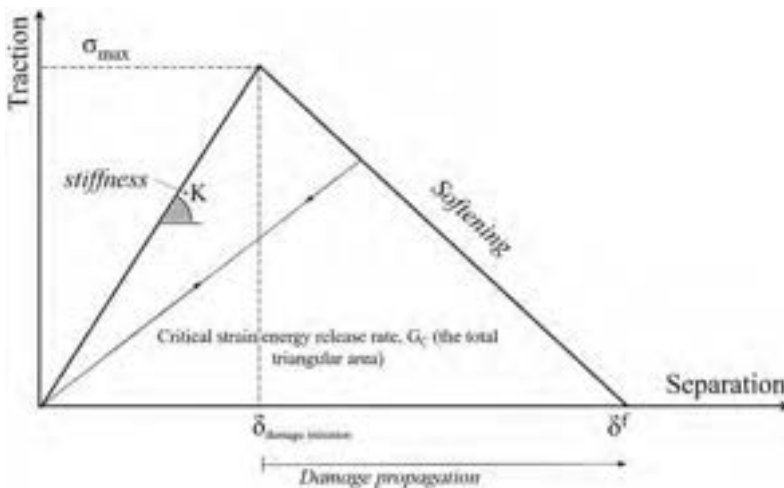


Fig. 15.4 A typical triangular CZM shape.

is one of the most common CZM shapes used for the damage analysis of adhesive joints. Certain parameters should be known to define the CZM shape. The most important parameter experimentally obtained is the fracture energy. Initial stiffness is the second parameter that can be considered as a penalty parameter if a zero cohesive thickness is considered in simulation. However, for finite cohesive elements, this parameter is often defined by the modulus (tensile and shear) of the adhesive divided by the thickness of the cohesive layer. The third key factor is the maximum traction, which is usually defined based on the tensile (shear) strength test results. Depending on the shape of the CZM, more parameters might be required. Further details about the different CZM shapes and techniques are presented in [113].

In the CZM approach, continuum mechanics criteria are often considered for damage onset; for damage propagation, energy-based criteria are used [114]. Unlike the continuum-based models, CZM is known to be less sensitive to the mesh size.

The different CZM law shapes allow considering different adhesive behaviors. CZM is also applicable for very ductile adhesives using a trapezoidal traction separation law. However, the triangular law is the most common CZM shape, well suited for more brittle adhesives. However, it should be noted that changing the CZM shape can significantly increase the computational costs. Some authors have studied the influence of different CZM shapes on the damage behavior of bonded joints. Chandra et al. [115] compared bilinear and exponential CZM shapes and found that in the tested conditions, the bilinear model is accurate enough to predict the damage. Alfonso also compared different TSLs and concluded that the material stiffness and interface toughness play key roles in choosing the most suitable TSL shape. Akhavan-Safar et al. [113] presented a detailed answer to the question of which CZM shape should be selected. Besides predicting adhesive behavior under static loading conditions, CZM is also able to take into account the effects of different loading and environmental conditions such as fatigue, impact, creep, and humidity [108,109,112,116]. Additional details on the CZM method and extraction of traction separation laws are discussed in Chapters 16, 17, and 32, including for mixed-mode fracture tests.

A comparison between the CZM and CDM methods showed that CZM results in more accurate predictions. On the other hand, the CDM approach is able to predict the crack path while CZM by itself does not [117].

15.6.3.3 *Extended finite element modeling*

Using similar concepts to CZM, XFEM as a damage criterion was developed where the crack is allowed to propagate through the elements (and not necessarily at their boundary). This is one of the main advantages that XFEM offers when compared to the CZM-based approaches. For crack propagation, no remeshing of the model ahead of the crack tip is required. XFEM has been recently considered in some studies for the fatigue analysis of materials [118–121]. A combination of XFEM and the cohesive zone (CZ) approach is also advanced in some studies [122,123]. However, more research is still needed to assess the performance and capabilities of XFEM to take into account different loading and environmental conditions, especially for 3D models.

15.7 Hybrid analytical/numerical methods

One of the main weaknesses of analytical models is their inability to accurately determine the stress state at the end of joints. Also, these approaches rarely consider the effects of the interfaces. On the other hand, the GSIF-based methods discussed in Section 15.6 are limited because at singular points, the stress component goes to infinity and consequently the generalized stress intensity factor (GSIF) cannot be obtained easily using FEM. To solve this issue, Zhang et al. [124] proposed a ratio-based method. Accordingly, the ratio of the stress intensity factor for two SLJs with different overlap lengths and bondline thicknesses is almost constant along the interface. The method was later extended to SLJs with different substrate thicknesses [125]. Rastegar et al. [125] also combined the GSIF approach with the analytical methods to predict the strength of bonded SLJs. Based on Eq. (15.3), the GSIF as a function of distance is a function of λ and f_{ij} .

$$H(r) = r^\lambda \sigma_{ij}(r) / f_{ij} \quad (15.3)$$

where H represents the value of wedge corner GSIFs and f_{ij} is a nondimensional function of the order of singularity (λ), local edge geometry around the corner (θ), and the elastic properties of the substrate and adhesive.

Based on the ratio method, using Eq. (15.3), the ratios of H^2/H^1 should be measured where the superscripts 1 and 2 represent two joints.

$$\frac{H^2}{H^1} = \frac{r^{\lambda 2} \sigma_{ij}^2(r) / f_{ij}^2}{r^{\lambda 1} \sigma_{ij}^1(r) / f_{ij}^1} \quad (15.4)$$

A combined analytical-numerical approach was also considered in some studies to estimate the strength of bonded joints considering the GSIF ratio and by taking into account the closed form shear stress relation developed by Volkersen. Considering this combined technique, it would be possible to overcome the individual shortcomings of the GSIF and the analytical methods in the performance analysis of bonded joints.

As discussed in Section 15.5, the Volkersen model is associated with large errors in the stress analysis at bonding ends in SLJs. According to the Volkersen model, the shear stress distribution (τ) is given by the following relation:

$$\tau = P\omega \cos h(\omega x) / 2b \sin h\left(\frac{\omega L}{2}\right) + [(t_t - t_b) / (t_t + t_b)] \omega L \sin h(\omega x) / 2 \cos h\left(\frac{\omega L}{2}\right) \quad (15.5)$$

where:

$$\omega = \sqrt{G_a [1 + t_t / t_b] / E t_a t_t} \quad (15.6)$$

where b is the joint width, x is the longitudinal coordinate with the origin located in the middle of the adhesive layer, P is the applied tensile load, t_t and t_b are the top and bottom substrate thicknesses, respectively, L is the overlap length, t_a is the adhesive thickness, and E and G are the substrate modulus and the adhesive shear modulus, respectively.

Using the proposed analytical method, the shortcomings of FEM such as mesh size dependency would not exist anymore. Accordingly, by knowing the reference GSIF (H_c^R) and considering the Volkersen relations, the critical GSIF for other joints can be obtained with no further finite element analysis or experiments. Although the Volkersen method cannot predict the failure load of SLJs precisely, its combination with the GSIF concept allows accurately predicting the critical GSIF ratios (H_c/H_{cR}). It should be noted that the proposed combined method works for SLJs with different geometries. The effects of joint geometry on the mechanical performance of bonded assemblies are briefly discussed in the next section.

15.8 Effects of joint geometry

15.8.1 Adhesive thickness

The effects of adhesive thickness on the joint strength have been extensively studied [68,69,79,126,127], some aspects of which will also be addressed in Chapter 18. In fracture tests using DCB and ENF samples, results show that the obtained energy is less sensitive to the thickness for brittle adhesives while the fracture energy increases with the adhesive thickness until a certain point is reached, where any further increase has no additional influence or can even reduce the obtained energy [127]. Although, based on the results of [128], adhesive thickness had no influence on the strength of butt joints, Reedy and Guess [129] showed that the butt joint strength varies with adhesive thickness. Their results showed that the influence of bondline thickness depends on the stiffness of the adherends. For joints with steel substrates, the strength of butt joints varied with the inverse cube root of bond thickness while in aluminum joints, it varied as the inverse fourth root of adhesive thickness. Naito et al. [130] also showed that increasing the adhesive thickness decreases the butt joint strength. Scarf joints have been also analyzed in terms of the bondline thickness. Effects of adhesive thickness in SLJs have been also investigated in several studies. According to FEM results and also based on analytical approaches such as those by Volkersen and Goland-Reissner, higher joint strength is predicted for joints with thicker bondlines because increasing the adhesive thickness leads to a more uniform stress and strain distribution along the adhesive layer. Negative effects of adhesive thickness were justified by the plasticity of the adhesive in some works [131,132]. However, this is not the case for joints with brittle adhesives. For this type of joint, the shear and peel stress components at the interface and bonding ends can explain the effects of adhesive thickness on joint strength, as [133,134] believes that there

is a strong interface constraint effect for joints with thinner bondlines. This effect causes higher joint strength. The effect of adhesive thickness on joint strength was deemed to be caused by the bending moment in the work of Grant et al. [135]. Adhesive thickness values of 0.1 to 0.5 mm were shown to be the optimum value in some studies [127,133,136]. Xu and Wei [137] used the cohesive interface concepts to take the effects of adhesive thickness into account in their failure criterion. A coupled stress/strain criterion was used by Moradi et al. [82] where they showed that the strength of SLJs decreases as the bondline thickness increases. Gleich et al. [133] believe that the only theory that could partially consider the effect of adhesive thickness is fracture mechanics, where a crack is assumed to be in the bondline. However, based on a distance method, Akhavan-Safar et al. [68] proposed a finite element method that can precisely predict the negative effects of adhesive thickness on the strength of bonded SLJs. They also showed that by taking the effects of stress triaxiality into account, the effects of the thickness of the bondline in DCB joints can be predicted [79]. Although adhesive thickness effects have been addressed in several works, this is still a challenging and open topic that needs further study, especially from the point of view of the failure load prediction models.

15.8.2 Overlap length

Generally, longer overlap lengths lead to a higher joint strength. However, extending the overlap length does not always result in an improvement in the joint strength. This is due to the nonuniform stress distribution along the bondline, especially for joints with a more brittle adhesive. This nonuniform stress distribution leads to a high stress level at the bonding ends and usually to a lower stress value around the middle of the joint. Increasing the overlap length usually increases the bending moments at the ends of the overlap in lap shear joints. This bending moment strongly limits the maximum strength of the joint. However, it should be noted that the effect of overlap length on the joint's strength is also a function of the adhesive behavior and the stiffness of the substrates. In the case of a high strength adherend with a linear elastic behavior until the joint failure, for very ductile (or flexible) adhesives, because the stress is more uniformly distributed along the overlap, almost a linear relation can be established between the joint strength and the overlap length in an SLJ. In this type of joint, the adhesive layer will experience significant plastic deformation before joint failure. Plastic flow, especially close to the bonding ends, makes the stress level limited at singular points, leading to improved mechanical performance of the joints. However, because the load-bearing capacity of more brittle adhesives is usually higher than that of ductile ones, structural load-bearing joints are usually bonded with high strength and less ductile adhesives. In this case, increasing the overlap length can improve the bond strength only until a certain length is reached. In these joints, strength is limited by the stress level at the bonding ends because the brittle adhesive has just a small resistant area. The adhesive at the middle of the joints does not significantly contribute to load bearing and the effective bonded area is limited to the zones close to the ends of

the overlap. In this case, increasing the overlap length will mainly increase the less effective area in the middle of the joint while the size of the resistant area at bonding ends will remain the same. To benefit from the lower stress level of the joints with ductile adhesives at bonding ends and also to take advantage of the high strength of joints with high-strength and more brittle adhesives, a bi-adhesive technique (mixed adhesive joint) was considered in some studies where the ductile adhesive is placed at bonding ends and in the middle of the joint, the high-strength and brittle adhesive transfers the loads [138,139]. Results showed that this technique can significantly improve the joint strength, especially for joints with bigger overlap lengths. Please note that the above discussion is more closely related to joints with high-strength adherends, with a linear elastic response until the joint failure. However, for more ductile substrates, the joint response to different overlap lengths will be vastly different. For joints with low-strength substrates, the adherends may experience plastic deformation before any adhesive fracture takes place. In this case, the joint strength is mainly limited by the strength of the adherends. For these joints, the increase in overlap length will not linearly increase the joint strength, even with ductile adhesives [140]. The story is again different when composite laminates are used as substrates instead of metal components. Delamination is a common failure mechanism in these cases and is the factor that most often limits the strength of bonded composite joints. However, this failure mechanism is often observed for joints with larger overlap lengths, where the bending moments create higher peel stress levels. Accordingly, similarly to the joints with brittle adhesives, the strength of joints with composite adherends can only be improved up to a certain overlap length. Using stiffer and less brittle adhesives will decrease the optimum overlap length in composite bonded joints. Accordingly, flexible and ductile adhesives are recommended for bonding composites.

15.8.3 Joint width and substrate stiffness

The effects of substrate stiffness and their interaction with overlap length were briefly discussed in the previous section. The influence of substrate stiffness on the joint strength has been already addressed by some authors [141–144]. Accordingly, increasing adherend thickness will increase joint stiffness and consequently decrease joint bending deformation, resulting in a more uniform stress distribution.

In contrast, the effects of the joint (substrate) width have received much less attention from authors. Nonetheless, increasing the joint width is still an effective way to simply improve the load-carrying capacity of a joint because the stress is often uniformly distributed along this direction [145]. However, it should be noted that in real applications, the stress per unit of width is often a critical design factor and increasing the width in these cases cannot be considered a solution to improve joint strength.

Based on the global yielding criterion discussed in [132], a linear increase in joint strength is also expected with joint width. An experimental and numerical study was conducted by Adin and Turgut [146] on Z joints with different widths. They obtained the same results where the strength of the joint increases by the width. In the work of

Gültekin et al. [145], the effect of joint width with respect to the overlap length was analyzed both experimentally and numerically. They found that increasing joint width not only can improve joint strength, but it can also increase the elongation at failure [145]. The main reason behind this behavior is the difference in the stress distribution in joints with different widths. However, the effect of width on the elongation of joints at failure still deserves further investigation.

15.9 Effects of strain rate

Adhesives are viscoelastic (and in some cases viscoplastic) materials, which means that their mechanical properties are a function of the strain (loading) rate applied to the joint. Higher strain rates often lead to higher stiffness, higher strength, and lower ductility of the bonded joints [147]. The opposite effect may be seen when very slow loading rates are applied, as also discussed in Chapter 20. Accordingly, the mechanical performance of the joints is often a function of the imposed rate and any prediction model must take these effects into account. Considering the effect of strain rate in the performance analysis of bonded structures is of paramount importance, especially in the automotive industry where the structures experience high strain rates in crash events (see Chapters 16 and 21 for further details).

To characterize adhesives in terms of strain rate, a simple approach is to test the adhesive at different crosshead rates using universal tensile test machines. However, strain rate effects can be also studied by a dynamic mechanical analysis (DMA). DMA is an established technique for the characterization of polymers and adhesives and can be employed for the characterization of viscoelastic materials. Using this approach, the bulk sample is subjected to a small oscillatory strain and the corresponding stress values can be measured. Another important experiment that is usually considered is the impact test, where the joint (or the bulk adhesive) is subjected to large loading rates [95,96]. The split Hopkinson pressure bar (SHPB), discussed in Chapter 21, is also a widely used approach that provides very high strain rates [148], often using pressurized air for inducing stress waves in long bars that will load the specimens at high rates. The results of these tests help to create safe designs against different loading rates, especially well suited for structures subjected to shock in service. Once the properties of the adhesives have been characterized as a function of the strain rate, FEM can be employed to evaluate the response of the bonded joints [95,96]. It is worth noting that even by keeping the loading rate constant during the test, the adhesive layer may experience different strain rates. This phenomenon has been studied by some authors [149].

15.10 Effects of aging

The degradation of mechanical properties of adhesives exposed to wet environments is one of the main known shortcomings of bonded joints. Extensive studies have been conducted [150–154] to analyze the sensitivity of the mechanical performance of

adhesives to prolonged exposure to humidity. Both the bulk adhesive and the adhesive/adherend interface can experience significant degradation due to the moisture aging mechanism. Moisture can reduce the strength, decrease the stiffness, and increase the ductility of many polymers [155]. It can also significantly degrade the interfacial adhesion properties [156]. Bound water aging occurs where the water molecules bind with the polymer chains and free water aging corresponds to the case where the free spaces of the adhesive are occupied by water molecules; these are the two main types of water uptake processes. After a drying process, the mechanical performance of the bonded joint can be recovered to its initial conditions in some but not all situations. A partial one-dimensional differential equation called Fick's law (proposed by Adolf Fick, see Eq. (15.7)) describes the water absorption behavior of adhesives exposed to a humid environment.

$$\frac{\partial c}{\partial t} = D \frac{\partial^2 c}{\partial x^2} \quad (15.7)$$

where t is time and D is the diffusion coefficient. c in Eq. (15.7) shows the concentration of water.

In real applications, water absorption and desorption procedures repeat frequently and cause cyclic aging phenomena that are considered in some studies [150,152–154]. Considering the aging environments is crucial in mechanical performance and durability analysis of bonded joints. Fig. 15.5 schematically shows the mechanical response of an adhesive joint at different aging levels. Strength prediction models must consider the effects of humidity. Due to the complexity of such problems, FEM is often used to simulate the mechanical performance of the aged adhesive joints where the properties of the elements are defined as a function of the level of water.

As described for the bulk adhesive, the adhesive-adherend interface properties also degrade due to water aging. The rate of interfacial aging is often higher than adhesive aging, leading to an interfacial failure. Also, some authors [150,152] have recently looked at the influence of the interfacial aging mechanisms on the strength of bonded joints. However, considering the interfacial aging phenomenon makes the analysis

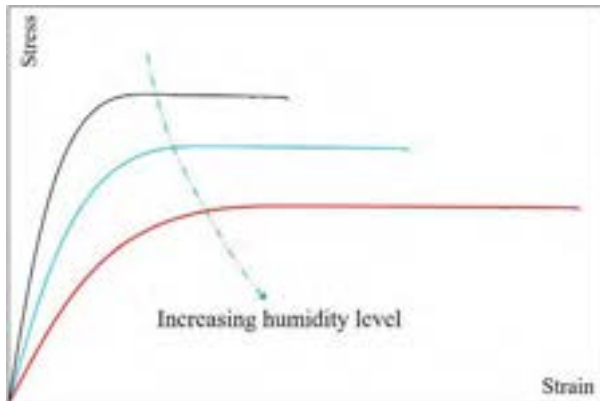


Fig. 15.5 Effects of humidity on the stress strain behavior of adhesives.

complex as no specific testing approach has yet been defined to characterize the interfacial strength of aged adhesive joints.

On the other hand, bound water is known to cause swelling (a dimensional expansion of the adhesive). Swelling can induce residual stresses within the adhesive layer, especially at the edges of the adhesive layer where the water has more direct access. These stresses are due to the restrictions posed by substrates against the adhesive dimensional expansion.

15.11 Effects of temperature

The mechanical performance of bonded joints is highly influenced by the in-service temperature. Generally speaking, increasing the temperature can significantly reduce joint strength and increase the ductility of the adhesives, mainly due to the increase in the mobility of the polymer chains at high temperatures. Not only does this cause a reduction in adhesive strength, but it also leads to the formation of residual stresses induced at high temperature that can also degrade the joint performance. This is especially harmful for joints with dissimilar substrates. Residual stresses are induced due to the difference in the thermal expansion coefficients of the adhesive and the adherends, which often differ by an order of magnitude. Based on the results obtained by the authors, single-lap joints subjected to thermal cycles can experience high levels of residual stresses. Based on the results, increasing the number of thermal cycles increases the longitudinal and transverse residual strains within the adhesive layer. The adhesive layer experiences compressive stresses along the longitudinal direction while thermal cycles induce tensile stresses in the transverse direction. Experimental results have also shown that increasing the adhesive thickness can reduce the residual thermal strains, as predicted by classic stress analyses [15].

It should be noted that in some specific cases, exposure to a high temperature for a specific time can actually improve the strength due to the post curing (and additional polymerization) that the adhesive experiences in this condition. Although high temperature reduces the stiffness and the strength of adhesives, it can improve the fracture energy. Fracture energy is a function of both the strength and ductility of the materials. Increasing the temperature increases the ductility and consequently can improve the fracture energy of the joint. However, this behavior depends on the adhesive system. Further details regarding the effect of temperature, test rate or duration, and aging phenomena can be found in [Chapter 20](#).

15.12 Conclusions

Adhesive bonds are used extensively in many industries. Considering these extensive applications, there is also a growing demand for methodologies that are suitable for predicting the performance of bonded joints. Researchers have long attempted to respond to these needs by introducing a wide range of models suited to different loading conditions, material types, and joint geometries. In this chapter, these models were

briefly discussed. After a brief introduction, the concepts of stress and strain components and the main sources of stress in bonded structures were introduced. Then the failure load prediction models were categorized into analytical approaches, numerical methods, and hybrid analytical-numerical techniques. The effects of joint geometry, strain rate, and environment on adhesive joint performance were also briefly discussed at the end of the chapter.

Considering all the available models, along with the progress in ease of use and capabilities of numerical tools, it can be concluded that analytical models are now finding less applicability in advanced applications, where the joint geometries, boundary conditions, loading conditions, and environmental effects greatly increase the problem complexity and several variables affect the results. Under such conditions, numerical techniques are most appropriate and thus several numerical models have also been proposed by researchers. The simplest of these models are based on continuum mechanics. Among them, models based on the critical distance may be better suited for joints where stresses (strains) at the connection ends are subjected to singular conditions. Models based on fracture mechanics are among the most widely used approaches for analyzing the performance of bonded joints. The presence of a precrack is the main assumption of these models, which makes them better suited for crack propagation studies and not the damage initiation phase. Damage mechanics methods have been attracting more attention lately, with CDM and CZM becoming the most popular damage mechanics-based methods. In contrast to CDM, the crack path should already be defined with the CZM approach. However, because the crack in bonded joints mainly propagates along the bondline, the need for defining the crack line in advance does not significantly limit the usefulness of CZM methods. XFEM is a recently developed extension to the previous approaches, where the crack can propagate not only at the boundary of the elements but also through the elements, which makes it less sensitive to the mesh size. Given the simplicity of the analysis methods and the capability of numerical techniques to solve complex problems, hybrid analytical-numerical methods have been considered by some researchers. The results show that these hybrid methods can accurately predict the performance of adhesively bonded structures. To optimize the mechanical performance of adhesive joints, it is necessary to have an understanding of the effects of joint geometry, strain rate, and environmental conditions on the mechanical behavior of adhesives. Considering the effects of these parameters is essential, as they can significantly alter the behavior of the adhesives. These parameters are mainly considered in the numerical models and especially in CZM-based approaches [10,95,96,109,113,116,157].

References

- [1] O. Volkersen, *Nietkraftverteilung in zugbeanspruchten nietverbindungen mit konstanten laschenquerschnitten*, Luftfahrtforschung I (1938) 15–41.
- [2] G.R. Wooley, D.R. Carver, *Stress Concentration Factors for Bonded Lap Joints*, Louisiana State University and Agricultural and Mechanical College. Division of Engineering Research, 1971.

- [3] G.R. Wooley, D.R. Carver, Stress concentration factors for bonded lap joints, *J. Aircr.* 8 (10) (1971) 817–820.
- [4] F. Erdogan, M. Ratwani, Stress distribution in bonded joints, *J. Compos. Mater.* 5 (3) (1971) 378–393.
- [5] G. Li, P. Lee-Sullivan, Finite element and experimental studies on single-lap balanced joints in tension, *Int. J. Adhes. Adhes.* 21 (3) (2001) 211–220.
- [6] P. Czarnocki, K. Piekarski, Non-linear numerical stress analysis of a symmetric adhesive-bonded lap joint, *Int. J. Adhes. Adhes.* 6 (3) (1986) 157–160.
- [7] G. Richardson, A. Crocombe, P. Smith, A comparison of two- and three-dimensional finite element analyses of adhesive joints, *Int. J. Adhes. Adhes.* 13 (3) (1993) 193–200.
- [8] R.M. Carneiro Neto, et al., Effect of creep on the mode II residual fracture energy of adhesives, *J. Appl. Polym. Sci.* 138 (47) (2021) 51387.
- [9] S. Jalali, et al., Effects of impact fatigue on residual static strength of adhesively bonded joints, *Proc. Inst. Mech. Eng. Part L* (2021), <https://doi.org/10.1177/1464420721994872>.
- [10] J. Monteiro, et al., Mode II modeling of adhesive materials degraded by fatigue loading using cohesive zone elements, *Theor. Appl. Fract. Mech.* 103 (2019), 102253.
- [11] J. Ebadi-Rajoli, et al., Progressive damage modeling of composite materials subjected to mixed mode cyclic loading using cohesive zone model, *Mech. Mater.* 143 (2020), 103322.
- [12] M. Costa, et al., A cohesive zone element for mode I modelling of adhesives degraded by humidity and fatigue, *Int. J. Fatigue* 112 (2018) 173–182.
- [13] A.J. Kinloch, E. Thrusabanjong, J.G. Williams, Fracture at bimaterial interfaces: the role of residual stresses, *J. Mater. Sci.* 26 (23) (1991) 6260–6270.
- [14] H.R. Daghyani, L. Ye, Y.W. Mai, Effect of thermal residual stress on the crack path in adhesively bonded joints, *J. Mater. Sci.* 31 (10) (1996) 2523–2529.
- [15] S. Safaei, et al., Effect of residual strains on the static strength of dissimilar single lap adhesive joints, *J. Adhes.* (2020) 1–20.
- [16] E. Marques, et al., Adhesive joints for low- and high-temperature use: an overview, *J. Adhes.* 91 (7) (2015) 556–585.
- [17] K.H. Lee, D.G. Lee, Smart cure cycles for the adhesive joint of composite structures at cryogenic temperatures, *Compos. Struct.* 86 (1) (2008) 37–44.
- [18] A. Agarwal, S.J. Foster, E. Hamed, Testing of new adhesive and CFRP laminate for steel-CFRP joints under sustained loading and temperature cycles, *Compos. Part B* 99 (2016) 235–247.
- [19] L.F. Da Silva, R. Adams, Stress-free temperature in a mixed-adhesive joint, *J. Adhes. Sci. Technol.* 20 (15) (2006) 1705–1726.
- [20] M. Goland, E. Reissner, The stresses in cemented joints, *J. Appl. Mech.* 11 (1) (1944) A17–A27.
- [21] O. Volkersen, Die Nietkraftverteilung in zugbeanspruchten Nietverbindungen mit konstanten Laschenquerschnitten, *Luftfahrtforschung* 15 (1938) 41–47.
- [22] M. Goland, The stresses in cemented joints, *J. Appl. Mech.* 17 (1944) 66.
- [23] L.J. Hart-Smith, Adhesive-Bonded Single-Lap Joints, National Aeronautics and Space Administration, 1973.
- [24] W. Renton, J. Vinson, Analysis of Adhesively Bonded Joints Between Panels of Composite Materials, 1977.
- [25] D. Allman, A theory for elastic stresses in adhesive bonded lap joints, *Q. J. Mech. Appl. Math.* 30 (4) (1977) 415–436.
- [26] I. Ojalvo, H. Eidinoff, Bond thickness effects upon stresses in single-lap adhesive joints, *AIAA J.* 16 (3) (1978) 204–211.

- [27] F. Delale, F. Erdogan, M. Aydinoglu, Stresses in adhesively bonded joints: a closed-form solution, *J. Compos. Mater.* 15 (3) (1981) 249–271.
- [28] S. Cheng, D. Chen, Y. Shi, Analysis of adhesive-bonded joints with nonidentical adherends, *J. Eng. Mech.* 117 (3) (1991) 605–623.
- [29] D. Bigwood, A. Crocombe, Elastic analysis and engineering design formulae for bonded joints, *Int. J. Adhes. Adhes.* 9 (4) (1989) 229–242.
- [30] D. Bigwood, A. Crocombe, Bonded joint design analyses, in: *Adhesion 13*, Springer, 1989, pp. 163–187.
- [31] D. Bigwood, A. Crocombe, Non-linear adhesive bonded joint design analyses, *Int. J. Adhes. Adhes.* 10 (1) (1990) 31–41.
- [32] A. Crocombe, D. Bigwood, Development of a full elasto-plastic adhesive joint design analysis, *J. Strain Anal. Eng. Des.* 27 (4) (1992) 211–218.
- [33] R. Adams, V. Mallick, A method for the stress analysis of lap joints, *J. Adhes.* 38 (3–4) (1992) 199–217.
- [34] C. Yang, S.-S. Pang, *Stress-Strain Analysis of Single-Lap Composite Joints Under Tension*, 1996.
- [35] D. Oplinger, Effects of adherend deflections in single lap joints, *Int. J. Solids Struct.* 31 (18) (1994) 2565–2587.
- [36] M. Tsai, D. Oplinger, J. Morton, Improved theoretical solutions for adhesive lap joints, *Int. J. Solids Struct.* 35 (12) (1998) 1163–1185.
- [37] Y. Frostig, O.T. Thomsen, F. Mortensen, Analysis of adhesive-bonded joints, square-end, and spew-fillet—high-order theory approach, *J. Eng. Mech.* 125 (11) (1999) 1298–1307.
- [38] F. Mortensen, O.T. Thomsen, Analysis of adhesive bonded joints: a unified approach, *Compos. Sci. Technol.* 62 (7–8) (2002) 1011–1031.
- [39] T. Sawa, K. Nakano, H. Toratani, A two-dimensional stress analysis of single-lap adhesive joints subjected to tensile loads, *J. Adhes. Sci. Technol.* 11 (8) (1997) 1039–1056.
- [40] G. Spies, *The Peeling Test on Redux-bonded Joints: A Theoretical Analysis of the Test Devised by Aero Research Limited*, Aircraft Engineering and Aerospace Technology, 1953.
- [41] D. Kaelble, Peel adhesion, *Adhes. Age* 3 (1960) 37–42.
- [42] K.-S. Kim, N. Aravas, Elastoplastic analysis of the peel test, *Int. J. Solids Struct.* 24 (4) (1988) 417–435.
- [43] A. Kinloch, C. Lau, J. Williams, The peeling of flexible laminates, *Int. J. Fract.* 66 (1) (1994) 45–70.
- [44] A.K. Moidu, A.N. Sinclair, J.K. Spelt, Analysis of the peel test: prediction of adherend plastic dissipation and extraction of fracture energy in metal-to-metal adhesive joints, *J. Test. Eval.* 23 (4) (1995) 241–253.
- [45] L. Hart-Smith, *Adhesive-Bonded Scarf and Stepped-Lap Joints*, 1973.
- [46] P. Grant, *Strength and stress analysis of bonded joints*, British Aircraft Corp. Ltd. Report, 50, 1976.
- [47] F. Mortensen, O.T. Thomsen, Simplified linear and non-linear analysis of stepped and scarfed adhesive-bonded lap-joints between composite laminates, *Compos. Struct.* 38 (1–4) (1997) 281–294.
- [48] J.E. Helms, C. Yang, S.-S. Pang, *A Laminated Plate Model of an Adhesive-Bonded Taper-Taper Joint Under Tension*, 1997.
- [49] D. Gleich, M. Van Tooren, P. De Haan, Shear and peel stress analysis of an adhesively bonded scarf joint, *J. Adhes. Sci. Technol.* 14 (6) (2000) 879–893.

- [50] Y. Nakano, T. Sawa, S. Arai, Stress analysis of an adhesive butt joint with two solid shafts subjected to torsional loading, *Int. J. Adhes. Adhes.* 9 (2) (1989) 83–87.
- [51] T. Sawa, Y. Nakano, K. Temma, Stress analysis of T-type butt adhesive joint subjected to external bending moments, *J. Adhes.* 24 (1) (1987) 1–15.
- [52] M. You, et al., Numerical analysis of adhesive thickness on butt-joints under impact, in: 2011 International Conference on Control, Automation and Systems Engineering (CASE), IEEE, 2011.
- [53] L.F. da Silva, et al., Analytical models of adhesively bonded joints—Part II: comparative study, *Int. J. Adhes. Adhes.* 29 (3) (2009) 331–341.
- [54] A.D. Crocombe, A. Tarek, A unified approach to adhesive joint analysis, in: *Proceeding of Adhesives, Sealants and Encapsulants*, vol. 85, Palastics and Rubber Institute, 1985.
- [55] N. Rahman, et al., Prediction of failure strength of adhesive joints using peel stress and CTOA, in: *Structural Dynamics and Materials Conference*, Denver, Colorado, 2011.
- [56] J.A. Harris, R.D. Adams, Strength prediction of bonded single lap joints by non-linear finite element methods, *Int. J. Adhes. Adhes.* 4 (2) (1984) 65–78.
- [57] K. Ikegami, et al., Strength of adhesively bonded scarf joints between glass fibre reinforced plastics and metals, *Int. J. Adhes. Adhes.* 10 (3) (1990) 199–206.
- [58] L. Goglio, M. Rossetto, E. Dragoni, Design of adhesive joints based on peak elastic stresses, *Int. J. Adhes. Adhes.* 28 (2008) 427–435.
- [59] L.J. Hart-Smith, *Adhesive Bonded Single-Lap Joints*, NASA, Langley Research Centre, 1973.
- [60] S.J. Lee, G.L. Lee, Development of a failure model for the adhesively bonded tubular single lap joint, *J. Adhes.* 40 (1992) 1–14.
- [61] H. Chai, Observation of deformation and damage at the tip of cracks in adhesive bonds loaded in shear and assessment of a criteria for fracture, *Int. J. Fract.* 60 (1993) 311–326.
- [62] L. Tong, Strength of adhesively bonded single lap and lap shear joints, *Int. J. Solids Struct.* 35 (20) (1998) 2601–2616.
- [63] M. Goland, E. Reissner, The stress in cemented joints, *J. Appl. Mech.* 66 (1944) A17–A27.
- [64] R.D. Adam, W.C. Wake, *Structural adhesive joints in engineering*, Elsevier applied science, London, 1984.
- [65] A.D. Crocombe, R.D. Adams, An elastoplastic investigation of the peel test, *J. Adhes.* 13 (1982) 241–267.
- [66] M. Ayatollahi, A. Akhavan-Safar, Failure load prediction of single lap adhesive joints based on a new linear elastic criterion, *Theor. Appl. Mech.* 80 (2015) 210–217.
- [67] H. Khoramshad, et al., Predicting static strength in adhesively bonded single lap joints using a critical distance based method: substrate thickness and overlap length effects, *Proc. Inst. Mech. Eng. Part L* 231 (1–2) (2017) 237–246.
- [68] A. Akhavan-Safar, M. Ayatollahi, L.F.M. da Silva, Strength prediction of adhesively bonded single lap joints with different bondline thicknesses: a critical longitudinal strain approach, *Int. J. Solids Struct.* 109 (2017) 189–198.
- [69] A. Akhavan-Safar, L. da Silva, M. Ayatollahi, An investigation on the strength of single lap adhesive joints with a wide range of materials and dimensions using a critical distance approach, *Int. J. Adhes. Adhes.* 78 (2017) 248–255.
- [70] C. Cruz-G, et al., On the evaluation of a critical distance approach for failure load prediction of adhesively bonded dissimilar materials, *Contin. Mech. Thermodyn.* (2020) 1–11.
- [71] A. Akhavan-Safar, et al., Residual static strength and the fracture initiation path in adhesively bonded joints weakened with interfacial edge pre-crack, *J. Adhes. Sci. Technol.* 32 (18) (2018) 2019–2040.

- [72] G. Sih, B. Macdonald, Fracture mechanics applied to engineering problems-strain energy density fracture criterion, *Eng. Fract. Mech.* 6 (2) (1974) 361–386.
- [73] S.R. Ranade, et al., Characterizing fracture performance and the interaction of propagating cracks with locally weakened interfaces in adhesive joints, *Int. J. Adhes. Adhes.* 82 (2018) 196–205.
- [74] D. Xie, et al., Fracture criterion for kinking cracks in a tri-material adhesively bonded joint under mixed mode loading, *Eng. Fract. Mech.* 72 (2005) 2487–2504.
- [75] B. Chen, D.A. Dillard, The effect of the T-stress on crack path selection in adhesively bonded joints, *Int. J. Adhes. Adhes.* 21 (5) (2001) 357–368.
- [76] B. Chen, D.A. Dillard, Numerical analysis of directionally unstable crack propagation in adhesively bonded joints, *Int. J. Solids Struct.* 38 (38–39) (2001) 6907–6924.
- [77] N.A. Fleck, J.W. Hutchinson, S. Zhigang, Crack path selection in a brittle adhesive layer, *Int. J. Solids Struct.* 27 (13) (1991) 1683–1703.
- [78] B. Chen, et al., Crack path selection in adhesively bonded joints: the roles of external loads and specimen geometry, *Int. J. Fract.* 114 (2) (2002) 167–190.
- [79] A. Akhavan-Safar, et al., The role of T-stress and stress triaxiality combined with the geometry on tensile fracture energy of brittle adhesives, *Int. J. Adhes. Adhes.* 87 (2018) 12–21.
- [80] P. Weissgraeber, D. Leguillon, W. Becker, A review of Finite Fracture Mechanics: crack initiation at singular and non-singular stress raisers, *Arch. Appl. Mech.* 86 (1) (2016) 375–401.
- [81] D. Leguillon, J. Laurencin, M. Dupeux, Failure initiation in an epoxy joint between two steel plates, *Eur. J. Mech. A Solids* 22 (4) (2003) 509–524.
- [82] A. Moradi, D. Leguillon, N. Carrère, Influence of the adhesive thickness on a debonding—an asymptotic model, *Eng. Fract. Mech.* 114 (2013) 55–68.
- [83] A. Akhavan-Safar, et al., Impact of geometry on the critical values of the stress intensity factor of adhesively bonded joints, *J. Adhes. Sci. Technol.* 31 (18) (2017) 2071–2087.
- [84] J. Klusák, T. Profant, M. Kotoul, Various methods of numerical estimation of generalized stress intensity factors of bi-material notches, *Appl. Comput. Mech.* 3 (2) (2009).
- [85] H. Groth, Stress singularities and fracture at interface corners in bonded joints, *Int. J. Adhes. Adhes.* 8 (2) (1988) 107–113.
- [86] J. Dundurs, Discussion: “Edge-bonded dissimilar orthogonal elastic wedges under normal and shear loading” (Bogy, DB, 1968, *ASME J. Appl. Mech.*, 35, pp. 460–466), 1969.
- [87] M. Ayatollahi, M. Mirsayar, M. Dehghany, Experimental determination of stress field parameters in bi-material notches using photoelasticity, *Mater. Des.* 32 (10) (2011) 4901–4908.
- [88] D. Lefebvre, D. Dillard, A stress singularity approach for the prediction of fatigue crack initiation in adhesive bonds. Part 1: theory, *J. Adhes.* 70 (1–2) (1999) 119–138.
- [89] D. Lefebvre, et al., The effect of surface treatments on interfacial fatigue crack initiation in aluminum/epoxy bonds, *Int. J. Fract.* 114 (2) (2002) 191–202.
- [90] D. Lefebvre, D. Dillard, J. Dillard, A stress singularity approach for the prediction of fatigue crack initiation in adhesive bonds. Part 2: experimental, *J. Adhes.* 70 (1–2) (1999) 139–154.
- [91] A. Akhavan-Safar, et al., Fracture energy assessment of adhesives—Part I: is GIC an adhesive property? A neural network analysis, *Proc. Inst. Mech. Eng. Part L* 235 (6) (2021) 1461–1476.
- [92] F. Delzendehrooy, et al., Fracture energy assessment of adhesives Part II: is GIIC an adhesive material property? (A neural network analysis), *J. Adv. Join. Process.* 3 (2021), 100049.

- [93] C. Borges, et al., Influence of mode mixity and loading rate on the fracture behaviour of crash resistant adhesives, *Theor. Appl. Fract. Mech.* (2020), 102508.
- [94] A. Akhavan-Safar, et al., Mode II fracture energy characterization of brittle adhesives using compliance calibration method, *Fatigue Fract. Eng. Mater. Struct.* 43 (9) (2020) 1928–1937.
- [95] C. Borges, et al., A strain rate dependent cohesive zone element for mode I modeling of the fracture behavior of adhesives, *Proc. Inst. Mech. Eng. Part L* 234 (4) (2020) 610–621.
- [96] P.D. Nunes, et al., Numerical assessment of strain rate in an adhesive layer throughout double cantilever beam and end notch flexure tests, *Proc. Inst. Mech. Eng. E J. Process. Mech. Eng.* (2020), <https://doi.org/10.1177/0954408920916007>.
- [97] M.R. Ayatollahi, et al., Effect of notch length and pre-crack size on mode II fracture energy of brittle adhesives, *Eng. Fract. Mech.* 212 (2019) 123–135.
- [98] S. Safaei, et al., A new technique to measure shear fracture toughness of adhesives using tensile load, *International Journal of Solids and Structures* 262-263 (2023), <https://doi.org/10.1016/j.ijsolstr.2022.112091>.
- [99] Aida Faria, et al., Novel mechanical characterization method applied to non-structural adhesives: adherend material sensitivity, *J. Mech. Solids* 1 (2022) 25–30, https://doi.org/10.24840/2975-8262_001-001_001799.
- [100] A. Ajdani, et al., Mixed mode fracture characterization of brittle and semi-brittle adhesives using the SCB specimen, *Int. J. Adhes. Adhes.* 101 (2020), 102629.
- [101] A. Akhavan-Safar, et al., Mixed mode I/III fracture behavior of adhesive joints, *Int. J. Solids Struct.* 15 (2020) 109–119.
- [102] L. Kachanov, *Introduction to Continuum Damage Mechanics*, vol. 10, Springer Science & Business Media, 1986.
- [103] J. García, et al., Characterization and material model definition of toughened adhesives for finite element analysis, *Int. J. Adhes. Adhes.* 31 (4) (2011) 182–192.
- [104] J. Chousal, M. De Moura, Mixed-mode I+ II continuum damage model applied to fracture characterization of bonded joints, *Int. J. Adhes. Adhes.* 41 (2013) 92–97.
- [105] A. Riccio, et al., Numerical investigation of constitutive material models on bonded joints in scarf repaired composite laminates, *Eng. Fract. Mech.* 173 (2017) 91–106.
- [106] Q. Zhang, et al., Investigation of tensile behavior and influence factors of composite-to-metal 2D-scarf bonded joint, *Eng. Struct.* 180 (2019) 284–294.
- [107] M.-H. Kim, H.-S. Hong, An adaptation of mixed-mode I+ II continuum damage model for prediction of fracture characteristics in adhesively bonded joint, *Int. J. Adhes. Adhes.* 80 (2018) 87–103.
- [108] R. Eghbalpoor, et al., A progressive damage model to predict the shear and mixed-mode low-cycle impact fatigue life of adhesive joints using cohesive elements, *Finite Elements in Analysis and Design* 216 (2023), <https://doi.org/10.1016/j.finel.2022.103894>.
- [109] A. Akhavan-Safar, et al., A modified degradation technique for fatigue life assessment of adhesive materials subjected to cyclic shear loads, *Proc. Inst. Mech. Eng. C J. Mech. Eng. Sci.* 235 (3) (2021) 550–559.
- [110] H. Hosseini-Toudeshky, et al., Prediction of interlaminar fatigue damages in adhesively bonded joints using mixed-mode strain based cohesive zone modeling, *Theor. Appl. Fract. Mech.* 106 (2020), 102480.
- [111] A. Akhavan-Safar, et al., Tensile fatigue life prediction of adhesively bonded structures based on CZM technique and a modified degradation approach, *Proc. Inst. Mech. Eng. G J. Aerosp. Eng.* 234 (13) (2020) 1988–1999.

- [112] R.C. Neto, et al., A customized shear traction separation law for cohesive zone modelling of creep loaded ENF adhesive joints, *Theor. Appl. Fract. Mech.* 119 (2022), 103336.
- [113] Akhavan-Safar, A., et al., *Cohesive Zone Modelling for Fatigue Life Analysis of Adhesive Joints*. Springer.
- [114] Z. Chen, R.D. Adams, L.F.M. da Silva, Prediction of crack initiation and propagation of adhesive lap joints using an energy failure criterion, *Eng. Fract. Mech.* 78 (6) (2011) 990–1007.
- [115] N. Chandra, et al., Some issues in the application of cohesive zone models for metal–ceramic interfaces, *Int. J. Solids Struct.* 39 (10) (2002) 2827–2855.
- [116] A. Akhavan-Safar, et al., Cohesive zone modelling–CZM, in: *Cohesive Zone Modelling for Fatigue Life Analysis of Adhesive Joints*, Springer, 2022, pp. 19–42.
- [117] S. Sugiman, H. Ahmad, Comparison of cohesive zone and continuum damage approach in predicting the static failure of adhesively bonded single lap joints, *J. Adhes. Sci. Technol.* 31 (5) (2017) 552–570.
- [118] I. Singh, et al., The numerical simulation of fatigue crack growth using extended finite element method, *Int. J. Fatigue* 36 (1) (2012) 109–119.
- [119] H. Pathak, A. Singh, I.V. Singh, Fatigue crack growth simulations of 3-D problems using XFEM, *Int. J. Mech. Sci.* 76 (2013) 112–131.
- [120] M. Sabsabi, E. Giner, F. Fuenmayor, Experimental fatigue testing of a fretting complete contact and numerical life correlation using X-FEM, *Int. J. Fatigue* 33 (6) (2011) 811–822.
- [121] Y. Xu, H. Yuan, Computational analysis of mixed-mode fatigue crack growth in quasi-brittle materials using extended finite element methods, *Eng. Fract. Mech.* 76 (2) (2009) 165–181.
- [122] G.N. Wells, L. Sluys, A new method for modelling cohesive cracks using finite elements, *Int. J. Numer. Methods Eng.* 50 (12) (2001) 2667–2682.
- [123] J. Mergheim, E. Kuhl, P. Steinmann, A finite element method for the computational modelling of cohesive cracks, *Int. J. Numer. Methods Eng.* 63 (2) (2005) 276–289.
- [124] Y. Zhang, N.-A. Noda, K. Takaishi, Effects of geometry on intensity of singular stress fields at the corner of single-lap joints, *World Acad. Sci. Eng. Technol.* 79 (2011) 911–916.
- [125] S. Rastegar, et al., Prediction of the critical stress intensity factor of single-lap adhesive joints using a coupled ratio method and an analytical model, *Proc. Inst. Mech. Eng. Part L* 233 (7) (2019) 1393–1403.
- [126] T. Pardoen, et al., Constraint effects in adhesive joint fracture, *J. Mech. Phys. Solids* 53 (9) (2005) 1951–1983.
- [127] L.F. da Silva, et al., Mode II fracture toughness of a brittle and a ductile adhesive as a function of the adhesive thickness, *J. Adhes.* 86 (9) (2010) 891–905.
- [128] D. Castagnetti, A. Spaggiari, E. Dragoni, Effect of bondline thickness on the static strength of structural adhesives under nearly-homogeneous shear stresses, *J. Adhes.* 87 (7–8) (2011) 780–803.
- [129] E. Reedy, T. Guess, Interface corner failure analysis of joint strength: effect of adherend stiffness, *Int. J. Fract.* 88 (4) (1997) 305–314.
- [130] K. Naito, M. Onta, Y. Kogo, The effect of adhesive thickness on tensile and shear strength of polyimide adhesive, *Int. J. Adhes. Adhes.* 36 (2012) 77–85.
- [131] A. Crocombe, A. Moul, The effect of the adhesive thickness on the strength of a bonded joint, in: *Adhesion 12*, Springer, Netherlands, 1988, pp. 174–192.
- [132] A.D. Crocombe, Global yielding as a failure criterion for bonded joints, *Int. J. Adhes. Adhes.* 9 (1989) 145–153.

- [133] D. Gleich, M. Van Tooren, A. Beukers, Analysis and evaluation of bondline thickness effects on failure load in adhesively bonded structures, *J. Adhes. Sci. Technol.* 15 (9) (2001) 1091–1101.
- [134] D.-B. Lee, et al., Effect of bond thickness on the fracture toughness of adhesive joints, *J. Eng. Mater. Technol.* 126 (1) (2004) 14–18.
- [135] L. Grant, R. Adams, L.F. da Silva, Experimental and numerical analysis of single-lap joints for the automotive industry, *Int. J. Adhes. Adhes.* 29 (4) (2009) 405–413.
- [136] J.M. Arenas, J.J. Narbón, C. Alía, Optimum adhesive thickness in structural adhesives joints using statistical techniques based on Weibull distribution, *Int. J. Adhes. Adhes.* 30 (3) (2010) 160–165.
- [137] W. Xu, Y. Wei, Influence of adhesive thickness on local interface fracture and overall strength of metallic adhesive bonding structures, *Int. J. Adhes. Adhes.* 40 (2013) 158–167.
- [138] A. Akhavan-Safar, et al., A review on bi-adhesive joints: benefits and challenges, *Int. J. Adhes. Adhes.* (2022), 103098.
- [139] F. Ramezani, et al., A comprehensive experimental study on bi-adhesive single lap joints using DIC technique, *Int. J. Adhes. Adhes.* 102 (2020), 102674.
- [140] L.F.M. da Silva, A. Öchsner, R.D. Adams, *Handbook of Adhesion Technology*, vol. 1, Springer, 2018.
- [141] A.M. Pereira, et al., Analysis of manufacturing parameters on the shear strength of aluminium adhesive single-lap joints, *J. Mater. Process. Technol.* 210 (2010) 610–670.
- [142] L.F. Da Silva, et al., Effect of material, geometry, surface treatment and environment on the shear strength of single lap joints, *Int. J. Adhes. Adhes.* 29 (6) (2009) 621–632.
- [143] A.B. Morais, et al., Strength of epoxy adhesive bonded stainless steel joints, *Int. J. Adhes. Adhes.* 27 (2007) 679–686.
- [144] M.D. Aydin, A. Özel, S. Temiz, The effect of adherend thickness on the failure of adhesively-bonded single-lap joints, *J. Adhes. Sci. Technol.* 19 (8) (2005) 705–718.
- [145] K. Gültekin, S. Akpınar, A. Özel, The effect of the adherend width on the strength of adhesively bonded single-lap joint: experimental and numerical analysis, *Compos. Part B* 60 (2014) 736–745.
- [146] H. Adin, A. Turgut, The effects of width on the strength of adhesively bonded Z joints subjected to tensile loads, *J. Adhes.* 89 (1) (2013) 1–18.
- [147] M. Perez, et al., Loading rate and temperature interaction effects on the mode I fracture response of a ductile polyurethane adhesive used in the automotive industry, *Materials* 15 (2022), <https://doi.org/10.3390/ma15248948>.
- [148] P. Nunes, et al., kQuasi-static and intermediate test speed validation of SHPB specimens for the determination of mode I, mode II fracture toughness of structural epoxy adhesives, *Eng. Fract. Mech.* (2022), 108231.
- [149] P. Nunes, et al., DCB tests at constant strain rate using crash-resistant epoxy adhesives: a numerical and experimental approach, *Proc. Inst. Mech. Eng. Part D* 235 (13) (2021) 3234–3242.
- [150] J. Da Costa, et al., Cyclic ageing of adhesive materials, *J. Adhes.* (2021) 1–17.
- [151] F. Delzendehrooy, et al., Investigation of the mechanical performance of hybrid bolted-bonded joints subjected to different ageing conditions: effect of geometrical parameters and bolt size, *J. Adv. Join. Process.* (2022), 100098.
- [152] J. Da Costa, et al., Effects of cyclic ageing on the tensile properties and diffusion coefficients of an epoxy-based adhesive, *Proc. Inst. Mech. Eng. Part L* 235 (6) (2021) 1451–1460.

-
- [153] M. Moazzami, et al., Influence of cyclic aging on adhesive mode mixity in dissimilar composite/metal double cantilever beam joints, *Proc. Inst. Mech. Eng. Part L* (2022), <https://doi.org/10.1177/14644207221074696>.
- [154] M. Moazzami, et al., Experimental and numerical analysis of cyclic aging in an epoxy-based adhesive, *Polym. Test.* 91 (2020), 106789.
- [155] F. Lopes, et al., The interaction of loading mode and humidity on the properties degradation of an epoxy adhesive subjected to strength, fracture, and fatigue tests, *J. Appl. Polym. Sci.* 140 (7) (2022), <https://doi.org/10.1002/app.53490>.
- [156] Guilherme do Vale, et al., Effects of mode mixity on the failure mechanism of aged adhesive joints, *J. Mech. Solids* 1 (2022), https://doi.org/10.24840/2975-8262_001-001_001838.
- [157] A. Rocha, et al., Numerical analysis of mixed-mode fatigue crack growth of adhesive joints using CZM, *Theor. Appl. Fract. Mech.* (2020), 102493.

This page intentionally left blank

Innovations in fracture testing of structural adhesive bonds

16

Stephan Marzi

University of Applied Sciences Mittelhessen, Institute of Mechanics and Materials, Gießen, Germany

16.1 Introduction

In recent years, adhesive bonding has been increasingly applied to join parts in light-weight structures that are subject to strict safety requirements. Gathering information about the structural integrity of such adhesive bonds is one of the basic requirements for a proper design of the individual connection as well as the entire structure. During the past decades, lots of research activities focused on fracture mechanics characterization of adhesive joints. Motivated by the manifold challenges arising from industrial applications, the focus has been put on modifications of established test setups to cover different loading conditions such as mixed-mode loading, fatigue, and aging, as well as creep or highly dynamic and impact loading. A literature review of fracture mechanics testing has been given by Chaves et al. [1]. More detailed information can also be found in relevant textbooks (e.g., [2, 3]).

Besides testing methods, related evaluation and data reduction methods have been improved in the past. Until the 1990s, most data reduction schemes were based on linear elastic fracture mechanics (LEFM), applying Griffith's theory and the Irwin-Kies equation to evaluate fracture toughness and critical energy release rate from experimental data.

In the last two decades, J-integral, which was proposed in the late 1960s independently by Cherepanov [4] and Rice [5], found its way into fracture testing of adhesive joints. The J-integral represents a quantity of nonlinear elastic field theory and allows the consideration of nonlinear mechanical behavior at the crack tip prior to fracture, as quite often occurs in polymer materials such as adhesives. When testing bonded beam-like specimens with elastic adherends, LEFM and J-integral agree with each other.

Further considerations of these approaches (e.g., [6, 7]) opened up the possibility of obtaining information about the stress state at the crack tip location and using these data as parameters for cohesive zone models (CZM). This class of models provides a simple and computational cost-efficient method to account for interface and bond failures in numerical simulations of large and complex structures, such as automotive crash simulations.

This chapter is intended to provide a comprehensive overview of the latest developments in fracture testing, particularly over the past two decades. First, established data reduction methods based on LEFM are briefly summarized and compared with

the J-integral approach, as the latter is increasingly used to evaluate experiments with nonlinear fracture behavior. Then, the focus is on new and further developments of fracture mechanics test setups that were applied to adhesive joints. Recent modifications of established test methods to cover special load and environmental conditions are discussed in the following two subsections. The chapter closes with an outlook on future trends.

16.2 Data reduction techniques

Fracture mechanics test methods must be sensitive with regard to the fracture energy, as this is the quantity of interest. In the past, several data reduction methods have been established to obtain the fracture energy from experimental data. Most data reduction methods rely on an accurate measurement of the crack length, but there are also crack-independent expressions that are preferred when the crack tip is difficult to detect.

16.2.1 Measurement of released energy and crack length

Probably the simplest solution is to determine the released energy, which is the energy delivered to growing the debond, by integrating the force-displacement data and then dividing by the area of the crack surface. This approach has two main disadvantages. In many cases, it is difficult to get an accurate measurement of the area of crack surface, especially if no arrest lines are detectable in the fracture pattern. In addition, the determined fracture energy represents an average value for the entire experiment and not an instantaneous quantity. However, if the adhesive fractures are very brittle, such a simple approach is often recommended, such as by DIN EN 6033:2016-02 [8]. Blackman et al. [9] postulated that in brittle fracture the force-displacement data upon unloading should be expected as a straight line to the origin and based on this assumption calculated the released energy without unloading the sample. Marzi et al. [10] proposed a modification of that simple proceeding, which is illustrated in Fig. 16.1. In experiments with stable crack growth on an elastic-plastic adhesive, they established different cumulated crack lengths and identified the critical energy release rate G_{Ic} as the slope of a linear regression between the released energy, which has been in difference to Blackman et al. [9] obtained in a load cycle and the associated crack length. The regression section with the axis of the released energy, W_{init} , was interpreted as the energy stored near the crack tip before the crack propagation. It was deduced from this that cracks should be of sufficient length if the fracture energy is assessed according to DIN EN 6033:2016-02 [8].

For more general cases, several data reduction schemes have been established to determine an instantaneous fracture energy. These can be divided into approaches based on LEFM and NLEFM. The procedures mentioned are described in more detail in the following subsections.

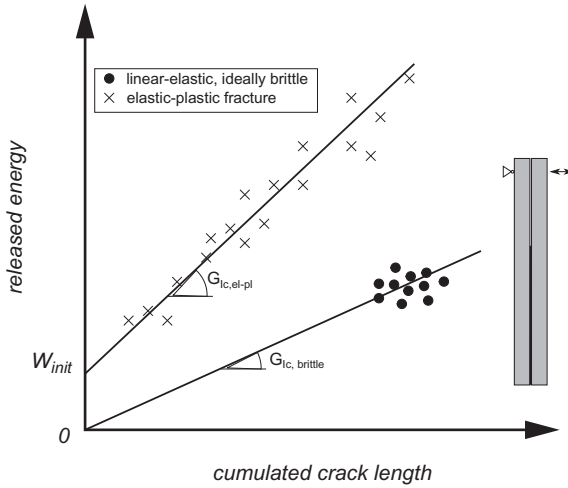


Fig. 16.1 A schematic illustration of released energy versus cumulated crack length for two kinds of adhesive joints.

16.2.2 The Irwin-Kies equation

In fracture mechanics tests as well as in real structures, crack propagation is usually not a continuous process in time. Cracks accelerate and slow down, or if stick-slip fractures occur, they may arrest for a while before the crack suddenly advances. Hence, an instantaneous fracture energy is required to more generally describe and understand a fracture.

Fig. 16.2 shows the displacement-force data as they may have been recorded during a fracture experiment on linear elastic material in force control. When force is increased from zero, the related displacement of the load introduction point increases proportionally to the force due to linear elastic behavior. At point ①, sudden fracture

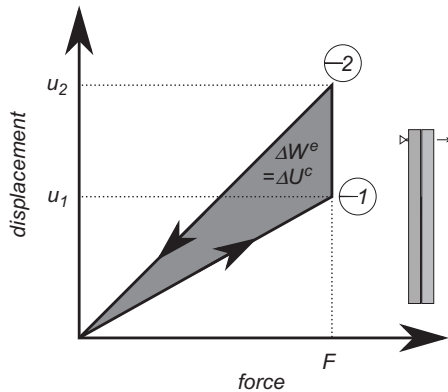


Fig. 16.2 Illustration of displacement versus force data from fracture test.

occurs and the displacement jumps from u_1 to u_2 while the force F remains constant. Afterward, the specimen is completely unloaded and due to the linear behavior, the recorded data show a straight line from point ② to the origin. Because the material behavior is considered as linear elastic, the amounts of complementary energy U^c and elastic energy W^e are the same. The released energy ΔW^e can then be determined by subtracting the elastically stored energy values in the states ② and ①, which graphically expresses the area of the shaded triangle in Fig. 16.2,

$$\Delta W^e = \frac{1}{2}F(u_2 - u_1) = \frac{1}{2}F\Delta u. \quad (16.1)$$

Division by the area $\Delta A_c = b\Delta a$ of the cracked surface gives the mean fracture energy,

$$\bar{G}_c = \frac{\Delta W^e}{b\Delta a} = \frac{F}{2b} \frac{\Delta u}{\Delta a}. \quad (16.2)$$

In these equations, b is the (constant) specimen width and Δa the change in crack length. The instantaneous fracture energy (or energy release rate) G_c is obtained in the limit case $\Delta a \rightarrow 0$, in which $\Delta u = u_2 - u_1 \rightarrow 0$,

$$G_c = \lim_{\Delta a \rightarrow 0} \bar{G}_c = \frac{F}{2b} \frac{du}{da}. \quad (16.3)$$

Introducing the infinitesimal compliance change $dC = du/F$ (infinitesimal crack growth occurs instantaneously at constant force) leads to

$$G_c = \frac{F^2}{2b} \frac{dC}{da}, \quad (16.4)$$

which is the well-known equation by Irwin and Kies [11].

The Irwin-Kies equation allows an instantaneous determination of the critical energy release rate. While the specimen width and the force can easily be measured in situ during an experiment, the change in compliance during crack growth dC/da has to be known in advance, for example, by performing preliminary tests. In addition, dC/da is not a constant value for most specimen geometries, which require an identification of the crack tip position during the experiment. The established methods for test evaluation based on the Irwin-Kies equation are briefly presented and discussed in Sections 16.2.3–16.2.5.

16.2.3 Simple beam theory (SBT)

One of the simplest approaches to get dC/da is derived from simple beam theory (SBT), which assumes clamping perfectly encastred of the cantilever beams at the crack tip and an infinitely stiff and brittle adhesive. The end deflection δ_0 of a single cantilever of length a , as shown in Fig. 16.3, with a rectangular cross section is given by

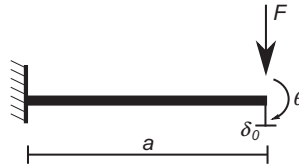


Fig. 16.3 Illustration of cantilever loaded by force.

$$\delta_0 = \left(\frac{a^3}{3EI} + \frac{a}{\kappa\mu A} \right) F = C(a)F, \quad (16.5)$$

where E and μ are Young's and shear modulus, respectively, $A = bh$ the area of the cross section, $I = bh^3/12$ the second moment of area, and $\kappa = 5/6$ the shear correction factor for a rectangular cross section. The first term in Eq. (16.5) contains the influence of the bending on the deflection, the second the influence of the shear force. Assuming further a Poisson ratio $\nu = 1/3$, which is a good approximation such as for metallic substrates, the compliance of the cantilever yields,

$$C(a) = \frac{4}{Eb} \left(\frac{a^3}{h^3} + \frac{a}{h} \right). \quad (16.6)$$

Deriving with respect to crack tip position a leads to

$$\frac{dC}{da} = \frac{4}{Eb} \left(\frac{3a^2}{h^3} + \frac{1}{h} \right) \quad (16.7)$$

for one single cantilever beam, and to

$$\frac{dC}{da} = \frac{8}{Eb} \left(\frac{3a^2}{h^3} + \frac{1}{h} \right) \quad (16.8)$$

for a double cantilever beam (DCB). Eq. (16.8) is recommended by relevant standards, e.g., in ISO 25217:2009-05 [12]. In DCB samples, dC/da depends on the actual crack length and is a constant for tapered DCB.

In impact testing, the force F is often not reliable for the evaluation due to noisy signals while the displacement δ_0 can be determined more reliably. If one neglects the small contribution of shear to the beam deflection, Eqs. (16.4) and 16.8 combine to

$$G_I = \frac{F^2}{2b} \frac{dC}{da} = \frac{F^2}{b} \frac{12a^2}{Eb h^3} = \frac{F^2 a^2}{bEI}. \quad (16.9)$$

After inserting

$$F = \frac{3EI}{2a^3} \delta_0, \quad (16.10)$$

Eq. (16.9) yields

$$G_I = \frac{9EI}{4ba^4} \delta_0^2, \quad (16.11)$$

which has been used, such as by Cognard [13], to evaluate wedge tests or by Xu and Dillard [14] to evaluate drop tower tests. A disadvantage is that Eq. (16.11) is very sensitive with regard to an exact determination of a (if the crack propagation values are of interest) because the crack length contributes in the fourth power in the denominator. In the case that the crack length cannot be reliably measured, crack-independent formulas to compute fracture energy may be preferred. Combining Eqs. (16.10) and 16.11 yields

$$G_I = \left(\frac{3}{2}\right)^{\frac{2}{3}} \frac{F^{\frac{4}{3}} \delta_0^{\frac{2}{3}}}{b(EI)^{\frac{1}{3}}}, \quad (16.12)$$

which is independent of crack length. A second crack-independent expression is obtained by considering the beam rotation θ at the load introduction point, which is

$$\theta = \frac{Fa^2}{2EI} \quad (16.13)$$

according to beam theory. Combining Eqs. (16.9) and 16.13 yields

$$G_I = \frac{2F\theta}{b}, \quad (16.14)$$

which is additionally independent of the bending stiffness EI . Consequently, only two instead of three of the five quantities F , δ_0 , a , θ , and EI contribute to the calculation of G , which reduces the measurement uncertainty from an experimental point of view. Eq. (16.14) further agrees with Eq. (16.25), which will be derived later from the J-integral.

For a comprehensive discussion of various expressions related to SBT, the reader is referred to Biel et al. [15].

16.2.4 Corrected beam theory (CBT)

The SBT usually underestimates compliance because it assumes a perfectly built-in beam. In reality, there will be additional compliance due to the adhesive layer. This additional compliance is considered in CBT by assuming a slightly longer crack length $a + \Delta$. The respective value for the extension Δ can be determined experimentally by linear regression by plotting $C^{1/3}$ over a for measurement data. Because Δ is an extrapolated intercept from a linear regression, it can be subject to a fairly large standard error of estimate. For further correction options, such as with regard to the influence of load blocks, reference is made to further literature (e.g., [16]).

16.2.5 Experimental compliance method (ECM)

Another approach to get dC/da is the experimental compliance (or Berry) method (ECM), where the logarithm of the compliance is plotted against the logarithm of the crack length for DCB tests. For tapered beam geometries, $C(a)$ should be linear. With this method, only the crack propagation values are used in the analysis; crack initiation is not taken into account. The interested reader is referred to further literature, such as [17].

16.2.6 The J-integral

In addition to linear elastic approaches for evaluating fracture tests, as used in relevant standards such as ISO 25217:2009-05 [12], the J-integral is becoming increasingly popular for determining the fracture energy. To better understand the advantages and limitations of that quantity from nonlinear field theory, a brief derivation is given below. More details can be found in Rice [5] or Eshelby [6].

The elastic energy density per unit undeformed volume W of an arbitrary nonlinear elastic body can be given as the function of the displacement vector in space \mathbf{u} , the material position vector \mathbf{a} , and the material displacement gradient tensor $\nabla_{\mathbf{a}}\mathbf{u} = \partial\mathbf{u}/\partial\mathbf{a}$,

$$W = \hat{W}(\mathbf{u}, \nabla_{\mathbf{a}}\mathbf{u}, \mathbf{a}). \tag{16.15}$$

From Hamilton’s principle,

$$\int W \, dV \rightarrow \text{minimum} \tag{16.16}$$

follows

$$\text{div} \underbrace{\frac{\partial W}{\partial(\nabla_{\mathbf{a}}\mathbf{u})}}_{=:\mathbf{P}} = \underbrace{\frac{\partial W}{\partial\mathbf{u}}}_{=\mathbf{b}}, \tag{16.17}$$

which is the balance law (equilibrium equations) in nonlinear field theory. In the most common cases in which the rigid body movement does not affect W , Eq. (16.15) is reduced to

$$W = \hat{W}(\nabla_{\mathbf{a}}\mathbf{u}, \mathbf{a}) \tag{16.18}$$

and Eq. (16.17) reduces to a conservation law,

$$\text{div} \frac{\partial W}{\partial(\nabla_{\mathbf{a}}\mathbf{u})} = \text{div } \mathbf{P} = \mathbf{0}, \tag{16.19}$$

which means that the first Piola-Kirchhoff stress tensor ${}^I\mathbf{P}$ is conserved, as its divergence in material coordinates disappears in the absence of body forces \mathbf{b} . In addition, W depends on \mathbf{a} only in the presence of inhomogeneities as plastic effects, residual stresses, or defects (as it is a crack tip). After introducing the stress-momentum tensor \mathbf{P} as a Legendre transform of W ,

$$\mathbf{P} = W\mathbf{g}_i \otimes \mathbf{g}_i - {}^I\mathbf{P}^T \cdot \nabla_{\mathbf{a}}\mathbf{u}, \tag{16.20}$$

with the three material base vectors \mathbf{g}_i ($i = 1, 2, 3$) and Einstein's summation convention, the explicit material gradient $\nabla_{\mathbf{a}}^{\text{ex}}$ of W yields

$$\nabla_{\mathbf{a}}^{\text{ex}}W = \text{div } \mathbf{P}. \tag{16.21}$$

The physical meaning of Eq. (16.21) can be interpreted by Noether's theorem [18]: If the material is homogeneous, then the stress-momentum tensor \mathbf{P} is a conserved quantity. In the case of inhomogeneities, its divergence gives the dissipated energy density per undeformed volume unit due to the inhomogeneity.

In the following, we dedicate ourselves to the application of Eq. (16.21) to the evaluation of fracture tests on adhesive bonds. We consider an adhesively bonded DCB specimen as shown in Fig. 16.4 of constant width b as body \mathcal{B} with boundary $\partial\mathcal{B}$. The body is homogeneous in the material direction \mathbf{g}_1 while it is inhomogeneous in material direction \mathbf{g}_2 due to dissimilar materials (adhesive and adherends). Obviously, the crack will propagate in material direction \mathbf{g}_1 and the crack tip is located on the boundary $\partial\mathcal{B}$, but not inside \mathcal{B} . Consequently, the body is free of inhomogeneities and the integral of Eq. (16.21) over the volume of the body vanishes,

$$\int_{\mathcal{B}} \nabla_{\mathbf{a}}^{\text{ex}}W \, dV = \int_{\mathcal{B}} \text{div } \mathbf{P} \, dV = \mathbf{0}. \tag{16.22}$$

Applying the divergence theorem, Eq. (16.22) can be transformed to a surface integral,

$$\oint_{\partial\mathcal{B}} (\mathbf{P} \cdot \mathbf{n}) \, dS = \mathbf{0}, \tag{16.23}$$

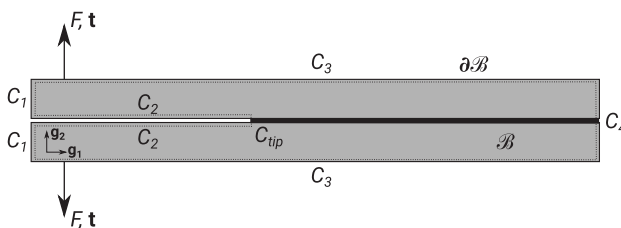


Fig. 16.4 DCB specimen as homogeneous body \mathcal{B} .

with \mathbf{n} being an outward pointing normal vector on $\partial\mathcal{B}$. Because the crack will propagate in material direction \mathbf{g}_1 , only the corresponding component of Eq. (16.23) is of interest for the analysis of fracture energy. More formally, W must not depend explicitly on \mathbf{a} in the direction of crack growth while such dependence is permissible in all other directions. The \mathbf{g}_1 -component of Eq. (16.23) yields under consideration of Eq. (16.20) after normalization on specimen width b

$$\oint_C (W\mathbf{n} - \mathbf{t} \cdot \nabla_{\mathbf{a}}\mathbf{u}) \cdot \mathbf{g}_1 \, ds = 0, \tag{16.24}$$

with $\mathbf{t} = {}^t\mathbf{P} \cdot \mathbf{n}$. Furthermore, the closed integration path C is divided into several subsections C_1 to C_4 and C_{tip} , as illustrated in Fig. 16.4. The contribution of C_{tip} to the integral in Eq. (16.24) is the energy release rate, and it is equal to the sum of contributions from C_1 to C_4 , which can be calculated from external loads. They are as follows:

- C_1 : $W = 0$ and $\mathbf{t} = \mathbf{0}$. Hence, the contribution is
- C_1 : $W = 0$ and $\mathbf{t} = \mathbf{0}$. Hence, the contribution is 0.
- C_2 : $\mathbf{n} \cdot \mathbf{g}_1 = 0$ and $\mathbf{t} = \mathbf{0}$ everywhere. Hence, the contribution is
- C_2 : $\mathbf{n} \cdot \mathbf{g}_1 = 0$ and $\mathbf{t} = \mathbf{0}$ everywhere. Hence, the contribution is 0.
- C_3 : $\mathbf{n} \cdot \mathbf{g}_1 = 0$ everywhere. The contribution is $\mathbf{t} \cdot \nabla_{\mathbf{a}}u \cdot \mathbf{g}_1 = -F_k\theta_k/b$ at locations where concentrated forces F_k act on the specimen. θ_k is the rotation of the adherend at the location of F_k .
- C_4 : $W = 0$ and $\mathbf{t} = \mathbf{0}$ if the specimen length is sufficiently large. Hence, the contribution is
- C_4 : $W = 0$ and $\mathbf{t} = \mathbf{0}$ if the specimen length is sufficiently large. Hence, the contribution is 0.

In summary, the energy release rate J_{tip} (or simply J) is defined as the quantity being in equilibrium with the external contributions,

$$J := \frac{\sum_{k=1}^N F_k\theta_k}{b}. \tag{16.25}$$

Eq. (16.25) was proposed by Paris and Paris [7] to evaluate DCB tests and is often used by many authors. A modification to take into account external torques instead of forces can be found in Fernlund et al. [19] and Loh and Marzi [20]. In summary, the following conclusions can be drawn from the presented derivation:

- The J-integral is a quantity from the theory of nonlinear elastic fields. It is not a quantity related to plasticity, as is sometimes stated.
- The potential W must exist and it must not depend explicitly on the material coordinates in the direction of crack growth. In all other directions, such an explicit dependence is permissible. This enables, for example, adhesive joints (where the adherends and adhesive consist of different materials), notches, or similar geometric features to be taken into account to ensure straight crack growth or to avoid plastic deformations within the adherends.
- The locations where the load is applied to the specimen are arbitrary. This is due to the characteristics of the stress-momentum tensor, the divergence of which only depends on material inhomogeneities and not on the load.

- The inhomogeneity is assumed to be a point. In the case of large damage zones in front of the crack tip, as often occurs with thick, soft adhesive layers, J-integral cannot be suitable for the test evaluation.
- The crack tip must be the only material inhomogeneity. Adherends must not deform plastically during the tests. However, the plastic energy dissipation at the point of the crack tip can be merged with the energy needed to form new surfaces. This allows elastic-plastic adhesives to be analyzed on the basis of the J-integral as long as plasticity and damage occur locally at the crack tip and there is no need to distinguish between them.
- If elastic-plastic adhesive joints are studied, the specimen must be monotonically loaded, as all local nonlinear effects at the crack tip are assumed to be elastic.
- Nonlinear mechanical response of the adhesive layer is allowed while it is not necessary to know the crack tip position. There is no influence of dC/da (or assumptions made about it).

However, when applied to beam-like specimens (such as those commonly used for bonded joints), there is obviously no difference between J-integral and SBT, as both methods provide the same expressions for calculating fracture energy (Eqs. 16.14 and 16.25). Rather, the two methods open up different perspectives for the interpretation and understanding of fracture processes. In contrast to beam theory, the J-integral is a more general approach, used for example to assess the integrity of a complex structure and not just for test evaluation.

As a disadvantage of using the J-integral to evaluate tests, the required accurate measurement of the adherend rotations at the load introduction points increases the experimental effort significantly. Various types of sensors and methods for measuring the rotations can be found in the literature:

- Incremental shaft encoders, for example, in Andersson and Stigh [21]
- Inclinometers, for example, in Manterola et al. [22]
- Digital image correlation, for example, in Sun and Blackman [23]
- Self-made sensors based on linear variable differential transformers (LVDT), for example, in Stigh et al. [24]
- Self-made sensors based on video analysis, for example, in Stigh et al. [25]
- Potentiometers (no references, possibly due to poor resolution at small angles)

16.2.7 Direct extraction of constitutive equations (CZM)

The failure of adhesive joints due to mechanical loading is commonly predicted in finite element (FE) simulations using cohesive zone models (CZMs). This class of fracture models was introduced by Dugdale [26] and Barenblatt [27]; several types of specific models are available in commercial FE software today. The constitutive equations of these CZMs are traction-separation laws (TSL) that have been extracted directly from experimental data by several authors (e.g., [25, 28–31]).

As already stated in the original publication by Rice [5], the J-integral can be obtained by integration of the TSL at the crack tip in the one-dimensional case of peel loading (Mode I),

$$J = \int_0^u \sigma(\hat{u}) d\hat{u}, \text{ or} \quad (16.26)$$

$$dJ = \sigma(\hat{u}) d\hat{u} \quad (16.27)$$

with the peel crack opening displacement (COD) u and the corresponding peel stress σ . The TSL in Mode I, $\sigma(u) = dJ/du$, is then obtained directly from experimental data. From a very practical point of view, such a derivation can be problematic due to scatter of the experimental data. Several approaches for overcoming difficulties, such as fitting data through analytical functions or using filters to smooth data prior to numerical derivation, can be found in the literature.

Extension of the preceding to the case of mixed-mode loading yields

$$J = \int_0^{\delta} \mathbf{t}(\hat{\boldsymbol{\delta}}) \cdot d\hat{\boldsymbol{\delta}}, \text{ or} \quad (16.28)$$

$$dJ = \mathbf{t}(\hat{\boldsymbol{\delta}}) \cdot d\hat{\boldsymbol{\delta}}, \quad (16.29)$$

with the traction vector $\mathbf{t} = [\sigma, \tau_2, \tau_3]^T$ and the COD vector $\boldsymbol{\delta} = [u, v, w]^T$. However, in contrast to the one-dimensional case, Eq. (16.29) can only be integrated to Eq. (16.28) if the vector field of traction $\mathbf{t}(\boldsymbol{\delta})$ fulfills the requirements for integrability,

$$\nabla_{\boldsymbol{\delta}} \times \mathbf{t} = \mathbf{0}, \quad (16.30)$$

or in other words, the curl of \mathbf{t} must vanish. This can be interpreted as traction being the gradient of J with respect to the COD, $\mathbf{t} = \nabla_{\boldsymbol{\delta}} J$. In such a case, J-integral would play the role of a (pseudo)potential, from which the constitutive equations of the CZMs can be derived. However, it is not to be expected that such assumptions of the model agree with the real fracture behavior, therefore caution should be exercised when extracting TSLs directly from mixed-mode fractures. If, on the other hand, one considers the material behavior as ideally linear elastic and expects the fracture to be ideally brittle, then it is expected that the traction follows from a linear elastic potential and direct identification of TSLs would be possible, even with mixed-mode loading.

16.3 Advances in quasistatic single-mode testing

When describing the load on a crack tip and the resulting crack propagation, a distinction is traditionally made between three fracture modes, as shown in Fig. 16.5. Fracture testing of adhesive joints under single Modes I and II has been intensively investigated by many researchers in the past, and are also the focus of Chapters 17 and 32. Hence, most of the latest innovations in test setups can be found for Mode III. The following subsections give a comprehensive overview of established or newer experimental setups in single-mode testing and methods with focus on the latter. Modifications of established methods due to special purposes such as environmental conditions, fatigue, or rate dependency are discussed in Sections 16.5 and 16.6.

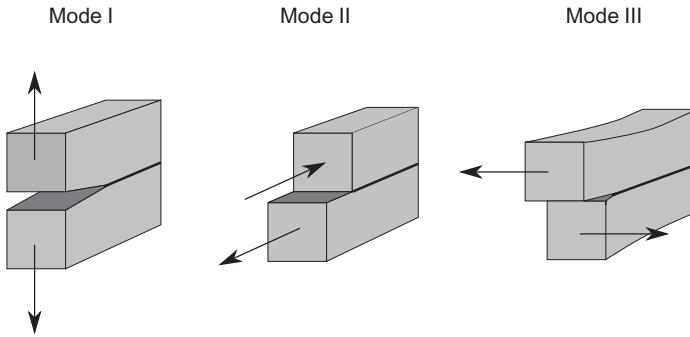


Fig. 16.5 Classic fracture Modes I, II, and III.

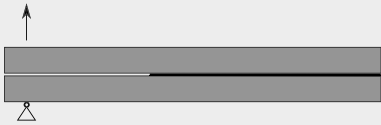
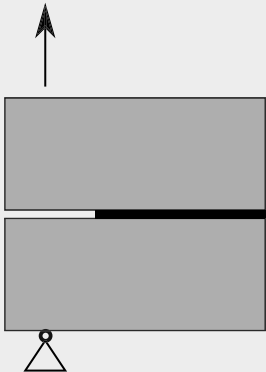
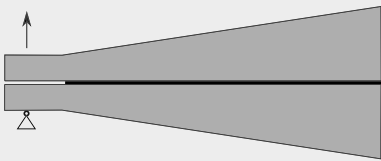

16.3.1 Mode I

Because Mode I loading is the most critical and easiest to test for adhesive bonds, corresponding test methods were the first ones to be developed and are already well established. Table 16.1 gives a short overview of available test methods in pure Mode I. Among them, DCB and TDCB are the most widespread, as they are also standardized in ISO 25217:2009-05 [12] or in ASTM D3433-99 [32], which recommend test evaluation according to LEFM. In the last two decades, test evaluation of DCB tests using the J-integral approach has become increasingly popular. Andersson and Stigh [21, 33] applied the approach of Paris and Paris [7] to adhesive joints. They made their own test setup in which they could measure the force and the rotations at the load application points. Taking into account an additional measurement of the COD, they evaluated a TSL for usage in CZMs. Differences between their approach and approaches from LEFM have been discussed by Biel et al. [15]. An experimental comparison between the different approaches used on different sample types on the same elastic-plastic adhesive showed good correlation between the individual methods and samples, as reported by Marzi et al. [29].

Cabello et al. [43] proposed an analytic approach to determine the peel stress distribution along the bondline of DCB samples of thick hyperelastic adhesive bonds. The method is based on beam theory with (hyper)elastic foundation and overcomes difficulties arising from theoretical assumptions when using approaches based on the Irwin-Kies equation or the J-integral. From an experimental point of view, the beam deflection has to be determined accurately, such as by digital image correlation, to apply the method. In the case of thick soft adhesive joints, this approach based on (hyper)elastic beam foundation is preferable to the more classical evaluation methods, which are more advantageous for thin stiff adhesive joints.

Khayer Dastjerdi et al. [35, 36] proposed DCB samples with rigid adherends to obtain TSLs in Mode I directly from experimental data based on an equilibrium approach. The assumption of rigid adherends leads to very simple kinematics and allows the direct calculation of stress-elongation relationships within the adhesive layer. The fracture energy is then obtained by integrating the TSL. While the fracture energy is most often the main variable extracted from DCB tests and TSLs represent a kind of additional information, this approach with RDCB samples works in reverse.

Table 16.1 Mode I tests.

Sketch	References
<p>Double cantilever beam (DCB)</p> 	<p>[12, 15, 16, 32, 34]</p>
<p>Rigid double cantilever beam (RDCB)</p> 	<p>[35–37]</p>
<p>Tapered double cantilever beam (TDCB)</p> 	<p>[12, 16, 32, 34, 38, 39]</p>
<p>Wedge test</p> 	<p>[13, 22, 40–42]</p>

The wedge test is standardized in ISO 11343:2019-10 [40] for high impact velocities, but the test is also used for quasistatic or creep loading rates [44]. Because the adherends usually consist of thin sheet metal, the plastic energy dissipation within adherends and the friction between wedges and adherends have a considerable influence on the test data. Therefore, wedge tests are not suitable for obtaining information about the fracture behavior of an adhesive itself. Instead, they are often used to compare the performance of different adhesives applied to the same adherend, to monitor quality during the manufacturing process, or to study long-term fracture behavior of bonded joints exposed to temperature or humidity (e.g., [45–47]). However, Taylor and Williams [48] improved their experimental setup by using a circular impactor

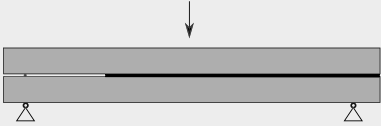
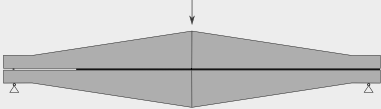
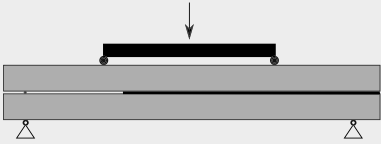



instead of a classic wedge. Renart et al. [42] developed a test methodology for wedge-driven tests that is similar to the methods recommended by the standards for DCB tests. It is not necessary to measure the crack length, but the coefficient of friction is assumed to be constant during the experiment. It is evident that the force on the wedge and the displacement of the wedge are the most important metrics in such tests. Manterola et al. [22] proposed a novel approach to obtain J-integral from wedge test data. They obtained the peeling force from the force pushing on the wedge by geometrical considerations, as proposed by Renart et al. [42], and measured the rotation of the adherends by inclinometers.

16.3.2 Mode II

Shear failure is generally not considered to be the most critical loading for adhesively bonded joints, which behave more sensitively to peel stresses. Among the individual shear modes, however, the in-plane case Mode II is the most frequently examined in the literature. Table 16.2 gives an overview of test setups that have been used in the past to investigate Mode II fracture in adhesive joints. In the late 1970s, the end-notched flexure (ENF) test, which is a fairly simple three-point bend test configuration, was proposed by Barrett and Foschi [49], who studied the fracture of wood in Mode II. The stability of crack propagation in ENF tests, however, depends on the chosen sample dimensions and the current position of the crack tip. More detailed information on the stability of ENF tests is found in Chai and Mall [50]. For example, a centrally loaded ENF specimen of span L is stable if the crack length exceeds $L/\sqrt[3]{24} \approx 0.35L$. Chai [51, 52] applied the ENF test to rather brittle adhesive joints and used evaluation methods based on LEFM. Leffler et al. [53] proposed an extension of the evaluation formulas to take into account effects due to the compliance of adhesive layers. Stigh et al. [25] and Marzi et al. [29] calculated the J-integral up to crack propagation in ENF tests of crash-optimized adhesive joints by evaluating forces and rotations at the load introduction points. The rotations were extracted manually from a video recording. To reduce measurement inaccuracies and to achieve an in situ measurement of the rotations, other sensors such as incremental encoders, inclinometers, or potentiometers appear more promising, but are more expensive. A comparison between the classic evaluation formulas, which are mainly based on the Euler-Bernoulli beam theory, and the J-integral approach is given by Biel and Stigh [54], who found that the results obtained with the different methods are pretty much the same from a practical point of view. However, a more ductile fracture will require large samples while more brittle joints will require smaller samples. Stigh and Biel [55] applied an additional compressive force near the crack tip in ENF tests and observed an increase in fracture energy with increasing compressive force.

The tapered end-notched flexure (TENF) test has been studied, for example, by Qiao et al. [56] and Marzi [57]. The main idea of tapering the specimens is to create a kind of Iso- G specimen where a constant force is measured as the crack propagates. In other words, the TENF test in Mode II is the equivalent of the TDCB test in Mode I.

Table 16.2 Mode II tests.

Sketch	References
<p>End-notched flexure (ENF)</p> 	<p>[25, 49, 51–54]</p>
<p>Tapered end-notched flexure (TENF)</p> 	<p>[56, 57]</p>
<p>4-Point end-notched flexure (4ENF)</p> 	<p>[58, 59]</p>
<p>Twice notched flexure (TNF)</p>	
	<p>[60]</p>
<p>End-loaded split (ELS)</p>	
	<p>[17, 61]</p>
<p>Independently loaded mixed-mode shear test (ILMMS)/end-loaded shear joint (ELSJ)</p>	
	<p>[62–64]</p>

The 4ENF test differs from the classic ENF test in that transverse forces at the crack tip and in the region of the process zone are avoided. In contrast to the classic ENF test, there is no compression region in front of the crack tip that could influence the crack propagation. It is therefore expected that crack propagation in 4ENF tests is more stable than in classic ENF tests. An analytical comparison between classic ENF and 4ENF can be found in Cricri [65].

A further modification to the ENF test has been proposed by Cricri [60]. The so-called twice notched flexure (TNF) test promises the direct evaluation of CZMs in shear and is expected to be stable. The applicability of the TNF test is currently proven by numerical simulations, but experimental data cannot be found in the literature at this point in time.

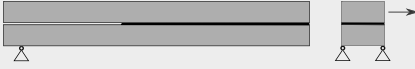

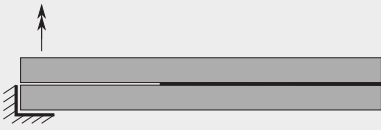
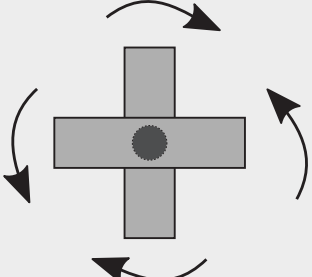
Another well-established test configuration in Mode II is the end-loaded split (ELS) test, which enables stable crack propagation. Blackman et al. [61] compared classic evaluation methods based on LEFM that can be applied to ELS tests. They proposed an alternative effect crack length approach to overcome problems observed due to minor cracks prior to macroscopic crack propagation.

All the above-mentioned test setups apply a shear load to the crack tip by bending the adherends. Possible equilibrium problems of the sample are avoided, but the adherends must deform purely elastically during the entire test. This requirement can present an experimental challenge, as reported by Borges et al. [66]. Another difficulty from an experimental point of view is friction, which on the one hand leads to energy losses and on the other hand can negatively affect the kinematics (e.g., in ELS tests). If one considers the classic “definitions” of fracture modes, which is loading of a crack tip as shown in Fig. 16.5, it seems obvious to load a specimen as shown in the figure. In the late 1980s, Sancaktar et al. [62] proposed the independently loaded mixed-mode specimen (ILMMS) test, which was reinvented as end-loaded shear joint (ELSJ) by Marzi et al. [63] approximately 20 years later. Both test setups load the crack tip in some kind of “natural” Mode II as suggested by Fig. 16.5, and both publications deal with elastic-plastic adhesive joints. The main difference comes from the methods by which the tests were evaluated. Sancaktar et al. [62] used approaches from LEFM to calculate G_{IIc} from maximum load and specimen dimensions while the evaluation by Marzi et al. [10] requires unloading of the samples and measurement of cumulated crack length (see Fig. 16.1). Unfortunately, there is no comparison between the two methods in the literature. Despite its “natural” type of Mode II loading, the ILMSS/ELSJ tests could not prevail over bending tests due to their experimental equilibrium difficulties. However, the ILMMS test has only recently been used by Baş and Sancaktar [64] to study mixed-mode fracture as will be discussed in Section 16.4.1.

16.3.3 Mode III

While fracture of adhesive bonds in Modes I and II has been investigated in many research activities in the past, there was almost no activity in Mode III fracture. Table 16.3 gives an overview of existing experimental methods in Mode III, starting with the pioneering work of Chai [51] at the end of the 1980s. Chai [51] concentrated on shear fracture and presented, in addition to an ENF test in Mode II, a DCB test that was loaded in Mode III in a very similar way, as shown in Fig. 16.5. The fracture energy G_{IIIc} was determined by using the Irwin-Kies equation while dC/da was calculated using beam theory. Chai [51] examined a brittle adhesive and found a linear increase of G_{IIIc} with the thickness of the adhesive layer. At the same time, Donaldson [67] published the split cantilever beam (SCB)—a very similar experimental setup in

Table 16.3 Mode III tests.

Sketch	References
Split (cantilever) beam test (SBT/SCB)	
	[51, 67–69]
Split cantilever beam (SCB)	
	[24]
Out-of-plane loaded DCB (ODCB)	
	[20, 70]
Torque shells	
	[71]

which he investigated Mode III fracture of composite materials that he bonded between aluminum beams.

In the following 25 years, Mode III fracture of adhesive bonds fell out of focus, even in the field of composite fractures; there are only a few publications on Mode III from this period (e.g., [72]). Davidson and Sediles [73] and Johnston et al. [68] published results on composite failure in Mode III (as well as in mixed mode) and Lee et al. [69] presented fatigue test results on DCB samples bonded with aluminum foam in Mode III. These authors used the split beam test (SBT), which—apart from minor modifications—is the setup of Donaldson [67]. Stigh et al. [24] presented a further developed SCB test. The adherends of the SCB test are C-shaped so that their shear center is in the middle of the adhesive layer. As a result, the adherends are not subjected to any torsional loading and there is no transverse torque in the

clamping, to ensure the equilibrium of the specimen. SCB tests were successfully performed on structural tape; the tests were evaluated according to a J-integral approach. The SCB test has a disadvantage in the event that adhesive layers of different thicknesses are of interest because in this case, different beam geometries are required. Loh and Marzi [20] presented a further development of the SBT test by Chai [51], which they called the out-of-plane loaded double cantilever beam (ODCB) test. The beams have been loaded with external torque instead of force, which allowed the Irwin-Kies equation to be applied without having to measure the current position of the crack tip during the experiment. The tests were carried out in a biaxial axial/torsional test machine, which made it possible to control the Mode I contributions to the fracture energy to zero. Schrader and Marzi [70] modified the test setup to reduce the inertia of the clamps and carried out Mode III tests on a crash-optimized adhesive at increased load rates. Nevertheless, the ODCB test requires a huge experimental effort compared to SBT and SCB tests, which is obviously not justified by advantages over these tests. However, the ODCB test has great potential for basic research, if it is extended to mixed mode. Reference is made to [Section 16.4.2](#) for this.

Cricià et al. [71] presented a so-called torque shell test to study the fracture of adhesively bonded joints in Mode III. In contrast to the beam-like tests, which have been discussed before, a circular crack front has been observed in those tests. Nevertheless, the torque shells show more similarities with continuum mechanics test setups such as the napkin ring tests (see, e.g., [74]) than with classic fracture mechanics tests, as there is no unloaded free end of the adhesive layer. However, the kinematics of the torque shells are quite complicated compared to napkin ring tests and crack propagation is observed. Obviously, for this reason, the authors consider the torque shells to be fracture tests in Mode III and therefore this test method is also listed here for the sake of completeness.

16.4 Novel developments in mixed-mode testing

The continued developments of fracture tests in recent years have concentrated more on mixed mode than on single mode. Of the four possible superimpositions of mode mixities, most efforts were made to investigate in-plane mixed-Mode I+II while only scarce publications are found for mixed-Mode II+III [73, 75]. The latter could be due to the fact that the two shear fracture Modes II and III are treated as equivalent for isotropic materials such as adhesives. This treatment is supported by the results of Fernlund et al. [75] and Chai [76], who found no significant differences between the two shear modes for thin adhesive layers within the experimental scatter.

All of the experimental methods listed below have in common that they assume that the total fracture energy G_{tot} (or J_{tot}) consists of portions from the individual modes,

$$G_{tot} = G_I + G_{II} + G_{III}, \quad (16.31)$$

which enables a definition and quantification of mode mixity based on ratios of these quantities. Various possibilities for defining mode mixity can be found in the literature, exemplary in the case of mixed-Mode I+II (in which $G_{III} \equiv 0$).

$$\psi_1 = \frac{G_I}{G_{tot}}, \tag{16.32}$$

$$\psi_2 = \tan^{-1} \left(\frac{G_{II}}{G_I} \right), \text{ or} \tag{16.33}$$

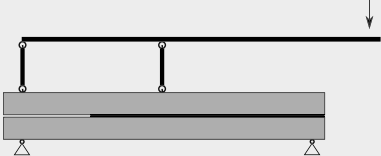

$$\psi_3 = \tan^{-1} \sqrt{\frac{G_{II}}{G_I}}. \tag{16.34}$$

All definitions are clear and can be converted into one another. However, ψ_1 ranges between 0 (pure Mode II) and 1 (pure Mode I), whereas ψ_2 and ψ_3 through 0 (Mode I) and $\pi/2$ (or 90 degrees) (mode II), respectively. By using the square root in Eq. (16.34), ψ_3 agrees with other possible definitions in the limit case of LEFM, wherein mode mixity can be defined in the form of ratios between single-mode components of COD or traction vector. Based on numerical studies using cohesive zone models, Conroy et al. [77] proposed a semianalytical mode partition in beam-like geometries, which accounts for the damage state at the crack tip by incorporating a cohesive length scale parameter.

16.4.1 Mixed-Mode I+II

Mixed-Mode I+II, which is a superimposition of peel and in-plane shear loading, has been studied very intensively in recent years. Tables 16.4 and 16.5 give an overview of established and newly developed setups, which arise from the basic idea with beam-like adherends. Table 16.6 shows two further, nonbeam-like test setups that have been proposed to investigate mixed-Mode I+II fractures.

Table 16.4 Mixed-Mode I+II tests (1).

Sketch	References
Mixed-mode bending (MMB)	
	[39, 78–82]
Single-leg bending (SLB)	
	[83–85]

Continued

Table 16.4 Continued

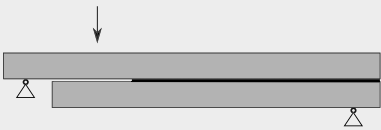
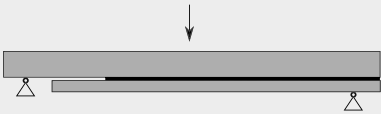
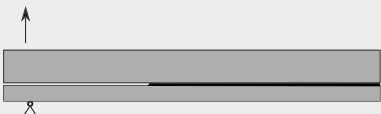
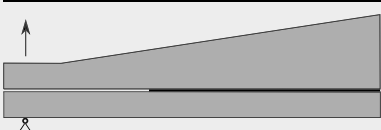



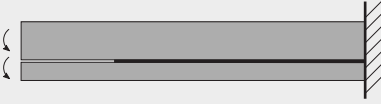
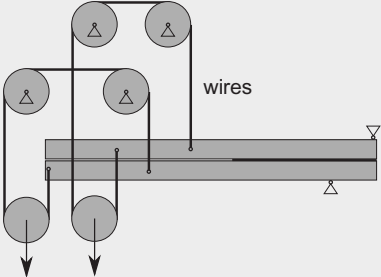
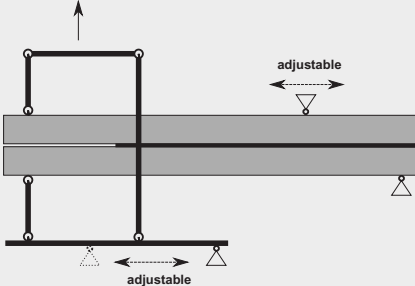
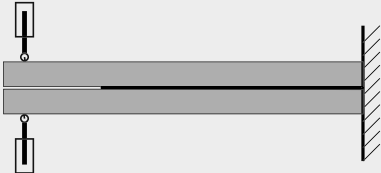
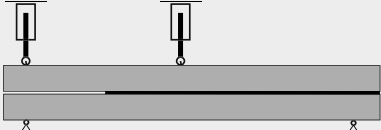
Sketch	References
<p>Over-leg bending (OLB)</p>  <p>The diagram shows a horizontal beam with a central crack. A downward-pointing arrow is positioned above the center of the beam. The beam is supported at both ends by triangular supports. The top part of the beam is shaded gray, and the bottom part is white.</p>	[86]
<p>Asymmetric single-leg bending (ASLB)</p>  <p>The diagram shows a horizontal beam with a central crack. A downward-pointing arrow is positioned above the center of the beam. The beam is supported at both ends by triangular supports. The top part of the beam is shaded gray, and the bottom part is white.</p>	[84, 87]
<p>Asymmetric double cantilever beam (ADCB)</p>  <p>The diagram shows a horizontal beam with a central crack. An upward-pointing arrow is positioned above the center of the beam. The beam is supported at both ends by triangular supports. The top part of the beam is shaded gray, and the bottom part is white.</p>	[88, 89]
<p>Asymmetric tapered double cantilever beam (ATDCB)</p>  <p>The diagram shows a tapered beam with a central crack. An upward-pointing arrow is positioned above the center of the beam. The beam is supported at both ends by triangular supports. The top part of the beam is shaded gray, and the bottom part is white.</p>	[90, 91]
<p>Asymmetric end-notched flexure (AENF)</p>  <p>The diagram shows a horizontal beam with a central crack. A downward-pointing arrow is positioned above the center of the beam. The beam is supported at both ends by triangular supports. The top part of the beam is shaded gray, and the bottom part is white.</p>	[87, 92, 93]
<p>Asymmetric 4-point end-notched flexure (4AENF)</p>  <p>The diagram shows a horizontal beam with a central crack. A downward-pointing arrow is positioned above the center of the beam. The beam is supported at both ends by triangular supports. The top part of the beam is shaded gray, and the bottom part is white.</p>	[94]
<p>Cracked lap joint (CLS)</p>  <p>The diagram shows a horizontal beam with a central crack. A downward-pointing arrow is positioned above the center of the beam. The beam is supported at both ends by triangular supports. The top part of the beam is shaded gray, and the bottom part is white.</p>	[19, 95–97]

Table 16.5 Mixed-Mode I+II tests (2).

Sketch	References
<p>DCB with uneven bending moments (DCB-UEB)</p> 	<p>[101, 106]</p>
<p>Creep DCB test with uneven bending moments</p> 	<p>[105]</p>
<p>Load jig proposed by Fernlund and Spelt [92]</p> 	<p>[66, 92, 107, 108]</p>
<p>Dual actuator loading (DAL)</p> 	<p>[109–113]</p>
<p>Controlled mixed-mode bending (CMMB)</p> 	<p>[114]</p>

Continued

Table 16.5 Continued


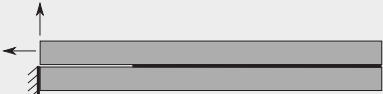
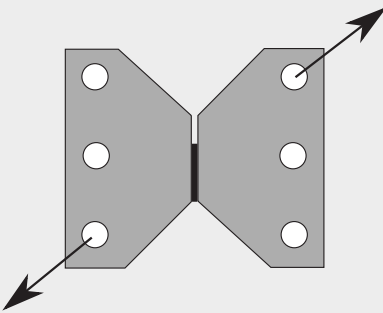
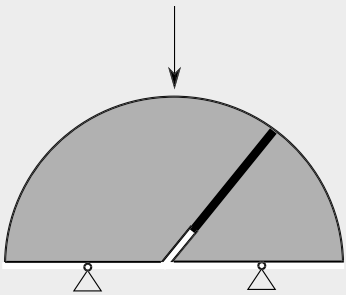
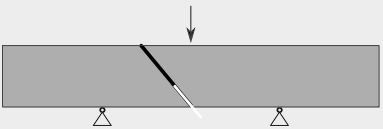
Sketch	References
Mixed-mode double cantilever beam (MCB)	
	[99, 115]
Independently loaded mixed-mode test (ILMM)	
	[62, 64]

Table 16.6 Mixed-Mode I+II tests (3).

Sketch	References
Compact mixed-mode (CMM) test	
	[28, 116–121]
Semicircular bend specimen (SCB)	
	[122–124]
Bi-material inclined notch short bend beam (BISBB)	
	[125]

In history, one of the first fracture tests in mixed-Mode I+II was the mixed-mode bending (MMB) test, which was proposed by Crews and Reeder [78], Crews and Reeder [79], as well as Hooper et al. [80] for composite materials, and which became standardized for composites in the early 2000s [98]. When applied to adhesive joints, the MMB test appears to work well for brittle adhesives while large samples are required to avoid plastic deformation of the adherends in more ductile joints. An advantage of the MMB test is the possibility of realizing different mode mixities by simply varying the load jig but not the specimen dimensions. Högberg and Stigh [99] presented an analytical study of MMB tests on adhesive joints and discussed several mode decomposition methods from the literature. Stamoulis et al. [82] performed MMB tests on a crash-optimized structural adhesive and identified a fracture envelope based on numerical simulations. They did not observe plastic adherend deformation, although they used comparatively thin and short beam dimensions.

The single-leg bending (SLB) test, which was introduced by Davidson and Sundararaman [100] for composite testing, has been applied to adhesive joints by Ji et al. [84]. They realized different mode mixities by choosing different heights of the beam-like adherends and presented traction-separation laws under certain mixed-mode conditions for a rather brittle adhesive joint. In addition, they proposed a decomposition of the J-integral into single-mode contributions by dividing the sample deformation into a symmetrical Mode I component and an asymmetrical Mode II component. Szekrényes and UJ [86] proposed the over-leg bending (OLB) test, which is similar to the SLB test, but here the load is applied in front of the crack tip instead of in the middle of the specimen. The approach of forcing different mode mixities through different beam heights can also be found in some other publications, where asymmetric DCB [88, 89, 101], TDCB [90, 91], SLB [84, 87], ENF [87, 92, 93], or 4ENF [94] have been used. Moreira et al. [87] discussed samples with asymmetric beam adherends in detail and focused on possible decompositions of the fracture energy into single modes. Based on their results, they proposed a strategy to identify fracture envelopes for rather brittle adhesive bonds in composite materials. It should be noted, however, that the respective value of the mode mixity (and thus the identified fracture envelope) strongly depends on the selected decomposition of the fracture energy.

Another traditional test for examining the mixed-Mode I+II fracture of adhesive joints is the cracked lap joint (CLS) test, which was proposed by Brussat et al. [95] in the late 1970s. CLS specimens are easy to manufacture and can be tested with conventional clamping devices and testing machines. For this reason, they are a preferred type of fatigue or impact test specimen [102–104] with regard to adhesive joints and composites.

Sørensen et al. [101] loaded the asymmetrical DCB specimen with uneven bending moments, which required rather stiff clamping at the opposite end of the specimen. They presented test results for a brittle adhesive and adherends made of composites and evaluated the initial fracture resistance of the joint as a function of mode mixity. The load with uneven bending moments and zero force was realized by a kind of wire arrangement, which was inspired by the work of Plausinis and Spelt [105], who were already using wires to apply external moments to DCB samples in mixed-mode creep

tests. The setup of Sørensen et al. [101] was later used by Lundsgaard-Larsen et al. [106], who carried out experimental investigations on sandwich samples. However, the wires and the requirement for a stiff clamping cause enormous experimental effort, which makes the setup unsuitable for widespread use.

Fernlund and Spelt [92] proposed a load jig to test adhesive joints in mixed-Mode I +II. In contrast to the MMB test, their test setup is able to use a large number of mode mixities, including single modes, as limit cases by changing the support positions. Fernlund and Spelt [92] calculated G_I and G_{II} by splitting the load on the sample into a symmetrical and an asymmetrical portions and analyzed stable and unstable crack propagations due to different loading conditions. They verified the results experimentally by testing a rather brittle adhesive joint. However, their experimental setup was quite large and heavy and, from a practical point of view, did not fit into climatic chambers. This circumstance inspired Costa et al. [108] to further develop the setup and the associated test evaluation. The original proceeding by Fernlund and Spelt [92] required measurement of the actual crack tip position to calculate G_C , but neither fracture process zone nor root rotation has been considered. Costa et al. [108] proposed an indirect evaluation method, which estimates the actual position of the crack tip by two LVDT measurements and is therefore also suitable for use in climatic chambers. Borges et al. [66] further developed the device for use at increased speeds and impacts.

What these test setups have in common is that they can be used in an ordinary testing machine. The mixed-mode loading is achieved by selecting the appropriate sample dimensions (in the form of different beam heights of adherends) or by adapting the associated load jig. Therefore, these setups are relatively easy to implement and appear to be suitable for industrial use. However, from an academic point of view, they have some limitations as the mode mixity is neither continuously variable between single modes nor can it be specified or changed during an experiment.

Dual actuator tests, which allow mode mixity control, overcome those limitations. In the literature, there are two different types of such tests for mixed-Mode I+II. Singh et al. [109] proposed the dual actuator loading (DAL) test, which is a combination of ELS and DCB tests. This experimental setup was applied to different types of adhesive joints such as wood [110] or composite [113]. Walander et al. [114] replaced the load jig of an MMB setup by two independent actuators and called it a controlled mixed-mode bending (CMMB) test. The applicability of the DAL test was proven by Chaves et al. [111], who carried out analytical and numerical studies of this test setup. Such analytical or numerical studies have not yet been found for the CMMB test, but both tests appear very promising for gaining deeper insights into mixed-mode fracture. In contrast to the CMMB test, however, the DAL test appears to be suitable for fatigue tests or for use with climatic chambers. In the future, such dual actuator tests could be the first choice to extract cohesive zone models directly from experimental data. From an industrial point of view, however, dual actuator tests appear too complex for everyday use compared to tests in conventional testing machines.

All the above-mentioned test setups achieve the Mode II load component by bending of adherends. With regard to Fig. 16.5, mixed-Mode I+II could also be achieved by more or less simple superimposition of Mode I and “natural” Mode II loading. This is the path taken by Sancaktar et al. [62], who proposed the Independently Loaded

Mixed-Mode (ILMM) test for rather brittle adhesive joints. Baş and Sancaktar [64] reused that test setup very recently to study the fracture of epoxy-based adhesive joints at quasistatic and elevated loading rates up to 500mm/min. While the Mode II load was applied by a testing machine, the Mode I load was implemented by a small hydraulic actuator that could be placed directly on the specimen. The hydraulic pressure was then kept constant during an experiment. This very innovative approach made it possible to implement a kind of double actuator load without having to produce a complex and expensive load device. In addition, the weight of the entire test setup is rather low compared to tests with load jigs, which is very promising in the case of fatigue or impact loads. After theoretical considerations, Högberg and Stigh [99] proposed the same idea of loading, but called it the mixed-mode double cantilever beam (MCB) test. Högberg et al. [115] performed MCB tests on a brittle adhesive and assessed the constitutive behavior of the adhesive layer based on J-integral by an inverse approach. This is in contrast to the publications of Sancaktar et al. [62] and Baş and Sancaktar [64], who evaluated their test results using methods from LEFM. With a view to possible future studies on fatigue or impact fracture, the ILMM/MCB tests appear promising due to the low weight, but technical difficulties due to the hydraulic Mode I actuator (ILMM) or the clamping (MCB) are to be expected at the same time.

In addition to the classic fracture tests with beam-like adherends that are subjected to bending, three further test setups (see Table 16.6), which are of alternate designs, should be mentioned for the sake of completeness. The first one is based on the classical device by Arcan et al. [126], which was originally designed to apply uniform plane-stress states. In contrast to some authors [127–130], who carried out ARCAN tests on adhesive joints in the classical way, Pang [117] proposed the compact mixed-mode (CMM) test, which was used earlier by Valentin and Caumes [116] to study wood fracture and is very similar to the classical ARCAN test, but there is an initial crack inside the adhesive. Originally, the CMM test was assessed using LEFM methods with the concept of stress intensity factors. Choupani [120] presented a detailed analytical and numerical study of the CMM test and compared the results with experimental data. The numerical analysis included a calculation of the J-integral. But because a rather brittle adhesive joint was tested in the experiments, there were no significant differences between the individual approaches. The CMM test was recently used by Pironi and Nicoletto [119] and Chen et al. [121] in fatigue loading. At this point, a strict distinction must be made between the CMM test, which is a fracture mechanics test due to the presence of an initial crack, and the classic ARCAN test. The latter was recently used by Sousa et al. [129, 130] in the fatigue loading of adhesive joints and was misleadingly referred to by the authors as a mixed-mode experiment.

The semicircular bend (SCB) test was proposed by Chong and Kuruppu [122] for mixed-mode testing on rocks. Ajdani et al. [123] first applied the SCB test to brittle and semibrittle adhesive joints and then to ductile adhesive joints [124]. The authors stated that the SCB test has some advantages over classic fracture tests such as MMB tests or the apparatus by Fernlund and Spelt [92] or Costa et al. [108]. Because no load jig is required, the test becomes more cost-effective and the risk of possible errors—as

can occur in other tests due to the deformation of a load jig—is minimized. The relatively stiff design of adherends significantly reduces the risk of plastic deformation of adherends, which is a problematic issue when applying bending to beam-like specimens.

The so-called bi-material inclined notch short bend beam (BISBB) test, which has been recently proposed by Aliha et al. [125], has similarities with the scarf joint in three-point bending [131]. However, it is a fracture test due to the presence of an initial crack tip. The authors carried out analytical and numerical investigations of the BISBB test and found the test suitable to cover the entire range of mode mixities between pure single Modes I and II. So far, the evaluation of BISBB tests has been based on LEFM.

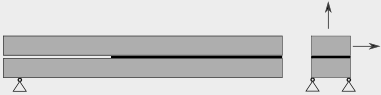
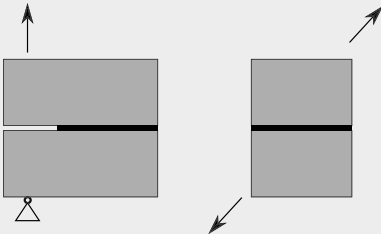
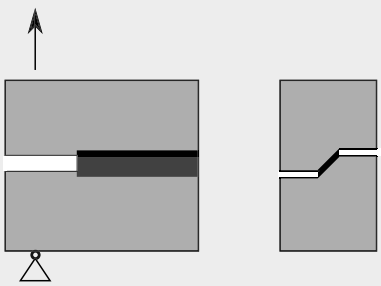
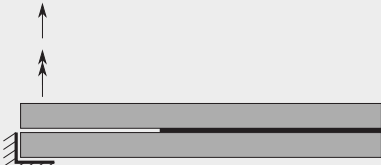
As a brief interim conclusion, it should be noted that apparently many researchers have a great interest in mixed-Mode I+II, resulting in continued releases of newly developed specimens, tests, test devices, or load jigs.

16.4.2 Mixed-Mode I+III

Fractures caused by combined peel and out-of-plane shear loading, the so-called mixed-Mode I+III, have not been researched very intensively in the past. Table 16.7 gives an overview of the methods and samples that can be found in the literature on this topic. In the early 1990s, Chai [132] published a modified DCB specimen, which was loaded additionally to peel by force acting out of plane. Closed-form solutions for G_I and G_{III} allowed a test evaluation by the Irwin-Kies-equation. Chai [132] has presented fracture envelopes for a particular adhesive of different layer thickness in the Mode I–III plane. The main disadvantage over modern testing methods was the application of the Mode I load by a screw that was held in place during the experiment.

After about 25 years, the test setup of Chai [132] was reinvented by Safaei et al. [133], who applied mixed-Mode I+III loading to bulk samples of a brittle polymer, and 3 years later by Akhavan-Safar et al. [134], who concentrated on rather brittle adhesive bonds. Because the tested joints were brittle, the tests were evaluated by concepts of stress intensity factors (LEFM) with the help of numerical simulations. While these authors carried out their tests by inserting DCB samples into a load rig that allowed the choice of different load directions, Watson et al. [37] decided to redesign the samples and to use conventional support. They made RDCB samples in a manner similar to what Khayer Dastjerdi et al. [35, 36] used in Mode I tests; however, the bond is located on a slope that was introduced into the adherends in the direction of the sample thickness. To differentiate between the individual sample geometries and mode mixities, they used the nomenclature rigid DCB in pure Mode I, bonded shear specimen (BSS) in pure Mode III, and mixed-mode specimen (MM) for mixed-Mode. Watson et al. [37] carried out tests on ductile elastic-plastic adhesive joints with three different nominal layer thicknesses in the individual Modes I and III as well as with two mode mixities in between. In addition to fracture envelopes, they specified the constitutive behavior for cohesive zone modeling for each individual layer thickness.

Table 16.7 Mixed-Mode I+III tests.

Sketch	References
<p>Modified DCB test</p>  <p>The sketch shows a horizontal beam with a central crack. A vertical arrow points upwards from the center of the beam. Below the beam, there are two triangular supports, one on the left and one on the right.</p>	<p>[132]</p>
<p>Test setup by Safaei et al. [133]</p>  <p>The sketch shows a horizontal beam with a central crack. A vertical arrow points upwards from the center of the beam. Below the beam, there is a triangular support on the left. To the right of the beam, there is a vertical rectangular block with a diagonal crack. Two arrows point away from the block, one upwards and to the right, and one downwards and to the left.</p>	<p>[133, 134]</p>
<p>Modification of rigid DCB for mixed-mode testing</p>  <p>The sketch shows a horizontal beam with a central crack. A vertical arrow points upwards from the center of the beam. Below the beam, there is a triangular support on the left. To the right of the beam, there is a vertical rectangular block with a diagonal crack. Two arrows point away from the block, one upwards and to the right, and one downwards and to the left.</p>	<p>[37]</p>
<p>Mixed-mode controlled DCB (MC-DCB)</p>  <p>The sketch shows a horizontal beam with a central crack. A vertical arrow points upwards from the center of the beam. Below the beam, there is a triangular support on the left. To the right of the beam, there is a vertical rectangular block with a diagonal crack. Two arrows point away from the block, one upwards and to the right, and one downwards and to the left.</p>	<p>[135–138]</p>

Loh and Marzi [135–138] decided to overlay their ODCB test [20] with Mode I loading, which was possible because the tests were performed in a biaxial axial/torsional testing machine. They calculated J-integral independently for both modes during the experiments in situ and controlled the tests on constant ratios J_{III}/J_I . These tests, which the authors called mixed-mode controlled double cantilever beam (MC-DCB) tests, were carried out successfully on both a hyperelastic and a crash-optimized adhesive. In the case of the hyperelastic adhesive, rather large samples

about 1m in length were used to allow the process zone to develop fully. A plateau in $J_{tot} = J_I + J_{III}$ during crack propagation was reported, but the crack propagation started much earlier than the plateau was reached. A plateau in J_{tot} was also observed in the tests with the elastic-plastic adhesive when the crack propagated. In contrast to their results, which were obtained with the hyperelastic adhesive, Loh and Marzi [137, 138] aimed to extract traction-separation laws for cohesive zone modeling from experimental data in the elastic-plastic adhesive. Therefore, they made use of the capability of their dual actuator test to run different paths in the mixed-Mode I+III plane up to fracture. Experimental difficulties arose from further force and moment components that occur in the clamping to achieve equilibrium. These external loads contribute to the J-integral, but their influence is negligibly small, as from additional measurements and from the numerical simulations by Bödeker and Marzi [139] could be shown. However, more research is needed to gain a deeper understanding of the tests and to further validate the proposed methods. In summary, the MC-DCB test—similar to the dual actuator tests in mixed-Mode I+II—appears very interesting and innovative from an academic point of view. However, due to its complexity, it is most likely not suitable for industrial use.

16.4.3 Mixed-Mode I+II+III

Combining all three modes of fracture in a single experiment is a challenge that has so far only been addressed by a very few authors, as summarized in Table 16.8. The main difficulty is a reliable decomposition of fracture energy due to the inhomogeneous stress state of the crack tip, which becomes more complicated when three modes are involved. In addition to test setups that have been applied to adhesive bonds, developments are also mentioned below that appear to be applicable to adhesive connections in the future.

The first attempts of mixed-Mode I+II+III experiments on adhesively bonded joints were undertaken in the 1990s. Vintilescu [140] extensively discussed the idea of using a SCB test with unsymmetrical adherends combined with out-of-plane

Table 16.8 Mixed-Mode I+II+III tests.

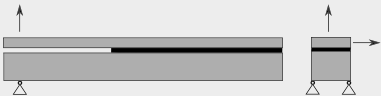
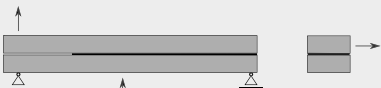
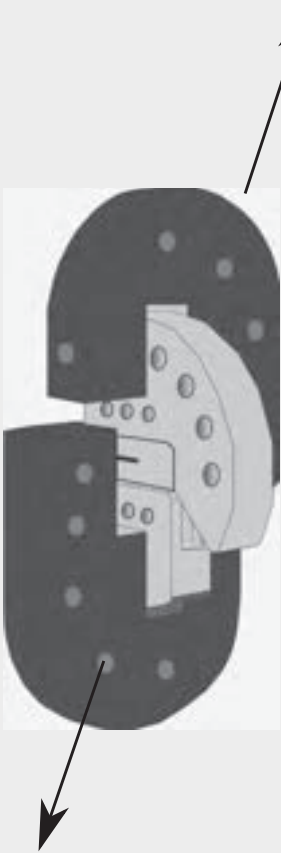
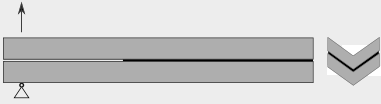
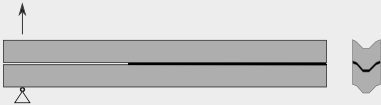
Sketch	References
Obliquely loaded unequal-adherend SCB specimen	
	[140]
Shear torsion bending (SBT)*	
	[73]

Table 16.8 Continued

Sketch	References
<p>All-fracture-mode (AFM)/compact tension-shearing and tearing (CTST)^a</p>	
	<p>[141–145]</p>
<p>V-specimen</p>	
	<p>[146]</p>
<p>Mixed-mode double cantilever beam (MMDCB)</p>	
	<p>[146]</p>

^a Comment: Not yet applied to adhesive bonds.

loading. In other words, the DCB loaded in mixed-Mode I+III according to Chai [51] was further modified by introducing a Mode II loading by different heights of adherend beams. The obliquely loaded unequal-adherend SCB specimen is easy to assemble using conventional clamping devices, even if transverse forces and torques are to be expected due to the fulfillment of equilibrium conditions. The evaluation of test results, including decomposition of fracture energy into individual modes, was made possible by means of the analytical approaches of LEFM due to the validity of the superimposition principle. Because the current value of the mode mixity depends on the crack length and the selected beam dimensions, it is expected that the mode mixity will change during the crack growth in a single experiment. A possible disadvantage of the experimental setup results from the fact that mixed-Mode I+III is combined with Mode II loading, so that the limit case of mixed-Modes II+III is not covered, because the load in Mode II is initiated by the same force component as in Mode I.

Davidson and Sediles [73] developed a setup for composite testing and superimposed an MMB test configuration in mixed-Mode I+II and an SCB test configuration in Mode III. Their shear-torsion-bending (STB) test allows loading under any ratio of the three individual fracture modes. This makes the test setup one of the only ones that can apply a mixed-Mode II+III load. The STB test has not yet been applied to adhesive bonds and even for composites, the authors only presented experimental results in Mode III. However, the applicability of the test in the entire range of mode mixities has been proven by numerical simulations and seems applicable to adhesive bonds in the future.

The intrinsic approach to combining all three fracture modes follows from Fig. 16.5. Richard and Kuna [141] proposed the all-fracture-mode (AFM) specimen, which was a DCB (or more precisely a compact tension (CT)) geometry, which has been placed in a load device to apply force components in all of the individual modes. They studied the fracture of rather brittle PMMA and aluminum and assessed their tests according to concepts based on stress intensity factors. Their results were picked up almost 30 years later by Razavi and Berto [142], who again conducted fracture tests on PMMA in a combination of all three modes. In addition to an extensive experimental test matrix, they investigated the development of a plastic process zone at the crack tip using numerical simulations. Ayhan and Demir [143, 144] and Demir et al. [145] presented further numerical studies and experimental results on aluminum with this type of test setup, which they called the compact tension-shearing and rearing (CTST) test. Unfortunately, the test setup has not been applied to bonded joints so far, although it appears to be an extension of the CMM for additional Mode III loading.

Just recently, Dagorn et al. [146] designed two beam geometries for testing under highly dynamic conditions. Both geometries are V-shaped in the direction of the beam width. They differ only slightly in their particular shape and are referred to as V-specimen and mixed-mode double cantilever beam (MMDCB). Using such beam geometry instead of a constant slope as used by Watson et al. [37] avoids lateral loads in the fixture, which is an advantage in dynamic test conditions. The special shape of the beams was chosen so that almost a homogeneous mode mixity is achieved regardless of the crack length. This is important for the applicability of the new specimen and

has been confirmed by numerical simulations. However, the authors did not explicitly distinguish between Modes II and III and combined them to form one single shear fracture mode, as is common with cohesive zone models. From a very practical point of view, it seems impossible to obtain Mode III without having parts of Mode II due to the finite width of the adhesive layer. This is a difficulty of all test setups that deal with such mixed modes as they were presented and discussed in [Sections 16.3.3](#) and [16.4.2](#). Hence, Dagorn et al. [146] pointed out the presence of all three fracture modes in their publication. However, their aim was to carry out high-speed tests and not to achieve different mode mixities in shear.

16.5 Extending experimental methods to fatigue, aging, and creep

This chapter provides an overview of the latest developments in fracture testing to investigate effects such as fatigue, creep, or aging on bonded joints. The focus is on the methods and experimental setups that have recently been used for this purpose. For an overview of the effects of such test conditions for certain types of adhesive, reference is made to further literature (e.g., [147, 148]).

16.5.1 Fracture testing in fatigue

The propagation of cracks in adhesive joints due to fatigue loading has been studied by many researchers in the past, and is also the subject of [Chapter 19](#). The most common fatigue tests are DCB or, even if they are not fracture tests, lap shear tests. Stiff adhesives are preferably tested in force control while displacement control is used for rather soft adhesives at frequencies up to 10Hz to avoid heating. The crack propagation is, however, influenced by the test control chosen. In DCB tests, for example, the force control leads to an increasing bending moment at the crack tip as the crack propagates. The increase in the load at the crack tip accelerates the crack propagation speed per load cycle during the experiment. The opposite effect occurs with the displacement control and the crack propagation per load cycle tends to stall during the test, resulting in a fatigue threshold, which is a useful property. A possible disadvantage of displacement control is that a larger G in the beginning may lead to larger plastic zones that affect subsequent crack propagation.

To achieve constant crack propagation per load cycle, constant G specimens with tapered geometries (e.g., TDCB) are used. Jin et al. [149] tested width-tapered double-cantilevered-beam (WTDCB) specimens in which the fracture energy was independent of the crack length. However, because the width contributes only linearly to the sample compliance while the influence of the height is third order, ordinary TDCB samples appear to be more practical. Nevertheless, tapered geometries are generally not preferred because they have a higher mass, and different crack propagation rates per load cycle are required to obtain a Paris law characterization of the bond system.

One of the experimental challenges in fatigue testing is the determination of the current crack length. Classical approaches to determining the current position of

the crack tip are based on the change in compliance during crack growth or on video recordings. Obviously, both approaches have their limits, as the determination of dC/da depends on the choice of data reduction method and the evaluation of videos can be strongly influenced by human judgment. Clerc et al. [150] successfully used acoustic emission sensors to detect the actual crack tip location in 4ENF tests on adhesively bonded wood. Even if the idea of using acoustic emissions to monitor crack tips was already investigated specifically for composite materials and composite bonds in the past, successful application to 4ENF fatigue tests should be highlighted. In Mode II in particular, the application of both the compliance method and the visual inspection can be problematic from a practical point of view.

To investigate crack propagation in mixed-Mode I+II, the CLS test is preferred by some authors [102–104]. The samples are easy to produce and can be clamped in testing machines using conventional clamping, making the CLS test easy to implement. Azari et al. [151] realized mixed-Mode I+II loads in fatigue tests through the use of asymmetrical DCB tests, which have similar advantages to CLS tests. A relatively new test setup was implemented by Pirondi and Nicoletto [119] and Chen et al. [121], who applied a fatigue load to the relatively new CMM specimen, as can be seen in Fig. 16.6. A similar ARCAN fatigue test was presented by Sousa et al. [129, 130], but their samples were made without an initial crack.

Rocha et al. [152] carried out fatigue tests in mixed-Mode I+II by using the apparatus by Costa et al. Costa et al. [108], as shown in Fig. 16.7. Especially in the case of fatigue tests, the test setup seems to be quite complicated due to the many pins,

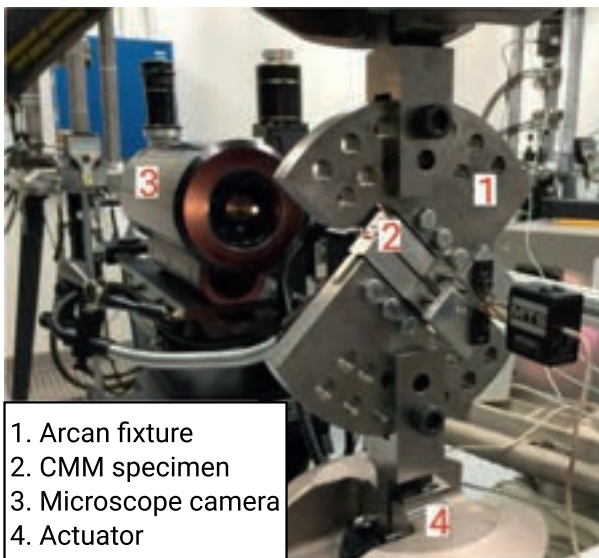


Fig. 16.6 CMM test setup in fatigue loading.

From Q. Chen, H. Guo, K. Avery, H. Kang, X. Su, Mixed-mode fatigue crack growth and life prediction of an automotive adhesive bonding system, *Eng. Fract. Mech.* 189 (2018) 439–450, ISSN 0013-7944, <https://doi.org/10.1016/j.engfracmech.2017.11.004>.

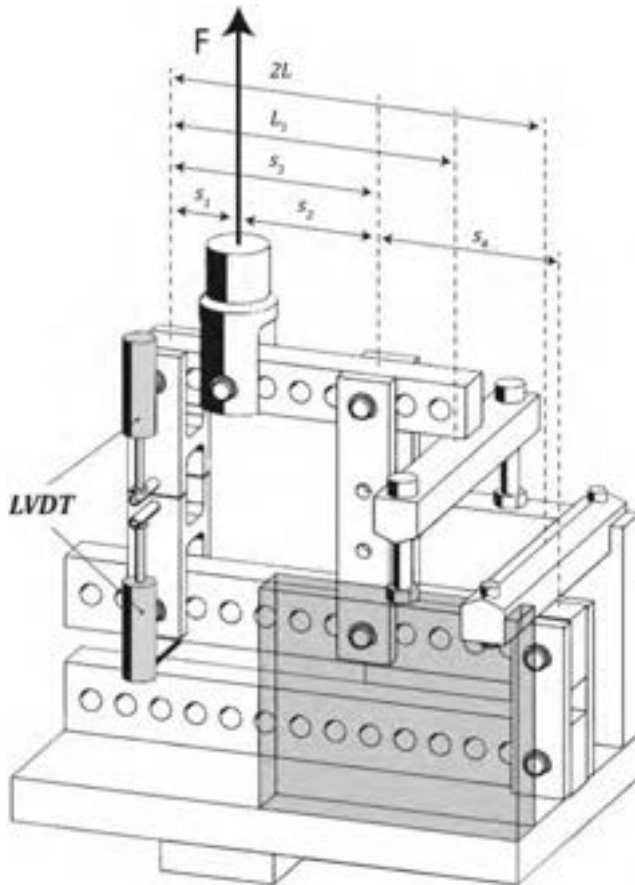


Fig. 16.7 Apparatus by Costa et al. [108] in fatigue loading.

From C.S.P. Borges, P.D.P. Nunes, A. Akhavan, E.A.S. Marques, R.J.C. Carbas, L. Alfonso, L. F.M. Silva, Influence of mode mixity and loading rate on the fracture behaviour of crash resistant adhesives, *Theor. Appl. Fract. Mech.* 107 (2020) 102508, ISSN 0167-8442, <https://doi.org/10.1016/j.tafmec.2020.102508>.

bearings, and friction in between. Nevertheless, the authors successfully achieved results at test frequencies up to 10Hz at a load ratio $R = 0.1$ for three different adhesives.

Chen et al. [153] investigated fracture in adhesive bonds using coach peel (CP) and lap shear (LS) tests. These tests are not fracture mechanics tests and are usually used to obtain S-N curves, but Chen et al. [153] used in their evaluation of fatigue fracture an approach proposed by Heyes et al. [154] to calculate the J-integral. The approach seems promising, even if further investigations should be carried out in the future in order to show the limits of the method, for example, caused by plasticity or by stiffness ratios between adherends and adhesive.

16.5.2 The influence of aging

The durability of polymeric materials such as adhesives is of considerable interest for industrial applications, as also addressed in [Chapter 20](#). In addition to strength and stiffness, the fracture energy of an adhesive bond can also be influenced by the aging of the materials. At this point, it is common to distinguish between aging effects that alter the microstructure of the adhesive, such as by moisture transport into the bulk, and effects that might affect the adhesion to the adherends such as corrosion. Because natural aging occurs on a timescale of up to years, accelerated testing methods are used in laboratories to obtain data for the joint design. For full information on this subject, see Possart and Brede [155], who cover all aspects of bond aging, including fracture mechanics.

In the past decade, there has been relevant work in the field of fracture testing under aging conditions published by the University of Toronto (e.g., [156–158]). The research focused on closed (CDCB) and open (ODCB) double cantilever beam specimens exposed to accelerated aging conditions. The main difference between both types of specimen is the manufacturing process. CDCB samples are conventional DCB samples in which, for example, the penetration of moisture during aging takes a long time due to the small surface area and the large width of the adhesive joint. In contrast, ODCB samples (see also [159, 160]) are separated after bonding, then degrade under aging conditions. Before testing, the two aged adherends with adhesive are bonded together again. It is evident that the CDCB test appears to be more suitable for comparing aged and unaged conditions. Ameli et al. [156–158] presented a strategy to obtain a dependence of the fracture energy on the exposure index using both kinds of samples. The interested reader is referred to further literature at this point.

Patil et al. [161] proposed a strategy to further use the experimental data in a cohesive zone model. They used a fairly simple bilinear traction-separation law, but added a degradation parameter D_{deg} to the constitutive equations. The purpose of D_{deg} was to equally degrade both model parameters, fracture energy G_C and peak traction T ,

$$G_{C,\text{deg}} = D_{\text{deg}} G_C, \text{ and} \quad (16.35)$$

$$T_{\text{deg}} = D_{\text{deg}} T. \quad (16.36)$$

The evolution of the degradation parameter D_{deg} with exposure index EI_T was specified as the power function,

$$D_{\text{deg}} = f(EI_T) = c_1 (EI_T)^{c_2} \quad (16.37)$$

with two parameters c_1 and c_2 at constant relative humidity. The variation of the exposure index EI_T over the specimen width was specified in the FE model by assigning degraded parameters to the cohesive elements. Consequently, the resolution of the selected mesh should be able to map the gradient of the exposure index in the direction of the sample width. The numerical work can be seen as a first step toward possibly combining moisture transport and fracture analysis in a single model in the future.

16.5.3 Creep fracture

While in the previous subsection the focus was on changing the fracture properties through long-term nonmechanical effects, tests of the fracture behavior under permanent mechanical load are the subject of this section. In terms of creep fracture, tests should be preferred in which the load at the crack tip is kept constant during the entire test. However, because, as with fatigue tests, the current position of the crack tip can influence the actual value of G_C , it is expected that the critical energy release rate will change during the test. In contrast to fatigue tests, which for obvious reasons have to be carried out in testing machines, creep tests are preferred with dead weights for reasons of cost. Plausinis and Spelt [105] realized a constant G load by applying pure bending to a DCB sample through a wire construction. In contrast to the load caused by forces, the load caused by pure bending moments means that G is independent of the crack length. Nevertheless, the experimental setup is quite complicated and a possible assembly with climatic chambers to investigate the temperature dependence of a fracture is difficult due to the wires. Therefore, Al-Khanbashi and El-Said [162] loaded DCB samples in a self-made creep test stand with a temperature chamber. The load was implemented cost effectively using dead weights, but as a drawback G_C depends on the actual crack length. To overcome these difficulties, one might prefer tapered geometries such as TDCB tests, where G is proportional to the force applied regardless of crack length. Pitti et al. [163] carried out experimental studies on the creep rupture of wood, which appear promising for future use in adhesive bonds. They introduced a mixed-mode crack growth (MMCG) specimen, which is a TDCB sample subjected to mixed-Mode I+II loading in an ARCAN device, as shown in Fig. 16.8. If one thinks of adapting such a structure to carry out creep rupture tests on bonded joints, the size of the dead weights required for crack propagation can become problematic. For that reason, Carneiro Neto et al. [164, 165] preferred to run ENF tests on adhesive bonds in a conventional testing machine, even if a single test lasted at least 30 days. Independent of aspects such as cost efficiency, which are more of interest for later industrial application than for academic progress, experimental results on creep rupture in an adhesive bond in Mode II were obtained. However, the large dead loads required and the ineffectiveness of the use of testing machines could be the main reasons for the fact that only a few publications are found on the creep rupture behavior of adhesive bonds, such as in Mode II or in mixed mode. Instead of fracture tests, most authors prefer creep tests on butt joint or lap shear tests (e.g., [166, 167]), but these are not fracture mechanics tests and are more sensitive to stiffness and strength than to fracture energy. Schrader et al. [168] carried out creep

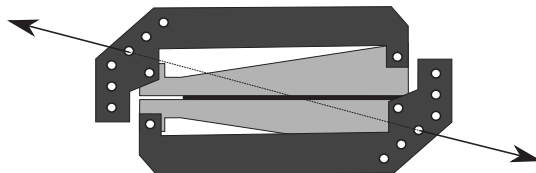


Fig. 16.8 TDCB in mixed-mode (MMCG specimen).

DCB tests on a rubber-like adhesive bond in a testing machine that was controlled by computer in such a way that the applied value of the J -integral was kept constant during the test. The main motivation for this solution, which is rather complicated compared to the use of tapered geometries (or even wires and dead weights), was to take into account nonlinearities related to the fracture behavior by a constant- J control.

16.6 Experimental challenges in impact and high-rate testing

Among other things, structural adhesive joints can be exposed to high loading speeds, such as occur in automobile crash applications or drop loads from mobile phones or tools. For a comprehensive review on high-rate testing of adhesive joints, reference is made to Machado et al. [169], to Sato and Marzi [170] or to [Chapter 21](#) of this book. The following sections focus on the latest developments in the field of fracture testing with a breakdown according to test methods.

16.6.1 Drop towers and pendulums

The simplest experimental setups in impact and high-speed tests are drop towers and pendulums. What they have in common is that they convert potential energy into kinetic energy, which leads to a maximum impact speed of

$$v_{\max} = \sqrt{2gh + \frac{2}{m}E_{\text{pre}}}, \quad (16.38)$$

with impactor mass m , the constant of gravity g , the initial height h above the impact position, and possibly additional potential energy E_{pre} , which, for example, can be stored in precompressed springs. Eq. (16.38) illustrates the speed of simple drop towers and pendulums without additional potential energy. To achieve an impact speed of 7m/s, a height of $h \approx 2.5\text{m}$ would be required, which is in the range of typical room heights for laboratories. Energy-driven experiments can be carried out with both drop towers and pendulums, in which the impactor is slowed after it hits the sample. To achieve an almost constant test speed during the test, the impactor mass should be selected to be sufficiently large. However, a large mass increases the kinetic energy, which has to be completely dissipated or converted back into potential energy during or after the test. Drop towers have the advantage that the load is always straight down to the ground, but the kinetic energy remaining after the test has to be dissipated in some way. In contrast, the load line of a pendulum is circular and can only be approximated to be straight for a short (test) distance, but the remaining kinetic energy is converted back into potential energy, which in turn increases the safety aspect. For the sake of completeness, rotary impact testers should also be mentioned here. Marzi et al. [171] performed T-peel tests on structural adhesive bonds in one such rotary impact device, but in general these devices are very rarely used today.

The most common impact tests on adhesive joints are dynamic wedge impact tests, as standardized in ISO 11343:2019-10 [40]. In addition to this established test method, other innovative developments with drop towers and pendulums have been published in the last two decades. Xu and Dillard [14] tested DCB samples in a drop tower, as shown in Fig. 16.9. The authors did not exhaust the maximum drop height of 1.25m and carried out their tests from a height of 450mm, resulting in an impact velocity of 1.6m/s. In spite of this comparatively low speed, no measurement of forces was carried out because strong vibrations in the force signals were assumed in advance due to the construction of the entire test setup, which excludes a reliable determination of the fracture energy with the Irwin-Kies equation. To overcome those issues, Eq. (16.11) has been used to evaluate the fracture energy based on a high-speed DIC measurement of the opening displacement at the load points.

Regarding mixed-mode loading, Ashcroft et al. [102] performed impact fatigue tests on CLS specimens in a pendulum. The pendulum hit the specimen at an impact speed of 1.5m/s, then the pendulum, which rebounded after the impact, was caught again and released again after 15 s. The sample was loaded by several such successive impacts. The authors highlighted some experimental details that should be considered to make successful measurements at high speed. Piezo strain gauges should be used instead of traditional electrical resistance gauges to suppress noise and to achieve high sampling rates. In addition, the position of the strain gauges, depending on the current

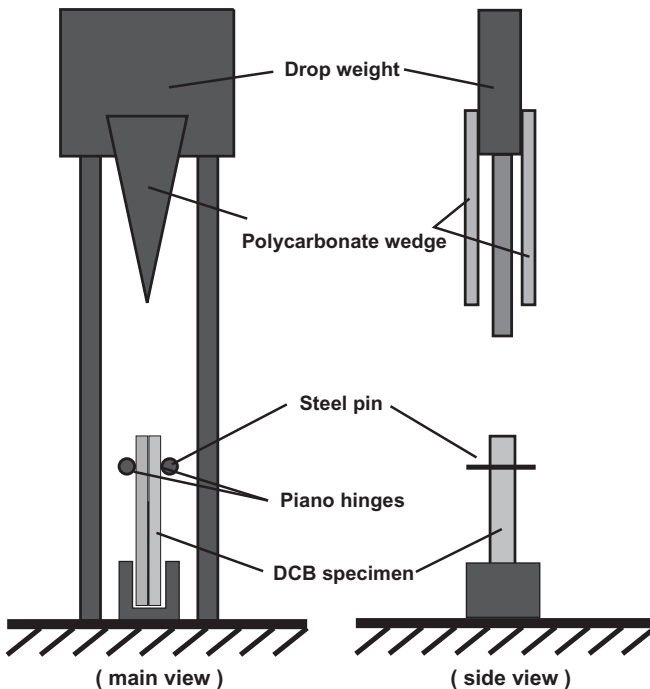


Fig. 16.9 DCB test setup in drop tower.

crack tip position, turned out to be critical. It was recommended to use multiple strain gauges in multiple locations to get the best signals throughout the experiment.

Valès et al. [172] successfully carried out ARCAN tests in a drop tower at heights of up to 500mm, which means impact velocities of about 3m/s. The implemented test setup is shown in Fig. 16.10. They used quite extensive measurement technology to be able to record the mechanical behavior of the sample during the test. Due to noise in the recorded signals, some post-processing operations were necessary to extract strains, strain rates, and stresses from the measured data. The ARCAN test is not a fracture test, but in the future, the test setup of Valès et al. [172] can of course also

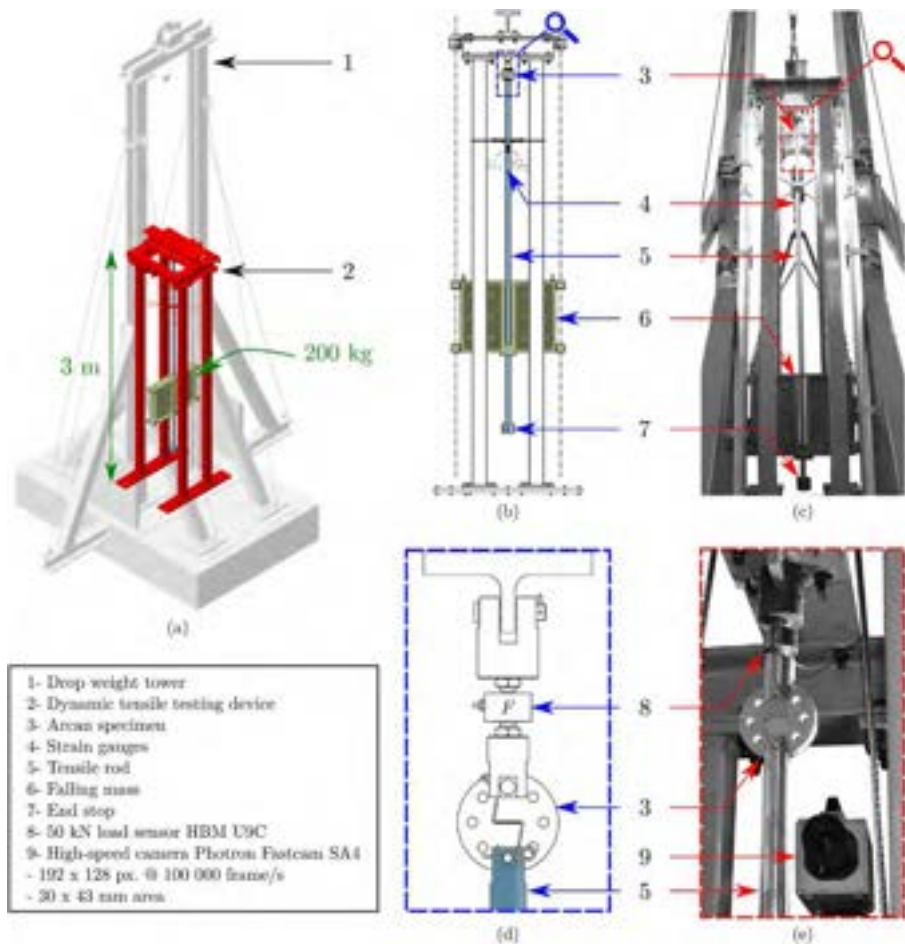


Fig. 16.10 Drop tower test setup for ARCAN samples.

From B. Valès, S. Marguet, R. Créac'hacdec, L. Sohier, J.-F. Ferrero, P. Navarro, An experimental method dedicated to the dynamic characterization of structural adhesives under drop weight conditions, *Int. J. Adhes. Adhes.* 90 (2019) 106–125, ISSN 0143-7496, <https://doi.org/10.1016/j.ijadhadh.2019.01.031>.

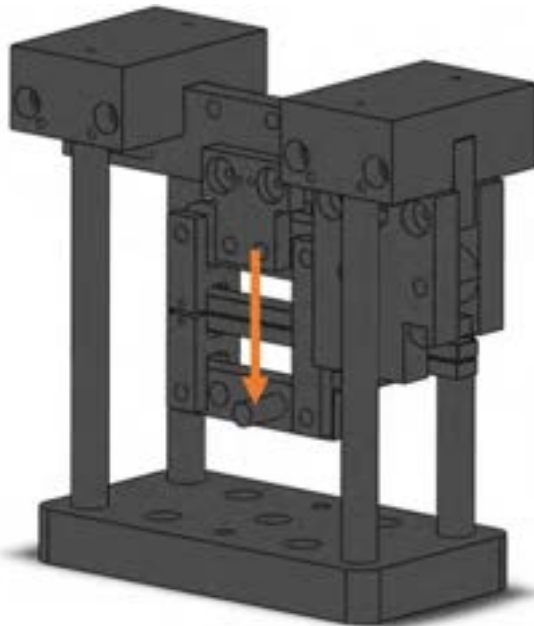


Fig. 16.11 Drop tower test setup for mixed-mode apparatus.

From C.S.P. Borges, P.D.P. Nunes, A. Akhavan, E.A.S. Marques, R.J.C. Carbas, L. Alfonso, L. F.M. Silva, Influence of mode mixity and loading rate on the fracture behaviour of crash resistant adhesives, *Theor. Appl. Fract. Mech.* 107 (2020) 102508, ISSN 0167-8442, <https://doi.org/10.1016/j.tafmec.2020.102508>.

be used with CMM specimens, which are very similar to the ARCAN specimens but contain an initial crack.

With the focus on impact tests of adhesive bonds in mixed mode, Borges et al. [66] successfully used a modification of the apparatus from Costa et al. [108] in a drop tower. Fig. 16.11 illustrates the modified apparatus with the arrow representing the impact load. Samples of two epoxy adhesives were tested at two mode mixities and impact velocities up to 3m/s. The authors found a dependency of the fracture behavior on the loading speed by comparing experimental data at quasistatic, intermediate, and impact test speeds. Unfortunately, the authors did not provide any information about the difficulties in testing and evaluating the recorded data as expected in such a complicated test setup.

It can be concluded that drop towers and pendulums appear to be good choices for testing at impact speeds in the 1–3 m/s range.

16.6.2 Split Hopkinson bars

Split Hopkinson pressure bars (SHPB) are established for highly dynamic load cases, such as those that can occur in ballistics, to obtain stress-strain data from materials at strain rates between 10^2s^{-1} and 10^4s^{-1} . The concept of SHPBs is based on the

propagation of stress waves in a one-dimensional bar. Such a load wave is generated by striking a fairly short striker bar (which has been accelerated by, for example, a gas gun) on a significantly longer input bar. The stress wave propagates through the input bar, which is connected to an output bar via the sample. Parts of the stress waves are reflected at every inhomogeneity, especially at the interfaces between the bars and the sample. The strain measurement on the bars enables the determination of transmitted and reflected waves, which can be converted into stress-strain relations by using the one-dimensional wave equation. Because the speed of propagation of stress waves in a material depends on the linear elastic properties and the density, the design of a specific SPHB configuration (beam lengths and material) must be in accordance with the planned experiment.

Lišner et al. [173–175] modified an SHPB for tensile testing and performed butt joint, lap shear, and scarf joint tests on a structural adhesive bond. They achieved test speeds of up to 3m/s, which is in the range of the drop tower tests cited in the previous subsection. The aim of the work was to extract rate-dependent parameters for cohesive zone modeling. The specimens used are quite sensitive to the stiffness and strength of the joint, but the fracture energy can only be roughly estimated. As a consequence, Lišner et al. [176, 177] further modified the test setup to work with fracture mechanics samples, such as the wedge double cantilever beam (WDCB) in Mode I, the ENF test in Mode II, and the SLB test in mixed-Mode I+II. The individual test configurations are shown in Fig. 16.12. It should be noted that fracture testing in the split Hopkinson bar is possible with a compression bar configuration that is generally less complicated than a tensile configuration as used in the previous work. In addition, different setups were used for WDCB and ENF/SLB tests. While the WDCB setup is more traditional with input and output bars, the output bar was replaced by a more rigid support in ENF and SLB tests. Similar to Xu and Dillard [14], it was found that forces acting on the sample due to the effects of friction and strong noise in the signals due to dynamic

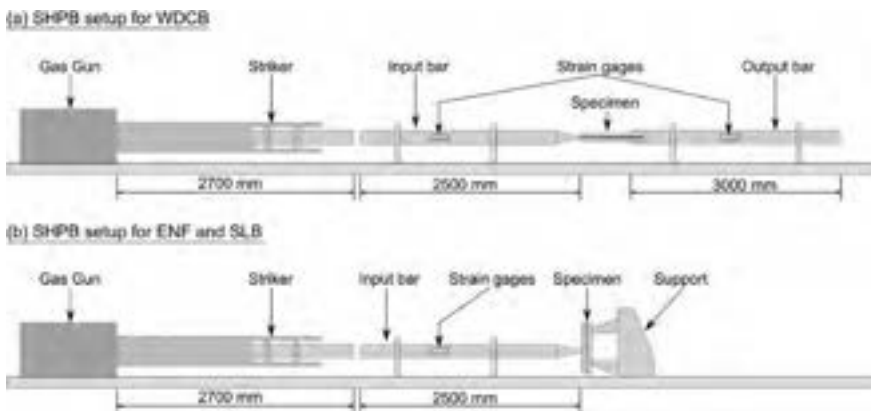


Fig. 16.12 SHPB configuration for fracture testing.

From M. Lišner, E. Alabort, B. Erice, H. Cui, B.R.K. Blackman, N. Petrinic, On the dynamic response of adhesively bonded structures, *Int. J. Impact Eng.* 138 (2020) 103479.

loading cannot be measured reliably. Therefore, Lißner et al. [176, 177] also calculated the fracture energy from the specimen compliance and the load point displacement, which was determined by means of digital image correlation (DIC) from measurements with high-speed cameras. Impact speeds of up to 4m/s were achieved, which is higher than the values found in publications on drop tower and pendulum tests.

16.6.3 Servohydraulic testing machines

Fracture tests at increased loading speeds are often carried out in servohydraulic testing machines. The main reason for this is that there are such machines in many laboratories for performing fatigue tests. The machines usually work in a closed control loop and achieve loading speeds of up to 1m/s, which is significantly below the capabilities of the devices mentioned in the previous subsections. As examples of newer fracture tests in such machines, Marzi et al. [178] and Dagorn et al. [146] carried out DCB, TENF, and mixed-mode tests at a test speed of 100mm/s while Schrader and Marzi [70] examined Mode III fractures by realizing angular displacement rates of up to 120 degrees/s.

For test velocities above 1m/s, there are special high-speed test machines with maximum test velocities between 20 and 25m/s. Such machines operate in an open loop, in which the hydraulic valves open instantly to accelerate a piston. Pohlitz et al. [179] used a modified load train of reduced inertia to perform CT tests at a relatively low velocity of 1m/s in such a machine. They compared load measurements with a piezoelectric load cell with strain gauges and found the signals from the piezoelectric cells to be more reliable under dynamic test conditions, which is in agreement with the observations from pendulum tests reported by Ashcroft et al. [102].

Blackman et al. [181], Karac et al. [182], and Gao et al. [183] performed DCB and TDCB tests in a speed range between 5 and 15m/s, which is the highest test speed found in the literature for fracture testing on adhesive bonds or composites. Fig. 16.13 illustrates their test setup, using a high-speed camera to monitor the crack growth during the experiment. As the test speed increased, the calculation of the fracture energy became difficult due to several changes in the fracture behavior, which was divided into four different types of fracture. Therefore, the authors were forced to propose different data reduction schemes depending on the sample type and observed fracture behavior. Nevertheless, from an experimental point of view, the high test speeds were successfully achieved, even if, especially in TDCB tests, the high inertia of the samples led to significant oscillations in the measurement signals. To overcome difficulties related to noisy signals and force measurement, Sun and Blackman [23] proposed a DIC method to obtain the fracture energy in Mode I and the associated traction-separation law for cohesive zone modeling at the same time from experimental data. The basic idea of the method is to obtain both the displacement and the rotation of the load application points as well as the COD from DIC measurements. Sun and Blackman [184] expanded the DIC method to obtain crack length under Mode I loading by evaluating beam deflection. Sun et al. [180] successfully applied these methods to high-speed DIC measurements in DCB tests at speeds

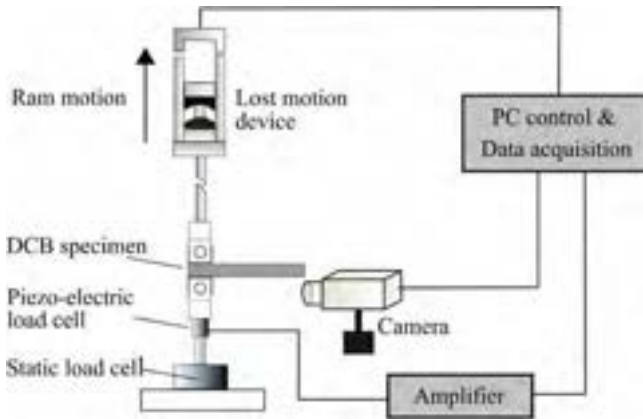


Fig. 16.13 DCB test in high-speed test machine.

From F. Sun, R. Zhang, B.R.K. Blackman, Determination of the mode I crack tip opening rate and the rate dependent cohesive properties for structural adhesive joints using digital image correlation, *Int. J. Solids Struct.* 217–218 (2021) 60–73, ISSN 0020-7683, <https://doi.org/10.1016/j.ijsolstr.2021.01.034>.

up to 1m/s. They confirmed the applicability of the DIC method on two different types of adhesive, one rather brittle and one more ductile. In DCB experiments at higher speeds, the method has not yet been used due to limitations in the maximum available frame rate of the cameras used.

16.7 Conclusions and future trends

In the past, fracture mechanics approaches to assessing the structural integrity of adhesive bonds have been increasingly improved. To gain a deeper understanding of the fracture under mixed-mode loading, many new types of test setups with appropriate evaluation methods were developed specifically for combinations of peel and in-plane shear loading. Load cases involving out-of-plane shear Mode III loading have rarely been considered, but in recent years there has been increasing, visible interest in these failure modes. Even if, according to the current state of research, there is no need to differentiate between Modes II and III with regard to fracture behavior, testing in Mode III appears to be more advantageous in some cases, especially for ductile adhesive joints. With regard to data reduction methods, LEFM approaches based on the Irwin-Kies equation are established, with the use of nonlinear approaches according to the J-integral enjoying increasing popularity. The latter has the advantage that it is not necessary to know or estimate the current crack length, but additional measurements required, such as of beam rotations, increase the experimental effort. Because cohesive zone modeling has now become an established method for designing structural adhesive connections with regard to fracture mechanics performance, test methods that allow the required model parameters to be determined appear to be the most popular in the future. With regard to fracture tests under special conditions

such as fatigue, aging, creep, or impact, further development of both established and new experimental methods will be required. This is because, first, to generate data on the performance of structural bonds under these conditions, and second, to provide the opportunity to gain a deeper understanding of the fracture that occurs under such conditions. As an example, a change in the fracture behavior between stable and stick-slip crack growth with increasing test speed in Mode I is reported in the literature while no corresponding experimental data have been found in other fracture modes so far. The increasing use of rubber-like adhesives in structural bondings requires the development of suitable testing and evaluation methods that take into account the large deformations of these adhesives prior to fracture.

In summary, fracture mechanics tests are a very powerful tool to characterize the structural integrity of bonded joints under all relevant loading conditions. In the future, however, further developments will be necessary to expand and improve the methods.

References

- [1] F.J.P. Chaves, L.F.M. da Silva, M.F.S.F de Moura, D.A. Dillard, V.H.C. Esteves, Fracture mechanics tests in adhesively bonded joints: a literature review, *J. Adhes.* 90 (12) (2014) 955–992, <https://doi.org/10.1080/00218464.2013.859075>.
- [2] L.F.M. da Silva, A. Öchsner, R.D. Adams, *Handbook of Adhesion Technology*, Springer Science & Business Media, Berlin Heidelberg, 2011, ISBN: 978-3-642-01168-9.
- [3] R.D. Adams, *Adhesive Bonding—Science, Technology and Applications*, Woodhead Publishing, Cambridge, 2021, ISBN: 978-0-323-85143-5.
- [4] G.P. Cherepanov, Crack propagation in continuous media: PMM vol. 31, no. 3, 1967, pp. 476–488, *J. Appl. Math. Mech.* 31 (3) (1967) 503–512.
- [5] J.R. Rice, A path independent integral and the approximate analysis of strain concentration by notches and cracks, *J. Appl. Mech.* 35 (2) (1968) 379–386.
- [6] J.D. Eshelby, The elastic energy-momentum tensor, *J. Elast.* 1573-2681, 5 (3) (1975) 321–335.
- [7] A.J. Paris, P.C. Paris, Instantaneous evaluation of J and O-star, *Int. J. Fract.* 38 (1) (1988) R19–R21.
- [8] E.N. DIN 6033:2016-02, *Aerospace Series—Carbon Fibre Reinforced Plastics—Test Method—Determination of Interlaminar Fracture Toughness Energy—Mode I—GIC*, DIN, 2016, <https://doi.org/10.31030/2385071>. Tech. Rep.
- [9] B. Blackman, J.P. Dear, A.J. Kinloch, S. Osiyemi, The calculation of adhesive fracture energies from double-cantilever beam test specimens, *J. Mater. Sci. Lett.* 10 (5) (1991) 253–256.
- [10] S. Marzi, O. Hesebeck, M. Brede, F. Kleiner, A rate-dependent cohesive zone model for adhesively bonded joints loaded in mode I, *J. Adhes. Sci. Technol.* 23 (6) (2009) 881–898, <https://doi.org/10.1163/156856109X411238>.
- [11] G.R. Irwin, J.A. Kies, Critical energy rate analysis of fracture strength, *Welding J. Suppl.* 33 (1954) 193s.
- [12] ISO 25217:2009-05, *Adhesives—Determination of the Mode I Adhesive Fracture Energy of Structural Adhesive Joints Using Double Cantilever Beam and Tapered Double Cantilever Beam Specimens*, International Organization for Standardization, 2009.
- [13] J. Cognard, The mechanics of the wedge test, *J. Adhes.* 20 (1) (1986) 1–13.

- [14] S. Xu, D.A. Dillard, Determining the impact resistance of electrically conductive adhesives using a falling wedge test, *IEEE Trans. Compon. Packag. Technol.* 26 (3) (2003) 554–562, <https://doi.org/10.1109/TCAPT.2003.817646>.
- [15] A. Biel, U. Stigh, An analysis of the evaluation of the fracture energy using the DCB-specimen, *Arch. Mech.* 59 (4-5) (2007) 311–327.
- [16] B. Blackman, A. Kinloch, Fracture tests on structural adhesive joints, in: D.R. Moore, A. Pavan, J.G. Williams (Eds.), *Fracture Mechanics Testing Methods for Polymers, Adhesives and Composites*, European Structural Integrity Society, vol. 28, Elsevier, 2001, pp. 225–267, [https://doi.org/10.1016/S1566-1369\(01\)80036-4](https://doi.org/10.1016/S1566-1369(01)80036-4).
- [17] D.R. Moore, J.G. Williams, A. Pavan, *Fracture Mechanics Testing Methods for Polymers, Adhesives and Composites*, Elsevier, 2001.
- [18] E. Noether, Invariantenprobleme, *Nachr. Ges. Wiss. Gottingen, Math.-Phys. Kl.* 2 (1918) 235–267.
- [19] G. Fernlund, M. Papini, D. McCammond, J.K. Spelt, Fracture load predictions for adhesive joints, *Compos. Sci. Technol.* 0266-3538, 51 (4) (1994) 587–600, [https://doi.org/10.1016/0266-3538\(94\)90091-4](https://doi.org/10.1016/0266-3538(94)90091-4).
- [20] L. Loh, S. Marzi, An out-of-plane loaded double cantilever beam (ODCB) test to measure the critical energy release rate in mode III of adhesive joints, *Int. J. Adhes. Adhes.* 0143-7496, 83 (2018) 24–30 (Special issue on joint design).
- [21] T. Andersson, U. Stigh, The stress-elongation relation for an adhesive layer loaded in peel using equilibrium of energetic forces, *Int. J. Solids Struct.* 0020-7683, 41 (2) (2004) 413–434, <https://doi.org/10.1016/j.ijsolstr.2003.09.039>.
- [22] J. Manterola, J. Renart, J. Zurbitu, A. Turon, I. Urresti, Mode I fracture characterisation of rigid and flexible bonded joints using an advanced Wedge-Driven Test, *Mech. Mater.* 0167-6636, 148 (2020) 103534, <https://doi.org/10.1016/j.mechmat.2020.103534>.
- [23] F. Sun, B.R.K. Blackman, A DIC method to determine the Mode I energy release rate G , the J-integral and the traction-separation law simultaneously for adhesive joints, *Eng. Fract. Mech.* 0013-7944, 234 (2020) 107097, <https://doi.org/10.1016/j.engfracmech.2020.107097>.
- [24] U. Stigh, A. Biel, D. Svensson, Cohesive zone modelling and the fracture process of structural tape, *Procedia Struct. Integr.* 2452-3216, 2 (2016) 235–244, <https://doi.org/10.1016/j.prostr.2016.06.031> (21st European Conference on Fracture, ECF21, 20–24 June 2016, Catania, Italy).
- [25] U. Stigh, K.S. Alfredsson, A. Biel, Measurement of cohesive laws and related problems, in: *ASME International Mechanical Engineering Congress and Exposition*, Volume 11: *Mechanics of Solids, Structures and Fluids*, 2009, pp. 293–298, ISBN: 978-0-7918-4384-0, <https://doi.org/10.1115/IMECE2009-10474>.
- [26] D.S. Dugdale, Yielding of steel sheets containing slits, *J. Mech. Phys. Solids* 8 (1960) 100–104.
- [27] G.I. Barenblatt, The mathematical theory of equilibrium cracks in brittle fracture, *Adv. Appl. Mech.* 77 (1962) 55–129.
- [28] Y. Zhu, K.M. Liechti, K. Ravi-Chandar, Direct extraction of rate-dependent traction-separation laws for polyurea/steel interfaces, *Int. J. Solids Struct.* 0020-7683, 46 (1) (2009) 31–51, <https://doi.org/10.1016/j.ijsolstr.2008.08.019>.
- [29] S. Marzi, A. Biel, U. Stigh, On experimental methods to investigate the effect of layer thickness on the fracture behavior of adhesively bonded joints, *Int. J. Adhes. Adhes.* 0143-7496, 31 (8) (2011) 840–850, <https://doi.org/10.1016/j.ijadhadh.2011.08.004>.
- [30] U. Stigh, A. Biel, T. Walander, Shear strength of adhesive layers—models and experiments, *Eng. Fract. Mech.* 0013-7944, 129 (2014) 67–76, <https://doi.org/10.1016/j.engfracmech.2014.07.033> (Macrofracture analysis and testing).

- [31] C. Wu, S. Gowrishankar, R. Huang, K. Liechti, On determining mixed-mode traction-separation relations for interfaces, *Int. J. Fract.* 202 (2016) 1–19, <https://doi.org/10.1007/s10704-016-0128-4>.
- [32] A.S.T.M. D3433-99, Standard Test Method for Fracture Strength in Cleavage of Adhesives in Bonded Metal Joints, ASTM International, 2012.
- [33] T. Andersson, U. Stigh, Verification of an experimental method to measure the stress-elongation law for an adhesive layer using a DCB-specimen, in: *Proceedings of 10th International Conference on Fracture. Advances in Fracture Research*, Elsevier, 2001. ICF100752OR.
- [34] B.R.K. Blackman, A.J. Kinloch, M. Paraschi, W.S. Teo, Measuring the mode I adhesive fracture energy, GIC, of structural adhesive joints: the results of an international round-robin, *Int. J. Adhes. Adhes.* 0143-7496, 23 (4) (2003) 293–305, [https://doi.org/10.1016/S0143-7496\(03\)00047-2](https://doi.org/10.1016/S0143-7496(03)00047-2).
- [35] A. Khayer Dastjerdi, M. Pagano, M.T. Kaartinen, M.D. McKee, F. Barthelat, Cohesive behavior of soft biological adhesives: experiments and modeling, *Acta Biomater.* 1742-7061, 8 (9) (2012) 3349–3359, <https://doi.org/10.1016/j.actbio.2012.05.005>.
- [36] A. Khayer Dastjerdi, E. Tan, F. Barthelat, Direct measurement of the cohesive law of adhesives using a rigid double cantilever beam technique, *Exp. Mech.* 53 (2013), <https://doi.org/10.1007/s11340-013-9755-0>.
- [37] B. Watson, M.J. Worswick, D.S. Cronin, Quantification of mixed mode loading and bond line thickness on adhesive joint strength using novel test specimen geometry, *Int. J. Adhes. Adhes.* 0143-7496, 102 (2020) 102682, <https://doi.org/10.1016/j.ijadhadh.2020.102682>.
- [38] E.J. Ripling, S. Mostovoy, H.T. Corten, Fracture mechanics: a tool for evaluating structural adhesives, *J. Adhes.* 3 (2) (1971) 107–123, <https://doi.org/10.1080/00218467108081158>.
- [39] G. Stamoulis, N. Carrere, Linear elastic analysis of the loading rate dependency of the fracture properties of structural adhesives in the mixed mode I+II plane, *Eng. Fract. Mech.* 0013-7944, 225 (2020) 106840, <https://doi.org/10.1016/j.engfracmech.2019.106840>.
- [40] ISO 11343:2019-10, Adhesives—Determination of Dynamic Resistance to Cleavage of High-Strength Adhesive Bonds Under Impact Wedge Conditions—Wedge Impact Method, International Organization for Standardization, 2019.
- [41] D.A. Dillard, D.J. Pohlit, G.C. Jacob, J.M. Starbuck, R.K. Kapania, On the use of a driven wedge test to acquire dynamic fracture energies of bonded beam specimens, *J. Adhes.* 87 (4) (2011) 395–423, <https://doi.org/10.1080/00218464.2011.562125>.
- [42] J. Renart, J. Costa, G. Santacruz, S. Lazcano, E.V. González, Measuring fracture energy of interfaces under mode I loading with the wedge driven test, *Eng. Fract. Mech.* 0013-7944, 239 (2020) 107210, <https://doi.org/10.1016/j.engfracmech.2020.107210>.
- [43] M. Cabello, J. Zurbitu, J. Renart, A. Turon, F. Martínez, A non-linear hyperelastic foundation beam theory model for double cantilever beam tests with thick flexible adhesive, *Int. J. Solids Struct.* 0020-7683, 80 (2016) 19–27, <https://doi.org/10.1016/j.ijsolstr.2015.10.017>.
- [44] D. Plausinis, J.K. Spelt, Designing for time-dependent crack growth in adhesive joints, *Int. J. Adhes. Adhes.* 0143-7496, 15 (3) (1995) 143–154, [https://doi.org/10.1016/0143-7496\(95\)91625-G](https://doi.org/10.1016/0143-7496(95)91625-G).
- [45] H. Parvatareddy, A. Pasricha, D.A. Dillard, B. Holmes, J.G. Dillard, High temperature and environmental effects on the durability of Ti-6Al-4V/FM5 adhesive bonded system, *ASTM Spec. Tech. Publ.* 1302 (1997) 149–174.
- [46] Y. Bertholet, F. Iker, X.X. Zhang, J.-P. Raskin, T. Pardoën, Steady-state measurement of the interface fracture resistance in wafer bonding, in: *15th European Conference of Fracture*, 2004.

- [47] H.K. Singh, K.-T. Wan, J.G. Dillard, D.A. Dillard, P. Reboa, J. Smith, E. Chappell, A. Sharan, Subcritical delamination in epoxy bonds to silicon and glass adherends: effect of temperature and preconditioning, *J. Adhes.* 84 (7) (2008) 619–637.
- [48] A.C. Taylor, J.G. Williams, Determining the fracture energy of structural adhesives from Wedge-Peel tests, *J. Adhes.* 87 (5) (2011) 482–503, <https://doi.org/10.1080/00218464.2011.575337>.
- [49] J.D. Barrett, R.O. Foschi, Mode II stress-intensity factors for cracked wood beams, *Eng. Fract. Mech.* 0013-7944, 9 (2) (1977) 371–378, [https://doi.org/10.1016/0013-7944\(77\)90029-7](https://doi.org/10.1016/0013-7944(77)90029-7).
- [50] H. Chai, S. Mall, Design aspects of the end-notch adhesive joint specimen, *Int. J. Fract.* 36 (1) (1988) R3–R8.
- [51] H. Chai, Shear fracture, *Int. J. Fract.* 37 (1988) 137–159.
- [52] H. Chai, Micromechanics of shear deformations in cracked bonded joints, *Int. J. Fract.* 58 (1992) 223–239.
- [53] K. Leffler, K.S. Alfredsson, U. Stigh, Shear behaviour of adhesive layers, *Int. J. Solids Struct.* 0020-7683, 44 (2) (2007) 530–545, <https://doi.org/10.1016/j.ijsolstr.2006.04.036>.
- [54] A. Biel, U. Stigh, Comparison of J-integral methods to experimentally determine cohesive laws in shear for adhesives, *Int. J. Adhes. Adhes.* 0143-7496, 94 (2019) 64–75, <https://doi.org/10.1016/j.ijadhadh.2019.04.014>.
- [55] U. Stigh, A. Biel, Shear properties of an adhesive layer exposed to a compressive load, *Procedia Mater. Sci.* 3 (2014) 1626–1631.
- [56] P. Qiao, J. Wang, J.F. Davalos, Analysis of tapered ENF specimen and characterization of bonded interface fracture under Mode-II loading, *Int. J. Solids Struct.* 0020-7683, 40 (8) (2003) 1865–1884, [https://doi.org/10.1016/S0020-7683\(03\)00031-3](https://doi.org/10.1016/S0020-7683(03)00031-3).
- [57] S. Marzi, Measuring the critical energy release rate in mode II of tough, structural adhesive joints using the tapered end-notched flexure (TENF) test, *Eur. Phys. J. Spec. Top.* 206 (2012) 35–40, <https://doi.org/10.1140/epjst/e2012-01584-4>.
- [58] R.H. Martin, B.D. Davidson, Mode II fracture toughness evaluation using four point bend, end notched flexure test, *Plast. Rubber Compos.* 28 (8) (1999) 401–406.
- [59] A.J.S. Leal, R.D.S.G. Campilho, Numerical evaluation of the ENF and 4ENF tests for the shear toughness estimation of adhesive joints, *Compos. Struct.* 0263-8223, 202 (2018) 333–343, <https://doi.org/10.1016/j.compstruct.2018.01.107> (Special issue dedicated to Ian Marshall).
- [60] G. Cricri, Cohesive law identification of adhesive layers subject to shear load The Twice Notched Flexure Test, *Procedia Struct. Integr.* 12 (2018) 492–498.
- [61] B.R.K. Blackman, A.J. Kinloch, M. Paraschi, The determination of the mode II adhesive fracture resistance, GIIC, of structural adhesive joints: an effective crack length approach, *Eng. Fract. Mech.* 0013-7944, 72 (6) (2005) 877–897, <https://doi.org/10.1016/j.engfracmech.2004.08.007> (Prospects in Fracture Papers from a Conference held to Celebrate the 65th Birthday of Professor J.G. Williams, FRS, FEng Imperial College London, July 2003).
- [62] E. Sancaktar, H. Jozavi, J. Baldwin, J. Tang, Elastoplastic fracture behavior of structural adhesives under monotonic loading, *J. Adhes.* 23 (4) (1987) 233–262, <https://doi.org/10.1080/00218468708075409>.
- [63] S. Marzi, O. Hesebeck, M. Brede, F. Kleiner, An end-loaded shear joint (ELSJ) specimen to measure the critical energy release rate in mode II of tough, structural adhesive joints, *J. Adhes. Sci. Technol.* 23 (15) (2009) 1883–1891, <https://doi.org/10.1163/016942409X12508517390716>.

- [64] G.S. Başı, E. Sancaktar, Mixed-mode fracture behavior of epoxy-based impact adhesives, *Int. J. Adhes. Adhes.* 0143-7496, (2021) 103012, <https://doi.org/10.1016/j.ijadhadh.2021.103012>.
- [65] G. Cricri, Cohesive law identification of adhesive layers subject to shear load—an exact inverse solution, *Int. J. Solids Struct.* 0020-7683, 158 (2019) 150–164, <https://doi.org/10.1016/j.ijsolstr.2018.09.001>.
- [66] C.S.P. Borges, P.D.P. Nunes, A. Akhavan, E.A.S. Marques, R.J.C. Carbas, L. Alfonso, L. F.M. Silva, Influence of mode mixity and loading rate on the fracture behaviour of crash resistant adhesives, *Theor. Appl. Fract. Mech.* 0167-8442, 107 (2020) 102508, <https://doi.org/10.1016/j.tafmec.2020.102508>.
- [67] S.L. Donaldson, Mode III interlaminar fracture characterization of composite materials, *Compos. Sci. Technol.* 0266-3538, 32 (3) (1988) 225–249, [https://doi.org/10.1016/0266-3538\(88\)90022-X](https://doi.org/10.1016/0266-3538(88)90022-X).
- [68] A.L. Johnston, B.D. Davidson, K.K. Simon, Assessment of split-beam-type tests for mode III delamination toughness determination, *Int. J. Fract.* 185 (2013) 31–48, <https://doi.org/10.1007/s10704-013-9897-1>.
- [69] J. Lee, J. Cho, G. Zhao, C. Cho, An investigation on the fatigue behavior of DCB specimen bonded with aluminum foam at Mode III, *J. Mech. Sci. Technol.* 30 (2016) 4475–4478, <https://doi.org/10.1007/s12206-016-0915-x>.
- [70] P. Schrader, S. Marzi, Mode III testing of structural adhesive joints at elevated loading rates, *Int. J. Adhes. Adhes.* 0143-7496, 113 (2022) 103078, <https://doi.org/10.1016/j.ijadhadh.2021.103078>.
- [71] G. Cricri, M. Perrella, S. Sessa, N. Valoroso, A novel fixture for measuring mode III toughness of bonded assemblies, *Eng. Fract. Mech.* 0013-7944, 138 (2015) 1–18, <https://doi.org/10.1016/j.engfracmech.2015.03.019>.
- [72] P. Robinson, D.Q. Song, A new mode III delamination test for composites, *Adv. Compos. Lett.* 1 (5) (1992). 096369359200100501.
- [73] B.D. Davidson, F.O. Sediles, Mixed-mode I+II+III delamination toughness determination via shear-torsion-bending test, *Compos. Part A* 42 (2011) 589–603.
- [74] A. Jouan, A. Constantinescu, A critical comparison of shear tests for adhesive joints, *Int. J. Adhes. Adhes.* 0143-7496, 84 (2018) 63–79, <https://doi.org/10.1016/j.ijadhadh.2018.02.035>.
- [75] G. Fernlund, H. Lanting, J.K. Spelt, Mixed mode II-mode III fracture of adhesive joints, *J. Compos. Technol. Res.* 17 (4) (1995) 317–330.
- [76] H. Chai, Bond thickness effect in mixed-mode fracture and its significance to delamination resistance, *Int. J. Solids Struct.* 0020-7683, 219–220 (2021) 63–80, <https://doi.org/10.1016/j.ijsolstr.2021.03.006>.
- [77] M. Conroy, A.J. Kinloch, J.G. Williams, A. Ivankovic, Mixed mode partitioning of beam-like geometries: a damage dependent solution, *Eng. Fract. Mech.* 0013-7944, 149 (2015) 351–367, <https://doi.org/10.1016/j.engfracmech.2015.06.061>.
- [78] J.H. Crews, J.R. Reeder, A Mixed-Mode Bending Apparatus for Delamination Testing, National Aeronautics and Space Administration, Langley Research Center, 1988.
- [79] J.R. Reeder, J.H. Crews Jr, Mixed-mode bending method for delamination testing, *AiAA J.* 28 (7) (1990) 1270–1276.
- [80] S.J. Hooper, Y. Khourchid, P. Sriram, Application of the MMB specimen in the measurement of mixed mode interlaminar fracture toughness, in: *Key Engineering Materials*, 120, Trans Tech Publ, 1996, pp. 361–388. vol.

- [81] F. Ducept, P. Davies, D. Gamby, Mixed mode failure criteria for a glass/epoxy composite and an adhesively bonded composite/composite joint, *Int. J. Adhes. Adhes.* 0143-7496, 20 (3) (2000) 233–244, [https://doi.org/10.1016/S0143-7496\(99\)00048-2](https://doi.org/10.1016/S0143-7496(99)00048-2).
- [82] G. Stamoulis, N. Carrere, J.Y. Cognard, P. Davies, C. Badulescu, On the experimental mixed-mode failure of adhesively bonded metallic joints, *Int. J. Adhes. Adhes.* 51 (2014) 148–158.
- [83] C.S. Hong, S.H. Yoon, Modified end notched flexure specimen for mixed mode interlaminar fracture in laminated composites, *Int. J. Fract.* 43 (1990) R3–R9.
- [84] G. Ji, Z. Ouyang, G. Li, On the interfacial constitutive laws of mixed mode fracture with various adhesive thicknesses, *Mech. Mater.* 0167-6636, 47 (2012) 24–32, <https://doi.org/10.1016/j.mechmat.2012.01.002>.
- [85] J. Jokinen, O. Orell, M. Wallin, M. Kanerva, A concept for defining the mixed-mode behaviour of tough epoxy film adhesives by single specimen design, *J. Adhes. Sci. Technol.* 34 (18) (2020) 1982–1999, <https://doi.org/10.1080/01694243.2020.1746606>.
- [86] A. Szekrényes, J. UJ, Over-leg bending test for mixed-mode I/II interlaminar fracture in composite laminates, *Int. J. Damage Mech.* 16 (1) (2007) 5–33, <https://doi.org/10.1177/1056789507060774>.
- [87] R.D.F. Moreira, M.F.S.F de Moura, F.G.A. Silva, A novel strategy to obtain the fracture envelope under mixed-mode I+II loading of composite bonded joints, *Eng. Fract. Mech.* 0013-7944, 232 (2020) 107032, <https://doi.org/10.1016/j.engfracmech.2020.107032>.
- [88] F. Xiao, C.-Y. Hui, E.J. Kramer, Analysis of a mixed mode fracture specimen: the asymmetric double cantilever beam, *J. Mater. Sci.* 28 (20) (1993) 5620–5629.
- [89] V. Sundararaman, B.D. Davidson, An unsymmetric double cantilever beam test for interfacial fracture toughness determination, *Int. J. Solids Struct.* 0020-7683, 34 (7) (1997) 799–817, [https://doi.org/10.1016/S0020-7683\(96\)00055-8](https://doi.org/10.1016/S0020-7683(96)00055-8).
- [90] S. Park, D. Dillard, Development of a simple mixed-mode fracture test and the resulting fracture energy envelope for an adhesive bond, *Int. J. Fract.* 148 (2008) 261–271, <https://doi.org/10.1007/s10704-008-9200-z>.
- [91] S. Marzi, An extension of MAT 240 to consider the failure of structural adhesive joints in crash simulations, in: *German LS-Dyna Forum, Conference Proceedings, Bamberg, 2010. B-II-1-B-II-12*.
- [92] G. Fernlund, J.K. Spelt, Mixed-mode fracture characterization of adhesive joints, *Compos. Sci. Technol.* 50 (1994) 441–449.
- [93] V. Sundararaman, B.D. Davidson, An unsymmetric end-notched flexure test for interfacial fracture toughness determination, *Eng. Fract. Mech.* 0013-7944, 60 (3) (1998) 361–377, [https://doi.org/10.1016/S0013-7944\(98\)00017-4](https://doi.org/10.1016/S0013-7944(98)00017-4).
- [94] Q. Liu, P. Qiao, Mixed mode fracture characterization of GFRP-concrete bonded interface using four-point asymmetric end-notched flexure test, *Theor. Appl. Fract. Mech.* 0167-8442, 92 (2017) 155–166, <https://doi.org/10.1016/j.tafmec.2017.06.009>.
- [95] T. Brussat, S. Chiu, S. Mostovoy, Fracture mechanics for structural adhesive bonds, Lockheed-California Co., Burbank, CA, 1977. Technical Report.
- [96] G. Fernlund, J.K. Spelt, Failure load prediction of structural adhesive joints: Part 1: Analytical method, *Int. J. Adhes. Adhes.* 0143-7496, 11 (4) (1991) 213–220, [https://doi.org/10.1016/0143-7496\(91\)90003-Z](https://doi.org/10.1016/0143-7496(91)90003-Z).
- [97] G. Fernlund, J.K. Spelt, Failure load prediction of structural adhesive joints: Part 2: Experimental study, *Int. J. Adhes. Adhes.* 0143-7496, 11 (4) (1991) 221–227, [https://doi.org/10.1016/0143-7496\(91\)90004-2](https://doi.org/10.1016/0143-7496(91)90004-2).
- [98] ASTM International, Standard Test Method for Mixed Mode I-mode II Interlaminar Fracture Toughness of Unidirectional Fiber Reinforced Polymer Matrix Composites.

- Annual book of ASTM Standards, ASTM International, 2004. Tech. Rep. ASTM D6671-04.
- [99] J.L. Högberg, U. Stigh, Specimen proposals for mixed mode testing of adhesive layer, *Eng. Fract. Mech.* 0013-7944, 73 (16) (2006) 2541–2556, <https://doi.org/10.1016/j.engfracmech.2006.04.017> (Fracture of Polymers, Composites and Adhesives).
- [100] B.D. Davidson, V. Sundararaman, A single leg bending test for interfacial fracture toughness determination, *Int. J. Fract.* 78 (2) (1996) 193–210.
- [101] B.F. Sørensen, K. Jørgensen, T.K. Jacobsen, R.C. Østergaard, DCB-specimen loaded with uneven bending moments, *Int. J. Fract.* 141 (2006) 163–176, <https://doi.org/10.1007/s10704-006-0071-x>.
- [102] I.A. Ashcroft, J.P. Casas-Rodriguez, V.V. Silberschmidt, Mixed-mode crack growth in bonded composite joints under standard and impact-fatigue loading, *J. Mater. Sci.* 43 (20) (2008) 6704–6713.
- [103] D. Samborsky, A. Sears, P. Agastra, J. Mandell, Mixed mode static and fatigue crack growth in wind blade paste adhesives, in: Collection of Technical Papers—AIAA/ASME/ASCE/AHS/ASC Structures, Structural Dynamics and Materials Conference, 2011, <https://doi.org/10.2514/6.2011-1755>.
- [104] I. Floros, K. Tserpes, Fatigue crack growth characterization in adhesive CFRP joints, *Compos. Struct.* 0263-8223, 207 (2019) 531–536, <https://doi.org/10.1016/j.compstruct.2018.09.020>.
- [105] D. Plausinis, J.K. Spelt, Application of a new constant G load-jig to creep crack growth in adhesive joints, *Int. J. Adhes. Adhes.* 0143-7496, 15 (4) (1995) 225–232, [https://doi.org/10.1016/0143-7496\(96\)83703-1](https://doi.org/10.1016/0143-7496(96)83703-1).
- [106] C. Lundsgaard-Larsen, B.F. Sørensen, C. Berggreen, R.C. Østergaard, A modified DCB sandwich specimen for measuring mixed-mode cohesive laws, *Eng. Fract. Mech.* 75 (2008) 2514–2530.
- [107] S. Azari, M. Eskandarian, M. Papini, J.A. Schroeder, J.K. Spelt, Fracture load predictions and measurements for highly toughened epoxy adhesive joints, *Eng. Fract. Mech.* 0013-7944, 76 (13) (2009) 2039–2055, <https://doi.org/10.1016/j.engfracmech.2009.05.011>.
- [108] M. Costa, R. Carbas, E. Marques, G. Viana, L.F.M. da Silva, An apparatus for mixed-mode fracture characterization of adhesive joints, *Theor. Appl. Fract. Mech.* 0167-8442, 91 (2017) 94–102, <https://doi.org/10.1016/j.tafmec.2017.04.014> (Mixed Mode Fracture: Recent Developments).
- [109] H. Singh, A. Chakraborty, C. Frazier, D. Dillard, Mixed mode fracture testing of adhesively bonded specimens using a dual-actuator load frame, *Holzforschung* 64 (2010) 353–361, <https://doi.org/10.1515/HF.2010.041>.
- [110] E. Nicoli, D.A. Dillard, C.E. Frazier, A. Zink-Sharp, Characterization of mixed-mode I/II fracture properties of adhesively bonded yellow-poplar by a dual actuator test frame instrument, *Holzforschung* 66 (5) (2012) 623–631, <https://doi.org/10.1515/hf-2011-0171>.
- [111] F.J.P. Chaves, M.F.S.F de Moura, L.F.M. da Silva, D.A. Dillard, Numerical analysis of the dual actuator load test applied to fracture characterization of bonded joints, *Int. J. Solids Struct.* 0020-7683, 48 (10) (2011) 1572–1578, <https://doi.org/10.1016/j.ijsolstr.2011.02.006>.
- [112] F.J.P. Chaves, M.F.S.F de Moura, L.F.M. da Silva, D.A. Dillard, Fracture characterization of bonded joints using the dual actuator load apparatus, *J. Adhes. Sci. Technol.* 28 (5) (2014) 512–524, <https://doi.org/10.1080/01694243.2013.845357>.
- [113] E. Panettieri, G. Leclerc, J. Jumel, J. Guitard, Mixed-mode crack propagation tests of composite bonded joints using a dual-actuator load frame—constant and variable GII/

- GI conditions, *Eng. Fract. Mech.* 0013-7944, 202 (2018) 471–486, <https://doi.org/10.1016/j.engfracmech.2018.09.015>.
- [114] T. Walander, Influences of Temperature, Fatigue and Mixed-Mode Loading on the Cohesive Properties of Adhesives Layers (Ph.D. thesis), Chalmers University Göteborg 2015.
- [115] J.L. Högberg, B.F. Sørensen, U. Stigh, Constitutive behaviour of mixed mode loaded adhesive layer, *Int. J. Soild Struct.* 44 (2007) 8335–8354.
- [116] G. Valentin, P. Caumes, Crack propagation in mixed mode in wood: a new specimen, *Wood Sci. Technol.* 23 (1989) 43–53, <https://doi.org/10.1007/BF00350606>.
- [117] H.L.J. Pang, Mixed mode fracture analysis and toughness of adhesive joints, *Eng. Fract. Mech.* 51 (1995) 575–583.
- [118] H.L.J. Pang, C.W. Seetoh, A compact mixed mode (CMM) fracture specimen for adhesive bonded joints, *Eng. Fract. Mech.* 0013-7944, 57 (1997) 57–65.
- [119] A. Pirondi, G. Nicoletto, Mixed mode I/II fatigue crack growth in adhesive joints, *Eng. Fract. Mech.* 73 (2006) 2557–2568, <https://doi.org/10.1016/j.engfracmech.2006.04.009>.
- [120] N. Choupani, Mixed-mode cohesive fracture of adhesive joints: experimental and numerical studies, *Eng. Fract. Mech.* 0013-7944, 75 (15) (2008) 4363–4382, <https://doi.org/10.1016/j.engfracmech.2008.04.023>.
- [121] Q. Chen, H. Guo, K. Avery, H. Kang, X. Su, Mixed-mode fatigue crack growth and life prediction of an automotive adhesive bonding system, *Eng. Fract. Mech.* 0013-7944, 189 (2018) 439–450, <https://doi.org/10.1016/j.engfracmech.2017.11.004>.
- [122] K. Chong, M.D. Kuruppu, New specimen for fracture toughness determination for rock and other materials, *Int. J. Fract.* 26 (2) (1984) R59–R62.
- [123] A. Ajdani, M.R. Ayatollahi, A. Akhavan-Safar, L.F.M. da Silva, Mixed mode fracture characterization of brittle and semi-brittle adhesives using the SCB specimen, *Int. J. Adhes. Adhes.* 0143-7496, 101 (2020) 102629, <https://doi.org/10.1016/j.ijadhadh.2020.102629>.
- [124] A. Ajdani, M.R. Ayatollahi, L.F.M. da Silva, Mixed mode fracture analysis in a ductile adhesive using semi-circular bend (SCB) specimen, *Theor. Appl. Fract. Mech.* 0167-8442, 112 (2021) 102927, <https://doi.org/10.1016/j.tafmec.2021.102927>.
- [125] M.R.M. Aliha, H.G. Kucheki, M. Mirsayar, Mixed mode I/II fracture analysis of bi-material adhesive bonded joints using a novel short beam specimen, *Appl. Sci.* 11 (11) (2021) 5232.
- [126] M. Arcan, Z. Hashin, A. Voloshin, A method to produce uniform plane-stress states with applications to fiber-reinforced materials, *Exp. Mech.* 18 (4) (1978) 141–146.
- [127] J.Y. Cognard, R. Créac’hacdec, L.F.M. da Silva, F.G. Teixeira, P. Davies, M. Peleau, Experimental analysis of the influence of hydrostatic stress on the behaviour of an adhesive using a pressure vessel, *J. Adhes.* 87 (2011) 804–825.
- [128] R. Créac’hacdec, G. Jamin, J.Y. Cognard, P. Jousset, Experimental analysis of the mechanical behaviour of a thick flexible adhesive under tensile/compression-shear loads, *Int. J. Adhes. Adhes.* 0143-7496, 48 (2014) 258–267, <https://doi.org/10.1016/j.ijadhadh.2013.09.040>.
- [129] F. Sousa, A. Akhavan-Safar, R. Goyal, L.F.M. Silva, The influence of mode mixity and adhesive system on the fatigue life of adhesive joints, *Fatigue Fract. Eng. Mater. Struct.* 43 (2020), <https://doi.org/10.1111/ffe.13301>.
- [130] F.C. Sousa, A. Akhavan-Safar, G. Rakesh, L.F.M. da Silva, Fatigue life estimation of adhesive joints at different mode mixities, *J. Adhes.* (2020) 1–23.
- [131] T. Wah, The adhesive scarf joint in pure bending, *Int. J. Mech. Sci.* 0020-7403, 18 (5) (1976) 223–228, [https://doi.org/10.1016/0020-7403\(76\)90003-5](https://doi.org/10.1016/0020-7403(76)90003-5).
- [132] H. Chai, Experimental evaluation of mixed-mode fracture in adhesive bonds, *Exp. Mech.* 32 (1992) 296–303.

- [133] S. Safaei, M.R. Ayatollahi, B. Saboori, Fracture behavior of GPPS brittle polymer under mixed mode I/III loading, *Theor. Appl. Fract. Mech.* 91 (2017) 103–115.
- [134] A. Akhavan-Safar, M.R. Ayatollahi, S. Safaei, L.F.M. da Silva, Mixed mode I/III fracture behavior of adhesive joints, *Int. J. Solids Struct.* 0020-7683, 199 (2020) 109–119, <https://doi.org/10.1016/j.ijsolstr.2020.05.007>.
- [135] L. Loh, S. Marzi, Mixed-mode I+III tests on hyperelastic adhesive joints at prescribed mode-mixity, *Int. J. Adhes. Adhes.* 0143-7496, 85 (2018) 113–122.
- [136] L. Loh, S. Marzi, A mixed-mode controlled DCB test on adhesive joints loaded in a combination of modes I and III, *Procedia Struct. Integr.* 13 (2018) 1318–1323, <https://doi.org/10.1016/j.prostr.2018.12.277>.
- [137] L. Loh, S. Marzi, A novel experimental methodology to identify fracture envelopes and cohesive laws in mixed-mode I+III, *Eng. Fract. Mech.* 0013-7944, 214 (2019) 304–319 (Corrected in Ref. [138]).
- [138] L. Loh, S. Marzi, Corrigendum to “A novel experimental methodology to identify fracture envelopes and cohesive laws in mixed-mode I+III” [*Eng. Fract. Mech.* 214 (2019), 304–319], *Eng. Fract. Mech.* 0013-7944, 263 (2022) 108294, <https://doi.org/10.1016/j.engfracmech.2022.108294>.
- [139] F. Bödeker, S. Marzi, Applicability of the mixed-mode controlled double cantilever beam test and related evaluation methods, *Eng. Fract. Mech.* 0013-7944, 235 (2020) 107149, <https://doi.org/10.1016/j.engfracmech.2020.107149>.
- [140] I.V. Vintilescu, Mixed-Mode I-II-III Fracture of Adhesive Joints (Master’s thesis), University of Toronto 1997.
- [141] H.A. Richard, M. Kuna, Theoretical and experimental study of superimposed fracture modes I, II and III, *Eng. Fract. Mech.* 0013-7944, 35 (6) (1990) 949–960, [https://doi.org/10.1016/0013-7944\(90\)90124-Y](https://doi.org/10.1016/0013-7944(90)90124-Y).
- [142] M. Razavi, F. Berto, A new fixture for fracture tests under mixed mode I/II/III loading, *Fatigue Fract. Eng. Mater. Struct.* 42 (2019), <https://doi.org/10.1111/ffe.13033>.
- [143] A.O. Ayhan, O. Demir, A novel test system for mixed mode-I/II/III fracture tests—Part 1: Modeling and numerical analyses, *Eng. Fract. Mech.* 0013-7944, 218 (2019) 106597, <https://doi.org/10.1016/j.engfracmech.2019.106597>.
- [144] A.O. Ayhan, O. Demir, Computational modeling of three-dimensional mixed mode-I/II/III fatigue crack growth problems and experiments, *Comput. Struct.* 0045-7949, 243 (2021) 106399, <https://doi.org/10.1016/j.compstruc.2020.106399>.
- [145] O. Demir, A.O. Ayhan, S. İriç, A novel test system for mixed mode-I/II/III fracture tests—Part 2: Experiments and criterion development, *Eng. Fract. Mech.* 0013-7944, 220 (2019) 106671, <https://doi.org/10.1016/j.engfracmech.2019.106671>.
- [146] N. Dagorn, G. Portemont, J. Berthe, F. Rasselet, B. Bourel, F. Lauro, Development of a mixed mode double cantilever beam specimen for the fracture characterization of adhesives under high displacement rate, *Eng. Fract. Mech.* 0013-7944, 242 (2021) 107467, <https://doi.org/10.1016/j.engfracmech.2020.107467>.
- [147] G. Jhin, S. Azari, A. Ameli, N.V. Datla, M. Papini, J.K. Spelt, Crack growth rate and crack path in adhesively bonded joints: comparison of creep, fatigue and fracture, *Int. J. Adhes. Adhes.* 0143-7496, 46 (2013) 74–84, <https://doi.org/10.1016/j.ijadhadh.2013.05.009>.
- [148] X.-L. Zhao, Y. Bai, R. Al-Mahaidi, S. Rizkalla, Effect of dynamic loading and environmental conditions on the bond between CFRP and steel: state-of-the-art review, *J. Compos. Constr.* 18 (3) (2014) A4013005.
- [149] H. Jin, G.M. Miller, N.R. Sottos, S.R. White, Fracture and fatigue response of a self-healing epoxy adhesive, *Polymer* 0032-3861, 52 (7) (2011) 1628–1634, <https://doi.org/10.1016/j.polymer.2011.02.011>.

- [150] G. Clerc, A.J. Brunner, S. Josset, P. Niemz, F. Pichelin, J.W.G. Van de Kuilen, Adhesive wood joints under quasi-static and cyclic fatigue fracture mode II loads, *Int. J. Fatigue* 0142-1123, 123 (2019) 40–52, <https://doi.org/10.1016/j.ijfatigue.2019.02.008>.
- [151] S. Azari, M. Papini, J.K. Spelt, Effect of adhesive thickness on fatigue and fracture of toughened epoxy joints—Part I: Experiments, *Eng. Fract. Mech.* 0013-7944, 78 (1) (2011) 153–162, <https://doi.org/10.1016/j.engfracmech.2010.06.025>.
- [152] A.V.M. Rocha, A. Akhavan-Safar, R. Carbas, E.A.S. Marques, R. Goyal, M. El-zein, L. F.M. da Silva, Fatigue crack growth analysis of different adhesive systems: effects of mode mixity and load level, *Fatigue Fract. Eng. Mater. Struct.* 43 (2) (2020) 330–341.
- [153] Q. Chen, H. Guo, K. Avery, X. Su, H. Kang, Fatigue performance and life estimation of automotive adhesive joints using a fracture mechanics approach, *Eng. Fract. Mech.* 0013-7944, 172 (2017) 73–89, <https://doi.org/10.1016/j.engfracmech.2017.01.005>.
- [154] P. Heyes, G. Björkman, A. Blows, T. Mumford, P. Briskham, A fracture mechanics approach to durability calculations for adhesive joints, *SAE Int. J. Mater. Manuf.* 5 (1) (2012) 215–225.
- [155] W. Possart, M. Brede, *Adhesive Joints: Ageing and Durability of Epoxies and Polyurethanes*, Wiley, 2019, ISBN: 9783527341856. <https://books.google.de/books?id=ykNxDwAAQBAJ>.
- [156] A. Ameli, M. Papini, J.K. Spelt, Hygrothermal degradation of two rubber-toughened epoxy adhesives: application of open-faced fracture tests, *Int. J. Adhes. Adhes.* 0143-7496, 31 (1) (2011) 9–19, <https://doi.org/10.1016/j.ijadhadh.2010.10.001>.
- [157] A. Ameli, N.V. Datla, S. Azari, M. Papini, J.K. Spelt, Prediction of environmental degradation of closed adhesive joints using data from open-faced specimens, *Compos. Struct.* 0263-8223, 94 (2) (2012) 779–786, <https://doi.org/10.1016/j.compstruct.2011.09.017>.
- [158] A. Ameli, S. Azari, M. Papini, J.K. Spelt, Characterization and prediction of fracture properties in hygrothermally degraded adhesive joints: an open-faced approach, *J. Adhes. Sci. Technol.* 27 (10) (2013) 1080–1103.
- [159] T. Chang, E.A. Sproat, Y.-H. Lai, N.E. Shephard, D.A. Dillard, A test method for accelerated humidity conditioning and estimation of adhesive bond durability, *J. Adhes.* 60 (1–4) (1997) 153–162.
- [160] D.A. Dillard, B. Chen, T. Chang, Y.-H. Lai, Analysis of the notched coating adhesion test, *J. Adhes.* 69 (1–2) (1999) 99–120.
- [161] O. Patil, A. Ameli, N.V. Datla, Predicting environmental degradation of adhesive joints using a cohesive zone finite element model based on accelerated fracture tests, *Int. J. Adhes. Adhes.* 76 (2017) 54–60.
- [162] A. Al-Khanbashi, E.M. El-Said, Effect of bond thickness on creep lifetime of adhesive joints under mode I, *J. Adhes. Sci. Technol.* 19 (7) (2005) 595–610, <https://doi.org/10.1163/1568561054352478>.
- [163] R.M. Pitti, F. Dubois, O. Pop, A proposed mixed-mode fracture specimen for wood under creep loadings, *Int. J. Fract.* 167 (2) (2011) 195–209.
- [164] R.M. Carneiro Neto, A. Akhavan-Safar, E.M. Sampaio, J.T. Assis, L.F. da Silva, Effect of creep on the mode II residual fracture energy of adhesives, *J. Appl. Polym. Sci.* 138 (47) (2021) 51387.
- [165] R.M. Carneiro Neto, A. Akhavan-Safar, E.M. Sampaio, J.T. Assis, L.F.M. da Silva, Assessment of the creep life of adhesively bonded joints using the end notched flexure samples, *Eng. Fail. Anal.* 1350-6307, 133 (2022) 105969, <https://doi.org/10.1016/j.engfailanal.2021.105969>.

- [166] B.W. Townsend, D.C. Ohanehi, D.A. Dillard, S.R. Austin, F. Salmon, D.R. Gagnon, Characterizing acrylic foam pressure sensitive adhesive tapes for structural glazing applications—Part II: Creep rupture results, *Int. J. Adhes. Adhes.* 0143-7496, 31 (7) (2011) 650–659, <https://doi.org/10.1016/j.ijadhadh.2011.06.018>.
- [167] R.A. Queiroz, E.M. Sampaio, V.J. Cortines, N.R.F. Rohem, Study on the creep behavior of bonded metallic joints, *Appl. Adhes. Sci.* 2 (1) (2014) 1–12.
- [168] P. Schrader, C. Schmandt, S. Marzi, Mode I creep fracture of rubber-like adhesive joints at constant crack driving force, *Int. J. Adhes. Adhes.* 0143-7496, 113 (2022) 103079, <https://doi.org/10.1016/j.ijadhadh.2021.103079>.
- [169] J.J.M. Machado, E.A.S. Marques, L.F.M. da Silva, Adhesives and adhesive joints under impact loadings: an overview, *J. Adhes.* 94 (6) (2018) 421–452, <https://doi.org/10.1080/00218464.2017.1282349>.
- [170] C. Sato, S. Marzi, High-rate loading and impact in adhesively bonding joints, in: R.D. Adams (Ed.), *Adhesive Bonding*, second ed., Woodhead Publishing, 2021, pp. 257–293, ISBN: 978-0-12-819954-1, <https://doi.org/10.1016/B978-0-12-819954-1.00015-0>.
- [171] S. Marzi, A. Biel, O. Hesebeck, 3D optical displacement measurements on dynamically loaded adhesively bonded T-peel specimens, *Int. J. Adhes. Adhes.* 0143-7496, 56 (2015) 41–45, <https://doi.org/10.1016/j.ijadhadh.2014.07.013> (Special Issue on Impact Phenomena of Adhesively Bonded Joints).
- [172] B. Valès, S. Marguet, R. Créac’hacdec, L. Sohier, J.-F. Ferrero, P. Navarro, An experimental method dedicated to the dynamic characterization of structural adhesives under drop weight conditions, *Int. J. Adhes. Adhes.* 0143-7496, 90 (2019) 106–125, <https://doi.org/10.1016/j.ijadhadh.2019.01.031>.
- [173] M. Lißner, E. Alabort, H. Cui, A. Pellegrino, N. Petrinic, On the rate dependent behaviour of epoxy adhesive joints: experimental characterisation and modelling of mode I failure, *Compos. Struct.* 0263-8223, 189 (2018) 286–303, <https://doi.org/10.1016/j.compstruct.2018.01.019>.
- [174] M. Lißner, E. Alabort, B. Erice, H. Cui, N. Petrinic, A rate dependent experimental and numerical analysis of adhesive joints under different loading directions, *Eur. Phys. J. Spec. Top.* 227 (1) (2018) 85–97.
- [175] M. Lißner, E. Alabort, H. Cui, R. Rito, B.R.K. Blackman, N. Petrinic, Experimental characterisation and numerical modelling of the influence of bondline thickness, loading rate, and deformation mode on the response of ductile adhesive interfaces, *J. Mech. Phys. Solids* 130 (2019) 349–369.
- [176] M. Lißner, E. Alabort, B. Erice, H. Cui, B.R.K. Blackman, N. Petrinic, On the dynamic response of adhesively bonded structures, *Int. J. Impact Eng.* 138 (2020) 103479.
- [177] M. Lißner, B. Erice, E. Alabort, D. Thomson, H. Cui, C. Kaboglu, B.R.K. Blackman, M. Gude, N. Petrinic, Multi-material adhesively bonded structures: characterisation and modelling of their rate-dependent performance, *Compos. Part B Eng.* 1359-8368, 195 (2020) 108077, <https://doi.org/10.1016/j.compositesb.2020.108077>.
- [178] S. Marzi, A. Rauh, R.M. Hinterhölzl, Fracture mechanical investigations and cohesive zone failure modelling on automotive composites, *Compos. Struct.* 0263-8223, 111 (2014) 324–331, <https://doi.org/10.1016/j.compstruct.2014.01.016>.
- [179] D.J. Pohlit, D.A. Dillard, G.C. Jacob, J.M. Starbuck, Evaluating the rate-dependent fracture toughness of an automotive adhesive, *J. Adhes.* 84 (2) (2008) 143–163.
- [180] F. Sun, R. Zhang, B.R.K. Blackman, Determination of the mode I crack tip opening rate and the rate dependent cohesive properties for structural adhesive joints using digital

- image correlation, *Int. J. Solids Struct.* 0020-7683, 217-218 (2021) 60–73, <https://doi.org/10.1016/j.ijsolstr.2021.01.034>.
- [181] B.R.K. Blackman, A.J. Kinloch, F.S. Rodriguez Sanchez, W.S. Teo, J.G. Williams, The fracture behaviour of structural adhesives under high rates of testing, *Eng. Fract. Mech.* 0013-7944, 76 (18) (2009) 2868–2889, <https://doi.org/10.1016/j.engfracmech.2009.07.013> (Fracture of Polymers, Composites and Adhesives).
- [182] A. Karac, B.R.K. Blackman, V. Cooper, A.J. Kinloch, S. Rodriguez Sanchez, W.S. Teo, A. Ivankovic, Modelling the fracture behaviour of adhesively-bonded joints as a function of test rate, *Eng. Fract. Mech.* 0013-7944, 78 (6) (2011) 973–989, <https://doi.org/10.1016/j.engfracmech.2010.11.014>.
- [183] T. Gao, A. Kinloch, B. Blackman, F. Sanchez, S.-k. Lee, C. Cho, H.-j. Bang, S. Cheon, J. Cho, A study of the impact properties of adhesively-bonded aluminum alloy based on impact velocity, *J. Mech. Sci. Technol.* 29 (2015) 493–499, <https://doi.org/10.1007/s12206-015-0109-y>.
- [184] F. Sun, B.R.K. Blackman, Using digital image correlation to automate the measurement of crack length and fracture energy in the mode I testing of structural adhesive joints, *Eng. Fract. Mech.* 0013-7944, 255 (2021) 107957, <https://doi.org/10.1016/j.engfracmech.2021.107957>.

Understanding fracture mode-mixity and its effects on bond performance

17

Bamber Blackman^a, Fengzhen Sun^b, Sofia Teixeira de Freitas^c, Silvio de Barros^d, Marcio Moreira Arouche^c, and Alojz Ivankovic^e

^aDepartment of Mechanical Engineering, Imperial College London, South Kensington Campus, London, United Kingdom, ^bTongji University, Shanghai, China, ^cAerospace Structures and Materials Department, Faculty of Aerospace Engineering, Delft University of Technology, Delft, Netherlands, ^dLINEACT CESI Engineering School, Paris, France, ^eUniversity College Dublin, Dublin, Ireland

17.1 Introduction

The use of structural adhesives to join engineering components and structures has become very popular due to the many advantages structural adhesive bonding brings. These advantages include the avoidance of the need to drill holes or introduce local damage to the adherends, the improved stress distribution of adhesively bonded joints compared with mechanically fastened or welded joints, the ability to join dissimilar adherends and the improvement in structural rigidity, the reduction of vibration, and improved fatigue resistance, all of which make structural adhesive bonding a very highly employed joining technique.

To optimize joint performance, many studies [1,2] have shown that tensile opening forces (mode I) should be minimized and that in-plane shear forces (mode II) should be maximized, hence tensile butt joints are typically avoided in design, and joints loaded in shear such as the single- or double-lap joint are preferred. To further optimize joint performance, the stress concentrations associated with the ends of the joint overlap should be reduced by employing tapered adherends.

To measure adhesive joint performance, extensive use has been made of fracture mechanics since the pioneering initial studies by Ripling, Mosovoy, and Patrick in the 1960s [3]. Their work focused mainly on mode I loading of joints employing metallic adherends and led to the popular ASTM standard [4]. As structural joint designs were improved, there was increased interest in mode II and mixed-mode loading (i.e., combinations of modes I, II, and III acting together) and many workers explored test methods that combined modes, most commonly modes I and II. Although there have been many notable contributors to the understanding of the mixed-mode fracture behavior in adhesive joints such as [5–7], there is a lack of standardized tests developed specifically for these structures.

To analyze mixed-mode fracture tests, most workers have followed the energy release rate (G) approach and have combined this with beam theory methods to determine the rate of change of compliance C with crack length a , that is, to determine dC/da . This is then combined with the Irwin-Kies equation [8] to calculate the critical value of G for fracture, G_c . Initially, linear elastic fracture mechanics (LEFM) theory was followed, where one assumption is that any in-elastic deformation is limited in size to a very small zone at the crack tip and that the specimen behaves in a linear-elastic manner overall. Such assumptions are valid for brittle adhesives, but as adhesives have been manufactured with greatly improved toughness or ductility, the size of the in-elastic deformation zone at the crack tip has greatly increased, requiring the use of cohesive zone models to combine the approaches of fracture mechanics and classical strength of materials. The use of cohesive zone models and the concept of the cohesive zone length (damage length) have become increasingly important in the analysis of fracture in adhesively bonded joints under mixed-mode loading, as will be discussed in more detail later in this chapter as well as in [Chapter 32](#) with digital image correlation (DIC) methods.

17.2 Brief summary of test methods to introduce mixed-mode loading

The accurate measurement of the fracture energy (G_c) is one key research campaign for characterization of the fracture behavior of laminated composites and adhesively bonded joints. Over the last few decades, many methodologies and data reduction schemes have been proposed to quantify the fracture energy for mode I, mode II, and mixed I/II mode loading [9]. Double cantilever beam (DCB) specimens loaded with pure bending moments provide a very accurate and robust way to determine the mode I fracture toughness (G_{Ic}) without the need for measuring crack lengths; however, this method does rely on the use of a specially designed loading jig [10]. Instead, specimens loaded with a transverse load are more often adopted, but this gives rise to the problem that the crack length must be determined. To measure the mode II fracture toughness (G_{IIc}), end notched flexure (ENF) tests using a three-point bending apparatus are extensively employed due to the test convenience; however, the crack growth in the specimens is intrinsically unstable and thus only initiation values of G_{IIc} are usually obtained [11]. Another way to determine the value of G_{IIc} is by using the end-loaded split (ELS) specimen, which is tested in a sliding clamp that only allows the specimen to slide freely in the horizontal direction, and the crack growth is relatively stable [12]. In addition, prior to the ELS test, a correction to the end clamping needs to be determined [12].

In practice, very rarely does failure in engineering structures occur under pure mode loading conditions. Crack growth under a combination of opening and shear modes is more commonly encountered, making it necessary to characterize the fracture behavior of structural adhesive joints under mixed-mode loading. The mixed mode flexure (MMF) specimen, also known as the single leg bending (SLB) specimen, and the fixed ratio mixed mode (FRMM) specimen are convenient choices to

complement the results obtained with the pure mode tests. The MMF configuration is very similar to the ENF test, and it is tested using a three-point bending rig, but only the upper arm at one end of the specimen is loaded. The FRMM test employs the same clamping arrangement as the mode II ELS test, but only one arm is loaded in this case. Symmetric MMF and FRMM specimens yield a constant mode-mixity G_{II}/G of $3/7$.

Apart from the constant mode-mixity tests, a range of mode-mixity can be obtained by altering the relative thickness of the substrates such as the asymmetric DCB (ADCB) and asymmetric FRMM (AFRMM) specimens, although this raises the question of how to partition the mode-mixity correctly; this will be discussed in detail in the following section. The ADCB and AFRMM specimens are the generalization of the standard DCB and FRMM specimens using different beam thicknesses or different materials for the substrates. The specimens are manufactured and tested in the same manner as the DCB and FRMM tests. ADCB specimens are simpler to test than AFRMM specimens, but the achievable range of mode-mixity is much more limited in the ADCB than in the AFRMM case.

Another strategy to induce mixed-mode fracture is loading a symmetric adhesive joint with an apparatus designed to apply different load combinations such as those used in mixed-mode bending (MMB) [13], Arcan fixtures [14], and the rig developed by Fernlund and Spelt [15]. The MMB test is the only standardized mixed-mode I/II test available [16]. Although this standard was initially developed for unidirectionally fiber-reinforced polymer (FRP) composites, it has been successfully used to test multidirectional FRPs and adhesive joints. The MMB test covers a wide range of mode I to mode II loadings by adjustment of the loading and lever fulcrum positions in the test apparatus [13]. This type of test combines opening and in-plane sliding displacement modes, and the applied loading usually is treated as the superposition of the applied loadings of the DCB and ENF tests. Its advantage is that a range of mixed-mode I/II load cases can be studied without having to change the specimen geometry, but it does require a complex fixture and bonded steel hinged tabs, which may introduce a geometrical nonlinearity.

Another mixed-mode loading apparatus was introduced by Fernlund and Spelt [15]. The load jig consists of a link-arm system that allows the force acting on the upper and lower substrates of the test specimen to be varied by altering the load jig geometry. The links in the load jig are connected to each other with dowel pins to facilitate the geometry change. The nominal phase angle of loading is independent of the specimen crack length, and it also allows mode ratios from pure mode I to pure mode II to be obtained. Important features are that all mixed-mode ratios can be generated with a single equal-adherend DCB specimen, and the mixed-mode ratio is independent of crack length. Recently, Costa et al. [17] developed a more compact apparatus based upon the Fernlund and Spelt method. These authors demonstrated, using mixed-mode and classical models (ATDCB, SLB, DCB, and ENF), the validity of the results obtained with the new apparatus.

Arcan et al. [14] proposed a biaxial fixture, commonly known as the Arcan fixture, to produce biaxial states of stress. The compact nature of the Arcan fixture enables the shear properties in all in-plane directions to be obtained in a relatively simple manner. Various mixed-mode combinations can be achieved by rotating the loading direction.

However, although the Arcan test covers all the mixed-mode ratios, including the pure mode I to mode II, the results can only be obtained by a numerical (finite element) analysis, which involves the singularity at the crack tip. The cracked-lap shear (CLS) was also an attempt to construct a mixed-mode testing approach, and it was popular for fatigue testing in the aerospace industry because of its nominally constant energy release rate as a function of debonding length [18]. However, one distinctive feature of the CLS is the eccentric loading path that leads to geometrical nonlinearity, as was identified in the ASTM round-robin activity [19]. Thus, large deflections have to be considered in analytical and numerical analyses. Due to these limitations, other tests have become more popular.

Finally, mixed-mode loading of adhesive joints or interfaces has been achieved via the use of dual actuator loading frames [7,20,21], where the loading of each specimen arm is independently controlled. Challenges here include the maintenance of a constant mode-mixity during quasistatic tests [20] and the maintenance of constant local separation rates with changing mode-mixity in higher rate tests [21].

17.3 Mixed-mode partitioning schemes

17.3.1 Introduction

The mixed-mode loading situation raises fundamental questions that are not relevant to the pure mode case. For example, to what extent do the two loading modes interact when applied simultaneously to modify the resistance of the joint from that which would be predicted from a simple linear addition of the separate mode contributions? Indeed, it is frequently observed that such a linear addition is a poor descriptor of mixed-mode fracture resistance, and that a stronger interaction exists [22]. So, to define the correct degree of interaction (fracture criterion), it is important to be able to partition the total loading correctly into its constituent parts. In terms of fracture energy, the mixed-mode fracture resistance G_c must be partitioned into the mode I and mode II components.

17.3.2 Local and global partitioning schemes for monolithic specimens

Attempts to partition mixed-mode loading into pure mode components have traditionally taken either a local or a global approach. In the local approach, the stress singularity at the crack tip is assumed to control fracture. This requires that the region controlled by the singular field (K-dominant zone) engulfs the crack tip process zone (plastic and/or damage zone). The singular field stress distributions are determined at the crack tip and these are partitioned into the mode I and II components, K_I and K_{II} , which can then be written in terms of the associated energy release rate components, G_I and G_{II} , respectively. In the global approach, the bending moments applied to the specimen are considered but the details of the local stress or strain fields ahead of the crack tip are neglected. Williams [23] proposed that these applied moments could be

partitioned into components that induce pure mode I (M_I) and pure mode II (M_{II}). Fig. 17.1 shows a cracked beam-like geometry subjected to pure bending moments of M_I on the upper beam and kM_I on the lower beam [24]. The upper beam has a thickness of h_1 and the lower beam a thickness of h_2 , and the ratio of heights is $\gamma = h_1/h_2$.

Local and global partitioning approaches have been reviewed by Conroy et al. [24], and an application of the global approach is discussed further in Section 17.4. As is shown in Fig. 17.2a, when the test specimen has a symmetric geometry, as is the case for the mixed-mode bending (MMB) specimen, then the local and global partitioning approaches produce identical results for the applied mixed-mode partition ratio, G_{II}/G . Note that for $\gamma = 1$, when the applied moment ratio $k = -1$, then pure mode I loading is obtained and when $k = 1$, then pure mode II is obtained. However, as is shown in Fig. 17.2b, for an asymmetric geometry, in this case the AFRMM specimen, then the local and global partitioning approaches produce very different results. Fig. 17.2b shows the mixed-mode partition ratio G_{II}/G as a function of the beam height ratio γ , where the two approaches only agree when $\gamma = 1$. It is noteworthy therefore that if only symmetric specimens are used, the two partitioning approaches produce identical results in monolithic specimens.

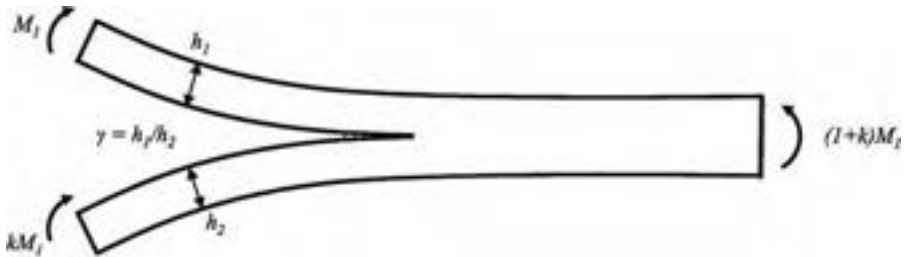


Fig. 17.1 Beam-like geometry subjected to pure bending moments (M_I and kM_I) [24].

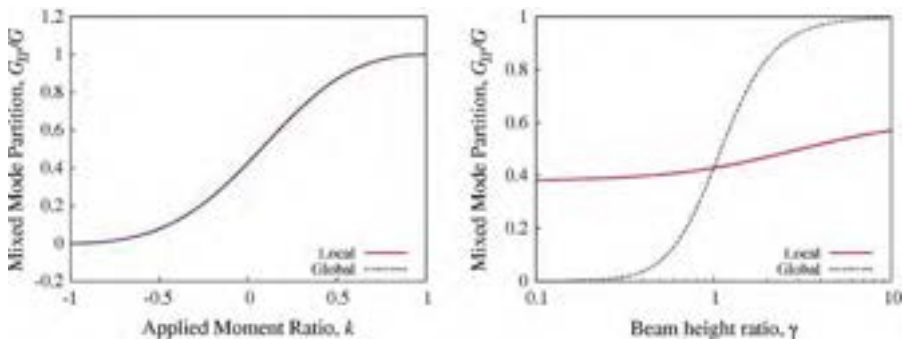


Fig. 17.2 Local and global partitioning: (a) symmetric specimens such as MMB; (b) asymmetric specimens such as AFRMM [24].

17.3.3 A damage-based partitioning scheme

For highly fracture-resistant materials, including joints bonded with toughened adhesives, the length of the fracture process zone (the cohesive zone) can be significantly larger than the extent of the singular field. For these materials, the global approach has traditionally found greater success. Conroy et al. [24] noted from their numerical studies that as the degree of damage increased, that is, as the size of the cohesive zone increased, then the global partitioning approach becomes more accurate. Conversely, as the amount of damage decreased, then the local partitioning approach becomes more accurate. Conroy et al. [24] proposed a damage-dependent partitioning method that was termed the semianalytical cohesive analysis (SACA), which is now discussed.

Conroy et al. [24] proposed that the partitioning approach should acknowledge the state of damage in the specimen. They allowed this to be scaled via a singularity factor f between a lower bound given by the local solution and an upper bound given by the global solution, where f was given by:

$$f = \frac{\left(\frac{G_{II}}{G}\right) - \left(\frac{G_{II}}{G}\right)_W}{\left(\frac{G_{II}}{G}\right)_{HS} - \left(\frac{G_{II}}{G}\right)_W} \quad (17.1)$$

where $(G_{II}/G)_W$ and $(G_{II}/G)_{HS}$ are the mixed-mode ratios given by the global and local solutions, respectively, and (G_{II}/G) is the predicted mixed-mode partition ratio according to this semianalytical cohesive analysis (SACA) method. To employ the SACA method, a normalized damage length parameter was defined for the specimen, l_{nd} , where this is given by:

$$l_{nd} = \frac{l_{cz}}{a_c} \quad (17.2)$$

where l_{cz} is the cohesive zone length and a_c is the smallest characteristic dimension of the specimen. The cohesive zone lengths in modes I and II were determined analytically and the singularity factor was then given by Eq. (17.3) or (17.4), depending upon whether the value of l_{nd} was less than 0.3.

$$f = 1 \text{ if } l_{nd} \leq 0.3 \quad (17.3)$$

$$f = 0.9682e^{-0.24l_{nd}} + 0.0983e^{-0.2l_{nd}} \text{ otherwise} \quad (17.4)$$

Based upon Eqs. (17.3) and (17.4), partitioning via the local singular field approach was considered accurate for cohesive zone lengths up to 30% of the smallest characteristic length. The singularity factor f was dependent upon material properties and specimen geometry. Conroy et al. [24] applied the method to various test cases based upon composite materials in the literature with excellent results. The method is evaluated for a structural adhesive joint in the next section.

17.3.4 Evaluation and discussion of mixed-mode partitioning

Mixed-mode partitioning schemes were investigated experimentally by Alvarez et al. [25] for structural adhesive joints in which carbon fiber-reinforced composite adherends had been bonded with a toughened aerospace film adhesive grade AF163-2 OST. These authors employed various test specimens, including ADCB, FRMM, and AFRMM. The experimental results were partitioned according to the global approach and according to two forms of the local approach: the first one based on the crack tip element (CTE) method of Davidson et al. [26], which was termed the singular field (CTE-SF), and the second method was a nonsingular field (CTE-NSF) version of Davidson's method. They also explored the use of the SACA method.

Alvarez et al. [25] found that for this relatively tough adhesive joint, the global partitioning approach [23] was generally accurate across the range of mixed-mode ratios (G_{II}/G) attained, but showed the largest percentage errors at the smallest mixed-mode ratios. Additionally, as has frequently been noted in the literature, the global partitioning approach is anomalous for the ADCB test, where it predicts (G_{II}/G)=0, that is, mode I, for all arm thickness ratios. The local approach via Davidson's CTE-SF method was accurate at the smallest mixed-mode ratios and Davidson's CTE-NSF method was accurate at intermediate ratios, but both became nonphysical at higher mixed-mode ratios, such as for (G_{II}/G)>0.5. The SACA method, in which the singularity factor f was determined for the adhesive joint based upon the material properties of the adhesive and the adherends and the specimen geometry, gave the most accurate mixed-mode partitioning across the entire range $0 < (G_{II}/G) \leq 1$. In Fig. 17.3, the mixed-mode failure envelope was

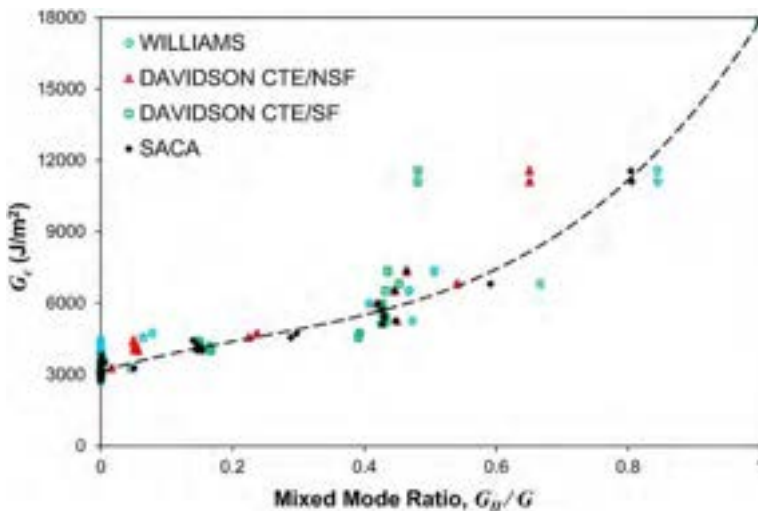


Fig. 17.3 Comparison of the failure locus obtained from the experimental results partitioned via the global approach (Williams [23]); the singular and nonsingular field versions of Davidson's analysis, CTE/NSF and CTE/SF; and the SACA method [25].

drawn using the B-K criterion. Note that failure envelopes are discussed in more detail in Section 17.5 of the present chapter.

17.4 Application of global partitioning to mixed-mode bi-material interface joints

In this section, the mixed-mode fracture behavior of a bi-material adhesively bonded joint is investigated. The strain-based method (SBM) is described, evaluated, and tested on a composite-to-metal bonded joint using the MMB test.

17.4.1 Analytical framework: Introducing the longitudinal strain-based criterion

17.4.1.1 Strain energy release rate

The strain energy release rate (SERR) is one of the most important parameters to consider for characterizing the fracture behavior of cracked structures. For linear elastic behavior, the total SERR can be obtained by the balance of fracture energy through the following equation:

$$G = \frac{1}{B} \left(\frac{\delta U_e}{\delta a} - \frac{\delta U_s}{\delta a} \right) \quad (17.5)$$

where B is the width of the specimen, U_e is the external work performed, U_s is the strain energy, and a is the crack length. The analysis considers a region ABCD mechanically affected by the presence of a crack under pure bending moments, as shown in Fig. 17.4.

The upper and lower arm thicknesses are h_1 and h_2 , and the bending moments applied to the upper and lower arms are M_1 and M_2 , respectively. The angles Φ_0 , Φ_1 , and Φ_2 represent the slopes of the beam, upper arm, and lower arm, respectively. When the crack grows a length δa from O on section AB to O' on section CD, the external work is:

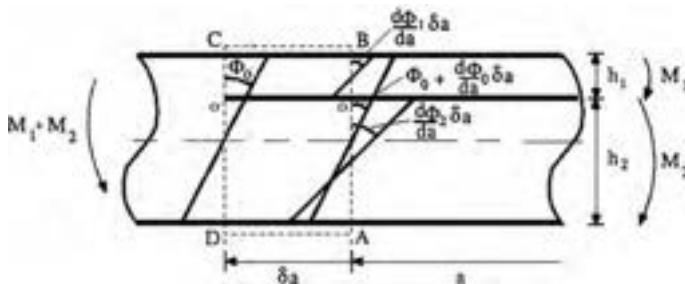


Fig. 17.4 Beam analysis under pure bending moments [27].

Reprinted with permission from Taylor & Francis Ltd, <http://www.tandfonline.com>.

$$\frac{\delta U_e}{\delta a} = M_1 \left(\frac{\delta \phi_1}{\delta a} - \frac{\delta \phi_0}{\delta a} \right) + M_2 \left(\frac{\delta \phi_2}{\delta a} - \frac{\delta \phi_0}{\delta a} \right) \quad (17.6)$$

For pure bending, the change in angle is given by:

$$\frac{\delta \phi}{\delta a} = \frac{M}{EI} \quad (17.7)$$

where M is the moment, E is the flexural modulus, and I is the second moment of area. Similarly, the strain energy is:

$$\frac{\delta U_s}{\delta a} = \frac{M_1^2}{2E_1 I_1} + \frac{M_2^2}{2E_2 I_2} - \frac{(M_1 + M_2)^2}{2E_{eq} I_{eq}} \quad (17.8)$$

where E_1 , I_1 , E_2 , I_2 , E_{eq} , and I_{eq} are the flexural longitudinal moduli and second moments of the area in the section of the crack tip of the upper arm, lower arm, and total specimen, respectively. Substituting Eqs. (17.6) and (17.8) in Eq. (17.5), it can be reduced to the equation of the total fracture energy:

$$G = \frac{1}{2B} \left(\frac{M_1^2}{E_1 I_1} + \frac{M_2^2}{E_2 I_2} - \frac{(M_1 + M_2)^2}{E_{eq} I_{eq}} \right) \quad (17.9)$$

Eq. (17.9) allows determining the total fracture energy released from a crack between two arms. However, it is essential for the characterization of the mechanical behavior to define the contribution of mode I and mode II fracture.

17.4.1.2 Williams' global partitioning approach

In the late 1980s, Williams [23] proposed a fracture partitioning method (WM) based on the assumptions that: (i) pure mode I exists when opposite moments act on the joint arms; and (ii) pure mode II is obtained when the curvatures of the two arms are the same. This means:

$$M_1 = M_{II} - M_I \quad (17.10)$$

$$M_2 = \psi M_{II} + M_I \quad (17.11)$$

Where the bending stiffness ratio between upper and lower arms is:

$$\psi = \frac{E_2 I_2}{E_1 I_1} \quad (17.12)$$

Substituting Eqs. (17.10) and (17.11) in Eq. (17.9), the equation of the total fracture energy can be reduced to:

$$G = \frac{1}{2B} \left[M_I^2 \left(\frac{\psi + 1}{E_2 I_2} \right) + M_{II}^2 \left(\frac{\psi + \psi^2}{E_2 I_2} - \frac{(1 + \psi)^2}{E_{eq} I_{eq}} \right) \right] \quad (17.13)$$

Notice that no cross-product term is observed. Therefore, the partitioning can be obtained by rewriting Eq. (17.13) as a function of M_I and M_{II} :

$$f(M_I, M_{II}) = f_I(M_I) + f_{II}(M_{II}) \quad (17.14)$$

G_I , G_{II} , and the total G are then given by:

$$G_I = \frac{M_I^2}{2B} \left(\frac{\psi + 1}{E_2 I_2} \right) \quad (17.15)$$

$$G_{II} = \frac{M_{II}^2}{2B} \left(\frac{\psi + \psi^2}{E_2 I_2} - \frac{(1 + \psi)^2}{E_{eq} I_{eq}} \right) \quad (17.16)$$

$$G = G_I + G_{II} \quad (17.17)$$

Finally, substituting Eqs. (17.10) and (17.11) in Eqs. (17.15) and (17.16), the mode I and mode II SERR can be written as:

$$G_I = \frac{(\psi M_1 - M_2)^2}{2B(\psi + 1)^2} \left(\frac{1}{E_1 I_1} + \frac{1}{E_2 I_2} \right) \quad (17.18)$$

$$G_{II} = \frac{(M_1 + M_2)^2}{2B(\psi + 1)} \left(\frac{1}{E_1 I_1} - \frac{(\psi + 1)}{E_{eq} I_{eq}} \right) \quad (17.19)$$

Analytical models based only on simple beam analysis do not properly describe the crack propagation mechanism [28]. The two arms are not fixed against rotation at the crack tip, as assumed in the beam analysis. To account for these effects in the mode I fracture, Williams [29] proposed a correction factor, based on Kanninen's [30] elastic foundation model. Then, Wang and William [31] extended the same correction factor for the mode II fracture component. The incorporation of crack tip correction factors in the beam model, Eqs. (17.18) and (17.19), resulted in the so-called corrected beam theory (CBT). In this method, an effective crack length is used to account for the contribution of shear deformation to the energy release rate.

The works of Williams [22], Hashemi et al. [32], and Ducept et al. [33] indicated that CBT produces reliable values for the total fracture energy and partitioning ratio of symmetric cracks. However, Ducept et al. [34] showed that WM does not provide reliable results of the fracture mode partitioning of cracks between asymmetric arms. The assumptions for the pure modes do not describe with precision the interaction between mode I and mode II fractures. Therefore, it is not recommended for the characterization of asymmetric cracks.

17.4.1.3 Strain-based partitioning method

Arouche et al. [27,35] introduced a new criterion for fracture mode partitioning, the strain-based partitioning method (SBM). The main difference to the WM lies on the condition for pure mode I: it incorporates the requirement of strain equivalence between the faying surfaces for ensuring pure mode I, as identified by Ouyang [36] and confirmed by Wang et al. [37]. In the case of pure mode II, similarly to WM, the SBM assumes that it is produced when both arms have the same curvature, as observed by Mollón et al. [38], assuming that the curvature of the neutral axis is the same as the faying surfaces. Therefore, the partitioning assumptions become: (i) the longitudinal strain distribution at the faying surfaces of both arms must be identical to produce pure mode I, and (ii) pure mode II is obtained when the curvature in the two arms is the same. This gives:

$$M_1 = M_{II} - M_I \quad (17.20)$$

$$M_2 = \psi M_{II} + \beta M_I \quad (17.21)$$

Where the longitudinal strain ratio between upper and lower arms is:

$$\beta = \frac{E_2 h_2^2}{E_1 h_1^2} \quad (17.22)$$

Substituting Eqs. (17.20) and (17.21) in Eq. (17.9), the total SERR is obtained:

$$G = \frac{1}{2B} \left[\begin{aligned} &M_I^2 \left(\frac{\psi + \beta^2}{E_2 I_2} - \frac{(\beta - 1)^2}{E_{eq} I_{eq}} \right) + M_{II}^2 \left(\frac{\psi + \psi^2}{E_2 I_2} - \frac{(1 + \psi)^2}{E_{eq} I_{eq}} \right) + \\ &M_I M_{II} \left(\frac{2\psi\beta - 2\psi}{E_2 I_2} - \frac{2(1 + \psi)(\beta - 1)}{E_{eq} I_{eq}} \right) \end{aligned} \right] \quad (17.23)$$

Eq. (17.23) shows that the mode I fracture energy affects the mode II fracture energy and vice versa. Consequently, the equation can only be written in the form of:

$$f(M_I, M_{II}) = f_I(M_I) + f_{II}(M_{II}) + f_c(M_I, M_{II}) \quad (17.24)$$

Eq. (17.24) displays a coupling function $f_c(M_I, M_{II})$ beyond the functions of pure mode I and pure mode II— $f_I(M_I)$ and $f_{II}(M_{II})$, respectively. This implies that the fracture mode partitioning is obtained when the coupling function $f_c(M_I, M_{II})$ is zero. This is achieved in the condition of $\beta = 1$. Therefore, the specimen design condition of longitudinal strain equivalence has to be satisfied. It means:

$$E_1 h_1^2 = E_2 h_2^2 \quad (17.25)$$

In this case, the mode I and mode II equations of fracture energy are the same as in WM—Eqs. (17.18) and (17.19). However, WM does not reinforce any specific specimen design because it was derived for symmetric specimens in which β is always equal to 1. It ignores the coupling function that contributes to the total fracture energy. This is the reason why WM is inaccurate if applied to asymmetric specimens where the longitudinal strain-based design criterion is not applied ($\beta \neq 1$).

17.4.2 Application in MMB test in composite-to-metal bonded joints

17.4.2.1 MMB test

Reeder and Crews [38] developed the MMB test as a combination of the DCB and the ENF tests. In the MMB test, a load (P) is applied through a roller attached to a lever and loaded just above the midplane of the test specimen. The test loading is decomposed into opening (P_I) and shear (P_{II}) loadings in a constant ratio determined by the lever length (c). The original procedure was later redesigned to minimize geometrical nonlinearity effects [39] and to take into account the weight of the lever (P_g) and the distance of the lever center of gravity (c_g) [40]. Later, Chen et al. [41] proposed a modification to the test apparatus to avoid preloading on the specimens caused by the weight of the lever. The MMB test scheme is shown in Fig. 17.5. The MMB test has proved to be an easy and reliable method for measuring a wide range of mixed-mode ratios with only one specimen geometry [33,42]. The loads applied to the specimen are shown in Fig. 17.6.

The resulting bending moments are:

$$M_1 = \frac{Pc + P_g c_g}{L} a \quad (17.26)$$

$$M_2 = \frac{P(L - c) + P_g(L - c_g)}{2L} a \quad (17.27)$$

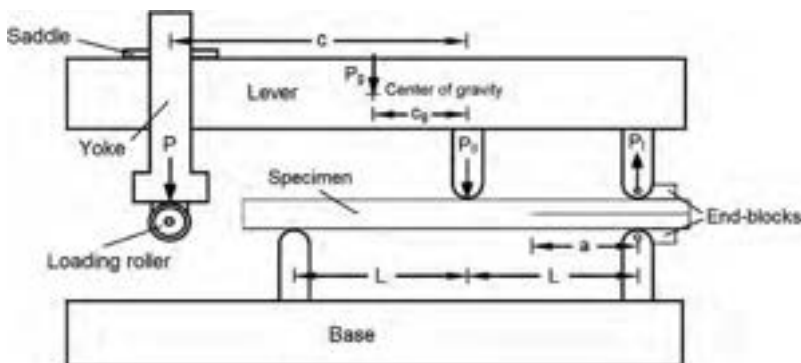


Fig. 17.5 MMB test scheme.

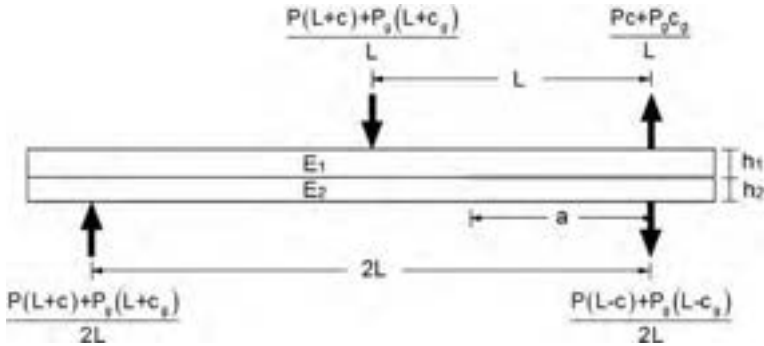


Fig. 17.6 MMB specimen free body diagram.

Then, the mode I and mode II SERR of an MMB test specimen can be obtained by replacing Eqs. (17.26) and (17.27) in Eqs. (17.18) and (17.19).

17.4.2.2 Numerical model

A virtual MMB test was chosen to evaluate the SBM. The geometric features of the two-dimensional (2D) model are a 70 mm half-span (L) and a 50 mm crack length (a). The upper and lower arm thicknesses (h_1 and h_2 , respectively) and materials (E_1 and E_2 , respectively) are the parameters varied in the analysis [27].

17.4.2.3 Asymmetric crack within the same material

The first parametric study was performed on an asymmetric crack within the same material. The upper and lower arms have the same elastic modulus (E_1 and E_2) of 70 GPa and a Poisson’s ratio (ν_1 and ν_2) of 0.33. In order to verify the influence of the fracture mode ratio in the accuracy of the analytical methods, three different conditions were considered: low ($c=117$ mm), intermediate ($c=61$ mm), and high ($c=42$ mm) mode II ratio. Table 17.1 shows the three cases of geometrical asymmetry. The upper arm thickness (h_1) is varied in a wide range of geometries applied to the MMB test specimen while the lower arm thickness (h_2) remains at 3.0 mm. The crack length is kept at 50 mm and the test load (P) is 100 N.

Analytical and numerical results of the total fracture energy (G) are presented in Fig. 17.7. Fig. 17.7a–c show the three cases of low (case 1), intermediate (case 2),

Table 17.1 Study cases of geometrical asymmetry.

Case	Lever length, c (mm)	h_1 (mm)	h_2 (mm)	E_1 ; E_2 (GPa)	ν_1 ; ν_2
1	117	$1.5 < h_1 < 6.0$	3.0	70	0.33
2	61	$1.5 < h_1 < 6.0$	3.0	70	0.33
3	42	$1.5 < h_1 < 6.0$	3.0	70	0.33

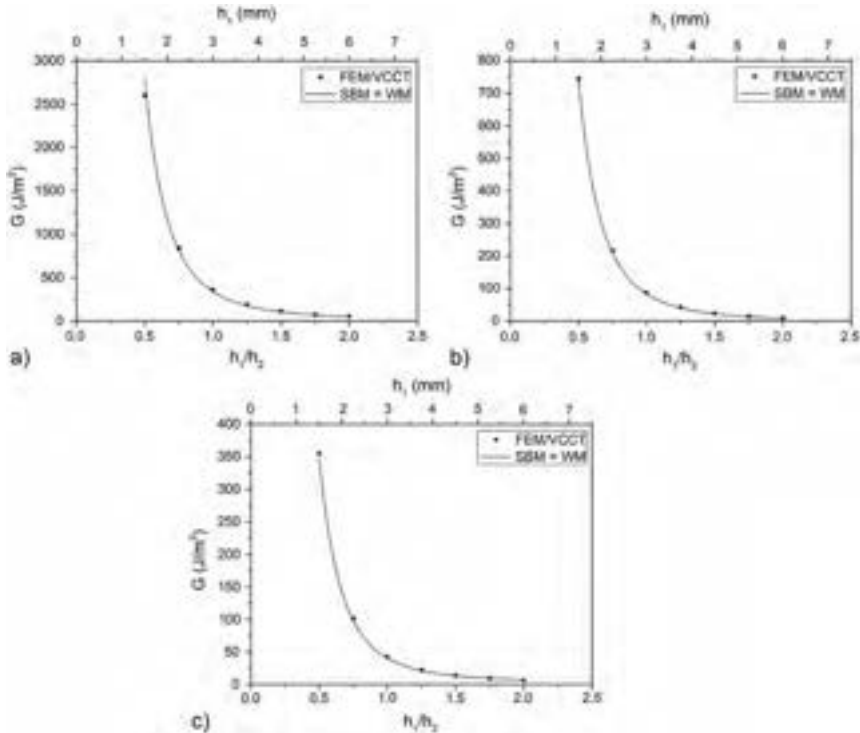


Fig. 17.7 Total fracture energy with the variation of the specimen thickness: cases (a) 1—low, (b) 2—intermediate, and (c) 3—high mode II [27].

Reprinted with permission from Taylor & Francis Ltd, <http://www.tandfonline.com>.

and high (case 3) mode II fracture, respectively. Overall, the total fracture energy obtained from analytical solutions based on beam analysis are in very good agreement with the numerical results.

Fig. 17.8 shows the analytical and numerical fracture mode ratio (G_{II}/G). Notice that the SBM implies that the specimen design condition is satisfied ($\beta = 1$) and, for this condition, gives the same result of WM. Fig. 17.8a shows the results for low mode II (case 1). When $\beta = 1$, the specimen is symmetric in the crack plane ($h_1/h_2 = 1$) and both analytical methods show good agreement with numerical results. As β differs from 1, WM gives significant discrepancies from the FEM/VCCT results. This shows that WM is only valid for the condition $\beta = 1$. Similar results are observed as the mode II fracture ratio increases, in Fig. 17.8b and c (cases 2 and 3, respectively). Moreover, the limitation of WM to predict the fracture partitioning ratios on asymmetric cracks within the same material is noticeable. This can be explained by the influence of the mode I and mode II coupling on the fracture energy.

Table 17.2 shows the results and errors of the analytical model in comparison with the numerical model for the condition of symmetric crack. Slight errors between -4.2% and -6.0% are observed in the calculation of the total fracture energy and between 2.6% and 7.6% in the fracture mode ratio. In the particular condition of a symmetric crack, the literature suggests crack tip corrections to account for the effect of crack tip rotation under mode I [29] and mode II [31] fracture. The analytical

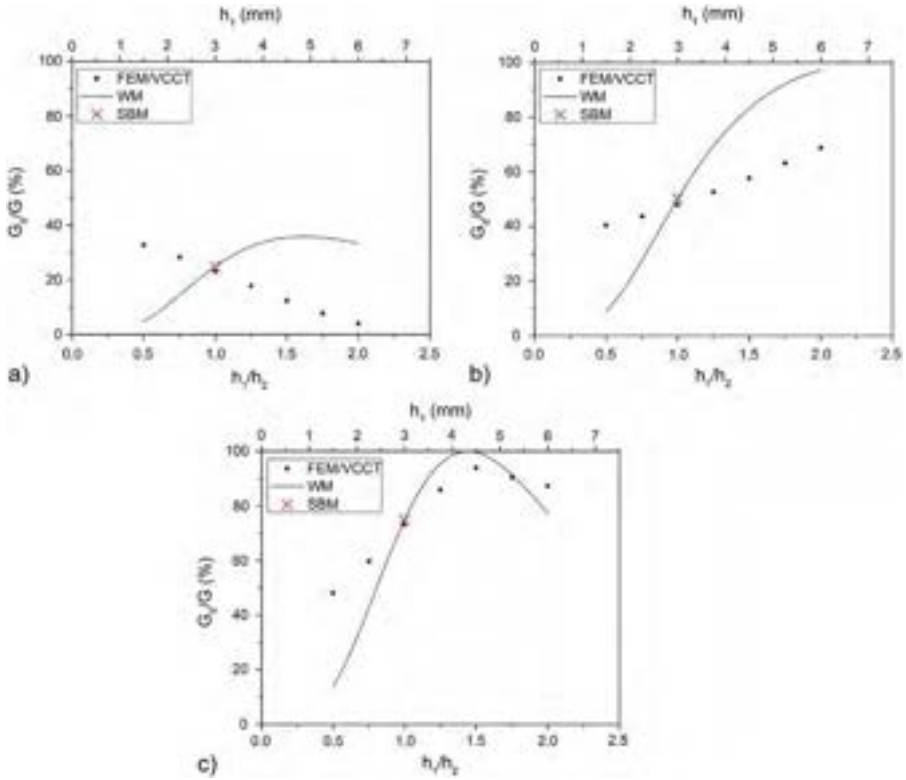


Fig. 17.8 Fracture mode ratio with the variation of specimen thickness: cases (a) 1—low, (b) 2—intermediate, and (c) 3—high mode II [27].

Reprinted with permission from Taylor & Francis Ltd, <http://www.tandfonline.com>.

Table 17.2 Results and errors of the analytical model in the condition of symmetric specimen in the crack plane.

Case	Numerical model		Analytical model				Analytical model with crack tip corrections			
	G (J/m ²)	G_{II}/G (%)	G (J/m ²)	Error (%)	G_{II}/G (%)	Error (%)	G (J/m ²)	Error (%)	G_{II}/G (%)	Error (%)
1	362.3	23.2	340.7	-6.0	24.9	7.6	364.7	0.6	24.1	4.0
2	87.7	47.9	83.1	-5.2	50.2	4.8	87.9	0.3	49.1	2.5
3	42.4	73.1	40.6	-4.2	75.0	2.6	42.5	0.2	74.1	1.4

method with the application of these correction factors presented insignificant errors for the calculation of the total fracture energy and errors lower than 4.0% for the fracture mode ratio (see Table 17.2). In both cases, the use of correction factors resulted in more accurate results. This shows that the effect of crack tip rotation during the experiments may have a nonnegligible effect on the fracture behavior, although the simple analytical model proved to be reliable.

17.4.2.4 Bi-material crack

A second parametric study was carried out on a crack at a bi-material interface with asymmetric geometry. The upper arm has a thickness (h_1) of 2.12 mm and the lower arm has a thickness (h_2) of 3.0 mm. To verify the influence of the fracture mode ratio in the accuracy of the analytical methods, three different conditions were considered: low ($c = 95$ mm), intermediate ($c = 49$ mm), and high ($c = 34$ mm) mode II ratio. Table 17.3 shows the three cases of bi-material crack. The upper arm elastic modulus (E_1) is varied in a wide range of reasonable materials applied to MMB test specimens. The lower arm has an elastic modulus (E_2) of 70 GPa and both arms have a Poisson's ratio (ν_1 and ν_2) of 0.33. The crack length is kept at 50 mm and the test load (P) is 100 N, likewise the previous cases.

Analytical and numerical results of the total fracture energy (G) are presented in Fig. 17.9. Both analytical methods give the same results for any material. Fig. 17.9a, b, and c show the three cases of low, intermediate, and high mode II fracture, respectively. Both analytical methods are in very good agreement with the FEM/VCCT results, hence, the analytical methods based on beam analysis provide reliable results of the total fracture energy on bi-material cracks.

Fig. 17.10 shows the analytical and numerical fracture mode ratio (G_{II}/G). For the applied parameters, the strain-equivalent geometry ($\beta = 1$) is achieved when E_1/E_2 equals 2.0. In the case of low mode II (case 4), shown in Fig. 17.10a, the SBM shows good agreement with the FEM/VCCT despite the remarkable asymmetry of the materials and geometry. However, as β differs from 1, WM gives significant discrepancies from the FEM/VCCT results. This shows that the analytical method based on beam analysis is only valid for when the strain-equivalence condition is respected. Similar results are observed as the mode II fracture ratio increases, presented in Fig. 17.10b and c (cases 5 and 6, respectively). Moreover, it is shown once more that WM only predicts accurate fracture mode ratios when the condition of strain equivalence is satisfied ($\beta = 1$). For any other geometry, the coupling effect between fracture modes is not taken into account and therefore incorrectly predicts the fracture mode ratios. The influence of the mode I and mode II coupling may have a large effect on the fracture mode of bi-material cracks. This reinforces the requirement of the strain-based design criterion for obtaining the correct partitioning ratio.

Table 17.4 shows the results and errors of the analytical model in comparison with the numerical model for the particular condition of strain equivalence proposed in the SBM (see Eq. (17.23)). Errors between 1.0% and -8.1% are observed in the calculation of the total fracture energy and between 1.1% and -8.6% in the fracture mode

Table 17.3 Study cases of a crack at a bi-material interface.

Case	Lever length, c (mm)	h_1 (mm)	h_2 (mm)	E_1 (GPa)	E_2 (GPa)	ν_1 ; ν_2
4	95	2.12	3.0	$35 \leq E_1 \leq 210$	70	0.33
5	49	2.12	3.0	$35 \leq E_1 \leq 210$	70	0.33
6	34	2.12	3.0	$35 \leq E_1 \leq 210$	70	0.33

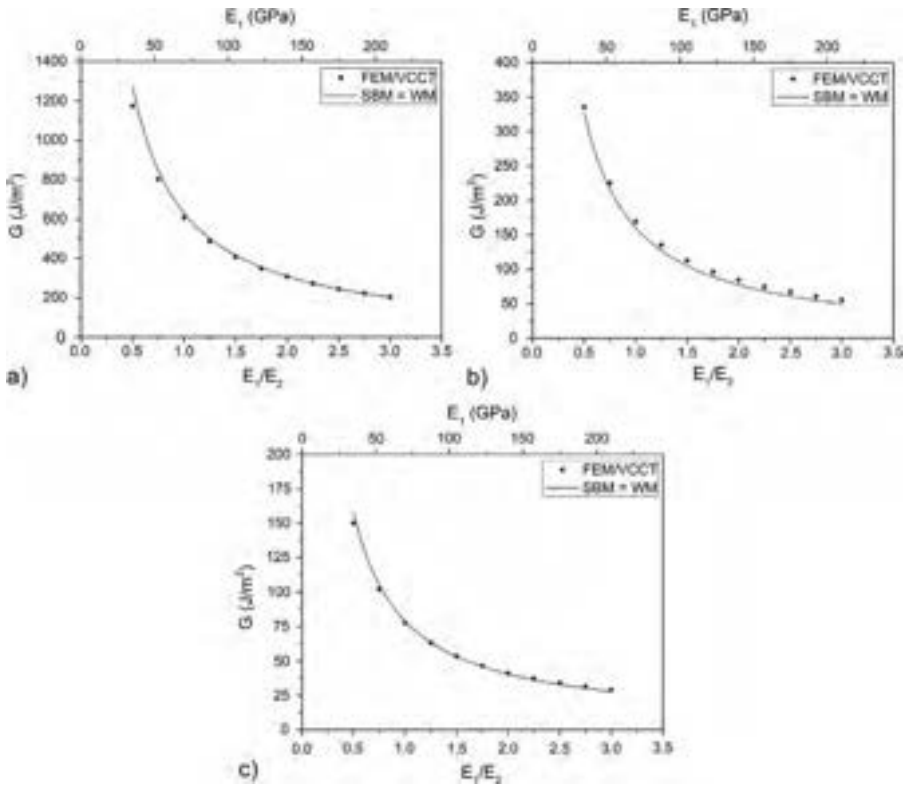


Fig. 17.9 Total fracture energy with the variation of the specimen material: cases (a) 4—low, (b) 5—intermediate, and (c) 6—high mode II [27]. Reprinted with permission from Taylor & Francis Ltd, <http://www.tandfonline.com>.

ratio. These errors are in a similar degree as cases 1, 2, and 3 of symmetric condition, presented in Table 17.2. Therefore, it can be implied that the effect of crack tip rotation is also a major cause of the errors produced in cases 4, 5, and 6 of bi-material cracks using the SBM.

17.4.2.5 Application of the SBM to composite-to-metal bonded joints

To evaluate the SBM and validate the previous numerical analysis, a test campaign has been conducted in which MMB tests were performed [27,35]. Composite-to-metal bonded joints were manufactured in thin and thick geometries. The geometry of the joint was designed to satisfy the criterion of strain equivalence ($\beta=1$). The mechanical properties of the materials are shown in Table 17.5.

Table 17.6 shows the test matrix. The half-span (L) of the test is 70mm and the initial crack length (a_0) of 30mm was obtained after bonding the end blocks.

The total fracture energy and mode ratio were obtained at crack propagation using the SBM and the FEM assuming cohesive failure in the adhesive. Fig. 17.11a and b show the total fracture energy of Tests 1 and 2 in thick specimens. The SBM produced

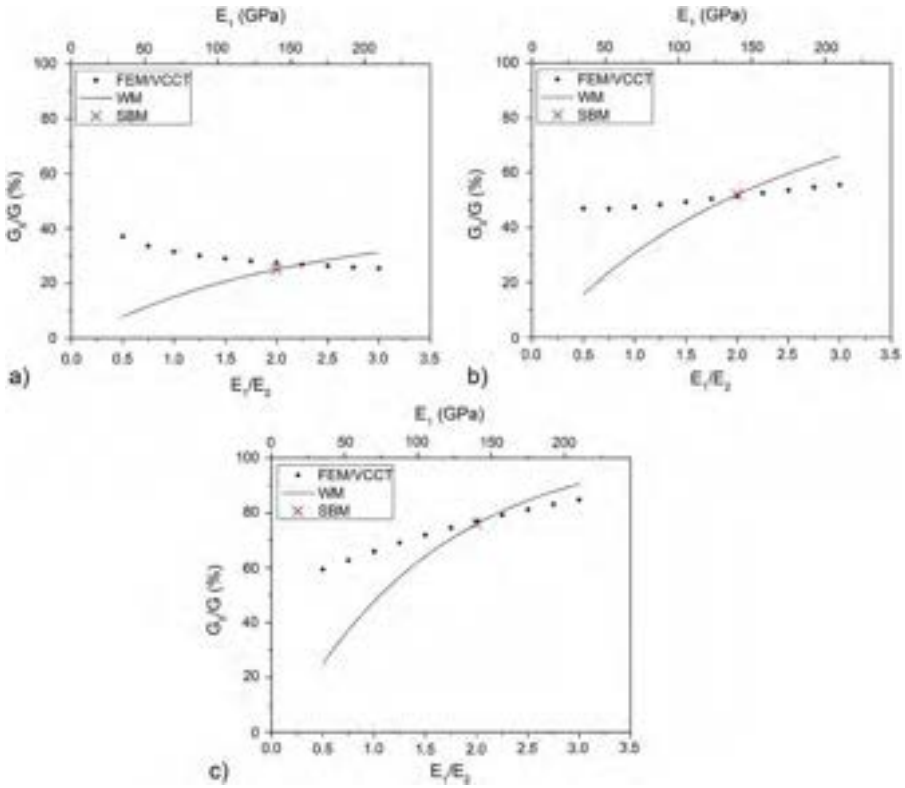


Fig. 17.10 Fracture mode ratio with the variation of specimen material: cases (a) 4—low, (b) 5—intermediate, and (c) 6—high mode II [27].

Reprinted with permission from Taylor & Francis Ltd, <http://www.tandfonline.com>.

Table 17.4 Results and errors of the analytical model in the condition of strain equivalence.

Case	Numerical model		Strain-based method (SBM)			
	G (J/m ²)	G_{II}/G (%)	G (J/m ²)	Error (%)	G_{II}/G (%)	Error (%)
4	306.0	27.5	309.0	1.0	25.1	-8.6
5	84.2	51.5	77.4	-8.1	52.1	1.1
6	41.3	77.0	40.5	-2.0	76.0	-1.3

Table 17.5 Mechanical properties of the materials.

Material	Elastic modulus, E_{11} (GPa)	Poisson's ratio, ν_{12}
Steel	200	0.27
Composite 0/90	46	0.24
Adhesive	2.25	0.38

Table 17.6 Test matrix.

Test	Specimen	Metal arm thickness, h_1 (mm)	Composite arm thickness, h_2 (mm)	Lever length, c (mm)	Lever center of gravity, c_g (mm)	Lever weight, P_g (kg)
1	Thick	6.35	13.35	78	31	17.6
2	Thick	6.35	13.35	78	31	17.6
3	Thin	3.18	6.34	110	40	17.6
4	Thin	3.18	6.34	110	40	17.6

an error of 27.8% in the first measurement of crack propagation and this reduces as the crack length increases, down to 11.4% in the last propagation point. The fracture mode ratio (G_{II}/G) presented nearly constant values of 23.5% in the SBM and 21.5% in the FEM, as observed in Fig. 17.11c. A constant fracture mode ratio is expected from the MMB test. The total fracture energy of Tests 3 and 4, in thin specimens, are presented in Fig. 17.12a and b, respectively. In this geometry, the SBM produced an error of 13.2% in the first measurement of crack propagation and this reduced as the crack length increases, down to 2.6% in the last propagation point. The analytical method produced more accurate results in the thin specimens compared to the thick ones. Moreover, the analytical solution showed more accuracy as the crack length increases due to the reduction of transverse shear effect that is not considered in the analytical

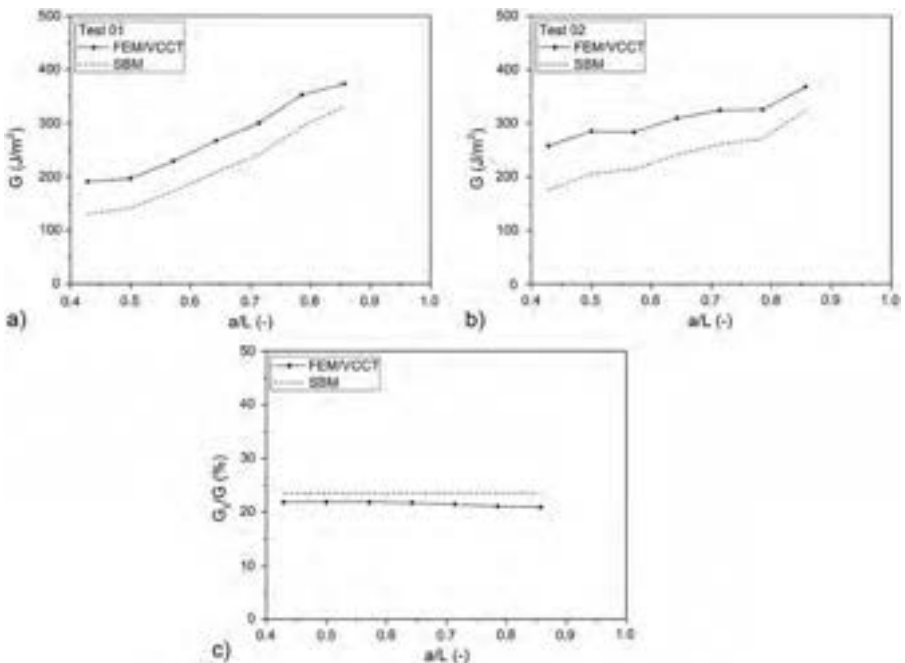


Fig. 17.11 Total fracture energy and mode ratio of thick specimens [27].
 Reprinted with permission from Taylor & Francis Ltd, <http://www.tandfonline.com>.

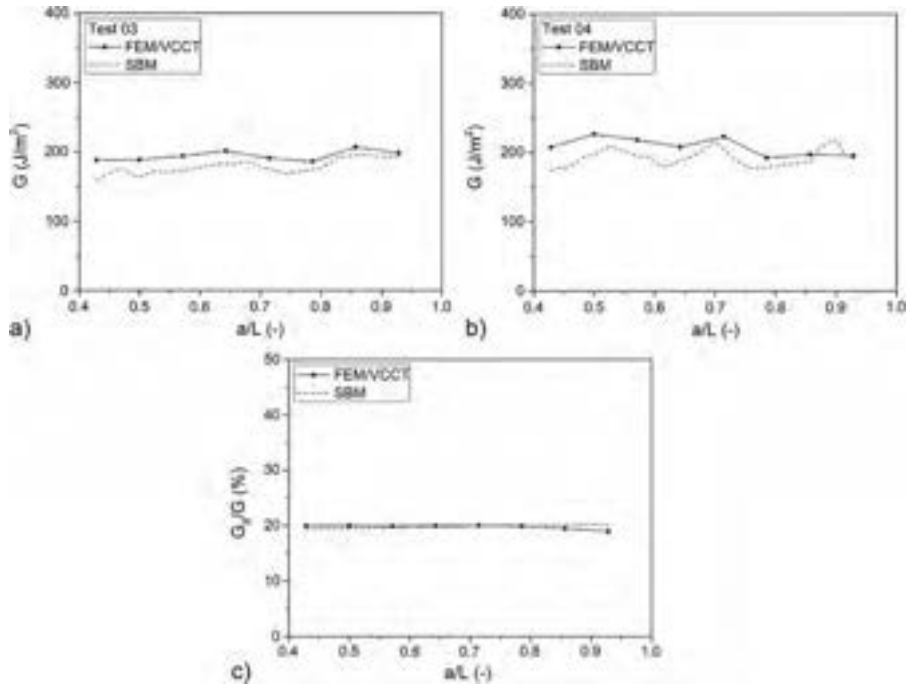


Fig. 17.12 Total fracture energy and mode ratio of thin specimens [27].

Reprinted with permission from Taylor & Francis Ltd, <http://www.tandfonline.com>.

model but can be significant in a specimen with relatively large thickness. Finally, thin specimens presented a nearly constant fracture mode ratio (G_{II}/G) of 19.8% from both the SBM and the FEM, as shown in Fig. 17.12c. This shows the accuracy of the analytical solution and agrees with the results obtained from the parametric study in the previous section. Overall, the SBM gives reliable results for the calculation of the total fracture energy and mode ratio of cracks at a bi-material interface as long as the shear effects are negligible.

17.5 Mixed-mode fracture behavior

17.5.1 Crack stability

Crack stability is an important issue in the fracture testing of adhesively bonded joints, as only for stable cracking can the change in applied force (and hence the compliance) be measured for a growing crack. A crack is unstable if an infinitesimal change in displacement is accompanied by a finite change in the crack length. The stability of crack growth may be judged from the sign of dG/da . Stable crack growth occurs if:

$$\frac{dG}{da} \leq 0 \quad (17.28)$$

The energy release rate was defined as the Irwin-Kies equation [8]:

$$G = \frac{P^2}{2b} \frac{dC}{da} \quad (17.29)$$

where P is the applied load and C is the compliance defined by δ/P (δ is the displacement) and b is the specimen width. In this form, linear elastic behavior is assumed and in the following, G_c is assumed to be independent of rate. Considering the crack propagates very quickly with the displacement increment, the loading process is analogous to a condition of fixed grips. Eq. (17.29) can be transformed as:

$$G = \frac{\delta^2}{2bC^2} \frac{dC}{da} \quad (17.30)$$

Combing Eqs. (17.28) and (17.30) leads to the stability criterion for fracture tests [23]:

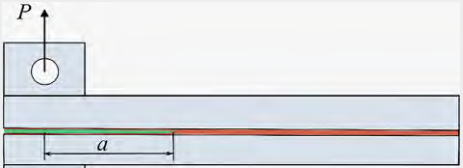
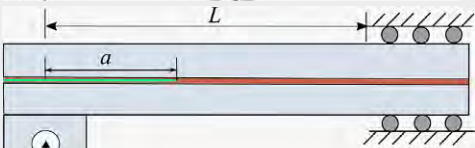
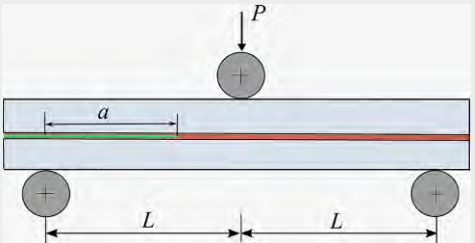
$$\frac{1}{2} C \frac{d^2C}{da^2} \frac{1}{(dC/da)^2} \leq 1 \quad (17.31)$$

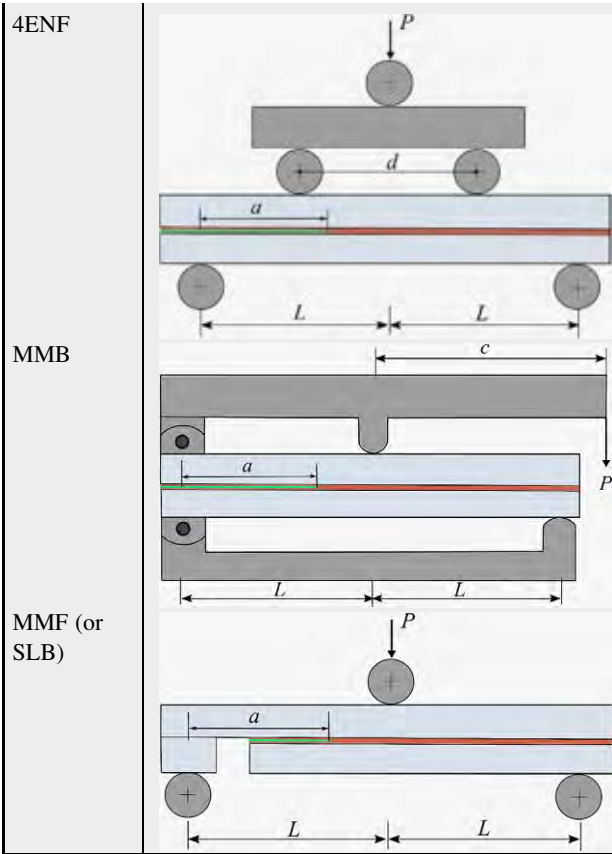
Based on this theory, the stability criteria for a variety of fracture tests have been successfully derived, as documented in Table 17.7. Specimen precracking is always recommended prior to a fracture test, as unstable crack growth can occur when testing the specimen directly from an insert. The resistance to crack initiation from an inserted release film (positioned in the adhesive layer during manufacture of the joint) may impose a greater initial crack resistance with $(dG/da) > 0$. Precracking the specimen so that the crack length can extend by a short distance from its initial length can improve stability.

However, unstable fracture behavior can still occur despite the initial crack length satisfying the above criteria, as crack stability is highly dependent upon the adhesive properties. An unstable fracture is more likely to occur in joints bonded with a brittle adhesive while joints bonded with a tougher adhesive tend to result in stable fracture behavior [47]. Moreover, crack stability is very sensitive to the mixed-mode ratio. While stable fracture can be obtained in the adhesively bonded CFRP under mode I and mode II loadings, an unstable crack may appear in the mixed mode I/II loading. Researchers, such as [48], also reported that the crack in glass epoxy laminates bonded with Redux 420 epoxy adhesive propagated very rapidly and unstably under mode I dominated loading, whereas the propagation became more stable under mode II dominated loading, when the fracture resistance was greater.

The fracture behavior of asymmetric specimens suggests that the size of the cohesive zone may be a critical factor governing the stability of crack growth in adhesive joints [46]. In the AFRMM joints loaded via the thinner arm (mode I dominated), the crack was found to grow stably within the adhesive. In contrast, in the case loaded with the thicker arm (mode II dominated), the response became rather unstable with the crack propagating to the clamping point abruptly, associated with a change in the type of failure from cohesive in the adhesive layer to interlaminar in the CFRP substrates.

Table 17.7 Specimen configuration and stability criteria for fracture testing of laminated composites and adhesive joints loaded in displacement control.

Fracture tests	Specimen configurations	Stability criteria	References
DCB and ADCB		Always stable	[32]
ELS		$a/L \geq 0.56$	[32]
3ENF		$a/L \geq 0.68$	[32]



Always stable. Enough space between the loading pin and the crack tip should be allowed to rule out any unwanted effects from the compressive stresses of the loading pin.

[43]

$$a/L \geq \left[\frac{(c+L)^2}{4(3c-L)^2 + 3(c+L)^2} \right]^{\frac{1}{3}}$$

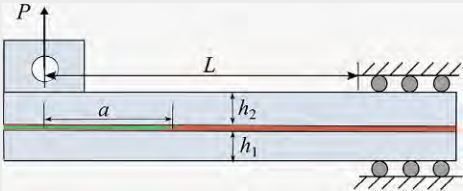
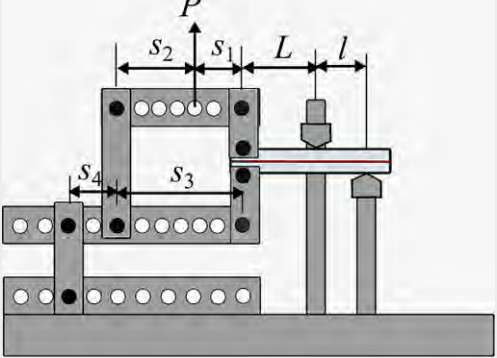
[44]

$$a/L \geq 0.49$$

[45]

Continued

Table 17.7 Continued

Fracture tests	Specimen configurations	Stability criteria	References
FRMM ($h_1 = h_2$)		$a/L \geq 0.41$	[32]
AFRMM ($h_1 \neq h_2$)		$a/L \geq \frac{\alpha}{1+\alpha} \left[\frac{(1+\alpha)^2(1+\alpha^3)}{2((1+\alpha)^2+3\alpha^4)} \right]^{\frac{1}{3}}$ $\alpha = \frac{h_2}{h_1} = \frac{\text{Loaded arm}}{\text{Unloaded arm}}$	[46]
SPELT		$a/L \geq \left[\frac{1+l/L}{1+\beta^*(\psi)} \right]^{\frac{1}{3}}$ <p>ψ is the nominal phase angle of loading, and $\beta^*(\psi)$ is the dimensionless geometry parameter</p>	[15]

The FEA simulation suggests extensive damage accumulated ahead of the crack tip in the AFRMM specimen loaded via the thicker arm, leading to much longer cohesive zones than those loaded inversely. In addition, the length of the cohesive zone decreased rapidly after reaching a maximum. This abrupt reduction could explain the unstable nature of these tests (Fig. 17.13).

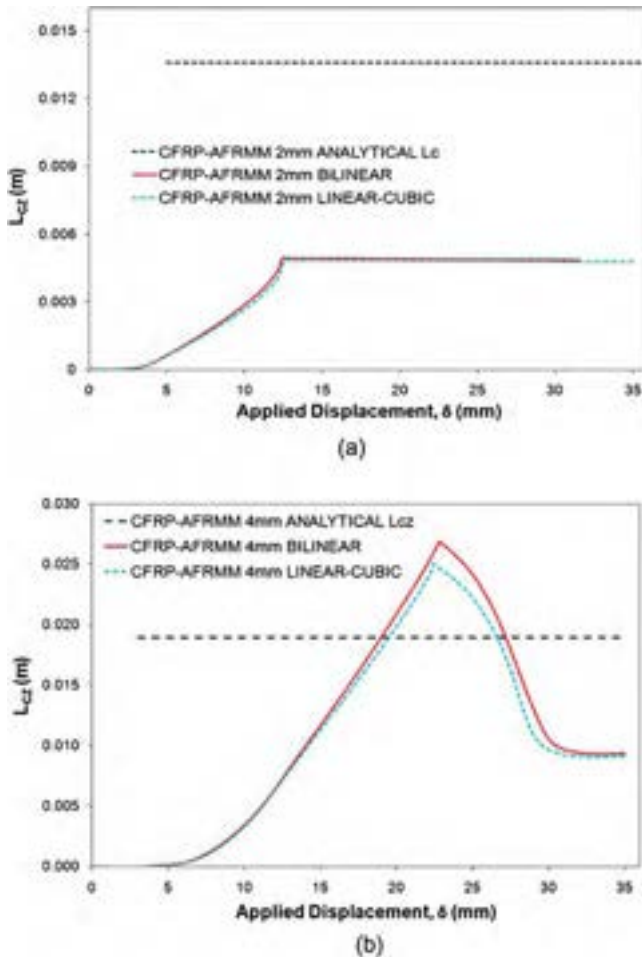


Fig. 17.13 The cohesive zone length as a function of applied displacement in AFRMM specimens loaded at (a) the thinnest and (b) the thickest arms from FEA simulations, assuming a bilinear and a linear cubic traction separation law, and from an analytical method. The analytical estimate was calculated by adding the contributions of the pure mode components of G_{IC}^m and G_{IIIC}^m , that is, $l_{CZ}^m = l_{CZ, I}(G_{IC}^m) + l_{CZ, II}(G_{IIIC}^m)$ [46].

17.5.2 Crack paths

Crack path is a major concern for the fracture analysis of layered materials. Due to the existence of elastic mismatch, microdefects, and residual stresses on the interface, it is quite challenging to predict the crack paths analytically. Fleck et al. [49] established LEFM theories to predict the crack path in adhesively bonded structures under mode I with finite mode II loading, based on the experimentally established fact that a crack advancing continuously in an isotropic, homogeneous, brittle solid selects a trajectory where local stress intensity factor $K_{II} = 0$. The remote field in the asymptotic problem in Fig. 17.14 is specified by K_I^∞ , K_{II}^∞ , T^∞ , and σ^0 , where K_I^∞ and K_{II}^∞ are the remote values of the mode I and mode II stress intensity factors, respectively; T^∞ is the remote T -stress; and σ^0 is the σ_{xx} component of residual stress preexisting in the adhesive due to thermal mismatch or other sources. The solution to the elasticity problem (as shown in Fig. 17.14) provides the local K_I , K_{II} , and T at the crack tip within the layer, and is given by the following equations, with c_I and c_{II} and $\phi_H(\alpha, \beta) + \omega(\alpha, \beta)$ being tabulated in [49].

Note that the parameter β used in this section has a different definition to β defined elsewhere in the chapter. The local (K_I, K_{II}) depends only on the remote loads K_I^∞ and K_{II}^∞ , and the two sets are connected by the energy release rate due to conservation of the J -integral:

$$K_I + iK_{II} = \left(\frac{1 - \alpha}{1 + \alpha}\right)^{1/2} (K_I^\infty + K_{II}^\infty) e^{i\phi} \tag{17.32}$$

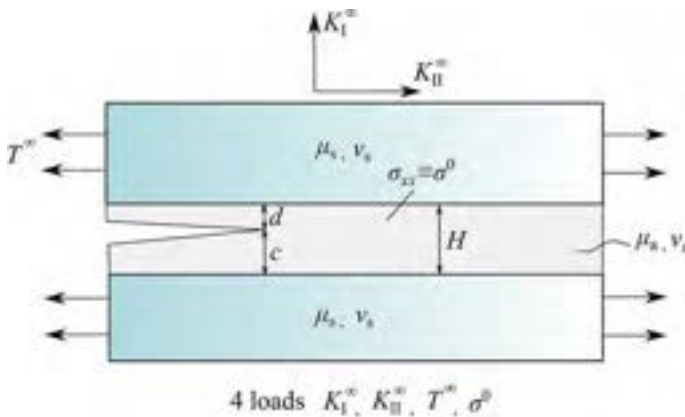


Fig. 17.14 The elasticity problem. Redrawn after N.A. Fleck, J.W. Hutchinson, Z. Suo, Crack path selection in a brittle adhesive layer, Int. J. Solids Struct. 27 (1991) 1683–703.

where ϕ can be interpreted as a phase angle shift between the remote and local stress intensities, $\phi \equiv \tan^{-1}(K_{II}/K_I) - \tan^{-1}(K_{II}^\infty/K_I^\infty)$. ϕ is only a function of structures, that is, $\phi = \phi(c/H, \alpha, \beta)$:

$$\phi = \varepsilon \ln\left(\frac{H-c}{c}\right) + 2\left(\frac{c}{H} - \frac{1}{2}\right)[\phi_H(\alpha, \beta) + \omega(\alpha, \beta)] \quad (17.33)$$

where α, β are Dundurs elastic mismatch parameters, $\varepsilon = (1/2\pi) \ln[(1-\beta)/(1+\beta)]$, c/H is the crack location as illustrated in Fig. 17.14, the function $\omega(\alpha, \beta)$ is tabulated in [50] and ϕ_H is given in Hutchinson et al. [51].

The local T-stress depends linearly on all four loading parameters.

$$T = \frac{1-\alpha}{1+\alpha} T^\infty + \sigma^0 + c_I \frac{K_I^\infty}{\sqrt{H}} + c_{II} \frac{K_{II}^\infty}{\sqrt{H}} \quad (17.34)$$

where the two nondimensional functions, $c_I(c/H, \alpha, \beta)$ and $c_{II}(c/H, \alpha, \beta)$, are given in [49].

A necessary condition for the existence of a straight path within the layer is the location of a path with $K_{II} = 0$. Such a path will only be stable if $T < 0$. Symmetry indicates that a crack along the center line of a layer joining identical materials and subject to remote pure mode I loading will be under pure mode I locally. When the base specimen carries some mode II in addition to mode I, the crack may find a pure mode I path off the center line. When the mode II component is sufficiently large, typically $\tan^{-1}(K_{II}^\infty/K_I^\infty) \geq 15$ degrees, the crack runs along the adhesive/substrate interface and the measured G_c is the mode-dependent interfacial fracture energy. For values of K_{II}^∞/K_I^∞ outside the range of possible retention of the crack within the layer (such as, $\tan^{-1}(K_{II}^\infty/K_I^\infty)$ greater than 0–10 degrees depending on the mismatch), the crack will be driven toward one interface or the other—toward the lower interface if $K_{II}^\infty > 0$ and toward the upper if $K_{II}^\infty < 0$ [52].

For tough adhesive systems in which LEFM may not still be valid, there exists considerable experimental evidence that suggests that the type of loading affects the crack propagation path (i.e., loci of failure). Mixed mode I/II tends to drive the crack toward the interface of the adhesive joint. For instance, Blackman et al. [53] reported that the adhesively bonded CFRP joints loaded in mixed-mode ($G_I/G_{II} = 4/3$) failed via a delamination mechanism, with the crack switching from the position of the cohesive precrack to a path within the composite substrate, in contrast to the cohesive failure that occurred under the pure mode I or mode II loading. Blackman et al. pointed out that this type of failure was related to the transverse tensile stresses (σ_{yy}) exerted on the CFRP substrates. If the transverse stresses exceeded the transverse strength (σ_{yyc}), fracture could take place in the composite arms. An approximation to the transverse stress, σ_{yy} , on a single substrate for the loading modes was developed that indicated that the greatest transverse stresses were produced by mixed-mode loading using the FRMM specimen, which has only a single arm being loaded.

17.5.3 Failure envelopes

A comprehensive review of failure envelopes, including information on the type of responses modeled in each case, can be found in [54]. These criteria were initially developed for composite materials, but there is much evidence showing they are also valid for adhesive joints. The most widely used empirical criteria for the failure of adhesive joints are the power criterion [55] (Eq. 17.35) and the B-K criterion [42] (Eq. 17.36). Both criteria were implemented in several commercial finite element analysis codes.

$$\left(\frac{G_I}{G_{Ic}}\right)^m + \left(\frac{G_{II}}{G_{IIc}}\right)^n = 1 \tag{17.35}$$

$$G_{I/IIc} = G_{Ic} + (G_{IIc} - G_{Ic}) \left(\frac{G_{II}}{G_I + G_{II}}\right)^n \tag{17.36}$$

Fig. 17.15 presents the fracture toughness as a function of the mode-mixity (G_{II}/G) for the unidirectionally reinforced carbon fiber composite substrates bonded with the epoxy adhesive, 3M-D460 [56]. The power law captured the failure envelope of the adhesive joints when the exponents $m=0.63$ and $n=1.43$, and indeed the power law criterion with a single exponent of 1.0 has been able to provide a satisfactory fit.

It has been reported that the B-K failure criterion successfully described the failure behavior of adhesive joints employing metallic substrates. Fig. 17.16 shows the fracture toughness of the crash-resistant epoxy adhesive SikaPowers-498 measured under various values of mixed-mode ratio using TDCB and MMB tests [57]. Fig. 17.17 gives another example of the fracture toughness of Araldite-2015 bonded metallic joints determined by DCB and MMB tests [58]. For both sets of experimental data, there was a steady increase in the fracture resistance as the mixed-mode ratio increased from 0 (pure mode I) to 1 (pure mode II). The B-K model captured the fracture behavior as a function of mixed-mode ratio closely.

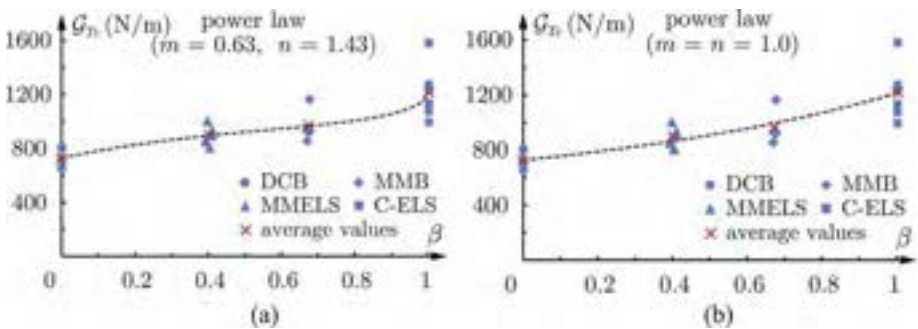


Fig. 17.15 Values of G -total (G_{Tc}) as a function of mixed-mode ratio $\beta = G_{II}/G_{Tc}$ for: (a) exponents $m=0.63$ and $n=1.43$ and (b) a single exponent of 1.0 [56].

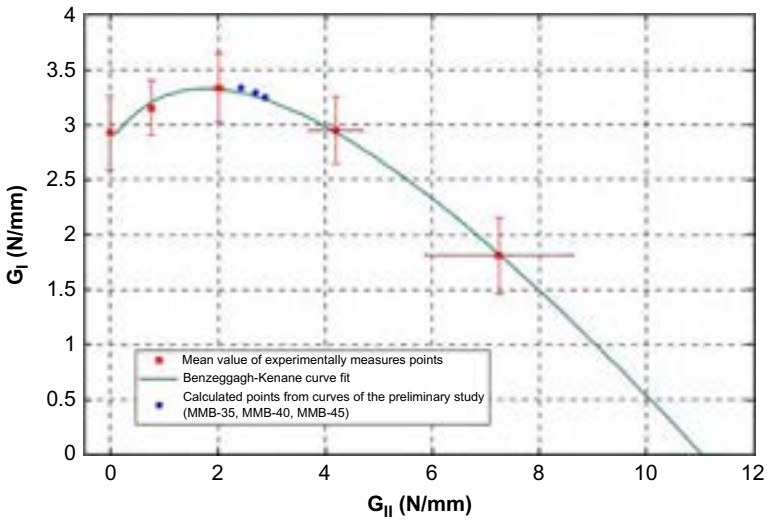


Fig. 17.16 Mixed-mode fracture data measured on joints employing metallic substrates bonded with SikaPower 498 adhesive, fitted using the B-K criterion [57].

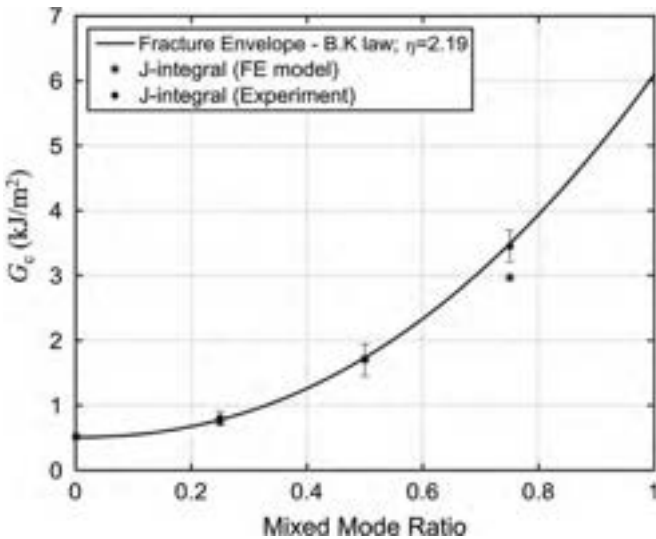


Fig. 17.17 Mixed-mode fracture data measured on joints employing metallic substrates bonded with Araldite 2015 adhesive, fitted using the B-K criterion [58].

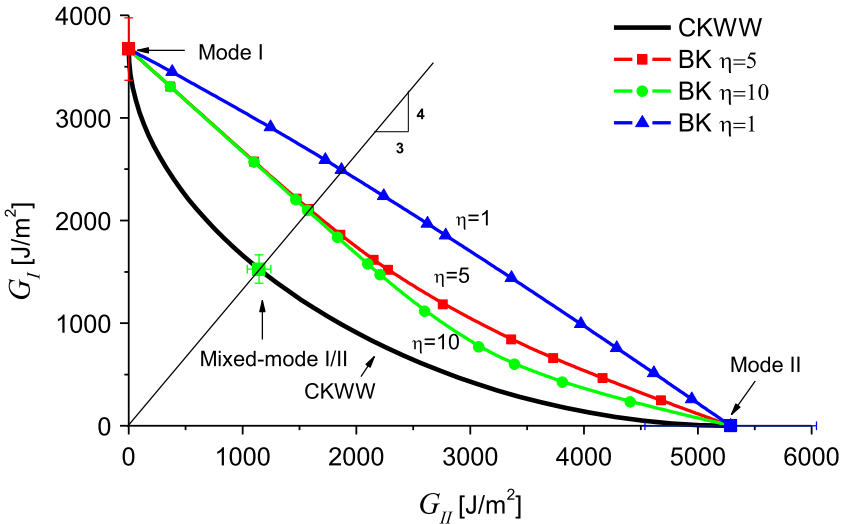


Fig. 17.18 Comparison of the use of the CKWW and BK criteria for construction of the failure envelope for joints bonded with a toughened automotive adhesive XD4600, when substrate delamination occurred [59].

The B-K model requires that the fracture toughness value always increases as the contribution of mode II is increased, that is, $G_{Ic} < G_{I/IIc} < G_{IIc}$; however, such a monotonically increasing trend is not always measured for adhesive joints. Fig. 17.18 presents B-K criteria constructed for joints bonded with the toughened automotive adhesive XD4600 under quasistatic loading [59]. Different values of η were used for the B-K criterion, but it was not possible for this model to fit the low mixed-mode I/II values produced when a switch in crack propagation path to interfacial failure or composite delamination occurred. Clearly, these joints that showed substrate delamination under mixed-mode loading did not comply with the “monotonic increase” requirement. Similar nonmonotonic behavior caused by the failure mechanism changing from cohesive (in the adhesive) to adhesive (on the carrier cloth/adhesive interface) under the mixed-mode loading was also reported by Dillard et al. [60]. However, the Charalambides, Kinloch, Wang, and Williams (CKWW) criterion [61] (in Eq. (17.37)) was found to be capable of capturing the nonmonotonic fracture envelope due to the criterion having two fitting parameters, κ and φ , which enabled the fitting of more complex failure envelopes.

$$\left(\frac{G_I}{G_{Ic}} - 1\right) \left(\frac{G_{II}}{G_{IIc}} - 1\right) - \left[\kappa + \varphi \left(\frac{G_I}{G_I + G_{II}}\right)\right] \left(\frac{G_I}{G_{Ic}}\right) \left(\frac{G_{II}}{G_{IIc}}\right) = 0 \quad (17.37)$$

Fig. 17.19 displays another example of fitting failure envelopes [62]. The fracture toughness determined at the point of the maximum load, in which the discrete value for $\beta = 0.25$ violates a monotonic trend, that is, in the range of $\beta < 0.25$ the G_c decreases with increasing mixity but when $\beta > 0.25$ it increases. The B-K criterion

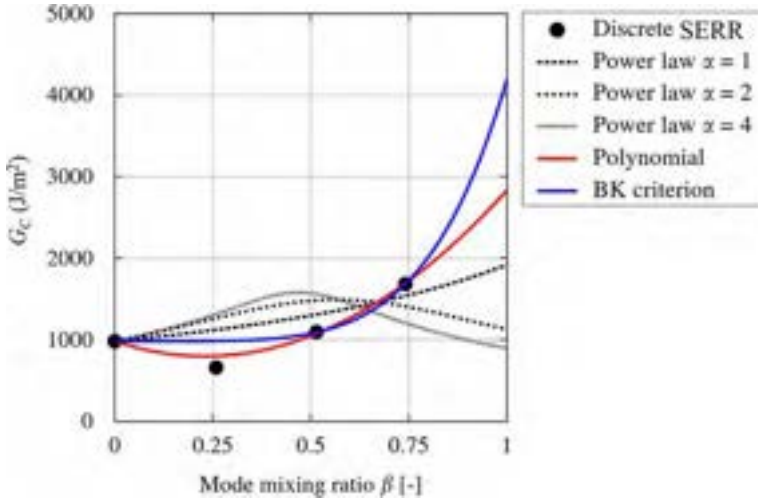


Fig. 17.19 Comparison of the use of the various failure criteria for construction of the failure envelopes for unidirectional Hexcel IM7/8552 carbon/epoxy composite bonded with film adhesive Cytec FM 300M [62].

and the power law with $\alpha_1 = \alpha_2 = 1$, both of which require a monotonical increase in G_c values, did not yield good approximation of the G_c value at $\beta = 0.25$. Instead, the best fit of the G_c values is obtained by the second order polynomial, clearly capturing the transition in the G_c value at $\beta = 0.25$.

17.6 Conclusions and outlook

The characterization of fracture in adhesively bonded joints under mixed-mode (I/II) loading conditions has been discussed. While standardized tests for adhesive joints in mixed-mode are not yet available, much use has been made of methods developed initially for composite laminates such as the mixed-mode bend test, the fixed-ratio mixed-mode test with both symmetric and asymmetric geometry, and the asymmetric double cantilever beam. Most analyses utilize LEFM and corrected beam theory to determine the fracture resistance as a function of mixed-mode ratio.

Efforts to partition the mixed-mode (I/II) fracture resistance into pure mode components have typically followed either a local singular field approach or a global approach. The application of these partitioning strategies to adhesively bonded joints has led to the conclusion that neither strategy works well across the wide spectrum of adhesives in common usage. The local singular field approach has been shown to be more suitable when brittle adhesives are employed (when the damage zone ahead of the crack tip is very limited in size.) Conversely, the global partitioning approach is shown to be more suitable when toughened adhesives are employed (when the damage zone ahead of the crack tip is larger.) A semianalytical cohesive zone analysis has been shown to work equally well across the wide spectrum of adhesives in use. This

approach utilizes a singularity factor that scales from the local to the global solutions and therefore has wide applicability.

The limitations of global partitioning have been further explored with the goal to design and analyze adhesive joints with dissimilar adherends—a bi-material interface joint. The definition of mode I loading in the mixed-mode case has been modified by the incorporation of a longitudinal strain criteria. Further, the coupling between mode I and II components and their contribution to the total mixed-mode fracture energy has been considered and the technique has been verified numerically. Such an approach offers advantages for the design of adhesive joints with dissimilar adherends and their analysis.

Finally, the issues of crack stability, crack path selection, and failure envelopes for mixed-mode loading were considered.

In terms of future trends, as adhesives become more highly toughened they present larger damage zones at the crack tip and the use of LEFM becomes increasingly inaccurate. As such, nonlinear methods such as the J -integral (also described in Chapter 16), and the adaptation of the inclinometer test methods to mixed-mode testing will increasingly be required. Also, developments in experimental techniques such as digital image correlation, which can be used to simultaneously track the crack growth, measure the traction-separation law, and determine J_c , will become more popular [47,63]. Also, as materials become more complex, especially layered or laminated materials that can be incorporated into adhesively bonded joints, then there is significant scope to design more fracture-resistant systems where knowledge of the failure paths under mixed-mode loading can be exploited.

References

- [1] A.J. Kinloch, *Adhesion and Adhesives: Science and Technology*, Chapman & Hall, London, 1987.
- [2] L.F.M. Da Silva, A. Öchsner, R.D. Adams, *Handbook of Adhesion Technology*, Springer-Verlag Berlin Heidelberg, Heidelberg, 2011.
- [3] E.J. Ripling, S. Mostovoy, R.L. Patrick, Measuring fracture toughness of adhesive joints, *Mater. Res. Stand.* 4 (1964) 129–134.
- [4] ASTM D3433-93, Standard Test Method for Fracture Strength in Cleavage of Adhesives in Bonded Metal Joints, 1993.
- [5] K.M. Liechti, T. Freda, On the use of laminated beams for the determination of pure and mixed-mode fracture properties of structural adhesives, *J. Adhes.* 28 (1989) 145–169.
- [6] S. Li, J. Wang, M.D. Thouless, The effects of shear on delamination in layered materials, *J. Mech. Phys. Solids* 52 (2004) 193–214.
- [7] H.K. Singh, A. Chakraborty, C.E. Frazier, D.A. Dillard, Mixed mode fracture testing of adhesively bonded wood specimens using a dual actuator load frame, *Holzforschung* 64 (2010) 353–361.
- [8] G.R. Irwin, J.A. Kies, Critical energy release rate analysis of fracture strength of large welded structures, *Weld. J.* 33 (1954) 193–198.
- [9] Chaves F.J.P., Silva L.F.M., De Moura M.F.S.F., Dillard D.A., Esteves C., Chaves F.J.P., et al. Fracture mechanics tests in adhesively bonded joints: a literature review *J. Adhes.* 90 2014; 8464.F.J.P. Chaves, L.F.M. Silva, M.F.S.F. De Moura, D.A. Dillard, C. Esteves, F.J.

- P. Chaves, et al., Fracture mechanics tests in adhesively bonded joints: a literature review, *J. Adhes.* 90 (2014) 955–992.
- [10] B.F. Sørensen, P. Brethe, P. Skov-Hansen, Controlled crack growth in ceramics: the DCB specimen loaded with pure moments, *J. Eur. Ceram. Soc.* 16 (1996) 1021–1025.
- [11] L.A. Carlsson, J.W. Gillespie, R.B. Pipes, On the Analysis and Design of the End Notched Flexure (ENF) Specimen for Mode II Testing, *J. Compos. Mater.* 20 (1986) 594–604.
- [12] B.R.K. Blackman, A.J. Kinloch, M. Paraschi, The determination of the mode II adhesive fracture resistance, G_{IIc} , of structural adhesive joints: an effective crack length approach, *Eng. Fract. Mech.* 72 (2005) 877–897.
- [13] J.R. Reeder, J.H. Crews, Nonlinear analysis and redesign of the Mixed-Mode bending Delamination test, Langley Research Center Hampton, Virginia, 1991.
- [14] M. Arcan, Z. Hashin, A. Voloshin, A method to produce uniform plane-stress states with applications to fiber-reinforced materials - a specially designed specimen yields material properties under pure shear or uniform plane-stress conditions, *Exp. Mech.* 18 (1978) 141–146.
- [15] G. Fernlund, J.K. Spelt, Mixed-mode fracture characterization of adhesive joints, *Compos. Sci. Technol.* 50 (1994) 441–449.
- [16] ASTM: D6671M, Standard Test Method for Mixed Mode I-Mode II Interlaminar Fracture Toughness of Unidirectional Fiber Reinforced Polymer Matrix Composites, 2006.
- [17] M. Costa, R. Carbas, E. Marques, G. Viana, L.F.M. da Silva, An apparatus for mixed-mode fracture characterization of adhesive joints, *Theor. Appl. Fract. Mech.* 91 (2017) 94–102.
- [18] Y.H. Lai, M.D. Rakestraw, D.A. Dillard, The cracked lap shear specimen revisited - a closed form solution, *Int. J. Solids Struct.* 33 (1996) 1725–1743.
- [19] W.S. Johnson, Stress analysis of the cracked-lap-shear specimen - an ASTM round-robin, *J. Test. Eval.* 15 (1987) 303–324.
- [20] E. Panettieri, G. Leclerc, J. Jumel, J. Guitard, Mixed-mode crack propagation tests of composite bonded joints using a dual-actuator load frame_Constant and variable G_{II}/G conditions, *Eng. Fract. Mech.* 202 (2018) 471–486.
- [21] T. Yang, V. Gandhi, R. Huang, K.M. Liechti, Rate dependent fracture along a silicone / epoxy interface under mixed-mode loading conditions, *Int. J. Solids Struct.* (2022) (in press).
- [22] J.G. Williams, The fracture mechanics of delamination tests, *J. Strain Anal. Eng. Des.* 24 (1989) 207–214.
- [23] J.G. Williams, On the calculation of energy release rates for cracked laminates, *Int. J. Fract.* 36 (1988) 101–119.
- [24] M. Conroy, A.J. Kinloch, J.G. Williams, A. Ivankovic, Mixed mode partitioning of beam-like geometries: a damage dependent solution, *Eng. Fract. Mech.* 149 (2015) 351–367.
- [25] D. Álvarez, F.J. Guild, A.J. Kinloch, B.R.K. Blackman, Partitioning of mixed-mode fracture in adhesively-bonded joints: experimental studies, *Eng. Fract. Mech.* 203 (2018) 224–239.
- [26] B.D. Davidson, S.J. Gharibian, L. Yu, Evaluation of energy release rate-based approaches for predicting delamination growth in laminated composites, *Int. J. Fract.* 105 (2000) 343–365.
- [27] M.M. Arouche, S. Teixeira de Freitas, S. de Barros, Evaluation of the strain-based partitioning method for mixed-mode I+II fracture of bi-material cracks, *J. Adhes.* 98 (2022) 577–605.
- [28] J.G. Williams, Large displacement and end block effects in the “DCB” interlaminar test in Modes I and II, *J. Compos. Mater.* 21 (1987) 330–347.

- [29] J.G. Williams, End corrections for orthotropic DCB specimens, *Compos. Sci. Technol.* 35 (1989) 367–376.
- [30] M.F. Kanninen, A dynamic analysis of unstable crack propagation and arrest in the DCB test specimen, *Int. J. Fract.* 10 (1974) 415–430.
- [31] Y. Wang, J.G. Williams, Corrections for mode II fracture toughness specimens of composites materials, *Compos. Sci. Technol.* 43 (1992) 251–256.
- [32] S. Hashemi, A.J. Kinloch, J.G. Williams, The analysis of interlaminar fracture in uniaxial fibre-polymer composites, *Proc. R. Soc. Lond. A* 427 (1990) 173–199.
- [33] F. Ducept, P. Davies, D. Gamby, An experimental study to validate tests used to determine mixed mode failure criteria of glass/epoxy composites, *Compos. A: Appl. Sci. Manuf.* 28 (1997) 719–729.
- [34] F. Ducept, D. Gamby, P. Davies, A mixed-mode failure criterion derived from tests on symmetric and asymmetric specimens, *Compos. Sci. Technol.* 59 (1999) 609–619.
- [35] M.M. Arouche, W. Wang, S. Teixeira de Freitas, S. de Barros, Strain-based methodology for mixed-mode I+II fracture: a new partitioning method for bi-material adhesively bonded joints, *J. Adhes.* 95 (2019) 385–404.
- [36] Z. Ouyang, G. Ji, G. Li, On approximately realizing and characterizing pure mode-I interface fracture between bonded dissimilar materials, *J. Appl. Mech.* 78 (2011) 1–12.
- [37] W. Wang, R. Lopes Fernandes, S. Teixeira De Freitas, D. Zarouchas, R. Benedictus, How pure mode I can be obtained in bi-material bonded DCB joints: a longitudinal strain-based criterion, *Compos. Part B Eng.* 153 (2018) 137–148.
- [38] V. Mollón, J. Bonhomme, A. Argüelles, J. Viña, Influence of the crack plane asymmetry over G II results in carbon epoxy ENF specimens, *Compos. Struct.* 94 (2012) 1187–1191.
- [39] J.R. Reeder, J.H. Crews, Redesign of the mixed-mode bending delamination test to reduce nonlinear effects, *J. Compos. Technol. Res.* 14 (1992) 12–19.
- [40] J.R. Reeder, A bilinear failure criterion for mixed-mode delamination, in: *Composite Materials: Testing and Design*, ASTM STP 1206, vol. 11, American Society for Testing and Materials, Philadelphia, 1993, pp. 302–322.
- [41] J.H. Chen, R. Sernow, E. Schulz, G. Hinrichsen, Modification of the mixed-mode bending test apparatus, *Compos. A: Appl. Sci. Manuf.* 30 (1999) 871–877.
- [42] M.L. Benzeggagh, M. Kenane, Measurement of mixed-mode delamination fracture toughness of unidirectional glass/epoxy composites with mixed-mode bending apparatus, *Compos. Sci. Technol.* 56 (1996) 439–449.
- [43] C. Schuecker, B.D. Davidson, Evaluation of the accuracy of the four-point bend end-notched flexure test for mode II delamination toughness determination, *Compos. Sci. Technol.* 60 (2000) 2137–2146.
- [44] Y.J. Yum, A.H. You, Pure mode I, II and mixed mode interlaminar fracture of graphite/epoxy composite materials, *J. Reinf. Plast. Compos.* 20 (2001) 794–808.
- [45] A. Szekrényes, Crack stability of fracture specimens used to test unidirectional fiber reinforced material, *Exp. Mech.* 50 (2010) 473–482.
- [46] D. Alvarez Feito, Fracture mechanics of carbon fibre reinforced plastics to Ti-alloy adhesive joints (Ph.D. thesis), Imperial College London, 2012.
- [47] F. Sun, B.R.K. Blackman, A DIC method to determine the Mode I energy release rate G, the J-integral and the traction-separation law simultaneously for adhesive joints, *Eng. Fract. Mech.* 234 (2020), 107097.
- [48] F. Ducept, P. Davies, D. Gamby, Mixed mode failure criteria for a glass/epoxy composite and an adhesively bonded composite/composite joint, *Int. J. Adhes. Adhes.* 20 (2000) 233–244.

-
- [49] N.A. Fleck, J.W. Hutchinson, Z. Suo, Crack path selection in a brittle adhesive layer, *Int. J. Solids Struct.* 27 (1991) 1683–1703.
- [50] R. Huang, Z. Suo, J.H. Prevost, W.D. Nix, Inhomogeneous deformation in metallic glasses, *J. Mech. Phys. Solids* 50 (2002) 1011–1027.
- [51] J.W. Hutchinson, M.E. Mear, J.R. Rice, Crack paralleling an interface between dissimilar materials, *J. Appl. Mech.* 54 (1987) 828–832.
- [52] J.W. Hutchinson, Z. Suo, Mixed mode cracking in layered materials, *Adv. Appl. Mech.* 29 (1991) 63–191.
- [53] B.R.K. Blackman, A.J. Kinloch, F.S. Rodriguez-Sanchez, W.S. Teo, The fracture behaviour of adhesively-bonded composite joints: effects of rate of test and mode of loading, *Int. J. Solids Struct.* 49 (2012) 1434–1452.
- [54] J.R. Reeder, 3-D mixed mode delamination fracture criteria - an Experimentalist's perspective, in: B. Sankar, A. Waas, M. Hyer (Eds.), *Damage in Composites*, Destech Publications, Lancaster, PA, 2013, pp. 129–146.
- [55] E.M. Wu, R.C. Reuter, Crack Extension in Fiberglass Reinforced Plastics, Report No. 275, University of Illinois, Urbana, IL, 1965.
- [56] I. Simon, L. Banks-Sills, Mixed mode I/II interlaminar initiation fracture toughness of a secondary bonded pultrusion composite laminate, *Theor. Appl. Fract. Mech.* 114 (2021), 103018.
- [57] G. Stamoulis, N. Carrere, J.Y. Cognard, P. Davies, C. Badulescu, On the experimental mixed-mode failure of adhesively bonded metallic joints, *Int. J. Adhes. Adhes.* 51 (2014) 148–158.
- [58] M.Z. Sadeghi, J. Zimmermann, A. Gabener, K.U. Schroeder, The applicability of J-integral approach in the determination of mixed-mode fracture energy in a ductile adhesive, *Int. J. Adhes. Adhes.* 83 (2018) 2–8.
- [59] F.S. Rodriguez-Sanchez, Fracture Behaviour of Automotive Adhesive Joints, Imperial College London, 2008 (Ph.D. thesis).
- [60] D.A. Dillard, H.K. Singh, D.J. Pohlit, J.M. Starbuck, Observations of decreased fracture toughness for mixed mode fracture testing of adhesively bonded joints, *J. Adhes. Sci. Technol.* 23 (2009) 1515–1530.
- [61] M. Charalambides, A.J. Kinloch, Y. Wang, J.G. Williams, On the analysis of mixed-mode failure, *Int. J. Fract.* 54 (1992) 269–291.
- [62] C. Balzani, W. Wagner, D. Wilckens, R. Degenhardt, S. Büsing, H.G. Reimerdes, Adhesive joints in composite laminates - A combined numerical/experimental estimate of critical energy release rates, *Int. J. Adhes. Adhes.* 32 (2012) 23–38.
- [63] F. Sun, R. Zhang, B.R.K. Blackman, Determination of the mode I crack tip opening rate and the rate dependent cohesive properties for structural adhesive joints using digital image correlation, *Int. J. Solids Struct.* 217-218 (2021) 60–73.

This page intentionally left blank

Bondline thickness: Fracture mechanics perspective

18

Sofia Teixeira de Freitas^a and Michal K. Budzik^b

^aAerospace Structures and Materials Department, Faculty of Aerospace Engineering, Delft University of Technology, Delft, Netherlands, ^bDepartment of Mechanical and Production Engineering, Aarhus University, Aarhus, Denmark

18.1 Introduction

Judging if the bondline is thick or thin is far from an easy task. For structural bonding, the common assumption is to consider the bondline as thin if its thickness is very small compared to the other dimensions of the joint. In doing so, we assume that the bondline thickness is much higher than, for example, the roughness of the joined surfaces, and thus, well above the atomic length scale. However, there is no absolute definition of a thick or thin bondline. For example, a 1-cm thick bondline will certainly be recognized as very thick by the aerospace industry where a few millimeters thick composite plates are bonded, but can be seen as a rather thin in civil engineering applications while bonding/joining concrete slabs or beams. Historically, motivated and driven by aerospace industry development of lightweight materials and structures, thin bondlines were of the highest importance and, thus, studied the most extensively. Thin bondlines have been assumed in building analytical models, as well as data reduction schemes and standards [1]. However, with the expansion of adhesive bonding to marine, wind energy, civil engineering, and other industries, thicker bondlines are encountered very often [2]. The number of works discussing the effects of adhesive layer thickness on the strength and toughness of the joint is considerable [3–12]. In these works, the thickness of the bondline ranges from nanometers to centimeters.

The early tests indicated the dependence of adhesive joint strength on adhesive thickness, for example [13], leading to conclusions often diverging from expectations. For instance, according to the continuum theory, an increase in adhesive thickness and, thus, its volume, should not affect the strength of the joint (strength, as we know, is derived from the cross section area of the joint and, thus, not related to the thickness) while the joint toughness should be improved (here, the thickness leads to a larger volume over which the energy flows). Contrary to this, the strength was shown to decrease with increasing the adhesive thickness. In a more recent study, such a decrease is observed once the so-called optimum bondline thickness is exceeded [10]. In addition, once the adhesive thickness increases above a certain value, the adhesive can be regarded as experiencing a three-dimensional stress state and critical stress gradients due to geometrical (edges and corner) and material (an adhesive is usually of different materials than the joined adherends) discontinuities [14–17].

The continuum mechanics stress analysis was no longer sufficient and the tools of fracture mechanics are now intertwined to fully comprehend and predict adhesive joint failure. Within the fracture mechanics framework and corner stress fields, pioneer works involving elastic-plastic analysis a joint revealed the existence of a critical thickness and of a plastic radius at the tip of the crack [18]. The following sections will be used to build a theoretical framework linking these two aspects with the adhesive thickness. The majority of the content will focus on fracture mechanics and will be built around the concept that the adhesive joint can store the mechanical energy within the adherends, within the bondline, or split between the two.

18.2 From thin to thick adhesive layers

Analysis of the adhesive joints can be divided into strength and toughness (or fracture) approaches, as discussed in detail in Chapter 14. Fig. 18.1A–C shows three typical test specimens often used to investigate strength and fracture in adhesive joints.

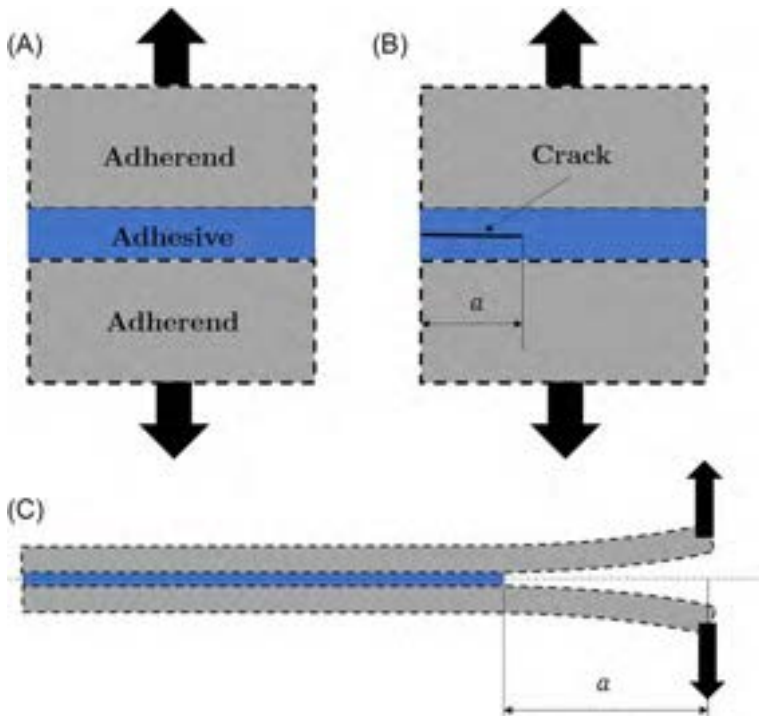


Fig. 18.1 Schematic representation of adhesively bonded specimens used to test the strength and toughness properties of joints. (A) The butt joint for testing strength; (B) the bonded single edge notch test (SENT) for testing fracture toughness; (C) the double cantilever beam (DCB) for testing fracture energy.

In the strength approach, such as using the butt joint in Fig. 18.1A, the focus is on evaluating the stress distribution and the stress level at which the bondline fails. The more general 3D stress analysis, for which limited closed-form solutions exist [19], can be reduced to the frequently used Volkersen and Goland and Reissner models developed for joints under shear loading [20, 21]. The details of such can be found in [22] as well as in Chapter 15 and will not be repeated here.

In the toughness approach, the interest lies in the measure of the energy levels at which the joints fail and the crack propagates. The fracture toughness, tested using single edge notch test specimens (SENT), as shown in Fig. 18.1B, is expressed in the units of stress per square root of length while the fracture energy, tested using the double cantilever beam (DCB) geometries, as shown in Fig. 18.1C is expressed in units of work per area.

These two toughness concepts, and the geometries proposed in Fig. 18.1A–C, will be used throughout this chapter to outline the importance of the energy flow through the adhesive joint. Looking to the extreme cases of both approaches, it is often the case that in the butt joint, the adherends can be assumed as perfectly rigid, thus not experiencing any deformations and not storing any energy, as shown in Fig. 18.1A and B. On the opposite extreme case, in the DCB-like specimens, as shown in Fig. 18.1C, the adhesive deformation is assumed negligible compared to the deformations experienced by the adherends.

Recall some of the small deformation continuum mechanics equations in which the stress tensor components σ_{ij} are defined as:

$$\sigma_{ij} = C_{ijkl}\epsilon_{kl} \quad (18.1)$$

where C_{ijkl} are the components of the stiffness matrix. For isotropic and elastic materials, the stiffness matrix components can be expressed through Young's modulus E and Poisson's ratio ν [23]. The associated strain tensor can be found from:

$$\epsilon_{ij} = \frac{1}{E^*} [\sigma_{ij} - \nu(\sigma_{kk}\delta_{ij} - \sigma_{ij})] \quad (18.2)$$

where $E^* = f(E, \nu)$ is material stiffness depending on, for example, the assumed stress state, and $\delta_{ij} = \begin{cases} 1 & \forall i = j \\ 0 & \forall i \neq j \end{cases}$ is the Kronecker's delta. Thus, under unidirectional applied stress, the strain field is not unidirectional and the so-called Poisson ratio effects can become visible once the adhesive thickness increases and the adhesive is characterized by a high Poisson's ratio. Such effects are important from both the strength and toughness perspectives, leading to rapid stress and strain gradients near the edge and the corner.

Consider butt joint testing using the specimen similar to the one shown in Fig. 18.1A in which the rigid adherends, $E \rightarrow \infty$, are joined with a relatively soft adhesive with modulus $E_a \ll E$, as illustrated in Fig. 18.2A. Experimentally, a force P or displacement Δ is applied to the adherends, leading to the stress inside the joint $\sigma_{zz} = \sigma_{zz}(x, y)$, that is, the load is perpendicular to the bondline, as shown in Fig. 18.2A \rightarrow B'. Thus:

$$\sigma_{zz} = -\nu(\sigma_{xx} + \sigma_{yy}). \quad (18.3)$$

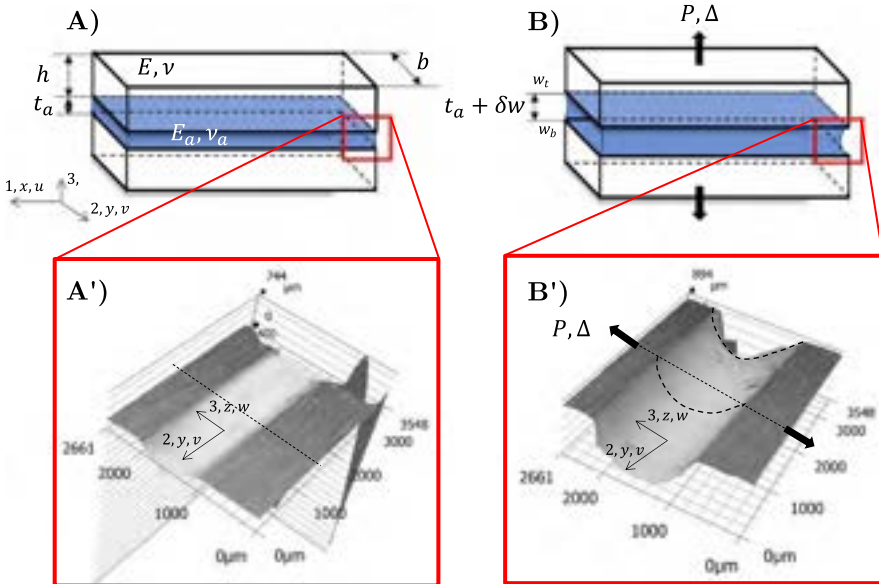


Fig. 18.2 (A) Schematic representation of the butt joint before the load is applied and (A') the corresponding picture of the edge and corner vicinity obtained using three-dimensional scanning microscopy. (B) and (B') The same specimen but after the remote tensile load is applied. (B') emphasizes the role of Poisson's ratio. In the experiment, the joint consisted of aluminum blocks bonded with methyl methacrylate (MMA) adhesive with $\nu_a = 0.45$.

This configuration, being only one of the versions of the butt joint, is usually regarded as a simple and convenient test to evaluate bondline strength. During the loading, the strain in the thickness direction is given by $\epsilon_{zz} = (w_t - w_b)/t_a$, where w_t and w_b are the displacements of the top and bottom adherends and t_a is the initial thickness of the adhesive; see Fig. 18.2. At the center of the adhesive layer, the σ_{ii} stress components are building up due to a nonzero Poisson's ratio, that is, Eq. (18.3). However, along, for example, the adhesive/adherend interface, assuming that the adherend material can be considered as nondeformable, the Poisson's ratio contraction is unconstrained, leading to visible bondline deformation, as shown in Fig. 18.2, A' \rightarrow B'.

Additional shear components, σ_{ij} with $i \neq j$, are thus present. Consequently, strains, and stresses, must be functions of position within the adhesive layer, including through the adhesive thickness direction. The distance and the associated load transfer over which the strains and stresses vary give through the thickness direction rise to the vivid studies of confinement and constraint effects [24, 25].

18.2.1 Energy approach and fracture mechanics

Fracture mechanics dates back to the work of Griffith, who used the energy approach to describe the failure of brittle, elastic solids [26]. Many of the initial works focused on applying Griffith balance to adhesive joint geometries [27–29]. Consider the total

elastic energy stored in the adhesive joint as U being the sum of energies stored in the adhesive U_a and the adherends U_b , i.e., $U = U_a + U_b$. For the butt joint geometry presented in Fig. 18.2 and a material system such that $E_a \ll E$, that is, the extreme case where the adherends can be considered as rigid, the total energy is given to the one stored in the elastic adhesive layer, U_a (as $U_b \approx 0$), and can be defined as:

$$U \equiv U_a = \frac{1}{2} \int_V \sigma_{ij} \epsilon_{ij} dv = \frac{1}{2} b t_a \int_l \sigma_{ij} \epsilon_{ij} dx \quad (18.4)$$

with v being adhesive layer volume, and l and b being the extension of the bonded region along the x and y directions, respectively. Acknowledging the limitations of the above approach, we observe that the stored energy is proportional to the adhesive thickness. Ignoring effects due to the kinetic energy, or the plastic zone dissipation, we define the elastic strain energy release rate (SERR or ERR for short):

$$\mathcal{G} = - \frac{dU}{dA} \quad (18.5)$$

where A is the surface area of the crack. For geometries with constant width b (such as those usually used for testing) where the crack propagated the distance a , $A = ba$. Notice that because we consider an elastic case and assuming laboratory loading conditions through controlled displacement, the stored energy balances out the work done by the external forces.

Consider now a fracture mechanics derivative of the butt joint—SENT specimen geometry depicted in Fig. 18.3A. Let us examine the material case studied previously, i.e., the adherend deformation is very small compared to the deformation of the bondline, $U \approx U_a$ under the remote stress field $\sigma_{ij} \epsilon_{ij} = \sigma \epsilon$, see Fig. 18.3B. Combining Eqs. (18.4) and (18.5) yields:

$$\mathcal{G} = \frac{1}{2} t_a \frac{d}{da} \left(\int_a^l \sigma \epsilon dx \right) \propto t_a \quad (18.6)$$

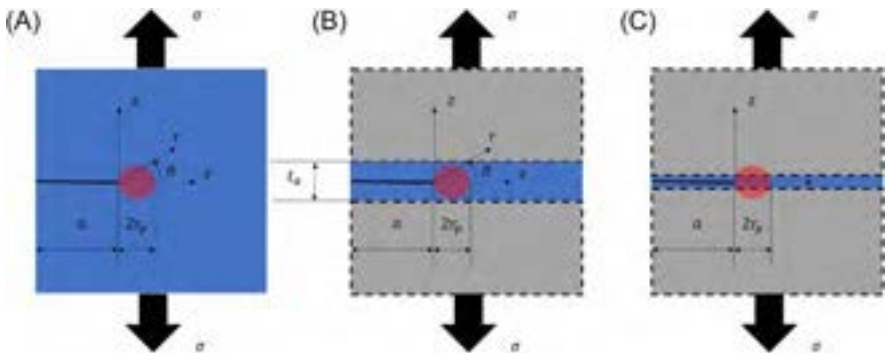


Fig. 18.3 A schematic representation of (A) a specimen with a side crack of length a , under remote loading σ —the SENT fracture specimen, (B) SENT with thick and (C) thin adhesive layer.

with l corresponding to the length of the adhesive layer. The result is equivalent to the one derived by Gent [30] for “soft” adhesives. The \mathcal{G} depends on the adhesive thickness and increases until fracture. In a generic manner, $\mathcal{G} = \mathcal{G}_c$ once the crack begins to propagate defining the Griffith’s fracture criterion. \mathcal{G}_c is called the fracture energy and for isotropic, homogeneous materials it is deemed as material constant under the assumption of equilibrium and a self-similar fracture process. While we can be encouraged by the simplicity of the solution, unfortunately adhesive joints are not homogeneous materials but structures, and thus, the presented theory needs further refinement.

18.2.2 Stress near the crack tip and emergence of material length scale

With the details behind fracture mechanics provided in Chapters 14 and 16, let us return to the SENT specimen and consider the testing of a homogeneous material, such as a bulk adhesive, under remote Mode I loading conditions; see Fig. 18.3A. Assuming the plane stress conditions at the crack tip for the sake of simplicity, the Mode I stress field is described as [31–33]:

$$\sigma_{zz} = \frac{K_I}{\sqrt{2\pi r}} \cos \frac{\theta}{2} \left(1 + \sin \frac{\theta}{2} \sin \frac{3\theta}{2} \right) + \dots \quad (18.7)$$

where r and θ are the distance from the crack tip and the angle measured from the expected crack growth plane, respectively. The K_I is called the Mode I stress intensity factor that at the crack onset, yields $K_I \equiv K_{Ic}$. K_{Ic} is defined as the fracture toughness and it is regarded as a material constant. The dropped higher order terms, indicated in Eq. (18.7) by the dots, become negligible as $r \rightarrow 0$ and practically as $r \leq 0.1a$. For $r \rightarrow 0$, the elastic solution tends to a nonphysical infinite stress denoting mathematical singularity. For large r , the solution ceases and the stress level converges to the Saint-Venant simplification.

The toughness, or resistance to crack growth, of a material is governed by the energy dissipated during the fracture process. For the perfect elastic-brittle materials, such as Griffith’s materials, like glass, this energy can be deduced from the rupturing energy of primary chemical bonds. This is not the case for structural adhesives where a large damage zone in front of the crack front is likely to develop; toughening strategies for adhesives are discussed in detail in Chapter 8. In this zone, a significant amount of energy will be dissipated, usually of orders of magnitude higher than the energy predicted by atomic bonding calculations.

Returning to the discussion of the SENT specimen fracture, we assume a physical limit to the stress due to a plastic limit, that is, $\sigma(r=0) = \sigma_y$ such that $\sigma = \sigma_y \forall r \leq r_p$ where r_p defines the region in which a material undergoes plastic deformation. Substituting σ_y and r_p into Eq. (18.7), after rearrangement:

$$2r_p = n \frac{K_{Ic}^2}{\sigma_y^2}. \quad (18.8)$$

Eq. (18.8) defines an intrinsic material property initially derived by Irwin [34] and an important material length scale. In addition, $K_{Ic}^2 = E^* \mathcal{G}_c$, thus, $\mathcal{G}_c \propto r_p$ —the fracture energy is a measure of the plastic radius, or the plastic radius is a measure of resistance to fracture. n , stated explicitly in Eq. (18.8), is a constant of order 1 that can be attributed to the current crack tip stress state. However, the existence of r_p holds important implications for adhesive joints.

Consider that the adhesive occupies a finite domain of thickness t_a with material properties (E_a, ν_a) significantly different than the surrounding (E, ν) and that $E_a \ll E$ and $\nu_a \geq \nu$, as in most practical cases. Taking t_a and r_p interactions, the following cases can be recognized: if $t_a > r_p$, both length scales can coexist without affecting each other, and for example increasing t_a does not increase r_p ; see Fig. 18.3B; once $t_a \leq 2r_p$, as shown in Fig. 18.3C the stress distribution in the crack tip region will be altered by t_a promoting the high level of stress triaxiality along the bonded plane [24, 25]. In the limit case of $t_a \approx 0$, the adhesive layer can be regarded as the crack growth plane, justifying an initial, aerospace-motivated approach to adhesive joint analysis. It is now well understood that the adhesive confinement affects the evaluated values of fracture parameters and this has been related with the altering of the development of the plastic zone [18, 35–37].

18.2.3 Edge and corner stress fields

The previously outlined analysis was not explicitly concerned by the fact that the stress and the strain vary in the vicinity of the interfaces between the two materials [14], that is, the edge and the corner effects. For SENT geometries, for example, such simplification is only justified if $t_a < a$ and $t_a > 2r_p$, but not otherwise. This disclosure is very important, as just after joint manufacturing $a \approx 0 < t_a$ is deemed. For DCB geometries, as depicted in Fig. 18.4, we can assume $t_a \ll a$ only if $t_a < r_p$. The bottom row of Fig. 18.4 shows the (tensorial) shear strain component ϵ_{xz} gathered for the three t_a cases (from the left): $t_a \ll 2r_p$; $t_a \approx 2r_p$, and; $t_a > 2r_p$ using digital image correlation (DIC) (see Chapter 32 for details about the DIC technique). Only color maps (the same shear strain range is used for all the cases) are given, limiting our discussion to the qualitative.

In this example, an elasto-plastic adhesive has been used to bond two aluminum adherends. Significant differences between the three cases are recorded. For $t_a \ll 2r_p$, as shown in Fig. 18.4A, the shear stresses are forming the so-called shear bands inside the adherends. A single stress field can be associated with the crack tip. The energy is then stored mainly in the adherends, and the bondline can be effectively seen as a crack growth plane. For the $t_a \approx 2r_p$, as shown in Fig. 18.4B, the intensity of the shear band inside the adherends decreases, the marking the fact that more of the deformation occurs within the adhesive layer. However, with similar resolution of the DIC results as in the previous case and contrary to a single crack tip field, the strain localizes near the corners. The energy is thus distributed between the adhesive and the adherends. Finally, for the $t_a > 2r_p$, as shown in Fig. 18.4C, the adherends do not experience significant deformation compared to the adhesive. The adhesive corners and, at

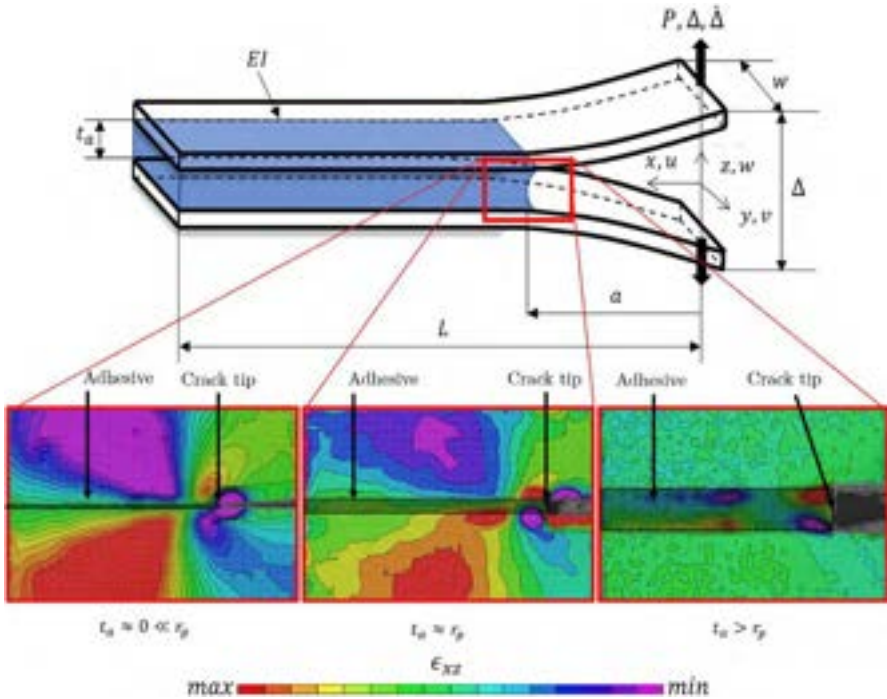


Fig. 18.4 Comparison of ϵ_{xz} shear strain field near the crack front for the joints with different adhesive thicknesses. *Top row*: Schematic representation of DCB specimen used for testing. *Bottom row*: The results obtained with the two-dimensional DIC, for the three adhesive thickness cases (from left): $t_a = 0.5 \text{ mm} \ll 2r_p$; $t_a = 2.5 \text{ mm} \approx 2r_p$, and; $t_a = 10 \text{ mm} > 2r_p$.

some distance away, the adhesive/adherend interface are localizing the strains. As depicted in Fig. 18.4, and recognized in [36], two main mechanisms of plastic dissipation in adhesive joints exist: dissipation at the crack tip inside the r_p , and shear near corners and edges. Using the same adhesive material in the same geometrical configuration of the adherends under the same loading conditions, the failure localization and failure load can be regarded as controlled by the adhesive thickness. The corners and the edges are often crack onset locations and are likely to become growth paths, as will be further shown in this chapter by experimental results. The stress intensity factor and the crack tip stresses need to be quantitatively linked with the adherends, or specifically with the adhesive/adherend properties mismatch. Mathematically, the resulting stresses have a complex form, and, for Mode I loading, the real part reads as:

$$\sigma = \mathcal{R}(K r_\epsilon^{-1/2+i\epsilon}) \quad (18.9)$$

where $\epsilon = \frac{1}{2\pi} \ln\left(\frac{1-\beta}{1+\beta}\right)$ is the bi-material exponent [16] dependent on the Dundurs parameter β [15]. For completeness, both Dundurs parameters are defined as [38]:

$$\alpha = \frac{(1 - \nu_2)/\mu_2 - (1 - \nu_1)/\mu_1}{(1 - \nu_2)/\mu_2 + (1 - \nu_1)/\mu_1}, \quad (18.10)$$

$$\beta = \frac{1}{2} \frac{\mu_1(1 - 2\nu_2) - \mu_2(1 - 2\nu_1)}{\mu_1(1 - \nu_2) + \mu_2(1 - \nu_1)}, \quad (18.11)$$

with $\mu_i = \frac{E_i^*}{2(1 + \nu_i)}$, and $E_i^* = \begin{cases} E \text{ plane stress} \\ \frac{E}{1 - \nu_i^2} \text{ plane strain} \end{cases}$ [17].

Contrary to the homogeneous case, a pair of bi-material constants α and β is introduced linking the respective ν_i and E_i^* . As the contrast between the joined materials increases, the stress gradient near their edge and corner increases. Once the mismatch vanishes, the homogeneous material solution, as shown in Eq. (18.7) is recovered. The results, such as in [16], indicate that the failure load decreases upon increasing the bondline thickness even above the $t_a \gg 2r_p$. To complete discussion, we acknowledge that the corner, or 3D singularity, is “stronger” than the edge, two-dimensional (2D), ones [39]. Fig. 18.5A and B schematize the emerging corner stress field.

The situation depicted arises if t_a is large enough so that the stress fields, distributed over r_e , as shown in Eq. (18.9) from each corner, do not interact. As in the case of crack tip singularity and r_p , as $t_a \rightarrow 0$, the corner stresses are constrained between the adherend material. Under such circumstances, the crack will likely initiate in the middle of the adhesive layer. The situation becomes more complex once both r_p and r_e coexist [40].

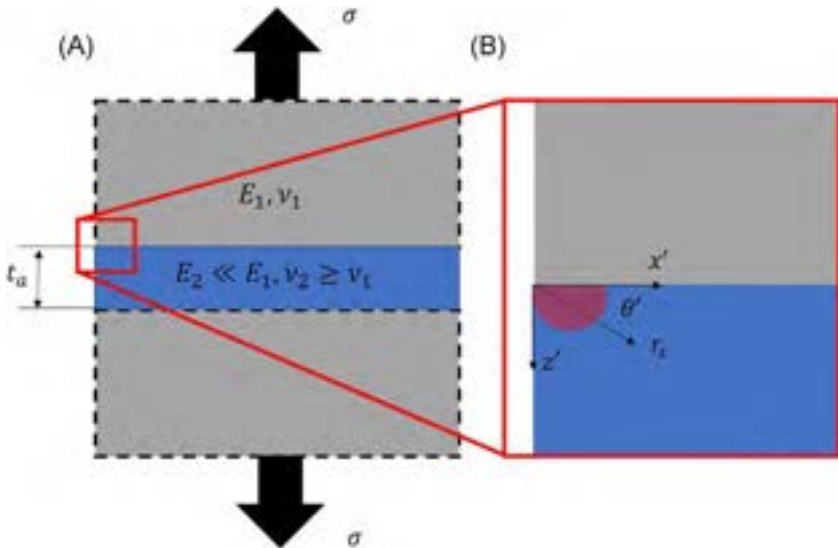


Fig. 18.5 Schematic representation of Mode I stress field near the bi-material corner.

(A) The butt joint under remote tensile loading σ . (B) Close-up on the corner region where a local stress field emerges.

18.3 Adhesive thickness analysis using double cantilever beam (DCB) configuration

18.3.1 The adhesive/adherend energy flow

In the following sections, the effect of adhesive thickness on effective fracture properties obtained from DCB testing will be discussed. With the geometry defined in Fig. 18.4, following the simple beam theory [41], the compliance C is expressed as:

$$C \equiv \frac{\Delta}{P} = \frac{2a^3}{3EI}. \quad (18.12)$$

where the adherend is characterized via the beam bending rigidity $EI = E \frac{bh^3}{12}$. No explicit term for the adhesive layer is provided with the assumption that only the adherend is deforming and, thus, storing energy, implying $a \gg t_a$ and $t_a < r_p \approx 0$. The total elastic energy becomes $U = U_b = \frac{1}{2}P\Delta = \frac{1}{2}P^2C$ and marks the second extreme case for which the adhesive deformation is ignored. Substituting U_b into Eq. (18.5) we obtain:

$$\mathcal{G} = \frac{1}{2} \frac{P^2}{b} \frac{\partial C}{\partial a} \quad (18.13)$$

expressing the essence of the compliance method for calculating \mathcal{G} and with Eq. (18.12) yielding:

$$\mathcal{G} = \frac{1}{2} \frac{P^2}{b} \frac{a^2}{EI}. \quad (18.14)$$

Substituting for rectangular cross section bonded adherends, $I = bh^3/12$:

$$\mathcal{G} = 12 \frac{P^2 a^2}{Eb^2 h^3}. \quad (18.15)$$

The adhesive layer contribution is not included, but this should not imply it is not affecting the results; the adhesive layer plays a role in stress and energy flow.

Assuming equilibrium crack growth conditions, $\mathcal{G} = \mathcal{G}_c = const.$, the amount of energy released from both the adherend and the adhesive should be constant, thus:

$$-\frac{dU_b}{bda} + \frac{1}{2}t_a \frac{d}{da} \left(\int_a^l \sigma_a \epsilon_a dx \right) = \mathcal{G}. \quad (18.16)$$

For the beam problem investigated, the second term on the left side needs to be evaluated from the spatially varying stresses and strains within the adhesive layer, that is, $\sigma_a \wedge \epsilon_a = f(x)$. This is rarely performed. One of the well established frameworks mitigating such evaluation is called the effective crack length approach [42, 43]. In this approach, the integral term, related to the adhesive layer, becomes part of a lumped

parameter a_e , and expressing the effective crack length that differs from the actual, observed, or apparent one, a . In specific, $a_e > a$ due to the finite stiffness of the adhesive layer not captured by Eq. (18.15). Taking an adhesive of stiffness E_a , increasing t_a leads to bigger a_e . Such a value is then used in Eq. (18.15) instead of a . Not following such a procedure leads often to significant misinterpretations. Eq. (18.16) is however aimed at expressing an important concept and paradigm. Considering stress and fracture analyses, it is important to recognize where the energy is stored, either in the adhesive, as in Eq. (18.4), or the adherend, as in Eq. (18.14), or a combination of the two, as in Eq. (18.16). We usually follow only one of the two extreme paths. Some analyses assume the adhesive layer to be sufficiently thin, such as simple beam theory for DCB (Eq. 18.14), while others assume just the opposite, for example, soft adhesives with rigid adherends for which all the energy is stored in the adhesive and this drives the fracture; Eq. (18.6). While these approaches can be very appropriate in very specific situations, the adhesive thickness is one of the geometrical length scales that easily converts one into another. One of the models enabling treatment of both cases is based on the assumption that the bondline can be represented as a continuous series of springs, resulting in the beam on elastic foundation formulation.

18.3.2 Interpretation using elastic foundation models

The popularization of laminated composite materials required improved representation of interfaces, for example through the so-called elastic foundation models [44]. The foundation, or the interface/bondline as in our case, is represented by the distributed springs. Such an idea have been implemented successfully to many problems related to composites and adhesive bonding to predict stresses in the vicinity of the crack front [21, 45–48]. The well-recognized model is due to Kanninen [49]. Originally devised within the context of crack onset and arrest in laminated composite material, it proposes the governing beam problem to be formulated as:

$$\frac{d^4 w}{dx^4} + 4\lambda^4 H(x)w = 0 \quad (18.17)$$

where $w(x)$ is the searched solution of the beam deflection, $H(x)$ is the Heaviside step function valued as:

$$H(x) = \begin{cases} 0 & \forall x < a \\ 1 & \forall x \geq a \end{cases} \quad (18.18)$$

and $\lambda = \lambda_{MK}$ is found from:

$$\lambda_{MK}^4 = \frac{k_{MK}}{4EI} \quad (18.19)$$

This is obtained from the characteristic root of the governing equation, Eq. (18.17), with the physical interpretation of the wave number. The inverse of λ is denoting the length of the region over which significant tensile stresses, are distributed.

Usually, this region is much longer than the validity of the local, asymptotic analysis, given by Eq. (18.7). If laminated material is considered, the thickness of the interface is assumed to be 0, and the constant k , i.e., the effective stiffness of the interface, can be associated with the (finite) transverse stiffness of the beam material. For instance, for the case of a beam made of isotropic material with a rectangular cross section of width b and thickness h , $k = \frac{2Eb}{h}$ under the assumption that the stresses can develop within the half of the beam thickness:

$$\lambda_{MK} = \frac{\sqrt{6}}{h}. \quad (18.20)$$

We should not disregard this solution. Even if $t_a \approx 0$, but adherends such as composite or wood (in general, materials with transverse properties similar to the one of the bondline material) are bonded, the Kanninen model can be used successfully. To the first approximation, the stress inside the bonded region can be evaluated from:

$$\sigma_{zz}(x) = E\epsilon_{zz} = \frac{k_{MK}}{b} w(x) = \frac{E}{2} \frac{w(x)}{h} \propto Ee^{-\lambda x}. \quad (18.21)$$

This analysis considerably affected the field of adhesion and bonding, and the approach has ever since been followed, expanded, and recently reviewed [48]. For adhesive bonding, in most cases the effective adhesive layer stiffness is significantly lower than that of the adherend, owing either to the increased thickness or much lower modulus of elasticity. Thus, representation of the adhesive layer as the elastic foundation while ignoring transverse adherend stiffness can be found in [17, 21, 46] to list only a few positions. We follow the analysis provided in [17] where the effective foundation stiffness is approximated by $k_{SK} = \frac{E'_a}{t_a}$ with E'_a . Accounting for the plane strain conditions in the adhesive layer, that is, $E'_a = E_a(1 - \mu_a^2)$, from Eq. (18.17) with $\lambda \Rightarrow \lambda_{SK}$:

$$\lambda_{SK}^4 = \frac{6}{t_a h^3} \frac{E'_a}{E}. \quad (18.22)$$

The adhesive thickness is explicitly introduced and controls the region of nonzero beam curvature (i.e., link to the effective crack length approach) and, equivalently, the stress distribution within the adhesive layer, namely λ_{SK}^{-1} . Carrying out the ERR derivation, Eq. (18.5) yields:

$$\mathcal{G} = \frac{1}{2} \frac{(Pa)^2}{bEI} \left(1 + \frac{1}{\lambda_{SK} a} \right)^2 \quad (18.23)$$

We notice that contrary to the monomial form of Eq. (18.15), a polynomial form of a more general Eq. (18.16) is restored. In specific, the second term on the right side is linked with the integral, i.e., the adhesive, term of Eq. (18.16), while the first term with

the beam bending, dU_b/da . Indeed, setting $\lambda_{SK}a \gg 1$ in the denominator of Eq. (18.23), the second term approaches 0 and the entire bracket approaches unity. Eq. (18.14) can then be seen as an asymptotic solution for $U \rightarrow U_b$ and any nonzero adhesive thickness and stiffness will lead to misinterpretations if the limit, beam analysis, is used.

18.4 Effect of adhesive thickness on failure modes and fracture properties

18.4.1 Case study from thin to thick

The case study hereby presented focuses on the adhesive bondline thickness effect on Mode I fracture behavior of steel-to-steel bonded joints. A structural epoxy adhesive with bondline thicknesses from 0.4 to 10 mm is investigated using the DCB test. The case study becomes relevant for the application of structural adhesive bonding in maritime and civil engineering structures. The manufacturing tolerance in such structures can lead to “extra” thick bondlines in the order of centimeter scale. In this section the main findings of this case study are described. The detailed experimental procedure can be found in [50]. The adhesive used was a bi-component epoxy paste Araldite 2015 (Huntsman). First the influence of the adhesive thickness on the failure modes, fracture toughness values, and stress field ahead of the crack tip are shown. These results are then used to discuss and justify the trend of the fracture toughness. Finally, a few considerations are given regarding the strain rate dependency with the adhesive thickness.

18.4.1.1 Failure modes

Fig. 18.6 gives an overview of the crack path for representative specimens of 0.4, 1.1, 4.1, and 10.1 mm. Firstly, it can be observed that the crack path did not follow the mid-plane of the adhesive layer. This alternating crack path, recognized in the prior literature, such as [51, 52], is more pronounced with the increasing thickness, with the

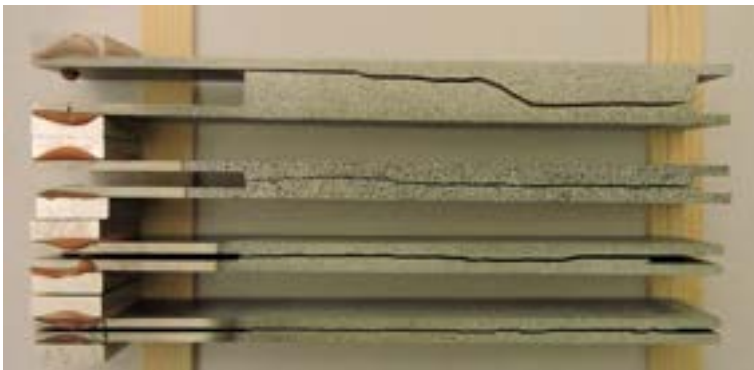


Fig. 18.6 Typical failure modes of each bondline thickness (from bottom to top: 0.4, 1.1, 4.1, 10.1 mm).

extreme case being the 10.1 mm thick adhesive layer where the crack path deflected from one interface to the other. Despite the alternating crack path, the failure was consistently cohesive owing to robust surface treatment procedure, i.e., no interface failure was observed. A more quantitative representation of the crack path profile for different positions along the specimen width (y) is shown in Fig. 18.7. For each adhesive thickness, one representative specimen is presented.

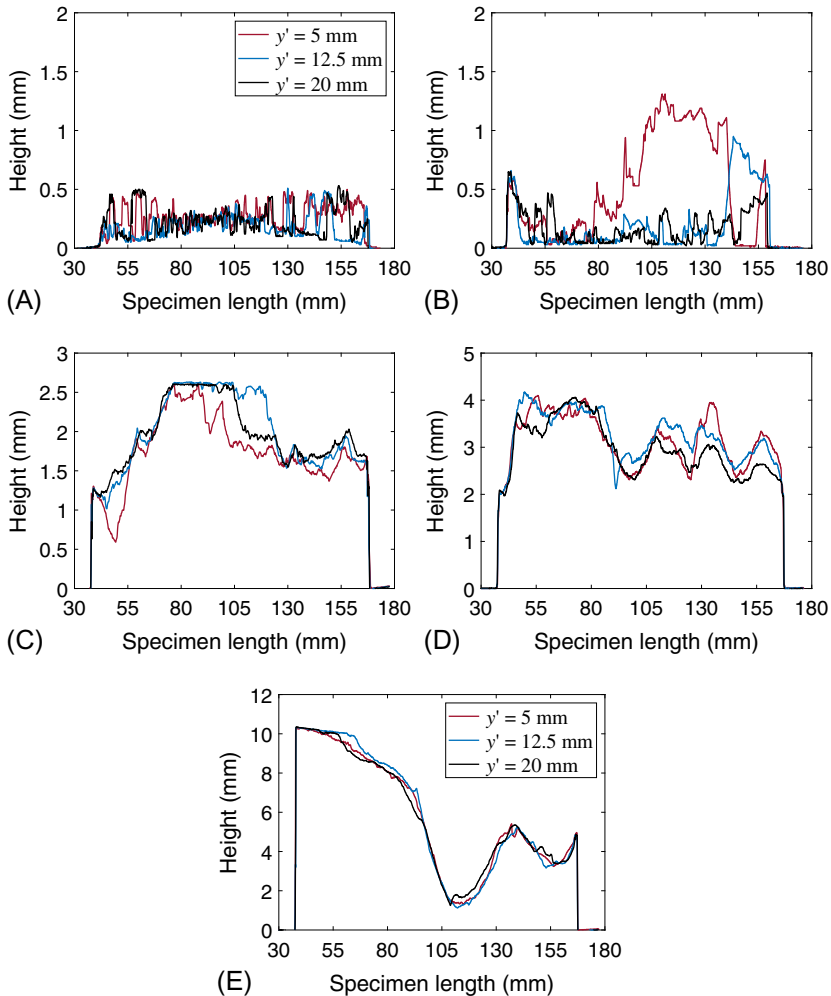


Fig. 18.7 Height profile (0 is position of the interface) of the remaining adhesive layer on the failure surface in respect to the reference adherend surfaces along the specimen's length direction of the representative specimens: (A) Bondline thickness ($t_a = 2t$) of 0.4 mm; (B) $t_a = 2t = 1.1$ mm; (C) $t_a = 2t = 2.6$ mm; (D) $t_a = 2t = 4.1$ mm; (E) $t_a = 2t = 10.1$ mm. The height profile is plotted at $y' = 5, 12.5$ and 20 mm, where y' is the coordinate in the specimen width direction [50]. Notice, that the adhesive thicknesses deviations along the specimen length justify the few cases where the height profile is higher than the average adhesive thickness.

18.4.1.2 Fracture energy

Fig. 18.8 gathers the fracture energy values as a function of the adhesive thickness. The fracture energy was determined using the elastic foundation models described earlier, as in Eq. (18.23), considering 3D plane strain.

18.4.1.3 Stress fields ahead of the crack tip

Besides the values for fracture energy in Fig. 18.8 the predicted deformation zone ahead of the crack tip of each bondline thickness is also plotted as $2r_p + \lambda_{j-\text{exp}}^{-1}$ where $j = 0.4, 1.1, 2.6, 4.1, 10.1$ mm and $\lambda_{j-\text{exp}}^{-1}$ corresponds to the value of the experimental λ^{-1} of thickness of j mm, that is, the length of the elastic process zone; see Eq. (18.22). The value $2r_p$ corresponds to the plastic process zone length; see Eq. (18.8). For the given case, this value is equal to 1.08 mm, assuming the plane strain conditions. The energy dissipation mainly occurs in the plastic deformation zone. However, the elastic process length also affects the recorded externally applied displacement. The experimental elastic fracture process length, $\lambda_{j-\text{exp}}^{-1}$ was determined using experimental data, load, and crack length, and was defined as the distance over which the positive peel stress is distributed up to the yield strength of the bulk adhesive. Fig. 18.9 shows the peel stress ahead of the crack tip derived using Eq. (18.21).

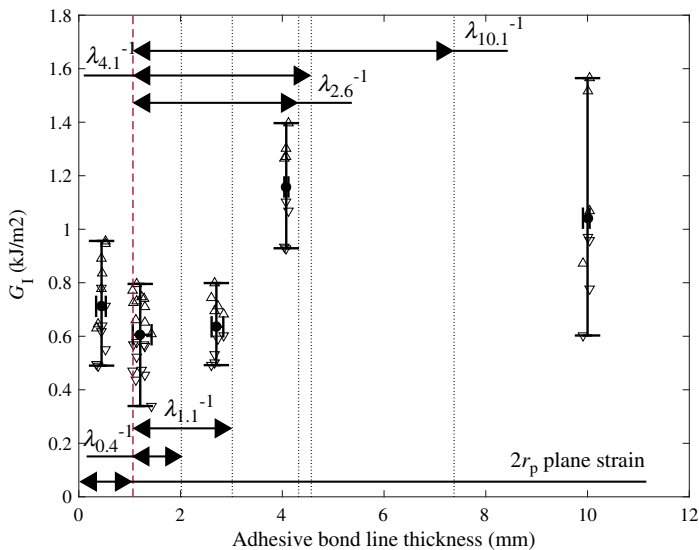


Fig. 18.8 Mode I fracture energy as a function of adhesive thickness. Two error bars are also plotted, giving the range of scatter on the thickness and G_I . The red dashed line gives the limit of $2r_p$ considering plane strain conditions. The black dashed lines give the limit of $2r_p + \lambda_{j-\text{exp}}^{-1}$, where $j = 0.4, 1.1, 2.6, 4.1, 10.1$ mm, and the $\lambda_{j-\text{exp}}^{-1}$ is the length of the elastic tensile stress region ahead of the crack tip estimated experimentally [50].

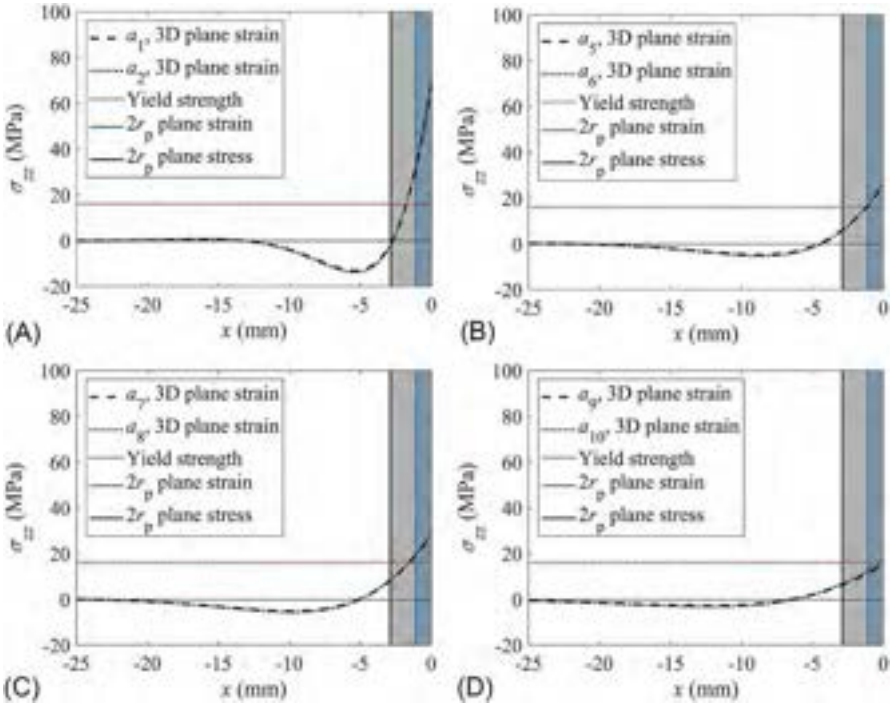


Fig. 18.9 Peel stresses ahead of the crack tip (located at $x = 0$). Two arbitrary points in the propagation region were selected for each representative specimen: crack length and load a_i, P_i respectively [50]. (A) $t_a = 2t = 0.4$ mm: σ_{zz} ; (B) $t_a = 2t = 2.6$ mm: σ_{zz} ; (C) $t_a = 2t = 4.1$ mm: σ_{zz} ; (D) $t_a = 2t = 10.1$ mm: σ_{zz} .

18.4.1.4 Explaining fracture energy trend

Fig. 18.10 shows a schematic illustration of Mode I fracture energy as a function of adhesive thickness as stated by Kinloch and Shaw [5]. If applied to the case study hereby presented, the highest Mode I fracture toughness would be expected in the specimens with 1.1 mm adhesive thickness because $2t \approx 2r_p$ ($2r_p = 1.08$ mm), and decrease from 1.1 to 0.4 mm and from 1.1 to 10.1 mm. Although this is not the case for the bondline investigated in this case study, because 4.1 mm adhesive thickness results in the highest toughness as shown in Fig. 18.8, the theory can still support the overall trend while the stress fields ahead of the crack tip previously presented give interesting insights in to the deformation zone ahead of the crack tip.

In the specimens with thin bondlines of 0.4 mm, the effect of the adherend constraint is more pronounced, leading to higher confinement of the crack tip and higher local peel stresses. This is clearly shown in Fig. 18.9A with the highest peel stresses ahead of the crack tip in comparison with the remaining adhesive thicknesses and the expansion of the plastic deformation zone length higher than $2r_p$ (plane strain conditions), resulting in a more elongated deformation zone with an elliptical shape, as reported by Kinloch and Shaw [5].

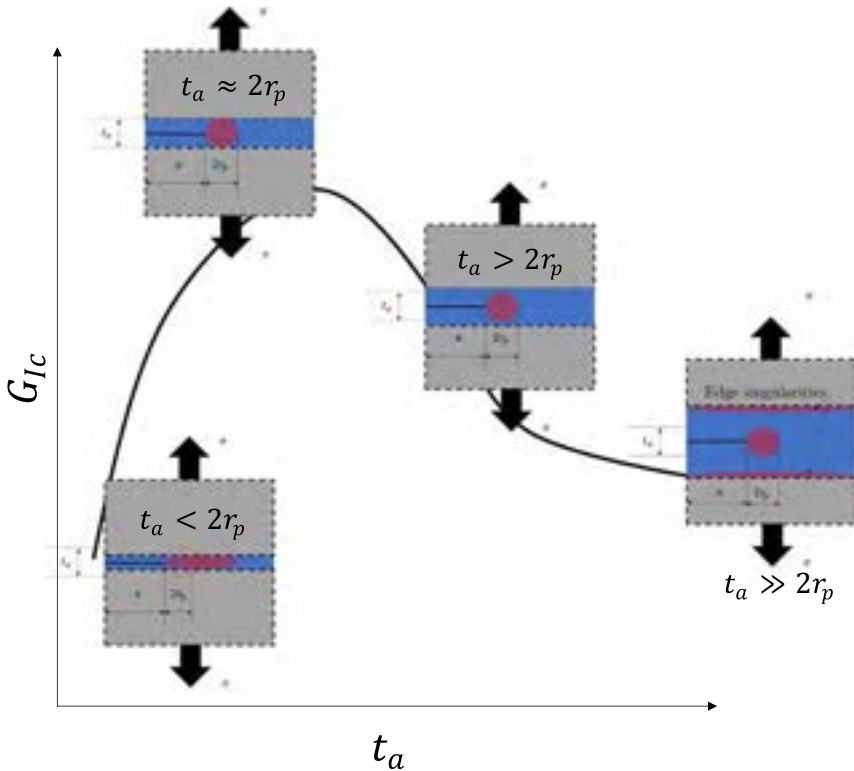


Fig. 18.10 Schematic illustration of Mode I fracture toughness as a function of adhesive thickness.

Adopted from A.J. Kinloch, S.J. Shaw, The fracture resistance of a toughened epoxy adhesive, *J. Adhes.* 12 (1) (1981) 59–77.

By increasing the bondline thickness to 2.6 mm, the adherend constraint gets smaller. This is seen in Fig. 18.9B in which the plastic deformation zone length decreases in comparison with 0.4 mm and it seems to converge to $2r_p$ (plane strain). In the range of bondline thicknesses of 0.4 to 2.6 mm, an increase on the average value of G_{Ic} as the physical constraint becomes less pronounced for thicker bondlines and, naturally, the deformation zone becomes larger in volume. However, the experimental results show a different trend. Similar average G_I values are obtained in the range of a 0.4–2.6 mm thick adhesive layer. It is important to note that the failure surfaces and crack paths present some differences. In the thinnest specimens, the surfaces displayed several densely packed peaks (Fig. 18.7A) characteristic for high stress triaxiality. For the thicker specimens of bondlines of 1.1 and 2.6 mm, the failure surfaces appear smoother and the changes on the crack path plane location might have prevented the full development of the deformation zone, leading in the end to similar results of G_I . Despite the fact that λ_{exp}^{-1} increases with the bondline thickness as shown is Fig. 18.8, this seems not to affect the average value of G_I in the bondline thicknesses

range of 0.4–2.6 mm, which shows that energy dissipation mainly occurred in the plastic deformation zone.

In the specimens with a bondline of 4.1 mm, the adherend constraining effect should get even lower and the deformation zone should be fully developed, leading to higher energy dissipation before crack propagation, and consequently, higher G_I values. There was indeed an increase of approximately 84% in the average value of G_I from a bondline of 2.6 mm to a bondline of 4.1 mm, resulting in the joint with highest toughness. According to Kinloch and Shaw [5], the plastic deformation zone for this bondline thickness should have a height equal to $2r_p$ and a length longer than $2r_p$. The results in Fig. 18.9C agree with this theory regarding the increase in the length of the deformation zone. However, it should be noted that these predictions of the peel stresses assume perfectly cohesive crack propagation (i.e., at the midthickness of the bondline), which is not representative of the real crack path profile of the 4.1 mm thick adhesive bond line specimens (see Fig. 18.7D). In fact, the change on the crack plane must have affected the shape, size, and direction of the deformation zone, namely in the regions where the crack propagated close to one of the interfaces. Consequently, the real deformation zone length might be different from the estimated. Nevertheless, it seems that the deformation zone could develop more in the specimens with a bondline thickness of 4.1 mm than in the ones with a 2.6 mm thick adhesive bondline, as shown by the higher average G_I value obtained.

Finally, in the specimens with a bondline of 10.1 mm, the crack grew alternating between the two interfaces (but always within the adhesive layer as observed by the naked eye and confirmed by attenuated total reflectance Fourier transform infrared (ATR-FTIR) spectroscopy surface analysis [53]). Such bondlines, following Eq. (18.21) and Fig. 18.9, experience the lowest peel stresses; however, as shown in Fig. 18.4, they are the most likely to localize shear stresses near corners and edges. Consequently, the crack onset and the propagation are occurring most likely under mixed-mode conditions, breaking the symmetry conditions of the DCB configuration. As a consequence of the crack path location, the deformation zone was physically constrained just in one side, which might have reduced its size, and, subsequently, the Mode I fracture toughness. The estimation of $\lambda_{\text{exp}}^{-1}$ and the plastic deformation zone from Fig. 18.9D might not be representative of the experiment due to the crack plane location.

The research done in the past has proved that there is a dependence of the fracture energy of adhesive joints on bonding thickness, regardless of the nature of the adhesives. In the present case study, the average Mode I fracture toughness, $G_{I \text{ av.}}$, presented similar values for the specimens with adhesive bondline thicknesses in the range of 0.4–2.6 mm, and it increased by approximately 63% for the joints of a 4.1 mm thick bondline. A further increase in the thickness of the adhesive layer led to a decrease of about 10% in $G_{I \text{ av.}}$ (in comparison with the 4.1 mm thick bond layer). These results show that the increase in bond thickness does not always lead to an increase in the critical fracture energy. This is consistent with the outlined theoretical framework. The trend of these results can be attributed to: (a) the crack path, which influences the stress field ahead of the crack tip and, consequently, the size of the deformation zone, and (b) the differences in the fracture surfaces' topography.

18.4.1.5 Strain rate dependency

While testing adhesive joints of different thicknesses, a common approach is to use a similar rate of applied displacement. Bearing in mind that the adhesives are polymers usually prone to time-dependent phenomena, maintaining the rate of loading while testing different adhesive thicknesses can result in misinterpretation. It is important to note the relationship between the strain rate and the adhesive thickness. Recalling the case depicted in Fig. 18.3B, undeformable adherends bonded with a relatively soft adhesive of thickness t_a . The strain in the thickness direction z experienced by the adhesive is given by:

$$\epsilon_{zz} = \frac{w(x)}{t_a} = \frac{w_t - w_b}{t_a}. \quad (18.24)$$

(Recall that w_t and w_b are displacements of the top and bottom adherends—see Fig. 18.2) Differentiating this formula with respect to time, the strain rate is given by:

$$\dot{\epsilon}_{zz} = \frac{\dot{w}(x)}{t_a} \quad (18.25)$$

This shows that as the adhesive thickness t_a increases, the strain rate decreases in the exact same proportions, which bears severe consequences [54]. The simple linear relation is, however, not always the case. For instance, for DCB testing, the rate of crack growth and strain rate at the crack tip are a function of crack position and changes during testing, that is, the rates are slower at the end of the test than in the beginning [55]. Significant research has been done on strain rate dependence of the Mode I fracture energy. However, the literature is not unanimous on their relation. Blackman et al. [56, 57] have reported a decrease in fracture toughness under Mode I loading G_{Ic} with increased strain rate, but the majority of researchers report the opposite, an increase of fracture toughness with the increase in strain rate [58–61]. A phenomenological model, [62] based on the fracture process zone size dependence on time, indicates that for shorter times, and thus, higher strain rates, the process zone converges toward elastic solution. For longer times and lower rates, the process zone can easily grow without an actual growth of the crack. Thus, if one uses the apparent crack length approach (crack position observed from the side with a camera), the extension of the process zone will lead to higher deformations and recorded displacements while keeping the crack length constant at a given force, thus overestimating the fracture energy. On the contrary, by using the effective crack length approach, the extension of the process zone will be interpreted as an extension of a_e that is counteracting the increased displacements. For the DCB case study here presented, the strain rate decreases as the adhesive thickness increases. Taking into account the results from the majority of the literatures, this could imply that the decrease in the fracture toughness from 1.1 to 2.6 mm and from 4.1 to 10.1 mm could be partly due to the difference in the strain rates. Nevertheless, all the cited literature varied the strain rate by varying the displacement crosshead rate of the tests while the adhesive thickness was kept constant. In the case study here presented, the strain rate varied by varying the adhesive thickness while the displacement crosshead rate of the test was kept constant. Further studies are needed to prove whether the similitude between these two holds.

18.4.2 Crack initiation competition in thick bonded joints

With a bondline thickness on the centimeter scale, one feature to be recognized is the stress gradient that arises at the bi-material adhesive-adherend edges and corners [15, 16, 38, 63]. The differences in material properties and geometry singularities at these locations result in opening stresses, as shown in Eq. (18.9), that can trigger fracture onset. Interestingly, this feature can be used as a fracture trigger to increase the fracture toughness of the bonded joint. The control over the number and the location of the

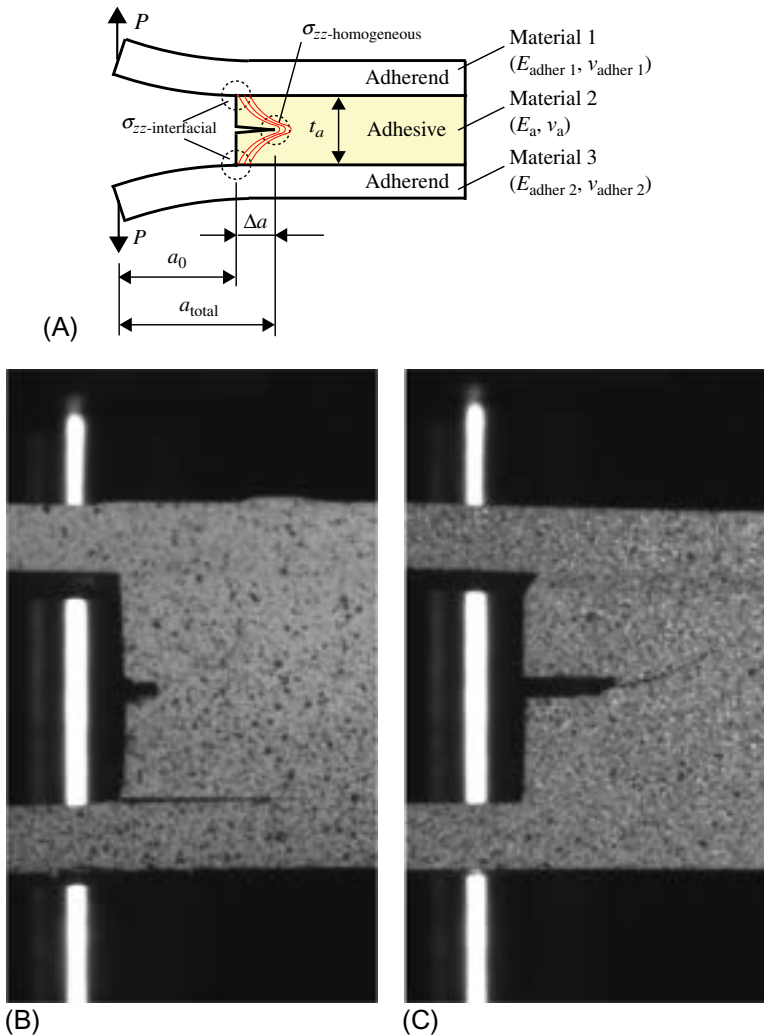


Fig. 18.11 (A) Fracture scenario in study: influence of Δa length on fracture onset in adhesive joint with finite thickness adherends under global Mode I loading; (B) Fracture onset close to the interface; (C) Fracture onset at the precrack [40].

plastic zones resulting from fracture onset in elasto-plastic adhesives can be of high benefit to increase and tailor the resistance to fracture and overall performance of the joint.

In this section, the relation between fracture initiation at the corner and bi-material singularities and the fracture initiation at the midthickness adhesive is studied. Fig. 18.11A represents the fracture scenario at hand. The case study here investigated considers an adhesive of thickness $t_a = 2t \approx 10$ mm. A precrack of length Δa is cut at midthickness of the adhesive bondline. Steel and glass fibre reinforced polymer (GFRP) were used as adherends. DCB bonded joints made of single adherend material (steel-steel and GFRP-GFRP) and bi-material (steel-GFRP) adherends bonded with a structural epoxy adhesive were tested. Details of the manufacturing and experimental setup can be found in [40].

Fig. 18.11B and C shows examples of the two possible fracture onsets encountered. The fracture competition between the corner singularities and the precrack can be described as the fracture onset will occur at the precrack tip if Δa is sufficiently large to create a singular stress field around the precrack tip, in which the threshold stress is reached prior than at the bi-material edges and corners. In the subsequent sections the roles of the adherend-adhesive modulus mismatch and the precrack length in this crack onset competition are demonstrated.

18.4.2.1 Role of adherend-adhesive modulus mismatch

At the adherend-adhesive edge, stresses arise due to material mismatch the values of which are dependent upon the material and geometrical properties. This dependency can be quantified using the Dundurs [15] parameters α and β , previously presented by Eqs. (18.10) and (18.11), respectively ($1 =$ adherend and $2 =$ adhesive). The parameter α can be interpreted as a measure of the stiffness dissimilarity between the two materials: for $\alpha > 0$, the adherend material is rigid relative to the adhesive. The parameter β is related to the oscillatory crack path near the crack onset. Table 18.1 lists both parameters for the case study at hand for the steel-epoxy as well as for the GFRP-epoxy interface.

Both Dundurs parameters are higher for the steel-epoxy interface, which means that, in the case of fracture onset close to the interface at bi-material bonded joints, the fracture location is more likely to occur at the steel-epoxy interface, the one with the highest adherend-adhesive modulus mismatch. Experimental and numerical evidence of this fact is confirmed in [53] and [40], respectively. Fig. 18.12 shows the

Table 18.1 Dundurs parameters for different material combinations under plane strain conditions [40].

Adherend/ adhesive	G_{adher} (GPa)	G_a (GPa)	ν_{adher} (-)	ν_a (-)	α (-)	β (-)
Steel/epoxy	80769	752	0.300	0.33	0.98	0.25
GFRP/epoxy	3897	752	0.252	0.33	0.65	0.15

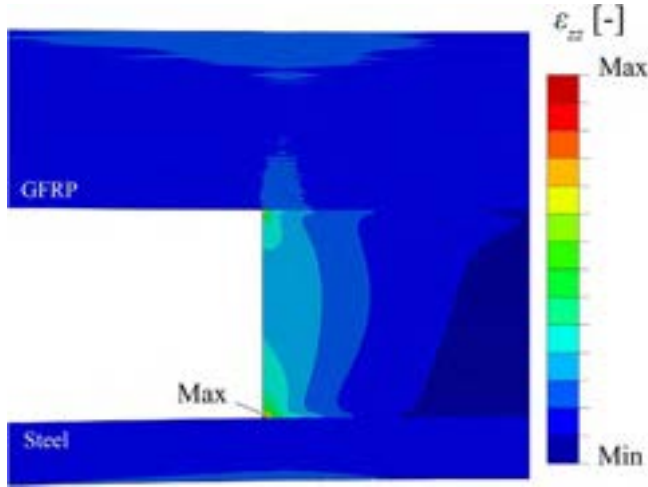


Fig. 18.12 Evolution of strain field, ε_{zz} for bi-material bonded joint GFRP-steel. No precrack is modeled, $\Delta a = 0$ mm.

Adapted from R.L. Fernandes, M.K. Budzik, R. Benedictus, S. Teixeira de Freitas, Multimaterial adhesive joints with thick bond-lines: crack onset and crack deflection, *Compos. Struct.* 266 (2021) 113687.

numerical evidence. The strain distribution is not symmetric and the highest strain values are found close to the steel-epoxy interface.

18.4.2.2 Role of precrack length

In this section, the role of $\Delta a \neq 0$ mm in the fracture onset locus of thick bi-material bonded joints is analyzed.

Up to a certain bondline thickness, the fracture onset is dominated by a singular stress field around the existing precrack tip in the adhesive. However, for thicker bondlines, geometric and material discontinuities, such as corners and adherend-adhesive interfaces create local stresses where the failure might occur first; see [Figs. 18.5](#) and [18.11B](#). To avoid this fracture onset locus to fully explore the cohesive properties of the adhesive, a certain critical precrack length Δa_{crit} must be fulfilled such that the threshold stress is attained first at the precrack tip rather than at corners. The criterion to define Δa_{crit} follows the Griffith's diffusion line approach, which proposes that for a crack in a homogeneous material of well-defined length a , a region of material adjacent to the free surfaces is unloaded [64]. Applying this concept to adhesive joints translates into Δa being sufficiently long such that the corners near the interfaces are unloaded, as shown in [Fig. 18.11A](#) by the red diffusion lines.

According to [65], in an infinite plate with a crack, the unloaded region is approximated by a triangle with the base length corresponding to Δa and a height of $2\pi\Delta a$. For the case study here presented in [Fig. 18.11A](#), this would mean that as long as $t_a = 2t \geq 4\pi\Delta a$, the corners are unloaded and the crack onsets at the crack tip. It is

made clear that the Δa_{crit} is dependent on the bondline thickness. To demonstrate this relation, experimental tests and numerical simulations were performed varying Δa . Fig. 18.13 shows the resulting strain field obtained numerically (refer to [40] for details on the numerical simulations).

From the experimental results, it was found that for $r_p < t$ and $\Delta a > 0$, a ratio of $\frac{\lambda^{-1}}{\Delta a} \leq 2$ leads to cohesive fracture onset (i.e., at mid-adhesive thickness). Replacing λ by Eq. (18.19) with $t_a = 2t$, the empirical relation for cohesive fracture onset can also be expressed as $(8E_a B/E_x^f I)(\Delta a_{crit.})^4 \geq 2t$, so that for a given material mismatch, for the DCB geometry, $(\Delta a_{crit.}/h_{adher})^4 \sim (t/h_{adher})$ is the scaling relation for transition into cohesive fracture onset.

In summary, for $\Delta a < \Delta a_{crit.}$, the stress singularity near the bi-material corner rules over the stress singularity at the precrack tip. The bi-material corner with the highest modulus mismatch, characterized by the highest Dundurs parameters, dictates the region of fracture initiation; for $\Delta a \geq \Delta a_{crit.}$ the stress singularity at the precrack tip is dominant, resulting in cohesive fracture onset.

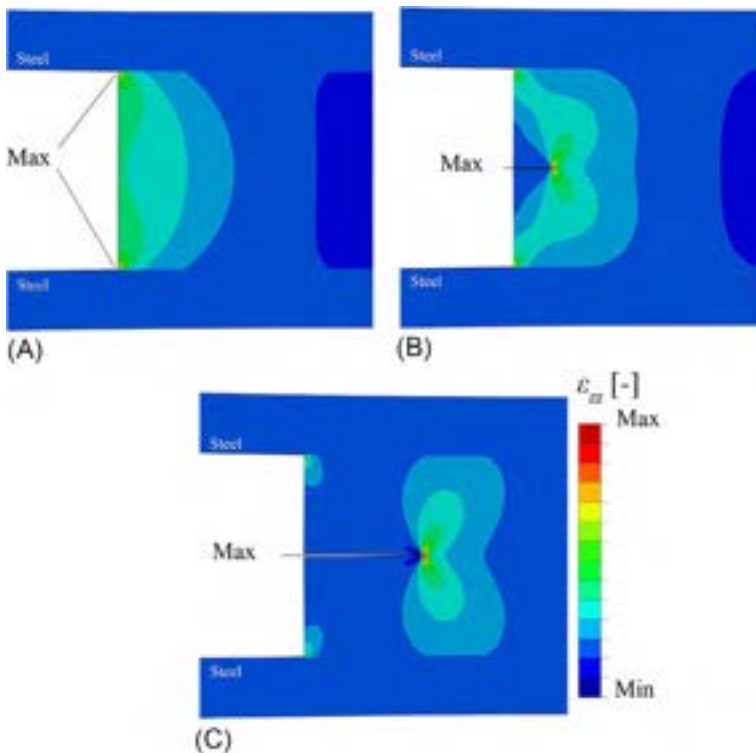


Fig. 18.13 Evolution of strain field, ϵ_{zz} , in steel-steel joint with increasing Δa . (A) $\Delta a = 0$ mm; (B) $\Delta a = 2$ mm; (C) $\Delta a = 6$ mm.

Adapted from R.L. Fernandes, M.K. Budzik, R. Benedictus, S. Teixeira de Freitas, Multimaterial adhesive joints with thick bond-lines: crack onset and crack deflection, Compos. Struct. 266 (2021) 113687.

18.5 Summary and future directions

Conventionally, the bondline thickness has been regarded as a consequence or medium to address some of the performance requirements (thin, stiff bondlines for aerospace) or to address manufacturing process limitations, mainly tolerances (thicker bondlines used in transportation and civil engineering applications). With the development of wind energy as well as marine and civil engineering markets and the focus on lightweight structures, thick bondlines became also a necessity. The new, thicker bondlines became a new and critical length scale for a joint and require different analysis and evaluation due to different load transfer mechanisms and failure modes. These have not always been adopted and are not part of either standard or certification procedure. However, the increased thickness does not need to be considered as a consequence but rather a design feature to be explored. This additional new dimension opens new design routes and expands the design freedom. The adhesive thickness can be used to optimize properties, shape load response, and add functionalities; it can also lead to the development of greener solutions with new materials and limited usage. Recently, use of the mechanical metamaterials as a substitution for traditional bondlines has been proposed [66]. While offering significant volumes, such systems can weigh only a percentage of today's thick bondline systems while maintaining satisfactory mechanical properties. Only time will tell if such a geometrical approach gains widespread acceptance.

References

- [1] G.P. Anderson, S.J. Bennett, K.L. DeVries, *Analysis and testing of adhesive bonds*, NASA, 1977. Tech. rep.
- [2] M.K. Budzik, M. Wolfahrt, P. Reis, M. Kozłowski, J. Sena-Cruz, L. Papadakis, M. Nasr Saleh, K.V. Machalicka, S. Teixeira de Freitas, A.P. Vassilopoulos, Testing mechanical performance of adhesively bonded composite joints in engineering applications: an overview, *J. Adhes.* 98 (14) (2021) 2133–2209.
- [3] S. Mostovoy, E.J. Ripling, Fracture toughness of an epoxy system, *J. Appl. Polym. Sci.* 10 (9) (1966) 1351–1371.
- [4] S. Mostovoy, E.J. Ripling, Effect of joint geometry on the toughness of epoxy adhesives, *J. Appl. Polym. Sci.* 15 (3) (1971) 661–673.
- [5] A.J. Kinloch, S.J. Shaw, The fracture resistance of a toughened epoxy adhesive, *J. Adhes.* 12 (1) (1981) 59–77.
- [6] S. Mall, G. Ramamurthy, Effect of bond thickness on fracture and fatigue strength of adhesively bonded composite joints, *Int. J. Adhes. Adhes.* 9 (1) (1989) 33–37.
- [7] C. Yan, Y.-W. Mai, L. Ye, Effect of bond thickness on fracture behaviour in adhesive joints, *J. Adhes.* 75 (1) (2001) 27–44.
- [8] L.F. Kawashita, A.J. Kinloch, D.R. Moore, J.G. Williams, The influence of bond line thickness and peel arm thickness on adhesive fracture toughness of rubber toughened epoxy-aluminium alloy laminates, *Int. J. Adhes. Adhes.* 28 (4–5) (2008) 199–210.
- [9] P. Davies, L. Sohier, J.-Y. Cognard, A. Bourmaud, D. Choqueuse, E. Rinnert, R. Créac'hacdec, Influence of adhesive bond line thickness on joint strength, *Int. J. Adhes. Adhes.* 29 (7) (2009) 724–736.

- [10] J.M. Arenas, J.J. Narbón, C. Alía, Optimum adhesive thickness in structural adhesives joints using statistical techniques based on Weibull distribution, *Int. J. Adhes. Adhes.* 30 (3) (2010) 160–165.
- [11] G. Ji, Z. Ouyang, G. Li, On the interfacial constitutive laws of mixed mode fracture with various adhesive thicknesses, *Mech. Mater.* 47 (2012) 24–32.
- [12] M.K. Budzik, J. Jumel, M.E.R. Shanahan, 4-Point beam tensile test on a soft adhesive, *Mater. Des.* 46 (2013) 134–141.
- [13] D.J. Alner, *Aspects of Adhesion*, vol. 6, University of London Press, 1965.
- [14] J. Dundurs, T. Mura, Interaction between an edge dislocation and a circular inclusion, *J. Mech. Phys. Solids* 12 (3) (1964) 177–189.
- [15] D.B. Bogy, On the problem of edge-bonded elastic quarter-planes loaded at the boundary, *Int. J. Solids Struct.* 6 (9) (1970) 1287–1313.
- [16] E.D. Reedy, T.R. Guess, Interface corner failure analysis of joint strength: effect of adherend stiffness, *Int. J. Fract.* 88 (4) (1997) 305–314.
- [17] S. Krenk, Energy release rate of symmetric adhesive joints, *Eng. Fract. Mech.* 43 (4) (1992) 549–559.
- [18] W.D. Bascom, R.L. Cottingham, R.L. Jones, P. Peyser, The fracture of epoxy-and elastomer-modified epoxy polymers in bulk and as adhesives, *J. Appl. Polym. Sci.* 19 (9) (1975) 2545–2562.
- [19] B. Zhao, Z.-H. Lu, Y.-N. Lu, Closed-form solutions for elastic stress-strain analysis in unbalanced adhesive single-lap joints considering adherend deformations and bond thickness, *Int. J. Adhes. Adhes.* 31 (6) (2011) 434–445.
- [20] L.F.M. Da Silva, T.N.S.S. Rodrigues, M.A.V. Figueiredo, M.F.S.F. De Moura, J.A.G. Chousal, Effect of adhesive type and thickness on the lap shear strength, *J. Adhes.* 82 (11) (2006) 1091–1115.
- [21] M. Goland, E. Reissner, The stresses in cemented joints, *J. Appl. Mech.* 11 (1) (1944) A17–A27.
- [22] D.A. Dillard, *Fundamentals of Stress Transfer in Bonded*, Elsevier, 2002.
- [23] W. Flügge, *Tensor Analysis and Continuum Mechanics*, vol. 4, Springer, 1972.
- [24] T. Pardoen, T. Ferracin, C.M. Landis, F. Delannay, Constraint effects in adhesive joint fracture, *J. Mech. Phys. Solids* 53 (9) (2005) 1951–1983.
- [25] F. Van Loock, M.D. Thouless, N.A. Fleck, Tensile fracture of an adhesive joint: the role of crack length and of material mismatch, *J. Mech. Phys. Solids* 130 (2019) 330–348.
- [26] A.A. Griffith, M. Eng, The phenomena of rupture and flow in solids, *Phil. Trans. R. Soc. Lond. A* 221 (582–593) (1921) 163–198.
- [27] P.P. Gillis, J.J. Gilman, Double-cantilever cleavage mode of crack propagation, *J. Appl. Phys.* 35 (3) (1964) 647–658.
- [28] E.J. Ripling, S. Mostovoy, R.L. Patrick, Measuring fracture toughness of adhesive joints, *Mater. Res. Stand* 4 (3) (1964) 129–134.
- [29] K. Kondo, Analysis of double cantilever beam specimen, *Adv. Compos. Mater.* 4 (4) (1995) 355–366.
- [30] A.N. Gent, Fracture mechanics of adhesive bonds, *Rubber Chem. Technol.* 47 (1) (1974) 202–212.
- [31] H.M. Westergaard, Bearing pressures and cracks, *J. Appl. Mech.* 6 (2) (1939) A49–A53.
- [32] H.M. Westergaard, *Theory of Elasticity and Plasticity*, vol. 367, Harvard University Press Cambridge, 1952.
- [33] G.C. Sih, On the Westergaard method of crack analysis, *Int. J. Fract. Mechanics* 2 (4) (1966) 628–631.

- [34] G.R. Irwin, Analysis of stresses and strains near the end of a crack traversing a plate, *J. Appl. Mech.* 24 (1957) 361–364.
- [35] E.H. Andrews, A.J. Kinloch, Mechanics of adhesive failure. II, *Proc. R. Soc. Lond. A. Math. Phys. Sci.* 332 (1590) (1973) 401–414.
- [36] P. Martiny, F. Lani, A.J. Kinloch, T. Pardoen, A multiscale parametric study of mode I fracture in metal-to-metal low-toughness adhesive joints, *Int. J. Fract.* 173 (2) (2012) 105–133.
- [37] S.R. Ranade, Y. Guan, D.C. Ohanehi, J.G. Dillard, R.C. Batra, D.A. Dillard, A tapered bondline thickness double cantilever beam (DCB) specimen geometry for combinatorial fracture studies of adhesive bonds, *Int. J. Adhes. Adhes.* 55 (2014) 155–160.
- [38] A.R. Akisanya, C.S. Meng, Initiation of fracture at the interface corner of bi-material joints, *J. Mech. Phys. Solids* 51 (1) (2003) 27–46.
- [39] A. Dimitrov, H. Andrä, E. Schnack, Efficient computation of order and mode of corner singularities in 3D-elasticity, *Int. J. Numer. Methods Eng.* 52 (8) (2001) 805–827.
- [40] R.L. Fernandes, M.K. Budzik, R. Benedictus, S. Teixeira de Freitas, Multi-material adhesive joints with thick bond-lines: crack onset and crack deflection, *Compos. Struct.* 266 (2021) 113687.
- [41] J.J. Benbow, F.C. Roesler, Experiments on controlled fractures, *Proc. Phys. Soc. Sect. B* 70 (2) (1957) 201.
- [42] B.R.K. Blackman, H. Hadavinia, A.J. Kinloch, M. Paraschi, J.G. Williams, The calculation of adhesive fracture energies in mode I: revisiting the tapered double cantilever beam (TDCB) test, *Eng. Fract. Mech.* 70 (2) (2003) 233–248.
- [43] M. Budzik, J. Jumel, M.E.R. Shanahan, Adhesive compliance effect in mode I separation: profilometry approach, *Int. J. Adhes. Adhes.* 31 (3) (2011) 135–145.
- [44] S.P. Timoshenko, S. Woinowsky-Krieger, *Theory of Plates and Shells*, McGraw-Hill, 1959.
- [45] M.A. Biot, Bending of an infinite beam on an elastic foundation, *J. Appl. Math. Mech.* 2 (3) (1922) 165–184.
- [46] G.J. Spies, The peeling test on redux-bonded joints: a theoretical analysis of the test devised by aero research limited, *Aircr. Eng. Aerosp. Technol.* 25 (3) (1953) 64–70.
- [47] A.D. Kerr, Elastic and viscoelastic foundation models, *J. Appl. Mech.* 31 (3) (1964) 491–498.
- [48] D.A. Dillard, B. Mukherjee, P. Karnal, R.C. Batra, J. Frechette, A review of Winkler's foundation and its profound influence on adhesion and soft matter applications, *Soft Matter* 14 (19) (2018) 3669–3683.
- [49] M.F. Kanninen, An augmented double cantilever beam model for studying crack propagation and arrest, *Int. J. Fract.* 9 (1) (1973) 83–92.
- [50] R. Lopes Fernandes, S. Teixeira de Freitas, M.K. Budzik, J.A. Poulis, R. Benedictus, From thin to extra-thick adhesive layer thicknesses: fracture of bonded joints under mode I loading conditions, *Eng. Fract. Mech.* 218 (2019), 106607.
- [51] B. Chen, D.A. Dillard, J.G. Dillard, R.L. Clark Jr, Crack path selection in adhesively-bonded joints: the role of material properties, *J. Adhes.* 75 (4) (2001) 405–434.
- [52] B. Chen, D.A. Dillard, The effect of the T-stress on crack path selection in adhesively bonded joints, *Int. J. Adhes. Adhes.* 21 (5) (2001) 357–368.
- [53] R. Lopes Fernandes, S. Teixeira de Freitas, M.K. Budzik, J.A. Poulis, R. Benedictus, Role of adherend material on the fracture of bi-material composite bonded joints, *Compos. Struct.* 252 (2020), 112643.
- [54] C.M. Landis, T. Pardoen, J.W. Hutchinson, Crack velocity dependent toughness in rate dependent materials, *Mech. Mater.* 32 (11) (2000) 663–678.

- [55] S. Heide-Jørgensen, M.K. Budzik, Effects of bondline discontinuity during growth of interface cracks including stability and kinetic considerations, *J. Mech. Phys. Solids* 117 (2018) 1–21.
- [56] B.R.K. Blackman, A.J. Kinloch, F.S. Rodriguez Sanchez, W.S. Teo, J.G. Williams, The fracture behaviour of structural adhesives under high rates of testing, *Eng. Fract. Mech.* 00137944, 76 (18) (2009) 2868–2889, <https://doi.org/10.1016/j.engfracmech.2009.07.013>.
- [57] A. Karac, B.R.K. Blackman, V. Cooper, A.J. Kinloch, S. Rodriguez Sanchez, W.S. Teo, A. Ivankovic, Modelling the fracture behaviour of adhesively-bonded joints as a function of test rate, *Eng. Fract. Mech.* 00137944, 78 (6) (2011) 973–989, <https://doi.org/10.1016/j.engfracmech.2010.11.014>.
- [58] I. Georgiou, A. Ivankovic, A.J. Kinloch, V. Tropsa, Rate dependent fracture behaviour of adhesively bonded joints, in: *European Structural Integrity Society*, vol. 32, Elsevier, 2003, pp. 317–328, [https://doi.org/10.1016/S1566-1369\(03\)80105-X](https://doi.org/10.1016/S1566-1369(03)80105-X).
- [59] T. Carlberger, A. Biel, U. Stigh, Influence of temperature and strain rate on cohesive properties of a structural epoxy adhesive, *Int. J. Fract.* 03769429, 155 (2) (2009) 155–166, <https://doi.org/10.1007/s10704-009-9337-4>.
- [60] M. May, O. Hesebeck, S. Marzi, W. Böhme, J. Lienhard, S. Kilchert, M. Brede, S. Hiermaier, Rate dependent behavior of crash-optimized adhesives—experimental characterization, model development, and simulation, *Eng. Fract. Mech.* 00137944, 133 (2015) 112–137, <https://doi.org/10.1016/j.engfracmech.2014.11.006>.
- [61] C.S.P. Borges, P.D.P. Nunes, A. Akhavan-Safar, E.A.S. Marques, R.J.C. Carbas, L. Alfonso, L.F.M. Silva, A strain rate dependent cohesive zone element for mode I modeling of the fracture behavior of adhesives, *Proc. Inst. Mech. Eng. L J. Mater. Des. Appl.* 20413076, 234 (4) (2020) 610–621, <https://doi.org/10.1177/1464420720904026>.
- [62] J. Jumel, S. Chauffaille, M.K. Budzik, M.E. Shanahan, J. Guitard, Viscoelastic foundation analysis of single cantilevered beam (SCB) test under stationary loading, *Eur. J. Mech. A Solids* 39 (2013) 170–179.
- [63] J.W. Hutchinson, M.E. Mear, J.R. Rice, Crack paralleling an interface between dissimilar materials, *J. Appl. Mech.* 54 (1987) 828–832.
- [64] N. Perez, *Fracture Mechanics*, Springer, 2017, <https://doi.org/10.1007/b118073>.
- [65] Z.P. Bazant, L. Cedolin, *Stability of Structures: Elastic, Inelastic, Fracture and Damage Theories*, World Scientific, 2010.
- [66] A.E. Athanasiadis, M.A. Dias, M.K. Budzik, Can confined mechanical metamaterials replace adhesives? *Extreme Mech. Lett.* 48 (2021) 101411.

This page intentionally left blank

Evaluating and predicting fatigue behavior in adhesively bonded joints

19

Ian Ashcroft^a and John-Alan Pascoe^b

^aUniversity of Nottingham, Nottingham, United Kingdom, ^bDelft University of Technology, Delft, The Netherlands

19.1 Introduction

Like most other engineering materials, adhesives suffer from fatigue, that is, the degradation of material properties and eventual failure due to repeated load cycles below the static strength of the material. Evaluating the fatigue life of an adhesive joint is therefore crucial to ensuring the durability of an adhesively bonded structure. Besides looking purely at research on adhesive bonds, we can also draw lessons from research on delamination of composites, which often involves similar materials (e.g., epoxy systems) in similar geometries (cracking of a thin layer between two stiffer adherends).

Over the years, a number of different approaches have been developed for evaluating the fatigue life of adhesive bonds. These can be grouped into four categories:

1. **Stress/strain-life approaches** that link the applied stress or strain amplitude to the fatigue life of the joint, without further consideration of the physical damage processes.
2. **Strength/stiffness wearout models** in which the strength and/or stiffness of the joint is gradually reduced as a function of the number of applied load cycles. Final failure occurs when the strength or stiffness reaches a critical value.
3. **Fracture mechanics models** that model the growth of the physical crack(s) in the adhesive joint. Final failure occurs when the crack reaches a critical size.
4. **Damage mechanics** that represent the damage in the material by a damage parameter, which usually can range from 0 (undamaged) to 1 (fully damaged), and in which damage will progressively increase as a function of fatigue cycles until failure occurs. Damage mechanics approaches are usually implemented within finite element analyses.

This chapter will first cover some general considerations in evaluating fatigue in adhesive joints and then discuss the available experimental techniques. Next, a more in-depth discussion will be presented on the four categories of prediction models mentioned above. Finally, the influence of various features of the joint (e.g., adhesive thickness and joint geometry) and the influence of environmental effects on the fatigue life will be discussed.

19.2 General considerations for fatigue of adhesives

The fatigue behavior of an adhesive bond will depend on many factors. These include the amplitude and frequency of the applied load cycles, the environmental conditions, the adherend and adhesive materials and geometry, and the surface treatment applied before the bonding process. These factors do not just influence the rate at which specific fatigue mechanisms propagate, but can also change which fatigue mechanisms occur in the first place.

Adhesively bonded joints are multimaterial structures and therefore can suffer from different failure modes, as illustrated in Fig. 19.1. Bonded joints can fail through cohesive failures of either the adherends (Fig. 19.1a) or the adhesive (Fig. 19.1b). In metals, cohesive adherend failure typically takes the form of a transverse crack through the thickness of the adherend, initiated at a stress concentration near the end of the bond line (Fig. 19.1a). In fiber-reinforced composites, on the other hand, if the interlaminar interface is weaker than the adhesive, delamination of the ply or plies closest to the adhesive may occur (Fig. 19.1a). Cohesive failure of the constituent materials of the joint failure can also occur due to a failure of the adhesion between the adhesive and one of the adherends (Fig. 19.1c). It is also possible for a joint to fail through a combination of cohesive failure in both the adhesive and the adherend (Fig. 19.1d) or by a mix of both cohesive and interfacial failure. In the case of metal adherends, the stress concentration generated by the presence of a crack in the adhesive can initiate a crack in the adherend as well. In the case of composite adherends, the crack can migrate into the composite and continue growing as a delamination. In some cases, the crack can even migrate back to the bondline at a later stage, for example in the scarf joints investigated by Goh et al. [1]. The propensity of the crack to migrate depends on the joint geometry and the lay-up of the adherends [2]. In general, a crack will find it more difficult to migrate through a layer where the fibers are aligned parallel to the (local) loading direction, and easier to migrate through a layer where the fibers are aligned perpendicular to the loading direction. This is because in the second case, the crack can propagate through the layer as a purely matrix crack, without needing to break any fibers.

When trying to predict or analyze the fatigue behavior of a specific structure in service, it's important to ensure that any analyses or experiments used to support this are based on the same failure mode. If the failure mode seen in service does not match that seen in the lab, or assumed in the analysis, then that analysis result or experimental data are not applicable to the case under examination.

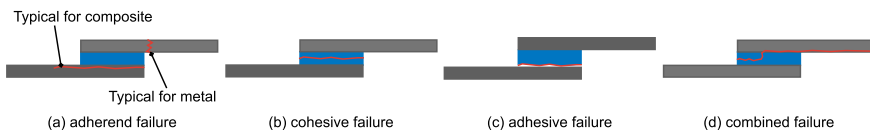


Fig. 19.1 The different failure modes that can occur in an adhesive bond.

19.3 Experimental techniques

Experimental data are essential for evaluating the fatigue performance of adhesive bonds. Although various fatigue models exist, they all require experimental data on the fatigue behavior of some kind, and thus specific fatigue experiments are needed. Tests can be performed for different reasons, such as part of material screening and selection, to provide input for predictive models or to validate fatigue analyses. In the case of tests performed to provide input for predictive models, the type of model will determine the test objectives. For stress or strain-life approaches, the objective is to determine the number of cycles until failure at different load levels and thus only the applied load needs to be determined accurately. To support damage mechanics or wearout models, the objective is to obtain the residual strength or stiffness as a function of the number of cycles. Measurement of the residual stiffness requires some consideration to ensure a sufficiently accurate measurement can be obtained. To support fracture mechanics models, tests need to determine the fracture mechanics parameters and accurately measure the crack growth rate. Thus, specimens need to be selected in which the crack length can be readily measured. For experiments aiming to detect fatigue crack initiation, configurations can be selected where initiation can be detected through strain measurements, such as Refs. [3–8].

Typically, the test specimen geometries used for fatigue testing are similar to those used for quasistatic testing, but with a cyclic load applied instead of a monotonic one. Some commonly used fatigue test geometries are shown in Fig. 19.2. Besides the coverage in this chapter, some test methods are also discussed in more detail in Chapters 14, 16, 17, 20–22, and 32. Testing aimed at finding the fatigue life commonly makes use of lap joints, which are covered by the BS EN ISO 9664:1995 and ASTM D3166-99 standards. For the crack growth parameters needed for fracture mechanics models, test geometries such as the double cantilever beam (DCB, mode I, Fig. 19.2d), end notch flexure (ENF, mode II, Fig. 19.2e), or mixed-mode bending (MMB, mixed-mode, Fig. 19.2f) can be employed. As of yet, no test standards have been published for fatigue crack growth tests, but for double cantilever beam tests, the quasistatic standards ASTM D3433-99 or ISO 25217 can be used as a basis for the specimen

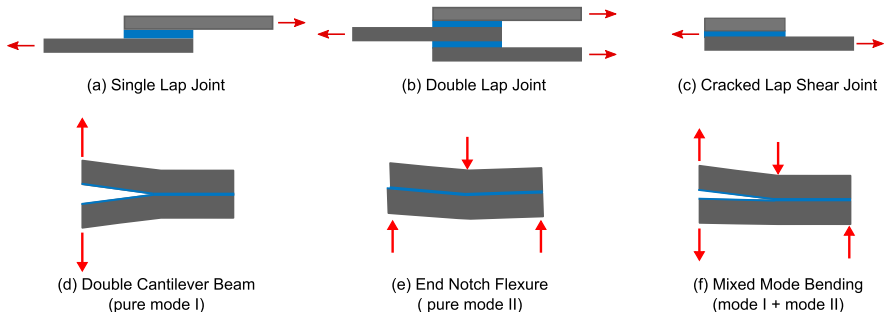


Fig. 19.2 Examples of commonly used fatigue test geometries.

geometry. It is important to note that the standard fracture mechanics tests assume that the crack occurs at the midplane between two arms made of the same material. Therefore, special care needs to be taken when investigating the bonding of two dissimilar materials (e.g., metal to fiber-reinforced polymer). A typical approach is to adjust the thickness of each arm so that the bending stiffness is equal [9–12], although in that case the strains at the interface might still be quite different, resulting in different behavior, even if the global strain energy release rate appears to be the same.

If the goal of a test is to measure the crack propagation rate, a longer overlap length than employed for quasistatic tests may be desirable to avoid premature failure of the specimen. For testing the behavior of long bond lines, such as those of bonded stiffeners, the cracked lap shear (CLS) configuration (Fig. 19.2c) is a popular choice. This configuration can reproduce the stress concentration caused by a stiffener run-out and can therefore be used to investigate the fatigue initiation behavior. It also reproduces the change of mode-mixity as the crack grows. Lai et al. [13] have provided a closed-form solution for this configuration.

An extensive review of available testing methods for adhesive bonds has recently been provided by Budzik et al. [14]. They point out that there are only a limited number of generic test standards (this is even more the case for fatigue) and that in practice, much testing is conducted using industry- and/or application-specific methods. This situation is likely in part due to the difficulty of generalizing experimental results. The stress distribution in an adhesive joint is complex and highly dependent on both the joint geometry and the adherend properties. Furthermore, if a geometry is used in which multiple cracks may occur (e.g., a double strap joint), these cracks can interact with each other [15]. Therefore, it can be difficult to transfer results obtained in a certain experiment to predict the behavior of a joint with a different geometry, even if the same adhesive and adherends are used. Additionally, it should be kept in mind that the adherend properties will influence the test results. Thus, without extensive analysis, a test will give information on the combination of adherend and adhesive under the specific joint configuration and loading mode, rather than on the material properties of the adhesive itself. As a recent example, Sahin and Alkpinar [16] investigated the effect of adherend thickness on the fatigue strength of bonded single-lap joints. They found that an increase of the adherend thickness resulted in an increased fatigue strength in terms of the applied force, but by a much smaller factor than the increase in adherend thickness. For example, increasing the adherend thickness from 2 to 5 mm increased the fatigue strength by only 24% due to the change in bending moments and flexural stiffnesses of the adherends. Thus, a change in adherend thickness needs to be accounted for when comparing two different cases.

When conducting tests to predict the behavior of an operational structure, particular attention should be paid to using the same manufacturing process for both test specimens and the final structure, as changes in the manufacturing procedure will affect the fatigue life [17]. An illustrative case study here is the wing root joint of the F/A-18 fighter jet, also discussed in Chapter 23. This is a stepped-lap joint in which a titanium lug is adhesively bonded to a composite skin, as shown in Fig. 19.3. In order



Fig. 19.3 The F/A-18 wing root joint.

to investigate possible safety concerns, and to support a life extension program, Seneviratne et al. tested the residual strength and remaining fatigue life of specimens cut from retired aircraft wings that had been used in service [18]. These tests showed that the remaining strength and fatigue life were satisfactory, and the specimens failed through cohesive failure in either the adhesive or adherend (as required) in all cases. Nevertheless, at a later stage large disbonds were discovered on a number of aircraft in service, and these were investigated by Mueller et al. [19]. The investigation found that the disbonds took the form of *adhesive* failure, rather than the cohesive failure that occurred in the Seneviratne et al. test program. After further investigation, it was concluded that the most likely cause was a failure to sufficiently rinse off fluorine-containing residue during the surface treatment. Effectively, the insufficient rinsing in the specimens examined by Mueller et al. meant that they had undergone a slightly different manufacturing process than the specimens used by Seneviratne et al., which were taken from a different aircraft than the failures examined by Mueller et al. This resulted in a change of failure modes when the joints were subjected to fatigue loading, which meant that the results obtained by Seneviratne et al. were not applicable, even though they were obtained from nominally identical joints. These results highlight the potential impact of surface treatment and manufacturing processes, and imperfections in those processes, on the behavior of the joint. For further discussion of surface issues, see [Chapter 9](#). As a general lesson, this case study shows the importance of carefully evaluating under which conditions experimental results can actually be applied to operational structures.

19.4 Stress/strain-life approaches

19.4.1 The stress-life approach

This constitutes one of the earliest approaches to predicting fatigue, as pioneered by Wöhler [20] in his studies of failure in iron and steel in the railways. It is an empirical approach based on testing samples under constant sinusoidal loading at various load levels. The number of cycles to failure (N_f) is then plotted as a function of a variable such as stress or strain amplitude. Where the loading is low enough that the deformation is predominantly elastic, a stress variable (S) is usually chosen and the resultant plot is termed an S - N curve, or a Wöhler plot; this is known as the stress-life approach. Under these conditions, a long fatigue life would be expected and hence this is sometimes termed high cycle fatigue (HCF). The S - N data are either plotted as a log-linear or a log-log plot and a characteristic equation can be obtained by empirical curve fitting. The constants in the curve-fitted equations are dependent on many factors,

including material, geometry, surface condition, environment, and mean stress. Hence, caution should be used when trying to apply $S-N$ data beyond the samples used to generate the data. The standard stress-life method gives no indication of the progression of damage, although in some cases the onset of cracking is indicated on the plot in addition to the complete failure, hence allowing the initiation and propagation phases to be differentiated. The above factors mean that the $S-N$ curve is of rather limited use in predicting fatigue behavior; however, it is still useful in fatigue modeling as a validation tool, such as with [21,22].

A further limit in the application of $S-N$ curves to fatigue prediction in bonded joints is that there is no unique relation between the easily determined average shear stress in the adhesive layer and the maximum stress. For this reason, load rather than stress is often used in total-life plots for bonded joints; these are known as $L-N$ curves. A typical $L-N$ curve for epoxy-bonded double-lap joints can be seen in Fig. 19.4. The $L-N$ curve can be divided into a low cycle fatigue (LCF) region below approximately 1000 cycles, a high cycle fatigue (HCF) region between approximately 1000 and 100,000 cycles, and an endurance limit region, which in this case starts at approximately 100,000 cycles. The endurance limit is defined by a load below which an infinite fatigue life is predicted. However, not all materials exhibit a clearly defined endurance limit, in which case it may be instead defined as the load at which fatigue failure hasn't occurred after a large number of cycles representative of the application, typically 10^6 .

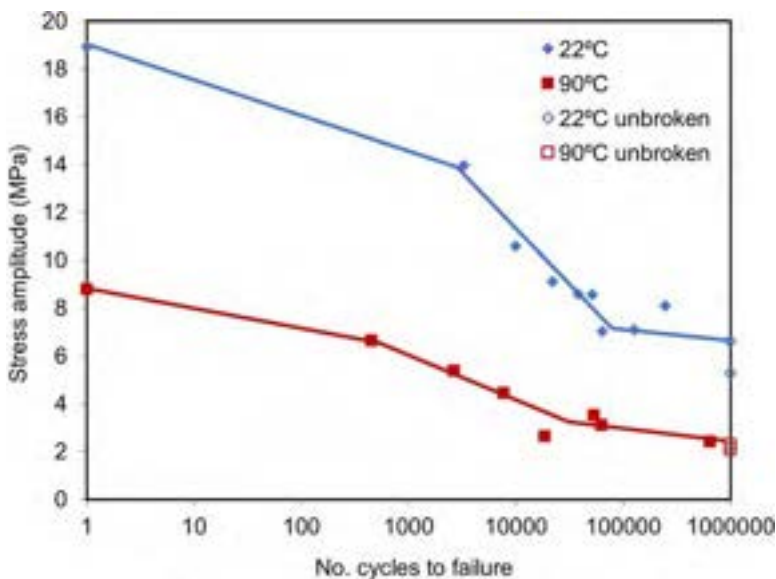


Fig. 19.4 Load-life ($L-N$) curve for bonded lap joints.

Data from I.A. Ashcroft, D.J. Hughes, S.J. Shaw, M.A. Wahab, A. Crocombe, Effect of temperature on the quasi-static strength and fatigue resistance of bonded composite double lap joints, *J. Adhes.* 75(1) (2001) 61–88.

Fatigue life not only depends on the stress amplitude but also on the mean stress, as either increasing the mean or increasing the amplitude tends to result in a reduction of the fatigue life. The relationship between amplitude and mean on the fatigue life can be illustrated in constant-life diagrams, in which a given fatigue life is plotted against both mean and amplitude.

19.4.2 Damage initiation and crack growth phases of damage

Although the S - N curve can be used to predict life to failure for a particular load or stress that sits on the experimental plot, it tells us nothing of the evolution of damage in a component. A particular deficiency in the standard stress-life approach is that no differentiation is made between the crack initiation and growth phases. In some cases, efforts have been made to differentiate between the initiation and propagation phases in the S - N behavior of bonded joints [4,23–28]. Shenoy et al. [26] used a combination of back-face strain measurements and sectioning of partially fatigued joints to measure damage and crack growth as a function of number of fatigue cycles. It was seen from the sectioned joints that there could be extensive internal damage in the joint without external signs of cracking; therefore, the determination of an initiation phase from external observations alone is likely to lead to an overestimation. Shenoy et al. [26] identified three regions in the fatigue life of an aluminum/epoxy single-lap joint: an initiation period (CI) in which damage starts to accumulate, but a macrocrack has not yet formed; a stable crack growth (SCG) region in which a macrocrack has formed and is growing slowly; and a fast crack growth region (FCG), which leads to rapid failure of the joint. They found that the percentage of life spent in each region varies with the fatigue load. At low loads, the fatigue life is dominated by crack initiation, whereas crack growth dominates at high loads. This is illustrated schematically in the extended L - N curve of Fig. 19.5. It can also be seen in the figure that the back-face strain signal associated with each phase of fatigue damage can be used to monitor damage.

19.4.3 Variable amplitude fatigue

The S - N curve is only directly applicable to constant amplitude fatigue, whereas in most practical applications for structural joints, a variable amplitude fatigue spectrum is more likely. A simple method of using S - N data to predict variable amplitude fatigue is that proposed by Palmgren [29] and further developed by Miner [30]. The Palmgren Miner (P-M) rule can be represented by:

$$\sum \frac{n_i}{N_{fi}} = 1 \quad (19.1)$$

where n_i is the number of cycles in a constant amplitude block, and N_{fi} is the number of cycles to failure at the stress amplitude for that particular block and can be obtained from the S - N curve. It can be seen by using Eq. (19.1) that the fatigue life of a sample in variable amplitude fatigue can be predicted from an S - N curve obtained from

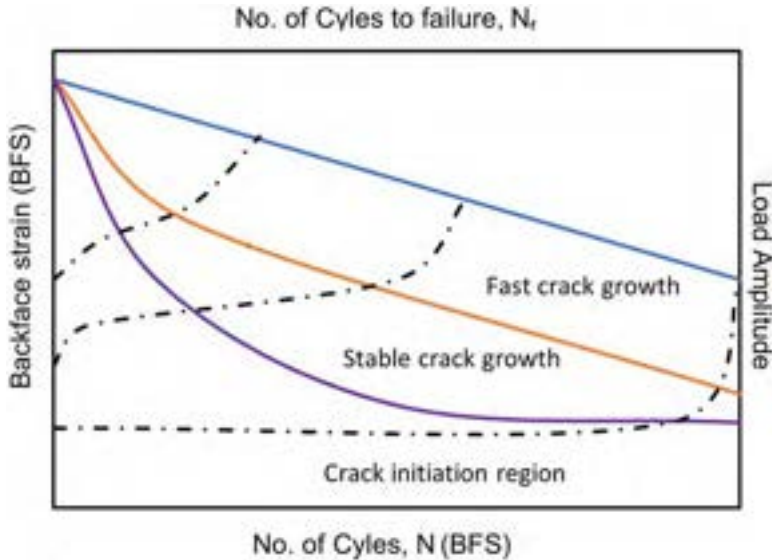


Fig. 19.5 Extended $L-N$ diagram.

From V. Shenoy, I.A. Ashcroft, G.W. Critchlow, A.D. Crocombe, M.M. Abdel Wahab, An investigation into the crack initiation and propagation behaviour of bonded single-lap joints using backface strain, *Int. J. Adhes. Adhes.* 29(4) (2009) 361–371.

constant amplitude fatigue testing of similar samples. However, there are a number of serious limitations to this method, primarily the assumptions that damage accumulation is linear and that there are no load history effects. Modifications to the P-M rule have been suggested to address some of the deficiencies, such as with [31–35]. However, any improvements are at the expense of increased complexity and/or increased testing requirements and the basic flaw in the method, that it bears no relation to the actual progression of damage in the sample, is still not addressed. Erpolat et al. [36] used the P-M law and the extended P-M law, in which cycles below the endurance limit also contribute to damage accumulation, to predict failure in an epoxy-CFRP double lap joint subjected to a variable amplitude (VA) fatigue spectrum. The resulting Miner's sum was significantly less than 1, varying between 0.04 and 0.3, and decreased with increasing load. This indicates that load sequencing is causing damage acceleration, that is, that the P-M rule is nonconservative.

19.4.4 Fatigue limit

Wöhler [20] noted a stress below which a nominally infinite life is seen, which is termed the fatigue or endurance limit. If a fatigue limit is seen, then it may be possible to use the data from one sample to predict the fatigue limit for a different geometry or loading condition. The approach is similar to that for predicting failure under quasistatic loading, and similar multiaxial failure criteria, such as von Mises or maximum principal stress, should be used. Wahab et al. [37] compared the predicted

fatigue limit (or fatigue threshold) in bonded lap-strap joints using a variety of stress- and strain-based failure criteria. It should be noted that many materials do not have a well-defined fatigue limit, in which case a high number of cycles such as 10^7 may be used to indicate a nominal fatigue limit for predictive purposes.

19.4.5 The strain-life approach

Under high stress amplitudes, plastic deformation occurs and the fatigue life is considerably shortened. This is known as low cycle fatigue (LCF). Under constant stress amplitude fatigue with strain hardening, the strain amplitude decreases after the first cycle, and the subsequent hysteresis loop is repeated a number of times before micro-cracking occurs. In LCF, the high loads and plastic deformation mean that the fatigue life is dominated by crack initiation as failure occurs quickly once a crack has formed. This behavior can be seen in Fig. 19.5 and also explains the change in gradient of the $L-N$ curve in Fig. 19.4 in the LCF region. In constant strain amplitude testing, if there is a positive strain mean then the mean tends to decrease as the sample is fatigued, a phenomenon known as plastic shakedown. This can be compared with the effect of creep in constant stress amplitude testing, which leads to an increase in the mean strain with cycling. The strain-life approach is more difficult to implement than the stress-life method, particularly for complex systems such as bonded joints. Structural bonded joints tend to be used in HCF applications and hence the strain-life method has seen little application to adhesively bonded joints.

19.5 Strength/stiffness wearout

An alternative phenomenological approach to the total life methods described above is to characterize fatigue damage as a function of the reduction in the strength or stiffness of the joint during its fatigue life. Stiffness wearout has the advantage that it can be detected by nondestructive testing techniques; however, it is not directly linked to a failure criterion and may not be very sensitive to the early stages of damage. The strength wearout method provides a useful characterization of the degradation of residual strength with fatigue cycling but requires extensive destructive testing.

19.5.1 Strength wearout approach

In the strength wearout method, the joint's strength is initially equal to the static strength, S_u , but decreases to $S_R(n)$ as damage accumulates through the application of n fatigue cycles. This degradation can be represented by:

$$S_R(n) = S_u - f(S_u, S_{\max}, R)n^\kappa \quad (19.2)$$

where κ is a strength degradation parameter, S_{\max} is the maximum stress, and R is the ratio of minimum to maximum stress (i.e., $R = S_{\min}/S_{\max}$). Failure occurs when

the residual strength equals the maximum stress of the spectrum, that is, when $S_R(N_f) = S_{\max}$.

Shenoy et al. [38] proposed a modified version of this equation that they termed the normalized nonlinear strength wearout model (NNLSWM), which is given by:

$$L_n = 1 - \frac{(L_u - L_{\max})}{L_u} (N_n)^\eta \quad (19.3)$$

The normalized residual failure load, L_n , and normalized cycles to failure, N_n , are defined as:

$$L_n = L_R(n)/L_u$$

$$N_n = n/N_f$$

where $L_R(n)$ is the quasistatic failure load after n fatigue cycles, L_u is the quasistatic failure load prior to fatigue loading, and N_f is the number of cycles to failure. Fig. 19.6 shows an experimental plot of L_n against N_n for various fatigue loads, together with the best fit of Eq. (19.3). It can be seen that the proposed phenomenological model agrees well with the experimental results. A single curve can be reasonably drawn for the entire range of fatigue loads, wherein the experimental parameter η is independent of the applied fatigue load.

Schaff and Davidson [40,41] extended Eq. (19.2) to enable the residual strength degradation of a sample subjected to a variable amplitude loading spectrum to be predicted. However, they noted a crack acceleration effect in the transition from one constant amplitude (CA) block to another, a phenomenon they termed the cycle mix effect, and proposed a cycle mix factor, CM, to account for this. Erpolat et al. [42] proposed a modified form of Shaff and Davidson's cycle mix equation to model the degradation of CFRP-epoxy double-lap joints subjected to a variable amplitude

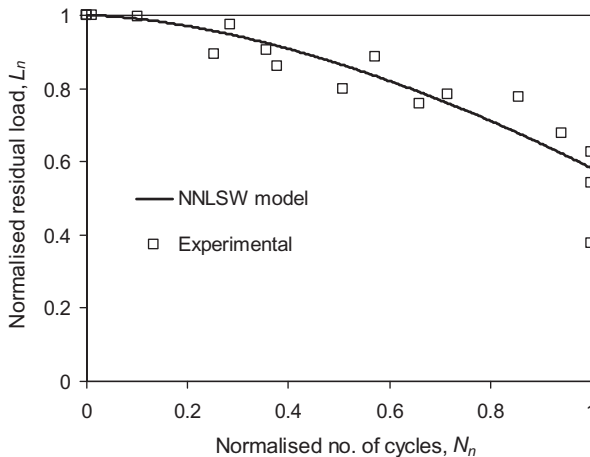


Fig. 19.6 Normalized nonlinear strength wearout model (Shenoy et al. [39]).

fatigue spectrum. They showed that this model represented the fatigue life of bonded joints under variable amplitude fatigue more accurately than Palmgren-Miner's law. Shenoy et al. [39] proposed further modifications to this approach based upon a nonlinear strength wearout model with a damage-dependent cycle mix parameter. It is worth noting that whereas crack acceleration is seen after overloads in brittle thermosetting plastics, such as epoxies, the opposite is frequently reported for ductile metals, where plastic deformation can cause crack blunting, strain hardening, and/or plasticity-induced crack closure [43]. It could be postulated, therefore, that in more ductile adhesives in which failure is dominated by plastic yielding rather than crack growth, overloads may be less detrimental or even beneficial in terms of fatigue life.

19.5.2 Stiffness wearout approach

As with strength degradation, the stiffness degradation rate can be considered a power function of the number of load cycles, using a similar equation to 2 [44–46]. A failure criterion for a stiffness-based wearout model is not as straightforward as that for the strength-based wearout models. One approach is to relate the degraded stiffness, $E(N_f)$, to stress, such as:

$$\frac{E(N_f)}{E(0)} = \frac{S_{\max}}{S_u} \quad (19.4)$$

where $E(0)$ is the initial stiffness.

19.6 Fracture mechanics

The fracture mechanics-based approaches to fatigue aim to predict the growth of physical cracks in the adhesive bond. The fatigue life of the bond is reached when the crack reaches a critical length. This is usually defined as the crack length at which unstable fracture occurs if the maximum design load is applied. An important advantage of these kinds of approaches is that they can be used to analyze the effect of defects on the fatigue life [47], unlike stress/strain-life approaches, which are usually based on (nominally) “defect-free” specimens.

Typically, researchers aim to predict the crack growth rate based on linear elastic fracture mechanics (LEFM) theory (see also Chapters 15–17 and 32). LEFM was first applied to the prediction of fatigue crack growth in metals by Paris and coworkers [48]. Some 15 years later, Mostovoy and Ripling [49] adopted this approach for fatigue crack growth in adhesives. For this, Mostovoy and Ripling modified the equation proposed by Paris by replacing the stress intensity factor range ΔK with the strain energy release rate range (SERR) ΔG to obtain an equation of the form:

$$\frac{da}{dN} = Cf(G)^n \quad (19.5)$$

where da/dN is the crack growth rate, C and n are empirical parameters found by curve fitting, and $f(G)$ is a function of the strain energy release rate. It should be noted that ΔG is proportional to $(K_{\max}^2 - K_{\min}^2)$, which is not equal to $\Delta K^2 = (K_{\max} - K_{\min})^2$. Therefore the substitution of ΔG for ΔK is not directly equivalent in a physical sense [50]. Nevertheless, Mostovoy and Ripling were able to successfully correlate the crack growth rate to ΔG . As an alternative to ΔG , other researchers have suggested $f(G) = G_{\max}$ or $f(G) = \Delta\sqrt{G} = \sqrt{G_{\max}} - \sqrt{G_{\min}}$. As long as the empirical parameters C and n are calibrated to match the choice of $f(G)$, all three choices can result in good fits of experimental crack growth data. Many variations on the basic form of Eq. (19.5) have been proposed over the years, for example to deal with the R -ratio or mode-mixity effects, and reviews can be found in Refs. [51–53].

LEFM assumes a linear elastic material behavior and is therefore usually only applied for brittle adhesives such as epoxies (including toughened epoxy systems). In cases where the adhesive exhibits significant amounts of plasticity during fatigue loading, the SERR may not be the most appropriate controlling parameter. In these cases, the J -integral (discussed in detail in Chapter 16) may prove to be a suitable alternative to the SERR. Several researchers have therefore proposed fatigue and/or crack growth models based on the J -integral as the controlling parameter [37,54–56], but there does not yet seem to be widespread adoption of this approach. For both the J -integral and LEFM approaches, the key issue is how to relate the chosen driving force representation (e.g., J_{\max} or ΔJ) to the crack growth rate. To date, no physical theory has been formulated that can justify the form of Eq. (19.5), and thus, fracture mechanics approaches rely on empirical correlations. Nevertheless, given sufficient input data, these methods can still produce accurate predictions. Care does need to be taken to ensure that the input data match the prediction case, as for example R -ratio, mode-mix, and environmental effects are known to affect the values of the fitting parameters C and n . Also, other factors such as manufacturing quality and loading frequency may also affect the crack growth behavior.

19.6.1 Numerical techniques

For simple geometries, analytical equations are available to calculate the strain energy release rate, as for example provided in the ASTM D5528-13 (DCB), ASTM D6671M-19 (MMB), and ASTM D7905M-14 (ENF) standards. The crack length after a certain number of cycles can then be predicted by inserting the strain energy release rate equation into Eq. (19.5) and integrating. For more complex geometries, however, simple equations for the strain energy release rate are not available, and thus finite element analysis (FEA) is called for. With FEA, one popular method for calculating the strain energy release rate is the virtual crack closure technique (VCCT), originally developed by Rybicki and Kanninen [57], based on an argument by Irwin [58]. The basic assumption is that the energy released when extending the crack by a certain increment is the same as the work required to close the crack by the same increment. Thus, the strain energy release rate at a certain node in a finite element mesh can be computed based on the nodal forces, and the displacements of the nodes behind the

crack tip. An overview of earlier development and applications of VCCT has been provided by Krueger [59]. More recently, guidelines for implementing VCCT-based fatigue analyses have been published by NASA [60]. Because the VCCT allows calculation of the strain energy release rate within the numerical analysis, it can be combined with Eq. (19.5) to predict the crack growth rate. The VCCT has downsides, however, including that remeshing is required when a crack grows and that an initial crack is always required. Also, the VCCT cannot model crack initiation.

To improve on the limitations of VCCT, recent research efforts have focused on the use of cohesive zone models (CZM) to predict fatigue crack growth, such as [61–72]. The cohesive zone models are based on the works of Dugdale [73] and Barenblatt [74], and were applied to the fatigue of adhesive bonds by Pirondi and Moroni [75,76]. While the details of implementations differ, the CZMs are all based on a constitutive law linking traction to the separation of nodes. As separation is increased, the traction first increases until a critical separation is reached, after which it decreases, thereby simulating the initiation of damage. The irreversible nature of the damage is simulated by introducing one or more damage parameters, which are used to degrade the stiffness of the element. Fatigue damage can be simulated by incrementing the damage parameters based on the loading and the number of cycles that have been applied. Rather than simulating the effect of each individual cycle, which would be computationally very costly, a cycle jump strategy is usually applied in which the crack growth rate is effectively assumed to remain constant for a certain increment of cycles. The increment of the damage parameters due to fatigue is usually chosen such that it will produce the crack growth rate predicted by Eq. (19.5). Therefore, although one can argue that the cohesive model is more representative of the actual material behavior, it is important to realize that when it comes to representing fatigue behavior, cohesive zone-based models still rely on an empirical correlation to predict the crack growth.

19.6.2 R-ratio effect

Many researchers have noted that the ratio of minimum to maximum stress in a cycle, the R -ratio-affects the crack growth rate. That is, if G_{\max} or ΔG is held constant and the R -ratio is changed, then a different crack growth rate is obtained. This should not be very surprising, as the combinations of a particular G_{\max} or ΔG value and two different R -ratios specify two different load cycles, which then also produce two different crack growth rates. The qualitative effect of changing the R -ratio can be predicted by considering the amount of cyclic work, U_{cyc} , that would be applied. For example, if the amount of cyclic work is reduced (e.g., by keeping G_{\max} constant and increasing R), then the crack growth rate will be lower [77]. The effect of R -ratio on cyclic work when holding different LEFM parameters constant is illustrated in Figs. 19.7 and 19.8.

If ΔG is held constant and the R -ratio is changed, then U_{cyc} remains constant. Thus, one might expect the crack growth rate to also remain constant. This is indeed sometimes seen [77]. However, in other cases, increasing the R -ratio while keeping ΔG constant results in a reduction in the crack growth rate [50,78]. The likely reason for this is that keeping ΔG constant while increasing R also requires increasing G_{\max} . In Ref. [77], which investigated an epoxy adhesive, increasing G_{\max} was correlated to

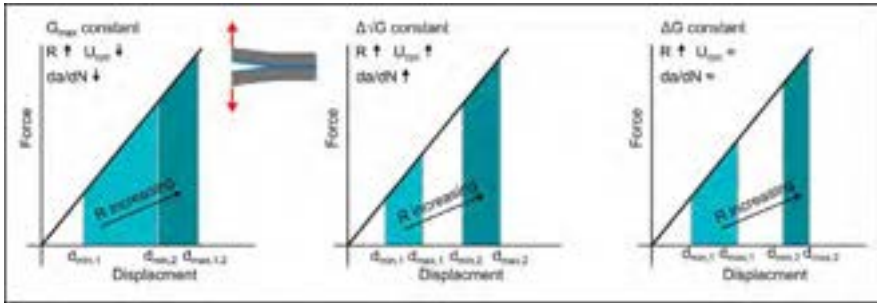


Fig. 19.7 Effect of changing R -ratio on cyclic work (U_{cyc}) and crack growth rate (da/dN) while holding different LEFM parameters constant.

an increase of the resistance to crack growth, that is, the amount of energy required to advance the crack by a unit distance, which results in a reduction of the crack growth rate. The previous discussion is mainly based on data from epoxy adhesives and matrices, though a similar effect of R -ratio on the Paris curve has been reported for a thermoplastic PEEK-based composite [79]. Interestingly, Jia and Davalos [80] reported a different behavior for the case of a resorcinol-formaldehyde adhesive used to bond wood to a fiber-reinforced polymer. There, an increasing da/dN for a constant ΔG resulted in an increased crack growth rate. Further research is still needed to understand the physics of this R -ratio effect.

This lack of understanding means that there is as yet no theoretical model that can a priori quantitatively predict the R -ratio effect on the crack growth rate. Instead, an empirical model is needed that can account for the R -ratio. The most basic approach is to experimentally determine the values of the coefficient and exponent in Eq. (19.5) for different R -ratios. This will require a substantial experimental effort, and is therefore undesirable. Instead, the basic form of Eq. (19.5) can be modified to either explicitly include the R -ratio as an input variable, or to describe the load cycle by two parameters. Various options have been presented in the literature, mainly based on data from epoxy systems. One possibility is the use of the Hartman-Schijve equation, as proposed by Jones and Kinloch [81,82]:

$$\frac{da}{dN} = D(\Delta\kappa)^n = D \left[\frac{\Delta\sqrt{G} - \Delta\sqrt{G_{thr}}}{\sqrt{1 - \sqrt{G_{max}/A}}} \right]^n \tag{19.6}$$

where $\Delta\sqrt{G_{thr}}$ is the value of $\Delta\sqrt{G}$ at the threshold below which no significant fatigue crack growth occurs and A is the critical value of G_{max} , at which the crack growth rate asymptotically goes to infinity. A is therefore close to the quasistatic fracture toughness G_c , but not necessarily equal to it. Because this expression uses two parameters to specify the fatigue cycle (i.e., G_{max} and $\Delta\sqrt{G}$), it can uniquely define the cycle. In addition to this, Jones and Kinloch suggest accounting for the R -ratio by varying the value of $\Delta\sqrt{G_{thr}}$ [81]. Similarly, adjusting the value of $\Delta\sqrt{G_{thr}}$ and A ,

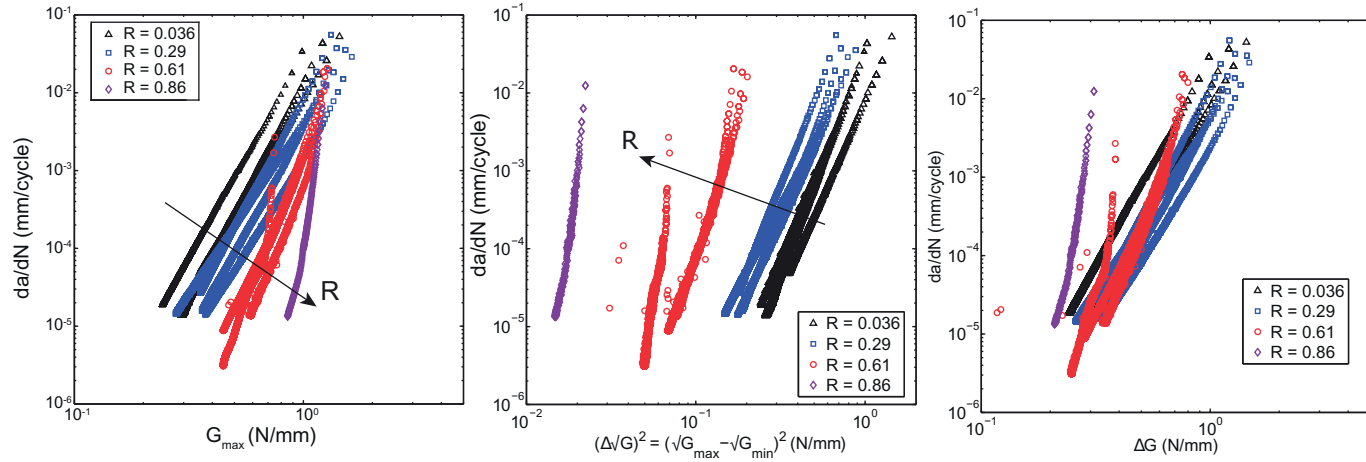


Fig. 19.8 Effect of different R -ratios depending on the chosen LEFM similitude parameter. Data showing crack growth in an epoxy adhesive from [77].

based on experimental data, can capture the effect of temperature, mode mix, and adhesive thickness and collapse the data onto a single master curve [82]. The other two parameter models are those of Khan [83]:

$$\frac{da}{dN} = C_1 G_{\max}^{n_1} + C_2 \Delta G^{n_2} \quad (19.7)$$

and Atodaria et al. [84]:

$$\frac{da}{dN} = C \left[\left(\sqrt{G} \right)_{\text{average}}^{\gamma} \left(\Delta \sqrt{G} \right)^{1-\gamma} \right]^n \quad (19.8)$$

$$\sqrt{G_{\text{average}}} = \left[\frac{1}{k} \sum_{\sqrt{G_{\text{thr}}} }^{\sqrt{G_{\text{max}}}} \left(\sqrt{G} \right)^w \right]^{\frac{1}{w}} \quad (19.9)$$

where the range from $\sqrt{G_{\text{thr}}}$ to $\sqrt{G_{\text{max}}}$ is divided into k increments, w is an experimentally determined weight factor, and γ is an empirical mean stress sensitivity parameter. Instead of using two parameters to describe the load cycle, one can instead explicitly include the R -ratio in the equation, as in the model of Allegrri et al. [85]:

$$\frac{da}{dN} = C \left(\frac{G_{II,\max}}{G_{IIc}} \right)^{\frac{n}{(1-R)^2}} \quad (19.10)$$

Eq. (19.10) is formulated in terms of the mode II SERR, but of course a similar formulation could be made for mode I crack growth. The models mentioned above only give limited insight into the physical mechanisms underlying the fatigue crack growth process. Nevertheless, as an engineering approach they can provide accurate crack growth rate predictions under different R -ratios, if suitable experimental data are available.

19.6.3 Mode mix

In structural applications, bonded joints will often be subjected to mixed-mode loading (also discussed in Chapters 17 and 32), and the mode-mixity can vary along the crack front. In some cases, especially if there is tension-compression fatigue inducing buckling in the adherends, the mode-mix could even change depending on the phase of the load cycle. Therefore, understanding the effect of mode-mixity on crack growth rate and/or fatigue life is an area of active research [63,72,86–92].

In general, it can be stated that crack growth under mode I loading for a given applied G -value is much faster than under mode II, and that mixed-mode crack growth rates will be somewhere in between [88,90,92]. However, Dillard et al. [93] have shown that in some cases the quasistatic fracture toughness under mode II loading is lower than under mode I loading. Similarly, the critical total energy release rate

($G_T = G_I + G_{II}$) could be lower than the critical rate for either of the pure modes. Dillard et al. explained this behavior by suggesting that shearing could steer the crack to areas that had lower resistance to crack growth. While Dillard et al. investigated quasistatic crack growth, there is a good chance their results will also hold for fatigue crack growth. This suggests that simply basing crack growth calculations on the mode I behavior might not always be conservative for fatigue. Instead, the fatigue crack growth rates should be characterized for a range of mode-mix ratios, or using a geometry that will reproduce the mode-mixity that will be encountered in the intended design (e.g., the CLS configuration).

A very straightforward approach to dealing with mode-mixity is to simply compute the total SERR, G_T , and insert this into an equation with the form of Eq. (19.5). However, in this case the coefficient and exponent will be different for different mode-mix ratios [90,94]. Kenane and Benzeggagh therefore proposed explicitly making both the exponent and coefficient in the Paris equation (Eq. 19.5) functions of the ratio G_{II}/G_T [94]. Instead of varying the Paris parameters, Jones et al. [81,95] propose using Eq. (19.6), but with a value of $\Delta\sqrt{G_{th}}$ that depends on the mode-mix. An alternative approach has more recently been proposed by Quaresimin et al. [90]. In their approach, which was validated experimentally for a two-part epoxy adhesive, the crack growth rate at mode-mixity values G_{II}/G_T below 0.5 is predicted purely based on the mode I component, with ΔG_I as the controlling parameter. For mode-mixity values above 0.5, the controlling parameter is instead ΔS , where S is the average of the maximum principal stress in a given control volume, which is taken to be representative for the process zone. Prediction of mixed mode crack growth can also be addressed numerically via a cohesive zone model, as for example in the work of Robinson et al. [96], de Moura and Gonçalves [71], Tserpes and Floros [72], Zhang et al. [63], Hosseini-Toudeshky et al. [62], Rocha et al. [70], and Moreira et al. [86]. The precise approach taken differs, but all the mentioned works assume that a cohesive element is fully damaged when exceeding a criterion of the form:

$$\left(\frac{G_I}{G_{Ic}}\right)^{\alpha/2} + \left(\frac{G_{II}}{G_{IIc}}\right)^{\alpha/2} = 1 \quad (19.11)$$

Additionally, a damage parameter is introduced in the constitutive law of the cohesive element, which allows the fatigue-driven damage progression to be modeled, usually by matching the crack growth rate given by some variation of Eq. (19.5).

Most researchers simply take $\alpha = 2$, that is, a linear fracture criterion, but Robinson et al. [96] preferred an elliptical criterion with $2 \leq \alpha \leq 4$. Zhang et al. also use a linear criterion, but introduce a coupling in the traction-separation relations [63]. Rocha et al. [70] instead make use of the Benzeggagh-Kenane criterion [97]. Tserpes and Floros have shown that such a technique (if suitable experimental calibration data are available) can predict not just the crack length, but also for example the twisting of the crack front that occurs in a cracked lap shear specimen based on an epoxy adhesive [72].

19.6.4 Variable amplitude

So far, only a few researchers have attempted to apply fracture mechanics-based models to variable amplitude fatigue. Erpolat et al. [42] applied a numerical integration of Eq. (19.5) to predict the crack length, thereby assuming a linear damage accumulation. However, when compared to experiments on a single part epoxy paste adhesive, they found that the prediction tended to underestimate the crack length, especially after an overload. They attributed this to the model not taking into account that the overload creates a damage zone ahead of the crack tip, which accelerates the crack growth in subsequent cycles. This argument seems reasonable for brittle adhesives, but may not apply to more ductile adhesives. Ashcroft suggested taking the overload effect into account by shifting the constant amplitude fatigue crack growth rate vs the SERR range curve [98]. More recently, Hosseini-Toudeshky et al. [99] and Khoramishad et al. [100] proposed using CZM-based progressive damage models to predict the effect of VA fatigue loading. Khoramishad et al. [100] also presented an experimental validation with data from a toughened epoxy film adhesive, which showed good agreement with the model.

19.7 Effect of joint features

Various geometrical and material features of a joint will affect its fatigue performance. The adherend stiffness (i.e., elastic modulus and dimensions) and geometrical shape (e.g., tapered vs constant thickness adherends) will affect the stress distribution in the joint, and thereby also the fatigue life. The overlap length will (beyond a certain minimum length) typically not affect the peak stresses. However, the longer the overlap, the further a crack can grow before the remaining material fails. In this way, the overlap length can still affect the fatigue life of the joint.

The importance of the surface treatment on joint strength has already been discussed, and this is also dependent on failure mode. If the damage mode remains a cohesive failure of the adhesive, the surface treatment does not have a large effect. For example, the study of Azari et al. [101] suggested that as long as the crack propagates within the adhesive sufficiently far from the interface, it is not affected by the surface roughness.

Chapter 18 focuses on the effects of adhesive thickness on various properties. Regarding its effect on crack growth rate specifically, this has been investigated by a number of researchers, including Azari et al. [102,103], Chai [104], Krenk et al. [105], Abou-Hamda et al. [106], Mall and Ramamurthy [107], Xu et al. [108], Schmueser [109], Joseph et al. [110], Wilson [111], and Pascoe et al. [112]. In general, it is reported that an increase in bondline thickness results in a lower crack growth rate (at the same applied SERR), which is attributed to a removal of constraint, allowing more plasticity to occur. However, Krenk et al. [105], Schmueser [109], and Pascoe et al. [112] reported a higher crack growth rate for increasing thickness (all for epoxy adhesives). Pascoe et al. further noted that the energy dissipation per unit of crack growth did not appear to be affected by the adhesive thickness, but that a higher thickness resulted in more energy dissipation per cycle, suggesting more energy was

available for crack growth. Chai [104] reported a nonmonotonic behavior for one of the adhesives investigated (PEEK resin). This nonmonotonic behavior was explained by Kinloch and Shaw [113] and Yan et al. [114], who proposed that there is an optimum thickness at which the fracture toughness of the adhesive is maximized. Below this optimum thickness, the plastic zone cannot fully develop while above the optimum thickness, according to Kinloch and Shaw, the plastic zone is less constrained in the thickness direction and therefore does not extend as far ahead of the crack tip. On the other hand, Yan et al. suggested that there is more crack tip blunting, and thus easier void coalescence at higher thicknesses. From the literature, we can thus draw the conclusion that the highest fatigue life can be obtained if the adhesive has the optimum thickness, which can in principle be found by modeling the plastic zone at the crack tip, noting that the plastic zone size is time and temperature dependent.

A step beyond changing the bondline thickness to affect the fatigue life is the inclusion of specific features in the bond to slow or even arrest the growth of cracks. Kruse et al. [115] investigated two options for this: (i) inserting bolts through the adhesive joint, and (ii) using a laser to expose fibers at the surface of a CFRP adherend. The latter approach is used to create through-thickness reinforcement of the adhesive layer. Both approaches appeared to be promising. Chowdhury et al. [116] reported that hybrid joints, combining both fasteners and adhesive, had a higher fatigue life than purely bolted or purely bonded joints. Rather than inserting a bolt through the entire thickness, Löbel et al. [117] and Steinmetz et al. [118] developed a crack stopper based on inserting a different polymer into the bondline. All these strategies of course involve additional manufacturing effort, and thus a careful trade-off is needed at the design stage to decide whether such crack-stopping capability is worth the additional cost. Within the aerospace industry, these approaches are of interest due to the difficulty of certifying adhesive bonds for safety critical structures. Having a proven capability to arrest cracks through a design feature of the bond is seen as a potential strategy for enabling certification [115], as discussed in more detail in [Chapter 23](#).

19.8 Environmental and loading effects

Both the environment and the loading rate can affect the fatigue life. Ramírez et al. [119] recently reviewed the existing literature on the effect of the two most important environmental aspects, temperature and moisture. The review notes that environment and fatigue can have a synergistic effect, where adverse environments (high temperatures and high levels of moisture) cause acceleration of (fatigue) damage accumulation. Ramírez et al. further noted that investigations of environmental effects on fatigue are still largely empirical, and that available models are also still heavily reliant on test data for calibration. A general model for the effect of temperature and moisture on fatigue is still lacking [119].

It is important to note that different adhesives will have a different sensitivity to temperature and moisture. For example, recently Houjou et al. [120] (epoxy), Mu et al. [121] (epoxy), Tan et al. [122] (polyurethane), and Xie et al. [123] (epoxy + sand bonding medium) reported a reduced fatigue life at an increased test temperature. On the other hand, Pugstaller and Wallner [124] saw little difference in the crack growth

rates in tests conducted at 23°C and 60°C on a steel laminate bonded with a waterborne epoxy varnish. They suggested this was due to 60°C being far away from the adhesive's glass transition temperature. An even more remarkable result was found by van den Akker et al. [125]. They investigated fatigue-driven disbonding of composite stiffeners bonded with an epoxy film adhesive, aged by exposure to 90% relative humidity at 80°C for 280–396 days and then tested at room temperature. In this case, the disbond growth rate was found to be slower in the aged panels. Van den Akker et al. attributed this to moisture causing plasticization of the adhesive, which resulted in an increased fracture toughness. Taken together, the results discussed above show the importance of understanding the properties of the specific adhesive being used in a particular application. Even which combination of temperature and moisture will result in the worst-case fatigue behavior may differ from adhesive to adhesive.

A final important effect on fatigue of adhesives is the effect of the loading frequency. At high frequencies, self-heating of the adhesive may occur, in which case the elevated temperature can accelerate the fatigue process. In addition, if the temperature reaches or exceeds the glass transition temperature, sudden stiffness changes may occur, resulting in changes of deformations and redistribution of stresses. Many practical applications will not encounter such high frequencies in service. Nevertheless, the self-heating effect limits the highest loading frequencies that can be applied in laboratory tests, forming an obstacle to conducting accelerated fatigue tests.

At the other end of the scale, at very low frequencies, the adhesive will spend long periods of time in the highly loaded portion of the cycle, and thus interactions between creep and fatigue mechanisms can occur. For adhesive bonds, not much work has been published on this topic. Landes and Begley [126], Nikbin et al. [127], and Saxena [128] all developed time-dependent fracture mechanics parameters to take the creep effect into account. Al-Ghamdi [129] proposed four different methods for dealing with combined creep and fatigue. The first method is to fit a purely empirical crack growth law to experimental data. The second method is to assume that creep and fatigue methods are competing, with the growth rate determined by the dominant mechanism. The third method is to partition the crack growth into a component that is time dependent (i.e., creep-driven) and one that is load cycle dependent (i.e., fatigue driven). The fourth method is an extension of the third method, including an empirical term to account for interaction between creep and fatigue mechanisms. A partition method has also been proposed by Movahedi-Rad et al. [130]. In their method, a stress vs time-to-failure curve is predicted based on a combination of the cyclic loading and creep contributions. Each of the individual contributions is scaled based on the energy dissipation in each damage mode. Given that in practical applications adhesive joints may spend a significant portion of their life at high loads, further research into creep-fatigue interactions is called for.

19.9 Damage mechanics

Damage mechanics is an approach to predicting failure in a material by relating the applied load to a deterioration in mechanical properties, which may include stiffness, strength and/or fracture resistance, and resistance to fatigue loading. The aim in

damage mechanics is to enable a quantitative representation of load-induced microdamage, such as that commonly observed in areas of high stress concentration prior to the formation of a macrocrack. In an adhesively bonded joint, stress and, hence, any load-induced damage, will tend to be localized. Hence, we may have some areas of the joint undamaged, some areas in various states of damage, and some areas having failed. The net effect of this variation in damage across the joint will always be a net decrease in resistance to further loading compared to the joint prior to loading. A feature of fatigue loading is that the damage across the joint will progressively increase as a function of fatigue cycles until there is sufficient damage to cause complete failure of the joint. An advantage of the damage mechanics approach, compared to other fatigue modeling methods, is that it more closely represents damage evolution as a function of cycling and hence is better placed to determine the residual strength and stiffness at any point in the fatigue life. It can also be used with NDE techniques as part of a health monitoring scheme. The disadvantages of damage mechanics methods are that they tend to be more complex and require more input parameters than alternative fatigue modeling methods.

Two forms of progressive damage modeling that have been used with adhesive joints are cohesive zone modeling (CZM), where the failure is localized along a plane, and continuum damage modeling (CDM), where the damage is in a more extended damage, or process, zone. CZM can be viewed as an extension to the fracture mechanics approach for modeling fatigue behavior, and as such is discussed in the previous section. Hence, this section will be limited to the application of CDM to the prediction of fatigue failure in adhesively bonded joints.

Continuum damage mechanics (CDM) requires a damage variable, D , to be defined as a measure of the severity of the material damage [131–133]. It is assumed that D is equal to 0 for undamaged material and $D = 1$ represents the complete rupture of the material. A simple method of defining D is to relate damage to a reduction in stiffness:

$$D = 1 - \frac{E_D}{E} \quad (19.12)$$

where E and E_D are the Young's modulus of the undamaged and damaged material, respectively. A damage equivalent effective stress, σ_{eff}^* , can be related to damage as:

$$\sigma_{\text{eff}}^* = \frac{\sigma^*}{(1 - D)} \quad (19.13)$$

where σ^* is the damage equivalent stress, which is defined as:

$$\sigma^* = \sigma_{\text{eq}} \left[\frac{2}{3} (1 + \nu) + 3(1 - 2\nu) \left(\frac{\sigma_H}{\sigma_{\text{eq}}} \right)^2 \right]^{\frac{1}{2}} \quad (19.14)$$

where σ_{eq} is the von Mises equivalent stress and σ_H is the hydrostatic stress. σ_{eff}^* can be used as a quasistatic failure criterion. However, to apply the CDM approach to fatigue,

Lemaitre [131,132] derived the following equation for the rate of damage accumulation as a function of fatigue cycles, $\delta D/\delta N$:

$$\frac{\delta D}{\delta N} = \frac{2B_0 \left[\frac{2}{3}(1+\nu) + 3(1-2\nu) \left(\frac{\sigma_H}{\sigma_{eq}} \right)^2 \right]^{s_o}}{(\beta_o + 1)(1-D)^{\beta_o+1}} \left(\sigma_{eq,max}^{\beta_o+1} - \sigma_{eq,min}^{\beta_o+1} \right) \quad (19.15)$$

where s_o , B_o , and β_o are material- and temperature-dependent coefficients, and $\sigma_{eq,max}$ and $\sigma_{eq,min}$ are maximum and minimum von Mises equivalent stresses in a fatigue cycle, respectively. Eq. (19.15) can be integrated for constant amplitude fatigue loading. Using the boundary conditions ($N=0 \rightarrow D=0$) and ($N=N_R$ [number of cycles to rupture] $\rightarrow D=1$):

$$N_R = \frac{(\beta_o + 1) \left(\sigma_{eq,max}^{\beta_o+1} - \sigma_{eq,min}^{\beta_o+1} \right)^{-1}}{2(\beta_o + 2)\beta_o \left[\frac{2}{3}(1+\nu) + 3(1-2\nu) \left(\frac{\sigma_H}{\sigma_{eq}} \right)^2 \right]^{s_o}} \quad (19.16)$$

Abdel Wahab et al. [134] used this CDM approach to predict fatigue thresholds in CFRP/epoxy lap-strap joints and double-lap joints. They found that the predictions using CDM compared favorably with those using fracture mechanics. The method was extended to predict fatigue damage in bulk adhesive samples [135] and aluminum/epoxy single-lap joints by Hilmy et al. [136]. A simplified equation for small stress ratio values was also derived, assuming an initial condition of $D=0$;

$$D = 1 - \left[1 - A(\beta + m + 1) \Delta\sigma_{eq}^{\beta+m} R_v^{\frac{\beta}{2}} N \right]^{\frac{1}{\beta+m+1}} \quad (19.17)$$

where $\Delta\sigma_{eq}$ is the von Mises stress range, R_v is the triaxiality function (which is the square of the ratio of the damage equivalent stress to the von Mises equivalent stress), m is the power constant in the Ramberg-Osgood equation, and A and β are experimentally determined damage parameters. The number of cycles to failure (N_f) can be determined from the equation when $D=1$ and $N=N_f$ at the fully damaged state as:

$$N_f = \frac{\Delta\sigma_{eq}^{-\beta-m} R_v^{-\frac{\beta}{2}}}{A(\beta + m + 1)} \quad (19.18)$$

A and β are experimentally determined damage parameters. Abdel Wahab et al. [134] used two points from constant amplitude fatigue experiments of CFRP-epoxy double-lap joints to determine these parameters for a particular adhesive at a particular temperature, and showed that Eq. (19.18) could accurately predict a stress life (S - N) curve.

Wahab et al. [137] extended this approach to the low cycle fatigue of bulk adhesive. In this case, the damage evolution curves were derived assuming isotropic damage and

a stress triaxiality function equal to one. Application of this method to single-lap joints [138] required determination of the triaxiality function to account for the multiaxial stress state in the joint, and it was seen that this value varied along the adhesive layer. The dependency of the triaxiality function on the joint type was further investigated by Wahab [139,140] in later work.

Although the CDM approach described above enabled the progressive degradation of the adhesive layer to be characterized, it did not allow the initiation and propagation phases of fatigue to be explicitly modeled. Ashcroft et al. [141] used a simple CDM-based approach to progressively model the initiation and evolution of damage in an adhesive joint, leading to crack formation and growth. In this approach, the damage rate dD/dN was assumed to be a power law function of the localized equivalent plastic strain range, $\Delta\varepsilon_p$, that is,

$$\frac{dD}{dN} = C_D (\Delta\varepsilon_p)^{m_D} \quad (19.19)$$

where C_D and m_D are experimentally derived constants. The rate of damage was determined from FEA using Eq. (19.19) and the element properties were degraded as:

$$\begin{aligned} E &= E_0(1 - D) \\ \sigma_{yp} &= \sigma_{yp0}(1 - D) \\ \beta &= \beta_0(1 - D) \end{aligned} \quad (19.20)$$

where E_0 , σ_{yp0} , and β_0 are the Young's modulus, yield stress, and plastic surface modifier constant for the parabolic Mohr-Coulomb model, respectively, and $D = 1$ represents a fully damaged element, which was used to define the macrocrack length. E , σ_{yp} , and β are the values of the Young's modulus, yield stress, and plastic surface modifier constant, respectively, after incorporating the material damage. Shenoy et al. [142] showed that this method could be used to predict total-life plots, the fatigue initiation life, fatigue crack growth curves, and strength and stiffness wearout plots; hence, they termed this a unified fatigue methodology (UFM). Shenoy et al. [143] later showed that this approach could also be applied to variable amplitude fatigue.

Walander et al. [144] experimentally studied mode I fatigue crack growth in rubber- and polyurethane-based adhesives using a double-cantilever beam specimen. A damage growth law with a constitutive relation for the adhesive material degradation was implemented in a commercial finite element code. The presented damage evolution law was of the form:

$$\frac{dD}{dN} = \alpha \left(\frac{\sigma}{1-D} - \sigma_{th} \right)^\beta \quad (19.21)$$

The material parameters: α , β , and σ_{th} , were determined experimentally and good correlation between the experimental data and the proposed damage law for fatigue was reported.

19.10 Summary

This chapter has summarized the current state of the art with regard to evaluating and predicting fatigue of adhesive bonds, which is critical to ensuring their long-term structural integrity. Four broad categories of fatigue models exist, which are stress/strain-life models, strength/stiffness wearout models, damage mechanics, and fracture mechanics. All adhesive fatigue models are still strongly reliant on experimental data for calibration, and an underlying physical theory for predicting the fatigue behavior is still lacking. When generating experimental data, care needs to be taken that the experiments are sufficiently representative of the application of interest, especially ensuring that the same failure mode is observed. Additionally, consideration should be given to stress distributions within the joint (including the proportions of peel and shear stresses) as well as the effects of manufacturing processes, loading frequency, and operational environment.

References

- [1] J.Y. Goh, S. Georgiadis, A.C. Orifici, and C.H. Wang, "Effects of bondline flaws on the damage tolerance of composite scarf joints," *Compos. Part A Appl. Sci. Manuf.*, vol. 55, pp. 110–119, 2013.
- [2] J. Kupski, S. Teixeira de Freitas, D. Zarouchas, P.P. Camanho, and R. Benedictus, "Composite layup effect on the failure mechanism of single lap bonded joints," *Compos. Struct.*, vol. 217 December 2018, pp. 14–26, 2019.
- [3] A. Graner Solana, A.D. Crocombe, and I.A. Ashcroft, "Fatigue life and backface strain predictions in adhesively bonded joints," *Int. J. Adhes. Adhes.*, vol. 30, no. 1, pp. 36–42, 2010.
- [4] Z. Zhang, J.K. Shang, and F.V. Lawrence, "A backface strain technique for detecting fatigue crack initiation in adhesive joints," *J. Adhes.*, vol. 49, no. 1–2, pp. 23–36, 1995.
- [5] D.R. Lefebvre, B.K. Ahn, D.A. Dillard, and J.G. Dillard, "The effect of surface treatments on interfacial fatigue crack initiation in aluminum/epoxy bonds," *Int. J. Fract.*, vol. 114, no. 2, pp. 191–202, 2002.
- [6] M.Z. Sadeghi *et al.*, "Damage detection in adhesively bonded single lap joints by using backface strain: proposing a new position for backface strain gauges," *Int. J. Adhes. Adhes.*, vol. 97, 2019, p. 102494, 2020.
- [7] D.R. Lefebvre and D.A. Dillard, "A stress singularity approach for the prediction of fatigue crack initiation in adhesive bonds. Part 1: theory," *J. Adhes.*, vol. 70, no. 1–2, pp. 119–138, 1999.
- [8] D.R. Lefebvre, D.A. Dillard, and J.G. Dillard, "A stress singularity approach for the prediction of fatigue crack initiation in adhesive bonds. Part 2: experimental," *J. Adhes.*, vol. 70, no. 1–2, pp. 139–154, 1999.
- [9] G. Zambelis, T. Da Silva Botelho, O. Klinkova, I. Tawfiq, and C. Lanouette, "Evaluation of the energy release rate in mode I of asymmetrical bonded composite/metal assembly," *Eng. Fract. Mech.*, vol. 190, pp. 175–185, 2018.
- [10] G. Zambelis, T. Da Silva Botelho, O. Klinkova, I. Tawfiq, and C. Lanouette, "A new approach in testing fatigue fracture mechanics properties in asymmetrical bonded composite/metal assemblies," *Compos. Part B Eng.*, vol. 158, 2018, pp. 390–399, 2019.

- [11] L. Adamos and T. Loutas, "Challenges in the fatigue crack growth characterization of metal/composite joints: a compliance-based investigation of a Ti/CFRP joint," *Int. J. Fatigue*, vol. 148, p. 106233, 2021.
- [12] W.D. Hartley *et al.*, "Fracture characterization of overmold composite adhesion," *J. Thermoplast. Compos. Mater.*, vol. 35, no. 7, pp. 977–997, 2022.
- [13] Y.H. Lai, M.D. Rakestraw, and D.A. Dillard, "The cracked lap shear specimen revisited—a closed form solution," *Int. J. Solids Struct.*, vol. 33, no. 12, pp. 1725–1743, 1996.
- [14] M.K. Budzik *et al.*, "Testing mechanical performance of adhesively bonded composite joints in engineering applications: an overview," *J. Adhes.*, 2021.
- [15] J.A. Pascoe, C.D. Rans, and R. Benedictus, "Characterizing fatigue delamination growth behaviour using specimens with multiple delaminations: the effect of unequal delamination lengths," *Eng. Fract. Mech.*, vol. 109, pp. 150–160, 2013.
- [16] R. Sahin and S. Akpınar, "The effects of adhering thickness on the fatigue strength of adhesively bonded single-lap joints," *Int. J. Adhes. Adhes.*, vol. 107, p. 102845, 2021.
- [17] A.I.M. Foletti, J. Sena Cruz, and A.P. Vassilopoulos, "Fabrication and curing conditions effects on the fatigue behavior of a structural adhesive," *Int. J. Fatigue*, vol. 139, p. 105743, 2020.
- [18] W. Seneviratne, J. Tomblin, and M. Kittur, "Durability and residual strength of adhesively-bonded composite joints: the case of F/A-18 A-D wing root stepped-lap joint," in *Fatigue and Fracture of Adhesively-Bonded Composite Joints*, A.P. Vassilopoulos, Ed. Cambridge: Elsevier, 2015, pp. 289–320.
- [19] E.M. Mueller, S. Starnes, N. Strickland, P. Kenny, and C. Williams, "The detection, inspection, and failure analysis of a composite wing skin defect on a tactical aircraft," *Compos. Struct.*, vol. 145, pp. 186–193, 2016.
- [20] A. Wöhler, "Versuche über die Festigkeit der Eisenbahnwagenachsen," *Zeitschrift für Bauwes.*, vol. 10, 1867.
- [21] A.J. Kinloch and S.O. Osiyemi, "Predicting the fatigue life of adhesively-bonded joints," *J. Adhes.*, vol. 43, no. 1–2, pp. 79–90, 1993.
- [22] M.M. Abdel Wahab, I.A. Ashcroft, A.D. Crocombe, and P.A. Smith, "Numerical prediction of fatigue crack propagation lifetime in adhesively bonded structures," *Int. J. Fatigue*, vol. 24, no. 6, pp. 705–709, 2002.
- [23] J.A. Harris and P.A. Fay, "Fatigue life evaluation of structural adhesives for automotive applications," *Int. J. Adhes. Adhes.*, vol. 12, no. 1, pp. 9–18, 1992.
- [24] A.D. Crocombe, C.Y. Ong, C.M. Chan, M.M. Abdel Wahab, and I.A. Ashcroft, "Investigating fatigue damage evolution in adhesively bonded structures using backface strain measurement," *J. Adhes.*, vol. 78, no. 9, pp. 745–776, 2002.
- [25] A.G. Solana, A.D. Crocombe, M.M.A. Wahab, and I.A. Ashcroft, "Fatigue initiation in adhesively-bonded single-lap joints," *J. Adhes. Sci. Technol.*, vol. 21, no. 14, pp. 1343–1357, 2007.
- [26] V. Shenoy, I.A. Ashcroft, G.W. Critchlow, A.D. Crocombe, and M.M. Abdel Wahab, "An investigation into the crack initiation and propagation behaviour of bonded single-lap joints using backface strain," *Int. J. Adhes. Adhes.*, vol. 29, no. 4, pp. 361–371, 2009.
- [27] M. Dessureault and J.K. Spelt, "Observations of fatigue crack initiation and propagation in an epoxy adhesive," *Int. J. Adhes. Adhes.*, vol. 17, no. 3, pp. 183–195, 1997.
- [28] M. Qaresimin and M. Ricotta, "Fatigue behaviour and damage evolution of single lap bonded joints in composite material," *Compos. Sci. Technol.*, vol. 66, no. 2, pp. 176–187, 2006.
- [29] A. Palmgren, "Die lebensdauer von kugellagen," *Z. Ver. Dtsch. Zucker Ind.*, vol. 68, pp. 339–41, 1924.

- [30] M.A. Miner, "Cumulative damage in fatigue," *J. Appl. Mech.*, vol. 12, pp. 159–64, 1945.
- [31] S.M. Marco and W.L. Starkey, "A concept of fatigue damage," *Trans. Am. Soc. Mech. Eng.*, vol. 76, pp. 626–662, 1954.
- [32] D.L. Henry, "A theory of fatigue damage accumulation in steel," *Trans. Am. Soc. Mech. Eng.*, vol. 9, no. 13, p. 918, 1955.
- [33] H.L. Leve, "Cumulative damage theories," in *Metal Fatigue: Theory and Design*, NY, USA: John Wiley & Sons, 1969, pp. 170–203.
- [34] M.J. Owen and R.J. Howe, "The accumulation of damage in a glass-reinforced plastic under tensile and fatigue loading," *J. Phys. D. Appl. Phys.*, vol. 5, no. 9, pp. 1637–1649, 1972.
- [35] I.P. Bond, "Fatigue life prediction for GRP subjected to variable amplitude loading," *Compos. Part A Appl. Sci. Manuf.*, vol. 30, no. 8, pp. 961–970, 1999.
- [36] S. Erpolat, I.A. Ashcroft, A.D. Crocombe, and M.M. Abdel-Wahab, "A study of adhesively bonded joints subjected to constant and variable amplitude fatigue," *Int. J. Fatigue*, vol. 26, no. 11, pp. 1189–1196, 2004.
- [37] M.M.A. Wahab, I.A. Ashcroft, A.D. Crocombe, D.J. Hughes, and S.J. Shaw, "Effect of environment on the fatigue of bonded composite joints. Part 2: fatigue threshold prediction," *Compos. Part A Appl. Sci. Manuf.*, vol. 32, no. 1, pp. 59–69, 2001.
- [38] V. Shenoy, I.A. Ashcroft, G.W. Critchlow, A.D. Crocombe, and M.M. Abdel Wahab, "Strength wearout of adhesively bonded joints under constant amplitude fatigue," *Int. J. Fatigue*, vol. 31, no. 5, pp. 820–830, 2009.
- [39] V. Shenoy, I.A. Ashcroft, G.W. Critchlow, A.D. Crocombe, and M.M. Abdel Wahab, "An evaluation of strength wearout models for the lifetime prediction of adhesive joints subjected to variable amplitude fatigue," *Int. J. Adhes. Adhes.*, vol. 29, no. 6, pp. 639–649, 2009.
- [40] J.R. Schaff and B.D. Davidson, "Life prediction methodology for composite structures. Part I—constant amplitude and two-stress level fatigue," *J. Compos. Mater.*, vol. 31, no. 2, pp. 128–157, 1997.
- [41] J.R. Schaff and B.D. Davidson, "Life prediction methodology for composite structures. Part II—spectrum fatigue," *J. Compos. Mater.*, vol. 31, no. 2, pp. 158–181, 1997.
- [42] S. Erpolat, I.A. Ashcroft, A.D. Crocombe, and M.M. Abdel-Wahab, "Fatigue crack growth acceleration due to intermittent overstressing in adhesively bonded CFRP joints," *Compos. Part A Appl. Sci. Manuf.*, vol. 35, no. 10, pp. 1175–1183, 2004.
- [43] D.M. Neto, E.R. Sérgio, M.F. Borges, L.P. Borrego, and F.V. Antunes, "Effect of load blocks on fatigue crack growth," *Int. J. Fatigue*, vol. 162, p. 107001, 2022.
- [44] A.T. Dibenedetto and G. Salee, "Fatigue crack propagation in, graphite fiber reinforced nylon 66," *Polym. Eng. Sci.*, vol. 19, no. 7, pp. 512–518, 1979.
- [45] J.N. Yang, D.L. Jones, S.H. Yang, and A. Meskini, "A stiffness degradation model for graphite/epoxy laminates," *J. Compos. Mater.*, pp. 753–769, 1990.
- [46] H.A. Whitworth, "Cumulative damage in composites," *J. Eng. Mater. Technol.*, vol. 112, no. 3, pp. 358–361, 1990.
- [47] Y. Liu, X. Zhang, S. Lemanski, H.Y. Nezhad, and D. Ayre, "Experimental and numerical study of process-induced defects and their effect on fatigue debonding in composite joints," *Int. J. Fatigue*, vol. 125, 2018, pp. 47–57, 2019.
- [48] P.C. Paris, M.P. Gomez, and W.E. Anderson, "A rational analytic theory of fatigue," *Trend Eng.*, vol. 13, pp. 9–14, 1961.
- [49] S. Mostovoy and E.J. Ripling, "Flaw tolerance of a number of commercial and experimental adhesives," in *Adhesion Science and Technology*, no. 9B, L.-H. Lee, Ed. New York: Plenum Press, 1975, pp. 513–562.

- [50] C. Rans, R.C. Alderliesten, and R. Benedictus, "Misinterpreting the results: how similitude can improve our understanding of fatigue delamination growth," *Compos. Sci. Technol.*, vol. 71, pp. 230–238, 2011.
- [51] J.A. Pascoe, R.C. Alderliesten, and R. Benedictus, "Methods for the prediction of fatigue delamination growth in composites and adhesive bonds—a critical review," *Eng. Fract. Mech.*, vol. 112–113, pp. 72–96, 2013.
- [52] I.A. Ashcroft and A. Mubashar, "Fatigue," in *Adhesive Bonding—Science, Technology and Applications*, second ed., R.D. Adams, Ed. Duxford: Woodhead Publishing, 2021, pp. 317–361.
- [53] M.M. Abdel Wahab, "Fatigue in adhesively bonded joints: a review," *ISRN Mater. Sci.*, vol. 2012, no. c, pp. 1–25, 2012.
- [54] P. Gaur and R.S. Prasad, "Investigation of fatigue crack propagation in adhesively bonded joints using fatigue testing, finite element analysis and neural networks," *Appl. Eng. Lett.*, vol. 4, no. 4, pp. 136–149, 2019.
- [55] Q. Chen, H. Guo, K. Avery, X. Su, and H. Kang, "Fatigue performance and life estimation of automotive adhesive joints using a fracture mechanics approach," *Eng. Fract. Mech.*, vol. 172, pp. 73–89, 2017.
- [56] W.J. Lai and J. Pan, "Stress intensity factor solutions for adhesive-bonded lap-shear specimens of magnesium and steel sheets with and without kinked cracks for fatigue life estimations," *Eng. Fract. Mech.*, vol. 131, pp. 454–470, 2014.
- [57] E.F. Rybicki and M.F. Kanninen, "A finite element calculation of stress intensity factors by a modified crack closure integral," *Eng. Fract. Mech.*, vol. 9, no. 4, pp. 931–938, 1977.
- [58] G.R. Irwin, "Analysis of stresses and strains near the end of a crack traversing a plate," *J. Appl. Mech.*, vol. 24, no. 3, pp. 361–364, 1957.
- [59] R. Krueger, "Virtual crack closure technique: history, approach, and applications," *Appl. Mech. Rev.*, vol. 57, no. 1–6, pp. 109–143, 2004.
- [60] L.R. Deobald *et al.*, "Guidelines for VCCT-Based Interlaminar Fatigue and Progressive Failure Finite Element Analysis," NASA/TM–2017-219663, 2017.
- [61] M.F.S.F. De Moura and J.P.M. Gonçalves, "Cohesive zone model for high-cycle fatigue of adhesively bonded joints under mode I loading," *Int. J. Solids Struct.*, vol. 51, no. 5, pp. 1123–1131, 2014.
- [62] H. Hosseini-Toudeshky, F. Shebanian, H.R. Ovesy, and M.S. Goodarzi, "Prediction of interlaminar fatigue damages in adhesively bonded joints using mixed-mode strain based cohesive zone modeling," *Theor. Appl. Fract. Mech.*, vol. 106, p. 102480, 2020.
- [63] W. Zhang, Z. Tang, Y. Yang, J. Wei, and P. Stanislav, "Mixed-mode debonding behavior between CFRP plates and concrete under fatigue loading," *J. Struct. Eng.*, vol. 147 (5), p. 04021055, 2021.
- [64] K. Tserpes *et al.*, "A review on failure theories and simulation models for adhesive joints," *J. Adhes.*, pp. 1–61, 2021.
- [65] R.D.F. Moreira, M.F.S.F. de Moura, F.G.A. Silva, F.M.G. Ramírez, and F.D.R. Silva, "Numerical comparison of several composite bonded repairs under fatigue loading," *Compos. Struct.*, vol. 243, p. 112250, 2020.
- [66] A. Pirondi and F. Moroni, "Improvement of a cohesive zone model for fatigue delamination rate simulation," *Materials (Basel)*, vol. 12, no. 1, pp. 1–17, 2019.
- [67] A. Pirondi, G. Giuliese, and F. Moroni, "Fatigue debonding three-dimensional simulation with cohesive zone," *J. Adhes.*, vol. 92, no. 7–9, pp. 553–571, 2016.
- [68] A. Pirondi, G. Giuliese, F. Moroni, A. Bernasconi, and A. Jamil, "Comparative study of cohesive zone and virtual crack closure techniques for three-dimensional fatigue debonding," *J. Adhes.*, vol. 90, no. 5–6, pp. 457–481, 2014.

- [69] A. Pironi and F. Moroni, "Simulation of mixed-mode I/II fatigue crack propagation in adhesive joints with a modified cohesive zone model," *J. Adhes. Sci. Technol.*, vol. 25, no. 18, pp. 2483–2499, 2011.
- [70] A.V.M. Rocha *et al.*, "Numerical analysis of mixed-mode fatigue crack growth of adhesive joints using CZM," *Theor. Appl. Fract. Mech.*, vol. 106, 2019, p. 102493, 2020.
- [71] M.F.S.F. de Moura and J.P.M. Gonçalves, "Cohesive zone model for high-cycle fatigue of composite bonded joints under mixed-mode I+II loading," *Eng. Fract. Mech.*, vol. 140, pp. 31–42, 2015.
- [72] K. Tserpes and I. Floros, "Fatigue crack growth simulation in adhesively bonded composite joints," *Fatigue Fract. Eng. Mater. Struct.*, vol. 42, no. 7, pp. 1430–1440, 2019.
- [73] D.S. Dugdale, "Yielding of steel sheets containing slits," *J. Mech. Phys. Solids*, vol. 8, no. 2, pp. 100–104, 1960.
- [74] G.I. Barenblatt, "The mathematical theory of equilibrium cracks in brittle fracture," in *Advances in Applied Mechanics*, 1962, vol. 7, pp. 55–129.
- [75] A. Pironi and F. Moroni, "A progressive damage model for the prediction of fatigue crack growth in bonded joints," *J. Adhes.*, vol. 86, no. 5–6, pp. 501–521, 2010.
- [76] F. Moroni and A. Pironi, "A procedure for the simulation of fatigue crack growth in adhesively bonded joints based on the cohesive zone model and different mixed-mode propagation criteria," *Eng. Fract. Mech.*, vol. 78, no. 8, pp. 1808–1816, 2011.
- [77] J.A. Pascoe, R.C. Alderliesten, and R. Benedictus, "On the physical interpretation of the R-ratio effect and the LFM parameters used for fatigue crack growth in adhesive bonds," *Int. J. Fatigue*, vol. 97, pp. 162–176, 2017.
- [78] R. Jones, A.J. Kinloch, and W. Hu, "Cyclic-fatigue crack growth in composite and adhesively-bonded structures: the FAA slow crack growth approach to certification and the problem of similitude," *Int. J. Fatigue*, vol. 88, pp. 10–18, 2016.
- [79] J. Andersons, M. Hojo, and S. Ochiai, "Empirical model for stress ratio effect on fatigue delamination growth rate in composite laminates," *Int. J. Fatigue*, vol. 26, no. 6, pp. 597–604, 2004.
- [80] J. Jia and J.F. Davalos, "Study of load ratio for mode-I fatigue fracture of wood-FRP-bonded interfaces," *J. Compos. Mater.*, vol. 38, no. 14, pp. 1211–1230, 2004.
- [81] R. Jones, W. Hu, and A.J. Kinloch, "A convenient way to represent fatigue crack growth in structural adhesives," *Fatigue Fract. Eng. Mater. Struct.*, vol. 38, no. 4, pp. 379–391, 2015.
- [82] R. Jones, A.J. Kinloch, J. Michopoulos, and A.P. Iliopoulos, "Crack growth in adhesives: similitude and the Hartman-Schijve equation," *Compos. Struct.*, vol. 273, p. 114260, 2021.
- [83] R. Khan, "Delamination Growth in Composites Under Fatigue Loading," Delft University of Technology, 2013.
- [84] D.R. Atodaria, S.K. Putatunda, and P.K. Mallick, "Delamination growth behavior of a fabric reinforced laminated composite under mode {I} fatigue," *J. Eng. Mater. Technol.*, vol. 121, no. 3, pp. 381–385, 1999.
- [85] G. Allegri, M.I. Jones, M.R. Wisnom, and S.R. Hallett, "A new semi-empirical model for stress ratio effect on mode II fatigue delamination growth," *Compos. Part A Appl. Sci. Manuf.*, vol. 42, no. 7, pp. 733–740, 2011.
- [86] R.D.F. Moreira, M.F.S.F. de Moura, F.G.A. Silva, J.P.A. Reina, and T.M.S. Rodrigues, "A simple strategy to perform mixed-mode I+II fatigue/fracture characterisation of composite bonded joints," *Int. J. Fatigue*, vol. 158, 2021, p. 106723, 2022.
- [87] F. Castro Sousa, A. Akhavan-Safar, G. Rakesh, and L.F.M. da Silva, "Fatigue life estimation of adhesive joints at different mode mixities," *J. Adhes.*, vol. 98, no. 1, pp. 1–23, 2022.
- [88] J. Monteiro *et al.*, "Influence of mode mixity and loading conditions on the fatigue crack growth behaviour of an epoxy adhesive," *Fatigue Fract. Eng. Mater. Struct.*, vol. 43, no. 2, pp. 308–316, 2020.

- [89] F.C. Sousa, A. Akhavan-Safar, R. Goyal, and L.F.M. da Silva, "The influence of mode mixity and adhesive system on the fatigue life of adhesive joints," *Fatigue Fract. Eng. Mater. Struct.*, vol. 43, no. 10, pp. 2337–2348, 2020.
- [90] M. Quaresimin, P.A. Carraro, G. Meneghetti, and M. Ricotta, *Mixed-Mode Fatigue of Bonded Joints in Composites: Experiments and Modelling*, no. 2011. Elsevier, 2015.
- [91] M. Shahverdi, A.P. Vassilopoulos, and T. Keller, "Mixed-mode fatigue failure criteria for adhesively-bonded pultruded GFRP joints," *Compos. Part A Appl. Sci. Manuf.*, vol. 54, pp. 46–55, 2013.
- [92] D. Bürger, "Mixed-Mode Fatigue Disbond on Metallic Bonded Joints," Delft University of Technology, 2015.
- [93] D.A. Dillard, H.K. Singh, D.J. Pohlit, and J.M. Starbuck, "Observations of decreased fracture toughness for mixed mode fracture testing of adhesively bonded joints," *J. Adhes. Sci. Technol.*, vol. 23, no. 10–11, pp. 1515–1530, 2009.
- [94] M. Kenane and M.L. Benzeggagh, "Mixed-mode delamination fracture toughness of unidirectional glass/epoxy composites under fatigue loading," *Compos. Sci. Technol.*, vol. 57, no. 5, pp. 597–605, 1997.
- [95] R. Jones, S. Stelzer, and A.J. Brunner, "Mode I, II and mixed mode I/II delamination growth in composites," *Compos. Struct.*, vol. 110, no. 1, pp. 317–324, 2014.
- [96] P. Robinson, U. Galvanetto, D. Tumino, G. Bellucci, and D. Violeau, "Numerical simulation of fatigue-driven delamination using interface elements," *Int. J. Numer. Methods Eng.*, vol. 63, no. 13, pp. 1824–1848, 2005.
- [97] M.L. Benzeggagh and M. Kenane, "Measurement of mixed-mode delamination fracture toughness of unidirectional glass/epoxy composites with mixed-mode bending apparatus," *Compos. Sci. Technol.*, vol. 56, no. 4, pp. 439–449, 1996.
- [98] I.A. Ashcroft, "A simple model to predict crack growth in bonded joints and laminates under variable-amplitude fatigue," *J. Strain Anal. Eng. Des.*, vol. 39, no. 6, pp. 707–716, 2004.
- [99] H. Hosseini-Toudeshky, M. Jahanmardi, and M.S. Goodarzi, "Progressive debonding analysis of composite blade root joint of wind turbines under fatigue loading," *Compos. Struct.*, vol. 120, pp. 417–427, 2015.
- [100] H. Khoramshad, A.D. Crocombe, K.B. Katnam, and I.A. Ashcroft, "Fatigue damage modelling of adhesively bonded joints under variable amplitude loading using a cohesive zone model," *Eng. Fract. Mech.*, vol. 78, no. 18, pp. 3212–3225, 2011.
- [101] S. Azari, M. Papini, and J.K. Spelt, "Effect of surface roughness on the performance of adhesive joints under static and cyclic loading," *J. Adhes.*, vol. 86, no. 7, pp. 742–764, 2010.
- [102] S. Azari, M. Papini, and J.K. Spelt, "Effect of adhesive thickness on fatigue and fracture of toughened epoxy joints—part I: experiments," *Eng. Fract. Mech.*, vol. 78, no. 1, pp. 153–162, 2011.
- [103] S. Azari, M. Papini, and J.K. Spelt, "Effect of adhesive thickness on fatigue and fracture of toughened epoxy joints—part II: analysis and finite element modeling," *Eng. Fract. Mech.*, vol. 78, no. 1, pp. 138–152, 2011.
- [104] H. Chai, "On the correlation between the mode I failure of adhesive joints and laminated composites," *Eng. Fract. Mech.*, vol. 24, no. 3, pp. 413–431, 1986.
- [105] S. Krenk, J. Jönsson, and L.P. Hansen, "Fatigue analysis and testing of adhesive joints," *Eng. Fract. Mech.*, vol. 53, no. 6, pp. 859–872, 1996.
- [106] M.M. Abou-Hamda, M.M. Megahed, and M.M.I. Hammouda, "Fatigue crack growth in double cantilever beam specimen with an adhesive layer," *Eng. Fract. Mech.*, vol. 60, no. 5–6, pp. 605–614, 1998.

- [107] S. Mall and G. Ramamurthy, "Effect of bond thickness on fracture and fatigue strength of adhesively bonded composite joints," *Int. J. Adhes. Adhes.*, vol. 9, no. 1, pp. 33–37, 1989.
- [108] X.X. Xu, A.D. Crocombe, and P.A. Smith, "Fatigue crack growth rates in adhesive joints tested at different frequencies," *J. Adhes.*, vol. 58, no. 3–4, pp. 191–204, 1996.
- [109] D.W. Schmueser, "A fracture mechanics approach to characterizing cyclic debonding of varied thickness adhesive joints to electroprimed steel surfaces," *J. Adhes.*, vol. 36, no. 1, pp. 1–23, 1991.
- [110] R. Joseph, J.P. Bell, A.J. Mcevily, and J.L. Liang, "Fatigue crack growth in epoxy/aluminum and epoxy/steel joints," *J. Adhes.*, vol. 41, no. 1–4, pp. 169–187, 1993.
- [111] G.S. Wilson, "Fatigue Crack Growth Prediction for Generalized Fiber Metal Laminates and Hybrid Materials," Delft University of Technology, 2013.
- [112] J.A. Pascoe, N. Zavatta, E. Troiani, and R.C. Alderliesten, "The effect of bond-line thickness on fatigue crack growth rate in adhesively bonded joints," *Eng. Fract. Mech.*, vol. 229, p. 106959, 2020.
- [113] A.J. Kinloch and S.J. Shaw, "The fracture resistance of a toughened epoxy adhesive," *J. Adhes.*, vol. 12, no. 1, pp. 59–77, 1981.
- [114] C. Yan, Y.W. Mai, and L. Ye, "Effect of bond thickness on fracture behaviour in adhesive joints," *J. Adhes.*, vol. 75, no. 1, pp. 27–44, 2001.
- [115] T. Kruse, T. Körwien, S. Heckner, and M. Geistbeck, "Bonding of CFRP primary aerospace structures—crackstopping in composite bonded joints under fatigue," in *20th International Conferences on Composite Materials*, 2015.
- [116] N.M. Chowdhury, J. Wang, W.K. Chiu, and P. Chang, "Static and fatigue testing bolted, bonded and hybrid step lap joints of thick carbon fibre/epoxy laminates used on aircraft structures," *Compos. Struct.*, vol. 142, pp. 96–106, 2016.
- [117] T. Löbel, D. Holzhüter, M. Sinapius, and C. Hühne, "A hybrid bondline concept for bonded composite joints," *Int. J. Adhes. Adhes.*, vol. 68, pp. 229–238, 2016.
- [118] J. Steinmetz *et al.*, "The working principles of a multifunctional bondline with disbond stopping and health monitoring features for composite structures," *J. Compos. Sci.*, vol. 5, no. 2, pp. 1–17, 2021.
- [119] F.M.G. Ramírez, M.F.S.F. de Moura, R.D.F. Moreira, and F.G.A. Silva, "A review on the environmental degradation effects on fatigue behaviour of adhesively bonded joints," *Fatigue Fract. Eng. Mater. Struct.*, vol. 43, no. 7, pp. 1307–1326, 2020.
- [120] K. Houjou, K. Shimamoto, H. Akiyama, and C. Sato, "Effect of test temperature on the shear and fatigue strengths of epoxy adhesive joints," *J. Adhes.*, 2021.
- [121] W.L. Mu, Q.H. Xu, J.X. Na, H. Wang, W. Tan, and D.F. Li, "Influence of temperature and humidity on the fatigue behaviour of adhesively bonded CFRP/aluminium alloy joints," *J. Adhes.*, 2021.
- [122] W. Tan, N. Jingxin, W. Guangbin, H. Chen, and H. Meng, "Effect of temperature on the fatigue performance and failure mechanism of a flexible adhesive butt joint," *J. Adhes.*, 2021.
- [123] G. hua Xie, Z.a. Tao, Y. Sun, S.q. Li, and A.A. Gedi, "An investigation of hygrothermal effect on fatigue behavior of adhesively bonded anchorages for FRP tendon," *Constr. Build. Mater.*, vol. 316, 2020, p. 126044, 2022.
- [124] R. Pugstaller and G.M. Wallner, "Development of a fracture-mechanics based fatigue testing method for epoxy/electrical steel laminates with thin adhesive layer," *Eng. Fract. Mech.*, vol. 258, p. 108045, 2021.
- [125] B.P.H. van den Akker, M.V. Donadon, R. Loendersloot, L.A. de Oliveira, and M.A. Arbelo, "The influence of hygrothermal aging on the fatigue behavior and residual

- strength of post-buckled co-bonded stiffened panels subjected to compressive loading,” *Compos. Part B Eng.*, vol. 194, , p. 108023, 2020.
- [126] J.D. Landes and J.A. Begley, “A fracture mechanics approach to creep crack growth,” in *Mechanics of Crack Growth*, ASTM STP 590, American Society for Testing and Materials, 1976, pp. 128–148.
- [127] K.M. Nikbin, G.A. Webster, and C.E. Turner, “Relevance of nonlinear fracture mechanics to creep crack growth,” in *Crack and Fracture*, ASTM STP 601, American Society for Testing and Materials, 1976, pp. 47–62.
- [128] A. Saxena, “Creep crack growth under non-steady-state conditions,” in *Fracture Mechanics*, ASTM STP 905, American Society for Testing and Materials, 1986, pp. 185–201.
- [129] A.H. Al-Ghamdi, “Fatigue and Creep of Adhesively Bonded Joints,” Loughborough University, 2004.
- [130] A.V. Movahedi-Rad, G. Eslami, and T. Keller, “A novel fatigue life prediction methodology based on energy dissipation in viscoelastic materials,” *Int. J. Fatigue*, vol. 152, 2021, p. 106457, April.
- [131] J. Lemaitre, “How to use damage mechanics,” *Nucl. Eng. Des.*, vol. 80, no. 2, pp. 233–245, 1984.
- [132] J. Lemaitre, “A continuous damage mechanics model for ductile fracture,” *J. Eng. Mater. Technol.*, vol. 107, no. 1, pp. 83–89, January 1985.
- [133] L. Kachanov, *Introduction to Continuum Damage Mechanics*. Dordrecht: Martinus Nijhoff, 1986.
- [134] M.M. Abdel Wahab, I.A. Ashcroft, A.D. Crocombe, and S.J. Shaw, “Prediction of fatigue thresholds in adhesively bonded joints using damage mechanics and fracture mechanics,” *J. Adhes. Sci. Technol.*, vol. 15, no. 7, pp. 763–781, 2001.
- [135] I. Hilmy, M.M. Abdel Wahab, I.A. Ashcroft, and A.D. Crocombe, “Measuring of damage parameters in adhesive bonding,” *Key Eng. Mater.*, vol. 324–325, no. 1, pp. 275–278, 2006.
- [136] I. Hilmy, M.M. Abdel Wahab, A.D. Crocombe, I.A. Ashcroft, and A.G. Solana, “Effect of triaxiality on damage parameters in adhesive,” *Key Eng. Mater.*, vol. 348–349, no. 2, pp. 37–40, 2007.
- [137] M.M.A. Wahab, I. Hilmy, I.A. Ashcroft, and A.D. Crocombe, “Evaluation of fatigue damage in adhesive bonding: part 1: bulk adhesive,” *J. Adhes. Sci. Technol.*, vol. 24, no. 2, pp. 305–324, 2010.
- [138] M.M.A. Wahab, I. Hilmy, I.A. Ashcroft, and A.D. Crocombe, “Evaluation of fatigue damage in adhesive bonding: part 2: single lap joint,” *J. Adhes. Sci. Technol.*, vol. 24, no. 2, pp. 325–345, 2010.
- [139] M.M.A. Wahab, I. Hilmy, I.A. Ashcroft, and A.D. Crocombe, “Damage parameters of adhesive joints with general triaxiality part I: finite element analysis,” *J. Adhes. Sci. Technol.*, vol. 25, no. 9, pp. 903–923, 2011.
- [140] M.M.A. Wahab, I. Hilmy, I.A. Ashcroft, and A.D. Crocombe, “Damage parameters of adhesive joints with general triaxiality, part 2: scarf joint analysis,” *J. Adhes. Sci. Technol.*, vol. 25, no. 9, pp. 925–947, 2011.
- [141] I.A. Ashcroft, V. Shenoy, G.W. Critchlow, and A.D. Crocombe, “A comparison of the prediction of fatigue damage and crack growth in adhesively bonded joints using fracture mechanics and damage mechanics progressive damage methods,” *J. Adhes.*, vol. 86, no. 12, pp. 1203–1230, 2010.
- [142] V. Shenoy, I.A. Ashcroft, G.W. Critchlow, and A.D. Crocombe, “Unified methodology for the prediction of the fatigue behaviour of adhesively bonded joints,” *Int. J. Fatigue*, vol. 32, no. 8, pp. 1278–1288, 2010.

- [143] V. Shenoy, I.A. Ashcroft, G.W. Critchlow, and A.D. Crocombe, “Fracture mechanics and damage mechanics based fatigue lifetime prediction of adhesively bonded joints subjected to variable amplitude fatigue,” *Eng. Fract. Mech.*, vol. 77, no. 7, pp. 1073–1090, 2010.
- [144] T. Walander, A. Eklind, T. Carlberger, and U. Stigh, “Fatigue damage of adhesive layers—experiments and models,” *Procedia Mater. Sci.*, vol. 3, pp. 829–834, 2014.

Durability and accelerated characterization of adhesive bonds

20

Scott W. Case^{a,b}, Arit Das^{b,c}, Michael J. Bortner^{b,c}, David A. Dillard^{b,d}, and Christopher C. White^e

^aVia Department of Civil and Environmental Engineering, Virginia Tech, Blacksburg, VA, United States, ^bMacromolecules Innovation Institute, Virginia Tech, Blacksburg, VA, United States, ^cDepartment of Chemical Engineering, Virginia Tech, Blacksburg, VA, United States, ^dDepartment of Biomedical Engineering and Mechanics, Virginia Tech, Blacksburg, VA, United States, ^eExponent, Inc., Bowie, MD, United States

20.1 Introduction

A key challenge in testing adhesives is to balance the speed and simplicity of tests with the “usefulness” of the results. Hundreds of test methods have been developed and applied to adhesive systems. For example, the Adhesive and Sealant Council [1] lists 34 standard test and test specifications; Duncan [2] lists 43 “key standards” published by ISO and ASTM and suggests that many more national, industry, and company-specific tests are used for joint tests. However, as he notes, standard tests may not be the most accurate or appropriate tests for many purposes. Many of those tests can only be used for qualitative or comparative measurements and only a few are likely suitable for developing design data.

Hartshorn [3] has suggested that adhesives are tested for one of three reasons: (1) to guide the development or selection of an adhesive for a particular use; (2) to monitor the production quality of an adhesive; and (3) to assure the effectiveness of the bonding process employed. As he notes, “One problem, always present in the use of structural adhesives, is how to determine the reliability of the bonded structure. This may be at the time of manufacture, to ensure that a good joint has been produced, or during service, to monitor behavior under operating conditions. It is often impractical, or impossible, to use the types of test methods employed to determine mechanical properties....”

A significant amount of data related to the durability of structural adhesive joints has been gathered from outdoor aging studies or laboratory simulations thereof. Typically, the exposure conditions may be grouped into one of: (1) temperature: moderate climate, normally in northern latitudes; (2) desert: hot, dry climate; (3) tropical: hot, wet climate; and (4) marine: corrosive, coastal environment. Wilson et al. [4] discussed the need for a series of tests to evaluate the long-term durability of bonded aluminum systems. Among the needs were tests to screen and select different bonding

systems, provide information regarding the influence of environment on the systems (including the pretreated surface and the adhesive/adherend interface), and to answer manufacturing questions such as the acceptable range of pretreatment and the best adhesive curing conditions.

A key component for durability assessment is often determining the severity and duration of the exposure conditions, and how results from such exposure can be used to predict system or product durability in actual service. With desired service lives often on the order of several years or decades, there is considerable interest to be able to extrapolate long-term durability from short-term testing. Any accelerated test will, by definition, represent a more extreme condition for one of the damage drivers (e.g., temperatures, humidity levels, concentration levels, cyclic frequencies, shorter diffusion paths, etc.) than seen in-service to speed up the degradation effects. To compare performance in accelerated exposure tests to that obtained in real environments, it is often desirable to conduct some limited parallel studies to provide validation for the acceleration scheme. For example, in their study, Wilson et al. [4] attempted to compare results for systems evaluated in two different acceleration procedures: combined stress/humidity and neutral salt spray tests. They found that their accelerated salt spray test had a time acceleration factor of five compared with outdoor marine exposure in the United Kingdom; their combined stress/humidity test had a time acceleration factor of approximately 60 in comparison with outdoor exposure in Australia. However, they caution that the results are specific to the particular system examined and the particular exposure site, and that only by comparing results from various locations can confidence in the overall environmental performance be obtained. While this caution was appropriate for their correlation, stronger connections to underlying mechanisms (e.g., [5]) allow greater confidence in the acceleration scheme.

20.2 Correlating environmental exposure to mechanistic changes in polymer structure

The reduced weight, increased stiffness, and enhanced fatigue resistance of adhesives have resulted in their utilization as a fastening mechanism in many structural applications [6–8]. Adhesive bonds based on both thermoplastics and thermosets are ubiquitous in the automotive (see Chapter 24), marine and general industrial (see Chapter 26), and aerospace (see Chapter 23) sectors, and are subjected to various loading modes and a wide range of environmental factors. The durability of adhesives exposed to various environmental conditions is largely governed by chemical composition, morphology, and microstructure of the respective polymers. As such, the properties of adhesive bonds can be significantly impacted upon exposure to environmental factors such as temperature, moisture, irradiation, etc. [9,10]. Such environmental exposures can critically affect the interface between the adherend and the adhesive, and if left unaddressed, can lead to catastrophic failures. The effect of common exposure factors, including moisture, temperature, ultraviolet (UV) radiation, and chemicals present during service life, among others, on the performance of adhesive bonds has been a topic of significant interest over the past decades. The

changes in durability and properties of an adhesive in response to environmental exposure can originate from physical and chemical aging of the polymer, as will be discussed later in this section. Hence, having a thorough mechanistic understanding of the aging process is highly desirable to provide important recommendations regarding the service life of the components bonded using such adhesives. Such an approach will help guide the design and fabrication of adhesives and bonded systems with enhanced durability and reliable performance.

20.2.1 *Types of environmental exposures*

Temperature plays a key role in dictating the mechanical properties and service life of polymer-based adhesives. At increased temperatures, adhesives have reduced yield stress and modulus while at lower temperatures, they are quite stiff and often higher yield stresses [11]. The glass transition temperature (T_g) of the adhesives can be tuned based on their chemistry and architecture, including as discussed for various chemical families in Chapters in Part I of this book. Adhesives are often selected, in large part, based on their T_g . For example, structural adhesives for ambient to high-temperature applications typically should exhibit higher T_g s [12] than the service environment temperatures to retain their integrity. Exceptions to this guideline include the silicone-based adhesives used for semistructural applications (see Chapter 6) and low T_g polyurethanes. Moreover, it is worth reminding the reader that unless specifically mentioned, the discussions presented in this section are representative of adhesives that do not typically include two T_g values, such as the polyurethane-based systems discussed in Chapter 3.

The temperature-dependent transition from a rigid (glassy) to a more flexible (rubbery) material must be controlled through careful manipulation of the polymer's T_g [13]. If the service temperature approaches the T_g , which can be depressed by sorbed moisture or other diluents, the time-dependent behavior of adhesives can lead to increased creep, as well as potentially changing the locus of failure, such as from cohesive to an interfacial failure regime [14]. Prolonged exposure to temperatures approaching the T_g of the adhesive can result in significant creep deformation and even delayed failures, such as the Big Dig failure discussed in Chapter 14. Moreover, the failure mechanism can often transition from cohesive to interfacial due to the environmental degradation facilitated by the high-temperature exposure leading to substantial reduction in the strength and durability of the adhesive bonds.

Adhesive bonds are susceptible to environmental moisture due to their molecular mobility that is sometimes enhanced by plasticizers. The extent of water diffusion as well as the nature of the interaction between the polymer chains and water control the adhesive properties. Upon diffusion into the polymer matrix, the moisture can simultaneously chemically degrade the adhesive through chain scission and corrode the substrate surface through hydration [15]. The water molecules can migrate into adhesively bonded joints through bulk diffusion or ingress along interfaces or flaws, and alter the physico-chemical properties of the adhesive as well as of the interface or interphase, thereby significantly affecting the strength and durability of the bonds [16]. This is unfortunate because water is almost always present in environments to

which most adhesive joints are exposed. Entering the polymer network, the moisture can cause the polymer to swell, negatively impacting the strength and T_g of the polymer [17,18], leading to the generation of internal stresses and in some cases cracks, which can also form with subsequent drying. The reduction in T_g of the adhesive is controlled by the water present within the apparent free volume of the polymer (bound water) [17].

Depending on the end application, a number of functional parts and structures are often simultaneously exposed to temperature and humidity [19]. In many instances, the durability of the bonds exposed to thermal aging in the absence of imposed moisture is found to be superior to that exhibited by the bonds exposed to thermal aging under humid conditions [20,21]. The water diffusion rate is accelerated at higher temperatures due to enhanced chain mobility. Further, the individual detrimental effects of thermal and moisture exposure on the fatigue behavior of adhesive bonds have been found to be less than that encountered during a combined exposure [22,23].

20.2.2 Examples of adhesives exposed to environmental factors

The strength of single-lap joints bonded using two different adhesives, a polyurethane-based one and an epoxy-based one, was studied at different temperatures (-40°C , 20°C , and 80°C) [11]. For the polyurethane-based adhesive, the highest average shear strength was achieved at -40°C . The T_g of the soft phase for this adhesive was -60°C that resulted in a more ductile response at lower temperatures, leading to enhanced strength of the bonded joints [24]. In contrast to the polyurethane-based adhesive, the lap shear strength of the epoxy adhesive joint was found to decrease both at -40°C (due to loss of ductility) and 80°C (due to loss of adhesion strength), compared to the value at 20°C . Similar work employing single-lap joints was performed to characterize the fatigue performance of a rubbery polybutadiene and a glassy epoxy adhesive at different temperatures (-30°C , 20°C , and 90°C) [25]. The fatigue properties of the polybutadiene bonded joints were relatively independent of temperature while those of the glassy epoxy were enhanced at lower temperatures. Furthermore, the effect of temperature on the toughness of an automotive-grade epoxy adhesive was evaluated by Banea et al. [26]. The mode I fracture toughness (G_{Ic}) was independent at temperatures below the T_g of the epoxy while the G_{Ic} values reduced significantly when tested at temperatures above the T_g (see Chapter 1 for detailed discussion of epoxies).

The fatigue behavior of adhesive bonds, discussed in more detail in Chapter 19, can be also strongly affected by prior or concurrent environmental exposure. The effect of moisture exposure on the fatigue performance of adhesively bonded aluminum and glass fiber-reinforced epoxy joints was investigated by Mariam et al. [27]. The adhesively bonded joints were exposed to water at 50°C for a variable duration (20–120 days). The fatigue strength of fiber-reinforced epoxy joints decreased significantly compared to that of the aluminum joints due to the permeable nature of the epoxy resin that allowed increased diffusion of water. However, in the aluminum joints, the presence of moisture corrodes the interface between the substrate and the adhesive, which highlights the necessity of appropriate surface treatments to retain

adequate durability (see also [Chapter 9](#)). In this regard, the fatigue threshold fracture energies (G_{th}) of chromic acid and phosphoric acid-etched aluminum joints were measured to be 45 and 310 J m^{-2} , respectively, as compared to 560 J m^{-2} when tested without exposing the joints to moisture aging [28]. Moreover, the locus of joint failure transitioned from interfacial to cohesive when the surface treatment was changed from chromic acid to phosphoric acid. Along similar lines, the fatigue performance of epoxy-bonded aluminum lap joints was probed in the presence of moisture (96% relative humidity) and a silicon-based surface treatment [29]. The fatigue life of the moisture-exposed untreated joints was inferior to that of their surface-treated counterparts. This was attributed again to the differences in the failure mechanisms: the treated joints undergoing cohesion failure through the adhesive while the untreated joints failed at the interface of the adhesive and substrate.

The effect of different levels of moisture exposure (63% and 95% relative humidity) on the static shear properties of adhesively bonded aluminum joints was studied by Jurf and Vinson [30]. The authors found that the shear properties of the bonded joints reduced upon exposure due to the diffusion of water molecules into the adhesives. Interestingly, the presence of moisture impacted the static properties in a manner similar to exposing the joints to higher temperatures or reducing the T_g of the adhesive. The fatigue performance of carbon fiber-reinforced plastics/epoxy lap-strap joints was investigated at different temperatures (-50°C , 25°C , and 90°C) and different levels of relative humidity [31]. The fatigue resistance decreases when they are exposed to temperatures closer to the T_g of the adhesive. The moisture absorption into the adhesive has a plasticizing effect and reduced its T_g . At lower temperatures, the samples failed due to cracks propagating within the adhesive layer while at higher temperatures, the cracks propagated across the interface between the adhesive and the substrate.

20.2.3 Mechanistic changes in polymer structure

Exposure to each of the environmental factors described above alters the molecular structure of the adhesives to varying extents, resulting in the observed behavior, as discussed in the preceding sections. For example, if adhesives are maintained at temperatures lower than their T_g s, they often retain their properties for extended time periods. However, when the adhesives are subjected to high temperatures for prolonged periods of time, the polymer chains slowly reorganize and affect the mechanical properties of the adhesively bonded joints. During the initial period of exposure, the polymer segments with more mobility in the regions with low crosslinking migrate away from the regions with higher crosslinking, leading to phase separation. This difference in the mobility between the polymer segments can lead to the appearance of two T_g s, as has been reported for epoxy systems [32]. However, as the exposure period lengthens, the mobile segments tend to aggregate and form a more packed system, thereby losing their mobility. The chemical nature as well as the curing characteristics and thermal history dictate the T_g of an adhesive, and are therefore critical to the performance of the adhesives at higher temperatures [33,34].

In case of exposure to moisture, the robustness of the adhesive layer is severely impacted. The absorption of 1% of water by an epoxy resin can lead to a T_g reduction

of about 10°C due to the plasticization of the polymer [35]. The reduction in the adhesive bond strength postexposure is attributed to the increased molecular mobility of the adhesive and plasticization effects. It is worth noting that the effect of water absorption is less pronounced in the regions with higher crosslinking density. Adhesively bonded joints can be subjected to significant levels of residual stresses due to the combined effects of absorbed water and coefficient of thermal expansion mismatch between the substrate and the adhesive. Generally, adhesives are prone to swelling when exposed to moisture for prolonged periods. However, the thermal stress build-up during curing can be reduced through the swelling of the adhesive due to moisture diffusion [36]. It is worth noting that the relaxation of the adhesive does not lead to residual stress generation and the properties of the bonded joints remain unaltered [37,38]. The environmental conditions that the adhesives are exposed to dictate the extent of moisture uptake. The equilibrium moisture uptake increases as the moisture content of the environment increases due to the increase in the driving force for diffusion [10,36,39,40]. The equilibrium moisture uptake is also controlled by the environmental temperature; generally increasing with temperature [17,41–43] but in some cases can also be independent of the temperature [10,44]. Environmental moisture often reduces the durability of the adhesively bonded joints by altering the adhesive-adherend interface through lowering the thermodynamic work of adhesion, disrupting native oxide layers, and even corroding the adherend surface, resulting in failure of the bonded systems [45]. The extent of wetting and interaction between the adhesive and the adherend can be affected by the degree of moisture absorption during curing of the adhesive bonds.

Other than water, adhesives have been aged in other liquids such as acetone, ethylene glycol, aviation fuel, dichloromethane, etc. As with moisture exposure, the presence of solvents may plasticize and swell the polymer matrix. Environmental stress cracking and crazing are commonly observed when susceptible adhesives are exposed to certain solvents [46,47]; however, the relationship between solvent uptake and the strength of the adhesive bonds has not yet been widely studied.

The combined effect of long-term exposure to different environmental factors on the durability of polyamine-based adhesive bonds has also been explored [48]. Based on the kinetic theory, the increase in temperature results in increased diffusion of moisture into the adhesives. The exposure time can also have a significant effect on the properties of the bonds. The effect of moisture exposure at relatively lower temperatures is generally reversible, with the bonds recovering their properties once dried [45,49,50]. Interestingly, the moisture exposure at higher temperatures for short durations can result in improved mechanical properties of the bonds, likely due to plasticization or postcuring effects. But if the exposure time is increased, the properties are negatively affected [12]. Gurumurthy et al. investigated the initiation and growth of cracks between polymer interfaces in response to hydrothermal conditions [51,52]. The threshold energy release rate (G_{th}) of the interface between an anhydride-cured epoxy and a polyimide reduced upon increasing either the exposure temperature or the relative humidity of the exposure environment. The crack growth rate dependence on the energy release rate (G^*) above G_{th} is more complex and the behavior can be described using two different regimes [51]. Initially, the crack growth rate exhibits

a power law increase with G^* that corresponds to a stress-activated hydrolysis reaction rate-controlled regime while at higher G^* values, the crack growth rate does not change with G^* in a transport-controlled regime [51]. Subsequent work from the same group found that the hydrothermal crack growth per unit temperature cycle cannot be explained using classical Paris law [52]. The experimental findings were accurately modeled accounting for the crack growth due to the thermal fatigue as well as the interfacial stress-assisted hydrolysis of the ester bonds (thermal) [52]. Moreover, the authors reported that the performance of the adhesively bonded joints was inferior if the exposure temperature was changed slowly. The effects of air and saline water exposure on the fatigue performance of adhesive bonds were characterized by Liechti et al. [53] using cracked lap shear specimens employing a polyurethane-based adhesive. At higher temperatures, the fracture toughness of the saline water-exposed adhesive bonds decreases. At room temperature, the authors reported the power law exponent of the classical Paris law increased as the exposure medium was changed from air to salt water.

It is evident from the above discussion that extended exposure to environmental factors can lead to a reduction in the properties of adhesives, thereby limiting their reliability and applicability. Depending on the nature of changes occurring during the exposure, the aging of an adhesive can be categorized into physical and chemical aging.

20.2.3.1 Physical aging in polymer structure

Physical aging is one of the most common aging mechanisms encountered in polymer and glassy materials [54–57]. The major distinction among the other aging mechanisms (chemical, hydrothermal, etc.) and physical aging is the profound physical changes in the polymer microstructure that are induced due to long-term thermal exposures to temperatures lower than the T_g of the polymer. The arrangement of the polymer chain network changes without altering the chemical microstructure. Mechanistically, a typical physical aging process is invariably associated with a simultaneous reduction in the free volume and changes in the molecular configuration on the polymer backbone. During such exposure, the polymers usually undergo increased levels of volumetric relaxations and/or a decrease in enthalpic relaxations, as dictated by classical thermodynamics [58]. As a result, the toughness of the material diminishes appreciably, which may have an adverse effect on the industrial applicability of the parts, especially those manufactured with the goal of exhibiting acceptable mechanical performance when subjected to sub- T_g temperatures over extended time periods. Generally, the negative effects of physical aging on the properties can be reversed by exposing the material to temperatures above its T_g , as will be discussed in a later section, though is often impractical for many applications.

Physical aging is prevalent for both thermoplastic and thermoset adhesives. Research has focused more heavily on the effect of physical aging on the constitutive properties (such as modulus) of the adhesives than on their strength and fracture properties. Generally, most of the thermoset adhesives (e.g., epoxy based and often thermally cured) are amorphous in nature. The primary difference between the

aforementioned classes of adhesives is the covalent crosslinks that control the stiffness of the polymer network. Increased crosslink density limits polymer chain mobility and hinders its ability to reconfigure into a crystalline state. Therefore, the extent of physical aging is impeded by the presence of a more crosslinked network. However, the crosslink density and chemical nature of the covalent linkages have minimal effect on the aging kinetics [59].

The degree of curing (and therefore, the crosslink density) of epoxy networks is controlled by both the curing time and temperature. Hence, the processing conditions and cure staging affect the extent of physical aging in such epoxy network structures. Postcuring, the permanent deformations in molecular structure (induced by the curing parameters) can lead to the development of substantial levels of residual stresses in the materials [60–63]. However, the mobility of the polymer chains reduces significantly at increased degrees of cure, and therefore the long-range conformational motion of the polymer backbone is restricted. Hence, a combination of synthetic modifications and physics-guided process parameter selection is of paramount importance to optimize the crosslink density in the networks to obtain desired properties.

20.2.3.2 Chemical aging in polymer structure

In contrast to physical aging, the chemical structure of an adhesive changes irreversibly during chemical aging due to chain scission, chain branching, and chemical crosslinking. Chemical degradation of adhesives is common during prolonged temperature exposure. Temperature-induced chemical aging can result in a reduction of the length of polymer chains due to chain scission that reduces the entanglement density of the polymer. As a result, the properties of the polymer deteriorate drastically upon such exposures. For example, polyurethane-based adhesives undergo thermo-oxidative degradation (through oxidation of the methylene group to ketone) in air at around 150°C [64]. At higher temperatures (150–250°C), the urethane linkages serve as the site of thermal decomposition and are cleaved into isocyanate and alcohol, resulting in depolymerization of the matrix [65]. However, it is worth noting that during the degradation of polymer, it is possible that several side reactions might result in the formation of new crosslinks in the network that can counteract the effects of chemical aging to a certain extent.

Chemical aging is often increasingly likely in adhesives exposed to moisture. Again, taking the example of polyurethane-based systems, studies on the effect of moisture exposure are relatively scarce, so there is a lack of consensus about the degradation mechanism upon chemical aging. Tailored synthesis of polyurethane networks through controlled stoichiometry has exhibited potential in limiting the extent of water absorption into the matrix, the main reason behind the failure of some adhesively bonded joints [66]. The authors postulated that the reduction in the bond strength was due to the coupled effects of polyurethane hydrolysis and hydration of the surface oxide layer in the substrate. In contrast, the possibility of potential chemical reactions upon moisture exposure was ruled out through spectroscopic characterizations, and the plasticization effect of water was held responsible for the deterioration in adhesive bond performance [67]. Generally, the chemical degradation of polyester

polyurethanes is caused by hydrolysis of ester groups [68] while the ether groups in polyether polyurethanes are stable against moisture exposure, although the urethane linkages are susceptible to hydrolysis [69]. The effect of hydrolysis is more severe in aromatic polyether polyurethanes compared to the aliphatic varieties.

Chemical aging of adhesives can also be induced due to the presence of oxygen in the ambient environment. The oxygen reacts with the adhesives, resulting in permanent changes in the network macrostructure. The oxidation of polymer chains occurs through a free radical chain reaction that results in chain scission and degrades the adhesives [70–73].

20.3 Test methods for characterizing durability

Experimentally characterizing the durability of adhesively bonded joints adds several additional challenges to the slate of test methods used to measure adhesive performance. Questions include how many environments and at what intensities (e.g., temperatures, moisture levels, chemical concentrations, etc.); the duration of exposure conditions and at what intervals; whether constant, cyclic, or other profiles for environmental challenges are appropriate; whether exposure occurs while specimens are under mechanical loads; and whether exposure and testing are performed at the same or a different temperature or set of environmental factors. For tests that are destructive in nature, each test condition may require a sufficient number of replicates to obtain statistically valid insights. And, environmental exposure can alter the mode or locus of failure, so different degradation mechanisms are frequently involved, complicating comparisons and direct inferences. Exposure time, space for exposure, number of required specimens, and costs associated with personnel, equipment, and data analysis often dictate restrictions on test matrices, necessitating compromises between what is desired and what is practical. Good judgment, including based on prior experience with related systems, often guides the decision process in established industries, as discussed in several Chapters in Part IV of this book, though surprises, sometimes very consequential, still occur.

20.3.1 Tests of adhesives as materials

One important concept in evaluating adhesive durability is the need to test the *bond system* rather than just the adhesive as a *material*. The *bond system* or *material system* consists of, for example, the adherends, surface cleaning and treatment, primers, and the adhesive, as well as the dispensing and curing processes used in fabrication. This system evaluation is needed as long-term exposures to loading and environmental challenges can induce a range of degradation mechanisms on these components, either individually or as combined within the bond. Thus, in many situations, tests of bonded joints, prepared in a manner similar to the intended products or applications, are advisable for meaningful durability assessment. Nonetheless, the adhesive is a dominant part of any bonded joint, and as with any polymer, it is sensitive to time, rate, and temperature, along with perhaps susceptibility to other environmental exposure

factors. Thus, characterizing an inherently time- and temperature-dependent component, the adhesive, is often a critical link in a joint's ability to transfer stress from one adherend to the other over the service life.

Testing of adhesives as *materials* rather than part of a *bond system* is convenient for several reasons. To the extent that adhesives can be cast or formed into films or coupons, they lend themselves naturally to the wide range of polymer test procedures, including thermal analysis and tests assessing constitutive properties, strength and fracture measurements, and other temperature-dependent viscoelastic characterizations. Furthermore, without the presence of (often) impervious adherends, the diffusion of environmental agents into the materials can be accelerated significantly, thus allowing for more rapid characterization in the presence of environmental factors of interest. Recognizing the difficulty of having a durable adhesive bond without a durable adhesive, the characterization of bulk adhesives as a *material* is often a first step in determining the likely success of a proposed *bond system*, providing specimens representative of the adhesive within the intended bond can be fabricated.

Among neat adhesive tests that might be appropriate, one might suggest chemical characterization, thermal analysis, and mechanical characterization. Typical test techniques for each of these are briefly described below.

Chemical characterization: Structural adhesives are often formulated by the manufacturers to optimize the desired mechanical properties (tensile, shear, compression, peel, etc.), depending on the anticipated market needs. Because the synthetic chemistry controls the properties of the polymer, routine chemical characterizations are conducted during product development and often serve as valuable components of the quality control acceptance process. Fourier transform infrared (FTIR) spectroscopy is one of the most popular techniques used to analyze adhesives. FTIR provides a route to evaluate adhesives at different aging stages through monitoring the changes in the network structure as well as to characterize chemical functionalities that either appear or disappear during the curing and aging processes [74]. The change in intensity of the characteristic absorption band of a particular functional group during aging with respect to a stable band can be used to quantitatively estimate the amount of that group present in the adhesive [75]. Coupling attenuated total reflectance (ATR) with FTIR allows for minimal sample preparation requirements, faster sampling, and enhanced reproducibility. FTIR and ATR-FTIR have been frequently employed by multiple researchers to characterize the chemical nature of the various kinds of adhesives [40–43]. Complementary to the FTIR technique, FT-Raman spectroscopy can also be used to study the chemical functionalities of adhesives [44]. By monitoring the intensities of the characteristic peaks, a spatial distribution of the concentration of the adhesive across the adhesive-adherend interface as well as the extent of diffusion of the resin into the interface can be obtained [46]. However, it is worth mentioning that the properties and long-term performance of the adhesives are not only controlled by their chemical nature but also the degree of crystallinity, crosslink density, molecular size distribution, and types and amounts of additives incorporated into the matrix [47]. Therefore, detailed investigations on the relative impacts of such factors on adhesive performance must be performed.

Thermal analysis: There are several test techniques that fall under thermal analysis and are often conducted on neat polymer samples. Differential scanning calorimetry (DSC), thermogravimetric analysis (TGA), dynamic mechanical analysis (DMA), and thermomechanical analysis (TMA) can all be quickly conducted during thermal scans to understand the thermal landscape of the polymer. These tests can all be conducted over a range of heating rates and/or loading rates or frequencies to gain insights into the rate dependence of the samples. Conducting TGA over several thermal ramp rates, for example, might suggest kinetics of thermal degradation that can be essential for predicting the thermal stability of adhesives [76]. The chemical reactions taking place during thermal degradation can be probed using an FTIR-coupled TGA technique, and the corresponding weight loss can be correlated with the release of certain gases from the sample [77]. DMA tests are commonly performed at various frequencies and temperatures to generate master curves for constitutive properties, using accelerated characterization techniques. Repeated thermal cycles, such as first and second heat from the lowest temperature to highest and back, provide additional information about the degree of cure, physical aging, extent of crystallization, and other factors. All these issues may be relevant for adhesive performance, long-term stability, and material durability.

Mechanical characterization: Because structural adhesives must often bear significant applied stresses over a long duration, mechanical characterization can be a critical complement in development and screening processes. Typical tests include tensile coupons loaded to failure to obtain stress-strain relationships, modulus, yield behavior, and strain to break. When conducted at different crosshead rates and temperatures, insights into the time-dependence of these properties can also be obtained. Fracture tests such as compact tension (CT), single edge notch bend (SENB), and perhaps tearing tests also provide useful insights into the adhesive's ability to resist fracture, including the effects of rate.

20.3.2 Tests of adhesives as bonded systems

While tests of adhesives as *materials* can provide valuable insights into the mechanical and other properties of this crucial component of *bond systems*, most durability assessments of bonded joints are incomplete without exposure of representative bonded specimens to service-relevant loading and environmental exposure. Minford [78] made this point clearly; his results are reproduced in Fig. 20.1, where tensile coupons of a bulk epoxy adhesive showed good durability over time when exposed to water, but significant decreases in tensile strength when exposed to ethanol. In contrast, when aluminum single-lap joints bonded with this same adhesive were exposed to ethanol, there was little degradation in joint strength, but the lap joint strength dramatically decreased with exposure to water, presumably because water was able to degrade the interfacial region in the bond. By testing bonded joints relevant to the intended purpose, one not only brings in the various components and interfaces of interest, but also the processing procedures for adherend cleaning, surface preparation, adhesive dispensing, and curing and storage conditions, thus exposing all these and their representative assembly to the challenges of time, temperature, and

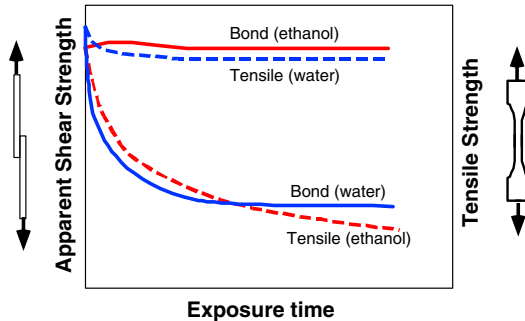


Fig. 20.1 Illustration of the differing effects of water and ethanol exposure on bulk epoxy tensile coupons and on aluminum lap shear joints bonded with the same epoxy. Adapted from J.D. Minford, Durability evaluation of adhesive bonded structures, in: L.-H. Lee (Ed.), Adhesive Bonding, Springer Science+Business Media, New York, 1991.

environmental exposure. In addition, whereas bulk polymer coupons may be relatively stress free, bonded joints composed of materials with different coefficients of thermal (and/or hygral) expansion often result in significant residual stresses.

These residual stresses within the bond can play a significant role in bond durability. In the absence of other mechanically applied loads, residual stresses alone can sometimes be sufficient to lead to debonding in thicker coatings [79] and adhesive layers, especially where assembly stresses may further increase the residual stress state. Residual stresses increase the base stress level, so the subsequent application of mechanically induced stresses can be more likely to reach the yield stress, thresholds for fatigue or subcritical damage, or other limit states that may affect performance or durability. Indeed, in some cases these residual stresses may be more significant than the mechanically induced stresses some joints may experience. In addition, residual stresses resulting from adhesive shrinkage can lead to cracking or other damage, especially in constrained configurations. Furthermore, these cracks can serve as pipelines to allow environmental liquids to ingress deeply into the bonds, significantly accelerating degradation. Residual stresses can alter the locus of failure [80,81] and increase susceptibility to environmental stress cracking, especially in thermoplastic adhesives [47,82]. Residual stresses can affect dimensional stability, complicating assembly or appearance [83]. Finally, although many residual stresses tend to relax to some extent due to viscoelastic processes, in some cases thermal [84,85] or hygral [86] cycling can lead to increased residual stresses due to ratchetting phenomena. Crystallization and other shrinkage phenomena are possible, including leaching, blooming, outgassing, or other egress mechanisms.

Perhaps the most common method to assess environmental effects in materials as well as bonded joints involves exposing specimens to relevant environments, removing individual specimens, typically at periodic intervals, and testing specimens for their mechanical or other properties. Such tests are frequently performed because the equipment required to expose relatively large numbers of specimens to environments of interest are often available, and in some cases are quite inexpensive relative

to test frames. The ability to expose many specimens simultaneously is often significantly less expensive than would be required for long-duration testing on multiple load frames equipped with relevant exposure capabilities. For example, outdoor exposure or subjecting specimens to liquid immersion at ambient temperatures requires little specialized equipment and minimal investment. However, exposure to some nonambient temperatures requires ovens or environmental chambers, which become more expensive, especially if controlled humidity exposure is also required. In some cases, however, the use of saturated salt solutions can provide exposure at desired relative humidity levels without the expense of humidification control systems. Exposure chamber costs can go up for more specialized systems including weatherometers, salt-spray units, etc. The ability to expose numerous specimens at a time, however, may make these units cost-effective when amortized over the life of the unit. This leads to the popularity of this method, where significant quantities of specimens are often preexposed to the environment of interest and tested after removal from the chamber. In some cases, these subsequent tests are conducted at the same conditions as the preexposure step. This is especially important in cases where the properties are expected to vary significantly if tested at different conditions. For example, specimens often reach thermal equilibrium quite quickly, so they may need to be tested in chambers at the desired temperature. On the other hand, moisture ingress or damage states induced during preexposure are not expected to change quickly for some specimens, likely permitting short tests at ambient conditions. Thus, preconditioning large numbers of samples in dedicated chambers, removing subsets of specimens often at predetermined time intervals, and testing has been a very popular approach for durability assessment.

There are, however, distinct advantages to testing specimens that are simultaneously exposed to environmental and mechanical challenges, as this is often more representative of in-service conditions and may even accelerate degradation phenomena. The so-called 'Boeing wedge' test (see ASTM D3762 and ISO 10354) marked a significant advance in durability testing by introducing an initial debond, thus creating the "perfect storm" for accelerated characterization—the simultaneous application of stress plus environment in the presence of a loaded crack tip. These tests have been advocated for durability characterization for a wide range of material systems [87]. Cognard has provided an analysis method to convert crack length data into applied energy release rate estimates, provided the adherends remain linear elastic [88], resulting in:

$$G = \frac{9EI\Delta_{\text{wedge}}^2}{4ba^4} \quad (20.1)$$

where EI is the Young's modulus times the second moment of area of the symmetric adherends, Δ_{wedge} is the thickness of the wedge, b is the width of the bond, and a is the crack length. Examples to illustrate its application include determining the lowered susceptibility of Ti-6Al-4V/FM-5 bonds to reduced air pressure (and thus oxygen activity) relevant for the intended service altitude and temperature by converting debond length data (up to 80 weeks) to the evolving applied energy release rate, as

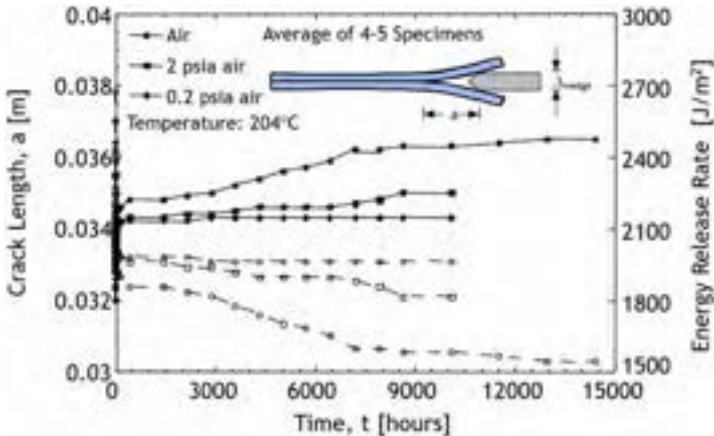


Fig. 20.2 Increasing crack length data, along with inferred energy release rate reductions, for chromic acid anodized Ti-6Al-4V/FM-5 polyimide bonded wedge specimens aged at 204°C at ambient and reduced atmospheric pressures. A preliminary version of this appeared in Ref. [91] for air exposure.

Source: © D. A. Dillard and issued, CC BY-SA 4.0. Available at: <http://hdl.handle.net/10919/112968>. (Accessed 22 December 2022).

shown in Fig. 20.2 [89]. The susceptibility of the same system to liquids of interest for aerospace applications is shown as debond propagation rate vs applied energy release rate in Fig. 20.3, where Cognard's analysis [90] has again been used to convert crack length data into applied energy release rate estimates for these linear elastic adherends; the analysis becomes more complex if plastic or viscoelastic deformation of adherends occurs.

To highlight the importance of combining stress and environment to generate the “perfect storm” for effective accelerated aging studies, we can consider the fatigue crack growth data collected for steel/epoxy specimens using the double-cantilever beam (DCB) test geometry shown in Fig. 20.4. In these tests, some samples had a drop of water applied with an eyedropper at the crack tip during testing. For those samples, it was observed that the crack growth rate increased by approximately a factor of 50 over dry samples at the same applied energy release rate. At the lowest energy release rates (corresponding to the slowest crack growth rates/longest times), the crack growth rate approached that of the dry samples, suggesting that evaporation of the water placed at the crack tip may have occurred. Other self-loading specimens have also been suggested, including the curvature mismatch test (Fig. 20.5) [92]. This is similar in principle to the wedge test, except that the applied energy release rate can remain constant with debond propagation rather than decreasing rapidly as in the wedge test, perhaps making this test more useful for more flexible adhesives.

Exposure during testing is now a common test for automotive applications (see illustrations and representative results in Chapter 24). This method involves multiple short single-lap joints, connected in series within a stress tube that was then loaded,

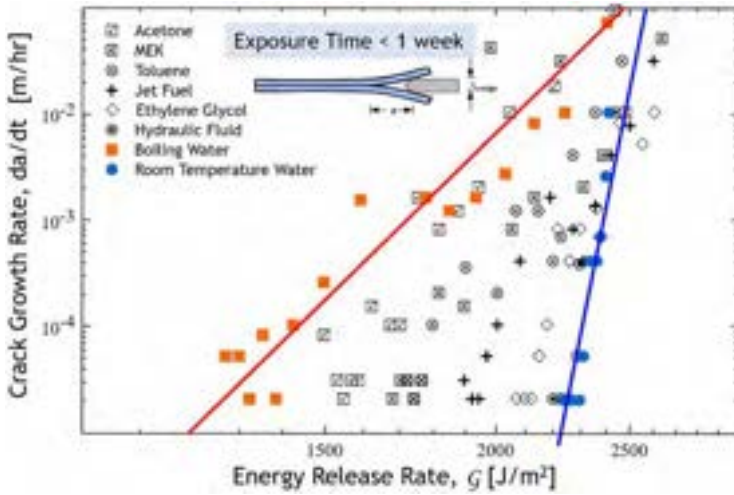


Fig. 20.3 Illustration of wedge test data collected for Ti-6Al-4V adherends bonded with FM-5, a high-temperature polyimide. Data were collected over 162h, suggesting that the debond rates in various liquids at room temperature were bounded by room temperature and boiling water exposure. Prior partial versions of this appeared in Refs. [91] and [47].

Source: © D. A. Dillard and issued, CC BY-SA 4.0. Available at: <http://hdl.handle.net/10919/112968>. (Accessed 22 December 2022).

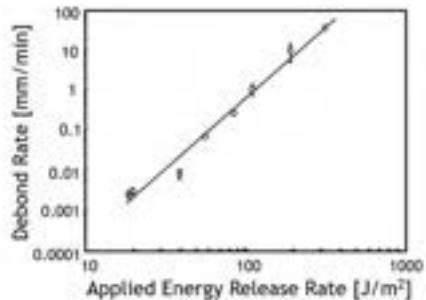


Fig. 20.4 Illustration of the effect of adding a drop of water to the crack tip of steel/epoxy DCB specimens. Details on Adhesive E are provided in Ref. [93].

Source: © D. A. Dillard and issued, CC BY-SA 4.0. Available at: <http://hdl.handle.net/10919/112968>. (Accessed 22 December 2022).

typically by a compressed coil spring. These tubes were then suspended above water baths to maintain temperature and humidity control, or exposed to cyclic and/or salt-spray conditions. When one specimen breaks in the chain of specimens, it can be replaced by a blank that allows for continued testing of the other specimens in the tube. These tests are an important advance over the expose then test sequence, as they

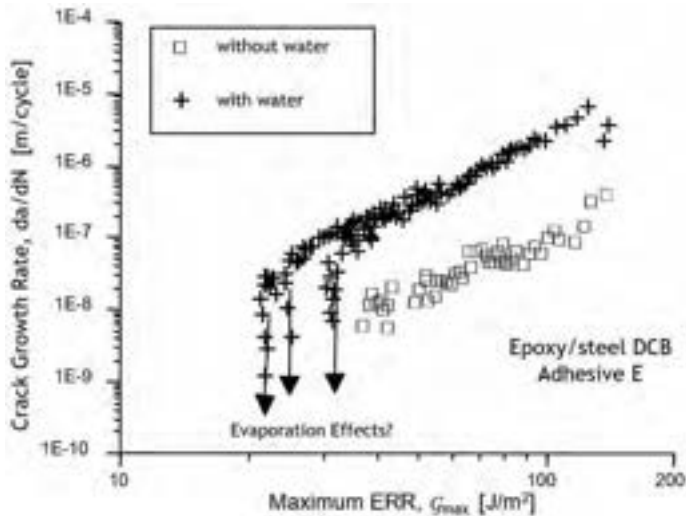


Fig. 20.5 Curvature mismatch test geometry and data for an acrylic PSA.

Source: © D. A. Dillard and issued, CC BY-SA 4.0. Available at: <http://hdl.handle.net/10919/112968>. (Accessed 22 December 2022).

simultaneously expose to environment and stress. Furthermore, the presence of the environment at the bond edges, where stress concentrations or singularities occur leads to the “perfect storm” of environmental exposure and stress singularities at the same location within the samples.

Further explorations of the synergistic effects of combining mechanical and environmental factors were conducted in the NIST SPHERE [94]. The NIST SPHERE was designed with significant industry collaboration to explore the interaction of four environmental stresses (ultraviolet (UV) radiation, heat flow/temperature, moisture, and applied mechanical stress). It was able to produce precisely controlled environments of temperature and humidity typical of in-service systems. The UV, created from a metal halide UV source, was the only environmental stress that was “accelerated.”

The SPHERE further advances the importance of combined weathering stresses similar to the example presented previously in the fatigue crack growth example. The SPHERE is able to combine a variety of environmental stresses at the same time. Fig. 20.6 illustrates how the combined environmental stresses produce unique results. In this figure, the greatest changes in sealant modulus were observed for the samples with $\pm 25\%$ movement, 50°C , and 50% relative humidity. Testing the same samples at 0% relative humidity produced the second-largest decrease in modulus. From this figure, it is possible to see that movement, heat, or moisture alone does not yield the same experimentally observed behavior as when these factors are combined.

In parallel, multienvironmental outdoor exposure instrumentation and test methods, including mechanical deformation induced by thermal mismatch of fixture components during temperature fluctuations, were developed (Fig. 20.7) [95]. The

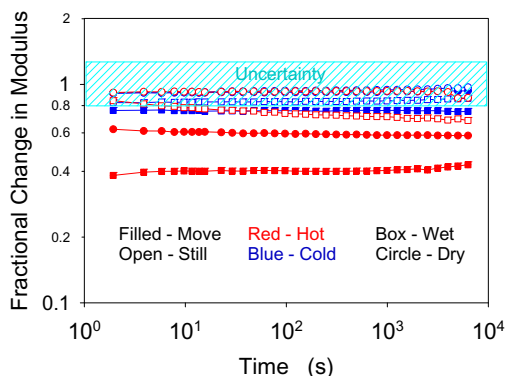


Fig. 20.6 ASTM 1735 modulus after a 30-day exposure of a commercial sealant divided by the ASTM 1735 modulus before exposure is shown as a function of exposure time. Each line represents the average of four replicates. The “cold” samples were run at 30°C while the “hot” samples were run at 50°C.

testing methods are described in ASTM 1589 method B. These outdoor testing methods, while slower than laboratory-based methods, can demonstrate the effect of weather on the long-term viability of the sealant. They also illustrate how a relatively simple device can be used to introduce combined mechanical and environmental loading. For example, in Fig. 20.8, a 4-year exposure of a sealant demonstrates how the sealant experiences daily deformations, but relatively more compression in the summer and tension in the winter. Twice a year, the sealants were removed and forced back to the initial configuration (12.5 mm width) for 10 days. Initially, the sealant can respond and accommodate the deformation by returning to the initial configuration. Over time, the sealant demonstrates a decreasing ability to accommodate the deformation. As the sealant is still subjected to the same mechanical environmentally induced strains, this is interpreted as an increase in internal stress within the sealant. This increase in internal stress is a measure of the degradation or change due to combined environmental exposure.

The NIST SPHERE approach also investigated the role of simultaneous mechanical, UV, temperature, and humidity effects on building joint sealant samples [96]. The building joint sealant samples were monitored using ASTM C1735, a stress relaxation test method. Mechanical stress imposed during weathering changed the network structure of the sealant as determined by changes to the measured stress relaxation modulus. In one experiment, four sealant chemistries were evaluated by ASTM C1519, a test method with both weathering and cyclic movement. The four sealant chemistries were evaluated with ASTM C1735 before and after weathering. Prior to weathering, two formulations exhibited very similar stress relaxation behavior. After weathering, one showed no change in shape but a change in modulus, whereas a second formulation showed both a change in shape and an increase in modulus. Other studies have shown that imposing a mechanical deformation on the sealant will result in a change in the molecular structure as measured by stress relaxation modulus

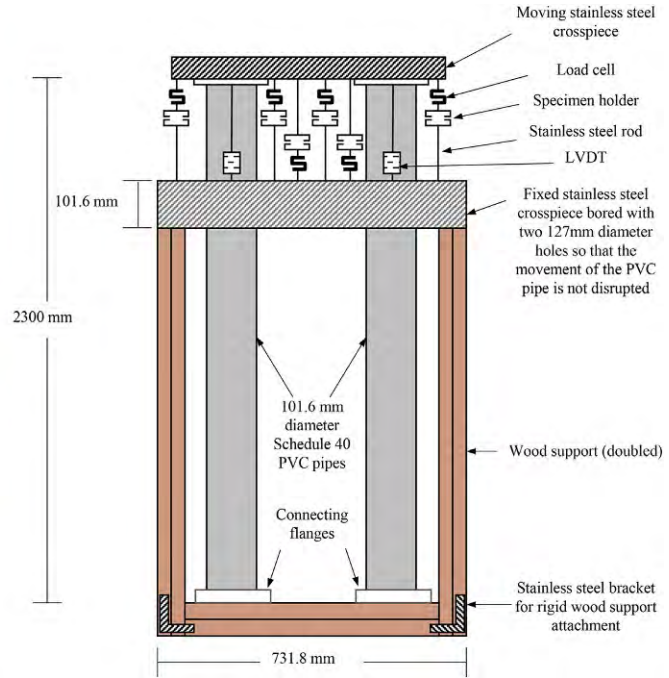


Fig. 20.7 The ASTM 1589 Method B testing apparatus.

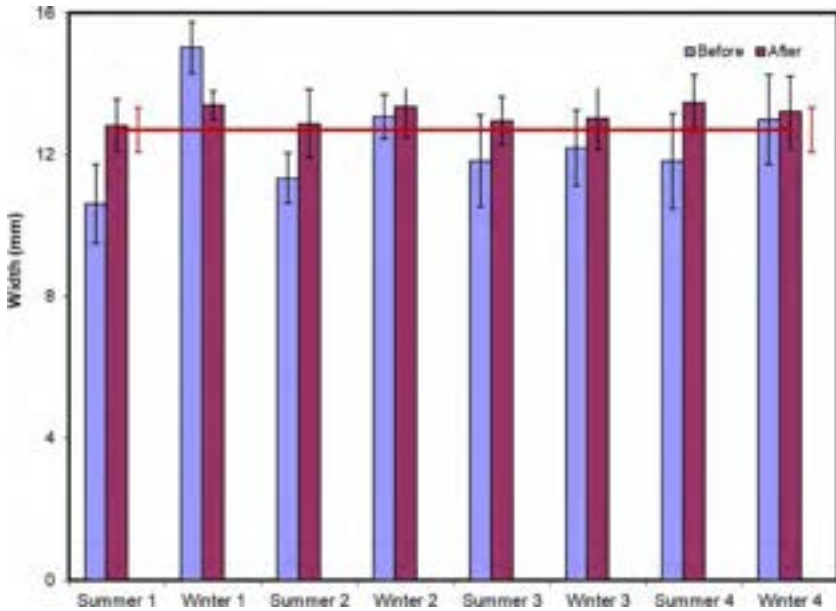


Fig. 20.8 A 4-year exposure using ASTM 1589 method B tester. Every season the sealant width showed a compression or tension set (before). After a season of exposure, the sealant is forced back into the original dimension (after). Over the 4 years of exposure, the sealant demonstrates a decreasing ability to respond to the dynamic stress.

(ASTM C1735) [97]. In these studies, it was found that the combination of heat, movement, and moisture resulted in the largest decrease in modulus.

The ability to combine the multienvironmental SPHERE exposure and the monitored outdoor exposure admits a true prediction of changes due to environmental exposure occurring in service. This is accomplished by carefully monitoring changes in relevant properties of the materials during SPHERE exposure (through FTIR, visual, or mechanical characterization) and producing a database of rate of change for a specific environmental condition. The creation of this database was enabled by the unique capabilities of the SPHERE, particularly its 32 separately controlled environmental chambers. The resulting database of experimentally determined rate constants was then used to create a statistically based material response surface, where the rate of change for the experimentally determined property of interest could be determined for a specific weather profile.

A prediction of property change for a specific outdoor exposure could be determined by breaking the weather conditions into a series of shorter time intervals (1 h), then determining the average conditions of that time interval (temperature, moisture, UV). Using the material's response surface generated from the laboratory experimental data allowed for the determination of a rate of change. By multiplying that rate of change by the time interval, the extent of change during that time interval was estimated. These estimates were summed to generate a time series estimate for the

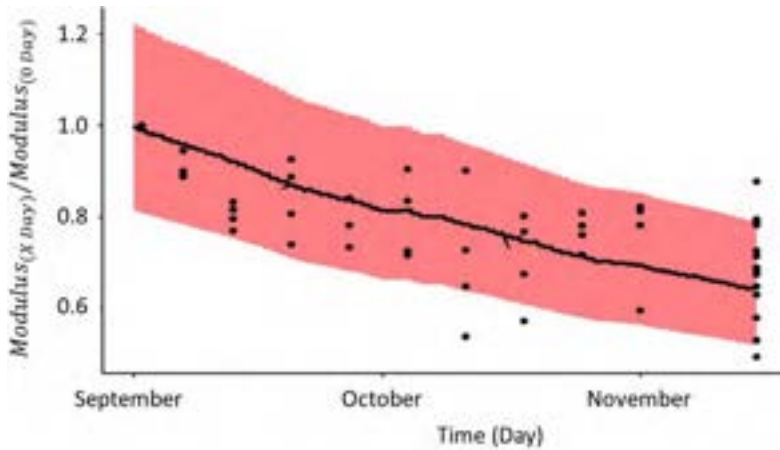


Fig. 20.9 The prediction based on SPHERE data (*solid line* (average) and 95% uncertainty (*shaded area*)) well predicts the stiffness change in the sealant measured using ASTM 1589 (*black dots*) for a 3-month period of outdoor Florida exposure.

material property change. Validation of this approach was achieved by exposing samples in an outdoor environment with monitored environmental conditions and resulting material property change [98]. This is a significant achievement, as modulus change in sealants significantly affects the induced stresses in typical displacement-defined loading conditions.

Comparing the laboratory-generated predictions with the observed outdoor changes resulted in confidence in this approach [5]. Fig. 20.9 shows such a result. In Fig. 20.9, the SPHERE-generated prediction of modulus change (given by the solid black line) and the associated 95% confidence interval are combined with measurements (shown as the black dots) from the same sealant that experienced the exact modeled environment. In this study, the sealant used was specifically formulated to degrade rapidly. There is excellent agreement between the measured outdoor modulus change in the sealant and the laboratory-generated SPHERE prediction. Generating this data for a sample with decades of expected in-service performance would require significantly more effort.

One accelerating factor that is often overlooked is that of the test specimen geometry and its dimensions. Indeed, the time for environmental degradation to take place involves both the time for the environment to diffuse into the adhesive as well as the time associated with the degradation process itself. The diffusion time is akin to an incubation time, in that the degradation process cannot begin until sufficient quantities of the agent reach that location within a specimen. This is inherently a nonuniform process, typically governed by some type of diffusion process. Although non-Fickian processes are common in polymers and adhesive layers, a simple Fickian diffusion model is often insightful [99]. The equations for heat transfer and diffusion are the same [100–102], but the thermal diffusivity is often 5–6 orders of magnitude greater than the mass diffusivity [103]. This means that specimens reaching thermal

equilibrium in several minutes could take years to reach moisture saturation when introduced to a humid or aqueous environment. Because diffusion times scale with the square of the diffusion distance, making specimens smaller can significantly reduce the time required for diffusion to take place. Several implementations of this approach have been suggested. Diffusion into neat adhesive samples is not hindered by adherends, which are often impervious to diluent ingress, thus forcing ingress within the plane of the adhesive. Thinner samples can thus reduce time to equilibrium concentration significantly. Related approaches have been applied to adhesives applied to a single adherend, resulting in a coating and interface that are susceptible to increased diffusion through the thin adhesive layer [104–106]. These methods offer the possibility to gain insights into bond durability in a small fraction of the time required for the exposure of traditional bonded joints.

A significant consideration for accelerated characterization is how one can detect precursor damage events that might lead to failure. If one can detect such damage events, often occurring well before final separation or failure, one gains advanced information about durability, and may be able to shorten the durability testing requirement. Methods that have been used include the backface strain measurement method [107–110] and dielectric impedance spectroscopy [111,112]. Characterizing debond growth rates under fatigue loading or creep scenarios provides rates of debonding, often over a range of applied energy release rates. This allows one to make design predictions using either the fail-safe approach, where thresholds can be identified, or the safe-life approach, where one can predict evolving crack length. These can be applied to structural bonds, including with standard fracture specimens such as the DCB and in peel testing, including extensions to softer adhesive systems [113].

20.4 TTSP and accelerated characterization

Polymers exhibit viscoelastic behavior due to chain relaxation, which controls the viscosity, diffusion, and mechanical properties of these materials. The time-temperature superposition principle (TTSP, also known as frequency-temperature superposition or the method of reduced variables) is a common procedure to extend the time over which the material behavior is studied [114]. Simply stated, the approach allows one to conduct a series of tests (e.g., storage and loss modulus measurements at several frequencies or stress relaxation or creep as a function of time) at different temperatures. The resulting data are then plotted as a function of $\log(\omega)$ or $\log(t)$ and then shifted horizontally from a reference temperature T_r by a shift factor $\log(a_T)$ where $\log(a_T) = \log(\tau_T/\tau_r)$ and τ_T and τ_r are the characteristic relaxation times at T and T_r , respectively [115]. Polymer physics makes a strong case for the validity of temperature as an accelerating parameter for TTSP applications, though other parameters are also possible. For example, the Doolittle equation can be used to derive the Williams-Landel-Ferry (WLF) equation through increases in free volume associated with thermal expansion [116]. Strictly speaking, the use of TTSP is restricted to “thermorheologically simple” where the shift factor is identical for all relaxation times; in practice, relaxation times associated with different transition regions shifting by

different amounts, becoming “thermorheologically complex,” with judgment required to decide if a valid or usable master curve can be constructed.

Free volume reduces intermolecular frictional forces by enhancing molecular mobility, so in addition to temperature, other factors increasing free volume are expected to induce similar acceleration. Examples of this include sorbed water or diluents as well as tensile mean stress states that result in the dilation of polymers, which can also increase free volume. Again, it is important to distinguish between increases in volume due to additional free volume that enhances mobility and voiding or other damage that may lead to failure, which are not associated with changes in free volume at the continuum level. Knauss and Emri [117–119] proposed a simple extension of the WLF model that includes increases in free volume associated with diluent ingestion and hydrostatic stress state. Schapery [120] introduced an alternate nonlinear viscoelastic constitutive model based on a shift factor associated with the applied stress level to develop a time-temperature-stress superposition. Gamby and Blugeon [121] used this approach to characterize the behavior of an FM-73 adhesive.

20.4.1 Impact of physical aging on TTSP

The thermo-mechanical response of epoxy networks is a strong function of the thermal history to which they are exposed during curing. As discussed in detail in [Chapter 31](#), the evolution of the viscoelastic properties of epoxy systems during curing has been predicted using a time conversion superposition principle with adequate levels of accuracy [122]. The viscoelastic properties as a function of different degrees of cure have been studied using similar superposition techniques that successfully describe the effect of crosslink density on the material response [123–125]. However, the impact of the crosslink density of the network structures on physical aging was not accounted for, and was investigated by other researchers [126–128]. Based on these findings, with an increase in crosslink density of the networks, the time to achieve structural equilibrium increases (due to reduced mobility) [127,128], while the rates of enthalpy relaxation [129] and total enthalpy relaxation decrease [129]. The behavior is attributed to the limited number of molecular rearrangements at higher levels of crosslinkages. As the motion of the polymer chains reduces, the network structure exhibits decreased propensity to reduce the available free volume and conformational enthalpy through relaxation.

[Fig. 20.10](#) highlights the importance of crosslink density in governing the aging behavior of a model system (polyphenylene oxide/epoxy) through detailed time-aging time superposition and time-temperature superposition analysis [127]. As evident from the plot, the characteristic relaxation timescales are strongly dependent on the crosslink density of the network. The physical aging behavior of such network systems was found to be remarkably analogous to thermoplastic glasses [56]. The effect of crosslink length on the aging of epoxy systems has also been investigated [130]. The results suggest that with increasing crosslink lengths, the relaxation dynamics of the polymer chains are noncooperative in nature, which reduces the severity of the physical aging process. On the other hand, for thermoplastic adhesives the physical aging behavior is notably different. The molecular architecture in thermoplastic

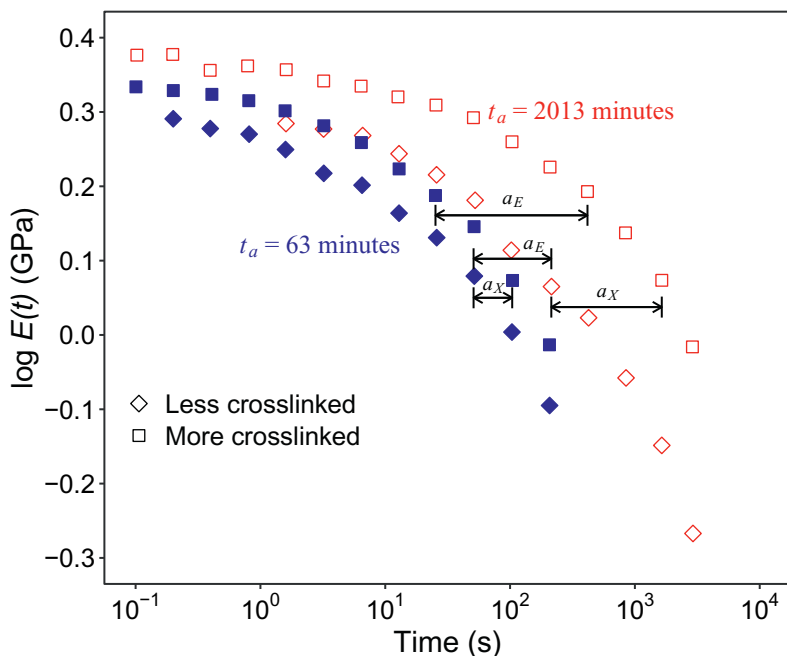


Fig. 20.10 Relaxation modulus vs time for DGEBA/PPO systems with two different aging levels (filled markers, 63 min; open markers, 2013 min) and two different crosslink densities. Here, a_E is the aging shift factor and a_X is the shift factor to longer aging times as crosslink density increases.

Reprinted with permission from G.M. Odegard, A. Bandyopadhyay, Physical aging of epoxy polymers and their composites, *J. Polym. Sci. B* 49(24) (2011) 1695–1716, John Wiley & Sons Ltd. The original data were obtained from A. Lee, G.B. McKenna, Viscoelastic response of epoxy glasses subjected to different thermal treatments, *Polym. Eng. Sci.* 30(7) (1990) 431–435.

systems allows for a relatively higher degree of conformational changes during aging compared to the thermoset counterparts (where conformational changes are limited by the cured network structure).

20.4.2 Reversing physical aging effects

Thermal rejuvenation is an interesting approach to counter the effects of physical aging on the network structures, and the associated mechanism for epoxies has been a topic of significant research [56,131–133]. Briefly, the thermal history can be effectively erased by exposing the aged polymer network to temperatures above its T_g . Annealing temperatures of approximately $T_g + 40^\circ\text{C}$ coupled with exposure times of 10–15 min are sufficient for rejuvenating the networks [134], although the conditions are dependent on the material properties of the polymer. Moreover, the cooling profiles postannealing to temperatures below T_g dictate the characteristics of the rejuvenated polymer.

Interestingly, the thermal rejuvenation can also be achieved at temperatures lower than the T_g of the polymer. The classical definition of physical aging is based on the free volume theory and the rejuvenation of glassy materials was attributed to the sizeable amounts of mechanical deformations [133]. However, subsequent research suggests that rejuvenation simply imparts a quenching effect on the material and can remove the effects of prior aging. Researchers have successfully rejuvenated epoxy networks at sub- T_g temperatures and termed the set temperature as “erasure temperature” [131,135]. The mechanism behind sub- T_g rejuvenation is known as the localization effect, which is related to the temperature-dependent changes to the configurations on the polymer backbone. The effects of physical aging can be removed by exploiting such molecular transitions (dictated by the polymer stereochemistry) at sub- T_g temperatures.

Fig. 20.11 shows the results from an attempt to partition physical and chemical aging for the fracture energies of DCB specimens consisting of chromic acid anodized Ti-6Al-4V adherends bonded with FM-5 polyimide adhesive that were aged 12 months at 204°C. Aging was conducted in three different pressure environments: ambient air pressure and partially evacuated chambers at absolute pressures corresponding to service altitude (13.8 kPa (2 psia)) and an order of magnitude lower pressure to further reduce oxygen activity (1.38 kPa (0.2 psia)) [89]. Following ASTM

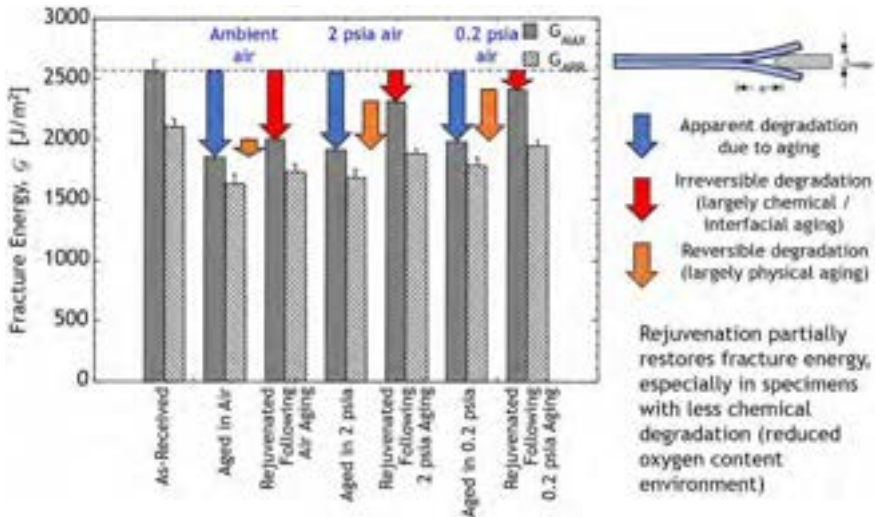


Fig. 20.11 Illustration of DCB results for CAA Ti/FM 5 DCB specimens aged 12 months at 204°C in different pressure environments. Colored arrows are shown to suggest that the total degradation (*blue arrows*) can be partitioned, with the relative magnitudes of permanent reductions in G_{max} , assumed to be from chemical degradation of adhesive or the interface (*red arrows*) and degradation thought to be associated with physical aging (*orange arrows*), which is reversed by rejuvenation. An earlier version of this appears in Ref. [89].

Source: © D. A. Dillard and issued, CC BY-SA 4.0. Available at: <http://hdl.handle.net/10919/112968>. (Accessed 22 December 2022).

D3433, both maximum and arrest fracture energies are shown. As described in the caption, some of the total degradation seen after aging was reversible following rejuvenation (assumed to be due to physical aging), while some was irreversible. Chemical aging of the polyimide or interface was thought to be responsible for the irreversible portion of the degradation. As pressure and hence oxygen concentration decreased, chemical aging due to oxidation, for example, would be reduced. Physical aging likely played a larger role in measured fracture energy reductions for these specimens, likely because densification reduced the molecular mobility and energy dissipation mechanisms. This approach offers a possible framework to partitioning irreversible damage from apparent damage that is reversed by rejuvenation.

20.5 Examples and a case study

TTSP has been widely employed for adhesives and other polymeric materials for constitutive properties. There have perhaps been fewer applications to strength and fracture properties, though TTSP's merits and utility have been shown in a number of publications. Here, we provide two classic examples for pressure-sensitive adhesive (PSA) tapes, and present a recent case study for a polyurethane adhesive.

A good example of the application of TTSP is the work of Kaelble [136], who studied the peel strength of cellophane bonded to cellophane with a polyisobutylene-based adhesive using the 90° peel test. The results were then shifted to a common reference temperature with temperature shift factors. A summary of those results is illustrated in Fig. 20.12. Note that in addition to shifted data, this plot includes a number of measurements made at the 25°C reference temperature (red x symbols). In Kaelble's

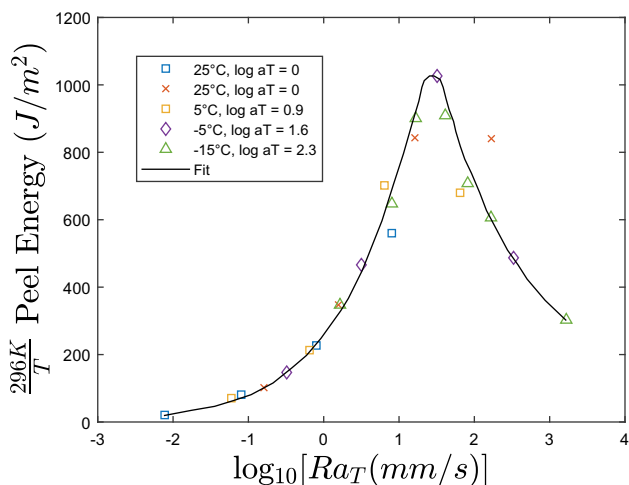


Fig. 20.12 Peel data for polyisobutylene-based adhesive reduced at a reference temperature of 25°C.

Adapted from D.H. Kaelble, Theory and analysis of peel adhesion: rate-temperature dependence of viscoelastic interlayers, *J. Colloid Sci.* 19 (5) (1964) 413–424.

words, “[c]omparison of the reduced data and direct test data indicates reasonably good agreement.” Here, the range of rates spanned by using TTSP (approximately five decades) is not that much greater than the range obtained at any individual temperature (approximately three decades).

Gent and Petrich [137] also used time-temperature superposition to reduce T-peel data for two similar butadiene-styrene copolymer adhesives (labeled A and B) with similar number average molecular weights. Adhesive B was chosen to give a greater degree of rubber-like behavior at room temperature. The peel strength versus shifted rate data exhibit a complicated behavior consisting of a steady increase in peel force with rate of peel up to a critical rate, followed by an abrupt transition to much smaller peel forces. At the same time, the mode of failure changed from cohesive failure of the polymer layer to interfacial failure. Gent and Petrich explained this behavior in terms of the transition from liquid-like to rubber-like behavior of the polymer at the first peak and the transition from rubber-like to glass-like behavior at high rates. This was confirmed by comparing the peel force/shifted rate plot with the plot of the Young’s modulus and rate of extension where the peaks did, in fact, align with the transitions. To confirm the hypothesis that the low-rate transition was associated with liquid-like flow, they crosslinked polymer A to prevent that flow from occurring. For the crosslinked material, the first peak no longer appeared along with only interfacial failure. Interestingly, for polymer B only a single peak was observed. Again, this was explained in terms of the liquid-like flow, which in this case was limited by the higher molecular weight chains (Fig. 20.13).

To further illustrate the applicability of TTSP to evaluating the durability of an adhesive system of industrial interest, we consider a case study from the work of Anderson [138] where a polyurethane adhesive was evaluated. Storage modulus, loss

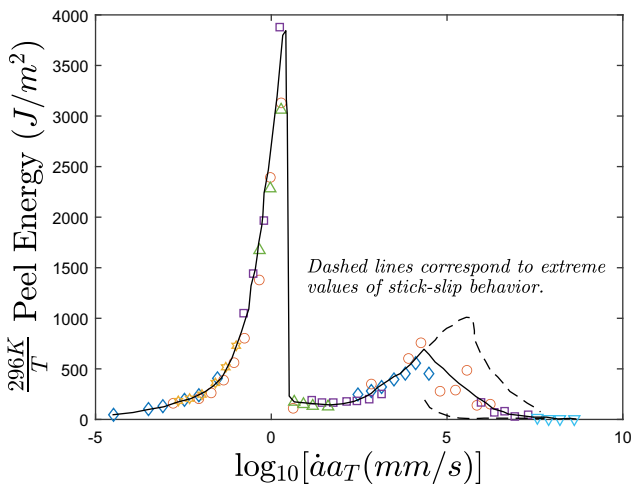


Fig. 20.13 Master peel force vs shifted rate plot for butadiene-styrene copolymer adhesive (Gent and Petrich polymer A) adhering to Mylar. The dashed lines correspond to the extreme values of stick-slip behavior.

Adapted from A. Gent, R. Petrich, Adhesion of viscoelastic materials to rigid substrates, Proc. R. Soc.Lond. A Math. Phys. Sci. 310 (1502) (1969) 433–448.

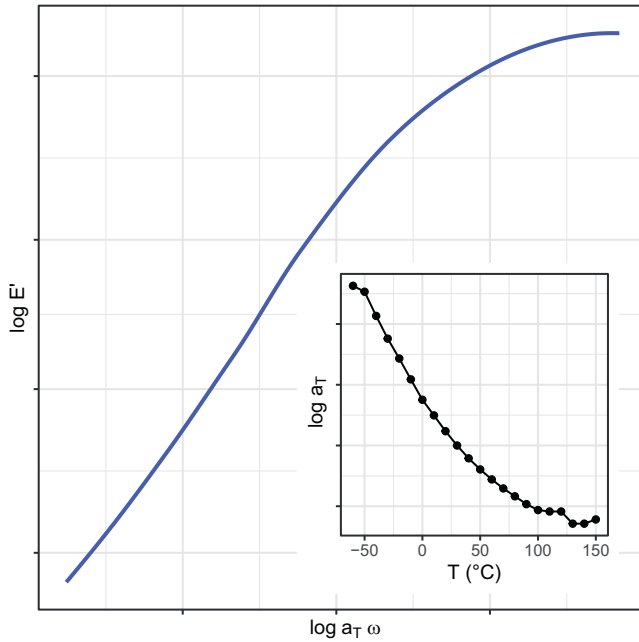


Fig. 20.14 Master curve of storage modulus as a function of reduced frequency and associated shift factors for a polyurethane adhesive [138].

modulus, and $\tan \delta$ master curves were conducted using frequency sweeps ranging from 1 to 100 Hz at 22 different temperatures ranging from -60°C to 110°C . The data were then horizontally shifted in reference to the data at 30°C to develop master curves. The resulting master curve for the storage modulus (E') is shown in Fig. 20.14. (Note that at the sponsor's request, the ordinate scales have been removed.)

Once the DMA tests were completed, T-peel samples were prepared and tested. These T-peel specimens consisted of two 2024 aluminum adherends bonded together using the same polyurethane adhesive. During the peel tests, both load and displacement were measured. Unlike some other fracture test geometries, T-peel samples are often made with relatively thin adherends that may experience significant plastic deformation during the tests. To determine the fracture energy of the adhesive, the ICPeel analysis [139] was used to partition the dissipated energy into that dissipated through plastic work in bending the adherends and the energy dissipated within the adhesive (the fracture energy). Samples were tested at various displacement rates and temperatures in the unaged condition, after exposure to isothermal aging conditions (unstressed), and after being subjected to cyclically varying temperature (with and without moisture present). In total, nearly 200 T-peel samples were tested. Additional details are provided in Ref. [138].

The fracture energy values for the unaged samples were plotted as a function of a_T -Rate for each of the temperatures at which tests were conducted using the temperature shift factors obtained from the DMA tests to develop a master curve of fracture energy vs reduced crosshead rate. The resulting plot is shown in Fig. 20.15. While there is considerable scatter in the fracture energy, the overall trend is clear. In fact,

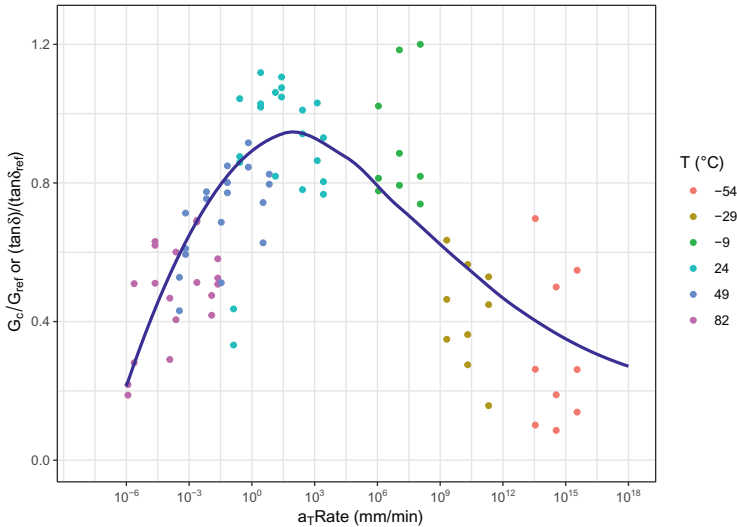


Fig. 20.15 Master curve of average fracture energy from T-peel tests conducted at several rates and temperatures (*symbols*) for a polyurethane adhesive bonded to aluminum, and $\tan \delta$ from DMA tests for the same polyurethane adhesive (*solid line*) (all referenced to 30°C). The shift factors from the DMA data were used to shift the T-peel results and a process zone size of 100mm was used to calculate an equivalent rate for the $\tan \delta$ data [138].

if the values for $\tan \delta$ are appropriately scaled, we see that the trend in the fracture energy mimics that of the loss tangent. This is not surprising given that both the fracture energy and the loss tangent are measures of the adhesive's ability to dissipate energy. Similar correlations have been reported for other adhesive systems [140,141], as also discussed in Chapter 21.

Additional results were collected for the aged samples. The experimental data showed that 400+ thermal cycles introduced changes in fracture energy that were statistically insignificant in comparison with their unaged counterparts. Additionally, samples aged for up to 2000h in a dry environment or 500h in a wet environment showed no significant reduction in fracture energies. However, specimens aged for more than 500h in a wet environment were observed to have a significant decrease in fracture energy values in comparison with those of the unaged system.

These examples (and others) illustrate that we can use temperature to accelerate or decelerate the influence of loading rates and that by careful interpretation of the data, we can connect the observed behavior of the joint to the properties of the adhesive. Additionally, within limits, we can tailor the properties of the adhesive to control the behavior of the joints.

20.6 Summary: Status and future needs

Of the existing techniques for accelerated testing of adhesives, TTSP and the related time-temperature-stress superposition and time-temperature-diluent concentration superposition (e.g., [142]) have the best grounding in polymer physics and are

relatively simple to employ. The examples above show that they are useful in accelerating behavior in laboratory conditions. However, with real systems there are almost always questions about whether the assumptions of TTSP are met. Most critically, in practice there are often multiple degradation mechanisms that may be occurring simultaneously. Investigators have been successful in correlating accelerated laboratory tests with real-time outdoor exposure. However, such correlations have been limited to a particular adhesive system in a particular environment—at least when it comes to quantitative estimates necessary for reliability predictions (qualitative rankings are possible). Translating results from one application to another can be a challenge. For example, while the automotive, aerospace, and electronics industries have significant experience studying the effects of aging on epoxy adhesives, the results are nearly impossible to apply to civil engineering applications because of the differences in loading conditions, types of environmental exposure, the substrate materials, the manufacturing processes, and the expected service lifetimes. As computational power becomes more readily available at low cost and as numerical analysis tools are developed to take advantage of that power and to provide more accurate stress analyses, refined test methods will be needed to provide inputs to those models.

References

- [1] ASC, Adhesive Standard Test Methods, 2022. https://www.ascouncil.org/page/Test_Methods/-Adhesive-Standard-Test-Methods.htm. (Accessed 21 December 2022).
- [2] B. Duncan, Developments in testing adhesive joints, in: D.A. Dillard (Ed.), *Advances in Structural Adhesive Bonding*, Woodhead Publishing, 2010, pp. 389–436 (Chapter 14).
- [3] S.R. Hartshorn, The durability of structural adhesive joints, in: S.R. Hartshorn (Ed.), *Structural Adhesives: Chemistry and Technology*, Springer US, Boston, MA, 1986, pp. 347–406.
- [4] I. Wilson, P.G. Sheasby, A. Maddison, The significance of environment for performance of structural adhesive bonding, *SAE Trans.* 106 (1997) 6–14.
- [5] C. White, D. Hunston, K. Tan, Predicting material in-service performance using the NIST SPHERE, in: *Proceedings of the 4th European Weathering Symposium, Budapest, 2009*.
- [6] L.F.M. da Silva, P.J.C. das Neves, R.D. Adams, J.K. Spelt, Analytical models of adhesively bonded joints—part I: literature survey, *Int. J. Adhes. Adhes.* 29 (3) (2009) 319–330.
- [7] L.D.R. Grant, R.D. Adams, L.F.M. da Silva, Experimental and numerical analysis of single-lap joints for the automotive industry, *Int. J. Adhes. Adhes.* 29 (4) (2009) 405–413.
- [8] A. Mubashar, I.A. Ashcroft, G.W. Critchlow, A.D. Crocombe, Strength prediction of adhesive joints after cyclic moisture conditioning using a cohesive zone model, *Eng. Fract. Mech.* 78 (16) (2011) 2746–2760.
- [9] H.M. Hand, C.O. Arah, D.K. McNamara, M.F. Mecklenburg, Effects of environmental exposure on adhesively bonded joints, *Int. J. Adhes. Adhes.* 11 (1) (1991) 15–23.
- [10] C.D.M. Liljedahl, A.D. Crocombe, M.A. Wahab, I.A. Ashcroft, Modelling the environmental degradation of the interface in adhesively bonded joints using a cohesive zone approach, *J. Adhes.* 82 (11) (2006) 1061–1089.
- [11] M.D. Banea, L.F.M. da Silva, The effect of temperature on the mechanical properties of adhesives for the automotive industry, *Proc. Inst. Mech. Eng. L J. Mater. Des. Appl.* 224 (2) (2010) 51–62.

- [12] G. Viana, M. Costa, M.D. Banea, L.F.M. Da Silva, A review on the temperature and moisture degradation of adhesive joints, *Proc. Inst. Mech. Eng. L J. Mater. Des. Appl.* 231 (5) (2017) 488–501.
- [13] E.A.S. Marques, L.F. Da Silva, M.D. Banea, R.J.C. Carbas, Adhesive joints for low-and high-temperature use: an overview, *J. Adhes.* 91 (7) (2015) 556–585.
- [14] F.M.G. Ramírez, M.F.S.F. de Moura, R.D.F. Moreira, F.G.A. Silva, A review on the environmental degradation effects on fatigue behaviour of adhesively bonded joints, *Fatigue Fract. Eng. Mater. Struct.* 43 (7) (2020) 1307–1326.
- [15] J. Comyn, Diffusion and adhesion, in: J. Comyn (Ed.), *Polymer Permeability*, Springer Netherlands, Dordrecht, 1985, pp. 177–215.
- [16] A.N. Rider, N. Brack, S. Andres, P.J. Pigram, The influence of hydroxyl group concentration on epoxy–aluminium bond durability, *J. Adhes. Sci. Technol.* 18 (10) (2004) 1123–1152.
- [17] M.Y.M. Chiang, M. Fernandez-Garcia, Relation of swelling and Tg depression to the apparent free volume of a particle-filled, epoxy-based adhesive, *J. Appl. Polym. Sci.* 87 (9) (2003) 1436–1444.
- [18] L.S.A. Smith, V. Schmitz, The effect of water on the glass transition temperature of poly(methyl methacrylate), *Polymer* 29 (10) (1988) 1871–1878.
- [19] G. Viana, M. Banea, L. da Silva, A review on the temperature and moisture degradation of adhesive joints, *Proceedings of the Institution of Mechanical Engineers, Part L: Journal of Materials: Design and Applications.* 231 (5) (2017) 488–502, <https://doi.org/10.1177/1464420716671503>.
- [20] P. Galvez, J. Abenojar, M.A. Martinez, Effect of moisture and temperature on the thermal and mechanical properties of a ductile epoxy adhesive for use in steel structures reinforced with CFRP, *Composites Part B* 176 (2019) 107194, <https://doi.org/10.1016/j.compositesb.2019.107194>.
- [21] F. Zhang, H.-P. Wang, C. Hicks, X. Yang, B. Carlson, Q. Zhou, Experimental study of initial strengths and hygrothermal degradation of adhesive joints between thin aluminum and steel substrates, *International Journal of Adhesion and Adhesives* 43 (2013) 14–25, <https://doi.org/10.1016/j.ijadhadh.2013.01.001>.
- [22] J.A.M. Ferreira, P.N. Reis, J.D.M. Costa, M.O.W. Richardson, Fatigue behaviour of composite adhesive lap joints, *Composites Science and Technology* 62 (10–11) (2002) 1373–1379, [https://doi.org/10.1016/S0266-3538\(02\)00082-9](https://doi.org/10.1016/S0266-3538(02)00082-9).
- [23] W.-L. Mu, Q.-H. Xu, J.-X. Na, H. Wang, W. Tan, D.-F. Li, Influence of temperature and humidity on the fatigue behaviour of adhesively bonded CFRP/aluminium alloy joints, *The Journal of Adhesion* 98 (10) (2022) 1358–1376, <https://doi.org/10.1080/00218464.2021.1896362>.
- [24] D.M. Segura, A.D. Nurse, A. McCourt, R. Phelps, A. Segura, Chemistry of polyurethane adhesives and sealants, in: P. Cognard (Ed.), *Handbook of Adhesives and Sealants*, Elsevier Science, 2005, pp. 101–162 (Chapter 3).
- [25] J.A. Harris, P.A. Fay, Fatigue life evaluation of structural adhesives for automotive applications, *Int. J. Adhes. Adhes.* 12 (1) (1992) 9–18.
- [26] M.D. Banea, L.F.M. da Silva, R.D.S.G. Campilho, Mode I fracture toughness of adhesively bonded joints as a function of temperature: experimental and numerical study, *Int. J. Adhes. Adhes.* 31 (5) (2011) 273–279.
- [27] M. Mariam, M. Afendi, M.S. Abdul Majid, M.J.M. Ridzuan, A.I. Azmi, M.T.H. Sultan, Influence of hydrothermal ageing on the mechanical properties of an adhesively bonded joint with different adherends, *Compos. Part B Eng.* 165 (2019) 572–585.

- [28] M. Fernando, W.W. Harjoprayitno, A.J. Kinloch, A fracture mechanics study of the influence of moisture on the fatigue behaviour of adhesively bonded aluminium-alloy joints, *Int. J. Adhes. Adhes.* 16 (2) (1996) 113–119.
- [29] M.W. Rushforth, P. Bowen, E. McAlpine, X. Zhou, G.E. Thompson, The effect of surface pretreatment and moisture on the fatigue performance of adhesively-bonded aluminium, *J. Mater. Process. Technol.* 153–154 (2004) 359–365.
- [30] R.A. Jurf, J.R. Vinson, Effect of moisture on the static and viscoelastic shear properties of epoxy adhesives, *J. Mater. Sci.* 20 (8) (1985) 2979–2989.
- [31] I.A. Ashcroft, M.M.A. Wahab, A.D. Crocombe, D.J. Hughes, S.J. Shaw, The effect of environment on the fatigue of bonded composite joints. Part 1: testing and fractography, *Compos. A: Appl. Sci. Manuf.* 32 (1) (2001) 45–58.
- [32] D. Fata, W. Possart, Aging behavior of a hot-cured epoxy system, *J. Appl. Polym. Sci.* 99 (5) (2006) 2726–2736.
- [33] R.J.C. Carbas, E.A.S. Marques, L.F.M. da Silva, A.M. Lopes, Effect of cure temperature on the glass transition temperature and mechanical properties of epoxy adhesives, *J. Adhes.* 90 (1) (2014) 104–119.
- [34] Y. Zhang, R.D. Adams, L.F.M. da Silva, Effects of curing cycle and thermal history on the glass transition temperature of adhesives, *J. Adhes.* 90 (4) (2014) 327–345.
- [35] R.A. Pethrick, Design and ageing of adhesives for structural adhesive bonding—a review, *Proc. Inst. Mech. Eng L J. Mater. Des. Appl.* 229 (5) (2015) 349–379.
- [36] W.K. Loh, A.D. Crocombe, M.M. Abdel Wahab, I.A. Ashcroft, Modelling anomalous moisture uptake, swelling and thermal characteristics of a rubber toughened epoxy adhesive, *Int. J. Adhes. Adhes.* 25 (1) (2005) 1–12.
- [37] S. Sugiman, A.D. Crocombe, I.A. Ashcroft, Modelling the static response of unaged adhesively bonded structures, *Eng. Fract. Mech.* 98 (2013) 296–314.
- [38] C.D.M. Liljedahl, A.D. Crocombe, M.A. Wahab, I.A. Ashcroft, The effect of residual strains on the progressive damage modelling of environmentally degraded adhesive joints, *J. Adhes. Sci. Technol.* 19 (7) (2005) 525–547.
- [39] A. Ameli, N.V. Datta, M. Papini, J.K. Spelt, Hygrothermal properties of highly toughened epoxy adhesives, *J. Adhes.* 86 (7) (2010) 698–725.
- [40] A.D. Crocombe, Y.X. Hua, W.K. Loh, M.A. Wahab, I.A. Ashcroft, Predicting the residual strength for environmentally degraded adhesive lap joints, *Int. J. Adhes. Adhes.* 26 (5) (2006) 325–336.
- [41] D.-W. Suh, M.-K. Ku, J.-D. Nam, B.-S. Kim, S.-C. Yoon, Equilibrium water uptake of epoxy/carbon fiber composites in hygrothermal environmental conditions, *J. Compos. Mater.* 35 (3) (2001) 264–278.
- [42] M.R. Vanlandingham, R.F. Eduljee, J.W. Gillespie Jr., Moisture diffusion in epoxy systems, *J. Appl. Polym. Sci.* 71 (5) (1999) 787–798.
- [43] J. Zhou, J.P. Lucas, The effects of a water environment on anomalous absorption behavior in graphite/epoxy composites, *Compos. Sci. Technol.* 53 (1) (1995) 57–64.
- [44] Y. Zhang, R.D. Adams, L.F.M.d. Silva, Absorption and glass transition temperature of adhesives exposed to water and toluene, *Int. J. Adhes. Adhes.* 50 (2014) 85–92.
- [45] M. Mubashar, I.A. Ashcroft, G.W. Critchlow, A.D. Crocombe, Moisture absorption–desorption effects in adhesive joints, *International Journal of Adhesion and Adhesives* 29 (8) (2009) 751–760, <https://doi.org/10.1016/j.ijadhadh.2009.05.001>.
- [46] D.A. Dillard, J.A. Hinkley, W.S. Johnson, T.L.S. Clair, Spiral tunneling cracks induced by environmental stress cracking in LaRCTM-TPI adhesives, *J. Adhes.* 44 (1–2) (1994) 51–67.

- [47] H. Parvatareddy, J.G. Dillard, J.E. McGrath, D.A. Dillard, Solvent effects on high temperature polyimides and their bonded joints, *J. Adhes.* 69 (1–2) (1999) 83–98.
- [48] N. Su, R.I. Mackie, W.J. Harvey, The effects of ageing and environment on the fatigue life of adhesive joints, *Int. J. Adhes. Adhes.* 12 (2) (1992) 85–93.
- [49] K. Houjou, K. Shimamoto, H. Akiyama, C. Sato, Effect of cyclic moisture absorption/desorption on the strength of epoxy adhesive joints and moisture diffusion coefficient, *The Journal of Adhesion* 98 (11) (2022) 1535–1551, <https://doi.org/10.1080/00218464.2021.1926242>.
- [50] M.R. Bowditch, The durability of adhesive joints in the presence of water, *International Journal of Adhesion and Adhesives* 16 (2) (1996) 73–79, [https://doi.org/10.1016/0143-7496\(96\)00001-2](https://doi.org/10.1016/0143-7496(96)00001-2).
- [51] C.K. Gurumurthy, E.J. Kramer, C.-Y. Hui, Water-assisted sub-critical crack growth along an interface between polyimide passivation and epoxy underfill, *Int. J. Fract.* 109 (1) (2001) 1–28.
- [52] C.K. Gurumurthy, E.J. Kramer, C.Y. Hui, Hydro-thermal fatigue of polymer interfaces, *Acta Mater.* 49 (16) (2001) 3309–3320.
- [53] K.M. Liechti, G.A. Arzoumanidis, S.-J. Park, Fatigue fracture of fully saturated bonded joints, *J. Adhes.* 78 (5) (2002) 383–411.
- [54] G.B. McKenna, Y. Leterrier, C.R. Schultheisz, The evolution of material properties during physical aging, *Polym. Eng. Sci.* 35 (5) (1995) 403–410.
- [55] L.C.E. Struik, Physical aging in amorphous glassy polymers, *Ann. N. Y. Acad. Sci.* 279 (1) (1976) 78–85.
- [56] L.C.E. Struik, Physical aging in plastics and other glassy materials, *Polym. Eng. Sci.* 17 (3) (1977) 165–173.
- [57] L.C.E. Struik, *Physical Aging in Amorphous Polymers and Other Materials*, Elsevier, 1978.
- [58] A. Bandyopadhyay, G.M. Odegard, Molecular modeling of physical aging in epoxy polymers, *J. Appl. Polym. Sci.* 128 (1) (2013) 660–666.
- [59] W.D. Cook, Ageing and yielding in model epoxy thermosets, *Polymer* 40 (5) (1999) 1209–1218, [https://doi.org/10.1016/S0032-3861\(98\)00343-7](https://doi.org/10.1016/S0032-3861(98)00343-7).
- [60] M. Alcoutlabi, G.B. McKenna, Effects of confinement on material behaviour at the nanometre size scale, *J. Phys. Condens. Matter* 17 (15) (2005) R461.
- [61] M. Alcoutlabi, G.B. McKenna, S.L. Simon, Analysis of the development of isotropic residual stresses in a bismaleimide/spiro orthocarbonate thermosetting resin for composite materials, *J. Appl. Polym. Sci.* 88 (1) (2003) 227–244.
- [62] M. Merzlyakov, G.B. McKenna, S.L. Simon, Cure-induced and thermal stresses in a constrained epoxy resin, *Compos. A: Appl. Sci. Manuf.* 37 (4) (2006) 585–591.
- [63] P. Prasatya, G.B. McKenna, S.L. Simon, A viscoelastic model for predicting isotropic residual stresses in thermosetting materials: effects of processing parameters, *J. Compos. Mater.* 35 (10) (2001) 826–848.
- [64] T. Servay, R. Voelkel, H. Schmiedberger, S. Lehmann, Thermal oxidation of the methylene diphenylene unit in MDI-TPU, *Polymer* 41 (14) (2000) 5247–5256.
- [65] T. Gupta, B. Adhikari, Thermal degradation and stability of HTPB-based polyurethane and polyurethaneureas, *Thermochim. Acta* 402 (1) (2003) 169–181.
- [66] Zain, N.M., Ahmad, S.H., and Ali, E.S., "Durability of green polyurethane adhesive bonded aluminum alloy in dry and hydrothermal ageing conditions." *J. Appl. Polym. Sci.*, 2014. 131(23). N.M. Zain, S.H. Ahmad, E.S. Ali, Durability of green polyurethane adhesive bonded aluminum alloy in dry and hydrothermal ageing conditions, *J. Appl. Polym. Sci.* 131 (23) (2014) 41151, <https://doi.org/10.1002/app.41151>.

- [67] J.E. Huacuja-Sánchez, K. Müller, W. Possart, Water diffusion in a crosslinked polyether-based polyurethane adhesive, *Int. J. Adhes. Adhes.* 66 (2016) 167–175.
- [68] T. Pretsch, I. Jakob, W. Müller, Hydrolytic degradation and functional stability of a segmented shape memory poly(ester urethane), *Polym. Degrad. Stab.* 94 (1) (2009) 61–73.
- [69] T.M. Chapman, Models for polyurethane hydrolysis under moderately acidic conditions: a comparative study of hydrolysis rates of urethanes, ureas, and amides, *J. Polym. Sci. A Polym. Chem.* 27 (6) (1989) 1993–2005.
- [70] A. Bahrololoumi, H. Mohammadi, V. Moravati, R. Dargazany, A physically-based model for thermo-oxidative and hydrolytic aging of elastomers, *International Journal of Mechanical Sciences* 194 (2021), 106193, <https://doi.org/10.1016/j.ijmecsci.2020.106193>.
- [71] D.J. Harrison, W.R. Yates, J.F. Johnson, Aging of pressure-sensitive adhesives III. Studies of surface oxidation with multidetector size exclusion chromatography, *Journal of Applied Polymer Science* (1986) 1393–1401, <https://doi.org/10.1002/app.1986.070310523>.
- [72] R. Jozef, R. Lyda, N. Igor, V. Vladimír, P. Jozef, J. Ivica, C. Ivan, Thermooxidative stability of hot melt adhesives based on metallocene polyolefins grafted with polar acrylic acid moieties, *Polymer Testing* 85 (2020), 106422, <https://doi.org/10.1016/j.polymertesting.2020.106422>.
- [73] K. Li, K. Wang, M.-S. Zhan, W. Xu, The change of thermal–mechanical properties and chemical structure of ambient cured DGEBA/TEPA under accelerated thermo-oxidative aging, *Polymer Degradation and Stability* 98 (11) (2013) 2340–2346, <https://doi.org/10.1016/j.polymdegradstab.2013.08.014>.
- [74] S. Rolere, S. Liengprayoon, L. Vaysse, J. Sainte-Beuve, F. Bonfils, Investigating natural rubber composition with Fourier Transform Infrared (FT-IR) spectroscopy: a rapid and non-destructive method to determine both protein and lipid contents simultaneously, *Polym. Test.* 43 (2015) 83–93.
- [75] A. Muhr, Y. Marco, P.Y. Le Gac, Formation of crust on Natural Rubber after long periods of ageing, in: *Constitutive Models for Rubber VII—Proceedings of the 7th European Conference on Constitutive Models for Rubber, ECCMR, 2011*.
- [76] V. Seebauer, J. Petek, G. Staudinger, Effects of particle size, heating rate and pressure on measurement of pyrolysis kinetics by thermogravimetric analysis, *Fuel* 76 (13) (1997) 1277–1282.
- [77] A. Williams, H. Günzler, *Handbook of Analytical Techniques*, Wiley-VCH, 2001.
- [78] J.D. Minford, Durability evaluation of adhesive bonded structures, in: L.-H. Lee (Ed.), *Adhesive Bonding*, Springer Science+Business Media, New York, 1991.
- [79] R.J. Farris, C.L. Bauer, A self-delamination method of measuring the surface-energy of adhesion of coatings, *J. Adhes.* 26 (4) (1988) 293–300.
- [80] B. Chen, D.A. Dillard, J.G. Dillard, Effect of the T-stress in the adhesively bonded joints on the locus of failure in rubber toughened epoxy system, in: J.H. Constable (Ed.), *3rd International Conference on Adhesive Joining and Coating Technology in Electronics Manufacturing 1998, Proceedings, 1998*, p. 364.
- [81] N.A. Fleck, J.W. Hutchinson, Z.G. Suo, Crack path selection in a brittle adhesive layer, *Int. J. Solids Struct.* 27 (13) (1991) 1683–1703.
- [82] D.A. Dillard, J.A. Hinkley, W.S. Johnson, T.L. St. Clair, Spiral tunneling cracks induced by environmental stress cracking in LaRC-TPI adhesives, *J. Adhes.* 44 (1994) 51–67.
- [83] K.A. Patankar, D.A. Dillard, K.D. Fernholz, Characterizing the constitutive properties and developing a stress model for adhesive bond-line readout, *Int. J. Adhes. Adhes.* 40 (2013) 149–157.

- [84] G.R. Humfeld, D.A. Dillard, Residual stress development in adhesive joints subjected to thermal cycling, *J. Adhes.* 65 (1–4) (1998) 277–306.
- [85] D.A. Dillard, S. Guo, B. Chen, J.-H. Yu, Adhesive layer shrinkage in bonds subjected to thermal cycling, *Mech. Time-Depend. Mater.* 7 (1) (2003) 21–39.
- [86] F.W. Crossman, R.E. Mauri, W.J. Warren, Moisture-altered viscoelastic response of graphite/epoxy composites, in: J.R. Vinson (Ed.), *Advanced Composite Materials—Environmental Effects*, ASTM STP 658, American Society for Testing and Materials, 1978, pp. 205–220.
- [87] R.D. Adams, J.W. Cowap, G. Farquharson, G.M. Margary, D. Vaughn, The relative merits of the Boeing wedge test and the double cantilever beam test for assessing the durability of adhesively bonded joints, with particular reference to the use of fracture mechanics, *Int. J. Adhes. Adhes.* 29 (6) (2009) 609–620.
- [88] J. Cognard, Quantitative measurement of the energy of fracture of an adhesive joint using the wedge-test, *J. Adhes.* 22 (2) (1987) 97–108.
- [89] H. Parvatareddy, J. Dillard, J. McGrath, D. Dillard, Environmental aging of the Ti-6Al-4V/FM-5 polyimide adhesive bonded system: implications of physical and chemical aging on durability, *J. Adhes. Sci. Technol.* 12 (6) (1998) 615–637.
- [90] J. Cognard, The mechanics of the wedge test, *J. Adhes.* 20 (1) (1986) 1–13.
- [91] H. Parvatareddy, A. Pasricha, D.A. Dillard, B. Holmes, J.G. Dillard, High temperature and environmental effects on the durability of Ti-6Al-4V/FM5 adhesive bonded system, in: *High Temperature and Environmental Effects on Polymeric Composites: 2nd Volume*, ASTM International, 1997.
- [92] D.A. Dillard, Stresses between adherends with different curvatures, *J. Adhes.* 26 (1) (1988) 59–69.
- [93] M.D. Rakestraw, M.W. Taylor, D.A. Dillard, T. Chang, Time dependent crack growth and loading rate effects on interfacial and cohesive fracture of adhesive joints, *J. Adhes.* 55 (1–2) (1995) 123–149.
- [94] J. Chin, E. Byrd, N. Embree, J. Garver, B. Dickens, T. Finn, J. Martin, Accelerated UV weathering device based on integrating sphere technology, *Rev. Sci. Instrum.* 75 (11) (2004) 4951–4959.
- [95] C.C. White, K.T. Tan, E.P. O’Brien, D.L. Hunston, J.W. Chin, R.S. Williams, Design, fabrication, and implementation of thermally driven outdoor testing devices for building joint sealants, *Rev. Sci. Instrum.* 82 (2) (2011) 025112.
- [96] C.C. White, D.L. Hunston, K.T. Tan, J.J. Filliben, A.L. Pintar, G. Schueneman, A systematic approach to the study of accelerated weathering of building joint sealants, *J. ASTM Int.* 9 (5) (2012) 1–17.
- [97] A.L. Pintar, C.C. White, D.L. Hunston, J.J. Filliben, Predicting field degradation of sealants using accelerated testing from the NIST solar SPHERE, in: C.C. White, H. Miyauchi (Eds.), *Durability of Building and Construction Sealants and Adhesives*, STP1604-EB, 6, ASTM International, West Conshohocken, PA, 2018. <https://doi.org/10.1520/STP1604-EB>.
- [98] A.L. Pintar, C.C. White, L.P. Sung, Bayesian Hierarchical models for service life prediction of polymers, in: C.C. White, C.M. Nickols, J. Pickett (Eds.), *Service Life Prediction of Polymers and Coatings: Enhanced Methods*, Elsevier, 2020.
- [99] J. Comyn, Environmental (durability) effects, in: R.D. Adams (Ed.), *Adhesive Bonding*, second ed., Woodhead Publishing, 2021, pp. 193–213 (Chapter 7).
- [100] J. Crank, *The Mathematics of Diffusion*, Clarendon Press, Oxford, 1956.
- [101] J. Crank, P. Nicolson, A practical method for numerical evaluation of solutions of partial differential equations of the heat-conduction type, *Math. Proc. Camb. Philos. Soc.* 43 (1) (1947) 50–67.

- [102] A. Fick, V. On liquid diffusion, *Lond. Edinb. Dubl. Philos. Mag. J. Sci.* 10 (63) (1855) 30–39.
- [103] C.-H. Shen, G.S. Springer, Moisture absorption and desorption of composite materials, *J. Compos. Mater.* 10 (1) (1976) 2–20.
- [104] T. Chang, E.A. Sproat, Y.-H. Lai, N.E. Shephard, D.A. Dillard, A test method for accelerated humidity conditioning and estimation of adhesive bond durability, *J. Adhes.* 60 (1–4) (1997) 153–162.
- [105] R.K. Giunta, R.G. Kander, Failure surface analysis of polyimide/titanium notched coating adhesion specimens, *J. Adhes.* 77 (3) (2001) 183–214.
- [106] J. Wylde, J. Spelt, Measurement of adhesive joint fracture properties as a function of environmental degradation, *Int. J. Adhes. Adhes.* 18 (4) (1998) 237–246.
- [107] A.A.M.A. Campos, A.M.P. de Jesus, J.A.F.O. Correia, J.J.L. Morais, Fatigue crack growth behavior of bonded aluminum joints, *Procedia Eng.* 160 (2016) 270–277.
- [108] D.R. Lefebvre, D.A. Dillard, A stress singularity approach for the prediction of fatigue crack initiation in adhesive bonds. Part 1: theory, *J. Adhes.* 70 (1–2) (1999) 119–138.
- [109] A.G. Solana, A.D. Crocombe, M.M.A. Wahab, I.A. Ashcroft, Fatigue initiation in adhesively-bonded single-lap joints, *J. Adhes. Sci. Technol.* 21 (14) (2007) 1343–1357.
- [110] J. Weiland, M.Z. Sadeghi, J.V. Thomalla, A. Schiebahn, K.U. Schroeder, U. Reisgen, Analysis of back-face strain measurement for adhesively bonded single lap joints using strain gauge, Digital Image Correlation and finite element method, *Int. J. Adhes. Adhes.* 97 (2020) 102491.
- [111] M.R.P. Elenchezian, V. Vadlamudi, P.K. Banerjee, C. Dave, A. Mahmood, R. Raihan, K.L. Reifsnider, Quality assessment of adhesive bond based on dielectric properties, in: *SAMPE Conference Proceedings, SAMPE*, 2017.
- [112] P.K. Banerjee, M.R.P. Elenchezian, V. Vadlamudi, R. Raihan, K.L. Reifsnider, Predicting adhesive bond performance based on initial dielectric properties, in: *Proceedings of the American Society for Composites—Thirty-Second Technical Conference, American Society for Composites*, 2017, pp. 840–849.
- [113] N.E. Shephard, Stresses and fracture of elastomeric bonds, in: D.A. Dillard, A.V. Pocius (Eds.), *The Mechanics of Adhesion*, Elsevier, 2002, pp. 351–388.
- [114] M. Van Gorp, J. Palmen, Time-temperature superposition for polymeric blends, *Rheol. Bull.* 67 (1) (1998) 5–8.
- [115] N. Heymans, Constitutive equations for polymer viscoelasticity derived from hierarchical models in cases of failure of time-temperature superposition, *Signal Process.* 83 (11) (2003) 2345–2357.
- [116] J.D. Ferry, *Viscoelastic Properties of Polymers*, third ed., Wiley, New York, 1980.
- [117] W.G. Knauss, I.J. Emri, Non-linear viscoelasticity based on free-volume consideration, *Comput. Struct.* 13 (1–3) (1981) 123–128.
- [118] W.G. Knauss, I. Emri, Volume change and the nonlinearly thermoviscoelastic constitution of polymers, *Polym. Eng. Sci.* 27 (1) (1987) 86–100.
- [119] C.F. Popelar, K.M. Liechti, A distortion-modified free volume theory for nonlinear viscoelastic behavior, *Mech. Time-Depend. Mater.* 7 (2) (2003) 89–141.
- [120] R.A. Schapery, On the characterization of nonlinear viscoelastic materials, *Polym. Eng. Sci.* 9 (4) (1969) 295–310.
- [121] D. Gamby, L. Blugeon, On the characterization by Schapery's model of non-linear Viscoelastic materials, *Polym. Test.* 7 (2) (1987) 137–147.
- [122] S.L. Simon, G.B. McKenna, O. Sindt, Modeling the evolution of the dynamic mechanical properties of a commercial epoxy during cure after gelation, *J. Appl. Polym. Sci.* 76 (4) (2000) 495–508.
- [123] D. Adolf, R. Chambers, Verification of the capability for quantitative stress prediction during epoxy cure, *Polymer* 38 (21) (1997) 5481–5490.

- [124] D. Adolf, J.E. Martin, Time-cure superposition during crosslinking, *Macromolecules* 23 (15) (1990) 3700–3704.
- [125] D.B. Adolf, J.E. Martin, R.S. Chambers, S.N. Burchett, T.R. Guess, Stresses during thermoset cure, *J. Mater. Res.* 13 (3) (1998) 530–550.
- [126] W.D. Cook, M. Mehrabi, G. Edward, Ageing and yielding in model epoxy thermosets, *Polymer* 40 (5) (1999) 1209–1218.
- [127] A. Lee, G.B. McKenna, Effect of crosslink density on physical ageing of epoxy networks, *Polymer* 29 (10) (1988) 1812–1817.
- [128] A. Lee, G.B. McKenna, Viscoelastic response of epoxy glasses subjected to different thermal treatments, *Polym. Eng. Sci.* 30 (7) (1990) 431–435.
- [129] J.M. Hutchinson, D. McCarthy, S. Montserrat, P. Cortes, Enthalpy relaxation in a partially cured epoxy resin, *J. Polym. Sci. B* 34 (2) (1996) 229–239.
- [130] S. Montserrat, Physical aging studies in epoxy resins. I. Kinetics of the enthalpy relaxation process in a fully cured epoxy resin, *J. Polym. Sci. B* 32 (3) (1994) 509–522.
- [131] J.K. Lee, J.Y. Hwang, J.K. Gillham, Erasure below glass-transition temperature of effect of isothermal physical aging in fully cured epoxy/amine thermosetting system, *J. Appl. Polym. Sci.* 81 (2) (2001) 396–404.
- [132] G.B. McKenna, Mechanical rejuvenation in polymer glasses: fact or fallacy? *J. Phys. Condens. Matter* 15 (11) (2003) S737–S763.
- [133] L.C.E. Struik, On the rejuvenation of physically aged polymers by mechanical deformation, *Polymer* 38 (16) (1997) 4053–4057.
- [134] J.M.G. Cowie, R. Ferguson, The ageing of polyvinyl methyl ether as determined from enthalpy relaxation measurements, *Polym. Commun.* 27 (9) (1986) 258–260.
- [135] J.K. Lee, J.Y. Hwang, Erasure behavior of isothermal physical aging effect below glass transition temperature in a fully cured epoxy resin. Differential scanning calorimetry measurement, *Polym. J.* 35 (2) (2003) 191–196.
- [136] D.H. Kaelble, Theory and analysis of peel adhesion: rate-temperature dependence of viscoelastic interlayers, *J. Colloid Sci.* 19 (5) (1964) 413–424.
- [137] A. Gent, R. Petrich, Adhesion of viscoelastic materials to rigid substrates, *Proc. R. Soc. Lond. A Math. Phys. Sci.* 310 (1502) (1969) 433–448.
- [138] G.D. Anderson, Long-term durability characterization and prediction of a urethane-based adhesive, in: *Engineering Mechanics* (M.S. Thesis), Virginia Tech, Blacksburg, VA, 2020. <https://vtechworks.lib.vt.edu/handle/10919/98825>.
- [139] College, I". ICPeel. 2022 [cited 2022 August 19, 2022]; Available from: <https://www.imperial.ac.uk/mechanical-engineering/research/mechanics-of-materials/composites-adhesives-and-soft-solids/adhesion/test-protocols/>. Imperial College, Fracture Test Protocols, 2022.
- [140] D.A. Dillard, D.J. Pohlit, G.C. Jacob, J.M. Starbuck, R.K. Kapania, On the use of a driven wedge test to acquire dynamic fracture energies of bonded beam specimens, *J. Adhes.* 87 (4) (2011) 395–423.
- [141] X. Shuangyan, D.A. Dillard, Determining the impact resistance of electrically conductive adhesives using a falling wedge test, *IEEE Trans. Compon. Packag. Technol.* 26 (3) (2003) 554–562.
- [142] C.W. Feng, C.W. Keong, Y.P. Hsueh, Y.Y. Wang, H.J. Sue, Modeling of long-term creep behavior of structural epoxy adhesives, *Int. J. Adhes. Adhes.* 25 (5) (2005) 427–436.

High-rate testing of structural adhesives

21

Evan L. Breedlove, Chaodi Li, Chao Chen, and Luis Trimiño
3M Company, Corporate Research Laboratory, Maplewood, MN, United States

21.1 Introduction

Structural adhesives are commonly applied in applications where high strain-rate performance is a critical engineering concern, including the automotive, aerospace, and consumer electronics industries [1,2]. As with all other polymers, structural adhesives exhibit rate-dependent mechanical properties. Depending on the glass transition temperature and backbone chemistry, properties may vary by several orders of magnitude over a comparable range of rates [3]. Additionally, adhesives may go through a ductile to brittle transition at elevated rates, qualitatively changing the failure behavior of the material [4]. In other words, structural adhesive properties can differ substantially from the quasistatic rates typically reported in tech data sheets, and these differences can have significant consequences for engineering design. Consequently, accurate high strain rate characterization is critical in many industries.

Definitions of high strain rates vary, but generally strain rates exceeding 10^3 s^{-1} and up to 10^4 – 10^5 s^{-1} are considered to be “high rate” and require special measurement techniques. Note that rates exceeding 0.1 s^{-1} are too large to be measured in dogbone tensile tests on most conventional loadframes. Strain rates between 0.1 and 10^3 s^{-1} are classified as intermediate strain rates. They are notoriously challenging to measure because they suffer from the inertial and vibration challenges of high-rate testing and yet are not amenable to many of the solutions employed in high-rate testing. Different techniques are appropriate for different ranges of strain rate and strain amplitude within the high strain rate spectrum (Fig. 21.1). This chapter will primarily focus on high strain rates, with some discussion of methods that are appropriate for intermediate rates.

21.2 The physics of high-rate testing

High strain rate testing differs from conventional, quasistatic testing in more respects than just the speed of the test. First, high rates entail unique challenges in data acquisition due to the effects of circuit dynamics and discrete sampling. Second, high rates generate nontrivial contributions from inertia due to rapid acceleration, effects that can typically be ignored at quasistatic rates. Finally, high-rate loading often induces vibration in the test specimen and/or test apparatus. These vibrations can be of the same magnitude as the measurement, resulting in poor signal-to-noise ratio.

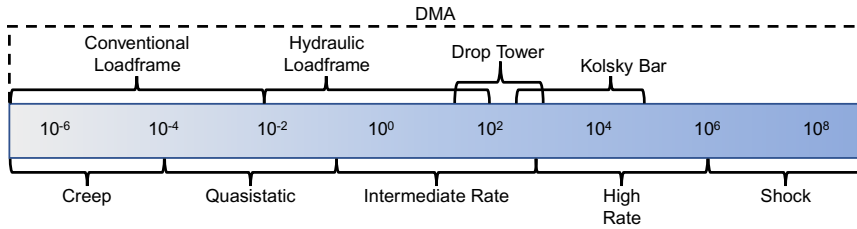


Fig. 21.1 Test rates and associated methods. See also [5,6] for extensive reviews of high-rate testing methods.

21.2.1 High-rate sampling

High-rate tests typically occur over a duration significantly shorter than 1 s. For instance, a strain rate of 1000 s^{-1} will yield a strain of 100% in only 1 ms. To obtain meaningful test data, experiments must therefore be conducted with data acquisition rates exceeding 10,000 Hz. Under these conditions, analog circuit dynamics and discrete sampling effects become salient. These issues are distinct and potentially confounding.

The goal in sensor and amplifier selection is to obtain a measurement system resonant frequency that exceeds the main frequency band of the measured signal so that it is not distorted. Sensor resonance issues explain the dominance of piezoelectric force sensors in high-rate testing. Strain gage-based load cells consist of a deformable structure with strain gages attached to struts. The deformation of these struts generates the force measurement. This construction is mechanically bulky and results in a low resonant frequency. In contrast, a piezoelectric sensor generates a strong electrical signal with relatively little motion. This allows for a high resonant frequency, typically on the order of 30–70 kHz. This is often sufficiently high for many applications.

Digital sampling is an additional factor that must be considered. The well-known Shannon sampling theorem, also referred to as the Nyquist frequency, states that digital sampling must occur at least twice the frequency of the highest frequency component in the measured signal [7]. For example, a 1 ms impulse would have frequency content up to about 1000 Hz. This means that data must be collected at a minimum rate of 2000 Hz. Sampling at lower frequencies will also cause aliasing. In essence, higher frequency data will appear as a ghosted artifact superimposed on the actual data.

21.2.2 Inertial effects

Inertia affects test results in several ways. First, inertia means that forces are not uniform throughout the load train. In a quasistatic test, acceleration is negligible. This means that the force measured on either side of a component will be in equilibrium. For instance, in a quasistatic tensile test, it does not matter if the force is measured at the grips or after some extension rods attaching the grips to the crosshead (Fig. 21.2). This convenience is actually a specially simplified case. Newton's second law states

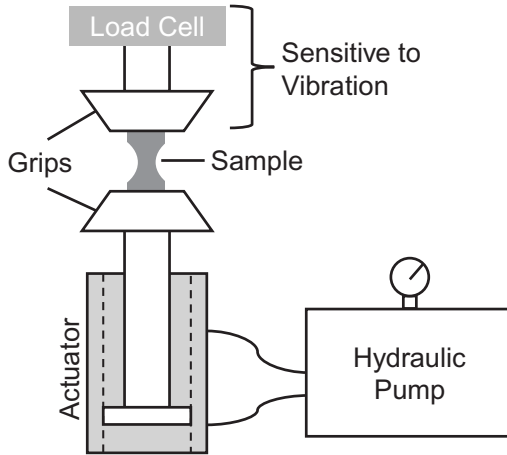


Fig. 21.2 Typical load train for servohydraulic loadframe tensile test. Note large mass between sample and load cell, which is a concern for vibrations.

$$\sum_i F_i = ma_{net} \quad (21.1)$$

which means that when a mass (m) has a nonzero net acceleration (a_{net}), the forces (F_i) must not sum to zero. In other words, there must be a force imbalance as a material accelerates. In Fig. 21.3, if this test were conducted at a high rate, then the acceleration of the grips would cause a force imbalance between the force acting on the bond and the force acting on the load cell. In fact, the acceleration can be thought of as an additional force. This analytical approach, named after Jean d'Alembert [8], restates Newton's second law as

$$\sum_i F_i - ma_{net} = 0 \quad (21.2)$$

so that there is an inertial force with magnitude ma_{net} and sign opposite the acceleration. This change in perspective makes clear why inertia will confound force measurements if not carefully managed. Well-designed high-rate tests explicitly address this issue by modifying the force sensor setup to measure forces directly on the bond or through components that experience limited acceleration, by designing the test to run at constant velocity (i.e., no acceleration), and/or explicitly accounting for inertia in the force measurement.

Inertia therefore affects force sensor placement. When a sample is accelerating, it is necessarily not in force equilibrium. Force equilibrium is a common assumption in material property analysis. For instance, a tensile stress/strain curve does not provide accurate modulus if the dogbone is not in a uniform, uniaxial state of stress.

In any test, the initial application of a force to one side of a specimen induces the propagation of a stress wave that proceeds to reflect back and forth in the specimen. Even if the specimen is deforming at a constant rate on average, wave propagation

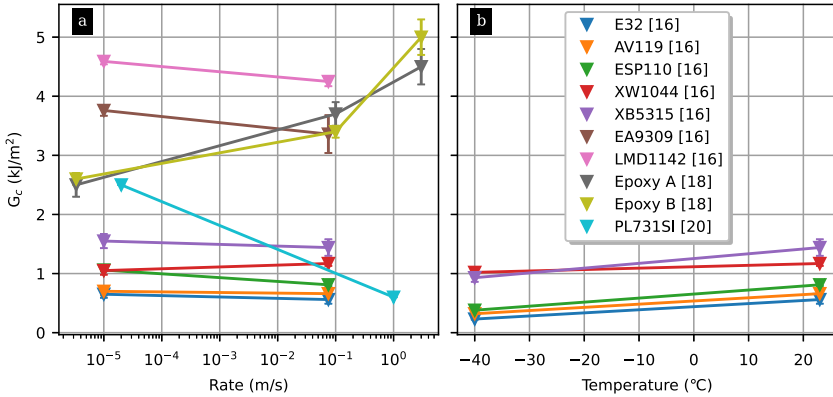


Fig. 21.3 The critical strain energy release rate (G_c) exhibits sensitivity in (a) rate and (b) temperature. Colder temperatures mirror faster rates, and G_c can be correlated with $\tan(\delta)$, suggesting that rate and temperature effects reflect the rheology of the polymer. Data adapted from the literature B.R.K. Blackman, A.J. Kinloch, A.C. Taylor, Y. Wang, The impact wedge-peel performance of structural adhesives, *J. Mater. Sci.* 35(8) (2000) 1867–1884; C.S.P. Borges, P.D.P. Nunes, A. Akhavan-Safar, E.A.S. Marques, R.J.C. Carbas, L. Alfonso, L. F.M. Silva, A strain rate dependent cohesive zone element for mode I modeling of the fracture behavior of adhesives, *Proc. Inst. Mech. Eng. Part L J. Mater. Des. Appl.* 234(4) (2020) 610–621; D.A. Dillard, D.J. Pohlit, G.C. Jacob, J.M. Starbuck, R.K. Kapania, On the use of a driven wedge test to acquire dynamic fracture energies of bonded beam specimens, *J. Adhes.* 87(4) (2011) 395–423.

causes local acceleration and consequent force heterogeneity. After multiple wave reflections, a standing wave (i.e., vibration) is established, in which the force at either extent of the specimen is equal [9–11]. Practically, it takes about four wave reflections for this to occur [12]. Therefore, given a specimen of length l , Young’s modulus E , and density ρ , the speed of wave propagation is $c = \sqrt{\frac{E}{\rho}}$, and the minimum time to equilibration is

$$t_{eq} = \frac{4l}{c} = 4l\sqrt{\frac{\rho}{E}} \tag{21.3}$$

For an adhesive specimen with Young’s modulus of 1 GPa, a density of 1 g/cm^3 , and a length of 25 mm, $t_{eq} = 0.1$ ms. For a quasistatic tensile test, this is an insignificant period of time, but for a high-rate test, it is longer than the typical duration of a test. Eq. (21.3) indicates that the equilibration time may be shortened by increasing the modulus or decreasing the specimen length. Clearly, force equilibrium is a lesser concern for higher modulus adhesives, but practically this means high-rate tests are often designed with short specimens because length has the strongest influence on equilibration time.

Note that reducing sample size is not a trivial solution. Quasistatic tests are often conducted with larger specimens for practical reasons, such as ensuring a uniaxial

stress state, improving dimensional tolerance, and ensuring strong signal-to-noise ratio. This last issue is a significant trade-off in high-rate test design because samples need to be sufficiently large to generate a force that exceeds the sometimes substantial noise floor.

21.2.3 Vibration

In the previous section, it was noted that multiple stress wave reflections set up a standing wave in test specimens, which is also known as vibration. Mechanical systems generally exhibit second-order behavior and vibrate with a resonant frequency when deformed. More specifically, deformable bodies such as adhesive test specimens and test apparatus components behave like a network of infinite interconnected second-order systems, yielding an infinite number of resonances and antiresonance. However, the vibrational behavior will be dominated by a primary or *fundamental* frequency. To a first approximation, the resonant frequency is given by $\sqrt{k/m}$, where k is the stiffness and m is the mass. Test apparatus components such as extension rods potentially have moderate k and high m , leading to low resonant frequencies. In contrast, adhesive specimens tend to have large stiffness due to their relatively short length and low mass, leading to resonant frequencies that may be larger than test component resonances. However, the vibrations of test components can still confound a measurement when they are picked up by force and displacement sensors. Managing these vibrations is a significant concern in some test method designs [13].

Note that for a vibration to occur, there needs to be sufficient time for stress waves to traverse and reflect along the extent of an object. The interaction of these reflecting waves creates a standing wave, and the standing wave is the vibration that is observed [9]. Therefore, another strategy for eliminating vibrations is to create a test apparatus in which wave propagation is significantly slower than the timeframe of the test. This is a key element in Kolsky bar test design, which will be discussed in Section 21.7.

21.3 Rate-dependent properties in structural adhesives

Several different structural adhesive properties are measured in high-rate tests. The most basic is modulus. Rate-dependent modulus (i.e., viscoelasticity) can vary over two to four orders of magnitude depending on the glass transition temperature, filler, backbone chemistry, and crosslinking [3,4,14]. Structural adhesives are also not always thermorheologically simple [15], sometimes limiting the application of time-temperature superposition methods that are commonly used with pressure-sensitive adhesives. Other bulk properties also typically exhibit rate sensitivity, including yield stress and strain, hardening exponent, and bulk modulus, which can have a complex relationship with rate [4], as discussed in Chapter 15 and Chapter 20.

Due to the focus on fracture mechanics analysis for structural adhesives, fracture toughness and/or critical strain energy release rate (G_C) are also commonly measured as a function of rate. Studies have alternately found that G_C decreases [16,17] or increases [18,19] with rate (Fig. 21.3a). Correlation between G_C and $\tan(\delta)$ suggests

that variation in fracture toughness is related to the polymer rheology [17], which accounts for rising or falling G_C depending on the rate and temperature relative to the glass transition. Indeed, the temperature dependence of G_C typically mirrors the effect of rate, with colder temperatures analogous to higher rates (Fig. 21.3b), which is consistent with the time-temperature superposition principle (see Section 21.4). Because many structural adhesives are used in their glassy state, this would account for the observations of decreasing G_C with rate. While the underlying mechanism remains a topic of study, fracture behavior is nevertheless rate and temperature sensitive and warrants investigation for high-rate and/or cold-temperature applications.

In high strain rate loading conditions, polymers may undergo substantial plastic strain prior to failure. Yielding and post yield deformation can lead to significant additional energy dissipation compared to quasistatic loading conditions. While such energy can be dissipated in most metals, many polymers deform in mostly adiabatic-like conditions due to the short heat exchange time in high strain rate, and the heat results in a significant temperature rise in the polymer [20]. Adiabatic behavior is expected when the strain rate is above a critical strain rate. For example, for polycarbonate polymer, the critical strain rate is about 0.2 s^{-1} [21]. Chou et al. [22] found that mechanical work was completely converted into heat after a certain level of strain had been attained at high strain rates ($\sim 50 \text{ s}^{-1}$). Research has shown such a temperature rise in mechanical tests at high rates in a variety of polymers [5]. Different testing techniques, including thermocouples and infrared measurement systems, have been developed to measure such temperature rises [21–24]. The temperature rises range from a few degrees Celsius to more than 40°C . The heating effect is particularly important for polymers because they show a much greater temperature dependence of mechanical properties than metals [21]. Such a temperature increase may lead to significant thermal softening of the materials. The competition between thermal softening and strain hardening may dictate polymer behavior after yielding [24]. Increased material temperature may cause the plastic flow stress at the higher strain rates to fall below the quasistatic values [21]. The temperature rises ahead of cracks may also contribute to the formation of craze-like regions and voids in polymers under high strain rate conditions. The temperature rise may then dramatically affect the toughness of the material and bonded joint performance [14].

The energy dissipated by an adhesive bond is also commonly measured. When the bond is not damaged, this quantity appears similar to the phase lag ($\tan(\delta)$) in complex modulus measurements. When the bond is destroyed, this quantity appears similar to fracture toughness. Taking these values as a fraction of initial potential energy delivered during an impact test creates an attractive metric that can be compared across multiple rates. Despite the interpretative appeal, energy measurement at high rates can be problematic. First, many sources of energy dissipation exist in a high-rate test beyond the deformation of the adhesive bond. Moreover, energy is an insufficient initial condition to determine the displacement history to which an adhesive is subjected. The stiffness of the adhesive itself determines the duration and peak force. Furthermore, isoenergetic impacts that differ by velocity and mass will have significantly different momentum transfer because momentum scales linearly with velocity but energy

scales with the square. Finally, because many structural adhesives are viscoelastic, differences in rate lead to fundamentally different material properties, which means that mass and velocity are not interchangeable sources of energy. Consequently, high-rate tests must be carefully designed to ensure the valid measurement of fracture toughness and/or viscoelastic dissipation.

21.3.1 Dynamic response of polymers and constitutive material modeling

Material constitutive models that describe the mechanical responses of materials at high strain rates are required for structure designs where the impact loading conditions are critical. Different experimental techniques have been applied to characterize material dynamic responses, as discussed in this chapter. A typical stress-strain curve of a polymer consists of several distinctive characteristics: stress increases with strain, often nonlinearly if the polymer is in a rubbery state, until it reaches a peak stress; the peak stress is followed by strain softening and then strain hardening [5]. The high strain rate deformation behavior of polymers is significantly affected by temperature-dependent material modulus as well as viscoelastic and thermal softening. Therefore, the constitutive material model should capture these characteristic features: temperature- and strain rate-dependent initial elasticity, yielding, strain softening, strain hardening, etc. At high strain rates, polymer materials usually change their behavior from ductile to brittle. The yield stress also generally increases with strain rate. However, adiabatic heating may result in thermal softening, which competes with pure rate effects. For polymers, the effects of temperature and strain rate are analogous, with an increase in strain rate akin to a decrease in temperature [15,25]. Many researchers have applied time-temperature superposition (TTS) equivalence in modeling simulations, including as discussed in [Chapter 20](#) and [Chapter 31](#). A generalized Maxwell model is often used to represent the strain rate-dependent viscoelastic characteristics. Boyce et al. [26] and Mulliken and Boyce [20] extended TTS to capture rate, temperature, and pressure-dependent yield behavior. The well-known Johnson-Cook and Cowper-Symonds models are two common plasticity models for capturing rate-dependent postyield behavior. While they were developed for capturing behavior in metals, they have been widely applied with structural adhesives [27]. Pressure dependency can be captured through the Drucker-Prager model, which expresses yield stress as a function of pressure [2]. For more complex combinations of rate and pressure sensitivity along with viscoelasticity, it is necessary to resort to fully nonlinear constitutive models such as the Bergstrom-Boyce model [28] or the successor three-network model (TNM) [29] and more general constitutive models such as parallel rheological framework (PRF) models [30].

Various computational models have also been developed to investigate the failure of adhesively bonded joints in high strain rates. Cohesive contact or cohesive zone models are the most common numerical implementation, and these represent the force displacement of a fracturing bond using a traction-separation law that can be expressed in a rate-dependent form. For the high rate, the parameter sets need to

be calibrated with appropriate strain rate tests [31]. However, there are limited strain rate-dependent debonding models available in commercial finite element codes due to the complexities of the interactions.

21.4 DMA methods

Dynamic (thermo)mechanical analysis, commonly abbreviated as DMA or DMTA, is an important technique for measuring rate- and temperature-dependent properties in polymers, though it is not typically listed among high-rate test methods. DMA rests on the principle of TTS. TTS relates low temperatures to high rates, and conversely high temperatures to low rates. The underlying mechanism is the mobility of polymer chains at the molecular scale [15,25,32]. High rates and cold temperatures both impede molecular motion and lead to an increase in modulus. By testing a material at a range of different rates and temperatures, it is possible to determine this relationship.

In a typical DMA test, a sample is sinusoidally deformed at a small strain for a fixed set of frequencies and temperatures. Many different deformation modes may be used, including tension, compression, bending, torsion, and lap shear. The choice of deformation mode depends on the relevant properties and dimensions of the adhesive. Tensile, compressive, and shear moduli may differ depending on the composition of the adhesive [33,34], and bending averages between tension and compression.

When a sample is deformed sinusoidally, it will respond with a sinusoidally varying stress at the same frequency and with some level of phase lag [25]. The sinusoidal stress and strain may be represented as complex-valued phasors such that

$$\sigma^* = E^*(\omega)\epsilon^* \quad (21.4)$$

where the starred quantities represent the complex-valued measures and properties. The complex-valued modulus E^* may be decomposed into real and imaginary components

$$E^* = E' + jE'' \quad (21.5)$$

where the in-phase real component E' is called the storage modulus and the out-of-phase imaginary component is called the loss modulus. The storage modulus is associated with the elastic, nondissipative behavior of the material. The loss modulus is the stiffness of the polymer associated with dissipation. As a material becomes more dissipative, the ratio of E'' to E' grows. This ratio is related to the tangent of the phase lag δ between the stress and the strain and is commonly reported in DMA experiments

$$\tan(\delta) = \frac{E''}{E'} \quad (21.6)$$

The amplitude of the complex-valued modulus can also be reported as

$$|E^*| = \sqrt{E'^2 + E''^2} \quad (21.7)$$

where the amplitude $|E^*|$ is commonly labeled E^* and referred to as the complex modulus.

The storage, loss, and complex moduli as well as the $\tan(\delta)$ are alternative ways of reporting the same rate-dependent information about a polymer's modulus. Large frequencies are related to large strain rates, but frequencies and time are not equivalent. The conversion from frequency-dependent modulus to time-dependent modulus typically requires an intermediate model such as the Prony series. This conversion has been described in detail [35–39]. Strain rates and frequencies are often approximately related (e.g., $1 \text{ Hz} \sim 1 \text{ s}^{-1}$), following the logic that a straight line approximates a quarter period of a sine wave [20,40]. However, the straight-line approximation amounts to a triangular wave, which does not have the same frequency content as a single-frequency sine wave. The errors in this approximation are moderate at low and high frequencies, but can be substantial when frequencies correspond within the glass-transition region of the polymer [41].

The typical TTS analysis procedure is to shift data at a particular rate and temperature to an effective rate for a reference temperature. In this construction, low-temperature data shift to higher rates for a room-temperature reference temperature, and high-temperature data shift to lower rates. For each temperature, the magnitude of the multiplicative factor between the actual and effective frequencies required to create overlap with the remaining test data is recorded. The full set of these shift factors form a curve, which is frequently modeled with the Williams-Landel-Ferry (WLF) equation [32]; however, it should be noted that this relationship is most applicable at temperatures above the glass transition. As structural adhesives are often used below their glass transition temperature, other relationships such as the Arrhenius equation often provide a better fit. A curve showing the modulus as a function of frequency, shifted to a reference temperature, is called a DMA master curve. A master curve covers frequencies that are not practical to measure directly, which is the primary utility of DMA and TTS. DMA measurements are only made at small strains and the TTS shifting procedure presumes thermorheological simplicity [25]; nevertheless, DMA measurements are among the most straightforward to conduct and provide valuable insight into the temperature- and rate-dependent trends in an adhesive's behavior. Moreover, TTS behavior appears to account for large-strain behavior, at least when adiabatic heating [5,42,43] and beta transitions [20] are accounted for.

21.5 Servohydraulic methods

Servohydraulic loadframes provide a convenient way to extend beyond quasistatic rates into intermediate rates and the low range of high strain rates. Servohydraulic loadframes are easily adapted to higher rates and allow for test methods that are comparable to common quasistatic tests.

As with screw-driven loadframes, servohydraulic loadframes consist of a controlled uniaxial actuator and a corresponding displacement sensor and load cell (Fig. 21.2). Actuator position is measured by a linear variable differential transformer (LVDT), which is a common sensor for position measurement in mechanical testing. LVDTs exhibit good position fidelity even to moderately high speeds and are suitable for applications with a defined/constrained displacement, as with the stroke of a loadframe actuator. Specimen displacement/strain is typically measured by an extensometer or digital image correlation (DIC) system (as discussed in Chapter 32, depending on the test geometry, as with slower versions of loadframe-based tests. The force is measured by a load cell connected between one of the grips, typically the stationary one so as to avoid inertial loading on the load cell.

Hydraulic loadframes are able to achieve higher rates and forces than screw-driven machines because of their actuation. The actuator piston's position is determined by the flow of (essentially) incompressible oil into the actuator [44], so that the velocity of the actuator $v(t)$ is related to the volumetric flow rate of oil $V(t)$ by the cross-sectional area A so that

$$V(t) = Av(t) \quad (21.8)$$

Similarly, the force is determined by the oil pressure p and the actuator cross-sectional area so that

$$F = pA \quad (21.9)$$

Combining Eqs. (21.8) and (21.9) shows that the target volumetric flow rate for a given operating pressure depends on the applied force and displacement rate:

$$V(t) = \frac{F}{p}v(t) \quad (21.10)$$

Operating pressures are typically limited by yield stress in the actuator wall and safety concerns [44] and are typically in the range of 3000 psi (20.7 MPa). This means that volumetric flow rate must increase for increasing target force and rate. Achieving sufficiently high volumetric flow rate requires substantial oil accumulation and more sophisticated valve design to allow for rapid oil inflow; therefore, hydraulic loadframes for high-rate testing are specially designed instruments that differ for lower-rate and fatigue-rated instruments. These instruments achieve a maximum rate of 20–30 m/s [45].

Most common quasistatic structural adhesive tests can be conducted on a servohydraulic loadframe at higher strain rates. Examples include dogbone tensile testing (ASTM D638 [46]), unconstrained compression (ASTM D695 [47]), and strength tests such as butt tension (ASTM D2095 [48]) and thick-adherend lap shear (ASTM D5656 [49]). These latter tests require some care in interpretation because the mass of butt tension and shear substrates can be substantial. Most high-rate tests are conducted so that the actuator applies a tensile force. High-rate compressive tests are

possible; however, it can be difficult to control the actuator without damaging the load train because of the large forces the actuator can generate and the unavoidable positional overshoot that occurs when an actuator is driven under high-speed displacement control. In contrast, impact forces in drop towers and a Kolsky bar do not have active displacement control, meaning the maximum delivered force is limited by the potential energy delivered to the instrument.

During the initial actuation, the velocity is not constant as the actuator piston accelerates. This acceleration results in data loss because the specimen is stretching for a period where the strain rate is nonconstant and below the target. Such data are not suitable for typical property measurements like modulus. A slack adapter is a typical solution. A slack adapter consists of a rod that slides in a hollow sleeve between the grips and engages through a conical seat. The gradual engagement of the conical seat helps prevent severe vibrations from sudden engagement. Rubber coating on the seat also helps suppress vibrations [11,45]. However, the vibrations at engagement can still be significant. The sudden loading of the slack adapter can cause the instrument fixtures to vibrate at their natural frequency [50].

Recent studies have focused on improving data quality at intermediate strain rates and extending tests into higher strain rates. Xiao studied the high-rate system in detail both experimentally and through the analysis of a lumped-parameter vibration model [11]. Similar to Xia [13], Xiao concluded that vibrational ringing in the entire load train sets an upper limit on the practical strain rate for hydraulic loadframe testing, which is also reflected in the Society of Automotive Engineer's practice standard recommendation to have a test frame resonance exceeding 4000 Hz [51]. Xiao also notes that dynamic equilibrium is a concern in designing even at the moderate rates for hydraulic tests because the specimen gage length also tends to be longer than in drop tower and Kolsky bar tests. As discussed in Section 21.2.2, at least four wave transit times are needed to establish stress equilibrium in a sample [12]. Depending on the modulus of the adhesive, this can require on the order of a millisecond. In some cases, sample size and modulus may be more significant limiting factors than the maximum velocity of the loadframe.

Efforts to increase the useful rate range of servohydraulic testing have focused on minimizing vibrations. Xia et al. proposed a modification to the force sensor and grips in tensile tests that increased the stiffness of the load train [13]. The new force sensor design consisted of an integrated force sensor and shoulder grip, where a strain gage applied to the neck of the shoulder grip detected the force applied to the grip. The increase in resonant frequency significantly improved measurement quality.

As discussed in Section 21.2.3, standing waves created by multiple reflections of stress waves are what cause vibrations. Therefore, rather than attempting to increase the resonance frequency through stiffening, another strategy for addressing vibration is to create a component so long that the wave transit time is longer than the test duration, thus eliminating the possibility of standing waves. This is the principle behind the Kolsky bar discussed in Section 21.7. Several authors have evaluated hybrid systems in which the load sensor is a long, strain-gaged rod and the actuation is provided by a servohydraulic system. Othman et al. [52] created a system with an 820 mm long load-sensing bar that showed significantly lower levels of oscillation compared with a

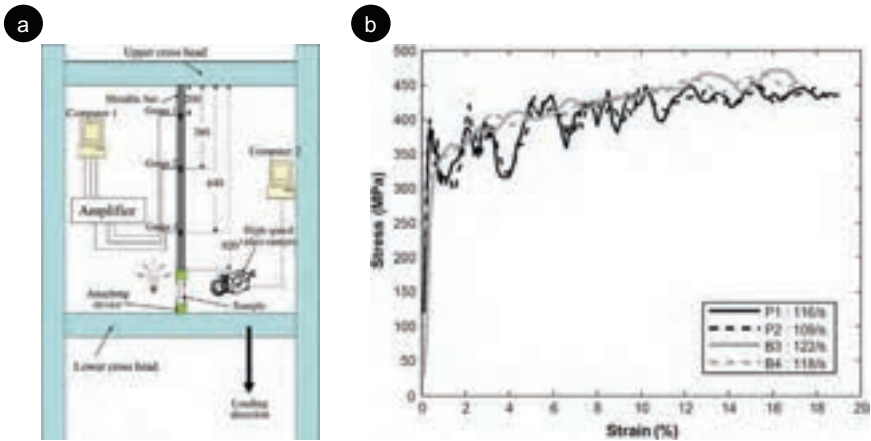


Fig. 21.4 (a) Hybridized servohydraulic loadframe with transmission bar and (b) correlation between the transmission bar measurement (B3 and B4) with piezoelectric load cells (P1 and P2).

Reproduced with permission from R. Othman, P. Guégan, G. Challita, F. Pasco, D. LeBreton, A modified servo-hydraulic machine for testing at intermediate strain rates, *Int. J. Impact Eng.* 36(3) (2009) 460–467.

conventional hydraulic setup and good agreement overall (Fig. 21.4). This instrument design was limited to short duration loading of about 1 ms. This restriction is because the duration of the force applied to the specimen dictates the physical length of the stress wave in the bar such that $l = Ct$ where l is the stress wavelength, C is the speed of sound in the bar, and t is the duration of the test. Longer duration tests would result in the reflected leading edge of the wave interfering with the strain gage measurement at later time points. Othman et al. demonstrated longer test durations by employing wave separation analytical methods [52].

Wave separation methods can be avoided by employing a longer load sensing bar; however, for intermediate strain rates where test durations are comparatively long duration (milliseconds instead of microseconds), the sensing bar length requirement can be substantial. Gilat et al. constructed a similar hybrid device with a 40m long load-sensing bar [53]. The system yielded excellent data quality for intermediate strain rate tests; however, the bar length is impractical for most laboratories. Whittington et al. [54] suggested a modification of the Gilat et al. design using a serpentine bar (Fig. 21.5). The serpentine bar collapses the length of the sensor bar into a series of nested tubes that are designed such that they each possess identical wave impedance, thus eliminating any wave reflection at their intersection. The serpentine bar behaves mechanically like a conventional bar with a length equivalent to the unnested length.

Improvements in force measurement and vibration suppression do not require modification of typical quasistatic tests, such as tensile and lap shear tests; however, fracture tests cannot be directly adapted to intermediate and high rates without some modification. Blackman et al. investigated double cantilever beam (DCB) and tapered

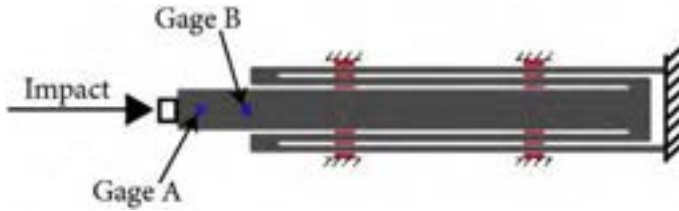


Fig. 21.5 Serpentine transmission bar, allowing for vibration-free measurement of very long (i.e., intermediate rate) pulses.

Reproduced with permission from W.R. Whittington, A.L. Oppedal, D.K. Francis, M.F. Horstemeyer, A novel intermediate strain rate testing device: the serpentine transmitted bar, *Int. J. Impact Eng.* 81 (2015) 1–7.

double cantilever beam (TDCB) Mode I fracture specimens using an open-loop control hydraulic loadframe, with actuator speeds reaching 15 m/s [14]. They used a kinetic energy correction to remove the inertial effects of the substrates from the fracture energy calculation and determined the crack length using high-speed videography.

Another strategy for high-rate fracture testing currently being explored is to reduce the substrate mass that must accelerate. Pohlit et al. used a compact tension specimen. They found a greater than 30% reduction in fracture toughness when increasing cross-head speeds from 10^{-6} to 1 m/s, observing good correlation with the decrease in $\tan(\delta)$ over a similar range and concluding that TTS could reasonably be applied [55]. Watson et al. applied the rigid DCB (RDCB), which utilizes substrates with a width-to-thickness ratio close to one, for structural adhesive fracture testing [56]. Like the TDCB specimen, the rigidity of the specimen obviates the need for crack-length measurement; however, the mass of the RDCB is much lower, and the authors observed that this would minimize the kinetic energy correction in high-rate testing. Finally, Dillard et al. employed a conventional DCB sample, but applied actuation by means of a wedge. The wider wedge, as compared to the wedge impact test described in the next section, forces a separation of the substrates; however, the shorter moment arm between the applied force and the crack tip minimizes the inertia and stored elastic energy in the substrates, permitting rates up to 1 m/s [57].

21.6 Drop weight, falling striker, and pendulum impact tests

Dropping a test piece in free fall is an attractive way to evaluate impact resistance because of the simple boundary conditions [58]. However, quantitative force measurement can be challenging in this format, limiting the potential for property determination. Furthermore, the energy available at a given drop height may not always be sufficient to induce failure, and yet adding mass or increasing the drop height in guided free fall can substantially alter the impact in undesirable ways. This means that it may not be possible to determine failure properties at lower speeds using a guided

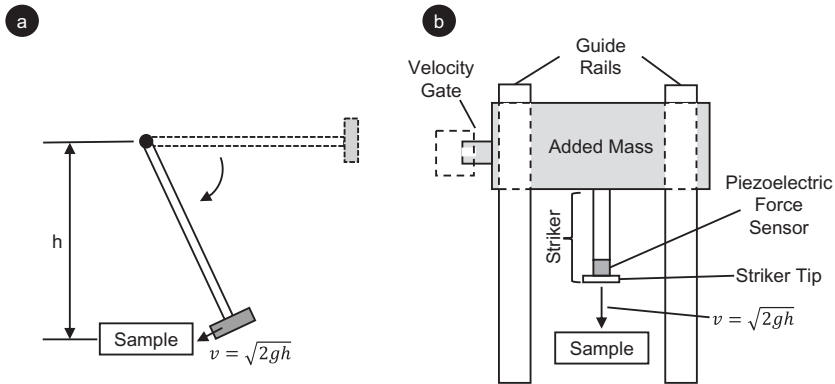


Fig. 21.6 Schematic representation of (a) the pendulum apparatus and (b) drop tower apparatus. Both configurations have a mass propelled by gravity that strikes the sample, and the impact velocity is governed by the release height. Stored energy devices (e.g., springs) can be used to launch the mass, thus increasing the velocity.

free fall methodology. A related set of tests called drop weight tests, falling striker tests, or pendulum tests all solve this problem by keeping the test object stationary and striking it with a falling or swinging striker that can be instrumented (Fig. 21.6). The striker can be equipped with significant added mass, can be dropped from different heights, and can even be launched with springs to increase the impact velocity. Furthermore, the displacement of the striker can generally be tracked, making it possible to determine the mechanical work delivered to the object over time as the integral of force times displacement.

In the drop weight test, also called a drop tower or a falling striker, a striker falls through a guide tube or is attached to a carriage that runs on rails, and the final velocity is determined by the release height according to

$$v = \sqrt{2gh} \quad (21.11)$$

Both configurations allow the striker to travel freely in one dimension without tumbling and ensure a consistent strike location. In a pendulum configuration, a hammer is affixed to the end of a pendulum arm, and the hammer is adjusted to strike the test object held in an anvil at the bottom of the pendulum swing. The impact velocity is also determined by the drop height according to the conservation of energy. The pendulum arrangement translates the difference in height of the hammer to an angular sweep of the pendulum arm. If the pendulum arm mass is much lower compared to the hammer, then the impact velocity is also given by Eq. (21.11).

In principle, a drop tower can perform any test a pendulum can perform; however, in practice, pendulums are useful in several scenarios. First, a pendulum can generally manage a larger mass because the only bearing is the revolute joint at the pendulum pivot. Rotational bearings have better dynamic friction and durability than linear

bearings. Also, any excess potential energy that is not dissipated during the impact is easily dissipated in the upswing postimpact. In contrast, a falling weight set-up requires some sort of catching device to arrest the striker. For large impact energies, this secondary impact may be substantial. Finally, as described below, pendulums can measure energy dissipated by a test object, and therefore can be substantially less expensive when used in this mode. However, instrumented pendulums are also frequently used in research.

On the other hand, pendulums are generally limited in their impact velocity because the maximum free fall distance is controlled by the pendulum length. Also, the angular momentum of the pendulum arm becomes more substantial as the length increases and as the velocity increases. Furthermore, the hammer construction best accommodates test geometries in which the hammer skives off some protruding portion of the test object. There are commonly used workarounds, particularly for wedge impact, but for more general test geometries a drop tower is more versatile. Drop towers are particularly preferred if some portion of the test object is to be punched out (e.g., see the blister test below).

Drop towers and pendulums may be instrumented or uninstrumented. Uninstrumented tests focus on energy dissipated by the adhesive, which is related to toughness. In the case of a pendulum, this information is directly measurable from the initial and final angular position of the pendulum (i.e., the change in initial and final potential energy). For an uninstrumented drop tower, the Bruceton staircase method can be used to determine a threshold energy. Such an approach is used in Gardner and Dupont impact tests (see below).

Instrumented tests also provide force, displacement, and velocity vs time, and by extension, the mechanical work done vs time. This negates the need for a staircase method because the work delivered to the test object is directly measured during the test, regardless of how much excess energy is available in the striker. Furthermore, force and displacement data vs time provide richer insight into the failure process. It is possible to determine a peak nominal stress, which is useful for failure modeling, and differences in the failure process between materials with comparable failure energies can be observed. Finally, instrumented results provide important troubleshooting data, revealing artifacts such as inertial spikes.

Pendulums often lack a force sensor, but they may or may not have displacement sensing. In the simplest configuration, a protractor is mounted with the pendulum. This allows a user to determine the release angle. The maximum angle postimpact can also be measured by attaching a friction dial to the pendulum/protractor; as the pendulum swings it pushes the friction dial, stopping at the peak of its upswing. The difference between the release and final angle provides the energy absorbed. Modern digital variations on this arrangement use an angular encoder to determine initial and final angular position. These systems typically record the angle as a function of time throughout the impact, making it possible to determine the velocity and position vs time, and based on energy balance, the energy dissipated vs time throughout the impact event.

Drop towers typically lack direct displacement sensing. LVDT stroke length and calibration would be problematic for a wide range of drop heights and risk damage

to the LVDT. Optical and laser-based methods are expensive. Most importantly, direct displacement measurement is unnecessary. Instead, displacement can be determined from force sensing plus measurement of the velocity just before the impact, measured using a light gate. Assuming the only forces acting on the striker/carriage assembly are the force applied to the striker by the test object, which is measured by the load cell, and the weight of the carriage, the displacement is computed from a simple force balance as:

$$x(t) = \int_0^t \int_0^t \frac{mg - f(t)}{m} dt^2 + \int_0^t v_0 dt \quad (21.12)$$

Provided there are not significant unaccounted-for forces (e.g., a large lateral load), this is an accurate method with displacement resolution equal to $\frac{S_f}{m} \Delta t^2$ where S_f is the force sensitivity and Δt is the time step. However, it should be noted this approach measures the displacement and velocity of the striker, not necessarily the displacement of the bond. This is an important distinction, as discussed further below.

Force sensors in drop towers and pendulums often consist of a piezoelectric load cell situated at the end of the striker with some replaceable striker tip. The striker tip protects the load cell and allows for different contact geometries. The mass and length of the tip are typically small and do not negatively impact the accuracy of the force measurement; however, the tip geometry can influence the stress distribution in the test, and consequently the way in which adhesive failure evolves. Therefore, tip geometry is an important factor that should be accounted for when describing and comparing test methods [59]. Strain gage-based force sensors were historically more common but have increasingly been replaced by piezoelectric sensors. Strain gage sensors are more temperature sensitive and tend to be less stiff, leading to a lower resonant frequency.

It should be noted that the load cell location on the striker tip ensures accurate measurement of the forces acting on the striker (and by extension, accurate displacement), but the forces acting on the striker are not necessarily the forces acting on the adhesive bond. For instance, the striker does not directly impact the adhesive in many drop tower tests; rather, the striker impacts a substrate, which in turn delivers a stress to the adhesive. The inertia and deformation of the substrate virtually guarantee that the force delivered to the adhesive itself will be different than the value recorded, as discussed in [Section 21.2.1](#). This can be problematic for drop tower tests that measure the energy dissipated during an impact as the toughness of the adhesive. Toughness and dissipated energy are related concepts, but the toughness specifically refers to the energy delivered to the material at the time of failure. In practice, drop tower energy dissipation measurements are an overestimate of toughness because the striker records mechanical work done to accelerate and deform the substrates and fixtures.

Drop tower and pendulum tests are incredibly versatile, but they also suffer from several significant limitations. First, tests are destructive by design. It is possible in principle to run a drop tower or pendulum test at low enough energy to avoid failure, but this is challenging in practice. Second, fixture compliance is a general concern for

drop tower tests because it leads to an overestimate of displacements and energy dissipation, a reduction in peak force, and vibrations in the measured data. Commercial drop towers such as the CEAST line of instrumented drop towers emphasize modularity and flexibility, which comes at the expense of a more complex and compliant fixturing load train. Teller et al. developed an alternative drop tower design that situates all fixturing directly on the concrete floor [60,61]. This greatly reduces compliance, and they have reported an improvement in force measurement accuracy and a reduction in vibration. They employed high-speed DIC for displacement measurement rather than using the force sensor-based method; therefore, it is not clear if this design change improved displacement measurement accuracy.

Song et al. developed another solution to fixture vibration by hybridizing the drop tower with a Kolsky bar/split Hopkinson bar [62]. In their apparatus, which they named a Dropkinson bar, the impact is delivered by a typical striker; however, force is not measured in the striker. Instead, the delivered force is measured by a long force-sensing bar attached to the test object fixture. As with typical Kolsky bar measurements, the induced strain wave is measured by means of strain gages affixed to the bar, and knowing the modulus of the bar, the force can be recovered.

Note that system compliance is mostly a concern when it is on the same order as the test object compliance. As with the guided free fall tower, the drop tower fixtures and test object can be thought of as springs in series. This gives an overall compliance at the moment of impact

$$k_{effective} = \frac{1}{\frac{1}{k_{obj}} + \frac{1}{k_{tower}}} \quad (21.13)$$

In this situation, the tower compliance will not significantly affect the load history during impact or interact with the test object dynamics if $1/k_{tower} \ll 1/k_{obj}$. This is the case for most common tests for which drop towers are designed (e.g., film puncture ASTM D3763 [63]), but it is not necessarily true for many common structural adhesive tests [64–66].

An additional limitation arises from the indirect measurement of displacement. As described above, the displacement is computed from the force on the load cell. This measurement scheme accurately yields the displacement of the striker; however, this is not necessarily the displacement of the test object. To illustrate this issue, consider a test in which the carriage is more massive than the test object to minimize the velocity change in the striker assembly. Assuming no energy is dissipated in the impact and the final velocity of the carriage is 98% of the initial velocity, the conservation of momentum yields:

$$v_{obj} = m_{carriage} \frac{0.02v_{init}}{m_{obj}} \quad (21.14)$$

If $0.02 * m_{carriage} / m_{obj} > 1$, then the object will depart at a larger velocity than the striker. This means that the displacement history of the striker will not reflect the displacement history of the test object. By extension, the work done by the striker is not

equal to the work done on the bond. Additionally, due to load train compliance, the striker may displace without a corresponding stretch in the adhesive bond. Therefore, in general, the dissipated energy will be overestimated.

As with guided free fall, free fall affords limited velocity range. Because the impact velocity goes like the square root of the drop height, increasing drop height yields diminishing returns for the impact velocity. In practice, impact velocities from free fall alone do not exceed 6 m/s due to typical ceiling heights. Larger velocities are achievable by adding springs that launch the carriage and provide additional potential energy to increase the impact velocity.

Finally, drop towers and pendulums suffer from a limitation common to all high-speed testing. It is not possible to instantaneously change the velocity of the test object from zero to a target velocity without an infinite acceleration and by extension an infinite impact force. Consequently, the force measured by the load cell during initial impact will include forces due to the inertia of the test object. In other words, the force exerted by the striker will exceed the force exerted on the bond due to the acceleration of the test object. To illustrate this effect, consider the force acting on a 100 g test object being struck with a velocity of 4 m/s. To illustrate the amplitude of inertial force, assume there is no bond and no gravity. The impulse required to accelerate such a test object from rest is

$$P = \int_0^t F(\tau) d\tau = mv \quad (21.15)$$

Assuming a triangular pulse with a duration of 25 μ s, which is typical in drop tower experiments, the peak force will reach approximately 40 kN. In reality, the spike is not as prominent due to the compliance of the fixtures and test object, but the point is that the force required to accelerate a substrate can be substantial if the timeframe is sufficiently short. If the failure of the adhesive occurs within this time frame, the inertial spike will obscure the true failure data. If the failure occurs at a later time and larger extension, the inertial spike could lead to spurious conclusions if it is wrongly interpreted as the adhesive response. For instance, recording the peak force in a series of drop tests on different materials could obscure differences in failure among the adhesives if the inertial spike is larger than the final failure load.

A wide range of adhesive tests can be conducted using drop towers and pendulums, including several standard tests. These tests can be broadly classified as bulk property tests and bonded assembly tests. Bulk property tests are derived from similar quasistatic variants. Early bulk impact resistance was semiquantitatively assessed using the Gardner test (ASTM D5420) [67–69]. Rather than recording a mechanical property, it uses the Bruceton staircase method to assign a relative impact resistance based on puncturing a coupon of cured adhesive or alternatively a blister-style coupon. A Gardner apparatus has no instrumentation and consists merely of a weight that can be released from controlled heights and a hemispherical probe that is driven into the sample when impacted by the weight. While this test is rarely used in the literature, it is still common in industry due to its simplicity and low cost.

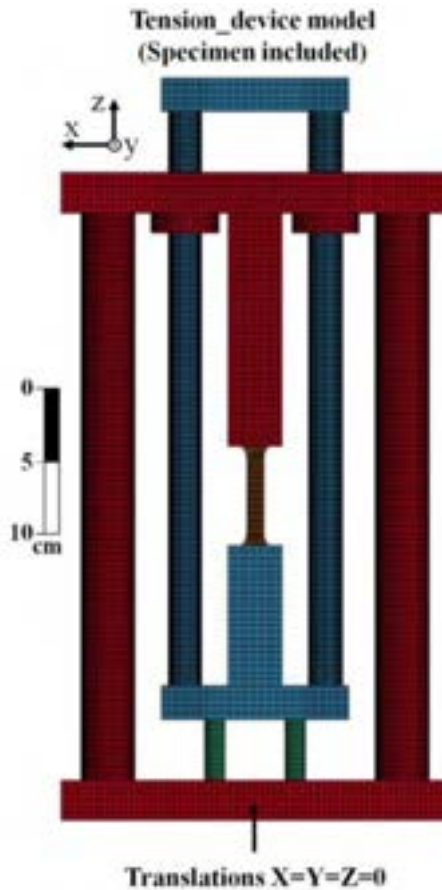


Fig. 21.7 Apparatus for converting the compression of a drop tower impact into tensile loading. Reproduced with permission from N. Perogamvros, T. Mitropoulos, G. Lampeas, Drop tower adaptation for medium strain rate tensile testing, *Exp. Mech.* 56(3) (2016) 419–436.

Intermediate to high strain rate tensile tests with dogbone specimens similar to ASTM D638 and ISO 527 can be conducted on a drop tower using a specialized fixture and high-speed DIC. Perogamvros et al. developed a rig that converts a compressive impact on a platform to tensile loading on a dogbone specimen [70] (Fig. 21.7). Similar fixtures exist for commercial drop towers.

While compression tests are possible in principle, examples are largely absent from the literature. The previously mentioned Dropkinson machine is one example of a hybridized compression technique [62]. High-rate compression tests are generally feasible on servohydraulic machines due to the short gage length of compression samples, and Kolsky bar methods are favored for higher rates due to a less noisy force signal, more accurate strain measurement, and better control over strain rate.

High-rate bulk failure properties are also sometimes assessed by Charpy (ASTM D6110 [71]) and Izod (ASTM D256 [72]) impact toughness tests. Despite their names,

these tests do not measure a true intrinsic toughness due to a number of factors, including fixture effects and imperfections in specimen notching. Rather, the standards themselves note that these are useful comparative tests. Both tests report the energy dissipated during impact with a notched or unnotched specimen. In the Izod test, the specimen is cantilevered out of a rigid clamp. In the Charpy tests, the sample is loaded in three-point bending. Both standards stipulate pendulum testing, and the respective toughnesses are easily computed by the change between initial and final pendulum angle; however, both have been adapted to the drop tower and are commonly performed on either instrument.

Substantial focus has been given to high-rate behavior of bonded assemblies, particular joint strength. Lap shear tests are particularly common. The ASTM D950 [73] test was developed for evaluating wood adhesives and has been adapted in industry to other structural adhesives. The test consists of a small puck bonded to another substrate. A pendulum hammer skives the puck off, recording the energy dissipated during the impact. As with the Charpy and Izod tests, this is not a true toughness, but can be a useful comparative measure. Care must be taken to ensure that the hammer does not drive the puck into the substrate and dissipate additional energy through friction. Due to the circular arc of the pendulum, this can be a particular issue for adhesives with large strains to break.

Viana et al. investigated rate- and temperature-dependent lap shear failure of a commercial one-part epoxy through both servohydraulic and drop tower testing [74]. They independently characterized the adhesive modulus, yield stress, and fracture energy as well as the plasticity of the substrates. They showed good agreement between experimental results and the independently predicted lap shear behavior. However, substantial substrate yield was observed in the tests, and direct interpretation of the nominal shear failure load was not a good indicator of the adhesive strength. Based on this inverse assessment of strength, they showed an increase in overall joint toughness with increasing rate. Goglio et al. similarly investigated the lap shear strength of a commercial two-part epoxy using a novel pendulum test set-up [75] (Fig. 21.8a). They noted the classic result due to Volkens [76] and Goland and Reissner [77] that the stress distribution in a lap joint is highly nonuniform, making average stress a poor representation of the actual strength. Therefore, they employed an analytical solution by Bigwood and Crocombe [78] to estimate the peak peel and shear forces as well as the stress intensity factor relative to the average stress. By varying substrate thickness and using two substrates of differing thickness, they were able to create different combinations of peel and shear stress. They demonstrated that the impact failure stresses lay outside the rectangular failure locus created by the normal and shear stresses under quasistatic loads (Fig. 21.8b), echoing the results by Viana et al. showing an increase in toughness with rate.

The tensile strength of joints may also be evaluated by means of a pendulum or drop tower. The conventional butt tension specimen used at quasistatic rates (ASTM D2095) [48] is not well suited to high-rate testing [64]. Rather, variations of napkin ring or blister specimens have been evaluated (Fig. 21.9). The napkin-ring specimen consists of a butt joint formed between two equally sized tubes, resulting in an annular bond. This specimen is more common in Kolsky bar testing and is discussed further in

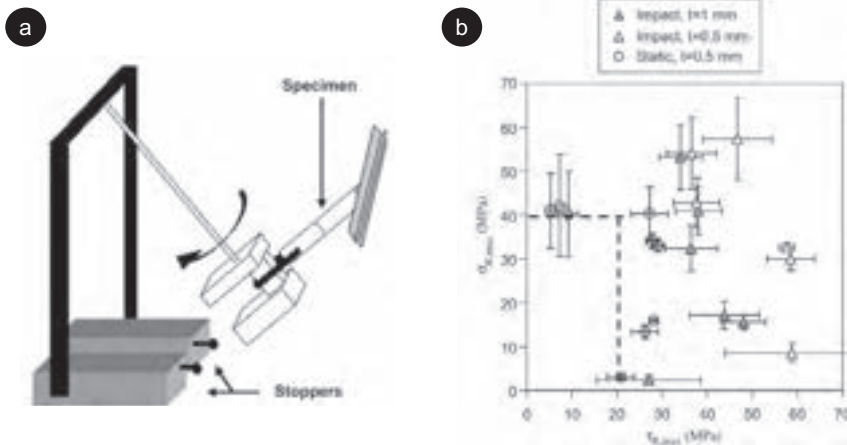


Fig. 21.8 (a) Apparatus for generating tensile loading on a lap shear specimen using a pendulum. Varying substrate thickness produces different ratios of tensile and shear stress at failure. (b) High-rate data for a two-part epoxy fell outside the typical rectangular failure locus for quasistatic rates.

Reproduced with permission from L. Goglio, M. Rossetto, Impact rupture of structural adhesive joints under different stress combinations, *Int. J. Impact Eng.* 35(7) (2008) 635–643.

Section 21.7. The blister specimen also creates an annular bond between a circular puck and window frame with a circular cutout. The puck is loaded in compression, pushing it away from the window frame and nominally loading the bond in tension. Several authors have evaluated tensile strength in epoxies using the blister configuration using a drop tower [59,65,66]. Carpenter et al. noted that the fixturing, striker selection, and striker tip selection could all influence the measured adhesive strength [59]. Breedlove et al. compared blister tests conducted by drop tower and Kolsky bar

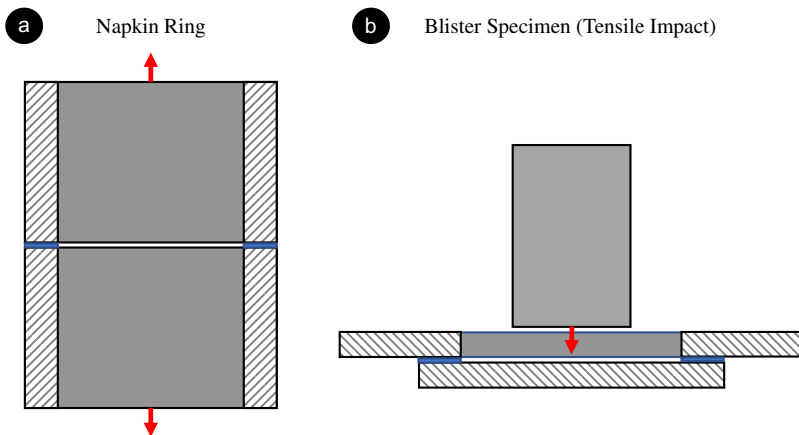


Fig. 21.9 Schematics of napkin ring and blister specimens, used to characterize tensile bond failure at high rates. The adhesive is shown in blue.

with napkin ring tests conducted on a Kolsky bar [64]. They observed significant differences in the stress history among the three different test configurations and concluded that compliance in the drop tower load train as well as flexure in the blister specimen puck led to artificially low peak force and an inflation of measured energy dissipation.

Particular attention has been given to the measurement of Mode I and Mode II fracture toughnesses at high rates. The impact wedge peel test is a Mode I test (ASTM D3762 retracted [79], ISO 11343 [80]), which is common in the automotive industry [16]. In this test, a wedge is driven between two flexible substrates that are bonded by a structural adhesive (Fig. 21.10a), causing the bond to fail and the substrates to deform [16]. Variations on the design of the wedge, the fixturing of the sample, and the loading of the wedge have been proposed [17,81], and the ISO 11343 standard does not specify the exact sample shape [16,80], but the general principle behind the test is the same.

The primary result from a wedge peel test is the average cleavage force. The ISO 11343 standard specifies that this should be taken as the average force after discarding the first 25% of the signal and the final 10% of the signal. This procedure is intended to remove both the initial peak, associated with brief unstable crack growth as the impact first occurs and the semisharp crack first propagates, and the final moments when the bond is no longer intact. Unfortunately, the standard does not differentiate between stable and unstable crack growth (Fig. 21.10b). Because unstable crack growth is associated with measurement of a near-zero force, the 25%/10% procedure causes the cleavage force to be averaged within the initial peak. This leads to the spurious result that unstable crack growth yields a larger average cleavage force in the wedge peel test, suggesting higher toughness, which is incorrect. Blackman et al. considered this issue at length and provided recommendations for careful application of wedge peel [16].

In addition to distinguishing between stable and unstable crack growth, care must also be taken when comparing results between different sample geometries and/or

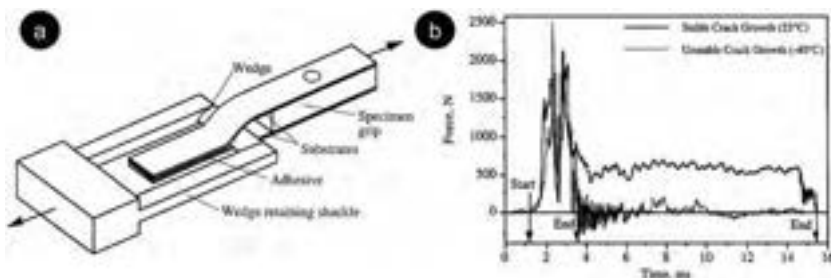


Fig. 21.10 (a) Schematic of the impact wedge test specimen and shackle for driving the wedge through the bond. (b) Both stable and unstable crack growth may be observed. Unstable growth is characterized by a force spike that falls to near zero with no force plateau associated with stable growth. Standard analysis is not appropriate for unstable growth.

Adapted with permission from B.R.K. Blackman, A.J. Kinloch, A.C. Taylor, Y. Wang, The impact wedge-peel performance of structural adhesives, *J. Mater. Sci.* 35(8) (2000) 1867–1884.

preparation methods. Blackman et al. also investigated different sample preparation techniques [16], and observed that these differences influenced the length of the initial unstable peak, and therefore influenced the duration/length of the stable crack growth regime. Consequently, the total energy dissipated by the fracture was dependent on the geometry; however, the plateau cleavage force was not. Therefore, impact energies should not be used for material comparison across sites or different sample preparation techniques.

Although the impact energies are not intrinsic, Mode I fracture energies may be extracted from wedge peel tests. Blackman et al. observed that 2 m/s impact speeds resulted in crack tip opening displacement rates comparable to DCB tests conducted at 0.03 to 0.12 m/s [16]. Thouless et al. originally proposed a method for determining the critical strain energy release rate (G_c) by evaluating the shape of the plastically deformed substrates [82]. The results underpredicted G_c compared with reference values, and it was suggested that the incorporation of root rotations (a correction for the large deflections compared to typical Timoshenko beam analysis) could be the culprit [83–85]. Taylor and Williams applied this analysis with root rotation corrections and found good agreement with independently measured G_c values [86]. They further demonstrated that measuring the force during the test or the crack length could be used with similar precision; however, analysis based on the force history requires knowledge of the friction coefficient between the wedge and the adhesive.

Wedge-peel has been successfully employed to study the rate sensitivity of fracture behavior in adhesives. Often, it is observed that fracture toughness decreases with increasing rate and/or decreasing temperature [16], although increases with rate have also been observed (Fig. 21.3). This decrease is associated with a transition to more brittle modes of fracture [87]. Xu and Dillard similarly observed that fracture toughness decreased with temperature, and further correlated the fracture toughness with the temperature-dependent $\tan(\delta)$, suggesting the variation in toughness was related to the rheological variation in the adhesive's internal energy dissipation [17]. Following the TTS principle, this suggests that the decrease in fracture toughness with increasing rate is related to the same phenomenon. Wedge peel methods have also been extended to the study of interfacial failure. Sun et al. employed an asymmetric specimen to vary mode-mixity and steer cracks to the interface between a commercial rubber-toughened epoxy and a dual-phase steel substrate [81]. They did not observe any rate sensitivity in the cohesive or adhesive toughness for crack velocities between about 0.1 to 1000 mm/s, and it was noted that interfacial toughnesses were approximately 40% lower than bulk toughness.

One final class of drop tower test that is more application-focused remains an area of active research. Crush tubes are structures integrated into automobile bodies that provide for progressive structural collapse with significant energy dissipation [88]. Crush tubes are designed to induce a progressive axial folding of the tube under axial loading instead of buckling. Modern lightweight designs preclude extruded or spot-welded crush tubes, necessitating adhesive bonding. Furthermore, adhesively bonded crush tubes exhibit improved toughness, fatigue resistance, and vibration response compared with spot welds [89] and better stiffness and strength compared with hybrid joining techniques (e.g., adhesive plus rivets) [90]. These adhesives have particularly

demanding high-rate toughness requirements, and direct assessment of their performance in high-rate crumpling of crush tubes is essential [91]. Consequently, crush tube testing is largely an industry screening test; however, there have been several notable advancements in recent years.

First, classic crush tubes without adhesive bonds could be analytically evaluated, with classic closed-form, rate-dependent predictions for crush force developed by Abramowicz and Jones [92,93]; however, multimaterial, bonded crush tubes do not allow such straightforward analysis. Trimiño demonstrated that both cohesive zone models and tie-break models could realistically capture adhesive performance in crush tube tests [91]. Han et al. similarly demonstrated that tie break-based simulations exhibit good agreement with tests for adhesively bonded composite crush tubes [94]. The good performance of tie break methods suggest that energy dissipation in the adhesive during the crushing process is not a significant contributor and rather the loss of strength past peak stress is more significant in compromising the structure. Ramakrishnan et al. used cohesive zone models to evaluate cylindrical lap joints in crush tubes and developed design guidelines based on a design of experiments and analysis of simulation results, which were subsequently validated through testing [95,96].

The second area of innovation concerns testing crush tubes. The extremely large energy dissipation of the structures requires impact masses up to 200 kg. Coupled with the fact that impact velocities up to 20 m/s are relevant for automotive crash performance, crush tube testing towers can become prohibitively large and expensive. Omer et al. rotated the drop tower into a horizontal orientation, creating a sled-style apparatus [97]. Sled testing is common in vehicle crash tests and allows for much larger impact masses and eliminates the challenge of height constraint, provided sufficient propulsion is supplied. Other authors have sought to scale crush tubes to smaller geometries while still maintaining prediction of full-scale structures. Such scaling is challenging in practice because induced strain rates do not scale with the change in length scale and stiffness. Oshiro and Alves introduced the indirect similitude method, which employs an alternative nondimensionalization of the impact problem to arrive at a scaled impact velocity to maintain appropriate rate-dependent material properties [98]. Trimiño et al. applied this method for adhesively bonded crush tubes and concluded that scaled results were in good agreement with conventional tests, provided that the adhesive constitutes a small fraction of the crush tube structure [99]. This opens the possibility that crush tubes can be more readily and affordably studied without the use of a large and expensive test apparatus.

21.7 Kolsky bar/split-Hopkinson bar

The high-speed test methods considered thus far have focused on evaluating the impact resistance of complex test objects and/or material properties at intermediate speeds. At higher velocities, inertial and vibration artifacts as well as practical speed limits become a significant impediment. In servohydraulic and drop tower tests, the length scale is such that stress waves can reflect repeatedly through the duration

of a test. These reflected waves create standing waves, which are the physical basis of vibrations. One strategy to eliminate standing waves is to create a test apparatus in which the stress wave propagation path is much longer than the time required for a stress wave to traverse the apparatus. A Kolsky bar is such an apparatus. The Kolsky bar, also known as a split-Hopkinson bar, is a one-dimensional mechanical waveguide. The principle mimics the determination of optical properties based on the incident, reflected, and transmitted amplitudes of light. These three quantities imply a particular refractive index mismatch at an interface. Similarly, the incident, reflected, and transmitted stress wave amplitudes imply a particular mismatch of mechanical impedance, thus yielding the material properties at high rates.

The Kolsky bar test consists of a test object situated between incident and transmission bars (Fig. 21.11a). The incident bar is sized so that incident and reflected waves pass along the incident bar without overlapping, and the transmission bar is longer than the length of the transmitted wave. Strain gages placed near the center of the bars are thus able to record an isolated strain wave as it passes by without interference from reflected waves.

A strain pulse is often generated in the incident bar by firing a striker bar out of a gas gun, which impacts the incident bar (Fig. 21.11b). Based on plane-wave propagation in a one-dimensional elastic medium, the strain pulse is proportional to the strain rate in the sample according to

$$\dot{\epsilon} = \frac{C}{L_s}(\epsilon_I - \epsilon_R - \epsilon_T) \quad (21.16)$$

where C is the speed of sound in the bar given by $\sqrt{E/\rho}$, L_s is the sample gage length, $\dot{\epsilon}$ is the strain rate in the sample, and the incident, reflected, and transmitted bar strains ϵ are indicated by subscripts I , R , and T , respectively [9,100]. Note that the strain rate is proportional to the amplitude of the pulse in the bars, and the total strain is obtained by integrating the strain rate. Therefore, the maximum imposed strain is proportional to the pulse duration, which is determined by the length of the striker bar according to

$$T = \frac{2L}{C} \quad (21.17)$$

where L is the length of the striker bar.

The Kolsky bar eliminates the complexity of vibrating test apparatuses because the extent of the bars ensures that waves cannot reflect multiple times and create standing waves within the timeframe of the test. As with any dynamic tests, the force acting on the adhesive bond is not uniform if the adhesive is deforming at a nonconstant strain rate; however, once approximately constant strain rate is established, the forces acting on either face of the test object are equal. Under these conditions, the force and displacement may be computed as

$$F(t) = AE\epsilon_T(t) \quad (21.18)$$

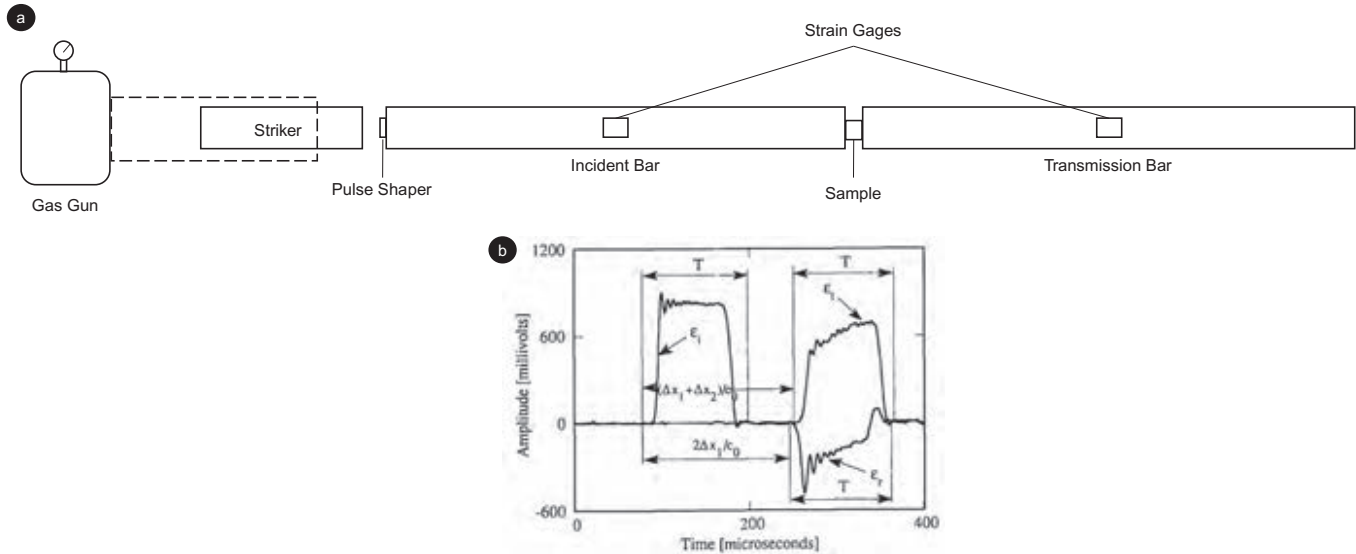


Fig. 21.11 (a) The typical Kolsky bar apparatus consists of incident and transmission bars, between which the sample is situated. A pulse is generated in the incident bar by some means, typically a gas gun that fires a striker bar. The incident, reflected, and transmitted pulses are measured by strain gages. (b) Typical incident, reflected, and transmitted waves measured in a compression experiment.

Reproduced with permission from J. Lifshitz, H. Leber, Data processing in the split Hopkinson pressure bar tests, *Int. J. Impact Eng.* 15(6) (1994) 723–733.

$$\epsilon(t) = -\frac{2C}{L_s} \int_0^t \epsilon_R(\tau) d\tau \quad (21.19)$$

where A is the bar cross-sectional area and E is the bar modulus [9]. The incident stress wave must transit the sample approximately four times before stress equilibrium is achieved, as shown in Eq. (21.3) [12]. If the time equilibrium is too long, the sample may reach failure before stress equilibrium is achieved.

Interfacial friction and radial inertia are additional concerns in Kolsky bar tests. The literature on this topic is extensive [9,101,102]. The key issue is that for samples with a diameter-to-thickness ratio greater than one, frictional forces and the inertia required to accelerate the sample radially due to Poisson effects both become significant [103,104]. Low-viscosity lubrication (e.g., vegetable oil is frequently used) between the sample and the bars is essential to minimize friction [102,105]. Typical adhesive compression samples are only a few millimeters thick and with a diameter of 12 mm or more. Sample diameter is limited by the Poisson effect. During compression, the diameter increases. If the sample diameter exceeds the bar diameter, the sample will no longer be under a state of uniaxial stress. Conservatively taking the sample as incompressible, the maximum initial sample diameter can be computed for a given bar diameter and final strain by [9].

$$d_0 = d_{bar} \sqrt{1 - \epsilon_{max}} \quad (21.20)$$

Often, firing a simple striker bar is insufficient for structural adhesive testing. First, a simple striker bar will create an approximately trapezoidal wave. According to Eq. (21.16), the abrupt change in strain wave amplitude will result in a corresponding rapid change in strain rate, and consequently large acceleration of the sample. When the sample is accelerating, it cannot be in stress equilibrium, and by extension relationships Eqs. (21.18) and (21.19) are not true. Furthermore, waves with a wavelength shorter than the bar diameter (i.e., higher-frequency waves) propagate with a slower velocity, complicating analysis and making it desirable to filter them out of the incident pulse [106,107]. Finally, a trapezoidal pulse will not yield a constant strain rate if the adhesive strain hardens. This results from the requirement that under stress equilibrium, the bar strains must obey

$$\epsilon_I + \epsilon_R = \epsilon_T \quad (21.21)$$

which means

$$\epsilon_R = \epsilon_T - \epsilon_I \quad (21.22)$$

Eq. (21.18) says that the force applied to the sample is proportional to the transmitted strain. Therefore, Eq. (21.22) indicates that if the incident pulse is trapezoidal and the material strain hardens, then the reflected pulse cannot be trapezoidal. But the strain rate is proportional to the reflected pulse by Eq. (21.19); therefore, the incident pulse must not be trapezoidal to maintain a constant strain rate if the material strain hardens.

Ideally, the incident pulse should look similar to the response of the sample. If a dummy sample is placed in the wave path prior to the sample, it will create such a modified incident wave [108]. In practice, this is typically done by placing a pulse shaper, which is a small disk or stack of disks of material with properties comparable to the sample, between the striker and incident bar [109]. The introduction of the pulse shaper not only helps maintain a constant strain rate but also slows the rise time of the pulse and filters out high-frequency wave components. Frew et al. developed an analytical approach for selecting a pulse shaper for strain-hardening metals [110]; however, for polymers, there is no analytical solution for pulse shaping [111]. Unfortunately, pulse shaping remains a recognized and essential artform. Often, heat-treated copper is used as a pulse shaper [110]. Other common pulse shapers are lead, acrylonitrile butadiene styrene (ABS), silicone rubber, and paper [9,111]. In principle, a pulse shaper made of the adhesive material would provide good performance; however, examples of this technique are not readily evident in the literature.

The Kolsky bar testing is often explained as a compressive instrument, and the earliest methods were compression mode, but the principle is not restricted to compressive waves. Kolsky bar structural adhesive tests have been performed on tensile specimens [112–114], lap shear specimens [115,116], torsional specimens [117], and even combined compression-torsional loading [118]. In each of these, the principle is the same: a one-dimensional wave travels down the bar, and the incident, reflected, and transmitted waves reveal the forces and displacements acting on the sample. Some of the innovations over the past 10 years have focused on enhancing these other deformation modes or creating methods of multimodal loading. Other work has focused on improved force sensitivity or faster equilibrium. These advancements have allowed for new adhesive fracture tests. New bar designs have also stretched the lower rate range of Kolsky bar testing into the intermediate range. Finally, methods are beginning to emerge that take advantage of the Kolsky bar loading method, but that employ alternative means to measure and analyze loading on the sample.

Chen et al. pioneered Kolsky tension bar testing using threaded cylindrical dumbbell specimens [119]. The specimens threaded directly into the bars. The authors used a hollow transmission bar to improve signal quality. They successfully tested Epon 828, finding minimal rate sensitivity from quasistatic to high rates in the modulus, yield, and failure strain. This contrasted with a $2\times$ rate-dependent variation in yield stress in compression.

Gilat et al. subsequently investigated epoxy resins E-862 and PR-520 in tension and torsional shear [4]. Torsional Kolsky bar tests are conducted using the same one-dimensional wave propagation theory as used for tensile and compression modes; however, a torsional wave is created by clamping the incident bar, applying a torque, and then abruptly releasing the clamp. They used both flat and cylindrical dogbones that were cemented to adapters on the bar. Strain gages on the dogbones were used to measure the strain. For E-862, they observed that the material maintained good ductility in shear across rates with increasing yield stress and decreasing maximum strain. In contrast, they found that the tensile yield stress was relatively insensitive to rate,

with a much more brittle response. PR-520 showed similar behavior, except that the maximum shear strain was not affected by rate.

Goglio et al. investigated a two-part commercial epoxy in both tension and compression [27]. They employed an unusual set-up to create a tensile pulse. Rather than directly applying a tensile wave, they positioned a split ring between the two bars. The split ring transmitted a compressive pulse, preventing any loading on the tensile dogbone. The compression wave then reflected off the free end of the second bar, becoming a tensile pulse. The reflected tensile pulse then loaded the threaded dogbone, with the split ring carrying no tensile load. The authors additionally investigated two different cure conditions. They found that heat curing caused an increase in yield stress and more pronounced strain hardening. Similarly, tensile tests showed a larger yield stress and modulus for heat-cured samples. Yield stress increased with rate for both deformation modes and curing conditions (Fig. 21.12).

The specimen geometries in early Kolsky tension tests of structural adhesives either bonded the specimens to the bars or used cylindrical dogbones with threads. Both geometries can be problematic for commercial adhesives because many adhesives are not readily machined, and removal of specimens after bonding can be challenging. Consequently, more recent studies have employed more conventional gripping methods. Trimiño et al. studied several automotive-grade two-part epoxies using a flat dogbone and clevis configuration [112]. Slots were cut into the bars,

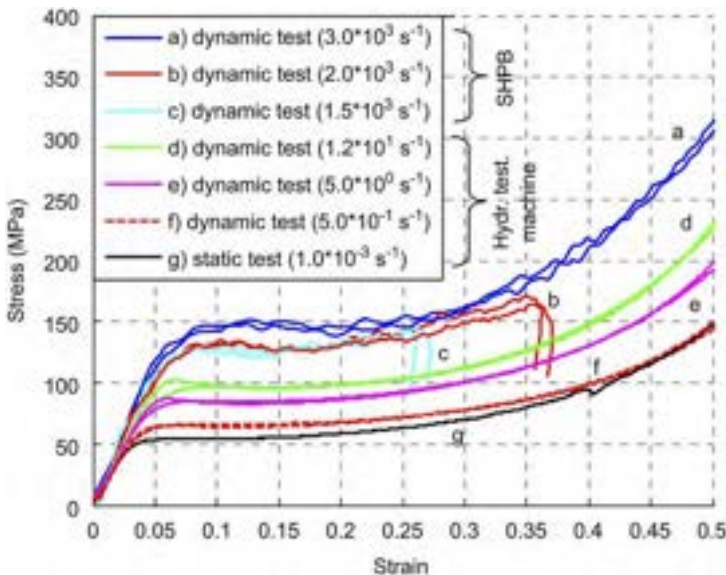


Fig. 21.12 Rate-dependent variation in compressive stress-strain response of a two-part toughened epoxy. These results are typical of Kolsky bar compression results for epoxies. Reproduced with permission from L. Goglio, L. Peroni, M. Peroni, M. Rossetto, High strain-rate compression and tension behaviour of an epoxy bi-component adhesive, *Int. J. Adhes. Adhes.* 28(7) (2008) 329–339.

and the samples were held into place with a bolt passing through the tabs of the dogbone. Breedlove later compared several different gripping methods, concluding that wedge-type grips and clevis grips yield comparable stress-strain responses and sample stress equilibrium provided that DIC is used to measure strains [114]. He suggested that Kolsky bar grips should be chosen for compatibility with the sample (e.g., to minimize sample tear out) and to maximize test efficiency.

One of the most sophisticated Kolsky bar experiments involves generating superimposed waves with different deformation types. This is particularly challenging because wave speeds for different deformation modes are not the same, meaning that the experiment must be specially designed to synchronize loading in multiple modes [120,121]. Claus et al. recently developed a system of wedges that converts a compressive wave into a combined compression-torsion wave just before interaction with the sample [118]. They demonstrated their method on a simulated polymer explosive binder, which has properties similar to structural adhesives. This method is of particular interest in structural adhesive characterization because yield and fracture properties are often pressure-dependent in filled polymer systems.

Chen et al. introduced the hollow transmission bar for measuring low-impedance material (i.e., lower modulus) [122]. The lower impedance of the transmission bar (i.e., larger strain for same applied force) improves the signal-to-noise ratio in measured stress. Note that the hollow transmission bar requires modification of Eqs. (21.18)–(21.19) to account for the different impedances in the incident and transmission bars. Chen et al. later introduced an embedded quartz crystal near the bar faces to produce a load cell with extremely high performance frequency response [123]. The impedance of quartz is nearly identical to aluminum, making it an ideal inclusion into the bar without creating undesirable wave reflections. This is particularly valuable for improving the force measurement on the incident side of the sample to confirm force equilibrium. The large impedance difference between metal bars and polymeric adhesive samples typically creates a very large reflection, which makes the incident force measurement noisy. The quartz crystal method largely solves this problem. Casem et al. later improved on the design to passively eliminate the inertial loading created by the platens affixed to either crystal face [124].

Another focus area in Kolsky bar research is improving stress equilibrium. Pulse shapers are largely able to solve this issue for conventional compression and tension specimens; however, achieving stress equilibrium can be challenging for tests involving substrates, such as DCB specimens, because the wave transit time through the sample is relatively long compared to the duration of the test. Failure to symmetrically load a DCB sample leads to mixed-mode loading. One particularly clever solution to this problem is to generate simultaneous pulses on both bars, so that either side of the specimen is simultaneously and symmetrically loaded. While this approach greatly improves stress equilibrium, it is also extremely challenging to accomplish in practice because the two pulses must arrive with microsecond precision. Nie et al. developed a Kolsky bar apparatus in which both bars are loaded with an electromagnetic pulse [125]. The pulse generators are essentially large voice coils that can be synchronized to ensure precise pulse timing. Compression validation mirrored traditional Kolsky bar experiments with pulse shaping. They demonstrated symmetric loading on a

composite DCB sample. Not only can this method ensure Mode I loading on traditional DCB specimens, it also enables intentional mixed mode loading using two-actuator methodologies such as those developed by Singh, Chaves, and Dillard et al. [126–128] as well as Wu and Liechti et al. [129].

Yokoyama initially studied a commercial cyanoacrylate adhesive using conventional butt tension specimens [130]. The adhesive was bonded to both steel and aluminum substrates, which were threaded into the bars. He observed an increase in tensile strength with rate, with the steel substrates showing an approximately $2\times$ larger strength, and a decrease in the absorbed energy with rate. Yokoyama et al. later considered a commercial two-part epoxy using a top hat specimen, similar to a napkin ring, made from either aluminum or titanium. The top-hat specimen is press fit into a hollow transmission bar, and a tensile stress is applied to the adhesive by pressing on the head of the hat (Fig. 21.13a). Because the force is applied in compression, conventional compression bar set-ups and pulse-shaping techniques can be applied; however, the authors determined through finite element analysis that the central loading creates a bending stress that leads to heterogeneous stress distribution through the bond. They found that tensile strength increased with rate but decreased with bond thickness (Fig. 21.13b). The differences between aluminum and titanium substrates were minimal, with aluminum producing slightly higher strengths.

The reality of a Kolsky bar that can symmetrically load a sample has potential for more complex DCB-inspired test geometries. Dagorn et al. recently hybridized the DCB and arcan geometries (Fig. 21.14) to create specimen capable of creating mixities among Modes I, II, and III [131]. This test geometry showed good correlation with conventional single-leg bending (SLB) tests, and, unlike SLB tests, they observed that the test could be adapted to the symmetric-loading Kolsky bar of Nie et al. [125].

Nunes et al. investigated high rate Mode I and II fracture in two commercial rubber-toughened one-part epoxies [132]. They used a butt tension geometry similar to Yokoyama [130] to determine Mode I fracture toughness, and they used a lap shear geometry that could be attached to the bars through the same threaded joint to evaluate Mode II. Results showed good agreement with reference data. Similar to Gilat et al. [4], they found little rate sensitivity in the butt tension stiffness, but they did see rate sensitivity in shear. Both deformation modes exhibited increasing maximum stress and fracture energy with rate and decreasing maximum strain.

Kolsky bar tests are typically conducted for high strain rates (Fig. 21.1), but in principle they can be conducted for intermediate strain rates as well. Intermediate speed Kolsky bar tests have the advantage of avoiding many of the vibration, load train compliance, and displacement measurement challenges of other methods; however, Eq. (21.16) indicates that lower strain rates require longer pulses to achieve the same total strain. This means that intermediate rate Kolsky bars must be much longer. Gilat et al. constructed a 40 m long bar capable of testing materials between 50 and 500 s^{-1} [53]. Several recent innovations aim to fold a long waveguide into a smaller space. The serpentine bar discussed in Section 21.6 can also be used in a Kolsky bar to generate very long pulses [54]. The millipede bar is another folded bar design [133]. Instead of concentrically nested tubes, the millipede bar is a square bar that zigzags

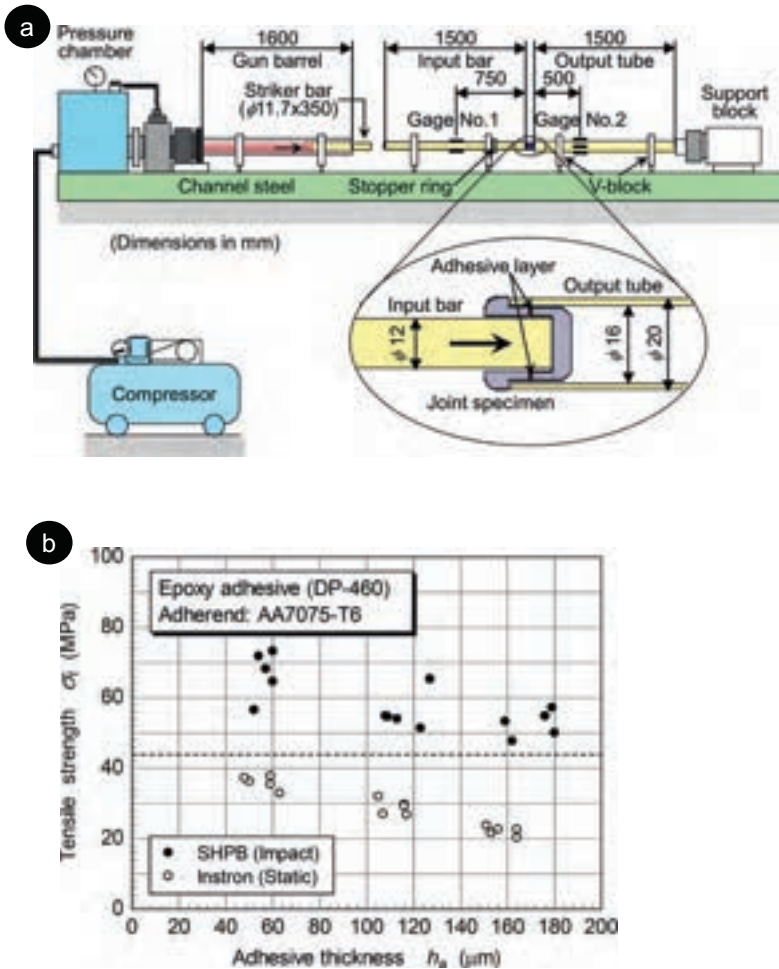


Fig. 21.13 (a) Illustration of the top hat specimen, similar to a napkin ring specimen, and Kolsky bar loading method. (b) Variation in failure stress with rate and bond thickness for an aluminum substrate.

Reproduced with permission from T. Yokoyama, K. Nakai, Determination of the impact tensile strength of structural adhesive butt joints with a modified split Hopkinson pressure bar, *Int. J. Adhes. Adhes.* 56 (2015) 13–23.

back and forth. Surprisingly, this geometry does not appreciably distort the transmitted wave nor introduce additional undesirable bending waves. Folded bars have yet to be applied to structural adhesive testing, but they have the potential to address the gap in testing in the low 100 s/s strain rate range.

Several of the studies described above leveraged high-speed DIC to obtain accurate strain measurements in scenarios where the traditional Kolsky bar equations did not apply. The virtual fields method (VFM) builds on DIC technology, allowing for the

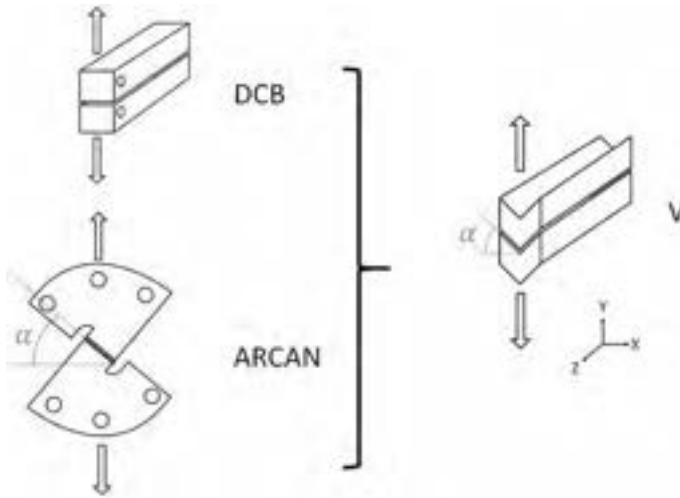


Fig. 21.14 The hybridized DCB specimen to induce mixed mode fracture.

Reproduced with permission from N. Dagorn, G. Portemont, J. Berthe, F. Rasselet, B. Bourel, F. Lauro, Development of a mixed mode double cantilever beam specimen for the fracture characterization of adhesives under high displacement rate, *Eng. Fract. Mech.* 242 (2021) 107467.

determination of stress fields and material properties from DIC measurements if the boundary conditions are well known [134,135]. Fletcher et al. used VFM to develop the image-based inertial impact (IBII) test, in which a Kolsky bar is used to apply a pulse to a panel [136]. This pulse launches the panel and causes it to deform under the trapped wave. The reflected compressive pulse creates a tensile pulse that can subsequently cause tensile failure in the specimen. Because the specimen is ballistic during the imaging, the boundary conditions are trivial. Guige et al. adapted the IBII specimen to test adhesive strength in an epoxy [137]. The method shows promise for high-rate adhesive failure testing as it is not constrained by the stress equilibrium requirement in conventional Kolsky bar testing.

21.8 Advancements and gaps in high-speed testing

The past 10 years of high-speed structural adhesive testing have largely seen improvements in test methodology. Technological advancements in servohydraulic load-frames, drop towers, and Kolsky bars have all collectively improved the accuracy and quality of data and made high-rate testing more accessible. There are now several methods suitable for high-rate testing adhesives in tension, compression, and shear as well as fracture testing. While there is certainly room for additional test innovation, this has set the stage for broader high-rate characterization of structural adhesives, particularly across a broader range of chemistries and fillers. Furthermore, foundational

work, primarily in epoxies, has demonstrated that adhesives exhibit complex rate-dependent behavior, but many questions remain. In what ways do these behaviors link back to chemistry and fundamental properties? Does TTS always apply to yield stress [43]? Why do shear properties appear more sensitive to rate than tensile properties for some adhesives [4]? Why does fracture energy decrease with rate in some situations [14,17,57] and increase in others [18,19,132]? Or is fracture energy tied to the rheological dissipation, thus attaining a peak and then decreasing so that increases, decreases, and lack of sensitivity are simply a window of the broader rate-dependent behavior [17]? Advancements in high-rate structural adhesive testing have started to address these questions and created a rich set of methodologies for deeper investigation.

References

- [1] J.J.M. Machado, E.A.S. Marques, L.F.M. da Silva, Adhesives and adhesive joints under impact loadings: an overview, *J. Adhes.* 94 (6) (2018) 421–452.
- [2] L.F.M. da Silva, A. Ochsner, R.D. Adams (Eds.), *Handbook of Adhesion Technology*, Springer-Verlag, Berlin, 2011.
- [3] S. Marzi, O. Hesebeck, M. Brede, F. Kleiner, A rate-dependent cohesive zone model for adhesively bonded joints loaded in mode I, *J. Adhes. Sci. Technol.* 23 (6) (2009) 881–898.
- [4] A. Gilat, R.K. Goldberg, G.D. Roberts, Strain Rate Sensitivity of Epoxy Resin in Tensile and Shear Loading, 2005.
- [5] C.R. Siviour, J.L. Jordan, High strain rate mechanics of polymers: a review, *J. Dyn. Behav. Mater.* 2 (1) (2016) 15–32.
- [6] J.E. Field, S.M. Walley, W.G. Proud, H.T. Goldrein, C.R. Siviour, *Review of Experimental Techniques for High Rate Deformation and Shock Studies*, 2004.
- [7] J.S. Bendat, A.G. Piersol, *Engineering Applications of Correlation and Spectral Analysis*, Wiley-Interscience, New York, NY, 1993.
- [8] C. Truesdell, *Essays in the History of Mechanics*, Springer-Verlag, New York, 1968.
- [9] W. Chen, B. Song, *Split Hopkinson (Kolsky) Bar*, Springer Science, New York, 2011.
- [10] D.A. Gorham, Specimen inertia in high strain-rate compression, *J. Phys. D. Appl. Phys.* 22 (12) (1989) 1888–1893.
- [11] X. Xiao, Dynamic tensile testing of plastic materials, *Polym. Test.* 27 (2008) 164–178.
- [12] G. Ravichandran, G. Subhash, Critical appraisal of limiting strain rates for compression testing of ceramics in a split Hopkinson pressure bar, *J. Am. Ceram. Soc.* 77 (1) (1994) 263–267.
- [13] Y. Xia, J. Zhu, K. Wang, Q. Zhou, Design and verification of a strain gauge based load sensor for medium-speed dynamic tests with a hydraulic test machine, *Int. J. Impact Eng.* 88 (2016) 139–152.
- [14] B.R.K. Blackman, A.J. Kinloch, F.S. Rodriguez Sanchez, W.S. Teo, J.G. Williams, The fracture behaviour of structural adhesives under high rates of testing, *Eng. Fract. Mech.* 76 (18) (2009) 2868–2889.
- [15] J.D. Ferry, *Viscoelastic Properties of Polymers*, John Wiley and Sons, New York, 1980.
- [16] B.R.K. Blackman, A.J. Kinloch, A.C. Taylor, Y. Wang, The impact wedge-peel performance of structural adhesives, *J. Mater. Sci.* 35 (8) (2000) 1867–1884.

- [17] S. Xu, D.A. Dillard, Determining the impact resistance of electrically conductive adhesives using a falling wedge test, *IEEE Trans. Compon. Packag. Technol.* 26 (3) (2003) 554–562.
- [18] C.S.P. Borges, P.D.P. Nunes, A. Akhavan-Safar, E.A.S. Marques, R.J.C. Carbas, L. Alfonso, L.F.M. Silva, A strain rate dependent cohesive zone element for mode I modeling of the fracture behavior of adhesives, *Proc. Inst. Mech. Eng. Part L J. Mater. Des. Appl.* 234 (4) (2020) 610–621.
- [19] T. Carlberger, A. Biel, U. Stigh, Influence of temperature and strain rate on cohesive properties of a structural epoxy adhesive, *Int. J. Fract.* 155 (2) (2009) 155–166.
- [20] A.D. Mulliken, M.C. Boyce, Mechanics of the rate-dependent elastic-plastic deformation of glassy polymers from low to high strain rates, *Int. J. Solids Struct.* 43 (5) (2006) 1331–1356.
- [21] P.C. Dawson, G.M. Swallowe, Z. Xinwu, Temperature rises during high rate deformation of polymers. *Le, J. Phys.* IV 01 (C3) (1991) C3-701–C3-706.
- [22] S.C. Chou, K.D. Robertson, J.H. Rainey, The effect of strain rate and heat developed during deformation on the stress-strain curve of plastics, *Exp. Mech.* 13 (10) (1973) 422–432.
- [23] M. Garg, A.D. Mulliken, M.C. Boyce, Temperature rise in polymeric materials during high rate deformation, *J. Appl. Mech. Trans. ASME* 75 (1) (2008) 0110091–0110098.
- [24] Z. Li, J. Lambros, Strain rate effects on the thermomechanical behavior of polymers, *Int. J. Solids Struct.* 38 (2001) 3549–3562.
- [25] C.W. Macosko, *Rheology: Principles, Measurements, Ad Applications*, Wiley VCH, New York, NY, 1994.
- [26] M.C. Boyce, S. Socrate, P.G. Llana, Constitutive model for the finite deformation stress-strain behavior of poly(ethylene terephthalate) above the glass transition, *Polymer (Guildf)* 41 (6) (2000) 2183–2201.
- [27] L. Goglio, L. Peroni, M. Peroni, M. Rossetto, High strain-rate compression and tension behaviour of an epoxy bi-component adhesive, *Int. J. Adhes. Adhes.* 28 (7) (2008) 329–339.
- [28] J. Bergstrom, M.C. Boyce, Constitutive modeling of the large strain time-dependent behavior of elastomers, *J. Mech. Phys. Solids* 46 (5) (1998) 931–954.
- [29] H. Chen, P. Song, T. Commins, A. Graham, A.R. Trivedi, C.R. Siviour, Characterization and modelling of bisphenol-a type epoxy polymer over a wide range of rates and temperatures, *Polymer (Guildf)* 249 (2022), 124860.
- [30] I. Lapczyk, J.A. Hurtado, S.M. Govindarajan, A parallel rheological framework for modeling elastomers and polymers, in: 182nd Fall Technical Meeting of the Rubber Division, American Chemical Society, Cincinnati, OH, 2012.
- [31] K. Park, G.H. Paulino, Cohesive zone models: a critical review of traction-separation relationships across fracture surfaces, *Appl. Mech. Rev.* 64 (6) (2011), 060802.
- [32] M.L. Williams, R.F. Landel, J.D. Ferry, The temperature dependence of relaxation mechanisms in amorphous polymers and other glass-forming liquids, *J. Am. Chem. Soc.* 77 (14) (1955) 3701–3707.
- [33] K. Vijayakumar, J.G. Ashoka, A bilinear constitutive model for isotropic bimodulus materials, *J. Eng. Mater. Technol.* 112 (3) (1990) 372–379.
- [34] Y. Nakamura, M. Yamaguchi, M. Okubo, T. Matsumoto, Effect of particle size on mechanical properties of epoxy resin filled with angular-shaped silica, *J. Appl. Polym. Sci.* 44 (1) (1992) 151–158.
- [35] J. Bergström, *Mechanics of Solid Polymers*, William Andrew Publishing, 2015.

- [36] M. Ghorban Ebrahimi, M. Saleh, M.A.M. Gonzalez, Interconversion between viscoelastic functions using the tikhonov regularisation method and its comparison with approximate techniques, *Road Mater. Pavement Des.* 15 (4) (2014) 820–840.
- [37] S.W. Katicha, G.W. Flintsch, Fractional viscoelastic models: master curve construction, interconversion, and numerical approximation, *Rheol. Acta* 51 (8) (2012) 675–689.
- [38] S. Kaneko, S. Nagasawa, Estimation of viscoelastic resistance and subduction profile of acrylic based pressure sensitive adhesive sheet subjected to wedge indentation, *J. Adv. Mech. Des. Syst. Manuf.* 13 (1) (2019) 1–17.
- [39] H.F. Brinson, C. Brinson, *Polymer Engineering Science and Viscoelasticity*, Springer Science, New York, 2008.
- [40] W.P. Cox, E.H. Merz, Correlation of dynamic and steady flow viscosities, *J. Polym. Sci.* 28 (118) (1958) 619–622.
- [41] E.L. Breedlove, A.O. Moughton, A.T. Hedegaard, J. McAllister, C. Li, Quantifying error and the potentially misleading conclusions of the Cox-Merz approximation, in: *Proceedings of the Adhesion Society*, 2021.
- [42] C. Bauwens-Crowet, J.C. Bauwens, G. Homès, Tensile yield-stress behavior of glassy polymers, *J. Polym. Sci.* 7 (4) (1969) 735–742.
- [43] Siviour, C.R., Walley, S.M., Proud, W.G., and Field, J.E., 2005, The high strain rate compressive behaviour of polycarbonate and polyvinylidene difluoride. *Polymer (Guildf)* C. R. Siviour, S.M. Walley, W.G. Proud, J.E. Field, The high strain rate compressive behaviour of polycarbonate and polyvinylidene difluoride, *Polymer* 46 (26) (2005) 12546–12555.
- [44] O. Gomis-Bellmunt, L.F. Campanile, *Design Rules for Actuators in Active Mechanical Systems*, Springer-Verlag, London, 2010.
- [45] T. Bhujangrao, C. Froustey, E. Iriondo, F. Veiga, P. Darnis, F.G. Mata, Review of intermediate strain rate testing devices, *Metals* 10 (7) (2020) 1–24.
- [46] ASTM, Standard Test Method for Tensile Properties in Plastics, 2010. D638-10.
- [47] ASTM, Standard Test Method for Compressive Properties of Rigid Plastics, 2010. ASTM D695-10.
- [48] ASTM International, Standard Test Method for Tensile Strength of Adhesives by Means of Bar and Rod, 2015.
- [49] ASTM, Standard Test Method for Thick-Adherend Metal Lap-Shear Joints for Determination of the Stress-Strain Behavior of Adhesives in Shear by Tension Loading, 2010. D5656-10.
- [50] S. Sahraoui, J.L. Lataillade, Analysis of load oscillations in instrumented impact testing, *Eng. Fract. Mech.* 60 (4) (1998) 437–446.
- [51] High Strain Rate Tensile Testing of Polymers, SAE International, 2017.
- [52] R. Othman, P. Guégan, G. Challita, F. Pasco, D. LeBreton, A modified servo-hydraulic machine for testing at intermediate strain rates, *Int. J. Impact Eng.* 36 (3) (2009) 460–467.
- [53] A. Gilat, T.A. Matrka, A new compression intermediate strain rate testing apparatus, *EPJ Web Conf.* 6 (2010).
- [54] W.R. Whittington, A.L. Oppedal, D.K. Francis, M.F. Horstemeyer, A novel intermediate strain rate testing device: the serpentine transmitted bar, *Int. J. Impact Eng.* 81 (2015) 1–7.
- [55] D.J. Pohlit, D.A. Dillard, G.C. Jacob, J.M. Starbuck, Evaluating the rate-dependent fracture toughness of an automotive adhesive, *J. Adhes.* 84 (2) (2008) 143–163.
- [56] Watson, B., Liao, C.-H., Worswick, M.J., and Cronin, D.S., 2018, Mode I traction-separation measured using rigid double cantilever beam applied to structural adhesive. *J. Adhes.* B. Watson, C.-H. Liao, M.J. Worswick, D.S. Cronin, Mode I traction-separation

- measured using rigid double cantilever beam applied to structural adhesive, *J. Adhes.* 96 (8) (2018) 717–737.
- [57] D.A. Dillard, D.J. Pohlit, G.C. Jacob, J.M. Starbuck, R.K. Kapania, On the use of a driven wedge test to acquire dynamic fracture energies of bonded beam specimens, *J. Adhes.* 87 (4) (2011) 395–423.
- [58] E. Tempelman, M.M.S. Dwaikat, C. Spítás, Experimental and analytical study of free-fall drop impact testing of portable products, *Exp. Mech.* 52 (9) (2012) 1385–1395.
- [59] S. Carpenter, Effects of sample preparation method on adhesive tensile impact testing, in: *Annual Meeting of the Adhesion Society*, 2018.
- [60] S.S. Teller, E.C. Schmitt, J.S. Bergström, A new high strain-rate biaxial experiment to validate constitutive MODELS for polymers, in: *Proceedings of the ASME 2016 International Mechanical Engineering Congress and Exposition*, Phoenix, AZ, 2016.
- [61] E.C. Schmitt, S.S. Teller, J.S. Bergstrom, D. Beynor, System and Method for High Strain Rate Testing of Material Using Gravity Driven Drop Tower, 2022.
- [62] B. Song, B. Sanborn, J. Heister, R. Everett, T. Martinez, G. Groves, E. Johnson, D. Kenney, M. Knight, M. Spletzer, Development of ‘Dropkinson’ bar for intermediate strain-rate testing, *EPJ Web Conf.* 183 (2018) 02004. *DYMAT 2018 - 12th Int. Conf. Mech. Phys. Behav. Mater. under Dyn. Load.*
- [63] ASTM, Standard Test Method for High Speed Puncture Properties of Plastics Using Load and Displacement Sensors, ASTM International, 2014.
- [64] Breedlove, E.L., 2023, A comparison of high-rate tensile failure methods for structural adhesives. *Dynamic Behavior of Materials, Volume 1*, In Press E.L. Breedlove, R. Powers, M. Kennedy, M. Al Tameemi, J. Priester, A comparison of high-rate tensile failure methods for structural adhesives, in: S. Mates, V. Eliasson, P. Allison (Eds.), *Dynamic Behavior of Materials, 1*, Springer, Cham, 2023, pp. 113–121.
- [65] K. Gollins, N. Elvin, F. Delale, Characterization of adhesive joints under high-speed normal impact: part I—experimental studies, *Int. J. Adhes. Adhes.* 98 (2020), 102529.
- [66] S. Yildiz, Y. Andreopoulos, F. Delale, A. Smail, Adhesively bonded joints under quasi-static and shock-wave loadings, *Int. J. Impact Eng.* 143 (2020), 103613.
- [67] D.E. Floyd, D.E. Peerman, H. Wittcoff, Characteristics of the polyamide-epoxy resin system, *J. Appl. Chem.* 7 (5) (1957) 250–260.
- [68] A.C. Soldatos, A.S. Burhans, Cyclonaliphatic epoxy resins with improved strength and impact coupled with high heat distortion temperature, *Ind. Eng. Chem. Prod. Res. Dev.* 9 (3) (1970) 296–300.
- [69] Standard Test Method for Impact Resistance of Flat, Rigid Plastic Specimen by Means of a Striker Impacted by a Falling Weight (Gardner Impact), ASTM International, 2016.
- [70] N. Perogamvros, T. Mitropoulos, G. Lampeas, Drop tower adaptation for medium strain rate tensile testing, *Exp. Mech.* 56 (3) (2016) 419–436.
- [71] ASTM, Standard Test Method for Determining the Charpy Impact Resistance of Notched Specimens of Plastics, 2010. ASTM D6110-10.
- [72] ASTM, Standard Test Methods for Determining the Izod Pendulum Impact Resistance of Plastics, 2010. ASTM D256-10.
- [73] ASTM, Standard Test Method for Impact Strength of Adhesive Bonds, 2003. ASTM D950-03.
- [74] G. Viana, J. Machado, R. Carbas, M. Costa, L.F.M. da Silva, M. Vaz, M.D. Banea, Strain rate dependence of adhesive joints for the automotive industry at low and high temperatures, *J. Adhes. Sci. Technol.* 32 (19) (2018) 2162–2179.
- [75] L. Goglio, M. Rossetto, Impact rupture of structural adhesive joints under different stress combinations, *Int. J. Impact Eng.* 35 (7) (2008) 635–643.

- [76] O. Volkersen, Die nietkraftverteilung in zugbeanspruchten nietverbindungen mit konstanten laschenquerschnitten, *Luftfahrtforschung* 15 (1938) 41–47.
- [77] M. Goland, E. Reissner, The stresses in cemented joints, *J. Appl. Mech.* 11 (1) (1944) A17–A27.
- [78] D.A. Bigwood, A.D. Crocombe, Elastic analysis and engineering design formulae for bonded joints, *Int. J. Adhes. Adhes.* 9 (4) (1989) 229–242.
- [79] ASTM, Standard Test Method for Adhesive-Bonded Surface Durability of Aluminum (Wedge Test), 2003. ASTM D3762-03.
- [80] ISO, Determination of Dynamic Resistance to Cleavage of High-Strength Adhesive Bonds under Impact Wedge Conditions—Wedge Impact Method, 2019. ISO 113432019.
- [81] C. Sun, M.D. Thouless, A.M. Waas, J.A. Schroeder, P.D. Zavattieri, Rate effects for mixed-mode fracture of plastically-deforming, adhesively-bonded structures, *Int. J. Adhes. Adhes.* 29 (4) (2009) 434–443.
- [82] M.D. Thouless, J.L. Adams, M.S. Kafkalidis, S.M. Ward, R.A. Dickie, G.L. Westerbeek, Determining the toughness of plastically deforming joints, *J. Mater. Sci.* 33 (1) (1998) 189–197.
- [83] A.J. Kinloch, J.G. Williams, Comments on ‘determining the toughness of plastically deforming joints’, *J. Mater. Sci. Lett.* 17 (10) (1998) 813–814.
- [84] Q.D. Yang, M.D. Thouless, Reply to comments on “Determining the Toughness of Plastically Deforming Joints”, *J. Mater. Sci. Lett.* 18 (1999) 2051–2053.
- [85] A.J. Kinloch, J.G. Williams, Further comments on ‘Determining the Toughness of Plastically Deforming Joints’, *J. Mater. Sci. Lett.* 18 (24) (1999) 2049.
- [86] A.C. Taylor, J.G. Williams, Determining the fracture energy of structural adhesives from wedge-peel tests, *J. Adhes.* 87 (5) (2011) 482–503.
- [87] C. Sun, M.D. Thouless, A.M. Waas, J.A. Schroeder, P.D. Zavattieri, Ductile-brittle transitions in the fracture of plastically-deforming, adhesively-bonded structures. Part I: experimental studies, *Int. J. Solids Struct.* 45 (10) (2008) 3059–3073.
- [88] P. Du Bois, C.C. Chou, B.B. Fileta, T.B. Khalil, A.I. King, H.F. Mahmood, H.J. Mertz, J. Wismans, *Vehicle Crashworthiness and Occupant Protection*, 2004.
- [89] L. Peroni, M. Avalle, G. Belingardi, Comparison of the energy absorption capability of crash boxes assembled by spot-weld and continuous joining techniques, *Int. J. Impact Eng.* 36 (3) (2009) 498–511.
- [90] A.H. Ibrahim, D.S. Cronin, Mechanical testing of adhesive, self-piercing rivet, and hybrid jointed aluminum under tension loading, *Int. J. Adhes. Adhes.* 113 (2022), 103066.
- [91] L.F. Trimiño, *Analysis and Performance of Adhesively Bonded Crush Tube Structures*, University of Waterloo, 2012.
- [92] W. Abramowicz, N. Jones, Dynamic axial crushing of square tubes, *Int. J. Impact Eng.* 2 (2) (1984) 179–208.
- [93] W. Abramowicz, N. Jones, Dynamic axial crushing of circular tubes, *Int. J. Impact Eng.* 2 (3) (1984) 263–281.
- [94] X. Han, S. Hou, L. Ying, W. Hou, H. Aliyev, On the fracture behaviour of adhesively bonded CFRP hat-shaped thin-walled beam under axial crushing load: an experimental and modelling study, *Compos. Struct.* 215 (2019) 258–265.
- [95] M.U. Ramakrishnan, *Analysis of Tubular Adhesive Joints in Aluminum and Composite Structures under Crush and Tensile Loads*, University of Michigan-Dearborn, 2021.
- [96] M.U. Ramakrishnan, P. Mallick, Behavior of adhesive lap joints in aluminum tubes for crashworthy structures, in: SAE Technical Paper 2022-01-0873, 2022.

- [97] K. Omer, L. ten Kortenaar, C. Butcher, M. Worswick, S. Malcolm, D. Detwiler, Testing of a hot stamped axial crush member with tailored properties—experiments and models, *Int. J. Impact Eng.* 103 (2017) 12–28.
- [98] R.E. Oshiro, M. Alves, Scaling impacted structures, *Arch. Appl. Mech.* 74 (1) (2004) 130–145.
- [99] L.F. Trimiño, D.S. Cronin, Non-direct similitude technique applied to the dynamic axial impact of bonded crush tubes, *Int. J. Impact Eng.* 64 (2014) 39–52.
- [100] P.S. Follansbee, C. Frantz, Wave propagation in the split Hopkinson pressure bar, *J. Eng. Mater. Technol.* 105 (1) (1983) 61–66.
- [101] T.L. Warren, M.J. Forrestal, Comments on the effect of radial inertia in the Kolsky bar test for an incompressible material, *Exp. Mech.* 50 (8) (2010) 1253–1255.
- [102] F. Lu, Y. Lin, X. Wang, L. Lu, R. Chen, A theoretical analysis about the influence of interfacial friction in SHPB tests, *Int. J. Impact Eng.* 79 (Supplement C) (2015) 95–101.
- [103] B. Song, Y. Ge, W.W. Chen, T. Weerasooriya, Radial inertia effects in Kolsky bar testing of extra-soft specimens, *Exp. Mech.* 47 (5) (2007) 659.
- [104] W.W. Chen, Experimental methods for characterizing dynamic response of soft materials, *J. Dyn. Behav. Mater.* 2 (1) (2016) 2–14.
- [105] E.L. Breedlove, D. Lindeman, C. Li, Kolsky bar testing of pressure sensitive adhesives, in: L.E. Lamberson (Ed.), *Dynamic Behavior of Materials, Volume 1*, Springer International Publishing, Cham, 2020, pp. 73–84.
- [106] D. Bancroft, The velocity of longitudinal waves in cylindrical bars, *Phys. Rev.* 59 (1941) 588.
- [107] J.C. Gong, L.E. Malvern, D.A. Jenkins, Dispersion investigation in the split Hopkinson pressure bar, *J. Eng. Mater. Technol.* 112 (3) (1990) 309–314.
- [108] S. Ellwood, L.J. Griffiths, D.J. Parry, Materials testing at high constant strain rates, *J. Phys. E* 15 (3) (1982) 280–282.
- [109] A.M. Bragov, A.K. Lomunov, Methodological aspects of studying dynamic material properties using the Kolsky method, *Int. J. Impact Eng.* 16 (2) (1995) 321–330.
- [110] D.J. Frew, M.J. Forrestal, W. Chen, Pulse shaping techniques for testing brittle materials with a split Hopkinson pressure bar, *Exp. Mech.* 42 (1) (2002) 93–106.
- [111] T.Z. Jiang, P. Xue, H.S.U. Butt, Pulse shaper design for dynamic testing of viscoelastic materials using polymeric SHPB, *Int. J. Impact Eng.* 79 (Supplement C) (2015) 45–52.
- [112] L.F. Trimiño, D.S. Cronin, Evaluation of numerical methods to model structural adhesive response and failure in tension and shear loading, *J. Dyn. Behav. Mater.* 2 (1) (2016) 122–137.
- [113] B. Song, W. Chen, S.T. Montgomery, M.J. Forrestal, Mechanical response of an alumina-filled epoxy at various strain rates, *J. Compos. Mater.* 43 (14) (2009) 1519–1536.
- [114] E.L. Breedlove, Kolsky Bar tensile gripping methods for structural adhesives, in: S. Mates, V. Eliasson (Eds.), *Dynamic Behavior of Materials, Volume 1*, Springer International Publishing, Cham, 2022, pp. 27–33.
- [115] O. Sen, S.A. Tekalur, C. Jilek, The determination of dynamic strength of single lap joints using the split Hopkinson pressure bar, *Int. J. Adhes. Adhes.* 31 (6) (2011) 541–549.
- [116] G. Challita, R. Othman, Finite-element analysis of SHPB tests on double-lap adhesive joints, *Int. J. Adhes. Adhes.* 30 (4) (2010) 236–244.
- [117] B.A. Gama, S.L. Lopatnikov, J.W. Gillespie, Hopkinson bar experimental technique: a critical review, *Appl. Mech. Rev.* 57 (1–6) (2004) 223–250.
- [118] B. Claus, J. Chu, M. Beason, H. Liao, B. Martin, W. Chen, Dynamic experiments using simultaneous compression and shear loading, *Exp. Mech.* 57 (9) (2017) 1359–1369.

- [119] W. Chen, F. Lu, M. Cheng, Tension & compression tests under quasi-static & dynamic loading, *Polym. Test.* 21 (2) (2002) 113–121.
- [120] D. Rittel, S. Lee, G. Ravichandran, A shear-compression specimen for large strain testing, *Exp. Mech.* 42 (1) (2002) 58–64.
- [121] H. Huang, R. Feng, A study of the dynamic tribological response of closed fracture surface pairs by Kolsky-bar compression-shear experiment, *Int. J. Solids Struct.* 41 (11–12) (2004) 2821–2835.
- [122] W. Chen, B. Zhang, M.J. Forrestal, A split Hopkinson bar technique for low-impedance materials, *Exp. Mech.* 39 (2) (1999) 81–85.
- [123] W. Chen, F. Lu, B. Zhou, A quartz-crystal-embedded split Hopkinson pressure bar for soft materials, *Exp. Mech.* 40 (1) (2000) 1–6.
- [124] D. Casem, T. Weerasooriya, P. Moy, Inertial effects of quartz force transducers embedded in a split Hopkinson pressure bar, *Exp. Mech.* 45 (4) (2005) 368–376.
- [125] H. Nie, T. Suo, X. Shi, H. Liu, Y. Li, H. Zhao, Symmetric split Hopkinson compression and tension tests using synchronized electromagnetic stress pulse generators, *Int. J. Impact Eng.* 122 (2018) 73–82.
- [126] H.K. Singh, A. Chakraborty, C.E. Frazier, D.A. Dillard, Mixed mode fracture testing of adhesively bonded wood specimens using a dual actuator load frame, *Holzforschung* 64 (2010) 353–361.
- [127] F.J.P. Chaves, M.F.S.F. De Moura, L.F.M. Da Silva, D.A. Dillard, Fracture characterization of bonded joints using the dual actuator load apparatus, *J. Adhes. Sci. Technol.* 28 (5) (2014) 512–524.
- [128] F.J.P. Chaves, M.F.S.F. De Moura, L.F.M. Da Silva, D.A. Dillard, Numerical analysis of the dual actuator load test applied to fracture characterization of bonded joints, *Int. J. Solids Struct.* 48 (10) (2011) 1572–1578.
- [129] C. Wu, R. Huang, K.M. Liechti, Simultaneous extraction of tensile and shear interactions at interfaces, *J. Mech. Phys. Solids* 125 (2019) 225–254.
- [130] T. Yokoyama, Experimental determination of impact tensile properties of adhesive butt joints with the split Hopkinson bar, *J. Strain Anal. Eng. Des.* 38 (3) (2003) 233–245.
- [131] N. Dagorn, G. Portemont, J. Berthe, F. Rasselet, B. Bourel, F. Lauro, Development of a mixed mode double cantilever beam specimen for the fracture characterization of adhesives under high displacement rate, *Eng. Fract. Mech.* 242 (2021), 107467.
- [132] P.D.P. Nunes, E.A.S. Marques, R.J.C. Carbas, A. Akhavan-Safar, L.F.M. da Silva, Quasi-static and intermediate test speed validation of SHPB specimens for the determination of mode I, mode II fracture toughness of structural epoxy adhesives, *Eng. Fract. Mech.* 262 (2022), 108231.
- [133] R.Y. Leonard III, *Compact Stress Waveguides in Solid Mechanics*, Mississippi State University, 2021.
- [134] F. Pierron, H. Zhu, C.R. Siviour, Beyond Hopkinson's bar, *Philos Trans. A Math. Phys. Eng. Sci.* 372 (2014).
- [135] F. Pierron, M. Grediac, *The Virtual Fields Method: Extracting Constitutive Mechanical Parameters from Full-Field Deformation Measurements*, 2012.
- [136] L. Fletcher, F. Davis, S. Dreuilhe, A. Marek, F. Pierron, High strain rate elasto-plasticity identification using the image-based inertial impact (IBII) test part 1: error quantification, *Strain* 57 (2) (2021) 1–36.
- [137] A. Guigue, L. Fletcher, R. Seghir, F. Pierron, in: J. Kimberley, L.E. Lamberson, S. Mates (Eds.), *IBII test for high strain rate tensile testing of adhesives BT—dynamic behavior of materials*, vol. 1, Springer International Publishing, Cham, 2019, pp. 301–305.

Application of high-throughput methodologies and artificial intelligence for adhesion testing

22

Kshitish A. Patankar^a, Tom Kalantar^a, Simon Cook^a, Edoardo Nicoli^a, Brad Tuft^b, and Matthew Crimmins^a

^aCore Research and Development, The Dow Chemical Company, Midland, MI, United States, ^bDow Performance Silicones, Product Development, The Dow Chemical Company, Midland, MI, United States

22.1 Introduction

Polymer interfaces play a major role in numerous technologies and industries, ranging from biomedical to aerospace. Although critical, understanding the systematic influence of molecular architecture on the interfacial properties and adhesion is not trivial. Many relevant factors, such as surface chemistry, geometry, strain/stress history, environmental conditions, etc., make it an even more daunting task to truly understand interfaces and adhesion properties. It is commonly understood that although many material solutions exist for controlling interfacial properties, rigorous design of experiments (DOE) involving said variables is required to understand the impact of a given formulation on the interfacial properties and develop a data-driven empirical predictive model [1]. Such formulation studies based on complete DOEs can take a significant amount of time, thereby delaying product development. Driven by the advances in biomedical and pharmaceutical industries, new research methods based on combinatorial methodologies have gained traction as a means to facilitate our understanding of the complexities of polymer adhesion. Soft adhesives (subambient glass transition temperature) and the development of high-throughput workflows to characterize their performance have been topics of discussion of several academic and industrial endeavors [2–5]. Although this book focuses on structural bonding, which usually includes rigid (higher than ambient glass transition temperature) adhesives, a brief discussion of high-throughput workflows developed for soft adhesives is appropriate because these workflows highlight the logic and thinking that can accelerate the discovery process and subsequent formulation development for all classes of adhesives. A brief introduction to high-throughput (HT) methods is important to understand the underlying considerations for the development, implementation, and use of HT workflows for adhesive characterization.

22.2 Background

Combinatorial and HT methods and workflows were initially adopted to accelerate the process of drug discovery and then implemented widely across chemical industry research and development (R&D) processes [6,7]. HT methods are useful in enabling an increase in the rate of screening and characterizing new materials, including polymeric materials such as plastics, paints, coatings, and adhesives [7]. This may be accomplished by approaches as simple as processing multiple samples in series or parallel using existing standard benchtop methods, to approaches involving full parallelization and full automation of a fully integrated workflow. The key result of the use of HT is that discovery, screening, and optimization processes are accelerated 5–100 times in rate and/or productivity over classical benchtop methods.

HT methods take advantage of design of experiment (DOE) methodologies, miniaturization, parallelization, and automation to rapidly prepare libraries of test materials and screen them against desired characteristics to identify and characterize trends (structure-property relationships) and identify “hits,” or successful candidate samples. These hits can then become the focus of more in-depth HT characterization and optimization studies as well as bench-scale and pilot-scale activities aimed at rapid materials design, optimization, and scale up as required [8–10]. The large numbers of parameters that can be studied quickly via HT methods enable the researcher to evaluate a vast composition space quickly (in parallel or in rapid serial fashion) for many performance characteristics (output responses) [11]. This broad coverage enables the development of response surface models as well as the identification of local and global maxima and minima while also enabling the researcher to focus on an optimal solution very rapidly [9,12]. The result is, at a very basic level, rapid identification of positive results and elimination of materials or formulations not relevant to the desired outcomes. From an industrial perspective, this “fast-to-fail” approach can result in a significant reduction of time to market [6].

The process of using HT in an overall R&D work process (see schematic in Fig. 22.1) starts with a solid hypothesis based on previous experience, experimental results, literature precedent, predicative models, or simulation. Following a determination that HT methods are the most appropriate for the intended development effort, a



Fig. 22.1 R&D process flow showing the place of HT in the overall work process [10,13–17].

carefully planned experimental design is created. This may be done with commercial DOE software or other methods such as Bayesian next best experiment techniques. Materials are prepared, blended or formulated, processed, and then screened for key material and application properties via a few simple screens that quickly identify hits and eliminate samples of no further interest. Hits might then progress to bench-scale validation using traditional methods, and then to pilot and development scale as warranted. The entire HT experimental effort is supported by databases and software that enable the experimental design, tool and robot operation, collection, storing, analyzing, visualizing, mining, and modeling of the collected data [18]. More than one cycle though this process may be useful, with the first to screen the broad space followed by one or more cycles focused on materials of interest or to optimize around a specific balance of properties. The final steps in the process are to optimize and validate at the bench scale, validate and refine the properties, then scale-up to commercialize.

One of the key obstacles to accelerating product development is the size of the vast compositional space, and the limited time and resources available to explore it [11]. HT approaches combined with optimized DOE and data analysis tools, using rapid screens to evaluate large combinatorial libraries in parallel, enable faster coverage of the same parameter space, or coverage of a much larger space [6,14,19,20] with a similar effort. Being able to scan such a large parameter space can increase the likelihood of finding unexpected hits as well as obtaining a view of the full structure-property relationships for the system [9,20,21]. In one example, a coatings study conducted at Dow Chemical (2 nested DOEs with 8 variables, 8 responses, 432 formulations, 1728 coatings, and >23,000 data points collected) was completed in 8 weeks via HT methods, vs the 39 weeks required for a benchtop study for a similar DOE with one-third the number of formulations [15]. In addition, hits were found in the HT study in an experimental space that was not included in the benchtop study simply due to time and resource limitations [15]. An example of how an experimental space can quickly explode when all the relevant variables are taken into consideration can be found in Table 22.1. This is an example of a DOE from the development of a one-component (1 k) moisture cure polyurethane adhesive, and underscores the need for the use of HT methods. The experimental space for a comprehensive formulation study can grow exponentially to account for the numerous variables, their different “levels,” and sample replicates.

HT methods are simply enabling tools applicable to many but not all research challenges. A simple rule of thumb of when HT may be applicable is as follows: if the research problem is unique, or if the number of needed experiments is expected to be small, one might be better off using classical benchtop methods. However, in situations where research challenges are likely to recur, and where there are many parameters to be considered, establishing and using HT methods can be advantageous [10,12]. One important note is that although HT methods are great accelerators, they do not guarantee success. Success still depends on a carefully designed experimental program to test a technically sound hypothesis followed by rigorously designed screening tests and careful use of data capture and analysis methods to capture learnings.

Table 22.1 An illustration of the complexity of testing a one-component adhesive formulation.

Adhesive formulation variables	Number of levels/components
Polyol	3
Isocyanate	3
Ratios of isocyanate: polyol	3
Levels of solid filler (assuming only one filler)	3
Levels of cure catalyst	3
Levels of rheology modifier	3
Total number of combinations of formulation variables	729
Number of formulations in 1/8 factorial DOE	91
<i>Die^a shear testing variables</i>	
Replicates per substrate and cure condition	5
Substrates	3
Cure times	3
Tests for initial adhesion testing	45
Additional replicates to be tested after environmental exposure	15
Total die shear replicates to be tested per formulation	60
Total number of die shear samples in overall DOE in a 1/8 factorial DOE	5460

^a Details of die shear testing are discussed in detail later in this chapter.

22.3 Considerations in HT workflow and screen development

In designing an HT workflow, one has two primary options: (1) develop an accelerated serial or linear workflow similar to the traditional workflow but mitigate the rate-limiting bottlenecks to enable faster workflow output; or (2) develop a parallel workflow in which libraries of samples are carried through the workflow in parallel. Both approaches are valid, and the choice depends on the specific research needs [16]. Effective workflow development generally requires the removal of bottlenecks in the process, reducing the time or complexity of steps that limit the rate of throughput. However, even if there are one or more steps in the potential HT workflow that cannot be automated or accelerated, it does not preclude the utility of an overall HT workflow; such step(s) can be performed manually. Even if there is a bottleneck, automation of the rest of the workflow can still significantly reduce overall R&D time and effort [10]. Additionally, the HT effort should be compared at all stages to the cost/effort of doing the work via traditional methods. If the sample number is small, or the workflow steps are too complex to automate, HT may not be advantageous [12].

Screen development is extremely important. Screens should be developed based on the end use of the material under development [12]. They must be applicable broadly enough or be so easily repurposed that they can be applied to many different research

challenges with minimal modification. Ideally, a screen should be able to provide full quantitative characterization data comparable to that from a standard benchtop test (ASTM methods, for example). However, such a screen may be too complex to miniaturize, automate, or run in a parallel format. One should therefore choose screens that might be simplified versions of standard screens, be rapid and directional, and correlate with standard tests (indicative of end use properties), provided that the correlation can be established. A useful screening test will enable one to distinguish “good” (desirable) from “bad” (undesirable) samples rapidly on a small scale. To ensure data quality, sample libraries need to include positive and negative controls, internal standards, and duplicate/replicate samples. A good screen should also enable the rapid and reliable relative ranking of the desirability of a library of samples and be able to reliably identify trends in the data [17,18,22]. “Good” samples can eventually be identified and further characterized using traditional, standardized, and perhaps more resource-intensive, analyses.

The degree of integration and automation of the HT workflows depends on the needs of the research challenge. In a research program where the incoming samples are expected to be uniform, and the sample preparation and screens applied are the same every time, one might establish a fully integrated and automated HT workflow, eliminating all human interaction with the samples. In the case where development targets change often, one might opt to establish a more flexible, less integrated, less automated HT workflow. The different elements of the workflow are tied together by common library formats and software and database systems to ensure complete and seamless interoperability [10]. Demanding complete tool and workflow flexibility to handle every possible type of sample requires a great deal of workflow complexity, especially if high speed and high data quality are also required. A useful approach here is to consider a proposed workflow in light of the 80/20 rule: enabling the last 20% will be 80% of the cost and complexity of the system under design; limiting the design to handle only the first 80% will result in a much lower cost, lower complexity, and more reliable workflow.

Having discussed the HT concepts, we now turn to a discussion of HT development specific to addressing adhesion-related challenges.

22.4 Previous instances of HT in adhesion science

Several conventional methods are used to characterize adhesion or interfacial strength. Some of the common methods include the peel, tack, probe test, and lap shear, edge peel, and double-cantilever beam experiments [23]. Of these methods peel, probe, and tack experiments are primarily used to quantify the adhesion of soft adhesives, such as pressure-sensitive adhesives. Free-edge peel tests focus on bonding of thin glassy or semicrystalline polymers (e.g., coatings in electronic applications). Double-cantilever beam and lap shear experiments are conventionally used to quantify the adhesion of glassy polymers, such as epoxies or polyurethanes, that are used in various structural applications. HT methodologies for probing soft adhesion have been developed for the probe, edge delamination, and peel test [2,4,24]. The multilens

contact adhesion test (MCAT) is a probe-type test in which an array of probes is brought in contact with a flat complementary substrate, and the two components are subsequently separated as in a conventional probe test [1]. The MCAT analysis leads to two important quantities that enable quantitative and comparative assessment of multiple systems. The first quantity is hysteresis, which is related to the total energy dissipated during the failure of an interface for elastic materials. The second quantity determined from the contact history is the strain at final failure. To quantify the interfacial strength using MCAT, the strain energy release rate (\mathcal{G}) is treated as a fitting parameter for defining a curve to best fit the contact history for elastic systems. \mathcal{G} is then plotted as a function of the normalized contact radius or the interfacial crack velocity (da/dt) to identify the critical strain energy release rate (\mathcal{G}_c). The edge delamination test, consisting of delaminating a polymer film from the substrate due to the thermal mismatch brought on by the sudden quenching of the coated substrate from a thermal equilibrium, can be designed as a combinatorial HT test. Chiang [24] and Song [25] discuss the utility of this test by designing their libraries with thickness and temperature gradients for a film coated on a metal substrate. These techniques demonstrate how discrete samples and conventional testing methods can be combined with gradient and HT methodologies to increase the efficiency of experimentation and knowledge discovery [26].

Despite the availability of several combinatorial methodologies for characterizing flexible adhesives, there is a dearth of combinatorial method development for characterizing structural adhesives. Adhesive failure or debonding can be viewed from a fracture or strength perspective. The double-cantilever beam (DCB) test is a common technique to characterize \mathcal{G}_c for adhesively bonded joints [23] while the lap shear test is commonly employed in industry to characterize the apparent shear strength of a bond (ASTM D1002). Despite several disadvantages of this test (axial asymmetry, presence of unaccounted-for peel stresses, bending of substrates, nonuniform shear stress distribution along the bondline, poorly understood impact of adhesive thickness, overlap length, etc.), its simple design and easy analysis make it the most used test to differentiate between or rank adhesives based on their failure mode (adhesive or cohesive) and strength. In the next section, we discuss an HT workflow developed at Dow Chemical to characterize the shear strength and failure modes of adhesives. Another aspect of this workflow is the development of methods for the rapid characterization of adhesive reliability and longer-term durability under environmental conditions.

22.5 Workflow concept overview

The essential components of this workflow are: (a) preparation of the substrates; (b) automated adhesive dispensing; (c) automated shear strength testing; and (d) accelerated durability testing to characterize the failure mode and strain energy release rate. The discussion here will focus on developing an HT methodology for rigid substrates that can find applications in the construction, automotive, and electronic industries, among others. A schematic of this workflow is shown in Fig. 22.2.

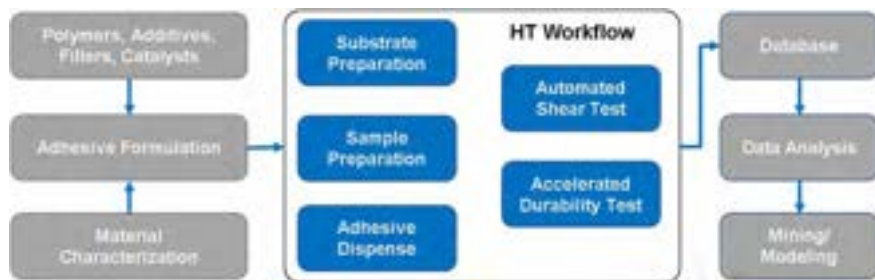


Fig. 22.2 HT workflow to characterize the shear strength of an adhesive, as well as the long-term durability of the adhesive bond. This schematic expands on the trapezoidal box in Fig. 22.1.

This methodology is intended to be a screening tool that can help rank adhesive formulations based on performance; however, a full characterization using standard methods is usually advisable on the chosen adhesive candidates (guided by HT) to confirm that they meet the desired performance standards. The new HT methodology along with the existing standard characterization tools (tensile, thermal, rheological, cure kinetics, etc.) accelerates formulation screening and reliability testing significantly. Of the workflow elements shown in Fig. 22.2, substrate preparation and adhesive dispensing are considered supporting workflows. The remaining two workflows, automated shear testing and accelerated durability, are the primary workflows since they are the source of the data generated and thus the quantitative assessment of the adhesive performance. As discussed above, an important aspect of HT is the data acquisition and processing for further analysis, which will be discussed later in this chapter. The workflow shown in Fig. 22.2 will be referred to as a general outline in the development of the remaining part of this chapter, focusing first on the automated shear test and then on the accelerated durability workflow.

22.6 Shear test: From workflow concept to integration

22.6.1 Automatic shear strength testing

The single-lap joint (SLJ) test is one of the oldest tests used to characterize adhesive strength in a shear mode. ASTM D1002 defines the test and the parameters to be noted after the test. Although very popular in the industry, the test itself does not lend itself to easy automation and cannot be easily done in an HT fashion. Die shear strength (DSS) testing, as described in IPC-TM-650, is routinely used in the electronics industry, where the bond integrity between a semiconductor die and a substrate is characterized. In some cases, the die is a cylindrical button stamped out of the desired substrate. A schematic of the test method is shown in Fig. 22.3.

The testing equipment is expected to have sufficient versatility to conduct a multitude of commonly used bond tests and various built-in automation features reduce subsequent automation and programming requirements. To characterize the failure

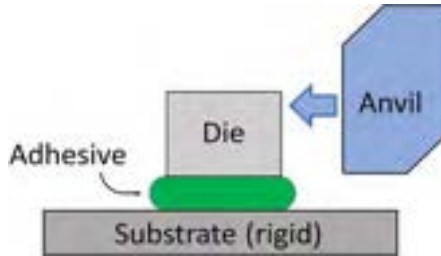


Fig. 22.3 A schematic representation of the die shear test.

mode after the test is complete, a commercial automated imaging tool, capable of rendering three-dimensional (3D) images of the newly formed surfaces, was implemented.

22.6.2 Preparation of the substrates and dies

Common rigid substrates of interest include steel, aluminum, plastic, glass, ceramic, wood, etc. Similarly, dies for DSS testing can also be chosen to suit the needs of the application. The adhesives under consideration in our laboratories range from low modulus, low glass transition elastomeric adhesives to high modulus, intermediate glass transition semirigid adhesives. Initial laboratory experiments suggest that a round die with a diameter of 12.5 mm was ideal for the machine capability and load cell ranges. Substrates were chosen so that they could be handled inside a frame with the same dimensions of a standard microtiter plate, approximately 128×86 mm. Substrate dimensions were approximately $120 \times 78 \times 3$ mm. Given the dimensions of the substrate, about 15 dies can be adhered to such a substrate in a 5×3 (i.e., 5 rows with 3 dies each) configuration. This configuration gives the researcher the flexibility of designing and conducting DOEs with appropriate replicates efficiently. It is imperative that the substrates, the dies, or both be treated with the appropriate surface treatment prior to the adhesion application. A typical surface treatment includes washing the surface with soap and water, then isopropanol or acetone, followed by applying a thin layer of a low molecular weight adhesion-promoting silane primer. An example of a primer is a moisture-cure multifunctional alkoxy silane coupling agent with a titanate catalyst in a solvent.

22.6.3 Automated adhesive dispensing

Three types of adhesive chemistries were considered while designing this workflow: one-component (1k) moisture cure, two-component (2k) thermal cure, and 1k hot-melt adhesives. There are many considerations when it comes to adhesive dispensing and the chemistry involved including adequate humidity control for 1k moisture cure adhesives, ovens for 2k thermal cure adhesives, appropriate adhesive thickness, dispense modes (pressure vs volume control) and accuracy of the dispense, the effect of overdensing vs underdispensing, etc. It is imperative that such provisions are necessary and considered in the HT tool development plan. The effect of adhesive

bondline thickness on the bond strength observed in an SLJ test is not clearly understood, thus this is an important parameter to consider. Numerous studies have investigated the effect of bondline thickness on bond strength; some analyses predict that the strength should increase with adhesive thickness while others hypothesize the presence of an optimum bondline thickness [27–33]. Considering this uncertainty, it was decided to focus on an adhesive bondline thickness relevant to the anticipated applications, in the range 0.5–1 mm. Other than the bondline thickness, the dispensing protocol should also minimize the variability of the area in the die covered with the adhesive as a way to reduce experimental error in the measurement of DSS.

22.6.4 Adhesive dispensing workflow

A pictorial representation of the adhesive dispensing workflow is shown in Fig. 22.4. This workflow is intended to prepare the specimens for die shear testing. A unique, miniaturized arrangement of substrates was designed. The arrangement consists of 15 dies, each about 12.5 mm in diameter and 6 mm in height, bonded to a substrate plate. The dies, stamped from aluminum shim stock, are cleaned, primed, and are placed in a “die carrier.” The die carrier has wells or holes to accommodate the dies. Six such carriers are placed in a “carrier tray.” Multiple carrier trays can then be prepared depending on the number of samples required based on the DOE. The adhesive is dispensed on the dies using an industrial dispenser. The substrate plate, made from metal, plastic, ceramic, wood, cement, etc., depending on the application, is placed on top of the adhesive in an automated fashion and the assembly is set to cure per the desired curing protocol. The bondline is controlled by spacers in the tray. After curing, the bonded specimen is inverted, meaning the substrate plate is now at the bottom with the bonded dies on top. The bonded plate is then moved to the die shear tester.

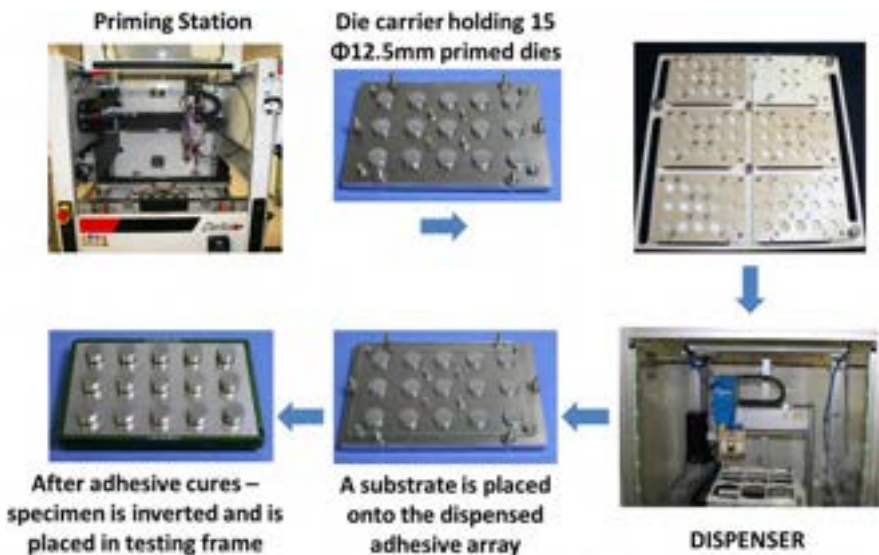


Fig. 22.4 The adhesive dispensing workflow.

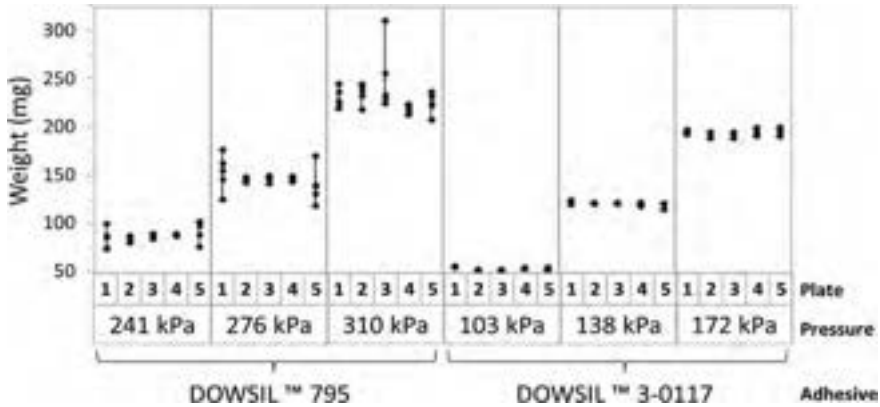


Fig. 22.5 Recorded weight of two 1 k moisture-cure silicone adhesives for Plates 1 through 5 at the indicated dispense pressures for a 5 s dispense.

To validate the adhesive dispensing workflow, two 1 k moisture cure silicone adhesives (open time > 15 min) were chosen. Because these adhesives were paste-like in consistency, the extrusion rate was used as an indirect measure of viscosity. Using a suitable dispenser, the adhesive was dispensed through an orifice of 4 mm in diameter at 448 kPa at ambient conditions (23°C, 10%–30% RH) and the extrudate was collected. The adhesives ranged in viscosity with DOWSIL 3-0117^a at the lower end (extrusion rate of 5 g/min) and DOWSIL 795 (extrusion rate of 1.95 g/min) at the higher end. The weight dispensed on each plate is a function of pressure and dispense time. Keeping the dispense time at 5 s, the weight dispensed as a function of pressure for the two adhesives is shown in Fig. 22.5. The weight was also measured for each “plate,” which represents five dies and was found to be internally consistent. Stepping through the applied pressure resulted in a step change in the adhesive dispensed with minimal variability. It is realized that the time/pressure setting will be different for different adhesives. Owing to shear thinning and thixotropic nature of the adhesives in general, variations can be observed between the weights dispensed at the beginning and the end of the dispense. The best practice is to discard the adhesive dispensed in the beginning and prepare the samples from the adhesive dispensed when the flow is uniform. Generally, higher pressures lead to higher variability; however, it has been noticed that the impact on the shear strength measurement is minimal.

22.6.5 Die shear testing workflow

The bonded specimens prepared in the adhesive dispensing workflow are then moved to the die shear strength (DSS) testing workflow. DSS was measured for the same set of adhesives bonded to aluminum substrates (Al 5052) at a displacement rate of 50 mm/min; results are shown in Fig. 22.6, utilizing a box plot analysis to indicate the spread of the data. The test is expected to have some scatter in the data owing

^a TM Trademark of The Dow Chemical Company (“Dow”) or an affiliated company of Dow.

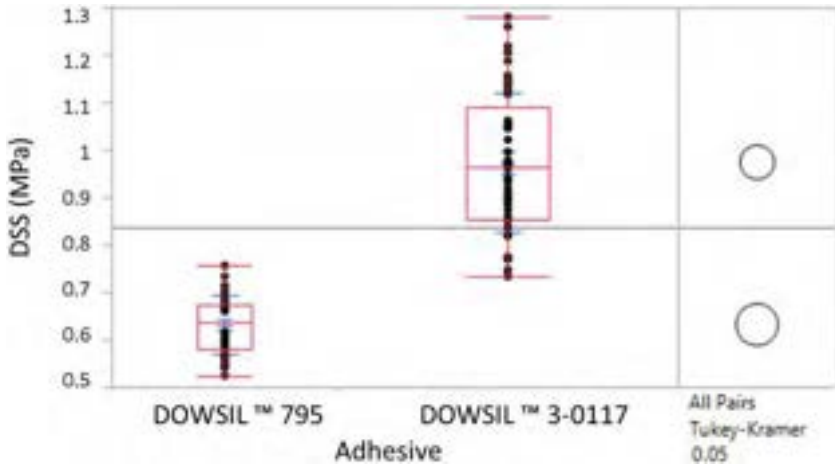


Fig. 22.6 Recorded DSS strength for an aluminum-aluminum bond with two 1 k moisture cure silicone adhesives at a displacement rate of 50 mm/min.

to the complications such as stringing of adhesives, adhesive overflowing out of the area bonded to the substrate, etc. The impact of these variables has also been studied in detail and found to have little influence on the DSS data. The results (Fig. 22.6) show that the two adhesives exhibit statistically different DSS; the ranking is correct relative to their known adhesive properties.^a

Another aspect of the validation work involved comparing strength values obtained on the same adhesive via the two different approaches, SLJ and DSS. Typical SLJ specimens were prepared using the standard ASTM D1002 with 25 mm × 25 mm of adhesive coverage. Care was taken to use the same displacement rate (50 mm/min) to characterize the shear strength. Only DSS data from one plate (five dies) was used for comparison because it is expected that there will be five replicates or data points per experiment in a DOE. Such a comparison is shown in Fig. 22.7. The data show that the lap shear strength of both adhesives was higher than that determined by the HT DSS test. Also, there is significantly more scatter in the SLJ data compared to the DSS data. Most strength-based adhesion measurements exhibit noticeable scatter and the fact that DSS does not exhibit as much scatter is encouraging. We hypothesize that the larger scatter observed in the SLJ data is the result of the geometric variability introduced with the manual procedures for SLJ specimen preparation. The geometric variability refers to the bondline thickness and specimen alignment in the manual SLJ preparation vs in the die shear specimen, with the use of jigs and automation in dispensing the specimen. Despite the difference in the observed DSS averages, it is nevertheless encouraging to see that the relative ranking observed in DSS was corroborated by the SLJ data, proving that DSS is an appropriate and correlating substitute screen for SLJ strength measurements.^a

In addition to being automation-friendly, the DSS test can acquire shear mode stress-strain plots (data shown in Fig. 22.8), from which one can estimate the shear modulus. Shear moduli calculated by this method generally compare well to Young's moduli measured from a tensile test.^a

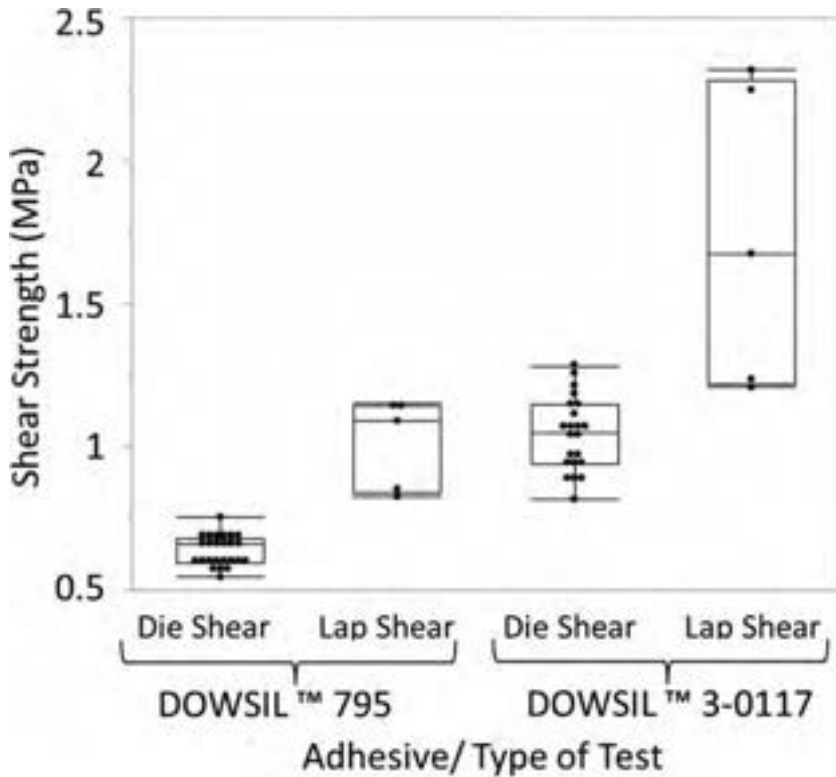


Fig. 22.7 Recorded DSS and SLJ strength for an aluminum-aluminum bond with two 1k moisture cure silicone adhesives at a displacement rate of 50mm/min.

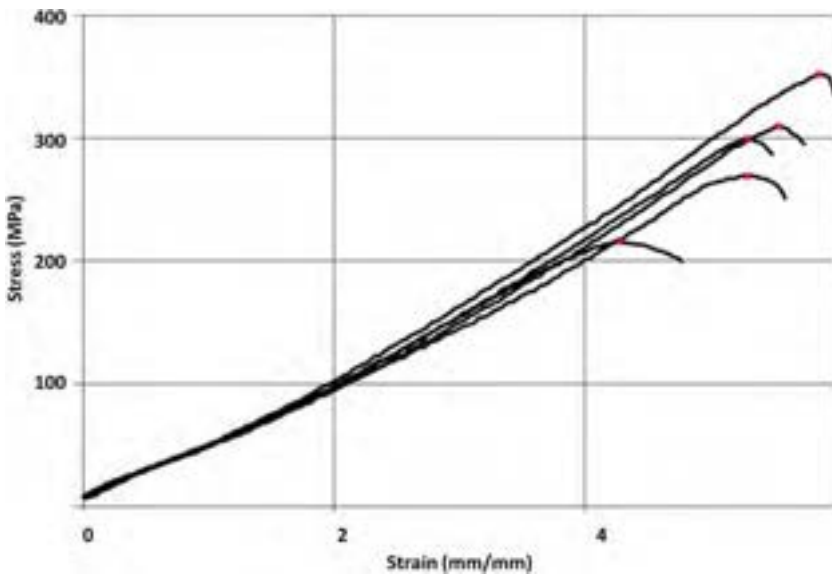


Fig. 22.8 Typical stress-strain plots obtained during a die shear test.

22.7 Durability: From workflow concept to integration

22.7.1 Initial considerations

In addition to using high-throughput DSS testing as a rapid performance screen for adhesive strength, to aid in product down-selection for a given application it is desirable to pair DSS testing with an HT method for screening adhesive bond durability. Specifically, the prediction of adhesion durability in the final joint assembly is greatly enhanced by including a durability screen such as a wedge test in the workflow. This test is also referred to as the wedge cleavage test or Boeing wedge test (BWT) and has been described in various standards (e.g., ISO 10354 and ASTM D3762). The adhesion durability performance demonstrated with this method is often a better predictor of “in-field” performance than are strength-at-failure tests, particularly in adhesive joints where it is atypical to transition to high stress loads over short time scales [34,35]. For example, relevant adhesive and sealant joints that do not undergo high dynamic loads but experience cyclic mechanical and environmental stresses are common in automotive electronics and construction sealant applications.

The wedge test is used to evaluate the durability of an adhesive on a given substrate by subjecting the adhesive joint to both mechanical stress from wedge insertion (wedge thicker than the bondline) and exposing the mechanically stressed joint to environmental stresses such as high heat and humidity, salt-spray cycling, thermal cycling, or water immersion. The combined exposure to mechanical and environmental stresses more closely mimics what adhesive-adherend pairings experience in joints that are not subjected to high stress loads over short time scales. To improve reproducibility with soft or elastomeric adhesives, a precrack is formed at the adhesive-adherend interface as a stress concentrator, which yields more predictable results in tests based on fracture mechanics. The crack will propagate over time through the bulk of the adhesive as long as the mechanical stress exceeds the local fracture toughness at the crack tip, or between the adhesive and the substrate interfaces if it exceeds the fracture energy of the adhesive-adherend bond. Both the local fracture toughness at the crack tip and the adhesive bond strength between the adhesive and substrate can be affected, typically being reduced, during exposure to environmental stress such as water ingress. With some assumptions, the strain energy release rate for crack propagation can be mathematically derived from the thickness and modulus of the deflected beam, the wedge thickness relative to the bondline thickness, and the final length of the crack (Eq. 22.1) [36].

$$G = \frac{3Et^3h^2}{16l^4} \quad (22.1)$$

where

G = strain energy release rate (per area)

E = Young's modulus of the substrate

t = substrate thickness

h = wedge thickness

l = crack length

A qualitative correlation of performance in a wedge test to long-term in-service performance has been demonstrated [37]. The wedge test is also advantageous for lab-based testing as it is inexpensive; straightforward to produce large sample sets to gain statistical insight; enables relatively rapid screening of many adhesives, substrate types, and surface treatments; and is effective to evaluate adhesion durability against expected field conditions. A drawback of the test is that the samples typically must be removed from the exposure environment to measure crack length, and the crack may propagate unevenly across the bond line width or may be difficult to view or measure.

22.7.2 Manual method for durability characterization

This section describes a manual method for producing wedge test specimens to evaluate adhesion durability. Understanding the manual production method clarifies areas for efficiency improvements for any potential use of an HT method to screen products based on adhesion durability results. A wedge test sample consists of the adhesive bonded to two adherends, a defined precrack as a defect to concentrate stress at the interface between the adhesive and the substrate of interest, and a wedge that is thicker than the bondline inserted between the two adherends at a set distance to produce a calculated strain energy release rate (Fig. 22.9).

To ensure failure at the crack tip, the surface opposite the precrack is primed with a silane coupling agent before assembly. In a typical lab workflow, the substrates opposite the precrack are 25 mm × 101 mm coupons of a die-cast or stamped corrosion-resistant aluminum alloy and are cleaned with solvent wipes and then primed to ensure that there is no adhesive failure along this interface during testing.

The testing substrate that the adhesive will be evaluated against is any surface of interest used in the application such as aluminum alloyed with magnesium or chromium for corrosion resistance, glass fiber-reinforced engineering-grade plastic resins, or surfaces treated by plasma, corona, or other reactive surface modification. The test substrate is typically cleaned in a manner that would be representative of the substrate's use in application, which is often "as is" or just a simple dry wipe to remove particulates or oil. To produce a precrack at the adhesive interface on the testing substrate, a piece of PTFE tape is first applied at a set distance from the edge of the coupon and the adhesive bead is dispensed starting first on the tape, then drawn across the sample (Fig. 22.10).

Hand-made specimens are produced with a hand-held adhesive dispenser or a small-scale automated dispensing robot. The bondline thickness of the wedge sample is typically controlled to between 0.5 and 2 mm in thickness to match the bondline thickness in the intended application. Bondline thickness is controlled using physical



Fig. 22.9 Edge view of a representative wedge test sample to evaluate adhesion durability.

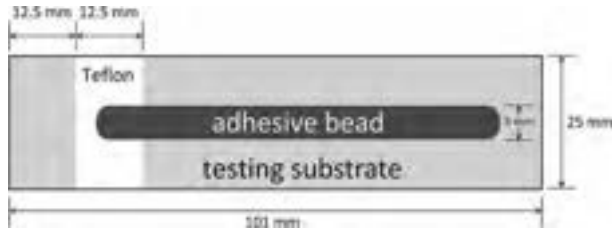


Fig. 22.10 Representative wedge test sample prior to placing spacers and the primed adherend on top. The PTFE tape is used to generate a sharp precrack in the bondline.

spacers such as size-controlled beads or a specific wire gauge. After dispensing the adhesive, the primed adherend (permanent substrate in Fig. 22.9) is placed on top of the uncured adhesive and spacers. Spring force binder clips then fasten the adhesive joint onto the spacers until completion of adhesive cure at the desired conditions. Following adhesive cure, the position of the Teflon tape is marked and the tape removed, which leaves the precrack open to environmental exposure. The wedge, which is thicker than the bondline, is inserted between the two adherends to an insertion line previously measured and marked to carefully control insertion distance, as this dramatically impacts the amount of strain energy on the precrack (see Eq. 22.1). Following wedge insertion, the sample is stored under accelerated environmental aging conditions relevant to the application such as -40°C to 125°C thermal cycling, 85°C , 85% relative humidity, water submersion, salt-spray corrosion cycling, etc. After environmental exposure the wedge sample is manually opened to measure the crack length and assign a failure mode—adhesive or cohesive—along the length of the adhesive bead.

22.7.3 High-throughput wedge test workflow

Similar to the accelerated adhesion performance characterization with the HT DSS test, applying automation and HT methodology to the wedge test significantly accelerates adhesion durability characterization. To enable integration with the HT adhesion characterization workflow, the wedge test is modified from the manual method previously presented. The most significant difference to adapt to an HT workflow is changing the testing substrate's physical dimensions to match the size of the substrates used in die shear testing (approximately $120 \times 78 \times 3$ mm). Changing the substrate's dimensions in this way enables the use of the same automated dispensing tools, sample carriers, and robotic positioning equipment as used in DSS testing. This larger substrate is the material against which the adhesive will be tested for the durability of an adhesive bond. The primed substrates opposite the precrack are aluminum coupons with dimensions of $108 \text{ mm} \times 6.4 \text{ mm} \times 1.6 \text{ mm}$. Because of modifications to the wedge test, including the thickness (3 mm) and rigidity of the testing substrate, estimating strain energy may require the use of beam on elastic foundation or finite element analysis methods rather than Eq. (22.1).

The larger testing substrate enables the generation of five replicates per plate. The increased size of this substrate has the added benefit of reducing cleaning time or cleaning errors, as there are fewer small substrates to handle and clean in any given study. Further, the step of placing the PTFE tape to generate a precrack is also simplified because the samples are wider and easier to handle and the number of individually taped substrates can be reduced by a factor of up to five (a single tape placement for five samples vs one tape placement per sample).

Liquid silicone formulations that are later cured to form elastomeric sealants or adhesives, similar to those described in the section on DSS testing, are applied directly to the cleaned and primed aluminum coupons. The positioning of the coupons is controlled using a 3D printed template and dispensing is controlled with an automated robotic dispenser (Fig. 22.11). The bondline thickness is controlled with offsets in the 3D printed template, which eliminates the repetitive and tedious manual placement of individual spacer elements on each sample. Performing the adhesion durability evaluation with this HT method significantly reduces the time and resources needed to produce large sample sets.

After the cure of the adhesive and after wedge insertion, samples are placed under accelerated environmental aging conditions. In the traditional manual setup, the wedge samples are opened by hand following environmental exposure to inspect for crack propagation and failure mode—adhesive or cohesive—along the adhesive bead. Crack propagation is also measured by hand and results are then manually recorded and uploaded for each specimen (Fig. 22.12). However, in the HT workflow, crack propagation can be measured nondestructively (ND) using an ultrasonic probe with a phased array, which substantially reduces the required number of samples needed in long environmental exposure experiments (as the samples can be evaluated nondestructively, returned to the exposure conditions, and evaluated again repeatedly). With this method, a coupling gel is applied to the bottom of the substrate and the ultrasonic probe is drawn across the precrack region for all five replicates per specimen. Results can be recorded as pass if there is no crack growth and fail

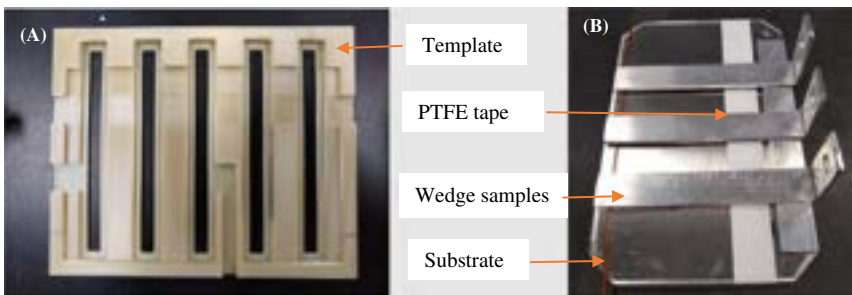


Fig. 22.11 (A) 3D printed template for the wedge test assembly using an HT approach; (B) Representative plaque with three out of a possible five wedge test samples already dispensed and assembled.



Fig. 22.12 (Left) Example of high-throughput wedge samples submerged in water; (Center) Example of adhesive failure across most of the bondline for an adhesive exposed to mechanical strain and water exposure; (Right) Example of cohesive failure after opening the sample following water submersion.

if there is 1 mm or more of crack growth, or as a quantitative measure of crack growth for each specimen. Scanning acoustic microscopy is also known and used as an ND method to measure defects in multilaminate structures such as crack growth in wedge specimens. However, this method typically requires immersion in water as a coupling medium for the sound waves, which would expose the precrack to water, a condition that is not desired in every situation. The portable ultrasonic probe instrument was selected for ND measurement of crack length based on ease of use and integration with the HT workflow and because it does not require significant handling or manipulation of the samples or additional confounding environmental exposure such as water submersion. Extended discussion on ND characterization of crack propagation is beyond the scope of this chapter.

Due to the efficiency of producing and analyzing large sample sets, using HT testing of adhesion durability performance can be useful for rapid screening. For example, if many adhesives, substrates, or environmental conditions are part of an intended study, even a simple pass/fail approach based on any detected adhesive failure in a joint can serve as a screen for solutions rather than a detailed quantitative analysis of crack growth on every sample. Using this pass/fail approach can rapidly identify key factors for the best solution space that inform and define boundaries for more detailed analysis in a significantly narrowed experimental space.

In summary, an automated and HT workflow can be used, at substantially reduced time and resource costs, minimum operator dependency, reduced level of repetitive manual tasks, and accelerated experimentation and project decision loops for faster innovation, to measure adhesion durability. Finally, with appropriate design, the adhesion durability workflow greatly expands existing automated adhesion strength testing tools and augments the available performance data needed to determine the best solutions for successful application outcomes over the intended adhesive joint's lifetime.

22.8 Supporting the adhesion HT workflow

22.8.1 Overview

The initial impetus for the development of these workflows was a need to enable more rapid, in-depth initial screening of adhesive test specimens. The key needs were simple, small-scale (minimal material requirement) screens that would quickly and reliably get at and correlate to fundamental adhesive properties in the areas of bond strength (DSS) and durability under stress (BWT). These screens, although demonstrated on elastomeric adhesives in this study, are expected to be applicable to other classes of adhesives, including high-strength structural adhesives (both methods were developed originally in their benchtop form to handle epoxy adhesives). The screens automated as described herein are of course not a full complement of characterization methods necessary for adhesive product development. These screens provide a rapid way to learn about the basic formulation properties as a function of components, cure conditions, etc., and then to quickly downselect to the “successful” samples for further in-depth, bench-scale characterization (often using customer-specific test methods), leading ultimately to product optimization and commercialization. In addition to the development of these HT tools, methods for handling the data they produce are also necessary. As shown in Fig. 22.2, the full adhesion HT workflow is integrated into a complete and larger workflow that includes a back end devoted to data collection and its analysis and modeling in light of the designs that were studied via the HT methods. Any attempt to use HT methods requires an accompanying data handling workflow, from capture to storage to analysis and modeling. The next section will outline some of the considerations necessary for success in this essential area.

22.8.2 Data management

One of the essential steps in any HT workflow process is the capture of the essential data from each of the process steps. Further, it is highly advantageous to automatically capture and store said data for later retrieval. It is advantageous to start with a data plan. A typical data plan will map out the data obtained from the equipment, the metadata associated with it, and the needs of the data consumers (lab experimenters, data scientists, etc.), then will attempt to compromise among the needs of the different user groups (including database efficiency). When considering the data obtained from the equipment, particularly for in-house developed systems, it is worth considering findable, accessible, interoperable, reusable (FAIR) scientific data principles [38] and human readable data formats such as comma separated variable (CSV), extensible markup language (XML), and JavaScript object notation (JSON). Additional data standards such as Allotrope and analytical information markup language (AnIML) [39,40] can also be highly advantageous in any data capture plan.

The process of parsing data from many instruments and systems becomes one of working with the generated data from the vendor and determining the best methodology to extract the data. In recent years, vendor data have become much easier to extract into a standard format, using an application programmable interface (API).

The next step in the process is mapping the different pieces of extracted data to a “standard” dataset, for example, “Max Force, N.” Note that aligning the units as well as the measured quantity is important for any data mining or modeling. Parsing to a standard format is typically referred to as data governance, which becomes more and more important as datasets grow exponentially larger.

In many automated systems, the equipment is controlled and data are extracted using a programming code (e.g., C# or Python). This code base sends instructions to the equipment to (for example) start the instrument(s) and read the data into code. This code then organizes the data into discrete variables and data arrays (for X-Y type data) ready for manipulation into tables or a database structure. In the case where the in-house generated code also controls the instrumentation, it is recommended that the data are stored in a local database (such as MySQL) to allow easy data manipulation. Once the data are extracted and parsed into discrete variables and arrays in code, it is highly recommended to have a quality assessment of the data before long-term storage. This allows a determination of whether the data are reflective of the test and allows suspect data, or data that have failed on the instrument, to be marked as such and not included on any data averaging coding. The workflow discussed above is shown in Fig. 22.13.

Data from many HT experiments are collected and stored in a database or a series of tables (hereinafter referred to as a database) similar to an SQL-type database such as Oracle, MS-SQL, MySQL, PostgreSQL, etc. The database systems are typically referred to as a system of record, meaning a system that stores data and records for the long term, typically in a manner that can be easily accessed by code for data analysis. When designing said database, the key is understanding the data plan. In general, the optimal way to lay out the database is in several layers, as discussed below.

The top level of many HT databases typically has a design reference (to link to the synthesis or other formulation and sample preparation details) and descriptions of the type of experiment, preferably including the methodology used. The sample table would have many rows for each design reference that reflect the individual samples (with a consistent reference) being formulated or tested. The data at this level reflect the overall composition or testing average type results. Another layer of tables would be replicate analyses that are performed to improve the power to detect a difference between samples. This table would hold all the individual testing data. This type of structure is illustrated for a DSS experiment in Fig. 22.14.



Fig. 22.13 High-level diagram of the HT data flow.

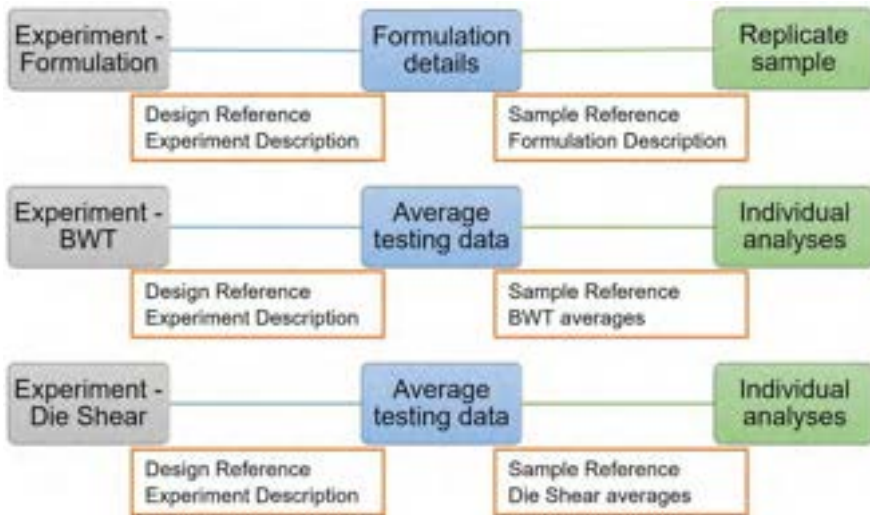


Fig. 22.14 A schematic representation of the different data levels for each HT experiment.

By carefully organizing the data in such a way, the formulation details can be easily joined to the testing details by the design reference and individual sample reference. This lends itself to automated data processing such as can be used for both individual sample exploration as well as data extraction into larger datasets for modeling. Commercial databases typically have end-user tools or APIs in place that allow easy access to the data with coding scripts while data tables held outside such systems can easily be combined using code.

22.9 Role of machine learning/artificial intelligence in adhesion science

The growth in computational power experienced in the past few decades has been a great enabler and complement to the laboratory HT techniques used in modern industrial research. Terms such as data science, artificial intelligence (AI), and machine learning (ML), once limited to computer science research and, since the early 2000s, applied to various Internet platforms, have recently become familiar also in materials science research. Data science is not an intrinsically novel science, as it is a field that combines the scientific method with the use of algorithms and statistics for extracting the maximum amount of useful information from a given dataset.

Traditionally, AI/ML advancements were led by the technology/Internet companies while traditional industries (such as materials or chemical manufacturers) have been slower in implementing AI approaches. However, the increase in data availability that HT techniques have recently provided has opened interesting opportunities for AI/ML approaches also for more traditional industries [41]. To some extent, the

technological advancements leading HT to gain a foothold in the industry have also led to generating data that AI/ML systems can use and benefit from [21,42]. Lastly, AI and ML are obviously used in research and industry for integrating the physics and hypotheses that are already part of shared knowledge to identify new correlation patterns [43,44] and for predicting new materials properties from existing databases, leading to reduced product development cycle times and shorter times to market.

Specifically related to adhesive applications, AI/ML tools can be used to analyze and correlate data that possibly span the range from chemical synthesis and formulation to finite element analysis and mechanical testing [45]. The desired optimization goals of adhesive-related studies can point to aspects such as the increase of adhesive joint strength [46,47], processing cost reductions [48], optimization of joint geometry [49], and extension of fatigue life [50]. In several of the mentioned studies, the application of AI/ML techniques is still in the initial stages, with the whole process being not fully autonomous from human interactions and supervision. Some of the complications limiting the field are as follows:

- The coexistence of variables of different nature, for example combining quantitative/numerical variables as for molecular weight and stress levels with time series data such as spectra.
- The general complexity of the design spaces, as properties of adhesively bonded joints do not depend solely on the bulk properties of the constitutive materials.
- The general relatively limited size of the available dataset [51], such as, for example, tests on a large number of geometries for training the models are not always economically feasible.

One practical problem with data is that often historical datasets were not intended to be developed as a single set but have been populated as a result of multiple separate efforts. In this common case, said datasets can result in sparse matrices (i.e., matrices of properties where many of the cell values are zero or unknown) that do not facilitate the development of reliable models. Applications of external constraints using physics- and reason-based hypotheses can help the system to perform model inversions [52] in this case and allow one to identify formulations that:

- Are physically plausible
- Minimize cost
- Use all available intermediates (including those not in training data)
- Incorporate institutional knowledge or regulatory constraints

The data voracity of the AI/ML approach is challenging the ways in which industrial researchers, and in this specific case adhesive developers and users, can make the most of these relatively new toolsets. AI/ML is solidly grounded on materials datasets that are, as much as possible, complete, in standardized format, and easily accessible. Several initiatives on open access information have constituted the basis for initial AI/ML developments in the materials science world. Also, much of the code has been written as open source software, benefitting from quick feedback and bug detection by the user community [53]. Commercial business opportunities, on the other hand, that rely on private data ownership and proprietary databases are by default created and closely maintained by smaller groups (i.e., within a single company). Future challenges and the velocity of implementation are expected to depend also on the balance of these contradictory interests [53].

22.10 Summary

High-throughput (HT) method development for discovery and commercialization in the chemical and materials industry has been implemented extensively in recent years. In this chapter, the development of HT methodology to characterize and test adhesives has been overviewed by outlining the essential workflow components, that is, identification and preparation of the substrates, automated adhesive dispensing, and automated shear strength testing and accelerated durability testing to characterize the failure mode and strain energy release rate. The vision behind this effort is to increase the rate of adhesive formulation screening by a factor of 5–100 and to improve significantly testing reliability. The shear strength workflow was validated by demonstrating that: (1) Die shear strength (DSS) differentiates between aluminum-aluminum assemblies bonded with different adhesives; and (2) although statistically not equivalent, the SLJ and DSS adhesion strength were ranked similarly for aluminum-aluminum assemblies. Custom-built templates were designed for the HT durability workflow to eliminate several steps from the manual durability screen, thereby simplifying, streamlining, and accelerating the testing process. Considerations for data collection and management workflow were discussed. Finally, although, AI and ML initiatives have hereto been slow to pervade adhesion research, recent trends are pointing in the direction of significantly increased use of such tools as they become more widely accessible.

Acknowledgments

The authors would like to express their sincere gratitude to the Dow Chemical Company for sponsoring this work. The authors would also like to thank numerous colleagues and experts in the area of HT and adhesion for valuable discussions.

References

- [1] A.J. Crosby, Combinatorial characterization of polymer adhesion, *J. Mater. Sci.* 38 (2003) 4439.
- [2] A. Chiche, W. Zhang, C.M. Stafford, A. Karim, A new design for high-throughput peel tests: statistical analysis and example, *Meas. Sci. Technol.* 16 (2005) 183.
- [3] J.C. Grunlan, et al., Combinatorial development of pressure-sensitive adhesives, *Macromol. Rapid Commun.* 25 (2004) 286.
- [4] A.J. Crosby, A. Karim, E.J. Amis, Combinatorial investigations of interfacial failure, *J. Polym. Sci., Part B: Polym. Phys.* 41 (833) (2003).
- [5] J.C. Meredith, A.P. Smith, A. Karim, E.J. Amis, Combinatorial materials science for polymer thin-film dewetting, *Macromolecules* 33 (26) (2000) 9747.
- [6] R. Hoogenboom, M.A.R. Meier, U.S. Schubert, Combinatorial methods, automated synthesis and high-throughput screening in polymer research: past and present, *Macromol. Rapid Commun.* 24 (1) (2003) 15.
- [7] M.A.R. Meier, R. Hoogenboom, U.S. Schubert, Combinatorial methods, automated synthesis and high-throughput screening in polymer research: the evolution continues, *Macromol. Rapid Commun.* 25 (1) (2004) 21.

- [8] J.R. Hattrick-Simpers, J.M. Gregoire, A.G. Kusne, Perspective: composition–structure–property mapping in high-throughput experiments: turning data into knowledge, *APL Mater.* 4 (5) (2016) 053211.
- [9] M.L. Green, I. Takeuchi, J.R. Hattrick-Simpers, Applications of high throughput (combinatorial) methodologies to electronic, magnetic, optical, and energy-related materials, *J. Appl. Phys.* 113 (23) (2013) 231101.
- [10] T.-C. Kuo, et al., High-throughput industrial coatings research at the Dow Chemical Company, *ACS Comb. Sci.* 18 (9) (2016) 507–526.
- [11] I.G. Clayson, et al., High throughput methods in the synthesis, characterization, and optimization of porous materials, *Adv. Mater.* 32 (44) (2020) 2002780.
- [12] H.E. Tuinstra, C.H. Cummins, Combinatorial materials and catalyst research, *Adv. Mater.* 12 (23) (2000) 1819.
- [13] R. Iden, et al., Combinatorial materials research in the polymer industry: speed versus flexibility, *Macromol. Rapid Commun.* 24 (1) (2003) 63–72.
- [14] J.N. Cawse, Experimental strategies for combinatorial and high-throughput materials development, *Acc. Chem. Res.* 34 (3) (2001) 213–221.
- [15] R. Cesaretti, et al., Overview of capabilities and applications of high throughput formulation research, in: *ChemSpec USA Conference*, Philadelphia, PA, 2011.
- [16] K.P. Peil, et al., Applications of high throughput research at the Dow Chemical Company, *Macromol. Rapid Commun.* 25 (1) (2004) 119–126.
- [17] B. Chisholm, et al., Combinatorial chemistry methods for coating development: III. Development of a high throughput screening method for abrasion resistance: correlation with conventional methods and the effects of abrasion mechanism, *Prog. Org. Coat.* 47 (2) (2003) 112–119.
- [18] W.F. Maier, K. Stöwe, S. Sieg, Combinatorial and high-throughput materials science, *Angew. Chem. Int. Ed.* 46 (32) (2007) 6016.
- [19] B. Colin, et al., Development of new high-throughput screening method to compare and to detect efficient catalysts for adhesive materials, *Int. J. Adhes. Adhes.* 68 (2016) 47–53.
- [20] J.G. de Vries, H.M. de André, The power of high-throughput experimentation in homogeneous catalysis research for fine chemicals, *Eur. J. Org. Chem.* 2003 (5) (2003) 799–811.
- [21] R.A. Potyralo, et al., Development of combinatorial chemistry methods for coatings: high-throughput adhesion evaluation and scale-up of combinatorial leads, *J. Comb. Chem.* 5 (4) (2003) 472–478.
- [22] B. Chisholm, et al., Combinatorial chemistry methods for coating development: VI. Correlation of high throughput screening methods with conventional measurement techniques, *Prog. Org. Coat.* 48 (2) (2003) 219–226.
- [23] A.J. Kinloch, *Adhesion and Adhesives: Science and Technology*, Chapman and Hall, 1987.
- [24] M.Y.M. Chiang, et al., Combinatorial approach to the edge delamination test for thin film reliability—concept and simulation, *Thin Solid Films* 437 (1) (2003) 197–203.
- [25] R. Song, et al., Combinatorial peel tests for the characterization of adhesion behavior of polymeric films, *Polymer* 46 (5) (2005) 1643–1652.
- [26] S.R. Ranade, et al., A tapered bondline thickness double cantilever beam (DCB) specimen geometry for combinatorial fracture studies of adhesive bonds, *Int. J. Adhes. Adhes.* 55 (2014) 155–160.
- [27] M. Rośkowicz, et al., The effect of adhesive layer thickness on joint static strength, *Materials* 14 (6) (2021) 1499.

- [28] L.F.M. da Silva, et al., Effect of adhesive type and thickness on the lap shear strength, *J. Adhes.* 82 (11) (2006) 1091–1115.
- [29] D.J. Alner, *Aspects of Adhesion*, vol. 6, University of London Press, 1965.
- [30] J.-Y. Cognard, et al., Influence of adhesive thickness on the behaviour of bonded assemblies under shear loadings using a modified TAST fixture, *Int. J. Adhes. Adhes.* 30 (5) (2010) 257–266.
- [31] H. Winter, *Fertigungstechnik von Luft- und Raumfahrzeugen: Aufsätze aus verschiedenen Aufgabengebieten der Fertigung und eine Bibliographie der Veröffentlichungen*, Springer-Verlag, 2013.
- [32] L. Grant, R.D. Adams, L.F. da Silva, Experimental and numerical analysis of single-lap joints for the automotive industry, *Int. J. Adhes. Adhes.* 29 (4) (2009) 405–413.
- [33] J.M. Arenas, J.J. Narbón, C. Alía, Optimum adhesive thickness in structural adhesives joints using statistical techniques based on Weibull distribution, *Int. J. Adhes. Adhes.* 30 (3) (2010) 160–165.
- [34] D.A. Dillard (Ed.), *Advances in Structural Adhesive Bonding*, CRC Press, Boca Raton, FL, 2010.
- [35] R. Jones, A. Baker, N. Matthews, V. Champagne (Eds.), *Aircraft Sustainment and Repair*, Elsevier, 2018.
- [36] R.D. Adams, et al., The relative merits of the Boeing wedge test and the double cantilever beam test for assessing the durability of adhesively bonded joints, with particular reference to the use of fracture mechanics, *Int. J. Adhes. Adhes.* 29 (2009) 609.
- [37] E.M. Petrie, Adhesive bonding of aluminum alloys, *Met. Finish.* 105 (9) (2007) 49–56.
- [38] GO FAIR Initiative. <https://www.go-fair.org/go-fair-initiative/>.
- [39] Allotrope Foundation. <https://www.allotrope.org/>.
- [40] ANIML Overview. <https://www.animl.org/overview>.
- [41] D. Morgan, R. Jacobs, Opportunities and challenges for machine learning in materials science, *Annu. Rev. Mater. Res.* 50 (1) (2020) 71–103.
- [42] P. Roberts, J. Frechette, High-throughput test paves the way for machine-learning-based optimization of adhesives, *ACS Cent. Sci.* 7 (7) (2021) 1102–1104.
- [43] Cova, T.F.G.G. and A.A.C.C. Pais, Deep learning for deep chemistry: optimizing the prediction of chemical patterns in *Front. Chem.*, 2019. 7(809). T.F.G.G. Cova, A.A.C.C. Pais, Deep learning for deep chemistry: optimizing the prediction of chemical patterns, *Front. Chem.* 7 (809) (2019), <https://doi.org/10.3389/fchem.2019.00809>.
- [44] M.H. Segler, M.P. Waller, Neural-symbolic machine learning for retrosynthesis and reaction prediction, *Chem. Eur. J.* 23 (25) (2017) 5966–5971.
- [45] R. Tamura, et al., Experimental design for the highly accurate prediction of material properties using descriptors obtained by measurement, *Sci. Technol. Adv. Mater. Methods* 1 (1) (2021) 152–161.
- [46] M.A. Mashrei, R. Seracino, M.S. Rahman, Application of artificial neural networks to predict the bond strength of FRP-to-concrete joints, *Constr. Build. Mater.* 40 (2013) 812–821.
- [47] E. Tosun, A. Çalık, Failure load prediction of single lap adhesive joints using artificial neural networks, *Alex. Eng. J.* 55 (2) (2016) 1341–1346.
- [48] S.P. Leo Kumar, State of the art-intense review on artificial intelligence systems application in process planning and manufacturing, *Eng. Appl. Artif. Intell.* 65 (2017) 294–329.
- [49] Z. Gu, et al., A parametric study of adhesive bonded joints with composite material using black-box and grey-box machine learning methods: deep neuron networks and genetic programming, *Compos. Part B* 217 (2021) 108894.

-
- [50] G.C. Silva, V.C. Beber, D.B. Pitz, Machine learning and finite element analysis: an integrated approach for fatigue lifetime prediction of adhesively bonded joints, *Fatigue Fract. Eng. Mater. Struct.* 44 (12) (2021) 3334–3348.
 - [51] S. Pruksawan, et al., Prediction and optimization of epoxy adhesive strength from a small dataset through active learning, *Sci. Technol. Adv. Mater.* 20 (1) (2019) 1010–1021.
 - [52] E. Tomba, M. Barolo, S. Garcia-Munoz, In-silico product formulation design through latent variable model inversion, *Chem. Eng. Res. Des.* 92 (2014) 534–544.
 - [53] L. Himanen, et al., Data-driven materials science: status, challenges, and perspectives, *Adv. Sci.* 6 (21) (2019) 1900808.

This page intentionally left blank

Part Four

Adhesive specification, quality control, & risk mitigation

This page intentionally left blank

Aerospace structural bonding: Qualification, quality control, substantiation, and risk mitigation

23

Cindy Ashforth^a, Guilherme Garcia Momm^b, Waruna Seneviratne^c, Ashley Trace^d, and Larry Ilcewicz^a

^aFederal Aviation Administration, Des Moines, WA, United States, ^bNational Civil Aviation Agency, São José dos Campos, Brazil, ^cNational Institute for Aviation Research, Wichita State University, Wichita, KS, United States, ^dThe Boeing Company, Seattle, WA, United States

23.1 Introduction

Bonding applications date back to the dawn of aviation [1]. Metal bonding emerged almost simultaneously as metallic airframes [1]. In the 1950s and 1960s, airplanes designed to fly higher, more often, and for decades demanded long-lasting bonded joints [1,2]. Today, adhesively bonded joints are widely used in aviation. They are substantiated as part of a *bonding system*, which in turn is certified as part of the aviation product. Bonding systems consist of four interrelated elements: adhesive, substrate, surface preparation, and bonding process. The adhesion, strength, durability, and thus performance of a bonding system are characterized as a whole. However, each element must also be characterized, controlled, and documented as part of a qualified bonding system.

This chapter defines the bonding system and how to qualify it, describes certification requirements, presents best practices for design and certification of bonded aircraft structures, and summarizes service experiences of bonded structures in aviation.

23.1.1 Terms and abbreviations

AC	Advisory circular
AMC	Approved means of compliance
Adhesion failure	Rupture of the adhesively bonded joint, such that the separation appears to be at the adhesive-adherend interface (sometimes referred to as interfacial failure)
Amine blush	A chemical reaction among water, carbon dioxide, and the amine component of epoxy that occurs prior to bonding, creating a waxy film that can reduce bond strength and performance

Continued

ARAC	Aviation Rulemaking Advisory Committee
Cohesion failure	Rupture of an adhesively bonded joint, such that the separation is within the adhesive
CFR	Code of Federal Regulations
CMH-17	Composite Material Handbook-17
EASA	European Aviation Safety Agency
FAA	Federal Aviation Administration
Fleet Leader	Airframe/component with the highest use
GA	General aviation
GLARE	Glass laminate aluminum-reinforced epoxy
ICAO	International Civil Aviation Organization
Limit Load	The maximum load expected in service
NDI	Nondestructive inspection
Sol-Gel	Solution-gelation technology is a surface preparation technique for metal substrates that deposits a thin film to promote adhesion through chemical interactions at the interface between the metal surface and the adhesive primer or adhesive
TA	Transport airplane
TCCA	Transport Canada Civil Aviation
Ultimate Load	Limit load multiplied by a safety factor of 1.5
Understrength Bond	Understrength bonds are manufacturing defects that result from underspecified or controlled manufacturing processes (chemistry). The resulting bond may have mechanical properties that are below the specification minimum values and/or require further consideration once discovered. Note that the terminology of “understrength bonds” has been adopted to distinguish bond phenomena that may still allow the use of damage tolerance principles in reliably controlling damage growth until found and repaired, whereas weak bonds may not
Weak Bond	A bond with mechanisms that cause continual strength degradation in a nonpredictable way, such as metal corrosion caused by bondline hydration

23.2 Certification regulations and guidance

Civil aviation regulations are found in Title 14, Code of Federal Regulations (14 CFR) [3]. The general requirements for design, production, and airworthiness approvals are found in part 21, which refers to requirements for specific products—for example, transport airplanes (TA), rotorcraft, and engines—in parts 23–35. General maintenance and repair requirements are in part 43. Other parts have requirements for operation and training, among other topics.

The Federal Aviation Administration (FAA) publishes guidance on how to satisfy regulations in advisory circulars (AC) and policies. The most relevant guidance referenced throughout this document is AC 20-107B, “Composite Aircraft Structure” [4]. This AC is harmonized with the European Aviation Safety Agency (EASA) Approved Means of Compliance (AMC) 20-29 [5] and attempts to address regulatory requirements using a safety management philosophy. These guidance materials were

reviewed by an FAA-tasks Aircraft Rulemaking Advisory Committee (ARAC), which provided industry's recommendations for future rulemaking and guidance related to structural bonding for transport airplane structures, as documented in the 2018 Final Report [6] and a subsequent 2021 Structural Bonding Extension Report [7].

AC 20-107B describes means of compliance unique to bonded structure and is supplemented by an additional policy [8] applicable to part 23 general aviation (GA) airplanes. However, applicants for design approvals may propose to use it for other product types. The FAA has also published nonregulatory research reports about bonding through the William J. Hughes Technical Center Library. For instance, the report DOT/FAA/AR-TN06/57 [9] identifies best industry practices in bonded structures and repairs.

It is important to note up front that the FAA does not certify adhesives or bonded joints independently. The FAA only provides design approvals for aviation *products* or *articles*.

- A product is an aircraft, aircraft engine, or propeller (14 CFR 21.1(b)(5)).
- An article is a material, part, component, or appliance (14 CFR 21.1(b)(2)).

Regulations are generally material-agnostic, with exceptions related to fatigue and damage tolerance for some products. When it comes to requirements for materials and processes, such as bonded joints, regulations require materials to be suitable and durable, adequately defined and controlled, have adequate strength and other properties based on tests, and account for the effects of the environment. Other regulations require bonding processes to be controlled by a specification with limitations based on test data. Lastly, strength properties and material design values must be based on enough material tests meeting approved specifications to establish design values on a statistical basis.

There was one regulation for fatigue and damage tolerance of GA airplanes that specifically referred to bonded joints: § 23.573(a)(5). This regulation was superseded at amendment 64 with a performance-based requirement. However, the regulation principles are still applied to GA airplanes and other products through AC 20-107B [4], paragraph 6.c. The regulation and guidance say in part that for bonded structure: *"the failure of which would result in catastrophic loss of the airplane, the limit load capacity must be substantiated by one of the following methods—(i) The maximum disbands of each bonded joint consistent with the capability to withstand the loads in paragraph (a)(3) of this section must be determined by analysis, tests, or both. Disbands of each bonded joint greater than this must be prevented by design features; or (ii) Proof testing must be conducted on each production article that will apply the critical limit design load to each critical bonded joint; or (iii) Repeatable and reliable nondestructive inspection techniques must be established that ensure the strength of each joint."* This concept has also been extended to repairs under policy PS-AIR-20-130-01, "Bonded Repair Size Limits" [8].

The former rule and existing guidance offer three ways to substantiate a bonded structure: (1) demonstrate that the bond sustains limit loads (defined in the regulations as the maximum load expected in service) with the bond failed between arresting

features; (2) perform limit load proof testing on every production article; or (3) implement a nondestructive inspection method that ensures the full strength of the bonded joint. As of the writing of this chapter, option 3 is not in use on any certified aircraft. Option 2 is occasionally selected for applications where redundant bondlines are impractical, the configuration of the bonded part lends itself to practical proof load fixturing, and production numbers are low enough to warrant full-scale testing of the part in question. By far, the most common option is to implement some sort of secondary load path such that if the bond is failed between arresting features, the remaining structure can maintain limit loads. Note that in all cases, a fully intact bonded structure must demonstrate ultimate load capability, which is defined as limit load with a safety factor of 1.5. It is also important to note that these criteria depend upon a robust material and process that ensures repeatable, high-quality bonds with adequate adhesion, durability, and strength. In other words, the secondary load path demonstrated between arresting features cannot be substituted for stringent material and process control. Arresting features may be in the form of fasteners or other features that stop bondline disbond progressions, such as reinforcing ribs or other sub-structures. Secondary load paths may be in the form of fasteners or additional bonded load paths.

The transport aircraft ARAC Structural Bond final report [7] further endorsed existing bonding guidance. The initial report [6] recommended significant updates on the importance of stringent structural bond material and process controls to avoid service issues in transport aircraft. Both reports highlighted that if you cannot achieve sufficient bondline process control, then current damage tolerance practices, including redundant load path between arresting features, are insufficient to protect the bonded structure.

Requirements and guidance for the structural substantiation of US military aircraft are given in the Joint Service Specification Guide for Aircraft Structures, JSSG-2006 [10], although they are modified and superseded with specific requirements for each program. An example of specific military bonding requirements can be found in Structures Bulletin EZ-SB-20-03, "Requirements for Bonded Structural Repairs and Guidance for Bonded Structural Repair Design and Certification" [11].

23.2.1 Industry publications

Industry publications supplement government regulations and guidance. In particular, the Composite Material Handbook, CMH-17 [12], is a repository of detailed background information and best practices for designing and manufacturing bonded structures. The handbook is expanding content on best practices for structural bonding in the upcoming revision H of volumes 1 and 3 [13]. In addition, the SAE [14] Commercial Aircraft Composite Repair Committee (CACRC) publishes guidance on standardization and training for commercial aircraft bonded repairs and modifications (e.g. [15]).

23.3 Bonding systems for both metal and composite bonds

23.3.1 Types of bonded joints

There are three different types of bonding—cocuring, secondary bonding, and cobonding—as shown in Fig. 23.1.

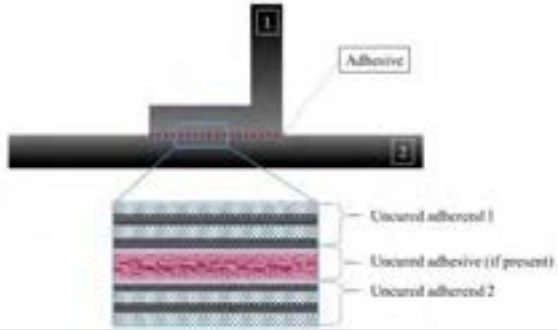
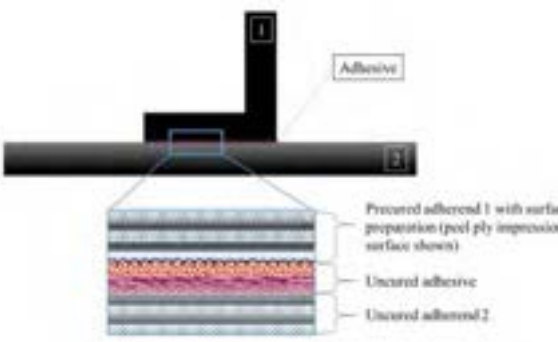
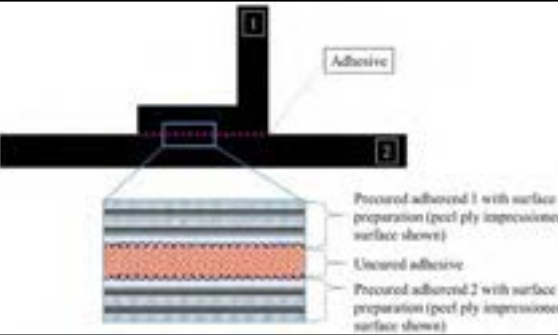
<p>Cocure</p> <p>Both adherends are uncured. Bonding occurs during the cure of both adherends.</p> <p>Note: may include adhesive.</p>	 <p>The diagram shows an L-shaped joint formed by two adherends, labeled 1 and 2, joined by an adhesive. A cross-sectional view below the joint shows the internal structure: two layers of uncured adherend (1 and 2) with a layer of uncured adhesive (if present) between them. The adhesive is shown as a red layer.</p>
<p>Cobond</p> <p>Adherend 1 is precured (or metal) and Adherend 2 is uncured. Surface preparation is applied to Adherend 1. Adherends are bonded during the cure of Adherend 2.</p> <p>Note: may not include adhesive.</p>	 <p>The diagram shows an L-shaped joint formed by two adherends, labeled 1 and 2, joined by an adhesive. A cross-sectional view below the joint shows the internal structure: a precured adherend 1 with surface preparation (peel ply impressed surface shown) and a layer of uncured adhesive between it and uncured adherend 2. The adhesive is shown as a red layer.</p>
<p>Secondary Bond</p> <p>Both adherends are precured (or metal). Surface preparation is applied to both adherends. Adherends are bonded during an additional bonding process.</p>	 <p>The diagram shows an L-shaped joint formed by two adherends, labeled 1 and 2, joined by an adhesive. A cross-sectional view below the joint shows the internal structure: two precured adherends (1 and 2) with surface preparation (peel ply impressed surface shown) and a layer of uncured adhesive between them. The adhesive is shown as a red layer.</p>

Fig. 23.1 Types of bonded joints.

Adapted from R.O. Olander, B.D. Flinn, A.C. Tracey, Nanomechanical Property Characterization of Composite Adhesive Bonding Systems, SAMPE, 2021.

While curing is fundamentally considered a type of bonding, the FAA does not recognize it as a "structural bond" as defined in AC 20-107B [4]. The advisory circular defines structural bonding as "a structural joint created by the process of adhesive bonding, comprising of one or more previously cured composite or metal parts." This distinction is because cocured joints typically result in stronger bonds associated with polymer matrix crosslinks and chemical bonds between the composite lamina matrix and adhesive (if used), similar to what occurs between the plies of a composite laminate. As such, FAA guidance only recognizes secondary bonding and cobonding as structural bonding processes, where at least one of the surfaces is precured (or metal) and requires surface preparation before bonding.

Sandwich structures, which consist of laminate skins cobonded or secondarily bonded to core materials such as foam, metallic, or nonmetallic honeycomb, are specific types of bonded structures that require unique guidelines. Detailed information unique to sandwich structures can be found in CMH-17 volume 6 [16].

23.3.2 Bonding systems

Adhesives are not certified independently; they are part of a bonding system, which in turn is certified as part of a product or article. A bonding system consists of four inter-related elements, as shown in Fig. 23.2. When any of the elements change, the bonding system is reevaluated.

Note: After defining the bonding system, the joint design is similarly defined and characterized, as discussed later in this chapter (Section 23.3.2.6).

The adhesion, strength, durability, and thus performance of a bonding system are characterized as a whole. Additionally, each element of that system must also be characterized, controlled, and documented [17,18].

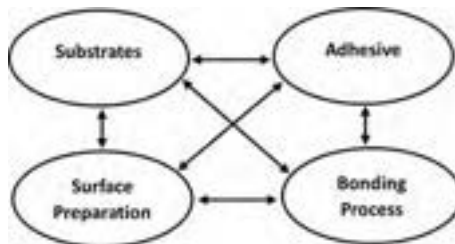


Fig. 23.2 Bonding system.

Adapted from K. Blohowiak, M. Dilligan, W. Grace, C. Park, M. Pihel, P. Van Voast, E. Kutscha, H. Ashton, Qualified bonded systems approach to certified bonded structure, NATO STO-MP-AVT-266, 2018, doi:10.14339/STO-MP-AVT-266-KN2-PDF.

23.3.2.1 *Substrate materials*

Substrate materials are the most straightforward to characterize and control. Metal substrates typically have published design values, such as those in the Metallic Material Properties Development and Standardization Handbook (MMPDS) [19]. Composite laminates have recommended protocols for characterization and control (e.g., implementation of controlled contamination areas for composite processing to limit prebond environmental exposures such as moisture, light, and solvents) in CMH-17 and elsewhere. In addition to chemical, physical, and thermal characterization (e.g., glass transition temperature, fiber areal weight, resin content, gel time, resin flow) of uncured and cured materials, typical mechanical properties include unnotched 0 and 90 degree tension and compression strengths and moduli, in-plane shear strength and modulus, and short beam shear strength, as well as some notched laminate properties [20].

23.3.2.2 *Adhesive materials*

Although the FAA and CMH-17 publish some best practices, there are no standard protocols for characterizing an adhesive material. Properties may be developed at this level purely for procurement and quality control purposes, or they may be developed to support analytical modeling. Typically, chemical, physical, and thermal adhesive properties (e.g., glass transition temperature, viscosity, gel time, pot life, adhesive flow, rheology, volatile content, density and film weight, infrared spectroscopy) are characterized. Common mechanical characterization tests include single-lap shear, flatwise tensile strength, roller peel, and fracture toughness. Exact test methods vary based on whether the adhesive is in film or paste form. These mechanical tests are often performed on metallic substrates to better isolate adhesive behavior and reduce bond process variability, even if the actual bonded structure comprises composite substrates.

Adhesive characterization tests should include determining sensitivity to environmental conditions during the bonding process and in service. For example, chemical and physical tests may be performed on test articles fabricated at a wide range of environmental conditions that may be present during the bonding process, including the repair environment. Mechanical properties are also evaluated at all extremes of the service environment. Not all tests are standardized. Ultimately, tests may be performed on uncured paste adhesive to determine the amount of time it can be exposed to various environmental conditions before developing amine blush [21]. In the end, it is important to fully characterize and understand adhesive performance under all processing and service conditions.

23.3.2.3 *Surface preparation*

During the process of certifying bonded structure, surface preparation is the most significant factor in long-term bond durability and is the cause of most bond failures in service [9]. Many failures are caused by ineffective processes, not just contamination. Successful bonding requires a clean and chemically active surface. A clean surface alone is not sufficient.

Adhesion, bond strength, and in-service bond durability critically depend on the interaction between the adhesive and prepared surfaces. Draft content for CMH-17 Volume 3 Revision H [13] highlights that in-service durability—specifically environmental durability—is the most important distinction between metal and composite bonds. Composites are known to be affected by the service environment and this effect is characterized and accounted for in the bonded joint design. Degradation at the interface between composite substrates and the adhesive is not anticipated during normal service when the surfaces are properly prepared. Metals, however, are susceptible to hydration of the interface, even when properly prepared. Given enough time in the service environment, moisture migrates to the adhesive-substrate interface and can disrupt bonding and/or hydrate (degrade) the metal oxide layer at the interface. It is critical to minimize and restrict moisture from accessing the interface and to prepare metal surfaces to resist its adverse effects. It is also important to develop adequate maintenance instructions to monitor this effect and initiate repair or replacement before bonded joint performance degrades below acceptable limits.

Common surface preparation techniques for composite substrates include removable surface plies (e.g., peel ply) and mechanical abrasion (e.g., hand sanding, grit blasting). Because abrasion surface preparation techniques are not as effective in activating the surface of thermoplastic substrates, energetic processes (e.g., plasma or corona processes, ultraviolet treatment, laser ablation [22–24]) are used to improve adhesion characteristics (see Fig. 23.3). Common methods for preparing metallic surfaces include etching, anodizing, and sol-gel, typically followed by applying an adhesive primer. Cleaning procedures are an important aspect of surface preparation techniques to prevent contamination of the interface.

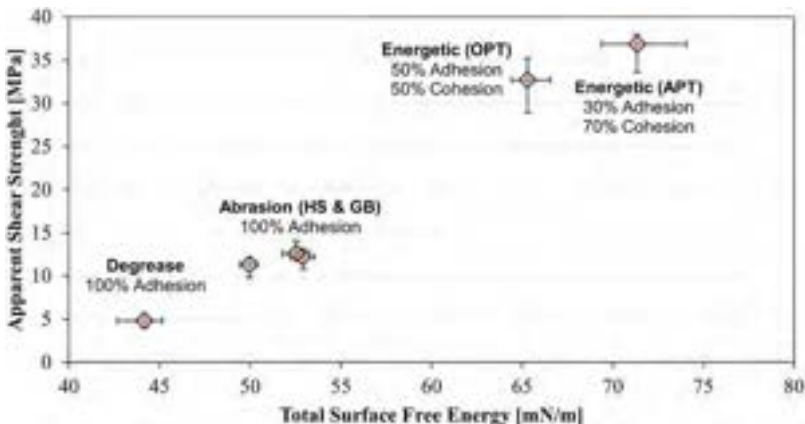


Fig. 23.3 Effects of surface preparation techniques on apparent shear strength of thermoplastic joints.

Adapted from W. Seneviratne, J. Tomblin, B. Saathoff, Thermoplastic Joining Materials Guidance Materials Guidance for Aircraft Design and Certification, 2021. https://www.wichita.edu/industry_and_defense/NIAR/Documents/jams-presentations-2021/Thermoplastic_Joining-Materials-Guidance-Seneviratne.pdf (Accessed 24 January 2022).

When developing surface preparation techniques, the performance of such preparation within all fabrication and bonding process tolerances must be validated with testing. The goal of surface preparation development should be that adhesion failure modes are avoided in any test type. Mode 1 testing is most sensitive to surface preparation and contamination. Some variables to evaluate include prebond moisture and environmental conditions, time between preparation and bonding, cure temperatures, ramp rates, and dwell times. Any materials that are part of the surface preparation, including solvents and other contact materials, should be controlled by a specification (e.g., wipers are controlled in accordance with AMS3819D [25]) to ensure consistent and repeatable performance as well as to prevent any unexpected changes to the material.

23.3.2.4 Bonding process

The bonding process encompasses assembly procedures, including adhesive application methods, tooling and fixturing, in-line quality control measurements (if applicable), curing, and postcure inspections. When establishing a bonding process, one important aspect is to quantify bondline thickness ranges and ensure that those are controlled in production. Bondline thickness variations can affect apparent bond strength, as shown in Fig. 23.4 and as discussed further in Chapter 18. Verification films and destructive inspection are methods for determining bondline thickness.

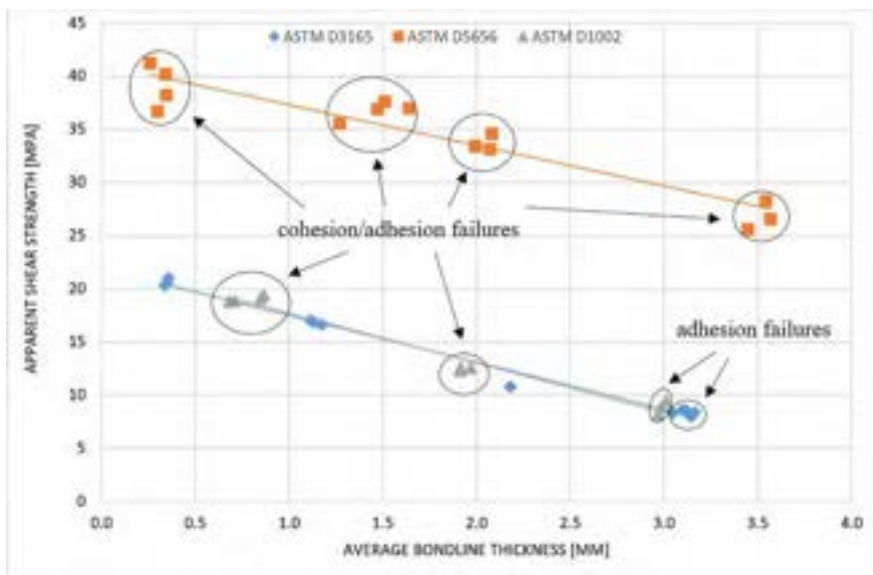


Fig. 23.4 Effects of bondline thickness on apparent shear strength and failure mode of a two-part adhesive system.

Adapted from J. Tomblin, P. Harter, W. Seneviratne, C. Yang, Characterization of bondline thickness effects in adhesive joints, *J. Compos. Technol. Res.* 24 (2002) 332–344.

Bondline thickness control depends on part fit-up tolerances and consistent tooling, pressure application, and heating rates. For film adhesives, scrim or carrier fabric in the adhesive films can play a role in bondline thickness control. Paste adhesive bonds sometimes incorporate glass beads, rods, or other spacers.

Applying film adhesive is typically more straightforward than paste adhesive. Similar to prepregs, film adhesives are b-staged resins and require freezer storage. Additionally, film adhesives are handled similarly to prepregs during processing (i.e., cut and laid up like prepreg plies). Paste adhesives are typically a one-part system that is refrigerated or a two-part system that can be stored at room temperature and mixed directly before bonding. Mixing procedures must be controlled to ensure proper chemistry. Pastes may or may not have fillers (e.g., metal particles, glass beads), which directly affects paste viscosity. Sometimes, particularly in general aviation applications, a thin layer of unfilled adhesive is applied to the substrates (often referred to as “primer”) before applying the filled adhesive. All adhesive materials must be controlled to a specification that includes definitions of out time, shelf life, and gel time/pot life.

During bonding, control of environmental conditions (e.g., humidity, temperature, out time) is recommended to ensure moisture saturation limits are not exceeded. Moisture can cause adverse effects on bondline quality, including bondline porosity and degradation in cured properties. In the case of paste adhesives, moisture can also lead to the formation of amine blush on the surface of the uncured adhesive [21]. Bond open time, especially when paste adhesives are used, must be characterized and controlled.

As with all composite materials, the cure cycle significantly affects the bonded structure’s final properties. Ramp rate, dwell temperature, and time affect the flow, viscosity, and crosslinking of the polymer (i.e., degree of cure). There are many ways to monitor this, such as with thermocouples in the substrate, in the bond, on the tooling, or even air temperature. The selected method must demonstrate that it produces a repeatable bond for each structural detail. Bonding may occur in or out of an autoclave and may or may not be accompanied by vacuum pressure.

After bonding, inspection methods can include visual inspection of adhesive squeeze-out and formation of adhesive fillets as well as traditional ultrasonic nondestructive inspection (NDI) methods. Note that these inspections do not directly measure adhesion and bond performance. Rigorous process controls and in-line quality controls (e.g., surface measurements, bath chemistry measurements, traveler/witness coupons) are required.

Paste adhesive processing is more complicated, as unique key process parameters include

- Mixing instructions for two-part adhesives and/or with fillers.
- Adhesive application with or without a layer of unfilled adhesive resin (typically called a primer in general aviation applications), shaping tools.
- Thickness control/measurement, such as the use of bonding rods or prebonding measurement techniques such as verification film or putty.

As a part of bond-process qualification, the sensitivity of mixing ratios within the specification limits must be understood to ensure that the chemical, physical, and mechanical properties are within the acceptable range.

23.3.2.5 Bonding system screening tests

Screening tests are used to qualitatively ensure a robust bonding system. (Note that the same tests may be used for quantitative structural substantiation, see [Section 23.4.1.3](#).) Three key attributes of a structural bond are adhesion, strength, and durability. Adhesion is the foundational attribute; without it, the other strength and durability attributes are irrelevant [26]. The purpose of evaluating the bonded joint as a whole is to ensure adhesive/substrate compatibility and that the surface preparation and bonding process produces adequate adhesion, durability, and strength. There are no standard protocols yet for this process. However, acceptable methods can include

Adhesion—Evaluating adhesion must be done with mechanical testing; mode I (opening/cleavage) tests interrogate interfacial interactions and are most sensitive to surface preparation and contamination.

Strength—Strength measurements typically include, at a minimum, shear and fracture performance. Shear strength is often evaluated with lap shear tests per ASTM D1002 [27], ASTM D3163 [28], or variations thereof to ensure that the bonded joint meets structural strength expectations. Critical fracture energy can be evaluated with mode I double cantilever beam (DCB) testing (e.g., modified ASTM D5528 [29]) and mode II end notch flexure (ENF) testing (e.g., modified ASTM D7905 [30]) to give measures of fracture performance. Other mixed-mode tests may also be used to ensure that the bonded joint performs acceptably in structural application.

Durability—Bonds must be shown to be durable in operating conditions, including both mechanical and environmental durability. For metal bonds in particular, environmental durability must be tested. Coupon-level tests with conservative pass/fail criteria, such as the wedge test (ASTM D3762 [31]) for metallic substrates, are effective methods to qualitatively evaluate long-term environmental performance. Other long-term durability testing can include elevated temperature creep, thermal/moisture cycling, and long-term thermal aging.

Coupon-level tests are appropriate for screening to ensure that the bond is successful and may be used as part of the building block approach. Note that lap shear tests per ASTM D1002 [27] are ineffective for demonstrating bond durability. While that can be an appropriate test for quality assurance, lap shear does not validate long-term bond durability.

As with surface preparation evaluations, any screening test adhesion failures, which indicate the lack of chemical bonding between the substrate and adhesive materials, are considered an unacceptable failure mode. If they are observed, the bonding system must be revised.

23.3.2.6 Design features

After characterizing the bonding system, design features must be considered when substantiating a bonded joint. This is necessary to ensure that the joint design can be scaled and reproduces the bonding system with structural details (e.g., reproduces cure temperature, maintains tolerances). Design features are also critical when generating strength and design values for a bonded joint. Even when all other elements—substrate, adhesive, surface preparation, and bonding process—are the same, the overall strength and performance of the bonded joint depend on its design, as depicted in Fig. 23.5. Joint design features are largely geometric, such as single or double overlap, partial or full scarf, or T-joint. When design allowables are created for a bonding system, physics-based models are generally inadequate to predict behavior across different adhesive joint designs; hence, semiempirical data are almost always required when providing strength and design values.

23.4 Bonded joint certification

Bonded joints must reliably and predictably transfer loads for the lifetime of the bonded component. The certification of a bonded joint consists of more steps than characterizing an adhesive or performing lap shear coupon tests. It is a combination of controlling the raw materials involved in the bonding process, controlling the process, developing design allowables, substantiating the structural strength, and substantiating fatigue and damage tolerance behavior supplemented with appropriate maintenance instructions.

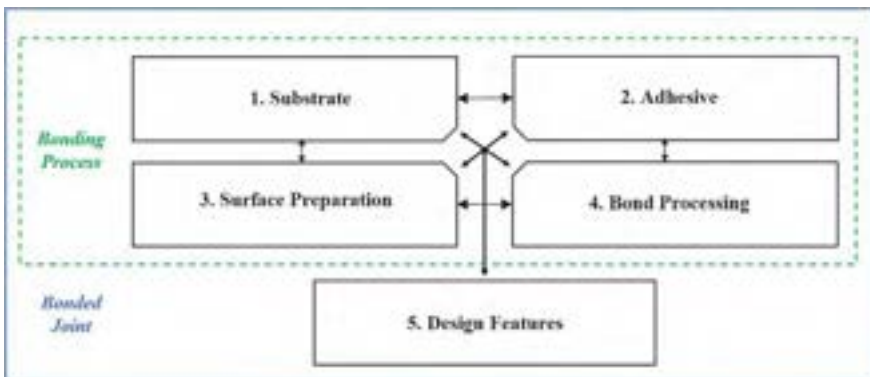


Fig. 23.5 Relationship between the elements of a bonding system and the bonded joint. Adapted from W. Seneviratne, J. Tomblin, B. Saathoff, Thermoplastic Joining Materials Guidance Materials Guidance for Aircraft Design and Certification, 2021. https://www.wichita.edu/industry_and_defense/NIAR/Documents/jams-presentations-2021/Thermoplastic_Joining-Materials-Guidance-Seneviratne.pdf (Accessed 24 January 2022).

23.4.1 Best practices for design and structural substantiation of bonded structures and repairs

23.4.1.1 Design and analysis

Bonded joints and attachments generally have the primary structural purpose of transferring shear loads. Local peel forces exist in bond stresses but are controlled using structural details designed to minimize such stress. The stress distribution and strength of a bonded joint or attachment depend on the substrate geometry (for example, adherend thickness, taper angles), bondline thickness, bond overlap length, and if using composite substrates, laminate lay-up or fiber architecture. Residual stresses are often important design considerations, depending on differences in thermal expansion and the stiffness of the attached substrates. Bonds between metallic and composite substrates typically yield significant residual stresses and, depending on design and application, there is potential for load and environmental history dependence [32].

Like most critical structures in aviation, bonded joints and attachments are designed with redundant features. Alternate load paths may use structural geometry, which often stabilizes the structure, and fasteners or added splices attached to a second bonding operation. Due to load transfer differences between bonded and fastened joints, the joint will typically be designed with the assumption that only the bond or only the fasteners are transferring loads over any given segment of the joint. When bonds are present, they dominate load-carrying capability until failure, and therefore require ultimate load capability. In contrast, the fasteners are designed to carry somewhere between limit and ultimate loads. The exact load that a designer will use depends on service experience, regulatory or internal company requirements, and selected design criteria (e.g., ranging from a failed bond of specified size to an entire bond failure).

The 2021 Transport Airplane Fatigue and Damage Tolerance ARAC report on structural bonding [7] had a special section dedicated to discussions on structural redundancy and other means of achieving sufficient structural performance in the presence of very rare, large disbonds (e.g., structural damage capability). Section 4.2.4.1 of the report [7] proposed damage tolerance design criteria within existing damage categories described by AC 20-107B [4] for composite bonded structures. This section also covered single-load path structures and recommended higher levels of structural bond process control to achieve reliability greater than multiloading path structures, combined with secondary considerations of damage tolerance design criteria to ensure disbonds are detected before reaching unsafe sizes. Other related structural considerations, posed as damage-tolerant design/maintenance goals and criteria, appear in Section 4.2.4.2 of this report [7].

Helicopter rotor blades are an example of critical structures that often do not have specific structural bond redundancy but adopt damage-tolerant design features and enhanced maintenance activities to ensure safe operation. Some critical bonded structures for many small airplanes and a few transport airplanes can achieve large structural damage capability without specific redundant structural details. They

demonstrate that they can sustain a rare large disbond of similar or larger sizes than redundant design features and still retain limit load residual strength (discussed in Section 4.2.4.1 of Ref. [7]). Depending on fatigue loads for these structures, such damage may not grow or could grow very slowly. However, like all damage of such magnitude, the possibility of large damage near limit load capability should be extremely rare. Per general damage tolerance principles, all disbonds lowering strength below ultimate load capability should require maintenance inspections. Inspection methods should be substantiated to ensure critical damage sizes can safely be detected and repaired.

Integrated product teams (IPT) are commonly used in composite design and are effective for addressing manufacturing, tooling, and maintenance issues. One common IPT goal is to design structural detail reliably produced in the factory to meet the performance requirements while minimizing manufacturing defects. Success in meeting such goals is often derived over time with experience gained in product size and product scaling [33]. An IPT needs to recognize the maintenance cost implications of field inspection and repair of bonded structural details, realizing that access and disassembly are difficult without design provisions.

Industry analyses used to design bonded joints and attachments range from crude models to simple two-dimensional analyses, which refine structural details. Crude models, which convert shear flow and other loads to average shear stress, assess bond capability with conservative design values to avoid failure. Despite conservatism, such an approach should test specific design details in structural substantiation or apply high overload factors to scaled structure to ensure joint reliability while avoiding failure modes with time-related load dependence.

Simple analyses and software-based tools predict local shear and peel stress distributions, helping to design joint parameters for optimal performance. The state of the art for USAF metal bonding is still largely defined by the Primary Adhesively Bonded Structure Technology (PABST) program from the late 1970s and early 1980s [34]. Some models include nonlinear elastic and plastic adhesive behavior for further joint optimization. Bond overlap length should be designed to ensure plastic deformation occurs without a risk to bond integrity or permanent damage. Design criteria and guidelines can apply constraints that minimize the need for bonded joint test data. One effective guideline is to design joint overlap length to carry all loads by adhesive plastic deformation, with sufficient elastic zone allowance away from the joint ends for creep resistance [35]. Additional joint design and analysis criteria, including fracture toughness-based analysis approaches, are discussed in Chapter 10 of reference [13].

Design criteria, analyses, and test data can also be used for the timely disposition of manufacturing defects and service damage. Advanced analysis methods that predict the effects of bond defects and damage scenarios continue to evolve; however, most depend on conservative assumptions and test data. This observation is especially true for dispositioning defects such as wrinkles or marcols (in-plane waviness) and damage as complex as that caused by foreign object impact.

23.4.1.2 Maintenance considerations

The design of bonded repairs uses many of the same design procedures and analysis tools applied to bonded joints and attachments. A typical scarfed bonded repair considers the patch geometries, scarf angles, and bondline thicknesses. Residual stresses due to differences in laminate lay-up, stiffness, and thermal expansion properties between the bonded patch and base part are considered in repair design and analysis (Fig. 23.6). Conservative knockdown factors are used to substantiate bonded repairs to account for manufacturing tolerances, such as for composite ply orientations and placement location.

Structural bonded repairs are limited by the same design objectives, guidelines, criteria, and constraints as base structural bonds for a component or part. Section 4.2.5 of the Structural Bonding Extension Report [7] provides several pages that summarize maintenance inspection and repair considerations, including design,

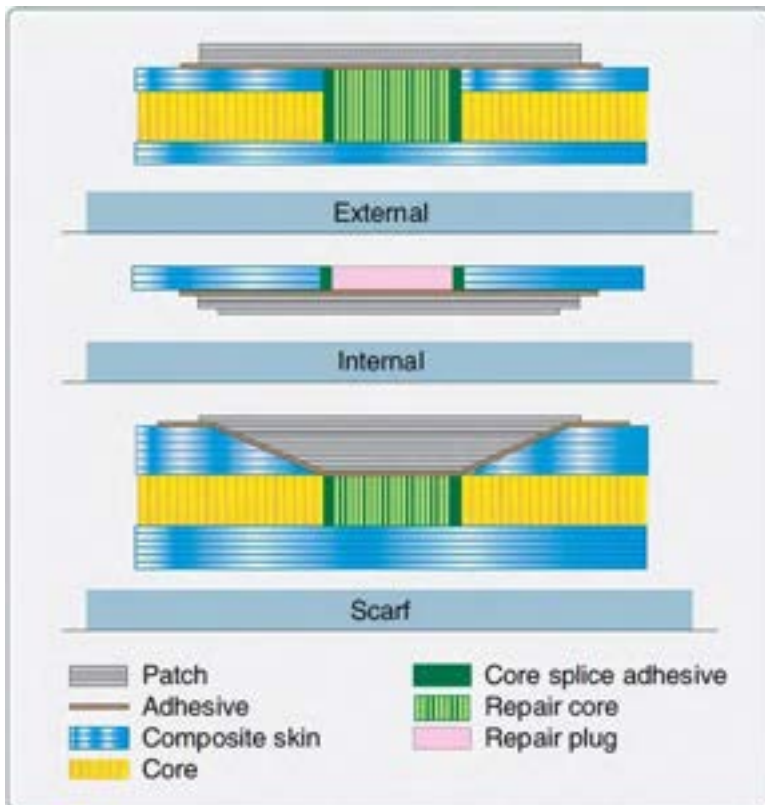


Fig. 23.6 Basic bonded repair joints [13].

repair size limits, and other references of note, including industry standards, best practices, and training details documented by the SAE CACRC [15] and CMH-17 [13].

Regulatory guidance for repair size limits appears in PS-AIR-100-14-130-001 [36]. It is essential to realize that bonding in field maintenance depots, including work on aircraft parts or components that cannot be removed from the structure, has greater challenges than that performed in a factory. As a result, the repair size limits are often constrained to a smaller size than allowed during design and manufacture because performance and reliability are much harder to achieve in field repairs. Size limits may also be set by the limitations of supporting test and analytical data, which are covered in Section 4.2.5 of the Structural Bonding Extension Report [7]. Large repair sizes, approaching those allowed in original manufacturing facilities, may be possible in the field with the right facilities and technician experience.

Section 4.2.5 of the Structural Bonding Extension Report [7] describes initiatives to expand the knowledge shared among aircraft manufacturers, operators (airlines, cargo companies), and maintenance organizations to document standards, best practice guidelines, training courses, and ultimately, detailed guidance for damage tolerance and related maintenance practices. The FAA, EASA, and Transport Canada Civil Aviation (TCCA) were the primary regulatory bodies involved, but workshops held throughout the world further helped the knowledge transfer by getting others involved. Finally, Sections 4.2.6 and 4.2.7 of Ref. [7] describe inspection considerations and aging limits to metal and composite bonding, respectively.

23.4.1.3 Structural substantiation

As discussed in AC 20-107B [4], a common approach for composite and bonded structural substantiation utilizes a building block to develop design data and calibrated analytical tools. The semiempirically refined analyses are applied for structural details, which range in size and assembly completeness (coupons, elements, subcomponents, and components), to address composite defect, damage, and environmental considerations. Alternative approaches, based on crude analyses and a conservative demonstration of strength at a large scale, typically have more constraints but can prove economical for certain product types, and designs are known to have adequate strength and durability. A building block approach allows more freedom to expand beyond the specific structural details, damages, defects, and repairs addressed in large-scale tests.

Design data development includes characterization for minimum and maximum service temperatures and the moisture content possible after years in service, typically established as conservative design criteria. A threat assessment of manufacturing defects and service damage should define the full scope of structural tests and analyses. Materials, conditions, and processes used for factory and field repair often differ and also need substantiation within the building block approach.

One should specifically look for adhesion failures during bonded joint testing. Any adhesion failures are considered unacceptable. The source of adhesion failures must be identified before additional tests and analyses. Test specimen adhesion failures

noted in multiple specimens typically indicate issues and sensitivities directly related to the materials and processes, suggesting potential chemical or processing incompatibilities.

Even after demonstrating consistent successful coupon behavior, adhesion failures may still exist with scaled part testing. Such challenges may relate to insufficient cure in local areas of elements and design details when heating is insufficient during key parts of the cure cycle. Apparent adhesion failures, which are actually assembly failures, may occur when there is insufficient adhesive to fill the joint or when there is inadequate contact between the substrates. This aspect is a primary reason for scaled building blocks and large part testing, which becomes as important for manufacturing process development as it is for final structural substantiation.

Understanding degradation mechanisms and tracking long-term performance are important for addressing the long-term durability of bonded joints. As discussed in previous sections, bond process qualifications and coordinated manufacturing/structural scaling trials help initiate these efforts, with the former using accelerated test procedures that conservatively force an assessment of the chemical bonding. Correlations between accelerated tests and tracking actual long-term performance further ensure some conservatism in the accelerated tests while gaining data at larger scales.

Additional reliability is ensured by tracking loading history and real-time environmental exposure to temperature, moisture, and other fluids found in service. It is essential to realize that many composite and metal bonded aging phenomena are not always obvious and may not yield evidence of adhesion failures in accelerated tests. Lesser process abnormalities, not as severe as those causing large areas of adhesion failures, may still age structural bonded joints and reduce performance over time [5]. Regular maintenance inspection and fleet monitoring to judge such structural aging becomes essential if the aging mechanisms invalidate maintenance programs, requiring more regular inspection or structural repair. Some metal bond aging phenomena may eventually impact the limit of validity for a given maintenance program [6,7]. An assessment of bonded structural joints should be part of any teardown assessments performed at the end of life.

Final substantiation of a product or article's static strength, fatigue, and damage tolerance use large representative component tests or subcomponents that contain full-scale details manufactured with production processes. For example, the rotorcraft industry has relied on bench testing rotor blade segments with unique test fixtures able to simulate real load conditions along the axis of the blade for high-cycle fatigue testing. Careful attention to test boundary conditions and attachments yields representative results. Building block analyses and tests support design value development for most of the effects of structural details, damage, defects, and repair, again with careful attention to the proper simulation of structural behavior.

Largest-scale building block tests provide final overall proof of the design and manufacturing characteristics of configured structures, including bonded joints, cut-outs, damage, repairs, and combined loads. This proof includes validation of load path predictions and final strength assessments based on structural detail design values tested in lower levels of the building blocks. However, the largest scale of testing is unable to test the strength of all load cases and damage scenarios, typically leading to conservative designs when the structure is driven by strength and damage tolerance,

including conservative design criteria assumptions that envelop a range of allowed damage and manufacturing defects. Even without the conservative damage or defect considerations, integrally bonded airframes may have secondary load paths and complex failure modes that are difficult to predict without careful consideration of manufacturing tolerances and load redistribution following individual failures.

In addition to the aforementioned building block tests that include extensive full-scale fatigue and environmental tests, military rotorcraft applications [37] are routinely inspected for bond quality and repairs according to the service repair manuals. Upon repair, they are balanced statically and dynamically in a whirl tower before installing back in a rotorcraft, where final balancing occurs. Teardown inspections of fleet leaders after a significant use are also practiced to investigate the bonded joint integrity and potential aging phenomena.

23.5 Bonded joint applications

Structural bonding has been used in aviation for more than a century [1]. The first civil airplane (D.H.104 Dove) applying metal bonding in primary structures was certified in the 1940s [1]. Since then, the use of bonding has expanded to encompass structures and repairs in all sorts of civil [18] and military [34,38] aeronautical products, encompassing small [39–42] to large [43–46] airplanes, rotorcraft [47–49], propellers [50], and engines [51,52].

23.5.1 Typical applications

In the TA world, turboprops (e.g., Fokker F27 Friendship), jets (e.g., DH 106 Comet, Boeing 727), and even supersonic airliners (e.g., Concorde) already employed structural bonding [1,53] more than six decades ago. Since then, the use of structural bonding has increased. Nonetheless, TA tends to be conservative in applications for any sensitive technologies (such as bonding), relying on large databases of experience starting with noncritical applications and progressively moving to critical structures. Moreover, relatively high load levels at many TA joints—such as at major fuselage splices or the attachment of spars and skin panels for wing or empennage torque boxes—pose more challenges for bonding. Limited peel and shear load carrying capacity cannot be tolerated to withstand fuel and cabin pressures and high loads resulting from these heavier TA structures [54,55]. Finally, some TA bonded structures demonstrated durability issues in-service [1,43]. As a result, TA bonding applications mostly encompass (low load) metallic, composite, or hybrid structures such as skin-to-stringer joints, longitudinal/circumferential continuing joints, doublers, cutout reinforcements, and crack arrest straps, often including secondary fasteners as a redundancy feature [1,43–46,56,57]. Sandwich structures are also frequently used in moveable surfaces, leading/trailing edges, fairings, nacelles, and interior structures such as floor panels and monuments [1,58–61]. More recently, bond applications also include fiber-reinforced aluminum (e.g., GLARE) fuselage panels [43,56].

For many decades, GA airplanes have also been using structural bonding. However, as GA airplane structures withstand comparatively low (relative to TA) and predominantly in-plane loads, many GA airplane applications of structural bonding exceed the extent of those in TA [39,55]. As examples of this extensive use, there are fully bonded major components (e.g., fuselage, wing, empennage) made of composite sandwich [39,41,42] or metallic stiffened panels [40].

The first use of structural bonding in main and tail rotor blades of rotorcraft also dated back to the 1950s [48]. These rotating parts withstand a high-cycle fatigue environment unlike anything experienced by airframes. Thus, rotor blades mainly utilize out of necessity fully bonded—often sandwich—structures with metallic (e.g., aluminum, titanium, stainless steel), composite, or hybrid joints [48,49,62]. The use of bonding has expanded to fuselage panels, fairings, and other discrete joints [48,49,62]; however, rotorcraft airframe parts have not had the same extensive bonding experience [18]. Newer rotorcraft applications are introducing composite bonded joints to primary structures, such as the Bell V280 bonded composite wing [63].

In addition to aircraft, bonding is also used in other aeronautic products. Propellers have relied on bonding since the beginning of aviation [1]. Structural bonding in propellers typically encompasses primary joints of metallic, composite, wood, or hybrid construction as well as secondary structures such as erosion sheath and deicing boots [50,64].

Elevated temperatures tend to limit structural bonding applications in engines. Nonetheless, there are examples of bonding in primary (e.g., first-stage compressor blades [52]) and secondary (e.g., ice impact protecting panels [51]) structures.

Finally, aeronautic military structural bonding applications dated before and extended beyond the aforementioned civil counterparts [1,34], particularly in repairs [65]. Unmanned systems such as Global Hawk (RQ-4) and Triton (MQ-4C) with a wingspan of more than 40 m are bonded with paste adhesives [66]. Every article is proof loaded upon manufacturing to demonstrate the bonded joint integrity.

23.5.2 Service experience

The previous section briefly described a range of typical structural bonding applications in aviation. Over the decades, these applications accumulated considerable in-service experience.

23.5.2.1 Civil

While bonded joints are by and large used successfully in civil aircraft, several notable accidents/incidents have bonded joint failure as a contributing factor [67]. In-service bonding data are particularly valuable considering the complexity of adhesion phenomena and aging, which is difficult to simulate numerically or even reproduce experimentally. Since the 1940s in the civil aviation world, member states of the International Civil Aviation Organization (ICAO) have investigated and documented aircraft accidents and incidents. The resulting documentation, such as technical reports, safety recommendations, and airworthiness directives, is often publicly

available in many online databases worldwide. The documentation of 73 bond-related accidents/incidents involving type-certified civil aircraft registered in 13 countries on five continents was recently reviewed elsewhere [67] to identify potential certification shortfalls. These occurrences were compiled according to the aeronautical product containing the failed bonded joint—TA, GA airplane, rotorcraft, propellers, and engines—and the associated root causes such as—design, production, operation, and maintenance.

In this review [67], bond-related occurrences involving TA included failures in the fuselage (e.g., skin lap joints), wing (e.g., trailing edges, nacelles), and control/high-lift surfaces of single-aisle, wide-body, and even supersonic airliners. In many cases, environmental interaction—such as ground-air-ground pressure difference, freeze/thaw cycles, and chemical attack—with substandard bonding (e.g., initial disbonds, weak bonds) led to metallic and composite sandwich panels debonding and in-flight detachment from the airplane. Some cases illustrated that structural redundancy could lessen the severity of events associated with poor bonding but not prevent them entirely, and exposed limitations of inspections to address substandard bonding. Fortunately, most of the reviewed bond-related events involving TA resulted in minor damage to aircraft and no injuries to the occupants.

The reviewed [67] bond-related events in the GA airplane world included failures in the wing, empennage, and landing devices of gliders, single-piston, and twin-turboprop airplanes. In most cases, production or maintenance issues, such as improper quality control, excessive moisture during cure, or lack of adherence to approved data, caused substandard bonding (such as inadequate adhesive thicknesses, voids, weak bonds) in composite structures. Unlike the TA cases, all the reviewed events involving GA airplanes resulted in severe or catastrophic damage to the aircraft. A third of the events led to fatal injuries to the occupants.

Most of the reviewed [67] bond-related accidents/incidents involved rotorcraft, from small piston-powered to large twin-turbine ones. These bond failures occurred primarily in (mostly metallic) main and tail rotor blades, despite examples of defective bonded joints in other structures such as mounts, bearings, shafts, and fuselage panels. In many cases, bonded structures not commonly classified as safety-critical—such as abrasion strips, tip cap, and balance mass—failed, contributing to the occurrences. As in the TA cases, there were examples of interaction between existing bond defects (e.g., voids and weak bonds) and the environment (e.g., moisture and contaminants), which led to progressive damage such as cracks and erosion. This progressive damage, coupled with the limitations of nondestructive inspection to identify substandard bonding and the inability of redundant design features/secondary fasteners to provide structural integrity in case of an improper bond, led to structural failure. Similar to the GA airplane cases, most of the reviewed events involving rotorcraft ended up in severe or catastrophic damage to the aircraft. At least a quarter of them inflicted fatal injuries to the occupants.

Substandard bonding in propellers installed in single/multipiston airplanes and regional airliners contributed to some of the reviewed [67] accidents/incidents. In most of these events, maintenance issues caused secondary structures—such as erosion sheath and deicing boots—to detach from a composite propeller, leading to minor damage to aircraft.

A few bond-related occurrences involving engines installed in regional and wide-body airliners were also identified [67]. In these events, the failure of metallic joints in primary structures (first-stage compressor blades) and metallic-composite joints in secondary ones (ice impact protecting panels) contributed to substantial damage to the airplanes.

The review [67] of these bond-related accidents/incidents supported the following observations:

- A wide range of aeronautical products (aircraft, engines, propellers) of different sizes, ages, and manufacturers typically contain bonded joints, whose failure can contribute to aircraft accidents/incidents. Rotorcraft—particularly the main and rotor blades—stand out.
- As a result of bonding's strong process dependence, issues that originated in production or during maintenance are common contributing factors to bond-related aircraft accidents/incidents.
- Potential unsafe conditions might arise even from substandard bonding in structures commonly classified as nonsafety-critical.
- Redundant design features such as secondary fasteners, or additional maintenance actions such as early retirement, inspections, and postbond tests, might not deliver the expected long-term joint performance in case of poor bonding.
- Forensic analyses of bonded structures that failed in-service commonly report evidence of bondline environmental degradation or adhesion failure.

23.5.2.2 *Military*

Military applications have also accumulated decades of generally positive bonding in-service experience in structures and repairs, though there are reports of bond-related accidents/incidents [1,65]. The F/A-18 wing root structure is one of the key examples of bonded primary structure certified and deployed on a military air vehicle. As shown in Fig. 23.7, the composite wing skin is attached to the titanium fuselage attachment lugs through this bonded joint. This hybrid bonded joint carries significant structural loads and has a complex stress distribution.

Decommissioned F/A-18 inner wing root stepped-lap joints were subjected to static and fatigue loads, NDI, and forensic analyses to assess the potential impact of aging on the joint structural performance [68]. Static strength tests conducted on test elements extracted from these joints indicated that the load-carrying capacity of the joint remained comparable to the test data generated for pristine specimens [68]. These results suggested that the service history—including environmental exposure—had no significant effects on the joint's residual strength. The protective exterior coatings did perform well. Further, the additional spectrum fatigue tests indicated that the remaining life of the joints is substantial, and the residual strength was unaffected by the additional fatigue cycles (as much as 10–30 additional lifetimes) induced under laboratory environmental conditions. Metallic failure was observed for the tension-dominant spectrum test with significant load severity (Fig. 23.8). Periodic microscopic and visual inspections showed that the fracture initiated in the metal and propagated into the composite as a delamination that propagated across the remaining length of the specimen. Furthermore, it was noted that the crack initiated as a corner crack on one side of the titanium and propagated across the width of the specimen.

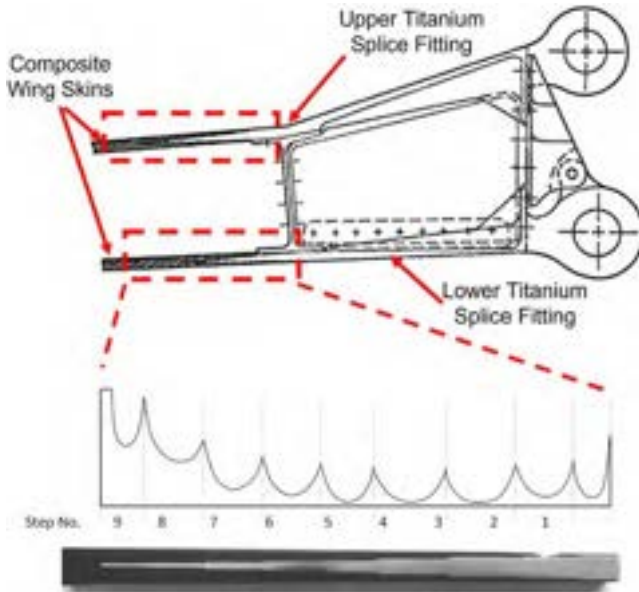


Fig. 23.7 F/A-18 inner wing composite to titanium double stepped-lap bonded joint. Adapted from W. Seneviratne, J. Tomblin, M. Kittur, A. Rahman, Aging evaluation of F/A-18 AD wing-root stepped-lap joint, in: NATO AVT-266 Research Specialist Meeting, Torino, Italy, 2018.

Even though the titanium has failed across the fillet region between steps 7 and 8 (see Fig. 23.8) and large delaminations were present, these specimens could transfer the fatigue loads across the remainder of the stepped-lap joint for a significant number of fatigue cycles. Although they were subjected to unrealistically high load severity factors, they survived over 5 lifetimes after one lifetime in service, indicating the bond system's reliability.

Detailed failure analysis conducted on test articles used for this study [68] showed primarily cohesive or substrate failure (initiated from plies near the interface), indicating proper surface preparation and no wear-out (aging) indications after a lifetime in fleet usage under operational conditions [69]. Also, it is noteworthy that the fatigue cracks were only observed when the spectrum loads were intensified significantly (as high as 45% of the design spectrum) and nucleated from titanium substrate. Initially, the spectrum loads applied to the elements only addressed the in-plane loading [68]. Subsequently, the research was expanded to a full-scale test demonstration of the inner wing to investigate more representative in-service loads. The full-scale test article consisted of the center fuselage, inner-wings, and trailing-edge flaps [70]. Both wings that had one lifetime in the fleet survived an additional lifetime of fatigue testing without any indications of damage growth in bonded joints or composite structure. After completing one lifetime of fatigue cycling in the laboratory environment, impact damages were inflicted on the wing-root stepped-lap joint area of the lower left-wing skin. Phased array NDI indicated that the overall length and width of each damage were

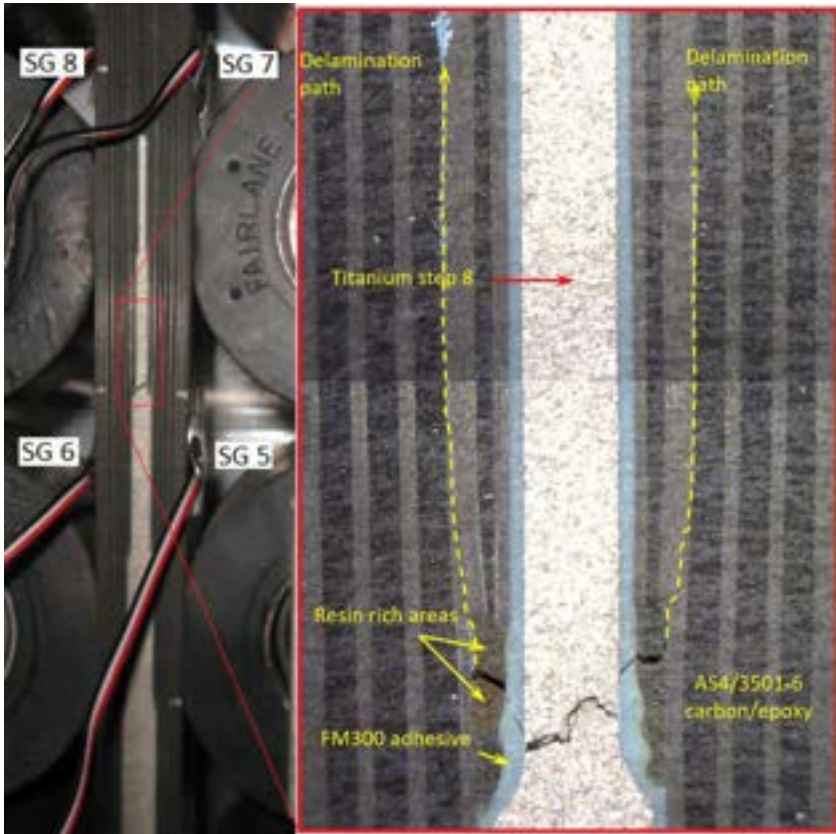


Fig. 23.8 Failure modes indicating metallic fracture for tension-dominant spectrum tests with high load severity.

Adapted from W. Seneviratne, J. Tomblin, M. Kittur, A. Rahman, Aging evaluation of F/A-18 AD wing-root stepped-lap joint, in: NATO AVT-266 Research Specialist Meeting, Torino, Italy, 2018.

approximately 150 mm. Following damage infliction, the test article was cycled for an additional 0.38 test life while conducting detailed periodic inspections around the damaged area. Additional fatigue cycles showed no damage growth or wearout around the impacted area, indicating the durability and damage tolerance of the bond system.

Nevertheless, a detailed investigation was conducted on a large anomaly on a wing skin of an F/A-18 found during in-service inspections [71]. A significant disbond (adhesion failure) was found in the stepped-lap joint. The presence of titanium-based oxides and the fluorine found in oxides revealed inadequate surface preparation causing poor adhesion. The interface crack (disbond) then propagated into the composite laminate (delamination) and further propagated, as shown in Fig. 23.8. Such isolated incidents show that the failure of any element of a qualified bonding system can cause joint failure. In the case of the F/A-18, the joint design and the overall wing design

contain multiple damage arrest features (e.g., multistep lap joint configuration and intermediate spars with bolted joints) that prevented a catastrophic failure of the wing even with the presence of a large disbond.

23.5.2.3 Overall observations

Consistent with current certification policies [4,8], service experience underscores the need for a "process control mentality" and thorough durability assessment to substantiate safe long-term operation of bonded structures. Particularly for safety-critical bonded structures, these policies encourage additional layers of protection such as added load path redundancy, damage growth arrest features, airframe environmental protection, damage tolerance-based maintenance actions, or advanced NDI techniques. Nonetheless, in-service data indicate that no combination of these additional layers of protection effectively can ensure the required minimum level of safety throughout the aircraft's operational life in case of substandard bonding. Furthermore, even relatively successful, well-established bonded joints (e.g., F/A-18 inner wing root) could perform poorly whenever any element of a qualified bonded system fails.

23.6 Conclusion

Bonded structures have been used in civil and military aviation applications for many years. While largely successful, some failures have occurred. Success depends on having a qualified bonding system consisting of four elements—adhesive, substrate, surface preparation and bonding process—with stringent characterization and control of each element to ensure adhesion, strength, and durability. After developing a bonding system, bonded joints must be substantiated with design details at structural scale, taking into account manufacturing and maintenance considerations. Redundant load paths are typically used as good design practice for critical structural details, including bonded joints, but are not a substitute for inadequate bonding processes.

Acknowledgments

The authors would like to thank Will Grace from The Boeing Company for reviewing and providing thoughtful edits to the chapter. We would also like to acknowledge the contributions of the CMH-17 task group that is writing content on bonded joints. This chapter reflects the same principles for safe qualification and certification.

References

- [1] P. Albericci, *Aerospace applications*, in: A.J. Kinloch (Ed.), *Durability of Structural Adhesives*, Applied Science Publishers, Barking, Essex, England, 1983, pp. 317–350.
- [2] R. Blomquist, *Adhesives—Past, Present and Future*, ASTM, Atlantic City, USA, 1963, pp. 182–215.
- [3] Title 14 of the Code of Federal Regulations (CFR). <https://www.ecfr.gov/current/title-14> (accessed December 22, 2022).

- [4] AC 20-107B Change 1—Composite Aircraft Structure, Federal Aviation Administration, 2010.
- [5] AMC 20-29—Composite Aircraft Structure, European Union Aviation Safety Agency, 2010.
- [6] C. Fualdes, M. Gruber, S. Haravan, D. Jury, T. Fukuoka, K. Jones, D.K. Nelson, E. Chesmar, Transport Airplane Metallic and Composite Structures Working Group (TAMCSWG)—Recommendation Report to FAA, TAMCSWG, 2018.
- [7] K. Fualdes, M. Davis, E. Chesmar, Transport Airplane Metallic and Composite Structures Working Group (TAMCSWG)—Recommendation Report to FAA Structural Bonding, TAMCSWG, 2021.
- [8] PS-ACE100-2005-10038—Bonded Joints and Structures: Technical Issues and Certification Considerations, Federal Aviation Administration, USA, 2005.
- [9] M.J. Davis, J. Tomblin, Best Practice in Adhesive-Bonded Structures and Repairs—DOT/FAA/AR-TN06/57, Federal Aviation Administration, 2007.
- [10] JSSG-2006—Joint Service Specification Guide: Aircraft Structures, United States Department of Defense, 1998.
- [11] G.A. Schoeppner, C.A. Babish IV, J.R. Calcaterra, EZ-SB-20-03—Requirements for Bonded Structural Repairs and Guidance for Bonded Structural Repair Design and Certification, Air Force Advanced Composites Office, 2020.
- [12] CMH-17, Composite Materials Handbook. www.cmh17.org (accessed December 22, 2022).
- [13] Composite Materials Handbook (CMH-17). Polymeric Matrix Composites Materials. Usage, Design, and Analysis, vol. 3, Rev. H, SAE International, Warrendale, PA, (in press).
- [14] SAE International, www.SAE.org (accessed December 22, 2022).
- [15] E. Chesmar, K.B. Armstrong, W. Cole, F. Museux, Care and Repair of Advanced Composites, third ed., SAE International, Warrendale, PA, 2020.
- [16] Composite Materials Handbook (CMH-17), Structural Sandwich Composites, vol. 6, SAE International, Warrendale, PA, 2013.
- [17] K. Blohowiak, M. Dilligan, W. Grace, C. Park, M. Pihel, P. Van Voast, E. Kutscha, H. Ashton, Qualified bonded systems approach to certified bonded structure, NATO STO-MP-AVT-266, 2018, <https://doi.org/10.14339/STO-MP-AVT-266-KN2-PDF>.
- [18] C. Ashforth, L. Ilcewicz, Certification of bonded aircraft structure and repairs, NATO STO-MP-AVT-266, 2018, <https://doi.org/10.14339/STO-MP-AVT-266-06-PDF>.
- [19] Metallic Materials Properties Development and Standardization (MMPDS-16), Battelle Memorial Institute, 2021.
- [20] J. Tomblin, Y.C. Ng, K.S. Raju, Material Qualification and Equivalency for Polymer Matrix Composite Material Systems: Updated Procedure—DOT/FAA/AR-03/19, Federal Aviation Administration, 2003.
- [21] B. Flinn, G. Iglesias, A. Stark, R. Kilgannon, Improving Adhesive Bonding of Composites Through Surface Characterization: Effect of Amine Blush on Bond Quality, 2015. https://depts.washington.edu/amtas/events/amtas_15fall/Flinn.pdf. (Accessed 14 February 2022).
- [22] G. Scarselli, D. Quan, N. Murphy, B. Deegan, D. Dowling, A. Ivankovic, Adhesion improvement of thermoplastics-based composites by atmospheric plasma and UV treatments, Appl. Compos. Mater. 28 (2021) 71–89, <https://doi.org/10.1007/s10443-020-09854-y>.

- [23] S. Chaechian, K. Schaerer, R. O’Kane, M.D. Halbasch, in: *A New Tailored UV Based Surface Activation Method for Bonding to Thermoplastics*, SAMPE 2019, SAMPE, Charlotte, NC, 2019, <https://doi.org/10.33599/nasampe/s.19.1628>.
- [24] A.C. Tracey, H. Dalal, M.A. Belcher, D.R. Ferriell, K.L. Hall, K.Y. Blohowiak, D.A. Blohowiak, B.S. Johnson, W.B. Grace, P.J. Van Voast, *Bonding the unbondable: thermoplastics!* in: *CAMX 2017*, Orlando, FL, 2017, pp. 1708–1720.
- [25] *AMS3819D—Cloths, Cleaning for Aircraft Primary and Secondary Structural Surfaces*, SAE International, 2020.
- [26] W.B.H. Grace, *The bonding system approach—characterizing and controlling the system for successful structural bonding*, in: *44th Annual Meeting, The Adhesion Society*, 2021.
- [27] *ASTM D1002-10—Standard Test Method for Apparent Shear Strength of Single-Lap-Joint Adhesively Bonded Metal Specimens by Tension Loading (Metal-to-Metal)*, ASTM International, 2019.
- [28] *ASTM D3163-01—Standard Test Method for Determining Strength of Adhesively Bonded Rigid Plastic Lap-Shear Joints in Shear by Tension Loading*, ASTM International, 2016.
- [29] *ASTM D5528-21—Standard Test Method for Mode I Interlaminar Fracture Toughness of Unidirectional Fiber-Reinforced Polymer Matrix Composites*, ASTM International, 2021.
- [30] *ASTM D7905-19—Standard Test Method for Determination of the Mode II Interlaminar Fracture Toughness of Unidirectional Fiber-Reinforced Polymer Matrix Composites*, ASTM International, 2019.
- [31] *ASTM D3762-03—Standard Test Method for Adhesive-Bonded Surface Durability of Aluminum (Wedge Test)*, ASTM International, 2010.
- [32] D. Lemme, L. Smith, *Ratcheting in a nonlinear viscoelastic adhesive*, *Mech. Time-Depend. Mater.* 22 (2018) 519–532, <https://doi.org/10.1007/s11043-017-9374-8>.
- [33] L. Ilcewicz, C. Ashforth, *Scaling crucial to integrated product development of composite airframe structures*, in: C.H. Zweben, P. Beaumont (Eds.), *Comprehensive Composite Materials II*, Elsevier, 2017.
- [34] J.J. Mazza, K.M. Storage, *Bonded repair in the United States Air Force and work to expand future capability*, *NATO STO-MP-AVT-266*, 2018, <https://doi.org/10.14339/STO-MP-AVT-266-04-PDF>.
- [35] L.J. Hart-Smith, *Stress analysis: a continuum mechanics approach*, in: A.J. Kinloch (Ed.), *Developments in Adhesive-2*, Applied Science Publishers, Barking, Essex, England, 1981, pp. 1–44.
- [36] *PS-AIR-100-14-130-001—Bonded Repair Size Limits*, Federal Aviation Administration, 2014.
- [37] *MIL-STD-3063—Rotorcraft Structural Integrity Program (RSIP)*, United States Department of Defense, 2018.
- [38] L.M. Smith, C.W. Rogers, *Bonded Bomber-B-58*, *SAE Trans.* 70 (1962) 477–486.
- [39] P. Brey, *Adhesive bonding experience at cirrus design*, in: *FAA Bonded Structures Workshop*, 2004. <https://transfer.niar.wichita.edu/?u=0HVB&p=e5RH>. (Accessed 23 December 2020).
- [40] J. Krone, *Structural metal bonding at Cessna Aircraft*, in: *FAA Bonded Structures Workshop*, 2004. <https://transfer.niar.wichita.edu/?u=0HVB&p=e5RH>. (Accessed 23 December 2020).
- [41] D. Koehler, *Structural bonding adhesive (Lancair)*, in: *FAA Bonded Structures Workshop*, 2004. <https://transfer.niar.wichita.edu/?u=0HVB&p=e5RH>. (Accessed 23 December 2020).

- [42] P. Harter, Certifying bonded structure: a new company's approach (Adam Aircraft), in: FAA Bonded Structures Workshop, 2004. <https://transfer.niar.wichita.edu/?u=0HVB&p=e5RH>. (Accessed 23 December 2020).
- [43] I. Meneghin, M. Pacchione, P. Vermeer, *Investigation on the Design of Bonded Structures for Increased Damage Tolerance*, Rotterdam, Netherlands, 2009.
- [44] P. Van Voast, K. Blohowiak, Critical materials & processes bonded joint issues, in: FAA Bonded Structures Workshop, 2004. <https://transfer.niar.wichita.edu/?u=0HVB&p=e5RH>. (Accessed 23 December 2020).
- [45] B. Raeckers, Overview of bonding processes at airbus, in: FAA Bonded Structures Workshop, 2004. <https://transfer.niar.wichita.edu/?u=0HVB&p=e5RH>. (Accessed 23 December 2020).
- [46] C. Voto, Alenia experience in metal bonding, in: FAA Bonded Structures Workshop, 2004. <https://transfer.niar.wichita.edu/?u=0HVB&p=e5RH>. (Accessed 23 December 2020).
- [47] L. Ilcewicz, C. Ashforth, Certifying innovative composite applications, in: AIAA SciTech Forum, AIAA, Orlando, FL, 2020.
- [48] C. Mark, Adhesive processing considerations (Bell Helicopters), in: FAA Bonded Structures Workshop, 2004. <https://transfer.niar.wichita.edu/?u=0HVB&p=e5RH>. (Accessed 23 December 2020).
- [49] E. Anamateros, E.L. Morra, U. Mariani, F. Scapinello, Agusta experience with bonded structures, in: FAA Bonded Structures Workshop, 2004. <https://transfer.niar.wichita.edu/?u=0HVB&p=e5RH>. (Accessed 23 December 2020).
- [50] J. Turnberg, Propeller continued airworthiness & service issues, in: FAA Bonded Structures Workshop, 2004. <https://transfer.niar.wichita.edu/?u=0HVB&p=e5RH>. (Accessed 23 December 2020).
- [51] K. Buettner, Investigation Report AX001-0/04, BFU, Germany, 2005. https://www.bfu-web.de/EN/Publications/Investigation%20Report/2004/Report_04_AX001-0_MUC_Fokker.pdf?__blob=publicationFile. (Accessed 11 August 2020).
- [52] Aviation Safety Investigation Report—200200646 ATSB, Australia, 2003. <https://www.atsb.gov.au/publications/safety-investigation-reports/?mode=Aviation&q=200200646> (Accessed 3 July 2020).
- [53] D.F. King, Aircraft Accident Report—6/89, AAIB, UK, 1989. <https://www.gov.uk/aaib-reports/6-1989-concorde-102-g-boaf-12-april-1989>. (Accessed 24 January 2021).
- [54] A. Fawcett, Cobonding primary structure—processing issues and related tests (Boeing), in: FAA Bonded Structures Workshop, 2004. <https://transfer.niar.wichita.edu/?u=0HVB&p=e5RH>. (Accessed 23 December 2020).
- [55] D.M. Hoyt, S. Ward, Composite bonded joints analysis, data, and substantiation—industry directions and technical issues, in: FAA Bonded Structures Workshop, 2004. <https://transfer.niar.wichita.edu/?u=0HVB&p=e5RH>. (Accessed 23 December 2020).
- [56] Along the Bond Line: Groundbreaking Aircraft Structures. http://www.fokker.com/sites/default/files/media/Files/Brochures/Fokker_Glare.pdf (Accessed 15 November 2019).
- [57] A. Beevers, Forensic Studies of Adhesive Joints: Part 2—Bonded Aircraft Structures, AEA Technology, UK, 1995. http://www.adhesivestoolkit.com/Docs/test/Procedures%20and%20Recommended%20Practice_files/P3r9pt2.pdf. (Accessed 14 November 2019).
- [58] I. Fidler, Improving operational repairability through SRM development: the operator's quest (British Airways), in: FAA Bonded Structures Workshop, 2004. <https://transfer.niar.wichita.edu/?u=0HVB&p=e5RH>. (Accessed 23 December 2020).

- [59] H. Loken, Bonding from a honeycomb core perspective (DuPont), in: FAA Bonded Structures Workshop, 2004. <https://transfer.niar.wichita.edu/?u=0HVB&p=e5RH>. (Accessed 23 December 2020).
- [60] G. Marengo, Experience in manufacturing Nomex composites sandwich structures, in: FAA Bonded Structures Workshop, 2004. <https://transfer.niar.wichita.edu/?u=0HVB&p=e5RH>. (Accessed 23 December 2020).
- [61] C. Kauffmann, FAA Workshop on Adhesive Bonding (Hurel-Hispano)—FAA Bonded Structures Workshop, 2004. <https://transfer.niar.wichita.edu/?u=0HVB&p=e5RH>. (Accessed 23 December 2020).
- [62] R. Harvey, Design, development & substantiation of bonded structures (Westland), in: FAA Bonded Structures Workshop, 2004. <https://transfer.niar.wichita.edu/?u=0HVB&p=e5RH>. (Accessed 23 December 2020).
- [63] G. Gardiner, Composites Help Bell V-280 Toward Future Vertical Lift, CompositesWorld, 2016. <https://www.compositesworld.com/articles/-composites-help-bell-v-280-toward-future-vertical-lift>. (Accessed 10 March 2022).
- [64] J.J. Barnett, K. Conradi, A.P. Simmons, Aircraft Accident Report 1/2006 EW/C2004/07/06, AAIB, UK, 2006. <https://www.gov.uk/aaib-reports/aar-1-2006-fairey-britten-norman-bn2a-mk-iii-2-trislander-g-bevt-23-july-2004>. (Accessed 24 July 2020).
- [65] Certification of Bonded Structures, Action Group 13 of The Technical Cooperation Program (TTCP), 2001.
- [66] W. Seneviratne, J. Tomblin, B. Saathoff, Thermoplastic Joining Materials Guidance Materials Guidance for Aircraft Design and Certification, 2021. https://www.wichita.edu/industry_and_defense/NIAR/Documents/jams-presentations-2021/Thermoplastic_Joining-Materials-Guidance-Seneviratne.pdf. (Accessed 24 January 2022).
- [67] G.G. Momm, L. Ilcewicz, C. Ashforth, D.C. Fleming, Bond-Related Aircraft Accidents/Incidents: a Review—DOT/FAA/TC-21/22, Federal Aviation Administration, 2021.
- [68] W. Seneviratne, J. Tomblin, M. Kittur, A. Rahman, Aging evaluation of F/A-18 AD wing-root stepped-lap joint, in: NATO AVT-266 Research Specialist Meeting, Torino, Italy, 2018.
- [69] W. Seneviratne, J. Tomblin, Evaluation of End-of-Life Residual Strength and Remaining Life of F/A-18 A-D Wing-Root Stepped-Lap Joint, NIAR, Wichita-KS USA, 2015.
- [70] W. Seneviratne, J. Tomblin, T. Cravens, C. Saathoff, B. Saathoff, Full-Scale Fatigue Test of F/A-18 Inner Wing After One Lifetime in Service, NIAR, Wichita-KS USA, 2015.
- [71] E.M. Mueller, S. Starnes, N. Strickland, The detection, inspection, and failure analysis of a composite wing skin defect on a tactical aircraft, *Compos. Struct.* 145 (2016) 186–193.

Automotive adhesives: Specification, qualification, and quality control

24

John Hill and Ahmad Rezaei Mojdehi
Ford Motor Co., Dearborn, MI, United States

24.1 Introduction

Adhesives are used extensively within automotive vehicles, including the obvious such as attaching the rearview mirror to the front windshield as well as safety critical items such as bonding friction material to brake pads. For this latter example, virtually every original equipment manufacturer (OEM) has moved away from using rivets to attach the friction pad to the steel backing plate to relying solely on phenolic adhesives. The benefits of using bonded pads include an increased contact area and longer lifespan as the height of the rivet head no longer determines the useful life. Other automotive applications include moisture-cure single-component (1 K) polyurethane (PU) adhesives to attach the glass windshield to the body as well as heat-cured epoxies within the body structure and closure (doors, hoods, liftgates, etc.) hems. Acrylic pressure-sensitive adhesives (PSAs) are often used to attach interior and exterior trim components, whereas methacrylate “threadlocking” adhesives are used within the engine to help secure fasteners. The breadth and depth are too great to be covered adequately within this chapter, therefore the focus is on the use of 1 K epoxy structural adhesives for body applications (see also [Chapter 1](#) on epoxy chemistries). The primary benefits of such adhesives include:

- (i) **Stiffness**—Increasing the stiffness of a vehicle generally leads to improved driving dynamics or “feel” as the vehicle responds in a more predictable manner. Stiffer vehicles also have improved noise vibration and harshness (NVH), what’s more commonly termed reduced “squeak and rattle.” The overall effect of a stiffer vehicle is one of improved quality both initially and at the end of life.
- (ii) **Crash**—Adhesives can help distribute or dissipate a crash load by changing the buckling mode of a structure, leading to improved energy management.
- (iii) **Fatigue**—Adhesives are commonly used to address fatigue-related issues associated with thin sheet metal joints. Adhesives help distribute the load over a wider area, leading to lower stresses and increased durability.
- (iv) **Mixed material**—Automotive body structures are made from a variety of materials optimized for performance and cost. Such mixed material construction cannot usually be joined using local fusion via resistance spot welding (RSW). A common alternative is a self-pierce rivet (SPR) augmented with an epoxy adhesive.

Automotive manufacturers don't formulate adhesives, but instead rely on well-known commercial suppliers with a global presence. Vehicle manufacturers typically have a global presence and usually engineer their products to meet global requirements rather than designing vehicles for unique markets. Economies of scale enable the development and costs associated with approval and certification to be spread over multiple units. An example is the Ford Focus, which was manufactured in 11 plants around the world in numerous guises such as the Mazda 3, Volvo C30 (former Ford partners), Ford Escape/Kuga, and Ford C-Max. The total global volume was greater than 1.5 million vehicles per year. It follows that the adhesive used within these vehicles are specified and approved to a single set of global requirements. Approval of such specifications usually requires a balloting process with input from multiple regions and from different entities such as design and manufacturing. The speed of manufacture is also an important consideration with high volume OEMs producing vehicles at 60–75 jobs per hour (JPH) or one every 48–60 s.

This chapter provides an overview of the specifications, qualifications, and controls used within the automotive industry along with specific examples for each section. The examples relate to a single-component, heat-cured epoxy used on the aluminum Ford F-150 truck launched in 2015. More than 110m of epoxy adhesive were used on this vehicle, as shown in Fig. 24.1, approximately three times the amount used on the outgoing steel variant launched in 2004 [1]. At sales volumes in excess of 1 million per year, this represents one of the highest uses of automotive adhesives globally.

There are numerous approaches to constructing a vehicle. However, after 130 years of iteration, most high-volume automotive manufacturers follow a similar process, as shown in Fig. 24.2. Highlighted in the flowchart are the stages where pumpable adhesives and sealers are applied to the structure and where they are subsequently cured. It should be noted that some manufacturing plants are fully integrated into a single site. However, it is not uncommon for subassemblies containing uncured adhesive to be

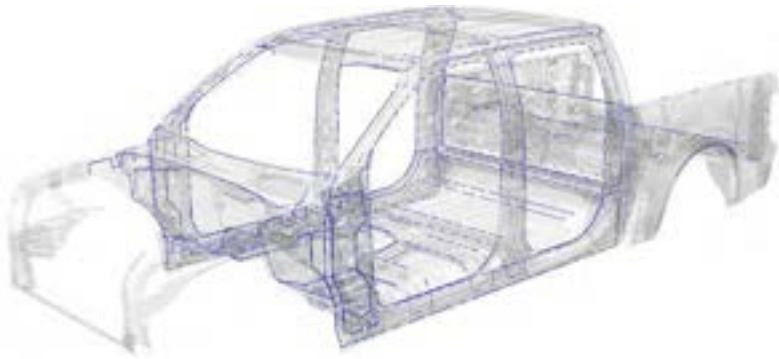
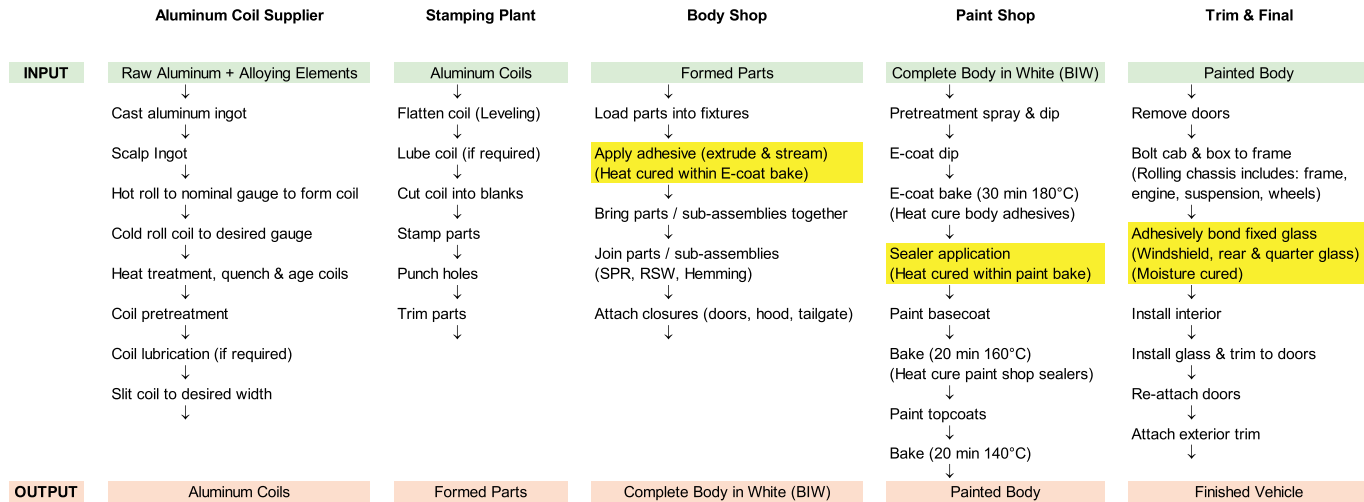


Fig. 24.1 2015 Aluminum Ford F-150 highlighting 110m of structural epoxy adhesive.



E-coat = Epoxy Electrocoat
 SPR = Self Pierce Rivet
 RSW = Resistance Spot Weld

Fig. 24.2 Flowchart showing the process steps in building an aluminum Ford F-150 (adhesive and sealer application highlighted).

shipped to different locations or even between countries. These manufacturing constraints can have a significant effect on the specification requirements of the adhesive, for example, humidity stability in the case of shipping subassemblies over long distances.

24.2 Specifications

Adhesive specifications for automotive use are typically broken down by application such as for glazing, closures, body structure, trim, etc. Each of these categories is broken down further by material type for example, sheet molding compound (SMC) hood, aluminum or steel body, or internal vs external trim. The specifications can also be classified by adhesive chemistry, such as 1 K oven-cure epoxy or 2 K PU. The specification details the performance requirement for each attribute, then references a test method such as ASTM, ISO, or a specific in-house test (for example a Ford laboratory test method, FLTM). The format of an adhesive specification used by Ford often takes the following form:

Performance Requirements:

- Lap shear strength
- T-peel strength
- Impact peel (plateau load or energy)
- Fatigue
- Corrosion performance (e.g., stress durability)

Material Characterization:

- Tensile modulus
- Poisson's ratio
- Differential scanning calorimeter (DSC) response
- Fourier transform infrared (FTIR) response

Manufacturing Requirements:

- Rheology
- Dispensing
- Sag, slump, and bridging resistance
- Wash-off resistance
- E-coat compatibility
- Welding and flammability acceptance
- Rivetability acceptance
- Odor rating (cured and uncured)
- Storage stability of sealed drums
- Humidity stability of open beads

Mapped on top of these requirements are multiple “noise factors” including: substrates (and coatings), bake conditions (minimum and maximum temperatures and times), lube type and coat weight, and conditioning (age, thermal, corrosion exposure). For example, lap shear testing would be performed at -40°C , 23°C , and 80°C . As a separate test, lap shear coupons would be exposed to a 6 weeks accelerated corrosion cycle prior to measuring their residual lap shear strength.

Defining these standards is a complex problem involving many aspects, such as minimal functional performance, best-in-class performance, and customer

expectations. How these tests are performed can also be an issue, for example, testing impact peel strength or T-peel and the effect of strain rate, or the effect of changing the yield strength of a 6000 aluminum alloy as a result of the adhesive bake cycle. It is possible to show an “apparent” increase in lap shear strength at the maximum bake condition based on changes in the alloy aging response between the minimum bake of 20 min at 160°C and the maximum bake of 40 min at 205°C. Changing the yield strength of the substrate also changes the deformation of the lap shear coupon and hence the stress distribution within the joint. Building full vehicle prototypes and testing them to destruction or beyond their expected service life is another way of helping to define the desired adhesive properties. For corrosion testing, this requires an accelerated test procedure that is designed to mimic a known degradation mode in a compressed timeframe. Such tests are typically cyclical in nature, with regard to wet and dry phases, high and low temperatures, percent relative humidity (RH), and salt concentration. Their duration can vary but are typically 6–12 weeks (1000–2000 h) [2]. These full vehicle corrosion test protocols are then reproduced at a laboratory level for coupon or small subassemblies [3]. One of the problems with accelerated testing is that they are designed to promote a specific failure mode rather than all potential modes. It is therefore useful to tear down used vehicles from areas with extreme conditions such as hot (Arizona), humid (Florida), high road salt (Michigan), etc., for evaluation. This holistic approach allows for the specifications to be adjusted accordingly.

24.2.1 Specification example—Stress durability (FLTM BV101-07)

One of the hardest requirements to achieve in automotive applications is a durable bond within a corrosive environment. The simplest test is to make a group of lap shear coupons, expose half of them to an accelerated cyclical corrosion cycle, then compare their residual strength against the nonaged control samples. The drawback of this approach is that it focuses on how well the joint is sealed (corrosion initiation) by the spew filet rather than how well it arrests a propagating corrosion crack. The opposite end of the test spectrum is when a bonded joint, lap shear, peel, or double cantilever beam (DCB) is exposed to an accelerated corrosion cycle while simultaneously being cyclically loaded. Such testing is complex and expensive to perform and is generally beyond the capability of most adhesive suppliers. Ford uses a simpler test whereby a string of bonded lap shear coupons (25.4 mm × 12.7 mm bond area) is subjected to a constant tensile load while exposed to a cyclical corrosion cycle [4]. The coupons are supported within a stainless steel fixture with a compressed spring at one end providing a 2400 N tensile load; see Fig. 24.3. The loaded fixture is dipped in a 5% concentration NaCl bath for 15 min, removed to drip dry at room temperature for 105 min, followed by 22 h exposure to 50°C and 90% RH within a humidity cabinet. The humidity cabinet was modified by cutting holes in the top to allow the spring to be kept at room temperature; see Fig. 24.4. The fixtures would be dipped daily five times per week until a coupon failed. The cycles to failure were noted, the coupon replaced with a blank, and the test continued until three failures were observed.

Fig. 24.5A shows the stress durability results for five 1 K epoxy adhesives, bonded under the same minimum and maximum bake conditions, to the same lot of A951 [5]

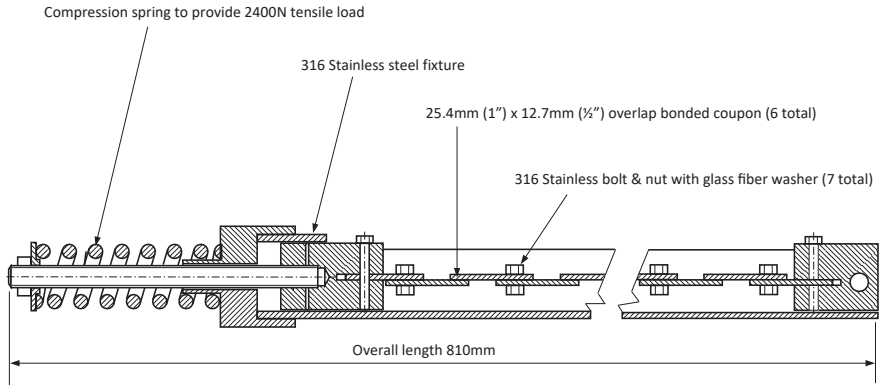
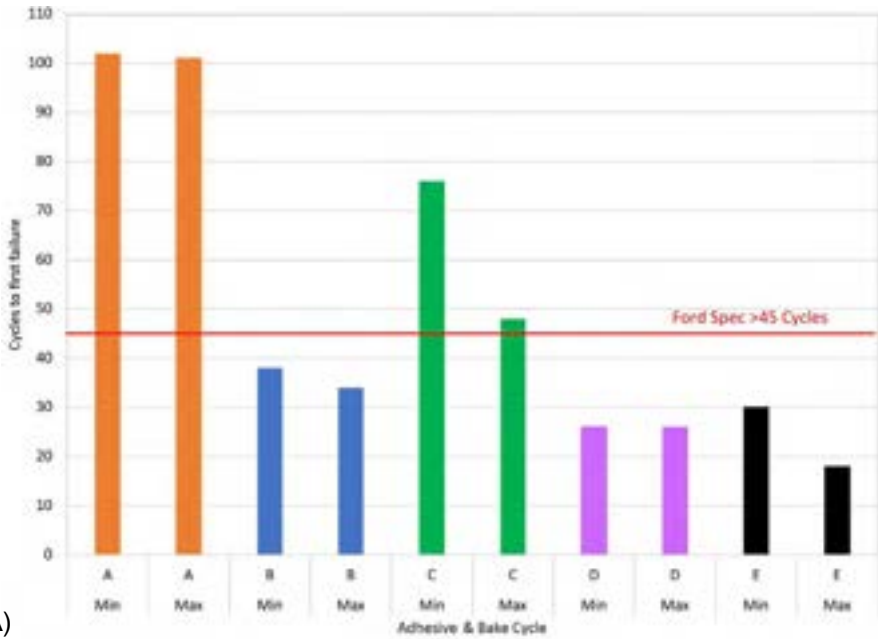


Fig. 24.3 Ford stress durability test fixture.



Fig. 24.4 Humidity cabinet loaded with stress durability fixtures.



(A)



A (102 cycles)



B (38 cycles)



C (76 cycles)



(B) D (26 cycles)



E (30 cycles)

Cohesive Failure

Adhesive Failure

Fig. 24.5 (A) Stress durability results for different 1K epoxy adhesives cured at minimum (20 min at 160°C) and maximum (40 min at 205°C) bake cycles. The substrate was a single batch of 2 mm thick 5754 aluminum pretreated with A951 and lubed with Quaker DC2-90 dry film. (B) Failure loci of different 1K epoxy adhesives after stress durability testing, as shown in A. All samples were cured under the minimum bake conditions (20 min at 160°C) on 2 mm thick 5754 aluminum pretreated with A951 and lubed with Quaker DC2-90 dry film.

pretreated 5754 aluminum substrates. It can be observed that several adhesives failed to meet the specification requirement of 45 cycles while others passed but exhibited a large variation between the minimum and maximum bake conditions. Fig. 24.5B shows a comparison of the failure loci among the five different adhesives after failure within the stress durability test. It is interesting to note that the failure mode determined by visual examination is reasonably consistent, predominantly adhesive with final failure being cohesive. Corrosion undercutting of the bond interface occurred, resulting in an adhesive failure mode and a reduction in bonded area. The spring on the top of the fixture was compressed to provide a constant load of 2400 N, which was distributed across the entire bond area. Undercut corrosion of this bond resulted in a reduced area and therefore higher stresses, resulting in catastrophic final failure of the joint. Although the failure loci are similar for all five adhesives, the number of cycles to failure varied dramatically from 26 (sample D) to 102 cycles (sample A).

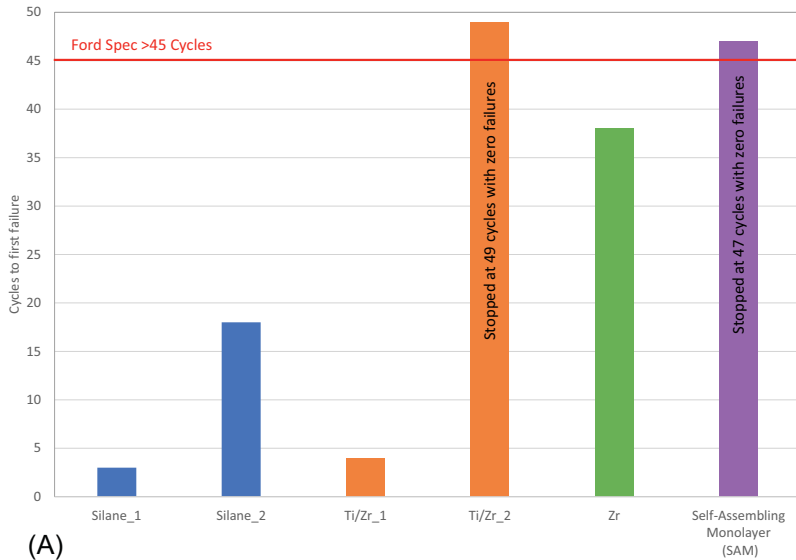
The BV101-07 stress durability test [4] was used on the 2015 Ford F-150 to help screen suitable adhesives as well as the development of a pretreatment process. For the former, adhesives were tested using a common substrate known to perform well within the test. For pretreatment development, a single adhesive known to perform well was used as a control. The pass requirement was 45 cycles for both tests. Fig. 24.6A shows the results of 6 different coil pretreatment processes used on the same 5754 aluminum alloy and tested with the same 1K epoxy adhesive using the same cure profile. Fig. 24.6B shows the failure loci associated with the pretreatment failures shown in Fig. 24.6A. High stress concentrations within the adhesive resulted in “stress whitening” and a lighter orange appearance. Regions of dark orange suggest that failure occurred within the pretreatment or substrate oxide rather than cohesively within the adhesive.

24.3 Qualification

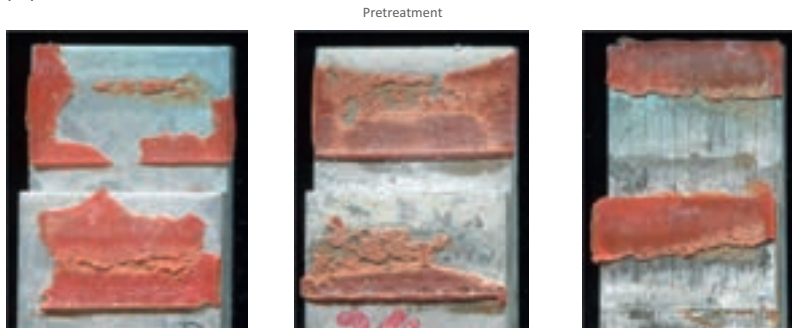
24.3.1 Design qualification

Qualification and quality control are similar in that they are concerned with achieving a designed performance. Qualification is a demonstration that the part or assembly has achieved a specific target, whereas quality control is primarily concerned with achieving a desired performance in a consistent manner. For automotive applications, qualification is often performed at full-vehicle or subsystem level by the OEM, whereas quality control is much more localized and specific and is often performed by the adhesive supplier.

Although the majority of vehicle design is performed within the virtual world using Computed Aided Engineering (CAE) simulation, there are still numerous qualification approvals that involve testing full vehicles to failure or beyond their life expectancy. Some of these tests are federally mandated such as those defined in the Federal Motor Vehicle Safety Standards (FMVSS) [6] including crashworthiness (#200) and integrity postcrash (#300). At the opposite end of the qualification spectrum are failures or partial failures that may cause a customer concern or perceived quality issue.



(A)



i) Silane-1 (3 cycles)

ii) Silane-2 (18 cycles)

iii) Ti/Zr-1 (4 cycles)



iv) Self-Assembling Monolayer (SAM) did not fail after 49 cycles. Sample pulled on load frame to observe failure mode

(B)

Fig. 24.6 (A) Stress durability results for different pretreatments on 2 mm thick 5754 aluminum lubed with Quaker DC2-90 dry film and bonded using the same 1 K epoxy adhesive. (B) Failure loci of the different pretreatments after stress durability testing, as shown in A. All samples were bonded using the same 1 K epoxy adhesive under the same cure conditions (30 min at 180°C) on 2 mm thick 5754 aluminum lubed with Quaker DC2-90 dry film.

Most manufacturers will use these federal in addition to global requirements to set their own internal standards designed to exceed these minimums. When launching a new vehicle, or the major refreshing of an existing model, they will aim to achieve the highest possible rating such as 5-Star Safety by the National Highway Traffic Safety Administration (NHTSA) [6] or to be a top pick within a consumer report.

Adhesives play a vital role in achieving the highest performance and quality standards and therefore become an important consideration in the qualification process. This requirement goes beyond just the adhesive in also ensuring that the substrate is prepared according to production intent. An example of this is crash testing (FMVSS 212) or the quasistatic roof crush (FMVSS 216a), whereby the front windshield plays a vital part in the crash response [6]. This requirement demands that the PU adhesive used to bond the glass has been applied correctly to both surfaces. Most manufactures use a moisture cure 1 K PU that is applied to the primed ceramic fret on the glass that mates with the clearcoat paint on the vehicle. This requires test vehicles to be painted through the full production paint process rather than offline in a prototype shop. The same is true for structural adhesive within the body structure, as it is essential that the substrates are representative of the intended production process.

Building and testing vehicles at a full-scale level is expensive and slow. A more efficient method is to test subsystems, for example a new adhesive on an F-150 truck box design. It is relatively easy to build a prototype box and attach it to an existing truck frame, which is run through the accelerated corrosion vehicle cycle [2]. For fatigue durability testing, a prototype box can be tested using a four-post test frame capable of simulating the expected life cycle in a compressed time frame.

24.3.2 Manufacturing qualification (or functional trial)

As thorough as the testing is within [Section 24.2](#), discrete specification testing fails to capture all interaction effects of the manufacturing processes. For this reason, manufacturing qualification (known as functional trials) is performed. For an existing process, this usually requires in-plant trials on specific adhesive dispensing robotic cells during production downtime. The trials typically involve purging the current adhesive with the new one and/or replacing the hoses. Several test assemblies would then be built prior to converting the cell back to the original adhesive until full approval is achieved. These assemblies would then be processed and tested to determine performance or to observe any downstream manufacturing concerns. For new vehicles or new facilities, the chosen adhesive would be used through the prototype build phases to demonstrate performance, then used to commission the manufacturing cell. The timeframe for these new installations can often exceed the shelf life of the adhesive (typically 3 months). To overcome this problem, robot dispense cells are often commissioned using small 20L pails of adhesives that are subsequently exchanged for 200L drums as the build volume is increased.

24.3.3 Qualification example—DSC kinetic cure model

For the 2015 Ford F-150 aluminum truck, a 1 K epoxy adhesive was chosen that cured within the e-coat bake oven (Fig. 24.2). It was essential that sufficient cure was obtained throughout the entire vehicle and was within the minimum and maximum profiles used for laboratory testing. Unfortunately, the thermal history of the adhesive through the e-coat bake oven is more complex than laboratory-prepared test coupons. Fig. 24.7 shows the minimum and maximum thermal traces taken from a prototype aluminum F-150. CAE thermal simulation of the vehicle within the oven helped identify the coldest locations, that is, rockers, the bottom of the A and B pillars, and mid-way up the B-pillar near the latch point. A prototype vehicle was built with more than 100 thermocouples embedded within the adhesive bondlines focusing specifically on the coldest areas. These thermal traces were then used as the input to an autocatalytic kinetic cure model to predict the degree of cure within the adhesive bond as a function of time and temperature.

A DSC (TA Instruments DSC250) was used to generate enthalpy curves for different ramp rates. These curves were then fitted using nonlinear regression analysis to the following form [7]:

$$\frac{dX}{dt} = A e^{\frac{-E_a}{RT}} \cdot X^m \cdot (1 - X)^n \quad (24.1)$$

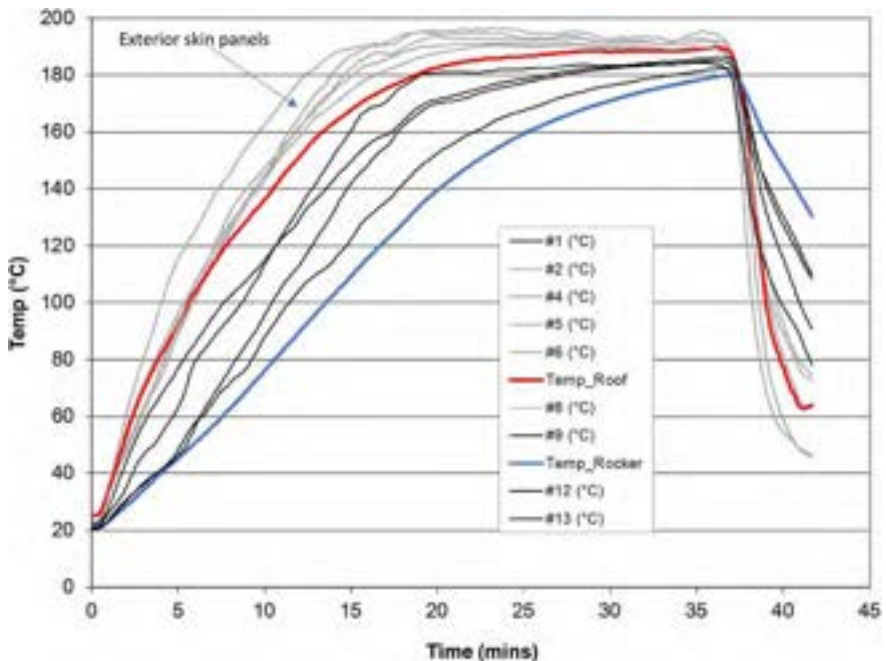


Fig. 24.7 Thermal profile of adhesive bond line within an F-150 truck processed through an e-coat oven.

where:

X = fractional conversion (degree of cure)

dX/dt = reaction rate (s^{-1})

m, n = reaction orders

T = temperature (K)

R = universal gas constant (8.32 J/mol)

A = pre-exponential factor (s^{-1})

E_a = activation energy (J/mol)

A finite difference model set up within a spreadsheet calculated the predicted cure for each incremental time step, that is, every second. The degree of cure was simply the cumulative sum for each time step. Fig. 24.8A shows a comparison of the DSC data to the autocatalytic model and Fig. 24.8B shows the same model applied to the thermal traces shown in Fig. 24.7. For the F-150, a minimum cure of 95% was defined, which necessitated upgrades to the e-coat oven to improve the heat-up rate as well as the temperature distribution. Adhesive samples taken from these cooler locations were run through the DSC to ensure that they were fully cured (>95%).

24.4 Quality control

Quality control is achieved through multiple levels and at varying frequencies. Similar to other high-volume manufacturing industries, the majority of the focus is on controlling the inputs rather than measuring and correcting defective outputs. One tool used to help with this process is failure mode and effects analyses (FMEA). These generally fall into two variants: DFMEA governing the **design** of the vehicle or use of adhesives within a component or subsystem, and PFMEA governing the manufacturing **process**. The requirements are rated in order of severity and detection. Items that score highly (undesirable) will be redesigned, or changes will be made to the manufacturing process to make it less risky, or some sort of detection will be added to help identify when a fault occurs.

At Ford, there are four levels of adhesive approval:

- (i) Initial approval (defined in Section 24.2 under specification).
- (ii) Functional trial (defined in Section 24.3.1).
- (iii) Annual retest (supplier provided such as slump, slide, and bridging).
- (iv) Every lot (supplier provided such as rheology yield stress and viscosity).

Control charts, run charts, and other statistical tools are utilized to ensure adequate control, ideally within 6 Sigma limits.

24.4.1 Manufacturing controls

Historically, manufacturing relied on the tear down of a vehicle or subassembly to verify the process, the frequency of which determined in part by the severity score in the DFMEA, which helped define the PFMEA. This frequency usually changes with the maturity of the process, for example, the first unit built may be torn down

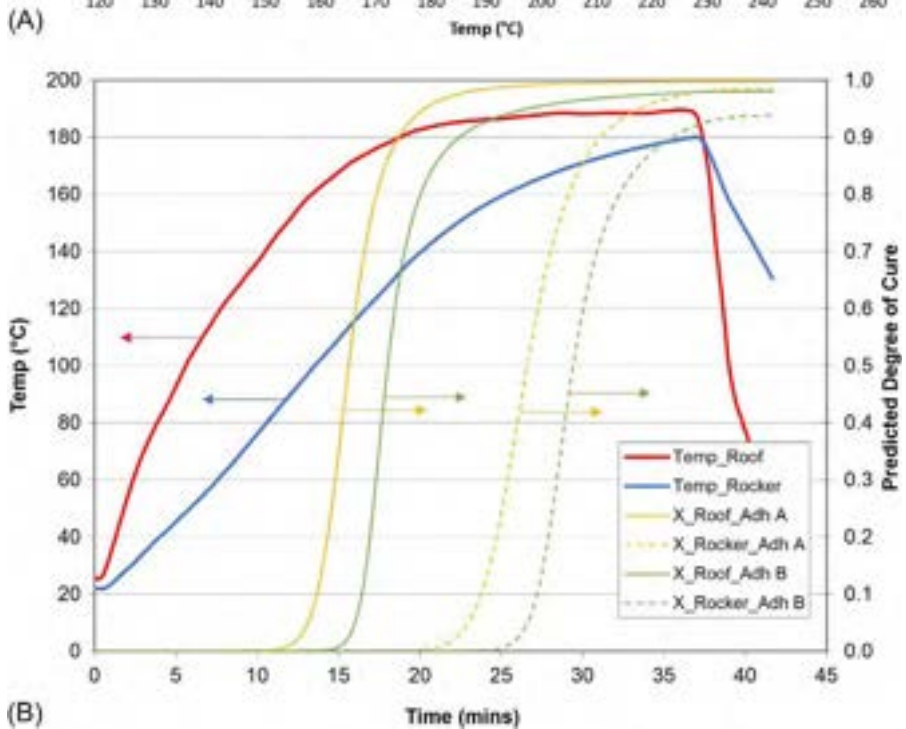
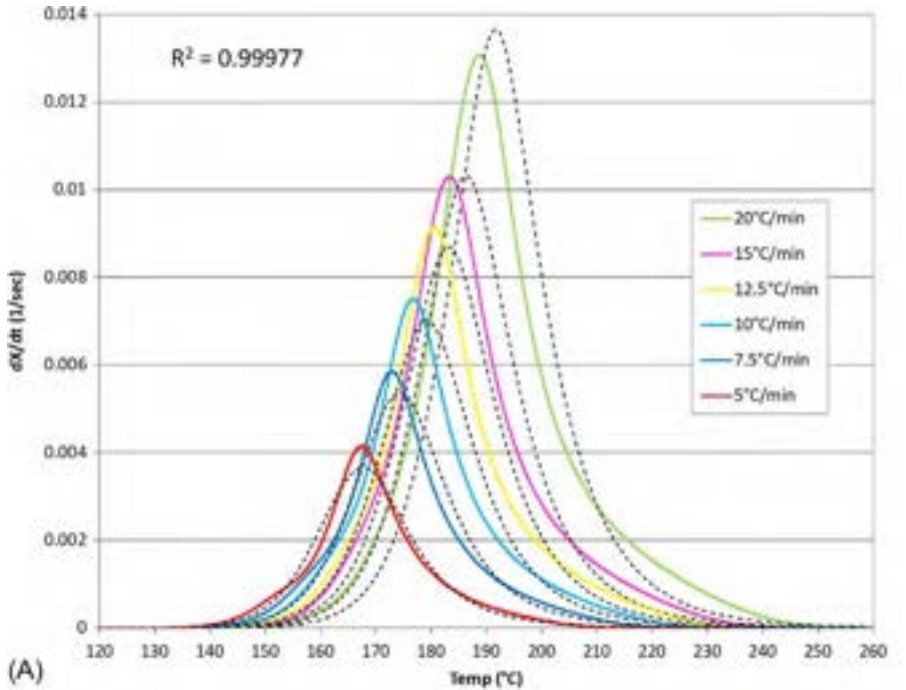


Fig. 24.8 (A) Comparison of DSC data (*solid lines*) to autocatalytic cure model (*dashed lines*). (B) Autocatalytic kinetic cure model applied to thermal traces.

to help refine the process or subassembly. Once manufacturing starts, typically progressive in volume, a tear down frequency is chosen to enable feedback and adjustment to the process. Full rate manufacturing capacity will trigger a given tear down rate to verify the process. As mentioned, this rate can be determined by the severity of the PFMEA score and the ability to contain suspect assemblies.

Assessment of adhesive joints for body construction is typically limited to detection of the presence of the adhesive and its coverage (or minimum bead width), as the tear down procedure usually occurs prior to cure within the e-coat bake oven. There are multiple reasons behind this decision:

- (i) Tear down should occur as close as possible to the process being assessed. Additional processes incur additional cost and delay the feedback response, putting more work in process (WIP) at risk.
- (ii) Tear down is a dirty process that is best contained within the body shop rather than the cleaner environment of the trim shop.
- (iii) Tearing down a body with cured structural adhesive is extremely difficult due to its strength. It is therefore considerably easier to tear apart a joint prior to cure.

Nondestructive evaluation (NDE) such as phased array ultrasonic probes is often used in lieu of destructive tear down or as an aid for setting up an adhesive dispensing cell to ensure adequate flange coverage or location. The time-consuming nature of these processes along with the skill required in using such tools usually limit their applicability.

In recent years, there have been numerous improvements to robotic adhesive dispensing systems, often referred to as in station process monitoring (ISPM), whereby defects are identified real time. Examples include pressure transducers to identify air bubbles or skips (<https://patents.google.com/patent/US10935477B2/>), displacement transducers to monitor dispensed volume, and ferromagnetic tagging to monitor the mix ratio of 2K systems. Vision systems are also used to detect bead shape and position on a panel. Some systems can repair a flaw, such as a skip, by selectively returning and reapplying a partial bead. The next generation of dispensing systems will include in station process control (ISPC), whereby the robot and dispense system will adjust in real time to ensure a perfect bead (<https://patents.google.com/patent/US20220288617A1/>).

24.4.2 Quality control example—Rheology characterization

Adhesive rheology has a significant effect on the manufacturing aspects of vehicle production. How the adhesive is pumped from a 200L barrel into a shot meter positioned on the end of a robot is governed by its viscosity at low shear rates (100–1000 s⁻¹). How the material behaves as it is extruded, swirled, or streamed onto a panel is dependent on its high shear rate response (10,000–100,000 s⁻¹). The shape of the adhesive bead dispensed on the panel is governed by its yield stress. This wide span in shear rate necessitates the use of time-temperature superposition (TTS) techniques to obtain an understanding of the yield and viscosity response beyond the direct measurement range of a laboratory rheometer. Fig. 24.9A shows the raw shear stress data for a 1K epoxy adhesive at different isothermal temperatures. The Cox-Merz rule [8] was implemented to measure the complex viscosity obtained from small amplitude

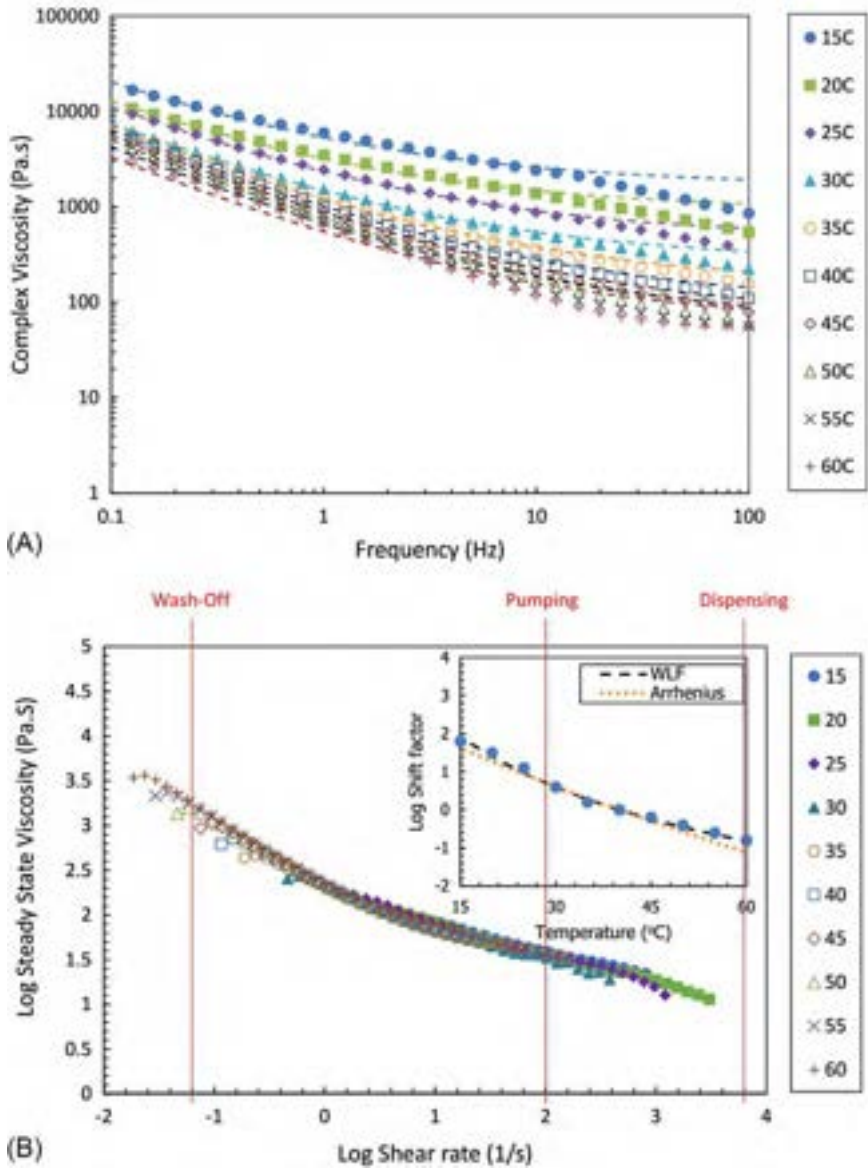


Fig. 24.9 (A) Time-temperature superposition (TTS) response for a 1K epoxy adhesive. Apparent Newtonian complex viscosity vs frequency obtained from small amplitude oscillatory shear tests from 15°C to 60°C. *Dashed lines* represent Casson fit to the data based on the Cox-Merz rule [8]. (B) Master curve for a 1K epoxy adhesive. Steady viscosity vs shear rate obtained by shifting the data to the reference temperature (40°C). Inset: Shift factor vs temperature (markers) and the corresponding WLF [9] and Arrhenius fits (*dashed lines*).

oscillatory (SAO) tests, enabling higher shear rates otherwise not accessible by standard steady-state rheology testing. Fig. 24.9B shows the master curve for the shear stress data shown in Fig. 24.9A. Also shown on Fig. 24.9B are the approximate shear rates associated with pumping the adhesive out of the barrel as well as dispensing.

Adhesive wash-off of a dispensed bead from a panel or out of a joint is a known issue in most OEM paint shops. Misplacement of an adhesive bead on a flange results in squeeze-out after application of the mechanical joint (e.g., self-pierce rivet or resistance spot weld). This squeezed-out adhesive is then subjected to significant spray pressure during the rinsing and dipping stages in the paint pretreatment line, leading to wash-off. These adhesive “blobs” could either redeposit on to a class A surface or contaminate the tanks and filters, leading to increased rework and maintenance costs. Rheological characterizations can also be used to identify the adhesive wash-off performance if appropriate shear stress and shear rate regimes are considered. Currently, most OEMs perform a separate adhesive wash-off test to simulate the rinsing process in a paint pretreatment line (e.g., spraying water, with a set pressure and flow rate, onto an adhesive bead for a period of time and measuring bead movement). However, developing a rheology test method that captures all aspects of adhesive performance related to rheology such as bead shape stability, sagging, wash-off, low speed dispensing (extrusion), and high-speed dispensing (streaming) would be of great practical importance, especially for developing next-generation adhesives at the research and development stage.

It is well documented that highly filled structural epoxy adhesives can age, resulting in an increase in viscosity that makes them harder to dispense as well as a reduction in yield stress that makes them lose their bead profile. It is for this reason that the specification requirements listed in Section 24.2 require testing of both fresh batches as well as those aged for 90 days at 32°C. Production-scale dispensing trials are performed using fresh and aged batches to show that they are within the capability of the equipment. From a quality control perspective, the adhesive supplier must measure the yield and viscosity of every batch prior to shipment. These measurements are performed using a laboratory rheometer but are limited to a single isothermal temperature (45°C) and a restricted shear range (~ 100 1/s). Determining the rheological properties at shear rates associated with dispensing involves extensive testing and complex TTS techniques, as shown in Fig. 24.9A and B. From a quality control perspective, it is impractical to fully characterize every production batch. Therefore, a single isothermal measurement over a limited shear range is a practical solution of ensuring consistency between batches. Upper and lower tolerance limits are then applied to these measurements and become part of the supplier’s control plan. The data are collected and plotted as control charts, including upper and lower specification limits (typically defined by the OEM) as well as control limits based on the capability of the equipment used to manufacture the adhesive. Once the specification and control limits have been established, then it’s possible to perform typical process control analysis to assess its capability. Fig. 24.10 shows the normalized Casson yield stress production quality control data for a 1 K epoxy adhesive considered for the F-150 truck.

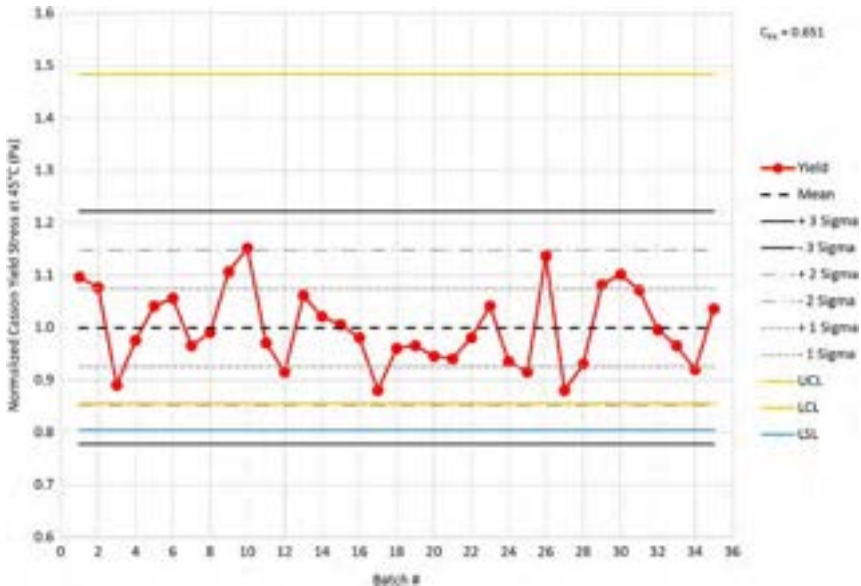


Fig. 24.10 Production run chart for Casson yield stress of a 1 K epoxy adhesive.

At first glance, the data in Fig. 24.10 look reasonable, as they fall within the ± 3 Sigma range and all the points are above the lower specification limit (LSL). However, closer examination shows a lack of process capability based on the distribution. The negative 3 Sigma limit based on the sample population is lower than the LSL. Although the population appears to be normally distributed, it is skewed toward this LSL. The standard method for measuring this asymmetry is the C_{PK} value, as defined by Eq. (24.2) [10].

$$C_{PK} = \frac{\text{Min}[(USL - \bar{x}), (\bar{x} - LSL)]}{3\sigma} \quad (24.2)$$

where:

USL = upper specification limit

LSL = lower specification limit

\bar{x} = mean

σ = standard deviation

For the data presented in Fig. 24.10, the C_{PK} value was 0.651. A value of 1 or greater means the data fall within the specification limits. In this example, a value of 0.651 indicates that the process falls outside these limits. It is often desirable to have a C_{PK} of 1.33 or greater as it shows 4 Sigma capability. A simple solution in this case would be to increase the target yield stress by increasing the filler content to centralize the process within the upper and lower control limits.

Data such as yield and viscosity are required for every batch and must be included on the shipping details, which are then checked against the specification requirement

before being accepted by Ford. Ford supplier technical assistance (STA) engineers work closely with adhesive suppliers to ensure their manufacturing processes are capable of meeting Ford's specification requirements. It is not uncommon for the adhesive formulators to have similar experts working with their suppliers, ensuring conformity of their raw ingredients. As per Ford, considerable effort is directed toward controlling and specifying the inputs to the process rather than fixing or adjusting the outputs to meet the specification.

24.5 Future trends

The 2015 aluminum F-150 saw a 280% increase in the use of structural epoxy adhesive within its body structure compared to the previous 2004 steel version [1]. Because steel has a tensile modulus of 207 GPa compared to only 69 GPa for aluminum, it follows that an aluminum copy of a steel vehicle would have only a third of the stiffness, leading to unacceptable performance and handling. To overcome this loss in modulus, aluminum vehicles use thicker panels, larger closed sections such as rockers, and more continuous joining such as adhesives. A combination of these strategies resulted in the 2015 aluminum F-150 being 5.8% stiffer and 45% lighter than the steel predecessor [1]. The adhesive alone contributed 20% to the overall stiffness of the cab. Other manufacturers have adopted a similar approach in using more adhesives to recover or improve stiffness while using lighter materials with a lower modulus. The ultimate vehicle is one where every component is optimized for weight, performance, and cost, leading to a mixture of materials needing to be joined. Adhesives offer one possible solution to this multimaterial problem, although the coefficient of thermal expansion (CTE) mismatch is a major challenge from a manufacturing perspective if the vehicles are to be processed through a conventional assembly plant (Fig. 24.2). CTE can be a concern from a structural perspective, for example a highly stressed bond within a corrosive environment, or from an appearance perspective. An example of the latter is bonding an aluminum roof skin onto a steel body through a conventional e-coat oven without buckling or local distortion. The most common solution has been to bond the prepainted aluminum roof on after the paint bake ovens within trim and final (Fig. 24.2) using a 2K PU adhesive.

In addition to changes in material choice, the time to develop and launch new vehicles is always being reduced. Computer simulation helps to compress both the design phase and manufacturing, but the quality of the predicted output is only as good as the input data. An improved understanding of adhesives with regard to their material properties and rate sensitivity as well as their rheological behavior helps all aspects of the design and manufacturing processes. This understanding leads to improved specifications, which in turn leads to improved adhesives.

References

- [1] M. Keller, F150 The future of tough, EuroCarBody 2015, in: 17th Global Car Body Benchmarking Conference, 20–22 October 2015, Bad Nauheim, Germany, 2015.

-
- [2] 12 Week Total Vehicle Accelerated Corrosion Test, Ford Corporate Engineering Test Procedure (CETP) 00.00-R-343, 2013.
 - [3] Laboratory Accelerated Cyclic Corrosion Test, Ford Corporate Engineering Test Procedure (CETP) 00.00-L-467, 2008.
 - [4] Stress Durability Test for Adhesive Lap-Shear Bonds, Ford Laboratory Test Method (FLTM) BV 101-07, 2017.
 - [5] J.M. Marinelli, et al., Acid Pretreatment for Adhesive Bonding of Vehicle Assemblies, US Patent 6,167,609, 2001.
 - [6] National Highway Traffic Safety Administration (NHTSA) Federal Motor Vehicle Safety Standards (FMVSS). <https://www.nhtsa.gov/vehicle-manufacturers/test-procedures>. (Accessed 1 March 2022).
 - [7] P.I. Karkanis, I.K. Partridge, D. Attwood, Modelling the cure of a commercial epoxy resin for applications in resin transfer moulding, *Polym. Int.* 41 (2) (1996) 183–191.
 - [8] W.P. Cox, E.H. Merz, Correlation of dynamic and steady flow viscosities, *Polym. Sci.* 28 (1958) 619–622.
 - [9] M.L. William, R.F. Landel, J.D. Ferry, The temperature dependence of relaxation mechanism in amorphous polymers and other glass-forming liquids, *J. Am. Chem. Soc.* 77 (14) (1955) 3701–3707.
 - [10] Process Capability Index. https://en.wikipedia.org/wiki/Process_capability_index. (Accessed 1 March 2022).

This page intentionally left blank

Construction adhesives: Qualification, specification, quality control, and risk mitigation

25

Till Vallée, Marvin Kaufmann, and Morten Voß

Fraunhofer Institute for Manufacturing Technology and Advanced Materials IFAM,
Adhesive Bonding Technology and Surfaces, Bremen, Germany

25.1 Scope and structure of this chapter

As in many other industries, the construction sector now recognizes adhesive bonding as a promising joining technique to either complement or supplement the conventional methods usually used. However, civil engineering comes with a series of peculiarities that requires a different approach for the acceptance and implementation of adhesives for structural applications. Being part of a book dedicated to *Advances in Structural Adhesive Bonding*, this chapter will neither redefine the different adhesive classes nor will it address generalities regarding bonding-related concepts. This chapter highlights some of the differences among civil engineering and automotive, aeronautics, or aerospace applications, and explores the effect thereof on the status of adhesive bonding in construction.

Among the first notable differences is the fact that over the last centuries, the construction sector has branched into several sectors, most often defined along the main material used. Accordingly, while all civil engineers share most of the structural engineering if expressed in terms of theoretical background, as related to mechanics and dynamics, they soon specialize in geotechnics, structural steel, reinforced concrete, timber engineering, and more recently, fiber-reinforced polymers, etc. Because the nature of the substrate fundamentally affects adhesive bonding, it is impossible not to separate the influences of these specializations when it comes to adhesion science. Dedicated sections of this chapter will address the main points to consider regarding structural bonding on the most important branches of civil engineering.

In the automotive, aeronautics, and aerospace industries, trained and skilled staff often manufacture the adhesively bonded joints following very precisely defined procedures to minimize imperfections. Manufacturing also occurs indoors under controlled and clean environments. Additionally, because of the much higher added value of the products and the relatively limited size of corresponding bonded areas, aspects from surface preparation to tailored curing cycles can easily be implemented. For civil engineering, however, such idealized situations can rarely be achieved, especially when bonding is to be performed onsite. A dedicated section will discuss related aspects, including methods for quality control and risk mitigation.

As already hinted at, while having split into different specializations, civil engineering remains homogeneous in terms of structural mechanics. Thus, structural verification is almost always carried out in terms of comparing a metric of stresses to that of strength. While higher-order concepts, such as fracture mechanics, are increasingly being considered for design purposes in industries such as aeronautics, civil engineers remain reluctant to use them. Several reasons explain this “lukewarm interest” [1], among them the disruption with regard to classical mechanics, the (very) extensive experimental characterization required, and the significant numerical effort involved. For structural steel, concrete, and timber engineering, and to some extent fiber-reinforced polymers, structural verification is cast into codes or standards that follow a common logic. Designing of most mechanical fasteners is quite straightforward (determination of stresses therein, using relatively simple mechanics) and knowledge about their resistance is obtained through relatively simple testing, resp. tabulated values); additionally, bolts and dowels are tabulated in standardized grades and dimensions. The largely standardized approach is to some extent also valid for welded joints. For bonded joints, things become more complicated due to the wide range of joint configurations, materials to be joined, surface preparation methods, and available adhesives as well as their respective time, rate, temperature, and environmental dependencies. The repercussions of this particular situation regarding the designing process of adhesively bonded structural joints will be discussed in a separate section.

25.2 Adhesive bonding for typical civil engineering materials

When discussing aspects related to adhesive bonding in different civil engineering specializations, different aspects have to be considered. The first is the materials or combinations thereof constituting the substrates, and the second is the typical joint typologies specific to each of these. Finally, although to some extent related, we have to consider the specific load and environmental conditions to which bonded joints are exposed.

25.2.1 Structural steel

For structural steel construction, two main classes of joining techniques are most widely used. The first is mechanical fasteners, first in the form of rivets [2,3], bolts [4], and beginning in the 20th century, welding [5,6]. The second is adhesive bonding, which is a joining technique for structural steel structures that was introduced as late as the 1950s [7,8] in the form of bonded joints in bridges that are still in service as of 2020. The current state of research on structural bonding of steel structures has been recently documented by Albiez et al. [9,10], in which a series of circular hollow sections (CHS, or tubes) has been extensively investigated, including = adhesive selection, large-scale tests, and numerical modeling. A set of even more recent papers by Albiez et al. [11,12] presents the results of extensive research on large-scale adhesively bonded offshore structures.

At first glance, bonding on steel seems unproblematic, as most technical data sheets of adhesives characterize lap shear strength on this substrate, provided the surfaces are adequately pretreated. As discussed in more detail in [Chapter 9](#), surface pretreatment [13–17] increases the bond strength by, among others, increasing surface tension, increasing surface roughness, producing a fresh stable oxide layer, or introducing new or increased amounts of chemical functionalities [18]. Surface treatment methods range from relatively simple methods such as degreasing with organic solvents (acetone, isopropanol, methyl ethyl ketone, etc.) [19] to specially formulated chemical etching (e.g., nitric-phosphoric acid solution). The degree of roughness of metallic adherends is, in particular among practitioners, a common design option to increase adhesive strength [20]; the idea behind this is based on the concept of mechanical interlocking [21]. However, for structural steel applications, almost all steel surfaces are coated in some way for corrosion control, either with galvanized zinc coatings [22,23] or polymeric coatings [24–26], which introduces an additional potential failure layer. Unlike bonding on bare and grit-blasted steel, bonding on galvanized zinc coating requires special attention, and is additionally dependent upon the specifics of the galvanization process, as significant differences were observed between “hot-dipped” [27] and “electroplated” [28] substrates. Bonding strength on organic coatings is very often limited by the capacity of the coating on the steel substrate [29,30], which results in significant strength reduction compared to bonding on the uncoated bare steel surface. It is important to note that surface pretreatment methods for galvanized and coated steel surfaces are restricted to preserve their integrity.

In a study on adhesively bonded steel joints, Vallée et al. [31] investigated a series of surface pretreatments including—in increasing order of complexity of the application—simple wiping of the surface with isopropanol, application of a primer, using a domestic cleaner (BrefPower from Henkel), and using an acid pickling cleaner (SurTec480 from SurTec). The authors showed that increasing the complexity of the surface pretreatment significantly enhanced the lap shear strength. However, they also demonstrated that the associated effort, lasting up to 45 min per joint, proved economically unrealistic under onsite conditions. Although significant differences were observed under idealized laboratory conditions (at +23°C), these benefits nearly vanished at +60°C, leading the authors to recommend the relatively basic wiping with a solvent. This example illustrates well the importance of balancing theoretically possible methods with the constraints of practical considerations, especially in light of the scale of many civil applications.

25.2.2 Timber engineering

The growing interest in adhesive bonding in timber engineering is largely due to the fact that traditional mechanical timber joining techniques represent a serious limitation on the use of timber in more demanding applications, such as multistory buildings [32,33] and bridges [34]. This limitation is particularly relevant when timber is used in conjunction with other materials, especially concrete [35], steel, or glass [36] in structural contexts. One of the most important factors that distinguishes adhesive bonding with timber is the very nature of the timber itself: a natural, anisotropic, hygroscopic, and inhomogeneous material [37], the bonding of which is discussed in more detail in

Chapter 13. This makes the analysis of bonded joints composed thereof nearly impossible using analytical formulas [38–40], for which reason stress determination relies on finite element analysis (FEA) [41,42].

Besides clear, or solid, softwood and hardwood, the construction sector makes wide use of so-called engineered wood products (EWP), such as glued laminated timber (GLT), laminated veneer lumber (LVL), cross-laminated timber (CLT), etc., which are by themselves dependent upon adhesives. The bonding of wood is not considered difficult per se [43–45]. While adhesive development initially focused on softwoods, current research shows that hardwoods can also be used to form strong and durable bonds [46,47]. For onsite bonding, it is almost necessary to use two-component (2K) adhesives, mostly 2K epoxies and 2K polyurethanes [46,48].

Discarding the mostly academic lap shear joints [42] seldom used in practice, the most prominent and successful bonded joint in timber engineering is certainly the glued-in rod (GiR). As its name strongly indicates, it consists of one (or multiple) steel and FRP rods bonded into solid wood or EWP; it is amply described in [49]. GiR has been the subject of numerous experimental studies on almost all aspects including rod type (threaded rods [50], rebars [51], G-FRP [52], etc.), adhesives (cold-cured, and accelerated curing 2K-epoxies and polyurethanes [53], etc.), and substrate (GLT, LVL [46] and CLT [54], etc.) Their extensive numerical modeling with FEA in conjunction with either fracture mechanics (FM [55]) or probabilistic methods (PM [41]) permitted a very good understanding of the failure mechanisms involved as well as accurate prediction of their load capacity. Contrary to what earlier researchers thought, joint strength was not dictated by the axial tensile strength of the wood (or EWP), but more so by the transverse tensile strength in conjunction with shear strength [41].

Experimental investigations on the influence of different manufacturing methods, imperfections, and defects on the load-bearing capacity of GiR have shown that this type of bonded joint is relatively robust. Kohl et al. [56] showed that various manufacturing methods of increasing complexity had a negligible influence on joint capacity. More significantly, the influence of various contaminations of oil, moisture, dust, and corrosion on the rods proved to have no statistically significant influence on joint strength. Only excessive amounts of sawdust led to a significant reduction of strength. Similar observations were made by Ratsch et al. [57].

A series of experiments has shown that the curing process of GiR, which normally lasts up to several days, can be dramatically shortened by the use of induction [53] and resistive [58] heating without significantly altering the mechanical performance of the joints. Besides shortening curing times, induction heating allowed the process to be carried out under low temperatures [59]. For the sake of completeness, similar positive experimental results were reported by Voß et al. [53] at room temperature and under low temperatures [60]; the authors also presented a numerical model for the curing progress within their GiR [61,62].

25.2.3 Concrete

Epoxy resin adhesives proved to produce very stiff and strong bonds to concrete that fail in a brittle manner [63,64]; they are favored if severe environmental factors are expected [65]. Furthermore, 2K polyurethane adhesives can also be used for bonding

concrete, such as to form steel-concrete hybrid beams, as done in [66]. For some material combinations, such as concrete-stainless steel, 2K methacrylate adhesives were also found to be suitable [67]. According to Chaudhary et al. [63], 2K epoxies and, in some cases, 2K polyurethanes are predominantly used nowadays for structural bonding and reinforcing of concrete-steel joints in the construction industry. Shear tests on bonded concrete-steel composite slabs have shown that shear stresses of up to 11 MPa can be transmitted in the adhesive joints (made of 2K epoxy resin adhesive), whereby the concrete cohesively fails close to the adhesive layer [63,68].

Steel bolts (heavy-duty anchors) adhesively bonded into holes drilled in concrete can transmit high tensile forces. For example, the Powerbond heavy-duty anchor system from the company fischer, which has obtained a European technical approval, can transmit approved tensile forces of up to 45.6 kN (anchorage depth 192 mm, M16 thread, normal concrete C20/25, adhesive: injection mortar) [69], which corresponds to an ultimate shear stress of 4.7 MPa. However, this method has one major drawback: the execution of a borehole in reinforced concrete with subsequent cleaning of the concrete surface requires significant effort.

For joining high-strength concrete components, the conventional joining techniques (embedded anchors) are not suitable, as these components are very delicate. The use of adhesives is an alternative solution that offers some advantages. Scheerer et al. [70] investigated the behavior of bonded microreinforced high-strength concrete-concrete joints using mineral mortars as adhesives. The following results were obtained for finger-jointed concrete slabs subjected to tensile loading, as commonly practiced in timber construction. If the flank inclination angle is steep enough, (ductile) failure of the reinforcement occurs in the joint area. In this case, brittle adhesive failure of the interfaces can be ruled out by appropriate design. The maximum transmissible forces are roughly comparable to those of undisturbed concrete components.

Surface treatment has a significant influence on the bond strength. There are various methods for treating concrete surfaces: sandblasting, mechanical grinding, brushing with a wire brush, high-pressure water jetting, and chemical methods for surface pretreatment. Sandblasting the concrete surface can provide the greatest improvement in transferring tensile and shear forces [63]. If other materials are involved, such as carbon fiber-reinforced polymers, the use of primers significantly improved bond strength [71].

25.2.4 Glass

The use of glass in architecture has steadily increased over the last decades, and structural glazing is now an integral part of civil engineering and architecture. Structural engineering had to follow by offering specific technical solutions for joining very dissimilar materials such as steel, concrete, and timber to glass. By the inherent very brittle nature of glass, connecting it is a challenging task, in particular if glass is to be part of the structural system. The natural reflex engineers developed toward the issue of brittleness was for a long time, and still is, to limit as much as possible the global structure from the critical glass elements; this is either achieved through mechanical

connectors or by the use of very flexible adhesives that greatly reduce stresses in general and stress peaks in particular. This design philosophy is perfectly mirrored in the reference code for structural glazing at the European level, the ETAG 002 [72], which implicitly enforces the limitation of silicones as adhesives. In North America, acrylics, such as pressure-sensitive tape [73,74], are also used. Silicones and acrylic tapes, by their relatively low stiffnesses compared to other adhesive classes commonly used for structural purposes, allow for large relative deformations, but at the price of relatively low strength. Added to that, effects such as silicone's significant tendency to creep. The associated low creep resistance, pose additional limits on the mechanical performance of silicone joints, as well as of hybrid structures joined thereof and in which glass is expected to be structurally active.

Among the first to report on adhesively bonded timber-glass connections were Kreher et al. [75] in an industrial implementation of timber-glass composite girders consisting of glass webs and wood flanges bonded by a hot-melt polyurethane. Based on laboratory tests, creep under "assumed maximum loads" was expected to stabilize after 4 weeks; measurements onsite showed deformations amounting to only a third of the expected value. Cruz and Pequeno [76] performed shear tests on Douglas fir bonded to laminated and tempered glass using silicones, polyurethanes, acrylates, and epoxies. The results showed a strong dependency of the fracture behavior on the adhesive stiffness, with two extreme situations occurring: adhesives exhibiting high strength and stiffness but brittle failure, and ductile and flexible adhesives with low mechanical resistance. The authors advocated the use of the "best balance" between these two. In subsequent research, Pequeno and Cruz [77] experimentally investigated hybrid timber-glass beams and panels with spans of up to 3200 mm in four-point bending. In comparison to equivalent traditional timber panels, capacity and stiffness were significantly higher, leading the authors to conclude that "timber provides ductility and glass offers stiffness," and these were successfully numerically modeled. Similar research was carried out by Kozłowski [78–80] and Blyberg et al. [81,82] on timber-glass I-beams, timber-glass columns, and timber-glass frames, all bonded using several types of adhesives. Among the counterintuitive findings of these studies was the fact that adhesively bonding glass need not always be performed using extremely soft silicones or acrylates, but that structural epoxies might represent a more appropriate substitute. This is interesting because structural epoxies exhibit much better behavior under environmental loads, and are thus more durable.

25.2.5 Fiber-reinforced polymers

Although joining of fibrous composite material is in principle possible by means of mechanical fasteners, for which a huge corpus of dedicated literature exists [83–87], it is generally agreed upon that adhesive bonding is a much more material adapted joining technique [88–92]. For the sake of completeness, the reader is reminded that hybrid joints, in which mechanical fasteners are combined with adhesives, aim at combining the best of two worlds [93–97].

The vast majority of experimental and numerical work related to adhesively bonded joints related to composites has been carried out on the arguably simplest

forms of bonded joints [98], either single- or double-lap joints, for which this article does not attempt to overview. Adhesively bonded joints composed of FRP tubes were analyzed both experimentally [99] and numerically [100] by Voß et al., who also pointed out that geometrical imperfections (such as offsetting and misalignment of the center lines) resulted in little influence on joint strength. Similar research was performed by Vallée et al. [93] on hybrid joints involving FRP tubes bonded and bolted to a flat profile, from which the authors concluded that most of the load was carried by the bonded connection, leaving almost no load share to the bolts. Budhe et al. [90] identified the most important parameters influencing the performance of bonded FRP joints, which include the bonding process itself, surface preparation, bondline thickness, joint configuration, overlap length, and the material properties of the FRP and the adhesive. However, the authors point out that, “*there is no generalized relationship between the bonded joint strength with respect to the geometric parameters (overlap length, bondline thickness and joint configuration) as there are other factors such as adhesive material properties (ductile or brittle), type of loading, adherend material, etc., involved.*” It will suffice at this point to remind that failure is highly dependent on the sharp stress peaks generated at the ends of the overlaps [101,102], that the load capacity increases with the overlap length [103,104], and that the transverse tensile strength of the laminate is at least as significant as its shear strength [105]. Although analytical methods are still advocated to analyze bonded joints of FRP [40], provided simple geometries are considered [106], the anisotropic nature of the material makes it almost mandatory to consider FEA [107]. For a realistic estimate of the load capacity, or strength, of adhesively bonded FRP joints, it is additionally necessary to account for the mechanics leading to failure, and for which several models compete [108], including fracture mechanics, cohesive zone element models, interface element models, multiple point constraint models, kinking crack models, repeating representative volume element (RVE), etc.

25.3 Structural verification

25.3.1 Civil engineering practice

Over the last two centuries, civil engineering has developed a relatively coherent conceptual framework for designing structures. While this chapter doesn't focus on these aspects, it is important to recognize some of the difficulties that designing adhesive bonding encounters in construction; the interested reader may consult [109,110] for more details. Structural analysis for construction strongly depends on the concept of verification, in which stresses are maintained below resistance. Most related procedures act at the level of cross-sections, with related geometrical quantities as (first and second) moments of area being central. For the most part, corresponding mechanics are developed for linear elements, typically beams, frames, etc. Adhesively bonded joints, however, cannot be described by such approaches. Their mechanics are clearly different. Stress determination has developed into a domain of its own [38–40], and is

currently almost exclusively performed numerically [106]. On the other hand, there is no clearly defined metric for what would constitute the “resistance of a bonded joint.”

25.3.2 What makes designing bonded joints so particular?

Three peculiarities of bonded joints make their designing so arduous: the stress peaks often predicted at their ends, the brittleness associated with some systems, and the inherent scatter in measured strength. Engineers have devised several techniques to circumvent the issues associated with stress peaks. These include considering the stresses at a distance [111], averaging over a zone [112], refining the modeling to account for fillets and roundings [113,114], empirical factors locally increasing the strength [102,115], etc. Such methods have no sound mechanical justification, and usually require calibration against experimental data.

To overcome such limitations, scientists and engineers have resorted to enhanced modeling techniques, such as fracture mechanics (FM [116]) or probabilistic methods (PM [117]). FM, including the cohesive zone modeling (CZM) derived thereof, creates disruption with regard to classical mechanics and usual design schemes, a reason for which "*many engineers show only lukewarm interest*" [1] in related procedures. FM is based upon a very extensive experimental characterization, and CZM requires determination and numerical implementation of cohesive laws, with both significantly depending upon geometrical specifications of the joints. Besides that, both methods are almost out of reach for the common civil engineer due to the numerical complexity they entail. Somewhat obscured by the dominant position FM and CZM take, alternatives such as PM remain quite underrepresented, despite offering a simple yet reliable approach to predict the strength of adhesively bonded joints that is compatible with the procedures common to civil engineering [105,118,119].

25.3.3 Suggestion

What are the reasons behind the noteworthy peculiarity of adhesive bonding? Both adhesive as a material and adhesive bonding as a joining technique have been widely investigated at almost all levels of complexity. Yet this accumulated knowledge has not diffused into useful codes and standards to safely dimension adhesively bonded joints. The dichotomy between available and implemented knowledge is mainly due to two reasons. The first is the lack of specific qualification of designers regarding the new technology and the sheer extension of specific knowledge required. The second is the attempt to clone “traditional” codes and standards where uniform approaches are desired. These issues have been recognized in other industries, such as railway and automotive [120], and more general solutions were offered that did not mimic traditional forms of coding but instead consider adhesive bonding as a process, and not merely a joint. This is, in essence, what modern codes regulating the use of adhesive bonding, such as DIN 2304 [121,122], aim to reach. By empowering the user, focusing on traceable processes, and adapting the requirements, including structural verification procedures, according to the level of safety required by any adhesively bonded connection, EN DIN 2304 is almost a stand-alone code that could

already be fully implemented in daily designing practice. While being extremely precise in the application, it remains very general in terms of compatibility with the requirement of any industry. Thus, it does not interfere with current civil engineering codes and standards, and has the potential to unleash the full potential of adhesive bonding.

25.4 Manufacturing, quality control and risk mitigation

25.4.1 Adhesive selection

The selection of appropriate adhesives is the single most crucial step for the design of any structural bond. It is also, at least for civil engineers, the most difficult one. On problem is the great diversity of adhesive classes [123] (acrylics, epoxies, polyurethanes, and silicones, to name the most relevant ones for construction), in one-component (1K) and two-component (2K) variants, and the literally thousands of different commercially available products on the market. Certainly as important as the previously mentioned is the difficulty civil engineers encounter in handling the different characteristics adhesives possess and which go beyond what they are used to, such as their temperature, load history, and moisture/environment dependence. Besides the purely mechanical aspects, such as strength and stiffness discussed at a later stage, adhesives possess many other properties that have to be accounted for. Excluding such aspects as ductility and brittleness, which may not be as stringent for bonding materials such as glass, aspects such as environmental conditions (in particular service temperature), durability (temperature, humidity, and other environmental agents), workability (e.g., aspects related to viscosity), and process (pot-life, time to cure, etc.) must be considered. These are linked to metrics such as glass transition temperature, rheology, curing kinetics, etc., for which civil engineers have not been prepared by their curricula.

Yet another aspect, to which no metric can easily be attached is the influence of the surface prior to bonding. There is a large consensus that surfaces have to be clean and grease-free (using solvent cleaning). It is also known that the capacity of adhesives to enhance the formation of chemical and mechanical bonds between the adherend and the adhesive is improved by a series of surface preparation methods [124], such as grit-blasting [125], plasma [17], laser [126], etc. The effect of the methods is either assessed by direct comparison of strength, such as lap shear, or by the analysis of chemical changes induced on treated coupons by a variety of techniques (XPS, CA, FTIR, etc.) However, it must be borne in mind that not everything that appears possible at the laboratory scale is also feasible under the conditions prevailing onsite, as factors such as cost and personnel qualification are paramount.

To add another layer of complexity, most of the previously mentioned aspects are heavily dependent upon the geometry and size of the considered joints. Most academic work, and the recommendations derived thereof, is performed on lap shear-sized samples. When scaling up joint size, most notably overlap length, the influence of the

properties of the adhesive become notably less dominant, as shown by Albiez et al. in [9–12]. In both studies, adhesives with significantly different mechanical properties on the bulk (tensile strength and stiffness) and lap-shear (lap-shear strength) levels led (with dimensions in tens of mm) to almost indistinguishable properties of large-scale joints (with dimensions counted in hundreds of mm). This feature, already known to scientists in the mid-1940s [127], makes it difficult for practitioners to simply scale up the strength of any joint from data known on another scale.

25.4.2 Influence of imperfections

Because of the difficulties associated with the bonding process, it is often argued that under the specific conditions prevailing in construction sites, it is not possible to meet the high-quality requirements for bonded joints typically encountered in other industries [128]. Aforementioned questions have received significant attention for metallic substrates or composite materials [129–132] as well as timber engineering [56,57,133]. Very early on, the use of adhesively bonded joints in timber engineering was subjected to very high standards to ensure that the “*joints are correctly designed, the work is done by experienced operatives, and strict quality control is exercised*” [134]. The question of the influence of typical defects and imperfections on the quality and joint capacity of bonded joints is regularly being asked by practitioners and regulating bodies. Mostly, the answer is to enforce extremely tight quality control to avoid defects [49,135]. Examples thereof are given by the few codes and standards that regulate GiR, such as DIN 1052-10:2012-05, which in practice prohibits any gluing operations outside controlled environments. Accordingly, from the perspective of codes and standards, the most important issues that prevent bonded joints from being used in practice are manufacturing quality, potential imperfections, defects, and the uncertainties related to the influence thereof on joint performance. However, studies such as that by Grunwald et al. [133] showed that for bonded joints composed of wooden substrates, the influence of defects on the load capacity was less pronounced than commonly assumed by practitioners.

Gonzales et al. [136] experimentally investigated typical imperfections encountered by practitioners when manufacturing GiR, and concluded that “*it is not imperative that the threaded rods be perfectly centered, nor correctly aligned in their bore holes*” to achieve reproducible results. Kohl et al. [56] reported on a large experimental campaign in which threaded rods were deliberately contaminated with various agents (oil, water, corrosion), and the performance of GiR made thereof, and compared the results to “perfectly clean” reference probes. The authors concluded that “*glued-in rod connections could be considered fairly robust with regard to manufacturing defects.*” Similar results were obtained by Ratsch et al. [57], who showed not only that only large voids resulted in significant reductions of joint strength but that results also depended upon the adhesive type, with polyurethanes being much more sensitive to moisture compared to epoxies. Similarly, Albiez et al. [9,10] highlighted the relatively minor effect of geometrical imperfections, such as misalignment and offsetting, on the load capacity of bonded joints for structural steel applications. In yet another study, Voß et al. [99] experimentally verified the

limited influence that various geometrical imperfections (center-line offset and misalignment, profile ovalization) have on the load-bearing capacity of adhesively bonded G-FRP tubes, despite the fact that these had a significant impact on the generated stresses [100].

25.5 Conclusions

25.5.1 Current situation

The status of structural bonding in the construction sector laid out in this chapter shows that adhesives are increasingly being used in combination with almost all materials used in civil engineering. While codes, standards, and regulations exist for some isolated applications (e.g., structural glazing, glued-in rods, etc.), there is yet no general ruling on how to proceed. This is in large part because adhesive bonding is difficult to encompass within the traditional means used in engineering.

There are multiple reasons for that, and the following are certainly the most critical. Adhesive bonding is a technology that is still in the midst of a substitution phase. This phase, which every newly introduced technology and material goes through, results in a series of drawbacks. Adhesive bonding may be misused, such as by just “replacing” other means of connections by a layer of adhesive, in the hope that no further changes are required. Practitioners inexperienced with adhesives are tempted to apply old recipes to new ingredients; this may lead them to take risks looking for designing procedures they think of being equivalent from other contexts, but which ultimately are not. Most practitioners look for formulas such as for the determination of stresses, verification methods to validate a design, reduction or adaptation factors to account for any deviation of perfect conditions, such as temperature, moisture or whatever etc. They also think exclusively in terms of the adhesive as being a material and completely discard the fact that although it is an important component, aspects such as joint geometry, scale, and time cannot be ignored to describe the bonded joint. Due to that, they think that each of the aforementioned aspects can singlehandedly be described by some fudge factor-labelled conversion factor. Oversensitive to questions of quality control, defects, nondestructive testing, etc., they think that absolute perfection is required for every single adhesively bonded joint, making the perfect the enemy of the good.

Aimed at shedding some light in that complexity, the rare attempts to standardize and codify adhesive bonding, such as that composite materials [137] introduce, ultimately add more confusion. Some codes prescribe specific designing methods, such as the use of outdated analytical formulas that end up restricting their use to a small subset of joint typologies [138], or by listing a fracture mechanics formula [139] but leaving the user clueless on how to use it. Others tackle problems such as temperature by imposing constraints on the glass transition temperature of the adhesive, discarding clear evidence that adhesive's T_g is not a natural limit if considered at the joint level. Some others, considering adhesive bonding's issues so insurmountable, simply impose a ban on any structural application. These severe limitations and useless

burdens contradict daily practice in other industries. For structural glazing, as an example, simple stress verifications are perfectly acceptable; in the railway industry, structural bonding has become commonplace.

If formulated this way, the conundrum's tenets are strikingly similar to those encountered by a joining technique that is now more than 100 years old, welding. Welding codes are usually distinct from other construction codes insofar as they impose qualification of the personnel involved at various process stages (the welding engineer), and stagger requirements according to the severity of the failure of welded joints [140].

25.5.2 Quality control and risk mitigation

There is obviously a need for a bonding-specific approach required for correct application of the technology, which has to be considered a "process" rather than a "material," as has been the case for decades with welding technology. Such approaches are nowadays used for structural bonding in the railway industry, both DIN 6701 [141] and DIN 2304 [142]. Both codes address in a straightforward manner all issues typically encountered by previous attempts to codify adhesive bonding, and appropriately ensure the required quality control and risk mitigation.

Adhesive bonding coordinators of adhesive bonding work—The definition of qualified personnel for all aspects related to adhesive bonding to ensure that the process is in safe hands, from the early stage of the design to structural verification and execution. Suitable persons for appointment as an adhesive bonding coordinator at a user or company are employees having responsibility for adhesive bonding and related tasks. Their suitability and technical knowledge (acquired through education, extra occupational training, and/or relevant experience) must be demonstrated and documented by means of recognizable documents issued by accredited third parties.

Classification of bonded joints in accordance with safety requirements—A code or standard shall classify adhesively bonded joints into safety classes based on the estimated consequences (intended by the component designer) should the adhesively bonded joint fail. Other requirements such as suitability for use with foods, fire protection regulations, emission regulations, and work safety when manufacturing bonded joints are not considered when classifying bonded joints under these standards. There are already other standards and regulations for these aspects.

Structural verification—Codes should not enforce a specific verification format, such as the variety of substrates, adhesives, joint typologies, and dimensions, and load type is too broad to be handled with one universal approach. Accordingly, dependent upon the aforesaid and considering the required safety level, different approaches, including experimental component testing, documented experience, and analytical and numerical modeling, shall be explicitly allowed, including in mutual combination provided the designer is adequately certified.

References

- [1] K.B. Broberg, Fracture mechanics? Theoria or tekhné? *Int. J. Fract.* 57 (1) (1992) 85–99, <https://doi.org/10.1007/BF00013009>.
- [2] T. Leslie, Built like bridges: iron, steel, and rivets in the nineteenth-century skyscraper, *J. Soc. Archit. Hist.* 69 (2) (2010) 234–261, <https://doi.org/10.1525/jsah.2010.69.2.234>.
- [3] A.R. de Jonge, Riveted Joints: a critical review of the literature covering their development, *Am. Soc. Mech. Eng.* (1945).
- [4] C. Batho, E.H. Bateman, *Investigations on Bolts and Bolted Joints, Second Report of the Steel Structures Research Committee*, London, 1934.
- [5] S.A. David, T. Debroy, Current issues and problems in welding science, *Science* 257 (5069) (1992) 497–502, <https://doi.org/10.1126/science.257.5069.497>.
- [6] J. Moody, *The Railroad Builders: A Chronicle of the Welding of the States*, Yale University Press, 1919.
- [7] A. Dörnen, G. Trittler, Kombinierte Eisenbahn-und Straßenbrücke über den Lippe-Seiten-Kanal der Chemischen Werke Hüls AG, *Marl. Der Stahlbau* 27 (1) (1958) 7–9.
- [8] J. Ritchie, P. Gregory, Improvements in bolted joint efficiency by the addition of cold-setting resin mixture, *Struct. Eng.* 37 (6) (1959) 1751–1777.
- [9] M. Albiez, T. Vallée, H. Fricke, T. Ummenhofer, Adhesively bonded steel tubes. Part I. Experimental investigations, *Int. J. Adhes. Adhes.* 90 (2019) 199–210, <https://doi.org/10.1016/j.ijadhadh.2018.02.005>.
- [10] M. Albiez, T. Vallée, T. Ummenhofer, Adhesively bonded steel tubes. Part II. Numerical modelling and strength prediction, *Int. J. Adhes. Adhes.* 90 (2019) 211–224, <https://doi.org/10.1016/j.ijadhadh.2018.02.004>.
- [11] M. Albiez, J. Damm, T. Ummenhofer, M. Kaufmann, T. Vallée, S. Myslicki, Hybrid joining of jacket structures for offshore wind turbines—determination of requirements and adhesive characterisation, *Eng. Struct.* 259 (2022), 114186, <https://doi.org/10.1016/j.engstruct.2022.114186>.
- [12] M. Albiez, J. Damm, T. Ummenhofer, H. Ehard, C. Schuler, M. Kaufmann, et al., Hybrid joining of jacket structures for offshore wind turbines—validation under static and dynamic loading at medium and large scale, *Eng. Struct.* 252 (2022), 113595, <https://doi.org/10.1016/j.engstruct.2021.113595>.
- [13] N. Anagreh, R. Dweiri, S. Masadeh, Characterization of adhesively bonded high strength steel surfaces treated with grit blasting and self-indicating pretreatment (SIP) adhesion mediator, *Mater. Test.* 59 (10) (2017) 891–902, <https://doi.org/10.3139/120.111094>.
- [14] J.L. Cotter, R. Kohler, The influence of surface pretreatment on the durability of adhesively-bonded aluminium alloys in humid and corrosive environments, *Int. J. Adhes. Adhes.* 1 (1) (1980) 23–28, [https://doi.org/10.1016/0143-7496\(80\)90030-5](https://doi.org/10.1016/0143-7496(80)90030-5).
- [15] J. Custódio, J.G. Broughton, H. Cruz, P. Winfield, Activation of timber surfaces by flame and corona treatments to improve adhesion, *Int. J. Adhes. Adhes.* 29 (2009) 167–172.
- [16] S. Ebnesajjad, C. Ebnesajjad, *Surface Treatment of Materials for Adhesive Bonding*, William Andrew, 2013.
- [17] C. Rodríguez-Villanueva, N. Encinas, J. Abenojar, M.A. Martínez, Assessment of atmospheric plasma treatment cleaning effect on steel surfaces, *Surf. Coat. Technol.* 236 (2013) 450–456, <https://doi.org/10.1016/j.surfcoat.2013.10.036>.
- [18] A. Baldan, Adhesively-bonded joints and repairs in metallic alloys, polymers and composite materials: adhesives, adhesion theories and surface pretreatment, *J. Mater. Sci.* 39 (1) (2004) 1–49, <https://doi.org/10.1023/B:JMSC.0000007726.58758.e4>.

- [19] D.S. Irwin, T.C. Johnson, *Comparison of Solvents for Cleaning Metal Surfaces*, Dow Chemical Company, Rocky Flats Plant, 1964.
- [20] C.W. Jennings, Surface roughness and bond strength of adhesives, *J. Adhes.* 4 (1) (1972) 25–38, <https://doi.org/10.1080/00218467208072208>.
- [21] K.W. Allen, Some reflections on contemporary views of theories of adhesion, *Int. J. Adhes. Adhes.* 13 (2) (1993) 67–72, [https://doi.org/10.1016/0143-7496\(93\)90015-2](https://doi.org/10.1016/0143-7496(93)90015-2).
- [22] A.R. Marder, The metallurgy of zinc-coated steel, *Prog. Mater. Sci.* 45 (3) (2000) 191–271, [https://doi.org/10.1016/S0079-6425\(98\)00006-1](https://doi.org/10.1016/S0079-6425(98)00006-1).
- [23] S. Shibli, B.N. Meena, R. Remya, A review on recent approaches in the field of hot dip zinc galvanizing process, *Surf. Coat. Technol.* 262 (2015) 210–215, <https://doi.org/10.1016/j.surfcoat.2014.12.054>.
- [24] M. Kitayama, K. Yoshida, T. Kamon, T. Michishita, K. Kaneta, Y. Suzuki, Examination of heavy-duty, ultra-thick coating systems for offshore steel structures, *ISIJ Int.* 25 (11) (1985) 1163–1170, <https://doi.org/10.2355/isijinternational1966.25.1163>.
- [25] M. Fukushima, S. Hashimoto, T. Tsuji, Development and progress of anti-corrosive coating in the marine atmosphere, in: W. Kato, B.C. Gerwick, M. Homma, R. Lenschow, O.T. Magoon, C.C. Mei, et al. (Eds.), *Ocean Space Utilization '85: Proceedings of the International Symposium Nihon University, Tokyo, Japan, June 1985*, vol. 2, Springer Japan, Tokyo, 1985, pp. 531–538.
- [26] A.A. Olajire, Recent advances on organic coating system technologies for corrosion protection of offshore metallic structures, *J. Mol. Liq.* 269 (2018) 572–606, <https://doi.org/10.1016/j.molliq.2018.08.053>.
- [27] G.W. Critchlow, K.H. Bedwell, M.E. Chamberlain, Pretreatments to improve the bondability of hot dipped galvanized mild steel, *Trans. IMF* 76 (6) (1998) 209–212, <https://doi.org/10.1080/00202967.1998.11871225>.
- [28] R.T. Foister, S.L.F. Niks, M.J. Barker, Strength loss mechanisms for adhesive bonds to electroplated zinc and cold rolled steel substrates subjected to moist environments, *J. Adhes.* 30 (1–4) (1989) 105–118, <https://doi.org/10.1080/00218468908048200>.
- [29] A. Momber, L. Fröck, T. Marquardt, Nachträgliches klebtechnisches Fügen von Haltern auf bereits beschichtete Stahloberflächen, *Stahlbau* 89 (11) (2020) 923–931, <https://doi.org/10.1002/stab.202000020>.
- [30] S. Myslicki, H. Kordy, M. Kaufmann, R. Créac'hacdec, T. Vallée, Under water glued stud bonding fasteners for offshore structures, *Int. J. Adhes. Adhes.* 98 (2020), 102533, <https://doi.org/10.1016/j.ijadhadh.2019.102533>.
- [31] C. Denkert, T. Gerke, R. Glienke, M. Dörre, M.K. Henkel, H. Fricke, et al., Experimental investigations on pre-tensioned hybrid joints for structural steel applications, *J. Adhes.* (2021) 1–36, <https://doi.org/10.1080/00218464.2021.2003786>.
- [32] V. Žegarac Leskovar, M. Premrov, A review of architectural and structural design typologies of multi-storey timber buildings in Europe, *Forests* 12 (6) (2021) 757, <https://doi.org/10.3390/f12060757>.
- [33] I. Smith, A. Frangi, Overview of design issues for tall timber buildings, *Struct. Eng. Int.* 18 (2) (2008) 141–147, <https://doi.org/10.2749/101686608784218833>.
- [34] M.P. Ansell, D. Smedley, Briefing: Bonded-in technology for structural timber, *Proc. Inst. Civil Eng. Construct. Mater.* 160 (3) (2007) 95–98, <https://doi.org/10.1680/coma.2007.160.3.95>.
- [35] T. Tannert, A. Gerber, T. Válee, Hybrid adhesively bonded timber-concrete-composite floors, *Int. J. Adhes. Adhes.* 97 (2020), 102490, <https://doi.org/10.1016/j.ijadhadh.2019.102490>.
- [36] T. Válee, C. Grunwald, L. Milchert, S. Fecht, Design and dimensioning of a complex timber-glass hybrid structure: the IFAM pedestrian bridge, *Glass Struct. Eng.* 1 (1) (2016) 3–18, <https://doi.org/10.1007/s40940-016-0007-4>.

- [37] T. Vallée, T. Tannert, S. Fecht, Adhesively bonded connections in the context of timber engineering—a review, *J. Adhes.* 93 (4) (2016) 257–287, <https://doi.org/10.1080/00218464.2015.1071255>.
- [38] O. Volkersen, Die Nietkraftverteilung in zugbeanspruchten Nietverbindungen mit konstanten Laschenquerschnitten, *Luftfahrtforschung* 15 (1/2) (1938) 41–47.
- [39] M. Goland, E. Reissner, The stresses in cemented joints, *J. Appl. Mech.* 11 (1944) A17–A27.
- [40] L.F. da Silva, P.J. das Neves, R.D. Adams, J.K. Spelt, Analytical models of adhesively bonded joints. Part I. Literature survey, *Int. J. Adhes. Adhes.* 29 (3) (2009) 319–330, <https://doi.org/10.1016/j.ijadhadh.2008.06.005>.
- [41] C. Grunwald, T. Vallée, S. Fecht, O. Bletz-Mühldorfer, F. Diehl, L. Bathon, et al., Rods glued in engineered hardwood products. Part II. Numerical modelling and capacity prediction, *Int. J. Adhes. Adhes.* 90 (2019) 182–198, <https://doi.org/10.1016/j.ijadhadh.2018.05.004>.
- [42] T. Tannert, T. Vallée, S. Hehl, Experimental and numerical investigations on adhesively bonded timber joints, *Wood Sci. Technol.* 46 (1–3) (2012) 579–590.
- [43] C.R. Frihart, Adhesive bonding and performance testing of bonded wood products, *J. ASTM Int.* 2 (7) (2005) 12952, <https://doi.org/10.1520/JAI12952>.
- [44] F. Stoeckel, J. Konnerth, W. Gindl-Altmatter, Mechanical properties of adhesives for bonding wood—a review, *Int. J. Adhes. Adhes.* 45 (2013) 32–41, <https://doi.org/10.1016/j.ijadhadh.2013.03.013>.
- [45] J. Custódio, J. Broughton, H. Cruz, A review of factors influencing the durability of structural bonded timber joints, *Int. J. Adhes. Adhes.* 29 (2) (2009) 173–185, <https://doi.org/10.1016/j.ijadhadh.2008.03.002>.
- [46] C. Grunwald, T. Vallée, S. Fecht, O. Bletz-Mühldorfer, F. Diehl, L. Bathon, et al., Rods glued in engineered hardwood products. Part I. Experimental results under quasi-static loading, *Int. J. Adhes. Adhes.* 90 (2019) 163–181, <https://doi.org/10.1016/j.ijadhadh.2018.05.003>.
- [47] S. Fecht, T. Vallée, T. Tannert, H. Fricke, Adhesively bonded hardwood joints under room temperature and elevated temperatures, *J. Adhes.* 90 (5-6) (2014) 401–419, <https://doi.org/10.1080/00218464.2013.836968>.
- [48] M. Verdet, A. Salenikovich, A. Cointe, J.-L. Coureau, P. Galimard, W. Munoz Toro, et al., mechanical performance of polyurethane and epoxy adhesives in connections with glued-in rods at elevated temperatures, *Bioresources* 11 (4) (2016), <https://doi.org/10.15376/biores.11.4.8200-8214>.
- [49] G. Tlustochowicz, E. Serrano, R. Steiger, State-of-the-art review on timber connections with glued-in steel rods, *Mater. Struct.* 44 (5) (2011) 997–1020, <https://doi.org/10.1617/s11527-010-9682-9>.
- [50] D.O. Chans, J.E. Cimadevila, E.M. Gutiérrez, Withdrawal strength of threaded steel rods glued with epoxy in wood, *Int. J. Adhes. Adhes.* 44 (2013) 115–212.
- [51] Z. Ling, H. Yang, W. Liu, W. Lu, D. Zhou, L. Wang, Pull-out strength and bond behaviour of axially loaded rebar glued-in glulam, *Constr. Build. Mater.* 65 (2014) 440–449, <https://doi.org/10.1016/j.conbuildmat.2014.05.008>.
- [52] C. Grunwald, M. Kaufmann, B. Alter, T. Vallée, T. Tannert, Numerical investigations and capacity prediction of G-FRP rods glued into timber, *Compos. Struct.* 202 (2018) 47–59, <https://doi.org/10.1016/j.compstruct.2017.10.010>.
- [53] N. Ratsch, S. Böhm, M. Voß, M. Adam, J. Wirries, T. Vallée, Accelerated curing of glued-in threaded rods by means of inductive heating. Part I. Experiments, *J. Adhes.* (2019) 1–26, <https://doi.org/10.1080/00218464.2019.1654864>.
- [54] G.S. Ayansola, T. Tannert, T. Vallée, Experimental investigations of glued-in rod connections in CLT, *Constr. Build. Mater.* (2022), 126680.
- [55] S. Myslicki, T. Vallée, O. Bletz-Mühldorfer, F. Diehl, L.C. Lavarec, Créac'Hcadec R., Fracture mechanics based joint capacity prediction of glued-in rods with beech laminated

- vener lumber, *J. Adhes.* 16 (3) (2018) 1–20, <https://doi.org/10.1080/00218464.2018.1538879>.
- [56] D. Kohl, N. Ratsch, S. Böhm, M. Voß, M. Kaufmann, T. Vallée, Influence of manufacturing methods and imperfections on the load capacity of glued-in rods, *J. Adhes.* 96 (8) (2020) 738–759, <https://doi.org/10.1080/00218464.2018.1508351>.
- [57] N. Ratsch, S. Böhm, M. Voß, M. Kaufmann, T. Vallée, Influence of imperfections on the load capacity and stiffness of glued-in rod connections, *Constr. Build. Mater.* 226 (2019) 200–211, <https://doi.org/10.1016/j.conbuildmat.2019.07.278>.
- [58] N. Ratsch, M. Burnett-Barking, S. Böhm, S. Myslicki, M. Voß, M. Adam, et al., Resistive curing of glued-in rods, *Constr. Build. Mater.* (2020), 121127, <https://doi.org/10.1016/j.conbuildmat.2020.121127>.
- [59] N. Ratsch, M. Burnett-Barking, S. Böhm, M. Voß, M. Adam, M. Kaufmann, et al., Accelerated curing of glued-in threaded rods by means of inductive heating. Part IV. Curing under low temperatures, *J. Adhes.* (2020) 1–26, <https://doi.org/10.1080/00218464.2020.1818562>.
- [60] M. Voß, T. Evers, T. Vallée, Low-temperature curing of adhesives—large-scale experiments, *J. Adhes.* (2022) 1–36, <https://doi.org/10.1080/00218464.2022.2059353>.
- [61] M. Voß, M. Kaufmann, T. Vallée, Curie-supported accelerated curing by means of inductive heating. Part I. Model building, *J. Adhes.* (2021) 1–44, <https://doi.org/10.1080/00218464.2021.1902810>.
- [62] M. Voß, M. Kaufmann, T. Vallée, Curie-supported accelerated curing by means of inductive heating. Part II. Validation and numerical studies, *J. Adhes.* (2021) 1–33, <https://doi.org/10.1080/00218464.2021.1951712>.
- [63] P. Kumar, A. Patnaik, S. Chaudhary, A review on application of structural adhesives in concrete and steel?: Concrete composite and factors influencing the performance of composite connections, *Int. J. Adhes. Adhes.* 77 (2017) 1–14, <https://doi.org/10.1016/j.ijadhadh.2017.03.009>.
- [64] R.A. Barnes, G.C. Mays, The transfer of stress through a steel to concrete adhesive bond, *Int. J. Adhes. Adhes.* 21 (6) (2001) 495–502, [https://doi.org/10.1016/S0143-7496\(01\)00031-8](https://doi.org/10.1016/S0143-7496(01)00031-8).
- [65] A. Çolak, T. Çoşgun, A.E. Bakırcı, Effects of environmental factors on the adhesion and durability characteristics of epoxy-bonded concrete prisms, *Constr. Build. Mater.* 23 (2) (2009) 758–767, <https://doi.org/10.1016/j.conbuildmat.2008.02.013>.
- [66] L. Bouazaoui, G. Perrenot, Y. Delmas, A. Li, Experimental study of bonded steel concrete composite structures, *J. Constr. Steel Res.* 63 (9) (2007) 1268–1278, <https://doi.org/10.1016/j.jcsr.2006.11.002>.
- [67] M. Kaluža, J. Hulimka, Methacrylate adhesives to create CFRP laminate-steel joints—preliminary static and fatigue tests, *Procedia Eng.* 172 (2017) 489–496, <https://doi.org/10.1016/j.proeng.2017.02.057>.
- [68] Y.N. Ziraba, M.H. Baluch, I.A. Basunbul, A.K. Azad, G.J. Al-Sulaimani, A.M. Sharif, Combined experimental-numerical approach to characterization of steel-glue-concrete interface, *Mater. Struct.* 1995 (28) (1995) 518–525.
- [69] Elevated technology. [April 26, 2022]; Available from: <https://www.fischer.group/en/press/press-releases/fischer-fixing-systems/thyssen-testturn>.
- [70] S. Scheerer, M. Curbach, *Leicht Bauen mit Beton: Klebverbindungen für Platten- und Scheibenbauteile aus hochfestem Beton*, 2022.
- [71] L. Ye, K. Friedrich, C. Weimer, Y.-W. Mai, Surface treatments and adhesion bonding between concrete and a CFRP composite, *Adv. Compos. Mater.* 7 (1) (1998) 47–61, <https://doi.org/10.1163/156855198X00048>.

- [72] ETAG 002, *Guidelines for European Technical Approval for Structural Sealant Glazing System(002)*, EOTA, 2012.
- [73] B.W. Townsend, D.C. Ohanehi, D.A. Dillard, S.R. Austin, F. Salmon, D.R. Gagnon, Characterizing acrylic foam pressure sensitive adhesive tapes for structural glazing applications. Part II. Creep rupture results, *Int. J. Adhes. Adhes.* 31 (7) (2011) 650–659, <https://doi.org/10.1016/j.ijadhadh.2011.06.018>.
- [74] B.W. Townsend, D.C. Ohanehi, D.A. Dillard, S.R. Austin, F. Salmon, D.R. Gagnon, Characterizing acrylic foam pressure sensitive adhesive tapes for structural glazing applications. Part I. DMA and ramp-to-fail results, *Int. J. Adhes. Adhes.* 31 (7) (2011) 639–649, <https://doi.org/10.1016/j.ijadhadh.2011.06.017>.
- [75] K. Kreher, J. Natterer, J. Natterer, Timber-glass-composite girders for a hotel in Switzerland, *Struct. Eng. Int.* 14 (2) (2004) 149–151, <https://doi.org/10.2749/101686604777963964>.
- [76] P.J.S. Cruz, J. Pequeno, Timber-Glass Composite Beams: Mechanical Behaviour & Architectural Solutions, Available from: http://cn.tttower.com/files/scientific-articles/02_Delft2008_b.pdf.
- [77] J. Pequeno, P. Cruz, Structural Timber-Glass Linear System: Characterization & Architectural Potentialities, *Glass Performance Days*, 2009.
- [78] M. Kozłowski, J. Hulimka, Load-bearing capacity of hybrid timber-glass beams, *Arch. Civil Eng. Environ.* 2 (2014).
- [79] M. Kozłowski, M. Kadela, J. Hulimka, Numerical investigation of structural behaviour of timber-glass composite beams, *Procedia Eng.* 161 (2016) 990–1000, <https://doi.org/10.1016/j.proeng.2016.08.838>.
- [80] M. Kozłowski, E. Serrano, B. Enquist, Experimental investigation on timber-glass composite I-beams, in: C. Louter, F. Bos, J. Belis, J.-P. Lebet (Eds.), *Challenging Glass 4 & COST Action TU0905 Final Conference*, CRC Press, 2014, pp. 261–268.
- [81] L. Blyberg, M. Lang, K. Lundstedt, M. Schander, E. Serrano, M. Silfverhielm, et al., Glass, timber and adhesive joints—innovative load bearing building components, *Constr. Build. Mater.* 55 (2014) 470–478, <https://doi.org/10.1016/j.conbuildmat.2014.01.045>.
- [82] L. Blyberg, E. Serrano, B. Enquist, M. Sterley, Adhesive joints for structural timber/glass applications: experimental testing and evaluation methods, *Int. J. Adhes. Adhes.* 35 (2012) 76–87, <https://doi.org/10.1016/j.ijadhadh.2012.02.008>.
- [83] A.M. Girão Coelho, J.T. Mottram, A review of the behaviour and analysis of bolted connections and joints in pultruded fibre reinforced polymers, *Mater. Des.* 74 (2015) 86–107, <https://doi.org/10.1016/j.matdes.2015.02.011>.
- [84] K.J. Jadee, A.R. Othman, Fiber reinforced composite structure with bolted joint—a review, *KEM* 471–472 (2011) 939–944, <https://doi.org/10.4028/www.scientific.net/KEM.471-472.939>.
- [85] A. Galińska, Mechanical joining of fibre reinforced polymer composites to metals—a review. Part I. Bolted joining, *Polymers (Basel)* 12 (10) (2020), <https://doi.org/10.3390/polym12102252>.
- [86] A. Galińska, C. Galiński, Mechanical joining of fibre reinforced polymer composites to metals—A review. Part II. Riveting, clinching, non-adhesive form-locked joints, pin and loop joining, *Polymers (Basel)* 12 (8) (2020) 1681, <https://doi.org/10.3390/polym12081681>.
- [87] S.D. Thoppul, J. Finegan, R.F. Gibson, Mechanics of mechanically fastened joints in polymer-matrix composite structures—a review, *Compos. Sci. Technol.* 69 (3–4) (2009) 301–329, <https://doi.org/10.1016/j.compscitech.2008.09.037>.
- [88] J.R. Vinson, Adhesive bonding of polymer composites, *Polym. Eng. Sci.* 29 (19) (1989) 1325–1331, <https://doi.org/10.1002/pen.760291904>.

- [89] G. Jeevi, S.K. Nayak, K.M. Abdul, Review on adhesive joints and their application in hybrid composite structures, *J. Adhes. Sci. Technol.* 33 (14) (2019) 1497–1520, <https://doi.org/10.1080/01694243.2018.1543528>.
- [90] Budhe S., Banea M.D., Barros S de, da Silva L.. An updated review of adhesively bonded joints in composite materials. *Int. J. Adhes. Adhes.* 2017;72:30–42. <https://doi.org/10.1016/j.ijadhadh.2016.10.010>.
- [91] I.A. Ashcroft, D.J. Hughes, S.J. Shaw, Adhesive bonding of fibre reinforced polymer composite materials, *Assem. Autom.* 20 (2) (2000) 150–161, <https://doi.org/10.1108/01445150010321797>.
- [92] E.A. Armanios, R.B. Bucinell, D.W. Wilson, L.J. Hart-Smith, Adhesive bonding of composite structures—progress to date and some remaining challenges, *J. Compos. Technol. Res.* 24 (3) (2002) 133, <https://doi.org/10.1520/CTR10566J>.
- [93] T. Vallée, T. Tannert, R. Meena, S. Hehl, Dimensioning method for bolted, adhesively bonded, and hybrid joints involving fibre-reinforced-polymers, *Compos. Part B: Eng.* 46 (2013) 179–187, <https://doi.org/10.1016/j.compositesb.2012.09.074>.
- [94] L.F.M. da Silva, A. Pironi, A. Öchsner (Eds.), *Hybrid Adhesive Joints*, Springer Berlin Heidelberg, Berlin, Heidelberg, 2011.
- [95] L.J. Hart-Smith, Bonded-bolted composite joints, *J. Aircr.* 22 (11) (1985) 993–1000, <https://doi.org/10.2514/3.45237>.
- [96] G. Kelly, Load transfer in hybrid (bonded/bolted) composite single-lap joints, *Compos. Struct.* 69 (1) (2005) 35–43, <https://doi.org/10.1016/j.compstruct.2004.04.016>.
- [97] J.H. Oh, Y.G. Kim, D.G. Lee, Optimum bolted joints for hybrid composite materials, *Compos. Struct.* 38 (1–4) (1997) 329–341, [https://doi.org/10.1016/S0263-8223\(98\)80014-7](https://doi.org/10.1016/S0263-8223(98)80014-7).
- [98] M.D. Banea, L.F.M. da Silva, *Adhesively bonded joints in composite materials: an overview*, *Proc. Inst. Mech. Eng. L: J. Mater. Des. Appl.* 223 (1) (2009) 1–18.
- [99] M. Voß, J. Haupt, Accelerated curing of adhesively bonded G-FRP tube connections. Part I. Experiments, *Compos. Struct.* 268 (2021), 113999, <https://doi.org/10.1016/j.compstruct.2021.113999>.
- [100] M. Voß, T. Vallée, M. Kaufmann, Accelerated curing of adhesively bonded G-FRP tube connections. Part III. Modelling of strength, *Compos. Struct.* 268 (2021), 113900, <https://doi.org/10.1016/j.compstruct.2021.113900>.
- [101] T. Vallée, J.R. Correia, T. Keller, Probabilistic strength prediction for double lap joints composed of pultruded GFRP profiles. Part II. Strength prediction, *Compos. Sci. Technol.* 66 (13) (2006) 1915–1930, <https://doi.org/10.1016/j.compscitech.2006.04.001>.
- [102] T. Keller, T. Vallée, Adhesively bonded lap joints from pultruded GFRP profiles. Part II. Joint strength prediction, *Compos. Part B: Eng.* 36 (4) (2005) 341–350, <https://doi.org/10.1016/j.compositesb.2004.11.002>.
- [103] T. Keller, T. Vallée, Adhesively bonded lap joints from pultruded GFRP profiles. Part I. Stress-strain analysis and failure modes, *Compos. Part B: Eng.* 36 (4) (2005) 331–340, <https://doi.org/10.1016/j.compositesb.2004.11.001>.
- [104] T. Vallée, J.R. Correia, T. Keller, Probabilistic strength prediction for double lap joints composed of pultruded GFRP profiles. Part I. Experimental and numerical investigations, *Compos. Sci. Technol.* 66 (13) (2006) 1903–1914, <https://doi.org/10.1016/j.compscitech.2006.04.007>.
- [105] T. Vallée, T. Keller, G. Fourestey, B. Fournier, J.R. Correia, Adhesively bonded joints composed of pultruded adherends: considerations at the upper tail of the material strength statistical distribution, *Probab. Eng. Mech.* 24 (3) (2009) 358–366, <https://doi.org/10.1016/j.proengmech.2008.10.001>.

- [106] L.F.M. da Silva, das Neves PC, Adams RD, Wang A, Spelt JK., Analytical models of adhesively bonded joints. Part II. Comparative study, *Int. J. Adhes. Adhes.* 29 (3) (2009) 331–341, <https://doi.org/10.1016/j.ijadhadh.2008.06.007>.
- [107] X. He, A review of finite element analysis of adhesively bonded joints, *Int. J. Adhes. Adhes.* 31 (4) (2011) 248–264, <https://doi.org/10.1016/j.ijadhadh.2011.01.006>.
- [108] M. Park, Modeling and analysis of composite bonded joints, *AJMIE* 2 (1) (2017) 1, <https://doi.org/10.11648/j.ajmie.20170201.11>.
- [109] T. Vallée, M. Kaufmann, R.D. Adams, M. Albiez, J.R. Correia, T. Tannert, Are probabilistic methods a way to get rid of fudge factors? Part I. Background and theory, *Int. J. Adhes. Adhes.* (2022).
- [110] T. Vallée, A. Groß, A critical look at the current status on the design regulations for structural adhesively bonded joints of fibre reinforced polymers, in: A. Ilki, M. Ispir, P. Inci (Eds.), *10th International Conference on FRP Composites in Civil Engineering*, Springer International Publishing, Cham, 2022, pp. 2390–2397.
- [111] D. Taylor, The theory of critical distances, *Eng. Fract. Mech.* 75 (7) (2008) 1696–1705, <https://doi.org/10.1016/j.engfracmech.2007.04.007>.
- [112] J.D. Clark, I.J. McGregor, Ultimate tensile stress over a zone: a new failure criterion for adhesive joints, *J. Adhes.* 42 (4) (1993) 227–245, <https://doi.org/10.1080/00218469308026578>.
- [113] R.D. Adams, N.A. Peppiatt, Stress analysis of adhesive-bonded lap joints, *J. Strain Anal.* 9 (3) (1974) 185–196, <https://doi.org/10.1243/03093247V093185>.
- [114] T. Vallée, T. Tannert, J. Murcia-Delso, D.J. Quinn, Influence of stress-reduction methods on the strength of adhesively bonded joints composed of orthotropic brittle adherends, *Int. J. Adhes. Adhes.* 30 (7) (2010) 583–594, <https://doi.org/10.1016/j.ijadhadh.2010.05.007>.
- [115] T. Vallée, T. Keller, Adhesively bonded lap joints from pultruded GFRP profiles. Part III. Effects of chamfers, *Compos. Part B: Eng.* 37 (4–5) (2006) 328–336, <https://doi.org/10.1016/j.compositesb.2005.11.002>.
- [116] A.-A. Griffith, The phenomena of rupture and flow in solids, *Philos. Trans. R. Soc. Lond. Ser. A, Contain. Papers Math. Phys. Charact.* 221 (582–593) (1921) 163–198, <https://doi.org/10.1098/rsta.1921.0006>.
- [117] A.M. Freudenthal, *Statistical Approach to Brittle Fracture. Fracture, An Advanced Treatise, II*, 1968, pp. 591–619.
- [118] T. Tannert, T. Vallée, S. Hehl, Probabilistic strength prediction of adhesively bonded timber joints, *Wood Sci. Technol.* 46 (1-3) (2012) 503–513.
- [119] T. Vallée, M. Kaufmann, R.D. Adams, M. Albiez, J.R. Correia, T. Tannert, Are probabilistic methods a way to get rid of fudge factors? Part II. Application, *Int. J. Adhes. Adhes.* (2022).
- [120] A. Groß, H. Lohse, New DIN 2304 standard and its use in practice, *Adhes. Adhes. Sealants* 12 (4) (2015) 12–17, <https://doi.org/10.1007/s35784-015-0534-4>.
- [121] A. Paul, K. Brune, Professional implementation of adhesive bonding processes, *Adhes. Adhes. Sealants* 13 (4) (2016) 10–13, <https://doi.org/10.1007/s35784-016-0033-2>.
- [122] DIN 2304-1:2020-04, *Klebtechnik_ - Qualitätsanforderungen an Klebprozesse_ - Teil_1: Prozesskette Kleben*, Beuth Verlag GmbH, Berlin, 2020, <https://doi.org/10.31030/3138880>.
- [123] B. Hussey, J. Wilson, Basic classes of adhesive, in: B. Hussey, J. Wilson (Eds.), *Structural Adhesives: Directory and Databook*, Springer US, Boston, MA, 1996, pp. 1–5.
- [124] D. Fernando, J.G. Teng, T. Yu, X.L. Zhao, Preparation and characterization of steel surfaces for adhesive bonding, *J. Compos. Constr.* 17 (6) (2013) 4013012, [https://doi.org/10.1061/\(ASCE\)CC.1943-5614.0000387](https://doi.org/10.1061/(ASCE)CC.1943-5614.0000387).

- [125] B. Wang, X. Hu, P. Lu, Improvement of adhesive bonding of grit-blasted steel substrates by using diluted resin as a primer, *Int. J. Adhes. Adhes.* 73 (2017) 92–99, <https://doi.org/10.1016/j.ijadhadh.2016.11.012>.
- [126] H.R. Jahani, B. Moffat, R. Mueller, D. Fumo, W. Duley, T. North, et al., Excimer laser surface modification of coated steel for enhancement of adhesive bonding, *Appl. Surf. Sci.* 127–129 (1998) 767–772, [https://doi.org/10.1016/S0169-4332\(97\)00738-1](https://doi.org/10.1016/S0169-4332(97)00738-1).
- [127] N.A. de Bruyne, The strength of glued joints, *Aircr. Eng. Aerosp. Technol.* 16 (4) (1944) 115–118, <https://doi.org/10.1108/eb031117>.
- [128] D.N. Markatos, K.I. Tserpes, E. Rau, S. Markus, B. Ehrhart, S. Pantelakis, The effects of manufacturing-induced and in-service related bonding quality reduction on the mode-I fracture toughness of composite bonded joints for aeronautical use, *Compos. Part B: Eng.* 45 (1) (2013) 556–564, <https://doi.org/10.1016/j.compositesb.2012.05.052>.
- [129] R.D. Adams, P. Cawley, A review of defect types and nondestructive testing techniques for composites and bonded joints, *NDT Int.* 21 (4) (1988) 208–222, [https://doi.org/10.1016/0308-9126\(88\)90333-1](https://doi.org/10.1016/0308-9126(88)90333-1).
- [130] R. Tamborrino, D. Palumbo, U. Galietti, P. Aversa, S. Chiozzi, V.A.M. Luprano, Assessment of the effect of defects on mechanical properties of adhesive bonded joints by using nondestructive methods, *Compos. Part B: Eng.* 91 (2016) 337–345, <https://doi.org/10.1016/j.compositesb.2016.01.059>.
- [131] T.T. Wang, F.W. Ryan, H. Schonhorn, Effect of bonding defects on shear strength in tension of lap joints having brittle adhesives, *J. Appl. Polym. Sci.* 16 (8) (1972) 1901–1909, <https://doi.org/10.1002/app.1972.070160804>.
- [132] H. Schonhorn, F.W. Ryan, T.T. Wang, Effects of symmetrical bonding defects on tensile shear strength of lap joints having ductile adhesives, *J. Appl. Polym. Sci.* 15 (5) (1971) 1069–1078, <https://doi.org/10.1002/app.1971.070150503>.
- [133] C. Grunwald, S. Fecht, T. Vallée, T. Tannert, Adhesively bonded timber joints—Do defects matter? *Int. J. Adhes. Adhes.* 55 (2014) 12–17, <https://doi.org/10.1016/j.ijadhadh.2014.07.003>.
- [134] J. Broughton, A. Hutchinson, Adhesive systems for structural connections in timber, *Int. J. Adhes. Adhes.* 21 (3) (2001) 177–186, [https://doi.org/10.1016/S0143-7496\(00\)00049-X](https://doi.org/10.1016/S0143-7496(00)00049-X).
- [135] M. Stepinac, V. Rajčić, F. Hunger, J.-W. van de Kuilen, R. Tomasi, E. Serrano, Comparison of Design Rules for Glued-In Rods and Design Rule Proposal for Implementation in European Standards, 2013.
- [136] E. Gonzales, T. Tannert, T. Vallee, The impact of defects on the capacity of timber joints with glued-in rods, *Int. J. Adhes. Adhes.* 65 (2016) 33–40, <https://doi.org/10.1016/j.ijadhadh.2015.11.002>.
- [137] J.L. Clarke, *Structural Design of Polymer Composites: Eurocomp Design Code and Background Document*, CRC Press, 2014.
- [138] I. van Straalen, J. Wardenier, L.B. Vogelesang, F. Soetens, Structural adhesive bonded joints in engineering—drafting design rules, *Int. J. Adhes. Adhes.* 18 (1) (1998) 41–49, [https://doi.org/10.1016/S0143-7496\(97\)00068-7](https://doi.org/10.1016/S0143-7496(97)00068-7).
- [139] L. Ascione, J.-F. Caron, P. Godonou, K. van Ijsselmuiden, J. Knippers, T. Mottram, et al., Prospect for New Guidance in the Design of FRP Support to the Implementation, Harmonization and Further Development of the Eurocodes, 2016.

-
- [140] R. Singh (Ed.), *Applied Welding Engineering*, Butterworth-Heinemann, Boston, 2012.
- [141] DIN. DIN 6701-3:2015-12, Adhesive Bonding of Railway Vehicles and Parts. Guideline for Construction Design and Verification of Bonds on Railway Vehicles(DIN 6701). Berlin: Beuth Verlag GmbH. <https://doi.org/10.31030/2351433>.
- [142] DIN. Adhesive Bonding Technology—Quality Requirements for Adhesive Bonding Processes. Part 1. Adhesive Bonding Process Chain (DIN 2304). Berlin: Beuth Verlag GmbH. <https://doi.org/10.31030/2399371>.

This page intentionally left blank

General industrial adhesive applications: Qualification, specification, quality control, and risk mitigation

26

Mario Madrid^a, Jani Turunen^b, and Wolfgang Seitz^c

^aHenkel AG & Co. KGaA, Düsseldorf, Germany, ^bValmet Technologies, Inc., Espoo, Finland,

^cAurora Lichtwerke GmbH, Eichstätt, Germany

26.1 Usage of adhesives in general industry

Although the transportation industries were early adopters of engineering adhesive solutions, there are many other industrial sectors where adhesively bonded joints are commonly chosen to meet joining needs and overcome assembly challenges. These industries have leveraged adhesive applications and adapted best qualification and quality control practices to meet their different needs. This chapter is intended to shed some light on applications in these industries, often grouped under the term “general industry,” for which adhesives have played a key role in the development of innovative designs as well as in the reduction of manufacturing and maintenance costs.

26.1.1 General industry end-user sectors, trends, and outlook

To facilitate an understanding of industrial drivers, needs, and the most relevant applications, the authors propose a high-level segmentation based on the following industry clusters or sectors:

- Capital goods: Encompassing heavy machines used for extraction, transformation, infrastructure, and manufacturing processes. Examples include centrifugal pumps and steam turbines.
- Durable goods: Typically, devices or machines acquired by consumers and expected to be used for a long period of time. These include refrigerators and loudspeakers, among many other examples.
- Consumable goods: Disposable, one-use, perishable, or replaceable components or items that are expected to last for a relatively short period of time or just be used once or for limited times. That is the case of filters and cutting tools as well as a range of less-structural products.

Just as the process and performance requirements of the joints and assemblies of the items and devices found in the sectors above vary greatly among industries, so do the adhesive technologies required to comply with them. Adhesive manufacturers and

industrial users have responded to these needs to meet the unique requirements to satisfy the evolving demands for efficient manufacturing, lightweighting, durable performance, and safety.

26.1.2 Engineering adhesive main functionality areas

Adhesive applications for general industrial sectors are not limited to providing structural integrity to load-bearing structures or attaching subcomponents to those structures. There are other functionalities highly relevant to achieve the intended performance of the final goods, ranging from thermal and/or electrical insulation/conductivity to mechanical integrity. Adhesives can also be used to hold wear-resistant components in place or even be applied as protective coatings themselves. The wide variety of needs in general industry greatly broadens the portfolio of engineering solutions needed to comply with every customer requirement, for which the term “engineering adhesives” is probably more appropriate [1].

Every engineering adhesive use case addressing a specific customer assembly challenge is often referred to as an application or “job to be done.” Indeed, customers typically demand complete assembly solutions beyond just the mere adhesive formulation meeting the assembly performance requirements. This leads not only to the need to set additional adhesive requirements for the manufacturing process, but also to the design and integration of the manufacturing and maintenance procedures within the customer operations.

Conceived as a full assembly solution, applications can be classified as follows:

- Assembly of primary structures, for which structural adhesives play a crucial role in the integrity of the main structure, reducing its weight and increasing its resistance to fatigue. Typical use cases can be found in wind turbine blades and recreational vehicles.
- Assembly of secondary structures, requiring structural adhesives to keep parts or components attached to the main structure, although not intended to contribute to its structural integrity. Adhesive usage for secondary structures may avoid substrate damage, reduce part count, and improve load transfer. That is the case for the assembly of displays in handheld devices, for example.
- Mechanical assembly, involving adhesives that fill and unitize mostly metal interfaces in machines to reinforce and seal them as well as improve the performance of mechanical and fluid management machines. Engineering adhesive usage for mechanical assembly may help prevent self-loosening of threaded parts, avoid reduction of clamping load between flanges, and eliminate leakage in machinery assemblies.
- Electrical assembly, for which adhesives are used to insulate electrical connections, transfer heat, and unitize subassemblies to improve electrical machinery efficiency and durability. Electrically insulating, curable resins play a fundamental role in modern electrical machines, providing electrical insulation and mechanical strength, reducing manufacturing costs, and facilitating heat dissipation in interphases where thermal conductivity is required.
- Electronics assembly, applied during the manufacturing process of printed circuit boards (PCBs) to facilitate and accelerate the assembly as well as to improve the performance and durability of the electronic components themselves. Electronics adhesives provide unique performance benefits including resistance to impact, capacity to absorb substrate deformation due to differential thermal expansion, and stability under harsh environments.

- Assembly automation, or the dispensing and control equipment necessary to the integration of engineering adhesives in the production lines. Durable goods manufactured in large series such as loudspeakers or light bulbs require highly automated assembly workstations. In contrast, capital goods such as machine tools often require a high degree of customization and are manufactured individually or in small batches. Therefore, engineering adhesives are applied using manual dispensing equipment.
- Surface protection, involving adhesives and coatings that hold or supplement wear protection elements or build a protective barrier themselves. Sometimes, gap-filling adhesives are used to rebuild a worn substrate. Engineering adhesives used for surface protection allow for the fast repair of damaged components versus long waiting times often required for spare part replacement. This significantly reduces downtime in critical machinery, thus reducing activity stoppage and limiting economic loss.

Finally, the literature sometimes refers to another application family that encompasses adhesive chemistries featuring significantly lower strength or load transfer capabilities. These so-called “nonstructural” applications are typically found in many consumable goods. Despite often having limited mechanical properties, these applications still need to comply with very demanding process requirements linked to the highly automated processes required for mass production. Likewise for the applications mentioned earlier, the adhesive qualification and specification are driven by engineers that also need to put in place stringent quality control and risk mitigation measurements that guarantee end products comply with the requirements.

26.1.3 Assembly of primary structures

Primary structures following monocoque construction principles and requiring structural adhesives became mainstream in the aerospace industry in the early 20th century but were rapidly adopted by cars and other transportation vehicles shortly thereafter. Bonded structures also became popular in general industry by the mid-20th century, where lightweight construction improves the performance and saves costs during operation, such as for the manufacture of yachts and trailers or in new designs of elevator cabins and their elements of construction.

It is worth noting that primary structures are intrinsically large constructions because they are often designed to ship goods, carry passengers, or hold bulky and/or heavy loads. Large construction sizes definitively have a direct impact on the requirements demanded of the engineering adhesives being chosen, as elaborated later in this section.

The performance requirements of structural adhesives for load-bearing primary structural applications are fundamentally determined by thermomechanical properties. High dynamic strength and durability within the operational temperature range are factors that top the list of requirements. The design of the overall joint configuration is crucial and oftentimes requires the use of sophisticated modeling techniques (finite element analysis, FEA) to assess and prevent the failure of the adhesive joint. In addition, the durability of the bonded joint must not be compromised, and therefore process requirements need to be carefully balanced with risk mitigation measurements. Designing both the structure itself and its manufacturing process should be

tackled together to guarantee satisfactory performance as well as anticipate the potential risk of failure of the structure. Notice that design requirements are especially stringent for the aerospace and civil engineering industries, where redundant joints are typically added for fail-safe designs. Structures involving significant risks and liabilities are not that usual in general industry, although when required, solutions such as hybrid bonded fastened joints [2] can be applied.

In contrast, for general industry applications, driving costs down by eliminating process bottlenecks becomes a more prominent factor in the design of adhesively bonded primary structures. Unfortunately, this becomes quite challenging because adhesives used for long or large structures are difficult to automate, as they need to be applied in larger volumes and fill larger bondline gaps with wider tolerances. The adhesive cure mechanism necessary to meet such requirements often relies on two-component adhesives, which greatly increases the complexity of the manufacturing process. This leads to an important investment in assembly automation, including metering and dispensing equipment as well as handling and lifting machinery and structures. This is rarely affordable for industries other than aerospace. Therefore, most assembly applications designed for primary structures in general industry are labor intensive.

Typically, primary structures were seldom repaired in general industrial applications, except for collision repair in the vehicle aftermarket. However, the regulatory framework is rapidly changing toward enabling the circularity of the economy, prolonging the service life of primary structures and thus reducing waste. That's the case of wind turbine blade repair, for example.

It is not uncommon to find primary structure applications being named after the structural elements being assembled, as in direct glazing when bonding the windshields to the vehicle body, blade bonding for wind turbines, or stiffener bonding for structural panels.

Finally, sealing applications are found in primary structures for which the selection of the appropriate sealant capable of absorbing and compensating both part tolerance and dimensional change under working conditions is paramount.

26.1.4 *Assembly of secondary structures*

For secondary structures, adhesive performance attributes are still key, but process requirements are probably more important. Secondary structures in general industry are often placed within primary structures, which provides extra protection against aging factors. In addition, secondary structures are often smaller and bonding is usually easier to automate. The challenge ultimately depends on developing easy-to-dispense, fast-cure adhesives that comply with the performance requirements.

Bonded joint size matters, especially when it comes to defining process requirements. Most structures in mid- to small-sized goods can be considered secondary. Provided that these constructions typically pose limited risks for the end user, both safety factors and quality parameters applied in their design and manufacturing are less stringent than those for primary structures.

Smaller items normally lead to subcomponent assemblies whose bondlines have narrower tolerances and thinner gaps. This allows selecting cure mechanisms based on one-component, surface-activated technologies. Automation is simpler, enabling production scale-up and the reduction of overall manufacturing costs. In service, the replacement of worn-out subcomponents is typically carried out by dispensing the adhesive from smaller containers that are far more convenient for maintenance operations.

Likewise in primary structures, applications in secondary structures are sometimes named after the type of subcomponent being assembled. This approach is common in the commercial literature, for instance it can be found in the documentation for hand-held device assembly, where application names such as “enclosure bonding” or “display bonding” are found. However, application names based on the substrate can be rather recommendable because the substrate nature is often a key factor determining the chemistry of the adhesive to be selected, therefore leading to polymer, metal, ceramics, composites, and natural materials bonding applications.

26.1.5 Mechanical assembly

While structural integrity is the primary demand for primary and secondary assemblies, guaranteeing the solidarity between components is the main function for mechanical assembly. Metal surface irregularities present in interfaces are often the root cause of mechanical failures in machines. For instance, micromovements between matching flanges or bolt-threaded flanks produce well-known, undesired phenomena such as fretting corrosion or self-loosening, respectively. Leakages in threaded connections and flanged joints are usually produced by solid sealants, such as PTFE or hemp, with limited capacity to block fluids from finding their pathway through the surface roughness. Increasing the surface flatness helps but does not solve the problem, and does involve higher machining costs.

The total consumption of mechanical assembly engineering adhesives is often far more relevant during maintenance because machines are manufactured once but serviced several times during their lifetime, especially for heavy machinery. Mechanical subcomponents as bearings or seals are subjected to fatigue and, thus, to wear and tear. Worn components might need to be replaced, which leads to the repeated use of mechanical assembly adhesives.

The classic mechanical assembly applications augmenting joint strength are threadlocking, retaining, and flange coupling. Although other applications such as form-in-place gasketing and thread sealing contribute to the strength of the joint, they primarily have a sealing function [3].

26.1.6 Electrical assembly

Electrical assembly refers to adhesively bonded joints typically found in electrical machines such as rotating machines, including motors and generators, and static devices, including transformers and batteries. The adhesives selected must maintain the required electrical properties such as electrical resistivity and dielectric strength at

the operating conditions during the lifetime of the electrical equipment. The literature often refers to the term “electrical insulating materials” [4], which encompasses not only curable resins (including adhesives, impregnation resins, and coatings) but also solid materials (including tapes, mica, plastics, and ceramics) and fluids (such as electrical oils or insulating gases). Standards such as IEC60034-1 [5] and NEMA MG1-12.43 [6] classify insulating materials in different classes according to their performance, which allows electrical engineers to select the appropriate insulating solutions required to build electrical machines.

The latest engineering adhesive developments are disrupting some of the traditional assembly processes, not only by enabling the automation of the manufacturing process but also by maximizing the efficiency of the electrical machines during operation.

Servicing electrical assemblies is expected to become an even more prominent market, mostly triggered by the adoption of electric vehicles. Going forward, the growth of the circular economy may further accelerate the development of repair and maintenance solutions for electrical assemblies. Among the most common electrical assembly applications are the impregnation of windings, the encapsulation (typically in the form of potting and casting) of windings and lamination stacks, and the bonding of lamination stacks or permanent magnets.

26.1.7 Electronics assembly

The electronics industry is probably one of the areas where engineering adhesives are most extensively used. Modern PCBs could not be as affordable and therefore as ubiquitous as they are today, if adhesives hadn't allowed this important industrial sector to accelerate and scale PCB manufacturing processes. Also, modern adhesives for microelectronics were specifically developed to enhance device performance while significantly reducing size, with remarkable advantages for many applications [7].

The electrical properties of the adhesives selected for electronics assembly are again fundamental; however, other requirements such as their uncured rheology or chemical purity play key roles in state-of-the-art electronics. The fastest surface mounting technology (SMT) pick and place machines can mount as many as 200,000 components per hour [8], or nearly 56 chips per second, which is only possible with chipbonders having unique rheological properties. On the other hand, the miniaturization of the components themselves makes them vulnerable to traces of halogens, heavy metals, or radioactive isotopes; this translates into expensive adhesive formulations made of contaminant-free, ultrapure raw materials.

With the progressive size reduction of microelectronics, servicing and repairing them has become quite challenging. However, regulations such as WEEE [9] and RoHS [10] in Europe are bringing back the need to reconsider the repair of electronics subcomponent assemblies as an option to prolong the life span of the machines containing electronics.

There is a wide variety of electronics assembly applications, including bonding, underfilling, and the encapsulation of electronic components on the board. Some

applications provide special properties to the bondlines, for instance in heat transfer or electrically conductive bonding applications.

26.1.8 Assembly automation

Sometimes underplayed by adhesive suppliers, but indisputably as important as the adhesives themselves at the very least, assembly automation equipment is an essential element of the total assembly solution demanded by the end-user industries [11]. In today's engineering adhesive market, the seamless marriage between adhesives and automation is undoubtedly essential to gain a competitive edge versus other alternative assembly methods such as welding or riveting, which managed to integrate assembly solutions and automation long ago.

As stated earlier, assembly automation is typically more viable for assemblies in secondary rather than primary structures. Mechanical, electrical, and electronics assemblies happen by nature in secondary structures; therefore, assembly automation is common in their manufacturing lines, especially for the latter [12].

26.1.9 Surface protection

Internal and external surfaces in machines and equipment are subjected to different deteriorating factors, ranging from corrosion to wear. Engineering adhesives play a key role in holding, supplementing, rebuilding, and/or reinforcing either the device components or the protective elements used, such as liners, plates, sleeves, or coatings.

These solutions are more common when servicing the equipment rather than in the manufacturing lines. Repair time is of paramount importance, so rapid cure engineering adhesives allow the end-user industries operating capital goods to get their equipment back to work much faster than other approaches, such as the replacement of the damaged components with spare parts.

The nature of surface degradation can be physical, chemical, or combined. The physical mechanisms range from cavitation to abrasion and erosion. They may occur in the presence of different media from dry solids (e.g., sand in wind turbines or rocks in crushing equipment) to fluids (e.g., slurries in flotation cells or water in refrigeration systems). The literature often refers to "wear" as the overarching term that encompasses all these physical surface deterioration phenomena. On the other side, chemical surface degradation mechanisms are often grouped under the common concept of "corrosion."

Mainstream surface protection applications range from those bonding protection elements, such as regular backing or rubber wear liner bonding, to those replacing them, as in metal [13] or rubber rebuild applications [14]. Some of the latest developments in this area simplify the application process, reduce the costs, increase worker safety, and eliminate the release of solvents [15]. Other surface protection applications are based on reinforcement solutions applied to prevent and/or repair leakage in deteriorated pipework, with thinner walls or even cracks, respectively [16]. Finally, state-of-the-art smart solutions integrate sensors to allow monitoring machinery behavior.

These new developments enable asset owners to anticipate machine failure, thus evolving service operations from the classic reactive, corrective repair works to the most modern predictive and prescriptive maintenance protocols [17].

26.2 Capital goods end-user sector

Capital goods include machinery and equipment used to extract and process raw materials, to transform these raw materials into intermediates, and finally to manufacture end products that consumers will later use. Other capital goods produce and/or manage resources and services demanded by urban and industrial areas. Agricultural and construction equipment are classic examples of capital goods, although there are many others not that broadly known but equally essential for the normal operation of the economy.

Some of the most remarkable adhesive applications for capital goods occur in heavy machines operating under the harshest conditions, typically outdoor and sometimes in highly contaminated environments at extreme temperatures. It is also worth mentioning that engineering adhesives are intensively used in every assembly step of the machinery value chain, from subcomponent manufacturing (e.g., to produce pneumatic and hydraulic components) to machine final assembly and onsite installation. They are also applied during maintenance and repair operations throughout the entire machine lifetime. Sometimes, machines are upgraded or even fully retrofitted to restore operation in a sort of second life, for which engineering adhesives often play a key role.

26.2.1 *Capital goods ecosystem: Industry drivers and needs*

To better understand the mainstream challenges faced by machines and the types of applications most demanded, capital goods can be clustered into four ecosystems: Extraction, transformation, infrastructure, and manufacturing. The urbanization megatrend, driven both by the progressive displacement of rural populations to cities and the rise of megacities, mostly in developing countries, translates into an increasing demand for resources such as raw materials (cement or iron) and energy. The sustainability megatrend, though, is curbing the demand for fossil fuels and urging both the development of alternative energy sources and the electrification of the transmission and distribution energy infrastructure.

The economics of capital goods are closely linked with concepts such as availability and reliability. Heavy machinery is a capital-intensive investment that only pays off when operating robustly and without unexpected malfunctions. Machinery lifespan can vary greatly between industries and even companies but, by and large, machinery users tend to keep older but well-maintained equipment and delay the acquisition of newer models if economically advantageous. Heavy machines may last from years to decades, depending on the intended application, costs of refurbishing versus replacing, and other issues. Indeed, very old but rugged

machine tools from the mid-20th century are frequently seen in many general industry workshops alongside the most modern computer numerical control machine centers (CNCs).

Root causes of failure in machinery vary among sectors, with wear being especially prominent in extractive industries such as mining or construction aggregates while corrosion more frequently leads to downtime for transformation industries such as pulp and paper production. For infrastructure, contamination often reduces machinery efficiency while for manufacturing industries, mechanical failure is the most frequent problem. Wear, corrosion, and contamination can be prevented with surface protection solutions while mechanical failure can be tackled through mechanical assembly solutions.

26.2.2 Adhesive applications for raw material extraction and transformation machinery

Most industries included in the extraction and transformation sectors (including mining, construction aggregates, oil and gas, and paper and pulp) handle hard materials and operate in harsh environments. Severe wear and corrosion can lead to downtime, and surface protection solutions based on engineering adhesives are often applied to delay and/or repair their adverse effects.

The equipment used in extraction industries such as mining ranges from the mobile machinery that retrieves and hauls minerals, rocks, and fossil raw materials to the processing equipment that progressively reduces rock size and concentrates the ore to facilitate its transportation and subsequent transformation. Dry-type equipment, such as crushers processing ore and rocks in mines and quarries, require backing compounds to supplement the wear liners. Wet-type equipment, such as slurry pumps, flotation cells, or mills, often involve wear protection liners that are typically made of rubber and use engineering adhesives when replaced or repaired. Finally, lifting and handling equipment, such as conveyor belts [18], requires engineering adhesives not only when manufactured but also when equipment is installed and then serviced during its lifespan (Fig. 26.1).

The mineral transformation process ranges from basic metals to construction aggregates. Metal mineral concentrates are transformed into metal forms using equipment such as furnaces or mills. Wear, combined with high temperatures, makes abrasion and corrosion the most prominent problems. Construction aggregates such as cement require special processing equipment such as kilns that also involve erosion and heat. Therefore, there is a need for high-temperature and wear-resistant surface protection solutions enabling operators to rapidly rebuild worn surfaces.

Other transformation processes worth mentioning are those used in the timber and pulp industries. Forestry equipment for cutting, delimiting, sawing, and grinding wood is subjected to high vibration and showcases numerous mechanical assembly applications while paper machines working in harsh chemical environments require surface protection solutions to protect an/or rebuild corroded areas.

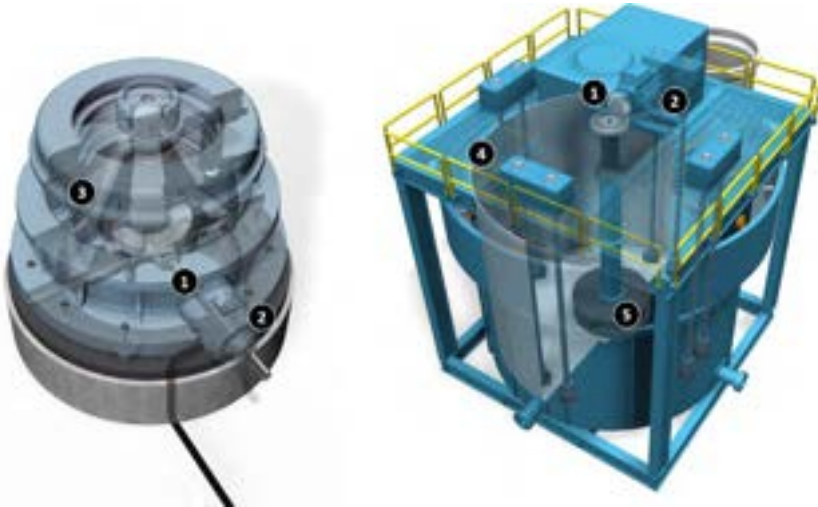


Fig. 26.1 Common engineering adhesive maintenance and repair applications for crushers and flotation cells, equipment typically used in the processing of minerals: (1) retaining of gears and bearings in rotating equipment; (2) threadlocking of rotating equipment threaded fasteners; (3) backing of steel wear liners; (4) bonding of rubber wear liners; (5) rebuild of rubber impeller. Credit: Henkel, Adhesive Technologies, www.henkel.com.

26.2.3 Adhesive applications for infrastructure machinery and equipment

The infrastructure sector encompasses the machinery, equipment, and premises required by several industries including transportation, telecommunication, energy, water, and waste. These industries continuously supply fundamental resources such as gas, electricity, or potable water as well as manage services such as communications or waste collection in rural, urban, and industrial areas. Corrosion and wear are relevant problems in infrastructure. However, contamination is probably the most prominent issue. Dust and dirt deposits reduce efficiency in power machines such as turbines or solar panels as well as in complementary equipment such as industrial fans.

The most relevant adhesive manufacturing applications in infrastructure are often related to the production of the capital goods involved, mostly for power-generation heavy machines such as turbines [19] and related equipment such as heat exchangers [20], fluid processing systems [21], or mechanical drives and transmissions. This is the case of the main wind turbine components, including the tower, the power train, and the rotor (that usually consists of a hub and three blades), for which engineering adhesives may be demanded in exceptionally large volumes (Fig. 26.2).

Nevertheless, as with the extraction and transformation sectors, the largest adhesive consumption for infrastructure typically occurs in service over the lifespan of the machines. For instance, gas, turbine, hydro, and wind turbines typically require

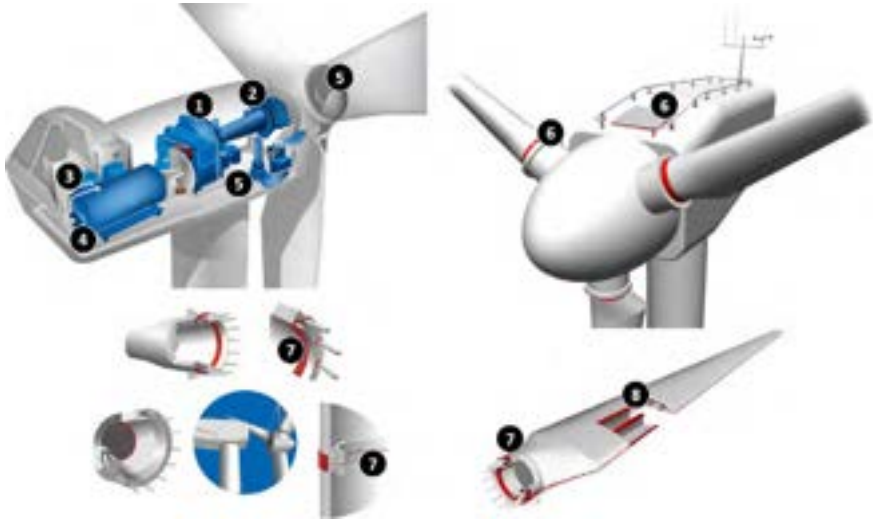


Fig. 26.2 Common engineering adhesive manufacturing applications for wind turbines: (1) gasketing of gearbox flanges; (2) flange coupling in the drivetrain; (3) thread sealing of oil pipes; (4) retaining bearings in the generator; (5) threadlocking of pitch and yaw driver fasteners; (6) sealing of rotor and nacelle components; (7) sealing and reinforcement of rotor and tower flanges; (8) bonding of blade shells, beams, and stiffeners. Credit: Henkel, Adhesive Technologies, www.henkel.com.

both planned and unplanned service protocols to maintain machine efficiency and minimize downtime. Maintenance operations involve the disassembly of the turbine, cleaning, repair/replacement of damaged components, and subsequent reassembly of the equipment, which requires the use of engineering adhesives and sealants as specified by the original equipment manufacturer (OEM).

Fluid management equipment such as pumps, valves, compressors, or pipes as well as transmission equipment such as gearboxes [22], brakes, or clutches are frequently used across all heavy industries but specially in power generation. Primary and secondary refrigeration systems installed in thermal power stations transport water and are subjected to severe corrosion and some wear. Therefore, regular inspection and maintenance are required to reduce plant downtime. These problems can often be addressed with surface protection solutions (Fig. 26.3).

26.2.4 Adhesive applications for manufacturing, industrial processing, and automation machinery

There are literally hundreds of industries manufacturing final goods. Among the largest ones by revenue are industries such as transportation (including automotive and aerospace), agriculture and farming, food and beverage [23], or textile and apparel. All these industries invest intensively in industrial processing machinery to scale-up outputs and reduce costs per unit produced. Just to name a few, an enormous

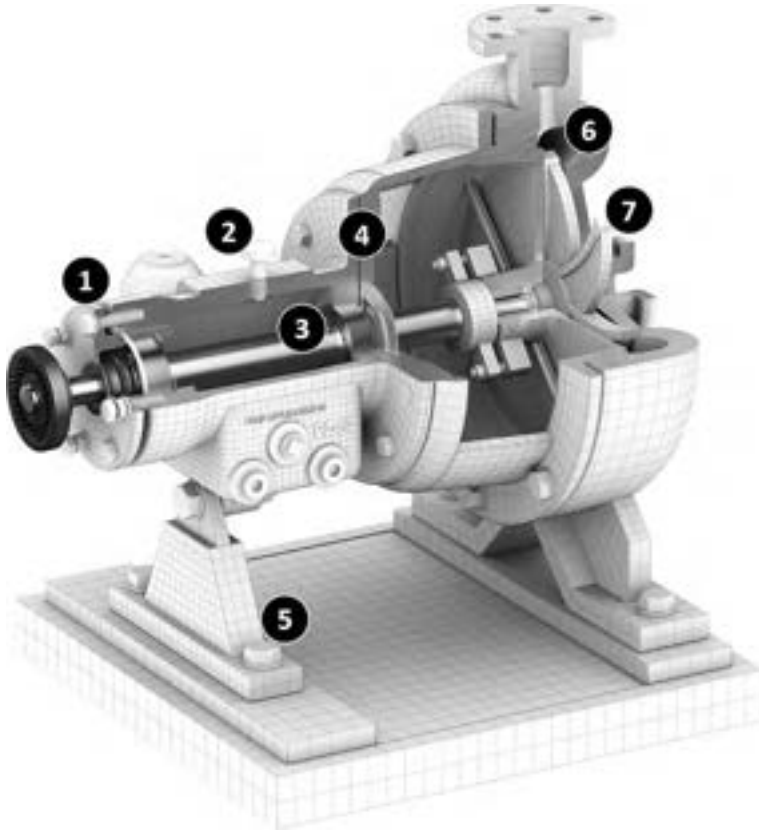


Fig. 26.3 Common engineering adhesive maintenance and repair applications for a centrifugal pump: (1) threadlocking of bearing housing fasteners; (2) thread sealing of oil plug; (3) retaining of bearings; (4) gasketing of pump flanges; (5) threadlocking of mounting bolts; (6) rebuild and protection of pump casing; (7) rebuild and protection of impeller.

Credit: Henkel, Adhesive Technologies, www.henkel.com.

number of machine tools [24], plastic injection machines, textile machinery, or food processing machinery can be found in many factories, and all of them must be operating reliably to avoid process disruption and economic loss.

Automation has been one of the areas of greatest development in recent decades. There is a range of automation equipment used in manufacturing lines as well as lifting and handling equipment, including conveyor belts, industrial robots [25], and elevators [26]. The use of adhesive solutions has undoubtedly contributed to the reliability and robustness of all this equipment, especially when it comes to mechanical assemblies required to drive and control motion (Fig. 26.4).

Engineering adhesives are applied in many applications, but typically in very low volumes. Regardless of the quantities required, these solutions have a significant

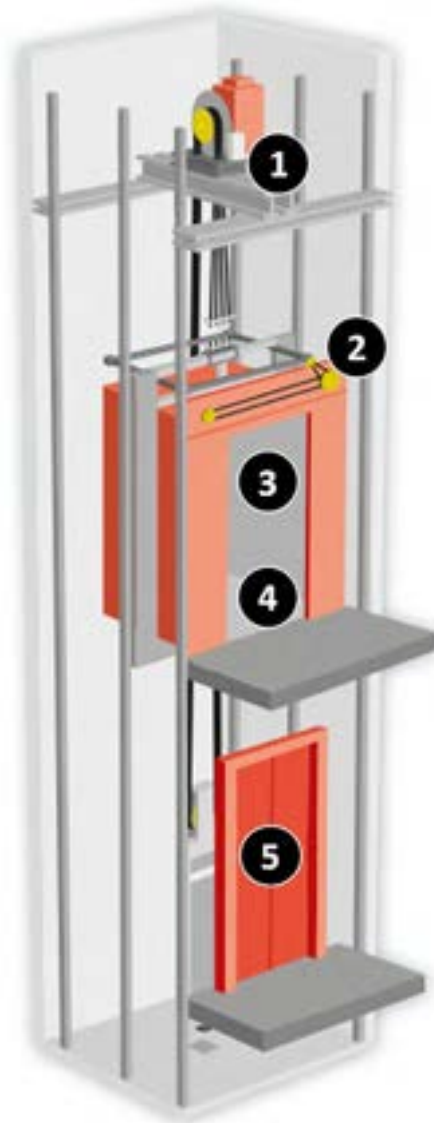


Fig. 26.4 Common engineering adhesive manufacturing applications for elevators: (1) threadlocking of motor fasteners; (2) threadlocking of door automation; (3) bonding of stiffeners to car side panels; (4) bonding of car floor; (5) bonding of stiffeners to landing doors.

Credit: Henkel, Adhesive Technologies, www.henkel.com.

impact on the performance and reliability of industrial processing machines. Most of these manufacturing applications involve mechanical assemblies carried out by the OEMs. Some of them are specified also for regular service operations, including the replacement of worn mechanical components such as bearings or bushings [27].

26.2.5 Adhesive qualification and specification in capital goods

The assembly solutions required to manufacture capital goods are designed and calculated by engineers who first define a list of performance requirements. Provided the high complexity and cost of some machinery components, simulation techniques and numerical calculations incorporating safety factors are often applied to design the joint configuration and determine the thermomechanical requirements.

Capital goods are often manufactured in very short series or even individually customized to satisfy end-user demands. Therefore, most component assembly operations are typically carried out by qualified workers using manual dispensing equipment. Adhesive working times should be long enough to allow operators to carry out the assemblies. However, machinery subcomponents manufactured in larger series are assembled in production lines, which leads to stringent process criteria. This is the case of some fluid management devices such as actuators or valves often demanding adhesives that cure quickly to reduce fixturing time.

Adhesive qualification normally starts with the preselection of adhesives matching the list of requirements. This is accomplished by initially assessing the technical documentation provided by the adhesive suppliers. Properties such as adhesion, durability, strength under different load modes, and heat resistance are then tested on lab specimens. This is followed by tests of prototypes and eventually actual parts, for which process requirements related to the adhesive manipulation and cure are validated.

Health and safety process considerations reducing operator risks and minimizing the release of toxic and/or environmentally harmful byproducts are also paramount. As applications are usually manual, workers should be protected against any health risks arising from the manipulation of adhesives.

Once the adhesive and the assembly process have been validated, the adhesive is specified at the design layouts. These specifications are relevant not only for the manufacture of the machine, but also during any maintenance operation that might require the replacement of worn or damaged components [28]. It is worth mentioning that maintenance and repair operations in capital goods often require special protocols. The original equipment manufacturers can standardize some of those procedures by qualifying and specifying the solutions required in the machine maintenance manual. Some asset owners, especially large utilities and infrastructure operators, may issue their own maintenance and repair procedures, or even subcontract machinery service to external companies specialized in equipment maintenance.

26.2.6 Adhesive quality control and risk mitigation in capital goods

Due to the nature of heavy machines, specific quality control operations are typically carried out mostly on critical assemblies that may entail a risk for machinery reliability. That is the case for threaded fasteners in wind turbine rotor assemblies for which clamping load is assessed after manufacturing and regularly during service over the entire wind turbine lifetime [29].

In primary structures and large-scale bonded joints, nondestructive techniques such as ultrasounds and thermography [30] can be used, especially when parts are initially identified as potentially defective by other means, such as through visual inspection.

Other adhesive applications are simply controlled alongside the customary machine performance tests as a whole or for the different subsystems, such as in the hydraulic, pneumatic, refrigeration, and lubrication systems [31] (Fig. 26.5).

26.3 Durable goods end-user sector

There are a wide variety of goods we use in our daily lives and for which we have a durability expectation, ranging from transportation vehicles to domestic appliances. The manufacturing and maintenance processes involved often require engineering adhesive solutions.

26.3.1 Durable goods ecosystem: Industry drivers and needs

Engineering adhesives are extensively used during the entire durable goods manufacturing value chain, from the production of the materials and subcomponents they are made of to the final durable good assembly process. The architecture of durable goods has evolved greatly since Henry Ford started the first assembly line for the mass production of an entire automobile in the early 20th century. Indeed, electrification and electronification, driven by increasing sustainability and connectivity requirements, have greatly reshaped durables. Some examples are the latest cordless power tool models, which offer unprecedented power and range, or the modern medical wearables that allow remote health monitoring.

Industry drivers such as miniaturization and ergonomics are further increasing the demand for solutions to handle higher power densities, increase robustness, and reduce weight of the end products. Both primary and secondary assembly solutions based on engineering adhesives not only elevate resistance to dynamic loads and impact, but also enable lightweight construction, help manage heat, and allow or hinder the transmission of radiofrequencies.

Traditionally, service operations were only economically viable for durable goods with high residual value. Some of the most relevant markets for adhesives arose around the car and ship aftermarkets. Emerging sustainability targets and state policies might lead to a wider range of durable goods being maintained and repaired instead of just being discarded.

26.3.2 Adhesive applications for materials construction

Adhesives are often utilized in the manufacture of materials, for instance as binders in composites such as chipboard, plywood, engineered stone, or FRP [32]. Also, many devices, machines, and vehicles are built with construction elements such as panels, which are often manufactured with engineering adhesives. Finally, there is extensive literature on repair applications for composite structures [33].

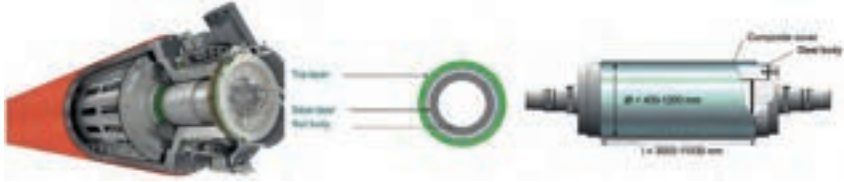
<p>Manufacturer: Valmet Device Type Paper Mill Roll / Capital Goods</p> 	<p>Country: Jyväskylä (Finland) Components Roll Cover to Steel Body</p>		
<p>ASSEMBLY REQUIREMENTS</p> <table border="0"> <tr> <td data-bbox="114 505 545 753"> <p>Performance Requirements</p> <ul style="list-style-type: none"> • Strong and durable adhesion on epoxy composite roll cover and steel body – above 10MPa shear strength after long-term immersion in water • Toughened adhesive coping with different component CTEs • Bondline operation temperature at 50°C, thermal resistance up to 80°C </td> <td data-bbox="545 505 1001 753"> <p>Process Requirements</p> <ul style="list-style-type: none"> • Suitable for manual application – no sensitive to humidity during adhesive spreading • No need of adhesive prebaking • Low volatiles – Maximum VOC level 250 g/liter, preferably <50 g/liter </td> </tr> </table>		<p>Performance Requirements</p> <ul style="list-style-type: none"> • Strong and durable adhesion on epoxy composite roll cover and steel body – above 10MPa shear strength after long-term immersion in water • Toughened adhesive coping with different component CTEs • Bondline operation temperature at 50°C, thermal resistance up to 80°C 	<p>Process Requirements</p> <ul style="list-style-type: none"> • Suitable for manual application – no sensitive to humidity during adhesive spreading • No need of adhesive prebaking • Low volatiles – Maximum VOC level 250 g/liter, preferably <50 g/liter
<p>Performance Requirements</p> <ul style="list-style-type: none"> • Strong and durable adhesion on epoxy composite roll cover and steel body – above 10MPa shear strength after long-term immersion in water • Toughened adhesive coping with different component CTEs • Bondline operation temperature at 50°C, thermal resistance up to 80°C 	<p>Process Requirements</p> <ul style="list-style-type: none"> • Suitable for manual application – no sensitive to humidity during adhesive spreading • No need of adhesive prebaking • Low volatiles – Maximum VOC level 250 g/liter, preferably <50 g/liter 		
<p>ADHESIVE QUALIFICATION AND SPECIFICATION</p> <table border="0"> <tr> <td data-bbox="114 810 545 1130"> <p>Compliance with Standards</p> <ul style="list-style-type: none"> • None </td> <td data-bbox="545 810 1001 1130"> <p>Tests passed</p> <ul style="list-style-type: none"> • Ageing tests: <ul style="list-style-type: none"> ○ Immersion in acidic water (pH 4.5), 3000 h ○ Dynamic loading, 1-2 MPa ○ 50°C continuous w/ 90°C peak temperature ○ Outcome: Above 10MPa / 70% initial shear strength retained • Hot strength test <ul style="list-style-type: none"> ○ 50°C continuous w/ 90°C peak temperature ○ Outcome: 20Mpa shear strength at 100°C </td> </tr> </table>		<p>Compliance with Standards</p> <ul style="list-style-type: none"> • None 	<p>Tests passed</p> <ul style="list-style-type: none"> • Ageing tests: <ul style="list-style-type: none"> ○ Immersion in acidic water (pH 4.5), 3000 h ○ Dynamic loading, 1-2 MPa ○ 50°C continuous w/ 90°C peak temperature ○ Outcome: Above 10MPa / 70% initial shear strength retained • Hot strength test <ul style="list-style-type: none"> ○ 50°C continuous w/ 90°C peak temperature ○ Outcome: 20Mpa shear strength at 100°C
<p>Compliance with Standards</p> <ul style="list-style-type: none"> • None 	<p>Tests passed</p> <ul style="list-style-type: none"> • Ageing tests: <ul style="list-style-type: none"> ○ Immersion in acidic water (pH 4.5), 3000 h ○ Dynamic loading, 1-2 MPa ○ 50°C continuous w/ 90°C peak temperature ○ Outcome: Above 10MPa / 70% initial shear strength retained • Hot strength test <ul style="list-style-type: none"> ○ 50°C continuous w/ 90°C peak temperature ○ Outcome: 20Mpa shear strength at 100°C 		
<p>QUALITY CONTROL</p> <table border="0"> <tr> <td data-bbox="114 1187 545 1333"> <p>Upon adhesive receipt</p> <ul style="list-style-type: none"> • Viscosity measurement – batch between parameters • Adhesive used within shelf life </td> <td data-bbox="545 1187 1001 1333"> <p>During assembly</p> <ul style="list-style-type: none"> • Process protocol specifies roll body temperature, manual application spreading tooling and adhesive volume • Visual inspection of the bondline </td> </tr> </table>		<p>Upon adhesive receipt</p> <ul style="list-style-type: none"> • Viscosity measurement – batch between parameters • Adhesive used within shelf life 	<p>During assembly</p> <ul style="list-style-type: none"> • Process protocol specifies roll body temperature, manual application spreading tooling and adhesive volume • Visual inspection of the bondline
<p>Upon adhesive receipt</p> <ul style="list-style-type: none"> • Viscosity measurement – batch between parameters • Adhesive used within shelf life 	<p>During assembly</p> <ul style="list-style-type: none"> • Process protocol specifies roll body temperature, manual application spreading tooling and adhesive volume • Visual inspection of the bondline 		
<p>RISK MITIGATION</p> <table border="0"> <tr> <td data-bbox="114 1390 545 1534"> <p>End-part Performance Tests</p> <ul style="list-style-type: none"> • Visual inspection of the finished roll • Small defects reworked on site • NDT to assess damage when large defects are detected during roll grinding </td> <td data-bbox="545 1390 1001 1534"> <p>Others</p> <ul style="list-style-type: none"> • End-user claims followed by root cause analysis and correction measures </td> </tr> </table>		<p>End-part Performance Tests</p> <ul style="list-style-type: none"> • Visual inspection of the finished roll • Small defects reworked on site • NDT to assess damage when large defects are detected during roll grinding 	<p>Others</p> <ul style="list-style-type: none"> • End-user claims followed by root cause analysis and correction measures
<p>End-part Performance Tests</p> <ul style="list-style-type: none"> • Visual inspection of the finished roll • Small defects reworked on site • NDT to assess damage when large defects are detected during roll grinding 	<p>Others</p> <ul style="list-style-type: none"> • End-user claims followed by root cause analysis and correction measures 		

Fig. 26.5 Example of engineering adhesive use case in capital goods: bonding of roll cover to steel body in paper mill roll.

Credit: Valmet, www.valmet.com.

Panels made of different structural elements are intended to provide high strength while being much lighter than monolithic plates. They may involve different designs, but the working principles are similar with thin “skins” attached to and separated by other components, thereby increasing the bending stiffness. For instance, stiffened panels are based on a skin reinforced with stiffening elements while sandwich panels are made of two outer skins and a low-density rigid inner core.

Stiffened panels are used in the construction of machinery enclosures and elevators. They are frequently made of steel. The solutions based on engineering adhesives have often replaced other assembly technologies such as welding or riveting, reducing process complexity and improving bending strength, vibration absorption, and noise reduction.

Sandwich panels are commonly used in recreational vehicles, cruise cabin walls, and signage. They are often manufactured following an industrial process called flat lamination, in which the adhesive is typically spread on the skins before being assembled with the inner core and subjected to high pressure and/or heat for consolidation and curing.

26.3.3 Adhesive applications in transportation

The transportation sector includes industries that likely have benefited the most from adhesives. Modern lightweight structures present in most transportation vehicles couldn't have been designed and fabricated without engineering adhesives. This holds true not only for aircraft [34], vehicles [35], and ships [36], but also for all sorts of recreational, commercial, and industrial vehicles, including construction and agricultural vehicles [37].

Obviously, the aerospace and automotive industries are large consumers of adhesives and therefore have dedicated chapters in this book (see [Chapters 23](#) and [24](#), respectively). But beyond these sectors, there are many others that are equally intensive in the use of adhesive solutions. From a volume usage perspective, recreational vehicles such as yachts, campers, and mobile homes are at the top, as structural adhesives are broadly used both for their primary and secondary structures. The same applies to trailers and racing sport vehicles, including racing boats, cars, and bicycles, as they intensively rely on composite materials for their construction. Finally, the newest micromobility vehicles such as scooters or wheelers also use structural adhesives to assemble secondary structures.

Passenger transportation vehicles such as cruise liners, ferries, passenger trains, and buses still use a fair amount of engineering adhesives, mostly for the assembly of windows and construction panels.

Mechanical assembly solutions are extensively used in transportation, mostly when assembling power trains. For instance, industrial and shipping vehicles such as off-highway vehicles, trucks, cargo ships, and freight trains require engineering adhesives, mostly to increase the reliability of their mechanical subcomponents.

Practically all vehicles are regularly maintained and repaired, which creates after-market opportunities for engineering adhesives. These markets are typically sizeable, especially for cars. However, the need to repair damaged cars and, therefore, the



Fig. 26.6 Common repair applications with structural adhesives in damaged light vehicles: (1) direct glazing of windshield; (2) bonding of side windows; (3) bonding of steel roof panel; (4) bonding of steel body quarters; (5) rebuild of plastic front bumper; (6) rebuild of plastic rocker panels; (7) rebuild of plastic rear bumper; (8) reinforcement of steel front side body frame; (9) reinforcement of steel pillars and central body frame components. Credit: Henkel, Adhesive Technologies, www.henkel.com.

consumption of adhesives could drop significantly as the adoption of advanced driver assistance systems (ADAS) and autonomous vehicles increases (Fig. 26.6).

26.3.4 Adhesive applications for electrical equipment

Most current devices integrate electrical subcomponents such as motors, generators, transformers, or batteries. As stated earlier, electrical assembly accounts for the highest volume of engineering adhesive applications in electrical machines. On the other side, electronics in general, but power electronics in particular, play a fundamental role to control and drive most modern electrical machines. Therefore, electronics assembly solutions account for a significant portion of engineering adhesive use cases as well. Finally, both secondary assembly and mechanical assembly applications are also common, mostly in rotative machinery [38].

It's worth noting that electrical machinery subcomponents, which are typically produced in separate manufacturing lines, can also be assembled with engineering adhesives. This is the case of components such as transformer lamination stacks or motor and generator rotors and stators [39].

Electrical machinery efficiency and long-term performance are compromised when systems overheat. As the power density of modern rotating devices such as brushless motors increases, the operating temperature reaches higher peaks, which in turn accelerates degradation of the polymers used in their construction. The use of



Fig. 26.7 Common engineering adhesive manufacturing applications in electric motors: (1) threadlocking of mechanical fasteners; (2) retaining of bearings; (3) bonding of magnets; (4) bonding of lamination stacks; (5) retaining of stator; (6) thermally conductive bonding of electronics heat sink; (7) assembly and encapsulation of electronics. Credit: Henkel, Adhesive Technologies, www.henkel.com.

engineering adhesives with thermal management properties contributes to reducing the working temperature, therefore significantly increasing electrical machinery performance and durability [40] (Fig. 26.7).

26.3.5 Adhesive applications for appliances, leisure, and home automation

Appliance is a broad term used for a wide range of devices designed to assist with various household and daily life needs. The Covid-19 pandemic has accelerated the change of many traditional patterns of cultural and societal behavior, bringing new ways of purchasing, learning, working, sporting, and even relating with others. The increasing connectivity, higher computational capacity, and ergonomic improvements of appliances around us are indeed behind these changes, as many of these features were not technically feasible just a few years ago. Home appliances are typically divided among three types:

- Small appliances such as coffee makers or microwaves.
- Major appliances, or white goods, such as dishwashers or refrigerators.
- Consumer electronics, or brown goods, such as computers or tablets.

Leisure devices, such as sports goods and loudspeakers, have also followed a similar development, as have security devices such as home automation or home security. Finally, professional devices such as power and gardening tools have improved in autonomy and portability.

The use of engineering adhesives to assemble the secondary structures for appliances has accelerated manufacturing processes while improving device performance,



Fig. 26.8 Common engineering adhesive manufacturing applications for a power tool: (1) retaining of gears and bearings; (2) threadlocking of mechanical fasteners; (3) bonding and sealing of enclosure; (4) tacking of electrical connections; (5) assembly and encapsulation of electronics; (6) thermally conductive gap filling of battery cells. Credit: Henkel, Adhesive Technologies, www.henkel.com.

such as enabling water-proof designs for high-end devices. The use of electronics assembly solutions is also highly remarkable at earlier stages of the manufacturing value chain [41] (Fig. 26.8).

26.3.6 Engineering adhesive qualification and specification in durable goods

Durable goods are often produced in large series. Manufacturers need to maximize outputs to keep costs down. Therefore, the applications with engineering adhesives must be adequately integrated into their production lines. This is accomplished by both selecting adhesives meeting all requirements and designing bonding assembly workstations with high levels of automation.

The first step in the qualification process consists of determining the adhesive process and performance requirements. Typically, CAD/CAM (computer-aided design/computer-aided manufacturing) software is used to design the bonded joint and thus derive adhesive mechanical properties. Likewise, the integration of the bonding process in the manufacturing line pushes process engineers to narrowly define key aspects such as cure mechanism, speed, and process conditions. This comprehensive set of requirements allows selecting a few adhesives worthy to perform the qualification tests.

The preselection of adhesives is then tested on lab specimens, which ideally should be made of the actual substrates. Shortlisted adhesives are subsequently tested in prototypes and, finally, in actual parts. The compliance with process requirements is eventually assessed in the very workstation, first in individual specimens, then in short series and finally in full batches.

Unlike with capital goods, the small size of durable goods allows subcomponent manipulation and assembly within workstations safer to operate, which expands the scope of viable chemistries during adhesive selection. The operators are not exposed to the risks associated with more harmful chemistries when these are applied in closed, safer chambers. For instance, assembly stations can manage and control the release of adhesive volatiles and/or byproducts as well as limit the direct contact of the adhesive with the workers. Regardless, manufacturers try to avoid the use of chemicals that may pose any risk to workers, the environment and, obviously, end users.

Except for vehicles [42], durable goods are rarely designed to be serviced and, therefore, engineering adhesives are seldom used for maintenance and repair. However, this situation is expected to change rapidly during this decade as the new sustainability regulatory frameworks oblige durable goods producers to design them through observing circular economy demands [43].

26.3.7 Engineering adhesive quality control and risk mitigation in durable goods

Both online and end-of-line quality control systems are usually integrated at the most critical assembly stages [44]. For instance, automated visual monitoring [45] guarantees that the adhesive was either applied or the parts assembled following the appropriate dispensing pattern. Low-load tests can also be carried out right after assembly. For sealing applications, assembly tightness can be assessed with low-pressure tests. At the end of the production line, performance tests are carried out on the manufactured durable good.

During production, the materials used and production conditions for each batch produced are closely tracked and recorded. This approach permits tracing defective batches of goods that may have even been already shipped, which can then be reclaimed and investigated to trigger any corrective actions. This allows the manufacturer to enhance production processes and mitigate risks in newer batches being produced (Fig. 26.9).


<p>Manufacturer: Aurora (former Ledvance) Location: Eichstätt (Germany)</p> <p>Device Type LED Bulb / Durable Goods</p> <p>Components Cup to Coated Glass Case</p>	
	
<p>ASSEMBLY REQUIREMENTS</p>	
<p>Performance Requirements</p> <ul style="list-style-type: none"> • Strong and durable adhesion on cup and case substrates – up to 40kh (reliability checks within 4kh in accelerated conditions) • Thermally conductive, above 2.0 W/mK • Flexible gap-filling adhesive to absorb differential CTEs and compensate part tolerances • Flammability rating UL94-V2 • Operating temperature range -10°C to 110°C • Electrical insulating properties 	<p>Process Requirements</p> <ul style="list-style-type: none"> • Suitable for automated production processes – automated dispensing • One or two component room temperature fast cure • Non-sag or paste-like viscosity enabling application in vertical surfaces but flowable enough to allow adhesive spreading • No surface preparation, Intrinsic adhesion to coated glass and aluminum (potential presence of silicone contamination)
<p>ADHESIVE QUALIFICATION AND SPECIFICATION</p>	
<p>Compliance with Standards</p> <ul style="list-style-type: none"> • Adhesive qualified as EHS REACH, ROHS, halogen free • Chemical compatibility tests to LEDs (DurisS5/S8/Seoul3030) • CREE compatibility tests to other optical parts (PC lens or glass cover) 	<p>Tests passed</p> <ul style="list-style-type: none"> • Short (<1% at 120°C/24h) and long-term (no fogging) low outgassing tests • Thermal cycling: 1000 cycles, -40°C to 120°C, 1000h • Temperature/Humidity test: 85%RH and 85°C, 1000h • High temperature test: 120°C, 1000h • Outcome of all tests: Passed without performance losses
<p>QUALITY CONTROL</p>	
<p>Upon adhesive receipt</p> <ul style="list-style-type: none"> • Cure and adhesion tests carried out for every new adhesive batch • Adhesive used within shelf life 	<p>During assembly</p> <ul style="list-style-type: none"> • On-line vision checks of bondline defects • Dispensing setup checks with every adhesive refill • Room temperature and humidity tracking
<p>RISK MITIGATION</p>	
<p>End-part Performance Tests</p> <ul style="list-style-type: none"> • End of line performance test of all bulbs 	<p>Others</p> <ul style="list-style-type: none"> • Samples retained for every bulb production batch • Claim tracking and batch reclaim when appropriate

Fig. 26.9 Example of engineering adhesive use case in durable goods: bonding of cup to coated glass case in LED bulb.

Credit: Aurora, www.aurora-licht.de/en.

26.4 Consumable goods end-user sector

Consumable goods are typically manufactured in mass production assembly lines and, therefore, adhesive solutions need to comply with highly demanding process requirements. Because durability requirements are sometimes more relaxed, nonstructural adhesives typically match both high process speed and low-price expectations. This typically happens when substrates based on polymers and natural materials are involved, for instance for consumables such as packaging or disposable articles.

However, for some industrial consumables with higher performance requirements, other substrates based on metals and ceramics can be present. Bonding such materials would require structural adhesives. Thus, consumables such as filters and cutting tools are built using engineering adhesives.

26.4.1 Consumable goods ecosystem: Industry drivers and needs

Consumable goods are intended to be replaced or disposed once used. The sustainability megatrend is heavily impacting this paradigm and driving new state policies meant to reduce waste and maximize resource utilization.

Overall, plastic packaging is currently coming under increased scrutiny, and expectations are that recycling and replacement with more biodegradable alternatives will have a strong effect along its entire value chain. On the other side, paper and cardboard derivatives, hit hard in recent years by the dramatic reduction of printed materials, are now experiencing a revival in the form of more sustainable packaging products.

One key driver for consumable goods is the compliance with very strict consumer regulatory frameworks, such as food safety directives. This often determines the assembly process and adhesive selection so adhesive suppliers must rapidly adapt to the current regulations.

26.4.2 Adhesive applications for industrial consumables

Abrasives are probably the most relevant industrial consumable and one of the largest adhesive-consuming industries. Sandpaper is typically manufactured with nonstructural adhesive binders. However, other disposables such as sand disks, flap disks, or polishing wheels may require engineering adhesives capable of withstanding higher operating temperatures and dynamic forces. Cutting tools also require high temperature-resistant, structural adhesives [46].

Filters are another good example of industrial consumables using adhesive solutions. Adhesive selection broadly varies depending on both process and performance requirements. Thus, most applications in standard air, water, and oil filters can be resolved with nonstructural adhesives. High-performance filters designed for special processes including reverse osmosis water desalination, chemical separation, or food processing are mostly fabricated using structural adhesives [47].

Tools and hardware may also need adhesives in their production, such as for handles being assembled for hammers or pliers.

26.4.3 Adhesive applications for nonindustrial consumables

Although most adhesive applications for nonindustrial consumable goods typically involve nonstructural adhesives, it is useful to recap the most relevant applications. Indeed, the largest industry consuming adhesives is packaging, where nonstructural adhesives are used not only to manufacture corrugated packaging materials such as paper, cardboard, and corrugated or flexible laminates but also to close cardboard parcels, seal cans, and attach labels.

Other nonindustrial consumable industries demanding large volumes of adhesives are nonwovens, including diapers or cloths, tobacco (especially cigarettes), and self-adhesive items such as labels, stickers, stamps, and envelopes. Most of these consumables use nonstructural adhesives as well.

26.4.4 Adhesive qualification and specification in consumable goods

The qualification of adhesives for consumable goods follows a process like that described for durable goods, starting with the definition of the adhesive requirements, followed by the assessment of the adhesives preselected and finally with the specification of the validated solutions. Substrate compatibility, product performance, and line processability are among the most common requirements demanded across all consumable manufacturing processes.

Also, it is important to note the high relevance of some specific requirements, especially in highly regulated industries such as those producing food, beverages, potable water, or medicines. These special requirements may limit enormously the breadth of compatible chemistries. Adhesive suppliers typically offer adhesives either compliant with the regulatory framework or, at the very least, tested and validated in conditions close to real situations.

26.4.5 Adhesive quality control and risk mitigation in consumable goods

Due to the special importance of the process requirements, properties affecting product cure and dispensing, such as its rheological profile, can be controlled at the reception of every new batch. In addition, adhesives are to be used within the shelf life and stored appropriately as recommended by the adhesive suppliers.

Consumable goods that might potentially be in contact with food and beverages must comply with very strict food safety regulations as defined by official organizations. The food safety regulatory framework can be complex and differ significantly between regions, therefore consumable good manufacturers and adhesive suppliers must closely comply with the legal requirements issued by regional bodies such as FDA [48], USDA [49], EFSA [50], FSA [51], or MHLW [52].

Acknowledgments

I would like to thank Juan Carlos del Real and Miguel Ángel Martínez for their friendship, loyalty, endless generosity, and commitment in the foundation of the Spanish Adhesion Society nearly 30 years ago. Also, special thanks to Juan Carlos for connecting me with Dr. David Dillard and his structural adhesives book project.

Other thanks go to Harri Jänkäväära from Henkel Norden for always being an inspiration and making possible the Valmet use case; Olaf Mündelein and Franz-Josef Gehr from Henkel Germany for their kind support developing the Aurora use case; Damir Biondic and Hugo Quintanilla, among the most knowledgeable general industrial market strategy experts I've ever known, and who taught and inspired me in many of the insights and views captured within this chapter; Keely Tate and Pinar Albas from Henkel Corporation for facilitating all the corporate images I needed; and Kourosh Bahrami and Eric Saunders for their constant support.

Special thanks go to my wife Yolanda and children Sergio and Ivan for your endless patience and encouragement.

This work is in memory of Alfredo Sánchez, who introduced me to the amazing world of engineering adhesives.

References

- [1] D.B. Richardson, T.Z. Blanzymski, E.N. Gregory, A.R. Hutchinson, L.M. Wyatt, Manufacturing methods, in: E.H. Smith (Ed.), *Mechanical Engineer's Reference Book*, twelfth ed., Butterworth-Heinemann, 1994, pp. 16-1–16-112, ISBN: 9780750611954, <https://doi.org/10.1016/B978-0-7506-1195-4.50020-8> (Chapter 16).
- [2] S. Maggiore, M.D. Banea, P. Stagnaro, G. Luciano, A review of structural adhesive joints in hybrid joining processes, *Polymers* 13 (22) (2021) 3961, <https://doi.org/10.3390/polym13223961>.
- [3] G. Haviland, *Machinery Adhesives for Locking, Retaining, and Sealing*, Routledge, 2019, ISBN: 9780203748565, <https://doi.org/10.1201/9780203748565>.
- [4] P.D. Surya Santoso, H. Wayne Beaty, Insulating materials, in: *Standard Handbook for Electrical Engineers*, seventeenth ed., McGraw-Hill, 2018, ISBN: 9781259642586, <https://www.accessengineeringlibrary.com/content/book/9781259642586/toc-chapter/chapter3/section/section21>.
- [5] International Electrotechnical Commission. <https://www.iec.ch/homepage>.
- [6] National Electrical Manufacturers Association. <https://www.nema.org/>.
- [7] S.L. Spitz, Chemicals in PCB manufacturing, in: F. Riley (Ed.), *The Electronics Assembly Handbook*, Springer, 1985, ISBN: 978-3-662-13163-3, https://doi.org/10.1007/978-3-662-13161-9_5.
- [8] Yamaha, Ultra-High-Speed Modular Z:TA-R YSM40R Achieves Revolutionary Productivity of 200,000 CPH Giving it the World's Fastest Speed on a Compact Platform. <https://global.yamaha-motor.com/business/smt/mounter/ysm40r/>.
- [9] European Commission, Waste from Electrical and Electronic Equipment (WEEE). https://ec.europa.eu/environment/topics/waste-and-recycling/waste-electrical-and-electronic-equipment-weee_en.
- [10] European Commission, Restriction of Hazardous Substances in Electrical and Electronic Equipment (RoHS). https://ec.europa.eu/environment/topics/waste-and-recycling/rohs-directive_en.

- [11] S. Ebnesajjad, A.H. Landrock, Adhesive applications and bonding processes, in: S. Ebnesajjad, A.H. Landrock (Eds.), *Adhesives Technology Handbook*, third ed., William Andrew Publishing, 2015, pp. 206–234, ISBN: 9780323355957, <https://doi.org/10.1016/B978-0-323-35595-7.00008-5> (Chapter 8).
- [12] How to Robot, Automated Adhesive Dispensing Systems—Types & Applications. <https://www.howtorobot.com/expert-insight/automated-adhesive-dispensing-systems-types-applications>.
- [13] Plant Engineering, Wear-Resistant Ceramic Coatings. <https://www.plantengineering.com/articles/wear-resistant-ceramic-coatings/>.
- [14] C. Chandrasekaran, Wear-resistant rubbers for ore and mining industries, in: C. Chandrasekaran (Ed.), *Plastics Design Library*, “Anticorrosive Rubber Lining”, William Andrew Publishing, 2017, pp. 21–28, ISBN: 9780323443715, <https://doi.org/10.1016/B978-0-323-44371-5.00003-7> (Chapter 3).
- [15] Weir, Weir Minerals Launches New Zero VOC Adhesive Range for Rubber Lining. <https://www.global.weir/newsroom/news-articles/weir-minerals-launches-new-zero-voc-adhesive-range-for-rubber-lining/>.
- [16] J.-S. Kim, J.-H. Jang, Y.-J. Kim, Efficient elastic stress analysis method for piping system with wall-thinning and reinforcement, *Nucl. Eng. Technol.* 1738-5733, (2021), <https://doi.org/10.1016/j.net.2021.08.026>.
- [17] Henkel, Henkel Launches Loctite Pulse during AUTOMA CONGRESS. <https://www.henkel.com/press-and-media/press-releases-and-kits/2021-10-05-henkel-launches-loctite-pulse-during-automa-congress-1371044>.
- [18] A. Biszczanik, K. Talaśka, D. Wilczyński, Analysis of the adhesive spread and the thickness of the adhesive bonded joint depending on the compressive force applied to bonded materials with different surface structure, *Int. J. Adhes. Adhes.* 0143-7496, 114 (2022), 103081, <https://doi.org/10.1016/j.ijadhadh.2021.103081>.
- [19] F. Sayer, A. Antoniou, A. van Wingerde, Investigation of structural bond lines in wind turbine blades by sub-component tests, *Int. J. Adhes. Adhes.* 0143-7496, 37 (2012) 129–135, <https://doi.org/10.1016/j.ijadhadh.2012.01.021>.
- [20] P. Paulraj, B. Paul, R. Peterson, Development of an adhesive-bonded counterflow micro-channel heat exchanger, *Appl. Therm. Eng.* 48 (2012) 194–201, <https://doi.org/10.1016/j.applthermaleng.2012.05.001>.
- [21] European Patent Office. <https://patents.google.com/patent/EP1533104B1/en>.
- [22] A.M. Waked, R.K. Al-Abbas, M.M. Sadek, Assessment of the thermal performance of bonded gearboxes, *Int. J. Adhes. Adhes.* 0143-7496, 11 (1) (1991) 30–36, [https://doi.org/10.1016/0143-7496\(91\)90058-P](https://doi.org/10.1016/0143-7496(91)90058-P).
- [23] A. Pirondi, F. Dazzi, L. Zomparelli, Adhesive joint use and aging in food machinery: a case-study on beverage filling systems, *Int. J. Adhes. Adhes.* 0143-7496, 107 (2021), 102852, <https://doi.org/10.1016/j.ijadhadh.2021.102852>.
- [24] Adhesively-bonded machine tools prototyped in Japan, *Mater. Des.* 0261-3069, 8 (5) (1987) 298, [https://doi.org/10.1016/0261-3069\(87\)90020-3](https://doi.org/10.1016/0261-3069(87)90020-3).
- [25] Henkel, Adhesives Solve Challenges of Robot Manufacturers. <https://www.henkel.com/resource/blob/146932/968cf8279f4535dfa7d0da62c692cc48/2013-05-31-adhesives-solve-challenges-of-robot-manufacturers-en-com-pdf-data.pdf>.
- [26] Henkel, Adhesives in Elevators on the Way Up. <https://www.henkel.com/resource/blob/146438/e665125e3fe2f456cfc319b7832a19bc/elevator-industry-adhesives-in-elevators-on-the-way-up-data.pdf>.
- [27] MinebeaMitsumi, Handling of a Bearing. https://product.minebeamitsumi.com/en/technology/bearing/ballbearings_cat-4_005.html.

- [28] V. Kakuevitskii, A. Redzyk, I. Ragutskii, D. Aronovich, A. Murokh, The use of anaerobic sealing materials to repair machines and equipment, *Polym. Sci. Ser. D* 3 (2010) 141–146, <https://doi.org/10.1134/S1995421210020140>.
- [29] R&D, Ultrasonic Clamp Load Testing: The Best Way to Ensure the Correct Bolt Pretension. <https://www.rd-as.com/insights/ultrasonic-clamp-load-testing-the-best-way-to-ensure-the-correct-bolt-pretension/>.
- [30] C.F.C. Bandeira, P.P. Kenedi, L.F.G. Souza, S. de Barros, On the use of thermographic technique to assess the fatigue performance of bonded joints, *Int. J. Adhes. Adhes.* 0143-7496, 83 (2018) 137–142, <https://doi.org/10.1016/j.ijadhadh.2018.02.016>.
- [31] The Alfing Special Machine Group, AMT Leak Test Systems. <https://www.aks-amt.alfing.de/en/products/amt/leak-test-systems.html>.
- [32] R.K. Behera, S.K. Parida, R.R. Das, Effect of pre-embedded adhesion failures and surface ply delaminations on the structural integrity of adhesively bonded single lap joints made with curved laminated FRP composite panels, *Int. J. Adhes. Adhes.* 0143-7496, 108 (2021), 102887, <https://doi.org/10.1016/j.ijadhadh.2021.102887>.
- [33] S. Psarras, T. Loutas, G. Galanopoulos, G. Karamadoukis, G. Sotiriadis, V. Kostopoulos, Evaluating experimentally and numerically different scarf-repair methodologies of composite structures, *Int. J. Adhes. Adhes.* 0143-7496, 97 (2020), 102495, <https://doi.org/10.1016/j.ijadhadh.2019.102495>.
- [34] A. Higgins, Adhesive bonding of aircraft structures, *Int. J. Adhes. Adhes.* 0143-7496, 20 (5) (2000) 367–376, [https://doi.org/10.1016/S0143-7496\(00\)00006-3](https://doi.org/10.1016/S0143-7496(00)00006-3).
- [35] J. Lin, L. Zhiguo, H. Yang, P. Wang, A design of experiments assessment of moisture content in uncured adhesive on static strength of adhesive-bonded galvanized SAE1006 steel, *Int. J. Adhes. Adhes.* 0143-7496, 31 (6) (2011) 478–485, <https://doi.org/10.1016/j.ijadhadh.2011.04.001>.
- [36] T. Alderucci, C. Borsellino, G. Di Bella, Effect of surface pattern on strength of structural lightweight bonded joints for marine applications, *Int. J. Adhes. Adhes.* 0143-7496, (2021), 103005, <https://doi.org/10.1016/j.ijadhadh.2021.103005>.
- [37] J. Antelo, A. Akhavan-Safar, R.J.C. Carbas, E.A.S. Marques, R. Goyal, L.F.M. da Silva, Replacing welding with adhesive bonding: an industrial case study, *Int. J. Adhes. Adhes.* 0143-7496, 113 (2022), 103064, <https://doi.org/10.1016/j.ijadhadh.2021.103064>.
- [38] Machine Design, Adhesives Hold Electric Motors Together. <https://www.machinedesign.com/archive/article/21815719/adhesives-hold-electric-motors-together>.
- [39] H. Thiede, A. Winkel, S. Mechtold, S. Böhm, Technology for the production of stator and rotor packets for electric motors by adhesive bonding, in: Conference: 37th Annual Meeting of the Adhesion Society at: San Diego, C, USA, 2014. https://www.researchgate.net/publication/298214510_Technology_for_the_Production_of_Stator_and_Rotor_Packets_for_Electric_Motors_by_Adhesive_Bonding.
- [40] X. Wang, B. Li, D. Gerada, K. Huang, I. Stone, S. Worrall, Y. Yan, A critical review on thermal management technologies for motors in electric cars, *Appl. Therm. Eng.* 1359-4311, 201 (Part A) (2022), 117758, <https://doi.org/10.1016/j.applthermaleng.2021.117758>.
- [41] Assembly Magazine, Appliance Assembly: Fastening or Bonding? <https://www.assemblymag.com/articles/85583-appliance-assembly-fastening-or-bonding>.
- [42] L. Yuchen, J. Broughton, P. Winfield, A review of innovations in disbonding techniques for repair and recycling of automotive vehicles, *Int. J. Adhes. Adhes.* 0143-7496, 50 (2014) 119–127, <https://doi.org/10.1016/j.ijadhadh.2014.01.021>.
- [43] K. Laitala, I.G. Klepp, V. Haugrønning, H. Throne-Holst, P. Strandbakken, Increasing repair of household appliances, mobile phones and clothing: experiences from consumers

- and the repair industry, *J. Clean. Prod.* 0959-6526, 282 (2021), 125349, <https://doi.org/10.1016/j.jclepro.2020.125349>.
- [44] A.W. Espie, J.H. Rogerson, K. Ebtahaj, Quality assurance in adhesive technology, *Int. J. Adhes. Adhes.* 0143-7496, 15 (2) (1995) 81–85, [https://doi.org/10.1016/0143-7496\(95\)98741-4](https://doi.org/10.1016/0143-7496(95)98741-4).
- [45] Y. Davidor, B.L. Davies, A vision system for the on-line quality control of adhesive beads, *Int. J. Adhes. Adhes.* 0143-7496, 8 (1) (1988) 33–38, [https://doi.org/10.1016/0143-7496\(88\)90055-3](https://doi.org/10.1016/0143-7496(88)90055-3).
- [46] A. Al-Samhan, S.M. Darwish, Factors influencing thermo-mechanical stresses developed in bonded tools, *Int. J. Adhes. Adhes.* 0143-7496, 25 (5) (2005) 379–388, <https://doi.org/10.1016/j.ijadhadh.2004.10.004>.
- [47] C.A. Scholes, J. Motuzas, S. Smart, S.E. Kentish, Membrane adhesives, *Ind. Eng. Chem. Res.* 53 (2014) 9523–9533, <https://doi.org/10.1021/ie501036p>.
- [48] Food and Drug Administration. <https://www.fda.gov/>.
- [49] U.S. Department of Agriculture. <https://www.usda.gov/>.
- [50] European Food Safety Authority. <https://www.efsa.europa.eu/en>.
- [51] Food Standards Agency. <https://www.food.gov.uk/>.
- [52] Ministry of Health, Food and Welfare. <https://www.mhlw.go.jp/english/>.

Biomedical adhesives: Qualification, specification, quality control, and risk mitigation

27

Juan Carlos del Real^a, Sara Lopez de Armentia^a, Eva Paz^a, Hermann Handwerker^b, and Felix Debor^b

^aInstitute for Research in Technology, ICAI School of Engineering, Universidad Pontificia Comillas, Madrid, Spain, ^bHenkel Technologies Industrial & Infrastructure, Henkel AG & Co. KGaA, Düsseldorf, Germany

27.1 Introduction

The progress and interest in polymeric adhesives for biomedical applications have increased exponentially in recent decades, as these adhesives have become promising alternatives to traditional wound-closure techniques and an interesting solution to apply in surgical procedures and the manufacture of medical devices.

The benefit of adhesives in medical devices can be recognized easily in the evolution of syringes. Until the mid-20th century, a medical syringe was built from various separate parts that needed to be assembled for use and disassembled for sterilization. Rigid glass barrels and rigid cannulas were connected by soft, deformable metal connectors forming a gentle clamp, and certain amounts of leakage were always accepted. With the availability of plastic materials and epoxy adhesives in the 1950s and 1960s, the connector part was made of plastic and the cannula already bonded in and 100% sealed by an adhesive. In parallel, the syringes were designed from plastic materials as well. The ease of manufacturing and the low cost of all these elements changed the use of the syringes toward single use, meaning syringes are disposable devices today. This enables having a fresh cannula with a fresh sharp tip. In addition, the bonding of the cannulas by an adhesive enabled reducing the needle diameter significantly. With a sharp needle tip and a small needle diameter, treatment with a cannula is far less painful than in the past. Adhesives enabled higher patient comfort, higher medical safety, lower costs, and a variety of needles specialized for medical use.

Similar examples can be found throughout the complete medical device range, and the majority of devices are built nowadays with adhesives.

Also in the surgery field, the use of adhesives can help with some issues that conventional solutions present. In 1961, the use of adhesives in medical procedures was reported for the first time, and it was for blood vessels [1]. The use of cyanoacrylates, also called *super glue*, was famed during the Vietnam war to stop bleeding through disposal cyanoacrylate sprays developed for use on the battlefield [2].

Meanwhile adhesives also have been explored for use as sealants, hemostatic agents, wound dressings, and drug delivery, demonstrating a high practical value in different fields of biomedicine.

One of the most promising applications is tissue sealing, as for example minimally invasive laparoscopic surgery or large-scale incompressible hemorrhage where sutures, staples, and wires are very difficult to apply. The application of sutures is time consuming and has several associated issues. However, the application of adhesives can overcome the disadvantages of these conventional sutures such as tissue damage, increased infection probability, and body fluid/air leakage. Additionally, they can help quickly close the wound and act as hemostats to control bleeding and provide a tissue-healing environment at the wound site.

There are numerous potential applications where adhesives can provide interesting benefits; these applications will be discussed later. It is important to consider that this great evolution has opened the door to the development of a multitude of adhesives with different characteristics and properties, depending on the final application requirements.

In this chapter, the main families of adhesives—natural and synthetic—used for biomedical applications are reviewed, highlighting their strengths and weaknesses, from the point of view of the requirements that these applications demand. Furthermore, adhesives used for clinical applications and in medical devices are explored, with some case studies. Finally, the certification process as well as safety, quality, and specifications demanded for adhesives used for biomedical applications are shown.

27.2 Biomedical adhesives

27.2.1 Requirement

The human body is a very particular working environment for adhesives, their use, application, and performance. Consequently, biomedical adhesives shall meet strict requirements and often need to be designed for the specific use case. This results in specific developments and limited overlap with standard industrial adhesives.

The most important requirement that a biomedical adhesive must satisfy is biocompatibility. The adhesive shall not negatively impact the patient whenever it comes in contact with the human body, short-term or long-term, or if by a bonded medical device or by a surgery procedure.

Specific for tissue adhesives, and depending on the particular application, are the additional requirements of biodegradation, high bonding strength in situ, elasticity, and wet adhesion, which is the responsible for broader durability issues. In the case of adhesives for medical devices, they need to withstand aggressive sterilization methods, especially in the case of reusable devices that are subjected to many sterilization cycles. Therefore, these adhesives need to present high thermal and/or chemical resistance.

In summary, the task that researchers face is to obtain an adhesive that meets the necessary biocompatibility and all the requirements of the targeted specific use.

27.2.1.1 *Biocompatibility and biodegradation*

A material (including adhesives) is biocompatible when its application does not produce any harmful effect on the human body. Such negative effects include affecting vital functions of the organism, allergic reactions, or other pathologies.

Biomedical adhesives are screened for biocompatibility depending on their use as a liquid adhesive, a cured adhesive, or extracts from cured adhesives.

In tissue adhesives, they are in close and potentially long-term contact with living tissue; therefore, these adhesives and their degradation products should exhibit a high degree of biocompatibility. It has been demonstrated that in addition to the possible damage produced by the adhesive, released adhesive components generated during biological resorption can also negatively affect the biocompatibility.

Conversely, adhesives used for medical devices are not necessarily in long-term contact with living tissue; however, they often have to meet biocompatibility requirements that mainly depend on two factors: the kind of contact and the exposure duration.

For this reason, exhaustive tests must be carried out to completely understand the interaction of the adhesive with the human body. This procedure has different stages: (i) it starts with *in vitro* essays based on cell cultures, (ii) it is followed by *in vivo* test and more comprehensive studies in experimental animals, and (iii) finally it ends with clinical studies.

In vitro tests to evaluate toxicity and possible harmful side effects include the assessment of cell viability and cytotoxicity. In addition, more than one assay should be carried out to determine cytotoxicity to avoid overestimation or underestimation of the toxicity.

Regarding *in vivo* tests, subcutaneous implantation in animals is one of the most used methodologies because it requires a small area for the animals, so it is easy to maintain and allows comparisons of tissue response in the same animal [3].

In regard to compatibility with the human body, another consideration is that persistent foreign bodies may have harmful long-term effects. Besides, a second operation is necessary to remove nondegradable materials. Therefore, in some applications, it may be desirable to have biologically absorbable materials [4].

27.2.1.2 *Mechanical performance*

The mechanical properties of biomedical adhesives must be appropriate for their correct performance. However, there is not a general requirement for all applications as every application has specific mechanical requisites. For example, for tissue adhesives, high softness and high elasticity are required to avoid tissue injury, and tissue sealant materials must also be tough and flexible to accommodate geometric changes during the healing process [4]. On the contrary, for medical devices, limited or no flexibility and high strength may be required to withstand mechanical forces, such as for bonded needles to withstand the penetration force into the skin and removal from the skin.

The type of biomechanical loading is another factor that must be considered. The attachment of the adhesive to a specific material, whether to tissue or nontissue, as well as its mechanical performance depend on the dynamic, stress mode, temperature, and cyclic or static application of the load.

27.2.1.3 *Wet adhesion*

Tissue adhesives require strong wet adhesion properties because internal organs are wet from blood, interstitial fluid, mucus, and different liquids, and they are exposed to multifaceted physiological conditions (e.g., pH, biological molecules, salts). The environment where the adhesive joint is immersed is a determining factor because the performance of adhesives in the presence of water or moisture is often drastically reduced compared with that in dry conditions. This effect is influenced by the hydrolysis of the adhesive, moisture-induced plasticization, swelling, and erosion [5]. Besides, water has an important effect on interfacial energies, that is, electrostatic, polar, and dispersion forces at the adhesion interface. Changes in interfacial energies lead to changes in the work of adhesion. In many cases, the work of adhesion is positive in dry conditions, whereas it is negative in water [5], meaning that the adhesion properties in wet conditions could be lower than in dry conditions.

To improve wet adhesion, researchers have studied how aquatic organisms (e.g., marine mussels, sandcastle worms, endoparasitic worms) survive by attachment underwater [5]. By understanding how nature achieves good adhesion underwater and on wet surfaces, some adhesives have been developed by mimicking the adhesion procedures. Some of these adhesion procedures in nature include: (i) the use of byssus (marine mussels) [6], (ii) the secretion of cement proteins (barnacles) [7], and (iii) the use of adhesive proteins (aquatic larvae and black fly pupae) [5].

For adhesives used in manufacturing medical devices, wet adhesion is normally not a requirement as the parts to be bonded are made from plastics, glass, metals, rubbers, or elastomers, surfaces that are typically dry.

27.2.2 *Natural adhesives*

Biopolymers are polymers derived from living organisms or are synthesized from natural resources. For this reason, they present a low tendency to be rejected by a body, which increases their biocompatibility. Furthermore, they present bioinertness, non-toxicity, and nonimmunogenicity, among other properties.

27.2.2.1 *Polysaccharides*

Polysaccharides are renewable materials that are readily available and are composed of repeat units of sugars, which make them biodegradable and nonimmunogenic. They have tissue-mimicking features, but often lack sufficient adhesive forces [4]. There are different adhesives based on polysaccharides; among the most used are chitosan, alginate, and hyaluronic acid.

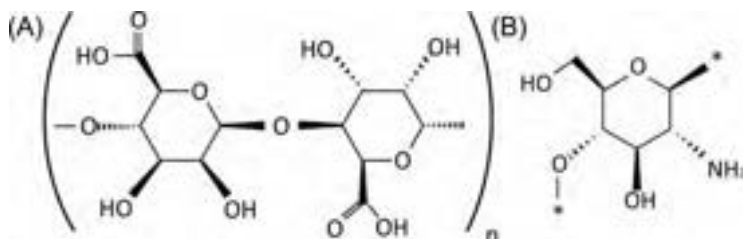


Fig. 27.1 Chemical structure of polysaccharides used as biomedical adhesives: (A) alginate, (B) chitosan.

Chitosan is obtained from the deacetylation of chitin, which is mainly extracted from the exoskeleton of arthropods and the cell walls of fungi. It presents a hydrophilic nature, thanks to its hydroxyl and amino groups (Fig. 27.1). As a natural polymer, it is biocompatible, biodegradable, and nontoxic. It also presents mucoadhesive properties that make it very interesting for carrier systems of mucosal drugs [8]. Unlike other polysaccharides, chitosan presents antimicrobial activity inhibiting the growth of some microorganisms, which makes it an important source of research for the pharmaceutical and biomedical industries [9].

Another polysaccharide explored to obtain adhesives is alginate. Alginate is mainly obtained from seaweed in the form of alginic acid. Its properties depend on its chemical composition (Fig. 27.1); the ratio of 1,4- β -D-mannuronic (M) and 1,4- α -L-guluronic (G) determines, for example, its viscosity. This ratio is determined by the types of algae used (rich in group M or group G). Commercially, three classes may be found: low viscosity (LV), medium viscosity (MV) and high viscosity (HV). As chitosan, alginate also presents mucoadhesive properties, but it does not have any antimicrobial activity [8].

In many studies [10,11], mucoadhesives made of a combination of chitosan and alginate have been developed.

Finally, hyaluronic acid is a polysaccharide from which adhesives can be obtained thanks to its high binding, bioactivity, and mucoadhesive properties [12]. Hyaluronic acid forms part of the extracellular matrix of the soft tissue of all vertebrates. It shows high biocompatibility and biodegradability while also playing an important role in the metabolism of the dermis and the wound-healing process. However, its clinical applications are limited by its low mechanical strength, adhesion, and elasticity. To reduce these drawbacks, photo-curable hyaluronic acid-based adhesives have been investigated [13].

27.2.2.2 Proteins

In general, protein-based adhesives present robust adhesion performance and excellent biocompatibility. Their sequence flexibility leads to improved mechanical and structural integrity as well as tunability. They are of special interest because wet adhesion in nature is, in many cases, promoted by proteins secreted by some living organisms.

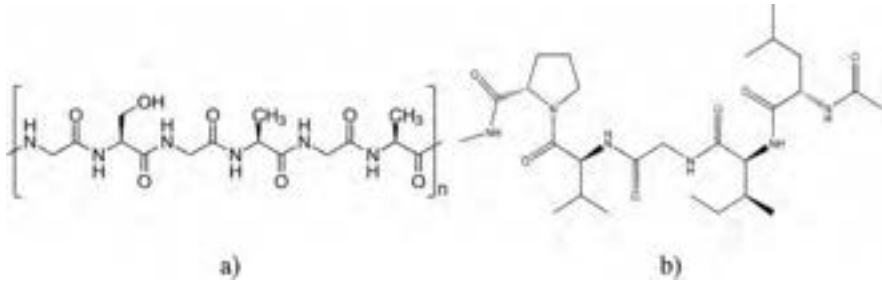


Fig. 27.2 Chemical structure of proteins used as biomedical adhesives: (a) silk fibroin, (b) elastin-like polypeptides.

Albumin is a protein, usually crosslinked by glutaraldehyde, found in the blood of mammals. It presents excellent adhesive strength (10^4 – 10^5 Pa) [14], but it has slow degradation rates and the presence of glutaraldehyde presents some safety concerns in certain areas of the body with high cellularity [15].

Silk fibroin is a natural proteinaceous material obtained from the cocoons produced by silkworms (Fig. 27.2). It has been studied in combination with other polymers or functionalizations, such as silk fibroin blended with polyvinyl alcohol and hyaluronic acid, and silk fibroin with polyethylene glycol. Silk fibroin contributes to the blend by different mechanisms: it increases hydrophobicity, improves mechanical strength, or alters degradability [16].

Elastin-like polypeptides have been widely studied as adhesives in the biomedical field, thanks to their robust adhesive performance in both dry and wet conditions, even outperforming the adhesive properties of commercially available cyanoacrylates [17].

Protein adhesives secreted by mussels, sandcastle worms, barnacles, and caddisfly larvae enable these organisms to firmly adhere to wet surfaces. Based on these proteins, some studies [18] were conducted that showed good biocompatibility and biodegradability as well as high adhesion.

Traditionally, proteins were directly extracted from animals, resulting in high production costs and low extraction efficiency. Therefore, efforts began to focus on producing proteins synthetically. However, synthetic routes to acquire proteins are usually tedious and sometimes weak in biocompatibility/biodegradability metrics (Table 27.1). For this reason, it is difficult to translate the exceptional properties of natural proteins into synthetic materials through conventional synthetic routes. Fortunately, genetic engineering is a powerful tool to design and fabricate proteins by incorporating specific moieties to obtain protein-based materials with desired functions [17].

A special group of adhesives is based on fibrin and collagen. Fibrin sealants mimic the final stages of blood clotting, and they are made from components obtained from human plasma. Collagen-based adhesives induce platelet adhesion and aggregation and activate coagulation factors. They adhere well to the wound and absorb blood and coagulation products [19].

Table 27.1 Advantages and disadvantages of natural adhesives.

	Advantages	Disadvantages
Polysaccharide-based adhesives	<ul style="list-style-type: none"> – Highly available. – Some of them present mucoadhesive properties. – Some of them have antimicrobial activity. – Biodegradable. – Nonimmunogenic. – Tissue-mimicking features. 	<ul style="list-style-type: none"> – Low adhesives forces. – Low mechanical properties.
Protein-based adhesives	<ul style="list-style-type: none"> – Robust adhesion performance. – Wet adhesion is promoted by proteins. – Mechanical and structural integrity and tunability. – Biocompatible. – Some of them show hemostatic properties. 	<ul style="list-style-type: none"> – Tedious synthetic routes of production

27.2.3 Synthetic

27.2.3.1 Cyanoacrylates

Cyanoacrylates (see also [Chapter 4](#)) show a very fast curing process that happens in seconds when they come in contact with Lewis bases, such as the moisture on surfaces. On tissues, mechanical interlocking and chemical adhesion are responsible for the good adhesion properties. Cyanoacrylates generate mechanical interlock thanks to their ability to flow into existing tissue crevices of. Also, the presence of NH_2 and NH groups in the tissue contributes to the polymerization initiation as well as to the adhesion.

They have been used in medicine and dentistry for several years due to their antiinflammatory features, antimicrobial properties, low foreign body response, and their high adhesion ability in moist environments [3].

However, cyanoacrylates have two main problems for use in medical in-body applications. Many studies have focused on them, and some interesting solutions have been found.

The first and main issue associated with cyanoacrylates is related to their degradation during their biological resorption. Cyanoacrylate adhesives degrade via hydrolysis, releasing small amounts of cyanoacetates and formaldehyde. These, in some cases, have shown cytotoxicity and inflammatory responses, resulting in the possible inhibition of the healing process [15]. However, their toxicity can be mitigated by increasing the length of their alkyl chain because monomers with short alkyl chains (e.g., methyl, ethyl) degrade faster than those with long chains.

Flexibility is the other problem for tissue bonding that these adhesives present. After curing, cyanoacrylates exhibit a hard and brittle structure, which is undesirable for *in vivo* tissue conditions. Polymer elasticity and strength can be modulated with the chain length: the longer the chain, the lower the stiffness and the strength [20].

For medical device bonding applications, cyanoacrylates are selected because of their high strength properties and very broad adhesion profile, which allows them to bond with nearly all combinations of materials. Their instant fixture and bonding capabilities allow fast processing of the parts, and this can even be accelerated by the use of light-curing cyanoacrylates, which offer a faster cure on demand.

27.2.3.2 Acrylics

Within acrylic adhesives (see also [Chapter 2](#)), an important group in the field of medical devices is light-curing acrylics. These adhesives are suitable for a wide range of polymers as polycarbonate, poly(acrylonitrile-*co*-butadiene-*co*-styrene), polyurethane, poly(vinyl chloride), poly(styrene-*stat*-acrylonitrile), poly(ethylene terephthalate), etc., and for metals as stainless steels and nitinol. Typical applications of medical light-cured adhesives include respiratory devices such as anesthesia masks, bag-valve-mask resuscitators, catheters, syringes, endoscopes, electronic medical devices, etc. [21]. These adhesives can incorporate fluorescent agents that facilitate in-line inspection for improved quality assurance. Formulations with secondary curing mechanisms are also available.

Another important application of acrylic adhesive in medicine is as pressure-sensitive adhesives (PSAs). Acrylic PSAs are made from higher alkyl esters of acrylic acid without the need for tackifiers, and they provide excellent physical properties. Nevertheless, many commercial acrylic PSAs for industrial use are formulated with other components such as tackifiers, antioxidants, pigments, and fillers. In the case of medical applications, acrylic PSAs free of those additions are preferred because they are less irritating to the skin. Acrylic PSAs present fast skin wetting as well as secure adhesion on skin within the application time, and they are completely removable after application. These properties make acrylic PSAs a good candidate to be used as adhesives for skin applications. They also present high tackiness, high cohesion strength, high stickiness, and ultraviolet (UV), solvent, and temperature stability [22]. Acrylic pressure-sensitive adhesives are available on the market, with most of them in the form of solvent-borne, waterborne, or solvent-free.

To reduce the quantity of organic solvents used, some authors [23,24] have developed UV-activated acrylic PSAs by adding a photoinitiator to the formulation. These pressure-sensitive adhesive products have a broad field of application in the medical devices industry, such as for bandages or transdermal drug delivery systems [25].

27.2.3.3 Epoxies

The main applications of epoxies (see also [Chapter 1](#)) in the biomedical field are in disposable and reusable devices as well as orthopedic devices and diagnostic equipment. They present high bond strength to a wide variety of adherends, excellent

mechanical and physical properties, and high chemical resistance. They present the ability to withstand extremely high temperatures, including most sterilization techniques as well as repeated sterilization.

Epoxy adhesives have been investigated in applications for bone in animal models, but they were not fully cured if there was any substance between the bone and the adhesive. Besides, even if cured completely, the curing time was unreasonable for real surgeries. For this reason, such usage was not transferred to human models [26].

27.2.3.4 Polyurethanes

Polyurethanes (see also [Chapter 3](#)) were first used in biomedicine during the 1950s, when it was used as a breast prosthesis coating. When considering the medical field, polyurethanes improve cell migration, sustain drug delivery, and ensure proper organ reconstruction. Also, polyurethanes show biocompatibility and antithrombogenic effects. However, their hydrophobic characteristics make it necessary to apply surface treatments to adapt for biomedical applications [27].

Polyurethane adhesives are also used in medical device manufacturing such as in fiber bundle end-cap bonding in dialyzers.

27.2.3.5 Others

Polyethylene glycol (PEG)-based adhesives present low adhesive strength and, for this reason, they are usually applied as sealants, preventing fluid and air leakage after surgery [14]. They present some advantages such as biocompatibility, hydrophilicity, and easy modification, among others. However, they show a high swelling rate, which results in a high degradation rate [4].

Silicone-based adhesive technologies (see also [Chapter 6](#)) have also been used for biomedical purposes thanks to the benefits of silicone chemistry, such as biocompatibility, gentleness to skin, breathability, and wear performance. This is especially true of the self-adhering silicone formulations that do not require any activation immediately prior to their use, making these the most promising solution. Silicone-based pressure-sensitive adhesives are very interesting for their skin friendliness. An additional benefit of silicone adhesives is that most of them are easy to remove from skin without negatively impacting the wound-healing process. In medical devices, silicone adhesives are used because of their high flexibility and softness, such as on highly flexible catheters as well as to bond silicone parts, as silicone adhesives have a good adhesion profile to silicone surfaces. [Tables 31.2 and 31.3](#) summarize the advantages and disadvantages of synthetic adhesives in tissue bonding and medical device applications.

Apart from the properties of the adhesives related to biological performance, there are other requirements regarding nonbiological properties. In [Fig. 27.3](#), some of these properties are compared to the adhesives mentioned above. In some cases, properties within the same family depend on the curing process; for this reason, some families appear more than once.

Table 27.2 Advantages and disadvantages of synthetic adhesives in tissue applications.

	Advantages	Disadvantages
Cyanoacrylates	<ul style="list-style-type: none"> – Fast curing. – Strong wet adhesion. – Antiinflammatory features. – Antimicrobial properties. – Low foreign body response. 	<ul style="list-style-type: none"> – Possible toxicity and inflammatory response of degradation products. – Hard and brittle cured structure.
Acrylics	<ul style="list-style-type: none"> – No need of additives. – Low skin irritability. – Fast skin wetting. – Secure adhesion on skin. – Complete removability. – Good chemical and thermal stability. 	<ul style="list-style-type: none"> – Possible chemical toxicity of solvents.
Epoxies	<ul style="list-style-type: none"> – High bond strength. – Good mechanical and physical properties. – High chemical resistance. – High thermal resistance. 	<ul style="list-style-type: none"> – Difficult to completely cure if there is any substance between bone and adhesive.
Polyurethanes	<ul style="list-style-type: none"> – Improve cell migration. – Sustain drug delivery. – Ensure organ reconstruction. – Biocompatible. – Antithrombogenic effects. 	<ul style="list-style-type: none"> – Its hydrophobic character makes it necessary to apply surface treatments.

Table 27.3 Advantages and disadvantages of synthetic adhesives in medical device applications.

	Advantages	Disadvantages
Cyanoacrylates	<ul style="list-style-type: none"> – Fast curing. – Very broad adhesion profile. – Light cure options. 	<ul style="list-style-type: none"> – Risk of blooming from excess.
Acrylics	<ul style="list-style-type: none"> – Cure on demand benefits. – Very fast curing. – Broad adhesion profile. – Invisible bondlines. – Good chemical stability. 	<ul style="list-style-type: none"> – Cure equipment needed. – Shadow areas risk partial cure.

Table 27.3 Continued

	Advantages	Disadvantages
Epoxies	<ul style="list-style-type: none"> – High bond strength. – Potting and sealing. – Good mechanical properties. – High chemical resistance. – High sterilization resistance. 	2K-epoxies <ul style="list-style-type: none"> – Mixing needed. – Long cure time. 1K-epoxies <ul style="list-style-type: none"> – Cure energy.
Polyurethanes	<ul style="list-style-type: none"> – High bond strength. – Potting and sealing. 	2K-polyurethanes <ul style="list-style-type: none"> – Mixing needed. – Long cure time.
Silicones	<ul style="list-style-type: none"> – High flexibility. – Adhesion to silicones. – Light cure options. 	<ul style="list-style-type: none"> – Low strength profile. – Reasonably long cure time.

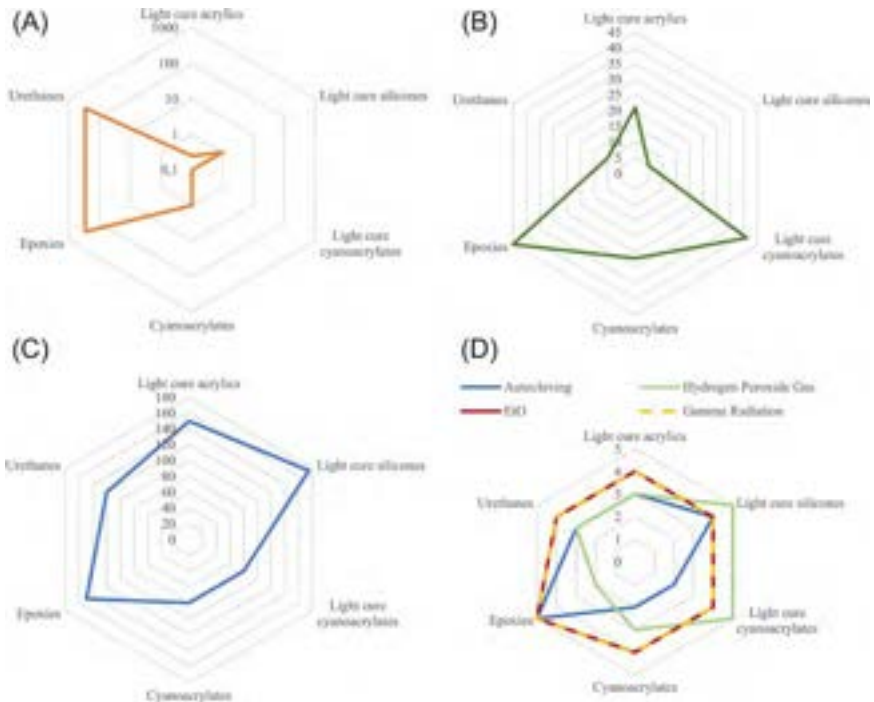


Fig. 27.3 Comparison of synthetic adhesives in terms of: (A) cure time (min), (B) maximum temperature (°C), (C) tensile strength (MPa), and (D) sterilization behavior from excellent (5) to very poor (1).

27.3 Clinical application of adhesives: Tissue adhesives

Tissue adhesives enable the innate wound-healing process to happen through tissue adhesion to tissue or tissue to nontissue (Table 27.4). They have been applied in different tissues, including skin, breast, cardiac, gastrointestinal, head and neck, hepatic, neurological, orthopedic, pediatric, thoracic, and bone as well as in dental and vascular surgery [28].

The properties of the adhesives have to be adapted to the tissue they will be in contact with because each kind of tissue has different properties. Depending on the level of mechanical strength, there are hard tissues (bone, tooth, cartilage) and soft tissues (most organs). Elastic modulus ranges from 0.5 kPa for brain tissue to 1 GPa for bone tissue (Fig. 27.4).

27.3.1 General surgery

In operating rooms, uncontrolled bleeding often occurs. The natural coagulation process of the body clearly helps prevent death from excessive bleeding. However, the formation of stable blood clots or insoluble fibrin is required and, especially in emergency situations, the assistance of hemostatic devices and agents is needed [29]. Polysaccharide-derived hemostatic materials have been widely explored. Fibrinogen, albumin, thrombin, gelatin, collagen, chitosan, cellulose, dextran alginate, starch, and

Table 27.4 Adhesive families used in tissue adhesive applications.

Clinical application	Adhesives
General surgery	<ul style="list-style-type: none"> – Polysaccharide-based – Poly(ethylene glycol) – Polyurethane – Polyester
Skin closure and cosmetic surgery	<ul style="list-style-type: none"> – Fibrin-based – Cyanoacrylate
Vascular surgery	<ul style="list-style-type: none"> – Protein-based – Polyurethane – Cyanoacrylate – Poly(ethylene glycol)
Laparoscopic surgery	<ul style="list-style-type: none"> – Fibrin-based
Dental adhesives	<ul style="list-style-type: none"> – Light-cure acrylic
Bone adhesives	<ul style="list-style-type: none"> – Protein-based – Acrylic – Polyester – Polyurethane – Cyanoacrylate
Medical tapes and drug delivery patches	<ul style="list-style-type: none"> – Acrylic

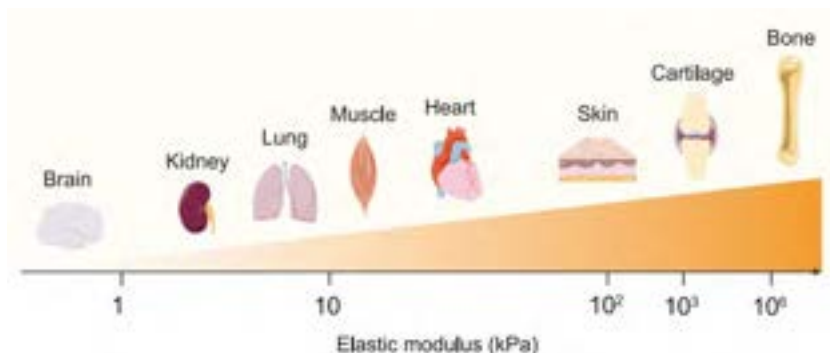


Fig. 27.4 Elastic modulus of different types of tissues.

Credit: Reprinted with permission from S. Nam, D. Mooney, *Polymeric tissue adhesives*, Chem. Rev. 121 (2021) 11336–11384.

hyaluronic acid have been used as local hemostatic agents, tissue adhesives, and sealants in biomedicine [29]. But it's not only polysaccharide-based adhesives that have been used in this field, as some synthetic adhesives with hemostatic properties have been put on the market, such as poly(ethylene glycol), polyurethanes, and polyesters.

27.3.2 *Skin closure and cosmetic surgery*

Topical skin adhesives are attracting attention due to their good scar cosmesis, infection prevention, easy skill acquisition, and lack of need for removal. The most commonly used adhesives for this purpose are cyanoacrylates [30], especially butyl cyanoacrylate, which was the first product to be broadly used for closing cutaneous wounds. They can be used in a wide range of surgeries such as abdominal, back, cardiovascular, face, neck, arms, legs, etc. [19].

In facial plastic surgery, cyanoacrylates and fibrin tissue adhesives are used. Cyanoacrylates have no hemostatic properties; therefore, their use is limited to superficial wound closure. They are widely used in areas where suture removal is painful, such as the eyelid or nose applications. Conversely, fibrin tissue adhesives present hemostatic properties. They can be autologous or homologous, depending on the source of the collected blood, from which the fibrinogen containing a platelet-rich plasma layer is obtained [31].

Cyanoacrylate adhesives have also been explored as alternatives to traditional suture closure in the repair of a cleft lip. The use of adhesives avoids dressing changes or suture removal under sedation [32].

27.3.3 *Vascular surgery*

Adhesives in vascular surgery are used to strongly bind tissues together, but they do not absorb blood or contribute to the physiological clotting cascade. Nevertheless, they can be used as an alternative to biologically active or absorbable hemostatic agents [33].

Protein-based adhesives may be used in vascular surgery. For example, adhesives based on mussel foot proteins (MFPs) [34], albumin, and collagen are used for applications such as hemostasis at a femoral arterial puncture site or surgical repair of vessels [35].

Regarding synthetic adhesives, polyurethanes are also used for the temporary endovascular occlusion of blood vessels below the neck up to 4 mm in diameter [35]. Polyethylene glycol-based adhesives that offer full mechanical sealing within a minute are also used in the repair of aortic dissections [33]. Cyanoacrylates are also widely used in vascular surgery. For example, cases of balloon-assisted embolization [36] and the closure of lower extremity superficial truncal veins [37] have been reported.

27.3.4 Laparoscopic surgery

The use of adhesives to close incisions from laparoscopic surgeries presents many advantages: they are easy to use, do not produce pain for the patient, and avoid the need for additional dressing. However, the use of adhesives requires a good-quality hemostasis to avoid blood clots.

Fibrin adhesives were used to fix a macroporous intraperitoneal prosthesis for the laparoscopic repair of incisional hernias. The use of these adhesives results in a low incidence of pain, hemorrhage, seroma development, and recurrence [38].

27.3.5 Dental adhesives

In dentistry, adhesives are used to obtain good retention of restorative materials inside the prepared cavity on the tooth. Improving contact also results in a reduction of bacterial leakage [39]. There are three types of systems: etch-and-rinse adhesives that require an acid etching treatment; self-etching adhesives that are responsible for simultaneous etching and adhesion to tooth substrates; and multimode or universal adhesives that can be used as self-etching or etch and rinse, depending on the specific case [40].

27.3.6 Bone adhesives

As an alternative to prostheses, bone adhesives are used to directly join broken fragments of bone together, being gradually replaced by the regrowing bone [41]. The first bone adhesives, developed in the 1940s, were based on gelatine, epoxy resins, and acrylates. However, they were not appropriate, but created the foundation for future research. Nowadays, epoxy adhesives have been discarded because of biocompatibility issues, and research on synthetic adhesives is focused on polyacrylic acid, polyester, polyurethanes, methacrylates, and cyanoacrylates. In terms of natural polymers, bone adhesives have been developed from a component of naturally secreted proteins [42,43]. Bone adhesives based on chitosan and dextran were also developed [44,45].

Furthermore, in recent years, scaffolds have been widely explored as a new alternative for autografts. When scaffolds start to be implemented, adhesives will play an important role in scaffold adhesion to assure anchoring in place and the adequate transmission of forces [15].

One particular case of bone joining application is acrylic bone cement; these materials are widely used in orthopedics, being the dominant fixation material in joint [arthroplasty](#) used to anchor the prosthesis to the bone. However, these are not always considered adhesives as they do not form a chemical bond with bone, but instead a mechanical bond.

Bone cements are constituted from two phases before mixing: a liquid phase and a solid phase. At the moment of cement application during surgery, both phases are mixed at room temperature, resulting in a viscous dough.

The polymerization and cure of the cement begin just after mixing both cement phases. Consequently, the viscosity of the cement gradually increases until it hardens completely, reaching its final mechanical properties several minutes after mixing.

27.3.7 Medical tapes and drug delivery patches

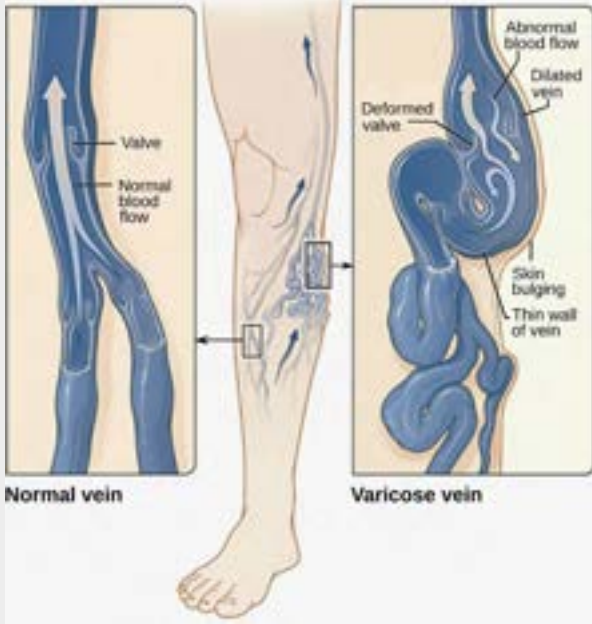
Medical skin adhesives patches are versatile tools used for different medical applications. The most widely used adhesive patches are commonly known as band aids. Usually, they are acrylic tapes for the treatment of minor skin wounds [46]. Nowadays, the possibility of using photocurable acrylic adhesives containing drugs has been explored [47]. Drug delivery through adhesive patches presents an important advantage compared to conventional administration procedures: the dosage is continuous and controlled, avoiding spikes and falls.

27.3.8 Others

Another common application of adhesives is the attachment of devices such as colostomy or diabetes medical devices, that is, glucose sensors and insulin infusion sets. Adhesives in these applications can produce skin side effects such as rashes and itching. Mainly, acrylate-based adhesives are used in these applications [48].

In regard to the future development of new bioadhesive formulations to expand their use in medicine, researchers have reported novel multifunctional bioadhesives with improved performance beyond the mechanical support to the repaired tissue. Multifunctional bioadhesives have added functions aimed at improving the outcome of the wound-healing process. Some examples include antimicrobial properties to minimize microbial adhesion; self-healing characteristics to prolong the service life of the adhesive; stimuli response to applied triggers such as pH, electricity, temperature, light, or changes in the wound environment to promote cellular migration; tissue-specific gene expression; and native tissue healing [14].

27.3.9 Case study

<p>Surgical procedure: Treatment of incompetent saphenous veins.</p> <p>Tissues: Vascular tissues. Veins</p> <p>Adhesive: Cyanoacrylate: <i>n</i>-butyl-2-cyanoacrylate (<i>n</i>-BCA) and <i>n</i>-butyl-5-cyanoacrylate</p>	 <p>The diagram illustrates the difference between a normal vein and a varicose vein. On the left, a 'Normal vein' is shown with a 'Valve' and 'Normal blood flow' indicated by an upward arrow. On the right, a 'Varicose vein' is shown with a 'Deformed valve', 'Abnormal blood flow' (indicated by a downward arrow), a 'Dilated vein', 'Skin bulging', and a 'Thin wall of vein'. A central illustration of a human leg shows the location of these veins, with arrows pointing to the corresponding diagrams.</p>
<p>Background</p>	
<p>Over the last two decades, thermal endovenous ablation with radiofrequency (RFA) or laser (EVLA) has replaced traditional surgery (high ligation and stripping to knee level) as a gold standard method for the treatment of chronic venous insufficiency (CVI). RFA and EVLA use tumescent anesthesia to minimize the risk of damage to the saphenous nerve and surrounding tissues [49]. Tumescent anesthesia, which involves multiple needle injections along the truncal vein pathway, causes pain and complications to the patients [37,50].</p> <p>New nonthermal and nontumescent ablation techniques have recently emerged to avoid some of these unwelcome effects. Cyanoacrylate closure (CAC) of refluxing saphenous veins consists of delivering cyanoacrylate adhesive to the vein, which induces inflammatory reaction and embolization of the vein [51]. CAC registers lower rates of adverse events with no difference in major adverse events, lower pain rates, less use of anesthesia and compression bandages, and shorter intervention and recovery times [52].</p>	
<p>Adhesive qualification and specification</p>	
<ul style="list-style-type: none"> • FDA PMA approval • CE Marked 	<ul style="list-style-type: none"> • Laboratory studies: Adhesive testing, material characterization, adhesive strength characterization, heat of polymerization, degradation rate • Animal studies • Additional studies. Biocompatibility ISO 10993-1 biocompatibility requirements. Adhesive polymerized and unpolymerized states (permanent implant in contact with circulating blood). Sterilization resistance testing ISO 11135-1. Packaging validation. Shelf life. • Clinical studies

Continued

Bonding procedure

- The adhesive can be applied by a catheter (5–7 F in diameter and 800–900 mm in length) by intravenous injections, with no need for general, spinal, or tumescent anesthesia. Once the adhesive has been injected, manual compression (30–90 s) is applied to facilitate complete bonding and sealing of the vein wall. This procedure is repeated several times, each 30 mm for the remaining segments of the vein.
- Puncture site and monitoring of the progress of the catheter and sealing of the vein is carried out by Doppler ultrasound.

27.4 Adhesives in medical device industry

27.4.1 Surgical instruments

One of the most important requirements for surgical instruments is that they have to resist multiple cycles of sterilization, usually performed by a cleaning process followed by steam sterilization. In minimally invasive procedures, many instruments are used, such as laparoscopes, endoscopes, arthroscopes, bronchoscopes, laryngoscopes, sigmoidoscopes, cystoscopes, etc. For this kind of applications, light-cure epoxy and light-cure silicone adhesives are used. Two-part epoxy cured by heat can also be used to bond surgical instruments, endoscopes, and light guides.

27.4.2 Medical disposables

Medical disposables include applications such as needles, syringes, catheters, tubes, connectors, etc. In these applications, light-cure acrylics, light-cure cyanoacrylates, and one-part heat-cure epoxies are the most common adhesives.

Disposables with transparent substrates are assembled using light-curing acrylics, such as lancets, syringes, injectors, hypodermics, and blood collection sets while non-transparent substrates use adhesives that are cured without light, such as the polypropylene moldings of drug administration guns bonded together with a cyanoacrylate adhesive [53].

In catheter assembly, light-cure acrylics, cyanoacrylates, and light-cure silicones can be found. Finally, for tubes and connectors, the preferred adhesives are acrylics, cyanoacrylates, and silicones, all of them light cure [54].

27.4.3 Reservoirs and enclosures

Reservoirs and housings in medical devices are typically made from transparent substrates to enable the monitoring of the fluid inside. Invisible, clear, and transparent adhesives are preferred. Light-cure acrylics and cyanoacrylates are the most widely used adhesives for fluid storage reservoirs and fluid monitoring devices [54]. Acrylic-based adhesives are used to bond polycarbonate medical devices such as cardiotomy reservoirs [53].

27.4.4 Blood filtration

Medical filtration applications include oxygenators, dialyzers, and filters. They are usually assembled by using adhesives as polyurethanes, light-cure acrylics, and epoxies [54]. In dialyzers (Fig. 27.5), polyurethane adhesives are used to bond and seal the ends of the fiber bundles. Like cardiotomy reservoirs, filters, blood pressure transducers, arteriography manifolds, and blood oxygenators are made of transparent polycarbonate. Therefore, they are also bonded by light curing. The bonding of end caps to the main tube of blood filters is done with epoxy adhesives [53].

27.4.5 Diagnostic equipment

The use of adhesives in diagnostic and imaging equipment includes electronic assemblies and, therefore, the range of adhesives used in these applications is huge. It includes anaerobics, cyanoacrylates, light-cure acrylics, epoxies, polyurethanes,

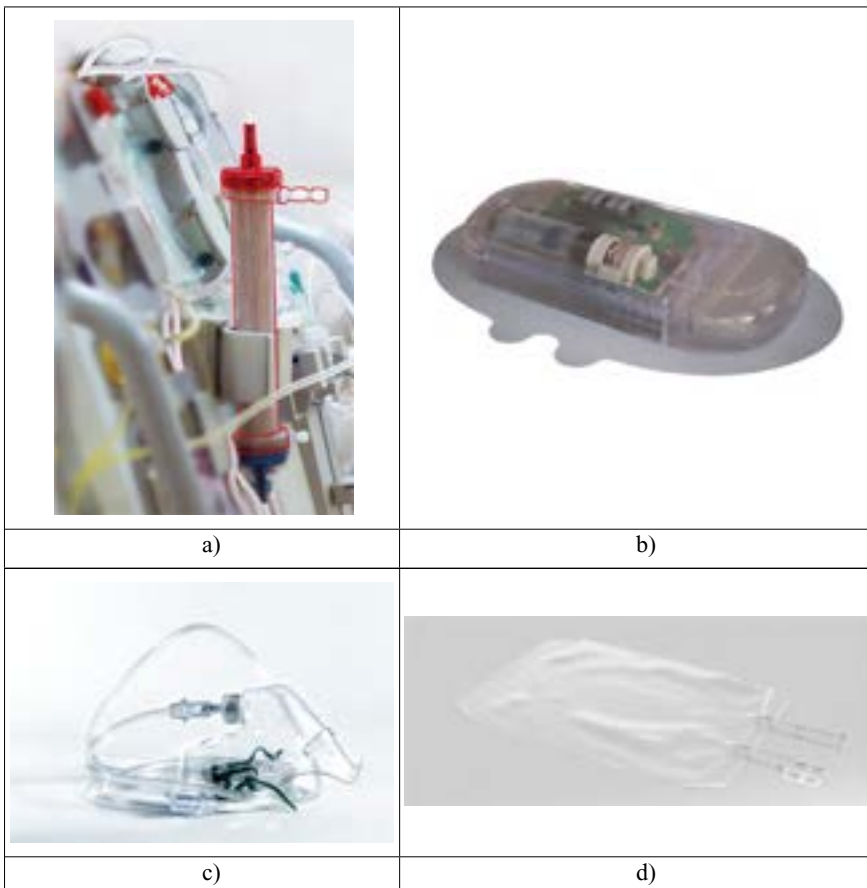


Fig. 27.5 Common applications of biomedical adhesives for medical devices: (a) dialyzer; (b) insulin patch pump; (c) mask for respiratory devices; (d) fluid bags.

silicones, and two-part acrylics [54] to bond the housings or the subcomponents (Fig. 27.5). For electronic assemblies, all types of electronic adhesives are used, such as electrically or thermally conductive adhesives and underfills as well as encapsulants such as glob tops, conformal coatings, and potting materials. In medical devices with high mechanical loads or high risk of bending or dropping, such as computerized topography scanners or wearables, underfills are used to protect the stress-sensitive electrical connections of the surface mounted device (SMD) from breaking and disconnecting, as the adhesive under the SMD absorbs the mechanical forces.


27.4.6 Others

The variety of medical devices is unlimited. The adhesives used in medical devices, such as in anesthesia and face masks, also have adhesive joints. In these cases, light-cure acrylic adhesives are employed to join the cushion, made of flexible PVC, to the dome, made of rigid PVC [53]. Adhesive families used in medical devices are summarized in Table 27.5.

Table 27.5 Adhesive families used in medical devices.

Medical device application	Common substrates	Adhesives
Medical disposables	Plastics (majority transparent), such as PC, acrylic, ABS, PP; Elastomers (majority transparent), such as silicones, TPU, TPE, plasticized PVC, PP Stainless steel, nitinol, glass (inert, like borax)	<ul style="list-style-type: none"> – Light-cure acrylics – Cyanoacrylates and light-cure cyanoacrylates – Epoxies, heat cure, or two component – Silicone, RTV cure, or light cure
Reservoirs and enclosures	Transparent plastics such as PC, acrylic, ABS	<ul style="list-style-type: none"> – Light-cure acrylics – Cyanoacrylates and light-cure cyanoacrylates
Blood filtration	PC, PP, polysulfone membrane	<ul style="list-style-type: none"> – Polyurethanes – Light-cure acrylics – Epoxies, two component
Diagnostic equipment	Unlimited variety of plastics, corrosion resistant metals, electronic substrates such as FR4 boards	<ul style="list-style-type: none"> – Anaerobics – Cyanoacrylates – Acrylics – Epoxies – Polyurethanes – Silicones – Electronic adhesives

27.4.7 Case study

<p>Device type: Hypodermic needle Materials: Polypropylene hub (plasma treated) to stainless steel cannula Adhesive: Light-curing acrylic</p>	
Assembly requirements	
<p>Performance requirements</p> <ul style="list-style-type: none">• Strong and durable assembly• Sterilization resistance (gamma/ETO)• High needle pull-out force• Low extractable and leachable profile	<p>Process requirements</p> <ul style="list-style-type: none">• Cannula sizes: G16 to G30• Adhesive dispensing after assembly• Fast LED cure• Suitable for highly automated high-speed production• In-line adhesive detection and quality inspection
Adhesive qualification and specification	
<ul style="list-style-type: none">• Compliance with ISO 10993 biocompatibility requirements• Clear adhesive joint• Fluorescent for in-line inspection• Viscosity 250 to 450mPas• Flow time into gap <8 s• Solvent free	<ul style="list-style-type: none">• Pull strength requirements according to ISO 7864• Accelerated aging tests: 60°C for 8 weeks• Sterilization resistance testing• DQ, IQ, OQ, PQ (design/installation/operational/performance qualification)

Quality control

Upon adhesive receipt

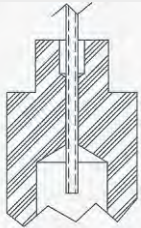
- Visual appearance
- Viscosity
- Needle pull-out force
- Curing depth
- Fixture time

During assembly

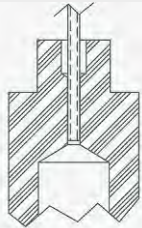
- In-line detection of adhesive after curing
- In-line testing of correct needle orientation
- In-line testing of minimum needle pull-out force
- Off-line statistical testing for maximum pull-out force

Bonding geometry

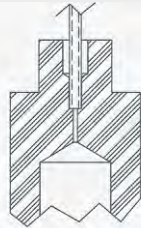
Common needle designs:



A. Protruding Cannula



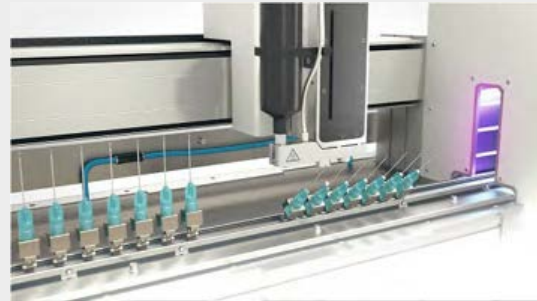
B. Recessed Cannula



C. Seated Cannula

- Typical design for hypodermic needles: Seated cannula
- Diametrical gap (cannula/hub): approx. 0.002" (0.05 mm)

Processing:



- Jet-dispensing of adhesive (shown in white) on preassembled needle before UV-curing station

27.5 Certification, safety, quality, and specifications

A biomedical adhesive often differs from other industrial adhesives because it must undergo a testing procedure to determine its biocompatibility. The biocompatibility assessment of a biomedical adhesive depends on various factors, such as the physico-chemical properties of the adhesive, the type of tissue it is in contact with, and the duration of that exposure.

Biomedical adhesives can be classified into two main applications: tissue adhesives and adhesives for medical devices. Tissue adhesives are specially formulated to use directly on the body, such as a suture or sealant in a surgical procedure. Adhesives for the medical devices industry are used in a variety of applications including syringes, airway masks, tubes, etc. From a regulatory point of view, both types of adhesives should be evaluated concerning their potential risks by themselves or being a part of a medical device.

27.5.1 Regulatory process in the United States and European Union for medical devices

Medical devices in the US market are regulated by the Food and Drug Administration (FDA), whose legal authority to regulate medical devices is based on the Federal Food Drug and Cosmetic Act (FD&C Act) [55].

The FDA classifies medical devices into three classes based on their risk, intended use, and different required controls to ensure product safety: Class I (general controls; with and without exemptions), Class II (general and special controls), and Class III (general controls, special controls, clinical studies, and premarket approval [PMA]) (Fig. 27.6).

Class I includes the lowest risk products and Class III those with the highest risk. The class to which products are assigned determines the type of premarket filing or application required for FDA premarket authorization or approval.

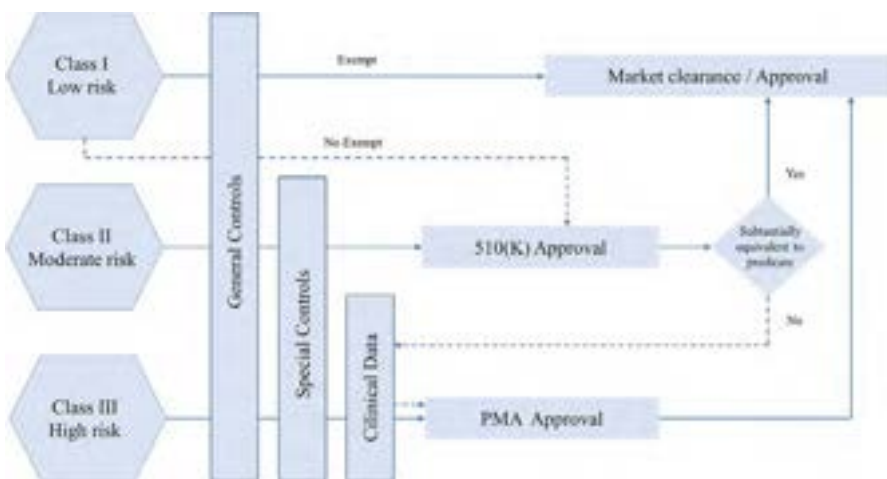


Fig. 27.6 FDA regulatory process for a new medical device.

Several types of premarket submissions can be made to the FDA:

- 510K
- Premarket approval application (PMA)
- DE NOVO
- Humanitarian device exemption
- Investigational device exemption

In order to legally market a device in the United States, the most common forms of premarket submissions to FDA are the 510(k) premarket notification submission and the PMA.

A 510(k) is a premarket submission made to the FDA to demonstrate that the device (class I and II) to be marketed is at least as safe and effective (substantially equivalent) to a legally marketed device. Submitters must compare their device to one or more similar legally marketed devices (predicates) and make and support their substantial equivalency claims [56].

The PMA is an FDA scientific and regulatory review process for evaluating the safety and effectiveness of Class III medical devices and is the most rigorous premarket submission. Due to the risk associated with Class III devices, PMA applications require additional data from laboratory and clinical studies that are not required under the 510k process.

The FDA classifies tissue adhesives into two groups, with the first being tissue adhesive for the topical approximation of skin (Class II) [57]. A typical application is the closure of surgical incisions and simple traumatic lacerations that have easily approximated skin edges. This group typically includes cyanoacrylate adhesives [58,59]. The other group is defined as a tissue adhesive for nontopical use (Class III) and in this case, its intended use is the adhesion of internal tissues in vascular, abdominal, or ophthalmological surgery [57]. Examples of commercial adhesives within this group include adhesives based on polyurethanes [60] or cyanoacrylates [61].

Because tissue adhesives are Class II and III devices, they require more rigorous testing and comprehensive evaluation. This would include the submission of valid scientific evidence demonstrating a reasonable assurance of safety and efficacy, including laboratory, animal, and clinical data as well as clinical trials, panel review, and a preapproval inspection.

Adhesives used in the assembly of medical devices must also comply with a series of controls because the device where they are used is also subject to regulatory requirements. In these cases, the materials from which they are manufactured and the cured adhesives used in their assembly are evaluated with biocompatibility study procedures similar to those of the final devices.

Within the European Union, the regulatory procedures for medical devices are carried out through the application of Medical Devices Regulation (MDR) [62] and is regulated at the member state level, but the European Medicines Agency (EMA) is involved in the regulatory process [63].

The products will be classified as Class I (low risk), Class IIA (medium risk), Class IIB (medium/high risk), and Class III (high risk), taking into account the intended purpose of the products and their inherent risks based on the invasiveness and duration of use of the devices [64,65].

The demonstration of conformity is primarily the responsibility of the manufacturer, and for most classes of products, conformity is subsequently assessed by a notified body. The higher the class of product, the more involved a notified body is in the conformity assessment. Annex I (general safety and performance requirements) and Annexes II (technical documentation) and III (technical documentation for postmarket surveillance) apply to all devices regardless of their class. Other relevant conformity assessment procedures (set out in Annexes IX to XI) depend on the class of the device. For some classes, the manufacturer has a choice between several procedures. Conformity assessment is described in Article 52 of the MDR [66].

27.5.2 Standards to determine biocompatibility of biomedical adhesives

27.5.2.1 USP class VI

For years, the evaluation of the biocompatibility of medical adhesives has been based on the US Pharmacopeia (USP) standards and protocols. The USP publishes biocompatibility protocols for polymeric materials used in medical devices or surgical equipment. Adhesives verified with established procedures and authorized bodies and properly classified are considered safe for use in the assembly of medical devices.

USP part <88> defines six plastic classes based on responses to a series of in vivo tests (see Table 27.6). The highest plastic class is USP Class VI, which requires the following three tests [67]:

- Implantation test: This test is designed for the evaluation of plastic materials and other polymeric materials in direct contact with living tissue.
- Acute systemic toxicity (systemic injection) test: This test is designed to evaluate systemic responses to extracts of materials under test following injection into mice.
- Intracutaneous test: This test is designed to evaluate local responses to the extracts of materials under test following intracutaneous injection into rabbits.

This type of testing is widely used in the medical device industry, and it provides first guidance in selecting a plastic material for a medical device, but the significance of the results and the level of safety assurance for medical devices are limited. For example, it would be possible to pass the USP Class VI tests and still be found to be cytotoxic, mutagenic, or sensitizing in other biological tests that may be required for biocompatibility evaluation of a medical device, according to ISO 10993-1. Therefore, such a test does not meet any device categorization and endpoint requirements. USP biocompatibility testing always gives only a portion of the information for material characterization.

27.5.2.2 ISO 10993 standards

In recent years, the USP tests have been superseded by the more robust ISO 10993 family of standards. The FDA and EMA agreed to use ISO 10993 guidelines to conduct biocompatibility testing [68]. The ISO 10993 series consists of more than 20 standards that guide the biocompatibility testing of medical devices and components.

Table 27.6 USP classification of plastics.

Plastic classes ^a						Tests to be conducted			
I	II	III	IV	V	VI	Test material	Animal	Dose	Procedure ^b
X	X	X	X	X	X	Extract of sample in sodium	Mouse	50 mL/kg	A (iv)
X	X	X	X	X	X	Chloride injection	Rabbit	0.2 mL/animal at each of 10 sites	B
	X	X	X	X	X	Extract of sample in 1 in 20	Mouse	50 mL/kg	A (iv)
	X	X	X	X	X	Solution of alcohol in sodium chloride injection	Rabbit	0.2 mL/animal at each of 10 sites	B
		X		X	X	Extract of sample in	Mouse	10 g/kg	A (ip)
				X	X	Polyethylene glycol 400	Rabbit	0.2 mL/animal at each of 10 sites	B
		X	X	X	X	Extract of sample in	Mouse	50 mL/kg	A(ip)
			X	X	X	Vegetable oil	Rabbit	0.2 mL/animal at each of 10 sites	B
			X		X	Implant strips on sample	Rabbit	Four strips/animal	C

^a Tests required for each class are indicated by “X” in appropriate columns.

^b Legend: *A(iv)*, systemic injection test (intravenous); *A(ip)*, systemic injection test (intraperitoneal); *B*, intracutaneous test; *C*, implantation test (intramuscular implantation).

Credit: (http://www.uspbep.com/usp29/v29240/usp29nf24s0_c88.html).

Like the USP standard, the ISO 10993 standard also distinguishes medical devices based on their contact with the body and their duration. However standard ISO 10993-1 [69] is intended as guidance to determine the potential biological risks arising from material components, the manufacturing process, and the clinical use of the medical device. It states that the evaluation and testing of medical devices are done as part of a risk management process based on ISO 14971 [62] to provide a robust system that gives scientific validity to the biological response evaluation process, complies with regulatory compliance laws, and offers greater assurance to the stakeholders regarding the biological safety of medical devices.

ISO 10993-1 is an important standard as it describes all relevant biological tests required for the material evaluation for medical devices. Subsequent ISO 10993 standards are more specific to the type of biocompatibility or toxicity tests. Fig. 27.7 is used to identify the required evaluation endpoints during risk assessment depending on the end use.

For all medical devices, a physical and/or chemical information assessment is required regardless of risk, use, or exposure duration of the device. Based on this information, the required endpoints are evaluated. The decision tree (Fig. 27.8) can be used to assess whether biocompatibility testing is required.

Device categories	Exposure duration	Physical and/or chemical information	Cytotoxicity	Sensitization	Irritation/ Irritation/ Irritation	Material-Mediated Toxicity	Acute systemic toxicity	Subacute systemic toxicity	Subchronic Toxicity	Chronic Toxicity	Implantation	Haemocompatibility	Genotoxicity	Carcinogenicity	Reproductive/Developmental	Biodegradability
Surface medical devices																
Skin	Limited (<24 hours)	●	●	●	●											
	Prolonged (24 hours to 30 days)	●	●	●	●											
	Permanent >30 days	●	●	●	●											
Mucosal Membrane	Limited (<24 hours)	●	●	●	●											
	Prolonged (24 hours to 30 days)	●	●	●	●											
	Permanent >30 days	●	●	●	●											
Intracutaneous or subcutaneous	Limited (<24 hours)	●	●	●	●											
	Prolonged (24 hours to 30 days)	●	●	●	●											
	Permanent >30 days	●	●	●	●											
Externally communicating devices																
Blood Path, indirect	Limited (<24 hours)	●	●	●	●											
	Prolonged (24 hours to 30 days)	●	●	●	●											
	Permanent >30 days	●	●	●	●											
Tissue, bone, device communicating	Limited (<24 hours)	●	●	●	●											
	Prolonged (24 hours to 30 days)	●	●	●	●											
	Permanent >30 days	●	●	●	●											
Circulating blood	Limited (<24 hours)	●	●	●	●											
	Prolonged (24 hours to 30 days)	●	●	●	●											
	Permanent >30 days	●	●	●	●											
Implant devices																
Tissue or bone	Limited (<24 hours)	●	●	●	●											
	Prolonged (24 hours to 30 days)	●	●	●	●											
	Permanent >30 days	●	●	●	●											
Blood	Limited (<24 hours)	●	●	●	●											
	Prolonged (24 hours to 30 days)	●	●	●	●											
	Permanent >30 days	●	●	●	●											

● ISO 10993-1 endpoints for evaluation
 ● Pre-clinical information needed for a risk assessment

Fig. 27.7 Endpoints to be addressed in a biological risk assessment. Adapted from: AnnexA-ISO 10993-1_2018.

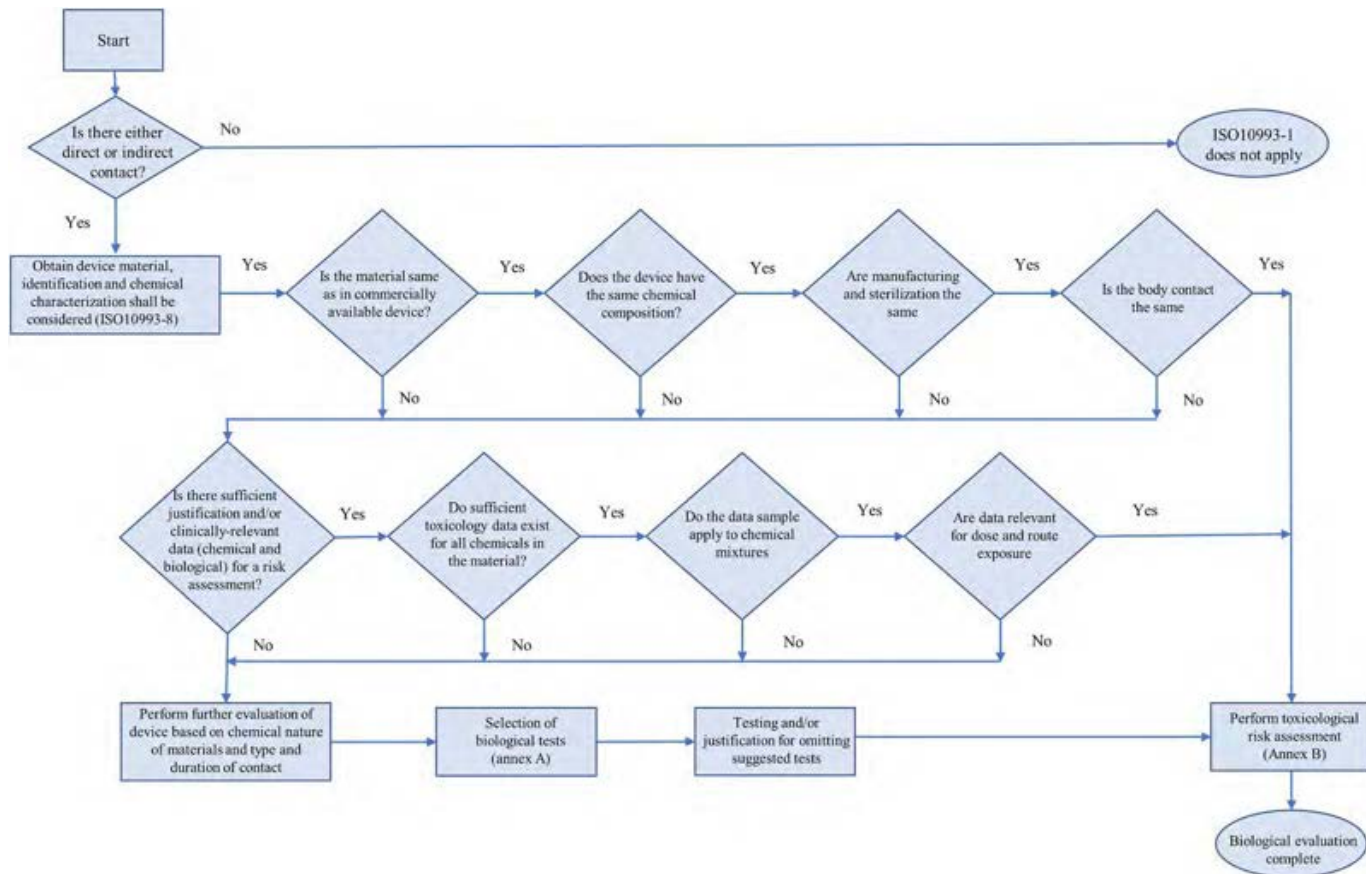


Fig. 27.8 Approach to a biological evaluation of medical devices as part of a risk management process. Adapted from: ISO 10993-1_2018.

For medical devices, the required testing varies by the nature, use, and duration of use of the device.

ISO 10993 biocompatibility tests typically applied as prescreening for adhesives used in medical devices by adhesive suppliers are as follows:

- ISO 10993-4 hemolysis. Selection of tests for interactions with blood.
- ISO 10993-5 cytotoxicity. In vitro cytotoxicity tests.
- ISO 10993-6 implementation. Tests of local effects after implantation.
- ISO 10993-10 intracutaneous: Sensitization and irritation. Irritation and delayed hypersensitivity tests.
- ISO 10993-11 systemic toxicity. Systemic toxicity tests.

Generally, the typical starting test method used to determine the biocompatibility of an adhesive is the ISO 10993-5 cytotoxicity test. This test helps to screen if the adhesive has any negative impact on mammalian cells; however, this test alone is not sufficient to meet the specifications of regulatory agencies.

To obtain the authorization to use and commercialize tissue adhesives, besides biocompatibility tests, they have to be subjected to some characterization tests such as viscosity, purity, setting time, heat of polymerization, physical and mechanical testing, shelf life, and sterility [70].

In addition, for tissue adhesives, animal tests are recommended to evaluate the potential for delayed healing and the effect of fumes produced during polymerization on tissue and skin to avoid chemical burns. Although clinical studies will not generally be required for most tissue adhesives, they are required in some cases when new formulations are used or the previously approved application is changed.

References

- [1] C.A. Carton, L.A. Kessler, B. Seidenberg, E.A. Hurwitt, Experimental studies in surgery of small blood vessels. II. Patching of arteriotomy using a plastic adhesive, *J. Neurosurg.* 18 (2) (1961) 188–194, <https://doi.org/10.3171/jns.1961.18.2.0188>.
- [2] C.A. Heisterkamp, R.L. Simmons, J. Vernick, T. Marsumoto, Solid organ injuries in Vietnam, *Arch. Surg.* 100 (1970) 109–112.
- [3] R.T. Moretti Neto, I. Mello, A.B. da Silveira Moretti, C.R.C. Robazza, A.A.C. Pereira, In vivo qualitative analysis of the biocompatibility of different cyanoacrylate-based adhesives, *Braz. Oral Res.* 22 (1) (2008) 43–47.
- [4] K. Zheng, Q. Gu, D. Zhou, M. Zhou, L. Zhang, Recent progress in surgical adhesives for biomedical applications, *Smart Mater. Med.* 3 (2022) 41–65, <https://doi.org/10.1016/j.smaim.2021.11.004>.
- [5] K.H. Park, K.Y. Seong, S.Y. Yang, S. Seo, Advances in medical adhesives inspired by aquatic organisms' adhesion, *Biomater. Res.* 21 (16) (2017).
- [6] H.G. Silverman, F.F. Roberto, Understanding marine mussel adhesion, *Mar. Biotechnol.* 9 (6) (2007) 661–681.
- [7] C. Liang, J. Strickland, Z. Ye, W. Wu, B. Hu, D. Rittschof, Biochemistry of barnacle adhesion: an updated review, *Front. Mar. Sci.* 6 (2019) 1–20.
- [8] J.R.A. Santos, A.T. Macedo, A.A. Santana, M.E.P. Souza, R.A. Holanda, G. Cruz, Green adhesives for biomedical applications, in: *Green Adhesives: Preparation, Properties and Applications*, 2020, pp. 85–120.

- [9] L.G. Confederat, C.G. Tuchilus, M. Dragan, Sha'at M, Dragostin OM., Preparation and antimicrobial activity of chitosan and its derivatives: a concise review, *Molecules* 26 (12) (2021) 3694.
- [10] L. Garcia Camargo, P. de Freitas Rosa Remiro, G.S. Rezende, S. Di Carla Santos, M. Franz-Montan, Â.M. Moraes, Development of bioadhesive polysaccharide-based films for topical release of the immunomodulatory agent imiquimod on oral mucosa lesions, *Eur. Polym. J.* 151 (2021), 110422.
- [11] G. Tejada, G.N. Piccirilli, M. Sortino, C.J. Salomón, M.C. Lamas, D. Leonardi, Formulation and in-vitro efficacy of antifungal mucoadhesive polymeric matrices for the delivery of miconazole nitrate, *Mater. Sci. Eng. C* 79 (2017) 140–150.
- [12] N. Pandey, L. Soto-Garcia, S. Yaman, A. Kuriakose, A.U. Rivera, V. Jones, et al., Polydopamine nanoparticles and hyaluronic acid hydrogels for mussel-inspired tissue adhesive nanocomposites, *Mater. Sci. Eng. C* (2021), 112589, <https://doi.org/10.1016/j.msec.2021.112589>.
- [13] Y. Zhang, Y. Zheng, F. Shu, R. Zhou, B. Bao, S. Xiao, et al., In situ-formed adhesive hyaluronic acid hydrogel with prolonged amnion-derived conditioned medium release for diabetic wound repair, *Carbohydr. Polym.* 276 (2022), 118752, <https://doi.org/10.1016/j.carbpol.2021.118752>.
- [14] R. Pinnaratip, M.S.A. Bhuiyan, K. Meyers, R.M. Rajachar, B.P. Lee, Multifunctional biomedical adhesives, *Adv. Healthc. Mater.* 8 (11) (2019) 1801568.
- [15] A.J. Vernengo, Adhesive materials for biomedical applications, in: *Adhesives—Applications and Properties*, 2016, pp. 99–136.
- [16] S.H. Kim, Y.J. Lee, J.R. Chao, D.Y. Kim, M.T. Sultan, H.J. Lee, et al., Rapidly photocurable silk fibroin sealant for clinical applications, *NPG Asia Mater.* 12 (2020) 46, <https://doi.org/10.1038/s41427-020-0227-6>.
- [17] J. Sun, J. Han, F. Wang, K. Liu, H. Zhang, Bioengineered protein-based adhesives for biomedical applications, *Chem. Eur. J.* 28 (2022), e202102902.
- [18] Z. Zeng, D. Liu, D. Li, X. Mo, An injectable double cross-linked hydrogel adhesive inspired by synergistic effects of mussel foot proteins for biomedical application, *Colloids Surf. B: Biointerfaces* 204 (2021), 111782, <https://doi.org/10.1016/j.colsurfb.2021.111782>.
- [19] S. Ebnesajjad, A.H. Landrock, Adhesives for medical and dental applications, in: *Adhesives Technology Handbook*, 2015, pp. 258–296.
- [20] G. Pascual, S. Sotomayor, M. Rodríguez, B. Pérez-Köhler, A. Kühnhardt, M. Fernández-Gutiérrez, et al., Cytotoxicity of cyanoacrylate-based tissue adhesives and short-term pre-clinical in vivo biocompatibility in abdominal hernia repair, *PLoS ONE* 11 (6) (2016), e0157920.
- [21] A. Vitale, G. Trusiano, R. Bongiovanni, UV-curing of adhesives: a critical review, in: *Progress in Adhesion and Adhesives*, 2018, pp. 101–154.
- [22] Z. Czech, A. Kowalczyk, J. Swiderska, Pressure-sensitive adhesives for medical applications, in: *Wide Spectra of Quality Control*, 2011, pp. 309–332.
- [23] Z. Czech, A. Kowalczyk, M. Ga, siorowska, J. Soroka, J. Kabatc, Novel pyridinium derivatives as very efficient photoinitiators for UV-activated synthesis of acrylic pressure-sensitive adhesives, *Int. J. Adhes. Adhes.* 31 (2011) 634–638.
- [24] H.J. Kim, Z. Czech, M. Bartkowiak, G.S. Shim, J. Kabatc, A. Licbarski, Study of UV-initiated polymerization and UV crosslinking of acrylic monomers mixture for the production of solvent-free pressure-sensitive adhesive films, *Polym. Test.* 105 (2022), 107424, <https://doi.org/10.1016/j.polymertesting.2021.107424>.
- [25] P.D. Palasz, UV Curable Adhesives Based on Acrylic Polymers, EP 3 091 043 A1, 2016.

- [26] Y. Zaokari, A. Persaud, A. Ibrahim, Biomaterials for adhesion in orthopedic applications: a review, *Eng. Regen.* 1 (2020) 51–63, <https://doi.org/10.1016/j.engreg.2020.07.002>.
- [27] L.C. Rusu, L.C. Ardelean, A.A. Jitariu, C.A. Miu, C.G. Streian, An insight into the structural diversity and clinical applicability of polyurethanes in biomedicine, *Polymers (Basel)* 12 (5) (2020) 1–22.
- [28] L. Ge, S. Chen, Recent advances in tissue adhesives for clinical medicine, *Polymers (Basel)* 12 (2020) 939.
- [29] D. Li, J. Chen, X. Wang, M. Zhang, C. Li, J. Zhou, Recent advances on synthetic and polysaccharide adhesives for biological hemostatic applications, *Front. Bioeng. Biotechnol.* 8 (2020) 926.
- [30] Y.H. Park, J.S. Choi, J.W. Choi, H.J. Kim, Incidence and risk factor of allergic contact dermatitis to 2-octyl cyanoacrylate and n-butyl cyanoacrylate topical skin adhesives, *Sci. Rep.* 11 (2021) 23762, <https://doi.org/10.1038/s41598-021-03319-3>.
- [31] D.M. Toriumi, V.K. Chung, Q.M. Cappelle, Surgical adhesives in facial plastic surgery, *Otolaryngol. Clin. N. Am.* 49 (3) (2016) 585–599, <https://doi.org/10.1016/j.otc.2016.02.012>.
- [32] P.D. Knott, J.E. Zins, J. Banbury, R. Djohan, R.J. Yetman, F. Papay, A comparison of dermabond tissue adhesive and sutures in the primary repair of the congenital cleft lip, *Ann. Plast. Surg.* 58 (2) (2007) 121–125.
- [33] J.K. Allotey, A.H. King, N.H. Kumins, V.L. Wong, K.C. Harth, J.S. Cho, et al., Systematic review of hemostatic agents used in vascular surgery, *J. Vasc. Surg.* 73 (6) (2021) 2189–2197, <https://doi.org/10.1016/j.jvs.2020.10.081>.
- [34] C. Xu, Y. Chen, Y. Si, Y. Yan, A.B. Kayitmazer, Y. Ding, et al., Injectable and biocompatible mussel-inspired adhesive for enhanced reendothelialization of injured artery, *Adv. Mater. Interfaces* 8 (2021) 2001955.
- [35] S. Nam, D. Mooney, Polymeric tissue adhesives, *Chem. Rev.* 121 (2021) 11336–11384.
- [36] R. Fujitsuna, F. Sugihara, D. Yasui, H. Saito, T. Ueda, S. Shirai, et al., Novel treatment of vascular injury from delayed hemodialysis catheter migration by transvenous balloon-assisted embolization with n-butyl cyanoacrylate, *Radiol. Case Rep.* 15 (2020) 1450–1454, <https://doi.org/10.1016/j.radcr.2020.05.077>.
- [37] K. Gibson, B. Ferris, Cyanoacrylate closure of incompetent great, small and accessory saphenous veins without the use of post-procedure compression: initial outcomes of a post-market evaluation of the VenaSeal System (the WAVES Study), *Vascular* 25 (2) (2017) 149–156.
- [38] S. Olmi, A. Scaini, L. Erba, E. Croce, Use of fibrin glue (Tissucol®) in laparoscopic repair of abdominal wall defects: preliminary experience, *Surg. Endosc. Other Interv. Tech.* 21 (2007) 409–413.
- [39] A. Tadin, L. Gavic, N. Galic, Biocompatibility of dental adhesives, in: *Adhesives—Applications and Properties*, 2016, pp. 29–57.
- [40] D. Dressano, M.V. Salvador, M.T. Oliveira, G.M. Marchi, B.M. Fronza, M. Hadis, et al., Chemistry of novel and contemporary resin-based dental adhesives, *J. Mech. Behav. Biomed. Mater.* 110 (2020), 103875, <https://doi.org/10.1016/j.jmbbm.2020.103875>.
- [41] K.O. Böker, K. Richter, K. Jäckle, S. Taheri, I. Grunwald, K. Borchering, et al., Current state of bone adhesives—necessities and hurdles, *Materials (Basel)* 12 (2019) 3975.
- [42] A. Kirillova, C. Kelly, N. von Windheim, K. Gall, Bioinspired mineral-organic bioresorbable bone adhesive, *Adv. Healthc. Mater.* 7 (17) (2018) 1800467.
- [43] K. Richter, G. Diaconu, K. Rischka, M. Amkreutz, F.A. Müller, A. Hartwig, Adsorption studies of mussel-inspired peptides, *Bioinspired Biomim. Nanobiomater.* 2 (2013) 45–53.

- [44] B. Hoffmann, E. Volkmer, A. Kokott, P. Augat, M. Ohnmacht, N. Sedlmayr, et al., Characterisation of a new bioadhesive system based on polysaccharides with the potential to be used as bone glue, *J. Mater. Sci. Mater. Med.* 20 (2009) 2001–2009.
- [45] B. Balakrishnan, D. Soman, U. Payanam, A. Laurent, D. Labarre, A. Jayakrishnan, A novel injectable tissue adhesive based on oxidized dextran and chitosan, *Acta Biomater.* 53 (2017) 343–354, <https://doi.org/10.1016/j.actbio.2017.01.065>.
- [46] I. Hwang, H.N. Kim, M. Seong, S.H. Lee, M. Kang, H. Yi, et al., Multifunctional smart skin adhesive patches for advanced health care, *Adv. Healthc. Mater.* 7 (15) (2018) 1800275.
- [47] P. Ossowicz-Rupniewska, P. Bednarczyk, M. Nowak, A. Nowak, W. Duchnik, Ł. Kucharski, et al., Sustainable uv-crosslinkable acrylic pressure-sensitive adhesives for medical application, *Int. J. Mol. Sci.* 22 (21) (2021) 11840.
- [48] L. Heinemann, S. Kamann, Adhesives used for diabetes medical devices, *J. Diabetes Sci. Technol.* 10 (6) (2016) 1211–1215.
- [49] L.H. Rasmussen, M. Lawaetz, L. Bjoern, B. Vennits, A. Blemings, B. Eklöf, Randomized clinical trial comparing endovenous laser ablation, radiofrequency ablation, foam sclerotherapy and surgical stripping for great saphenous varicose veins, *Br. J. Surg.* 98 (2011) 1079–1087.
- [50] T.Y. Tang, C.J.Q. Yap, S.L. Chan, S.X.Y. Soon, H.Y. Yap, S.Q.W. Lee, et al., Early results of an Asian prospective multicenter VenaSeal real-world postmarket evaluation to investigate the efficacy and safety of cyanoacrylate endovenous ablation for varicose veins, *J. Vasc. Surg. Venous Lymphat. Disord.* 9 (2) (2021) 335–345.e2, <https://doi.org/10.1016/j.jvsv.2020.03.020>.
- [51] T. Proebstle, J. Alm, S. Dimitri, L. Rasmussen, M. Whiteley, J. Lawson, et al., Three-year follow-up results of the prospective European Multicenter Cohort Study on Cyanoacrylate Embolization for treatment of refluxing great saphenous veins, *J. Vasc. Surg. Venous Lymphat. Disord.* 9 (2) (2021) 329–334, <https://doi.org/10.1016/j.jvsv.2020.05.019>.
- [52] E. García-Carpintero, M. Carmona, J.P. Chalco-Orrego, J. González-Enríquez, I. Imaz-Iglesia, Systematic review and meta-analysis of endovenous cyanoacrylate adhesive ablation for incompetent saphenous veins, *J. Vasc. Surg. Venous Lymphat. Disord.* 8 (2) (2020) 287–296, <https://doi.org/10.1016/j.jvsv.2019.09.010>.
- [53] S.M. Tavakoli, D.A. Pullen, S.B. Dunkerton, A review of adhesive bonding techniques for joining medical materials, *Assem. Autom.* 25 (2) (2005) 100–105, <https://doi.org/10.1108/01445150510700070>.
- [54] Henkel Adhesive Technologies, 2022. <https://www.henkel-adhesives.com/us/en/industries/medical/medical-devices.html>.
- [55] Title 21, Chapter 1, Subchapter H, in: Code of Federal Regulations, 2022, pp. 800–898. Available from: <https://www.ecfr.gov/current/title-21>.
- [56] Premarket Notification 510(k), Wiley Encyclopedia of Clinical Trials, 2020, Available from: <https://www.fda.gov/medical-devices/premarket-submissions-selecting-and-preparing-correct-submission/premarket-notification-510k>.
- [57] 21CFR878.4010, in: Code of Federal Regulations, 2008. Title 21, Volume 8, section 878, Available from: <https://www.ecfr.gov/current/title-21/chapter-I/subchapter-H/part-878/subpart-E/section-878.4010>.
- [58] U.S. Food and Drug Administration, Premarket Approval (PMA) for Tissue Adhesive for the Topical Approximation of Skin, vol. 510, Food and Drug Administration, 2008. Available from: <https://www.accessdata.fda.gov/scripts/cdrh/cfdocs/cfpma/pma.cfm?id=P960052>.
- [59] U.S. Food and Drug Administration, Premarket Approval (PMA) for Tissue Adhesive for the Topical Approximation of Skin, vol. 510, Food and Drug Administration, 2008.

Available from: <https://www.accessdata.fda.gov/scripts/cdrh/cfdocs/cfpma/pma.cfm?id=P050013>.

- [60] U.S. Food and Drug Administration, Premarket Approval (PMA) for Tissue Adhesive for Internal Use, vol. 510, Food and Drug Administration, 2015. Available from: <https://www.accessdata.fda.gov/scripts/cdrh/cfdocs/cfpma/pma.cfm?id=P130023>.
- [61] U.S. Food and Drug Administration, Premarket Approval (PMA) for Tissue Adhesive for Use in Embolization of Brain Arteriovenous Malformations, vol. 510, Food and Drug Administration, 2000. Available from: <https://www.accessdata.fda.gov/scripts/cdrh/cfdocs/cfpma/pma.cfm?id=p990040>.
- [62] Regulation (EU) 2017/745 of the European Parliament and of the Council of 5 April 2017 on medical devices, *Off. J. Eur. Union* 117 (2017) 1–175.
- [63] European Medicines Agency, Medical Devices, Available from: <https://www.ema.europa.eu/en/human-regulatory/overview/medical-devices>.
- [64] L. Peter, L. Hajek, P. Maresova, M. Augustynek, M. Penhaker, Medical devices: regulation, risk classification, and open innovation, *J. Open Innov. Technol. Mark. Complex.* 6 (2020) 42, <https://doi.org/10.3390/joitmc6020042>.
- [65] G.M. Taboada, K. Yang, M.J.N. Pereira, S.S. Liu, Y. Hu, J.M. Karp, et al., Overcoming the translational barriers of tissue adhesives, *Nat. Rev. Mater.* 5 (2020) 310–329, <https://doi.org/10.1038/s41578-019-0171-7>.
- [66] Group MDC, Guidance on Classification of Medical Devices, 2021, Available from: https://ec.europa.eu/health/system/files/2021-10/mdcg_2021-24_en_0.pdf.
- [67] The United States Pharmacopeia, 35th Revision: The National Formulary, thirtieth ed., *United States Pharmacopeial Convention*, Rockville, 2011.
- [68] U.S. Food and Drug Administration, Use of International Standard ISO 10993-1, “Biological Evaluation of Medical Devices-Part 1: Evaluation and Testing Within a Risk Management Process” Guidance for Industry and Food and Drug Administration staff, Food and Drug Administration, 2020. Available from: <https://www.fda.gov/media/85865/download>.
- [69] ISO 10993-1:2018, *Biological Evaluation of Medical Devices—Part 1: Evaluation and Testing Within a Risk Management Process*, 2018.
- [70] U.S. Food and Drug Administration, Tissue Adhesive for the Topical Approximation of Skin - Class II Special Controls Guidance for Industry and FDA Staff, in: *Guidance for Industry and FDA Staff*, Food and Drug Administration, 2007. Available from: <https://www.fda.gov/medical-devices/guidance-documents-medical-devices-and-radiation-emitting-products/tissue-adhesive-topical-approximation-skin-class-ii-special-controls-guidance-industry-and-fda-staff>.

Structural monitoring of adhesive joints using machine learning

28

A. Francisco G. Tenreiro^a, Gabriel M.F. Ramalho^b, António Mendes Lopes^{a,b}, and Lucas F.M. da Silva^{a,b}

^aAdvanced Joining Processes Unit, Institute of Science and Innovation in Mechanical and Industrial Engineering (INEGI), Porto, Portugal, ^bDepartment of Mechanical Engineering, Faculty of Engineering (FEUP), University of Porto, Porto, Portugal

28.1 Introduction

Recently, adhesive joining has gradually become an appealing and viable alternative to common joining methods, such as welding, riveting, or mechanical fastening. This change is observed in industrial sectors such as the automotive and aerospace industries, where a reduction of structural weight is required to achieve good levels of energetic efficiency while guaranteeing mechanical performance [1, 2]. This last aspect is of paramount importance because adhesive integrity may be compromised by environmental effects [3–5], diverse loading scenarios [5–8], or unwanted contamination during manufacture [3, 9, 10].

Given the inherent risks throughout the structural adhesive joint's life cycle, defects may appear in either the adhesive layer or in the adhesive-adherend interface, as shown in Fig. 28.1. Cracks may occur due to curing issues, shrinkage caused by thermal cycles, or stress loads (one-off or fatigue). Pockets of poor cure appear with incorrect component mixing or when insufficient heat occurs. Voids appear with relative movement of the adherends during the cure cycle or when insufficient adhesive is applied. Porosities typically exist because of entrapped air or volatile products (from chemical reactions of the curing cycle). Disbands are a type of void caused when adhesive isn't applied, or when it is unevenly applied on an adherend. Finally, weak adhesion (also known as a kissing bond) occurs when there is contact between the adhesive and the adherend, but a poor bond is actually formed. This perilous damage is caused by either poor surface preparation and cleaning, or bad curing procedures [11, 12]. Research has been done to mechanically characterize the influence of damage in bonded joints [12–14].

Normally, studying the mechanical performance of damaged adhesive joints will require destructive tests, which directly evaluate the joint's strength. However, this is inefficient and undesirable because this will require the destruction of structures, which is unfeasible in the manufacturing or maintenance stages. As such,

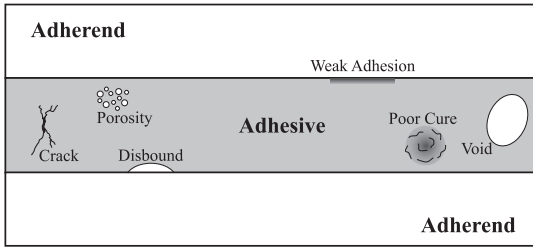


Fig. 28.1 Scheme of various defects in adhesive bonds.

nondestructive test and evaluation (NDT/NDE) methods are used to access the bond integrity by examining properties such as the stiffness or mass distribution [11, 15, 16].

Therefore, this chapter is structured as follows. Section 28.2 overviews several NDT methods to monitor adhesively bonded joints. Section 28.3 follows by listing the issues plaguing NDE to inspect joints in industrial environments, and presents structural health monitoring (SHM) as the next evolution. This section also tackles the theoretical background of two SHM methods—Lamb waves (LWs) and electro-mechanical impedance spectroscopy (EMIS)—and machine learning (ML) algorithms for damage detection. Section 28.4 tackles the use of LWs to detect weak adhesion while Section 28.5 showcases EMIS-based void detection with the help of two ML algorithms. Finally, Section 28.6 concludes this work.

28.2 Nondestructive testing and evaluation

28.2.1 Ultrasonic testing

Ultrasonic-based NDT is one of the most used adhesive integrity evaluation methods, given its versatility for material analysis. Various techniques exist, such as the pulse-echo technique shown in Fig. 28.2, where a probe first generates an ultrasonic pulse.

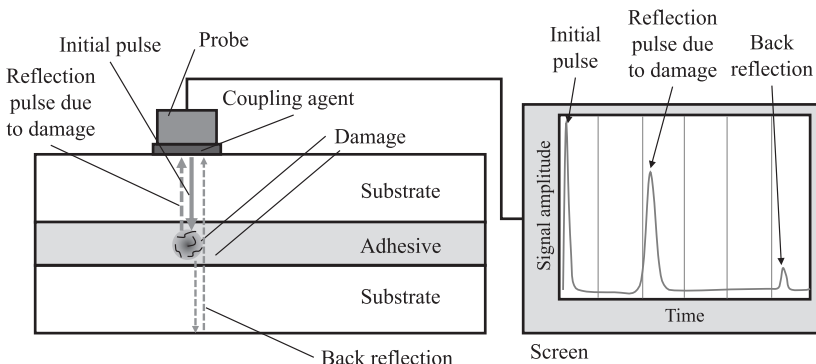


Fig. 28.2 Simplified pulse-echo ultrasonic NDT technique, with an A-scan result displayed on the screen.

there is any material discontinuity, part of the initial wave is reflected back while the remainder will continue until reaching the opposite end of the joint. Afterward, the remaining wave is reflected back toward the probe. One can distinguish the two reflected pulses because the time of flight of each pulse is different, as represented in Fig. 28.2 [11, 17].

The through-transmission technique is another ultrasonic NDE technique, and it uses two perfectly aligned transducers. A transmitter, generating an ultrasonic pulse, is placed on one side of the joint, and a receiving sensor reads the same wave on the opposite side. The measured signal amplitude by the receiver should diminish as the size of the damage increases. When porosities or microcracks are detected, the measured wave amplitude is smaller than the generated wave amplitude. Conversely, when large voids or unbounds are present, the pulse wave is blocked because the damage size is larger than the pulse width. This technique is usually adopted for the inspection of honeycomb structures, airplane fuselages and wings. However, this is only feasible when assess to both sides of the structure is possible. A variation of the through-transmission method exists where a reflecting plate is positioned on the opposite side of the joint.

As previously explained, ultrasonic signals can be presented as an A-scan, or as a scanned map of the whole surface known as a C-scan, with possible defects. As the sensor moves, the echo wave amplitude may change with damage. These amplitudes are then plotted as a function of the position [11, 15, 17].

Traditional ultrasonic-based NDT requires a coupling agent so that the sound wave can easily pass to the component under examination, as there is a large acoustic impedance between the air and any solid material. A commonly used coupling agent is water, which allows better matching of acoustic impedances. However, to perform one of these tests, large tanks are needed where one can immerse the component in water [17]. In the aeronautic industry, to avoid the use of impractical enormous tanks, water jets are also employed. Alternative ultrasound methods were developed such as laser ultrasonics or air-coupled ultrasound [11, 15, 18], but very little has been done to determine their effectiveness in examining adhesive joints. Yilmaz et al. [19] performed a comparative study on the performance of unbound detection on aluminum-epoxy adhesive joints. Results show that air-coupled ultrasonic tests performed worse than both water-coupled through-transmission and pulse-echo ultrasonic NDE.

Other shortcomings in defect detection exist. Defect detection in dissimilar adhesive joints is considerably harder because dissimilar adherends imply a mismatch of acoustic impedance. As such, different wave velocities and the occurrence of different wave reflections/transmissions between media occur [20, 21]. Smagulova et al. [20] developed a signal processing algorithm where void detection in dissimilar adherend joints is achieved from the measured peaks observed after multiple reflections and transmissions. Jasiūnienė et al. [21] inspected dissimilar hybrid joints with pulse-echo NDT, where additively manufactured titanium alloy substrate with an embedded pins was bonded to a carbon fiber-reinforced polymer (CFRP). Damage was detected on both adherends, but sensor scanning could only be performed from the side of the CFRP. Brotherhood et al. [22] studied the detectability of weak adhesion with ultrasonic NDE, concluding that readings of weak adhesion are sensitive to the transducer's contact pressure.

28.2.2 Shearography testing

Shearography is an optical-based method to nondestructively evaluate components. A small strain excitation is generated on the component, whose exposed surface is illuminated with a laser. The light rays are diffused from the surface and toward a beam-splitter, which acts as a prism separating beams of light. These are then reflected by mirrors and captured by a charge-coupled device (CCD) camera, as shown in Fig. 28.3 [23, 24]. Note that other set-ups exist, as detailed in reference [23].

Various strain-generation sources exist such as thermal sources, pressure excitation systems generating either vacuum or a small pressure, or dynamic actuators such as loudspeakers or piezoelectric elements [24, 25].

Taillade et al. [26] evaluated the capacity of shearography-based NDE to detect voids in concrete CFRP bonded joints using vacuum pressure to generate strain. A pressure differential of 10 kPa or less is enough to detect big voids, but the detection of small voids required a pressure difference of about 80 kPa. Kryukov and Böhm [25] studied the feasibility of detecting various defects in adhesive joints of similar and dissimilar materials. Damage was easier to detect when the substrates have lower stiffness, such as joints with aluminum or CFRP adherends. Conversely, when thick steel substrates were used, only pockets of uncured and unmixed adhesive were detected. Furthermore, weak adhesion was inconsistently detected. In steel-steel joints, this damage was detected despite the lack of clear damage boundaries in the resulting image. Conversely, weak adhesion is imperceptible in CFRP-steel joints.

Taiber et al. [27] used Terahertz shearography to evaluate the aging of adhesive joints. While changes in both polymeric substrates and adhesives are detected by transmission measurements, one cannot assign changes in either refractive or absorption indices to an aging factor.

Shearography is viewed as a promising structural adhesive examination method, given its applicability in the aeronautic industry [28]. This method can be automated with the adoption of deep learning and image-processing algorithms for defect detection [29]. However, research should be focused on reliably detecting damage sources in adhesive joints, and on evaluating the algorithm's aptitude in finding damage.

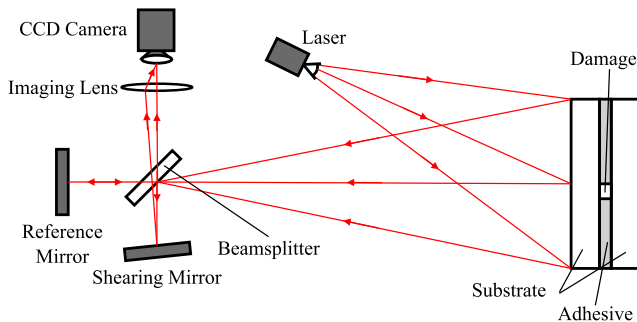


Fig. 28.3 Simplified shearography NDT setup for adhesive structure evaluation.

28.2.3 Infrared thermography testing

Another NDE technique is to measure the temperature distribution of a free surface of the bonded joint. This is the infrared thermography NDT method, where an infrared camera measures the temperature distribution contactlessly. Two main thermography methods exist, the first being the passive thermography method, where a camera monitors the temperature without the influence of a controlled thermal source. Therefore, the camera captures local temperature differences caused by outside influence (e.g., sun radiation, convective winds), which may indicate the presence of defects. Conversely, active thermography uses a heat source and detects damage by measuring the temperature gradients [30].

Active thermography can have various classification criteria, the most common one being the thermal excitation, that is, how the excitation occurs with time. In pulsed thermography (PT), a thermal source generates a pulse excitation, transferring heat in a small period of time, as schematized in Fig. 28.4A. Afterward, the joint cools and the resultant temperature gradients locate the existent defects. As shown in Fig. 28.4B, a heat step excitation is generated in stepped infrared thermography, heating the bonded parts, and the observed inhomogeneous temperature variations reveal the presence of defects. In lock-in thermography, a periodic thermal excitation is generated, as exemplified in Fig. 28.4C, and one analyses the thermal response with phase and magnitude values. Pulsed phase thermography (PPT) combines both the pulsed and lock-in thermography, in the sense that a heat pulse is generated and the frequency domain phase response is studied. Fig. 28.4D presents an alternative method where the excitation frequency is modulated, thus allowing the extraction of the phase information in one inspection [26, 30, 31].

Fernando et al. [32] used passive thermography to evaluate the degree of bonding of a polyurethane adhesive to fabric materials. This was done by comparing the peel

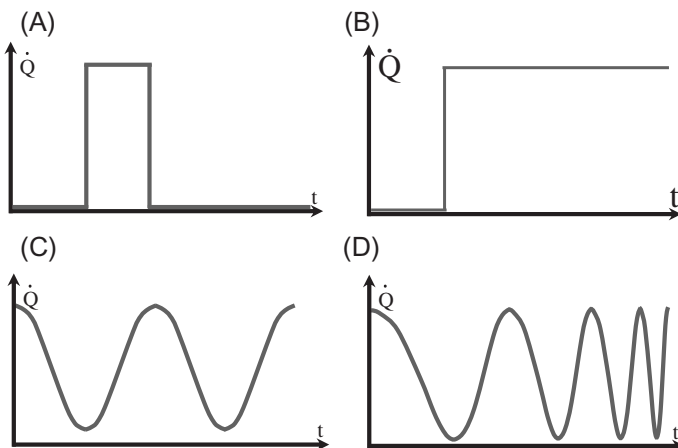


Fig. 28.4 Active thermography excitation methods. (A) Pulse thermography; (B) stepped thermography; (C) lock-in thermography; (D) stepped thermography.

strength, dependent of the curing temperature, with metrics calculated from the thermographic images. The standard deviation from the mean temperature, known as the *in-homogeneity factor*, Ra , correlates well with the observed peel strength. When the peel strength is below 1.6 N mm^{-1} , the Ra metric has values above 0.4, resulting in a steep temperature gradient. Conversely, when the peel strength is above 1.6 N mm^{-1} , Ra decreases to values between 0.1 and 0.3, thus indicating a more homogeneous temperature and adhesive distribution.

Taillade et al. [26] studied the void detection capability of PT in concrete CFRP bonded structures. Using heat transfer relations, the authors accurately estimated the depth of the defect. Hung et al. [24] used PT to detect voids in aluminum and composite joints. While void detection was possible with both spatial image analysis and logarithmic time-temperature plots, this was only possible with large diameter voids that are not deep in the adhesive layer. Grosso et al. [33] evaluated the detectability of voids in tubular glass fiber-reinforced polymer (GFRP) joints with PT. Various parameters were studied, such as the thickness of the collar connecting both tubular composite components, the heating time, and the power. Their research correlated these parameters with the temperature contrast between the zone where voids are present and the pristine adhesive zone, and determined that even with an increase of both the excitation's heating period and power, there is a thickness limit from which voids are undetectable.

Tighe et al. [31] analyzed both PPT and thermoelastic stress analysis (TSA), identical to stress pattern analysis by the measurement of thermal emission (SPATE), to detect weak adhesion in CFRP joints. PPT images of loaded joints enabled the location of defect zones. Furthermore because the use of small loads facilitates weak adhesion detection, a small vacuum chamber was built containing the heat source, thermal camera, and the tested joint. The generated vacuum allowed for testing of the structure without any plastic deformations, and weak adhesion was successfully detected. Kurpinski and Fidali [34] successfully used lock-in thermography to evaluate the distribution of adhesive.

Yilmaz et al. [35] performed one of the only statistical-based studies, where both thermography and ultrasonic tests were done on composite adhesive joints with artificially created voids. C-scans and thermal images were combined using data fusion methods to evaluate the detection of voids. This enabled easier void detection, but only if the sensor measurements are not contradictory.

28.3 Structural health monitoring

Various NDE technologies and their development in adhesive damage detection were described. However, despite thorough research, not all damage foci can be reliably detected. Furthermore, despite clear signs of improvements in NDT to tackle damage detection, reliability does not reach the desired standards.

SHM goes beyond NDT by performing in situ continuous structural monitoring. This method makes use of sensors that directly or indirectly measure the mechanical

properties of the evaluated component. The readings are then sent to an algorithm specialized in damage detection, location, characterization, etc. [36–38], as shown in Fig. 28.5A.

This technology is of particular interest to the aeronautic and aerospace industries [39, 40], where regular vehicular maintenance is mandated by law and components must be designed with high safety factors [41, 42]. This is true for structural adhesive joints, which are viewed as unreliable and are used in combination with mechanical joining methods. SHM aims to be versatile, as the algorithm continuously interrogates the structure for damage whether it is in static condition or in operation. This will enable enterprises to reduce maintenance check-ups with thorough and costly NDT procedures [37].

To characterize damage, an SHM hierarchical approach is required to process information from various sources, which was ported from the military domain to engineering, forming the field of *sensor and data fusion* [43]. Rytter proposed a hierarchical approach to evaluate damage foci, as shown in Fig. 28.5B [44].

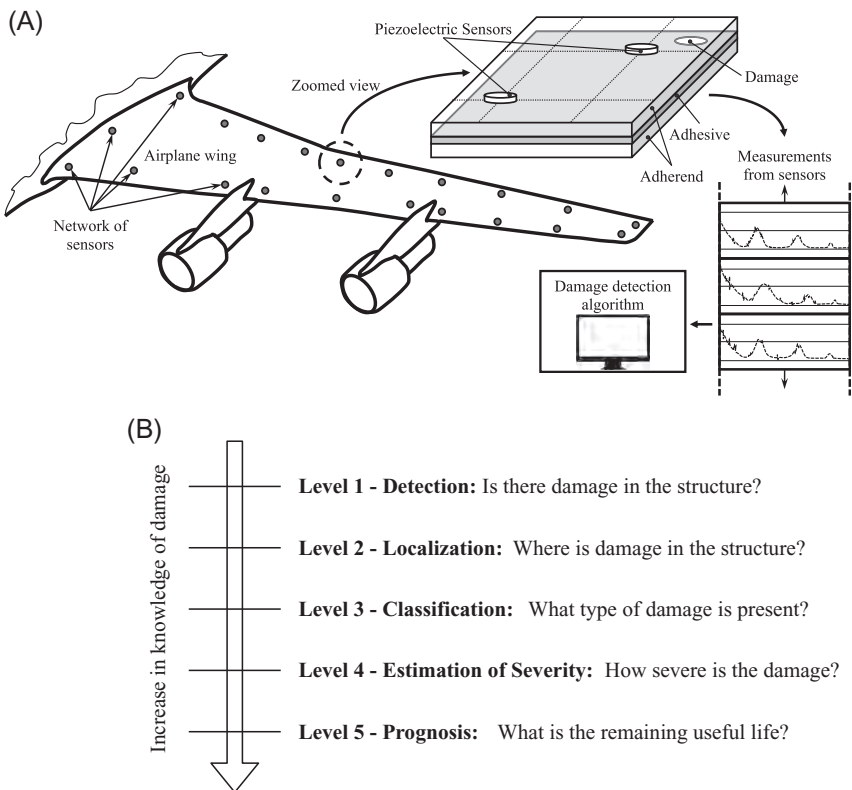


Fig. 28.5 Principles of SHM. (A) SHM methodology applied to an airplane wing; (B) SHM hierarchical approach to the analysis of damage.

In this hierarchical approach, one first examines the existence of damage (Detection). Second, the damage position is determined (Localization). Afterward, the algorithm needs to determine the type of each detected defect (Classification). In a fourth level, the SHM algorithm must evaluate the damage severity (Estimation of the severity). Lastly, the algorithm must calculate the remaining useful life of the monitored structure (Prognosis). Answering these questions in the established order will result in an increasing and precise knowledge of the damage state and the reliability of the structure [43, 45, 46]. Some researchers bundle the third and fourth level into a characterization level [47].

A variety of SHM methods exist, and these can be divided into two categories:

- **Passive SHM Systems**—This type of setup does not require a power source, and thus only sensors are used that monitor noise, low-frequency vibrations, or transient waves caused by small impacts as time goes by. Significant changes will result in damage detection.
- **Active SHM Systems**—In this architecture, a power supply is used as well as both actuators that generate a given excitation to the structure and sensors sensible to such excitations. The obtained measurements may yield conclusions regarding the presence of damage or lack thereof [36].

Various SHM systems have been developed, such as Lamb waves (LW) or shear horizontal waves [47–49], acoustic emissions [38, 50], electrical impedance spectroscopy (EIS) [51–53], infrared thermography [54], and electromechanical impedance spectroscopy (EMIS) [55, 56], among others. In this chapter, research on the use of LW and EMIS for damage detection in adhesive joints will be presented. However, first, a brief theoretical overview of these two SHM methods will be presented.

28.3.1 Lamb waves

LWs are a form of guided waves adopted in SHM, given their sensitivity to material alterations in their propagation path while also being able to travel long distances in slightly curved thin walls [57]. Lamb waves can be excited by various means, with the use of the piezoelectric elements one of the most commonly used, as schematized in Fig. 28.6A.

To generate LWs, a short pulse signal is required to reduce any type of interference that may originate from unwanted reflections. A way to achieve this is by means of a tapering function [58] in conjunction with the base signal, yielding an excitation signal such as the Hann window, described as

$$w(n) = 0.5 - 0.5 \cos\left(\frac{2\pi n}{M-1}\right), \quad (28.1)$$

where M is the number of points and $n = 0, 1, \dots, M-1$.

Despite the promising capabilities in detecting damage, LW, are highly complex signals because two different modes arise during wave generation: the symmetric mode, S_n , and the antisymmetric mode, A_n [59, 60]. These modes are better described with analytical dispersion curves, which are defined as

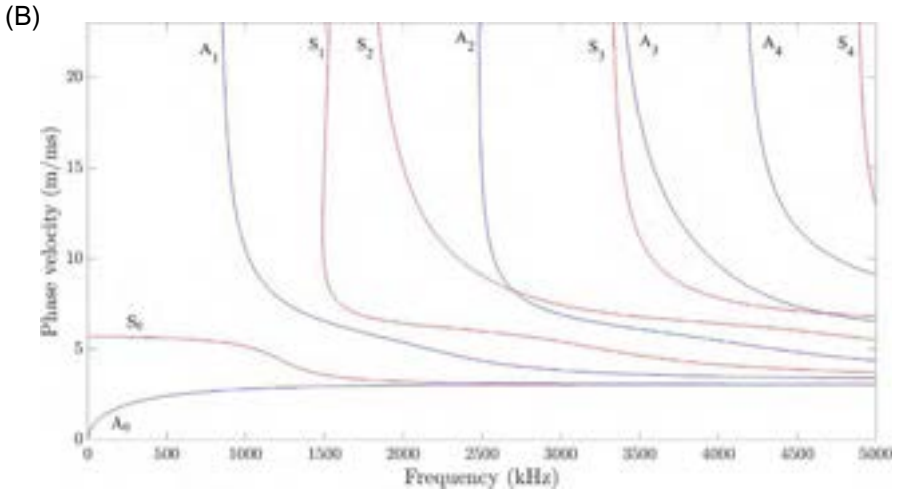
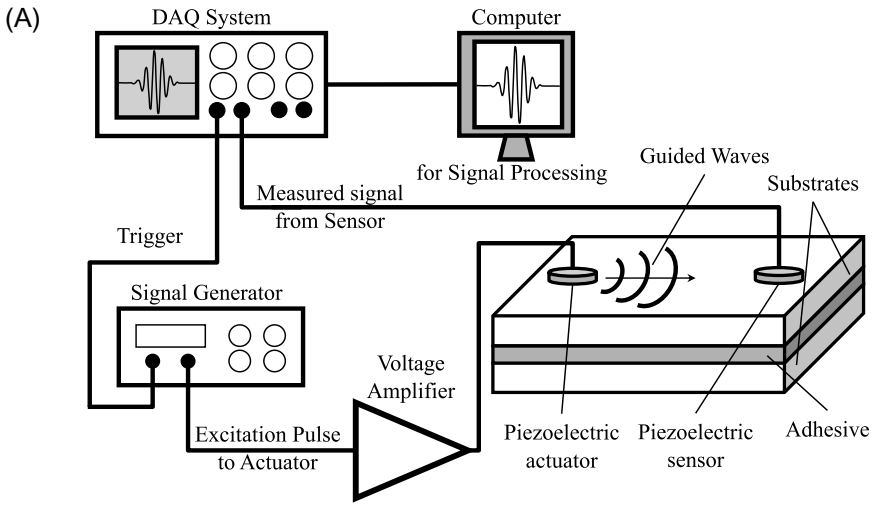


Fig. 28.6 Lamb wave behavior and generation. (A) Lamb wave generation and measurement setup; (B) Plot of symmetric and antisymmetric modes in a wave phase speed vs frequency graph.

$$\frac{\tan(qh)}{\tan(ph)} + \frac{4k^2qp}{(k^2 - q^2)^2} = 0, \tag{28.2}$$

$$\frac{\tan(qh)}{\tan(ph)} + \frac{(k^2 - q^2)^2}{4k^2qp} = 0, \tag{28.3}$$

with

$$p^2 = \frac{\omega^2}{c_L^2} - k^2, \quad q^2 = \frac{\omega^2}{c_T^2} - k^2, \quad k = \frac{2\pi}{\lambda}, \tag{28.4}$$

where p and q are placeholder variables, h stands for the plate's half-thickness, c_L and c_T denote the longitudinal and shear wave velocities, respectively, and k , λ , and ω are the wavenumber, wavelength, and angular frequency, respectively. The mathematical deduction of Eqs. (28.2)–(28.4) is quite extensive and is not presented in this chapter. For a detailed study, please consult references [36] and [61].

The calculation of the dispersion curves using Eqs. (28.2)–(28.4) yields many roots, and thus various modes exist for different frequency excitations [62, 63]. This is shown in Fig. 28.6B, which shows the calculated symmetric and antisymmetric modes for an aluminum plate of 2 mm thickness; a mass density, ρ , of 2500 kg m⁻³; a Poisson ratio, ν , of 0.33; and a Young's modulus, E , of 72.4 GPa.

Given this, various approaches can be adopted, such as the use of higher frequencies to obtain more data points, or the excitation of LW at lower frequencies to obtain cleaner data, thus requiring lower computational power for damage detection.

28.3.2 Electromechanical impedance spectroscopy

EMIS presents itself as a promising SHM method, benefiting from the coupled electromechanical behavior of piezoelectric wafer active sensors (PWAS) working simultaneously as actuators and sensors.

A generated sinusoidal voltage excites the PWAS, acting as an actuator, and converts the electric voltage signal into a mechanical stress solicitation. Concurrently, the same PWAS, acting as a sensor, converts the mechanical response to an electric signal, which is acquired by an impedance analyzer. This experiment is done for a wide range of frequencies, usually ranging from 1 kHz onward [55].

Because of this electromechanical coupled behavior, piezoelectric materials create an electric charge when subjected to mechanical stress, and will generate a mechanical strain under the influence of an electric field or, mathematically speaking,

$$\begin{cases} S_1 = \bar{s}_{11}^E T_1 + d_{31} E_3 \\ D_3 = d_{31} T_1 + \bar{\epsilon}_{33}^T E_3 \end{cases} \quad (28.5)$$

where S_1 represents the mechanical strain, T_1 is the mechanical stress, E_3 denotes the electric field, D_3 is the electrical displacement (charge per unit area), \bar{s}_{11}^E is the mechanical compliance at zero electric field, d_{31} stands for the piezoelectric induced strain coefficient, and $\bar{\epsilon}_{33}^T$ is the dielectric constant at zero stress [36, 64, 65].

These relations constitute the backbone of the physical modeling of the EMIS technique. These have been extensively used to mathematically relate the measured electrical impedance of the sensor, Z_e , with the mechanical properties of the structure. These are described by the mechanical impedance of the structure, $Z_{m,s}(\omega)$, which is defined as $Z_{m,s} = F/\dot{x}$, where F and \dot{x} are, respectively, the load and the velocity of an excited particle. For more on these mathematical models, please consult reference [55].

Liang et al. [66] were the first to propose a mathematical model that would describe this phenomenon, by estimating the electrical impedance for a one-dimensional (1D)

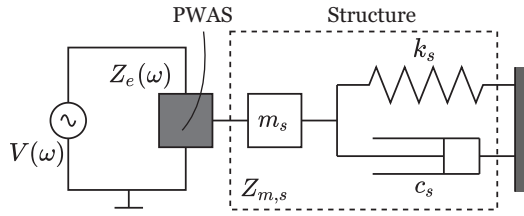


Fig. 28.7 Model of interaction between the PWAS and the 1D structure proposed by Liang et al. [66].

structure with mass, m_s , stiffness, k_s , and damping coefficient c_s , as shown in Fig. 28.7, such that

$$Z_e(\omega) = \left[j\omega \frac{w_P l_P}{h_P} \left(\bar{\epsilon}_{33}^T - \frac{Z_{m,s}(\omega)}{Z_{m,s}(\omega) + Z_{m,P}(\omega)} d_{31} \bar{Y}_{11}^E \right) \right]^{-1} \quad (28.6)$$

where w_P , l_P , and h_P are, respectively, the width, length, and thickness of the PWAS, and $Z_{m,P}$ is its mechanical impedance. One should note that j and ω correspond to the imaginary number, $j = \sqrt{-1}$, and the angular frequency, respectively. The variable \bar{Y}_{11}^E represents the complex Young's modulus of the piezoelectric material with a null electric field, and is defined as $\bar{Y}_{11}^E = |Y_{11}^E|(1 + j\eta)$, where η is the mechanical loss factor. Finally, the dielectric constant at zero stress, $\bar{\epsilon}_{33}^T$, is expressed as $\bar{\epsilon}_{33}^T = |\epsilon_{33}^T|(1 - j\delta)$, where δ is the dielectric loss factor.

As one can see from Eq. (28.6), the electric impedance, Z_e , has real and imaginary components, $\text{Re}(Z_e)$ and $\text{Im}(Z_e)$ respectively, but only the real component is sensitive to damage. With some signal processing, one can obtain a damage-sensitive reactance, as shown by Bhalla et al. [67].

This structural monitoring presents interesting advantages over other SHM methods, such as (a) the use of lightweight and inexpensive piezoelectric transducers, which can be implemented without hindering the stability of the structure; (b) the capability to monitor structures in the domain of high frequencies, where ambient noise and vibrations, commonly present in real-world applications, do not influence the obtained readings; and (c) the ability to use information from a wide frequency spectrum, with which one can detect minute damage foci [64, 68].

28.3.3 Algorithms and machine learning

Given the aim of SHM in detecting and determining relevant information regarding structural damage, advanced algorithmic approaches are required. In this manner, a plethora of algorithms has been adopted to tackle this in a hierarchical manner, as presented in Fig. 28.5B [36, 43, 46]. Indeed, this chapter does not aim at thoroughly describing all algorithmic methods, but a brief presentation is nonetheless required.

One of the simplest methods to tackle damage detection is the use of damage metrics, which compare sensor readings from a reference damageless structure and real-time measurements from the structure under examination. Afterward, depending on the calculated metric value, binary classification may occur, that is, damage is or is not detected [55].

Alternatively, one can detect damage with the help of model-driven algorithms, which are more complex than the previously mentioned damage metrics but can enable the extraction of more information. As such, these normally allow the answering of questions regarding not only damage detection, but damage localization and characterization. For instance, in EMIS, one can use impedance signals from various sensors to triangulate the position of the damage [69].

However, ML algorithms can also be used to study damage at any hierarchical level present in Fig. 28.5B. Here, features are extracted from the sensor measurements, which are then used as inputs for algorithms to detect and characterize the defect [43, 46]. Note that in ML, the extracted features of each instance i are gathered in input vector, \mathbf{x}_i , while y_i and $\sim y_i$ are, respectively, the label (the correct class) and the output (estimated class by the algorithm) of said instance. These algorithms will be focused on in this section.

However, before continuing, we must note that the algorithms presented herein are ML classification algorithms, in the sense that they aim to classify each and every data instance as being part of a given class. This does not have to correspond to the task of Level 3 of the hierarchical approach to the study of damage, where the damage evaluation algorithm aims to determine which type of damage is detected (e.g., void, crack, weak adhesion).

28.3.3.1 k -nearest neighbors

The k -nearest neighbors (kNN) algorithm is nonparametric, meaning that classification is not based on statistical assumptions and is only performed from the dataset.

Consider the training set $\tau = \{(\mathbf{x}_i, y_i)\}_{i=1}^n$, where i is the number of data instances. Each case i is composed by the feature vector \mathbf{x}_i , and y_i represents the label or response of said instance. Consider also that \mathbf{x}_t is a new feature vector for test, meaning that this vector is input for classification. To classify the new instance \mathbf{x}_t , one must first calculate the distance between this new data point and each member of the training set, or, mathematically speaking, $\text{dist}(\mathbf{x}_t, \mathbf{x}_i)$, for $i = 1, 2, \dots, n$. Various distances can be used, the most common being the Euclidean distance, the Manhattan distance, and the Minkowski distance.

$$\text{dist}(\mathbf{x}_t, \mathbf{x}_i) = \|\mathbf{x}_i - \mathbf{x}_t\|, \text{ for } i = 1, 2, \dots, n \quad (28.7)$$

With these distances calculated, a sorting of the training elements is done, where \mathbf{x}_1 becomes the closest instance to the datapoint \mathbf{x}_t and \mathbf{x}_n is the farthest point. From the training set, τ , one can construct the subset, κ , containing the k nearest elements, such that $\kappa = \{(\mathbf{x}_{(1)}, y_{(1)}), (\mathbf{x}_{(2)}, y_{(2)}), \dots, (\mathbf{x}_{(k)}, y_{(k)})\}$. From this subset, the classification of

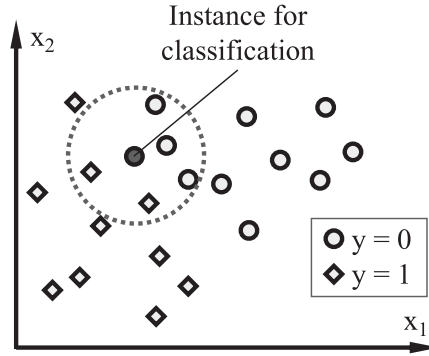


Fig. 28.8 Schematic representation of the kNN classification algorithm, where $k = 5$.

datapoint \mathbf{x}_i is attributed to the most frequent class in the κ subset [70, 71]. Fig. 28.8 exemplifies how the kNN algorithm performs classification, considering that $k = 5$.

In this chapter, the kNN algorithm is used for both LW and EMIS-based damage detection, where the Euclidean distance is adopted.

28.3.3.2 Naïve Bayes classifier

Consider again the dataset $\tau = \{(\mathbf{x}_i, y_i)\}_{i=1}^n$, where \mathbf{x}_i and y_i are the feature vector and label of instant i . Consider now that the vector \mathbf{x}_i contains a big set of features, such that $\mathbf{x}_i = (x_{i,1}, x_{i,2}, \dots, x_{i,m})$, with m the final feature in the vector. To use any normal classification model, a large dataset would forcibly be required to combat the *curse of dimensionality* [72].

However, in certain cases, one can simplify this algorithmic problem by assuming that all elements of the feature vector are conditionally independent from each other. As such, this means that the probability of obtaining a feature value of $P(x_{i,1} = c_1, x_{i,2} = c_2, \dots, x_{i,m} = c_m | y)$ is the same as multiplying each individual probability, or, in other words,

$$\begin{aligned} P(x_{i,1} = c_1, x_{i,2} = c_2, \dots, x_{i,f} = c_f | y_i) &= P(x_{i,1} = c_1 | y_i) \cdot \\ P(x_{i,2} = c_2 | y_i) \cdot \dots \cdot P(x_{i,m} = c_m | y_i) \end{aligned} \quad (28.8)$$

which is simpler and reduces the severity caused by the *curse of dimensionality*.

In this manner, the naïve Bayes classifier determines the posterior probability, $P(y_i | \mathbf{x}_i)$, as

$$P(y_i | \mathbf{x}_i) \propto P(y_i) \prod_{j=1}^f P(x_{i,j} | y_i) \quad (28.9)$$

or, in other words, it calculates the probability of instance i having target y_i , given that it is defined by the values in feature vector \mathbf{x}_i . The calculation of the probability $P(y_i)$ is equivalent to determining the ratio of class y_i in the training set τ .

During the training phase, these probabilities are estimated, and afterward, when testing is performed, the feature vector x_i is predicted as being of class y_i , when y_i yields the highest probability.

Different naïve Bayes classifiers make distinct assumptions on the probability $P(x_i|y)$. Here, this classification algorithm was adopted to classify the degree of weak adhesion with features from LW measurements. In this case, a normal distribution is defined to describe the probability $P(x_i|y)$ [72, 73].

28.3.3.3 Random forest

Random forest is a classification algorithm that originated by combining many individual decision trees, as schematized in Fig. 28.9 (hence the name random forest) to operate as an ensemble, where each decision tree is slightly different from the other. Decision trees are a form of nonparametric supervised learning method that operates on the principle that the combination of simple decision rules is able to predict the target value.

One advantage of this algorithm is that each tree behaves as an individual classification model and, therefore, any misclassification done by each individual tree is mitigated by the presence of other decision trees [72].

Note once again that this model is only used for the detection of weak adhesion with extracted features from LW. Because the features originate from vibrational signals with no visible correlations between damage cases, it is important to have an algorithm that is capable of determining the resemblances between the extracted features of each damage instance.

Gradient boosting

Gradient boosting shares the same decision tree roots as the random forest algorithm. However, while random forest uses various decision trees in parallel, the gradient boosting algorithm utilizes a sequence of simple decision trees trained in tandem, that is, the results obtained from the first decision tree are used as input for the next decision tree model, as shown in Fig. 28.10. These trees are then combined with the help of an additive model, whose internal weights are calculated with a gradient descent procedure [72].

This classification algorithm was also adopted to evaluate weak adhesion in adhesive joints using extracted information from LW measurements.

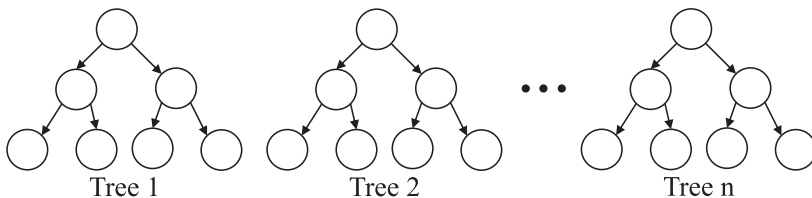


Fig. 28.9 Graphic representation of the random forest algorithm.

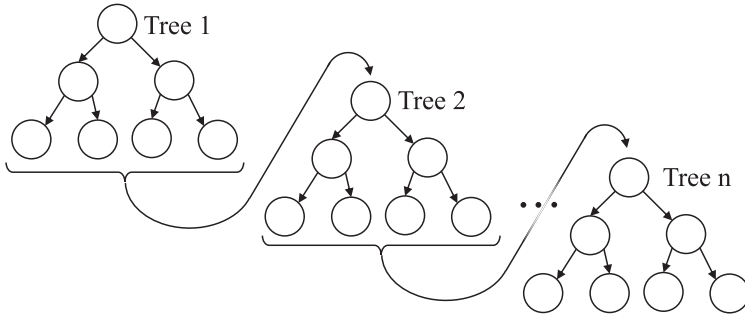


Fig. 28.10 Graphic representation of the gradient boost algorithm.

Artificial neural networks

Artificial neural networks (ANN), which were originally created to mimic the brain [74], are a family of ML algorithms, where the output is calculated as the successive composition of linear and nonlinear functions, and where internal parameters are cyclically optimized to improve the overall model fitting to the data.

Consider the training set, $\tau = \{(x_i, y_i)\}_{i=1}^n$, where i is the number of training instances, x_i is the input array containing m different features, and y_i is the label of instance i . This vector is given to the input layer, which feeds the values to the neurons of the first hidden layer. The number of nodes in each layer may vary from layer to layer.

In each node, two operations occur, the first being the linear combination of the input from the previous layer, or, in mathematical form

$$a = w_1\chi_1 + w_2\chi_2 + \dots + w_k\chi_k = \sum_{i=0}^k w_i\chi_i \quad (28.10)$$

where χ_i are the inputs, w_i is the weight of connection i , and $i = 1, 2, \dots, k$ describes the previous layer's neurons. The second operation, known as the activation function, is a nonlinear function that replicates the electrochemical activation of a neuron. From this, one obtains the output, which is either given to the neurons present in the next layer as input, or is the value obtained in the output layer.

These operations are performed for all neurons for each training instance, x_i , outputting an estimate target \tilde{y}_i . Now the ANN needs to evaluate the accuracy between the estimation, \tilde{y}_i , and the target, y_i . For this, the weights, w_i , need to be recalculated, which is done through the mechanism of backpropagation. In this manner, both the estimated and true targets, \tilde{y}_i and y_i , respectively, are evaluated with a loss function, or cost function, C_τ . Here, the cross-entropy loss function is used, such that

$$C_{\tau, \text{cs}} = - \sum_{i=0}^n y_i \log(\tilde{y}_i) \quad (28.11)$$

This function is then differentiated according to all node weights so that the obtained error between the estimated and true targets is adequately distributed. This procedure is normally done with optimization methods to optimize the network weights. Here, the scaled conjugate gradient (SCG) backpropagation is used [75] to train models for void detection with features from EMIS readings.

Periodically, ANN validation occurs with a second data subset, δ , with the aim of evaluating the network's performance as it is being trained. If there is no reduction of loss values obtained for the validation dataset, then one can progress to the testing phase, where another independent data subset, σ , is used to evaluate the performance of the trained model.

28.4 Weak adhesion detection using Lamb wave signals

In this section, a case study on Lamb wave-based damage detection (Level 1 of Fig. 28.5B) is presented, more specifically the detection of weak adhesion on adhesive joints. The obtained data are then studied with the help of ML algorithms to detect weak adhesion.

28.4.1 Numerical simulations

For one to use ML methods, one must have a robust and large dataset from which the algorithms can extract information. When the problem at hand is, for example, classification based on an image dataset, one can easily acquire large photograph sets or digitally generated image sets, but when the problem is based on the analysis of physical properties and phenomena, this task is increasingly difficult. In this case, one has two methods to create a dataset: either (a) the dataset for classification originates from an experimental setup subjected to the desired conditions, with sensors that measure the mechanical response that is then stored on a computer; or (b) the experiment is numerically simulated on a computer, with the results being as approximate as possible to real-life observations. The first approach has the benefit of using trustworthy measurements that can reliably show any structural change. However, it can be labor-intensive and costly to generate a large number of data points in different conditions, because it requires a lengthy manufacturing and testing procedure. Conversely the numerical simulation approach is less costly in this regard, but all simulated data should resemble experimental results.

Some considerations were formulated to simplify the problem at hand. First, all adhesives should contain a uniform weak adhesion defect to accentuate the effect of this defect while avoiding the needless use of complex numerical models. Second, the adhesive joints should be large, thus minimizing the effect of wave reflection caused by nearby walls, which would otherwise create more complex LWs. Consequently, finite element (FE) models can reliably match these two considerations while guaranteeing that these same considerations during specimen manufacture is considerably harder. Therefore, the dataset was created with simulations from various numerical models. Despite this, one should note that, especially for more complex

structures such as bonded joints in airplane primary structures, experimental data should be used in conjunction with numerical models of said structure for reliable monitoring.

The implementation of FE models was done with variable time-step ABAQUS dynamic explicit models, where single-lap joints (SLJ) composed of two $150 \times 150 \times 2$ mm aluminum plates were modeled with an overlap of 25 mm. One sensor is placed in the lower plate while an actuator is positioned on the top plate, as seen in Fig. 28.11. Both the sensor and the actuator are centered on the plates at a distance of 30 mm from the free end. The aluminum plate has a mass density, ρ , of 2500 kg m^{-3} ; a Poisson's ratio, ν , of 0.33; and a Young's modulus, E , of 72.4 GPa. In the models, both aluminum plates are joined with the Nagase T-836/R-810 epoxy-modified adhesive, with an adhesive thickness of 0.2 mm.

LWs were excited with Hann windowed 100 kHz sinusoidal force signals and a sampling frequency of 10^7 Hz was adopted, as it presents a compromise between high resolution and an acceptable number of data points. In these models, the excitation tried to replicate the behavior of piezoelectric elements. Piezoelectric actuators are normally glued to the surface and, as a voltage is applied to the ceramic elements, they excite the structure in the horizontal plane in all directions. Given the complexity of these simulations, there is a need to simplify the actuator, which was done by creating a square with horizontal forces occurring in three points on each side, as shown in Fig. 28.11.

An important step in the numerical modeling is to choose the mesh size in each coordinate direction. For the horizontal plane, the mesh size is defined by the wave size and should be smaller than the period of the wave. Therefore, in both horizontal directions, the mesh size is 1.5 mm for both the aluminum and adhesive. For the vertical direction, the mesh size is not conditioned by the wave but is limited by model

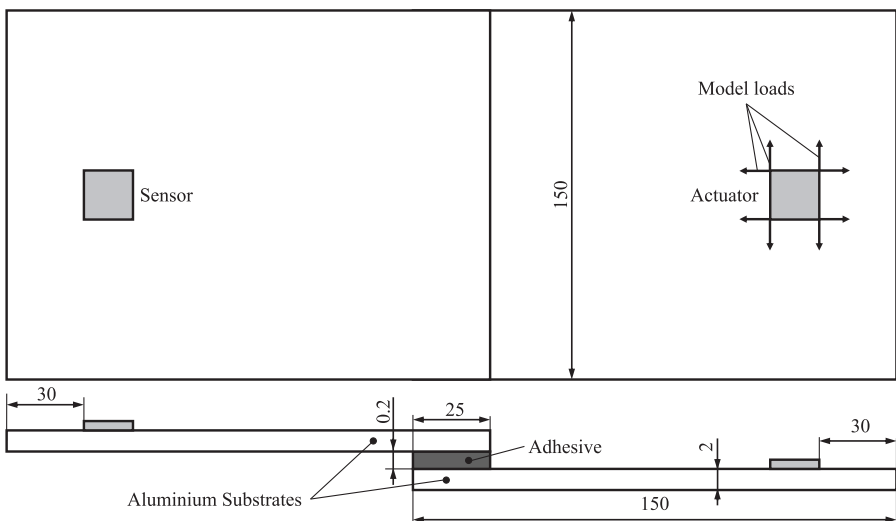


Fig. 28.11 Numerical model of the adhesive joint.

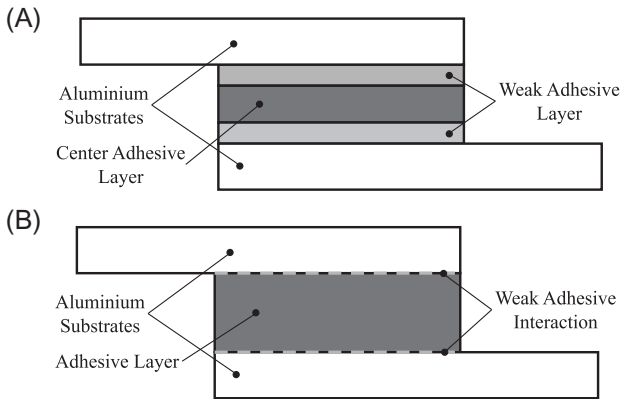


Fig. 28.12 Alternative numerical model strategies to recreate weak adhesion. (A) Three layer adhesive model; (B) One layer adhesive model with interactions.

geometry, as there is a need for more than one element to correctly depict the wave transmission. Thus, mesh sizes of 0.5 mm and 0.05 mm were respectively defined for the aluminum and adhesive.

Weak adhesion modeling can be done in two forms. The first method, schematized in Fig. 28.12A, is to create an adhesive part with three layers. A center thick layer is created with the properties of a fully cured adhesive while two thin border layers, placed at both interfaces, have altered structural properties, which vary with the degree of bond. The second method of modeling weak adhesion in FE models, as shown in Fig. 28.12B, is to create a single adhesive layer where the interaction properties between the adhesive and the substrate are defined according to the level of weak adhesion. As the problem at hand is an interaction property between the substrate and the adhesive, the second method was chosen, as it better represents the phenomenon of weak adhesion.

After running the numerical simulations, time series signals were obtained, each containing between 16,000 and 90,000 points, with a total of 1000 simulation tests, each one with a different level of adhesion. To visualize the difference caused by the weak adhesion plot comparison was done in Fig. 28.13 between a case of total adhesion and extremely weak adhesion. All time series created were subjected to preprocessing in the form of downsampling to 5000 points, thus equalizing the datasets.

28.4.2 Feature extraction

With the creation of a complete dataset, one must focus on the features needed to detect and classify weak adhesion in SLJs. There are two ways of selecting features for ML algorithms.

One approach is to select information by trial and error, where each possible feature combination is tested and the ones with better results are chosen. Various

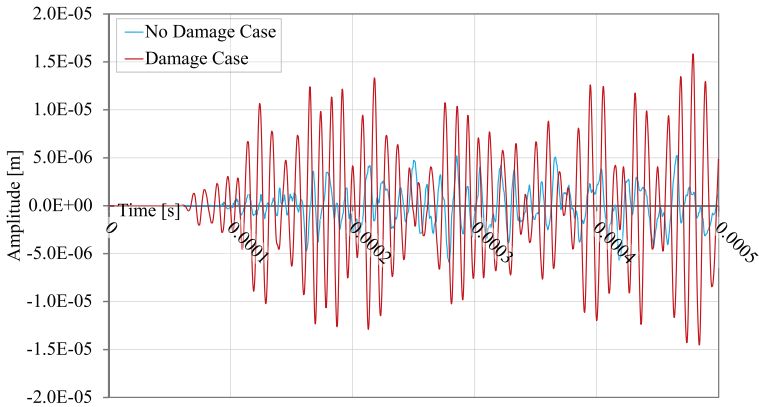


Fig. 28.13 Plot showing the obtained LW signals from SLJs with and without weak adhesion.

programming libraries that automatize the feature selection process exist, such as Python's opensource `TsFresh` module [76]. These modules test a multitude of variables as possible features for algorithmic classification, and list the features that allow for a better classification. With this feature selection process, one can implement this in any ML task and obtain good results without a profound understanding of the problem at hand.

The second method is to understand the relevant variables that can be selected as good features. This involves a deep and thorough knowledge of the phenomena, and thus, testing some features may be enough to evaluate the feature selection process and its effect in algorithm training. With this, one can evaluate possible deviations that may occur while also obtaining good results.

Of these two feature selection approaches, automatic feature extraction was chosen, as it allows for the creation of a more robust pipeline that can be used in any adhesive joint structure with the possibility of having weak adhesion. To create this automatic feature extraction pipeline, the `TsFresh` module was adopted, as it allows the study of large time series datasets. This library works in three phases:

1. In an initial phase, this module calculates a vast variety of metrics and features. These can be as simple as the time series mean value or the absolute energy of the signal, or they can be mathematically complex features such as the Benford correlation or the percentage of reoccurring data points in the signal.
2. In the second phase, all extracted features are evaluated, and those that are not considered relevant are removed. This procedure can be achieved with two alternative methods, one of them being the Benjamini-Hochberg method that controls the false discovery rate. The second method is the univariate hypothesis test, where the features with a P value lower or equal to 0.05 are removed, leaving only the relevant features for the classification of at least one class.
3. Last, the selected features are once again filtered, thus determining which features are able to describe all the classes in this classification task. This selection process can be seen in [Table 28.1](#), where all selection steps are demonstrated.

Table 28.1 The TsFresh classification-task oriented feature filtering steps results.

	Adhesive joint				
Classes	1	2	3	4	5
<i>Extracted features</i>	788				
Features with P value ≤ 0.05	681	636	599	598	590
Benjamini-Hochberg Selected features	657	559	555	571	571
Top features	244				

28.4.3 Classification metrics

To coherently evaluate the classification results, one needs to use metrics that can efficiently show the performance of the ML algorithm. A very simple and efficient method is the calculation of a confusion matrix, where all results are labeled as correctly or incorrectly classified by comparing their target class (defined in the input of the dataset) with the output of the algorithm. Fig. 28.14 shows an exemplary confusion matrix where each label on the x -axis represents the real level of damage in the SLJ, while the y -axis indicates the predicted damage level. Thus, the optimal classification result consists in all data instances being present in the diagonal of the matrix.

Despite the versatility of this indicator for performance evaluation, there is a need to quantify the values seen in this matrix. One metric usually adopted is the accuracy score, acc , which represents the ratio between correct predictions, that is, true positives, tp , and true negatives, tn , with the total number of instances assessed, which include all correctly predicted instances, tp and tn , as well as the false positive, fp , and false negative instances, fn . As such, the mathematical definition of the accuracy is

$$acc = \frac{tp + tn}{tp + fp + tn + fn} \tag{28.12}$$

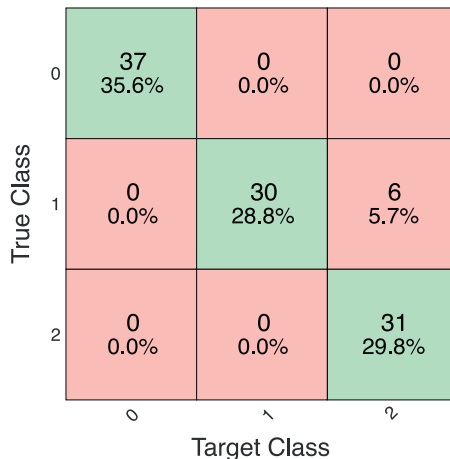


Fig. 28.14 Example of a confusion matrix.

Another commonly used metric is the precision score, p , and is defined as the ratio of correctly predicted positive observations, tp , with the total number of (true and false) positive observations, tp and fp . The precision measures the ability of a classifier not to label as positive a negative instance:

$$p = \frac{tp}{tp + fp} \quad (28.13)$$

A third metric is the recall score, r , which is the ratio between the correctly predicted positive observations, tp , with all the correctly and incorrectly classified observations of a given class, tp and fn , respectively. In mathematical terms, the recall r , is defined as

$$r = \frac{tp}{tp + fn} \quad (28.14)$$

This metric is used to measure the ability of the algorithm to detect all positive instances.

Finally, the last metric is the F1 score, $F1$, which is a weighted average of the recall, r , and the precision, p , and is defined as

$$F1 = \frac{2 \times p \times r}{p + r} \quad (28.15)$$

It is mainly used as a parameter when there is a large, uneven class distribution in the data.

Note that all classification scores are calculated by averaging the results for each class.

28.4.4 Results

Table 28.2 presents the classification metrics for weak adhesion detection using the kNN, the naïve Bayes' classifier, the random forest, and gradient boosting classifier models.

An important observation is that both the random forest and gradient boosting classification algorithms present great results independently of the feature selection. Furthermore, there is a decrease in accuracy with the trimming of features for the gradient boosting method while the accuracy metric for random forest remains constant with any of the three sets of features.

Meanwhile, one observes a slight increase of all performance metrics for the naïve Bayes if only the top features are used for weak adhesion classification. However, in a surprising twist, it is the kNN algorithm, which is the simplest classification method, that benefits most from this feature selection process. When all features are used for damage detection, an accuracy of 55% is attained while an impressive 98% accuracy score is attained when only the top features are used.

Table 28.2 Classification algorithm metrics—adhesion strength prediction on single-lap joint—80/20 data split.

Models		Adhesive joint dataset		
		Full features	Selected features	Top features
Naïve bayes	<i>acc</i>	0.948	0.948	0.981
	<i>p</i>	0.952	0.952	0.981
	<i>p</i>	0.945	0.945	0.982
	<i>F1</i>	0.948	0.948	0.982
k-nearest neighbors	<i>acc</i>	0.552	0.552	0.982
	<i>p</i>	0.566	0.566	0.981
	<i>p</i>	0.550	0.550	0.980
	<i>F1</i>	0.555	0.555	0.982
Gradient boosting	<i>acc</i>	0.996	1.00	0.993
	<i>p</i>	0.997	1.00	0.993
	<i>p</i>	0.996	1.00	0.993
	<i>F1</i>	0.996	1.00	0.993
Random forest	<i>acc</i>	1.00	1.00	1.00
	<i>p</i>	1.00	1.00	1.00
	<i>p</i>	1.00	1.00	1.00
	<i>F1</i>	1.00	1.00	1.00

28.5 Void detection using EMIS signals

While LWs prove themselves as able to detect weak adhesion in adhesive joints, bonded connections are prone to other forms of damage. In this manner, this section evaluates the capability of EMIS to detect voids in SLJs and to determine the void size. This will be performed with both the kNN and the ANN.

28.5.1 Numerical simulations

As in the previous case study, a philosophical question arose regarding the correct methodology to obtain data for damage detection. In this case, numerical simulations were created to replicate in an accurate manner the experimentally obtained electrical impedances in the EMIS method. Please note that the numerical modeling formulation was validated by Tenreiro et al. [77].

The dataset for algorithm training was created with a set of numerical models in ABAQUS 2017, which is based on the work of Zhaung et al. [78]. Direct steady-state linear dynamic models were performed on the frequency range between 50 kHz and 1.5 MHz, with a linearly distributed frequency interval of 5 kHz, corresponding to 291 sampling points. Note that the piezoelectric sensor was independently modeled from the remainder of the SLJ.

Table 28.3 Electric and mechanical properties of the PZT-5A piezoceramic material used in the finite element model.

Property	Unit	Notation	Value
Elastic modulus	GPa	E_1	60.97
		E_2	60.97
		E_3	53.19
Shear modulus	GPa	G_{13}	21.05
		G_{23}	21.05
		G_{12}	22.57
Poisson's ratio	(-)	ν_{13}	0.4402
		ν_{23}	0.4402
		ν_{12}	0.3500
Permittivity at constant strain	nF m ⁻¹	ϵ_1	15.31742
		ϵ_2	15.31742
		ϵ_3	15.05180
Piezoelectric strain coefficients	C N ⁻¹	d_{31}	$5.84 \cdot 10^{-10}$
		d_{32}	$5.84 \cdot 10^{-10}$
		d_{24}	$-1.71 \cdot 10^{-10}$
		d_{15}	$-1.71 \cdot 10^{-10}$
Mass density	kg m ⁻³	d_{33}	$3.74 \cdot 10^{-10}$
		ρ	7750

The properties of the PZT-5A piezoelectric element, which has a diameter of 3 mm and a thickness of 0.5 mm, are defined in Table 28.3. A mesh control of $3 \cdot 10^{-4}$ m was defined, using the piezoelectric type eight-node linear brick and reduced integration elements (C3D8R) mesh element.

The modeled SLJ consists of two aluminum adherends that are bonded together with a Hysol EA 9696 modified epoxy adhesive, whose properties are listed in Table 28.4. The SLJ geometric dimensions are presented in Fig. 28.15A, however, in most models, a void was introduced in one of nine locations of Fig. 28.15B. For each position, models were made with a void diameter defined as $D = \{2, 3, 4, 5, 6, 7, 8\}$ (mm). The SLJ has a general mesh size of $5 \cdot 10^{-4}$ m and a single bias mesh control was inserted for the adherends from the overlap area, increasing from $5 \cdot 10^{-4}$ m to $1 \cdot 10^{-2}$ m.

Table 28.4 Properties of the adhesives and adherend used in the finite element model.

Material	E (GPa)	ν (-)	η (-)	ρ (kg m ⁻³)
Aluminum Al 2024-T3	69.0	0.3	–	2710
Hysol EA 9696	2.55	0.41	0.005	1100

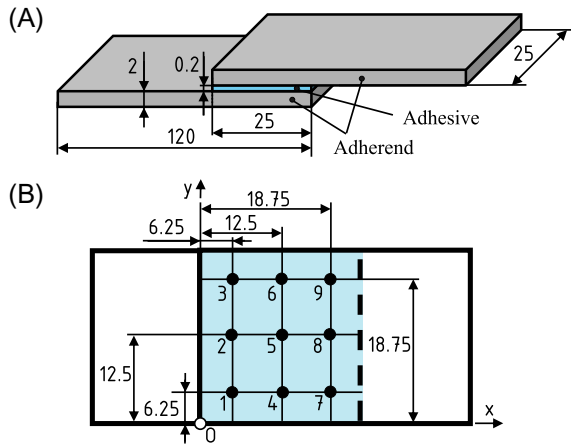


Fig. 28.15 Schematic representation of an SLJ modeled with dimensions in mm. (A) Geometry of the SLJ; (B) Void positioning in the overlap region.

As previously stated, the PWAS was modeled independently and then placed on top of the overlap region, with both parts being connected with a tie constraint interaction to guarantee that no relative movement between the components occurs.

The voltage excitation of 1 V was defined with two electric potentials, $E_u = 1 + 0j$ V and $E_l = 0 + 0j$ V, at each circular surface of the PWAS. From the simulations, the reactive electrical nodal charges (RCHG) were extracted from the sensor’s upper surface and summed, yielding the electric charge, $Q(\omega)$. The electrical impedance, $Z_e(\omega)$, is computed as

$$Z_e(\omega) = \frac{V(\omega)}{I(\omega)} = \frac{E_u - E_l}{j \omega Q(\omega)} \tag{28.16}$$

where $V(\omega)$ is the voltage and $I(\omega)$ is the generated electrical current.

Because this set of numerical experiments is composed of 64 different models, 63 of which have a void, more data for the case of damageless adhesive joints are required. As such, two approaches were concurrently followed:

- The calculation of impedance, $Z_e(\omega)$, was done considering both the presence and lack of electrical noise.
- The simulations were done with small variations of parameters.

In this first proposed approach, the operation of Eq. (28.16) was initially done with $V(\omega)$ having a value of $1 + 0j$ V, as previously indicated. Afterward, this operation was repeated in a similar fashion, where small variations of the voltage were created to replicate the effect of electrical noise. To achieve this, the voltage $V(\omega)$ was separated into its real and imaginary components, $\text{Re}(V(\omega))$ and $\text{Im}(V(\omega))$, respectively, which are modeled as Gaussian variables. As such, $V(\omega)$ is defined as

$$V(\omega) = \text{Re}(V(\omega)) + j \text{Im}(V(\omega)) \quad (28.17)$$

where $\text{Re}(V(\omega)) \sim N(1, 0.01 \cdot 1)$ V and $\text{Im}(V(\omega)) \sim N(0, 0.01 \cdot 1)$ V. This procedure was done four times for each simulation result.

For the other approach, an extra set of simulations was performed where a small variation in one specific parameter was defined, such as:

- A variation of ± 5 kPa on the elastic modulus of the adhesive material, yielding two more simulations.
- A variation of $\pm 1 \cdot 10^{-5}$ on the loss factor of the modified epoxy adhesive, yielding two more simulations.
- Finally, a small alteration to the excitation voltage was created. As such, the magnitude of the voltage source remains equal to 1 V, but the phase value changes from $\varphi(V) = 0$ degrees to $\varphi(V) = \pm 0.5$ degrees.

This was done to evaluate the robustness of algorithms in detecting voids as well as to obtain a broader dataset for void detection. Both type of results are then used in combination for void detection and void size differentiation.

Fig. 28.16 plots the simulation results of four models, three of which correspond to simulated measurements on SLJs with voids of 5 mm diameter while the fourth result is the impedance spectrum of a damageless SLJ. The coordinates correspond to the void placement of Fig. 28.15B.

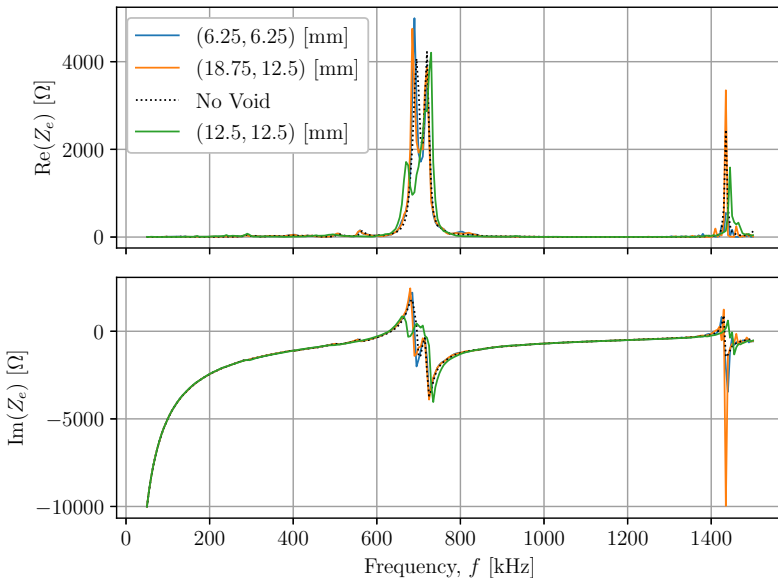


Fig. 28.16 Impedance spectra of simulated SLJs without void and with 5 mm diameter void (with both void center coordinates presented as (x, y)).

28.5.2 Development and performance of algorithms

Two main classification problems are tackled: damage detection and damage differentiation. In damage detection, the data instances can be divided into two classes, which correspond to damaged or undamaged SLJs. Alternatively, one can write this in mathematical terms as

$$y = \begin{cases} 0, & \text{if there is no void;} \\ 1, & \text{if there is void} \end{cases} \quad (28.18)$$

where y is the label, or target of the data instances. For the second type of classification, the void is differentiated according to its size. In this manner, the instances are separated into two classes, such that

$$y = \begin{cases} 0, & \text{if } D < 5 \text{ (mm);} \\ 1, & \text{if } D \geq 5 \text{ (mm)} \end{cases} \quad (28.19)$$

where D is the void diameter. For both problems, ANN and kNN algorithms were developed, using, respectively, Python 3.8 with the `scikit-learn` module [79] and MATLAB R2019b.

To develop efficient ML algorithms, features need to be extracted. One type of input feature usually used in EMIS-based algorithms is the peak information of the real component of the impedance [80]. Therefore, for this work, the three main peaks of the real component of the impedance, $\text{Re}(Z_e(\omega))$, and their respective ordinary frequency (in Hz), f , are used, yielding the feature vector

$$\mathbf{x} = [\text{Re}(Z_e(\omega))_1, f_1, \text{Re}(Z_e(\omega))_2, f_2, \text{Re}(Z_e(\omega))_3, f_3] \quad (28.20)$$

When formulating the kNN algorithms, the array \mathbf{x} was used as input while, for ANNs, preprocessing of the input data is required. In this particular case, data normalization was done. Afterward, the dataset must be divided into various subsets. For the kNN algorithm, 80% of the data was split for training and the remaining 20% was used for testing while for ANNs, 70% of the data was allocated for the training subset while 15% are used for validation and 15% for testing.

28.5.2.1 Damage detection

Artificial neural network

Fig. 28.17A shows the developed ANN model that uses the features presented in Eq. (28.20). Note that the data instances originate from both results obtained directly from the simulations as well as simulation results where electrical noise was added. This network contains one hidden layer with six nodes, and their respective activation function is the hyperbolic tangent sigmoid (*tansig*) activation function, such as

$$\nu = \text{tansig}(a) = \frac{2}{1 + e^{-2a}} - 1 \quad (28.21)$$

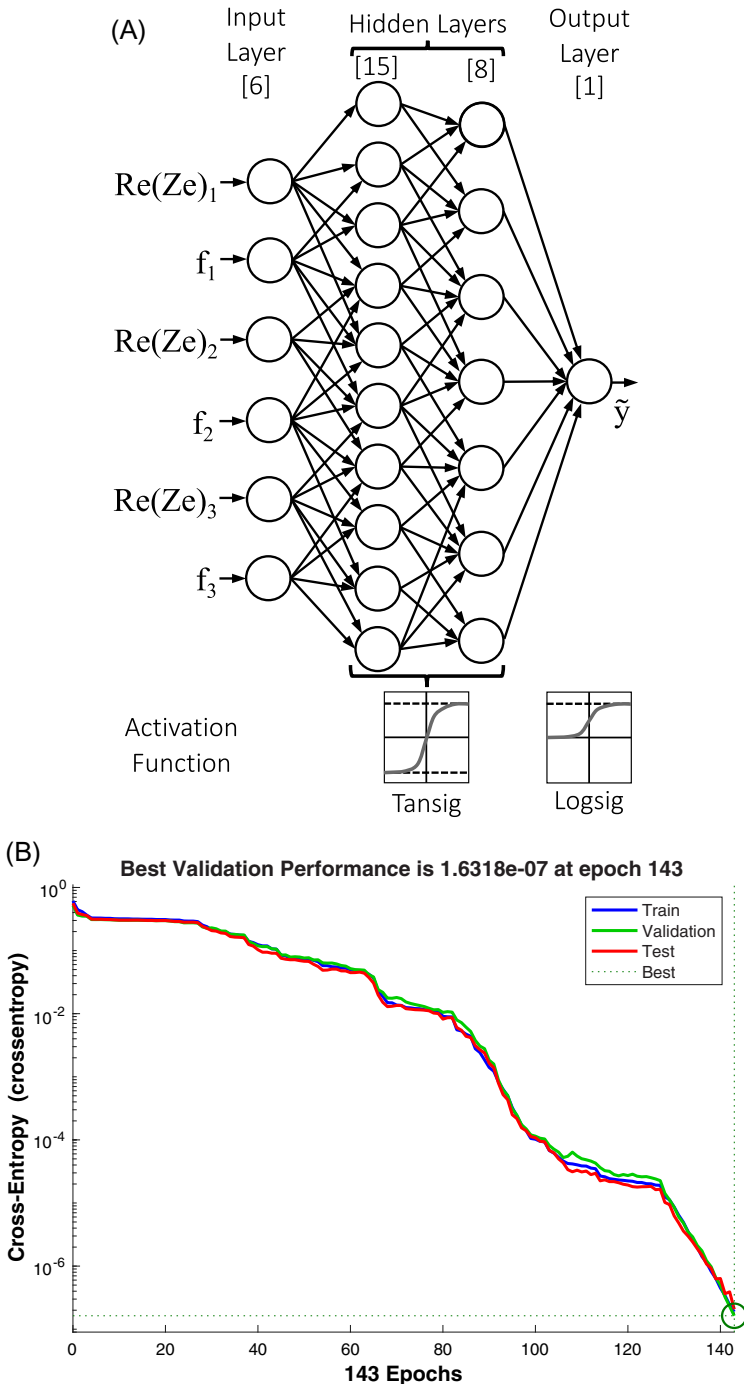


Fig. 28.17 ANN model for damage detection using simulation results with and without the addition of electrical noise. (A) Representative diagram of the ANN Model; (B) Performance of ANN.

where ν is the output of the node and a is the input of the activation function, as shown in Eq. (28.10). This ANN contains one output layer of one node with the log-sigmoid activation function, defined as

$$\nu = \text{logsig}(a) = \frac{1}{1 + e^{-a}} \quad (28.22)$$

The backpropagation method adopted herein is the scaled conjugate gradient backpropagation algorithm, with the following parameters: a Marquardt adjustment parameter of $\mu = 0.005$; a λ parameter to regulate the indefiniteness of the Hessian matrix, $\lambda = 5.0 \cdot 10^{-7}$; and a σ parameter to determine the change in weight of the second derivative approximation, $\sigma = 5.0 \cdot 10^{-5}$.

Fig. 28.17B displays the cross-entropy loss function for the training, validation, and testing subsets along the epochs. One observes that the performance of the validation dataset decreased throughout the training epochs, meaning that there is no overfitting of the data.

Fig. 28.18A and B show, respectively, the confusion matrix and the error histogram for the training, validation, and testing of this ANN model. Indeed, this algorithm can correctly detect the data instances corresponding to damaged adhesive joints. Observing the histogram in Fig. 28.18B, the median errors are of a very small order of magnitude, with the biggest difference between the target values, y , and the estimated values, $\sim y$, being approximately 0.000 5%. This is largely attributed to the fact that this training procedure was done with a big dataset, thus allowing for precise estimations while guaranteeing that there was no overfitting, as shown in the testing and validation confusion matrices of Fig. 28.18A.

k-nearest neighbors

Unlike with ANN, one only needs to split the dataset into train and test subsets to develop a kNN algorithm. In this manner, no validation occurs in the development of this classification algorithm, as previously explained in Section 28.3.3. Furthermore, only two parameters need to be defined: the distance metric used for classification, which, for this work, the Euclidean distance was adopted, and the k parameter, which was explained in Section 28.3.3. Here, a value of $k = 5$ was used.

Given the 80%-20% train-test split adopted, Fig. 28.19 presents a scatter plot of all the instances stored as training elements for damage detection in adhesive joints. Note that this data split was done in such a way as to guarantee the proportionality of classes in both data subsets.

Fig. 28.20A shows the confusion matrix of the testing subset (as it is the only subset with which the algorithm performs the classification task) while Fig. 28.20B presents the scatter plot of the test subset data instances. These results show that the kNN algorithm can correctly determine if the impedance information corresponds to an SLJ with or without a void. Note that the information was input as a feature vector in \mathbb{R}^6 , despite the fact that this corresponds to the information of the three largest peaks of the real component of the electric impedance, $\text{Re}(Z_e)$.

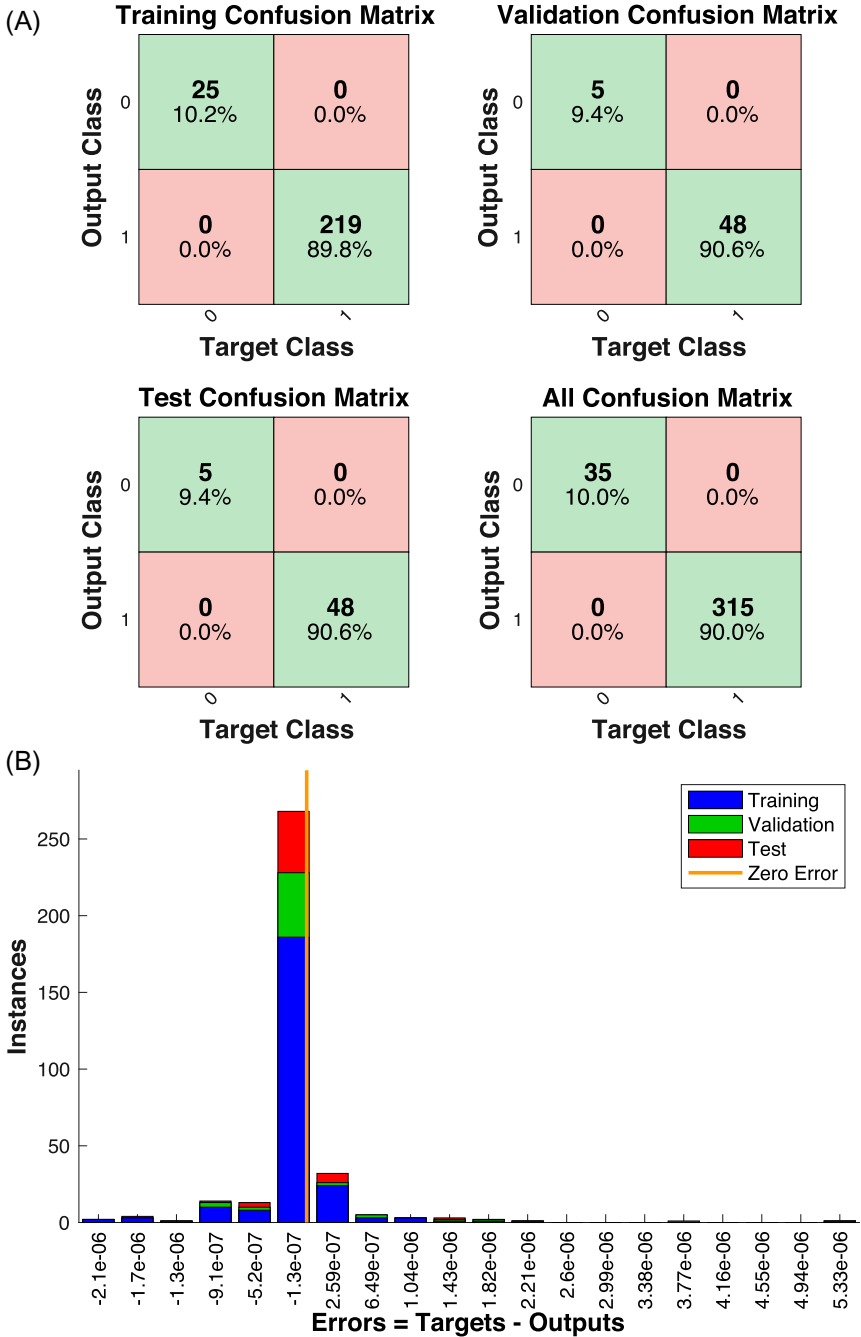


Fig. 28.18 Results of the ANN for damage detection using simulation results without the addition of electrical noise. (A) Confusion matrix results; (B) Error histogram.

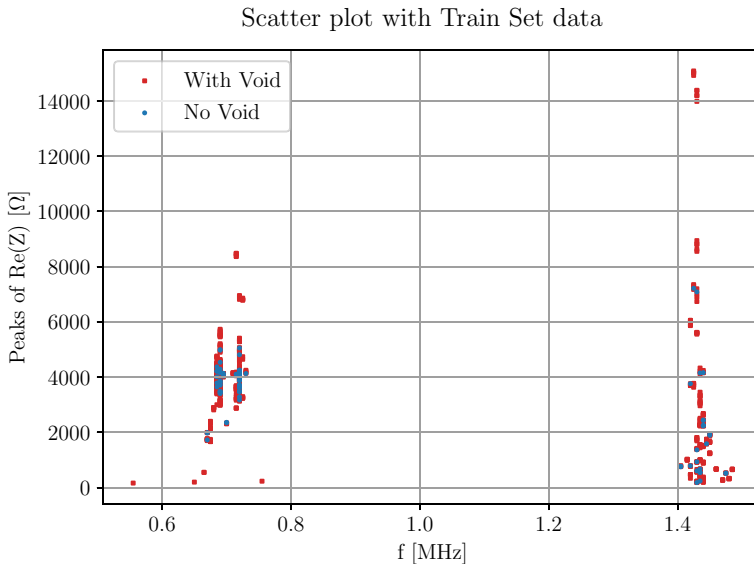


Fig. 28.19 Scatter plot of kNN training data instances.

28.5.3 Damage differentiation

28.5.3.1 Artificial neural network

Fig. 28.21A shows the developed ANN model, which is composed of a first hidden layer (15 nodes), and a second hidden layer (eight nodes), with the chosen activation function being the *tansig* function of Eq. (28.21). Likewise, the output layer contains only one node, whose activation function is the *logsig* shown in Eq. (28.22). Note that the training subset contained 80% of the original dataset while the testing and validation subsets each present the remaining 20% of the original dataset.

The training was performed with the scaled conjugate gradient backpropagation algorithm with the following parameters: a Marquardt adjustment parameter of $\mu = 0.005$; a λ parameter to regulate the indefiniteness of the Hessian matrix, $\lambda = 5.0 \cdot 10^{-7}$; and a σ parameter to determine the change in weight of the second derivative approximation, $\sigma = 1.0 \cdot 10^{-8}$.

Fig. 28.21B plots the performance for the training, validation, and testing subsets along the epochs. In this case, the performance of the validation, and testing datasets decreased throughout the training epochs, meaning that there is no overfitting of the data.

Fig. 28.22A and B plot, respectively, the confusion matrix and the error histogram for the training, validation, and testing of this model. The ANN can classify if the electric impedance features originate from an adhesive joint with a big or small diameter void. This can be shown by the fact that all training, validation, and testing data elements were correctly identified, as shown in the confusion matrix of Fig. 28.22A. Furthermore, the plot in Fig. 28.22B shows that the errors are small, that is, below 1%.

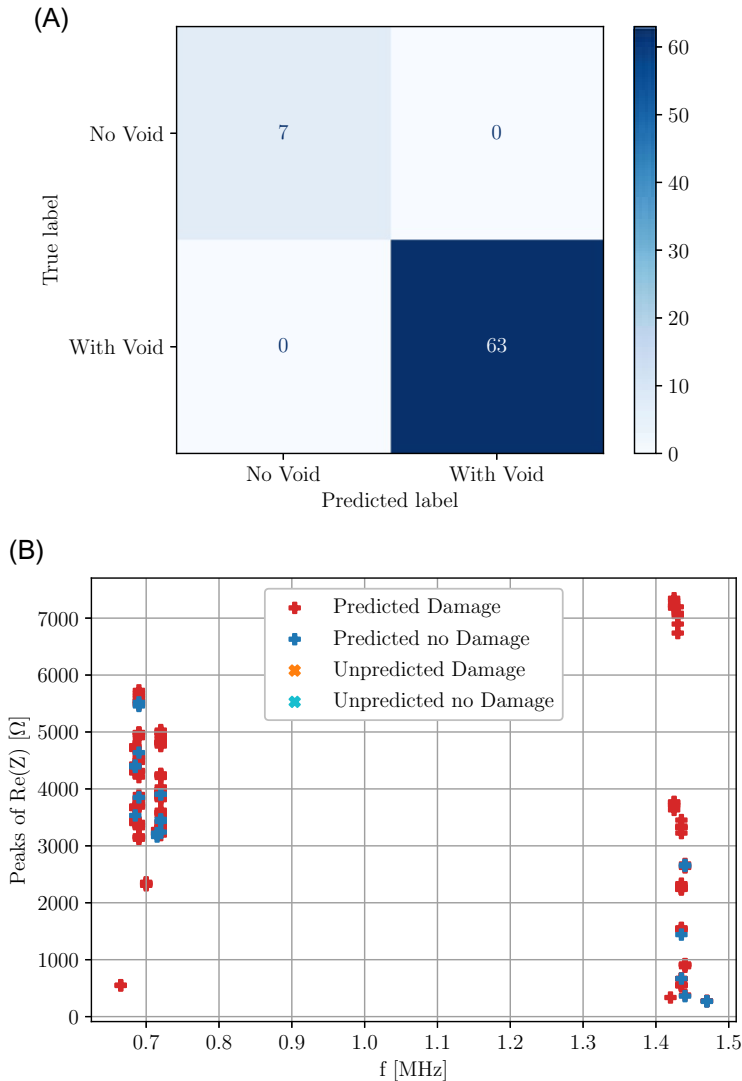


Fig. 28.20 Results of the kNN for damage detection using simulation results with and without the effect of electrical noise. (A) Confusion matrix results; (B) Scatter plot of kNN testing data instances.

28.5.3.2 *k*-nearest neighbors

As with the development of the previous kNN algorithms, a value of $k = 5$ is used. Fig. 28.23 shows the scatter plot of all the training data elements for damage differentiation.

Fig. 28.24A and B presents, respectively, the confusion matrix and the scatter plot of the test subset results. An accuracy of 90.5% was attained. Note that despite the fact

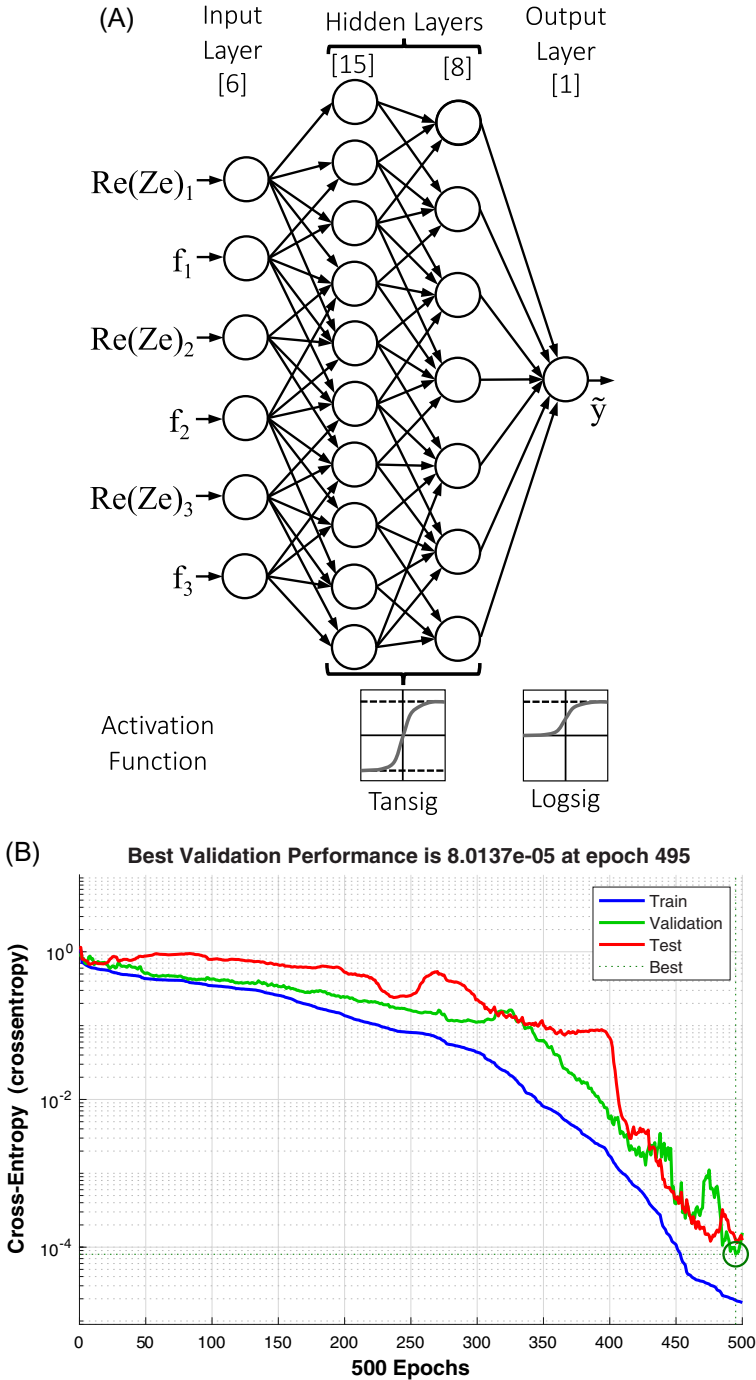


Fig. 28.21 ANN model for damage differentiation using simulation results with and without the addition of electrical noise. (A) Representative diagram of the ANN Model; (B) Performance of ANN.

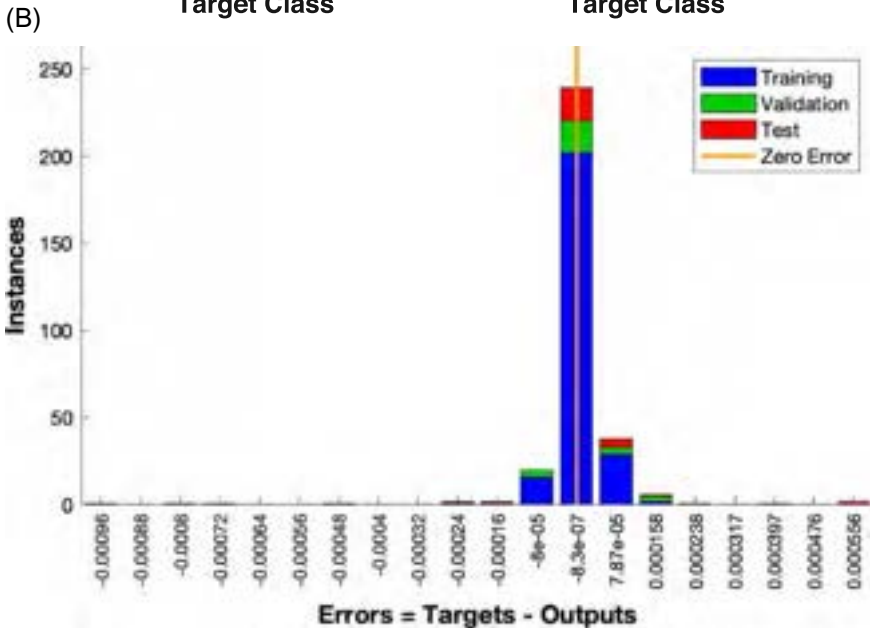
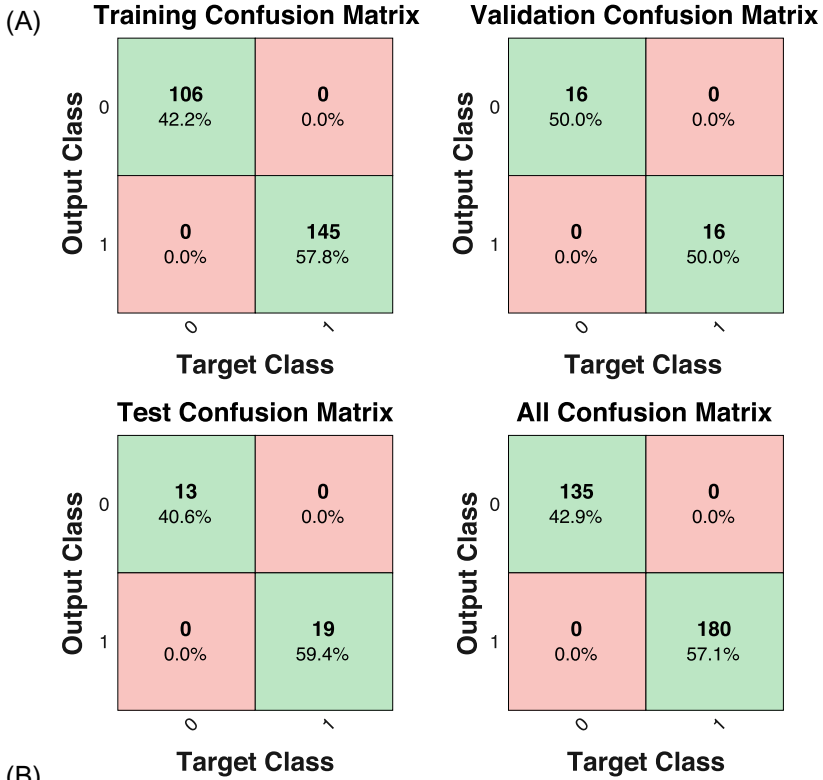


Fig. 28.22 Results of the ANN for damage detection using simulation results without the addition of electrical noise. (A) Confusion matrix results; (B) Error histogram.

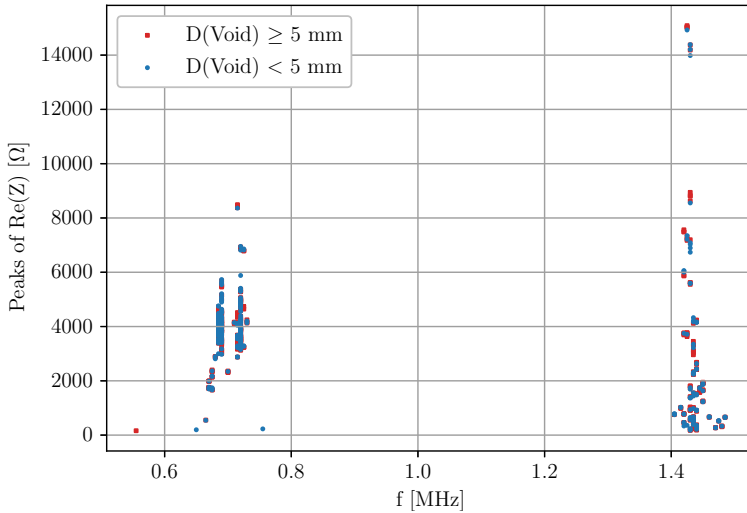


Fig. 28.23 Scatter plot of kNN training data instances.

that Fig. 28.24B plots the test elements in the \mathbb{R}^2 space, some instances were misclassified because of the extreme influence of one specific peak. For example, one can see that two distinct data instances contain a peak of $\text{Re}(Z_e)$ of approximately 700 Ω at a frequency of 670 kHz, one of which corresponds to a correctly predicted impedance reading from a joint with a big void while the other corresponds to an impedance measurement from an SLJ with a small void, which was misclassified as actually being from a big void. Indeed, upon closer observation of Fig. 28.23, most training instances containing a peak in the range between 0.6 and 0.8 MHz, and an impedance value between 0 and 1000 Ω , correspond to instances of the case where the void diameter is below 5 mm. As such, this test element can be seen as an outlier.

28.6 Conclusion

Recently, there has been an increase in research of NDT to improve damage detectability in structural adhesive joints. While improvements are observed, these methods still have limitations, especially when tackling the detection of weak adhesion. Concisely speaking, currently used NDE methods do not reach the desired technology readiness levels for reliable application in operational environments.

SHM, which presents itself as the successor of NDT to mechanical structures, aims to perform the detection, localization, characterization, and severity estimation of damage in a structure, and calculates the remaining useful life. Various technologies have presented themselves to aid SHM in this task, namely the use of ML algorithms to tackle damage detection in various structures and structural components, like, such as, adhesively bonded components. This was demonstrated with the use of both LW

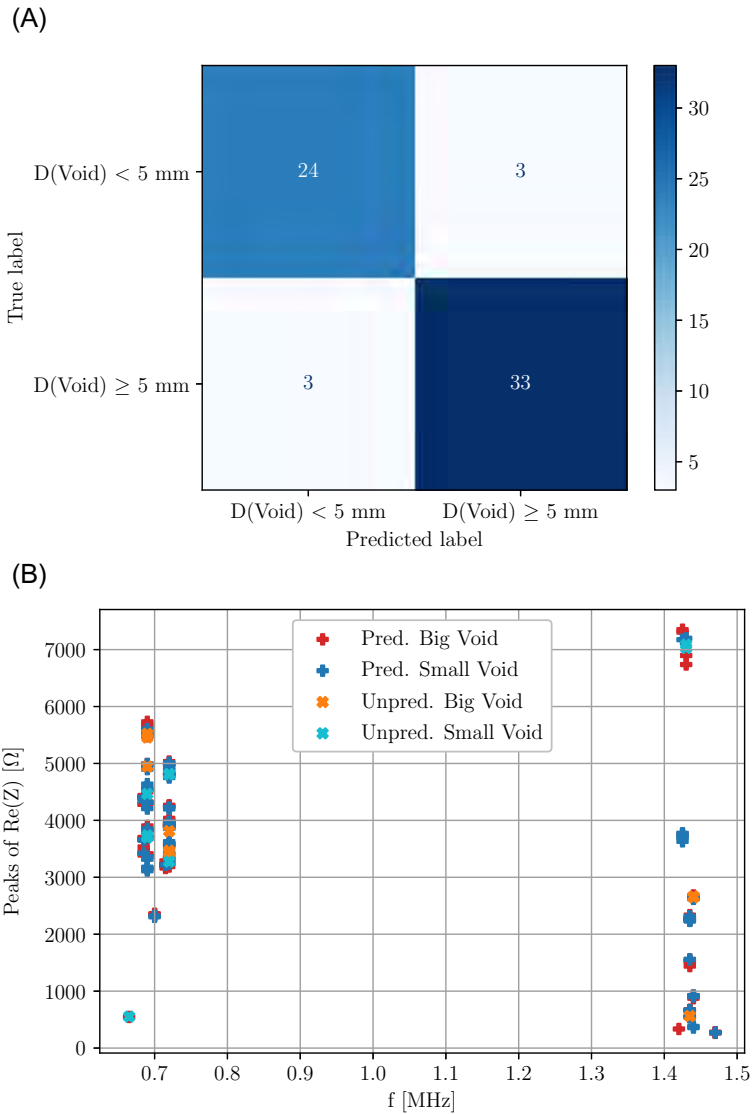


Fig. 28.24 Results of the kNN for damage detection using simulation results with and without the effect of electrical noise. (A) Confusion matrix results; (B) Scatter plot of kNN testing data instances.

and EMIS to monitor single-lap adhesive joints for weak adhesion and voids, respectively.

Features extracted from LW signals were used to develop various ML algorithms, such as the kNN, naïve Bayes classifier, random forest, and gradient booster algorithms. Before algorithm development, the data obtained were preprocessed in a

feature extraction pipeline, thus carefully selecting the most predominant features to be used by these ML algorithms. These algorithms then were trained to predict the level of weak adhesion in an SLJ.

Concurrently, features were extracted from EMIS readings of SLJs with and without voids, which were then used on both ANN and kNN algorithms to (a) detect voids and (b) determine if the void is of small or large diameter, that is, $D < 5$ (mm) or $D \geq 5$ (mm). Void detection was successfully performed with both algorithms, despite having an unbalanced dataset. Both algorithms were able to correctly label which instances originate from measurements of damageless adhesive joints and from SLJs with voids. This can be attributed to the fact that impedance readings from pristine adhesive joints are somewhat similar to each other, and impedance spectra from damaged joints are significantly different. Void differentiation, that is, void size classification, was also done, attaining excellent values of accuracy for both the ANN (accuracy of 100%) and the kNN algorithms (accuracy of 90.5%).

References

- [1] L.F.M. da Silva, A. Öchsner, R.D. Adams, *Handbook of Adhesion Technology*, second ed., Springer International Publishing AG, New York, NY, United States, 2018, ISBN: 978-3-319-55410-5.
- [2] J.J.M. Machado, E.A.S. Marques, L.F.M. da Silva, Adhesives and adhesive joints under impact loadings: an overview, *J. Adhes.* 94 (6) (2018) 421–452, <https://doi.org/10.1080/00218464.2017.1282349>.
- [3] F. Zhang, H.-P. Wang, C. Hicks, X. Yang, B.E. Carlson, Q. Zhou, Experimental study of initial strengths and hygrothermal degradation of adhesive joints between thin aluminum and steel substrates, *Int. J. Adhes. Adhes.* 43 (2013) 14–25, <https://doi.org/10.1016/j.ijadhadh.2013.01.001>.
- [4] J.J.M. Machado, E.A.S. Marques, A.Q. Barbosa, L.F.M. da Silva, Effect of hygrothermal aging on the quasi-static behaviour of CFRP joints varying the overlap length, *Compos. Struct.* 214 (2019) 451–462, <https://doi.org/10.1016/j.compstruct.2019.02.035>.
- [5] R. Avendaño, R.J.C. Carbas, E.A.S. Marques, L.F.M. da Silva, A.A. Fernandes, Effect of temperature and strain rate on single lap joints with dissimilar lightweight adherends bonded with an acrylic adhesive, *Compos. Struct.* 152 (2016) 34–44, <https://doi.org/10.1016/j.compstruct.2016.05.034>.
- [6] M. Lißner, E. Alabort, B. Erice, H. Cui, N. Petrinic, A rate dependent experimental and numerical analysis of adhesive joints under different loading directions, *Eur. Phys. J. Spec. Top.* 227 (1–2) (2018) 85–97, <https://doi.org/10.1140/epjst/e2018-00070-x>.
- [7] F.C. Sousa, A. Akhavan-Safar, R. Goyal, L.F.M. da Silva, Fatigue life estimation of adhesive joints at different mode mixities, *Fatigue Fract. Eng. Mater. Struct.* 98 (2020) 1–23, <https://doi.org/10.1080/00218464.2020.1804376>.
- [8] J.J.M. Machado, E.A.S. Marques, L.F.M. da Silva, Mechanical behaviour of adhesively bonded composite single lap joints under quasi-static and impact conditions with variation of temperature and overlap, *J. Compos. Mater.* 52 (26) (2018) 3621–3635, <https://doi.org/10.1177/0021998318766641>.
- [9] C.S.P. Borges, R. Brandão, A. Akhavan-Safar, E.A.S. Marques, R.J.C. Carbas, P. Weißgraeber, F. Schmid, L.F.M. da Silva, Influence of water and surfactant contamination

- on the mechanical and chemical properties of a silicone adhesive, before and after curing, *J. Adhes.* (2022). <https://doi.org/10.1080/00218464.2022.2082291>.
- [10] C.S.P. Borges, E.A.S. Marques, R.J.C. Carbas, C. Ueffing, P. Weißgraeber, L.F.M. da Silva, Review on the effect of moisture and contamination on the interfacial properties of adhesive joints, *Proc. Inst. Mech. Eng. C J. Mech. Eng. Sci.* 235 (3) (2021) 527–549, <https://doi.org/10.1177/0954406220944208>.
- [11] R.D. Adams, Nondestructive testing, in: L.F.M. da Silva, A. Öchsner, R.D. Adams (Eds.), *Handbook of Adhesion Technology*, Springer International Publishing AG, 2018, https://doi.org/10.1007/978-3-319-55411-2_42.
- [12] C. Jeenjitkaew, F.J. Guild, The analysis of kissing bonds in adhesive joints, *Int. J. Adhes. Adhes.* 75 (2017) 101–107, <https://doi.org/10.1016/j.ijadhadh.2017.02.019>.
- [13] F.M.F. Ribeiro, R.D.S.G. Campilho, R.J.C. Carbas, L.F.M. da Silva, Strength and damage growth in composite bonded joints with defects, *Compos. B Eng.* 100 (2016) 91–100, <https://doi.org/10.1016/j.compositesb.2016.06.060>.
- [14] E.F. Karachalios, R.D. Adams, L.F.M. da Silva, Strength of single lap joints with artificial defects, *Int. J. Adhes. Adhes.* 45 (2013) 69–76, <https://doi.org/10.1016/j.ijadhadh.2013.04.009>.
- [15] R.D. Adams, B.W. Drinkwater, Nondestructive testing of adhesively-bonded joints, *NDT&E Int.* 30 (2) (1997) 93–98, [https://doi.org/10.1016/S0963-8695\(96\)00050-3](https://doi.org/10.1016/S0963-8695(96)00050-3).
- [16] C.C.H. Guyott, P. Cawley, R.D. Adams, The non-destructive testing of adhesively bonded structure: a review, *J. Adhes.* 20 (2) (1986) 129–159, <https://doi.org/10.1080/00218468608074943>.
- [17] P.E. Mix, *Introduction to Nondestructive Testing: A Training Guide*, second ed., Wiley, Hoboken, NJ, United States, 2005, ISBN: 978-0-471-42029-3.
- [18] J.-P. Monchalán, Progress towards the application of laser-ultrasonics in industry, in: D.O. Thompson, D.E. Chimenti (Eds.), *Review of Progress in Quantitative Nondestructive Evaluation*, first ed., Springer, Boston, MA, United States, 1993, ISBN: 978-1-4613-6233-3, https://doi.org/10.1007/978-1-4615-2848-7_64.
- [19] B. Yilmaz, A. Asokkumar, E. Jasiūnienė, R.J. Kažys, Air-coupled, contact, and immersion ultrasonic non-destructive testing: comparison for bonding quality evaluation, *Appl. Sci.* 10 (19) (2020) 6757, <https://doi.org/10.3390/app10196757>.
- [20] D. Smagulova, L. Mazeika, E. Jasiūniene, Novel processing algorithm to improve detectability of disbonds in adhesive dissimilar material joints, *Sensors* 21 (9) (2021) 3048, <https://doi.org/10.3390/s21093048>.
- [21] E. Jasiūnienė, L. Mažeika, V. Samaitis, V. Cicėnas, D. Mattsson, Ultrasonic non-destructive testing of complex titanium/carbon fibre composite joints, *Ultrasonics* 95 (2019) 13–21, <https://doi.org/10.1016/j.ultras.2019.02.009>.
- [22] C.J. Brotherhood, B.W. Drinkwater, S. Dixon, The detectability of kissing bonds in adhesive joints using ultrasonic techniques, *Ultrasonics* 41 (7) (2003) 521–529, [https://doi.org/10.1016/S0041-624X\(03\)00156-2](https://doi.org/10.1016/S0041-624X(03)00156-2).
- [23] D. Francis, R.P. Tatam, R.M. Groves, Shearography technology and applications: a review, *Meas. Sci. Technol.* 21 (10) (2010) 102001, <https://doi.org/10.1088/0957-0233/21/10/102001>.
- [24] M.Y.Y. Hung, Review and comparison of shearography and pulsed thermography for adhesive bond evaluation, *Opt. Eng.* 46 (5) (2007) 051007, <https://doi.org/10.1117/1.2741277>.
- [25] I. Kryukov, S. Böhm, Prospects and limitations of eddy current shearography for non-destructive testing of adhesively bonded structural joints, *J. Adhes.* 95 (9) (2019) 874–886, <https://doi.org/10.1080/00218464.2018.1450144>.

- [26] F. Taillade, M. Quiertant, K. Benzarti, C. Aubagnac, Shearography and pulsed stimulated infrared thermography applied to a nondestructive evaluation of FRP strengthening systems bonded on concrete structures, *Construct. Build Mater.* 25 (2) (2011) 568–574, <https://doi.org/10.1016/j.conbuildmat.2010.02.019>.
- [27] J. Taiber, M. Kahlmeyer, A. Winkel, E.-M. Stübling, F. Taleb, M. Mikerov, S. Sommer, S. Böhm, M. Koch, Ageing condition determination of bonded joints by terahertz spectroscopy, in: L.F.M. da Silva, R.D. Adams, C. Sato, K. Dilger (Eds.), *Industrial Applications of Adhesives*, Springer Singapore, Singapore, 2021, pp. 127–138, https://doi.org/10.1007/978-981-15-6767-4_7.
- [28] Y.Y. Hung, Applications of digital shearography for testing of composite structures, *Compos. B Eng.* 30 (7) (1999) 765–773, [https://doi.org/10.1016/S1359-8368\(99\)00027-X](https://doi.org/10.1016/S1359-8368(99)00027-X).
- [29] Y. Ye, K. Ma, H. Zhou, D. Arola, D. Zhang, An automated shearography system for cylindrical surface inspection, *Measurement* 135 (2019) 400–405, <https://doi.org/10.1016/j.measurement.2018.11.085>.
- [30] R. Yang, Y. He, Optically and non-optically excited thermography for composites: a review, *Infrared Phys. Technol.* 75 (2016) 26–50, <https://doi.org/10.1016/j.infrared.2015.12.026>.
- [31] R.C. Tighe, J.M. Dulieu-Barton, S. Quinn, Identification of kissing defects in adhesive bonds using infrared thermography, *Int. J. Adhes. Adhes.* 64 (2016) 168–178, <https://doi.org/10.1016/j.ijadhadh.2015.10.018>.
- [32] W.D. Ruwandi Fernando, D.A. Tantrigoda, S.R.D. Rosa, D.R. Jayasundara, Infrared thermography as a non-destructive testing method for adhesively bonded textile structures, *Infrared Phys. Technol.* 98 (2019) 89–93, <https://doi.org/10.1016/j.infrared.2019.03.001>.
- [33] M. Grosso, I. de Araújo Soares, J.E.C. Lopez, S.D. Soares, J.M.A. Rebello, G.R. Pereira, Study on the limit detection of defects by pulsed thermography in adhesive composite joints through computational simulation, *Compos. B Eng.* 168 (2019) 589–596, <https://doi.org/10.1016/j.compositesb.2019.03.083>.
- [34] M. Kurpinski, M. Fidali, Detection of bonded joint defects by use of lock-in thermography, *Meas. Autom. Monit.* 62 (10) (2016) 333–336.
- [35] B. Yilmaz, A. Ba, E. Jasiuniene, H.-K. Bui, G. Berthiau, Evaluation of bonding quality with advanced nondestructive testing (NDT) and data fusion, *Sensors* 20 (18) (2020) 5127, <https://doi.org/10.3390/s20185127>.
- [36] V. Giurgiutiu, *Structural Health Monitoring with Piezoelectric Wafer Active Sensors*, second ed., Academic Press, Oxford, United Kingdom, 2014, ISBN: 978-0-12-418691-0, <https://doi.org/10.1016/C2013-0-00155-7>.
- [37] A. Güemes, A. Fernandez-Lopez, A.R. Pozo, J. Sierra-Pérez, Structural health monitoring for advanced composite structures: a review, *J. Compos. Sci.* 4 (1) (2020) 13, <https://doi.org/10.3390/jcs4010013>.
- [38] K. Ono, Review on structural health evaluation with acoustic emission, *Appl. Sci.* 8 (6) (2018) 958, <https://doi.org/10.3390/app8060958>.
- [39] S. Abbas, F. Li, J. Qiu, A review on SHM techniques and current challenges for characteristic investigation of damage in composite material components of aviation industry, *Mater. Perform. Charact.* 7 (1) (2018) 20170167, <https://doi.org/10.1520/MPC20170167>.
- [40] W.J. Staszewski, C. Boller, G.R. Tomlinson, *Health Monitoring of Aerospace Structures—Smart Sensor Technologies and Signal Processing*, first ed., Wiley, Chichester, United Kingdom, 2004, ISBN: 0-470-84340-3.
- [41] Federal Aviation Administration, *Federal Aviation Regulation—Part 5*, 2014. (sec. 23.57) <https://www.ecfr.gov/current/title-14/chapter-I/subchapter-C/part-23/subpart-5>. Federal Aviation Regulation.

- [42] European Union Aviation Safety Agency, Certification Specifications and Acceptable Means of Compliance for Large Aeroplanes, CS-25, 2020. (cS 25.625) Legal Regulation.
- [43] K. Worden, W.J. Staszewski, J.J. Hensman, Natural computing for mechanical systems research: a tutorial overview, *Mech. Syst. Signal Process.* 25 (1) (2011) 4–111, <https://doi.org/10.1016/j.ymssp.2010.07.013>.
- [44] A. Rytter, Vibration Based Inspection of Civil Engineering Structures (PhD thesis), University of Aalborg, Aalborg, Denmark, 1993.
- [45] C.R. Farrar, K. Worden, An introduction to structural health monitoring, *Philos. Trans. R. Soc. A Math. Phys. Eng. Sci.* 365 (1851) (2007) 303–315, <https://doi.org/10.1098/rsta.2006.1928>.
- [46] C.R. Farrar, K. Worden, *Structural Health Monitoring: A Machine Learning Perspective, first ed.*, Wiley, Chichester, United Kingdom, 2013, ISBN: 978-1-119-99433-6.
- [47] M. Mitra, S. Gopalakrishnan, Guided wave based structural health monitoring: a review, *Smart Mater. Struct.* 25 (5) (2016) 053001, <https://doi.org/10.1088/0964-1726/25/5/053001>.
- [48] G.M.F. Ramalho, A.M. Lopes, L.F.M. Silva, Structural health monitoring of adhesive joints using Lamb waves: a review, *Struct. Control Health Monit.* 29 (1) (2022), <https://doi.org/10.1002/stc.2849>.
- [49] M. Rucka, E. Wojtczak, J. Lachowicz, Lamb wave-based monitoring of shear failure of an adhesive lap joint, *Diagnostyka* 19 (4) (2018) 51–57, <https://doi.org/10.29354/diag/95176>.
- [50] K. Ono, Structural health monitoring of large structures using acoustic emission-case histories, *Appl. Sci.* 9 (21) (2019) 4602, <https://doi.org/10.3390/app9214602>.
- [51] J.A. Tenreiro Machado, A.M. Lopes, R de Camposinhos, Fractional-order modelling of epoxy resin, *Philos. Trans. R. Soc. A Math. Phys. Eng. Sci.* 378 (2172) (2020) 20190292, <https://doi.org/10.1098/rsta.2019.0292>.
- [52] C.-H. Kim, J.-H. Choi, J.-H. Kweon, Defect detection in adhesive joints using the impedance method, *Compos. Struct.* 120 (2015) 183–188, <https://doi.org/10.1016/j.compstruct.2014.09.045>.
- [53] M. Hübner, G. Dumstorff, M. Kahali Mogaddam, P. Plagemann, W. Lang, Online monitoring of the curing of adhesives with a miniaturised interdigital sensor using impedance spectroscopy, *J. Adhes. Sci. Technol.* 32 (7) (2018) 772–786, <https://doi.org/10.1080/01694243.2017.1385122>.
- [54] S. Bagavathiappan, B.B. Lahiri, T. Saravanan, J. Philip, T. Jayakumar, Infrared thermography for condition monitoring—a review, *Infrared Phys. Technol.* 60 (2013) 35–55, <https://doi.org/10.1016/j.infrared.2013.03.006>.
- [55] A.F.G. Tenreiro, A.M. Lopes, L.F.M. da Silva, A review of structural health monitoring of bonded structures using electromechanical impedance spectroscopy, *Struct. Health Monit.* (2021), <https://doi.org/10.1177/1475921721993419>. 1475921721993419.
- [56] Wongi Na, Jongdae Baek, A review of the piezoelectric electromechanical impedance based structural health monitoring technique for engineering structures, *Sensors* 18 (5) (2018) 1307, <https://doi.org/10.3390/s18051307>.
- [57] Z. Su, L. Ye, Y. Lu, Guided Lamb waves for identification of damage in composite structures: a review, *J. Sound Vib.* 295 (3-5) (2006) 753–780, <https://doi.org/10.1016/j.jsv.2006.01.020>.
- [58] K.F. Chen, S.L. Mei, Composite interpolated fast Fourier transform with the Hanning window, *IEEE Trans. Instrum. Meas.* 59 (6) (2010) 1571–1579, <https://doi.org/10.1109/TIM.2009.2027772>.
- [59] J.L. Rose, *Ultrasonic Guided Waves in Solid Media*, Cambridge University Press, New York, NY, United States, 2014.

- [60] Q.T. Deng, Z.C. Yang, Propagation of guided waves in bonded composite structures with tapered adhesive layer, *Appl. Math. Model.* 35 (11) (2011) 5369–5381, <https://doi.org/10.1016/j.apm.2011.04.042>.
- [61] V. Giurgiutiu, *Structural Health Monitoring of Aerospace Composites*, first ed., Elsevier, London, United Kingdom, 2016, ISBN: 978-0-12-409605-9.
- [62] B. Ren, C.J. Lissenden, Ultrasonic guided wave inspection of adhesive bonds between composite laminates, *Int. J. Adhes. Adhes.* 45 (2013) 59–68, <https://doi.org/10.1016/j.ijadhadh.2013.04.001>.
- [63] E. Siryabe, M. Renier, A. Meziane, M. Castaings, The transmission of Lamb waves across adhesively bonded lap joints to evaluate interfacial adhesive properties, *Phys. Procedia* 70 (3) (2015) 541–544, <https://doi.org/10.1016/j.phpro.2015.08.012>.
- [64] W. Yan, W.Q. Chen, Structural health monitoring using high-frequency electromechanical impedance signatures, *Adv. Civil Eng.* 2010 (2010) 1–11, <https://doi.org/10.1155/2010/429148>.
- [65] ANSI/IEEE, ANSI/IEEE Std 176-1987 Standard on Piezoelectricity, ANSI/IEEE, 1987, p. 74. Standard 176.
- [66] C. Liang, F.P. Sun, C.A. Rogers, Coupled electro-mechanical analysis of adaptive material systems-determination of the actuator power consumption and system energy transfer, *J. Intell. Mater. Syst. Struct.* 8 (4) (1997) 335–343, <https://doi.org/10.1177/1045389X9700800406>.
- [67] S. Bhalla, A. Surendra, C.K. Soh, Influence of structure-actuator interactions and temperature on piezoelectric mechatronic signatures for NDE, in: *Proceedings Volume 5062, Smart Materials, Structures, and Systems, 5062*, SPIE, Bangalore, India, 2002. vol. 0.1117/12.514762.
- [68] G. Park, H.H. Cudney, D.J. Inman, Impedance-based health monitoring of civil structural components, *J. Infrastruct. Syst.* 6 (4) (2000) 153–160, [https://doi.org/10.1061/\(ASCE\)1076-0342\(2000\)6:4\(153\)](https://doi.org/10.1061/(ASCE)1076-0342(2000)6:4(153)).
- [69] C. Kralovec, M. Schager, M. Mayr, Localization of damages by model-based evaluation of electro-mechanical impedance measurements, in: *Proceedings of the 9th European Workshop on Structural Health Monitoring*, July, NDT.net, Manchester, United Kingdom, 2018.
- [70] D.P. Kroese, Z.I. Botev, T. Taimre, R. Vaisman, *Data Science and Machine Learning: Mathematical and Statistical Methods*. Machine Learning & Pattern Recognition Series, first ed., CRC Press, Boca Raton, FL, United States, 2020, ISBN: 978-1-138-49253-0.
- [71] T.M. Mitchell, *Machine Learning*, McGraw-Hill, New York, NY, United States, 1997, ISBN: 978-0-07-042807-2.
- [72] S. Marsland, *Machine Learning: An Algorithmic Perspective*. Machine Learning & Pattern Recognition Series, second ed., CRC Press, Boca Raton, FL, United States, 2014, ISBN: 978-0-429-10250-9, <https://doi.org/10.1201/b17476>.
- [73] Z.-H. Zhou, *Ensemble Methods: Foundations and Algorithms*, Chapman and Hall/CRC, 2019.
- [74] W.S. McCulloch, W. Pitts, A logical calculus of the ideas immanent in nervous activity, *Bull. Math. Biol.* 52 (1/2) (1990) 99–115, <https://doi.org/10.1007/BF02459570> (Reprinted from the *Bull. Math. Biol.* 5 (1943) 115–133).
- [75] M.F. Møller, A scaled conjugate gradient algorithm for fast supervised learning, *Neural Netw.* 6 (4) (1993) 525–533, [https://doi.org/10.1016/S0893-6080\(05\)80056-5](https://doi.org/10.1016/S0893-6080(05)80056-5).
- [76] M. Christ, N. Braun, J. Neuffer, A.W. Kempa-Liehr, Time series feature extraction on basis of scalable hypothesis tests (tsfresh—a Python package), *Neurocomputing* 307 (2018) 72–77, <https://doi.org/10.1016/j.neucom.2018.03.067>.

-
- [77] A.F.G. Tenreiro, A.M. Lopes, L.F.M. da Silva, J.D.P. Amorim, Effect of mechanical properties and geometric dimensions on electromechanical impedance signatures for adhesive joint integrity monitoring, *Mech. Adv. Mater. Struct.* (2022) 1–16, <https://doi.org/10.1080/15376494.2022.2033891>.
- [78] Y. Zhuang, F. Kopsaftopoulos, R. Dugnani, F.-K. Chang, Integrity monitoring of adhesively bonded joints via an electromechanical impedance-based approach, *Struct. Health Monit.* 17 (5) (2018) 1031–1045, <https://doi.org/10.1177/1475921717732331>.
- [79] F. Pedregosa, G. Varoquaux, A. Gramfort, V. Michel, B. Thirion, O. Grisel, M. Blondel, P. Prettenhofer, R. Weiss, V. Dubourg, J. Vanderplas, A. Passos, D. Cournapeau, M. Brucher, M. Perrot, E. Duchesnay, Scikit-learn: machine learning in Python, *J. Mach. Learn. Res.* 12 (2011) 2825–2830.
- [80] M. Rautela, C.R. Bijudas, Electromechanical admittance based integrated health monitoring of adhesive bonded beams using surface bonded piezoelectric transducers, *Int. J. Adhes. Adhes.* 94 (2019) 84–98, <https://doi.org/10.1016/j.ijadhadh.2019.05.002>.

This page intentionally left blank

Part Five

Emerging technologies for structural bonding

This page intentionally left blank

Sustainable adhesives: Bioadhesives, chemistries, recyclability, and reversibility

29

Yuanqiao Rao and Grace Wan

The Dow Chemical Company, Midland, MI, United States

29.1 Introduction

In this chapter, we will describe how nature develops bioadhesives and how these materials and design strategies can be used to construct more sustainable adhesives. Then we will discuss sustainable materials for adhesives, including low-carbon options, biopolymers, and feedstocks from biomass. We are also interested in biodegradable adhesives to provide safer materials. Biodegradable adhesives are needed in applications where the use is temporary, the use time is short, and the persistence of the adhesive materials can expose microplastics. Biodegradable materials might not be preferred for use in structural adhesives, where longevity is more important. In addition to adhesives based on sustainable materials, the adhesives that enable the repair of engineering structures and the recycling of the structures will improve material circularity. These recyclable adhesives usually function through adhesion on demand and are called smart adhesives. Finally, we will discuss self-healing adhesives, which can reduce the energy and materials for adhesion repair and increase their lifetime in use.

29.2 Controlled adhesion in biological systems; multifunctional materials in nature

Adhesion exists in all biological systems, both subcellular and extracellular. Biological adhesives are crucial to the survival of living organisms. Terrestrial animals need to climb on various surfaces while marine animals need to anchor in the water. There are hundreds of references discussing bioadhesives [1]. In this section, we focus on a couple of examples of the most recent (post-2015) research on the chemistry of bioadhesives and how these molecules develop adhesion differently from synthetic adhesives.

In modern adhesive development, there are several strategies for obtaining good adhesion: covalent bonding, strong interfacial interactions such as ionic and hydrogen bonding, weak polar-polar interactions and van der Waals forces, molecular interdiffusion and mechanical interlocking, and the use of energy-dissipating materials, such as for pressure-sensitive adhesives. These adhesive mechanisms are delivered using

epoxies, polyurethanes, reactive acrylics, toughened acrylics, anaerobic acrylics, cyanoacrylates, and silicones. However, it was quickly realized that most existing commercial adhesion chemistries are nonexistent in nature. Therefore, the study of biological adhesive chemistry and mechanism has become increasingly attractive with the world's urgent need for sustainable adhesives. Several adhesion systems found in biology are notable examples of more sustainable adhesives. This section will discuss reversible adhesion to accommodate temporary adhesion needs, universal adhesion to varying compositions and structures, and underwater adhesion.

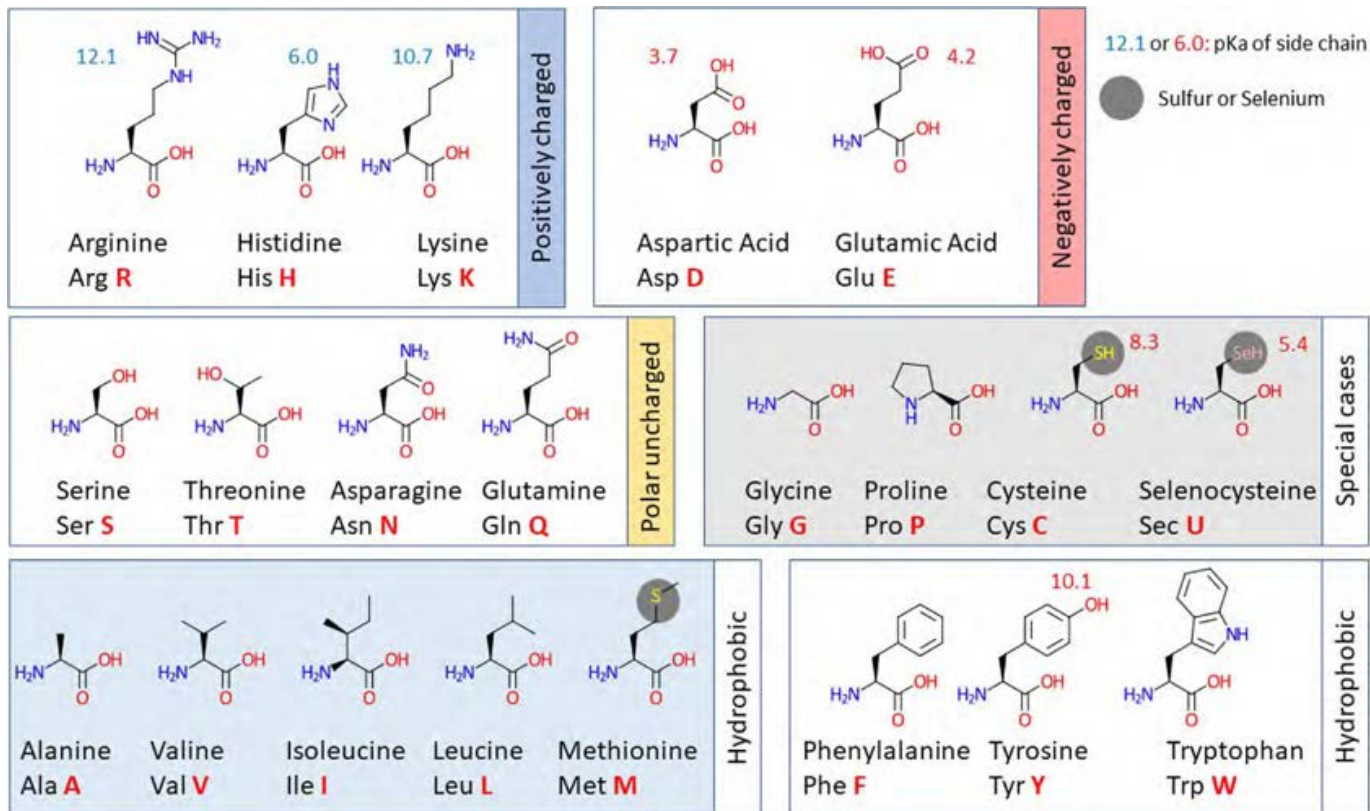
In living organisms, adhesive secretions usually contain specialized adhesive proteins. Bioadhesives are polyamides, an alternative name to describe the chemistry of proteins, which are rarely used in synthetic adhesives. Industrial polyamides are made through condensation polymerization, and there are no simple synthetic methods to carry out the condensation polymerization with amino acids. About 22 amino acids are used by living organisms to make proteins or polyamides. The chemical structures of these 22 amino acids are illustrated in Fig. 29.1 [2]. It is clearly shown that different side groups provide amino acids and the derived proteins with multiple degrees of charge, polarity, and hydrophobicity. These functional groups and their interactions/reactions form the foundation of various adhesion mechanisms in biological systems.

29.2.1 Universal adhesion

It is highly desired for an adhesive to adhere to substrates of varying composition and structure and maintain the adhesion under different environmental conditions. In a carnivorous plant, acyl glycerides and triterpenoids are released by the cells [3]. These acyl glycerides and triterpenoids are very hydrophobic. These OH groups are hypothesized to form strong interactions with hydrophilic surfaces while the hydrophobic groups help adhere to a hydrophobic surface. Additional hydrophobic surfaces are formed once the interface is established, reducing the adhesion's water sensitivity. These interactions and their contribution to the adhesion of the plant to both hydrophilic and hydrophobic surfaces are illustrated in Fig. 29.2. The physical properties of these compounds are soft, exhibiting large deformations under stress. These materials have similar physical properties to synthetic pressure-sensitive adhesives, which are often made of polyolefins, acrylics, or silicones. The adhesion strength between *Roridula gorgonias*, a carnivorous plant, and hydrophilic glass is about 2–3 kPa (using the pull-off force measurement), which is much lower than synthetic pressure-sensitive adhesives. However, this adhesive strength is not affected by the presence of water, unlike a synthetic pressure-sensitive adhesive (PSA).

29.2.2 Underwater adhesion

Underwater adhesion is challenging for synthetic adhesives because water can diffuse into the interface between two materials and solubilize or hydrolyze the interface, leading to adhesion loss. That is why underwater adhesion in aquatic animals attracts interest [3,4]. Several aquatic creatures, such as barnacles and mussels, rely on wet



Thomas Ryckmans 2021

Fig. 29.1 Chemical structures of 22 proteinogenic amino acids [2] (This work is provided under the terms of this creative commons public license ("CCPL" OR "LICENSE"). The work is protected by copyright and/or other applicable law any use of the work other than as authorized under this license or copyright law is prohibited).

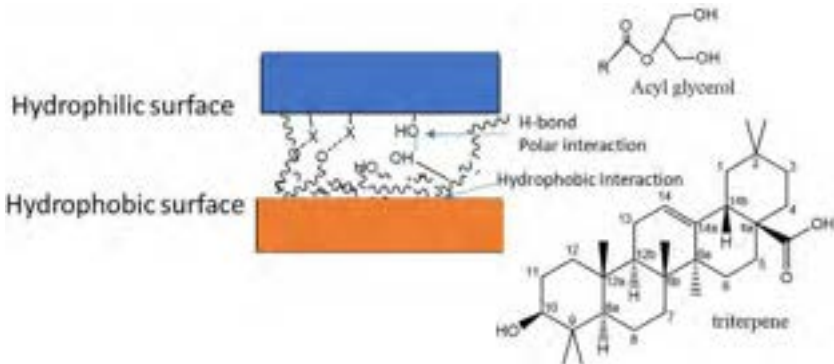


Fig. 29.2 Illustration of the modes of adhesion in a carnivorous plant.

adhesion for living. The strong underwater adhesion in these marine organisms originates from interactions of many diverse types: hydrophobic, electrostatic, covalent bonding, and supramolecular bonding.

Mussels and barnacles are two aquatic animals that utilize various chemistries to adhere to various surfaces under the water. These aquatic creatures secrete special proteins to assist the establishment of adhesion. Although the study of the adhesive mechanism of mussels started decades ago [5], there is still no agreement on the fundamental mechanism [6]. Initially, the adhesion was attributed to the 3,4-dihydroxyphenyl-L-alanine (DOPA) coordinating with the metal atoms on the substrate [5a]. Recent work has shown that the adhesion strength between a model compound containing DOPA and mica is not as strong as in nature [7]. It is now believed that the adhesion establishment is beyond just chelation; rather, it involves multiple proteins in a time-dependent process, layered structures, multiple interaction sites, and self-assembly. As described in Fig. 29.3, distinct types of proteins are released at various stages of adhesion. Pvfp-5 is the first protein released and is responsible for establishing contact with the substrate, especially displacing the hydrating surface layer. After that, Pvfp-3 and then Pvfp-6 were released. A detailed study [8] of protein surface interaction suggests that Pvfp-5 is responsible for interfacial strength. Pvfp-3 and Pvfp-6 form additional layers. It is suggested that Pvfp-3 prevents the oxidation of DOPA. All three proteins have both negative and positive charges and cysteine amino acids. These electrostatic and sulfur-sulfur bonding forces help the cohesion of the proteins and the overall structural assembly. Ou et al.'s molecular dynamics simulation illustrated the importance of the intramolecular structure of Pvfp-5 [6]. In this study, it was found that DOPA and positively charged basic amino acid residues form pairs. The charge interaction between the protein and the substrate was found to be the main driver for strong adhesion. This study highlights the importance of secondary structure in bioadhesives.

In summary, bioadhesives are polymers of a limited number of backbone chemistries: proteins, polysaccharides, and hydrocarbons, with various functional groups such as ionic, acid, hydroxyl, or amine. They often contain multiple functional groups

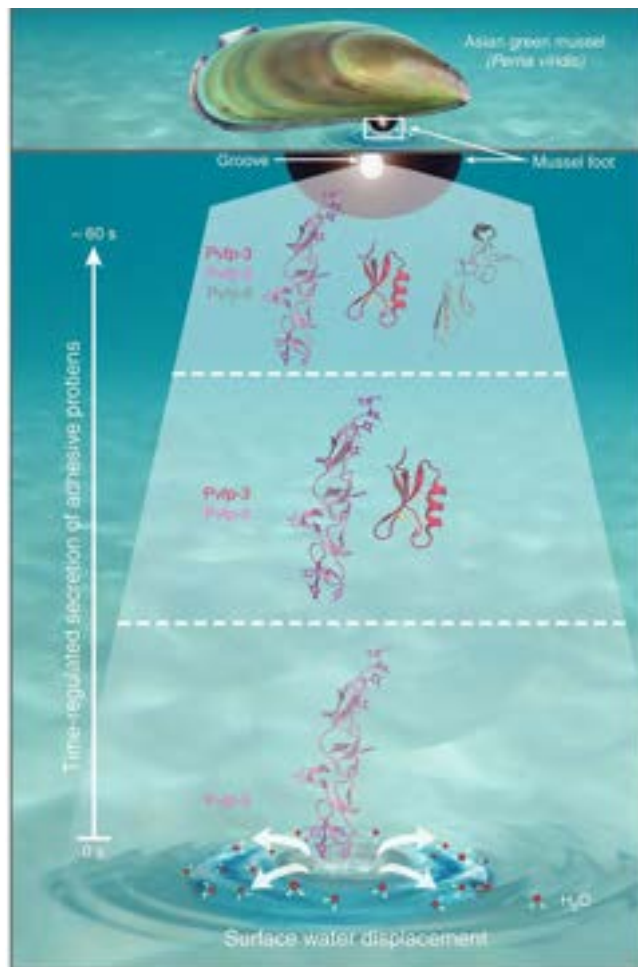


Fig. 29.3 Sequential secretion of adhesive proteins in mussels [8].

<https://www.nature.com/articles/ncomms9737#rightslink>, This work is licensed under a Creative Commons Attribution 4.0 International License.

in one polymer and form higher-level structures. These functional groups lead to various adhesive interactions with the surface: electrostatic, hydrogen bonding, polar, and hydrophobic interaction. The formation of the adhesive bonds is a multistep process. It starts with establishing a strong interaction with the surface, followed by the necessary secondary structure formation to strengthen and make the adhesion robust in various environments. In industrial applications, the direct replication of the bioadhesion, especially the hierarchical ordering, will not be achieved easily without a facile means to provide multiple functional groups and control the assembly of molecules. However, the special arrangement of multiple interactions and materials is a good example of sustainable adhesives.

29.3 Sustainable materials for adhesives

Sustainable materials are defined as materials that fit one or more of the following characteristics: made from a renewable source, enable recycling, or are nontoxic and biodegradable. Developing a sustainable adhesive may address only one of these aspects. However, a holistic sustainable solution that possesses high performance, has low environment impact, and is recyclable is desired. For instance, efforts to develop sustainable adhesives focus on eliminating toxic substances. Formaldehyde, a key ingredient in phenolic adhesives, is determined by the US National Toxicology Program as "known to be a human carcinogen and is desired to be eliminated" [9]. Toluene, *N*-methyl-2-pyrrolidone, and methyl ether ketone are solvents of concern. Bisphenol A, which is the workhorse in epoxy adhesive, is a concern because of the possible health effects on the brains of fetuses, infants, and children [10]. Monomeric isocyanate, which is needed to form polyurethane at room temperature, is toxic. Therefore, in recent years, better solvents such as ethyl acetate or water-based or solventless adhesives have been developed, benign epoxy monomers have been explored, and nonisocyanate polyurethanes have been created [11]. In this chapter, we survey research activities beyond the elimination of harmful substances. We will focus on materials aiming to replace petroleum-based chemicals for adhesives, including bio-derived materials for adhesives, recyclable adhesives, and biodegradable and compostable adhesives. We will also discuss smart adhesives and self-healing adhesives.

29.3.1 Bio-derived materials for adhesives

One method of reducing the carbon footprint is to reduce the use of petroleum-based materials. Recently, a biorefinery concept has been proposed that focuses on using sugars, starches, lignocellulose, oil-based crops, grasses, marine biomass, and their residues to make chemicals [12]. Traditional chemicals and new chemicals are proposed to be made via the biorefinery. In addition to biopolymers that can be formulated into adhesives, the intermediate chemicals from the biorefinery can be used as starting materials for adhesives. Some promising bio-derived chemicals include gluconic acid, lactic acid, malonic acid, propionic acid, citric and aconitic acids, xylonic acid, acetoin, furfural, levoglucosan, lysine, serine, and threonine [12a].

Traditional structural adhesives such as epoxies, urethanes, ureas, esters, phenolic resins, and acrylics can all benefit from bio-derived materials [11a]. Materials similar to petroleum-based ones can be made after the monomers are generated from biomass. However, it is often more desirable to use biopolymers directly to create adhesives.

29.3.2 Adhesives containing lignin and lignin derivatives

Among the most studied biopolymer-based adhesives are lignin-based adhesives. Lignin is the second most abundant biopolymer, next to cellulose. Chemically, lignin is based on crosslinked phenolic precursors. Because of its high content of phenolics,

lignin is hydrophobic, rigid, and chemically, biologically, and thermally stable. These attributes make lignin an ideal material for structural adhesives. Lignin derivatives can be formed through oxidation, enzymatic hydrolysis, and pyrolysis. Because of their abundance, lignin and lignin derivatives are used in creating phenolic [13], epoxy [14], and polyurethane adhesives [15]. Fig. 29.4 illustrates the heterogeneous chemical nature of lignin [15a].

There are two ways that lignin can be incorporated into an adhesive. The direct use of lignin products is preferred to reduce the mass of the overall carbon footprint most effectively. However, the inertness and the presence of only phenolic functional groups on lignin limit its reactivity and usefulness. To improve its chemical reactivity, monolignols and functional monolignols are produced. The depolymerization products of lignin, including monolignols of 4-hydroxy-3-methoxyphenylpropane (G) and 3,5-dimethoxy-4-hydroxyphenylpropane (S), can be used to make adhesives. Alternatively, the functionalized monolignols can be used as adhesive starting materials, as shown in Fig. 29.5 [15a].

Regarding the direct use of lignin products, lignin-containing phenol-formaldehyde adhesives have been used as wood adhesives for decades [16]. However, the incorporation of lignin usually decreases the adhesive performance. Recently, a 100% lignin-formaldehyde adhesive has been shown to have a comparable adhesive performance to its phenol counterpart [13a]. The authors attributed the performance improvement to the preparation of lignin precursors. In another paper, polyvinylpyrrolidone was mixed with phenol-modified lignin to avoid using

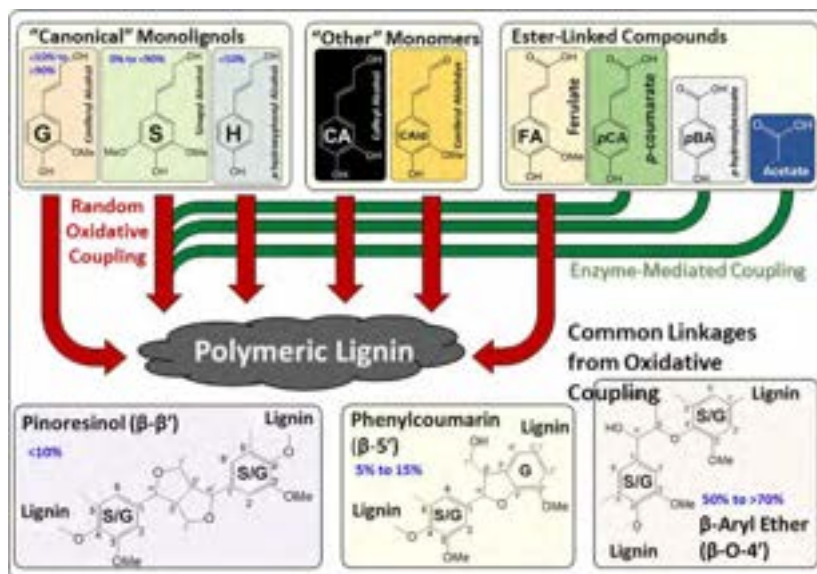


Fig. 29.4 Key compositional and structural features of lignin arising from lignin biosynthesis [15a]. <https://www.mdpi.com/2073-4360/11/7/1202>, Used under Creative Commons Copyrights.

formaldehyde, a substance of concern. The formed aqueous-based adhesive showed satisfactory lap shear strength as a wood adhesive [13b].

Urethane adhesives can be obtained by reacting ligninols with isocyanates [15a]. The success in creating a high-performance lignin-based PU adhesive depends on the reactivity of lignin toward isocyanates, and this reactivity can be modified through the derivatization of the lignin [17]. Not only can the use of lignin increase the biocarbon content, but it can also improve adhesive properties. For example, the addition of lignin into a PU adhesive improved the delamination resistance, cohesive failure, and gap-filling properties [15b].

The ligninols can be further functionalized into acrylics. Two monophenolic compounds, 4-propylsyringol (4pS) and 4-propylguaiacol (4pG), were obtained after the catalytical deconstruction of poplar wood and reaction with acryloyl chloride [18]. The glass transition temperatures (T_{gs}) of the polymers made from the radical polymerization of 4pS and 4pG are 98°C (P4pSA) and 169°C (P4pSMA), respectively. These high T_g bio-derived polymers when copolymerized with low T_g *n*-butyl acrylate polymers, derived from bio *n*-butanol, can form various copolymers that can be made into high-quality bioderived PSAs (Fig. 29.6).

Like lignols, an acrylic macromonomer can be formed from the chemicals generated from biomass; for example, L-lactide and ϵ -caprolactone were copolymerized with 2-hydroxyethyl methacrylate (HEMA). This macromonomer was copolymerized with other acrylic monomers through mini-emulsion polymerization and formulated into pressure-sensitive adhesives [19].

In summary, lignols and lignol derivatives are promising sustainable materials for various adhesives, such as wood adhesives, steel adhesives, and pressure-sensitive adhesives. Although the stability of lignin is advantageous in structure adhesives, lignin's resistance to biodegradation could be a cause for concern. In addition, microplastics could be of concern in many pressure-sensitive adhesives if the adhesive is not readily biodegradable. We will continue the discussion of biodegradable and compostable adhesives in the next section.

29.3.3 Biodegradable and compostable adhesives

Biodegradable and compostable adhesives can be bio-derived or petroleum based. However, it is preferred to create biodegradable and compostable adhesives using biomass-derived precursors. In this way, reducing the carbon footprint and eliminating the ecotoxicity of microplastics can be achieved simultaneously.

To prepare for our discussion, we will briefly introduce biodegradation. According to the Organization for Economic Cooperation and Development (OECD), an international organization on standards, biodegradation occurs when organic substances are decomposed by microorganisms (aerobic bacteria) into simpler substances such as carbon dioxide, water, and ammonia [20]. Biodegradation can happen in different media: freshwater, ocean water, wastewater, and soil. Compostability refers to the ability of the material to undergo biological decomposition in a compost site and be converted into CO₂, H₂O, inorganics, and biomass at a rate that is consistent with a known compostable material according to ASTM D6002. Therefore, compostability

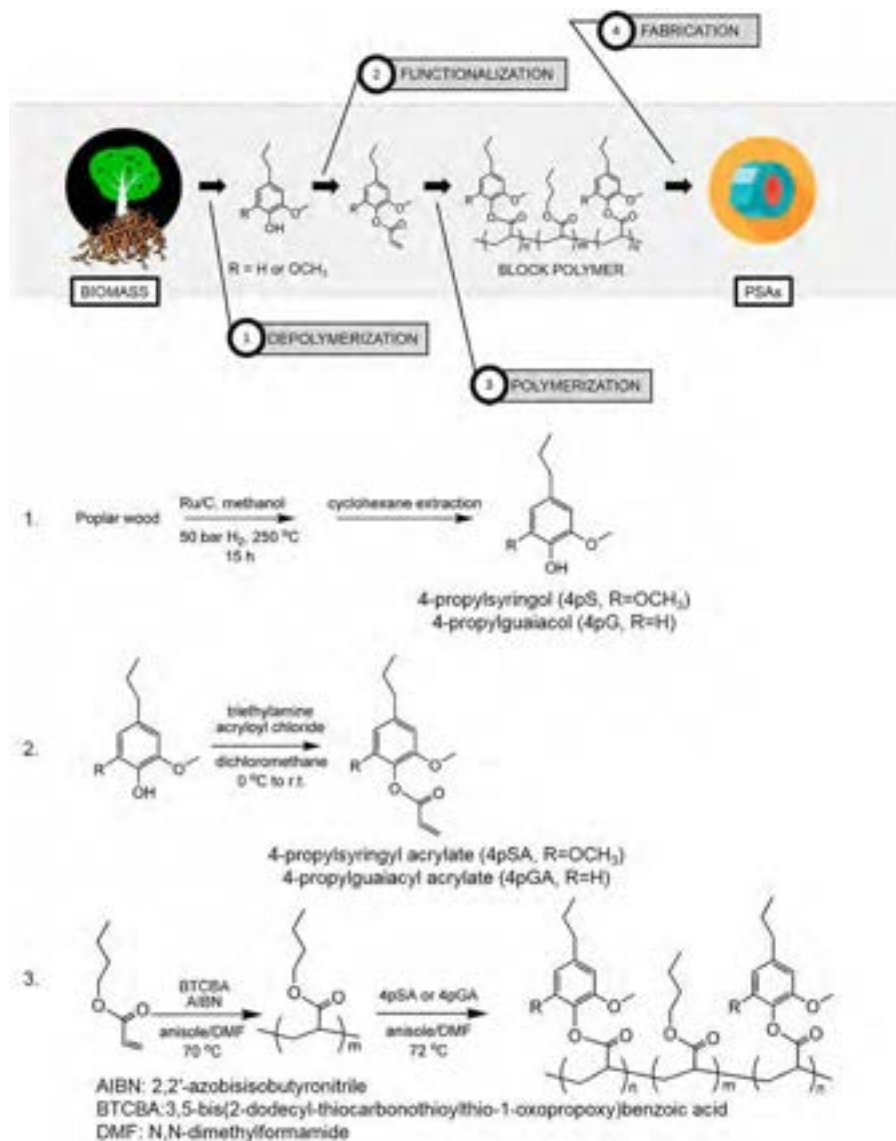


Fig. 29.6 Pressure-sensitive adhesive from lignin biomass [18].

S. Wang, L. Shuai, B. Saha, D.G. Vlachos and T.H. Epps, From tree to tape: direct synthesis of pressure sensitive adhesives from depolymerized raw lignocellulosic biomass, ACS Cent. Sci. 4 (6) (2018), 701–708, Publication Date: May 15, 2018, <https://doi.org/10.1021/acscentsci.8b00140>, ACS Author Choice with CC-BYlicense.

is a subcategory of biodegradability, defined explicitly as biodegradation in soil. The known biodegradable polymers include natural polymers such as polysaccharides, poly amino acids (protein), and polynucleotides (DNA and RNA) [21,22] as well as (bio)synthetic polymers such as polyesters and polyvinyl alcohol. These biodegradable polymers are great candidates for use in making biodegradable adhesives.

As an example of a polysaccharide, starch has been used as an adhesive for a long time. However, its hydrophilicity results in poor water resistance. Therefore, modification to improve its hydrophobicity is needed to make starch into a useful adhesive. Different chemical modifications can be used such as esterification, oxidation, etherification, and crosslinking, as detailed in Fig. 29.7 [23]. Starch can also be crosslinked by phosphoryl chloride, adipic acetic mixed anhydride, sodium trimetaphosphate (STMP), and mixtures of STMP and sodium tripolyphosphates (STPP) to form modified starches, which are approved as food-grade by the US Food and Drug Administration (FDA) [24]. Further, chemically modified starch can be crosslinked based on the available functional groups.

Most starch-based adhesives have been used for wood adhesion. In a recent study, starches were epoxidized first by reacting hydroxyl groups with epichlorohydrin. They were then crosslinked using diethylenetriamine to create a formaldehyde-free, water-resistant wood adhesive [25]. In another example, 100% biodegradable hot-melt adhesives were created using modified high amylose corn starch (HACS) and its propionate derivatives, polyvinyl alcohol (PVOH) and glycerol [26]. Better adhesive performance was achieved using expanded high amylose corn starch (DS = 0)

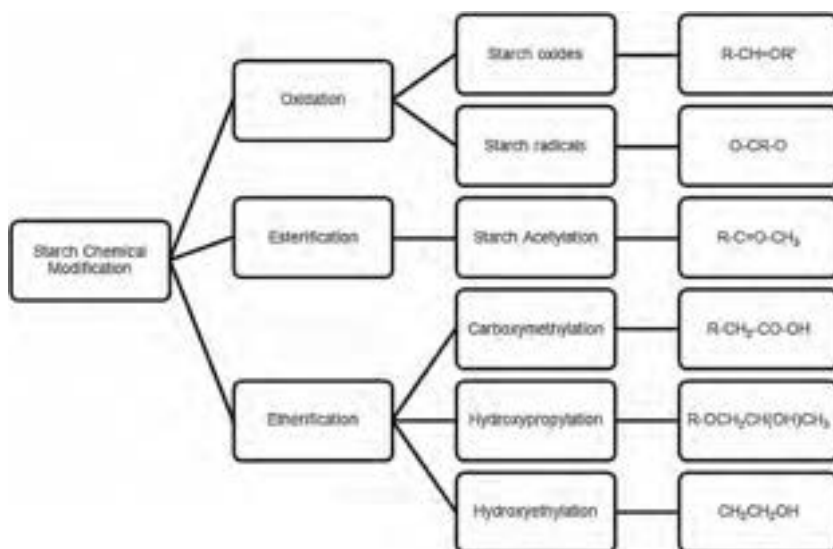


Fig. 29.7 Various chemical modifications of starch [23].

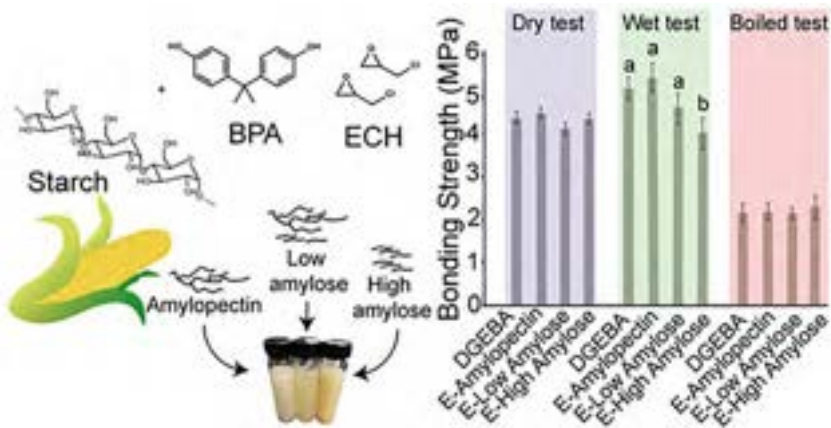


Fig. 29.8 Epoxidation of starch and the performance of crosslinked starch as a wood adhesive [25]. Reprinted (adapted) with permission from N. Tratnik, P.-Y. Kuo, N.R. Tanguy, P. Gnanasekar, N. Yan, Biobased epoxidized starch wood adhesives: effect of amylopectin and amylose content on adhesion properties, *ACS Sustain. Chem. Eng.* 8(49) (2020) 17997–18005.

than using native (nonexpanded) starch. The authors speculate that the expansion process promoted better noncovalent interactions with PVOH and glycerol and improved adhesion performance (Fig. 29.8).

In addition to starch, other polysaccharides also have been investigated as adhesives. An aqueous solution of a bacterial polysaccharide FucoPol was used to bond wood and showed good wet adhesion [27]. In addition, these authors compared the lap shear strength of diverse types of polysaccharides. Because of the variation in the structures and properties of various polysaccharides, polysaccharides are a rich material platform for exploration of their adhesive applications (Fig. 29.9).

It is no surprise that proteins have also been studied as adhesives. Collagen hydrolysate, a protein extracted from leather waste, has been used to make wood adhesives by crosslinking with silane coupling agents [28]. Because 90% of the leather waste is collagen hydrolysate, the authors believe in the potential of collagen hydrolysate as a low-cost biomaterial for adhesives. The water resistance of the adhesive was demonstrated and further improved by increased crosslinking density. We would like to remind the reader of the importance of protein in the water resistance of adhesives in biological systems and believe harvesting protein from biomass could be fruitful.

Soy protein and tannin have been reacted with other chemicals to make adhesives for many years [29,30]. However, soy protein-based adhesive has poor water resistance, similar to that of starch. When a crosslinker such as sodium hexametaphosphate is added, the wet adhesion of the soy protein adhesive was significantly improved [30b]. In another study inspired by mussel bioadhesives, calcium sulfoaluminate (CSA) was mixed with soy protein and acrylic acid [31]. CSA promoted the polymerization of acrylic acid and crosslinked with the organic phase to produce a wood

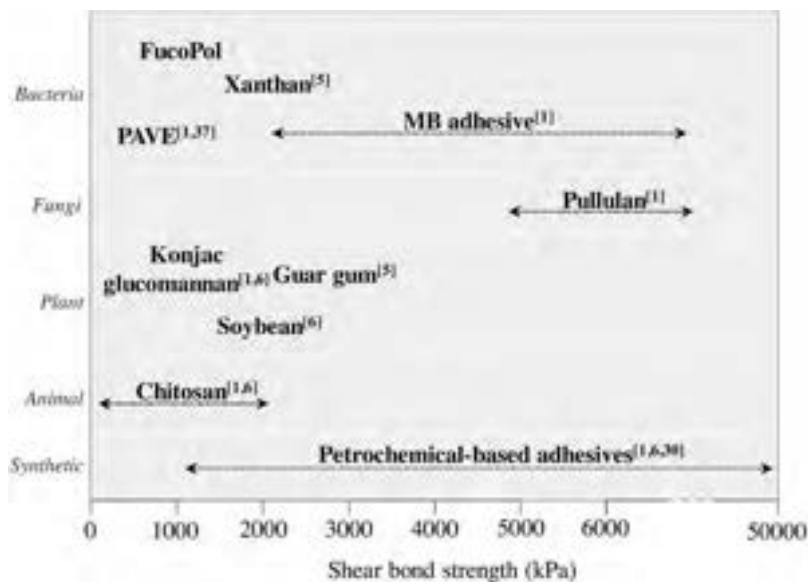


Fig. 29.9 Schematic representation of the shear bond strength values reported for different adhesives tested for bonding wood materials [27].

adhesive that had better adhesion strength than without CSA, and improved flame retardancy and reduced biofouling. Recently, Roman and Wilker's work suggested the potential of proteins as structural adhesives [32]. In their study, they formed a water-based adhesive when they mixed a protein and ascorbic acid. By adjusting the protein/ascorbic acid ratio, concentration, pH, and ion type and concentration, they demonstrated a lap shear strength of over 2 MPa for both aluminum and wood, which is comparable to Gorilla Glue, a synthetic adhesive [32]. The type of protein used is shown to have a significant impact on the adhesive strength. Bovine serum albumin (BSA) is shown to have the best adhesion properties. The correlation between the protein/ascorbic acid ratio is not monotonic; rather, there is a range of ratios that gives rise to good adhesive properties. The presence of amine-containing amino acids such as lysine in the protein to create crosslinking or hydrogen bonding may account for the good adhesive performance (Table 29.1).

In addition to natural polymers such as starch and protein, polyesters derived from biomass are promising materials for use as biodegradable adhesives. As described earlier, many chemicals can be produced from biomass. The formation of polyesters using these chemicals is hypothesized to replace petroleum-based polyesters and render the polymer biodegradable. Two bio-derived cyclic monomers, menthide and lactide, were copolymerized using ring-opening polymerization [34]. The resulting polymer was formulated into a pressure-sensitive adhesive. ϵ -decalactone (DL, castor oil) and lactide were also copolymerized and utilized in a pressure-sensitive

Table 29.1 Lap shear strength of various protein-containing adhesives for wood and metal adhesion [33].

Material	Class	Performed under optimized BSA conditions		Performed under optimized soy conditions	
		Aluminum adhesion (MPa)	Wood adhesion (MPa)	Aluminum adhesion (MPa)	Wood adhesion (MPa)
NW139C	Protein	0*	0*	0*	0*
Superset	Protein	0.1 ± 0.2*	0.2 ± 0.1*	0*	0.2 ± 0.1*
CM261C	Protein	0.2 ± 0.1*	0.6 ± 0.2*	0*	0.6 ± 0.2*
Prolia	Protein	1.1 ± 0.3*	1.9 ± 0.7*	0.5 ± 0.2*	0*
Sealmaster P30L	Polysaccharide	0.3 ± 0.4*	2 ± 1*	0.4 ± 0.1*	4 ± 1*
AP240	Polysaccharide	0.2 ± 0.2*	3 ± 2	0.2 ± 0.1*	1.7 ± 0.6
Gorilla Glue	Synthetic	3 ± 1	2.8 ± 0.3*	2 ± 1	1.4 ± 0.8
BSA	Protein	2.8 ± 0.7	4.0 ± 0.5	N/A	N/A
Soy	Protein	N/A	N/A	1.5 ± 0.2	2.0 ± 0.3

Deviations represent 90% confidence intervals, and asterisks identify data sets that were statistically ($P \leq .05$) different from the Maillard protein adhesives.

Reprinted with permission from J.K. Román, J.J. Wilker, Cooking chemistry transforms proteins into high-strength adhesives, *J. Am. Chem. Soc.* 141(3) (2019) 1359–1365, Copyright (2019) American Chemical Society.

adhesive [35]. It is known that high T_g and low T_g segments are needed to produce high-performance pressure-sensitive adhesives. In a study conducted by Chen et al., bio-derived poly(ϵ -decalactone) (PDL) was selected due to its low T_g , $\sim -50^\circ\text{C}$.

In comparison, bio-derived high T_g polyesters are less available. Based on the monomers used to produce a rigid and high T_g polyester (TCAs), Table 29.2 shows that different amounts of renewable content can be achieved. Using ϵ -decalactone, bio-based limonene oxide, and an anhydride, ABA block copolymers were prepared; their composition and properties are listed in Table 29.3.

These adhesives perform well compared to commercial petrochemical-based PSAs. The impact of chemical composition on the adhesion strengths has also been studied.

In summary, bio-derived materials are promising for creating low carbon footprint adhesives. Many biopolymers can be incorporated into adhesives to increase the bio-derived content. Biopolymers such as polysaccharides and proteins can be used as the major component to react with crosslinkers to form the adhesives. Additionally, biorefineries can provide a set of feedstock chemicals to create structural adhesives based on chemistries such as traditional epoxy, urethane, and acrylic adhesive chemistries. The monomers produced from biorefineries are different from those of petroleum-based monomers. Therefore, efforts are needed to improve the performance of adhesives prepared using bio-derived materials.

Table 29.2 Theoretical renewable content of polyesters from different epoxides/anhydrides (percentage values based on mass content of monomers).

anhydride/epoxide	PA	TCA 1	TCA 2	TCA 3	TCA 4
PD	0%	47%	0%	45%	81%
CHO	0%	41%	0%	39%	72%
LO	51%	75%	46%	77%	100%

Orange (potentially renewable) and green (fully renewable).

Modified use under creative commonCC BY4.0; T. T. D. Chen, L.P. Carrodeguas, G.S. Sulley, G.L. Gregory, C.K. Williams, Bio-based and degradable block polyester pressure-sensitive adhesives, *Angew. Chem. Int. Ed.* 59(52) (2020) 23450–23455.

29.4 Smart adhesives for recyclability: Reversible adhesion and adhesion on demand

Structural adhesives are commonly used to join dissimilar materials such as metals, inorganic, plastics, or rubbers to provide structural integrity in automotive, aerospace, military, biomedical, packaging, power production, and storage applications. Ideally, the adhesives will be "smart" and will debond at the end of their service life. Consequently, reversible adhesives have recently attracted significant attention, with some commercial products being available [36]. Two basic mechanisms are applied to debond adhesives with an external stimulus: cohesive failure by decreasing the adhesive mechanical strength via depolymerization, dissociation, or melting; and/or adhesive failure by reducing bonding between the adhesive and the substrate.

The choice of stimulus for debonding is a key consideration for the application and required lifetime of the adhesives. Stimuli may be physical or chemical but should allow debonding within a practical timeframe and without damaging the substrates. Another requirement for the stimulus is the low likelihood of exposure to the stimulus during product service to prevent premature failure. High temperatures and ultraviolet (UV) radiation are the most common debonding stimuli. Other debonding stimuli, including electric, magnetic, ultrasonic, or chemical treatments, are also reported and will be briefly reviewed.

Table 29.3 Various ABA block copolyesters and their composition and glass transition temperature.

Sample	TCA used	$M_{n,NMR}$ (kg mol ⁻¹)			Wt % _{Hard}	$M_{n,SEC}$ (kg mol ⁻¹) [Đ]		T_g (°C)	Renewable content (%)
		PDL	PE	Triblock		PDL	Triblock		
P1	TCA 1	29	7.7	37	21	34.3 [1.09]	39.1 [1.08]	-44, 72	95
P2	TCA 1	25	10.8	36	30	31.8 [1.09]	40.2 [1.07]	-40, 70	93
P3	TCA 1	23	15.5	37.9	41	28.8 [1.09]	40.9 [1.07]	-31, 79	90
P4	TCA 1	18	17	34.7	49	26.2 [1.08]	34.7 [1.06]	-21, 103	88
P5	TCA 2	24	16.5	40.4	41	34.3 [1.08]	45.3 [1.05]	-34, 79	78
P6	TCA 3	22	15.2	36.9	41	28.0 [1.07]	38.2 [1.05]	-31, 81	91
P7	TCA 4	22	14.4	36.2	40	27.7 [1.08]	38.1 [1.10]	-30, 70	100

PDL, poly (ϵ -decalactone); *PE*, a hard segment from reacting of TCA with LO.

Modified use under creative commonCC BY4.0; T. T. D. Chen, L.P. Carrodegua, G.S. Sulley, G.L. Gregory, C.K. Williams, Bio-based and degradable block polyester pressure-sensitive adhesives, *Angew. Chem. Int. Ed.* 59(52) (2020) 23450–23455.

This section reviews general strategies through polymer modification and additive approaches to achieve "adhesion on demand," enabling debondable adhesive systems. The technologies have been organized by the debonding trigger such as thermal, UV irradiation, chemical, etc. In terms of polymer chemistries, the primary focus is on epoxy and polyurethane systems, as structural adhesives are dominated by crosslinked epoxy and polyurethane chemistries. There is also a brief discussion on reversible adhesive systems found in nature.

29.4.1 Thermally debondable adhesives

Thermal treatment is the most widely studied approach for debondable adhesives. Although all polymeric adhesives can be thermally debonded through melting or decomposition, many strong structural adhesives are thermosets and decompose at extreme temperatures. Therefore, the main approaches for thermal debonding within a realistic temperature range are either to modify the polymer structures or to introduce thermally cleavable bonds. The substrates for thermal debonding should have some thermal conductivity and be stable up to the debonding temperature. Debonding on demand can be achieved by reducing the mechanical strength of the bulk adhesive by thermally degrading covalent bonds [37] or physical crosslinking such as hydrogen bonding [38].

29.4.1.1 Chemical modification with debonding features

Grafting or copolymerizing thermally responsive functional groups can chemically modify conventional adhesives. These functional groups can undergo thermal cleavage of the covalent bonds to decrease the polymers' crosslink density and/or molecular weight. A wide range of chemistries including carbamate [39], carbonate [40], acetal-ester [41], ester [42], poly peroxide [43], azo, and 2-ureido 4-pyrimidinone (UPy) motifs have been explored. Other strategies for thermal debonding include changes in miscibility, glass, and melting transitions.

Thermal labile bonds such as urethanes form from the reaction of an isocyanate with an active hydrogen compound such as acids, amine, or alcohol. At elevated temperatures, the urethane bonds reverse, regenerating free isocyanates and releasing carbon dioxide, leading to a polyurethane adhesive's loss of mechanical strength [44].

Luo et al. studied epoxy composites with polycaprolactone (PCL) [45]. The material is a miscible blend of PCL with diglycidyl ether of bisphenol-A/diaminodiphenylsulfone (DGEBA/DDS) epoxy. The cured material forms a "bricks and mortar" morphology in which the epoxy is formed of highly interconnected spheres ("bricks") that interpenetrate into a continuous PCL matrix ("mortar"). When heated above 60°C, the PCL liquefies and migrates to the interface, acting as a hot-melt adhesive with high adhesive strength on cooling. In addition, the PCL layer at the interface melts on reheating, allowing easy debonding. Commercially, this technology has been utilized by the Nitta corporation with the Landec Intelimer, a technology for electronic component manufacturing.

Cyclo-reversion reactions are also used for thermally induced debonding on demand. The Diels-Alder [4 + 2] reaction is the most common, as shown in Fig. 29.10. The Diels-Alder reaction forms a covalently crosslinked network that

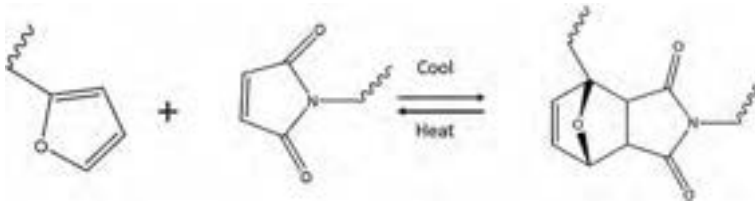


Fig. 29.10 Diels-Alder [4 + 2] reactions employed in debonding on demand.

breaks at elevated temperatures. As a result, the adhesive exhibits useful adhesive and mechanical properties at use conditions below the debonding temperature. This method of reversible bonding allows for optimal positioning at elevated temperatures. Upon cooling, the covalent crosslinks form again and the properties are restored [46].

Diels-Alder moieties can be incorporated into a wide range of polymers, including epoxies [47], urethanes [48], and polycarbonates, where the choice of crosslinkers and binders allows tuning of adhesive properties and debonding temperatures. For this approach, the compatibility of the diene/dieneophile with the polymer backbone must be considered to avoid unwanted side reactions and degradation.

Luo et al. synthesized epoxide-containing polymers with pendant thermally labile oxonorborene by radical polymerization [47]. The polymers can be crosslinked with a diamine and decrosslinked by thermal treatment at 160°C, which induces a retro Diels-Alder reaction to cleave pendant groups from the polymer backbone. This network degradation is irreversible upon heating.

29.4.1.2 Reversible adhesion: Dynamic covalent networks and vitrimers

Vitrimers are a class of materials formed through an associative mechanism [49]. Various dynamic networks such as transesterification, disulfide bond exchange, thiol-Michael exchange, transamination, trans-carbamoylation, imine exchange, trans-alkylation, and olefin dioxaborolane (boronic ester) exchange or silyl ether metathesis have been investigated for debondable adhesives [50].

Reversible adhesives using dynamic covalent bonds and vitrimers are recent developments in debondable adhesives. The covalent exchange is slow at the use temperature with the bonds having good mechanical strength and adhesion. Once triggered by heat, there is a rapid exchange of the covalent bonds, allowing debonding and reprocessing.

Among these methods, one approach is to incorporate trans-esterifiable functionality into an epoxy resin [51]. The choice of hardener, catalyst, epoxy prepolymer, and stoichiometry allows tuning of the adhesive and its mechanical properties. At ambient temperature, these resins act as elastomers/adhesives with a tensile strength of around 5 MPa. The material is debonded at elevated temperatures or in the presence of a catalyst such as $\text{Zn}(\text{acac})_2$.

Another commonly exploited debonding method is through disulfide bond exchange based on various networks, including epoxy resins. This was demonstrated

by Rowan and coworkers, who added cellulose nanocrystals to a di-sulfide-based adhesive, achieving lap shear strengths of 23 MPa for bonding to metals and up to 50 MPa with other substrates such as glass [52].

There is enormous potential for biologically derived materials and waste products in vitrimer and dynamic bond adhesives. Various natural products, including vegetable oils, rosin, and natural rubber, can be used beyond the current commercial adhesives [53], although there are some significant weaknesses for these vitrimers, such as lower strength and greater creep deformation. However, this is an emerging field with considerable potential for debondable adhesives.

29.4.1.3 Additive approaches

Another strategy for enabling debonding in adhesives is to add thermally activated additives that cause a reduction in modulus and adhesion at the adhesive-substrate interface. Approaches include incorporation of expandable microparticles such as chemical/physical foaming agents into commercial adhesive formulations [54], decomposable and evaporable organic additives [55], shape memory additives [56], and amphiphilic or crystalline nanoparticles [57].

Foaming agents can be applied to a wide range of commercial adhesives such as epoxies, urethanes, acrylates, and silicone matrixes. These foaming agents are nano-scale additives of carboxylic acids, azodicarbonamides, and nanocapsules of methylcyclohexane. Under microwave radiation or elevated temperatures, these additives expand, leading to debonding on demand within a few minutes. For example, Harris and coworkers incorporated cellulose nanocrystals into an epoxy thermoset, increasing the shear strength by 30% and reducing the thermal degradation temperature to 220°C [58].

29.4.2 Photo-debondable adhesives

Another common approach to debonding is to incorporate photo-responsive moieties into traditional adhesives by physical blending or chemical structural modification, as recently reviewed by Hohl and Weder [59]. Most developments in this area include photoinduced overcuring, degradation, isomerization, and dimerization [46,60]. Photo-triggered debondable adhesives can allow for rapid on-demand debonding; however, the limitations are that the substrates must be transparent, and that the parts will not be exposed to the debonding wavelengths during the product use lifetime.

29.4.2.1 Chemical modification for photo-debonding

Photoinduced overcuring

Photo-induced overcuring utilizes UV to increase the interfacial stress concentration through polymerization-induced shrinkage and to reduce tackiness through overcrosslinking, causing debonding at the adhesive-substrate interface. The major approaches are photo-initiated ring-opening or radical polymerization [61]. Bennett and Hittner reported that overcuring caused a reduction in adhesive strength when

oxirane ring-containing monomers were copolymerized into conventional pressure-sensitive adhesives. Various unsaturated multifunctional monomers or oligomers [62] including acrylates [63], itaconic acid [64], alcohols, thiols [65], and aziridines [66] have been shown to debond under UV radiation. Photo initiators and curable monomers are added into commercial adhesives by simply blending or grafting/copolymerizing them into existing polymer backbones. A wide range of photo initiators including 1-hydroxycyclohexyl phenyl ketone, triaryl sulfonium salts, acyl phosphine oxide, and benzophenone were evaluated. Although physical blending reduces the synthetic complexity, the free photo initiator or monomers may migrate to the surface or interface and lose their debonding effectiveness during the adhesive use lifetime.

Copolymerization of the photo initiator into the polymer backbone reduces these issues and improves adhesive lifetime and debonding efficiency [67]. Various adhesives, including acrylates, epoxies, polyesters, and vinyl block copolymers, have had photo initiators incorporated within. The debonding efficiency and residue level can be tuned by controlling the ratios of crosslinker to photo initiator. The primary concern is to maintain the mechanical properties of the adhesive during its use lifetime.

29.4.2.2 Photodegradation of crosslinkages: Covalent and supramolecular

Another strategy for UV-induced debonding is to degrade the bulk adhesives either through photodegradable covalent bonds or photo-induced solid-to-liquid phase changes of supramolecules.

There are several classes of photodegradable covalent bonds such as ortho-nitro-benzyl-esters [68], aromatic acyl oximes [69], polyperoxides, and aliphatic azo moieties. The latter two classes are less common because they are susceptible to thermal degradation gradually at ambient temperature. Typical photo-induced dissociation mechanisms are shown in Fig. 29.11.

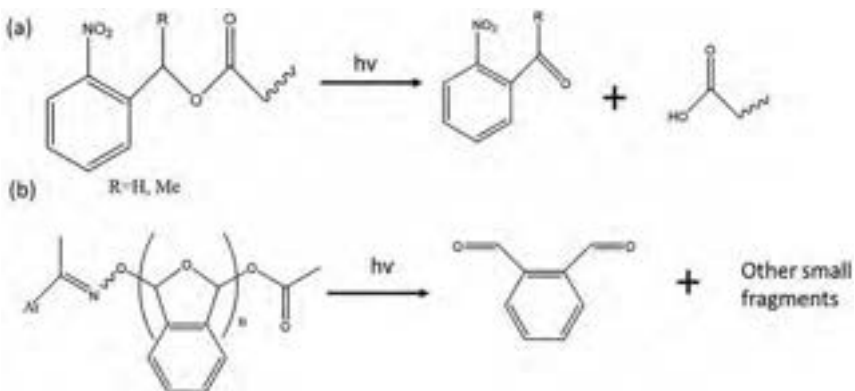


Fig. 29.11 Common photo-induced dissociation of (a) ortho-nitro-benzyl-esters, (b) aromatic acyl oximes.

UV radiation is also used to induce the degradation of noncovalent crosslinkages such as hydrogen bonding or metal-ion coordination. The 2-ureido 4-pyrimidinone (UPy) hydrogen bonding motif has been incorporated into a wide range of backbones such as polyacrylamides, polyvinyls, and polyureas to form polymers with excellent adhesive properties [70]. On UV irradiation, reversible dissociation of the hydrogen bonds occurs, converting the adhesive into a liquid and allowing debonding within minutes.

Supramolecular interactions such as metal-ligand motifs have also been utilized for UV-induced photo-dissociation and liquefaction. Gao et al. developed a poly (acrylic acid)-based adhesive with Fe(III)-carboxyl coordination complexes as crosslinkers [71]. Application of UV light reduced Fe(III) to Fe(II), triggering dissociation and a gel-sol transition allowing debonding on demand. Histidine-Ni(II) and catechol-Fe(III) complexes have also been utilized in debondable adhesives; however, these require additional photoacid generators and photoinitiators to enable debonding.

Photo-activated additives that can generate surfactants, photoacids, photobases, or radicals have been used for on-demand debonding of adhesives. For example, photoacid generators and photo radical initiators were used to degrade acid-sensitive crosslinkers such as esters, hemiacetals, carboxylates, and vinyl block copolymers [72]. The side chain of polymers such as poly(iso-butoxy-ethyl acrylate) or poly(isobornyl ester) can be photoacid cleaved and forms acrylic acid moieties.

Other technologies such as photo-induced isomerization and dimerization through the cycloaddition of 7-hydroxycoumarin derivatives, cinnamates, maleimides, and chitosan have also been reported for reversible bonding in epoxy, polyacrylate, and polyurethane adhesives [73].

29.4.3 Chemically triggered debondable adhesives

Chemical agents such as acids, bases, solvents, metal ions, and oxidizing or reducing agents can also serve as triggers to debond adhesives [74]. One issue with this approach is the accessibility of the adhesive to the debonding agent and the rate of chemical debonding in complex adhered structures.

Babra et al. developed a debondable polyurethane adhesive with good adhesion to metal, wood, plastic, and glass substrates. This adhesive contains a silyl protected phenol unit and undergoes fast degradation by fluoride such as from tetra-*n*-butylammonium fluoride [75].

Epoxy is a strong adhesive for glass and metal and is stable under various chemical and thermal conditions. Diacyl hydrazine moieties inserted in an epoxy resin can be oxidatively degraded by sodium hypochlorite into carboxylic acids and nitrogen gas, leading to a drop in polymer molecular weight, allowing debonding on demand [76].

29.4.4 Other triggered debondable adhesives (magnetically, electrically, and ultrasonically)

An oscillating magnetic field can be used to trigger debonding via heating of incorporated magnetic nanoparticles such as iron oxide (Fe_3O_4)-containing adhesives [77]. The magnetic stimulation generates local heat, which melts the adhesive or activates other debonding mechanisms such as crosslink degradation or blowing agent activation. The debonding time is highly dependent on the loading of Fe_3O_4 and can be tuned further by the addition of other nanoparticles such as graphene.

One niche debonding mechanism for conductive metal substrates is the application of a low voltage (10–50 V) to cause electrical debonding [78]. These adhesives contain inorganic or organic salt additives, often in the form of ionic liquids. When voltage is applied, the ions migrate to a metal-substrate interface, affecting the interfacial interaction and enabling debonding.

Ultrasound has also been used as a stimulus for adhesive debonding. Tachi and Suyama reported an acid-generating microcapsule, which was activated using 28 kHz ultrasonic irradiation for 20 min at 80°C [79]. When incorporated into a polyurethane system, the pressure-sensitive adhesive underwent debonding on demand via acid-catalyzed degradation.

29.5 Self-healing adhesives

Self-healing adhesives are a class of smart materials that contains self-healing material to retain adhesion after damage-repair cycles, enabling lifetime extension. Self-healing materials can be classified as autonomic or nonautonomic healing: autonomic healing requires no external intervention while nonautonomic healing requires an additional external stimulus such as heat or UV radiation.

For an autonomic healing adhesive, reactive repairing agents are typically incorporated into the polymer matrix in microcapsules. Nonautonomic healing typically involves intrinsic self-healing mechanisms that require external triggers such as heat or light to recover properties after damage. These intrinsic self-healing polymers rely on: (1) supramolecular interactions such as metal-ligand coordination, hydrogen bonding, and π - π stacking interaction [80], or (2) reversible dynamic covalent bonds using reversible Diels-Alder reactions, disulfide bonds, hindered urea bonds, boronic ester bonds, and so forth [49,81]. The intrinsic self-healing approaches provide the advantage of multicycle recoverability.

Recently, a series of autonomously intrinsic self-healable, high-adhesion elastomers (ASHA elastomers) healable through hydrogen bond interactions and molecular dynamics of a self-healable polymer poly (BCOE) have been reported [82].

29.5.1 Autonomic self-healing: Microcapsules or microvascular/fiber network systems

Thermoset epoxy adhesives with superior mechanical and adhesion properties have been widely used as structural adhesives in bonding dissimilar materials. However, the highly crosslinked epoxy is known to be brittle, and once a crack is initiated, it

is difficult to inhibit its propagation, leading to catastrophic failure. There is a substantial need to arrest the crack growth and enable self-repair once a crack occurs.

In 2001, White and coworkers developed an autonomically self-healing epoxy-based material by incorporating a microencapsulated healing agent (or monomer) and a chemical trigger (typically a catalyst or initiator) within an epoxy matrix [83]. The healing agents were microencapsulated low molecular weight monomers such as dicyclopentadiene (DCPD) with a solid phase chemical catalyst bis(tricyclohexylphosphine) benzylidene ruthenium (IV) dichloride (first-generation Grubbs' catalyst). The scanning electron microscope images of Grubbs' first-generation catalyst and DCPD-filled microcapsules are shown in Fig. 29.12. The propagating crack ruptures the microcapsules, releasing the healing agent and initiating the polymerization by contacting catalysts to block the crack propagation and restore the structural integrity. The ring-opening polymerization of DCPD with the first-generation Grubbs' catalyst is illustrated in Fig. 29.13.

Since then, considerable progress has been made. Single- and dual-capsule systems, new healing agents and catalyst systems, and fundamentals on diffusion, reaction kinetics, and morphology have been developed [84].

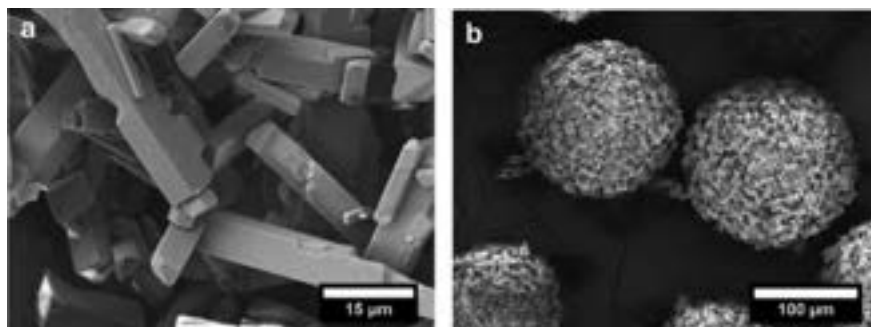


Fig. 29.12 Scanning electron microscope images of (a) as-received Grubbs' first-generation catalyst, (b) DCPD-filled microcapsules with poly(urea-formaldehyde) shell wall [84]. Reprinted with permission from H. Jin, G.F.M. Miller, N.R. Sottos, S.R. White, Fracture and fatigue response of a self-healing epoxy adhesive, *Polymer* 52(7) (2011) 1628–1634.

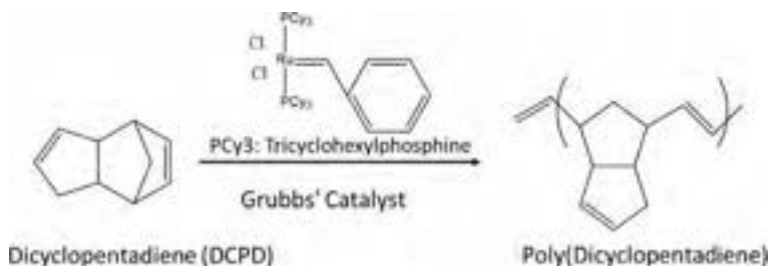


Fig. 29.13 Ring-opening polymerization of dicyclopentadiene (DCPD) with first-generation Grubbs' catalyst.

Ghazali et al. incorporated dual-capsule self-healing microcapsules into a standard epoxy adhesive to improve its mechanical and self-healing properties [85]. The resulting self-healing adhesive demonstrated recovery of both cohesion and adhesion properties under room temperature healing, achieving about 80% of its baseline Mode I fracture toughness (G_{IC}) by tapered double cantilever beam (TDCB) testing. Khoei and Kachoei also reported a self-healing epoxy adhesive that healed at room temperature using reactive amine nanocontainers [86]. However, a significant limitation to microencapsulation-based self-healing systems is that rupture of a microcapsule depletes the healing agent. Self-healing using this approach has limits on the number of times that damage to the same region can be healed.

29.5.2 Autonomic intrinsic self-healing (reversible dynamic bonds)

Autonomic intrinsic self-healing occurs through reestablishing physical crosslinking, including hydrogen bonding, ionic pairing, and/or metal-ligand interactions.

Zhang et al. reported supramolecular elastomers possessing excellent mechanical, reusable adhesion, and rapid self-healing properties [87]. They developed a polyamide-urea elastomer with metal-ligand and hydrogen bonds forming synergetic double dynamic bonds. At room temperature, this physical crosslinking endows the polyamide-urea elastomer with stretchability and rapid self-healing ability. For example, a representative polyamide-urea elastomer, DPPy1-Fe2, can fully restore its elastic modulus within 5 min at room temperature, and the elongation also reaches 3000% after 30 min of healing. Additionally, the unique dynamic bonds of the supramolecules enable them to adhere to different surfaces repeatedly. The shear strength of DPPy1-Fe2 is restored to an appreciable 80% after the first detachment-reattachment cycle, with excellent adhesive strength after multiple cycles.

Zhang et al. reported another type of autonomously intrinsic ASHA elastomers [82a,b]. The obtained elastomers exhibited high mechanical properties with elongation at break up to 2100% and toughness of 1.73 mJ m^{-3} . The damaged ASHA elastomers can be recovered under ambient conditions, without the need for external stimuli or encapsulated chemicals. These materials contain poly(2-[(butylamino)carbonyl]oxy ethyl acrylate) (poly(BCOE)) and curable elastomer (C-elastomer) as depicted in Fig. 29.14 [82a]. The C-elastomers, including silicone or polyurethane-based elastomer precursors, can be moisture-triggered to crosslink to high-toughness and high-adhesion materials. The elastomeric properties can be tuned by varying the poly(BCOE) to C-elastomer ratios. The self-healing process is illustrated in Fig. 29.15. The authors claim the fabrication process is simple, efficient, and scalable. These high-toughness, autonomous, and self-healable materials may be applicable in sealants, adhesives, and elastic devices.

29.5.3 Nonautonomic healing-thermal or light trigger

External triggers such as heat or light are often used to initiate the healing process for nonautonomic self-healing systems. Most reversible debonding systems with external triggers, discussed previously, can be applied to nonautonomic self-

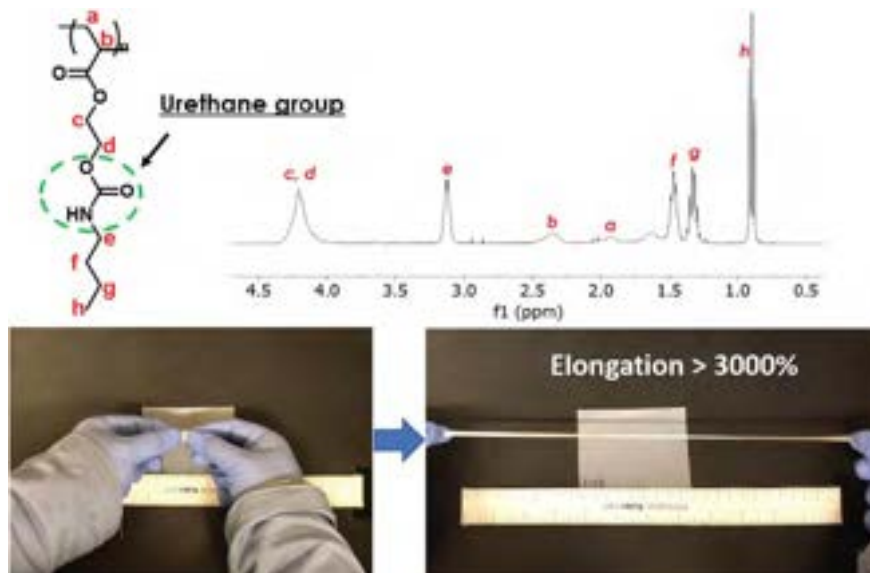


Fig. 29.14 The chemical structure, ¹H NMR, and elasticity demonstration of poly(BCOE)poly(2-[[[(butylamino)carbonyl]oxy]ethyl acrylate) [82a]. Reprinted with permission from Zhang, Z.; Ghezawi, N.; Li, B.; Ge, S.; Zhao, S.; Saito, T.; Hun, D.; Cao, P.-F., Autonomous Self-Healing Elastomers with Unprecedented Adhesion Force. *Adv. Funct. Mater.* 2021, 31(4), 2006298.

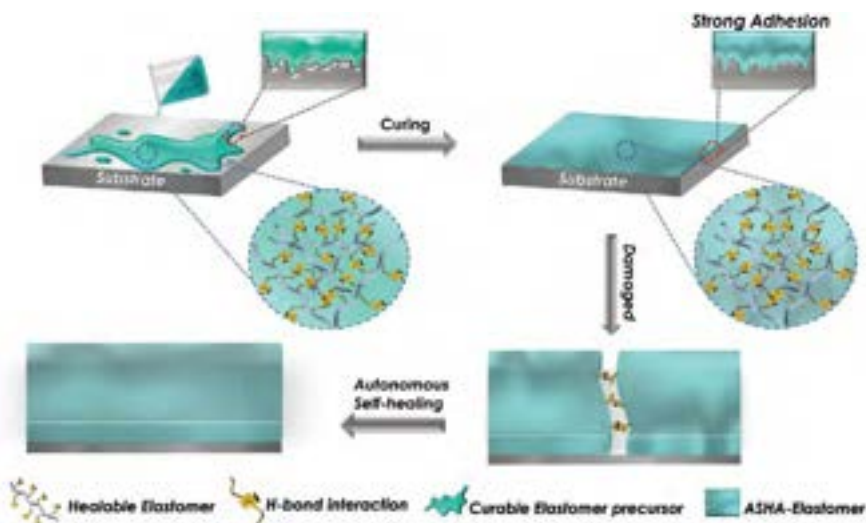


Fig. 29.15 Demonstration of the strong adhesion formation of the ASHA elastomer on an aluminum substrate and its self-healing process through hydrogen bond interactions and molecular dynamics of the self-healable polymer poly(2-[[[(butylamino)carbonyl]oxy]ethyl acrylate) [82a]. Reprinted with permission from Z. Zhang, N. Ghezawi, B. Li, S. Ge, S. Zhao, T. Saito, D. Hun, P.-F. Cao, Autonomous self-healing elastomers with unprecedented adhesion force, *Adv. Funct. Mater.* 31(4) (2021) 2006298.

healing adhesives if they meet adhesion performance requirements, healing efficiency, and the required healing time scale.

Tu et al. developed a self-healing polyurethane adhesive by adopting free radical polymerized hydroxyl-terminated polybutadiene (HTPB) as the soft segment and introducing aromatic disulfides into the polymer backbone [88]. The adhesive can achieve a self-healing efficiency up to 97% at 80°C, with an elongation at break of more than 700%.

Ahmadi and Ghanavati explored guanine as a hydrogen-bonding group to construct supramolecular polymeric systems based on poly (butyl methacrylate) [89]. The material was produced by a three-step reaction: a living radical copolymerization, deprotection of the functional comonomer, and grafting of the guanine group. A macroscopic scratch could be healed entirely at 40°C within 24 h, which is very promising for developing self-healing adhesives and coatings.

29.5.4 Renewable self-healing adhesives

Gong et al. reported self-healing adhesives with functional copolymers containing ethyl cellulose, fatty acid, vanillin, and an amine crosslinking agent through reversible addition-fragmentation chain transfer (RAFT) polymerization and Schiff base chemistry [90]. The presence of aldehyde groups from vanillin enables dynamic crosslinking, which can be reversed at 80°C. The shear strength could reach 0.81 MPa with a self-healing efficiency of 98.7%. Although the adhesive strength and self-healing efficiency need to be balanced for practical applications, this study demonstrated a self-healing adhesive from renewable ethyl cellulose.

Gao et al. also reported copolymers containing vanillin from lignin and fatty acid derivatives using diamines as crosslinkers [91]. The crosslinked lignin-based dynamic networks exhibited self-healing with 83.1% adhesion recovery after the first self-healing event. The damage and repair process could be carried out at least four times. This study has demonstrated the potential of lignin as a basis for high value-added materials such as adhesives.

29.6 Conclusions and outlook

Sustainability presents a difficult challenge and an exciting opportunity for research in the 21st century. Many technologies are being developed in parallel to address global warming, the scarcity of natural resources, and ecotoxicity. It is expected that new energy technology will shape the viability and significance of different sustainable solutions. Therefore, this is the time to be open minded and explore all viable solutions to reach a sustainable framework that satisfies technical, ecological, social, and economic requirements. Under this premise, adhesion is a critical area that needs innovation to support a sustainable future. The use of adhesives can be an impactful tool enabling substrate material recycling.

Commercial adhesives often rely on several petroleum-based chemistries such as epoxy, urethane, ester, and acrylate. These adhesives are typically not biodegradable,

and the production of these materials leads to carbon emissions. To address these shortcomings related to sustainability, different methods of making adhesives are needed. Nature usually uses a distinct set of backbones in its adhesives: polyamide (protein), polysaccharides, and hydrocarbons derived from them. Living organisms release bioadhesives to simultaneously use a suite of interactions: electrostatic, covalent, coordinative, hydrogen bonding, and hydrophobic interactions to adhere to surfaces. They also rely on higher-order structures to realize universal and strong adhesion in various environments. Although the characteristic self-assembly of bioadhesives is challenging to mimic, the strategy of enlisting multiple interactions can be considered. The use of the multiple functional groups on one type of backbone can be considered for improved adhesives. However, the presence of multiple functional groups in bioadhesives is made possible through the advanced catalysis of enzymes. We imagine new catalysts and methods to synthesize more sustainable adhesives will be required.

Biorefinery products and abundant biopolymers provide a new material platform for constructing adhesives. Different sets of chemicals can be produced through biorefining of abundant biomass, enabling the development of new materials to improve the sustainability of adhesives. These bio-derived feedstocks can be chemically transformed to take advantage of the adhesive chemistries mastered by material scientists. On the other hand, biopolymers can also be readily modified or used directly to construct adhesives. Lignin, starch, and protein have been demonstrated as adhesives, but more work is needed to meet the performance targets as commercial adhesives do.

Smart adhesives, including debondable and self-healing adhesives, are two paradigms that have the potential to improve sustainability by enabling recyclability and reducing waste. Debondable adhesives involve reversible adhesion by applying stimuli such as thermal, UV, or other triggers. By employing a trigger, the adhesion strength is often reduced to allow the delamination of the two substrates. This will enable the recycling of the two substrates separately and much more effectively.

A challenge for debondable adhesives is to control the debonding timeframe to allow for an economically viable recycle line. The major limiting factor for debonding time is the accessibility of the stimulus to the joint and to the adhesives. The challenge for self-healing adhesives is to develop both high strength and efficient self-healing properties, which may limit their applications. Future research should focus on designing and fabricating higher-performing reversible adhesive materials to make them more efficient and cost competitive.

Although much progress has been made, there are many obstacles to sustainable adhesive development. It requires a concerted effort to realize a new paradigm where adhesives can be made from renewable resources, are cost-competitive, and possess the best performance in applications. We expect rapid development in this area.

References

- [1] (a) K. Pathak, R. Malviya, *Introduction, theories and mechanisms of bioadhesion*, in: *Bioadhesives in Drug Delivery*, Wiley Global Headquarters, 2020, pp. 1–27.

- (b) R. Inamuddin, M.I. Boddula, A.M. Ahamed, Asiri, *Green Adhesives—Preparation, Properties and Applications*, John Wiley & Sons, 2020.
- (c) R.J. Narayan, 24.2.6 Bioadhesives, in: *ASM Handbook, Volume 23—Materials for Medical Devices*, ASM International, 2012.
- (d) M. Mishra, 8.1 Theories of bioadhesion, in: *Concise Encyclopedia of Biomedical Polymers and Polymeric Biomaterials*, vol. I–II, Taylor & Francis, 2012.
- (e) G. Perale, J. Hilborn, 2.5 Bioadhesives and medical glues, in: *Bioresorbable Polymers for Biomedical Applications—From Fundamentals to Translational Medicine*, Elsevier, 2017.
- [2] Amino Acid, F. W., *The Free Encyclopedia*. https://en.wikipedia.org/wiki/Amino_acid#:~:text=Amino%20acids%20are%20organic%20compounds,specific%20to%20each%20amino%20acid.&text=In%20the%20form%20of%20proteins,human%20muscles%20and%20other%20tissues.
- [3] D. Voigt, W. Konrad, S. Gorb, A universal glue: underwater adhesion of the secretion of the carnivorous flypaper plant *Roridula gorgonias*, *Interface Focus* 5 (1) (2015) 20140053.
- [4] V. Zheden, W. Klepal, S.N. Gorb, A. Kovalev, Mechanical properties of the cement of the stalked barnacle *Dosima fascicularis* (Cirripedia, Crustacea), *Interface Focus* 5 (1) (2015) 20140049.
- [5] (a) J.H. Waite, M.L. Tanzer, Polyphenolic substance of *Mytilus edulis*: novel adhesive containing L-dopa and hydroxyproline, *Science* 212 (4498) (1981) 1038–1040.
(b) Q. Lin, D. Gourdon, C. Sun, N. Holten-Andersen, T.H. Anderson, J.H. Waite, J.N. Israelachvili, Adhesion mechanisms of the mussel foot proteins mfp-1 and mfp-3, *Proc. Natl. Acad. Sci.* 104 (10) (2007) 3782–3786.
(c) L. Petrone, Molecular surface chemistry in marine bioadhesion, *Adv. Colloid Interf. Sci.* 195–196 (2013) 1–18.
- [6] X. Ou, B. Xue, Y. Lao, Y. Wutthinitikornkit, R. Tian, A. Zou, L. Yang, W. Wang, Y. Cao, J. Li, Structure and sequence features of mussel adhesive protein lead to its salt-tolerant adhesion ability, *Sci. Adv.* 6 (39) (2020) eabb7620.
- [7] T.H. Anderson, J. Yu, A. Estrada, M.U. Hammer, J.H. Waite, J.N. Israelachvili, The contribution of DOPA to substrate-peptide adhesion and internal cohesion of mussel-inspired synthetic peptide films, *Adv. Funct. Mater.* 20 (23) (2010) 4196–4205.
- [8] L. Petrone, A. Kumar, C.N. Sutanto, N.J. Patil, S. Kannan, A. Palaniappan, S. Amini, B. Zappone, C. Verma, A. Miserez, Mussel adhesion is dictated by time-regulated secretion and molecular conformation of mussel adhesive proteins, *Nat. Commun.* 6 (1) (2015) 8737.
- [9] (2011-06-10), N. T. P, Report on Carcinogens, fourteenth ed., 2016.
- [10] Bisphenol A (BPA): Use in Food Contact Application, 2021. <https://www.fda.gov/food/food-additives-petitions/bisphenol-bpa-use-food-contact-application>.
- [11] (a) S. Kumar, S. Krishnan, S. Mohanty, S.K. Nayak, Synthesis and characterization of petroleum and biobased epoxy resins: a review, *Polym. Int.* 67 (7) (2018) 815–839.
(b) A. Gomez-Lopez, S. Panchireddy, B. Grignard, I. Calvo, C. Jerome, C. Detrembleur, H. Sardon, Poly(hydroxyurethane) adhesives and coatings: state-of-the-art and future directions, *ACS Sustain. Chem. Eng.* 9 (29) (2021) 9541–9562.
- [12] (a) T. Werpy, G. Petersen, *Top Value Added Chemicals From Biomass*, vol. 1, US Department of Energy, 2005.
(b) F. Cherubini, The biorefinery concept: using biomass instead of oil for producing energy and chemicals, *Energy Convers. Manag.* 51 (7) (2010) 1412–1421.
- [13] (a) S. Kalami, M. Arefmanesh, E. Master, M. Nejad, Replacing 100% of phenol in phenolic adhesive formulations with lignin, *J. Appl. Polym. Sci.* 134 (30) (2017) 45124.

- (b) X. Gong, T. Liu, S. Yu, Y. Meng, J. Lu, Y. Cheng, H. Wang, The preparation and performance of a novel lignin-based adhesive without formaldehyde, *Ind. Crop. Prod.* 153 (2020) 112593.
- [14] J.R. Gouveia, G.E.S. Garcia, L.D. Antonino, L.B. Tavares, D.J. dos Santos, Epoxidation of kraft lignin as a tool for improving the mechanical properties of epoxy adhesive, *Molecules* 25 (11) (2020) 2513.
- [15] (a) M. Alinejad, C. Henry, S. Nikafshar, A. Gondaliya, S. Bagheri, N. Chen, S.K. Singh, D. B. Hodge, M. Nejad, Lignin-based polyurethanes: opportunities for bio-based foams, elastomers, coatings and adhesives, *Polymers* 11 (7) (2019) 1202.
(b) J. Lima García, G. Pans, C. Phanopoulos, Use of lignin in polyurethane-based structural wood adhesives, *J. Adhes.* 94 (10) (2018) 814–828.
(c) X. Ma, J. Chen, J. Zhu, N. Yan, Lignin-based polyurethane: recent advances and future perspectives, *Macromol. Rapid Commun.* 42 (3) (2021) 2000492.
- [16] B. Danielson, R. Simonson, Kraft lignin in phenol formaldehyde resin. Part 1. Partial replacement of phenol by kraft lignin in phenol formaldehyde adhesives for plywood, *J. Adhes. Sci. Technol.* 12 (9) (1998) 923–939.
- [17] C. Bonini, M. D’Auria, L. Emanuele, R. Ferri, R. Pucciariello, A.R. Sabia, Polyurethanes and polyesters from lignin, *J. Appl. Polym. Sci.* 98 (3) (2005) 1451–1456.
- [18] S. Wang, L. Shuai, B. Saha, D.G. Vlachos, T.H. Epps, From tree to tape: direct synthesis of pressure sensitive adhesives from depolymerized raw lignocellulosic biomass, *ACS Cent. Sci.* 4 (6) (2018) 701–708.
- [19] G. Pu, M.R. Dubay, J. Zhang, S.J. Severtson, C.J. Houtman, Polyacrylates with high biomass contents for pressure-sensitive adhesives prepared via mini-emulsion polymerization, *Ind. Eng. Chem. Res.* 51 (37) (2012) 12145–12149.
- [20] OECD, Biodegradation, 2001. <https://stats.oecd.org/glossary/detail.asp?ID=203>.
- [21] What Are Microplastics? 2015. <https://oceanservice.noaa.gov/facts/microplastics.html>.
- [22] Biopolymers. <https://www.nature.com/subjects/biopolymers>.
- [23] N. Masina, Y.E. Choonara, P. Kumar, L.C. du Toit, M. Govender, S. Indermun, V. Pillay, A review of the chemical modification techniques of starch, *Carbohydr. Polym.* 157 (2017) 1226–1236.
- [24] N. Shah, R.K. Mewada, T. Mehta, Crosslinking of starch and its effect on viscosity behaviour, *Rev. Chem. Eng.* 32 (2) (2016) 265–270.
- [25] N. Tratnik, P.-Y. Kuo, N.R. Tanguy, P. Gnanasekar, N. Yan, Biobased epoxidized starch wood adhesives: effect of amylopectin and amylose content on adhesion properties, *ACS Sustain. Chem. Eng.* 8 (49) (2020) 17997–18005.
- [26] Z. Zhang, D.J. Macquarrie, J.H. Clark, A.S. Matharu, Chemical modification of starch and the application of expanded starch and its esters in hot melt adhesive, *RSC Adv.* 4 (79) (2014) 41947–41955.
- [27] D. Araújo, V.D. Alves, J. Campos, I. Coelho, C. Sevrin, C. Grandfils, F. Freitas, M.A.M. Reis, Assessment of the adhesive properties of the bacterial polysaccharide FucoPol, *Int. J. Biol. Macromol.* 92 (2016) 383–389.
- [28] J. Zhou, T. Xu, X. Wang, C. Liu, X. Liao, X. Huang, B. Shi, A low-cost and water resistant biomass adhesive derived from the hydrolysate of leather waste, *RSC Adv.* 7 (7) (2017) 4024–4029.
- [29] (a) K. Li, X. Geng, J. Simonsen, J. Karchesy, Novel wood adhesives from condensed tannins and polyethylenimine, *Int. J. Adhes. Adhes.* 24 (4) (2004) 327–333.
(b) N.S. Hettiarachchy, U. Kalapathy, D.J. Myers, Alkali-modified soy protein with improved adhesive and hydrophobic properties, *J. Am. Oil Chem. Soc.* 72 (12) (1995) 1461–1464.

- [30] (a) S. Chen, Y. Chen, Z. Wang, H. Chen, D. Fan, Renewable bio-based adhesive fabricated from a novel biopolymer and soy protein, *RSC Adv.* 11 (19) (2021) 11724–11731.
(b) C. Yuan, M. Chen, J. Luo, X. Li, Q. Gao, J. Li, A novel water-based process produces eco-friendly bio-adhesive made from green cross-linked soybean soluble polysaccharide and soy protein, *Carbohydr. Polym.* 169 (2017) 417–425.
- [31] H. Pang, C. Ma, Y. Shen, Y. Sun, J. Li, S. Zhang, L. Cai, Z. Huang, Novel bionic soy protein-based adhesive with excellent prepressing adhesion, flame retardancy, and mildew resistance, *ACS Appl. Mater. Interfaces* 13 (32) (2021) 38732–38744.
- [32] Clear Gorilla Glue, Product Safety Datasheet, 2015.
- [33] J.K. Román, J.J. Wilker, Cooking chemistry transforms proteins into high-strength adhesives, *J. Am. Chem. Soc.* 141 (3) (2019) 1359–1365.
- [34] J. Shin, M.T. Martello, M. Shrestha, J.E. Wissinger, W.B. Tolman, M.A. Hillmyer, Pressure-sensitive adhesives from renewable triblock copolymers, *Macromolecules* 44 (1) (2011) 87–94.
- [35] H.M. Siebert, J.J. Wilker, Deriving commercial level adhesive performance from a bio-based mussel mimetic polymer, *ACS Sustain. Chem. Eng.* 7 (15) (2019) 13315–13323.
- [36] (a) D.J. Fortman, J.P. Brutman, G.X. De Hoe, R.L. Snyder, W.R. Dichtel, M.A. Hillmyer, Approaches to sustainable and continually recyclable cross-linked polymers, *ACS Sustain. Chem. Eng.* 6 (9) (2018) 11145–11159.
(b) M. Podgorski, B.D. Fairbanks, B.E. Kirkpatrick, M. McBride, A. Martinez, A. Dobson, N.J. Bongiardina, C.N. Bowman, Toward stimuli-responsive dynamic thermosets through continuous development and improvements in covalent adaptable networks (CANs), *Adv. Mater. (Weinheim, Ger.)* 32 (20) (2020) 1906876.
- [37] S. Ma, D.C. Webster, Degradable thermosets based on labile bonds or linkages: a review, *Prog. Polym. Sci.* 76 (2018) 65–110.
- [38] A.-C. Ferahian, D.K. Hohl, C. Weder, L. Montero de Espinosa, Bonding and debonding on demand with temperature and light responsive supramolecular polymers, *Macromol. Mater. Eng.* 304 (9) (2019) 1900161.
- [39] L. Wang, C.P. Wong, Syntheses and characterizations of thermally reworkable epoxy resins. Part I, *J. Polym. Sci., Part A: Polym. Chem.* 37 (15) (1999) 2991–3001.
- [40] L. Wang, H. Li, C.P. Wong, Syntheses and characterizations of thermally reworkable epoxy resins II, *J. Polym. Sci., Part A: Polym. Chem.* 38 (20) (2000) 3771–3782.
- [41] X. Zhang, G.-C. Chen, A. Collins, S. Jacobson, P. Morganelli, Y.L. Dar, O.M. Musa, Thermally degradable maleimides for reworkable adhesives, *J. Polym. Sci., Part A: Polym. Chem.* 47 (4) (2009) 1073–1084.
- [42] E. Themistou, A. Kanari, C.S. Patrickios, Thermolyzable polymer networks and star polymers containing a novel, compact, degradable acylal-based dimethacrylate crosslinker: synthesis, characterization, and thermolysis, *J. Polym. Sci., Part A: Polym. Chem.* 45 (24) (2007) 5811–5823.
- [43] E. Sato, M. Yuri, S. Fujii, T. Nishiyama, Y. Nakamura, H. Horibe, Liquid marble containing degradable polyperoxides for adhesion force-changeable pressure-sensitive adhesives, *RSC Adv.* 6 (61) (2016) 56475–56481.
- [44] (a) E. Delebecq, J.-P. Pascault, B. Boutevin, F. Ganachaud, On the versatility of urethane/urea bonds: reversibility, blocked isocyanate, and non-isocyanate polyurethane, *Chem. Rev. (Washington, DC, US)* 113 (1) (2013) 80–118.
(b) C. Gorsche, C. Schnoell, T. Koch, N. Moszner, R. Liska, Debonding on demand with highly cross-linked photopolymers: a combination of network regulation and thermally induced gas formation, *Macromolecules (Washington, DC, US)* 51 (3) (2018) 660–669.
- [45] X. Luo, K.E. Lauber, P.T. Mather, A thermally responsive, rigid, and reversible adhesive, *Polymer* 51 (5) (2010) 1169–1175.

- [46] N. Schuwer, R. Vendamme, Debondable adhesive systems, *RSC Green Chem. Ser.* 60 (2019) 310–338.
- [47] K. Luo, T. Xie, J. Rzyayev, Synthesis of thermally degradable epoxy adhesives, *J. Polym. Sci., Part A: Polym. Chem.* 51 (23) (2013) 4992–4997.
- [48] B.C. Mac Murray, T.H. Tong, R.D. Hreha, Reversible Thermoset Adhesive, US9260640, 2016.
- [49] N.J. Van Zee, R. Nicolay, Vitrimers: permanently crosslinked polymers with dynamic network topology, *Prog. Polym. Sci.* 104 (2020) 101233.
- [50] (a) E.E.L. Maassen, J.P.A. Heuts, R.P. Sijbesma, Reversible crosslinking and fast stress relaxation in dynamic polymer networks via transalkylation using 1,4-diazabicyclo [2.2.2] octane, *Polym. Chem.* 12 (25) (2021) 3640–3649.
(b) Y. Yang, F.-S. Du, Z.-C. Li, Highly stretchable, self-healable, and adhesive polyurethane elastomers based on boronic ester bonds, *ACS Appl. Polym. Mater.* 2 (12) (2020) 5630–5640.
- [51] (a) T. Liu, B. Zhao, J. Zhang, Recent development of repairable, malleable and recyclable thermosetting polymers through dynamic transesterification, *Polymer* 194 (2020) 122392.
(b) S. Zhao, M.M. Abu-Omar, Catechol-mediated glycidylation toward epoxy vitrimers/polymers with tunable properties, *Macromolecules (Washington, DC, US)* 52 (10) (2019) 3646–3654.
- [52] E. Cudjoe, K.M. Herbert, S.J. Rowan, Strong, rebondable, dynamic cross-linked cellulose nanocrystal polymer nanocomposite adhesives, *ACS Appl. Mater. Interfaces* 10 (36) (2018) 30723–30731.
- [53] Y. Zhu, F. Gao, J. Zhong, L. Shen, Y. Lin, Renewable castor oil and DL-limonene derived fully bio-based vinylogous urethane vitrimers, *Eur. Polym. J.* 135 (2020) 109865.
- [54] J. Bonaldo, M.D. Banea, R.J.C. Carbas, L.F.M. Da Silva, S. De Barros, Functionally graded adhesive joints by using thermally expandable particles, *J. Adhes.* 95 (11) (2019) 995–1014.
- [55] (a) M. Bauer, A. Concord, E. Langkabel, H. Luinge, G. Wachinger, Adhesive Composition Comprising Expandable Particles Modified by Encapsulation for Detachable Adhesive Joints in Aircrafts, WO2010128042, 2010.
(b) B. Lee, I. Son, J.H. Kim, C. Kim, J.Y. Yoo, B.W. Ahn, J. Hwang, J. Lee, J.H. Lee, Polymeric nanocapsules containing methylcyclohexane for improving thermally induced debonding of thin adhesive films, *J. Appl. Polym. Sci.* 135 (31) (2018) 46586.
- [56] (a) H.-Y. Hwang, Debondable adhesives using shape memory fibers, *Funct. Compos. Struct.* 2 (1) (2020) 015003.
(b) J.D. Rule, R.E. Behling, N.A. Lee, L.M. Lebow, Debondable Adhesive Articles Including Shape Memory Polymers and Methods of Making and Using the Same, WO2013012973, 2013.
- [57] R.R. Burch, Temperature Switchable Adhesive Assemblies With Temperature Non-Switchable Tack, US20120021215, 2012.
- [58] J.-S. Kang, A.J. Myles, K.D. Harris, Thermally-degradable thermoset adhesive based on a cellulose nanocrystals/epoxy nanocomposite, *ACS Appl. Polym. Mater.* 2 (11) (2020) 4626–4631.
- [59] D.K. Hohl, C. Weder, (De)bonding on demand with optically switchable adhesives, *Adv. Opt. Mater.* 7 (16) (2019) 1900230.
- [60] S.M. June, T. Suga, W.H. Heath, Q. Lin, R. Puligadda, L. Yan, D. Dillard, T.E. Long, Photoactive polyesters containing o-nitro benzyl ester functionality for photodeactivatable adhesion, *J. Adhes.* 89 (7) (2013) 548–558.
- [61] R.E. Bennett, M.A. Hittner, Pressure-Sensitive Adhesive Susceptible to Ultraviolet Light-Induced Detackification, WO8100309, 1981.

- [62] H.-S. Do, J.-H. Park, H.-J. Kim, UV-curing behavior and adhesion performance of polymeric photoinitiators blended with hydrogenated rosin epoxy methacrylate for UV-crosslinkable acrylic pressure sensitive adhesives, *Eur. Polym. J.* 44 (11) (2008) 3871–3882.
- [63] (a) H.-H. Chu, C.-K. Wang, K.S. Chuang, C.-Y. Chang, Removable acrylic pressure-sensitive adhesives activated by UV-radiation, *J. Polym. Res.* 21 (6) (2014) 1–7.
(b) M. Tunius, *Switchable Adhesives*, US9040076, 2015.
- [64] N. Schuewer, R. Vendamme, *Debondable Adhesive Composition of Unsaturated Polyester*, EP2957611, 2015.
- [65] J.K. Kim, W.H. Kim, D.H. Lee, Adhesion properties of UV crosslinked polystyrene-block-polybutadiene-block-polystyrene copolymer and tackifier mixture, *Polymer* 43 (18) (2002) 5005–5010.
- [66] J. Han, Y. Zhou, G. Bai, W. Wei, X. Liu, X. Li, Preparation of photo-crosslinkable acrylic copolymer and its debonding property on silicon wafer, *J. Adhes. Sci. Technol.* 36 (4) (2022) 424–436.
- [67] Z. Czech, A. Kowalczyk, J. Kabatc, J. Swiderska, L. Shao, Y. Bai, Influence of selected photoinitiators type II on tack, peel adhesion, and shear strength of UV-crosslinked solvent-borne acrylic pressure-sensitive adhesives used for medical applications, *Polym. Bull. (Heidelberg, Ger.)* 68 (2) (2012) 441–452.
- [68] M. Kim, H. Chung, Photo-responsive bio-inspired adhesives: facile control of adhesion strength via a photocleavable crosslinker, *Polym. Chem.* 8 (40) (2017) 6300–6308.
- [69] H. Hayashi, H. Tachi, K. Suyama, Synthesis and photo-degradation of polyphthalaldehydes with oxime ether terminals, *J. Photopolym. Sci. Technol.* 33 (3) (2020) 269–278.
- [70] (a) C. Heinzmann, S. Coulibaly, A. Roulin, G.L. Fiore, C. Weder, Light-induced bonding and debonding with supramolecular adhesives, *ACS Appl. Mater. Interfaces* 6 (7) (2014) 4713–4719.
(b) C. Heinzmann, I. Lamparth, K. Rist, N. Moszner, G.L. Fiore, C. Weder, Supramolecular polymer networks made by solvent-free copolymerization of a liquid 2-ureido-4[1H]-pyrimidinone methacrylamide, *Macromolecules (Washington, DC, U. S.)* 48 (22) (2015) 8128–8136.
- [71] Y. Gao, K. Wu, Z. Suo, Photodetachable adhesion, *Adv. Mater. (Weinheim, Ger.)* 31 (6) (2019) 1806948.
- [72] (a) Y. Fukamoto, E. Sato, H. Okamura, H. Horibe, A. Matsumoto, Control of adhesive strength of acrylate polymers containing 1-isobutoxyethyl and isobornyl esters in response to dual stimuli for dismantlable adhesion, *Appl. Adhes. Sci.* 5 (1) (2017) 6/1.
(b) H. Sugita, K. Itou, Y. Itou, N. Wada, T.U. Shin-Ya Kurita, Y. Hirose, K. Hatase, H. Matsumoto, D. Ichinohe, Multi-acrylate-based UV-curable dismantlable adhesives, *Int. J. Adhes. Adhes.* 104 (2021) 102758.
- [73] (a) J. Ling, M.Z. Rong, M.Q. Zhang, Photo-stimulated self-healing polyurethane containing dihydroxyl coumarin derivatives, *Polymer* 53 (13) (2012) 2691–2698.
(b) Z. Liu, J. Cheng, J. Zhang, An efficiently reworkable thermosetting adhesive based on photoreversible [4+4] cycloaddition reaction of epoxy-based prepolymer with four anthracene end groups, *Macromol. Chem. Phys.* 222 (2) (2021) 2000298.
- [74] Z.C. Soulie, *Adhesive System, Device for Implementation and Method for Activation or Deactivation of Adhesion*, FR2834902, 2003.
- [75] T.S. Babra, M. Wood, J.S. Godleman, S. Salimi, C. Warriner, N. Bazin, C.R. Siviour, I.W. Hamley, W. Hayes, B.W. Greenland, Fluoride-responsive debond on demand adhesives: manipulating polymer crystallinity and hydrogen bonding to optimise adhesion strength at low bonding temperatures, *Eur. Polym. J.* 119 (2019) 260–271.

- [76] T. Oguri, A. Kawahara, N. Kihara, Epoxy resin bearing diacylhydrazine moiety as a degradable adhesive for traceless oxidative removal, *Polymer* 99 (2016) 83–89.
- [77] S. Salimi, T.S. Babra, G.S. Dines, S.W. Baskerville, W. Hayes, B.W. Greenland, Composite polyurethane adhesives that debond-on-demand by hysteresis heating in an oscillating magnetic field, *Eur. Polym. J.* 121 (2019) 109264.
- [78] R. Heucher, S. Kopannia, C. McArdle, M. Stuve, J. Kolbe, Electrically Conductive Polyamide Hot-Melt Adhesives, WO2013135677, 2013.
- [79] H. Tachi, K. Suyama, Development of pressure-sensitive adhesives degradable on ultrasonic irradiation, *J. Photopolym. Sci. Technol.* 30 (2) (2017) 253–257.
- [80] C.-H. Li, J.-L. Zuo, Self-healing polymers based on coordination bonds, *Adv. Mater. (Weinheim, Ger.)* 32 (27) (2020) 1903762.
- [81] P. Chakma, D. Konkolewicz, Dynamic covalent bonds in polymeric materials, *Angew. Chem. Int. Ed.* 58 (29) (2019) 9682–9695.
- [82] (a) Z. Zhang, N. Ghezawi, B. Li, S. Ge, S. Zhao, T. Saito, D. Hun, P.-F. Cao, Autonomous self-healing elastomers with unprecedented adhesion force, *Adv. Funct. Mater.* 31 (4) (2021) 2006298.
(b) Y. Zhuo, V. Haakonsen, Z. He, S. Xiao, J. He, Z. Zhang, Enhancing the mechanical durability of icephobic surfaces by introducing autonomous self-healing function, *ACS Appl. Mater. Interfaces* 10 (14) (2018) 11972–11978.
- [83] S.R. White, N.R. Sottos, P.H. Geubelle, J.S. Moore, M.R. Kessler, S.R. Sriram, E.N. Brown, S. Viswanathan, Autonomic healing of polymer composites, *Nature (London)* 409 (6822) (2001) 794–797.
- [84] H. Jin, G.M. Miller, N.R. Sottos, S.R. White, Fracture and fatigue response of a self-healing epoxy adhesive, *Polymer* 52 (7) (2011) 1628–1634.
- [85] H. Ghazali, A.N.F. Amir, L. Ye, S. Dullah, Fracture toughness of epoxy adhesive containing dual-capsules self-healing system, *AIP Conf. Proc.* 2339 (1) (2021) 020055.
- [86] S. Khoee, Z. Kachoei, Design and development of novel reactive amine nanocontainers for a self-healing epoxy adhesive: self-repairing investigation using the lap shear test, *RSC Adv.* 5 (27) (2015) 21023–21032.
- [87] L. Zhang, D. Wang, L. Xu, A. Zhang, A supramolecular polymer with ultra-stretchable, notch-insensitive, rapid self-healing and adhesive properties, *Polym. Chem.* 12 (5) (2021) 660–669.
- [88] J. Tu, H. Xu, L. Liang, P. Li, X. Guo, Preparation of high self-healing efficient crosslink HTPB adhesive for improving debonding of propellant interface, *New J. Chem.* 44 (44) (2020) 19184–19191.
- [89] M. Ahmadi, M. Ghanavati, Dynamics of self-healing supramolecular guanine-modified poly(*n*-butyl methacrylate-co-hydroxyethyl methacrylate) copolymers, *Polymer* 211 (2020) 123117.
- [90] X. Gong, Z. Cheng, S. Gao, D. Zhang, Y. Ma, J. Wang, C. Wang, F. Chu, Ethyl cellulose based self-healing adhesives synthesized via RAFT and aromatic schiff-base chemistry, *Carbohydr. Polym.* 250 (2020) 116846.
- [91] S. Gao, Z. Cheng, X. Zhou, Y. Liu, J. Wang, C. Wang, F. Chu, F. Xu, D. Zhang, Fabrication of lignin based renewable dynamic networks and its applications as self-healing, antifungal and conductive adhesives, *Chem. Eng. J. (Amsterdam, Neth.)* 394 (2020) 124896.

This page intentionally left blank

Accelerated curing of bonded joints

30

Morten Voß and Till Vallée

Fraunhofer Institute for Manufacturing Technology and Advanced Materials IFAM,
Adhesive Bonding Technology and Surfaces, Bremen, Germany

30.1 Introduction

30.1.1 Scope of this chapter

While faster manufacturing due to accelerated curing is certainly an advantage in many industrial sectors, it falls far short of the mark in light of the manifold possibilities offered by modern adhesive bonding technology. Without any claim to completeness, the following positive effects may result with fast curing:

- Exploitation of new application fields for adhesively bonded joints.
- Greater variety of design for bonding processes.
- Faster manufacturing processes and shorter cycle times leading to time and money savings.
- Superior adhesive properties such as T_g or bond strength (both adhesive as well as cohesive).
- Improved resistance to fatigue, moisture diffusion, and elevated application temperatures.
- Manufacturing independent of ambient temperatures.

The choice of a reliable method for accelerated curing is largely determined by the manufacturing process, component geometry, and the type of adhesive. Accelerated curing of adhesives has been extensively investigated by many researchers [1–4] and in 2016, Javadi et al. [5] gave an overview of different methods thereof. Many of the available options rely on heat generation within the polymer to be cured. As a result, molecular mobility is increased, and thus faster polymerization is achieved. During this process, the curing kinetics play a decisive role, as some adhesives react poorly to external or internal heat supply while others react well. To provide a better overview of the existing approaches, the most common methods are summarized in Fig. 30.1.

Although there is plenty of literature available on accelerated curing processes, there are no clear guidelines or standards for their implementation as for adhesive bonding in general [6]. For practitioners, this results in a relatively confusing situation, as process conditions to be considered during practical application are usually not properly worked out. In addition, some of the available techniques are much better studied than others: For ultraviolet (UV)-curing adhesives, several review articles can be found [7–9] whereas for induction [10], microwave [11], or resistive curing, fewer are available. Furthermore, these review articles often focus on accelerated manufacturing of FRP rather than on fast curing in general.

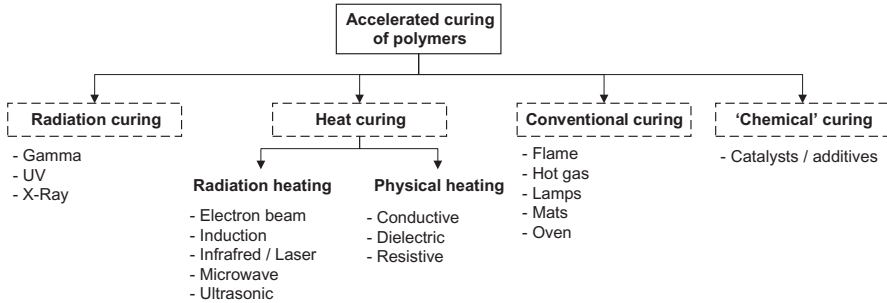


Fig. 30.1 Overview of existing approaches for accelerated curing of polymers.

This chapter uses experimental and numerical results on the accelerated curing of adhesives and adhesively bonded connections, using inductively heated Curie particles (CP), which are presented in a practitioner-friendly manner to highlight the complexity when accelerated curing is pursued. Induction heating is used as the most rapid and versatile heating technique, and CPs have been considered because of their property to generate heat up to their corresponding Curie temperature, if subjected to an electromagnetic field (EMF), but not beyond [12]. The combination of induction heating and CP is aimed at an accelerated curing process completely freed of the constraints of process control. Because of the complexity of the topic, and the various physical, chemical, and mechanical aspects involved, results are presented based upon a specific set of materials and joint geometries.

30.1.2 Induction heating

In essence, inductive heating represents a fast, noncontact method for accelerated curing [13]. Two main cases can be distinguished: metallic and nonmetallic adherends. In the first case, heat is generated by applying a high-frequency (HF) EMF, which leads to eddy currents within the metallic adherends such as steel or aluminum [14], that is then transmitted to the adhesive to be cured. Huang et al. [15] investigated the hybrid joining of an inductively heated aluminum sheet with different glass fiber-reinforced polymers (G-FRP) using an epoxy adhesive (see [Chapter 1](#) for details on this family of adhesives). They concluded that inductively joined specimens are superior in terms of tensile shear load and displacement when compared to specimens bonded at room temperature (RT). However, if metallic adherends are heated inductively, tight control of temperatures with external monitoring techniques (infrared (IR) camera, thermocouples, etc.) is always needed to prevent the joint from overheating, as for example in [16].

In the second case, when nonmetallic adherends are to be joined, research concentrates on using inductively heatable susceptors such as meshes [17], fibers [18], or particles [19] directly introduced into the adhesives to be cured. The use of metal meshes proved to be difficult due to handling limitations and the dependency on adhesive layer geometry. Additionally, it has not yet been clarified to what extent the state of stress inside the connection is negatively affected because some studies [17,20] observed a decrease in lap shear strength for specimens cured with mesh susceptors

in comparison to cold-cured references. The use of fiber- and wire-shaped steel susceptors for inductive curing of FRP was experimentally and numerically investigated by Mattheß et al. [21]. They concluded that fiber-shaped susceptors are more suitable for the curing process due to their superior heatability in comparison to the wire-shaped ones. However, because stainless steel was used as the susceptor material, the power of the induction device had to be adjusted continuously to prevent overheating.

30.1.3 Curie particles

The use of particulate susceptors for inductive curing has been studied by many researchers, such as [22–24]. However, many of the available studies considered particles such as zinc (Zn) [25], iron (Fe) [26], or magnetite (Fe_3O_4) [27]. All these materials can be heated significantly above the generally acceptable temperature range of 80–120°C for two-component (2K) adhesives, and 150–200°C for one-component (1K) adhesives. Therefore, overheating and the consequent irreversible damage of the adhesive cannot be prevented during the process. Some studies try to circumvent the problem by regulating the induction power with external monitoring techniques such as an IR camera [28] or thermocouples [29]. However, such monitoring results in additional costs, and may be too cumbersome for practical applicability. Furthermore, external temperature control is not possible for many components due to the inaccessibility of the adhesive layer.

To achieve simpler control of the heating process without external temperature monitoring, this study investigated accelerated curing with the help of Curie particles (CP). CPs are added to the adhesives and exposed to an HF EMF. During heating, no temperature monitoring is needed since the CP cannot, in principle, be heated above its Curie temperature (T_c), thus effectively protecting the adhesives from overheating. The feasibility of the process has already been demonstrated on small-scale glued-in rod (GiR) construction (also discussed in Chapter 25) in combination with a 1K-EPX [12,30]. These findings have since been extended by the authors to large-scale GiR specimens bonded with four commercially available 2K adhesives [31]. It was found that curing kinetics, and consequently the exothermic polymerization, contribute significantly to the adhesive heating behavior.

30.1.4 Curing kinetics and modeling

Kinetic modeling, that is, the determination of the relationship among the time, temperature, and level of cure of adhesives, has been extensively investigated in the past by many researchers [32–35] with a detailed overview given by Yousefi et al. in [36]; this is also discussed in Chapter 31. To understand the polymerization mechanisms, two main types of models can be distinguished in the literature: mechanistic [37] and phenomenological [38] models. Mechanistic models rely upon some presupposed model and reaction process, and derive curing kinetics ab initio. The latter can be performed at the molecular level [39] based upon mathematical models [40] or any other. They set a strong focus on qualitative understanding of the process rather than on a

precise quantification. Such an approach often requires detailed measurements of initial and intermediate reactant concentrations for validation, and are therefore more complex than phenomenological models. At the opposite side, phenomenological models focus on the quantitative description of metrics related to curing over time, without necessarily understanding them. For any phenomenological model, determination of the aforementioned metrics is at the center of attention for modeling adhesive curing; these can be derived by different techniques such as dielectric analysis (DEA), [41], IR spectroscopy [42], and differential scanning calorimetry (DSC) [43,44], among others [45].

During adhesive polymerization, existing reaction educts are converted into one or more reaction products. Within this process, the reaction rate $d\alpha/dt$ represents an essential parameter that describes the temporal change of the concentration of the reaction educts and products. Instead of individual reactant concentration changes, the conversion or curing degree α can be defined for the description of the curing progress. For α , the reaction speed v_r can be written as in Eq. (30.1); see Ref. [46].

$$v_r = \frac{d\alpha}{dt} \quad (30.1)$$

The determination of the reaction educt and product concentration is, however, difficult. Mostly for practical reasons, it is thus assumed that the released reaction heat during the polymerization correlates directly with the reaction progress. Therefore, the ratio between the heat $H(t)$ released up to any step t and the maximum releasable heat H_{Total} after complete curing ($\alpha = 1$) is posited to equal the curing degree α , which is expressed by Eq. (30.2).

$$\alpha(t) = \frac{H(t)}{H_{\text{Total}}} \quad (30.2)$$

The heat flow H can be determined directly in the DSC. Consequently, the measured curve for H can be used to determine the temporal progression of α by integrating Eq. (30.2). Likely the most classic example of a model used for the description of adhesive curing is the phenomenological model of Kamal and Sourour [47], which was used, for example, in Refs. [48–50]. This model represents an extension of a kinetic model developed by Horie et al. [51], who described an autocatalytic polymerization of primary amines with epoxy resin through hydroxyl groups. Kamal and Sourour generalized this model to Eq. (30.3); see Ref. [47].

$$\frac{d\alpha}{dt} = (k_1 + k_2\alpha^m) \cdot (1 - \alpha)^n \text{ with } k_{1,2}(T) = A_{1,2}e^{-\frac{E_{1,2}}{RT}} \quad (30.3)$$

Here, m and n represent the reaction orders, and the temperature-dependent parameters k_1 and k_2 follow an Arrhenius law. The parameter k_1 represents the initial reactivity of the resin for $\alpha = 0$ while k_2 takes into account the autocatalytic acceleration of the polymerization. Thus, in a purely autocatalytic behavior $k_1 = 0$ while for $k_2 = 0$, the reaction has n th-order kinetics. A detailed derivation of the Kamal and Sourour model

is given for example in Ref. [46] or [52], and shall not be discussed again in this chapter. Kamal and Sourour's model, along with many other kinetic models, is nowadays implemented in dedicated kinetic software. With the help of these programs, an evaluation of experimental data, such as dynamic or isothermal DSC data, can be carried out more easily.

30.2 Influence of accelerated curing on the adhesive

To evaluate the influence of accelerated curing with CPs on adhesives, an experimental campaign was carried out by Voß et al. [53,54]. The authors considered typical representatives of 2K epoxies (2K-EPX) and 2K polyurethanes (2K-PUR), and CPs exhibiting a Curie temperature of approximately 110°C.

30.2.1 Bulk properties

The curing behavior of the previously defined adhesives, without and with different CP content (10, 20, and 30 w/w-%) was investigated using a series of dynamic DSC measurements at constant heating rates of 2, 5, 10, 15, and 20 K/min [53]. The results of the kinetic characterization with CP at a heating rate of 10 K/min are presented and compared to the unfilled reference samples (see Fig. 30.2) the start, end, and peak of the polymerization occur at the same points in time for all adhesives. However, when increasing the CP content from 10 to 30 w/w-% for Fi390, DSC signals appear to be scaled down accordingly. This is also valid for the three remaining adhesives, as the DSC data for 30 w/w-% CP resembles a linearly scaled-down version of that of the unfilled reference. Accordingly, no catalytic effects were identified after adding the CP, which suggests that the polymerization was not altered at the chemical level, if compared to that of the unfilled adhesives.

Subsequently, an experimental program consisting of a room-temperature (RT, $23 \pm 2^\circ\text{C}$, 50% \pm 10% RH) oven as well as inductively cured dog-bone shaped AB and DMA specimens was done. To reveal the influence of the CP content, c_{particle} , on the adhesive characteristics, c_{particle} was increased in steps of 10 w/w-% in the range of 0–40 w/w-%. Fig. 30.3 shows the moduli of elasticity (MoE, top) and tensile strengths (TS, bottom) for the two adhesives. The blue bars indicate RT-cured series, whereas yellow and red bars stand for oven or inductively cured specimens, respectively. Globally, the results show that both MoE and TS are significantly dependent upon the CP content.

The DMA results are illustrated in Fig. 30.4, exemplarily for LP421. The data show that the mere addition of CP only influences the resulting stiffnesses (G' , G''), but not the magnitude of the glass transition temperature, T_g . Furthermore, the DMA shows that CP curing at elevated temperatures can result in a higher T_g , if compared to adhesives cured under common RT conditions (see Fig. 30.4b). A comparison of G' and G'' for inductively cured DMA samples showed clear differences, with a significantly lower T_g of 68.9 °C being measurable when testing is performed 0.5 h after inductive heating (see Fig. 30.4c dotted curves). In contrast, the tests of the inductively cured

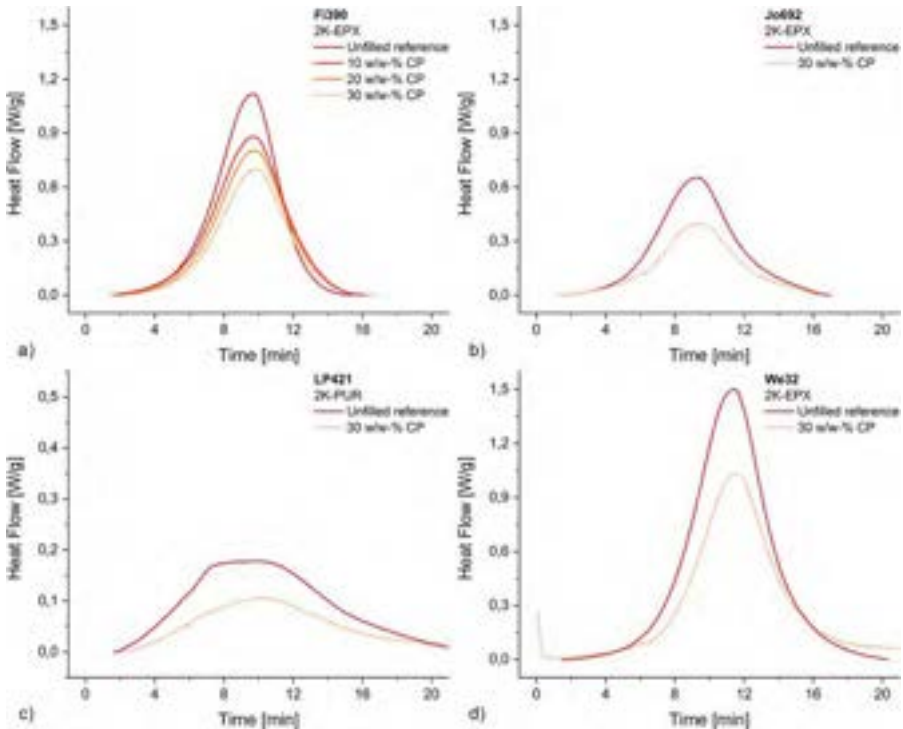


Fig. 30.2 Results of dynamic DSC measurements for the adhesives (a) Fi390, (b) Jo692, (c) LP421, and (d) We32 in dependency of CP content; temperature range 0–250°C, $dT/dt = 10\text{K/min}$.

specimens 10 days after inductive heating—a time lapse in which 2K curing at RT must have occurred—resulted in G' profiles and a T_g comparable to the unfilled reference. These results show that the adhesive was not fully cured at the end of the inductive heating phase, as shown by the mechanical tests carried out immediately (0.5 h) after the induction process. However, when inductively cured LP421 is left to cure at RT for a longer time span (10 days), the adhesive reaches a T_g similar to the RT-cured reference.

30.2.2 Lap shear strength

In a subsequent step [54], the influence of accelerated curing using CP on the second important metric for adhesives, lap shear strength, was investigated. Three different substrates were considered: aluminum, G-FRP, and wood. For wood and G-FRP, temperatures were not controlled, and the induction ran at full power; for aluminum, the time-temperature history was prescribed.

The mechanical results for all SLJ series produced with aluminum and G-FRP are shown in Fig. 30.5 with attained lap shear strengths, τ_u , being sorted by adherend

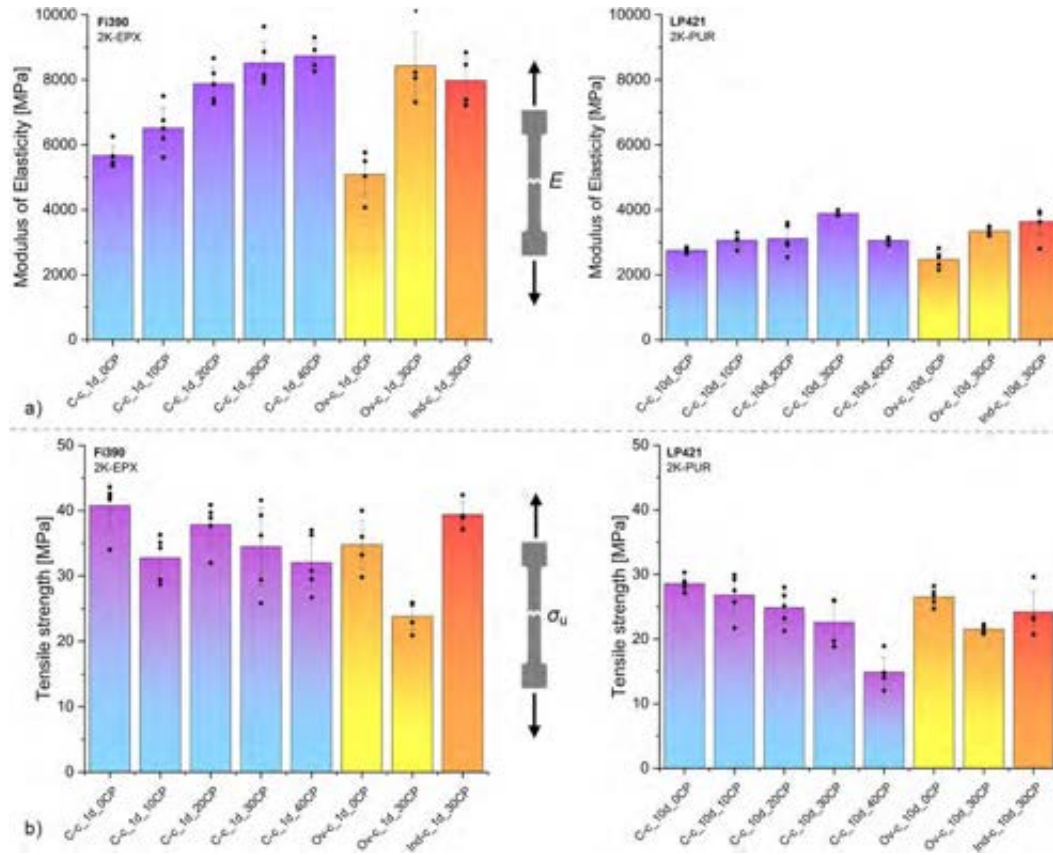


Fig. 30.3 Results of mechanical testing of AB specimens for the adhesives Fi390 (left) and LP421 (right) with (a) modulus of elasticity, E , and (b) tensile strength, σ_u ; Zwick|Roell UTM (50kN), $v=1$ mm/min, all tests performed at RT.

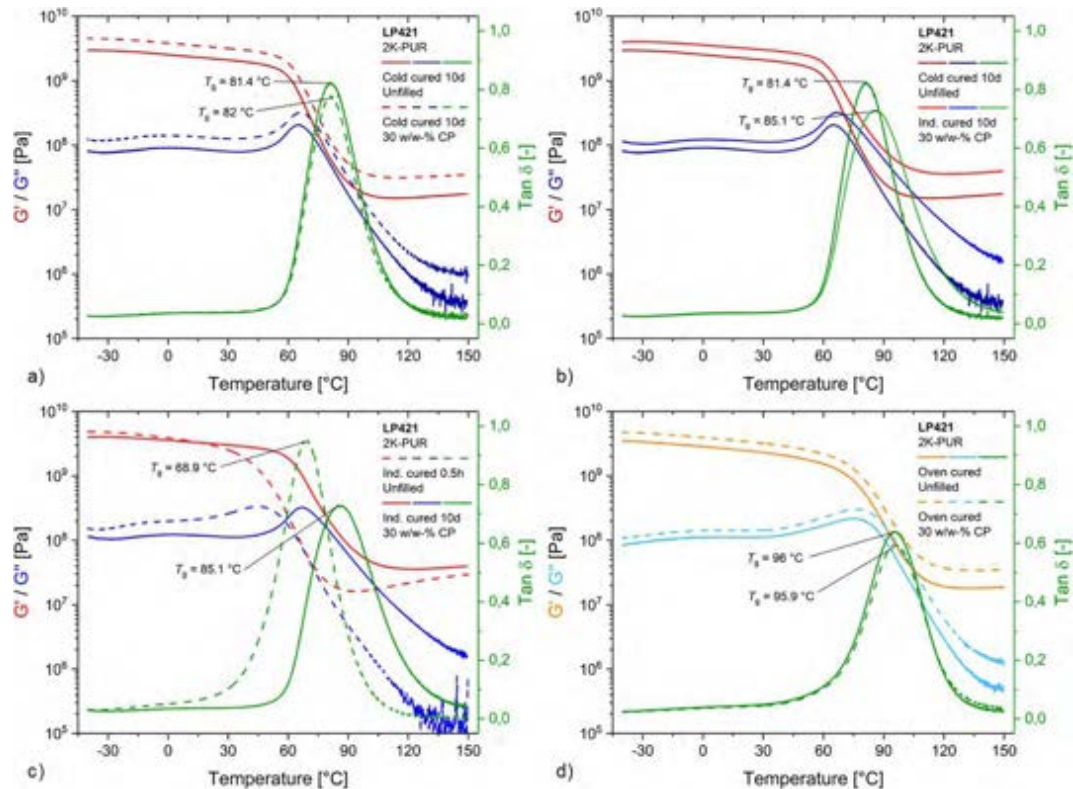


Fig. 30.4 Comparison of measured DMA curves for LP421, temperature range -40°C to $+150^\circ\text{C}$, $dT/dt = 2\text{K/min}$, $A = 20\mu\text{m}$, $f = 1\text{Hz}$.

material and adhesive. In addition, the curing degree α was calculated as a function of measured curing temperatures for the point in time mechanical testing was performed using appropriate kinetic models developed in Ref. [55].

Overall, the data shown in Fig. 30.5 make clear that adhesive strength is reduced with increasing CP content. Besides this aspect, related to the mere presence of CP, most inductively cured SLJ reached higher lap shear strengths compared to those attained for the reference sets. However, the lap shear strength of CP-cured joints appears to decrease with longer RT conditioning after induction, although it is still higher compared to the produced references in most cases. In summary, the SLJ experiments suggest that CP curing represents a suitable solution to accelerate adhesive cure on the lap shear scale. The other experimental results obtained on G-FRP and wood in essence confirm these findings.

Lap shear properties are changed fundamentally. Two counteracting effects were identified: Deterioration of lap shear characteristics attributable to the addition of CP,

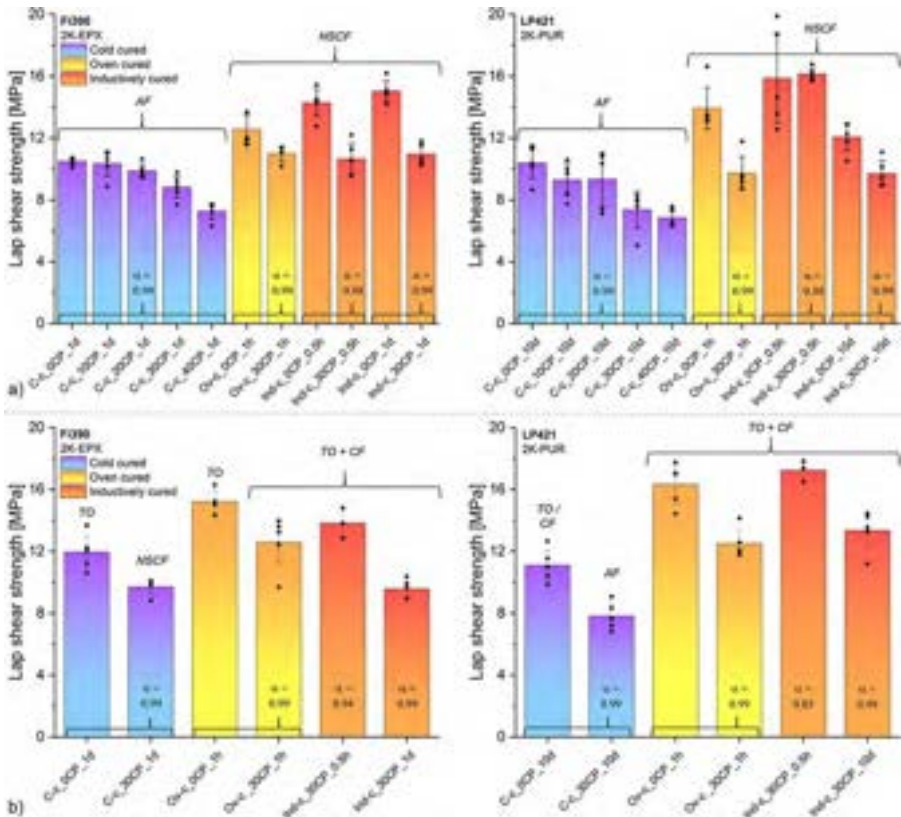


Fig. 30.5 Lap shear strengths of (a) aluminum and (b) G-FRP SLJ bonded with Fi390 (left) and LP421 (right); Zwick|Roell UTM (20kN), $v=2\text{mm/min}$, all tests performed at RT; AF=adhesive/adhesion failure, CF=cohesive failure, NSCF=Near-surface cohesive failure, TO=laminar tear off.

and improvements of compound characteristics as a result of curing at elevated temperatures. These observations are consistent with the findings on the bulk adhesive. It is strongly assumed that the build-up of stiffness and strength does not occur simultaneously. It appears that stiffness development continues to increase with further polymerization, whereas strength may not. This may be the reason for higher joint strengths right after the end of induction, if compared to samples additionally cured at RT after induction.

30.3 Accelerated curing of large-scale joints

To validate the findings obtained on the small-scale levels of adhesive bulk and lap shear samples, experiments were carried out at a much higher geometrical scale. Because of space restrictions in this chapter, the joint, a so-called GiR [56], is just briefly presented [57]. It consists of timber blocks ($120 \times 120 \times 330 \text{ mm}^3$) in which a glass fiber-reinforced polymer rod ($\varnothing 16 \text{ mm}$) has been inserted and adhesively bonded. The very same adhesives and Curie particles already described in Sections 30.2.1 and 30.2.2 were used.

30.3.1 Under laboratory conditions

In a first set of experiments, fully described in Ref. [57], induction heating was performed under room temperature for a duration of 10 min. Cold-cured reference joints were also manufactured for comparison purposes. The 10 min of induction time proved sufficient to achieve temperatures up to 110°C , depending upon the adhesive. However, significant differences of the heating behavior and associated temperature distributions within the GiR were found, depending upon the considered adhesive. Because the specimen geometry, experimental setup, CP content, and mixing procedure were identical, the differing heating behavior can be traced back to the underlying curing kinetics.

After the adhesives had cooled, the resulting load capacity, or joint strength, was experimentally determined. The results of the mechanical testing, illustrated in Fig. 30.6, proved relatively uniform for all considered 2K-EPX. Failure of the wood could be achieved for all cases, whereby load capacities and associated scattering values differed only slightly from each other. Because the wood was the weakest part of the tested joints, the achieved load capacities were limited by its strength. Most inductively cured series achieved comparable failure loads (and fracture patterns) if compared to the respective reference series.

The results indicated that the adhesives Jo692 and Fi390 were already completely cured 2 h after the inductive heating. In contrast, We32 showed a slightly different behavior, as it has not yet fully cured 2 h after induction curing has ended; this is an observation consistent with the kinetic characterization, which revealed a comparatively slow kinetic of We32. This might indicate that a less favorable residual stress condition (see Chapter 31) due to curing at elevated temperatures is responsible for the lowered load capacities. The experimental evidence that CP curing can accelerate the

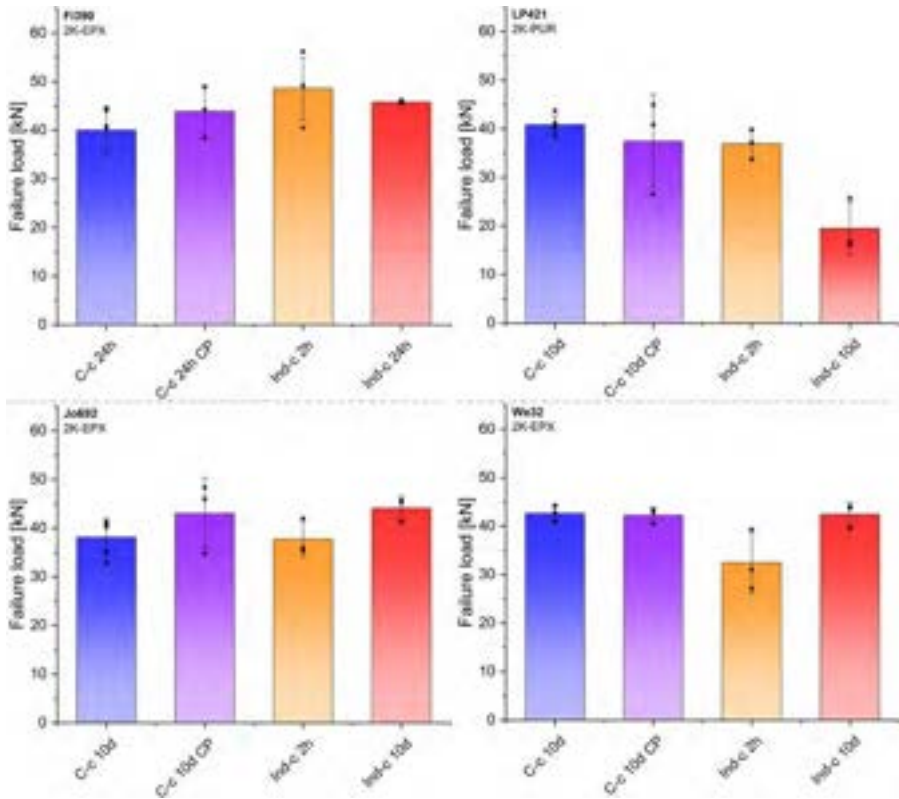


Fig. 30.6 Failure loads of large-scale GiR bonded with different 2K epoxy (Fi390, Jo692, We32) and polyurethane adhesives (LP421); C-c = RT-cured, Ind-c = Inductively cured, 2h/10d = mechanically tested after.

cure of 2K adhesives at a large component level has been provided. A relatively homogeneous heating behavior along the adhesive layer was achieved. For the epoxy adhesives, failure loads and fracture patterns were similar to the RT-cured reference series. The GiR experiments confirmed the prior observations and characterizations made at the level of bulk adhesive and lap shear samples. Parameters that significantly influenced the large-scale induction heating were the curing kinetics of the adhesives, the joint geometry, and the material properties of their components. Compared to the small-scale investigations, thermal inertia played a much more significant role.

30.3.2 Under low temperatures

In contrast to mechanical joining techniques, which can be manufactured under any ambient conditions, adhesively bonded joints always require some minimum temperatures, typically above +10°C, to cure safely. To overcome these restrictions, the very same GiR experiments presented in Section 30.3.1 were extended toward

low-temperature inductive curing at -10 and -30°C [58]. If compared to the experiments at room temperature, which lasted 10 min, induction time had to be increased by 2.5 min.

Resulting failure loads are visualized as bar charts for each considered adhesive in Fig. 30.7. Both load-displacement curves and representative fracture patterns, not discussed herein, can be found in the original article. The failure loads of all epoxy-based GiR proved almost insensitive to the manufacturing temperature (RT, -10°C or -30°C). As differences in fracture behavior between the EPX-bonded reference sets and the low-temperature GiR series were not observed, it can be summarized that the process is very well suited to enable low-temperature curing of 2K-EPX adhesives. The aforementioned results indicate that the general build-up of cohesion and adhesion is not hindered, although the joints were cured starting from low temperatures.

In contrast to the EPX adhesives, the mechanical results of the 2K-PUR under investigation behaved differently, with F_{\max} values being reduced to $\sim 50\%$ – 75% of the unfilled reference values depending on the considered low-temperature series. The reduction in joint capacity of the polyurethane series originates from moisture settlement on the cold adherends as soon as the sealing of the adherends is removed, which has been confirmed by additional experiments on the lap shear scale not presented herein.

Inductive CP-based curing of structural adhesives can be achieved under adverse environmental conditions, which shortens curing times from many days to minutes. Under lower temperatures, longer induction times may be needed. However, the required extension of the induction time only amounted to 2.5 min (from 10 to 12.5 min) and was only necessary for very low GiR temperatures of -30°C . All epoxy-bonded GiR exhibited fracture patterns and failure loads indistinguishable from the unfilled reference sets cured, a very promising result. In contrast to the epoxy adhesives, failure loads of GiR bonded with LP421 (2K-PUR) starting from low temperatures were reduced to $\sim 50\%$ – 75% of the reference values. It is strongly suspected that the deteriorated mechanical performance can be traced back to moisture settlement on the cold adherends.

30.4 Modeling accelerated curing processes

30.4.1 Principle

The experiments on different joint scales proved that CP-induced accelerated curing represents a highly complex process with various conditions influencing the adhesive heating and consequently curing behavior. Up to now, induction times needed to achieve full cure could only be determined through costly preliminary experiments. To contribute to a more efficient and controllable bonding process, a numerical model based on the finite element method (FEM) capable of predicting the curing degree in the dependency of curing temperature profiles and CP content was developed [59]. The model proved capable of predicting the curing degree, α , in the dependency of curing temperature, T_{cure} , and CP content, c_{particle} , using the exemplary application of GiR; the procedure illustrated in Fig. 30.8 has been applied. Key aspects were

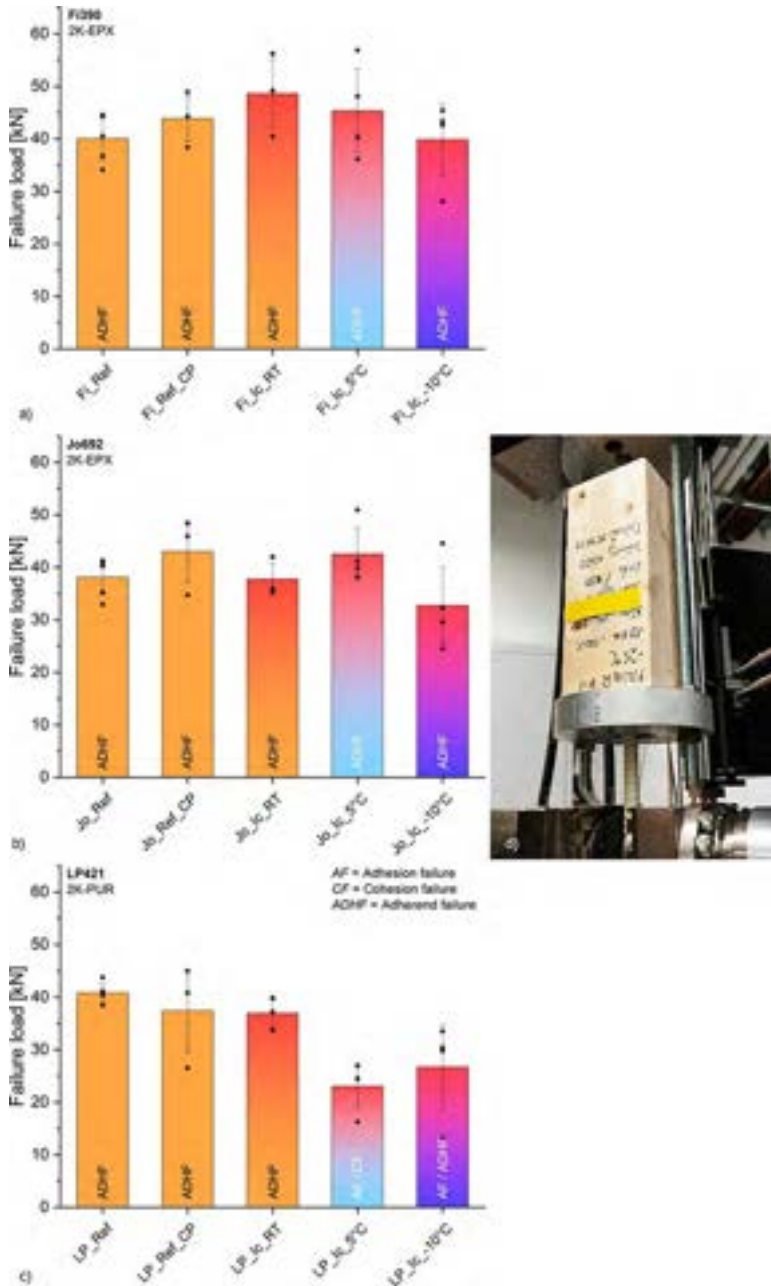


Fig. 30.7 Failure loads of low-temperature CP-cured GiR in comparison to inductively and RT-cured reference sets for (a) Fi390, (b) Jo692, and (c) LP421; (d) GiR positioning during mechanical testing, Zwick|Roell UTM (100kN), $v = 2 \text{ mm/min}$, all tests performed at RT; AF = Adhesive/adhesion failure, CF = Cohesive failure, ADHF = Adherend failure.

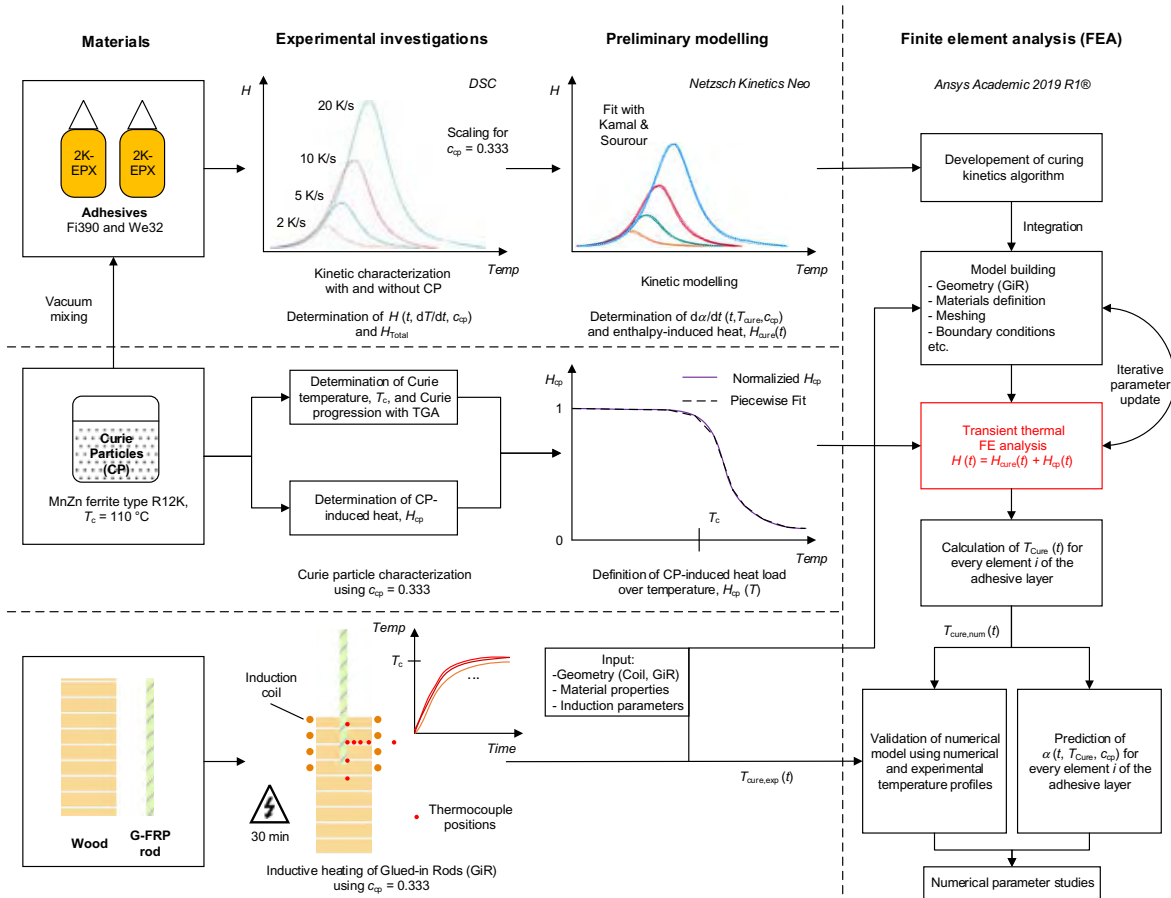


Fig. 30.8 Aspects considered for the numerical modeling of the curing process.

the integration of the Curie effect as full consideration of the polymerization's heat release into the FEA.

For the modeling, it was assumed that temperatures generated within the adhesive layer are attributable to two distinct heat sources: heat originating from CP exposed to the EMF, H_{cp} , and heat released by the exothermic polymerization, H_{cure} . The latter was known from the DSC characterization, with both the enthalpy release with temperature and time as well as the curing kinetics, that is, the progression of α , being implemented into the FEA. In addition to exothermic heat release, heat originating from the CP exposed to the EMF over time, $H_{cp}(t)$, and the Curie effect (switch-off at T_c) had to be integrated into the numerical model. For the following, it was assumed that H_{cp} is linearly proportional to the amount of "active" CP. In detail, the temperature-dependent change of H_{cp} resulting from the CP's "switch-off" behavior when the curing temperature reaches T_c was integrated into the FEA.

A typical output of the FEA is shown in Fig. 30.9 in the form of the temperature distribution within the global model. The FEA also allows one to plot the temperature development of any element of the adhesive layer in function of time; see Fig. 30.10. Furthermore, differences resulting from consideration or not of the exothermic energy release of the adhesive as well as the predicted curing degrees can be estimated.

The developed algorithm delivers a realistic impression of temperatures originating from CP curing. In addition, the Curie effect (switch-off at T_c) was successfully integrated into the FEA. The numerical model allows for better insights regarding the relationship between curing kinetics and heating behavior, including delayed curing,

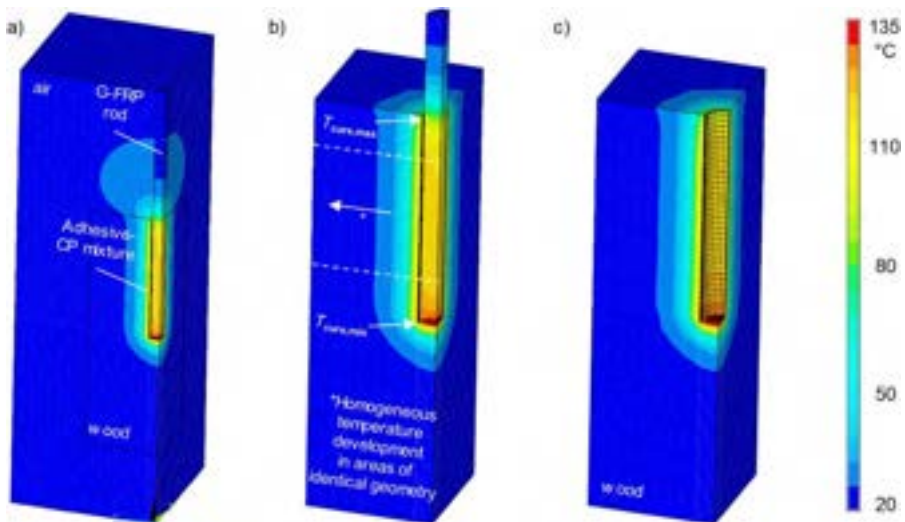


Fig. 30.9 Numerically calculated temperature distribution of GiR at the end of the inductive heating phase ($t = 10$ min) herein for Fi390, $c_{particle} = 0.333$, $t_a = 1$ mm, initial and ambient temperature set to 25°C , $H_{cure} = \text{on}$ (a) global model, (b) model without display of surrounding air layer, and (c) model with display of wooden block and adhesive layer.

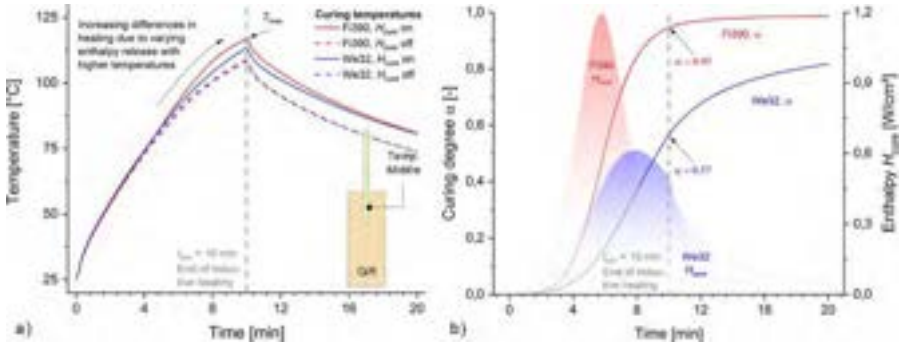


Fig. 30.10 (a) Numerically calculated temperatures in the middle of the adhesive layer for Fi390 (red) and We32 (blue) with and without inclusion of enthalpy release over time, $H_{cure}(t)$; (b) associated progression of curing degree, α , and released polymerization enthalpy, H_{cure} , over time.

on the level of large joints. In addition, the curing progress, $\alpha(t)$, can be predicted in the dependency of adhesive-CP temperatures, opening up the possibility to determine induction times needed to achieve full cure for different conditions numerically.

30.4.2 Validation and parametric studies

The numerical model was validated against a series of experimental temperature readings taken within the GiR joints, as illustrated by Fig. 30.11. The numerical predictions show a very good qualitative—and also mostly quantitative—agreement with the experimentally determined heating curves.

Based upon the validation, the influence of major design parameters can be evaluated. As an example among the several developed in Ref. [60], the influence of the adhesive layer thicknesses on the temperature development is illustrated in Fig. 30.12. As expected due to the Curie effect, temperatures start to flatten out at some point; this flattening tends to occur earlier for the thicker adhesive-CP layers. However, for the adhesive Fi390 at the very large $t_a = 4.0$ mm, computed temperatures, considering enthalpy development, exhibit an overshoot at $t_{sim} = 2-4$ min. Thus, with increasing adhesive-CP mass, that is, layer thickness, the influence of polymerization enthalpy on the heating behavior increases. Comparing the curing degrees, α , as shown in Fig. 30.12 (right), Fi390 generally cures faster in comparison to We32, with curing being already completed ($\alpha = 0.99$) for adhesive layer thicknesses of 4 and 2 mm at the end of the heating phase ($t = 10$ min), when shutting down the EMF.

The model validation was successfully carried out using thermocouple data recorded during CP heating at various locations of the GiR, which showed very good qualitative—and mostly also quantitative—agreement with the numerical predictions. It can thus be concluded that underlying experimental and analytical approaches for segregating the contributions resulting from the induction, H_{cp} , and exotherm, H_{cure} , were correctly implemented, and proved to be suitable for a realistic representation of

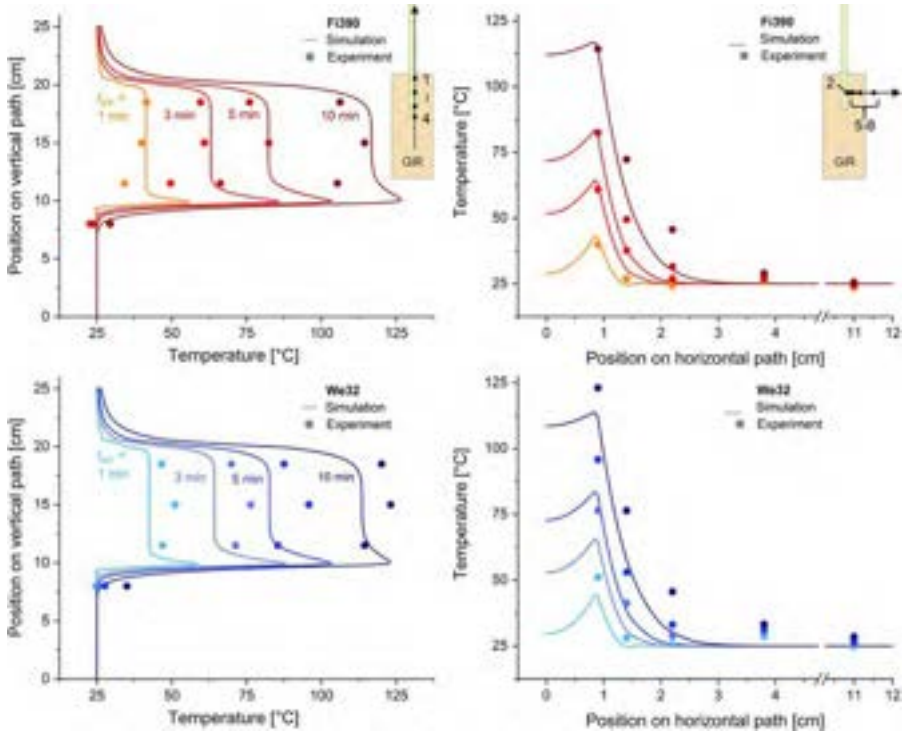


Fig. 30.11 Comparison between numerical and experimental temperature progressions for measuring points 2 and 5–8 for Fi390 (top) and We32 (bottom) for vertical (left) and horizontal GiR temperature path (right), $t_a = 1$ mm, $c_{\text{particle}} = 0.333$, $c_p = 981$ J/kg K, $\lambda = 0.33$ W/m·K, $T_{\text{start}} = 25^\circ\text{C}$, $t_{\text{ind}} = 30$ min.

the process. The numerical parameter studies made clear that almost all investigated parameters exhibit an influence on resulting temperatures. While adhesive layer thickness, CP content, induction time, and GiR starting temperature have a strong influence, the heat capacity and thermal conductivity of the adhesive-CP mixture have minor influences. The influence of the polymerization enthalpy proved to be very important; its significance increases with the thickness of the adhesive layer, the duration of the induction time, and the magnitude of the curing temperature of the GiR.

30.5 Conclusions

This chapter highlighted the main aspects related to the complex multiphysics problem represented by accelerated curing via inductively heated Curie particles as an exemplary accelerated curing technique. The process is influenced by various electromagnetic, thermic, chemical-kinetic, material engineering, mechanical, and process-related effects, tentatively summarized by Fig. 30.13. All these disciplines interact and

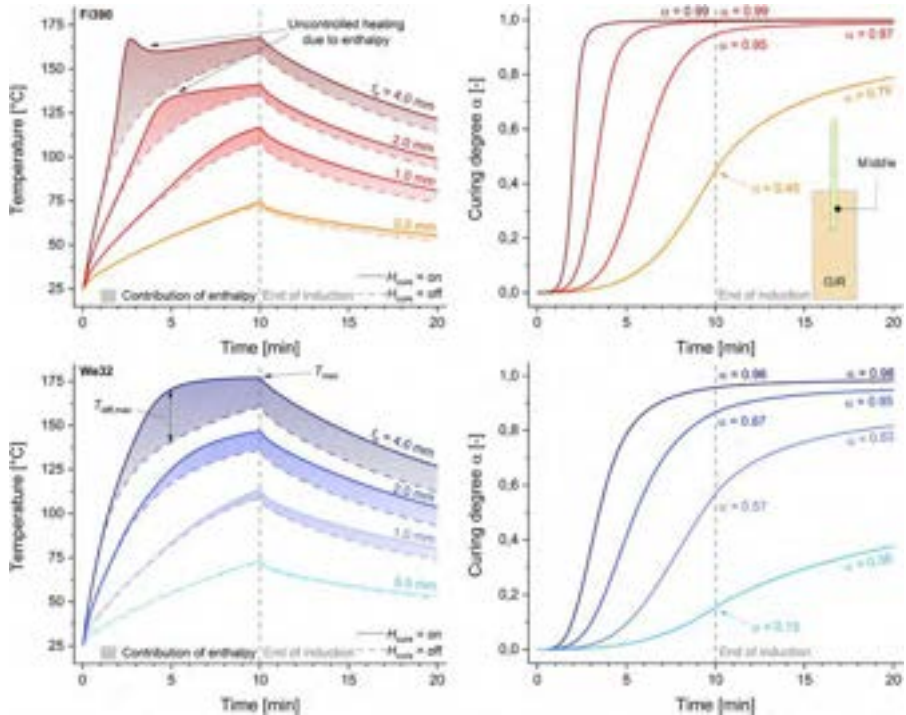


Fig. 30.12 Numerically calculated progression of curing temperature, T_{cure} (left), and curing degree, α (right), in the middle of the adhesive layer for different adhesive layer thicknesses, t_a , of Fi390 (top) and We32 (bottom), $c_{\text{particle}} = 0.333$, $c_p = 981$ J/kg K, $\lambda = 0.33$ W/m K, $t_{\text{ind}} = 10$ min, $T_{\text{start}} = 25^\circ\text{C}$.

determine the properties of the final bonded joint—an overriding cognition that may, in principle, also be applied to other accelerated curing techniques.

The mechanical properties of CP-bonded joints are influenced by the mechanical adhesive and CP properties, which are influenced by the curing history of the polymer. The latter, in turn, depends strongly upon the boundary conditions of the induction process (coil geometry, EMF intensity, induction time, etc.), joint configuration (geometry, adherends, etc.), and the electromagnetic, thermal, and kinetic properties of the adhesive and the CP, just to name a few uncovered interrelations. From these observations, it comes as no surprise that the derivation of generally valid recommendations to model and predict the outcome of the CP curing technique is arduous. Modeling the process opens up the possibility of raising the curing method to a qualitatively much higher level, which represents the first step toward standardization and controllability. For industrial applications [61], quantitative data, such as the exact magnitude of curing temperatures or resulting joint strengths, are necessary. Only on this basis can an efficient and target-oriented process integration into the production of a specific company be achieved.

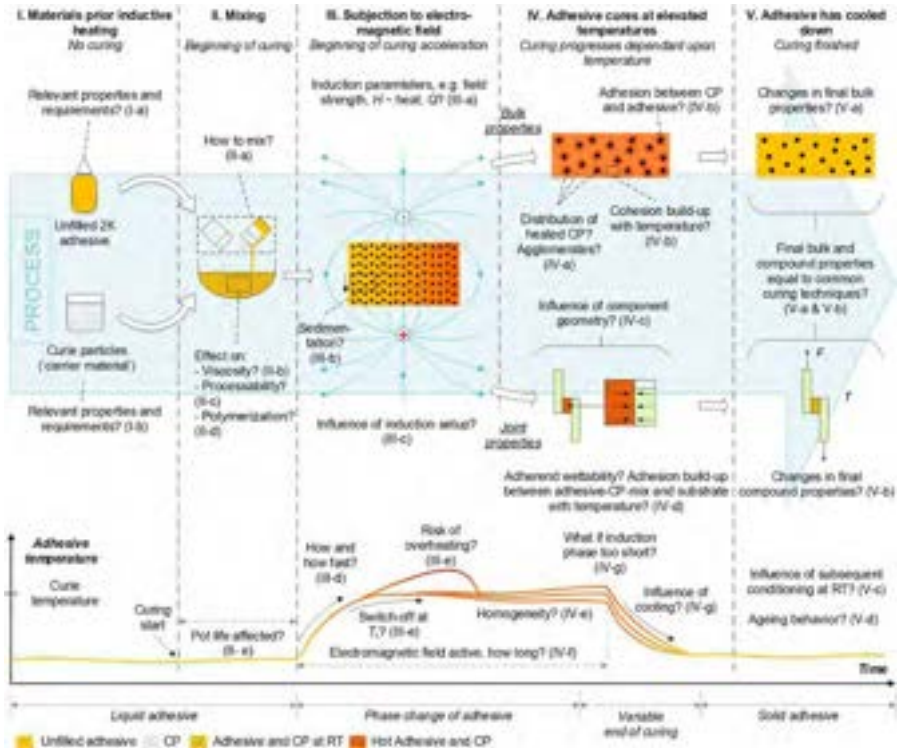


Fig. 30.13 Process chart of the CP curing technique along with associated scientific challenges and its heating principle.

References

- [1] S. Genty, P. Tingaut, M. Aufray, Fast polymerization at low temperature of an infrared radiation cured epoxy-amine adhesive, *Thermochim. Acta* 666 (2018) 27–35, <https://doi.org/10.1016/j.tca.2018.05.018>.
- [2] V.A. Kagan, R.J. Nichols, Benefits of induction welding of reinforced thermoplastics in high performance applications, *J. Reinf. Plast. Compos.* 24 (2005) 1345–1352, <https://doi.org/10.1177/0731684405048846>.
- [3] K. Wang, X. Yuan, M. Zhan, Comparison between microwave and thermal curing of a polyimide adhesive end-capped with phenylethynyl groups, *Int. J. Adhes. Adhes.* 74 (2017) 28–34, <https://doi.org/10.1016/j.ijadhadh.2016.12.008>.
- [4] J. Zhang, X. Ceng, J. Zhang, X. Guo, W. Huang, Effect of curing condition on bonding quality of scarf-repaired composite laminates, *Chin. J. Aeronaut.* (2019), <https://doi.org/10.1016/j.cja.2019.08.016>.
- [5] A. Javadi, H.S. Mehr, M. Sobani, M.D. Soucek, Cure-on-command technology: a review of the current state of the art, *Prog. Org. Coat.* 100 (2016) 2–31, <https://doi.org/10.1016/j.porgcoat.2016.02.014>.
- [6] DIN 2304-1:2020-04, *Klebertechnik—Qualitätsanforderungen an Klebprozesse—Teil_1: Prozesskette Kleben*, Beuth Verlag GmbH, Berlin, 2022.

- [7] A. Vitale, G. Trusiano, R. Bongiovanni, UV-curing of adhesives: a critical review, in: K.L. Mittal (Ed.), *Progress in Adhesion and Adhesives*, Volume 3, John Wiley & Sons, New York, 2018, pp. 101–154.
- [8] A. Endrueweit, M.S. Johnson, A.C. Long, Curing of composite components by ultraviolet radiation: a review, *Polym. Compos.* 27 (2006) 119–128, <https://doi.org/10.1002/pc.20166>.
- [9] V. Shukla, M. Bajpai, D.K. Singh, M. Singh, R. Shukla, Review of basic chemistry of UV-curing technology, *Pigm. Resin Technol.* 33 (2004) 272–279, <https://doi.org/10.1108/03699420410560461>.
- [10] T. Bayerl, M. Duhovic, P. Mitschang, D. Bhattacharyya, The heating of polymer composites by electromagnetic induction—a review, *Compos. A: Appl. Sci. Manuf.* 57 (2014) 27–40, <https://doi.org/10.1016/j.compositesa.2013.10.024>.
- [11] C.O. Mgbemena, D. Li, M.-F. Lin, P.D. Liddel, K.B. Katnam, V.K. Thakur, H.Y. Nezhad, Accelerated microwave curing of fibre-reinforced thermoset polymer composites for structural applications: a review of scientific challenges, *Compos. A: Appl. Sci. Manuf.* 115 (2018) 88–103, <https://doi.org/10.1016/j.compositesa.2018.09.012>.
- [12] T. Vallée, M. Adam, Inductively cured glued-in rods in timber using Curie particles, *Int. J. Adhes. Adhes.* 70 (2016) 37–45, <https://doi.org/10.1016/j.ijadhadh.2016.05.005>.
- [13] V. Kräusel, A. Fröhlich, M. Kroll, P. Rochala, J. Kimme, R. Wertheim, A highly efficient hybrid inductive joining technology for metals and composites, *CIRP Ann.* 67 (2018) 5–8, <https://doi.org/10.1016/j.cirp.2018.04.015>.
- [14] V. Rudnev, D. Loveless, R. Cook, *Handbook of Induction Heating*, second ed., CRC Press Taylor & Francis Group, Boca Raton, FL, 2017.
- [15] Z. Huang, S. Sugiyama, J. Yanagimoto, Adhesive–embossing hybrid joining process to fiber-reinforced thermosetting plastic and metallic thin sheets, *Procedia Eng.* 81 (2014) 2123–2128, <https://doi.org/10.1016/j.proeng.2014.10.296>.
- [16] R. Velthuis, *Induction welding of fiber reinforced thermoplastic polymer composites to metals*, Institut für Verbundwerkstoffe GmbH, Kaiserslautern, 2007.
- [17] S. Mahdi, H.-J. Kim, B.A. Gama, S. Yarlagadda, J.W. Gillespie, A comparison of oven-cured and induction-cured adhesively bonded composite joints, *J. Compos. Mater.* 37 (2003) 519–542, <https://doi.org/10.1177/0021998303037006776>.
- [18] C. Ageorges, L. Ye, M. Hou, Experimental investigation of the resistance welding for thermoplastic-matrix composites. Part I. Heating element and heat transfer, *Compos. Sci. Technol.* 60 (2000) 1027–1039, [https://doi.org/10.1016/S0266-3538\(00\)00005-1](https://doi.org/10.1016/S0266-3538(00)00005-1).
- [19] C. Severijns, S. Teixeira De Freitas, H. Poulis, On the assessment of susceptor-assisted induction curing of adhesively bonded joints, in: J. Abenojar Bzuendia (Ed.), *11th European Adhesion Conference*, 2016.
- [20] T.E. Tay, B.K. Fink, S.H. McKnight, S. Yarlagadda, J.W. Gillespie, Accelerated curing of adhesives in bonded joints by induction heating, *J. Compos. Mater.* 33 (1999) 1643–1664, <https://doi.org/10.1177/002199839903301704>.
- [21] D. Mattheß, D. Landgrebe, W.-G. Drossel, Inductive heating of glass fibre-reinforced thermoplastics using fibre- and wire-shaped stainless steel susceptors, *J. Thermoplast. Compos. Mater.* 30 (2017) 67–87, <https://doi.org/10.1177/0892705715583179>.
- [22] T. Bayerl, R. Schledjewski, P. Mitschang, Induction heating of thermoplastic materials by particulate heating promoters, *Polym. Polym. Compos.* 20 (2012) 333–342, <https://doi.org/10.1177/096739111202000401>.
- [23] C. Yungwirth, E. Wetzel, J. Sands, *Induction curing of a phase-toughened adhesive*, Army Research Laboratory, 2003, p. 30.

- [24] W. Suwanwatana, S. Yarlalagadda, J.W. Gillespie, Influence of particle size on hysteresis heating behavior of nickel particulate polymer films, *Compos. Sci. Technol.* 66 (2006) 2825–2836, <https://doi.org/10.1016/j.compscitech.2006.02.033>.
- [25] T. Lm, Y. Kwon, S. Choi, M. Shon, H. Jeon, S. Oh, G. Kim, Heating behavior and adhesion performance of induction-heated multilayered thermoplastic polyurethane adhesive film, *J. Adhes.* (2019) 1–12, <https://doi.org/10.1080/00218464.2019.1565757>.
- [26] D. Bae, P. Shin, S. Kwak, M. Moon, M. Shon, S. Oh, G. Kim, Heating behavior of ferromagnetic Fe particle-embedded thermoplastic polyurethane adhesive film by induction heating, *J. Ind. Eng. Chem.* 30 (2015) 92–97, <https://doi.org/10.1016/j.jiec.2015.05.007>.
- [27] D.H. Bae, M.Y. Shon, S.T. Oh, G.N. Kim, Study on the heating behavior of Fe₃O₄—embedded thermoplastic polyurethane adhesive film via induction heating, *Bull. Korean Chem. Soc.* 37 (2016) 1211–1218, <https://doi.org/10.1002/bkcs.10841>.
- [28] J.W. Hubbard, F. Orange, M.J.-F. Guinel, A.J. Guenther, J.M. Mabry, C.M. Sahagun, C. Rinaldi, Curing of a bisphenol E based cyanate ester using magnetic nanoparticles as an internal heat source through induction heating, *ACS Appl. Mater. Interfaces* 5 (2013) 11329–11335, <https://doi.org/10.1021/am4035575>.
- [29] N. Ratsch, S. Böhm, M. Voß, M. Adam, J. Wirries, T. Vallée, Accelerated curing of glued-in threaded rods by means of inductive heating. Part I. Experiments, *J. Adhes.* (2019) 1–26, <https://doi.org/10.1080/00218464.2019.1654864>.
- [30] M. Adam, A. Lühning, M. Popp, S. Fecht, T. Vallée, Pre-applicable structural adhesives for timber engineering: glued-in G-FRP rods, *Int. J. Adhes. Adhes.* 67 (2016) 121–127, <https://doi.org/10.1016/j.ijadhadh.2015.12.034>.
- [31] M. Voß, T. Vallée, Accelerated curing of G-FRP rods glued into timber by means of inductive heating using Curie-particles—large-scale experiments at room temperature, *J. Adhes.* (2020).
- [32] C. Garschke, P.P. Parlevliet, C. Weimer, B.L. Fox, Cure kinetics and viscosity modelling of a high-performance epoxy resin film, *Polym. Test.* 32 (2013) 150–157, <https://doi.org/10.1016/j.polymertesting.2012.09.011>.
- [33] S. Montserrat, J. Málek, A kinetic analysis of the curing reaction of an epoxy resin, *Thermochim. Acta* 228 (1993) 47–60, [https://doi.org/10.1016/0040-6031\(93\)80273-D](https://doi.org/10.1016/0040-6031(93)80273-D).
- [34] N. Rabearison, C. Jochum, J.C. Grandidier, A cure kinetics, diffusion controlled and temperature dependent, identification of the Araldite LY556 epoxy, *J. Mater. Sci.* 46 (2011) 787–796, <https://doi.org/10.1007/s10853-010-4815-7>.
- [35] C. Restrepo, T. Osswald, J. Hernández-Ortiz, Modeling and analysis of cure kinetics of aliphatic epoxy resin with and without diffusion, in: *70th annual technical conference of the Society of Plastics Engineers 2012 (ANTEC 2012): Orlando, Florida, USA, 2–4 April*, Red Hook, NY, Curran, 2012, p. 2012.
- [36] A. Yousefi, P.G. Lafleur, R. Gauvin, Kinetic studies of thermoset cure reactions: a review, *Polym. Compos.* 18 (1997) 157–168, <https://doi.org/10.1002/pc.10270>.
- [37] C.C. Riccardi, J. Dupuy, R.J.J. Williams, A simple model to explain the complex kinetic behavior of epoxy/anhydride systems, *J. Polym. Sci. B Polym. Phys.* 37 (1999) 2799–2805, [https://doi.org/10.1002/\(SICI\)1099-0488\(19991001\)37:19<2799:AID-POLB9>3.0.CO;2-N](https://doi.org/10.1002/(SICI)1099-0488(19991001)37:19<2799:AID-POLB9>3.0.CO;2-N).
- [38] Z. Liu, J. Xiao, S. Bai, W. Zhang, Study on phenomenological curing model of epoxy resin for prediction of degree of cure, *J. Therm. Anal. Calorim.* 109 (2012) 1555–1561, <https://doi.org/10.1007/s10973-011-2070-z>.
- [39] J.W. Holubka, R.D. Bach, J.L. Andres, Theoretical study of the reactions of ethylene oxide and ammonia: a model study of the epoxy adhesive curing mechanism, *Macromolecules* 25 (1992) 1189–1192, <https://doi.org/10.1021/ma00029a028>.

- [40] H. Esmonde, S. Holm, Fractional derivative modelling of adhesive cure, *Appl. Math. Model.* 77 (2020) 1041–1053, <https://doi.org/10.1016/j.apm.2019.08.021>.
- [41] R. Hardis, J.L. Jessop, F.E. Peters, M.R. Kessler, Cure kinetics characterization and monitoring of an epoxy resin using DSC, Raman spectroscopy, and DEA, *Compos. A: Appl. Sci. Manuf.* 49 (2013) 100–108, <https://doi.org/10.1016/j.compositesa.2013.01.021>.
- [42] A. Moroni, J. Mijovic, E.M. Pearce, C.C. Foun, Cure kinetics of epoxy resins and aromatic diamines, *J. Appl. Polym. Sci.* 32 (1986) 3761–3773, <https://doi.org/10.1002/app.1986.070320231>.
- [43] A. Bernath, L. Kärger, F. Henning, Accurate cure modeling for isothermal processing of fast curing epoxy resins, *Polymers* (2016) 8, <https://doi.org/10.3390/polym8110390>.
- [44] W. Jenninger, Calorimetric studies of isothermal curing of phase separating epoxy networks, *Polymer* 41 (2000) 1577–1588, [https://doi.org/10.1016/S0032-3861\(99\)00274-8](https://doi.org/10.1016/S0032-3861(99)00274-8).
- [45] A. Olusanya, A comparison of techniques for monitoring the cure of adhesives, *NPL Report CMMT (B)*, 1996, p. 104.
- [46] G. Hülder, Reaktionskinetik von Verbundmörtelsystemen für tragende Anwendungen im Bauwesen, *J. Plast. Technol.* (2010) 3.
- [47] S. Sourour, Kamal., Differential scanning calorimetry of epoxy cure: isothermal cure kinetics, *Thermochim. Acta* 14 (1976) 41–59.
- [48] G. Tripathi, D. Srivastava, Cure kinetics of ternary blends of epoxy resins studied by non-isothermal DSC data, *J. Appl. Polym. Sci.* 112 (2009) 3119–3126, <https://doi.org/10.1002/app.29781>.
- [49] X. Wang, J. Jin, M. Song, Y. Lin, Effect of graphene oxide sheet size on the curing kinetics and thermal stability of epoxy resins, *Mater. Res. Express* 3 (2016), 105303, <https://doi.org/10.1088/2053-1591/3/10/105303>.
- [50] N.C. Restrepo-Zapata, T.A. Osswald, J.P. Hernández-Ortiz, Method for time-temperature-transformation diagrams using DSC data: linseed aliphatic epoxy resin, *J. Appl. Polym. Sci.* 131 (2014) n/a-n/a, <https://doi.org/10.1002/app.40566>.
- [51] K. Horie, H. Hiura, M. Sawada, I. Mita, H. Kambe, Calorimetric investigation of polymerization reactions. III. Curing reaction of epoxides with amines, *J. Polym. Sci. Part A-1: Polym. Chem.* 8 (1970) 1357–1372.
- [52] C. Chen, Y. Li, Y. Gu, M. Li, Z. Zhang, An improved simplified approach for curing kinetics of epoxy resins by nonisothermal differential scanning calorimetry, *High Perform. Polym.* 30 (2018) 303–311, <https://doi.org/10.1177/0954008317693291>.
- [53] M. Voß, T. Vallée, Effects of Curie particle induced accelerated curing on thermo mechanical performance of 2K structural adhesives. Part I. Bulk properties, *J. Adhes.* (2021) 1–42, <https://doi.org/10.1080/00218464.2021.1909482>.
- [54] M. Voß, T. Vallée, Effects of Curie particle induced accelerated curing on thermo-mechanical performance of 2K structural adhesives. Part II. Lap shear properties, *J. Adhes.* (2021) 1–51, <https://doi.org/10.1080/00218464.2021.1884551>.
- [55] M. Voß, T. Vallée, Accelerated curing of G-FRP rods glued into timber by means of inductive heating—influences of curing kinetics, *J. Adhes.* 98 (2022) 1037–1075, <https://doi.org/10.1080/00218464.2020.1870450>.
- [56] G. Tlustochowicz, E. Serrano, R. Steiger, State-of-the-art review on timber connections with glued-in steel rods, *Mater. Struct.* 44 (2011) 997–1020, <https://doi.org/10.1617/s11527-010-9682-9>.
- [57] M. Voß, T. Vallée, Accelerated curing of G-FRP rods glued into timber by means of inductive heating using Curie-particles—large-scale experiments at room temperature, *J. Adhes.* 97 (2021) 1532–1560, <https://doi.org/10.1080/00218464.2020.1803067>.

-
- [58] M. Voß, T. Evers, T. Vallée, Low-temperature curing of adhesives—large-scale experiments, *J. Adhes.* (2022) 1–36, <https://doi.org/10.1080/00218464.2022.2059353>.
- [59] M. Voß, M. Kaufmann, T. Vallée, Curie-supported accelerated curing by means of inductive heating. Part I. Model building, *J. Adhes.* (2021) 1–44, <https://doi.org/10.1080/00218464.2021.1902810>.
- [60] M. Voß, M. Kaufmann, T. Vallée, Curie-supported accelerated curing by means of inductive heating. Part II. Validation and numerical studies, *J. Adhes.* (2021) 1–33, <https://doi.org/10.1080/00218464.2021.1951712>.
- [61] A. Elmahdy, I. van de Weyenberg, P. Cosemans, M. Adam, M. Voß, S. Heinrichs, T. Vallée, Some industrial examples of accelerated curing using curie particles, in: L.F. M. Da Silva (Ed.), *Industrial Applications of Adhesives: 1st International Conference on Industrial Applications of Adhesives*, Singapore, Springer Singapore Pte. Limited, 2021, pp. 15–30.

This page intentionally left blank

Residual stress development in curing processes: Material characterization and modeling

31

David Lindeman^a, Aaron Hedegaard^a, Chaodi Li^b, and Samuel Carpenter^a
^a3M Company, Saint Paul, MN, United States, ^b3M Company, Corporate Research Laboratory, Maplewood, MN, United States

31.1 Introduction

Adhesives are used extensively in the aerospace, automotive, and electronics industries [1–3]. Structural adhesives, such as epoxy-based adhesives, are commonly selected due to their excellent mechanical properties including low weight, high strength, and corrosion resistance. In typical applications, most structural adhesives must be cured to produce the crosslinking that converts the material from a viscous liquid to a glassy solid. Due to the crosslinking process and the reduction in free volume, chemical shrinkage strains are induced and may result in the generation of residual stresses in the bonded assembly [4,5]. The residual stresses can potentially damage sensitive components, lead to warpage of the assembly, or contribute to subsequent failure modes, such as fatigue [5–8]. In addition, because the curing reaction is often exothermic, thermal strains can also induce potentially harmful loads on the bonded components during the curing process. Finally, the mechanical properties of a cured adhesive often depend on curing conditions and processes. To properly design a bonded joint or assembly, it is therefore often necessary to understand the effects of the curing process.

Adhesive curing processes have been studied experimentally for decades [9], and new methods are enabling a more detailed characterization of the evolution of mechanical properties during cure. In addition, numerical methods have been developed that enable the simulation of curing processes and the development of residual stresses [7,10]. The fundamentals of adhesive curing processes and material property evolution are discussed in Section 31.2. The experimental methods used to quantify the evolution of material properties are outlined in Section 31.3. A numerical framework for simulating curing processes and predicting residual stresses is presented in Section 31.4. Finally, additional comments are given in Section 31.5.

31.2 Adhesive curing processes and material property evolution

The curing process in structural adhesives is commonly initiated by raising the temperature of the adhesive to a level that promotes the curing reaction. In some cases, however, the conversion process is initiated through exposure to ultraviolet (UV) light

or water [3]. During curing, the properties of structural adhesives typically evolve as complex functions of conversion and temperature [7,11–13]. As the curing reaction progresses and crosslinks are formed, the material transforms from a viscous liquid into a rubbery solid [11,12]. Following this gelation stage, additional conversion typically leads to the creation of a glassy solid upon cooling of the material [12,14–16].

The reactions associated with curing processes can often be described using kinetic relationships that define the conversion rate as a function of the current conversion level and temperature. For example, the Kamal equation [17] is defined as:

$$\dot{\alpha} = Ze^{\left(\frac{-E}{RT}\right)}(X + \alpha^m)(\alpha_{max}(T) - \alpha)^n \quad (31.1)$$

where α is the degree of conversion (a scalar that has a value of zero in the uncured state and a value of one in the fully cured state), E is the activation energy, R is the universal gas constant, T is the absolute temperature, and Z , m , and n are reaction constants. The term X is introduced to enable the definition of a nonzero conversion rate when $\alpha = 0$. The temperature-dependent term α_{max} is included so that curing conditions that result in a partially cured material ($\alpha < 1$) can be represented. In most practical applications, the curing conditions will be associated with $\alpha_{max} = 1$.

The conversion reaction is generally exothermic, and the volumetric heat generation rate q''' associated with the reaction can be defined as [18]:

$$q''' = \rho Q \dot{\alpha} \quad (31.2)$$

where ρ is the mass density and Q is the specific heat of reaction. Note that heat flow, heat flux, and volumetric heat generation are denoted by the symbols q , q'' , and q''' , respectively.

The evolution of the elastic and viscoelastic properties of the material is a complex function of the conversion and temperature histories. Theoretical and analytical descriptions of the evolution processes have been proposed [4,7]. Most often, evolution of the elastic and viscoelastic properties is characterized using experimental methods such as the time-temperature-cure superposition (TTCS) method [13], and both the elastic properties and viscoelastic shift function are defined as tabular functions of conversion and temperature.

Similarly, thermal expansion coefficient values are typically quantified using thermomechanical analysis (TMA) [19] and defined in a tabular form. Finally, the volumetric shrinkage coefficient γ associated with crosslinking can be determined by measuring the volume of specimens before and after cure. The incremental chemical strain $\Delta \epsilon_c$ can be defined in terms of the volumetric shrinkage and the increment in conversion $\Delta \alpha$:

$$\Delta \epsilon_c = \frac{\gamma}{3} \Delta \alpha \quad (31.3)$$

Due to the coupling of the mechanical properties and thermal strains to the spatially and temporally varying temperature field, the simulation of curing processes requires the use

of a coupled thermal-structural analysis [4,20,21]. Various material models have been used, including elastic, elastic-plastic, and viscoelastic models [4,6]. Early modeling efforts focused primarily on the evolution of the elastic modulus during curing and ignored viscoelastic effects. More recent works have included evolution of the viscoelastic properties using a temperature- and conversion-dependent shift factor [7,13].

31.3 Experimental methods

The sections below describe the experimental methods commonly used to measure the material properties associated with cured structural adhesives, and the methods used to characterize the evolution of properties as functions of conversion and temperature. In some cases, alternative test methods may exist, but the objective of these sections is not to review or compare test methods, but to provide examples of relevant methods and techniques. Note that experimental characterization is a necessary precursor to modeling efforts, and accurate characterization of the reaction kinetics and property evolution is critical to the development of accurate and predictive models. All of the experimental measurements and numerical predictions presented herein are associated with a single epoxy amine adhesive formulation; epoxy chemistries are discussed in detail in [Chapter 1](#).

31.3.1 Curing kinetics, heat of reaction, and specific heat

Differential scanning calorimetry (DSC) is a thermoanalytical technique useful for understanding the thermal transitions of a material. Using DSC methods, the curing kinetics, total heat of reaction, and specific heat (for both the uncured and cured material) can be measured. During a DSC test, a small amount of material (usually on the order of 5–10 mg) is placed in a sealed sample pan in a controlled temperature environment. The heat inflow or outflow required to maintain a specific temperature or produce a specific change in temperature is measured, and this information is used to derive the values of interest. In modern DSC systems, corrections for the thermal properties of the pan and equipment itself are automatically applied.

The kinetics associated with a curing reaction can be characterized by performing DSC measurements under isothermal conditions for a range of temperatures, or by ramping the temperature at a variety of rates. In general, isothermal tests are easier to perform and analyze, but require more time (due to the need to reach a steady-state condition at each temperature). The reader is referred to the documentation and publications available from the manufacturers of DSC systems for more information as well as the ASTM E698 test standard. The test output consists of time histories of excess heat as a function of temperature (e.g., [Fig. 31.1](#)) or temperature rate. These time histories can be integrated to obtain the total excess heat as a function of time and temperature (or temperature rate). By normalizing these curves, a scalar value for conversion (which varies from zero to one) is obtained (e.g., [Fig. 31.2](#)). These curves can be used to derive the parameters associated with a kinetic equation (see, for example, [Eq. 31.1](#)).

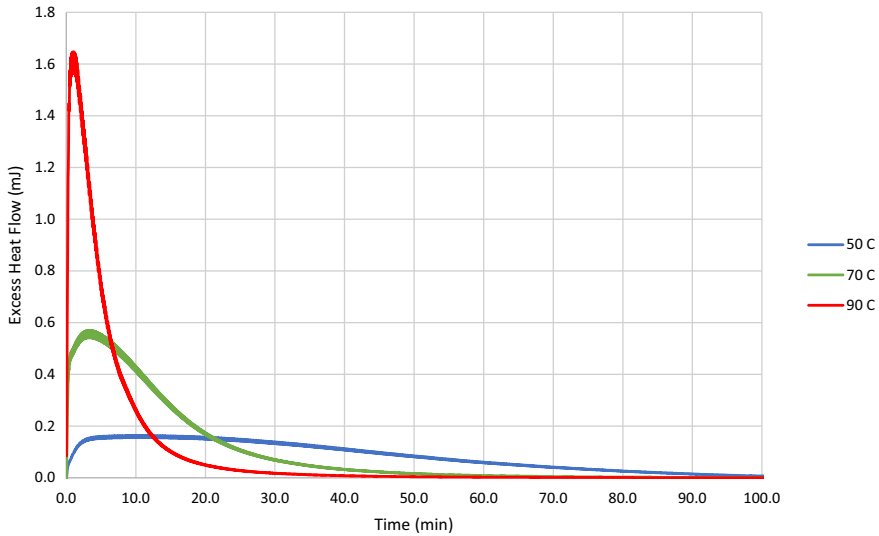


Fig. 31.1 Excess heat flow as a function of time for an epoxy/amine adhesive at various temperatures.

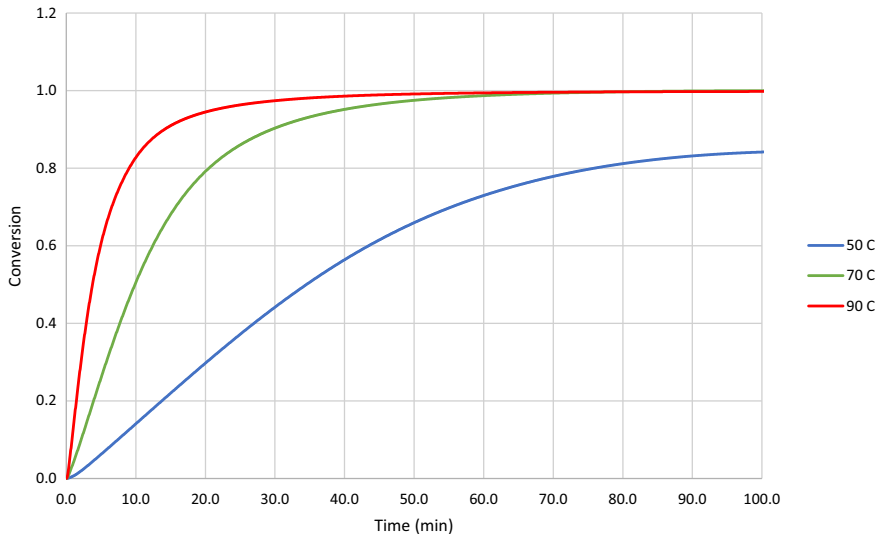


Fig. 31.2 Conversion as a function of time for an epoxy/amine adhesive at various temperatures.

For a fully cured material, the specific heat of reaction is simply the total excess heat (the area under an excess heat vs. time curve) divided by the mass of the sample. Note that under some conditions (in particular, low-temperature conditions), a DSC experiment may not yield a fully cured material (see, for example, the 50°C curve in

Fig. 31.1). Care should therefore be taken to use data associated with fully cured materials when determining the heat of reaction. For more information, see the ASTM E2160 test standard.

The specific heat C_p of a material is defined as the amount of energy required to raise the temperature of a mass of material by one degree. This value is typically temperature- and material-state dependent. DSC temperature ramps are often used to perform specific heat measurements (see, for example, the ASTM E1269 test standard). Alternatively, a modulated DSC (MDSC) temperature ramp can be used. In MDSC, a temperature modulation is superimposed over the standard temperature ramp, enabling the heat flow measurement to be split into reversible and nonreversible components. The specific heat as a function of temperature can be calculated from the reversible flow. Note that MDSC methods can be more accurate due to their ability to tease apart complex transition behavior and provide resolution improvements over standard methods. Additionally, heat flows and heat capacities can be determined from a single experiment.

31.3.2 Elastic and viscoelastic properties

Polymeric and prepolymeric materials are generally viscoelastic and exhibit a strain rate-dependent mechanical response and stress relaxation. Viscoelastic material properties are commonly characterized using dynamic mechanical analysis (DMA) methods (see, for example, the ASTM D4440 test standard [22]) in which samples are subjected to small, oscillatory shear (or compressive) strains $\varepsilon(t)$ (with magnitude ε_o often 1% or less) at various combinations of frequency ω and temperature:

$$\varepsilon(t) = \varepsilon_o \sin(\omega t) \quad (31.4)$$

Due to the viscoelasticity of the material, the measured stress response $\sigma(t)$ (of magnitude σ_o) lags the input strain by the phase angle δ :

$$\sigma(t) = \sigma_o \sin(\omega t + \delta) = \sigma_o \sin(\omega t) \cos(\delta) + \sigma_o \cos(\omega t) \sin(\delta) \quad (31.5)$$

This leads to the definition of a complex shear modulus $G^* = G' + iG''$, where the shear storage modulus G' and shear loss modulus G'' are defined as:

$$G' = \frac{\sigma_o}{\varepsilon_o} \cos(\delta) \quad (31.6)$$

$$G'' = \frac{\sigma_o}{\varepsilon_o} \sin(\delta) \quad (31.7)$$

and the phase angle is defined as:

$$\delta = \arctan\left(\frac{G''}{G'}\right) \quad (31.8)$$

Tests performed using a compressive load will yield the complex elastic modulus E^* , elastic storage modulus E' , and elastic loss modulus E'' .

If the test range is limited to the linear viscoelastic region (LVR) (the region in which stress is proportional to strain), then the storage and loss moduli provide a complete description of the mechanical response of the material over the measured frequency and temperature ranges. However, the practical frequency range currently available in DMA testing systems is generally restricted to 0.01–100 Hz, a range that may be too limited to characterize the response of materials used in high frequency or high strain rate applications, or to characterize the long-term response of the material.

To extend the frequency range characterized, time-temperature superposition (TTS) principles can be applied (as also discussed in [Chapter 20](#)). For *thermorheologically simple* materials (i.e., those materials for which the TTS principle holds), it is observed that the storage and loss moduli measured at one frequency-temperature pair are identical to those measured at a second frequency-temperature pair. This leads to an equivalence of frequency and temperature effects and enables storage and loss modulus curves to be shifted within frequency-temperature space. In practice, DMA tests are performed using a limited range of frequencies, but the tests are repeated over a range of temperatures. The equivalence between temperature and frequency allows the measured curves to be shifted as a function of temperature to obtain storage and loss modulus values over a much wider range of frequencies.

To perform the shifting, reference storage modulus, loss modulus, and phase angle curves (often the curves measured at room temperature) are selected, and the curves measured at other temperatures are shifted along the frequency axis until they superimpose to form a *master curve*. The shift factor A_{TTS} used for each curve/temperature is recorded and can be used to reshift the curves to a different reference temperature, if necessary. Note that $A_{TTS} \equiv 1$ for the reference curve/temperature. For higher temperatures, the shift factor is generally less than one (i.e., increasing temperature is equivalent to decreasing frequency). Likewise, for lower temperatures, the shift factor is typically greater than one (i.e., decreasing temperature is equivalent to increasing frequency).

If the measured curves do not all superimpose when shifted (i.e., if the material is *not* thermorheologically simple), then the shifting operation will be applicable only to a restricted temperature/frequency range. In these cases, high and/or low frequency DMA measurements must be performed to extend the frequency range. Fortunately, many structural adhesives *are* thermorheologically simple, and subsequent discussion will focus on materials for which TTS holds.

One key assumption of thermorheological simplicity is that the test specimen be chemically and structurally identical throughout the isothermal frequency sweep used in the DMA test. For structural adhesives that are completely cured or uncured (with the reaction inhibited to prevent conversion during the test), this requirement is not a problem. If the objective is to characterize a material as it cures, then, by definition, the chemical and structural state of the material must be allowed to evolve. This requires the application of TTCS principles.

TTCS is an extension of the TTS principle, wherein the equivalency of temperature and frequency is extended to include equivalency with conversion. Construction of a

TTCS master curve will therefore involve shifting in the temperature–frequency space as well as the conversion–frequency space, resulting in a temperature and conversion-dependent shift factor $A_{TTCS}(T, \alpha)$. If the reaction rate is very low (e.g., the material needs several hours to completely cure), then it may be possible to assume isoconversion conditions during a standard frequency-sweep DMA test [12,23,24]. Also, if the reaction can be halted mid-cure to allow time for DMA analysis (as demonstrated by Saseendran and coworkers [25]), then the isoconversion assumption holds as well. In practice, however, it is difficult to maintain an isoconversion state during a frequency-sweep DMA test (especially at higher temperatures) because the material will cure during the test. And, in general, the conversion level cannot be measured directly during the DMA test.

To overcome these challenges, a multiwave DMA test method can be used [13,26]. In this technique, a simple sinusoidal strain input (and frequency sweep) is replaced by a strain input signal consisting of multiple, superimposed sinusoidal signals of several frequencies, each with a unique amplitude and phase angle (Fig. 31.3). Using Fourier transforms, the input and output signals can be decomposed into individual frequency components, in effect allowing a frequency sweep to be performed using a single test cycle. The time required for each test cycle is short enough that the conversion level of the material can be assumed to be constant. By performing multiple tests with different temperature ramps (to achieve different temperature/conversion histories), the data required for construction of the TTCS master curve can be obtained [21,27].

Alternatively, individual DMA tests could be performed using various combinations of constant temperature and frequency, enabling measurement of the mechanical properties as the samples cure. This method would, however, require many more tests to fully characterize a material. A typical TTCS measurement might involve five or more temperatures and nine or more frequencies. Using TTCS, the measurements can be performed using only five tests, whereas using constant temperature/frequency tests would require 45.

A second challenge for TTCS analysis is determination of the conversion level during the test. Often, it is sufficient to use the measured cure kinetics (see Section 31.3.1) and the measured temperature history to infer the conversion level at any point during the test. However, this method may lead to errors because:

- 1) The volume of the test specimens used for DMA test is generally larger than that used for DSC tests, and therefore a nonuniform temperature field could exist within the material depending on the strength of the exotherm and the material diffusivity.
- 2) An unknown level of conversion could occur during the sample preparation and test initiation procedure.

Challenges associated with determination of the conversion level can be addressed by using *hyphenated rheology* techniques that enable direct measurement of the conversion level during a DMA test. In this approach, a chemical or thermal analysis is performed simultaneously with the mechanical analysis. Recent work by Radebe and coworkers discusses the use of a combined rheology-Fourier transform infrared (FTIR) spectroscopy instrument to correlate chemical conversion directly to rheological properties, circumventing the need to perform these experiments independently [28]. Previous work

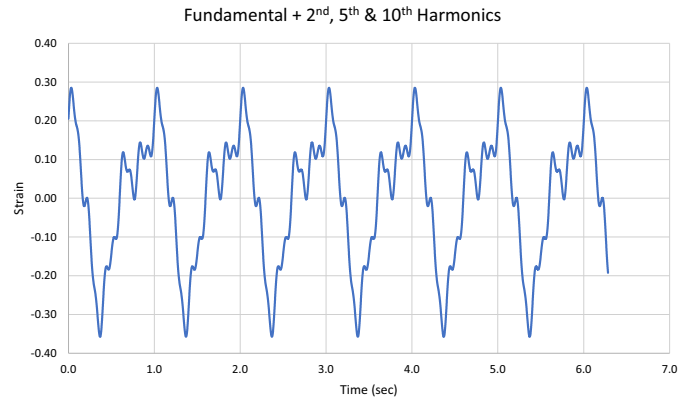
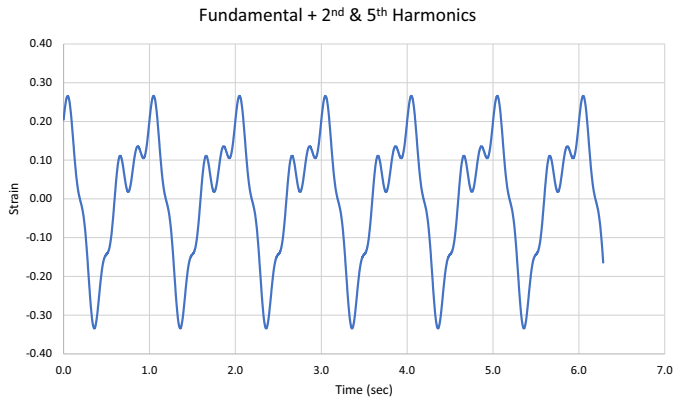
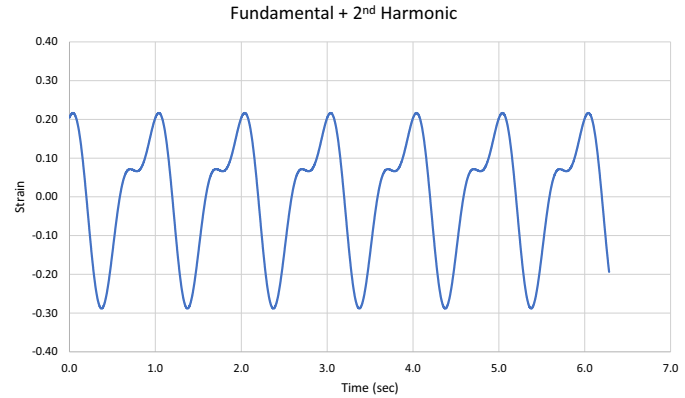
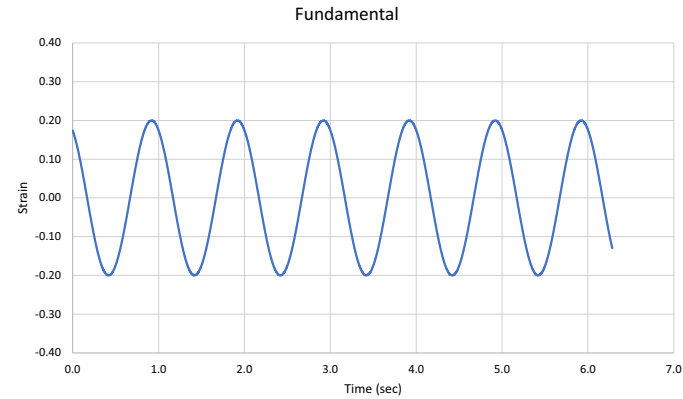


Fig. 31.3 Examples of multiwave oscillatory deformations. In each case, the Y-axis is the strain imposed on the sample while the X-axis is the time (in seconds). **Top left:** The fundamental oscillation at 1 Hz. **Top right:** Adding the second harmonic (2 Hz). **Bottom left:** Adding both the second and fifth harmonics. **Bottom right:** Adding the second, fifth, and 10th harmonics.

by Billotte and coworkers [29] has demonstrated the combination of heat flux and DMA measurements to monitor cure of a reacting resin via the heat of reaction, effectively combining DMA and thermal analysis in a single test to measure resin curing and the dynamic moduli. This study also tracked gap changes during the DMA measurement as well by holding the test specimen with a fixed compressive load and allowing the plate gap to adjust in response to chemical shrinkage. Work by Hedegaard and coworkers [13] further demonstrated that tracking the gap (and therefore, both thermal expansion and chemical shrinkage) in this way could be used to predict conversion and group TTCS data into isoconversion batches based on isoshrinkage states, even in the absence of other online thermal or chemical measurements. Knowledge of density as a function of conversion allowed for the quantitative evaluation of conversion during the DMA experiment.

Methods for controlling the initial cure level of the DMA samples have been documented by Hedegaard and coworkers [13]. In their experiments, prechilled plates were used to minimize conversion during sample preparation and test initiation.

TTCS characterization of an epoxy resin sample was demonstrated by Hedegaard and coworkers [13]. In their work, an ARES G2 strain-controlled rheometer was used to perform shear DMA measurements during curing, using 25 mm parallel plates. Tests were performed using temperature ramps between 0.5 °C/min and 5 °C/min, with the temperature ranging from 30 °C to 90 °C. Samples were repeatedly subjected to a multiwave strain oscillation during each experiment, enabling the collection of data over a range of temperatures, frequencies, and conversion levels.

Following acquisition, the data were grouped by conversion level, and TTS principles were applied to generate the master curves associated with each isoconversion level (Fig. 31.4). A reference temperature of 60 °C was used.

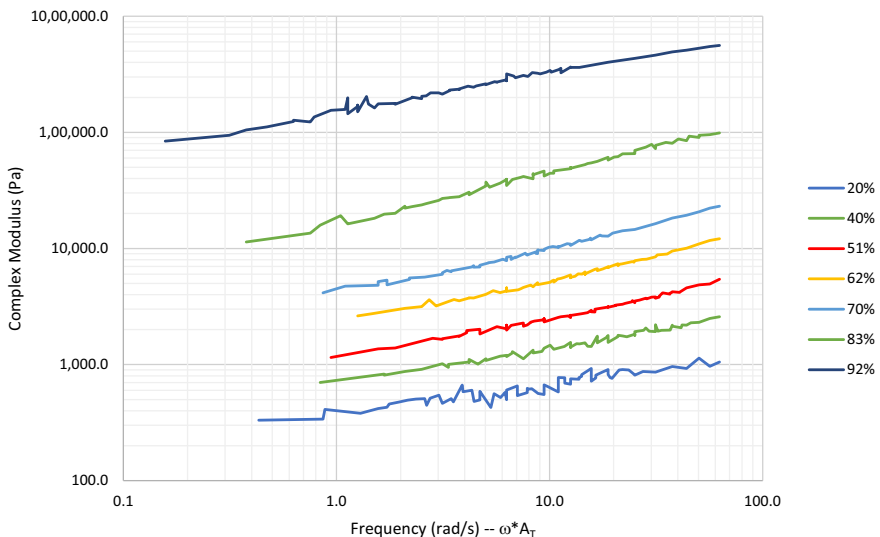


Fig. 31.4 TTS master curves of the complex shear modulus at various isoconversion states. Reference temperature was 60 °C.

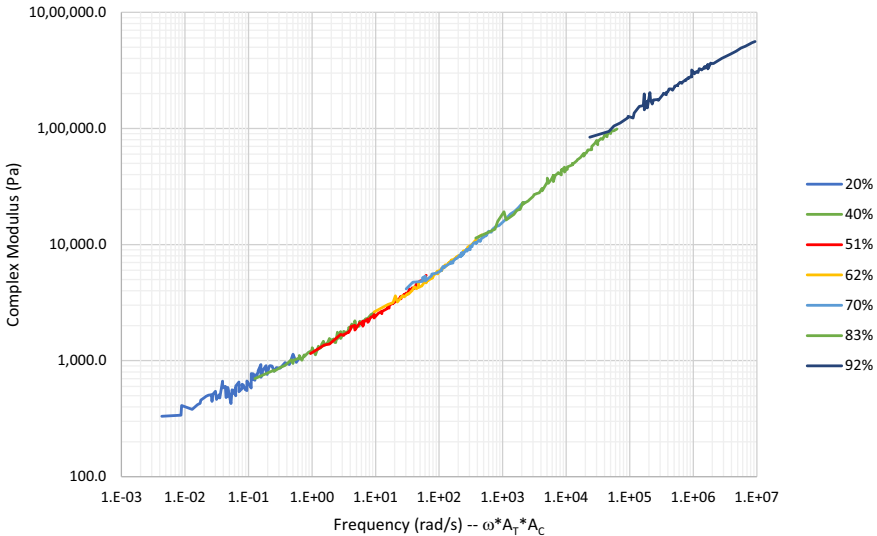


Fig. 31.5 TTCS master curve for complex modulus G^* , at reference conditions of 51% conversion and 60°C.

The isoconversion master curves were subsequently shifted by using TTCS principles to form a single master curve (Fig. 31.5). A reference conversion level of 51% was used.

For use in simulation of curing processes, the temperature- and conversion-dependent shift factor can be stored in a tabular form. Alternatively, common shift factor equations such as the Williams-Landel-Ferry (WLF) and Arrhenius equations can be fit to the data. Note that if shift factors are plotted vs. the difference between the experimental temperature value T and the conversion-dependent glass transition temperature $T_g(\alpha)$, the values collapse onto a single curve (Fig. 31.6). The plot includes the fit obtained for a WLF function described in terms of this temperature differential [12,13,30]:

$$A_{TTCS}(T, T_g(\alpha)) = \log \left[\frac{-C_1 * (T - T_g(\alpha) - (T_{ref} - T_g(\alpha_{ref})))}{C_2 + (T - T_g(\alpha) - (T_{ref} - T_g(\alpha_{ref})))} \right] \quad (31.9)$$

where T_{ref} and α_{ref} are the reference temperature and reference conversion used during TTCS, respectively, and C_1 and C_2 are the fitted WLF parameters.

The conversion-dependent glass transition temperature $T_g(\alpha)$ can be defined using the equations described by Hale and coworkers [31]. For many materials, the Havlicek and Dusek equation describes $T_g(\alpha)$ reasonably well over the full range of conversion, and is defined as:

$$\frac{1}{T_g(\alpha)} = \frac{1 - \alpha}{T_g(0)} + \frac{\alpha}{T_g(1)} + C\alpha(1 - \alpha) \quad (31.10)$$

where C is an experimentally determined fitting constant.

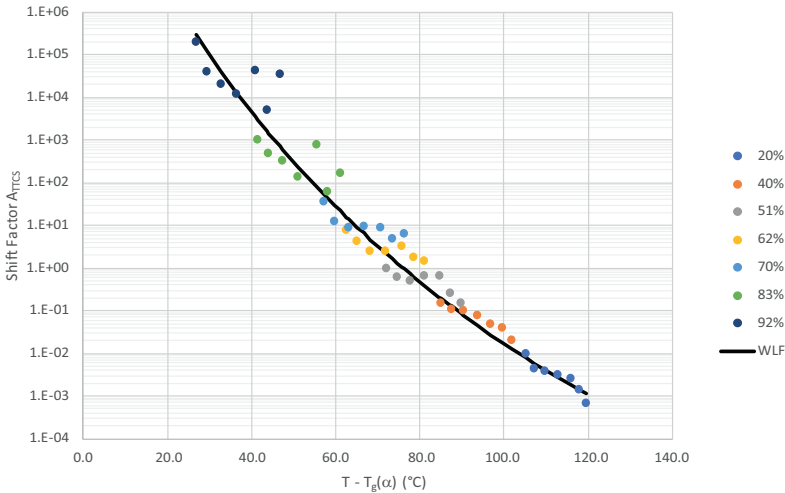


Fig. 31.6 Total TTCS shift factors plotted against $T - T_g(\alpha)$. The solid line shows the corresponding WLF model fit using Eq. (31.9).

Obtaining $T_g(\alpha)$ data can be challenging because the calorimetric or mechanical methods typically used in T_g determination can further advance the curing reaction. However, it can be measured directly using DSC temperature scans on resins at variable degrees of known conversion [32]. Alternatively, if direct measurements of T_g are not practical, then $T_g(\alpha)$ can be indirectly inferred by first determining the T_g of the fully cured resin (a simple task using either DMA or DSC) and then determining the function required to achieve superposition of the remainder of the isoconversion sets of shift factors from TTCS [13].

For time-domain analysis of curing processes, the frequency-domain storage modulus $G'(\omega)$ and loss modulus $G''(\omega)$ obtained using DMA must typically be used to derive a Prony series representation consisting of a finite number of relaxation modulus G_i and relaxation time τ_i pairs [Ref]. The Prony series parameters can be derived through optimization of the fit to the equations:

$$G'(\omega)|_{T_{ref}, \alpha_{ref}} = G_{\infty}(\alpha) + \sum \frac{G_i \omega^2 \tau_i^2}{1 + \omega^2 \tau_i^2}, G''(\omega)|_{T_{ref}, \alpha_{ref}} = \sum \frac{G_i \omega \tau_i}{1 + \omega^2 \tau_i^2} \quad (31.11)$$

where ω is the reduced frequency resulting from the TTCS shifting operations, and $G_{\infty}(\alpha)$ is the conversion-dependent long-term modulus of the material (included to capture the effects of gelation). This long-term modulus can be described using the equation [30]:

$$G_{\infty}(\alpha) = G_{\infty}(1) \left(\frac{\alpha^2 - \alpha_{gel}^2}{1 - \alpha_{gel}^2} \right)^{8/3} \quad (31.12)$$

where $G_{\infty}(1)$ is the plateau modulus at 100% conversion, and α_{gel} is the gel point conversion.

31.3.3 Thermal conductivity and thermal expansion

Accepted methods for the measurement of thermal conductivity include the use of a thermal interface material (TIM) tester following a testing procedure such as that outlined in ASTM D5470-17 [33]. In these tests, a material sample of thickness t and cross-sectional area A is placed between two platens, one of which is heated so that a constant temperature differential ΔT is maintained between the platens. The heat flow q required to maintain this temperature difference is measured, and an effective thermal conductivity k is calculated using the equation:

$$k = \frac{qt}{A\Delta T} = \frac{t}{RA} \quad (31.13)$$

where $R = \Delta T/q$ is the thermal resistance. The measured thermal conductivity includes the contact resistance across the two interfaces on either side of the sample material. Depending on the conductivity and wetting behavior of the sample material, contact resistances could significantly affect the measured conductivity. To account for this, tests are performed using multiple sample thicknesses. The inverse of the slope fit to a plot of $R \cdot A$ versus thickness yields the conductivity of the sample material (Fig. 31.7). For neat structural adhesives, thermal conductivity values of approximately 0.2–0.3 W/mK are typically observed. Common thermally conductive

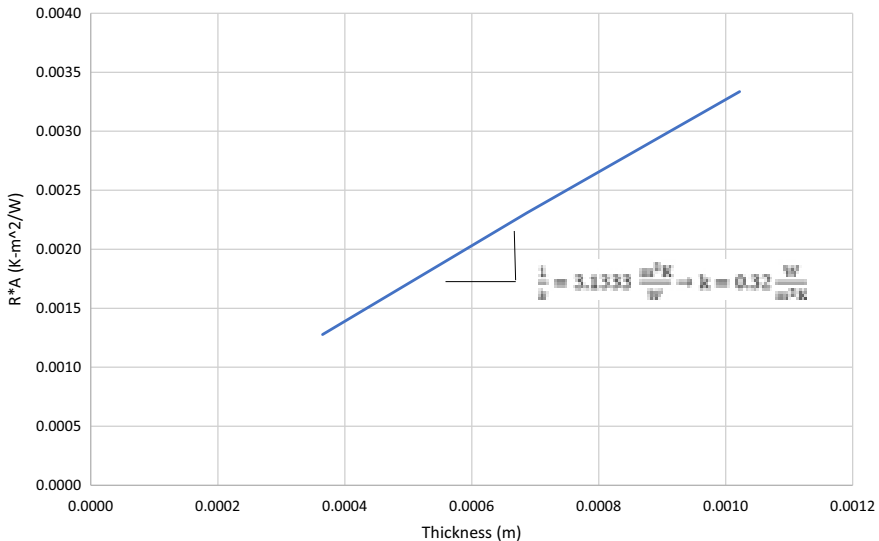


Fig. 31.7 Determination of thermal conductivity from the slope of thermal resistance vs. the thickness curve.

composite adhesives may reach 2–3 W/mK with high conductivity adhesives potentially reaching 10 W/mK. These higher conductivities are typically reached through the incorporation of significant amounts of high thermal conductivity inorganic fillers and can lead to a significant trade-off in the adhesive strength and mechanical properties of the material.

Alternatively, thermal conductivity can be measured using laser flash analysis (LFA). Although this technique measures the thermal diffusivity ϕ of a material, the diffusivity can be converted to a thermal conductivity if density ρ and heat capacity C_p are known:

$$k = \phi C_p \rho \quad (31.14)$$

Note that contact methods such as TIM are generally easier to use with soft materials with good wetting properties while LFA is more convenient for use with stiffer materials.

CTE values can be measured using thermal mechanical analysis (TMA) techniques, as described in ASTM E831. For solid materials such as a cured structural adhesive, a small cylindrical sample of thickness t is placed onto a TMA plate and a probe is brought into contact with the exposed surface using a small preload. The temperature is adjusted and the relative displacement between the plate and probe $u(T)$ is measured as a function of temperature. Frequently, the testing cycle is repeated to ensure the material is fully conditioned and nonreversible distortions have been worked out of the sample. Secant CTE values $\beta_s(T)$ are extracted once the measured thermal strain curves have stabilized using the equation:

$$\beta_s(T) = \frac{u(T)}{t} \frac{1}{(T - T_o)} \quad (31.15)$$

where T_o is the initial temperature used in the test.

In the cured state, many structural adhesives display a bilinear thermal expansion curve. For neat epoxy resin systems, expansion coefficient values below T_g are typically on the order of 70–100 ppm/C. Above T_g , expansion coefficient values on the order of 150–200 ppm/C are typical. Other classes of structural adhesives can show much higher values, depending on crosslink density. Typically, the addition of inorganic fillers (for example, fused silica or alumina) will lead to a reduction in the thermal expansion of the structural adhesive, and highly filled adhesives can have CTEs on the order of 30 ppm/C or less. The CTE of the liquid state can be measured with special volumetric probes that are standard options on modern TMAs. CTE values for structural adhesive in their liquid state are typically on the order of 200 ppm/C. Note that the CTE values associated with common substrates such as glass, aluminum, and steel are on the order of 3–23 ppm/C. The mismatch in thermal expansion between the substrates and the adhesive can therefore be of significant interest in many applications, and can induce significant temperature-induced stresses.

31.3.4 Density and chemical shrinkage

Density is commonly determined using Archimedes method, which involves the measurement of the volume of liquid displaced by a sample of known mass. A variety of commercial density balances are available to perform these measurements. Note that avoiding air entrainment in the material is very important for accurate measurement. Determination of the density of a fully cured adhesive is generally trivial. To characterize density as a function of conversion, however, special techniques may be required. For example, samples can be produced by dispensing and partially curing the adhesive between release liners or other substrates of known mass m_r and density ρ_r . DSC or FTIR techniques can be used to determine the cure state of the material at that point. The total mass m_t and (potentially conversion-dependent) density $\rho_t(\alpha)$ of the composite are then measured with a density balance, and the (potentially conversion-dependent) density of the adhesive $\rho_a(\alpha)$ is derived using the equation:

$$\rho_a(\alpha) = \frac{m_t - m_r}{\frac{m_t}{\rho_t(\alpha)} - \frac{m_r}{\rho_r}} \quad (31.16)$$

The density of the liquid ρ_l and solid ρ_s states can be compared to determine the total volumetric shrinkage γ of the material via the following equation, where a positive value for γ implies shrinkage of the adhesive:

$$\gamma = \frac{\rho_s - \rho_l}{\rho_l} \quad (31.17)$$

31.3.5 Model validation tests

The cure modeling procedure (described in Section 31.4) can be validated through comparison of the measured and predicted responses associated with simple curing experiments, including bilayer strip tests and the test described by Watts [9]. Bilayer strips are commonly used to study the effects of mismatched thermal expansion coefficients [34–38], but are only infrequently referenced in curing applications [8]. The Watts test was specifically designed to quantify the magnitude of chemical shrinkage strains and residual stresses.

In the bilayer strip test, adhesive is coated onto thin shims of uniform thickness. The samples are then processed through a curing and cooling cycle, and the resulting curl (typically represented using the symbol κ , and defined as the reciprocal of the radius of curvature) is measured. One method of measuring the curl involves the use of a *Kappa gauge* [39] (Fig. 31.8).

In the Watts test, an adhesive sample is dispensed onto a thick glass slide and centered within a brass ring. A thin glass cover slip is then pressed onto the assembly to form a nominally cylindrical adhesive specimen (Fig. 31.9). Following the curing, cooling, and relaxation cycle, the deflection profile of the cover slip is measured using a profilometer.

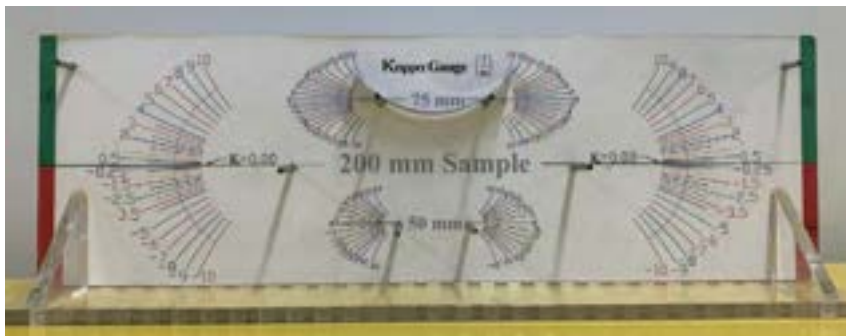


Fig. 31.8 Kappa gauge device.

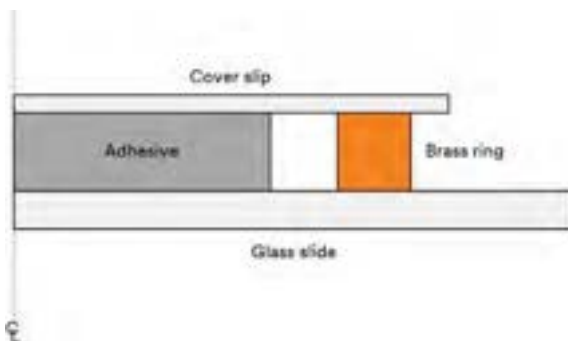


Fig. 31.9 Watts test geometry.

31.4 Modeling methods

31.4.1 Modeling framework

Because the mechanical properties and chemical strains evolve as a function of the conversion, and because the temperature-dependent conversion rate is often strongly influenced by the exothermic reaction, the simulation of curing processes must involve a coupling of the thermal and mechanical behaviors [4,20,21]. Due to the exotherm, a transient solution procedure is required for simulation of the heat transfer problem. Because inertial effects are negligible, a static or quasistatic solution procedure is generally sufficient for simulation of the mechanical response.

Coupled thermal-structural elements with temperature and displacement degrees of freedom are available within most commercial finite element programs. Conversion, however, must typically be represented using a *field variable*. User-defined subroutines are generally used to calculate the conversion rate as well as to update the total conversion, mechanical properties, thermal and chemical strains, and heat generation rate.

Various material models have been used, including elastic, elastic–plastic, and viscoelastic models [4,6]. Early modeling efforts focused primarily on the evolution of the elastic modulus during curing and ignored viscoelastic effects. More recent works have included evolution of the viscoelastic properties using a temperature- and conversion-dependent shift factor [7,13]. Thermal expansion has been addressed using constant, temperature-dependent, and temperature- and cure-dependent CTE values calibrated from experiments.

31.4.2 Modeling procedure

The conversion rate is calculated using an appropriate kinetic equation (see, for example, Eq. 31.1) or, alternatively, through interpolation from a table that defines conversion rate as a function of conversion and temperature. To obtain the total current conversion, an explicit time-integration procedure is typically used:

$$\alpha^{n+1} = \alpha^n + \dot{\alpha}(\bar{T}) \Delta t \quad (31.18)$$

where n denotes the time step number, $\bar{T} = (T^n + T^{n+1})/2$ is the average temperature during the time step, and Δt is the size of the time step.

Calculation of the conversion rate and update of the total conversion are typically done from within a user-defined subroutine designed for the calculation of field variables (e.g., the Abaqus USDFLD and/or UFIELD subroutines). The volumetric heat generation rate (see Eq. 31.2) is typically defined using a user-defined subroutine intended for specification of heat sources or sinks (e.g., the Abaqus HETVAL subroutine).

The current value of the elastic modulus is generally obtained by interpolation from a table defining the modulus as a function of conversion and temperature. Analytical forms can, of course, be used if available. Similarly, the viscoelastic shift factor is typically defined in a tabular form and calculated through interpolation. If the finite element code used supports tabular definition of properties as a function of temperature and field variable values, this interpolation process will be performed automatically, and the stress (and Jacobian) updates will be handled by the normal solution algorithms. If the finite element code used does not support this type of tabular definition, then a user-defined material subroutine will be required to update the elastic and viscoelastic properties, the viscous strains, the stresses, and the Jacobian (e.g., the Abaqus UMAT subroutine).

For a small-strain viscoelastic formulation, the viscous strain tensor $\boldsymbol{\epsilon}_i^{n+1}$ associated with the Prony series term i at time step $n+1$ is defined as [Abaqus Theory Manual, [40]]:

$$\begin{aligned} \boldsymbol{\epsilon}_i^{n+1} &= \boldsymbol{\epsilon}_i^n + \Delta \boldsymbol{\epsilon}_i \\ &= \boldsymbol{\epsilon}_i^n + \frac{\tau_i}{\Delta \tau} \left(\frac{\Delta \tau}{\tau_i} + e^{-\Delta \tau / \tau_i} - 1 \right) \Delta \boldsymbol{\epsilon} + \left(1 - e^{-\Delta \tau / \tau_i} \right) (\boldsymbol{\epsilon}^n - \boldsymbol{\epsilon}_i^n) \end{aligned} \quad (31.19)$$

where τ_i is the relaxation time associated with Prony series term i , $\boldsymbol{\epsilon}^n$ is the total strain tensor at time step n , and $\Delta\tau = \Delta t / A_{TTCS}(T, \alpha)$ is the reduced time increment calculated using the temperature- and conversion-dependent shift factor $A_{TTCS}(T, \alpha)$.

Using the conversion- and temperature-dependent shear modulus $\mu^{n+1} = \mu(\alpha^{n+1}, T^{n+1})$ value, the stress tensor $\boldsymbol{\sigma}^{n+1}$ at time step $n+1$ can be defined as:

$$\boldsymbol{\sigma}^{n+1} = 2\mu^{n+1} \left(\boldsymbol{\epsilon}^{n+1} - \sum_{i=1}^N g_i \boldsymbol{\epsilon}_i^{n+1} \right) \quad (31.20)$$

where g_i is the normalized shear modulus value associated with Prony series term i and N is the number of terms in the Prony series. The Jacobian can be derived through differentiation of the constitutive relationships as described, for example, in the *Abaqus Theory Manual* [40]. Alternatively, a numerical procedure can be used to derive the Jacobian [41].

The incremental thermal strain $\Delta\boldsymbol{\epsilon}_t$ can be defined as a function of a conversion- and temperature-dependent thermal tangent expansion coefficient $\beta_T(\alpha, T)$ and the temperature increment ΔT :

$$\Delta\boldsymbol{\epsilon}_t = \beta_T(\alpha, T) \Delta T \quad (31.21)$$

The incremental chemical strain is defined following Eq. (31.3). If the finite element code used supports the definition of *field expansions*, then the thermal and chemical strains can be defined using separate terms. If not, the thermal and chemical strains must be added to define a single, effective eigenstrain.

If the finite element code used supports the tabular definition of expansion coefficient values (thermal and/or field) as a function of temperature and field variables, then the simulation can be performed with the addition of a user-defined field only. If the finite element program used does not support this type of interpolation, then a user-defined subroutine for definition of thermal strains must be used (e.g., the Abaqus UEXPAN subroutine), and the resulting thermal strain must be interpreted as the total eigenstrain. Note that the output of separate thermal and chemical strain values could be achieved using state variables.

31.4.3 Model validation

As described in Section 31.3.5, the measured and predicted responses associated with simple curing experiments (including bilayer strip tests and the test described by Watts) can be used to validate cure modeling procedures and measured material properties. In both tests, a structural adhesive is dispensed onto a simple assembly, heated to initiate and maintain the curing process, then cooled. Following a relaxation period, the deformations are measured to quantify the effects of chemical shrinkage.

Assuming the deformed shape of the composite strip is a circular segment (and ignoring edge effects), the bilayer strip test can be simulated using a simple plane strain model representing an arbitrary periodic segment of the strip (Fig. 31.10).

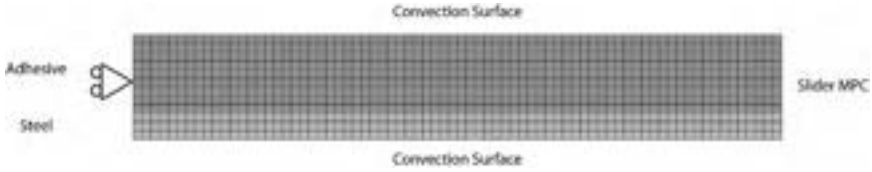


Fig. 31.10 Model of a bilayer strip.

Symmetry is assumed along one edge, and a periodic condition is enforced on the other using a multipoint constraint (MPC) that enforces a “planar surfaces remain planar” (i.e., “slider”) condition. Heating and cooling loads are applied to the exposed surfaces using specified convection coefficient and bulk temperature histories. The deformed coordinates of the nodes at the bottom of the metallic strip can be used to calculate the radius of curvature resulting from the residual chemical strains using a circle fitting algorithm [42]. A comparison of measured and predicted results is presented in Fig. 31.11. Note that the model correctly predicts the asymptotic approach to a limiting curl at higher coating thicknesses. Although the correlation does not appear exceptional, it should be noted that both the experimental characterization and the modeling procedures are complex and subject to sensitivity to several variables, including humidity and other environmental conditions.

The Watts test can be modeled using an axisymmetric approximation (Fig. 31.8). Again, thermal loads are applied using specified convection coefficient and bulk temperature histories. The adhesive interfaces are assumed to be perfectly bonded (mechanically and thermally), as is the interface between the glass slide and brass ring. A contact interface (that includes a thermal gap conductance) is used between the cover slip and brass ring.

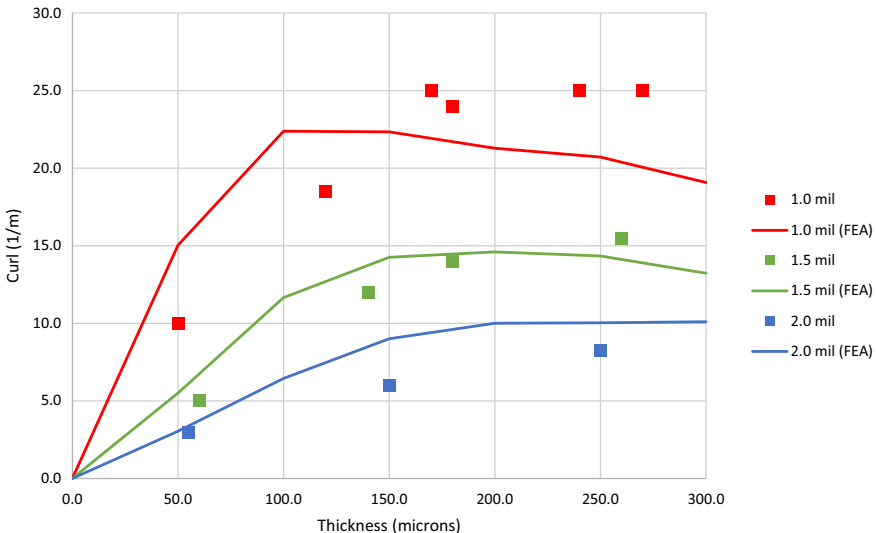


Fig. 31.11 Comparison of measured and predicted radius-of-curvature values.

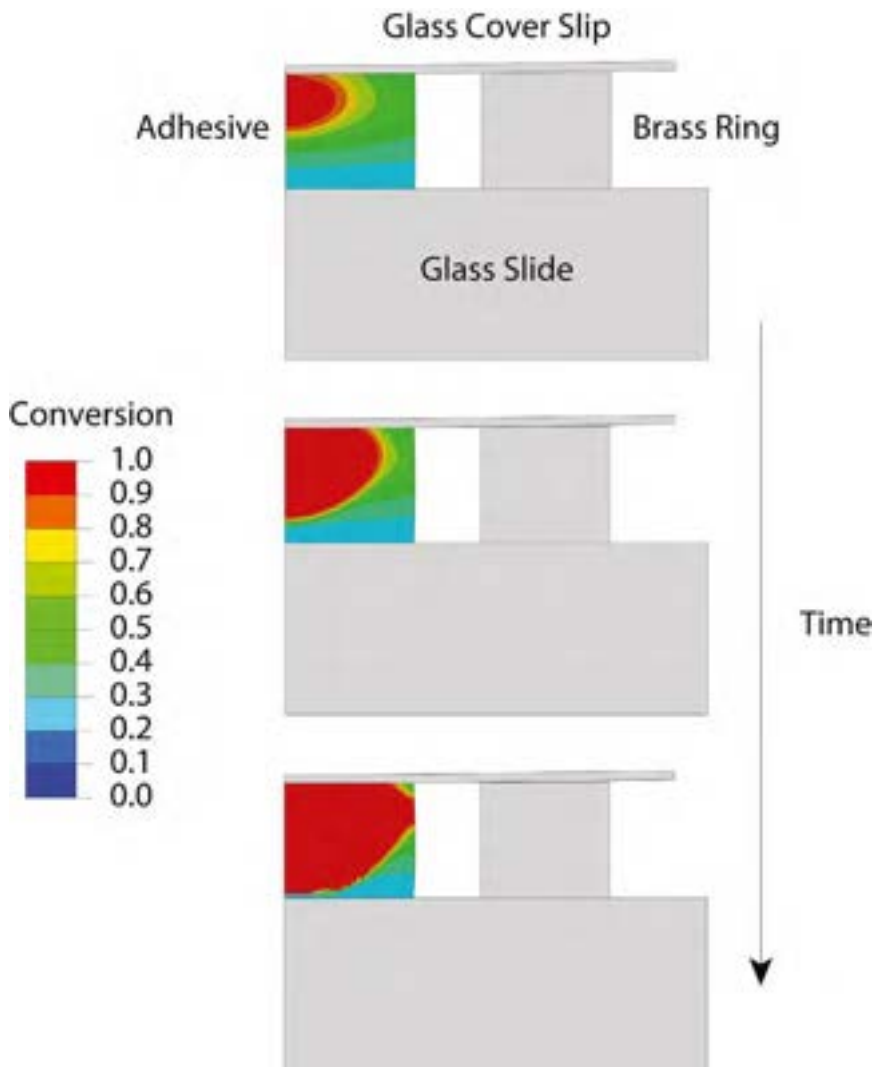


Fig. 31.12 Axisymmetric model of the Watts test showing conversion front history.

An illustration of the predicted conversion front propagation is presented in Fig. 31.12. Note that the reaction is predicted to initiate at the top center of the adhesive sample, and is found to propagate spherically outward.

The deflection profile on the top of the cover slip can be extracted directly from the predicted nodal displacements and compared to the measured values (Fig. 31.13). The predicted displacement profile is, in general, consistent with the measured profiles. Discrepancies can again be attributed to the complexity of the experimental characterization and modeling methods and, in this case, due to limitations in controlling the initial geometry of the adhesive sample in the Watts test.

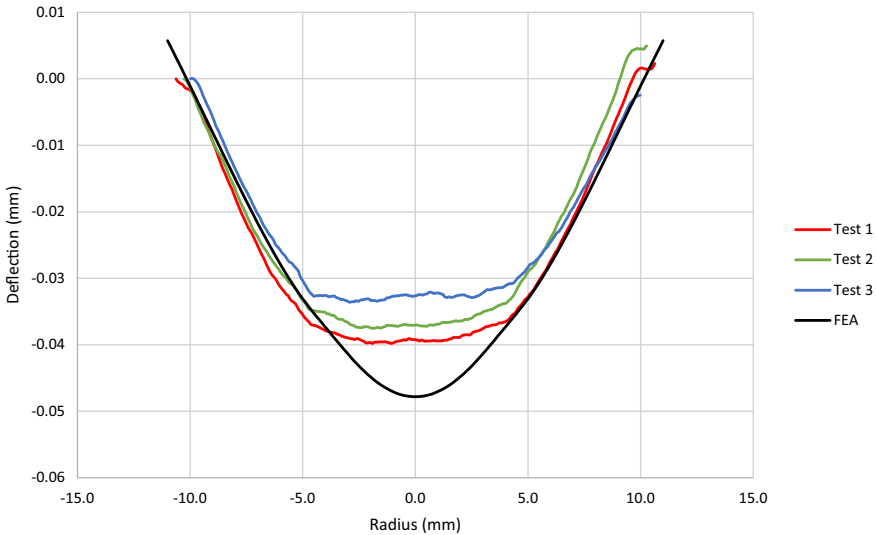


Fig. 31.13 Comparison of predicted and measured deflection profiles.

31.5 Additional notes

31.5.1 ABAQUS implementation of cure stress model

The cure modeling procedures described in this chapter are available within the commercial finite element program Abaqus (Dassault Systèmes) starting with version 2021 FD06 (released May 2021). The implementation uses the existing thermal-structural solution framework as well as the existing small-strain viscoelastic constitutive model (with temperature and field variable dependence). Parameter and property tables are used for the definition of the reaction kinetics, specific heat of reaction, and chemical shrinkage coefficient. The cure model is available as a “special purpose” material model that is activated using a material model name starting with “ABQ_CURE_MATERIAL.” For further information, see the *Abaqus Release Notes* and the *Abaqus Materials Guide* [43,44].

31.5.2 Experimental best practices

Measuring the viscoelasticity of a structural adhesive as it cures generally involves DMA testing performed in a rotational parallel plate (shear) configuration. Ideally, a large diameter plate is used when measuring low stiffness materials to maximize the signal-to-noise ratio. This may not be possible, however, because the modulus of the adhesive may vary by several orders of magnitude while curing. Curing studies are often conducted using a 25 mm parallel plate geometry for a more accurate

assessment of modulus prior to the gel point and may be repeated with 8 mm parallel plates to better characterize the material above the gel point. In either case, disposable plates are recommended as the plates become permanently adhered together by the end of each measurement. A gap of 0.5 mm is recommended as opposed to the more typical 1–2 mm, as thinner samples generate less total heat during the exothermic reaction and thus improve temperature control and reduce the role of the adhesive's thermal conductivity.

Zero axial force should be maintained throughout the curing DMA tests so that the plate gap adjusts to thermal expansion and chemical shrinkage in the specimen. This also permits the use of relative gap changes as an online proxy measurement for conversion. Other conversion-monitoring systems that can be combined with the DMA, such as FTIR and thermal analysis, should be used where available as they greatly simplify the matter of relating chemical conversion to viscoelastic properties.

A TTS master curve of the fully cured adhesive may be easily added to the TTCS master curve and may be obtained by either fully curing the resin between 8 mm parallel plates and then running the TTS experiment, or by curing the adhesive off the rheometer and then performing rectangular torsion DMA experiments.

Multiwave oscillatory measurements are recommended during curing studies whenever available, as they significantly reduce experimental time and eliminate the drift in conversion that happens when running frequencies sequentially as in a typical frequency sweep.

The choice of isothermal curing studies versus nonisothermal temperature ramp curing studies is primarily a question of the speed at which the curing reaction occurs. If the adhesive completely cures within a matter of minutes, then nonisothermal methods are preferred as the material can be loaded on the rheometer at low temperatures and then rapidly heated, such that minimal reaction occurs during sample dispensing and trimming. However, the TTCS analysis of nonisothermal curing data is more demanding of the analyst, as each experiment involves a continuous change in both conversion and temperature. As such, isothermal curing methods are preferred for slower curing adhesives (ones that take a matter of hours to fully cure) as it is the experimentally simpler of the two options.

References

- [1] M. Banea, L. Da Silva, R. Campilho, in: T. Amancio-Filho, L.-A. Blaga (Eds.), *Principles of Adhesive Bonding in Joining of Polymer-Metal Hybrid Structures: Principles and Applications*, John Wiley & Sons, 2018, pp. 3–27.
- [2] F. Chaves, L. da Silva, M. de Moura, D. Dillard, V. Esteves, Fracture mechanics tests in adhesively bonded joints: a literature review, *J. Adhes.* 90 (12) (2014) 955–992.
- [3] A. Pocius, *Adhesion and Adhesives Technology*, Carl Hanser Verlag, 2012, pp. 1–14 (Chapter 1).
- [4] J. Kropka, S. Spangler, M. Stavig, R. Chambers, Residual stress: prediction during polymer cure and effects on the strength of adhesive joints, Sandia Report SAND2013-8681, 2013.
- [5] K. Patankar, D. Dillard, K. Fernholz, Characterizing the constitutive properties and developing a stress model for adhesive bond-line readout, *Int. J. Adhes. Adhes.* 20 (2013) 149–157.

- [6] M. Abouhamzeh, J. Sinke, K. Jansen, R. Benedictus, Closed form expression for residual stresses and warpage during cure of composite laminates, *Compos. Struct.* 133 (2015) 902–910.
- [7] B. Patham, Multiphysics simulations for cure residual stresses and Springback in a thermoset resin using a viscoelastic model with cure-temperature-time superposition, *J. Appl. Polym. Sci.* (2013), <https://doi.org/10.1002/APP.38744>.
- [8] M. Zarrellia, I. Partridge, A. D'Amorea, Warpage induced in bi-material specimens: coefficient of thermal expansion, chemical shrinkage and viscoelastic modulus evolution during cure, *Composites Part A* 37 (2006) 565–570.
- [9] D. Watts, A. Cash, Determination of polymerization shrinkage kinetics in visible-light-cured materials: methods development, *Dent. Mater.* (1991) 281–287.
- [10] C. Li, Y. Wang, J. Mason, *The Effects of Curing History on Residual Stresses in Bone Cement During Hip Arthroplasty*, Wiley Interscience, 2004, <https://doi.org/10.1002/jbm.b.30016>.
- [11] D. Adolf, R. Chambers, A thermodynamically consistent, nonlinear viscoelastic approach for modeling thermosets during cure, *J. Rheol.* 51 (2007) 23.
- [12] Y. Eom, L. Boogh, V. Michaud, P. Sunderland, J. Manson, Time-cure-temperature superposition for the prediction of instantaneous viscoelastic properties during cure, *Polym. Eng. Sci.* 40 (6) (2000) 1281–1292.
- [13] A. Hedegaard, E. Breedlove, S. Carpenter, V. Jusuf, C. Li, D. Lindeman, Time-temperature-cure superposition (TTCS) methods for determining viscoelasticity of structural adhesives during curing, in: 44th Meeting of the Adhesion Society, 2021.
- [14] S. Simon, G.B. McKenna, O. Sindt, Modeling the evolution of the dynamic mechanical properties of a commercial epoxy during cure after gelation, *J. Appl. Polym. Sci.* 70 (2000) 495–508.
- [15] A.T. DiBenedetto, Prediction of the glass transition temperature of polymers: a model based on the principle of corresponding states, *J. Polym. Sci. Part B: Polym. Phys.* 25 (1987) 1949–1969.
- [16] F. Dimier, N. Sbirrazzuoli, B. Vergnes, M. Vincent, Curing kinetics and chemorheological analysis of polyurethane formation, *Polym. Eng. Sci.* 44 (3) (2004) 518–527.
- [17] M. Kamal, S. Sourour, Kinetics and thermal characterization of thermoset cure, *Polym. Eng. Sci.* (1973) 13–59.
- [18] F. Incropera, D. DeWitt, T. Bergman, *Fundamentals of Heat and Mass Transfer*, sixth ed., John Wiley, 2007 (Chapter 2).
- [19] C.M. Neag, Thermomechanical analysis in materials science, in: A.T. Riga, C.M. Neag (Eds.), *Material Characterization by Thermomechanical Analysis*, ASTM STP 1136, American Society for Testing and Materials, Philadelphia, 1991, pp. 3–21.
- [20] V. Costa, A. Sousa, Modeling of flow and thermo-kinetics during the cure of thick laminated composites, *Int. J. Therm. Sci.* 42 (2003) 15–22.
- [21] J.C. Dominguez, Thermosets (second edition), in: *Rheology and Curing Process of Thermosets*, 2018, pp. 115–146 (Chapter 4).
- [22] ASTM D4440-15, Standard Test Method for Plastics: Dynamic Mechanical Properties Melt Rheology, ASTM International, West Conshohocken, PA, 2015.
- [23] D. Adolf, J.E. Martin, Time-cure superposition during cross-linking, *Macromolecules* 23 (1990) 3700–3704.
- [24] D. Adolf, J.E. Martin, J.P. Wilcoxon, Evolution of structure and viscoelasticity in an epoxy near the sol-gel transition, *Macromolecules* 23 (2) (1990) 527–531.
- [25] S. Saseendran, M. Wysocki, J. Varna, Viscoelastic behavior of LY5052 epoxy resin in rubbery state during curing, in: 17th European Conference on Composite Materials (Conference Paper). Munich, Germany, 26–30th June, 2016.

-
- [26] TA Instruments, Rheology—Multi-Wave Oscillation, RH096, 2019.
- [27] B. Lucio, J.L. de la Fuente, Non-isothermal DSC and rheological curing of ferrocene-functionalized, hydroxyl-terminated polybutadiene polyurethane, *React. Funct. Polym.* 107 (2016) 60–68.
- [28] N.W. Radebe, C. Fengler, C.O. Klein, R. Figuli, M. Wilhelm, Rheo-IR: a combined setup for correlating chemical changes via FTIR spectroscopy and rheological properties in a strain-controlled rheometer, *J. Rheol.* 65 (2021) 681.
- [29] C. Billotte, F. Bernard, E. Ruiz, Chemical shrinkage and thermomechanical characterization of an epoxy resin during cure by a novel in situ measurement method, *Eur. Polym. J.* 49 (2013) 3548–3560.
- [30] H.H. Winter, F. Chambon, Analysis of linear viscoelasticity of a crosslinking polymer at the gel point, *J. Rheol.* 30 (1986) 367.
- [31] A. Hale, C.W. Macosko, H.E. Bair, Glass transition temperature as a function of conversion in thermosetting polymers, *Macromolecules* 24 (1991) 2610–2621.
- [32] M. Urbaniak, A relationship between the glass transition temperature and the conversion degree in the curing reaction of the EPY[®] epoxy system, *Polimery* 56 (3) (2011).
- [33] ASTM D5470-17, Standard Test Method for Thermal Transmission Properties of Thermally Conductive Electrical Insulation Materials, ASTM International, West Conshohocken, PA, 2017.
- [34] L. Freund, J. Floro, E. Chason, Extensions of the Stoney formula for substrate curvature to configurations with thin substrates or large deformations, *Appl. Phys. Lett.* 74 (1999) 1987.
- [35] H. Hsueh, D. Chiang, S. Lee, Modeling of relaxation of viscoelastic stresses in multi-layered thin films/substrate systems due to thermal mismatch, *Thin Solid Films* 518 (2010) 7497–7500.
- [36] G. Stoney, The tension of metallic films deposited by electrolysis, *Proc. R. Soc. Lond.* A82 (1909) 172.
- [37] Y. Zhang, Y. Zhao, Applicability range of Stoney's formula and modified formulas for a film/substrate bilayer, *J. Appl. Phys.* 99 (2006), 053513.
- [38] T. Chou, S. Yang, K. Chiang, Overview and applicability of residual stress estimation of film-substrate structure, *Thin Solid Films* 519 (2011) 7883–7894.
- [39] R. Swanson, Measurement of Web Curl. Association of Industrial Metallizers, Coaters and Laminators, AWEB Conference Proceedings, 2006.
- [40] Dassault Systèmes, Abaqus Theory Manual, 2021.
- [41] W. Sun, E.L. Charkof, M.E. Levenston, Numerical approximation of tangent moduli for finite element implementations of nonlinear hyperelastic material models, *J. Biomech. Eng.* (2008).
- [42] C. Rusu, T. Marius, P. Kuosmanen, E. Delp, Classical geometrical approach to circle fitting—review and new developments, *J. Electron. Imaging* 12 (1) (2003) 179–193.
- [43] Dassault Systèmes, Abaqus Materials Guide, 2021.
- [44] Dassault Systèmes, Abaqus Release Notes, 2021.

This page intentionally left blank

Digital image correlation: Advancing mechanical property characterization of adhesive joints

32

*Christopher M. Jackson^a, Jeffrey A. McGuire^b, Martin E. Losada^c,
Raffaella De Vita^b, and David A. Dillard^b*

^aCivil and Environmental Engineering Department, Virginia Tech, Blacksburg, VA, United States, ^bDepartment of Biomedical Engineering and Mechanics, Virginia Tech, Blacksburg, VA, United States, ^cCoatings Innovation Center, PPG Industries, Inc., Allison Park, PA, United States

32.1 Introduction

Imaging methods have been an essential tool in experimental stress analysis for decades, with a variety of techniques including photoelasticity [1], interferometry [2], shearography [3], caustics [4,5], and other photographic recording methods [6–8]. Though widely practiced for decades for a wide range of materials and applications, these methods have often found limited applications assessing stress or strain distributions in adhesive joints. Reasons likely include the inherent limitations of the techniques coupled with the unique complications associated with bonded joints, which are often opaque, multimaterial systems bonded with a relatively thin adhesive layer. However, a more recent innovation, digital image correlation (DIC) appears poised for expanded use in a wide range of applications, including adhesive bond evaluations. Although lacking the resolution of Moirè interferometry [2], DIC is often easier to use, as it does not require the sophisticated optics and isolation tables often needed with interferometric methods. And, as the method is agnostic to the materials being studied, it does not require the transparent, birefringent materials (or coatings) needed for photoelasticity. Furthermore, DIC's ability to determine both in-plane and out-of-plane deformations simultaneously, and at virtually any size scale, means it can span applications from microscopic to very large structures. In this chapter, we review recent applications of the DIC method to experimentally characterize adhesively bonded joints, with a special focus on fracture behavior characterization.

In the last decade, many researchers have found ways to use DIC for mechanical analyses of a wide variety of materials and engineering components and structures. DIC applications for soft biological tissues and kirigami-inspired films bonded to skin have been reported, suggesting further opportunities for use of such methods for soft matter and biomedical applications. For example, McGuire et al. [9] used DIC to characterize constitutive and tearing behavior at strains as high as 60% in biaxially loaded, multilayer vaginal tissue, and Zhao et al. [10] used the technique for the strain characterization of slit skin-covering prototype mimics for flexible electronics or

medical bandages. Results for elastomers include viscoelastic Poisson's ratio characterization of silicone rubber during creep [11]. DIC methods have been employed to characterize residual stress development, for example by measuring bilayer curvature during hygrothermal cycling of fuel cell proton exchange membranes [12]. DIC was used in assessing repair strategies for composite materials, a critical issue in the aerospace industry, Caminero et al. [13,14] to evaluate the performance of different adhesively bonded repairs for a variety of flaws. On a much larger scale, civil engineers have used DIC to analyze the fracture of reinforced concrete specimens [15,16]. With the increased use of composite materials in retrofits of civil structures, researchers have used DIC to evaluate the bond strength of fiber-reinforced polymer (FRP) adhesively joined to concrete [17] as well as optimal anchoring patterns of FRP to masonry [18]. These studies using DIC to measure deformations for a broad range of materials including composite and viscoelastic materials make it a viable choice to evaluate the mechanical properties of adhesively bonded joints—the focus of this chapter.

The inevitable combining of multiple materials and complex design features in adhesive bonds leads to stress concentrations (or even singularities), especially at bond terminations [19,20]. Researchers have found that DIC can provide great insights into the magnitudes of local strain fields as well as the extent of these high-strain regions, which may then allow stresses to be inferred. In fact, DIC offers an important tool to explore well-known behavior in bonded joints as well as characterize new material systems and geometries. Some reported applications relate DIC results to classic mechanics models, including Winkler's beam on elastic foundation (BoEF) [21–23], Volkersen's shear lag [10,24], and Goland and Reissner's predictions of adherend bending and the combined effects of shear lag and BoEF models on the shear and peel stresses within adhesively bonded single-lap joints (SLJs) [25]. Examples of these applications include extension to inferring shear strains in pressure-sensitive tapes [26], shear block tests [24], and Arcan specimens [27,28].

In addition to strain and stress analysis and the extraction of constitutive properties, the DIC method has also found numerous applications in experimental fracture mechanics studies of monolithic, composite, and adhesively bonded systems. For example, in monolithic material fracture, DIC has been used to predict the fatigue growth of metal compact tension specimens [29]. Pankow et al. [30] showed that DIC was much more accurate than far-field measurements for determining the fracture properties of a woven carbon fiber composite. DIC is proving to be especially attractive for the fracture property behavior of tougher systems, where simpler stress distribution models and analysis methods for linear elastic, monolithic material fracture become less applicable. Analytical methods to extract fracture energy from adhesively bonded joints, such as the widely used double cantilever beam (DCB), include simple beam theory (SBT), corrected beam theory (CBT) [31], experimental compliance method (ECM or Berry method), and the Paris and Paris J -integral method involving end rotations [32]. While each of these methods has strengths and weaknesses for converting experimental data into quantifiable fracture energy values, they reach limits of accuracy or applicability, especially with increasingly tougher adhesives that may require thicker adherends to limit yielding. DIC allows one to capture

end rotations needed for the J -integral method, explore shear deformations often neglected in the data reduction methods and of even greater significance for anisotropic materials such as wood or laminated composites, and measure root rotations and displacements to evaluate BoEF and other model relevance. DIC is proving to be an enabling technology to extract the traction-separation laws (TSL) needed for cohesive zone models (CZM) in modern fracture analysis using the finite element method, and the length scales over which these act, which are important in such characterizations [33]. Comparisons of DIC output with finite element predictions allow for the validation of model assumptions and boundary conditions [23], or the extraction of material properties through inverse methods.

Section 32.2 provides a brief background on the DIC method. In addition, relevant details and practical guidelines are given on its implementation, including as related to bonded joint systems. Applications for determining constitutive properties, obtaining deformation and strain fields in bonded joints, inspecting joint integrity, and optimizing joint designs are reviewed in Section 32.3. Section 32.4 summarizes recent applications of DIC to enhance several traditional data analysis methods for Mode I fracture energy determination in adhesive fracture specimens with extensions to Mode II loading also included. Section 32.5 provides background on the CZM approach and the significance of TSLs for this approach while also reviewing DIC as an enabling technology to facilitate the extraction of TSLs. Implementation of these methods for a recent extension to mixed-mode model development and calibration for a structural adhesive are discussed in Section 32.6.

32.2 Digital image correlation background

Over the last decade, DIC has emerged as the preeminent method for acquiring the deformation data of a specimen to better estimate mechanical properties. Pioneered by Ranson and colleagues [34,35] in the 1980s as a tool to determine strain fields based on relative motions of random but identifiable features on a surface, DIC instruments and analysis procedures are now commercially available from several vendors. DIC is a noncontact, optical method that measures the surface displacements of speckle patterns over a sequence of images acquired during a test. Advances in the capabilities, especially in the last decade, have made DIC a very practical tool for researchers to use in experimental mechanics studies. Basic details of the DIC procedure for most commercial packages will be covered in this section, but for more detailed information on how DIC works, one should refer to Sutton et al. [36].

To perform DIC, one may utilize existing distinguishing features on a surface, though it more commonly needs a method of applying a contrasting speckle pattern to the surface being analyzed. Equipment requirements typically include either one (for two-dimensional (2D)-DIC) or two (three-dimensional (3D)-DIC) high-resolution cameras, light sources, and some sort of DIC analysis software. Perhaps the most common manner for applying a speckle pattern is using black and white spray paints to achieve optimal contrast. Typically, white paint is used as the base layer and

black paint is misted over this as the speckling color. The size of the droplets will vary based on the dispensing tool (i.e., airbrush or can of spray paint) and should be selected based on the size of both the specimen and the region of interest. Other methods of speckling such as applying ink [37], powder particles [38], or laser etching [39] can be used when the specimens are made of materials more compliant than paint or if the tests are being conducted in extreme environments. Powerful light sources are often needed to properly illuminate specimens for good contrast resolution. Using 2D-DIC, one camera is sufficient for in-plane deformation determination, provided there are negligible out-of-plane displacements, and allows for a simpler calibration procedure requiring the user to input information on the frame reference distance. 3D-DIC uses two cameras and the calibration procedure is more involved, requiring a series of calibration plate images for the DIC software to determine the position of the cameras with respect to each other and the specimen. Advantages include the ability to determine out-of-plane deformation fields and greater robustness of the in-plane analysis. It is important that high-resolution cameras are used for DIC, as they may need to capture strains on the order of 10^{-5} mm/mm [36]. Fig. 32.1 shows a 3D-DIC system being used to image a portion of an end-notched flexure (ENF) test and with a reference image of the specimen from one of the cameras.

DIC analysis software calculates displacements by discretizing the speckled region of interest into overlapping groups known as subsets. Subsets are small, typically square regions with their own unique grayscale pattern generated from the speckle pattern. Using the reference image, the center point of each subset is determined. In each subsequent image taken during the deformation of the specimen, a correlation algorithm is used to calculate the updated locations of the deformed subsets and their corresponding centers. The difference between the reference and updated coordinates returns a displacement vector. The step size, which is the distance between subset centers, dictates the number of data points used in the software's analysis. To determine strain fields, the DIC software will differentiate the displacement fields. This is

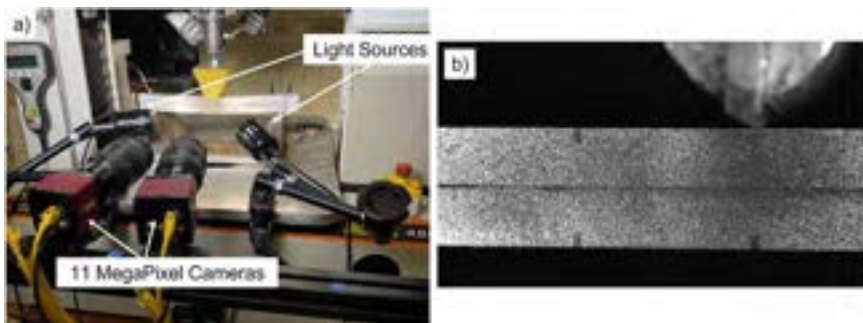


Fig. 32.1 (a) Example of a DIC system placed around an ENF test in a universal testing machine. Light source and camera placement must allow for proper illumination without obstructing the field of view. (b) A representative frame captured by one of the cameras, showing a speckled specimen in the vicinity of the loading tip.

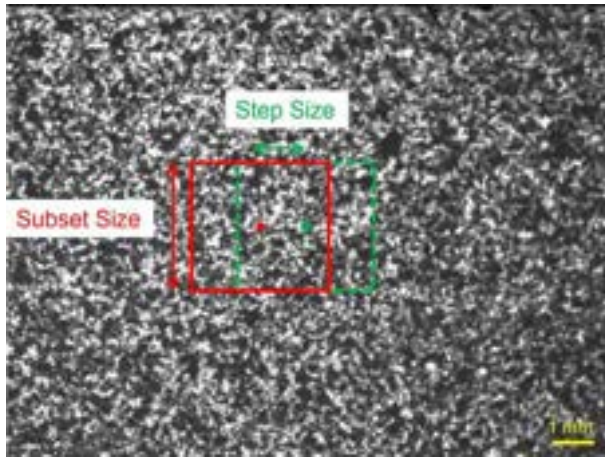


Fig. 32.2 Subset size and step size overlaid on a reference configuration speckle pattern for DIC. Subsets are generally square and step sizes will be offset in both the horizontal and vertical directions.

typically done via a Gaussian-weighted-averaging filtering operation that smooths the displacement data across a selected filtering length. A large step size will reduce the spatial resolution, reducing the accuracy of the differentiation used for strain calculations [36,40]. The filtering operation reduces noise, but can lead to erroneous measurements, thus user judgment is necessary to determine the validity of strain results, especially around discontinuities such as cracks or notches [40]. Examples of speckles, subsets, and step size are depicted in Fig. 32.2.

Getting the most accurate DIC measurements relies on a balance of the many parameters (i.e., field of view, speckle size, subset size, and step size) and may appear intimidating to new users; however, competence in the technique can be acquired rather quickly. Key factors that should be considered prior to running a DIC test are making sure the camera(s) can capture the full region of interest with sufficient resolution. When using DIC, it is very important to determine one's desired camera magnification, which may impact or be impacted by the experimental setup, desired resolution, and what is being measured [41]. If one wishes to capture a large, progressing fracture process zone (FPZ), they may opt for a wider view of the specimen. On the other hand, if more precise measurement of crack tip opening displacements is desired, then a higher magnification should be used. Determining the desired field of view is a very important step, affecting the choice of cameras, lenses, and setback distances. And, in some cases, multiple DIC setups may be required to obtain, for example, the overall specimen response as well as more detailed images in smaller regions of interest, such as the vicinity of a crack tip in fracture experiments.

The random speckling pattern should be adequate in both size and dispersion. For analysis, the user should primarily be concerned with selecting a subset size that is large enough to capture an adequate number of speckles but small enough to have

good spatial resolution. At a heavier computational cost, step size can also be made smaller as a means to increase spatial resolution. There are many other factors that can impact results, but these are some of the more commonly mentioned considerations. Failure to select proper parameters can reduce the accuracy of strain measurements by an order of magnitude [42].

While DIC can appear to be overwhelming with all the necessary preparations and parameters, commercial packages often are equipped with helpful user manuals and dedicated customer support. Additionally, there are a lot of high-quality studies discussing best practices for proper DIC analysis [36,40,42–46]. A quick online search will also show some popular open source packages for 2D-DIC such as Ncorr (<http://ncorr.com/index.php>) and other MATLAB-based codes (Mathworks).

32.3 DIC applications in adhesive and bonded joint testing

Having reviewed the DIC method, including its implementation and capabilities, we now turn the focus to opportunities to use the DIC method to enhance our understanding of material constitutive response, strain distributions, and joint displacements relevant to adhesive bonds, before focusing on fracture mechanics applications, starting in Section 32.4. Published examples as well as potential opportunities include the following:

32.3.1 *Extracting constitutive properties with DIC*

For adhesives that can be molded or cut from sheets, stress-strain constitutive properties are often obtained using quasistatic dogbone tensile specimens or bulk Iosipescu or Arcan shear specimens. The full stress-strain behavior of such adhesive samples may be determined by several methods, including DIC, which offers the added advantage of being able to extract Poisson's ratio from the 2D in-plane surface deformations, as shown for a neat polymeric tensile specimen in Fig. 32.3, without the need for biaxial extensometers. With lateral as well as longitudinal strains from DIC, one can determine true stress (here, assuming lateral strains are the same in both directions). Fig. 32.3a compares the stress-strain behavior of engineering stress and strain (Cauchy) to true stress and strain (Hencky). The negative of the slope of transverse strain over longitudinal strain for uniaxial stress states, defined as Poisson's ratio within the linear elastic region, is plotted in Fig. 32.3b. This same ratio may be used beyond yield into the plastic regime exhibited by a material, where isochoric deformation is approximated, so Fig. 32.3b shows this ratio's evolution as strain increases. Fig. 32.3c and d shows plots of lateral vs longitudinal strains for both engineering and true metrics; the latter's slope is approximately 1/2 over this range that is dominated by plastic flow, as expected. These DIC results suggest their utility for determining constitutive properties, including Poisson's ratio, which is seldom available on technical data sheets.

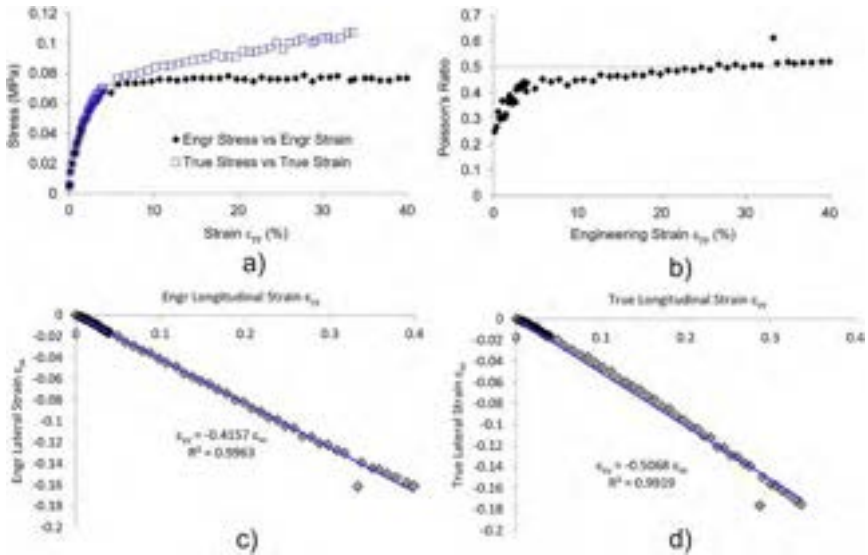


Fig. 32.3 Illustration of the application of DIC to characterize a polymeric tensile sample: (a) comparison of engineering and true stress-strain behavior; (b) labeled as “Poisson’s Ratio”, this is the negative of the ratio of true lateral to true longitudinal strain, with the *dashed line* representing a ratio of 1/2; (c) plot of engineering lateral vs longitudinal strains; and (d) plot of true lateral vs longitudinal strains.

Though characterization tests of monolithic tensile specimens have been widely used for bulk adhesives, stress-strain behavior in a neat adhesive tensile test may not always be representative of the response under the complex stress states and often extensive ductility seen in bonded joints with thin bondlines. Furthermore, some adhesives cannot be fabricated into sheet, film, or coupon form, as their relevant properties are not expressed unless prepared as bonded joints or by using their specific manufacturing process directly onto their intended substrate(s) (e.g., [47]). These, along with the interest to collect constitutive properties under realistic loading conditions and in more representative geometries, lead to the need to characterize in situ constitutive properties up to and including failure within relevant adhesive bonds.

Determining the constitutive properties of the resulting joints is often challenging, sometimes requiring specialized instrumentation capable of accurately quantifying the relatively small displacements arising within thin bondlines [48], as codified in ASTM D5656 and D3983. Moiré interferometry has been successfully used for such measurements [49], and recent applications of DIC are also showing success for this application. The large strain gradients in the vicinity of the thin bondline present challenges for most experimental methods. Refinements for determining shear strains within double-lap joints composed of carbon fiber-reinforced plastic (CFRP) adherends bonded with a structural film adhesive have been proposed [50] to improve measurements of the bondline shear strains.

Building on a prior study [28], a recent example utilized DIC to characterize the in situ constitutive behavior of several epoxy and polyurethane adhesives used to bond steel Arcan specimens that were loaded at different orientations to simultaneously characterize both normal and shear deformation modes [27] under the resulting combined loading. Fig. 32.4 shows an image grid of DIC image analysis patterns for vertical displacements taken for a polyurethane adhesive in an Arcan specimen loaded at a 50 degrees angle, thus resulting in an average bondline shear stress that is nominally 19% higher than the average normal stress within the adhesive layer. By analyzing the resulting strain fields, one can obtain stress-strain diagrams of average normal and shear values with respect to the bond plane, as shown in Fig. 32.5a. The initial slope of the shear behavior should correspond to the shear modulus of the adhesive, but that of the normal plot would be significantly higher than the Young's modulus, E , due to constraint effects, which theoretically could approach a limiting upper bound for

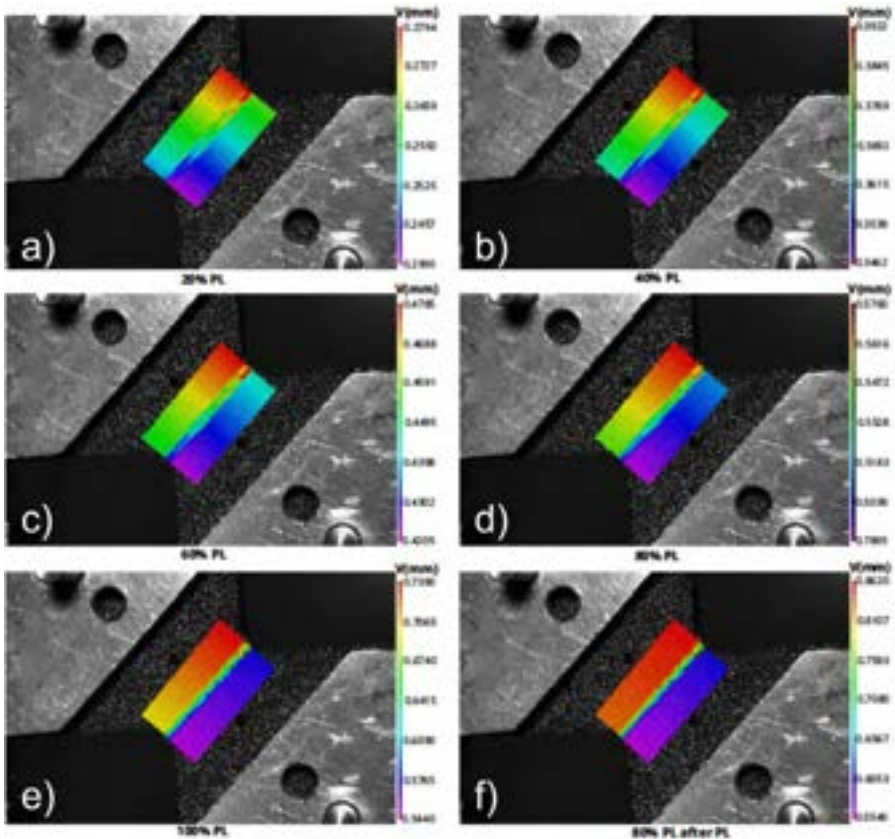


Fig. 32.4 Image grid of DIC analysis images for vertical displacement fields for a bonded Arcan specimen at various fractions of the peak load (PL) sustained: (a) 20%; (b) 40%; (c) 60%; (d) 80%; (e) 100%; (f) 80% after PL achieved. Contour rescaling is used, so these are relative displacements.

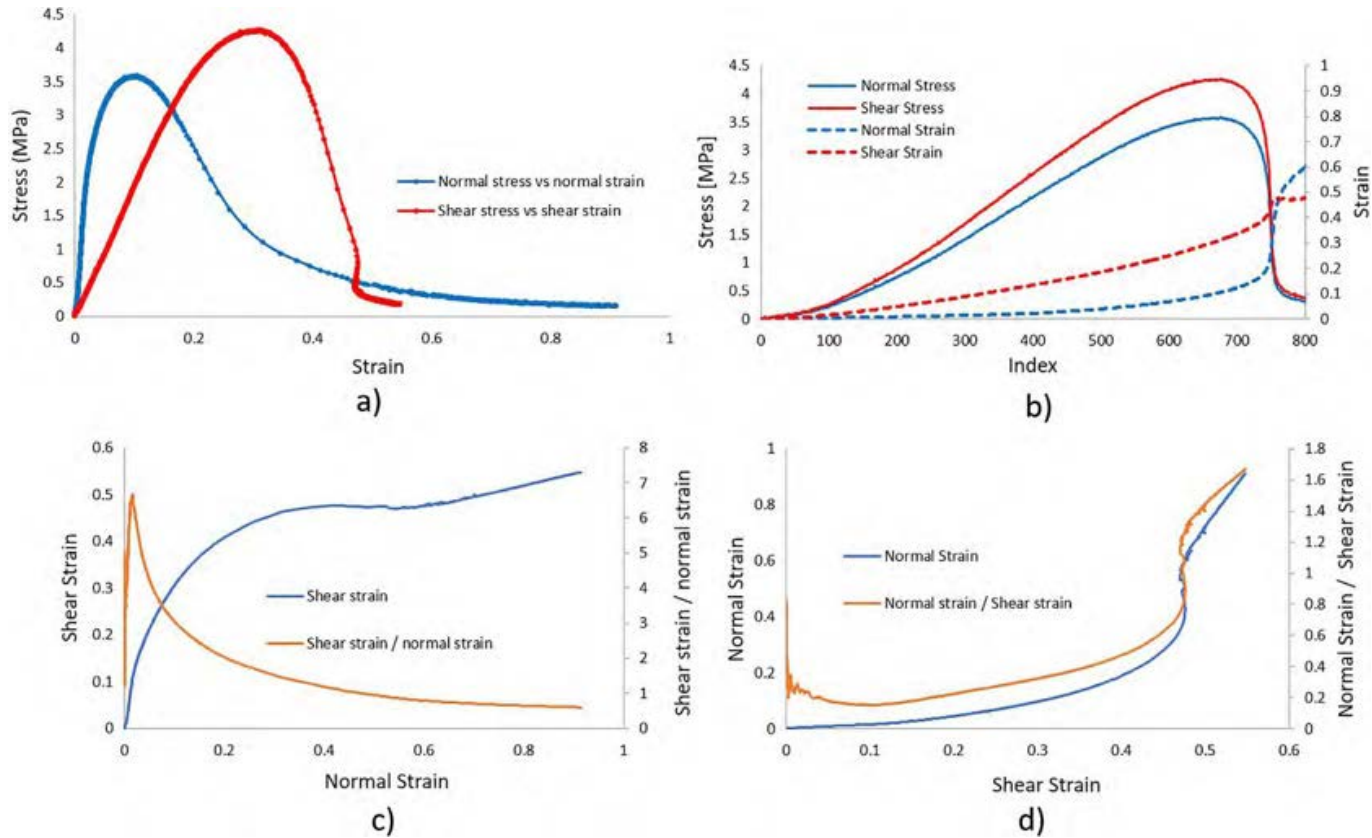


Fig. 32.5 DIC analysis results for an Arcan specimen loaded at 50 degrees: (a) normal stress vs normal strain and shear stress vs shear strain; (b) plots of normal and shear stress and strain traces as displacement proceeded (index is proportional to elapsed time); (c) shear strain vs normal strain and their ratio; (d) Normal strain vs shear strain and their ratio. All strains shown here are engineering strains.

uniaxial straining of $\frac{E(1-\nu)}{(1+\nu)(1-2\nu)}$, where ν is Poisson's ratio for thin bonds between rigid adherends of sufficient areal extent. In Fig. 32.5b, one sees the stress components (a fixed ratio for this Arcan orientation) and the strain components plotted as imposed crosshead displacement proceeds. None of these images suggests the occurrence of damage at approximately 1.7% normal strain, which becomes noticeable in Fig. 32.5c, as seen in the slope change of shear strain vs normal strain.

Plotting their ratio (in the same figure) results in a prominent peak, corresponding to a significant rate of increase of normal strain, believed to be associated with debond initiation or internal damage formation. Perhaps more informative, however, is a plot of the normal strain vs shear strain, and their ratio, as shown in Fig. 32.5d. The minimum in the ratio of normal strain to shear strain occurs at a shear strain of about 10.7%, suggesting the onset of debonding or possible cavitation that primarily affects the normal strain through relief of constraint. The ratio's slight downward trend prior to this likely arises from nonlinear behavior in the highly confined elastomer layer, resulting in very large shear stresses and strains around the bond periphery [51] that could affect local DIC measurements. Clearly, DIC offers opportunities to characterize in situ stress-strain behavior of adhesive bonds and also detect damage initiation and progression as testing proceeds.

32.3.2 Acquisition and applications of strain fields with DIC

Determining strain fields in adherends and bond, including to validate analytical and numerical model predictions

As a full-field technique for measuring deformations, DIC lends itself easily to evaluating strain fields within bonded systems. For example, Serrano and Enquist [24] used DIC to gain an understanding of bonded wood block deformations using ASTM D905, as shown in Fig. 32.6. This figure demonstrates the classical shear lag distribution for a soft material constrained by stiffer substrates subjected to compression loading. Furthermore the relatively high resolution of strain measurements allows for more advanced comparisons to finite element models, helping to tune material parameters to more accurately model local effects. An example will be shown in Section 32.3.3 for DIC use for edge-on imaging of SLJs exhibiting the well-known bending due to eccentric loading.

Determining adhesive layer strains from back face deformations

Depending on the relative stiffness of the adherends and adhesive layer, one may be able to estimate adhesive layer strains or slip by using DIC to measure adherend back face deformations, especially when referenced to a known position. In Fig. 32.7, for example, a single DIC setup would likely not be able to accurately capture deflections in an edge-on view of a pressure-sensitive adhesive (PSA) tape with a total thickness of 0.08 mm over the entire length of the bond (here approximately 40 mm). One could use multiple DIC cameras with different fields of view, but here a single system with a face-on view allows one to easily capture the back face deformations along the entire

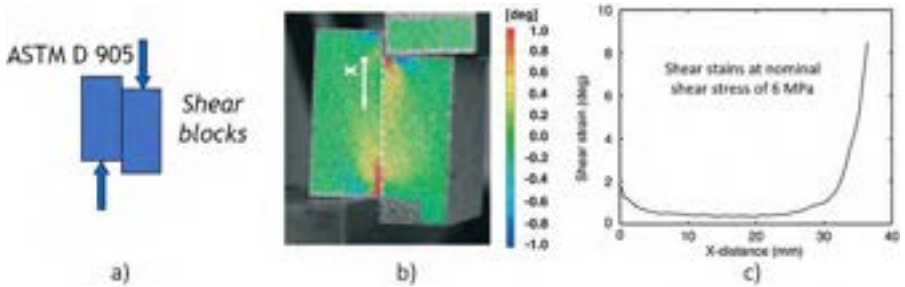


Fig. 32.6 Example of DIC used to determine shear strain distribution along the bondline of adhesively bonded wood blocks using ASTM D905: (a) schematic of test specimen; (b) DIC image of specimen loaded at 6 MPa nominal bondline stress, showing shear strain results. Serrano and Enquist [24] suggest that the adhesive layer is beginning to fail at the lower end of the bond, resulting in the larger and more extensive shear strains there; (c) shear strain as a function of distance down the bondline. Used with permission from E. Serrano, B. Enquist, Contact-free measurement and non-linear finite element analyses of strain distribution along wood adhesive bonds, *Holzforschung* 59 (2005) 641–646 for (b) and (c) images.

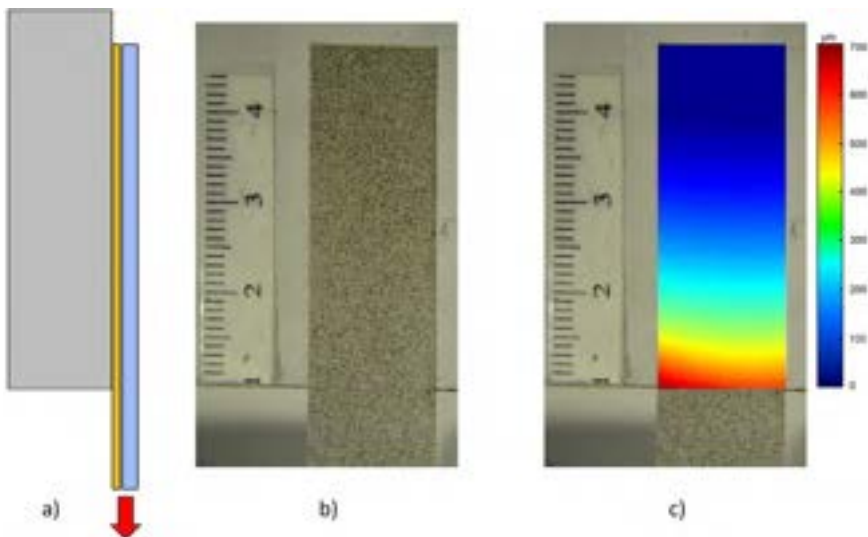


Fig. 32.7 Example of DIC used to capture tape backing deformations to infer underlying strain distribution within a pressure-sensitive adhesive tape subjected to a downward force of approximately 40 N: (a) schematic illustration of specimen; (b) image of speckle pattern along with scale in centimeter; and (c) DIC analysis of vertical deformations. See Mojdehi et al. [26] for experimental details and discussion.

bond length, shown here in the vertical direction when a PSA tape, bonded to a rigid substrate, is pulled downward. Because the backing itself is thin and several orders of magnitude stiffer than the adhesive, shear deformations within the backing were deemed negligible. Observed vertical displacements would then result primarily from shearing within the soft adhesive layer, allowing shear strains to be inferred by dividing back face displacements by the thickness of the PSA layer [26].

Nondestructive inspection and damage tracking

As a noncontact, full-field experimental imaging method, DIC offers a potential platform for nondestructive evaluation of adhesive bonds for some applications. For example, Liu et al. [52] used DIC to detect “kissing bonds” in CFRP/epoxy SLJs at loads perhaps as small as 50% of the subsequent failure load. Khafagy et al. [53,54] used DIC to investigate localized strains around intentional defects in double-lap shear specimens, a possible means to calibrate defect detection. He et al. [55] used DIC to track damage progression in the fatigue loading of composite SLJs. Sekiguchi et al. [56] monitored the yield progression under cyclic loading conditions in step-wise tailored SLJs composed of aluminum alloy adherends and a functionally graded, second-generation acrylic adhesive.

Design optimization

Adhesive joint optimization has attracted considerable interest since the extensive pioneering analytical studies of Hart-Smith for a wide range of lap joint configurations [57]. Optimization efforts have been explored for fundamental understanding of joint details, such as illustrated by Xu et al. [58] using photoelasticity for dissimilar material interfaces, and as widely practiced in industrial design of modern engineering components. In studies on carbon fiber repair, Caminero et al. [13,14] used DIC to determine the locus of failure for a set of patch repairs. Examining the failure load as well as the most severe deformations at the notched repairs, Caminero et al. described the optimal designs and techniques such as using double-sided repairs and carefully designing the adhesive layer, understanding the failure will be controlled by debonding. Studies like these allow for repairs to be judiciously selected, balancing the necessary strength, failure modes, and time/skill it may take to properly make the repair. In another example, Ramezani et al. [59] used DIC to explore bi-adhesive SLJ configurations that may offer synergistic advantages for bond performance.

32.3.3 Assessing deformations in single-lap joints

Due to its extensive industrial utility, single-lap joints have been widely used and studied. The peak force sustained divided by the bond area is referred to as the “apparent shear strength” in ASTM D1002-10 [60], hinting at underlying stress state complications. The SLJ is widely considered to be a shear test, but the failure of most SLJ joints is much more complex, often driven by peel stresses or initiation of plastic bending in the adherends themselves [57]. In addition to their wide industrial acceptance by both producers and users of adhesives for development, screening, and quality control

purposes, SLJs are often used by research groups as a test bed for model development, refinement, and validation, such as discussed in [Chapters 15](#) and [33](#).

Examples of DIC technique applications to SLJ include a systematic study by Bamberg et al. [61] of the effects of adherend yield, adhesive thickness, and overlap length for symmetric and hybrid high-strength steel (HSS) and aluminum alloy (AA) bonds joined by an epoxy adhesive. They have superimposed Lagrange vectors, whose directions are determined from displacements of selected points from initial to final locations. These Lagrange vectors and their relative orientations further highlight the stress transfer across the adhesive layer, as shown in [Fig. 32.8](#). Sun et al. [62] used DIC to study stresses and fracture in SLJs involving dissimilar (AA, steel, and woven CFRP) adherends.

For some applications, the extent of deformation can be just as important as the failure load, as discussed in [Chapter 7](#). Interestingly, standards such as ASTM D1002 make no mention about recording strain at peak load or final separation, nor of the more easily measured corresponding crosshead displacements. The reasons for this likely include the difficulty in measuring relative adherend motion across the

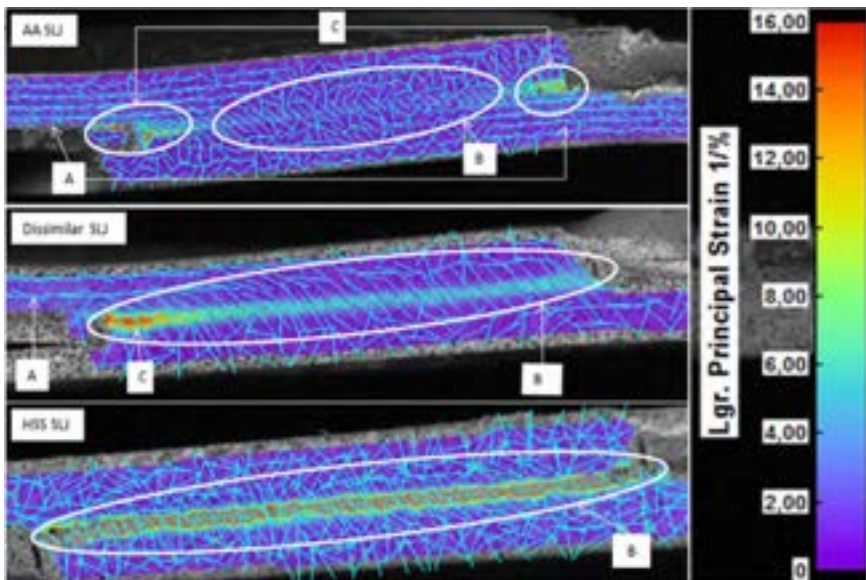


Fig. 32.8 DIC outputs for percent Lagrangian principal strains for AA (upper), hybrid AA/HSS (middle), and HSS (lower) SLJs with an overlap length of 12.5 mm, along with superimposed Lagrange vectors corresponding to relative displacements upon loading. Relative alignment suggests dominant straining, with A signifying yielding in aluminum adherends, B showing modest shear strains in adhesive as predicted by shear lag, and C suggesting regions of high peel stresses near ends with AA yielding.

Used with permission from P.A.M.G.P. Bamberg, U. Reisgen, A. Schiebahn, J.D.V. Barbosa, B. Marx, R.S. Coelho, Digital image correlation analysis of the effects of the overlap length, adhesive thickness and adherends yield strength over similar and dissimilar joints of high strength steel and aluminum alloys, *Int. J. Adhes. Adhes.* 83 (2018) 69–75.

bondline, as adhesive layer extensometers are not common and are typically used on thick adherend lap joints only (e.g., as in ASTM D5656). Widely available axial extensometers conceivably could be mounted on the adherends, but the results would be confounded by adherend stretching and the significant bending strains that naturally arise at bond terminations. Some entities request measurements of crosshead displacement of the universal test machines (UTM) used in such tests [63,64]. Despite the apparent simplicity, crosshead displacement measurements introduce several confounding factors, as even small extraneous displacements can be quite significant compared to the shear displacement in a thin bondline undergoing even large strains. Relatively large displacements can come from adherend yielding and the bending and alignment of these eccentric specimens as well as displacements associated with machine load train compliance, which varies with the specific UTM, and the fixtures used for a test. Using crosshead displacement measurements may be inappropriate for validating finite element analysis (FEA) models if load train compliance, wedge grip motion, grip slippage, etc., are not incorporated properly.

These issues are discussed in more detail in [Chapter 7](#), but DIC offers a useful option for accurately assessing specimen deformations, including with tougher structural adhesives. High strength adhesives further confound measurements of actual specimen displacement due to increasing amounts of adherend yielding prior to failure, but DIC is proving to be an appropriate tool for measuring the relative displacements of SLJ specimens. Strain fields for a deformed SLJ (Al 2024-T3 adherends bonded with PR-2930 epoxy by PPG Industries) loaded at 15500 N (96% of peak load) are shown in [Fig. 32.9](#), revealing a complex strain state near the ends of the overlap.

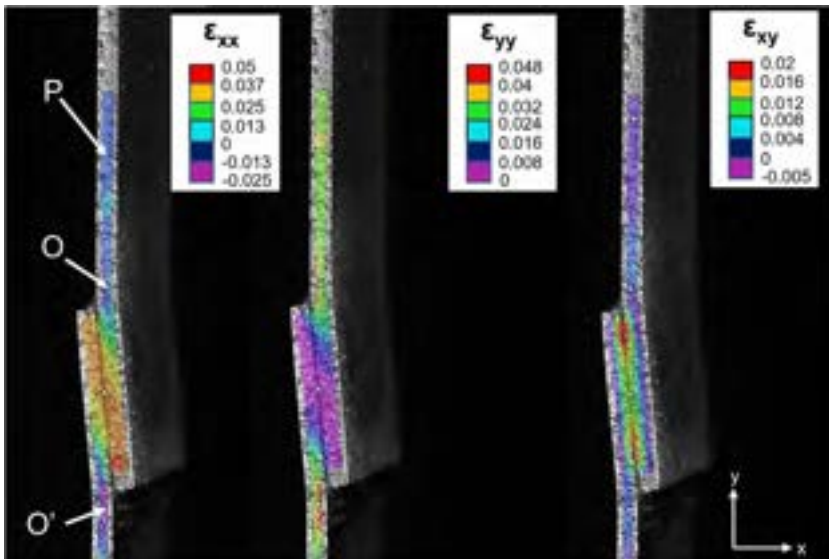


Fig. 32.9 DIC-determined strain fields for a single-lap joint specimen loaded at 96% of peak load.

Away from the bond, the adherends exhibit axial strains of 0.032–0.04, well beyond the yield strain of the aluminum. Rather than determining relative bondline displacements at the ends of the overlap, as was done by Bamberg et al. [61] and Sun et al. [62], our focus here was on assessing specimen deformation to help reconcile substantial differences between measured crosshead displacements and FEA predictions. The latter had imposed boundary conditions based on relative vertical displacement between the top and bottom grip end (i.e., elongating the region between the grips)—likely appropriate for the suspended specimen but failing to account for the relative motion of grip faces and the crosshead, which proved to be significant.

Some have considered adherend translation to measure the relative motion of one adherend to another, though this can be rather simplistic for many bonded joints in light of varying strain fields in Volkersen's shear lag model [65]. Exceptions to these complications likely include situations where bonds are quite short and adherends are very stiff relative to the adhesive layer. Viscoelastic creep or extensive plasticity within the adhesive layer makes the adhesive effectively softer, allowing some authors to successfully report adherend translation results [66,67]. When adhesives are sufficiently stiff, however, strains along the adherends and adhesive vary as predicted [25,65] or with added complexity if adherend or adhesive plasticity occurs.

Deeming it infeasible to image the entire specimen and retain sufficient DIC resolution, we imaged only the portion of the specimen shown in Fig. 32.9. Again, recalling our focus on the grip-to-grip motion as input into the FEA model, we considered three metrics: (1) relative longitudinal displacement between points O and O', (2) an estimate of the grip-to-grip or specimen deformation between the grips, obtained by combining the O-O' displacement with the remote adherend strain multiplied by the length of the nonoverlap portion of the specimen between the grips; and (3) the crosshead displacement as recorded by the load frame. For the specimen displacement estimate, one can assume that the nonbonded region of the specimen between the grips and point O is under a relatively uniform axial load and the longitudinal strains at point P can be multiplied by the total unbonded length, including if plastic deformation is occurring provided it be in the monotonically increasing portion of the adherend stress-strain behavior. This specimen deformation metric should then be useful for calibrating or validating FEA models, where boundary conditions are imposed as the ends of the grips. Fig. 32.10 shows the load trace plotted as a function of the three displacement metrics. Clearly, the displacement values are very different depending on the metric used, suggesting the utility of DIC for reconciling experimental and FEA model results, and cautioning one on the stark differences in "displacement." Even the O-O' displacement must be interpreted carefully, and does not represent bondline displacement. The relative motion of points at the ends of the bonded adherend (which are essentially unstrained in the axial direction) were only 70% as large as the O-O' displacement, reflecting the fact that adherend deformation (here including axial plasticity) is roughly 17 times as large as the deformation across the bondline at bond terminations.

Adherend yielding is seen in strain measurements collected at points P and O in Fig. 32.11. From these figures and our analysis, one finds that most of the deformation in this SLJ specimen is due to plastic deformations within the adherends, even

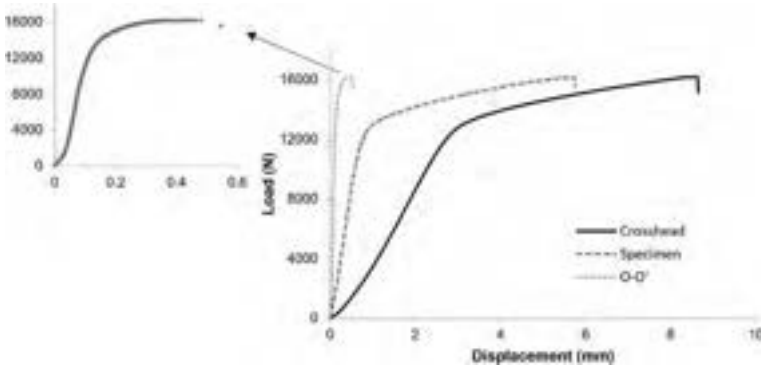


Fig. 32.10 Single-lap joint load trace plotted as a function of three different displacement metrics: crosshead displacement and bondline and specimen (grip-to-grip) displacements from DIC measurements. The O-O' line is shown on an expanded scale in the *inset*.

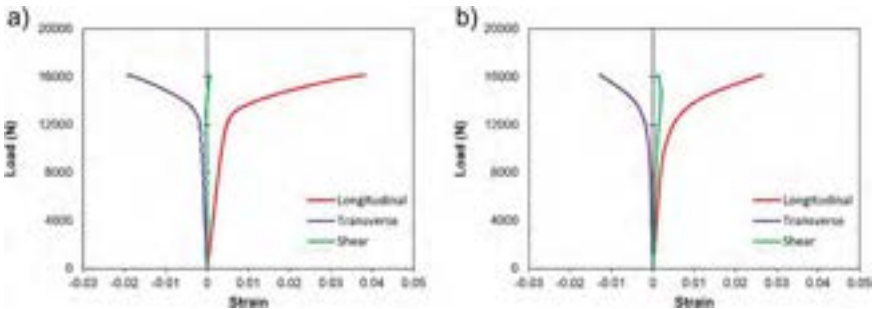


Fig. 32.11 Load vs DIC measured adherend strains collected at: (a) inspection point P; and (b) inspection point O as defined in Fig. 32.9.

considering the displacements between point O to O' that are very near the bonded region. As an interesting example of the ability of DIC to obtain useful data even across the relatively thin adherends, the Poisson's ratio suggested by the ratio of lateral to longitudinal strains prior to yielding results in a Poisson's ratio of 0.37, just slightly above the reported value of 0.33.

32.4 Augmenting traditional fracture analysis with DIC

This section will outline inroads DIC is making to enhance our understanding and characterization using traditional fracture analysis methods for adhesively bonded joints, focusing on Mode I fracture with some discussion on Mode II. Following this

content on traditional analysis, [Section 32.5](#) will then review the CZM approach that is increasingly used for fracture analysis, the extraction of TSLs, and implementation in FEA models, including for mixed-mode fracture conditions.

32.4.1 Fracture analysis of bonded joints

As structural adhesives are often used in applications where failure can have serious and life-threatening consequences, it is imperative that bonded joints be sufficiently damage tolerant, offering significant resistance to debonding typically through energy dissipation associated with fracture. This energy-based design is governed by fracture mechanics rather than strength criteria, as distinguished in [Chapter 14](#). As discussed in [Chapters 16](#) and [17](#), fracture is understood to potentially occur in three modes: I (opening), II (in-plane shearing), and III (tearing). Mode I fracture has received the greatest attention, as cracks in isotropic, monolithic materials tend to grow in a Mode I manner. The other fracture modes, and mixed-mode combinations, become more important in layered systems where the locus of failure is globally constrained to grow within a particular region, such as along an interface or within a thin adhesive layer between two tougher adherends. Even in these situations, however, experimental characterization often suggests that the Mode I fracture energy, G_{Ic} , is smaller than for Modes II and III [68], though exceptions have been reported [69,70]. For instances where the Mode I fracture energy is smaller than for other modes or combinations, characterizing Mode I fracture resistance is of greatest concern due to the understanding that it is often the critical mode of failure, and that using this smallest value, regardless of actual mode, can lead to conservative design. To test the Mode I fracture of adhesive bonds, the DCB has been the workhorse due to its simplicity in both experimental set up and analysis procedures available for determining fracture energy from measured data. Other specimen configurations are used to obtain Mode II and Mode III fracture energies, as well as combinations for mixed-mode characterization, especially of the in-plane modes, I and II, as described in more detail in [Chapter 17](#).

Cameras have been used to record crack propagation for such specimens, as crack length is often needed to determine the fracture energies. Their use allows for continuous monitoring or posttest determination of crack progression, better discernment of crack tip location, assessment of the process zone within which damage is occurring, and remote or automated tracking of tests as they progress. Recent applications of DIC to fracture testing are adding new insights into these test methods, offering new capabilities to more accurately extract fracture parameters and providing strain and deformation maps that can be used with finite element analyses for model validation and inverse method implementation to determine fracture parameters [71]. These are especially important as we increase adherend thickness to avoid adherend yielding to accommodate the testing of tougher adhesive systems, pushing the boundaries of established test methods and associated traditional analysis procedures. As discussed in [Chapter 16](#) and Sun and Blackman [72], traditional data reduction methods such as CBT [73], ECM, and more recently the compliance-based beam method (CBBM) [74] and the J -integral approach [32] are used for data analysis and determination of fracture energies, the latter two of which do not require crack length measurements [23].

32.4.2 Visualizing strain fields in bonded fracture specimens

The full-field displacement and 2D-strain maps obtained using DIC offer useful insights to refine our qualitative understanding of fracture specimen behavior. Although specimens such as the DCB test for Mode I or ENF test for Mode II characterization appear quite simple, they involve complex mechanics associated with layered, multimaterial systems. Most analytical analysis approaches and many FEA models of such specimens are 2D, yet with specimen widths that are typically 20–25 mm, such plane solutions have limitations, including their inability to capture anticlastic bending. In FEA of DCB specimens, conventional wisdom has been to assume the adherends, unless quite thin, are in a plane stress state, but that the thin, constrained adhesive layer is modeled as plane strain because of the constraint of the stiffer adherends. 3D FEA, of course, can more accurately address these nuances, but has been less commonly used for fracture specimen analysis due to added complexity and computational requirements. Also, if the adherends are orthotropic, such as wood or laminated composites, shear deformations become more significant, though are not always included in analytical models [75,76]. And as adhesive toughness improvements are made to meet the increasingly demanding challenges for automotive and other applications, thicker adherends may be needed to avoid adherend plasticity, raising further questions about common data analysis method assumptions often based on slender beam bending.

In exploring these and other issues, DIC then offers a means to capture the displacement and strain fields (albeit of the surface) of fracture specimens for insights and model comparisons. Unless otherwise noted, the examples in this chapter are for Al 2024-T3 adherends, 25 mm wide and of specified thickness, joined by a 0.25 mm thick bondline of PR-2930, a tough, one-component epoxy intended for automotive and aerospace applications developed by PPG Industries to meet the challenging performance requirements of MIL-PRF-32662 Group-I-classified adhesives, as discussed in [Chapter 7](#). Experimental and analysis details for these images and results are described in more detail in [77,78]. Some additional details regarding the input properties for the FEA model used for comparisons with experimental results in the following figures are also given in [Section 32.6](#).

Representative strain fields, as determined by DIC in a loaded DCB specimen, consisting of 19.1 mm thick aluminum adherends, are shown in [Fig. 32.12a](#). Also shown are schematic approximations of the expected normal stresses across the bondline, σ_n (which when multiplied by specimen width would be the vertical force per unit length along the beam), as also shown in [79]. In addition, schematic shear, V , and bending moment, M , diagrams are also suggested. These are conceptual, as the actual shear, and bending moment diagrams would represent successive integrations of the traction, once known. The DIC strain fields are ordered such that they have a nominal correlation with the adjacent schematic diagram, which is also rescaled and superimposed on the strain fields for illustration purposes. More details on ϵ_{yy} will be discussed in [Section 32.4.3](#), along with the BoEF and FPZ designations. V is expected to induce transverse shear stresses through the thickness. Interestingly, the very high shear strains appear just ahead of the crack tip, where the moment of the applied load is

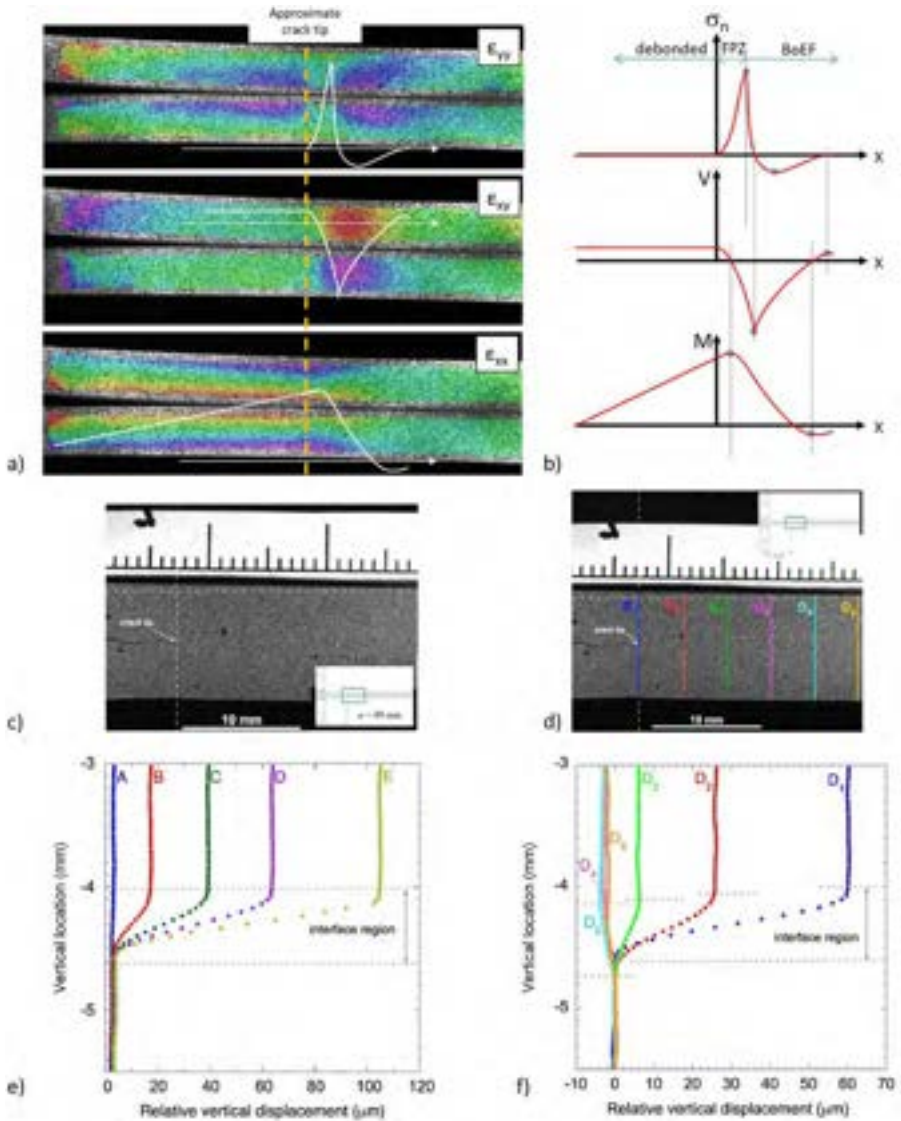


Fig. 32.12 Correlations of DIC strain fields with traction, shear, and moment diagrams: (a) DIC strain fields and (b) schematic representations of the tractions across the bondline along with shear (V) and bending moment (M) diagrams. The *circles* correspond with points of local maxima or minima, and align with zero-crossings on the figure above. These *curves* are then consistently scaled and superimposed on the strain fields in (a). Shown in (c) is a *vertical line* used to acquire vertical displacements for increasing load levels, A–E, plotted in (e). Panel (d) shows a set of *vertical lines* at various locations along the bondline, D1–D6, and shows the vertical displacements at each location for a given load. Panels (c)–(f) are taken from J.M. Gorman, M.D. Thouless, The use of digital-image correlation to investigate the cohesive zone in a double-cantilever beam, with comparisons to numerical and analytical models, *J. Mech. Phys. Solids* 123 (2019) 315–331.

reacted by a distributed couple—high tractions acting over a relatively short moment arm related to the characteristic length, as also seen in [23], and where anticlastic bending may enhance surface shear stresses [80]. Beam bending stresses induce longitudinal strains, ϵ_{xx} , that approach zero at the far left end where the loads are introduced, and ahead of the crack tip after the applied bending moment has been reacted by the couple mentioned above. These correlations with expected mechanics aid in understanding the DIC strain maps.

Strain fields were not shown across the bondline in this figure and several other figures in this chapter, as DIC software algorithms and subset size could result in misleading output. To avoid this issue and accurately obtain strains and rotations, earlier work by Gorman and Thouless [23] used linear fits of the u (horizontal) and v (vertical) displacements to accurately assess deflections, rotations, and strains, including within the adhesive layer. Fig. 32.12c and d are reproduced from their work and illustrate vertical lines along which displacements were measured for the respective figures below them. Fig. 32.12e and f illustrate relative vertical displacements at increasing load levels and at several positions ahead of the crack tip, respectively. Fig. 32.12f suggests both tensile and compressive deformations within the adhesive layer as one moves further ahead of the crack tip. Note that the transition regions between the steel adherends appear to be about double the actual adhesive bondline thickness of 250–300 μm . This artifact arises from the DIC subset size and algorithms, but is accurately addressed using the methods of [23] to robustly characterize the behavior, from which they then obtained traction separation laws, the extent of the cohesive zone, and a BoEF representation of tractions.

32.4.3 Using DIC for Mode I LEFM analysis

Linear elastic fracture mechanics (LEFM) methods have been the most commonly used techniques to extract fracture energies from fracture tests, as they typically only require measurements of load, displacement, and (usually) crack tip location. With improvements in structural adhesives, particularly high toughness formulations, researchers have found that LEFM approaches have not been adequate for determining the toughness of bonded systems. Gorman and Thouless [23] found deviations from true linear-elastic behavior at less than 10% of the force needed to propagate the crack on 4130 steel DCB adherends joined with a two-part structural adhesive. Subsequent studies by Sun and Blackman [72] used DIC to determine the validity of LEFM methods for a brittle epoxy, a tough epoxy, and a ductile polyurethane. The LEFM approaches were compared to the J -integral to determine their validity (LEFM and J -integral methods are discussed in detail in Chapter 16). The results of Sun and Blackman [72] showed that LEFM was adequate for the brittle and tough epoxies, but less appropriate for the ductile polyurethane. It was concluded that the LEFM results would be improved if the effective crack length was extended by a distance measured by the DIC system.

Gorman and Thouless [23], using their linear regression method, demonstrated a robust means to accurately characterize bondline deflections and adherend beam rotations, including in the vicinity of the crack tip, to account for crack tip rotations arising

from both bending moment and the applied shear. Building off of their recommendation for the improvement of effective crack length, Sun and Blackman [79] used a BoEF model to determine the optimal location of a crack tip extension that can be added to the measured crack length, a , to acquire an effective crack length, a_{eff} . Their process used DIC to acquire deflections at points along the neutral axis of both adherends and then fit a BoEF curve to the deflection data. The data showed that the best fit to the J -integral occurred when the extended crack tip was taken to be at the location corresponding to zero rotation, within the compression region ahead of the crack tip, approximating the cantilevered boundary condition, such as assumed by SBT. This is consistent with the understanding [81] that the compliance, from which LEFM methods are derived, is more significantly affected by root rotation at the crack tip rather than root deflections [23,76], as rotations result in increasingly large end displacements as the moment arm increases. Their optimal extended crack length determined via a BoEF model was quite close to the extended crack length the CBT calculates as the negative of the abscissa intercept of the $C^{1/3}$ vs a plot.

A magnified image of the ϵ_{yy} strain field in the vicinity of the crack tip for the DCB test of the PR-2930 bonded aluminum adherends, illustrated in Fig. 32.12, is shown in Fig. 32.13a [77,78]. The image provides an insightful visualization of the BoEF behavior that DCB joints often exhibit. In the wake of the crack (to the left of the crack tip), one observes compressive ϵ_{yy} along the formerly bonded surfaces, induced by Poisson's effect from the bending strains in the adherends. Directly ahead of the crack tip, one might expect significant tensile ϵ_{yy} strains in a region associated with the very large normal tractions across the bondline, as suggested in the schematic illustration of Fig. 32.13b. Instead, these strains are small because anticlastic bending [82], which locally forces edges of adherends together where the bending moment is large, likely

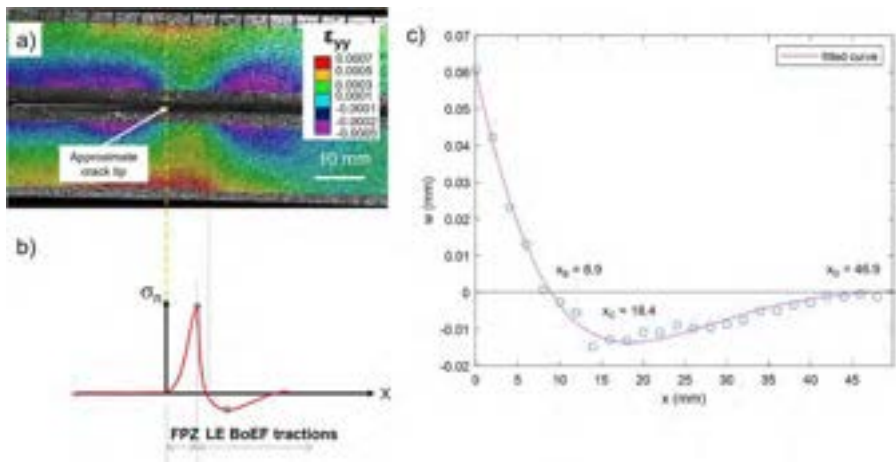


Fig. 32.13 Illustration of (a) a typical ϵ_{yy} strain field in the vicinity of the crack tip for a DCB specimen; (b) schematic illustration of normal stresses across the bondline, and (c) curve fit of a linear BoEF model to the DIC measure of neutral axis displacements ahead of the crack tip.

reducing the DIC strains, which are surface measurements. Averaged across the width of the specimen, this region consists of what are expected to be linear elastic adhesive tractions predicted by the classic BoEF model well in advance of the crack tip, as well as adhesive exhibiting nonlinear behavior, where damage has initiated and proceeds to separation at the crack tip [72]. This latter region is the FPZ, also known as the cohesive zone. Ahead of the tensile normal stress region is a region of compressive ϵ_{yy} near the adhesive layer, which can be attributed to the oscillatory decay tractions of BoEF behavior. On the top of the specimen in Fig. 32.13a there are machined notches to mark increments of 5 mm. By measuring the distance of the positive strain region between the two compressive regions, one can acquire a quick estimate of the size of the region with tensile tractions across the bond, though significant gradients and the complex stress field would require more refined analysis [23]. Nonetheless, it appears this is about 6–7 mm in length. Using the DIC approach given in [79], it was determined that the FPZ for this specimen is slightly shorter, on average about 5–6 mm in length. This length, when combined with the portion of the tensile region that remains linear elastic, is then quite consistent with the DIC estimate.

In Fig. 32.13c the deflection (w) vs location (x) data are fit with the BoEF equation given by Sun and Blackman [79] and the FPZ distance (x_B), point of zero rotation (x_C), and point of zero deflection (x_D) are given in Fig. 32.13c as well. The data shown in Fig. 32.13a reveal that the compressive region ahead of the crack tip is significantly longer than the FPZ, consistent with the BoEF model. The average CBT extended crack length for these DCB specimens was determined to be about 30 mm. This is much larger than Sun and Blackman's recommended crack length extensions at point x_C of 18.4 mm given in Fig. 32.13c. Perhaps the most significant reason for this large difference is because crosshead displacement was used for the CBT calculations, and this value may include some load train compliance. If the load train compliance is filtered from these specimens, there is much better agreement between the values, with the CBT extended crack length becoming approximately 18 mm. Simply using DIC to calculate load point displacements may yield improved results compared to the use of raw crosshead displacements. Thus, DIC offers opportunities to confirm behavior predicted by BoEF and CBT models as well as eliminate spurious machine compliance contributions to the analysis.

32.4.4 Using DIC for the Mode I J -integral method

The J -integral method is valid for both linear and nonlinear cases, and is reportedly a more robust analytical approach that can be used to determine fracture energy. For a DCB test where adherends remain linear elastic, Paris and Paris [32] demonstrated that the J -integral could be represented in the following closed form

$$J_I = P\theta \quad (32.1)$$

where θ is the relative rotation between the two adherends at the loading pins and P is the load per unit width applied to the arms of the DIC. This method relies on the assumption that both the strains and rotations remain small. This form is well-suited

for analysis with DIC, though the method used to determine the J -integral depends on the region of the specimen visible for imaging. For loads applied with loading blocks, the rotation data at the loaded ends can be obtained by creating a line of inspection points along the specimen (x -direction) axis and measuring the resulting slope as loading proceeds [72]. When drilled hole specimens are being used, the clevises will often obscure the end rotations unless specimen extensions are used. In this case, rotations can be measured at any unobstructed point between the loading point and the crack tip by taking the difference between measured rotations perpendicular to the x -axis for each adherend (i.e., $\theta = du/dy$). This method may also be useful where more resolution is desired in the vicinity of the crack tip, and a smaller field of view is captured by the DIC system. When rotations are not measured at the loading points, a bending correction term must also be included [41,23], leading to:

$$J_I = P\theta + 12(Px)^2/Eh^3 \tag{32.2}$$

where x is the distance of the inspection points from the loading point, h is adherend thickness, and E is the elastic modulus of the adherend. Stiff loading block corrections are also available for such specimens [23]. If rotations are taken at the crack tip, the $P\theta$ term represents the contribution arising from root rotation, and the right term is the SBT contribution; their combination is then akin to the CBT analysis. Illustrations of the two described DIC methods for measuring rotations are shown in Fig. 32.14a and b. Inclinometers have also been used to measure rotations at the ends

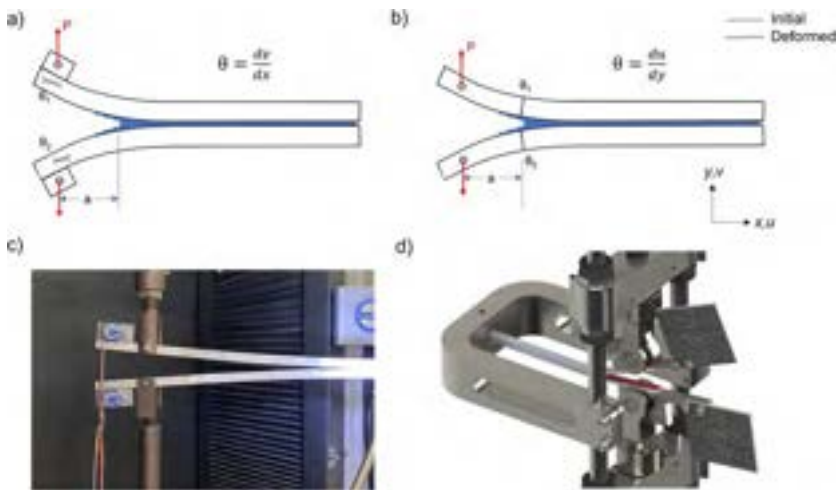


Fig. 32.14 Suggested inspection point locations for measuring rotations to determine J for DCB specimens using (a) slopes at load points, such as with loading blocks such that adherends are not obscured by clevises or (b) slopes away from load axis, here at the crack tip; (c) Inclinometers fixed to ends of DCB specimen to measure rotation; (d) Psylotech frame image with large speckled flags used with DIC to measure end rotations. The terms u and v refer to the displacement in the x and y directions, respectively.

of adherends, such as what is shown in Fig. 32.14c [77,83] and as discussed in Chapter 16. Additionally, Psylotech (Evanston, Illinois) has proposed test frame configurations with patterned flags to allow for DIC measurements of the rotation at the free ends of adherends, and an example can be seen in Fig. 32.14d. Similar DIC flags were used by Yang et al. [84] in a dual-actuator load frame that allowed for independent control of mode mixity [85].

Much of the published research shows J being determined at the precrack [23,41,72], but it can be measured as the crack grows along the bondline. For tough adhesive systems, there may be measured differences at the precrack and further away due to the initial lack of a developed crack tip in addition to changing shear and moment contributions, thus it may be necessary to collect rotation data at several points as the debond propagates.

32.4.5 DIC application to Mode II fracture testing

Mode II fracture, the in-plane shearing state, can be induced by sliding one adherend over another, and is commonly tested in either the ENF or end-loaded split (ELS) configurations. Mode II testing is complicated by the difficulty in seeing the crack tip, where sliding rather than opening displacements dominate. Complex fracture surfaces may result, including well-known hackle patterns [86], potentially leading to frictional contributions and other aspects. As the critical fracture energy for Mode II, G_{IIc} , is often greater than for Mode I, and because these geometries are less efficient (i.e., greater adherend bending stresses are required to induce a given energy release rate) [87], there may be concerns about larger plastic zones and more adherend yielding, invalidating some assumptions used to define many of the LEFM and J -integral approaches. Despite these difficulties in measuring Mode II fracture energies, determining G_{IIc} still remains necessary to more fully characterize adhesive failure behavior. Mode II fracture energy is often needed in models to predict response over a range of loading modes for many adhesive failures, including for CZMs for finite element modeling. Certain mixed-mode fracture models, such as the popular Benzeggagh-Kenane (B-K) and power law models, require inputs of Mode I and II fracture energies to set as bounds for the envelope and then use a power function to tune the shape of the fracture envelope between the points. These models are popular as they require relatively little input and can be used to model a wide range of load cases. When plastic deformation in the adherends during Mode II tests is very small or not observed, some closed-form solutions are available to determine the Mode II fracture energy. A closed form of J_{IIc} for the ENF test, which uses a three-point bending configuration, has been defined by Leffler et al. [88] as

$$J_{II} = \frac{9}{16} \frac{P^2 a^2}{EB^2 h^3} + \frac{3P\delta_s}{8Bh} \quad (32.3)$$

where δ_s is the sliding displacement between the two adherends at the crack tip. DIC can be used to either directly measure displacement at the crack tip or acquire the slope of the du/dy at the crack tip, as illustrated for a DCB in Fig. 32.14b. Using the slope

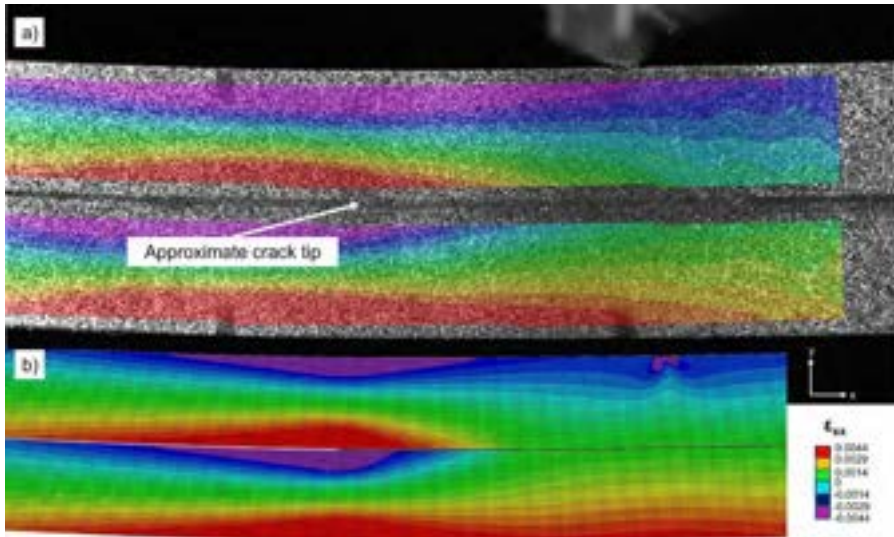


Fig. 32.15 (a) DIC and (b) FEA longitudinal strains (ϵ_{xx}) for an ENF specimen, with a crack propagated about halfway through the allowable distance. Strain levels were capped at the approximate yield strain for Al 2024-T3, suggesting significant regions of yield within the specimen.

method, one can extrapolate the slope to the location at approximately the interface to estimate the sliding displacement for each adherend (i.e., in the x -direction).

Fig. 32.15 shows both DIC and FEA longitudinal strain fields for an ENF specimen with 12.7 mm thick Al 2024-T3 adherends and a 0.25 mm thick adhesive layer of PR-2930 [77]. The contour map was limited to $+ / - 0.0044 \epsilon_{xx}$, the approximate yield strain for Al 2024-T3. As a result of this, regions that are red and purple are understood to be near or above the yield strain. The extensive degree of yielding observed in Fig. 32.15 would invalidate the data reduction methods based on linear elastic assumptions and necessitate the use of nonlinear finite element models to extract meaningful results, such as described in Section 32.6.

32.5 DIC utilization for traction-separation laws and finite element modeling

Finite element analysis offers a powerful numerical tool for modeling a wide range of problems, including stresses, strains, and energy release rates in adhesively bonded structures. Some FEA techniques to model fractures are virtual crack closure technique (VCCT) [89], the extended finite element method (XFEM) [90], and cohesive zone modeling, as also outlined in Chapter 15. VCCT is based on Griffith's principal assumption that the energy required to propagate a crack is equal to the energy that

would be necessary to close it, hence the term crack closure. This method assumes LEFM and must have the crack tip defined. The VCCT can be considered to be a local method, as Moreira et al. [91] showed it obtained the same mode partitioning as the Suo and Hutchinson approach [92] (see Chapter 17 for greater details on fracture mode partitioning).

32.5.1 Traction-separation laws for cohesive zone models

CZMs have been used in finite element codes to model the softening that occurs ahead of a crack tip, as high stresses cause small voids to nucleate and subsequently coalesce. The models were first introduced by Dugdale [93] and Barenblatt [94] to model the FPZ ahead of a crack tip in metals, then implemented into finite element codes by Hillerborg et al. [95]. CZMs utilize special elements (cohesive elements) to join continuum elements along the predetermined crack path. As the cohesive elements are displaced, they will eventually become damaged and degrade until they fail, at which point they are deleted. Based on many recent publications, CZMs are becoming one of the most popular methods for modeling the fracture of bonded joints. Interestingly, as discussed in Chapter 14 and in more detail in [96], they bridge the chasm between strength and fracture approaches, as they predict both the initiation of damage and flaws as well as their subsequent propagation. CZMs are governed by traction-separation constitutive. The capabilities of DIC to acquire high-resolution measurements of both displacement and strain make it a useful tool for acquiring the TSLs that govern CZMs.

TSL shapes can be modeled in many forms, including constant, bi-linear, trapezoidal, and exponential. For most structural adhesive modeling, a bi-linear or trapezoidal curve has been shown to suffice. Bi-linear curves are the simplest to implement and appear to be good fits for brittle adhesives whereas trapezoidal models have been shown to better model joints bonded with ductile adhesives [97]. In reality, all these shapes are simplified idealizations of actual traction-separation behavior, which has been shown to take on more complex shapes [28], though these simple TSL shapes have displayed powerful predictive capabilities [98]. The initial stiffness of the TSL is often difficult to acquire, though this value is usually less significant for modeling the global response of the system and can be approximated and tuned to improve model convergence. This is because higher initial stiffnesses are associated with steeper slopes, increasing the gradient that must be resolved when damage occurs. Common damage initiation criteria for CZMs are stress and displacement thresholds, using either a maximum value or a quadratic law for mixed-mode models. As damage accrues, tractions degrade or plateau due to stiffness penalties.

32.5.2 Using DIC for traction-separation law extraction

There are three often-cited methods for determining the TSL for each mode. These methods are described as the direct, indirect, and property identification methods. The direct method involves directly differentiating J to obtain a TSL, an approach enabled by DIC, as will be discussed below in more detail. The indirect method uses

an iterative process to back-calculate the TSL from a given set of data, often load vs displacement or load vs crack mouth opening displacement. When using indirect methods, judgment must be used to determine the bounds on the problem (i.e., TSL shape, coupling law, damage conditions) and whether the results are realistic for the class of material being tested. The property identification approach uses a combination of properties acquired from various tests. For example, a Mode II TSL developed via the property identification method may use an ENF test to acquire fracture energy, and the shear stiffness and traction from a thick adherend shear test.

Following the direct method, once J is determined, a TSL can be extracted by differentiating the J -integral with respect to the crack tip opening displacement, δ_n at a given point [99] measured with DIC [23]. For Mode I, the opening displacements, δ_n , at the crack tip are easily measured by DIC, and sliding displacements, δ_t , can similarly be measured when Mode II loading is also applied. The normal tractions can be represented by the following equation:

$$\sigma(\delta_n) = \frac{\partial J}{\partial \delta_n} \tag{32.4}$$

For a set of points along the centerlines of the beams, the differentiation process should be performed on a curve fit of J vs δ_n (commonly referred to as the R curve). Although the optimal curve form will vary depending on the joint geometry and type of adhesive being used, polynomial and piecewise linear forms have been shown to be strong fits for structural adhesives [41,72]. Fig. 32.16 shows a set of TSLs

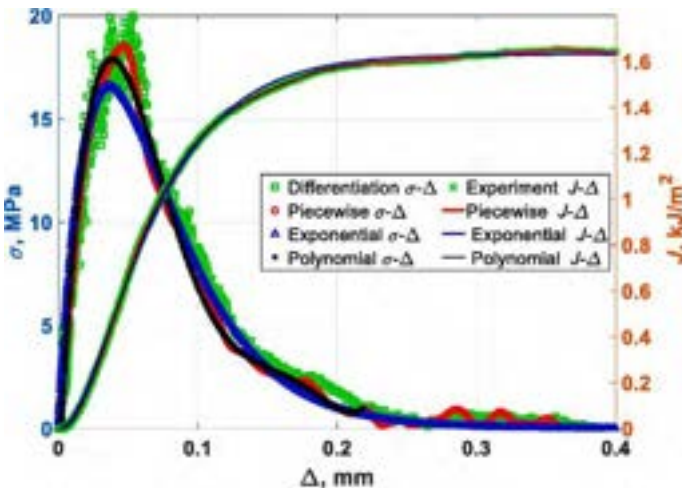


Fig. 32.16 R curve data for a ductile polyurethane and their corresponding TSLs acquired through differentiation of J with respect to δ_n (labeled Δ by authors). Used with permission from F. Sun, B.R.K. Blackman, A DIC method to determine the mode I energy release rate G , the J -integral and the traction-separation law simultaneously for adhesive joints, Eng. Fract. Mech. 234 (2020) 107097.

for a ductile polyurethane acquired by differentiating piecewise, exponential, and polynomial fits of the experimentally obtained J -integral as a function of δ_n , suggesting that the three fitting methods predict similar TSLs [72].

In a related approach, so called bond slip models have been used to extract TSLs using relative sliding motion between adherends loaded in shear, especially for civil structure reinforcement applications [100,101]. Bond-slip, the relative motion of a thinner adherend with respect to a more massive substrate to which it is bonded, decays with distance from the joint end and shifts as crack propagation proceeds, initiating at the end of the stiffer member (where Volkersen shear lag stresses are expected to be greatest) and propagating toward the end of the thinner member. Researchers have used DIC to measure the spatial variations in adherend strain as loading proceeds, then differentiated these to estimate shear stresses in the bondline. These stresses, along with the relative slip inferred across the interface, provide TSL representations of adhesive behavior. Using relatively compliant adherends bonded to very stiff steel, concrete, and fiber-reinforced composite substrates [102–104], translation measurements of the less stiff member allow the extraction of TSLs in shear for fracture propagation. This approach is akin to that seen in Fig. 32.7 [26] if debonding were to proceed.

32.5.3 Using DIC to acquire rate-dependent traction-separation laws

As structural adhesives are viscoelastic materials, their mechanical properties are dependent on time or rate and also temperature. The time-temperature superposition principle (TTSP) often serves as a guide in understanding and explaining their interactions. At either cooler temperatures or faster loading rates, adhesives typically become more glassy and brittle; at higher temperatures or slower loading rates, structural adhesives often exhibit greater ductility and enhanced energy dissipation capabilities. The literature on adhesive fracture is dominated by quasi-static testing because studies on the rate effect of fracture often require high-speed cameras and more capable loading equipment, as well as a more advanced experimental design due to the increased influence of dynamic effects. Long-term properties for viscoelastic adhesives also add complexity for experimental characterization and modeling. Building on earlier works [28,81] work, recent research has been published suggesting test techniques and analytical procedures for rate-effect tests on bonded joints, such as [105]. Rajan [41] tested the rate-dependent response of bitumen, a thermoplastic material used to bond roofing shingles, which are intended to endure a variety of loading rates due to wind. Their work used two DIC systems to record tests, a high-magnification system to capture the local displacements around the crack tip, and a low-magnification system to visualize and measure displacement and strain fields for the full specimen. To accommodate their methods with good DIC practice, two different speckle patterns were applied to the in-plane surfaces of the specimens: a finer speckle pattern applied to the high-magnification side and a coarser speckle pattern for the low-magnification side. The low-magnification system was used to measure the evolution of the FPZ. Their results showed a strong dependence of the TSL on displacement rate, with joints exhibiting more ductility at lower displacement rates. Similar results were obtained by Sun et al. [21], who used DIC to study the

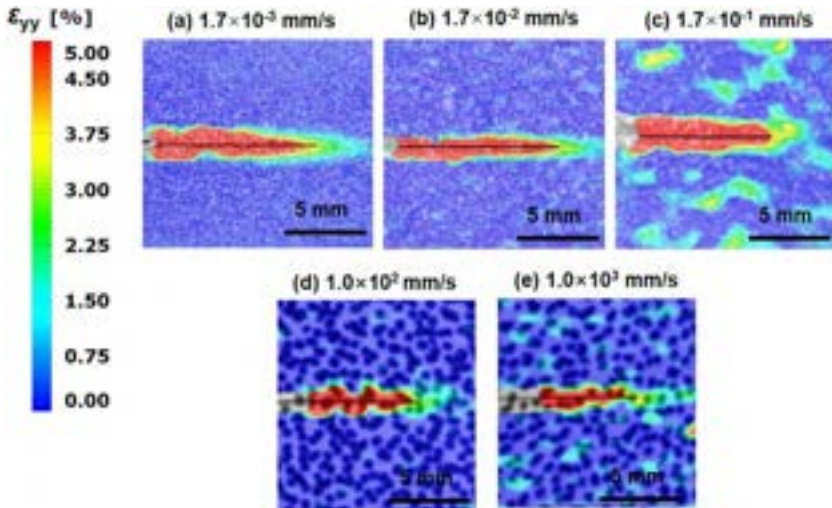


Fig. 32.17 Reduction of fracture process zone size with increasing rate, exhibiting the stiffening of the adhesive around the crack tip [21].

Used with permission from F. Sun, R. Zhang, B.R.K. Blackman, Determination of the mode I crack tip opening rate and the rate dependent cohesive properties for structural adhesive joints using digital image correlation, *Int. J. Solids Struct.* 217–218 (2021) 60–73.

correlation between loading rate and crack tip opening velocity for a ductile epoxy and ductile polyurethane. Their work showed that the shape of a TSL was strongly influenced by the strain rate at the crack tip. Thus, for modeling at various rates, a strain rate-dependent CZM model is necessary for some systems. For both the polyurethane in Sun et al.'s study and the bitumen in Rajan et al.'s study, J_c and σ increased to a critical rate and subsequently decreased at higher rates. Interestingly, Rajan et al.'s fastest loading rate correlated to both the lowest average crack tip strain and strain rate; however, they surmised that this occurred because large stresses quickly accrued at the crack tip, causing failure before the viscoelastic material could deform accordingly.

Images of a decreasing FPZ size with increasing displacement rate are shown Fig. 32.17, taken from [21]. They concluded that the shortening of the FPZ length can be attributed to the stiffening of the adhesive, and that the decrease in cohesive tractions and fracture energy may be due to the locus of failure shifting from cohesive failures to interfacial failures [21,106]. Results such as these suggest the value of DIC experiments to obtain TSLs, including associated rate dependence.

32.6 Case study: Using DIC with FEA to develop a mixed-mode fracture envelope

The focus of Chapter 17, mode mixity is of special importance for adhesively bonded joints, where cracks are often constrained to grow along an interface or within an adhesive layer, rather than in a Mode I fashion as is commonly seen in isotropic, monolithic

materials. Oftentimes, a mixed-mode coupling relationship to fill the envelope between Modes I (0 degrees) and II (90 degrees) must be fit to mixed-mode test results. While these mixed-mode coupling relationships have been empirically developed, they have been shown to be practical for modeling modern structural adhesives [107–110]. Using DIC, we can compare local displacement and strain fields acquired experimentally to CZM models. This information provides insights to both model information as well as capabilities and limitations of CZMs.

32.6.1 Traction-separation law determination

Cohesive zone modeling capabilities within Abaqus [111] were used to simulate crack growth for fracture specimens (Al 2024-T3 adherends bonded with a 0.25 mm layer of PR-2930 adhesive). Unlike data analysis methods based on linear elastic adherends, these simulations used nonlinear material models for monotonically loaded Al 2024-T3 adherends to account for energy dissipation within the adherends, as yielding was seen with thinner DCB adherends and most SLB and ENF specimens, regardless of thickness. TSLs were acquired using the property identification approach, collecting data from bulk adhesive tensile tests, thick adherend shear tests (TAST), and butt joints, in addition to the fracture tests. The TSLs used were bi-linear in shape and used a B-K coupling for mixed-mode fracture modeling. The main parameters for the PR-2930 CZMs can be seen in Table 32.1. E (normal) and G (shear) are the initial stiffnesses, t_n and t_s are the maximum traction values, and η represents the B-K parameter used to fit the B-K coupling law, given in Chapter 17, to mixed-mode data.

32.6.2 Evaluating cohesive zone model fit to DIC data

To check Mode I and Mode II TSL properties, FEA outputs are typically compared to the experimentally measured load vs displacement curves. The FEA curves seen in Fig. 32.18 use bi-linear Mode I and Mode II TSLs and show good fit to the data. However, to get these load vs displacement curve fits, it is necessary to either remove the machine compliance from the experimental data or to add springs to the boundaries of the FEA models to act as an analog for the machine compliance. This step can often be tedious, and can be bypassed by using DIC to measure local displacements by taking the difference in opening (Mode I) or sliding (Mode II) displacements between any set of symmetric points on each adherend.

Fig. 32.19 shows plots of both DIC and FEA local displacements vs load for the same specimens shown in 32.18. The local displacements shown in Fig. 32.19 are the opening and sliding displacements measured at the crack tip in the adherends at locations 2 mm from their respective bond interface. Care should be taken when

Table 32.1 PR-2930 cohesive zone model parameters.

E (MPa)	t_n (MPa)	G_{Ic} (kJ/m ²)	G (MPa)	t_s (MPa)	G_{IIc} (kJ/m ²)	η
2800	84	3.2	1000	65	14	2

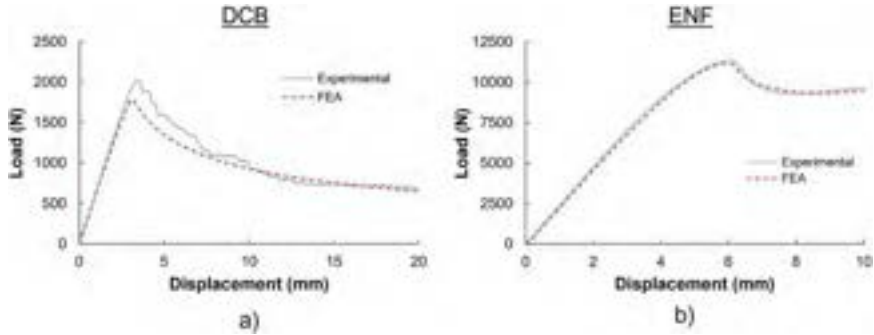


Fig. 32.18 Load-displacement curves for (a) DCB and (b) ENF tests comparing global load and crosshead displacement data for experimental and FEA results. The FEA curves use a spring boundary condition, tuned to account for load train compliance present in the experimental data.

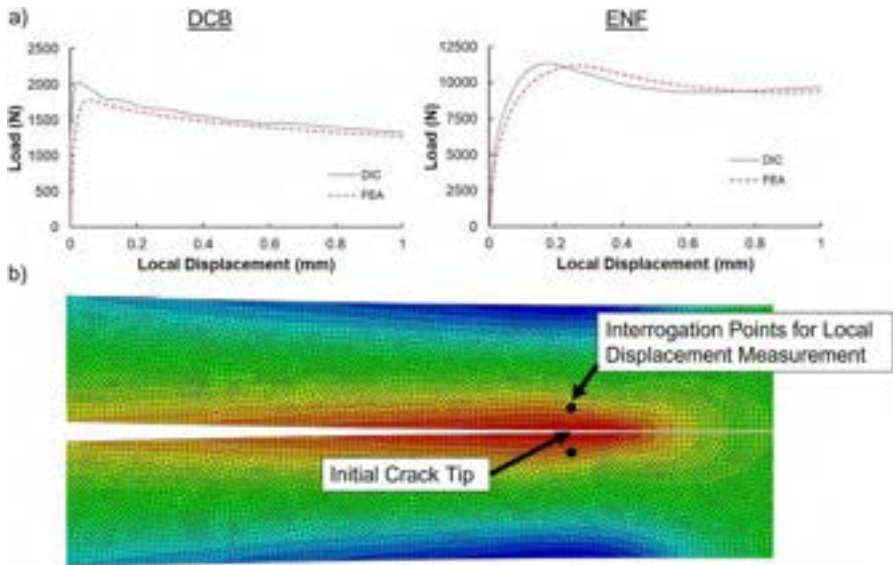


Fig. 32.19 Result comparison based on local displacements from FEA and DIC measurements: (a) comparison of local displacements for both the DCB and ENF specimens. Compared to the global data, the fit of the DCB TSL appears to be slightly better using the local data whereas the ENF specimen now appears worse. (b) FEA model with marked locations of the interrogation points used to gather the data. For both DIC and FEA, data was collected about 2 mm above and below the bondline interface at the initial crack tip.

using data near the adhesive layer, as it has been reported the smoothing algorithms used in DIC may produce erroneous data [23]. These more local measurements for evaluating CZMs show a better fit for the DCB FEA model, and a weaker fit for the ENF model. For the ENF model, this may be attributable to the bi-linear shape of the TSL, which has a much sharper stiffness degradation compared to the trapezoidal model. This is discussed in more detail in [78].

Strains can also be measured with DIC and compared to the strain data obtained from FEA. These measurements may prove to be insightful for further validations of models; However, the limitations of both FEA modeling and DIC should be considered when directly comparing strain fields. Such limitations may be the plane strain/stress FEA models often used and the resolution of the surface strain fields acquired from DIC. Fig. 32.20 compares in-plane strains taken at a point on a DCB specimen with 12.7 mm thick adherends. Despite some apparent differences, likely due to limitations of the model and measurement resolution, the ability of the 2D model to capture the global joint behavior as well as mimic the local strain curve shapes, shows the power of this modeling technique. The agreement for ϵ_{xx} appears very good. One suggestion for the offset of ϵ_{yy} peak locations and magnitudes seen in Fig. 32.20 is the anticlastic bending captured along specimen edges by DIC and ignored by the 2D plane stress FEA model. Anticlastic bending also causes shear stresses to vary across the cross section [80]. For a specimen loaded in bending, the maximum shear stresses occur along the edges of the specimen. This likely explains the difference in the magnitudes of ϵ_{xy} . While these suggestions seem mechanically plausible, a 3D FEA model would be necessary to validate them.

Once TSLs for Mode I and Mode II have been determined, the programmed coupling law should be evaluated for its fit to mixed-mode fracture tests, such as the mixed-mode bend (MMB), single-leg bend (SLB), and asymmetric adherend geometries of fracture tests. Using local displacements again, mixed-mode tests can be decomposed into opening and sliding displacements to determine the calibration factor used in mixed-mode coupling equations. Just like in the pure modes, the coupling law that provides the best fit to experimental data should be selected, and thus a CZM for a mixed-mode fracture envelope is developed. Fig. 32.21 shows a comparison of

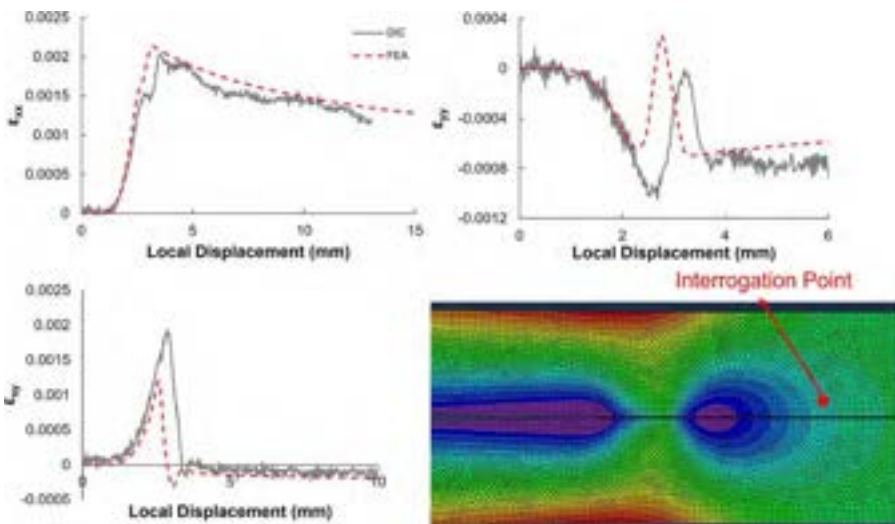


Fig. 32.20 Strain fields for a point along the bondline about 2 mm above the interface of a 0.25 mm thick bond. Because it increased monotonically, unlike load, the local displacement used in Fig. 32.19a is plotted on the abscissa.

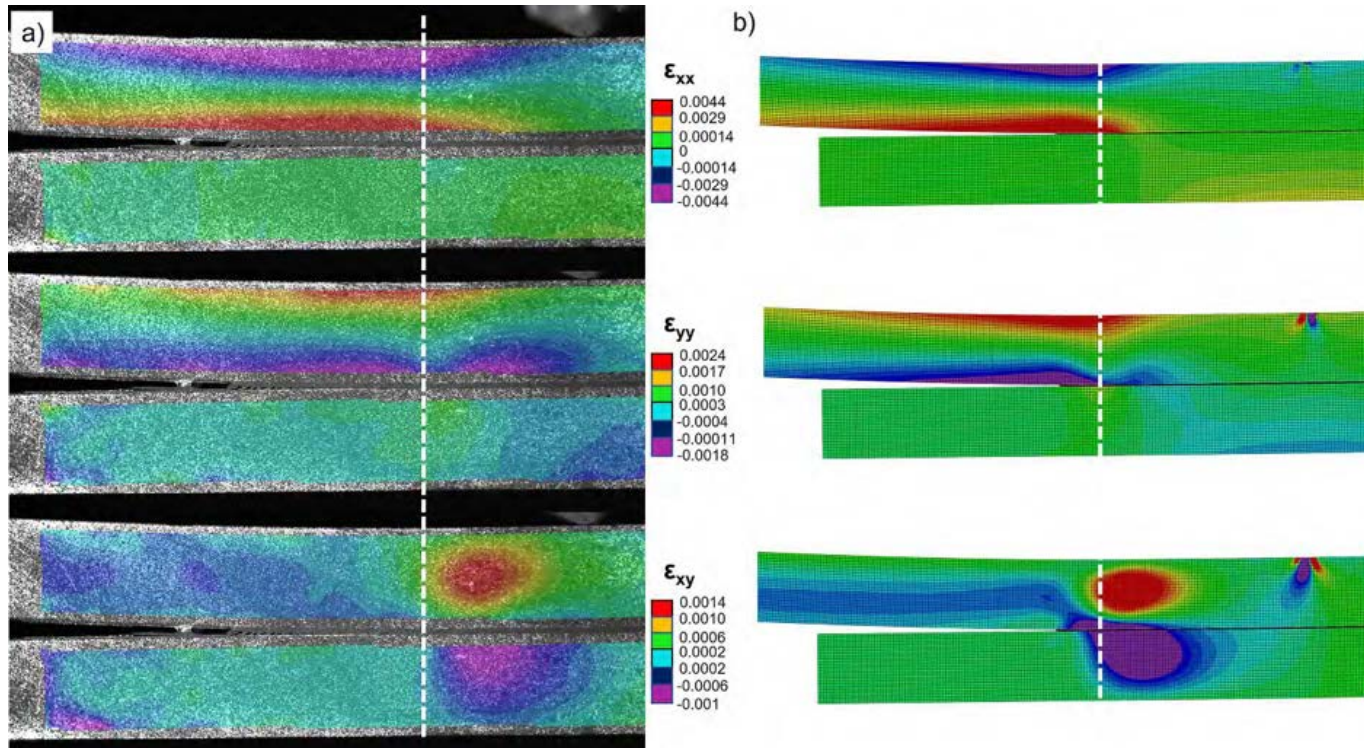


Fig. 32.21 (a) DIC and (b) FEA in-plane strain fields for an SLB test with the crack tip marked by a *dashed line*. The side-by-side images of these figures show how strain fields relate ahead of a crack tip, with longitudinal strains and transverse strains peaking near the crack tip. Transverse strains show BoEF behavior around the crack tip and shear strains show the complex transfer of forces at the edge of the bond.

both the DIC and FEA strain fields for an SLB specimen with 12.7 mm adherends. The model used a B-K coupling law with the data shown in [Table 32.1](#). The resolution of the full specimen strain field acquired by the DIC imaging is astonishing, smoothly conveying full fields with strains on the order of 10^{-4} . Just like what can be observed with the DCB specimen in [Fig. 32.13](#), the transverse strains exhibit a BoEF behavior, allowing one to estimate the location of the crack tip and size of the FPZ. Longitudinal strains are directed into the loaded upper adherend of the specimen, resulting in some degree of yielding, again showing the necessity of using FEA to sufficiently calibrate a TSL and model joint behavior. Furthermore, the visualization of the complex transfer of shear around the crack tip is an impressive capability, seldom seen in other imaging techniques.

32.7 Conclusions

While a number of optical techniques for measurement have been used in research, DIC has emerged as an increasingly popular method. The ability of DIC to measure a field of deformations in multiple axes is incredibly powerful, and not always available in other methods. This, coupled with its versatility, adaptability to various length scales, and relative ease of use, have led to numerous applications, including for adhesively bonded joints. This chapter has given a general overview of how DIC works and demonstrated various ways DIC has been employed to further the mechanical understanding of bonded joint behavior. Using DIC to obtain high-resolution measurements of strain fields has allowed for more accurate parameterization of constitutive properties and performance, and displacement results have been helpful for calibrating and validating numerical simulations. Using DIC for measuring adherend displacements has been shown to be useful for more accurately acquiring fracture parameters and FPZ details for both quasi static and rate-dependent applications as well as facilitating the extraction of TSLs from opening and sliding displacements across the bondline.

As a robust and versatile full-field imaging method, DIC provides rich details on in-plane and even out-of-plane displacements to aid our understanding and correlate with any number of locations within a specimen and FEA model. The high-resolution fields and data that DIC can acquire bode well for further improvements in methods for fitting of TSLs, particularly when using inverse methods. By taking a large set of DIC data points across a specimen, an inverse method could be applied in which a variety of TSLs are iteratively evaluated until a desired fit to the data is achieved. Some commercial DIC developers offer software with capabilities to compare DIC and FEA displacement fields, enabling the user to both refine their model and better understand its limitations. Such a feature appears to be a great tool for implementing inverse solvers to determine TSLs.

DIC has seen significant strides over the past several decades, and further improvements to experimental techniques as well as algorithms provide exciting opportunities for future research, including in the broad field of adhesion. The continued growth of adhesive bonding for an ever-increasing range of challenging applications will require an advanced understanding of mechanical parameters of adhesive materials to meet

performance and durability requirements of bonded structures. The implementation of the DIC method, as illustrated herein, confirms the possibilities of this method, including to calibrate and validate the results obtained with numerical simulations.

Acknowledgments

The authors would like to acknowledge helpful discussions with Dr. Robert Jensen and Dr. Marvin Pollum, and Profs. Bamber Blackman, Ian Ashcroft, Ian Maskery, Kenneth Liechti, and Michael Thouless, as well as Prof. Bilel Aidi, who also supplied Arcan images and data. CMJ also acknowledges support from the National Science Foundation's International Research Experience for Students Fellowship Program. PPG Industries acknowledges that research was sponsored by the US Department of Defense and was accomplished under Cooperative Agreement Award #HQ0034-15-2-0007 to NCMS. The views and conclusions contained in this report are those of the authors and should not be interpreted as representing the official policies, either expressed or implied, of the US government. The US government is authorized to reproduce and distribute reprints for government purposes notwithstanding any copyright notation herein.

References

- [1] M.M. Frocht, *Photoelasticity*, Wiley, 1941.
- [2] D. Post, B. Han, P. Ifju, *High Sensitivity Moiré: Experimental Analysis for Mechanics and Materials*, Springer Science & Business Media, 1997.
- [3] W. Steinchen, L. Yang, *Digital Shearography: Theory and Application of Digital Speckle Pattern Shearing Interferometry*, 100, CCH, 2003. vol.
- [4] J.F. Kalthoff, The shadow optical method of caustics, in: *Static and Dynamic Photoelasticity and Caustics*, Springer, 1987, pp. 407–522.
- [5] G.A. Papadopoulos, *Fracture Mechanics: The Experimental Method of Caustics and the Det.-Criterion of Fracture*, Springer Science & Business Media, 2012.
- [6] J.W. Dally, W.F. Riley, *Experimental stress analysis*, McGraw-Hill, 1978.
- [7] W.N. Sharpe, *Springer Handbook of Experimental Solid Mechanics*, Springer Science & Business Media, 2008.
- [8] G. Cloud, Optical methods in experimental mechanics, *Exp. Tech.* 33 (5) (2009) 13–17.
- [9] J.A. McGuire, S.D. Abramowitch, S. Maiti, R. De Vita, Swine vagina under planar biaxial loads: an investigation of large deformations and tears, *J. Biomech. Eng.* 141 (4) (2019) 041003.
- [10] R. Zhao, S. Lin, H. Yuk, X. Zhao, Kirigami enhances film adhesion, *Soft Matter* 14 (13) (2018) 2515–2525.
- [11] L.I. Farfan-Cabrera, J.B. Pascual-Francisco, An experimental methodological approach for obtaining viscoelastic Poisson's ratio of elastomers from creep strain DIC-based measurements, *Exp. Mech.* 62 (2) (2022) 287–297.
- [12] Y. Li, D.A. Dillard, Y.-H. Lai, S.W. Case, M.W. Ellis, M.K. Budinski, C.S. Gittleman, Experimental measurement of stress and strain in Nafion membrane during hydration cycles, *J. Electrochem. Soc.* 159 (2) (2011) B173.
- [13] M.A. Caminero, S. Pavlopoulou, M. Lopez-pedrosa, B.G. Nicolaisson, C. Pinna, C. Soutis, Analysis of adhesively bonded repairs in composites: Damage detection and prognosis, *Compos. Struct.* 95 (2013) 500–517.

- [14] M.A. Caminero, M. Lopez-Pedrosa, C. Pinna, C. Soutis, Damage monitoring and analysis of composite laminates with an open hole and adhesively bonded repairs using digital image correlation, *Compos. Part B Eng.* 53 (2013) 76–91.
- [15] B. Gencturk, K. Hossain, A. Kapadia, E. Labib, Y.-L. Mo, Use of digital image correlation technique in full-scale testing of prestressed concrete structures, *Measurement* 47 (2014) 505–515.
- [16] S.G. Shah, J.M. Chandra Kishen, Fracture properties of concrete-concrete interfaces using digital image correlation, *Exp. Mech.* 51 (2011) 303–313.
- [17] D. Corr, M. Accardi, L. Graham-Brady, S. Shah, Digital image correlation analysis of interfacial debonding properties and fracture behavior in concrete, *Eng. Fract. Mech.* 74 (2007) 109–121.
- [18] C. Caggegi, L. Chevalier, V. Pensée, M. Cuomo, Strain and shear stress fields analysis by means of Digital Image Correlation on CFRP to brick bonded joints fastened by fiber anchors, *Construct. Build Mater.* 106 (2016) 78–88.
- [19] E.D. Reedy Jr, Strength of butt and sharp-cornered joints, in: D.A. Dillard, A.V. Pocius (Eds.), *The Mechanics of Adhesion*, 2002, pp. 145–192.
- [20] R.D. Adams, R.D. Adams, J. Comyn, W.C. Wake, W.C. Wake, *Structural Adhesive Joints in Engineering*, Springer Science & Business Media, 1997.
- [21] F. Sun, R. Zhang, B.R.K. Blackman, Determination of the mode I crack tip opening rate and the rate dependent cohesive properties for structural adhesive joints using digital image correlation, *Int. J. Solids Struct.* 217–218 (2021) 60–73.
- [22] D.A. Dillard, B. Mukherjee, P. Karnal, R.C. Batra, J. Frechette, A review of Winkler's foundation and its profound influence on adhesion and soft matter applications, *Soft Matter* 14 (19) (2018) 3669–3683.
- [23] J.M. Gorman, M.D. Thouless, The use of digital-image correlation to investigate the cohesive zone in a double-cantilever beam, with comparisons to numerical and analytical models, *J. Mech. Phys. Solids* 123 (2019) 315–331.
- [24] E. Serrano, B. Enquist, Contact-free measurement and non-linear finite element analyses of strain distribution along wood adhesive bonds, *Holzforschung* 59 (2005) 641–646.
- [25] M. Goland, E. Reissner, The stresses in cemented joints, *J. Appl. Mech.* 11 (1944) A17–A27.
- [26] A.R. Mojdehi, D.P. Holmes, D.A. Dillard, Revisiting the generalized scaling law for adhesion: role of compliance and extension to progressive failure, *Soft Matter* 13 (41) (2017) 7529–7536.
- [27] B. Aidi, D.A. Dillard, Using DIC to characterize constitutive properties of adhesively bonded Arcan specimens, *Int. J. Adhes. Adhes.* (2023) (In preparation).
- [28] Y. Zhu, K.M. Liechti, K. Ravi-Chandar, Direct extraction of rate-dependent traction-separation laws for polyurea/steel interfaces, *Int. J. Solids Struct.* 46 (2009) 31–51.
- [29] J.M. Vasco-Olmo, F.A. Díaz, F.V. Antunes, M.N. James, Characterisation of fatigue crack growth using digital image correlation measurements of plastic CTOD, *Theor. Appl. Fract. Mech.* 101 (2019) 332–341.
- [30] M. Pankow, B. Justusson, M. Riosbaas, A.M. Waas, C.F. Yen, Effect of fiber architecture on tensile fracture of 3D woven textile composites, *Compos. Struct.* 225 (2019) 111139.
- [31] B. Blackman, J.P. Dear, A.J. Kinloch, S. Osiyemi, The calculation of adhesive fracture energies from double-cantilever beam test specimens, *J. Mater. Sci. Lett.* 10 (5) (1991) 253–256.
- [32] A.J. Paris, P.C. Paris, Instantaneous evaluation of J and C, *Int. J. Fract.* 38 (1988) R19–R21.
- [33] R.B. Sills, M.D. Thouless, Cohesive-length scales for damage and toughening mechanisms, *Int. J. Solids Struct.* 55 (1) (2015) 32–43.

- [34] W.H. Peters, W.F. Ranson, Digital imaging techniques in experimental stress analysis, *Opt. Eng.* 21 (3) (1982) 427–431.
- [35] T.C. Chu, W.F. Ranson, M.A. Sutton, Applications of digital-image-correlation techniques to experimental mechanics, *Exp. Mech.* 25 (3) (1985) 232–244.
- [36] M.A. Sutton, J.-J. Orteu, H. Schreier, *Image Correlation for Shape, Motion and Deformation Measurements: Basic Concepts, Theory and Applications*, vol. 1, Springer, 2009.
- [37] G. Lionello, C. Sirieix, M. Baleani, An effective procedure to create a speckle pattern on biological soft tissue for digital image correlation measurements, *J. Mech. Behav. Biomed. Mater.* 39 (2014) 1–8.
- [38] K.N. Jonnalagadda, I. Chasiotis, S. Yagnamurthy, J. Lambros, J. Pulskamp, R. Polcawich, M. Dubey, Experimental investigation of strain rate dependence of nanocrystalline Pt films, *Exp. Mech.* 50 (1) (2010) 25–35.
- [39] Y.J. Hu, Y.J. Wang, J.B. Chen, J.M. Zhu, A new method of creating high-temperature speckle patterns and its application in the determination of the high-temperature mechanical properties of metals, *Exp. Tech.* 42 (5) (2018) 523–532.
- [40] V.P. Rajan, M.N. Rossol, F.W. Zok, Optimization of digital image correlation for high-resolution strain mapping of ceramic composites, *Exp. Mech.* 52 (9) (2012) 1407–1421.
- [41] S. Rajan, M.A. Sutton, R. Fuerte, A. Kidane, Traction-separation relationship for polymer-modified bitumen under mode I loading: double cantilever beam experiment with stereo digital image correlation, *Eng. Fract. Mech.* 187 (2018) 404–421.
- [42] S. Amini, R.S. Kumar, A high-fidelity strain-mapping framework using digital image correlation, *Mater. Sci. Eng. A* 594 (2014) 394–403.
- [43] P.L. Reu, W. Sweatt, T. Miller, D. Fleming, Camera system resolution and its influence on digital image correlation, *Exp. Mech.* 55 (1) (2015) 9–25.
- [44] L. Yu, B. Pan, The errors in digital image correlation due to overmatched shape functions, *Meas. Sci. Technol.* 26 (4) (2015) 045202.
- [45] Y.L. Dong, B. Pan, A review of speckle pattern fabrication and assessment for digital image correlation, *Exp. Mech.* 57 (8) (2017) 1161–1181.
- [46] B. Pan, Digital image correlation for surface deformation measurement: historical developments, recent advances and future goals, *Meas. Sci. Technol.* 29 (8) (2018) 082001.
- [47] H. Yang, W. Zhang, R.D. Moffitt, T.C. Ward, D.A. Dillard, Multi-layer in-situ for evaluation of dynamic mechanical properties of pressure sensitive adhesives, *Int. J. Adhes. Adhes.* 27 (7) (2007) 536–546.
- [48] R.B. Krieger, *Stress Analysis Concepts for Adhesive Bonding of Aircraft Primary Structure*, ASTM International, 1988.
- [49] D. Post, R. Czarnek, J.D. Wood, D. Joh, *Deformations and strains in a thick adherend lap joint*, in: *Adhesively Bonded Joints: Testing, Analysis, and Design*, ASTM International, 1988.
- [50] K. Colavito, J. Gorman, E. Madenci, S. Smeltzer, Refinements in digital image correlation technique to extract adhesive strains in lap joints, in: *50th AIAA/ASME/ASCE/AHS/ASC Structures, Structural Dynamics, and Materials Conference 17th AIAA/ASME/AHS Adaptive Structures Conference 11th AIAA No*, 2009, p. 2504.
- [51] A.N. Gent, P.B. Lindley, The compression of bonded rubber blocks, *Proc. Inst. Mech. Eng.* 173 (1) (1959) 111–122.
- [52] Y. Liu, J. Johnston, A. Chattopadhyay, Non-destructive evaluation of composite adhesive kissing bond, in: *ASME International Mechanical Engineering Congress and Exposition*, vol. 56178, American Society of Mechanical Engineers, 2013. V001T01A035.
- [53] K.H. Khafagy, S. Datta, T.G. Stoumbos, D. Inoyama, A. Chattopadhyay, Experimental characterization and testing of adhesive bonding for space structure applications, in: *AIAA SCITECH 2022 Forum*, 2022, p. 0800.

- [54] K.H. Khafagy, T.G. Stoumbos, D. Inoyama, S. Datta, A. Chattopadhyay, In-situ investigation of temperature-dependent adhesive properties and failure modes in composite bonded joints, *Compos. Struct.* 300 (2022) 116113.
- [55] Z. He, Q. Luo, Q. Li, G. Zheng, G. Sun, Fatigue behavior of CFRP/Al adhesive joints—failure mechanisms study using digital image correlation (DIC) technique, *Thin-Walled Struct.* 174 (2022) 109075.
- [56] Y. Sekiguchi, M. Nakanouchi, K. Haraga, I. Takasaki, C. Sato, Experimental investigation on strength of stepwise tailored single lap adhesive joint using second-generation acrylic adhesive via shear and low-cycle shear tests, *Int. J. Adhes. Adhes.* 95 (2019) 102438.
- [57] L.J. Hart-Smith, *Adhesive-Bonded Single-Lap Joints*, 1973. Technical Report.
- [58] L.R. Xu, H. Kuai, S. Sengupta, A novel joint between dissimilar materials inspired by the mechanics of trees, *MRS Online Proc. Libr. (OPL)* 844 (2004) Y8.4.
- [59] F. Ramezani, M.R. Ayatollahi, A. Akhavan-Safar, L.F.M. Da Silva, A comprehensive experimental study on bi-adhesive single lap joints using DIC technique, *Int. J. Adhes. Adhes.* 102 (2020) 102674.
- [60] A.S.T.M. D1002-10, Standard Test Method for Apparent Shear Strength of Single-Lap-Joint Adhesively Bonded Metal Specimens by Tension Loading (Metal-to-Metal), ASTM International, West Consohocken, PA, 2010.
- [61] P.A.M.G.P. Bamberg, U. Reisingen, A. Schiebahn, J.D.V. Barbosa, B. Marx, R.S. Coelho, Digital image correlation analysis of the effects of the overlap length, adhesive thickness and adherends yield strength over similar and dissimilar joints of high strength steel and aluminum alloys, *Int. J. Adhes. Adhes.* 83 (2018) 69–75.
- [62] G. Sun, X. Liu, G. Zheng, Z. Gong, Q. Li, On fracture characteristics of adhesive joints with dissimilar materials—An experimental study using digital image correlation (DIC) technique, *Compos. Struct.* 201 (2018) 1056–1075.
- [63] A.R.L. CCDC, MIL-PRF-32662: Adhesive, High-Loading Rate, for Structural and Armor Applications, Aberdeen Proving Ground (MD): CCDC Army Research Laboratory (US), Aberdeen, MD, 2020. https://quicksearch.dla.mil/qsDocDetails.aspx?ident_number=283919.
- [64] A.R.L. CCDC, MIL-PRF-32662: Adhesive, High-Loading Rate, for Structural and Armor Applications—Frequently Asked Questions, Aberdeen Proving Ground (MD): CCDC Army Research Laboratory (US), Aberdeen, MD, 2020. <https://apps.dtic.mil/sti/citations/AD1110598>.
- [65] O. Volkersen, Die Nietkraftverteilung in zugbeanspruchten Nietverbindungen mit konstanten Laschenquerschnitten, *Luftfahrtforschung* 15 (1938) 41–47.
- [66] K.W. Allen, M.E.R. Shanahan, The creep behaviour of structural adhesive joints: Part I, *J. Adhes.* 7 (3) (1975) 161–174.
- [67] K.W. Allen, M.E.R. Shanahan, The creep behaviour of structural adhesive joints: Part II, *J. Adhes.* 8 (1) (1976) 43–56.
- [68] M. Charalambides, A.J. Kinloch, Y. Wang, J.G. Williams, On the analysis of mixed-mode failure, *Int. J. Fract.* 54 (3) (1992) 269–291.
- [69] D.A. Dillard, H.K. Singh, D.J. Pohlit, J.M. Starbuck, Observations of decreased fracture toughness for mixed mode fracture testing of adhesively bonded joints, *J. Adhes. Sci. Technol.* 23 (2009) 1515–1530.
- [70] M.D. Thouless, Fracture Resistance of an Adhesive Interface, *Scr. Metallurgica Mater.* 26 (6) (1992) 949–951.

- [71] I.A. Ashcroft, A. Mubashar, Numerical approach: finite element analysis, in: L.F.M. da Silva, A. Öchsner, R.D. Adams (Eds.), *Handbook of Adhesion Technology*, Springer International Publishing, 2018, pp. 701–739, ISBN: 978-3-319-55411-2, https://doi.org/10.1007/978-3-319-55411-2_25.
- [72] F. Sun, B.R.K. Blackman, A DIC method to determine the mode I energy release rate G , the J-integral and the traction-separation law simultaneously for adhesive joints, *Eng. Fract. Mech.* 234 (2020) 107097.
- [73] B.R.K. Blackman, A.J. Kinloch, F.S. Rodriguez-Sanchez, W.S. Teo, The fracture behaviour of adhesively-bonded composite joints: effects of rate of test and mode of loading, *Int. J. Solids Struct.* 49 (2012) 1434–1452.
- [74] M.F.S.F de Moura, R.D.S.G. Campilho, J.P.M. Gonçalves, Crack equivalent concept applied to the fracture characterization of bonded joints under pure mode I loading, *Compos. Sci. Technol.* 68 (2008) 2224–2230.
- [75] S Li, J Wang, M.D. Thouless, The effects of shear on delamination in layered materials, *J. Mech. Phys. Solids* 52 (2004) 193–214.
- [76] M.D. Thouless, Shear forces, root rotations, phase angles and delamination of layered materials, *Eng. Fract. Mech.* 191 (2018) 153–167.
- [77] C.M. Jackson, *Experimental and Numerical Methods for Characterizing the Mixed-Mode Fracture Envelope for a Tough Epoxy*, (Master's thesis), Virginia Tech, 2022.
- [78] C.M. Jackson, J.A. McGuire, M. Losada, I. Ashcroft, R. De Vita, D.A. Dillard, Using digital image correlation to construct a mixed-mode fracture envelope for a tough epoxy, *Eng. Fract. Mech.* (2023). In preparation.
- [79] F. Sun, B.R.K. Blackman, Using digital image correlation to automate the measurement of crack length and fracture energy in the mode I testing of structural adhesive joints, *Eng. Fract. Mech.* 255 (2021) 107957.
- [80] R.C. Hibbeler, *Mechanics of Materials*, Pearson, Hoboken, NJ, 2015.
- [81] C. Sun, M.D. Thouless, A.M. Waas, J.A. Schroeder, P.D. Zavattieri, Rate effects for mixed-mode fracture of plastically-deforming, adhesively-bonded structures, *Int. J. Adhes. Adhes.* 29 (4) (2009) 434–443.
- [82] R.J. Pomeroy, The effect of anticlastic bending on the curvature of beams, *Int. J. Solids Struct.* 6 (2) (1970) 277–285.
- [83] J. Manterola, J. Renart, J. Zurbitu, A. Turon, I. Urresti, Mode I fracture characterisation of rigid and flexible bonded joints using an advanced Wedge-Driven Test, *Mech. Mater.* 148 (2020) 103534.
- [84] T. Yang, V. Gandhi, R. Huang, K.M. Liechti, Rate dependent fracture along a silicon/epoxy interface under mixed-mode loading conditions, *Int. J. Solids Struct.* 257 (2021) 111129.
- [85] H.K. Singh, A. Chakraborty, C.E. Frazier, D.A. Dillard, Mixed mode fracture testing of adhesively bonded wood specimens using a dual actuator load frame, *Holzforschung* 64 (2010) 353–361.
- [86] H. Chai, Shear fracture, *Int. J. Fract.* 37 (2) (1988) 137–159.
- [87] Y.-H. Lai, D.A. Dillard, Using the fracture efficiency to compare adhesion tests, *Int. J. Solids Struct.* 34 (4) (1997) 509–525.
- [88] K. Leffler, K.S. Alfredsson, U. Stigh, Shear behaviour of adhesive layers, *Int. J. Solids Struct.* 44 (2007) 530–545.
- [89] E.F. Rybicki, M.F. Kanninen, A finite element calculation of stress intensity factors by a modified crack closure integral, *Eng. Fract. Mech.* 9 (4) (1977) 931–938.

- [90] T. Belytschko, T. Black, Elastic crack growth in finite elements with minimal remeshing, *Int. J. Numer. Methods Eng.* 45 (5) (1999) 601–620.
- [91] R.D.F. Moreira, M.F.S.F de Moura, F.G.A. Silva, A novel strategy to obtain the fracture envelope under mixed-mode I+II loading of composite bonded joints, *Eng. Fract. Mech.* 232 (2020) 107032.
- [92] Z. Suo, J.W. Hutchinson, Interface crack between two elastic layers, *Int. J. Fract.* 43 (1990) 1–18.
- [93] D.S. Dugdale, Yielding of steel sheets containing slits, *J. Mech. Phys. Solids* 8 (1960) 100–104.
- [94] G.I. Barenblatt, The mathematical theory of equilibrium cracks in brittle fracture, in: H. L. Dryden, T. von Kármán, G. Kuerti, F.H. van den Dungen, L. Howarth (Eds.), *Advances in Applied Mechanics*, vol. 7, Elsevier, 1962, pp. 55–129.
- [95] A. Hillerborg, M. Modéer, P.-E. Petersson, Analysis of crack formation and crack growth in concrete by means of fracture mechanics and finite elements, *Cem. Concr. Res.* 6 (1976) 773–781.
- [96] J.P. Parmigiani, M.D. Thouless, The effects of cohesive strength and toughness on mixed-mode delamination of beam-like geometries, *Eng. Fract. Mech.* 74 (2007) 2675–2699.
- [97] R.D.S.G. Campilho, M.D. Banea, J.A.B.P. Neto, L.F.M. da Silva, Modelling adhesive joints with cohesive zone models: effect of the cohesive law shape of the adhesive layer, *Int. J. Adhes. Adhes.* 44 (2013) 48–56.
- [98] L.F.M. da Silva, R.D.S.G. Campilho, *Advances in numerical modelling of adhesive joints*, in: *Advances in Numerical Modeling of Adhesive Joints*, Springer Berlin Heidelberg, Berlin, Heidelberg, 2012, pp. 1–93, ISBN: 978-3-642-23608-2, https://doi.org/10.1007/978-3-642-23608-2_1.
- [99] B.F. Sørensen, T.K. Jacobsen, Determination of cohesive laws by the J integral approach, *Eng. Fract. Mech.* 70 (14) (2003) 1841–1858.
- [100] H.-T. Wang, G. Wu, Y.-T. Dai, X.-Y. He, Determination of the bond-slip behavior of CFRP-to-steel bonded interfaces using digital image correlation, *J. Reinf. Plast. Compos.* 35 (18) (2016) 1353–1367.
- [101] H. Zhu, G. Wu, J. Shi, C. Liu, X. He, Digital image correlation measurement of the bond-slip relationship between fiber-reinforced polymer sheets and concrete substrate, *J. Reinf. Plast. Compos.* 33 (17) (2014) 1590–1603.
- [102] H.-T. Wang, G. Wu, Bond-slip models for CFRP plates externally bonded to steel substrates, *Compos. Struct.* 184 (2018) 1204–1214.
- [103] J. Shi, H. Zhu, Z. Wu, R. Seracino, G. Wu, Bond behavior between basalt fiber-reinforced polymer sheet and concrete substrate under the coupled effects of freeze-thaw cycling and sustained load, *J. Compos. Constr.* 17 (4) (2013) 530–542.
- [104] Y. Pang, G. Wu, H. Wang, D. Gao, P. Zhang, Bond-slip model of the CFRP-steel interface with the CFRP delamination failure, *Compos. Struct.* 256 (2021) 113015.
- [105] C.K. Desai, S. Basu, V. Parameswaran, Determination of traction separation law for interfacial failure in adhesive joints at different loading rates, *J. Adhes.* 92 (10) (2016) 819–839.
- [106] S. Ravindran, S. Sockalingam, K. Kodagali, A. Kidane, M.A. Sutton, B. Justusson, J. Pang, Mode-I behavior of adhesively bonded composite joints at high loading rates, *Compos. Sci. Technol.* 198 (2020) 108310.
- [107] F.A. Leone Jr, D. Girolamo, C.G. Davila, *Progressive damage analysis of bonded composite joints*, 2012. Technical Report.

-
- [108] S. Sugiman, A.D. Crocombe, I.A. Aschroft, Modelling the static response of unaged adhesively bonded structures, *Eng. Fract. Mech.* 0013-7944, 98 (2013) 296–314, <https://doi.org/10.1016/j.engfracmech.2012.10.014>.
- [109] M. May, H. Voß, S. Hiermaier, Predictive modeling of damage and failure in adhesively bonded metallic joints using cohesive interface elements, *Int. J. Adhes. Adhes.* 49 (2014) 7–17.
- [110] J.J.M. Machado, P.D.P. Nunes, E.A.S. Marques, L.F.M. da Silva, Numerical study of similar and dissimilar single lap joints under quasi-static and impact conditions, *Int. J. Adhes. Adhes.* 0143-7496, 96 (2020) 102501, <https://doi.org/10.1016/j.ijadhadh.2019.102501>.
- [111] M. Smith, *ABAQUS/Standard User's Manual, Version 6.9*, Dassault Systèmes Simulia Corp, United States, 2009.

This page intentionally left blank

Improving joint performance through graded materials and geometries

33

E.A.S. Marques^a, R.J.C. Carbas^b, A. Akhavan-Safar^b, and Lucas F.M. da Silva^a

^aDepartment of Mechanical Engineering, Faculty of Engineering (FEUP), University of Porto, Porto, Portugal, ^bInstitute of Science and Innovation in Mechanical and Industrial Engineering (INEGI), Porto, Portugal

33.1 Introduction

33.1.1 Stress distribution in common bonded joint geometries

While adhesives are generally known for exhibiting stress distributions that are generally smoother than those associated with other common joining methods, such as welding and mechanical fastening, they are still characterized by the existence of stress singularities, nonuniform peel distributions, and shear stress concentrations in critical areas of the joint [1]. One of the key tasks of a joint designer is to engineer solutions that reduce stress levels and/or distribute this stress over larger areas. As we will repeatedly see throughout this chapter, this can be achieved through geometrical modifications of the joint, but also through precise control over the adhesive and adherend properties.

Stresses acting on bonded joints can have vastly different origins. For example, peel stresses originate mostly from the eccentric load path found in most joints that bend the adherends away from each other and are especially severe in single-lap joints (SLJs) (Fig. 33.1). In contrast, shear stresses are mostly the result of differential straining between the adhesive and the adherends, which almost always exhibit large differences in modulus of elasticity and thus will deform in a vastly different manner under the same load, creating strains and stresses. Furthermore, adhesive ductility is also a key driver of the shear behavior exhibited by a bonded joint and will generally lower the development of shear stress peaks. Nonetheless, shear stresses are known to be much less harmful for joint performance than peel stresses, which can have deleterious effects not only on the performance of the adhesive itself but also on that of the adherends and the interfaces, causing delamination and debonding failures. Joint design is thus a discipline that is highly oriented toward the minimization of peel and shear stresses. Simple methods are available to mitigate the development of peel stresses in basic joint geometries [1]. For example, bonded doublers are often seen in bonded aerostructures where they provide local stiffening of generally thin skins, minimizing the bending action on the adhesive layer and thus creating significantly lowered peel stress concentrations.

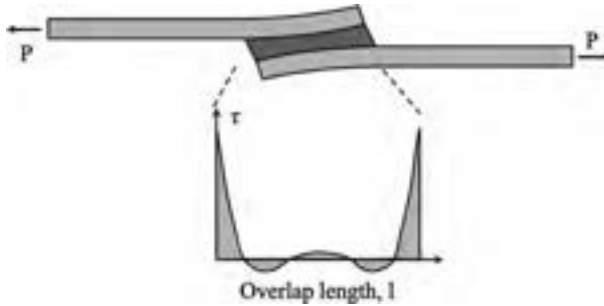


Fig. 33.1 Shear stresses in the adhesive generated by specimen asymmetry in an SLJ.

As stated above, the SLJ is the most commonly used joint geometry for testing and evaluation. It also has significant industrial relevance and implementation because it is quite simple to manufacture and well suited for lightly loaded thin structures. However, SLJs are eccentric in geometry because the adherends are not perfectly aligned, which leads to significant flexure in the adhesive layer under load, resulting in the inevitable formation of large peaks in the peel stress distribution at the ends of the overlap region [1]. In practice, most joints found in real-world applications will exhibit complex stress states due to the varied geometry of the adherends.

If one considers a mechanics of the material solution for this problem, where shear peak stresses will also develop in these same regions (Fig. 33.2), this complex mixed-mode loading will inevitably lead to early failure of the joint if one does not account for the combined effect of these two loading modes [2]. Increasing the overlap length and minimizing the adhesive layer thickness can aid in minimizing these effects, reducing the level of eccentricity, although it is fundamental to ensure that peak stress levels are not overcome. Furthermore, while one might consider that only tensile loads are damaging to SLJs, the use of these joints under compressive stresses should also be avoided because the eccentricity will progressively worsen as the joint becomes loaded. In the specific case of the single-strap joint, where the adherends are joined by a single splice plate, tensile loads will also inevitably generate a severe bending moment [3].

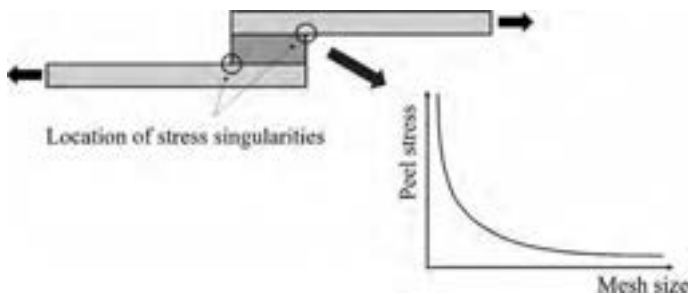


Fig. 33.2 Peak peel stresses within the adhesive and stress singularities in SLJs.

In contrast, the double-lap configuration is inherently better balanced because there is now geometrical symmetry and the bonded area is now doubled, providing a noticeable performance increase at the cost of some additional weight and manufacturing complexity. However, this is impractical in some situations. In these joints, the distribution of peel stress is still not perfectly constant, but instead exhibits tensile and compressive variations throughout the bonded layer without suffering from bending loads. Furthermore, compressive stresses will act mostly on the center of the joint, which can be seen as an advantage when dealing with delamination-prone composite materials. However, it might be argued that these compressive stresses might only be achieved through larger peel stresses acting on the edge of the joint, where stress singularities and the environment can play a more important role. Also, should debonding occur, these more detrimental tensile peel stresses proceed inward, altering the local stress state.

For bonding thicker substrates, scarf and step joints are often used because they reduce the abruptness associated with the edges of the overlapped regions, allowing for a more gradual load transfer that is able to involve more of the adhesive length. These were first proposed by Hart-Smith [4] for aerospace applications and can be seen as the original graded joints, as the tapered shapes do allow for a gradual transfer of stresses. The use of these joints with metallic substrates requires costly machining operations necessary to produce the steps, which in practice limits their application to the aerospace sectors. However, the growing use of layered composite substrates can somewhat facilitate the implementation of this technique. The smaller the dimension of the steps, the higher the load that can be transferred without the formation of large stress concentration peaks. However, the design of such joints is a balancing act for balancing the adherend stiffness throughout the adhesive layer length; it also requires control of the length and number of steps [4].

Finally, one can also consider the scarf joint geometry, which provides intermeshing ramps on the adherends and also allows for a gradual transference of stresses. Due to the accuracy needed to manufacture these ramps, they are also generally expensive [5]. However, they are able to efficiently eliminate joint eccentricities and also provide a joint without any protrusions or asymmetries, both of which are especially desirable for aeronautical applications [6]. More information on these types of joints and how they can be leveraged to reduce the stress concentrations is shown in the following subsections.

33.1.2 Classical methodologies to reduce stress concentrations in bonded joints

33.1.2.1 Fillets

Spew fillets are one of the most simple and cost-effective methods to reduce the stress distributions in SLJs. As discussed above, the stress concentrations in these joints are mostly located on the edges of the overlaps, where there is a severe geometrical discontinuity that forces stresses to become concentrated. Fillets simply extend and

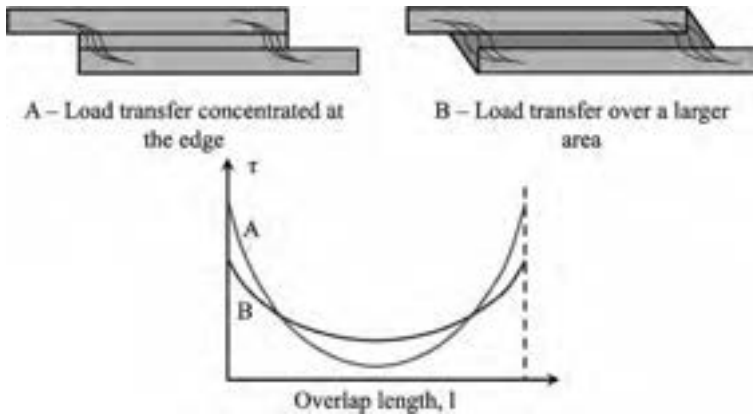


Fig. 33.3 The effect of spew fillets in the shear stress distribution in SLJs (stresses exaggerated for clearer representation). (The interface is effectively longer in B due to spew, but stresses in this region are not shown.)

smooth the stresses within this region, providing more adhesive material to spread the load and thus reducing peak stresses [7], as shown in Fig. 33.3.

In practice, fillets alter the load paths and change the peak stresses that are associated with the geometry of the edges of the overlap. Adhesive filleting is often the result of the excessive adhesive being squeezed out of the lap region when both substrates are pressed together and thus often represents no additional cost to the bonding operation [1,8,9]. The work of Adams and Harris also provided a major contribution to this field, showing the positive effect of filleting and even adherend-end rounding on joint performance [10]. The effectiveness of a spew fillet is dependent on multiple parameters, of which the most important are perhaps the shape of the fillet and the properties of the adhesive. For example, moving from tapered to rounded fillets can provide some increase in joint performance as a result of the reductions in stress concentration that are achieved. Furthermore, the use of a fillet in a joint with a brittle adhesive can have a more positive effect than found for a joint with the flexible and ductile adhesive because these adhesives will, through their elasticity and the capability to yield, inherently be less susceptible to stress concentrations. Experimental work, such as that of the classical work of Adams and Harris [10], shows that joint strength improvements of more than 50% can be achieved using spew fillets and rounded edges.

Composite materials, with their naturally lower interlaminar strength, can benefit greatly from the use of spew fillets to reduce the peel stresses and thus delay failure by delamination, as shown in the work of Tsai and Morton [11]. In this work, a combination of numerical analysis and experimental testing has led to the conclusion that adhesive shear and peel strain concentrations can be greatly reduced with the use of a fillet at the end of the overlap. Lang et al. [8] studied the effect of the spew fillet shape in the stress distribution of SLJs, considering the full and half triangular, full and half rounded, full rounded with fillet, oval, square, and arc geometries. The largest

reduction in peak stresses was attained with the use of the full rounded, oval shaped, and arc spew fillets because these provide the most gradual transfer of stresses between adherends. Later on, Belingardi et al. [9] used numerical modeling to perform a parametric analysis of the stress distribution generated by spew fillets. It was found that the spew fillets with a 45 degrees taper were a more advantageous solution to reduce shear and peel stress peaks, although all other configurations under analysis were still able to considerably reduce the stress peaks. However, the presence of the spew fillet can sometimes have a negative effect, as the work of da Silva and Adams has shown [12,13]. In this case, when SLJs are exposed to large temperature gradients, the use of spew fillets was found to be more susceptible to thermal stresses than simple square-end geometries.

33.1.2.2 Adherend rounding

As previously stated, the critical stresses in an SLJ will always occur at the edge of the overlap. We have discussed a method to control this by changing the geometry of the joint (double-lap joint) and of the adhesive layer, such as the use of spew fillets. However, it is also possible to control these stresses by acting on the adherend corners [10].

The work of Adams and Harris [10] was one of the first concerned with the geometry of corners in an adherend. Carrying out experiments with rounded adherend corners, they found that the simple rounding of the adherend corners will yield a significant joint strength increase, again providing additional paths for load transfer and minimizing stress concentrations. An analysis of the effect of rounded edges on the stress singularity was studied by Zhao et al. [14]. They concluded that the effect of this modification is also a factor of adhesive type, with joints bonded with brittle adhesives being more susceptible to the effect of adherend corner radius than ductile adhesives. The configurations under study are summarized in Fig. 33.4. Under ideal conditions, joints bonded with brittle adhesives and with highly rounded corners can show strength improvements of more than 40% when compared to adherends with sharp corners. In contrast, the same joints bonded with a ductile adhesive yield almost no noticeable strength improvement. As is the case for the spew fillets, the ductile nature of these adhesives naturally redistributes stresses throughout the joint and is thus unaffected by the presence of the rounded corner.

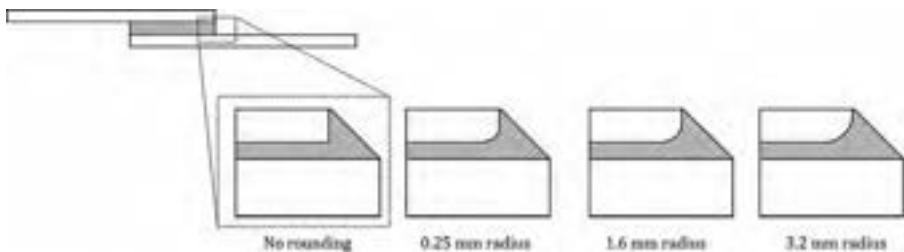


Fig. 33.4 Corners of SLJs with different degrees of rounding.

Adapted from X. Zhao, R. Adams, L. Da Silva, Single lap joints with rounded adherend corners: stress and strain analysis, *J. Adhes. Sci. Technol.* 25(8) (2011) 819–836.

33.1.2.3 Adherend shaping

It is possible to go beyond simple adherend rounding and implement geometrical modifications in the substrate that are much more substantial, giving rise to a set of techniques known as adherend shaping. Here, the main objective is to gradually control the stiffness of the adherend (and the joint) by providing less and less stiffening material as one approaches the critical stress concentration points [7]. Some possible tapered adherend shapes are shown in Fig. 33.5.

These techniques control the level of differential straining and thus can significantly flatten the shear stress distribution within the adhesive layer. Experimental work by Hart-Smith [15] has led to the conclusion that tapered joints with a ratio of 1:10 (increasing adhesive thickness near the edge of the overlap) will have an important effect on the joint strength. Furthermore, peel stresses are also controlled in this way, avoiding the failure of composite substrates [16].

Moving away from SLJs toward butt joints, one can find a type of adherend shaping that involves the implementation of changes in the edges of the substrates, with the aim of gradually reducing the local stiffness of the substrate in these regions. Xu et al. [17] conducted an experimental and numerical investigation seeking to remove the free edge stress singularities in dissimilar material butt joints, using edge geometries inspired by the shape and mechanics of bamboo and trees. The ultimate tensile strength of optimized butt joints was found to increase by 81% while the material volume was reduced by 15%. This work was followed by a purely numerical analysis [18], which identified the convex axisymmetric design as the best-performing geometrical modification for butt joints. Later, the work of Cognard et al. [19] adopted a machined beak in the edge of the adherends of Arcan-type specimens to minimize the very same edge effects and thus reach a more uniform tensile stress state during material characterization processes carried out with Arcan joints.

Composite joints are generally among those that can benefit the most from geometrical optimizations, given the very large susceptibility of their substrates to delamination. The work of Adams et al. [20] focused on double-lap joints combining carbon fiber-reinforced plastic (CFRP) adherends and steel substrates. By including both internal and external tapers in the substrates, the joint strength was found to increase significantly, increasing almost 300%. However, later work by da Silva et al. [13] found that these joints still remain susceptible to thermal stresses, which are found to still be very damaging to joint performance. An interesting development of these

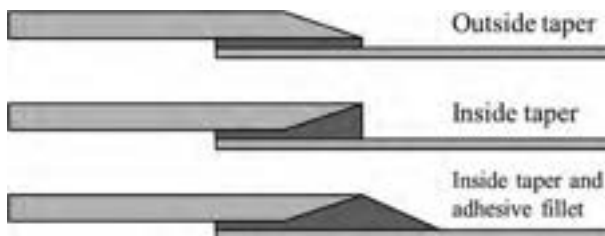


Fig. 33.5 Different possible specimen-shaping possibilities.

adherend shaping techniques is related to the use of advanced evolutionary structural optimization algorithms to remove material from adherends to improve joint performance. The aforementioned work of Xu et al. [17,18] uses such an evolutionary approach to design butt joints. Another example is the EVOLVE code prepared by Rispler et al. [21], which iteratively reduces maximum transverse stresses by removing unstressed portions from the joint structure.

It is well understood that the use of brittle adhesives with composites should be avoided to minimize the likelihood of delamination. However, if this cannot be avoided, the use of internal filleted adherends and spew fillets in the adhesive layers has been shown to provide a possible solution for avoiding premature joint strength. Nonetheless, this added complexity is often difficult to justify in many applications [1]. It is also important to take into consideration that tapering might not be useful for all types of joints. For example, strap joints are unsuited for tapering because the important peel stresses generated are mostly compressive in nature [15,22,23].

33.1.2.4 Wavy-lap geometry

One important development in adherend shaping is the wavy-lap joint geometry. This joint, first proposed by Goland and Reissner in Ref. [24] and later developed by Avila and Bueno [25] (see Fig. 33.6, top) has highly modified adherends that precisely control the stress distribution in the adhesive layer by ensuring that the peel stresses at the edges of the overlap are compressive in nature. This obviously has an important impact in joint strength and fatigue life but comes at the cost of a very complex and costly manufacture process. In this regard, many joint designers might prefer to assume a penalty with regard to performance and adopt a simpler geometry, such as tapers and the use of fillets.

A slightly less complex geometry was proposed by Fessel et al. [26] where the adherends are already prebent before any bonding takes place, ensuring that the final joint geometry is better aligned to the loading path and that stress concentrations are thus reduced (Fig. 33.6, bottom). Further testing showed that although important sensitivity to the adherend material and the overlap length was detected, this concept still allowed obtaining a strength improvement of almost 40% under static conditions, coupled with an important improvement in durability under fatigue conditions [27]. It should be noted that such configurations are designed for use in tension and might result in worse joint performance under compression conditions due to increased susceptibility to buckling failure, failing under conditions similar to those shown in the work of Guo et al. [28].

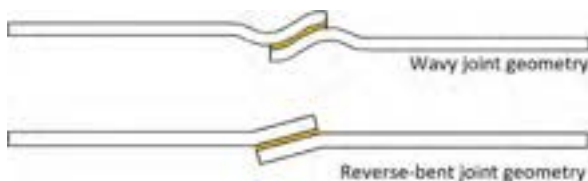


Fig. 33.6 Alternative joint geometries.

33.1.2.5 Scarf joint geometry

In scarf joints, adherend shaping is an integral part of the joint concept and geometry. In these cases, it is known that the use of adherends with almost identical stiffness provides the most efficient load path and almost complete elimination of stress concentrations because the eccentricity of the joint is almost fully eliminated [22]. However, as previously mentioned, the unfavorable cost-benefit equation of such joints makes their use only worthwhile for very high-end applications, such as those found in the aerospace sector.

In these aeronautical applications, the lamination of the adherends (or repair patches) is carefully coordinated to ensure perfect matching between the parts to be bonded. For isotropic adherends, Objois et al. [29] showed that peel and shear stresses are almost perfectly constant, although singularities can still be generated. Gunnion and Herszberg [30] showed the same for composites reinforced with unidirectional fibers. However, more complex layups with differently oriented plies and anisotropic behavior will often show oscillations in the stress distributions that, although undesirable, still have a limited impact on the joint performance. Nonetheless, Gunnion and Herszberg [30] strongly recommend the use of overlaminating plies on these joints, ensuring that the edges of the scarfs and steps are protected from peeling away.

The scarf angle is obviously the most important geometrical parameter associated with these joints because it controls both the length and size of the adhesive layer and the ratio between the peel and shear stresses in the joint. Low scarf angles will lead to very large overlap length with an increase of the bonded area and a reduction of peel stresses, as shown by Campilho et al. [31]. In fact, theoretically speaking it should be possible to attain any desired load-bearing capability by using very low scarf angles and thick adherends. Of course, this is entirely limited by practical concerns because the joint will become much larger, heavier, and even susceptible to creep failure if the adhesive is uniformly stressed well into a nonlinear portion of its shear behavior. This goes in line with the classic Hart-Smith design philosophy, which stresses that any design should target a stress level as low as possible to avoid creep failure [22].

33.1.2.6 Stepped-lap geometry

The stepped-lap joint is an alternative to scarf joint geometry that operates on the same principles and offers very similar behavior. This configuration is shown schematically in Fig. 33.7.

In this case, instead of a perfectly defined ramp, the joint geometry consists of a series of steps, which results in an average slope. The average slope length is analog to the taper angle of the tapered joint and controls the level of shear (or peel) stresses acting on the joint at a macroscale. At a microscale, each of the individual steps will in practice act as an individual lap joint with constant adherend dimensions. The geometrical complexity of these joints makes them highly sensitive to diverse factors. As was the case for the tapered joint, adherend stiffness balancing is paramount (as shown in Fig. 33.8), or else the joint will flex asymmetrically during service; this will generate large peel stresses. Furthermore, the length and thickness of the final steps are also

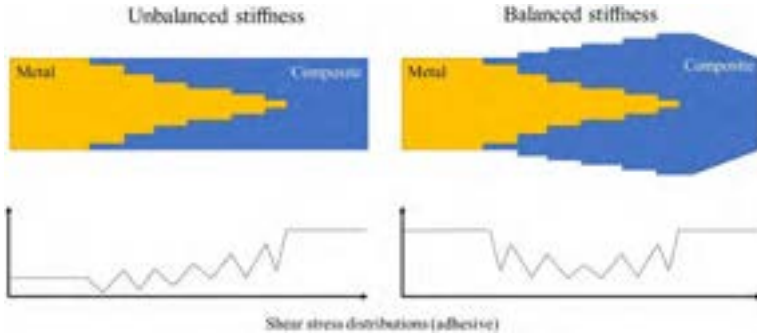


Fig. 33.7 Stepped-lap bonded joints with strength improvement by matching the stiffness of the adherends.

Adapted from L. Hart-Smith, *Adhesive-Bonded Scarf and Stepped-Lap Joints*, National Aeronautics and Space Administration, 1973.

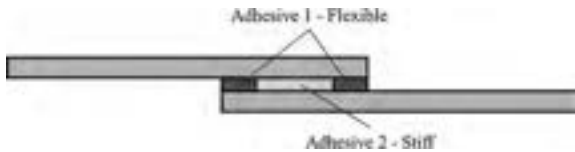


Fig. 33.8 The concept of a mixed adhesive joint manufactured using two different adhesives.

very important. The work of Hart-Smith [22] has shown that long and too-thick end steps should be in generally avoided, in addition to the use of constant thickness increments for all the steps. In fact, half-thickness increments for the final steps will instead lead to greatly improved stress distributions because the stress state at the surface of the adherends is more complex.

33.2 Mixed adhesive joints

33.2.1 Concept and operating principle

Mixed adhesive joints are another important alternative to control the stress field and the performance of bonded joints. They have the added benefit of improving the thermal behavior of the joint. In these joints, two or more adhesives are introduced in different locations of the same bonded layer, as shown in Fig. 33.8. The properties of the adhesives being used are usually highly dissimilar and interact in a synergistic manner to achieve increased joint performance.

33.2.2 Mechanical performance and production

At its most basic, a mixed adhesive joint will feature a ductile adhesive at the ends of the overlap and a stiff adhesive in the central portion of the adhesive layer. The ductile adhesive will be able to handle the highest deformations and stresses generated at this

critical area while the relatively unstressed stiff adhesive will be tasked to provide additional strength to the joint without being damaged. The design of a successful mixed adhesive joint is almost entirely dependent on the establishment of a balance between the performance of these two adhesives, seeking to create an adhesive layer that performs better than the sum of its separate parts. However, it should be noted that this balance is quite difficult to achieve and requires a detailed knowledge of the operation condition of the joints, such as the ambient temperatures and the stress levels. A mixed joint designed for a specific temperature range will thus be rendered useless if employed in a different temperature cycle with different loads.

Although mixed adhesive joints can seem to be a perfect solution for many applications, they are beset by some important practical problems, such as the difficulty in attaining perfect separation between both adhesives. While ideally one would seek to have a well-blended interface between the two adhesives, in practice this is very hard to achieve and often leads to the presence of defects. This can be avoided by using hard barriers such as nylon wires, silicone strips, and frames, but the introduction of these foreign elements has negative effects on the joint performance. Improved manufacture control can be attained with the use of film adhesives but their mechanical behavior ranges are quite limited, which leads to a reduced effectiveness of the mixed adhesive joint concept.

Another important issue related to the use of mixed adhesive joints is the difficulty in matching the curing processes of the different adhesives. Often, adhesive selection is strongly limited by the selection of adhesives that have compatible curing cycles, even if the properties of these adhesives are not ideal to explore the mixed adhesive joint concept to its fullest.

33.2.3 Performance under large thermal gradients

One important aspect associated with these joints is the fact that they can offer more than improved joint performance under quasistatic conditions and room temperature. In fact, mixed adhesive joints can also improve joint performance under demanding thermal conditions and wide temperature ranges. For example, mixed adhesive joints can be used in thermal protection systems for spacecraft, where the thermal shields must be bonded in a manner that is resistant to both the high temperatures associated with reentry in the atmosphere and to the extreme cold of outer space. This performance gain is attained by combining adhesives that are resistant to high temperatures with adhesives that behave well under very low temperatures. This concept works well because very stiff adhesives often have high glass transition temperatures (T_g) and are thus well suited for high temperatures while flexible adhesives often have T_g values below 0°C and are thus suitable for operation under extremely low temperatures. Thus, the mixed adhesive concept suits quite well the need for providing joints that offer good mechanical performance over an expanded temperature range (Fig. 33.9).

The excellent behavior of mixed adhesive joints at high temperature was first theorized by Hart-Smith [32], who determined that at low temperatures, one would

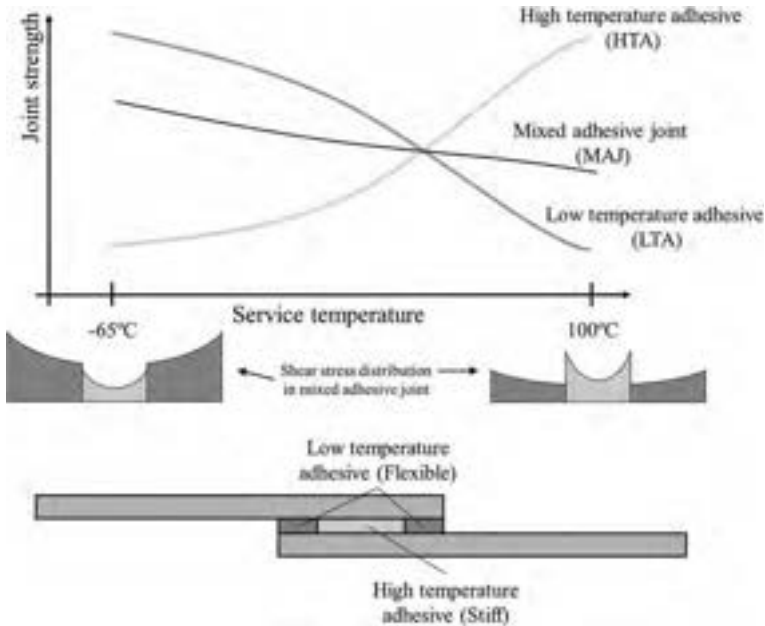


Fig. 33.9 Schematic representation of the synergistic effect of combining two adhesives that respond differently to temperature in the same bonded joint.

see most of the load being borne by the ductile, low-temperature adhesive while the inverse would certainly occur for very high temperatures. In this case, the low-temperature adhesive (with a very low T_g) would lose a significant portion of its load-carrying ability, which would be transferred mostly toward the high-temperature adhesive.

This concept was experimentally demonstrated in the work of da Silva and Adams [12,13], targeting an application in the aerospace sector. Using titanium and composite substrates to create dissimilar joints, the authors demonstrated an important strength improvement and, more importantly, stable mechanical behavior throughout a wide range of temperatures.

The concept of geometrical modifications of the adherends has been discussed at length in previous sections of this chapter. Some authors have tried to combine it with the mixed adhesive joint concept for improved performance gains. For example, the work of Marques and da Silva [16] explored the use of internal tapers and fillets in mixed adhesive joints (Fig. 33.10). They showed that while the use of the tapered patches with a stiff adhesive leads to a strength improvement of 30%, the same geometry does not bring any advantage for a mixed adhesive joint because the use of a ductile adhesive at the ends of the overlap provides an improvement to joint performance that is comparable to that associated with the use of the taper.

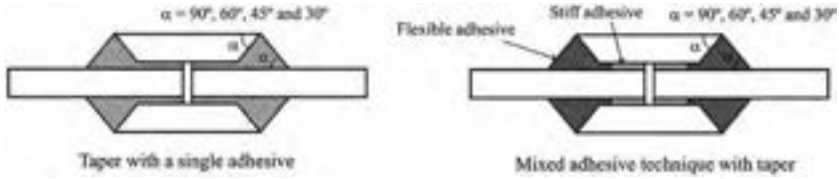


Fig. 33.10 Joint geometry combining mixed adhesive layer with tapered patches, as proposed by Marques and da Silva [16].

33.2.4 Performance under impact loads

Very limited work has been published on the behavior of mixed adhesive joints under impact conditions, and it is mostly focused on comparing the performance of mixed-adhesive joints with that of joints bonded with a single adhesive. The work of Marques et al. [33] studied specimens bonding ceramic protection tiles to metal plates, using three different adhesive layer configurations: One with a room temperature vulcanizing silicone only (RTV106), one with only a high-temperature epoxy (XN1244), and finally another configuration introducing both adhesives in the same joint (mixed joint). Under impact, all three joint configurations tested have shown an increase in failure loads under impact. Joints with the XN1244 epoxy exhibit the highest failure loads. Joints with RTV106 exhibit the highest strength gain, providing that the failure starts in the ceramic tile. The ceramic tile exhibits significant sensitivity to impact loads and is one of the most important factors in the overall joint strength, in this case with more importance than the mixed adhesive layer.

The works of Silva et al. [34] and Machado et al. [35] provide additional data on the impact testing of SLJs bonded with single adhesives and mixed adhesive layers, using metallic and composite substrates. The results show that some of the adhesive configurations under study (such as the combination of a brittle epoxy with a ductile acrylic-based adhesive) provide added performance under both quasistatic and impact conditions. The results of Fig. 33.11 show that energy absorption is significantly enhanced

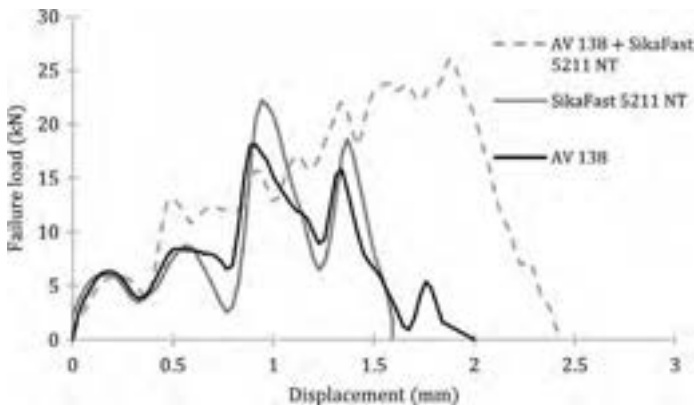


Fig. 33.11 Impact load-displacement curves showing the improved performance of the mixed adhesive joint over the single adhesive layers.

using this type of joint configuration, especially when composite substrates are used. However, the authors note that the impact performance of these mixed joints never exceeds that of a single layer of a custom-designed crash-resistant adhesive.

33.2.5 Modeling of mixed adhesive joints

As previously mentioned, the work of Hart-Smith [32] was the first to explore the concept of the mixed adhesive joint, referring initially to this concept as mixed-modulus adhesive joints, aware that it is the difference in the modulus of elasticity of the adhesives that brings this concept to fruition. Hart-Smith assessed the effectiveness of these joints mainly with the use of analytical shear lag models, which are able to determine the stress distribution on the adhesive layers as a function of the joint's geometrical parameters and the adherend and adhesive's properties. Such models are quite useful for the design of the mixed-mode joint because they facilitate balancing the contribution of each adhesive toward the load-bearing capability of the joint but lack the ability to precisely determine joint strength and to consider more complex joint geometries.

Nowadays, modeling of mixed adhesive joints is generally carried out with the aid of finite element models (FEM), using cohesive zone modeling (CZM) to predict damage propagation and failure of the adhesive layers. Such analysis is important to ascertain the sequence of failure of the joints because a mixed adhesive joint will perform optimally if both adhesive layers are loaded until failure in an almost simultaneous fashion, ensuring that both adhesive layers are providing maximum contribution toward the joint strength. The work of Marques et al. [36] undertook a geometrical study of mixed adhesive joints, using CZM to predict joint strength. In a first phase, experimental data were calibrated and used to validate a three-dimensional (3D) FEM of joints followed by a study of the performance of different geometrical configurations. Symmetrical and tapered joints were found to have lower failure loads than the standard mixed joint, but the tapered joint exhibited significantly lower stiffness, a beneficial characteristic for operation in large thermal gradients.

33.3 Functionally graded adhesives

33.3.1 Concept and operating principle

The use of mixed adhesives can be considered a rough version of a functionally graded adhesive because it already induces a discrete, stepwise variation of the adhesive properties as a function of the location in the overlap (Fig. 33.12). To provide maximum performance, the ideal would be to have a truly functionally modified adhesive with properties that vary continuously along the overlap, thus allowing for a more uniform stress distribution [37].

The main challenge associated with the design of a continuously graded joint is related to the manufacture of these joints, which is beset with serious practical issues. While some experimental work has shown the possibility of grading adhesive layers



Fig. 33.12 Schematic concept of the functionally graded joints obtained by induction heating, with the smooth variation of the properties of the adhesive layer being represented by a gradient.

along the overlap direction, grading an adhesive layer in the through thickness direction is still quite difficult. Related work has been done on functionally grading coating layers, providing thin coatings with higher thermal crack tolerance when compared to thicker uniform coatings [38]. Most of these solutions are based on ceramic and metallic compounds, with limited applicability to bonded joints [39]. Nonetheless, important advances in numerical modeling and simulation of the mechanical response of graded materials and interfaces have been laid by the work carried out with these materials [40,41].

The following subsections will list and detail some of the most important works carried out in the development of practical methodologies for graded bonded joints, mostly focusing on the development of functionally graded adhesive layers along the joint length and graded substrates along the thickness direction.

33.3.2 *Techniques for the manufacture of functionally graded adhesive layers*

33.3.2.1 *Differentiated cure with induction heating*

Carbas et al. [42] were among the first researchers to propose a practical method for obtaining functionally graded adhesives, developing an apparatus to provide a differential cure of bonded joints by induction heating. The application of differential cure ensures that the adhesive stiffness varies gradually along the overlap, with the degree of cure being maximum in the middle and minimum at the ends of the overlap. The first experimental study of SLJs with a functionally graded bondline was provided by Carbas et al. [43]. The authors previously characterized the adhesive used as a function of the cure temperature to understand the adhesive behavior for the different cure temperatures [44,45]. Carbas et al. [43] experimentally obtained functionally graded joints by induction heating, giving a graded cure of the adhesive along the joint (see Fig. 33.13). Experimental testing showed that the functionally graded joint provides improvements in ductility and strength when compared with joints cured isothermally.

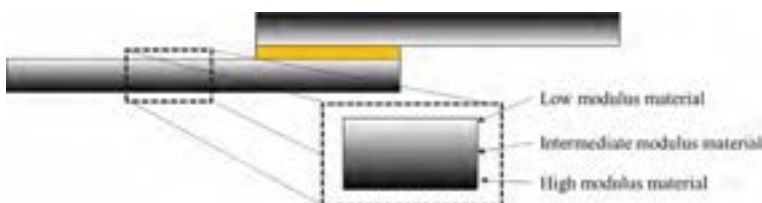


Fig. 33.13 Concept of functionally graded adherends.

The strength of the graded joints was more than 60% higher than reference joints with a homogeneous bondline cured at low or high temperature (brittle or ductile behavior, respectively).

The authors also studied the effect of postcuring on functionally graded joints obtained by induction heating to understand their performance when submitted to different postcure temperatures [44]. They performed three different postcuring conditions: at room temperature (without postcure) and with temperatures above and below the glass transition temperature of the fully cured network ($T_{g\infty}$). Carbas et al. [44] proved that functionally graded joints subjected to postcure at low temperatures (below $T_{g\infty}$) show a slight decrease of the strength while joints cured isothermally show a slight increase of the strength. In addition, with an increase of the postcure temperature (above $T_{g\infty}$), the functionally graded joints exhibit strength similar to that of the joints cured isothermally. It is important to note that any methodology to obtain functionally graded adhesive layers based on the curing process will exhibit sensitivity to temperature. Therefore, it is possible that exposure to service temperatures will make uniform the curing process and lead to the destruction of functional grading. Furthermore, other detrimental aspects are associated with a partially cured adhesive, such as reduced chemical stability and the health and safety concerns from unreacted species.

The authors then used the differential cure apparatus for the repair of wood beams used in civil engineering applications [46]. They analyzed two common types of defects on beams (cross-grain and compression failure) under bending loads. The damaged wood beams of the Portuguese *Pinus pinaster* species were repaired with CFRP patches. The repaired wood beams were cured by three different methods. Some were cured isothermally at room temperature, others isothermally at high temperature, and another set had a functionally graded adhesive layer achieved through differentiated cure. Two patch lengths for each type of wood beam damage were tested under a four-point bending load. They studied the behavior of repaired wood beams experimentally and numerically. The numerical analysis was done by FEM and CZMs were used to predict the fracture behavior (simulate the crack initiation and propagation) of adhesively bonded wood repairs. Experimental analysis allowed determining that the beams repaired with a graded bondline were able to withstand higher loads.

33.3.2.2 Control of the mixing ratio of adhesive components

Many adhesives are commercially supplied in two parts, a resin and a hardener that must be mixed at a predefined ratio to create a fully polymerized adhesive. Some researchers have found that altering this ratio offers the possibility of significantly varying the adhesive properties, opening the door to adhesive layers that are functionally graded in nature. The first of these techniques was proposed by Kawasaki et al. [47], who introduced a special numerically controlled adhesive application system able to vary the mixing ratios of the two components of acrylic-based adhesives. Large variations in the adhesive modulus and tensile strength were encountered, but this technique was not tested at the joint level because the system was developed mainly to produce bulk samples of adhesives. Nakanouchi et al. [48] further explored this

technique and expanded it to different adhesives, achieving a larger variation in mechanical properties. In a manner similar to the work of Kawasaki et al., Kumar et al. [49] used a 3D multimaterial printer to apply and precisely control the relative volume fraction between two polymer-based adhesives. Joint specimens were produced for bonding 3D printed adherends, and testing demonstrated an almost 100% increase in joint strength over the use of single adhesive layers. In a comparable work, Chiminelli et al. [50] produced graded adhesive dissimilar joints, bonding aluminum and composite adherends. A special adhesive applicator was able to control the ratio between two different epoxy resins. Testing the joints identified that while single adhesive led to the failure of the composite by delamination, the use of the graded joint enabled cohesive failure in the adhesive and an increase in the failure load of almost 70%.

33.3.2.3 Addition of particles or second phases

The addition of particles to an adhesive system can be used to locally control the mechanical properties of the adhesive layer. Adhesive manufacturers have long used rubber particles to enhance the toughness of generally brittle adhesives, but this assumes a uniform distribution of the particles throughout the adhesive. Some recent works have devised functionally graded joints via the addition of other types of particles such as nanoparticles or thermally expandable particles. The work of Carbas et al. [51] employed varied amounts of carbon black nanoparticles dispersed in a functionally graded manner through a bondline. The resultant joints were found to be functionally graded in nature and when tested under quasistatic conditions were found to have a higher joint strength than the joints using uniform distribution of the carbon black or those without any type of particle addition. Later, a similar study was carried out by Bonaldo et al. [52], but considering the use of thermally expandable particles (TEPs). These particles are capable of expanding when subjected to very high temperatures, causing the adhesive layer to debond on command. Thus, by using them to locally vary the adhesive layer properties in a gradual manner, one is also adding a self-dismantling capability to the joint. This work found that increasingly larger TEPs led to an increase in joint strength, but the effectiveness of the graded joint was only slightly better than the use of a homogeneous distribution of TEPs.

33.3.2.4 Addition of magnetic coated particles

As shown above, the addition of particles with properties to a polymeric matrix can represent a practical methodology for attaining a roughly functionally graded material, but this process requires particle introduction in a well-controlled manner to vary the adhesive properties according to a predefined gradient. The work of da Silva et al. [53] first provided a methodology to control the location of these particles based on the use of magnetized cork particles and carefully designed magnetic fields that will guide the particles toward areas of interest and will keep them away from areas where their presence is not necessary. This method can work in different ways. For example, if flexible and tough particles are used, the magnetic field is designed to carry the

particles toward the edge of the overlap. In contrast, if stiffer particles are used, such as the iron particles in another work from da Silva et al. [54], the magnetic field should instead be designed to move the particles toward the central portion of the overlap. Suitable flexible particles can be, for example, cork or rubber particles. As for stiff particles, iron spheres are preferable because they are already ferromagnetic and thus do not require a special coating to interact with the magnetic field. It is also important to mention that the adhesive rheology is highly important in these applications because it plays a key role in the mobility of the particles.

33.3.3 Modeling of functionally graded adhesives

Diverse theoretical studies have been conducted by Kumar [55] and Kumar and Scanlan [56] using analytical models for designing tubular adhesive joints with a functionally graded bondline. Carbas et al. [57] used a similar approach for SLJs with a functionally graded bondline. Kumar [55] studied a continuous (nonstepwise) functionally graded adhesive with a stepwise graded equivalent for different adhesive thickness and overlap length in a tubular joint. This study showed that the continuous functionally graded adhesive reduced the shear and peel stresses. Kumar and Scanlan [56], following the work of Kumar [55], developed analytical models to accurately predict the stress distribution in the members of the bonded assembly as a function of mechanical properties and geometry of the system under axial tensile load. This model captures accurate normal stresses in the adhesive and/or adherends. The study allowed predicting the stresses in stiff graded bonded systems and also allowed examining the effect of the loss of interface stiffness due to an existing defect and/or damage on structural response.

Carbas et al. [57] proposed a simple analytical model to study the behavior of SLJs with a functionally graded bondline. This simple analytical model was developed based on Volkersen's analysis [58], making use of power series expansions. The analytical model proposed successfully predicted the failure load of the functionally graded joints, showing that it is a valid tool to predict the maximum failure load. Also, it was shown that by increasing the adhesive thickness, the strength of functionally graded joints was also enhanced. This effect can be explained by the fact that the stress distribution becomes much more uniform than that of uniformly cured SLJs.

33.4 Functionally graded adherends

33.4.1 Concept and principle

A functionally graded adherend in a bonded joint will often have the main objective of ensuring that stresses transferred to the adhesive are redistributed through a larger area of the joint. This can be achieved in diverse ways. For example, it is possible to vary the stiffness of the adherend in the direction of the adhesive layer to minimize the differential straining between the adhesive and the adherend. Also, the stiffness through

the thickness of the adherend can be varied, creating a more flexible and softer zone near all the adhesive layer, providing a method to dissipate the stresses generated at the interface (Fig. 33.13) [59].

The concept of functionally graded adherends is already several decades old and diverse theoretical studies for SLJs with functionally graded adherends (see Fig. 33.14) have been conducted by multiple researchers, such as Ganesh and Choo [60], Boss et al. [61], Apalak and Gunes [62,63], and Gunes et al. [64]. The composition of both adherends used by Apalak and Gunes were ceramic (Al_2O_3) and metal (Ni) phases varying through the plate thickness between an Al_2O_3 Al_2O_3 -rich layer on the top surface and an Ni-rich layer on the bottom surface. Ganesh and Choo [60] and Boss et al. [61] considering grading of composites materials achieved using a braided preform with a continuously varying braid angle. The modulus grading of the adherend was achieved by varying the braid angle along the overlap length and geometrical grading was provided by varying the adherend thickness in the overlap region. They varied the braid angle measured to realistically evaluate the performance of adherend modulus grading in an SLJ. The authors obtained an increase of 20% joint strength with this technique due to a more uniform stress distribution. Boss et al. [61] also compared modulus grading with geometrical graded adherends in SLJs. This study showed that the modulus grading of the adherend reduced stresses and by combining modulus and geometrical grading, it was possible to obtain a better performance of SLJs.

Apalak and Gunes numerically investigated the 3D stress state of an SLJ with functionally graded adherends subjected to a tensile load [62] and to a flexural load [63], finding that the adhesive stress distribution was not highly affected. Gunes et al. [64] studied the effects of joint dimensions and volume fraction variation through the adherend thickness on the vibration characteristics of an SLJ with functionally graded adherends. This study showed that the natural frequencies of the adhesive joint are maximized, and its modal strain energy is minimized by increasing the overlap length and decreasing the plate thickness. Oppositely, the plate thickness should increase when decreasing the overlap length, seeking to ensure a more beneficial stress distribution and increased joint performance.

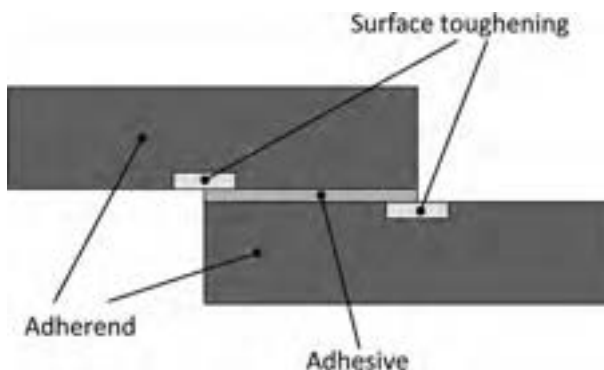


Fig. 33.14 Concept of a locally toughened SLJ.

Apalak et al. [65,66] studied tubular SLJs with adherends composed of a functionally gradient layer between a pure ceramic (Al_2O_3) layer and a pure metal (Ni) layer. A 3D stress analysis was carried out with functionally graded adherends in tension and subjected to an internal pressure. Through the thickness, the compositional gradient and the layer number did not affect considerably the normal and shear stress. However, by increasing the compositional gradient exponent, the peak stresses in the ceramic zone were found to decrease by 40%, whereas the peak stresses in the metal zone exhibited a negligible increase. Only the compositional gradient exponent had a considerable effect on the stress state when subjected to external loads. Gunes et al. [67] then studied the 3D free vibration analysis of a tubular SLJ with functionally graded adherends. This study used artificial neural networks and genetic algorithms to determine the natural frequencies and the corresponding modal strain energies. It was found that increasing the inner tube-inner radius, the outer tube thickness, and the compositional gradient exponent, the natural frequencies of the tubular adhesive joint were maximized. However, increasing the inner tube thickness had a negligible effect on the natural frequencies and corresponding modal strain energies.

Adhesively bonded functionally graded double containment cantilever joints were studied by Apalak and Ekici [68] and Apalak [69]. The functionally graded region through thickness is composed of a ceramic (Al_2O_3) on the top layer and a metal (Ni) on the bottom layer. The 3D stress states of the joint in tension and under a bending load were investigated. These studies used an artificial neural network model to obtain an optimal joint design. Apalak et al. [70] then analyzed thermal residual stresses in an adhesively bonded tubular SLJ for clamped plates with functionally graded substrates, subjected to an edge heat flux [71] and for clamped circular hollow plates [72]. The tubular SLJ was composed of ceramic (Al_2O_3) and metal (Ni) phases. The authors studied different compositions and distributions of functionally graded ceramic-metal and evaluated the strain and stress levels in the joints. The stress profiles across the adhesive layer remain the same, whereas von Mises and hoop stress levels at the adhesive-outer tube interface and at the adhesive-inner tube interface decrease uniformly. The compositional gradient exponent was found to have a considerable effect on the stress state of functionally graded tubular structures subjected to external loads, contrary to the thermal loads.

33.4.2 Techniques for the manufacture of graded substrates

33.4.2.1 Surface toughening of composite substrates

The addition of a ductile polymer material to a composite substrate can be used to improve the toughness of the composite and the joint, serving as a method to reduce delamination under quasistatic and impact loading conditions [73]. Depending on the location where the reinforcement is made, this technique can be known as local toughening, global toughening of the composite layup, or global toughening via the introduction of additional adhesive layers.

The concept of local toughening using polymers was first proposed by Schollerer et al. [74], whereupon a thermoplastic layer of polyvinylidene fluoride (PVDF) was

added to composite adherends in the overlap ends, cured in conjunction with the prepreg, as schematically shown in Fig. 33.14. The objective of this approach is to provide additional toughness to the areas of the adherend where peel stresses are most damaging. The ductile material is able to support these peel stresses and shield the composite material from delamination [74]. The authors reported a reduction in peel and shear stresses of around 40%, which results in a joint strength increase of more than 80%.

Global reinforcement of the substrate surface was proposed in parallel work carried out by Shang et al. [75]. In this case, CFRP adherends were coated with a very tough adhesive-based resin, reinforced with woven GFRP. This material was able to improve the joint strength and, most importantly, completely alter the failure mode from delamination of the CFRP adherends to cohesive failure of the adhesive failure, a much more benign type of failure.

33.4.2.2 Control of Z-pin content in composite substrates

Z-pins are a special type of reinforcement used in composite materials that provide additional strength in the through-the-thickness direction [76]. Composites reinforced with these materials will have much improved resistance to delamination and thus can be used to create joints that withstand higher mechanical loads [77,78]. Due to their small size, Z-pins can be finely adjusted to attain different reinforcement patterns, which can exhibit vastly different mechanical properties [79,80]. Specific layouts can be created for use in sandwich panels, allowing these materials to withstand larger loads [81]. When used as adherends for bonded joints, the Z-pin density can be adjusted to be maximum solely in the areas where higher peel stresses are expected (Fig. 33.15).

33.4.2.3 Geometrical modifications using additive manufacturing

New developments in additive manufacturing processes have opened the door to more precise control of both the shape and the mechanical properties of the adherends [82]. For example, using additive manufacturing, a commercial 3D printer can create a

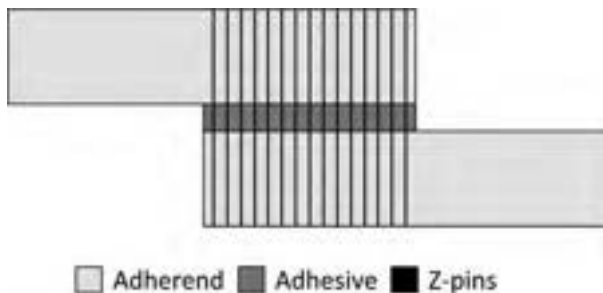


Fig. 33.15 Locally toughened composite adherends using Z-pin application.

substrate where the shape of the adherends is precisely controlled, using a specific tapering ratio that is designed to reduce the stresses acting on the adhesive layer and the joint.

Although 3D printing is not necessarily a very fast manufacturing process, the added agility and flexibility allow for shorter process times, especially in research and development settings. Furthermore, investments and operating costs are generally lower and the demand for skilled operators is reduced. However, most materials available for use with 3D printing are still generally weaker than those used with other manufacturing processes. Still, as this technology advances it will definitely occupy an increasingly greater space in the manufacture of adherends for bonded components. The added possibility of using different polymers in a single adherend provides another path for a truly graded material, something that was already demonstrated for bulk adhesive materials but is still not provided for printed adherends [49,83]. The work of Kumar et al. [82], which employs different 3D printed substrates, is illustrated in Fig. 33.16. It evaluates the effect of different ratios between the thickness of the free face of the adherend (e) and the thickness of the restrained face (h).

The use of a large tapering ratio ($e/h = 0.2$) leads to the greatest improvement in joint strength, reaching a failure load more than 80% larger than that found for the standard nontapered joint. This increased tapering ratio leads to a greatly reduced shear stress level, providing a level of improvement that is typical of joints with much more complex geometries. More recently, Vu et al. [84] used acrylic photopolymers printed in a multimaterial jetting process to produce fracture specimens with functionally graded characteristics in the through-the-thickness direction. The authors noted an increased design flexibility, which enables the possible control of the strength, stiffness, and toughness of the structure. A 62% increase in strength was found for both the average peel force and the apparent fracture energy for the specimens using the graded interface.

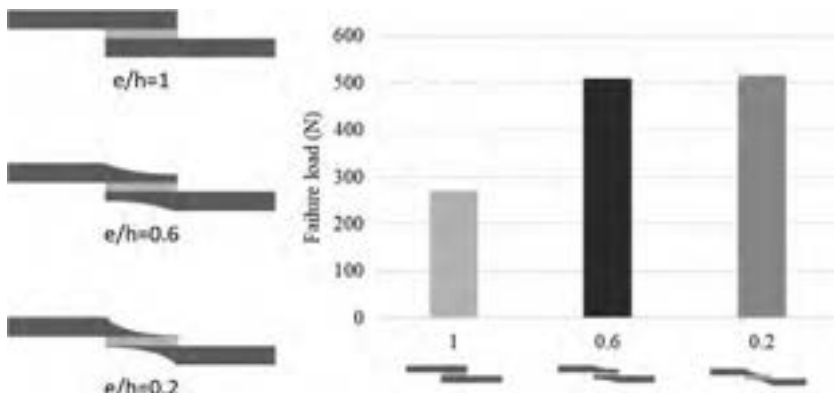


Fig. 33.16 Effect of 3D printed adherend shaping on joint performance.

33.4.2.4 Modeling of functionally graded adherends

Because the practical manufacture of functionally graded adherends is a complex task, the largest amount of publications in this field are dedicated to modeling processes, seeking novel concepts by performing analysis of the stress fields within these materials. One can encounter diverse studies that attempt to evaluate the effect of careful control of the modulus of adherends to counteract the stresses generated by the different loading directions. For example, some works are devoted to studying the effect of a graded modulus and graded geometrical parameters on the performance of SLJs under diverse conditions, such as shear and bending loads [62,85–87]. For tubular joints, diverse works have analyzed the effectiveness of graded adherends under internal pressure and tension loads [65,88].

Generally, the use of graded layers in these joints provides improved stress distribution, although the proposed geometries can be difficult to implement in practice. Some works have also explored the use of these materials to mitigate the effects of the residual thermal stresses for diverse types of joint geometries [66,70]. Furthermore, the use of functionally graded materials also allows controlling the thermal expansion and material density, mitigating the generation of residual stresses that might occur during the curing cycle of the adhesive [12]. Further analytical studies have been dedicated to analyses of the different aspects of joints with functionally graded adherends, such as the propagation of stress waves [89], the presence of interfacial stresses [90,91], the study of the free vibration modes [92–94], and strength prediction using damage mechanics [95].

Dos Reis et al. [96] developed a CZM for a joint with functionally graded adhesives, validating its performance against that of previously published data obtained with an analytical model. A subsequent work [97] used that same model to study the effect of different ratios of stiffness variation on the performance of SLJ adherends bonded with two very different adhesives. Stress analysis and failure load determination were carried out using CZM. The results showed that that the adhesive properties play a major role in the usefulness of the graded adherends. The brittle adhesive was found to be highly sensitive to the adherend configuration (almost a 50% strength improvement) while the tough adhesive did not show a similar sensitivity (less than 10%).

33.5 Conclusions

Adhesive layers are known to provide better stress distributions than those found with other classical joining methods, such as welding and mechanical fastening. However, the stress fields within bonded layers are still quite complex and can be damaging for many applications, especially where composite or laminated substrates are used. This document has shown that seeking ways to mitigate these harmful stresses in bonded joints has been the target of investigation for many decades. Researchers have adopted a wide range of concepts and ideas that seek to control the way the joints deform and how equalizing the way they load the transfer through the adherends and the adhesive,

thus leading to minimized stress concentrations. The first concepts attempted to reduce the stress concentration by shaping the joint and the adhesives, providing smoother geometries and larger areas of load transfer. While successful, these concepts usually are beset with added manufacturing complexity and costs, which has spurred the development of solutions that are based on the modification of the properties of the adhesive layer and the adherends. One of the most important of these concepts was the mixed adhesive joint, which selectively applies different adhesives in different locations of the adhesive layer, thus adjusting the properties of the adhesive to better handle the expected stresses and strains at a given location. This concept was found to work well, but it is still an imperfect, stepwise solution, whereas the final target would be to attain a constant variation of the adhesive properties with a functionally graded material. It has been shown that while the industrial use of a graded joint is still not fully feasible, multiple research works have fully developed the graded joint concept and its mechanics. Most recently, a limited but growing set of researchers also provided a set of techniques suitable for the manufacture of functionally graded adhesives and adherends. One important note is that most research carried out in this subject is performed in relatively simple joint geometries with relatively well-known stress fields. To further expand the use of these techniques to real-world joints with more complex stress states, it is essential to rely on numerical modeling that will allow precisely identifying the locations of the joints where modified properties provided strength improvements. Here, the use of evolutive models, using automated optimization processes is expected to be crucial because the complexity of these joints makes this a very time-consuming task. Furthermore, the practical implementation processes also represent a barrier, but it is expected that as manufacturing processes increasingly grow to rely on automated additive manufacturing procedures, the practical implementation of functionally graded adhesive joints will become more likely.

References

- [1] L.F.M. da Silva, A. Öchsner, R.D. Adams (Eds.), *Handbook of Adhesion Technology*, second ed., Springer Science & Business Media, Berlin, 2018.
- [2] A. Magalhaes, M. De Moura, Application of acoustic emission to study creep behaviour of composite bonded lap shear joints, *NDT E Int.* 38 (1) (2005) 45–52.
- [3] R.D. Adams, J. Comyn, W.C. Wake, *Structural Adhesive Joints in Engineering*, Springer Science & Business Media, New York, 1997.
- [4] L. Hart-Smith, *Adhesive-Bonded Scarf and Stepped-Lap Joints*, National Aeronautics and Space Administration, 1973.
- [5] F. Thamm, Stress distribution in lap joints with partially thinned adherends, *J. Adhes.* 7 (4) (1976) 301–309.
- [6] R.D.S.G. Campilho, M.F.S.F. De Moura, J.J.M.S. Domingues, Stress and failure analyses of scarf repaired CFRP laminates using a cohesive damage model, *J. Adhes. Sci. Technol.* 21 (9) (2007) 855–870.
- [7] L.F.M. da Silva, A. Öchsner, *Modeling of Adhesively Bonded Joints*, Springer, 2008.
- [8] T.P. Lang, P.K. Mallick, The effect of recessing on the stresses in adhesively bonded single-lap joints, *Int. J. Adhes. Adhes.* 19 (4) (1999) 257–271.

- [9] G. Belingardi, L. Goglio, A. Tarditi, Investigating the effect of spew and chamfer size on the stresses in metal/plastics adhesive joints, *Int. J. Adhes. Adhes.* 22 (4) (2002) 273–282.
- [10] R. Adams, J. Harris, The influence of local geometry on the strength of adhesive joints, *Int. J. Adhes. Adhes.* 7 (2) (1987) 69–80.
- [11] M.Y. Tsai, J. Morton, The effect of a spew fillet on adhesive stress distributions in laminated composite single-lap joints, *Compos. Struct.* 32 (1–4) (1995) 123–131.
- [12] L.F.M. da Silva, R.D. Adams, Adhesive joints at high and low temperatures using similar and dissimilar adherends and dual adhesives, *Int. J. Adhes. Adhes.* 27 (3) (2007) 216–226.
- [13] L.F.M. da Silva, R.D. Adams, Joint strength predictions for adhesive joints to be used over a wide temperature range, *Int. J. Adhes. Adhes.* 27 (5) (2007) 362–379.
- [14] X. Zhao, R. Adams, L. Da Silva, Single lap joints with rounded adherend corners: stress and strain analysis, *J. Adhes. Sci. Technol.* 25 (8) (2011) 819–836.
- [15] L. Hart-Smith, *Induced Peel Stresses in Adhesively Bonded Joints*, 1600, Douglas Aircraft Company, 1982, p. J9422A.
- [16] E.A.S. Marques, L.F.M. da Silva, Joint strength optimization of adhesively bonded patches, *J. Adhes.* 84 (11) (2008) 915–934.
- [17] L. Xu, H. Kuai, S. Sengupta, Dissimilar material joints with and without free-edge stress singularities: part I. A biologically inspired design, *Exp. Mech.* 44 (6) (2004) 608–615.
- [18] L. Xu, S. Sengupta, Dissimilar material joints with and without free-edge stress singularities: part II. An integrated numerical analysis, *Exp. Mech.* 44 (6) (2004) 616–621.
- [19] J.-Y. Cognard, et al., A study of the non-linear behaviour of adhesively-bonded composite assemblies, *Compos. Struct.* 76 (1–2) (2006) 34–46.
- [20] R. Adams, et al., Stress analysis and failure properties of carbon-fibre-reinforced-plastic/steel double-lap joints, *J. Adhes.* 20 (1) (1986) 29–53.
- [21] A.R. Rispler, et al., Shape optimisation of adhesive fillets, *Int. J. Adhes. Adhes.* 20 (3) (2000) 221–231.
- [22] L.J. Hart-Smith, *Designing to minimize peel stresses in adhesive-bonded joints, in: Delamination and Debonding of Materials*, ASTM International, 1985.
- [23] F.Z. Hu, C. Soutis, Strength prediction of patch-repaired CFRP laminates loaded in compression, *Compos. Sci. Technol.* 60 (7) (2000) 1103–1114.
- [24] M. Goland, E. Reissner, The stresses in cemented joints, *J. Appl. Mech.* 11 (1) (1944) A17–A27.
- [25] A.F. Avila, P.N.D.O. Bueno, An experimental and numerical study on adhesive joints for composites, *Compos. Struct.* 64 (3–4) (2004) 531–537.
- [26] G. Fessel, et al., Evaluation of different lap-shear joint geometries for automotive applications, *Int. J. Adhes. Adhes.* 27 (7) (2007) 574–583.
- [27] G. Fessel, et al., Fatigue performance of metallic reverse-bent joints, *Fatigue Fract. Eng. Mater. Struct.* 32 (9) (2009) 704–712.
- [28] S. Guo, D.A. Dillard, R.H. Plaut, Effect of boundary conditions and spacers on single-lap joints loaded in tension or compression, *Int. J. Adhes. Adhes.* 26 (8) (2006) 629–638.
- [29] A. Objois, B. Fargette, Y. Gilibert, The influence of the bevel angle on the micro-mechanical behaviour of bonded scarf joints, *J. Adhes. Sci. Technol.* 14 (8) (2000) 1057–1070.
- [30] A.J. Gunnion, I. Herszberg, Parametric study of scarf joints in composite structures, *Compos. Struct.* 75 (1–4) (2006) 364–376.
- [31] R.D.S.G. Campilho, et al., Tensile behaviour of three-dimensional carbon-epoxy adhesively bonded single-and double-strap repairs, *Int. J. Adhes. Adhes.* 29 (6) (2009) 678–686.

- [32] L. Hart-Smith, *Adhesive-Bonded Double-Lap Joints*, National Aeronautics and Space Administration, 1973.
- [33] Marques, E., L.F. da Silva, and C. Sato, Testing of dual adhesive ceramic-metal joints for aerospace applications. *Advances in Modeling and Design of Adhesively Bonded Systems*, 2013: p. 171–190. E. Marques, L.F. da Silva, C. Sato, Testing of dual adhesive ceramic-metal joints for aerospace applications, in: *Advances in Modeling and Design of Adhesively Bonded Systems*, Wiley, 2013, pp. 171–190.
- [34] M.R.G. Silva, E.A.S. Marques, L. Silva, Behaviour under impact of mixed adhesive joints for the automotive industry, *Lat. Am. J. Solids Struct.* 13 (5) (2016) 835–853.
- [35] J.J.M. Machado, et al., Improvement in impact strength of composite joints for the automotive industry, *Compos. Part B* 138 (2018) 243–255.
- [36] E. Marques, R. Campilho, L.F. da Silva, Geometrical study of mixed adhesive joints for high-temperature applications, *J. Adhes. Sci. Technol.* 30 (7) (2016) 691–707.
- [37] J. Marques, et al., An overview of manufacturing functionally graded adhesives—challenges and prospects, *J. Adhes.* 97 (2) (2021) 172–206.
- [38] K. Kokini, Y. Takeuchi, B. Choules, Thermal crack initiation mechanisms on the surface of functionally graded ceramic thermal barrier coatings, *Ceram. Int.* 22 (5) (1996) 397–401.
- [39] M. Sathish, N. Radhika, B. Saleh, A critical review on functionally graded coatings: methods, properties, and challenges, *Compos. Part B* 225 (2021) 109278.
- [40] X.-J. Xu, J.-M. Meng, A model for functionally graded materials, *Compos. Part B* 145 (2018) 70–80.
- [41] J.S. Moita, et al., Material distribution and sizing optimization of functionally graded plate-shell structures, *Compos. Part B* 142 (2018) 263–272.
- [42] R. Carbas, L. da Silva, G. Critchlow, Functionally graded joints by induction heating, in: *Provisional Patent Application Portuguese*, 2013. 107189.
- [43] R.J.C. Carbas, L.F.M. da Silva, G.W. Critchlow, Adhesively bonded functionally graded joints by induction heating, *Int. J. Adhes. Adhes.* 48 (2014) 110–118.
- [44] R. Carbas, et al., Effect of cure temperature on the glass transition temperature and mechanical properties of epoxy adhesives, *J. Adhes.* 90 (1) (2014) 104–119.
- [45] R. Carbas, et al., Effect of post-cure on the glass transition temperature and mechanical properties of epoxy adhesives, *J. Adhes. Sci. Technol.* 27 (23) (2013) 2542–2557.
- [46] R. Carbas, et al., Functionally graded adhesive patch repairs of wood beams in civil applications, *J. Compos. Constr.* 19 (2) (2014) 04014038.
- [47] S. Kawasaki, et al., Functionally graded adhesive joints bonded by honeymoon adhesion using two types of second generation acrylic adhesives of two components, *J. Adhes.* 92 (7–9) (2016) 517–534.
- [48] M. Nakanouchi, et al., Development of application method for fabricating functionally graded adhesive joints by two-component acrylic adhesives with different elastic moduli, *J. Adhes.* 95 (5–7) (2019) 529–542.
- [49] S. Kumar, B.L. Wardle, M.F. Arif, Strength and performance enhancement of bonded joints by spatial tailoring of adhesive compliance via 3D printing, *ACS Appl. Mater. Interfaces* 9 (1) (2017) 884–891.
- [50] A. Chiminelli, et al., Analysis of mixed adhesive joints considering the compaction process, *Int. J. Adhes. Adhes.* 76 (2017) 3–10.
- [51] R. Carbas, L. Da Silva, L. Andrés, Functionally graded adhesive joints by graded mixing of nanoparticles, *Int. J. Adhes. Adhes.* 76 (2017) 30–37.
- [52] J. Bonaldo, et al., Functionally graded adhesive joints by using thermally expandable particles, *J. Adhes.* 95 (11) (2019) 995–1014.

- [53] C.I.D. Silva, et al., Mechanical characterisation of graded single lap joints using magnetised cork microparticles, in: *Advanced Joining Processes*, Springer, 2020, pp. 153–174.
- [54] C. da Silva, et al., Functionally graded adhesive joints using magnetic microparticles with a polyurethane adhesive, *J. Adv. Join. Process.* 3 (2021) 100048.
- [55] S. Kumar, Analysis of tubular adhesive joints with a functionally modulus graded bondline subjected to axial loads, *Int. J. Adhes. Adhes.* 29 (8) (2009) 785–795.
- [56] S. Kumar, J. Scanlan, On axisymmetric adhesive joints with graded interface stiffness, *Int. J. Adhes. Adhes.* 41 (2013) 57–72.
- [57] R. Carbas, et al., Modelling of functionally graded adhesive joints, *J. Adhes.* 90 (8) (2014) 698–716.
- [58] O. Volkersen, Die Nietkraftverteilung in zugbeanspruchten Nietverbindungen mit konstanten Laschenquerschnitten, *Luftfahrtforschung* 15 (1/2) (1938) 41–47.
- [59] M. Dos Reis, et al., Functionally graded adherends in adhesive joints: an overview, *J. Adv. Join. Process.* 2 (2020) 100033.
- [60] V.K. Ganesh, T.S. Choo, Modulus graded composite adherends for single-lap bonded joints, *J. Compos. Mater.* 36 (14) (2002) 1757–1767.
- [61] J.N. Boss, V.K. Ganesh, C.T. Lim, Modulus grading versus geometrical grading of composite adherends in single-lap bonded joints, *Compos. Struct.* 62 (1) (2003) 113–121.
- [62] M.K. Apalak, R. Gunes, Investigation of elastic stresses in an adhesively bonded single lap joint with functionally graded adherends in tension, *Compos. Struct.* 70 (4) (2005) 444–467.
- [63] M.K. Apalak, R. Gunes, Elastic flexural behaviour of an adhesively bonded single lap joint with functionally graded adherends, *Mater. Des.* 28 (5) (2007) 1597–1617.
- [64] R. Gunes, M.K. Apalak, M. Yildirim, The free vibration analysis and optimal design of an adhesively bonded functionally graded single lap joint, *Int. J. Mech. Sci.* 49 (4) (2007) 479–499.
- [65] M.K. Apalak, Stress analysis of an adhesively bonded functionally graded tubular single lap joint subjected to an internal pressure, *Sci. Eng. Compos. Mater.* 13 (3) (2006) 183–212.
- [66] M.K. Apalak, R. Gunes, Thermal residual stresses in an adhesively-bonded functionally graded single-lap joint, *J. Adhes. Sci. Technol.* 20 (12) (2006) 1295–1320.
- [67] R. Gunes, M.K. Apalak, M. Yildirim, Free vibration analysis of an adhesively bonded functionally graded tubular single lap joint, *J. Adhes.* 87 (9) (2011) 902–925.
- [68] Z. Gul Apalak, R. Ekici, Elastic stresses in an adhesively bonded functionally graded double containment cantilever joint in tension, *J. Reinf. Plast. Compos.* 26 (13) (2007) 1291–1318.
- [69] Z.G. Apalak, Elastic flexural stresses in an adhesively bonded functionally graded double containment cantilever joint, *J. Thermoplast. Compos. Mater.* 23 (1) (2010) 35–56.
- [70] M.K. Apalak, R. Gunes, S. Eroglu, Thermal residual stresses in an adhesively bonded functionally graded tubular single lap joint, *Int. J. Adhes. Adhes.* 27 (1) (2007) 26–48.
- [71] M.K. Apalak, M.D. Bagci, Thermal residual stresses in adhesively bonded in-plane functionally graded clamped plates subjected to an edge heat flux, *J. Adhes. Sci. Technol.* 25 (15) (2012) 1861–1908.
- [72] M.K. Apalak, M.D. Demirbas, Thermal residual stresses in adhesively bonded in-plane functionally graded clamped circular hollow plates, *J. Adhes. Sci. Technol.* 27 (14) (2013) 1590–1623.
- [73] Shang, X., et al., Review on techniques to improve the strength of adhesive joints with composite adherends. *Compos. B. Eng.*, 2019. 177. X. Shang, et al., Review on techniques

- to improve the strength of adhesive joints with composite adherends, *Compos. B. Eng.* 177 (2019), 107363.
- [74] M.J. Schollere, et al., Surface toughening—a concept to decrease stress peaks in bonded joints, *J. Adhes.* 95 (5–7) (2018) 495–514.
- [75] X. Shang, et al., A strategy to reduce delamination of adhesive joints with composite substrates, *Proc. Inst. Mech. Eng. Pt. L: J. Mater. Des. Appl.* 233 (3) (2019) 521–530.
- [76] A.P. Mouritz, Review of z-pinned composite laminates, *Compos. A: Appl. Sci. Manuf.* 38 (12) (2007) 2383–2397.
- [77] I.K. Partridge, D.D.R. Cartié, Delamination resistant laminates by Z-Fiber[®] pinning: part I manufacture and fracture performance, *Compos. A: Appl. Sci. Manuf.* 36 (1) (2005) 55–64.
- [78] T.M. Koh, S. Feih, A.P. Mouritz, Experimental determination of the structural properties and strengthening mechanisms of z-pinned composite T-joints, *Compos. Struct.* 93 (9) (2011) 2222–2230.
- [79] M. Grassi, X. Zhang, Finite element analyses of mode I interlaminar delamination in z-fibre reinforced composite laminates, *Compos. Sci. Technol.* 63 (12) (2003) 1815–1832.
- [80] S.-C. Dai, et al., Experimental study on z-pin bridging law by pullout test, *Compos. Sci. Technol.* 64 (16) (2004) 2451–2457.
- [81] A.I. Marasco, et al., Mechanical properties balance in novel Z-pinned sandwich panels: out-of-plane properties, *Compos. A: Appl. Sci. Manuf.* 37 (2) (2006) 295–302.
- [82] S. Kumar, A. de Tejada Alvarez, Modeling and experimental evaluation of geometrically graded multi-material single-lap joints, in: 56th AIAA/ASCE/AHS/ASC Structures, Structural Dynamics, and Materials Conference, 2015.
- [83] M.A. Khan, S. Kumar, W.J. Cantwell, Additively manufactured cylindrical systems with stiffness-tailored interface: modeling and experiments, *Int. J. Solids Struct.* 152–153 (2018) 71–84.
- [84] I.Q. Vu, et al., Characterizing the effect of print orientation on interface integrity of multi-material jetting additive manufacturing, *Addit. Manuf.* 22 (2018) 447–461.
- [85] W.E. Guin, J. Wang, Theoretical model of adhesively bonded single lap joints with functionally graded adherends, *Eng. Struct.* 124 (2016) 316–332.
- [86] S. Amidi, J. Wang, Three-parameter viscoelastic foundation model of adhesively bonded single-lap joints with functionally graded adherends, *Eng. Struct.* 170 (2018) 118–134.
- [87] A. Afkar, M.N. Camari, Finite element analysis of mono- and bi-adhesively bonded functionally graded adherend, *J. Fail. Anal. Prev.* 14 (2) (2014) 253–258.
- [88] M.K. Apalak, Elastic stresses in an adhesively-bonded functionally-graded tubular single-lap joint in tension, *J. Adhes. Sci. Technol.* 20 (9) (2006) 1019–1046.
- [89] M. Dorduncu, M.K. Apalak, J.N. Reddy, Stress wave propagation in adhesively bonded functionally graded cylinders: an improved model, *J. Adhes. Sci. Technol.* 33 (2) (2018) 156–186.
- [90] M. Mustapha, et al., Interfacial stresses in plated beams with exponentially-varying properties, *J. Adhes. Sci. Technol.* 24 (6) (2010) 1063–1081.
- [91] I. Bensaid, B. Kerboua, Interfacial stress analysis of functionally graded beams strengthened with a bonded hygrothermal aged composite plate, *Compos. Interfaces* 24 (2) (2016) 149–169.
- [92] R. Gunes, et al., Free vibration analysis of adhesively bonded single lap joints with wide and narrow functionally graded plates, *Compos. Struct.* 92 (1) (2010) 1–17.
- [93] Z.G. Apalak, et al., Free vibration analysis of an adhesively bonded functionally graded double containment cantilever joint, *J. Adhes. Sci. Technol.* 28 (12) (2014) 1117–1139.

-
- [94] S. Wang, Y. Li, Z. Xie, Free vibration analysis of adhesively bonded lap joints through layerwise finite element, *Compos. Struct.* 223 (2019) 110943.
 - [95] P. Chen, et al., Numerical analysis of the strength and interfacial properties of adhesive joints with graded adherends, *Int. J. Adhes. Adhes.* 90 (2019) 88–96.
 - [96] M.Q. dos Reis, et al., Numerical modelling of multi-material graded joints under shear loading, *Proc. Inst. Mech. Eng. E: J. Process Mech. Eng.* 234 (5) (2020) 436–445.
 - [97] M. Dos Reis, et al., Numerical modelling of functionally graded adherends, *Proc. Inst. Mech. Eng. C J. Mech. Eng. Sci.* 235 (3) (2021) 508–517.

Architected adhesive joints with improved fracture toughness

34

Thomas Pardoen^a, Kevin T. Turner^b, and Michal K. Budzik^c

^aInstitute of Mechanics, Materials and Civil Engineering Ecole Polytechnique de Louvain-Louvain School of Engineering, Université Catholique de Louvain, Ottignies-Louvain-la-Neuve, Belgium, ^bDepartment of Mechanical Engineering and Applied Mechanics, University of Pennsylvania, Philadelphia, PA, United States, ^cDepartment of Mechanical and Production Engineering, Aarhus University, Aarhus, Denmark

34.1 Introduction

Assembly through adhesive bonding of primary and load-carrying components often requires the use of stiff and reliable joining materials with relatively high strength. Such materials often are limited by a relatively low toughness and a high sensitivity to initial flaws and cracks. Thus, much of the focus in the structural adhesive community has been on improving the damage tolerance of bondline materials. This has been achieved through a number of strategies, including reformulating adhesives, as discussed for several adhesive families in Part I, and introducing additional phases or materials (e.g., toughening phases at the nano- and microscales that dissipate energy during failure) as discussed in Chapters 7 and 8.

On the verge of the green transition, with the focus shifting toward optimized material usage, it is challenging and limiting to focus solely on adhesive chemistry and composition for improvement (e.g., because of the proprietary nature of formulations, long development times, inherent difficulty in realizing continued improvements, etc.). Hence, there is strong motivation to find extrinsic approaches based on structuring and geometry that can be used to toughen adhesive joints and applied to a broad range of materials, independent of chemistry and composition, while possibly also providing an opportunity for lightweighting. The focus of this chapter is on the use of architecture at the scale of tens to a hundred micrometers and above and is distinct from toughening strategies based on nanoscale particles and fibers [1,2]. Such architecture-based approaches have been used to realize bulk mechanical metamaterials (MM) with the goal to realize higher-performance materials, materials with unique combinations of properties, or unconventional properties (e.g., negative Poisson's ratio). The time has come to advance such a paradigm owing to progress in manufacturing, notably digital manufacturing, in the context of adhesive bonding. Contrary to the common paradigm of material continuity and isotropy, some emerging architected materials introduce predetermined defects that allow for extra energy dissipation. These “defects,” if correctly designed, can have a beneficial effect by improving toughness without significant loss of stiffness. Note that one of the basic toughening principles is to increase plastic dissipation by designing the joint thickness

to optimize the plastic zone size. This is the specific subject of Chapter 18, and the underlying principle of increasing plastic dissipation will be further exploited here through variations of this idea. In this chapter, we first review several principles that can be used to enhance toughness and then show several embodiments of these principles through architecting of joints.

34.2 Overview of working principles for extrinsic joint toughening

34.2.1 Enhancement through crack deflection

Consider Fig. 34.1 in which a bonded version of the single edge notched tensile (SENT) specimen is subjected to mode I fracture loading via a remote stress σ^∞ . If the bondline is of constant thickness t_a , Young's modulus E_a , and fracture energy \mathcal{G}_{Ic_a} , and without any flaws or shape variations, a crack growing along a path located in the middle of the adhesive thickness is expected. However, in the illustrated situation, one of the adherends (with Young's modulus E and fracture energy $\mathcal{G}_{Ic} \gg \mathcal{G}_{Ic_a}$) includes a pattern such that the adhesive thickness is locally affected, and the feature intersects the expected crack path. The detailed view of the feature in Fig. 34.1 illustrates the local crack growth scenario expected for this joint configuration. This discussion is simplified and qualitative. The crack propagates toward the feature under mode I loading (denoted as I). Once the tip reaches the feature, continued mode I crack propagation through the feature is energetically unfavorable as $\mathcal{G}_{Ic_a} \ll \mathcal{G}_{Ic}$. Instead, the crack propagates along the vertical edge of the feature. The crack grows along this path under, predominantly, mode II, and mode II generally requires additional energy [3]. Once the vertical edge is bypassed, the crack propagates under mode I either at the

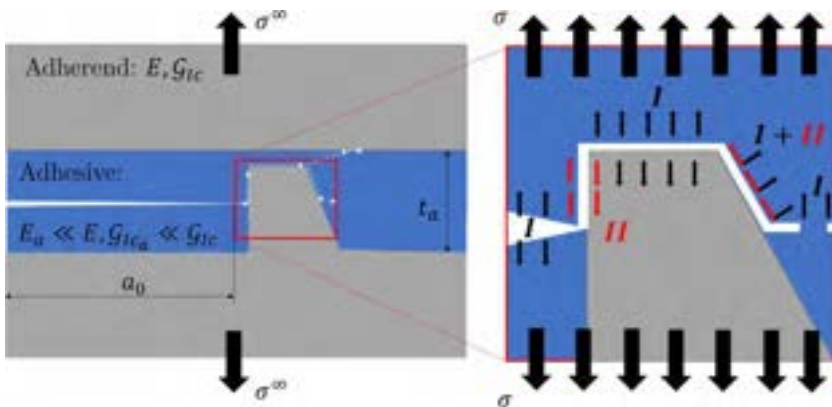


Fig. 34.1 Schematic representation of bonded single edge notch test specimen under mode I loading. The feature on one of the adherends deflects the crack from its original path and orientation. On the right, a detailed view of local stress distribution giving rise to different fracture modes.

interface (as in the figure) or cohesively inside the thin adhesive, requiring less energy. The trailing edge of the feature is arbitrarily oriented with respect to the loading direction and a mixed-mode I/II path is expected with intermediate energy expenditure I/II , before the mode I cohesive cracking process resumes.

Though simplified, this example captures the basic idea behind enhancing properties of adhesive joints through crack deflection. Analysis performed using interface fracture mechanics shows that the introduction of mixed-mode conditions leads to a significant increase of the apparent fracture toughness [4]. An entire family of failure criteria exists for determining interface fracture under mixed-mode conditions and crack deflection. The simple linear failure criterion for mixed-mode fracture is given by [5]:

$$\frac{\mathcal{G}_I}{\mathcal{G}_{Ic}} + \frac{\mathcal{G}_{II}}{\mathcal{G}_{IIc}} + \frac{\mathcal{G}_{III}}{\mathcal{G}_{IIIc}} = 1 \quad (34.1)$$

where \mathcal{G}_I , \mathcal{G}_{II} , and \mathcal{G}_{III} are the energy-release rates for mode I, II, and III fractures, respectively, and \mathcal{G}_{Ic} , \mathcal{G}_{IIc} , and \mathcal{G}_{IIIc} are the respective fracture energies, with a common (although not always respected) inequality $\mathcal{G}_{IIc} > \mathcal{G}_{IIIc} > \mathcal{G}_{Ic}$. Under a globally applied mode I fracture loading, the stresses and, thus, the related magnitudes of \mathcal{G}_I , \mathcal{G}_{II} , and \mathcal{G}_{III} are locally set by material heterogeneities and geometric features that can lead to crack deflection and an increase in the apparent fracture toughness. Choosing the ratio of adhesive/feature elastic and fracture properties, along with the shape and position of the crack-deflecting feature, can be used as a tool to control the toughness and crack growth process in general. Designing interfaces to exploit crack deflection is underexplored [6] to the authors' knowledge, though a significant number of works have theoretically investigated crack deflection [3,7,8] and proved the general validity of the concept [9].

34.2.2 *Blunt the propagating crack, relax the stress intensity factor at the tip*

Crack tip blunting is an efficient way to increase the apparent fracture toughness of a material. An elastic material containing a crack of length a under remote tensile loading σ^∞ can be effectively toughened through a straightforward, crack-blunting architecture. Consider an adhesive joint under remote tensile load σ^∞ similar to that previously discussed and depicted in Fig. 34.2a.

The shape of the crack tip region can be approximated by an ellipse with a major axis a and minor axis b . The maximum stress σ_{max} at the tip can be then expressed as:

$$\sigma_{max} = 2\sigma^\infty \frac{a}{b} \quad (34.2)$$

As the ratio $\frac{a}{b}$ increases, so does the maximum stress. In the limit of $a \rightarrow \infty$ or $b \rightarrow 0$, the crack is sharp and linear elastic fracture mechanics (LEFM) applies. Under LEFM, the stress at distance r from the front of the crack tip is (for mode I fracture along the crack growth plane):

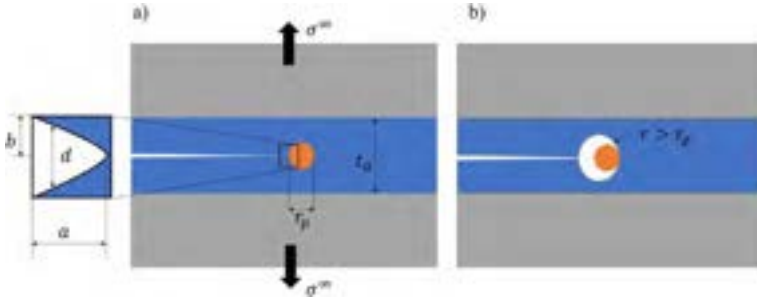


Fig. 34.2 Plastic zone radius r_p inside a bondline of thickness t_a under remote tensile stress σ^∞ (a). The local crack tip geometry can be approximated by an ellipse with major a and minor b (zoomed). The introduction of the geometrical feature of radius $r > r_p$ inside the bondline can be used to enhance fracture properties (b).

$$\sigma(r) \approx \frac{K_I}{\sqrt{2\pi r}} \tag{34.3}$$

where K_I is the stress intensity factor, and, in the elastic limit, $K_I^2 \propto EG_I$. Omitting effects at the atomic scale, many structural adhesives, including untoughened epoxy and polyester-based materials, behave in an apparent elastic-brittle manner. Considering bondlines made of such materials, the internal flaws and microcracks lead to singular stresses at their tips leading to failure at low loads. In addition, while being stiff, the brittle materials do not dissipate significant energy during fracture. In such cases, enabling unloading of the crack tip regions is an efficient solution for improving load capacity.

Locally at the crack tip, for elastic materials, the intensity/magnitude of the crack tip loading can be reformulated in terms of the crack tip opening displacement (CTOD), defined as:

$$d \sim \frac{K_I^2}{E\sigma_0} \sim \frac{G_I}{\sigma_0} \tag{34.4}$$

where σ_0 refers to the yield strength of the material. The brittle-ductile transition is controlled by a characteristic length scale of material, the plastic radius, $r_p = c \frac{K_I^2}{\sigma_0^2} = c \frac{EG_I}{\sigma_0^2}$, which describes the size of the plastic zone in front of the crack. Here, c is a constant that depends on, for example, the stress state at the crack tip, usually of order 1. Because all materials experience some level of plasticity, in elastoplastic fracture mechanics, d can be directly connected to the magnitude of the J integral. The concept is detailed in Chapter 16 through the following relationship:

$$d = \alpha \frac{J}{\sigma_0} \tag{34.5}$$

with α being the so-called Shih factor of order one, which depends on strain capacity and ratio $\frac{\sigma_0}{E}$. The critical CTOD, d_c , is an alternative fracture toughness indicator equivalent to $J_{Ic} = \mathcal{G}_{Ic} \propto \frac{K_{Ic}^2}{E}$ under small-scale yielding conditions. Both r_p and d_c can be formally related because $\frac{d_c^2}{r_p} \sim \frac{J_{Ic}}{E}$, with the geometric interpretation given in Fig. 34.2. Importantly, the magnitude of d_c offers a mean to quantify what can be considered a sharp crack in the context of fracture mechanics and what can be considered a notch. If the opening of the crack is initially larger than d_c , strictly speaking, the stress concentration cannot be assimilated to a pure crack. In other words, the tip radius of curvature is too low for the tip to be seen as a crack. This means that the maximum opening stress and maximum stress triaxiality ahead of the crack tip are lower than the fracture mechanics level as predicted by the HRR fields [10,11]. Extra energy must thus be dissipated to reinitiate a sharp crack. There are many examples showing that the apparent fracture toughness value indeed increases (and is no longer a true fracture toughness) above a certain threshold set by d_c (or sometimes a value larger than d_c but still connected to it). Thus, the toughening mechanism by blunting is to force the propagating crack to open above the threshold opening (typically d_c), which then arrests the crack and forces a reinitiation. Such “over-opening” can be triggered by forcing the crack to coalesce with cavities or microcracks. One implementation is to have particles with weak bonding to the matrix. As the crack gets very close to the particle, decohesion is created and the crack gets trapped by the void and over-opened. An alternative is to pattern the joint with preexisting open spaces [12–15].

34.2.3 Crack face bridging

The principle of toughening via bridging stems from basic fracture energy considerations and aims to increase sources of energy storage and dissipation by additional mechanisms instead of the fracture of bondline materials alone, that is, \mathcal{G}_c^a —the fracture energy of the adhesive material [16,17]. The creation of new crack faces in the material experiencing with bridging requires additional energy due to straining of the bridging material and eventual decohesion and/or failure of the ligaments, \mathcal{G}_c^p . The bridging phenomena can also equally be regarded as a reduction of the energy release rate; however, the net result remains the same—an increase in measured fracture energy. Thus, in general, the total fracture energy, expressed as \mathcal{G}_c^T , can be defined as a sum:

$$\mathcal{G}_c^T = \mathcal{G}_c^a + \mathcal{G}_c^p + \dots \quad (34.6)$$

where the three dots indicate other dissipation sources that can contribute to the work needed to fracture the joint (Fig. 34.3).

34.2.4 Architected bondlines and adherends

Consider a bonded tensile specimen shown in Fig. 34.4a under an applied tensile force P . For simplicity, neglecting any local effects on the stress distribution due to

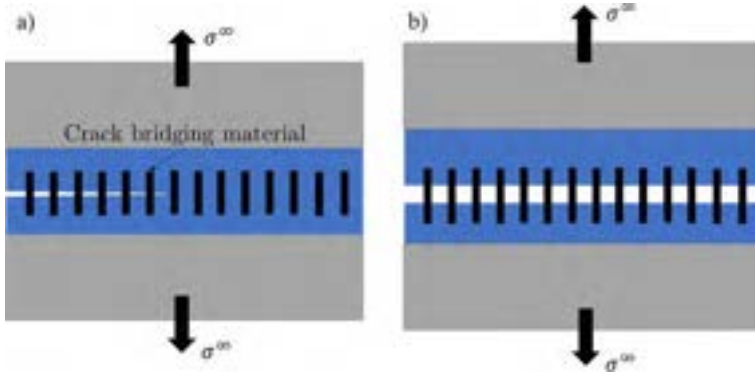


Fig. 34.3 Schematic representation of crack bridging phenomena: (a) initial configuration, and (b) after crack propagated through the bondline. In the presented case, under σ^∞ loading, the bridging material extends beyond the d_c of the adhesive material.

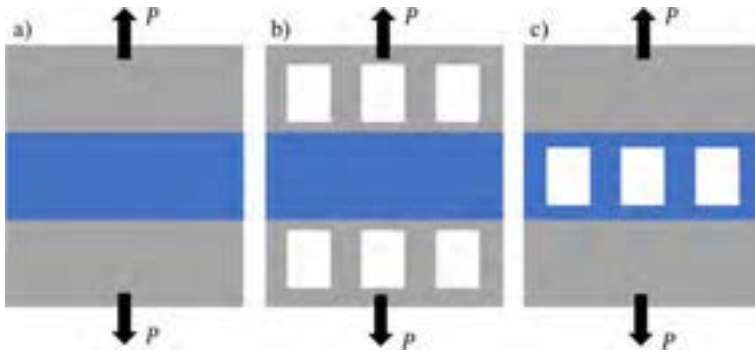


Fig. 34.4 Examples of using simple geometrical modifications to control failure loads and stress distribution: (a) reference butt joint; (b) joint with architected adherends; and (c) joint with architected bondline.

interfaces, edges, or corners, we assume the stress distribution is simply the average stress as given by:

$$\sigma \approx \frac{P}{A_i} = E_i \epsilon_i \tag{34.7}$$

where A_i is the cross-section area, E_i is the Young’s modulus, and ϵ_i is the strain. Index i is denoting either the adherend or the adhesive. The stress distribution is affected for the cases depicted in Figs. 34.4b–c because the geometry is spatially varying either in the adherend or in the adhesive domain, respectively. The effect of spatially varying stress can be used to manipulate strain localization, mitigate stresses at the usual failure loci, increase the compliance of the joint, or change the failure modes leading to different mechanical properties of the joint [18].

On the local scale, the analysis is more involved and we will only make use of fracture mechanics to outline the crucial aspect. Eq. (34.3) gives a simple relationship

between the stress field near discontinuities in the plates with a slit and can be rewritten as

$$\sigma(r) \approx \sqrt{\frac{\mathcal{G}_I E}{2\pi r}} \quad (34.8)$$

which can be rearranged to outline the extension of the asymptotic stress field:

$$r \approx \frac{1}{2\pi} \frac{\mathcal{G}_I E}{\sigma^2} \quad (34.9)$$

For any material with modulus E , there is a material parameter called cohesive length l_c for which $\mathcal{G}_I = \mathcal{G}_{Ic}$ and $\sigma = \sigma_f$ with σ_f denoting the failure stress [19,20]. Consequently,

$$\mathcal{G}_{Ic} \propto \frac{l_c \sigma_f^2}{E} \quad (34.10)$$

Thus, the fracture energy can be increased by increasing the cohesive length or the failure stress or by decreasing the modulus of the material. Of course, all the parameters are interlinked for homogeneous materials, but the effective E can be independently modified by careful geometrical manipulation. This is the key to architecting the local stress fields through geometry of the adherends and of the bondlines.

34.3 Embodiments of toughening principles through architecture

34.3.1 Stop holes as a crack blunting mechanism

As outlined in Section 34.2.2, forcing the crack to reinitiate can be an effective way for increasing fracture toughness of bondlines. Fig. 34.5 shows a realization of this concept through the introduction of holes running through the width of the interface [21].

Here, so-called “stop holes” are introduced through drilling or molding holes at regular intervals λ along the bondline with diameter D equaling, in the depicted case, that of the adhesive thickness (t_a). The critical parameter, as outlined previously, is D .

34.3.2 Alternating surface properties to force bridging and crack meandering

New concepts for achieving crack arrest and increased toughness of adhesive joints incorporate patterns for triggering bridging ligaments between the crack faces—resembling fiber bridging phenomena frequently observed in composite delamination. Here, two possible scenarios, shown in Fig. 34.6, have been exploited to improve the effective toughness: (i) bridging through the material embedded in the

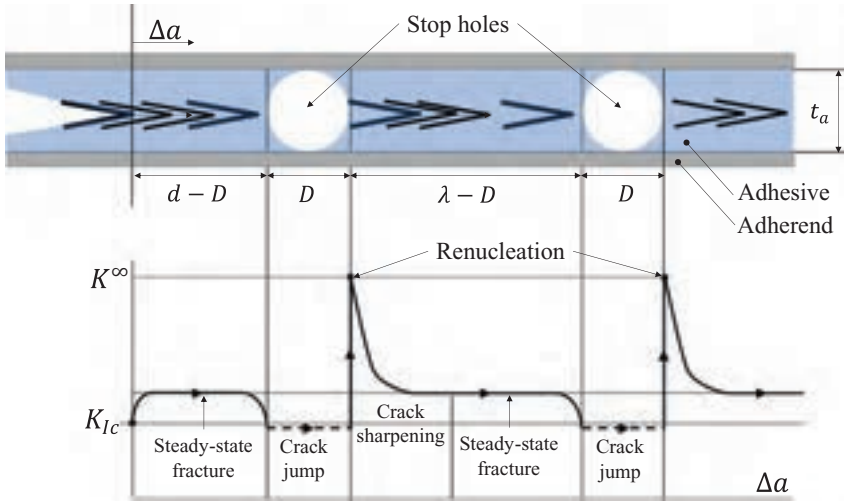


Fig. 34.5 Mechanism of toughening by crack blunting using holes with a diameter equal to the adhesive thickness ($t_a = D$). After the period of stable growth through the bondline (region $d - D$), the crack reaches the hole. With no material resistance, the crack jumps over distance D . Here, due to the curvature of the tip being smaller than at the crack tip, the energy required to reinitiate the crack is higher. This process is then repeated.

Adopted from K. Maloney, N. Fleck, Toughening strategies in adhesive joints, *Int. J. Solids Struct.* 158 (2019) 66–75.

adhesive [22] (Figs. 34.6a–b), and (ii) use of the bondline as the actual bridging ligaments [23] (Fig. 34.6c).

Both solutions were proven to be successful under mode I loading conditions, leading to a significant increase of bondline fracture energy as well as stabilization of the crack propagation process.

34.3.3 Design bondline geometry to control fracture toughness of joints

As discussed above in Section 24.2.4, the compliance of the bondline can play a central role in determining how stresses are distributed at the interface and particularly near the crack tip. A more compliant interface results in a larger elastic process zone and reduced stress levels at the crack tip [24]. This approach was implemented in DCB specimens made from PMMA, a model material chosen for its limited ductility (see Fig. 34.7a), structured with pillars at the interface as depicted schematically in Fig. 34.7b.

The pillar width, d , and spacing, s , of all the specimens were equal and the height of the pillars, t , was varied leading to pillars with aspect ratios (t/d) ranging from 0.5 to 9. The critical failure load of the specimens was a minimum for a pillar with an aspect ratio of 1 and then increased with increasing aspect ratio; see Fig. 34.7c. These trends were observed experimentally and were faithfully predicted by an analytical model

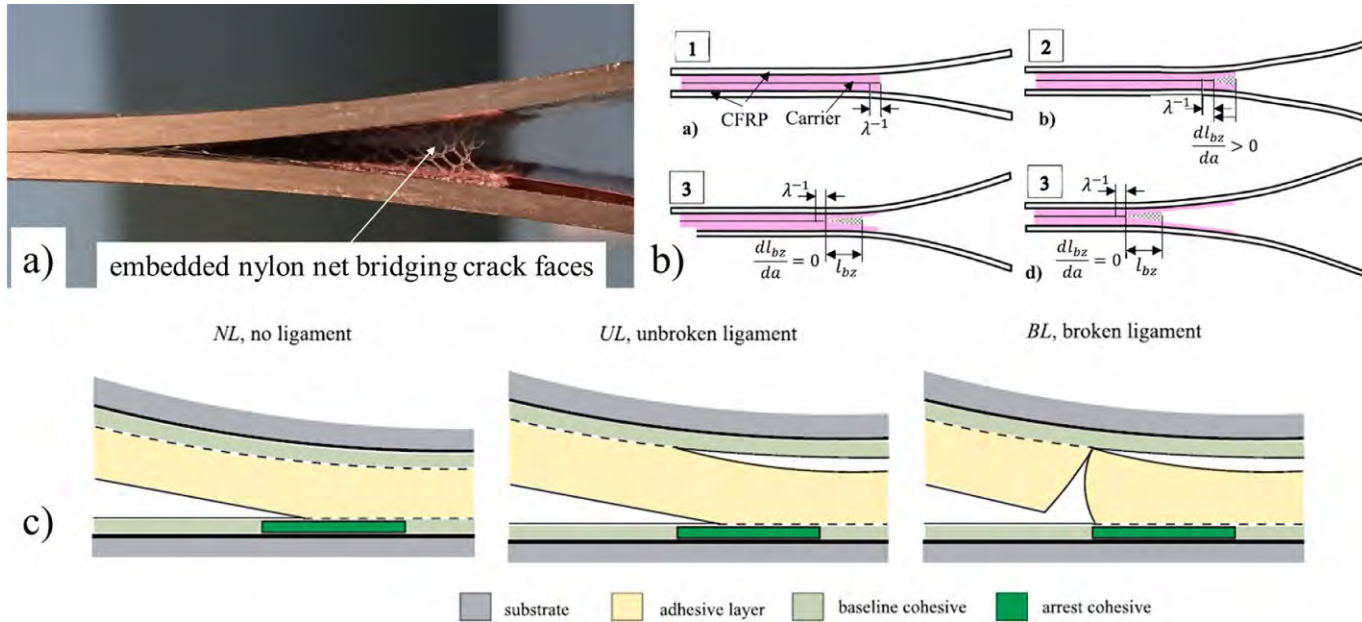


Fig. 34.6 Two realizations of toughening through intentional bridging phenomena. (a) Bridging of crack faces through an embedded nylon net with (b) showing the mechanism of fracture process [22]. (c) The mechanism of bridging with the adhesive triggered by designed surface patterning [23].

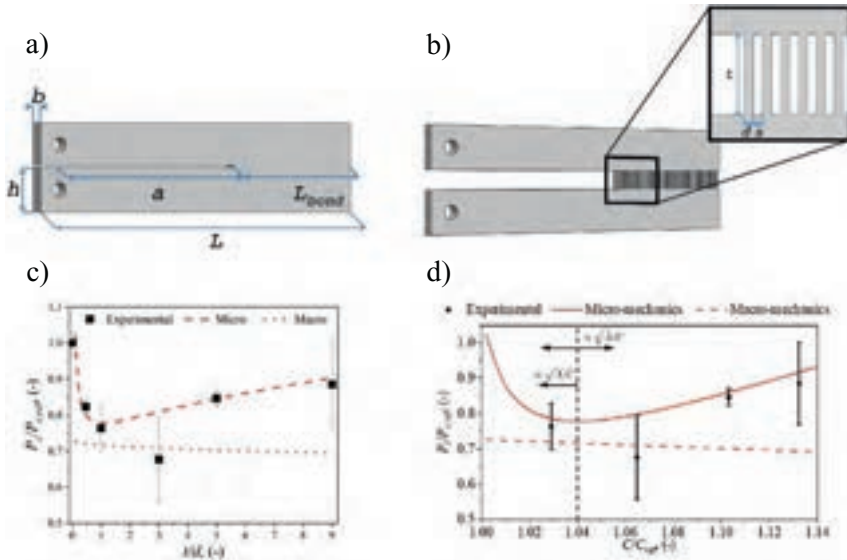


Fig. 34.7 Schematic representation of the DCB specimen with: (a) homogeneous bondline of length L_{bond} —the reference configuration, and (b) structured with pillar interface. The details of the architected region are given in the inset. (c) The critical fracture force (normalized with the fracture force of the homogeneous bondline) as a function of the pillar aspect ratio t/d in the architected region. (d) The normalized fracture force plotted against the normalized specimen compliance. In (c) and (d), model predictions are shown for a “micro” model that predicts failure by considering the failure of a single pillar and a “macro” model that homogenizes the array as a layer of reduced compliance. Only the micro model predicts the experimentally observed behavior.

Based on S. Heide-Jørgensen, M.K. Budzik, K.T. Turner, Mechanics and fracture of structured pillar interfaces, *J. Mech. Phys. Solids* 137 (2020) 103825.

that combines an elastic foundation and local pillar failure models (i.e., the micro model). The correct behavior was captured by the micromechanics-based theoretical model accounting for pillar geometry while the macroscopic model, based on homogenized properties, and the Winkler foundation model did not match the experimental results. This result shows that brittle adhesives can be toughened using architecture that locally adds compliance; see Fig. 34.7d.

As the pillar interface is not expected to yield optimal properties for all possible loading directions nor specific failure loads or stiffness, the basic concept can be further exploited. An example of using MM as interfaces was recently reported [25]. MMs are gaining significant attention from both the scientific and industrial communities as an attempt toward rational use of resources, leading to materials with tuned and carefully designed properties obtained by geometrical manipulations of the structure. In the work of Athanasiadis et al. [25], interfaces based on the three different unit cells—pillar, triangular, and hexagonal—were investigated theoretically and numerically; all are depicted in Fig. 34.8a. Using different geometries of the unit cell leads to

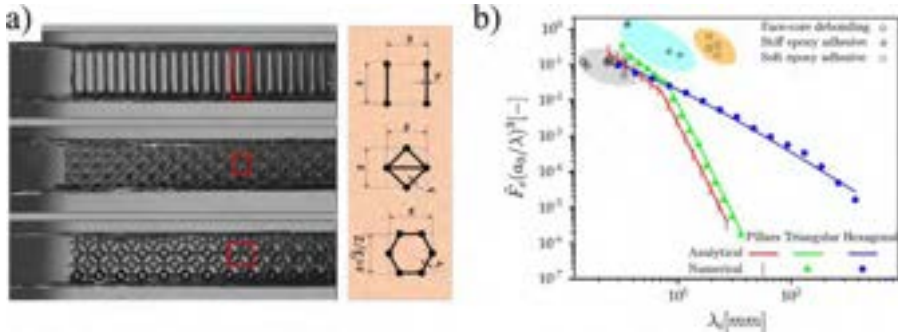


Fig. 34.8 (a) Concept of the metamaterial-based interfaces [25] yielding a range of process zone sizes λ_i and leading to a large spectrum of failure loads (b) through manipulating the geometry and size of the unit cell. The typical values used in homogenous systems are also included for reference.

different sizes of the fracture process zone, λ_i (i standing here for one of the three unit cells), and interface compliances. Noteworthy, λ is a constant for specific joint geometries with homogeneous bondlines. In the case of MM interfaces, it was shown that a full spectrum of λ can be generated by changing the type and dimensions of the unit cell. This in turn results in the range of critical fracture forces; see Fig. 34.8b. Such results open a new design approach in which the bondline will not only join two materials, but can be manipulated to give specific properties, responses under load, or failure modes.

34.3.4 Designing adherend geometry to control fracture toughness of joints

Another way of taking advantage of geometry is to exploit it in the design of the adherends. The adherends do not need to have uniform properties, for example the cross-sectional area and/or moment of inertia may vary along the length. The varying cross-sectional area and the second moment of the area introduce variations of the crack tip stress fields, such as extending or reducing the size of the process zone. Such observations were made by Kendall [26] and recently exploited for structural bonding [27]. In the latter study, the DCB specimen was used to evaluate the fracture properties of specimens with different adherend geometries. Contrary to homogenous adherends, the ones used in this study contained bio-inspired voids, circles, and squares with a characteristic dimension d , separated by distance l ; see Fig. 34.9a. Depending on the size of the voids and the distance between them, a significant improvement of fracture toughness was achieved. This is shown in Fig. 34.9b, with the inset showing the increase in the work of separation (WOS) as a function of the shape of the void for set values of d and l .

The adherend geometry can be also used to alter the crack front locus, deflecting the crack from the initial path and changing the local stress components; see Section 34.2.1. The concept of a rectangular zig-zag interface achieved by adherend

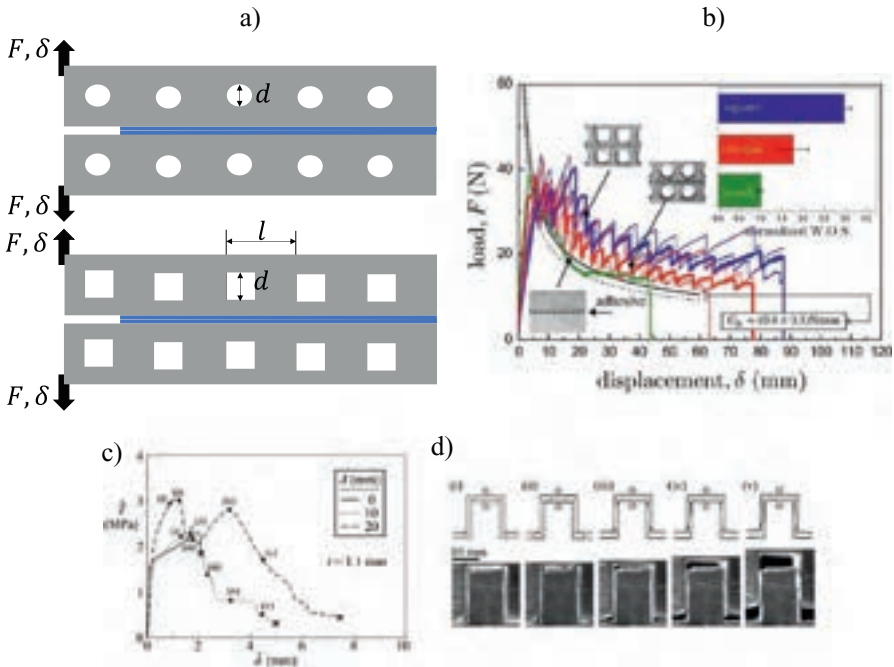


Fig. 34.9 Bio-inspired design of adhesive joint fracture through structuring of the adherends [23]: (a) adherend geometries explored, and (b) the resulting force-displacement curves indicating the increase of fracture toughness for specimens with structured adherends. Using adherends to deflect the crack and change local stress components [21]: (c) the average stress vs. displacement curves showing increase of failure loads and work of separation of structured specimens, and (d) the geometry and stages of failure of the joint.

design was exploited by Maloney and Fleck [21]. In Fig. 34.9c, the averaged stress \hat{T} is reported as a function of applied displacement $\hat{\delta}$. A significant increase in both the maximum stress and the WOS ($\approx \int \hat{T} d\hat{\delta}$) while increasing the adherend overlap distance A is manifested. The geometry relies on converting the globally applied tensile loading into a local stress state at the interface that is mixed mode (mode I and II). Fig. 34.9d shows different stages of joint failure, which are also indicated in Fig. 34.9c. It is observed that after the creation of mode I driven cavities near corners (stage (i) and (ii)), mode I propagation occurs (iii); however, the joint maintains integrity due to the transfer of part of the loading to shear stresses. Eventually, a mode II crack initiates (iv) and propagates (v) until the load-carrying capacity is fully lost.

34.3.5 Elastic toughening

Elastic heterogeneity along the crack path can be exploited for interface toughening as well. Kendall [26] investigated the peeling of a rubber strip with varying bending rigidity in the peeling direction, as shown in Fig. 34.10a.

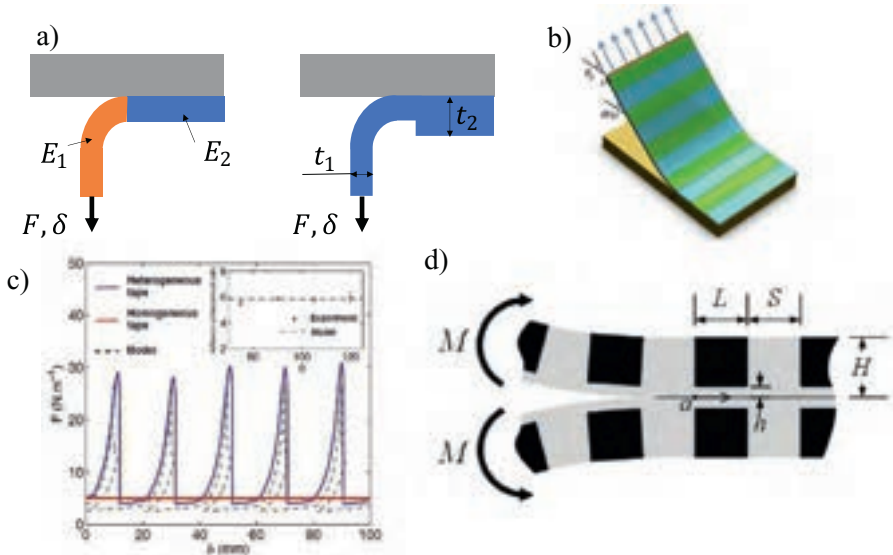


Fig. 34.10 Use of elastic toughening principles. (a) Two systems initially investigated by Kendall [26], that is, variation of peeling arm rigidity due to variable modulus and thickness. (b) Materials with periodic stiffness proposed by Xia et al. [28] (c) Effect of varying stiffness on measured peel force compared with the homogeneous stiffness material indicating significant increase of the peeling force despite the same interfacial adhesion properties [28]. (d) A DCB specimen made of material of varying modulus and thickness as analyzed by Luo and Turner [29].

Kendall found that the crack accelerated when going from a region of high stiffness to a region of low stiffness and slowed when moving from a region of low stiffness to a region of high stiffness. The regions of varying stiffness had a larger peel force than the homogenous case. Xia et al. [28] examined a similar problem of the peeling of a strip with periodic heterogeneity and showed that the peel force increased with local bending rigidity; for example, a factor of eight increase in bending rigidity led to an eight times increase in peel force. Recently, Luo and Turner [29] examined the fracture of DCB specimens with subsurface elastic heterogeneity and demonstrated that similar increases in failure load with increased bending rigidity can be achieved in these geometries, but that the stiff regions must be sufficiently long for the full potential to be realized.

34.3.6 Dissipative extra layer

In the case in which intrinsic toughening contribution due to plastic dissipation cannot be fully activated, for instance due to the need to use a very stiff specific adhesive with limited plastic dissipation, there is the option to include additional dissipative material layer(s). At least two options have been pursued in the literature, as shown in Fig. 34.11. The first working principle, illustrated in Fig. 34.11a, is simply to intercalate one layer in the stack of adherend and adhesive. When the crack runs in the adhesive sufficiently

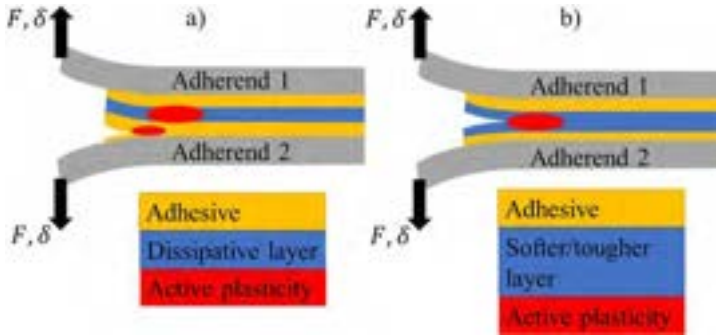


Fig. 34.11 Two working principles involving a dissipative interlayer (a) producing extra plastic dissipation while cracking remains inside the adhesive (cohesive, cohesive near the interface, of adhesive), (b) with the crack forced to propagate inside the extra layer being softer than the adhesive.

close to the extra layer, plasticity is induced owing to the large stress carried by the crack and leading to an extrinsic contribution. The second working principle (Fig. 34.11b) is to modify the adhesive layer to favor the presence of a softer but tougher layer that can trap the crack and dissipate more energy. In both cases, the extra layer must be compatible and show good adhesion with the adhesive to avoid premature interface decohesion. These two toughening ways are explained below.

(i) The toughening potential resulting from the introduction of an extra dissipative layer has been recently addressed using the model described in Fig. 34.12a. This is a small-scale yielding model in which the “thin layer” must be seen as the adhesive with thickness h_t [30]. Here, there is no adhesive layer on the other side of the dissipative layer such as in Fig. 34.11a, but the results should essentially be similar. The K field is applied far away from the crack tip region. In this work, the crack was forced to run at the interface between one adherend and the adhesive (adhesive cracking) but the results would not qualitatively change with a cohesive crack within the adhesive layer (= thin layer). The failure process is described by a traction separation law, as shown in Fig. 34.12b, with fracture energy Γ_0 and peak stress σ_c . One set of results considering an elastoplastic interlayer is shown in Fig. 34.12c in terms of the variation of the steady-state toughness Γ_{ss} normalized by Γ_0 as a function of the adhesive bond thickness normalized by the small-scale yielding estimate of the plastic zone size in the absence of interlayer R_0 . A very significant effect is observed when h_t/R_0 is small enough compared to the single layer/adhesive system. This analysis has been validated with experiments.

It is interesting to note in Fig. 34.12c that significant toughening is observed with a purely elastic interlayer as well. The reason is explained in Depinoy et al. [30] and results from additional plasticity in the adhesive layer due to extra bending associated with the deformation of the elastic interlayer. This can be considered another toughening principle associated with the flexible/compliant elastic interlayer.

This idea of introducing a dissipative interlayer has already been documented before, although not directly in the context of adhesive bonding [31,32]. The work

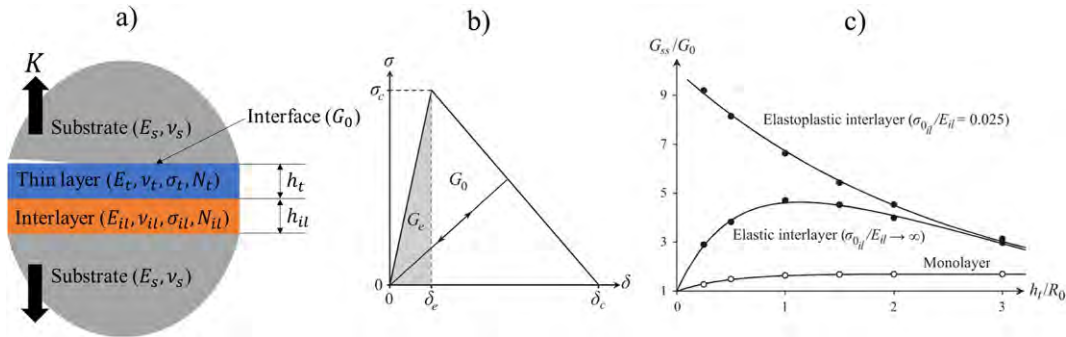


Fig. 34.12 The dissipative interlayer concept addressed by a small-scale yielding model with failure process (a) represented through a traction-separation law to provide results regarding increasing the steady-state fracture toughness (b). (c) Variation of the overall interface toughness for the three investigated cases: monolayer alone, elastic interlayer, and plastic interlayer (R_0 is a reference length corresponding to an estimate of the plastic zone size inside the thin layer).

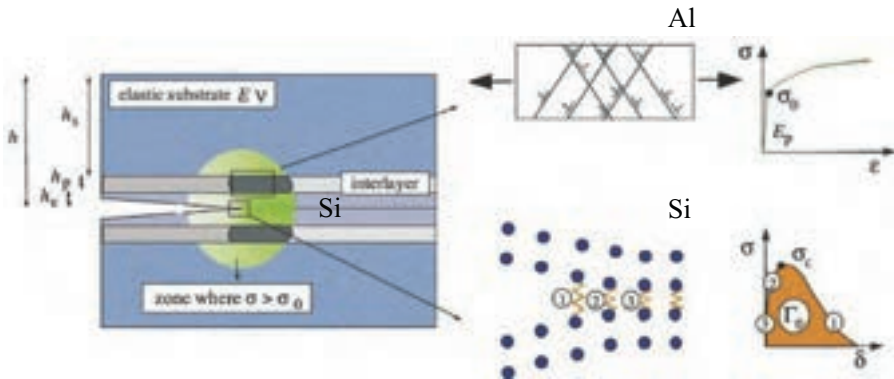


Fig. 34.13 Idea of interface toughening of silicon wafer bonding (Bertholet et al. [32]). Silicon (Si) wafers are typically bonded by molecular adhesion between the Si oxide surface layers. The idea was to introduce aluminum (Al) thin dissipative layers intercalated between Si and the Si oxide.

by Bertholet et al. [32] was on silicon wafer bonding. Silicon (Si) wafers are typically bonded by molecular adhesion between the Si oxide surface layers; see Fig. 34.13. The idea was to introduce aluminum (Al) thin dissipative layers intercalated between Si and the Si oxide. Very significant toughening was observed, with an increase of a factor between 2 and 5 due to the plasticity in the Al, as demonstrated experimentally and captured by a cohesive zone-based model. Wei and Hutchinson [31] previously addressed a similar problem from a purely computational viewpoint in the case of a thick dissipative interlayer with similar findings.

- (ii) The second option is the introduction of a softer but tougher layer with the crack forced to propagate into the soft layer, as shown in Fig. 34.11b. Even though the layer is tougher, the fact that it is softer leads to a crack trapping effect upon loading. The challenge is to experimentally realize such systems. One option has been recently proposed by Voleppe et al. [33] in which the interlayer is made of thermoplastic PEI, which can be cocured with a thermoset polymer. This research was made in the context of direct epoxy-based composite bonding through a thermoplastic layer. The cocuring process leads to interdiffusion and the creation of a graded layer. The idea is that one of the regions in the gradient is softer but much tougher owing to the presence of PEI. This requires careful control of the curing process to generate the right gradient and is not easily replicated, but the idea is worth pursuing, perhaps with a simpler approach. Ultimately, one could see the perforated bond layer addressed earlier in this chapter as a variant of this idea: the perforated layer is a soft region (due to the cavities) in which the crack is trapped and in which extra toughening is provided through crack arrest and blunting.

34.4 Summary and possible future trends

Recent trends in the toughening of adhesive joints through architecture were summarized and discussed. The main issue with architecting adhesive joints is how to avoid the introduction of a new source of damage/embrittlement due to new interfaces. It is

important to appreciate, as shown in the examples treated in this chapter, that fracture toughness includes a length scale and that dissipation will be significant if the volume under consideration is large enough. In other words, architected joints will reach full potential only if they are sufficiently thick. This may lead to important trade-offs concerning property optimization. For instance, for some architectures, the shear stiffness and strength of the joint may decrease significantly, and may impact other structural design constraints. There is thus a need to integrate this joint architecting approach into a wider vision of joint design, including opportunities to make the joints multifunctional.

References

- [1] A.J. Kinloch, J.H. Lee, A.C. Taylor, S. Sprenger, C. Eger, D. Egan, Toughening structural adhesives via nano-and micro-phase inclusions, *J. Adhes.* 79 (8–9) (2003) 867–873.
- [2] L. Daelemans, S. van der Heijden, I. De Baere, H. Rahier, W. Van Paepegem, K. De Clerck, Damage-resistant composites using electrospun nanofibers: a multiscale analysis of the toughening mechanisms, *ACS Appl. Mater. Interfaces* 8 (18) (2016) 11806–11818.
- [3] H. Ming-Yuan, J.W. Hutchinson, Crack deflection at an interface between dissimilar elastic materials, *Int. J. Solids Struct.* 25 (9) (1989) 1053–1067.
- [4] H.M. Jensen, Mixed mode interface fracture criteria, *Acta Metall. Mater.* 38 (12) (1990) 2637–2644.
- [5] J.P. Parmigiani, M.D. Thouless, The roles of toughness and cohesive strength on crack deflection at interfaces, *J. Mech. Phys. Solids* 54 (2) (2006) 266–287.
- [6] F.A. Cordisco, P.D. Zavattieri, L.G. Hector Jr., B.E. Carlson, Mode I fracture along adhesively bonded sinusoidal interfaces, *Int. J. Solids Struct.* 83 (2016) 45–64.
- [7] D. Martinez, V. Gupta, Energy criterion for crack deflection at an interface between two orthotropic media, *J. Mech. Phys. Solids* 42 (8) (1994) 1247–1271.
- [8] E. Martin, D. Leguillon, C. Lacroix, A revisited criterion for crack deflection at an interface in a brittle bimaterial, *Compos. Sci. Technol.* 61 (12) (2001) 1671–1679.
- [9] M. Alam, J.P. Parmigiani, J.J. Kruzic, An experimental assessment of methods to predict crack deflection at an interface, *Eng. Fract. Mech.* 181 (2017) 116–129.
- [10] T. Ikeda, A. Yamashita, D. Lee, N. Miyazaki, Failure of a ductile adhesive layer constrained by hard adherends, *J. Eng. Mater. Technol.* 122 (1) (2000) 80–85.
- [11] K.M. Liechti, E.C. Hanson, Nonlinear effects in mixed-mode interfacial delaminations, *Int. J. Fract.* 36 (3) (1988) 199–217.
- [12] S.R. Ranade, Y. Guan, R.B. Moore, J.G. Dillard, R.C. Batra, D.A. Dillard, Characterizing fracture performance and the interaction of propagating cracks with locally weakened interfaces in adhesive joints, *Int. J. Adhes. Adhes.* 82 (2018) 196–205.
- [13] C. Cuminatto, G. Parry, M. Braccini, A model for patterned interfaces debonding—application to adhesion tests, *Int. J. Solids Struct.* 75 (2015) 122–133.
- [14] S. Heide-Jørgensen, M.K. Budzik, Effects of bondline discontinuity during growth of interface cracks including stability and kinetic considerations, *J. Mech. Phys. Solids* 117 (2018) 1–21.
- [15] A. Pascuzzo, A. Yudhanto, M. Alfano, G. Lubineau, On the effect of interfacial patterns on energy dissipation in plastically deforming adhesive bonded ductile sheets, *Int. J. Solids Struct.* 198 (2020) 31–40.
- [16] C.H. Wang, L.R.F. Rose, A crack bridging model for bonded plates subjected to tension and bending, *Int. J. Solids Struct.* 36 (13) (1999) 1985–2014.

- [17] M. Perelmuter, Analysis of interaction of bridged cracks and weak interfaces, *Int. J. Mech. Sci.* 149 (2018) 349–360.
- [18] S. Kumar, B.L. Wardle, M.F. Arif, J. Ubaid, Stress reduction of 3D printed compliance-tailored multilayers, *Adv. Eng. Mater.* 20 (1) (2018) 1700883.
- [19] A. Hillerborg, M. Modéer, P.E. Petersson, Analysis of crack formation and crack growth in concrete by means of fracture mechanics and finite elements, *Cem. Concr. Res.* 6 (6) (1976) 773–781.
- [20] R.B. Sills, M.D. Thouless, Cohesive-length scales for damage and toughening mechanisms, *Int. J. Solids Struct.* 55 (2015) 32–43.
- [21] K. Maloney, N. Fleck, Toughening strategies in adhesive joints, *Int. J. Solids Struct.* 158 (2019) 66–75.
- [22] S. Heide-Jørgensen, S.T. de Freitas, M.K. Budzik, On the fracture behaviour of CFRP bonded joints under mode I loading: effect of supporting carrier and interface contamination, *Compos. Sci. Technol.* 160 (2018) 97–110.
- [23] R. Tao, X. Li, A. Yudhanto, M. Alfano, G. Lubineau, On controlling interfacial heterogeneity to trigger bridging in secondary bonded composite joints: an efficient strategy to introduce crack-arrest features, *Compos. Sci. Technol.* 188 (2020), 107964.
- [24] S. Heide-Jørgensen, M.K. Budzik, K.T. Turner, Mechanics and fracture of structured pillar interfaces, *J. Mech. Phys. Solids* 137 (2020), 103825.
- [25] A.E. Athanasiadis, M.A. Dias, M.K. Budzik, Can confined mechanical metamaterials replace adhesives? *Extreme Mech. Lett.* 48 (2021), 101411.
- [26] K. Kendall, Control of cracks by interfaces in composites, *Proc. R. Soc. Lond. A Math. Phys. Sci.* 341 (1627) (1975) 409–428.
- [27] A. Wagih, R. Tao, G. Lubineau, Bio-inspired adhesive joint with improved interlaminar fracture toughness, *Compos. A: Appl. Sci. Manuf.* 149 (2021), 106530.
- [28] S. Xia, L. Ponson, G. Ravichandran, K. Bhattacharya, Toughening and asymmetry in peeling of heterogeneous adhesives, *Phys. Rev. Lett.* 108 (19) (2012), 196101.
- [29] A. Luo, K.T. Turner, Adhesion of beams with subsurface elastic heterogeneity, *J. Mech. Phys. Solids* 159 (2022), 104713.
- [30] S. Depinoy, F. Strepenné, T.J. Massart, S. Godet, T. Pardoen, Interface toughening in multilayered systems through compliant dissipative interlayers, *J. Mech. Phys. Solids* 130 (2019) 1–20.
- [31] Y. Wei, J.W. Hutchinson, Models of interface separation accompanied by plastic dissipation at multiple scales, *Int. J. Fract.* 95 (1) (1999) 1–17.
- [32] Y. Bertholet, B. Olbrechts, B. Lejeune, J.P. Raskin, T. Pardoen, Molecular bonding aided by dissipative inter-layers, *Acta Mater.* 55 (2) (2007) 473–479.
- [33] Q. Voleppe, W. Ballout, P. Van Velthem, C. Bailly, T. Pardoen, Enhanced fracture resistance of thermoset/thermoplastic interfaces through crack trapping in a morphology gradient, *Polymer* 218 (2021), 123497.

Sensing stresses and damage in adhesive bonds using mechanophores

35

Jared A. Gohl, Nazmul Haque, and Chelsea S. Davis

School of Materials Engineering, Purdue University, West Lafayette, IN, United States

35.1 Introduction

As you return home from a day in the lab where every experiment worked exactly as planned (a fantasy, one would presume), you pull into your driveway and are greeted with a piercing shriek coming from your car. “Great. It’s time for new brakes,” you say to yourself sarcastically. You know that the engineers who designed your brake pads embedded little metal strips as wear indicators so that you can replace the pads before you have a catastrophic failure and crash the car. A wear indicator that signals that failure is imminent is a rare and difficult thing to engineer. In the context of structural adhesives, such a sensor or structural health monitoring system is even more complicated. Although progress has been made in the use of nondestructive inspection methods to assess defects and damage, traditional evaluation of adhesive systems often requires destructive testing, eliminating the opportunity to indicate performance degradation or failure onset prior to catastrophic failure. Some of the more common methods of performing nondestructive evaluation are explored in recent literature reviews and reference texts [1–4].

As the world continues to pursue sustainability in all aspects of life, advanced lightweight materials such as polymer composites and bonded composite joints become increasingly crucial to reaching these goals. However, these materials have a limited lifetime that is not completely understood. Fatigue failure of composite materials occurs as the adhesion between the polymer matrix and reinforcement material fails. For structurally bonded joints, failure can occur in several ways, enumerated in detail throughout this text (see [Chapter 19](#) for adhesive bond fatigue failure and prediction). When these materials are used as structural components in applications such as automobiles and wind turbines, catastrophic failure presents significant risk to life and property. Damage can accumulate within the adhesive joint throughout the life of the product yet remain internal and hidden from view. Due to the present lack of health monitoring systems for these structural adhesives, a safety factor is often applied that requires premature retirement of undamaged materials, leading to significant waste. However, recent advances in machine learning methods are being applied toward the structural health monitoring of adhesive joints (see [Chapter 28](#)). By combining the in situ information obtained through the activation of mechanophores described in this

chapter with machine learning efforts, more comprehensive datasets of stress fields in loaded joints can be generated to further refine these models. Advanced composite materials require a better understanding of stresses between the reinforcement material and the adhesive matrix as well as stresses developed in structural adhesive joints between composite parts.

One proposed solution to structural health monitoring within these various adhesive systems are mechanophores (MPs), the focus of this chapter. Mechanophores are stimuli-responsive materials that act as “molecular force probes,” sensitive to forces on the level of piconewtons. These molecules undergo a structural change upon the application of force, resulting in a detectable signal that can locally measure forces. Embedding these materials into adhesives could provide an indication of where stress is being concentrated and eventually be used to anticipate catastrophic failure. Mechanophores are an emerging technology and a long way from industrial implementation. However, as a nondestructive evaluation tool, MPs show great promise for use in research labs as a tool to aid the research and development process.

35.2 Introduction to mechanoresponsive materials

Current techniques for measuring deformation within adhesive joints include the use of embedded piezoelectric devices, photoelasticity, digital image correlation (DIC), ultrasound imaging, and observations of stress whitening. These techniques provide insight into the “ensemble” response of the polymer system but can potentially lead to incomplete pictures. DIC methods track changes in the external shape of a loaded specimen while piezoelectric sensors can provide localized strain measurements. Importantly, one must interpolate these surface or local strain observations to get a comprehensive understanding of how the joint is deforming. Photoelasticity relies on localized polymer chain alignment to provide stress gradients but is not feasible for all material systems (opaque, amorphous, networked, etc.). Further, as a transmission-based technique, it can be difficult to measure stress fields in three dimensions. Stress whitening and ultrasound imaging tend to provide a more global response of the deformation within the system. Mechanophores are a promising technology because they allow a highly localized measurement of the stresses within a polymer system, described in more detail below.

Mechanoresponsive materials undergo a molecular rearrangement or structural change upon the application of an external mechanical force, resulting in a change in the optical, electrical, or catalytic properties [5–7]. Mechanochemistry, the field studying mechanoresponsive materials and mechanophores, originated from the observation of a reduction in polymer molecular weight as polystyrene was processed [8]. Staudinger found that mechanically masticating polystyrene decreased the molecular weight of the polymers. While the average molecular weight of the polymers continued to decrease as the material was processed, the location of the polymer chain scission was unpredictable and occurred stochastically. This was one of the first reported observations of molecular bonds breaking through bulk mechanical damage.

Mechanoresponsive materials leverage intentionally weak or highly strained bonds within the system to provide a predictable failure point when the material is

mechanically loaded. As taught in introductory organic chemistry courses, unstrained carbon-carbon bonds are quite strong due to carbon containing four valence electrons. If heteroatoms such as oxygen or nitrogen are introduced into the polymer backbone, the failure point of the polymer chains becomes more predictable due to these “weaker” bonds in the system. Another example of a predictable failure point lies in cyclized carbon in three or four member rings that changes the bonding angle from 109.5° to 60° or 90° , respectively. This deviation from the equilibrium bond angle is energetically unfavorable, making the carbon-carbon bond more susceptible to breakage to reduce ring strain.

A significant advancement in the field of mechanoresponsive materials occurred when the researchers at the University of Illinois exploited this predictable bond breakage to develop advantageous chemistry [9]. They were the first to intentionally introduce a functional group within a polymer chain to induce selective, localized breakage. When broken, the azo moiety introduced into a polyethylene glycol (PEG) chain was capable of producing two PEG chains with almost identical mass. The newly produced polymer chains also had radical species at the ruptured ends, capable of further reactions. The term “mechanophore” was coined by Caster at the Army Research Office upon discussion of this work [7]. A recent review article from the Davis group shows graphical representations of common mechanophore activation mechanisms, highlighted in Fig. 35.1 [5].

One of the first “useful” mechanophores in the context of structural adhesives was spiropyran. Potisek et al. utilized a fluorescent molecule that was capable of isomerizing between a fluorescently inactive “closed” state and a fluorescently active “open” state and attached chemical tethers to either side of the labile bond [10]. By embedding this spiropyran mechanophore into a polymethylacrylate matrix and applying an external force, the samples changed color as a result of a mechanochromic change [10,11].

Early research on mechanochemistry mainly focused on understanding the mechanochemical degradation of polymers. However, over the past few years, this focus has shifted toward gathering information from mechanochemical responses without irreversibly deforming the polymer system [7]. The Craig group at Duke University completed many experiments quantifying the kinetics of mechanophore activation, shaping the field in the process. They studied the effects of loading pathways, concentration, temperature, and relaxation time on MP activation [12]. Since the pioneering work by Moore, White, and Sottos, the number and type of mechanophores reported in the literature continue to grow rapidly. A review article from 2021 reported more than 20 different types of mechanophores currently being studied [13].

35.3 Mechanochemistry for sensing stress in bulk adhesives

Mechanophores can be utilized to directly visualize stresses in polymeric materials (Fig. 35.2). By incorporating MPs into the polymer network of a structural adhesive such as a thermoset epoxy, local stress concentrations can be highlighted through MP activation. Depending on the molecule selected, the activation can be observed only

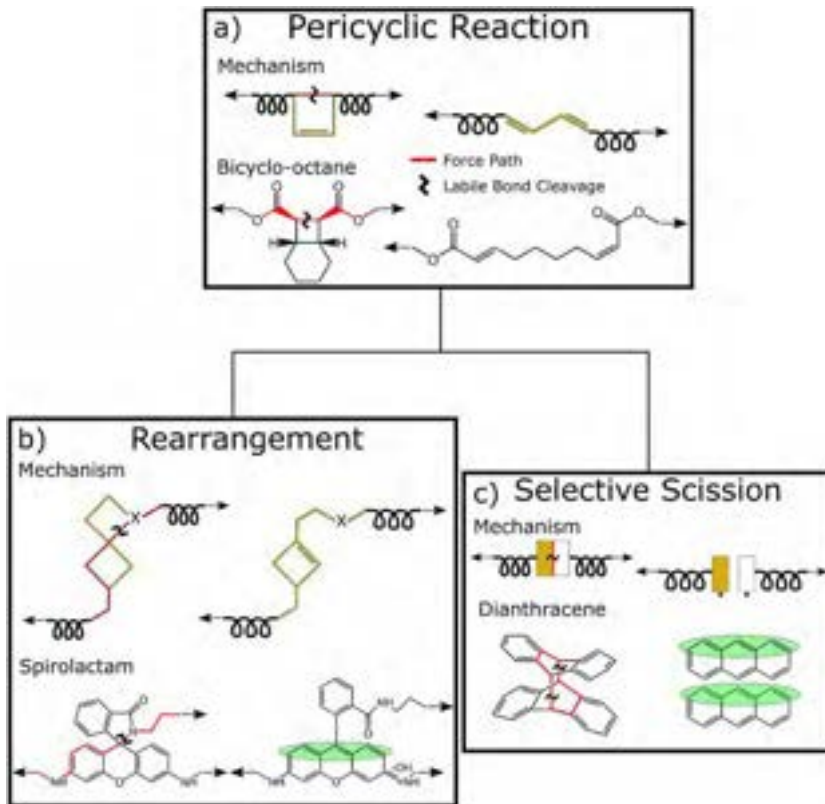


Fig. 35.1 Illustrated representation of various activation mechanisms of mechanophores indicating the transformation from an unactivated to an activated state: (a) highlights the cycloreversion mechanism; (b) shows the isomerization in spirolactam activation; and (c) indicates selective bond scission in dimeric anthracene [5].

Reproduced with permission from N. Deneke, M.L. Rencheck, C.S. Davis, An engineer's introduction to mechanophores, *Soft Matter* 16 (2020) 6230–6252, <https://doi.org/10.1039/d0sm00465k>.

while the structural adhesive joint is being loaded (Fig. 35.2c) [12] or can be persistent, observable long after the mechanical stimulus has been removed (Fig. 35.2d) [14].

The incorporation of mechanophores into bulk polymers allows for the visualization of internal damage of the adhesives. Weaker mechanophores such as spiropyran can be used to detect stress concentrations within the adhesive before significant damage has occurred [12] while stronger mechanophores such as anthracene-based Diels-Alder adducts will only activate once significant amounts of damage to the polymer network have occurred [15,16]. This range of activation thresholds allows both mechanophores to have unique use cases and provide details about the adhesive system.

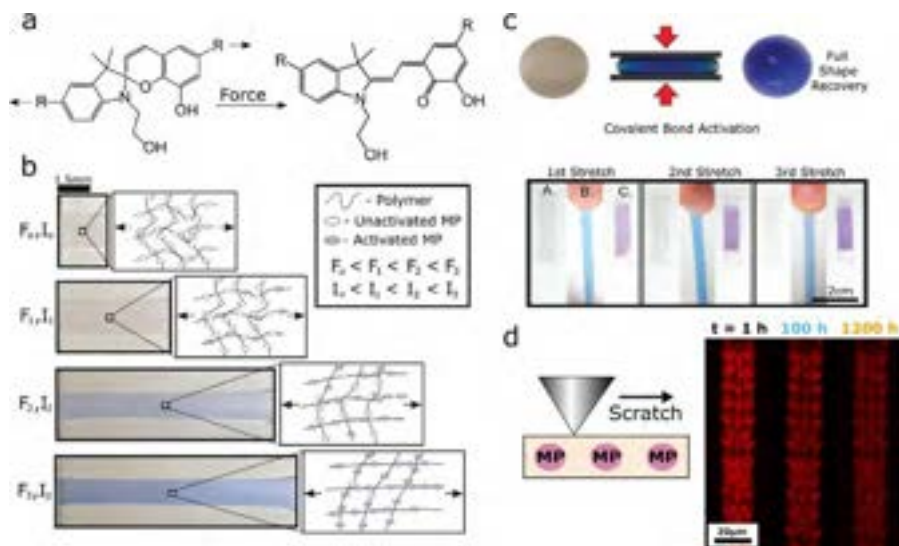


Fig. 35.2 Mechanoresponsive stress sensing in bulk polymer networks: (a) molecular structure highlighting the activation mechanism of spiropyran into merocyanine via isomerization; (b) the color of spiropyran in silicone changes with progressive strain steps [11]; (c) repeatable stretching and relaxation show cyclic spiropyran activation in bulk silicone [12]; and (d) instrumented scratching of bulk spiro-lactam-containing epoxy induces persistent fluorescence activation that lasts more than 50 days [14].

(b) Reproduced with permission from N. Deneke, M.L. Rencheck, C.S. Davis, An engineer's introduction to mechanophores, *Soft Matter* 16 (2020) 6230–6252, <https://doi.org/10.1039/d0sm00465k>, the Royal Society of Chemistry. (c) Modified from G.R. Gossweiler, G.B. Hewage, G. Soriano, Q. Wang, G.W. Welshofer, X. Zhao, S.L. Craig, Mechanochemical activation of covalent bonds in polymers with full and repeatable macroscopic shape recovery, *ACS Macro Lett.* 3 (2014) 216–219, <https://doi.org/10.1021/MZ500031Q>. (d) Modified from C.S. Davis, M.L. Rencheck, J.W. Woodcock, R. Beams, M. Wang, S. Stranick, A.M. Forster, J.W. Gilman, Activation of mechanophores in a thermoset matrix by instrumented scratch, *ACS Appl. Mater. Interfaces* 13 (2021) 55498–55506, <https://doi.org/10.1021/ACSAMI.1C15004>.

It should be noted here that mechanophores are force sensors. They are activated once a threshold stress is reached locally within the MP-functionalized polymer matrix. At small strains, most polymers, including epoxies commonly employed as structural adhesives, behave in a linear elastic manner. Thus, the temptation to use MPs as strain sensors or to think of them as such can be great. However, at large deformations or in the case of high stress localizations within a bonded joint, MPs provide a visual indication of the extent of the three-dimensional stress state in the loaded material. Local strain measurements such as differential image correlation (DIC) or embedded strain gauges such as fiberoptic Bragg gratings have the potential to be used in concert with mechanophores to provide a more comprehensive measurement of the deformation behavior.

35.3.1 *Mechanophores as research, development, and qualification tools*

Mechanophores that undergo scission activation or have a very high energy difference between the activated and inactive states are essentially irreversible, conducive for use as permanent damage sensors. Such “persistent” activation can be particularly useful for stiffer samples that are prone to forming microcracks and voids before catastrophic failure. Due to the angstrom scale displacements required to activate mechanophores in glassy polymer networks, the optical resolution limits of light-based microscopy tools can be circumvented. While optical microscopes are unable to resolve submicron cracks, they can detect the fluorescence resulting from mechanophore activation around nanoscale cracks within an adhesive.

Unlike the reversible mechanophore that loses color when the mechanical stimulus is removed, the fluorescence response of permanent damage sensors can be directly caused by bond scission [17]. Chen et al. showed how the mechanically induced bond scission in dioxetane caused an instantaneous visible light emission in both bulk polymers and polymer solutions [18]. This response was attributed to the difference in energy states of the two “halves” of the mechanophore after bond breaking. Another study with the same dioxetane mechanophore exhibited a mechanoresponse in a thermoplastic elastomer system that was localized at the point in the sample where fracture occurred [19]. Another example of a virtually irreversible mechanophore is the mechanically driven cycloreversion of anthracene-maleimide adduct, demonstrated via sonication [20]. In this system, fluorescence spectroscopy can be utilized to monitor the formation of cracks that were “detected” by the anthracene derivatives [21].

Epoxy-based thermosets are some of the most common polymers used for composite materials and structural adhesives, making them a good target system for implementing irreversible mechanophores. Davis et al. used a spirolactam mechanophore embedded into an epoxy network to visualize surface damage through scratching (Fig. 35.2d) [14]. The spirolactam mechanophore used in this study was synthesized from Rhodamine 110 as a synthetic precursor with only minor modification, making it one of the simplest mechanophores to synthesize to date. Using a nanoindenter to apply a scratch to the surface of the epoxy as well as fluorescence microscopy, the fluorescence intensity of the mechanophore was measured immediately after damage as well as 50 days later; the damage could still be detected with only a 50% decrease in intensity. The ability of the spirolactam/epoxy mechanophore system to detect surface scratches over an extended period of time demonstrates the potential for mechanophore utilization for the structural health monitoring of epoxy [22].

Embedding a chemiluminescent MP into a hydrogel elastomer, Ducrot et al. visually demonstrated the localization of stresses at a crack tip in a fracture event along with MP activation in the plastic zone ahead of the crack [22]. The mechanophore used in this study, bis(adamanty)l-1,2-dioxetane (BADOBA), releases a photon upon rupture. By incorporating these mechanophores into single, double, and triple network hydrogels, stress concentrations in front of the crack tip were observed (Fig. 35.3), providing visual insights into the relationship between toughness and stress concentration. The MP intensity increases at the crack tip around the plastic deformation zone

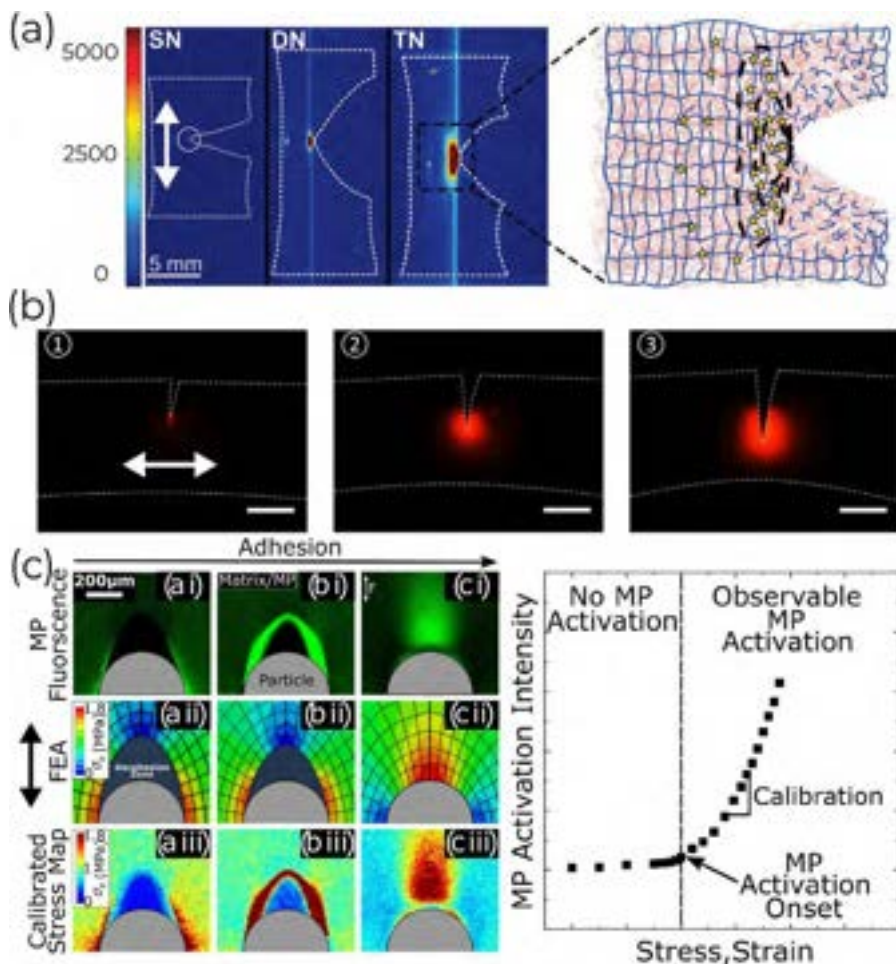


Fig. 35.3 Identifying localized stress by analyzing changes in MP activation intensity: (a) dioxetane MP bond breaking caused light emission in different networked elastomers [22]; (b) evolution of SP activation intensity in rubber toughened PMMA during single notched tensile test (2 mm scale bar) [23]; and (c) spiropyran MP activation in a glass particle-reinforced silicone matrix [24]. Tensile direction is indicated by *double-headed arrow* in each set of images.

Modified from (a) E. Ducrot, Y. Chen, M. Bulters, R.P. Sijbesma, C. Creton, Toughening elastomers with sacrificial bonds and watching them break, *Science* 344 (2014) 186–189, <https://doi.org/10.1126/science.1248494>; (b) A.D.N. Celestine, B.A. Beiermann, P.A. May, J.S. Moore, N.R. Sottos, S.R. White, Fracture-induced activation in mechanophore-linked, rubber toughened PMMA, *Polymer* 55 (1997) 4164–4171; (c) M.L. Rencheck, B.T. Mackey, Y.Y. Hu, C.C. Chang, M.D. Sangid, C.S. Davis, Identifying internal stresses during mechanophore activation, *Adv. Eng. Mater.* (2021) 2101080, <https://doi.org/10.1002/ADEM.202101080>.

as the crack propagates. By switching to a spiropyran mechanophore and performing a postmortem analysis of fractured surfaces, the stress distribution within elastomer samples was quantified, allowing for a tool to measure stress history in fractured adhesives [25].

Detailed work on understanding localized stress at the crack tip was conducted by Celestine et al. using rubber toughened PMMA [23,26]. An increase in the intensity and size of the SP activation zone along the crack path was observed during the fracture event. The size of the activated region was proportional to the size of the plastic zone, suggesting higher activation ahead of the crack tip due to increased plastic deformation [23]. Identification of the region of plastic deformation with a mechanophore led to further studies [26].

For the majority of mechanophore studies, the mechanochromic and fluorescent responses of the molecules were taken as a qualitative tool for visualizing stresses within the adhesive. To make this technology a feasible metrology for quantifying stresses, a shift must be made from qualitative visualization of stresses to quantitative correlation of fluorescence intensity to internal stresses. Utilizing a confocal microscope and a miniature load frame, Rencheck et al. obtained in situ micrographs of MP activation in a composite system, as shown in Fig. 35.3c [24]. By tailoring interfacial strength, they were able to observe both cavitation and debonding, as predicted by Gent and Park in 1984 [27].

The study was taken a step further as the simple composite was modeled using finite element analysis (FEA). By using a carefully constructed cohesive zone model (CZM) to represent the adhesion between the particle and the matrix, the model was able to replicate the failure modes observed in the tensile tests. By constructing a calibration curve of relative fluorescence intensity as a function of predicted stress from FEA, the team was able to quantify the stresses around the composite particle.

35.3.2 *Mechanophores as a tool for monitoring bulk adhesives in the field*

Mechanophores are an emerging technology. Field applications are not available at the time of publication, but their general potential can be speculated upon. The technology could adapt more mature structural health monitoring tools as a springboard toward implementation. Perhaps by combining embedded fiberoptic strain sensors with mechanophores within an adhesive joint, stresses and damage accumulation could be monitored. If the selected mechanophore undergoes a mechanochromic change, then embedding it into a transparent or translucent adhesive would allow for a qualitative damage indicator, facilitating quick inspection. Mechanophores are a natural extension of sensing technologies such as pH sensors or ion sensors. Coupling a mechanophore that releases another signal atom (i.e., mechanocatalysts) provides a convenient marker for damage within the system. As will be elaborated upon later in the chapter, mechanophores are quite difficult to utilize outside of the lab due to their sensitivity to harsh environmental conditions. However, by understanding these challenges, implementation in the field becomes one step closer.

35.4 Mechanochemistry for sensing interfacial damage

Interfacial mechanophores (iMPs) provide capabilities to measure angstrom to nanometer scale interfacial separation distances, nearly two orders of magnitude smaller than current optical capabilities. When an iMP is covalently attached to both surfaces that comprise the interface, the mechanophore can be activated upon adhesive failure. The diffraction limit of light dictates the size of interfacial separation that can be detected through traditional brightfield microscopy techniques. However, a fluorescence signal from activated mechanophores covalently bound across an interface can be observed, even if the newly separated surfaces are only angstroms apart. Fig. 35.4 highlights recent experimental efforts that have investigated the installation and subsequent activation of iMPs via various interfacial separation mechanisms.

The installation of interfacial mechanophores introduces an added layer of complexity, as they require asymmetric chemical functionality on the mechanophore, increasing the synthetic difficulty of fabricating the molecules. These dual functionalities must be surface specific, so interfacial mechanophores must be tailored to the chemistry of both sides of the interface. The first report of mechanochemical activation at a heterogeneous interface was from Li et al. in 2014 [31]. In this study, anthracene-maleimide mechanophores were placed at the interface between SiO₂ nanoparticles and poly (methyl acrylate) chains. Upon sonication of the polymer brush functionalized nanoparticles, the iMPs were activated. Since this initial work, a few studies have been published installing iMPs on silicon wafers or fiber surfaces, coating them with a polymer, and then using optical characterization methods to measure iMP activation upon interfacial separation [28–30]. Each experiment is represented in Fig. 35.4 and highlighted below.

35.4.1 Laser spallation-induced structural adhesive debonding

Anthracene interfacial mechanophores are robust damage sensors with a relatively high activation threshold [28]. Sung et al. asymmetrically functionalized these molecules with an amine group on one end and a vinyl group on the other. Reacting the vinyl group with triethoxysilane and a platinum catalyst created an iMP with silane functionality on one end that was capable of initiating polymerization. The molecules were covalently attached to silicon-based surfaces through liquid phase deposition. Epoxy resin was then added to the substrates and allowed to react with the amine groups on the unreacted side of the mechanophore, resulting in covalent attachment of the iMP between the silicon/epoxy interface. The samples were then mechanically tested using a laser spallation technique that produces uniform shock waves through the sample. Below a threshold stress, the mechanophores were not fluorescent, implying that they had not been activated. However, above this threshold stress value, the mechanophores activated as indicated by the bright fluorescence observed in the micrographs (Fig. 35.4a). Only the samples that were covalently attached to both the silicon and epoxy activated while control samples that were only physically entangled with the epoxy did not activate. By comparing covalently attached MP to physically entangled MP, this study demonstrated the necessity of covalent attachment to both surfaces to induce MP activation.

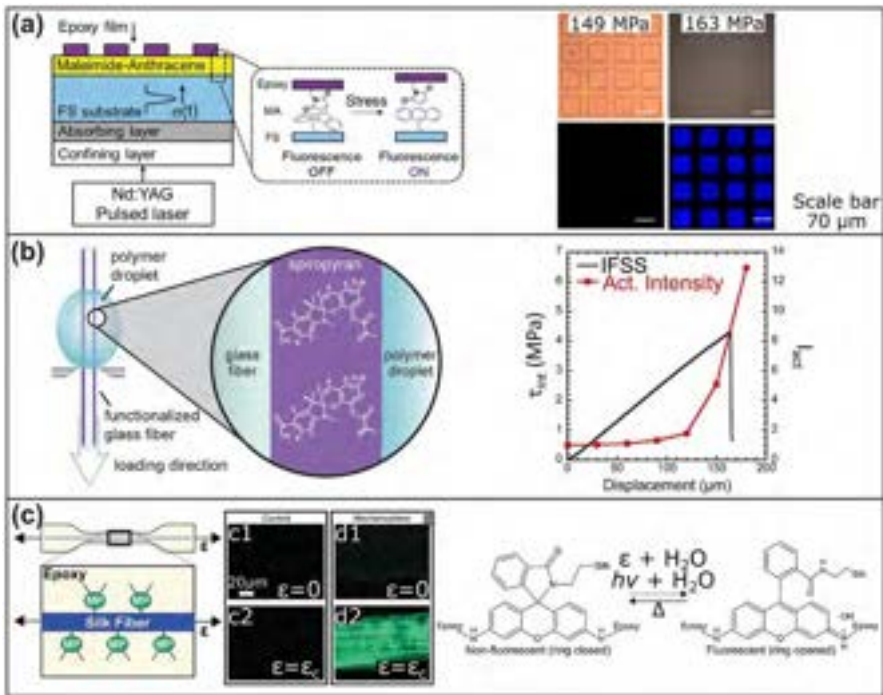


Fig. 35.4 Various experimental approaches to understand activation of interfacial mechanophores. (a) Anthracene-maleimide iMP activation at epoxy/fused SiO_2 interface via laser-induced stress waves [28]; (b) SP iMP activation during single fiber microdebond testing [29]; and (c) Spirolactam iMP at silk fiber/epoxy interface during single fiber tension [30]. Modified from (a) J. Sung, M.J. Robb, S.R. White, J.S. Moore, N.R. Sottos, Interfacial mechanophore activation using laser-induced stress waves, *J. Am. Chem. Soc.* 140 (2018) 5000–5003, <https://doi.org/10.1021/jacs.8b01427>. (b) M.E. Grady, C.M. Birrenkott, P. A. May, S.R. White, J.S. Moore, N.R. Sottos, Localization of spiropyran activation, *Langmuir* 36 (2020) 5847–5854, <https://doi.org/10.1021/acs.langmuir.0c00568>. (c) Reproduced with permission from J.W. Woodcock, R. Beams, C.S. Davis, N. Chen, S.J. Stranick, D.U. Shah, F. Vollrath, J.W. Gilman, Observation of interfacial damage in a silk-epoxy composite, using a simple mechanoresponsive fluorescent probe, *Adv. Mater. Interfaces* 4 (2017) 1601018, <https://doi.org/10.1002/admi.201601018>.

35.4.2 Single fiber microdebonding

Grady et al. utilized a similar approach to attach spiropyran to glass fibers in polymer to achieve interfacial mechanophores [29]. One end of the molecule was functionalized with a carboxylic acid and the other was functionalized with an initiator. The authors took advantage of the chemical sizing present on the “as received” commercial glass fiber that could react with the carboxylic acid on the iMP to attach to the surface. As a control, they also attached monofunctional spiropyran to the surface of half their samples. They then cured polymethyl methacrylate onto the fibers.

Using a microdebond testing set-up, they monitored the fluorescence intensity and interfacial shear stress as a function of displacement. It was shown that spiropyran, a low activation energy MP, does not require covalent attachment on both sides to be activated; however, greater sensitivity was observed when it was covalently attached to both the matrix and the fiber [29]. This study suggests that the mechanophore requires surface attachment to induce activation but not necessarily covalent attachment with the matrix.

35.4.3 Single fiber composite tensile testing

As previously mentioned, spirolactam mechanophores are relatively easy MPs to synthesize due to the commercial availability of Rhodamine 110, the synthetic precursor. Woodcock et al. synthesized interfacial spirolactam mechanophores between silk fibers and a polyether diamine epoxy matrix [30]. The lysine amino acids in silk have primary amines pendant to the main polypeptide chain, which were used to covalently attach the iMP. The other side of the spirolactam was then reacted with the epoxy matrix. Ex situ fluorescence lifetime measurements showed that spirolactam mechanophores require covalent attachments for interfacial activation. This study also showed that mechanophores are not limited to use in synthetic material systems, but are compatible with biomaterials such as silk fibers, too. In a follow-up study, it was demonstrated that this mechanophore can also be used to visualize far field damage in the matrix propagating from the interface [32].

35.5 Challenges to implementation

While mechanophores show promise as NDE tools for stress measurement in structural adhesives and polymer matrix composites, there are many challenges that researchers must overcome to realize this damage-sensing technology. First, while qualitative implementation of mechanophores as damage sensors is rather straightforward, quantifying stresses based on the observed intensity of the activation signal requires far more calibration and consideration specific to each system. Second, mechanophores, being organic molecules, are relatively susceptible to environmental forces such as elevated temperatures, ultraviolet (UV) irradiation, and oxidation, which can potentially limit the useful life of these molecular sensors. Third, a major obstacle to commercialization of this technology is the synthetic scale-up of the mechanophores.

35.5.1 Calibration of stress to mechanophore activation intensity

As the size of these force probes shrink from the macroscopic to the angstrom scale, fracture mechanics must integrate quantum mechanics to fully understand the relationship between bulk stresses and mechanophore activation. Merging these two fields may prove challenging due to the paradigms each group of scientists have when approaching problems. A physical chemist will view the problem as a game of probability and statistics. How likely is it that a mechanophore will break upon the addition

of a unit of energy to the system? There is never a definitive answer of what force will be required to activate a single mechanophore. “It depends.” It depends on the temperature of the system, the size of the activation barrier of the mechanophore, how the chemistry of the polymer matrix impacts that activation barrier, if there is a net charge in the system shifting the isomerization toward either the open or closed (activated or inactivated) form. The list of potential external influences is extensive, which is what the physical chemist expects. The engineer or physicist approaching the issue from a continuum mechanics and fracture mechanics framework, however, expects a definitive answer. “Below a threshold force value there is no activation and above it there is full activation.” This is also unlikely to be completely correct. There must be a paradigm shift on both ends of the problem to come up with a global approach to understanding mechanophore activation for a given system. The Craig group has done an excellent job of beginning this conversation by examining the effect of force on the equilibrium of the mechanophore [33].

Once the relationship among force, activation energy, and mechanophore activation has become well understood, another challenge presents itself for mechanoluminescent materials that become fluorescent upon activation. As with most other fluorometric techniques, mechanophore fluorescence intensity depends on the intensity of incident light, the concentration of the fluorophore within the field of view, the polymer network composition, and the sample geometry, necessitating unique calibration approaches. Fluorescence is a two-step phenomenon: the absorption of the incident photons (excitation) and the fluorescence of the emitted photons (emission) [34–36]. Absorption follows Beer’s law, which equates total absorption to the absorption coefficient of the molecule, the concentration of the molecule in the system, and the path length over which the light interacts with the sample [34]. The absorptivity constants depend on both the molecule itself as well as the chemical environment of the molecule. The path length is dependent on both the system and the measurement technique. The molecular concentration will vary from sample to sample unless explicitly controlled.

Changing from one adhesive formulation to another could significantly impact the interaction between the incident light and the mechanophore. As we shift focus to the second part of fluorescence (emission), the amount of emitted light depends on the amount of light absorbed, the intensity of the light, and the quantum efficiency of the molecule. The quantum efficiency is dependent on both the molecular structure of the mechanophore and the local chemical environment. By carefully controlling the formulation and instrument variables, researchers can construct calibration curves for a single sample type that relate the fluorescence intensity of activated mechanophores to the quantitative force or stress developed within the sample.

35.5.2 Environmental effects on mechanophore activation

Mechanophores with lower force activation thresholds also tend to be more susceptible to environmental factors such as pH or external irradiation (UV, thermal, etc.). Spiropyran is known for being essentially “turned off” by lowering the pH of the system, turning the molecule yellow and nonresponsive. Long periods of UV

radiation combined with oxygen degrade the mechanophore over time. These are issues that can be mitigated in the lab; however, they must be considered for field usage. For more extreme environments such as the underside of a car or on a wind turbine out at sea, heat, sunlight, and salinity must also be considered. Organic molecules tend to degrade at higher temperatures, presenting added technical challenges near engines or batteries.

35.5.3 Commercial availability of synthetically complex mechanophores

Due to the complexity of synthesis combined with the relatively low demand and instability of several mechanophores, we are unaware of any commercially available mechanophores as of the time of this writing. As with many technologies, the supply will grow to reach the demand for the product. Necessary steps to obtaining commercial mechanophores include optimization of the reactions at scales beyond milligrams. Complex multistep syntheses with low yields are not commercially feasible, especially with a push for cleaner processes and solvent-free methods in the chemical manufacturing industry.

Adding to the challenge of commercial feasibility is the specificity required to utilize mechanophores in a given system. Embedding a molecule into a glassy epoxy requires amine or epoxide functionality, whereas a silicone requires vinyl functionality. This specificity issue is worsened for interfacial mechanophores. Not only do the mechanophores need to bond to the adhesive itself but they also require special asymmetric functionality to attach across an interface. Preliminary work has been performed for silicon substrates functionalized with mechanophores, but attachment to metallic substrates or thermoplastic surfaces may prove challenging due to the lack of inherent functionality on their surfaces [28,29,31].

35.6 Conclusions and future trends

Mechanophores provide scientists with a great opportunity to change how the world approaches adhesives and composites. By embedding mechanophores as damage sensors in a structural adhesive joint to act as a stress concentration indicator, we can receive real-time feedback of stress localizations, fatigue, and the onset of debonding. By monitoring the structural health of bonded joints and composite interfaces, the service lifetimes of these components can be extended by reducing premature retirement. For large composite structures where catastrophic failure is costly to both life and property, this allows for a reduction in waste without compromising safety.

Mechanophores incorporated in the structural adhesive forming a bonded joint can indicate stress concentrations as they are loaded. Additionally, the incorporation of mechanophores within composites can allow for the rapid prototyping and testing of new reinforcement designs without the need for complex computer simulations to determine the stress concentrating effects.

Interfacial mechanophores show promise as a way to extend the service lifetime of massive composites structures such as wind turbines and lightweight automobile parts. Microelectronics could benefit from interfacial mechanophores that enable the detection of small-scale debonding of chip packaging at the chip-encapsulant interface. Further, interfacial damage sensors could be used as a sensing technology due to their advantages over traditional measurement systems. The sensitivity of mechanophores to the submicron interfacial separation of a buried interface will allow for the earlier detection of debonding events that can lead to component failure. Another advantage of attaching mechanophores across an interface is that the calibration of mechanophore response to stress magnitudes becomes unnecessary. Stresses are intensified across the interface so significantly that if the mechanophore is activated, the crack itself will have opened several nanometers. All mechanophores located at the interface where separation has occurred will be activated while those ahead of the propagating interfacial crack remain inactive. This allows the mechanophore to serve as an on/off interfacial separation indicator. Being able to detect submicron crack opening displacements would improve measurement techniques by several orders of magnitude.

In the near term, mechanophore technology must continue to be developed to be industrially feasible as a sensing technology. Chemists must continue to develop new robust mechanophores that are possible to synthesize at industrial scales and that are also chemically stable. Unavoidable environmental factors such as UV irradiation and oxidation are potential barriers to commercialization. Thankfully, new molecules are being synthesized monthly according to current literature trends. While chemists continue their synthetic efforts, research engineers are working to develop our understanding of mechanophore behavior in practical systems. The calibration of MP response to stresses within a material, the development of appropriate FEA models, and the optimization of the sensitivity and efficiency of the mechanophores are areas of active research.

Looking farther into the future, MP technologies will be implemented into many structural adhesive components as damage indicators. Just as color-changing, moisture-sensitive stickers indicate if electronics have gotten wet, mechanophore-laced adhesives will serve as either interfacial or bonded joint damage indicators. Recent work has shown the potential for mechanophores to detect microscopic scratches in epoxy coatings. Others have shown activation through shear stress, which will be useful in the evaluation of lap joints where the mechanophores could be used to highlight shear stress concentrations in loaded joints and signal if failure is imminent. Embedding MPs into automotive adhesives could provide indications of which adhesive joints are compromised after an accident, aiding repair shops in safe repair. From design and qualification perspectives, postmortem analysis of new joint designs can help to identify whether the load is disturbed evenly across the joint or is unintentionally being concentrated.

While there are several challenges associated with the implementation of mechanophores as a sensing technology, researchers have made steady progress in tackling these issues. Over the last couple of decades, the understanding of mechanophores has grown exponentially within the scientific community. The incorporation of mechanophores within structural adhesives, polymer matrix composites, and at the interface of dissimilar materials are all exciting avenues where this interesting technology can be deployed.

References

- [1] L.W. Schmerr, *Fundamentals of Ultrasonic Nondestructive Evaluation a Modeling Approach*, second ed., 2016. <http://www.springer.com/series/13337>.
- [2] N. Ida, N. Meyendorf (Eds.), *Handbook of Advanced Nondestructive Evaluation*, Springer, Cham, 2019. <https://doi.org/10.1007/978-3-319-26553-7>.
- [3] D.E. Bray, R.K. Stanley, *Nondestructive Evaluation: A Tool in Design, Manufacturing, and Service*, (2018). <https://doi.org/10.1201/9781315272993>. D.E. Bray, R.K. Stanley, *Nondestructive Evaluation: A Tool in Design, Manufacturing, and Service*, Taylor & Francis, 2018.
- [4] G. Busse, Nondestructive evaluation of polymer materials, *NDT E Int.* 27 (1994) 253–262, [https://doi.org/10.1016/0963-8695\(94\)90130-9](https://doi.org/10.1016/0963-8695(94)90130-9).
- [5] N. Deneke, M.L. Rencheck, C.S. Davis, An engineer’s introduction to mechanophores, *Soft Matter* 16 (2020) 6230–6252, <https://doi.org/10.1039/d0sm00465k>.
- [6] N. Willis-Fox, E. Rognin, T.A. Aljohani, R. Daly, Polymer mechanochemistry: manufacturing is now a force to be reckoned with, *Chem* 4 (2018) 2499–2537, <https://doi.org/10.1016/J.CHEMPR.2018.08.001>.
- [7] J. Li, C. Nagamani, J.S. Moore, Polymer mechanochemistry: from destructive to productive, *Acc. Chem. Res.* 48 (2015) 2181–2190, <https://doi.org/10.1021/acs.accounts.5b00184>.
- [8] H. Staudinger, W. Heuer, Highly polymerized compounds XCIII: the breaking up of the molecular fibers of the polystyrenes, *Berichte Der Dtsch. Chem. Gesellschaft B.* 67 (1934) 1159–1164, <https://doi.org/10.1002/cber.19340670708>.
- [9] K.L. Berkowski, S.L. Potisek, C.R. Hickenboth, J.S. Moore, Ultrasound-induced site-specific cleavage of azo-functionalized poly(ethylene glycol), *Macromolecules* 38 (2005) 8975–8978, <https://doi.org/10.1021/MA051394N>.
- [10] S.L. Potisek, D.A. Davis, N.R. Sottos, S.R. White, J.S. Moore, Mechanophore-linked addition polymers, *J. Am. Chem. Soc.* 129 (2007) 13808–13809, <https://doi.org/10.1021/JA076189X>.
- [11] D.A. Davis, A. Hamilton, J. Yang, L.D. Cremer, D. Van Gough, S.L. Potisek, M.T. Ong, P. V. Braun, T.J. Martínez, S.R. White, J.S. Moore, N.R. Sottos, Force-induced activation of covalent bonds in mechanoresponsive polymeric materials, *Nature* 459 (2009) 68–72, <https://doi.org/10.1038/nature07970>.
- [12] G.R. Gossweiler, G.B. Hewage, G. Soriano, Q. Wang, G.W. Welshofer, X. Zhao, S.L. Craig, Mechanochemical activation of covalent bonds in polymers with full and repeatable macroscopic shape recovery, *ACS Macro Lett.* 3 (2014) 216–219, <https://doi.org/10.1021/MZ500031Q>.
- [13] Y. Chen, G. Mellot, D. Van Luijk, C. Creton, R.P. Sijbesma, Mechanochemical tools for polymer materials, *Chem. Soc. Rev.* 50 (2021) 4100–4140, <https://doi.org/10.1039/d0cs00940g>.
- [14] C.S. Davis, M.L. Rencheck, J.W. Woodcock, R. Beams, M. Wang, S. Stranick, A.M. Forster, J.W. Gilman, Activation of mechanophores in a thermoset matrix by instrumented scratch, *ACS Appl. Mater. Interfaces* 13 (2021) 55498–55506, <https://doi.org/10.1021/ACSAMI.1C15004>.
- [15] C.P. Kabb, C.S. O’Bryan, C.D. Morley, T.E. Angelini, B.S. Sumerlin, Anthracene-based mechanophores for compression-activated fluorescence in polymeric networks, *Chem. Sci.* 10 (2019) 7702–7708, <https://doi.org/10.1039/c9sc02487e>.
- [16] B. Koo, E. Nofen, A. Chatopadhyay, L. Dai, Dimeric anthracene-based mechanophore for damage precursor detection in epoxy-based thermoset polymer matrix: characterization

- and atomistic modeling, *Comput. Mater. Sci.* 133 (2017) 167–174, <https://doi.org/10.1016/j.commatsci.2017.03.002>.
- [17] M.A. Ghanem, A. Basu, R. Behrou, N. Boechler, A.J. Boydston, S.L. Craig, Y. Lin, B.E. Lynde, A. Nelson, H. Shen, D.W. Storti, The role of polymer mechanochemistry in responsive materials and additive manufacturing, *Nat. Rev. Mater.* 61 (6) (2020) 84–98, <https://doi.org/10.1038/s41578-020-00249-w>.
- [18] Y. Chen, A.J.H. Spiering, S. Karthikeyan, G.W.M. Peters, E.W. Meijer, R.P. Sijbesma, Mechanically induced chemiluminescence from polymers incorporating a 1,2-dioxetane unit in the main chain, *Nat. Chem.* 47 (4) (2012) 559–562, <https://doi.org/10.1038/nchem.1358>.
- [19] Y. Chen, R.P. Sijbesma, Dioxetanes as mechanoluminescent probes in thermoplastic elastomers, *Macromolecules* 47 (2014) 3797–3805, https://doi.org/10.1021/MA500598T/SUPPL_FILE/MA500598T_SI_001.PDF.
- [20] K.M. Wiggins, J.N. Brantley, C.W. Bielawski, Polymer mechanochemistry: force enabled transformations, *ACS Macro Lett.* 1 (2012) 623–626, <https://doi.org/10.1021/MZ300167Y>.
- [21] Y.K. Song, K.H. Lee, W.S. Hong, S.Y. Cho, H.C. Yu, C.M. Chung, Fluorescence sensing of microcracks based on cycloreversion of a dimeric anthracene moiety, *J. Mater. Chem.* 22 (2012) 1380–1386, <https://doi.org/10.1039/c1jm13709c>.
- [22] E. Ducrot, Y. Chen, M. Bulters, R.P. Sijbesma, C. Creton, Toughening elastomers with sacrificial bonds and watching them break, *Science* 344 (2014) 186–189, <https://doi.org/10.1126/science.1248494>.
- [23] A.D.N. Celestine, B.A. Beiermann, P.A. May, J.S. Moore, N.R. Sottos, S.R. White, Fracture-induced activation in mechanophore-linked, rubber toughened PMMA, *Polymer* 55 (2014) 4164–4171, <https://doi.org/10.1016/J.POLYMER.2014.06.019>.
- [24] M.L. Rencheck, B.T. Mackey, Y.Y. Hu, C.C. Chang, M.D. Sangid, C.S. Davis, Identifying internal stresses during mechanophore activation, *Adv. Eng. Mater.* (2021) 2101080, <https://doi.org/10.1002/ADEM.202101080>.
- [25] Y. Chen, C.J. Yeh, Q. Guo, Y. Qi, R. Long, C. Creton, Fast reversible isomerization of merocyanine as a tool to quantify stress history in elastomers, *Chem. Sci.* 12 (2021) 1693–1701, <https://doi.org/10.1039/d0sc06157c>.
- [26] A.D.N. Celestine, N.R. Sottos, S.R. White, Strain and stress mapping by mechanochemical activation of spiropyran in poly(methyl methacrylate), *Strain* 55 (2019), <https://doi.org/10.1111/STR.12310>.
- [27] A.N. Gent, B. Park, Failure processes in elastomers at or near a rigid spherical inclusion, *J. Mater. Sci.* 19 (1984) 1947–1956, <https://doi.org/10.1007/BF00550265>.
- [28] J. Sung, M.J. Robb, S.R. White, J.S. Moore, N.R. Sottos, Interfacial mechanophore activation using laser-induced stress waves, *J. Am. Chem. Soc.* 140 (2018) 5000–5003, <https://doi.org/10.1021/jacs.8b01427>.
- [29] M.E. Grady, C.M. Birrenkott, P.A. May, S.R. White, J.S. Moore, N.R. Sottos, Localization of spiropyran activation, *Langmuir* 36 (2020) 5847–5854, <https://doi.org/10.1021/acs.langmuir.0c00568>.
- [30] J.W. Woodcock, R. Beams, C.S. Davis, N. Chen, S.J. Stranick, D.U. Shah, F. Vollrath, J. W. Gilman, Observation of interfacial damage in a silk-epoxy composite, using a simple mechanoresponsive fluorescent probe, *Adv. Mater. Interfaces* 4 (2017) 1601018, <https://doi.org/10.1002/admi.201601018>.
- [31] J. Li, T. Shiraki, B. Hu, R.A.E. Wright, B. Zhao, J.S. Moore, Mechanophore activation at heterointerfaces, *J. Am. Chem. Soc.* 136 (2014) 15925–15928, <https://doi.org/10.1021/ja509949d>.

-
- [32] J.W. Woodcock, R.J. Sheridan, R. Beams, S.J. Stranick, W.F. Mitchell, L.C. Brinson, V. Gudapati, D. Hartman, A. Vaidya, J.W. Gilman, G.A. Holmes, Damage sensing using a mechanophore crosslinked epoxy resin in single-fiber composites, *Compos. Sci. Technol.* 192 (2020) 108074, <https://doi.org/10.1016/j.compscitech.2020.108074>.
- [33] C.L. Brown, S.L. Craig, Molecular engineering of mechanophore activity for stress-responsive polymeric materials, *Chem. Sci.* 6 (2015) 2158–2165, <https://doi.org/10.1039/c4sc01945h>.
- [34] J.R. Lakowicz, Introduction to fluorescence, *Princ. Fluoresc. Spectrosc.* (1999) 1–23, https://doi.org/10.1007/978-1-4757-3061-6_1.
- [35] J.C. Zwinkels, P.C. DeRose, J.E. Leland, Spectral fluorescence measurements, *Exp. Methods Phys. Sci.* 46 (2014) 221–290, <https://doi.org/10.1016/B978-0-12-386022-4.00007-8>.
- [36] R.W. Welker, Size analysis and identification of particles, *Developments in Surface Contamination and Cleaning. Detection, Characterization, and Analysis of Contaminants* (2012) 179–213. <https://doi.org/10.1016/B978-1-4377-7883-0.00004-3>. R.W. Welker, Size analysis and identification of particles, in: *Developments in Surface Contamination and Cleaning. Detection, Characterization, and Analysis of Contaminants*, William Andrew Applied Science Publishers, 2012, pp. 179–213.

This page intentionally left blank

Index

Note: Page numbers followed by *f* indicate figures, *t* indicate tables, and *b* indicate boxes.

A

- Accelerated characterization, 695–699
- Accelerated curing, 991–996
 - bulk properties, 991–992, 992*f*
 - lap shear strength, 992–996, 993–994*f*
- Acid-base interaction, 330–331
- Acid-catalyzed Knoevenagel condensation, 142
- Acrylic structural adhesives
 - automotive, 72
 - bonding carbon-fiber composite, 97
 - bonding through dry lubricants, 97–98
 - bond strength and failure mode, 80–84, 80–81*f*
 - environmental durability, 82–84
 - rheological behavior, 82
 - chemical resistance, 84
 - composition-property relationship, 84–87
 - adhesive matrix, mechanical properties of, 84–87
 - dynamic mechanical analysis, 85–87, 86–87*f*
 - tensile testing, 85, 85*f*
 - corrosive environment, 84
 - EH&S compliance, 97
 - EH&S profile, additive impact on, 93
 - electric vehicle battery pack assembly, 96–97
 - cell to cooling plate, 96–97, 96*f*
 - environmental cycling, 84
 - environmental, health, and safety-friendlier
 - acrylic structural adhesives, 71–72
 - formulation components, 73, 73*t*
 - futures trends, 97–98
 - Hem-flange bonding, 93–94, 94*f*
 - high humidity exposure, 83–84
 - high temperature endurance, 83
 - historical perspective, 69–70
 - industrial assembly, 72–73
 - initiation and polymerization, 74–77
 - handling strength development, 79, 79*f*
 - mix ratio, 77–78, 77–78*f*
 - open time, 78–79
 - polymerization of methacrylates, 76–77
 - purge time, 80
 - redox initiation, 74–76, 75*t*
 - interfacial adhesion, 87–92
 - acrylic cure profile, 89–90, 89*f*
 - low surface energy thermoplastics, 89
 - thermoplastics and polymer composites, 88
 - odor, 92–93
 - low odor, 92–93
 - low toxicity, 92–93
 - nonflammable methacrylates, 92–93
 - rail/bus/trailer/recreation marine, 95–96
 - composite to composite, 95
 - composite to metals, 95–96
 - room temperature adhesion vs. high temperature
 - adhesion, 94, 95*f*
 - structural adhesives, 69
 - supply-chain uncertainty, 98
 - thermal shock, 84
 - toughened MMA-based acrylic adhesive, 70
 - toughened THFMA-based acrylic adhesive, 70–71, 71*t*
 - toughening of, 90–92
 - advancement in testing, 90
 - block copolymer elastomers, 91, 91*f*
 - other elastomers, 91–92
 - particulate rubbers, 90–91
 - transportation other than automotive, 72
 - untoughened MMA-based acrylic adhesive, 70
 - vehicle crash worthiness, 97
- Activation intensity, 1133–1134
- Addition-cure catalysts, 193
- Addition cure chemistry, 187–189
- Adherent
 - rounding, 1081, 1081*f*
 - shaping, 1082–1083, 1082*f*
- Adhesion
 - evaluation, 363–364
 - measuring, 292–303
 - promoters, 41, 193–194
 - science, 755–756
- Adhesive bonding, 468–469, 1040–1050
 - accelerated characterization, 695–699
 - adhesive joint stresses, 496–498
 - mechanical loading, 496–497
 - swelling stresses, 497–498
 - thermal stresses, 497
 - aging effects, 512–514, 513*f*
 - analytical approaches, 498–501
 - lap shear joints, 498–500, 499*f*
 - bonded joints, stress types in, 495–496, 495*f*

Adhesive bonding (*Continued*)

- butt joints, 501
- characterizing durability, test methods for, 683–695
 - adhesives as bonded systems, 685–695, 686*f*, 688–694*f*
 - adhesives as materials, 683–685
- cleavage stress, 496
- continuum-based numerical methods, 493–494
- continuum mechanics models, 502–503
 - critical distance-based models, 503
 - strain-based models, 502–503
 - stress-based models, 502
- damage mechanics methods, 505–507
 - cohesive zone modeling, 506–507
 - continuum damage models, 506
 - extended finite element modeling, 507
- durability, 442–445
 - cross-laminated wood products, adhesive effects in, 443–445, 444*f*
- examples, 699–702, 699–701*f*
- fracture mechanics methods, 503–505
- future needs, 702–703
- hybrid analytical/numerical methods, 508–509
- joint geometry, 509–512
 - adhesive thickness, 509–510
 - joint width, 511–512
 - overlap length, 510–511
 - substrate stiffness, 511–512
- mechanistic changes in polymer structure, 676–683
 - environmental exposures, 677–678
 - environmental factors, adhesives exposed to, 678–679
 - polymer structure, chemical aging in, 682–683
 - polymer structure, physical aging in, 681–682
- numerical methods, 501–507
- peel joints, 500
- peel stress, 496
- scarf and stepped joints, 500–501
- shear stress, 496
- strain rate effects, 512
- stress and strain concepts, 494–495, 494*f*
- temperature effects, 514
- tensile stress, 495
- time-temperature superposition principle (TTSP), 695–699
 - physical aging on, 696–697, 697*f*
 - physical aging reversing effects, 697–699, 698*f*
- Adhesive design, strength and fracture energy in, 466–480, 466*f*
- Adhesive dispensing workflow, 759–760, 759*f*
- Adhesive joints
 - categories, 643
 - damage mechanics, 662–665
 - environmental and loading effects, 661–662
 - experimental techniques, 645–647, 645*f*, 647*f*
 - fatigue of adhesives, general considerations for, 644
 - fracture mechanics, 653–660
 - mode mix, 658–659
 - numerical techniques, 654–655
 - R-ratio effect, 655–658, 656–657*f*
 - variable amplitude, 660
 - joint features, effect of, 660–661
 - measurements, 463–466, 464*f*
 - strength/stiffness wearout, 651–653
 - stiffness wearout approach, 653
 - strength wearout approach, 651–653, 652*f*
 - stresses, 496–498
 - mechanical loading, 496–497
 - swelling stresses, 497–498
 - thermal stresses, 497
 - stress/strain-life approaches, 647–651
 - damage initiation and crack growth phases, 649
 - fatigue limit, 650–651
 - fatigue limit/variable amplitude fatigue, 649–650, 650*f*
 - stress-life approach, 647–649, 648*f*
 - variable amplitude fatigue, 649–650, 650*f*
- Adhesives, 41–42, 47, 685–695, 686*f*, 688–694*f*
 - qualification and specification in consumable goods, 872
 - quality control and risk mitigation, 872
 - selection, 835–836
 - wood interactions, 422*f*, 434–436, 435*f*
- Advanced surface treatment, 334–337
 - corona treatment, 336
 - flame treatment, 335
 - plasma treatment and polymerization, 336–337
 - solvents and detergents, surface degreasing by, 335
 - UV treatment, 337
- Advancement in testing, 90
- Aerospace, 43–44, 54–55
 - bonded joint applications, 796–802
 - civil, 797–799
 - military, 799–802, 800–801*f*
 - overall observations, 802
 - service experience, 797–802
 - typical applications, 796–797
 - bonded joint certification, 790–796, 790*f*
 - bonded joints, 783–784, 783*f*
 - bonded structures and repairs, design and structural substantiation of, 791–796
 - design and analysis, 791–792

- maintenance considerations, 793–794
 - structural substantiation, 794–796
 - bonding systems, 784–790, 784*f*
 - adhesive materials, 785
 - bonding process, 787–789, 787*f*
 - design features, 790
 - screening tests, 789
 - substrate materials, 785
 - surface preparation, 785–787, 786*f*
 - certification regulations and guidance, 780–782
 - industry publications, 782
 - metal and composite bonds, bonding systems for, 783–790
 - terms and abbreviations, 779–780
 - Aging
 - effects, 343–344, 344*f*, 345*t*, 512–514, 513*f*
 - influence of, 557*f*, 558
 - Aliphatic amines, 17
 - Aliphatic polyetheramines, 20
 - Allyl-2-cyanoacrylate (ACA)-based adhesives, 145
 - Allyl cyanoacrylate polymerizes, 144–145
 - Amine accelerators, 34
 - Amines as copolymers, 121
 - Amino resins, 428
 - Anaerobic adhesive cure chemistry, 162–164, 163*f*
 - Anaerobic adhesives
 - anaerobic adhesive cure chemistry, 162–164, 163*f*
 - anaerobic products, new curatives for, 167–170, 168–170*f*
 - applications, 164–167
 - biorenewable sources, plasticizers from, 175
 - formulation chemistry of, 159–161, 160*f*, 160*t*
 - gasketing, 166–167, 167*f*
 - higher temperature performance, anaerobic products with, 175
 - introduction, 159
 - recent advances in, 167–175
 - retaining, 166, 166*f*
 - sustainability credentials, 171–175
 - methyl methacrylate (MMA), 171–172, 172*f*
 - overview, 171, 171*f*
 - renewable sources, oligomers from, 172–175, 173*f*, 174*t*
 - threadlocking, 164–165, 164*f*
 - thread sealing, 165, 165*f*
 - Anaerobic products, new curatives for, 167–170, 168–170*f*
 - Analytical approaches, 498–501
 - lap shear joints, 498–500, 499*f*
 - Anhydrides, 30
 - Applicable substrates and preparation, 43
 - Architected bondlines and adherends, 1109–1111, 1110*f*
 - Artificial neural network, 938, 940–941*f*
 - Army Research Laboratory (ARL), 482
 - Aromatic amines, 20–23, 21–23*t*
 - Assembly automation, 855
 - Assembly of primary structures, 851–852
 - Assembly of secondary structures, 852–853
 - Augmenting traditional fracture analysis, 1050–1059
 - bonded fracture specimens, visualizing strain fields in, 1052–1054
 - bonded joints, fracture analysis of, 1051
 - Mode II fracture testing, DIC application to, 1058–1059, 1059*f*
 - Mode I J-integral method, 1056–1058, 1057*f*
 - Mode I LEFM analysis, 1054–1056, 1055*f*
 - Automated adhesive dispensing, 758–759
 - Automatic shear strength testing, 757–758, 758*f*
 - Automation machinery, 859–861
 - Automotive adhesives, 44, 54
 - automotive manufacturers, 808
 - design qualification, 814–816, 815*f*
 - DSC kinetic cure model, 817–818
 - future trends, 824
 - manufacturers, 808
 - manufacturing qualification, 816
 - original equipment manufacturer (OEM), 807–808
 - qualification example, 817–818
 - quality control, 818–824
 - manufacturing controls, 818–820, 819*f*
 - rheology characterization, 820–824, 821*f*, 823*f*
 - specifications, 810–814
 - stress durability, 811–814, 812–813*f*
- ## B
- Bio-based adhesives, 430–433
 - Bio-based amines, 21–23*t*, 24
 - Bio-based epoxy resins, 13
 - Bio-based PUR, 128–129
 - Bio-based raw materials, 47
 - Biodegradable and compostable adhesives, 961–966, 963–965*f*, 966*t*
 - Bio-derived materials, 958
 - Bio-inspired dopamine, 340–343
 - Biological systems, controlled adhesion in, 953–957
 - Biomedical adhesives
 - biocompatibility, 879, 900–904
 - biodegradation, 900–904
 - certification, 898–904
 - European Union, 898–900
 - ISO 10993 standards, 900–904

- Biomedical adhesives (*Continued*)
 mechanical performance, 879–880
 medical device industry adhesives (*see* Medical device industry adhesives)
 natural adhesives, 880–882
 advantages and disadvantages of, 883*t*
 polysaccharides, 880–881, 881*f*
 proteins, 881–882, 882*f*
 quality, 898–904
 regulatory process, 898–900, 898*f*
 requirement, 878–880
 safety, 898–904
 specifications, 898–904
 synthetic
 acrylics, 884
 cyanoacrylates, 883–884
 epoxies, 884–885
 polyethylene glycol (PEG), 885–887
 polyurethanes, 885
 tissue adhesives (*see* Tissue adhesives)
 United States, 898–900
 USP class VI, 900
 wet adhesion, 880
- Biomedical cyanoacrylate adhesives, 150–151
- Biorenewable sources, plasticizers from, 175
- Bisphenol A diglycidyl ether (BADGE), 3
- Bisphenol alternative resins, 47
- Bisphenol A resin alternatives, 51–52, 51*f*
- Bisphenol glycidyl ether resins, 4–5, 5*f*
- Block copolymer elastomers, 91, 91*f*
- Bonded and coated structures, adhesion failure in, 304
- Bonded joints, 796–802
 accelerated curing, 991–996
 bulk properties, 991–992, 992*f*
 curie particles, 989
 curing kinetics and modeling, 989–991
 curing processes, modeling accelerated, 998–1003
 principle, 998–1002, 999–1002*f*
 validation and parametric studies, 1002–1003, 1003*f*
 induction heating, 988–989
 laboratory conditions, 996–997, 997*f*
 lap shear strength, 992–996, 993–994*f*
 large-scale joints, accelerated curing of, 996–998
 low temperatures, 997–998
 civil, 797–799
 military, 799–802, 800–801*f*
 overall observations, 802
 service experience, 797–802
 stress concentrations, 1079–1085
 fillets, 1079–1081, 1080*f*
 stress types in, 495–496, 495*f*
 typical applications, 796–797
- Bonded structures and repairs, design and structural substantiation of, 791–796
 design and analysis, 791–792
 maintenance considerations, 793–794
 structural substantiation, 794–796
- Bonding carbon-fiber composite, 97
- Bonding plastics
 advanced surface treatment, 334–337
 corona treatment, 336
 flame treatment, 335
 plasma treatment and polymerization, 336–337
 solvents and detergents, surface degreasing by, 335
 UV treatment, 337
 aging effect, 343–344, 344*f*, 345*t*
 challenge and surface characteristics, 332–334
 surface energy and solubility parameters, 332–334, 333*t*
 surface energy and wetting, temperature on, 334
 chemical treatment to, 337–343
 bio-inspired dopamine, 340–343
 catechol functionalization of latex, 343
 catechol grafting, 340–343, 341*f*, 342*t*
 organoboron chemistry, 338–340, 338–339*f*
 polyolefin adhesion, 345–351
 case studies, 348–351, 348*t*, 349–352*f*
 future trends, 352
 polyolefin specific adhesion, 346–347, 347*t*
 principles, 328–332
 substrates and adhesives, bonding formation between, 330–332
 acid-base interaction, 330–331
 covalent bonding, 330
 diffusion theory, 332
 electrostatic theory, 331
 mechanical interlocking, 331–332
 surface contact-wetting/spreading, 328–329, 329*t*
- Bonding systems, 784–790, 784*f*
 adhesive materials, 785
 bonding process, 787–789, 787*f*
 design features, 790
 screening tests, 789
 surface preparation, 785–787, 786*f*
- Bonding through dry lubricants, 97–98
- Bondline stiffness, 445–446
- Bondline thickness
 adhesive thickness analysis, 624–627
 adhesive/adherend energy flow, 624–625

- double cantilever beam (DCB) configuration, 624–627
 - elastic foundation models, interpretation using, 625–627
 - failure modes and fracture properties, 627–637
 - precrack length, 636–637, 637f
 - crack tip, stress near, 620–621
 - double cantilever beam (DCB) configuration, 624–627
 - adhesive/adherend energy flow, 624–625
 - elastic foundation models, 625–627
 - edge and corner stress fields, 621–623, 622–623f
 - energy approach, 618–620
 - failure modes and fracture properties, adhesive thickness on, 627–637
 - case studies, 627–633
 - failure modes, 627–628, 627–628f
 - fracture energy, 629, 629f
 - fracture energy trend, 630–632, 631f
 - stress fields, 629, 629f
 - fracture mechanics, 618–620, 619f
 - thick bonded joints, crack initiation competition in, 634–637
 - adherend-adhesive modulus mismatch, 635–636, 635t, 636f
 - crack tip and emergence of material length scale, 620–621
 - edge and corner stress fields, 621–623, 622–623f
 - energy approach and fracture mechanics, 616f, 618–620, 618–619f
 - optimum bondline thickness, 615–616
 - precrack length, 636–637, 637f
 - thin to thick adhesive layers, 616–623, 616f, 618f
 - thin to thick adhesive layers, 616–623, 616f, 618f
- Bond strength and failure mode, 80–84, 80–81f
- Boron trifluoride catalysts, 34
- Bulk epoxy polymers, 252–260
 - block copolymers, 255–256
 - chemical modification, 252
 - hybrid toughening, 259–260
 - inorganic rigid particles, 256–257
 - organic rigid particles, 257–259
 - rubber toughening (*see* Rubber toughening)
 - thermoplastic toughening, 255
- Butt joints, 501
- C**
- Calibration of stress, 1133–1134
- Capital goods
 - adhesive qualification and specification in, 862
 - adhesive quality control and risk mitigation, 862–863
 - end-user sector, 856–863
- Carbon nanotubes, 257–259
- Catechol functionalization of latex, 343
- Catechol grafting, 340–343, 341f, 342t
- Certification regulations and guidance, 780–782
 - industry publications, 782
- Characterizing durability, test methods for, adhesives as materials, 683–685
- Chemically triggered debondable adhesives, 973
- Chemical resistance, 84
- Civil engineering, 44–45
 - concrete, 830–831
 - fiber-reinforced polymers, 832–833
 - glass, 831–832
 - practice, 833–834
 - structural steel, 828–829
 - timber engineering, 829–830
- Cleavage stress, 496
- Cohesive zone modeling (CZM), 244, 525, 1064–1068
- Common bonded joint geometries, stress distribution in, 1077–1079
- Composite substrates
 - surface toughening of, 1095–1096
 - Z-pin content in, 1096, 1096f
- Composition-property relationship, 84–87
 - adhesive matrix, mechanical properties of, 84–87
 - dynamic mechanical analysis, 85–87, 86–87f
 - tensile testing, 85, 85f
- Compound annual growth rate (CAGR), 290–291
- Condensation-cure catalysts, 192–193
- Condensation cure chemistry (RTV), 181–187
- Constitutive equations (CZM), 534–535
- Construction adhesives
 - civil engineering materials, adhesive bonding for
 - concrete, 830–831
 - fiber-reinforced polymers, 832–833
 - glass, 831–832
 - structural steel, 828–829
 - timber engineering, 829–830
 - current situation, 837–838
 - manufacturing, quality control and risk mitigation, 835–837
 - adhesive selection, 835–836
 - influence of imperfections, 836–837
 - quality control and risk mitigation, 838
 - scope and structure, 827–828
 - structural verification
 - civil engineering practice, 833–834
 - designing bonded joints, 834
 - suggestion, 834–835

- Consumable goods
 ecosystem, 871
 end-user sector, 871–872
 adhesive qualification and specification in consumable goods, 872
 adhesive quality control and risk mitigation, 872
 consumable goods ecosystem, 871
 industrial consumables, adhesive applications for, 871
 nonindustrial consumables, adhesive applications for, 872
- Contact temperature, 364–366
- Continuum-based numerical methods, 493–494
- Continuum mechanics models, 502–503
 critical distance-based models, 503
 strain-based models, 502–503
 stress-based models, 502
- Core-shell rubbers, 254
- Corrected beam theory (CBT), 530
- Corrosive environment, 84
- Covalent and supramolecular, 972–973
- Covalent bonding, 330
- Crack blunting mechanism, stop holes as, 1111
- Crack face bridging, 1109
- Crack tip opening displacement (CTOD), 1107
- Creep fracture, 559–560
- Critical distance-based models, 503
- Crosslinkages, photodegradation of, 972–973
- Crosslinkers, 191–192
 RTV condensation-cure, 191–192, 192*t*
 RTV/LTV addition cure, 192
- Curatives, 39–40, 40*f*
- Cure stress model, ABAQUS implementation of, 1030
- Curie particles, 989
- Curing catalysts, 123
- Curing kinetics, 989–991, 1013–1015
- Curing processes, modeling accelerated, 998–1003
 principle, 998–1002, 999–1002*f*
 validation and parametric studies, 1002–1003, 1003*f*
- Curing processes, residual stress development
 cure stress model, ABAQUS implementation of, 1030
 curing kinetics, 1013–1015
 density and chemical shrinkage, 1024
 elastic and viscoelastic properties, 1015–1022, 1018–1021*f*
 experimental best practices, 1030–1031
 experimental methods, 1013–1024
 heat of reaction, 1013–1015
 material property evolution, 1011–1013
 modeling methods, 1025–1029
 modeling framework, 1025–1026
 modeling procedure, 1026–1027
 model validation, 1027–1029, 1028–1030*f*
 model validation tests, 1024
 specific heat, 1013–1015
 thermal conductivity and thermal expansion, 1022–1023
- α -cyanoacrylates esters
 acid-catalyzed Knoevenagel condensation, 142
 chemistry of, 138–139, 138–139*f*
 industrial synthesis/manufacture of, 139–142, 141*t*
 large bond gaps, adhesive curing through, 145–146
 recent developments, 143–146
 strengths, 143–146
 thermal resistance performance, 143–145, 144*f*
 weaknesses, 143–146
- Cyanoacrylate (CA) structural adhesives
 biomedical cyanoacrylate adhesives, 150–151
 chemistry of, 138–139
 cyanoacrylates and sustainability, 151–152
 α -cyanoacrylates esters
 acid-catalyzed Knoevenagel condensation, 142
 chemistry of, 138–139, 138–139*f*
 industrial synthesis/manufacture of, 139–142, 141*t*
 large bond gaps, adhesive curing through, 145–146
 recent developments, 143–146
 strengths, 143–146
 thermal resistance performance, 143–145, 144*f*
 weaknesses, 143–146
 definition, 137
 photocuring cyanoacrylates, 149–150, 150*f*
 sustainability, 151–152
 two-component (2K) cyanoacrylate adhesives, 146–149
 2K hybrid cyanoacrylate adhesives, 148–149, 148*f*
 two-component cyanoacrylate adhesives, 146–148, 147*f*
- Cycloaliphatic amines, 17–20, 18–19*t*
- Cycloaliphatic epoxy resins, 8–13, 11–12*t*
- ## D
- Damage-based partitioning scheme, 584
- Damage differentiation, EMIS signals, void detection
 artificial neural network, 938, 940–941*f*
 k-nearest neighbors, 939–942, 942*f*
- Damage mechanics, 505–507, 662–665

- cohesive zone modeling, 506–507
 - continuum damage models, 506
 - extended finite element modeling, 507
 - Density and chemical shrinkage, 1024
 - Designable open time followed by immediate curing, 130–132, 131*f*
 - Designing adherend geometry to control fracture toughness of joints, 1115–1116, 1116*f*
 - Diffusion theory, 332
 - Diffusion timescales, 379–380
 - Digital image correlation
 - adhesive and bonded joint testing, 1040–1050
 - augmenting traditional fracture analysis, 1050–1059
 - bonded fracture specimens, visualizing strain fields in, 1052–1054
 - bonded joints, fracture analysis of, 1051
 - Mode II fracture testing, DIC application to, 1058–1059, 1059*f*
 - Mode I J-integral method, 1056–1058, 1057*f*
 - Mode I LFM analysis, 1054–1056, 1055*f*
 - background, 1037–1040, 1038–1039*f*
 - extracting constitutive properties, 1040–1044, 1041–1043*f*
 - finite element modeling, 1059–1063
 - mixed-mode fracture envelope, 1063–1068
 - cohesive zone model fit, 1064–1068
 - mixed-mode bend (MMB), 1066–1068
 - single-leg bend (SLB), 1066–1068
 - traction-separation law determination, 1064
 - single-lap joints deformations, 1046–1050, 1047–1048*f*, 1050*f*
 - strain fields, acquisition and applications of, 1044–1046
 - adhesive layer strains, 1044–1046
 - analytical and numerical model predictions, 1044, 1045*f*
 - back face deformations, 1044–1046
 - design optimization, 1046
 - nondestructive inspection and damage tracking, 1046
 - traction-separation laws, 1059–1063
 - cohesive zone models, 1060
 - extraction, 1060–1062
 - rate-dependent traction-separation laws, 1062–1063, 1063*f*
- Digital tools, 242–244
- Dissipative extra layer, 1117–1120, 1118*f*
- Double cantilever beam (DCB), 528–529
- Drop towers and pendulums, 560–563, 561–563*f*
- Drop weight, 723–734
- DSC kinetic cure model, 817–818
- Dual cure chemistry, 196
- Durability, 763–767
 - adhesion HT workflow, 766*f*, 768–770
 - data management, 768–770, 769–770*f*
 - failure analysis, 210–211
 - goods ecosystem, 863
 - goods end-user sector, 863–870
 - adhesive applications in transportation, 865–866, 866*f*
 - appliances, 867–868
 - durable goods ecosystem, 863
 - electrical equipment, adhesive applications for, 866–867, 867*f*
 - engineering adhesive qualification and specification, 868–869
 - engineering adhesive quality control and risk mitigation, 869–870, 870*f*
 - home automation, 867–868
 - industry drivers and needs, 863
 - leisure, 867–868
 - materials construction, 863–865, 864*f*
 - high-throughput wedge test workflow, 765–767, 766*f*
 - initial considerations, 763–764
 - machine learning/artificial intelligence, 770–771
 - manual method for durability characterization, 764–765
- Dynamic (thermo)mechanical analysis, 718–719
- ## E
- EH&S compliance, 97
 - EH&S profile, additive impact on, 93
 - Elastic and viscoelastic properties, 1015–1022, 1018–1021*f*
 - Elastic toughening, 1116–1117, 1117*f*
 - Electrical assembly, 853–854
 - Electrical equipment, adhesive applications for, 866–867, 867*f*
 - Electrically conductive fillers, 195
 - Electric vehicle battery pack assembly, 96–97
 - cell to cooling plate, 96–97, 96*f*
 - Electron-beam and photo-cure induced addition chemistry, 189
 - Electronics
 - assembly, 854–855
 - communication, 55–56
 - Electrostatic theory, 331
 - EMIS signals, void detection using
 - damage detection, 934–937
 - damage differentiation, 938–942
 - development and performance of algorithms, 934–937
 - numerical simulations, 930–933, 931*r*, 933*f*
 - End-user sectors, trends, and outlook, 849–850
 - Energy, 45, 55

- Engineering adhesive
 main functionality areas, 850–851
 qualification and specification, 868–869
 quality control and risk mitigation, 869–870, 870*f*
- Engineering modeling packages, incorporation into, 244
- Enhancement through crack deflection, 1106–1107, 1106*f*
- Environmental cycling, 84
- Environmental durability, 82–84
- Environmental factors, adhesives exposed to, 678–679
- Environmental, health, and safety considerations, 38
- Epoxy adhesives
 accelerators and catalysts, 30–37, 31–33*t*
 amine accelerators, 34
 boron trifluoride catalysts, 34
 ionic liquids, 37
 metal salts, 37
 photoinitiation catalysts, 34–36, 35–36*t*
 additional resources, 56
 adhesive production, 41–42
 aerospace, 43–44
 aliphatic amines, 17
 aliphatic polyetheramines, 20
 anhydrides, 30
 applicable substrates and preparation, 43
 aromatic amines, 20–23, 21–23*t*
 automotive, 44
 bio-based amines, 21–23*t*, 24
 bio-based epoxy resins, 13
 bisphenol A diglycidyl ether (BADGE), 3
 bisphenol glycidyl ether resins, 4–5, 5*f*
 building, 44–45
 certificate of analysis, 37–38
 civil engineering, 44–45
 common applications, 42
 construction, 44–45
 cycloaliphatic amines, 17–20, 18–19*t*
 cycloaliphatic epoxy resins, 8–13, 11–12*t*
 electronics and communications, 45
 energy, 45
 environmental, health, and safety considerations, 38
 epoxy functional raw materials, 4–13
 epoxy novolac resins, 5
 epoxy reactions, 4*f*
 epoxy resins, 4–13
 curatives, 13–30
 specialty, 14–16*t*
 formulation and design, 39–41
 adhesion promoters, 41
 curatives, 39–40, 40*f*
 epoxy resins, 39
 fillers and rheology modifiers, 41
 tougheners, 41
 functional raw materials, 4–13
 general manufacturing, 44–45
 general property specifications, 37–38
 glycidyl amine resins, 8
 glycidyl ester resins, 8
 glycidyl ether resins and diluents, 5–8, 6–7*t*
 history of, 3
 industrial, 44–45
 latent curatives, 30
 major uses, 3–4
 marine, 45
 medical applications, 45–46
 minor uses, 3–4
 mixing and dispensing, 43
 novolac resins, 5
 processes and suppliers, 4–13
 reactions, 4*f*
 resins, 4–13, 39
 curatives, 13–30
 specialty epoxy resins, 13
 specialty vehicles and transportation, 46
 adhesives, 47
 aerospace, 54–55
 automotive, 54
 bio-based raw materials, 47
 bisphenol alternative resins, 47
 bisphenol A resin alternatives, 51–52, 51*f*
 construction, 55
 curatives, 52
 electronics and communication, 55–56
 energy, 55
 fatty acids, 49–51
 furans, 47–48, 48*f*
 general manufacturing, 53–56
 infrastructure, 55
 isosorbides, 48–49, 49*f*
 lignins, 50–51
 mixing and dispensing advances, 46–47
 raw material advances, 47–53
 sugars, 49–50
 tougheners, 52–53
 thiols, 24–30, 25–29*t*
 tougheners and flexibilizers, 37
 typical form factors and packaging of, 38–39
 use and properties of, 42–46
- Experimental compliance method (ECM), 531
- Extrinsic joint toughening, 1106–1111
 architected bondlines and adherends, 1109–1111, 1110*f*
 blunt the propagating crack, 1107–1109

- control fracture toughness of joints, design
 - bondline geometry to, 1112–1115, 1113*f*, 1115*f*
 - crack blunting mechanism, stop holes as, 1111
 - crack face bridging, 1109
 - crack tip opening displacement (CTOD), 1107
 - designing adherend geometry to control fracture toughness of joints, 1115–1116, 1116*f*
 - dissipative extra layer, 1117–1120, 1118*f*
 - elastic toughening, 1116–1117, 1117*f*
 - enhancement through crack deflection, 1106–1107, 1106*f*
 - force bridging and crack meandering, alternating surface properties to, 1111–1112
 - future trends, 1120–1121
 - toughening principles, embodiments of, 1111–1120
- F**
- Falling striker, 723–734
 - Fatigue limit, 650–651
 - Fatigue limit/variable amplitude fatigue, 649–650, 650*f*
 - Fatigue of adhesives, general considerations for, 644
 - Fatty acids
 - lignins, 50–51
 - sugars, 49–50
 - Fiber and platelet-type reinforcements, 272–274
 - bridging, 272–273, 273*f*
 - pull-out, 273–274, 273*f*
 - Fillers, 194–195
 - rheology modifiers, 41
 - Finite element analysis (FEA), 208–211, 244
 - Finite element modeling, 267–269, 268*f*, 1059–1063
 - Flame retardants, 195
 - FLASH DSC experiments, 364
 - Force bridging and crack meandering, alternating surface properties to, 1111–1112
 - Formaldehyde emissions, 433–434
 - Fracture mechanics, 128, 468–469, 503–505, 653–660
 - mode mix, 658–659
 - numerical techniques, 654–655
 - R-ratio effect, 655–658, 656–657*f*
 - variable amplitude, 660
 - Fracture mode-mixity
 - damage-based partitioning scheme, 584
 - mixed-mode bi-material interface joints, 586–598
 - bi-material crack, 594–595, 594*t*, 595*f*, 596*t*
 - composite-to-metal bonded joints, 590–598, 596–597*t*
 - longitudinal strain-based criterion, 586–590
 - MMB test, 590–591
 - same material, asymmetric crack within, 591–593
 - strain-based partitioning method, 589–590
 - strain energy release rate (SERR), 586–587, 586*f*
 - Williams' global partitioning approach, 587–588
 - mixed-mode fracture behavior, 598–609
 - crack paths, 604–605, 604*f*
 - crack stability, 598–603, 600–602*t*
 - failure envelopes, 606–609, 606*f*, 608–609*f*
 - mixed-mode partitioning schemes, 582–586
 - evaluation and discussion of, 585–586
 - monolithic specimens, local and global partitioning schemes for, 582–586
 - test methods to, 580–582
 - Fracture testing, 438–442, 555–557, 556*f*
 - cohesive zone models (CZM), 525
 - constitutive equations (CZM), 534–535
 - corrected beam theory (CBT), 530
 - data reduction techniques, 526–535
 - direct fracture energy methods, 440–442, 441*f*
 - experimental compliance method (ECM), 531
 - fatigue, 555–560
 - aging, influence of, 557*f*, 558
 - creep fracture, 559–560
 - fracture testing, 555–557, 556*f*
 - future trends, 566–567
 - impact and high-rate testing, 560–566
 - drop towers and pendulums, 560–563, 561–563*f*
 - servohydraulic testing machines, 565–566, 566*f*
 - Split Hopkinson pressure bars (SHPB), 563–565, 564*f*
 - Irwin-Kies equation, 527–528, 527*f*
 - J-integral, 531–534
 - mixed-mode I+II, 543–552, 543–546*t*
 - mixed-mode I+III, 550–552, 551*t*
 - mixed-mode I+II+III, 552–555, 552–553*t*
 - mixed-mode testing, novel developments in, 542–555
 - modified fracture mechanics methods, 438–440
 - quasistatic single-mode testing, 535–542
 - Mode I, 536–538, 536*f*, 537*t*
 - Mode II, 538–540, 539*t*
 - Mode III, 540–542, 541*t*
 - released energy and crack length, 526
 - simple beam theory (SBT), 528–530, 529*f*
- Free radical polymerization, 139
- Functionally graded adherends, 1098
 - concept and principle, 1093–1095, 1094*f*

- Functionally graded adhesives, 1089–1093
 adhesive components, mixing ratio control, 1091–1092
 concept and operating principle, 1089–1090, 1090*f*
 induction heating, differentiated cure with, 1090–1091, 1090*f*
 magnetic coated particles, 1092–1093
 modeling of, 1093
 particles/second phases, addition of, 1092
- Furans, 47–48, 48*f*
- Future opportunities, 481–484
- G**
- Gasketing, 166–167, 167*f*
- General industrial adhesive applications
 assembly automation, 855
 assembly of primary structures, 851–852
 assembly of secondary structures, 852–853
 automation machinery, 859–861
 capital goods
 adhesive qualification and specification in, 862
 adhesive quality control and risk mitigation, 862–863
 capital goods end-user sector, 856–863
 consumable goods end-user sector, 871–872
 adhesive qualification and specification in consumable goods, 872
 adhesive quality control and risk mitigation, 872
 consumable goods ecosystem, 871
 industrial consumables, adhesive applications for, 871
 nonindustrial consumables, adhesive applications for, 872
 durable goods end-user sector, 863–870
 adhesive applications in transportation, 865–866, 866*f*
 appliances, 867–868
 durable goods ecosystem, 863
 electrical equipment, adhesive applications for, 866–867, 867*f*
 engineering adhesive qualification and specification, 868–869
 engineering adhesive quality control and risk mitigation, 869–870, 870*f*
 home automation, 867–868
 industry drivers and needs, 863
 leisure, 867–868
 materials construction, 863–865, 864*f*
 electrical assembly, 853–854
 electronics assembly, 854–855
 end-user sectors, trends, and outlook, 849–850
 engineering adhesive main functionality areas, 850–851
 industrial processing machinery, 859–861, 861*f*
 industry drivers and needs, 856–857
 infrastructure machinery and equipment, 858–859
 manufacturing machinery, 859–861
 mechanical assembly, 853
 raw material extraction, adhesive applications for, 857
 surface protection, 855–856
 General manufacturing, 53–56
 General property specifications, 37–38
 Glycidyl amine resins, 8
 Glycidyl ester resins, 8
 Glycidyl ether resins, diluents, 5–8, 6–7*t*
- Google, 242
- Graded materials and geometries
 adherend rounding, 1081, 1081*f*
 adherend shaping, 1082–1083, 1082*f*
 bonded joints, stress concentrations in, 1079–1085
 fillets, 1079–1081, 1080*f*
 common bonded joint geometries, stress distribution in, 1077–1079
 functionally graded adherends, 1098
 concept and principle, 1093–1095, 1094*f*
 functionally graded adhesives, 1089–1093
 adhesive components, mixing ratio control, 1091–1092
 concept and operating principle, 1089–1090, 1090*f*
 induction heating, differentiated cure with, 1090–1091, 1090*f*
 magnetic coated particles, 1092–1093
 modeling of, 1093
 particles/second phases, addition of, 1092
 graded substrates, 1095–1098
 composite substrates, surface toughening of, 1095–1096
 composite substrates, Z-pin content in, 1096, 1096*f*
 mixed adhesive joints, 1085–1089
 concept and operating principle, 1085
 large thermal gradients, performance under, 1086–1087, 1087*f*
 mechanical performance and production, 1085–1086
 performance under impact loads, 1088–1089, 1088*f*
 scarf joint geometry, 1084
 stepped-lap geometry, 1084–1085, 1085*f*
 wavy-lap geometry, 1083, 1083*f*

Graded substrates, 1095–1098

 composite substrates

 surface toughening of, 1095–1096

 Z-pin content in, 1096, 1096*f*

H

Handling strength development, 79, 79*f*

Heat of reaction, 1013–1015

Heat stabilizers, 195

Hem-flange bonding, 93–94, 94*f*

High adhesion, 359–362

Higher temperature performance, anaerobic products with, 175

High humidity exposure, 83–84

High-rate sampling, 712

High-rate testing of structural adhesives

 drop weight, 723–734

 dynamic (thermo)mechanical analysis, 718–719

 falling striker, 723–734

 high-rate sampling, 712

 high-speed testing, advancements and gaps in, 743–744

 inertial effects, 712–715, 714*f*

 Kolsky bar/split-Hopkinson bar, 734–743, 736*f*, 739*f*, 742–743*f*

 pendulum impact tests, 723–734

 physics of, 711–715

 rate-dependent properties, 715–718

 dynamic response of polymers and constitutive material modeling, 717–718

 servohydraulic methods, 719–723, 722–723*f*

 structural adhesives, 715–718

 vibration, 715

High-speed testing, advancements and gaps in, 743–744

High temperature endurance, 83

High-throughput (HT) methodologies

 adhesion science, 755–756

 background, 752–753, 752*f*, 757*f*

 durability, 763–767

 adhesion HT workflow, 766*f*, 768–770

 data management, 768–770, 769–770*f*

 high-throughput wedge test workflow, 765–767, 766*f*

 initial considerations, 763–764

 machine learning/artificial intelligence, 770–771

 manual method for durability characterization, 764–765

 shear test, 757–762

 adhesive dispensing workflow, 759–760, 759*f*

 automated adhesive dispensing, 758–759

 automatic shear strength testing, 757–758, 758*f*

 shear testing workflow, 760–762

 substrates and dies, 758

 workflow and screen development, 754–755

 workflow concept, 756–757, 757*f*

Home automation, 867–868

Huang-Kinloch model, 264–267

 plastic void growth, 266–267

 plastic zone radius, 264–265

 rubber bridging, 267

 shear band yielding, 265–266

Hybrid analytical/numerical methods, 508–509

Hydrolysis reactions, 181–182

I

Improved fracture toughness, architected adhesive joints with

 extrinsic joint toughening, 1106–1111

 architected bondlines and adherends,

 1109–1111, 1110*f*

 blunt the propagating crack, 1107–1109

 control fracture toughness of joints, design

 bondline geometry to, 1112–1115, 1113*f*, 1115*f*

 crack blunting mechanism, stop holes as, 1111

 crack face bridging, 1109

 crack tip opening displacement (CTOD), 1107

 designing adherend geometry to control

 fracture toughness of joints, 1115–1116, 1116*f*

 dissipative extra layer, 1117–1120, 1118*f*

 elastic toughening, 1116–1117, 1117*f*

 enhancement through crack deflection,

 1106–1107, 1106*f*

 force bridging and crack meandering,

 alternating surface properties to,

 1111–1112

 future trends, 1120–1121

 toughening principles, embodiments of,

 1111–1120

Induction heating, 988–989

Industrial assembly, 72–73

Industrial consumables, adhesive applications for, 871

Industrial processing machinery, 859–861, 861*f*

Industry drivers and needs, 856–857, 863

Industry-specific standards, 462

Inertial effects, 712–715, 714*f*

Influence of imperfections, 836–837

Infrastructure machinery and equipment, 858–859

Interface, thermal history of, 366–367, 366–367*f*

- Interfacial adhesion, 87–92
 acrylic cure profile, 89–90, 89f
 low surface energy thermoplastics, 89
 thermoplastics and polymer composites, 88
- Interfacial geometry (IFG), 380–381
- Ionic liquids, 37
- Irwin-Kies equation, 527–528, 527f
- Isocyanates, 120
- Isosorbides, 48–49, 49f
- J**
- J-integral, 531–534
- Joint failure, addressing plasticity in, 469–480
- Joint features, effect of, 660–661
- Joint geometry, 509–512
 adhesive thickness, 509–510
 joint width, 511–512
 overlap length, 510–511
 substrate stiffness, 511–512
- K**
- 2K hybrid cyanoacrylate adhesives, 148–149, 148f
- k*-nearest neighbors, 939–942, 942f
- Knoevenagel process, 142
- Kolsky bar/split-Hopkinson bar, 734–743, 736f, 739f, 742–743f
- L**
- Lamb wave signals, weak adhesion detection using, 924–929
 classification metrics, 928–929, 928f
 feature extraction, 926–927, 927f, 928t
 numerical simulations, 924–926, 925f
 results, 929, 930t
- Lap shear joints, 498–500, 499f
- Lap shear strength, 401–403, 401t, 402f
- Large datasets, 483–484
- Large-scale joints, accelerated curing of, 996–998
 laboratory conditions, 996–997, 997f
 low temperatures, 997–998
- Large thermal gradients, performance under, 1086–1087, 1087f
- Latent curatives, 30
- Leisure, 867–868
- Lightweight fillers, 122–123
- Lignin and lignin derivatives, 958–961
- Linear elastic fracture mechanics (LEFM), 525
- M**
- Machine learning, adhesive joints using
 EMIS signals, void detection using
 damage detection, 934–937
 damage differentiation, 938–942
 development and performance of algorithms, 934–937
 numerical simulations, 930–933, 931t, 933f
- lamb wave signals, weak adhesion detection using, 924–929
 classification metrics, 928–929, 928f
 feature extraction, 926–927, 927f, 928t
 numerical simulations, 924–926, 925f
 results, 929, 930t
- nondestructive testing and evaluation, 910–914
 infrared thermography testing, 913–914, 913f
 shearography testing, 912, 912f
 ultrasonic testing, 910–911
- structural health monitoring (SHM), 910, 914–924, 915f
 algorithms and machine learning, 919–924
 artificial neural networks (ANN), 923–924
 electromechanical impedance spectroscopy, 918–919, 919f
 gradient boosting, 922, 922–923f
k-nearest neighbors (kNN), 920–921
 lamb waves, 916–918, 917f
 Naive Bayes classifier, 921–922
 random forest, 922–924
- Machine learning, advent of, 483–484
- Manufacturing machinery, 859–861
- Material improvements exceed standard assumptions, 481–482
- Material property evolution, 1011–1013
- Materials construction, 863–865, 864f
- Mechanical assembly, 853
- Mechanical interlocking, 331–332
- Mechanical loading, 496–497
- Mechanical performance and production, 1085–1086
- Mechanistic changes in polymer structure
 environmental exposures, 677–678
 polymer structure, chemical aging in, 682–683
 polymer structure, physical aging in, 681–682
- Mechanochemistry, 1125–1130
 bulk adhesives, 1130
 development, 1128–1130
 interfacial mechanophores (iMPs), 1131
 laser spallation-induced structural adhesive debonding, 1131, 1132f
 qualification tools, 1128–1130, 1129f
 research, 1128–1130
 sensing interfacial damage, 1131–1133
 single fiber composite tensile testing, 1133
 single fiber microdebonding, 1132–1133
- Mechanophores (MPs)
 activation, environmental effects on, 1134–1135
 sensing stresses and damage

- activation intensity, 1133–1134
 - calibration of stress, 1133–1134
 - future trends, 1135–1136
 - implementation, challenges to, 1133–1135
 - introduction to, 1124–1125
 - mechanochemistry, 1125–1130
 - bulk adhesives, 1130
 - development, 1128–1130
 - interfacial mechanophores (iMPs), 1131
 - laser spallation-induced structural adhesive debonding, 1131, 1132*f*
 - qualification tools, 1128–1130, 1129*f*
 - research, 1128–1130
 - sensing interfacial damage, 1131–1133
 - single fiber composite tensile testing, 1133
 - single fiber microdebonding, 1132–1133
 - mechanophore activation, environmental effects on, 1134–1135
 - synthetically complex mechanophores, commercial availability of, 1135
 - Medical device industry adhesives
 - blood filtration, 894
 - case studies, 896–897
 - diagnostic equipment, 894–895
 - medical disposables, 893
 - others, 895
 - reservoirs and enclosures, 893
 - surgical instruments, 893
 - Metal and composite bonds, bonding systems for, 783–790
 - Metal salts, 37
 - Methyl methacrylate (MMA), 149
 - Metrology standards, 460–461
 - MIL-PRF-32662, 242
 - Mixed adhesive joints, 1085–1089
 - concept and operating principle, 1085
 - large thermal gradients, performance under, 1086–1087, 1087*f*
 - mechanical performance and production, 1085–1086
 - Mixed-mode bend (MMB), 1066–1068
 - Mixed-mode bi-material interface joints, 586–598
 - bi-material crack, 594–595, 594*t*, 595*f*, 596*t*
 - composite-to-metal bonded joints, 590–598, 596–597*t*
 - longitudinal strain-based criterion, 586–590
 - MMB test, 590–591
 - same material, asymmetric crack within, 591–593
 - strain-based partitioning method, 589–590
 - strain energy release rate (SERR), 586–587, 586*f*
 - Williams' global partitioning approach, 587–588
 - Mixed-mode fracture behavior, 598–609
 - crack paths, 604–605, 604*f*
 - crack stability, 598–603, 600–602*t*
 - failure envelopes, 606–609, 606*f*, 608–609*f*
 - Mixed-mode fracture envelope, 1063–1068
 - cohesive zone model fit, 1064–1068
 - mixed-mode bend (MMB), 1066–1068
 - single-leg bend (SLB), 1066–1068
 - traction-separation law determination, 1064
 - Mixed-mode I+II, 543–552, 543–546*t*
 - Mixed-mode I+III, 550–552, 551*t*
 - Mixed-mode I+II+III, 552–555, 552–553*t*
 - Mixed-mode partitioning schemes, 582–586
 - evaluation and discussion of, 585–586
 - Mixing and dispensing, 43, 46–47
 - Mix ratio, 77–78, 77–78*f*
 - Mode I and mode II fracture behavior, 395–399, 396–398*f*
 - adhesive joints, failure mode of, 403–404, 403*f*
 - adhesive joints, fracture energies of, 404–406, 405*f*, 406*t*
 - Mode I fracture behavior, 409–411, 409–410*f*
 - Mode II fracture testing, DIC application to, 1058–1059, 1059*f*
 - Mode I J-integral method, 1056–1058, 1057*f*
 - Mode I LEFM analysis, 1054–1056, 1055*f*
 - Modeling framework, 1025–1026
 - Modeling procedure, 1026–1027
 - Model simplification, 209
 - Model validation, 210, 210*f*, 1027–1029, 1028–1030*f*
 - Model validation tests, 1024
 - Mode mix, 658–659
 - Mold temperature, 364–366
 - Molecular weight, 364–366
 - Monolithic specimens, local and global partitioning schemes for, 582–586
 - Multifunctional hybrid acrylate-cyanoacrylate monomer, 150
 - Multifunctional materials in nature, 953–957
- ## N
- Nondestructive testing and evaluation, 910–914
 - infrared thermography testing, 913–914, 913*f*
 - shearography testing, 912, 912*f*
 - ultrasonic testing, 910–911
 - Nondissociated nucleophilic base species, 138–139
 - Nonindustrial consumables, adhesive applications for, 872
 - Non-isocyanate polyurethane (NIPU), 127
 - Numerical methods, 501–507
- ## O
- Odor, 92–93
 - low odor, 92–93

- Odor (*Continued*)
 low toxicity, 92–93
 nonflammable methacrylates, 92–93
 Original equipment manufacturer (OEM), 807–808
 Open data, 483–484
 Open time, 78–79
 Opportunities, 462–463
 Organic rigid particles, 257–259
 carbon nanotubes, 257–259
 graphene and derivatives, 258–259
 Organoboron chemistry, 338–340, 338–339*f*
 Overmolded polyamide 6 interfaces, adhesion of, 364–370
- P**
- Particulate rubbers, 90–91
 Peel joints, 500
 Peel stress, 496
 Pendulum impact tests, 723–734
 Performance under impact loads, 1088–1089, 1088*f*
 Phenolics, 425–427, 431*t*
 Photocuring cyanoacrylates, 149–150, 150*f*
 Photo-debondable adhesives, 971–973
 chemically triggered debondable adhesives, 973
 covalent and supramolecular, 972–973
 crosslinkages, photodegradation of, 972–973
 photoinduced overcuring, 971–972
 triggered debondable adhesives, 974
 Photoinduced overcuring, 971–972
 Photoinitiation catalysts, 34–36, 35–36*t*
 Pigments, 122–123
 Plastic void growth, 266–267
 Plastic zone radius, 264–265
 Polyamide 6 (PA6) overmolding experiments, 359–360, 360–362*f*, 364–370, 379–380
 contact temperature, 364–366
 interface, thermal history of, 366–367, 366–367*f*
 mold temperature, 364–366
 molecular weight, 364–366
 surface properties, mold temperature on, 367–370, 368–370*f*
 Polycyanoacrylate polymers, 143–144
 Polyether ether ketone (PEEK), 389–390
 Polymeric isocyanate, 428–429
 Polymerization, 138
 methacrylates, 76–77
 Polymers, 190
 plasticizer (trimethylsiloxy-terminated PDMS polymer), 190–191
 silanol-terminated PDMS polymer, 190
 vinyl dimethylsiloxy-terminated PDMS polymer, 190
- Polyolefin adhesion, 345–351
 case studies, 348–351, 348*t*, 349–352*f*
 future trends, 352
 polyolefin specific adhesion, 346–347, 347*t*
 Polyols, 120–121
 Polyurethane, 429–430
 basic concepts, 103–106, 104–105*f*
 bio-based PUR, 128–129
 chemistry of, 111–114, 111–113*f*
 designable open time followed by immediate curing, 130–132, 131*f*
 formulation and raw materials of, 117–124, 118–119*t*
 fracture mechanics, 128
 mechanical properties, 106–109, 107–109*f*
 non-isocyanate polyurethane (NIPU), 127
 property relationships, 114–116, 114–117*f*
 raw materials, 120–123
 amines as copolymers, 121
 curing catalysts, 123
 isocyanates, 120
 lightweight fillers, 122–123
 pigments, 122–123
 polyols, 120–121
 regulatory aspects of, 124
 rheology modifiers, 122–123
 stabilizers, 123
 structural fillers, 121–122
 surface-active agents, 122–123
 structural polyurethane adhesives, 124–127
 application equipment, 126–127, 127*f*
 industrial use, 124–126, 124–126*f*
 surface pretreatments to, 106*t*
 thermomechanical and stability testing, 128
 thermomechanical properties, 109–111
 thermo-reversible PUR/debonding effects, 129–130
- Product forms, 181–189
 Production-level testing, cautions on, 468
 Purge time, 80
- Q**
- Qualified technical data, 242
 Quality control, 818–824
 manufacturing controls, 818–820, 819*f*
 methods, 437–438
 rheology characterization, 820–824, 821*f*, 823*f*
 risk mitigation, 838
 Quantifying crystallization, 379–380
 Quasistatic single-mode testing, 535–542
 Mode I, 536–538, 536*f*, 537*t*
 Mode II, 538–540, 539*t*
 Mode III, 540–542, 541*t*

R

- Rail/bus/trailer/recreation marine, 95–96
 - composite to composite, 95
 - composite to metals, 95–96
- Rate-dependent properties, 715–718
 - dynamic response of polymers and constitutive material modeling, 717–718
- Raw material advances, 47–53
- Raw material extraction, adhesive applications for, 857
- Reactive liquid rubbers, 253–254, 253f
- Redox initiation, 74–76, 75t
- Rheological behavior, 82
- Rheology modifiers, 122–123
- Rigid secondary phases, 269–272
 - crack deflection, 270–271, 270–271f
 - crack pinning, 269, 270f
 - debonding and plastic void growth, 271–272, 272f
- Room temperature adhesion vs. high temperature adhesion, 94, 95f
- R-ratio effect, 655–658, 656–657f
- RTV cure, physics of, 182–187, 183f, 185f
- Rubber bridging, 267
- Rubber-like toughening via microvoid toughening, 254–255
- Rubber toughening
 - core-shell rubbers, 254
 - reactive liquid rubbers, 253–254, 253f
 - rubber-like toughening via microvoid toughening, 254–255
- S**
- Scarf and stepped joints, 500–501
- Scarf joint geometry, 1084
- Self-healing adhesives, 974–978
 - autonomic intrinsic self-healing, 976
 - autonomic self-healing, 974–976
 - microcapsules or microvascular/fiber network systems, 974–976
 - nonautonomic healing-thermal/light trigger, 976–978
 - renewable self-healing adhesives, 978
- Semicrystalline thermoplastic interfaces
 - adhesion evaluation, 363–364
 - FLASH DSC experiments, 364
 - high adhesion, 359–362
 - interfacial geometry (IFG), 380–381
 - materials, 363
 - overmolding experiments, 362–364
 - polyamide 6 (PA6) overmolding experiments, 359–360, 360–362f, 364–370, 379–380
 - contact temperature, 364–366
 - interface, thermal history of, 366–367, 366–367f
 - mold temperature, 364–366
 - molecular weight, 364–366
 - surface properties, mold temperature on, 367–370, 368–370f
 - quantifying crystallization and diffusion timescales, 379–380
 - strong polymer interfaces requirements, 370–379
 - interdiffusion and crystallization, 372–376, 373f
 - PA6, interdiffusion and crystallization timescales for, 376–379, 377–378f
 - strong semicrystalline polymer interfaces, conditions needed for, 372
 - thermal modeling, 364
- Servo-hydraulic methods, 719–723, 722–723f
- Servo-hydraulic testing machines, 565–566, 566f
- Shear band yielding, 265–266
- Shear stress, 496
- Shear test, 757–762
 - adhesive dispensing workflow, 759–760, 759f
 - automated adhesive dispensing, 758–759
 - automatic shear strength testing, 757–758, 758f
 - shear testing workflow, 760–762
 - substrates and dies, 758
- Sheet molding compound (SMC), 289
- Siffness wearout approach, 653
- Silicone adhesive formulations, 190–196
- Simple beam theory (SBT), 528–530, 529f
- Single-lap joints deformations, 1046–1050, 1047–1048f, 1050f
- Single-leg bend (SLB), 1066–1068
- Soft secondary phases, 260–264
 - plastic void growth, 262–263, 262f
 - rubber bridging, 263–264
 - shear band yielding, 260–261, 261–262f
- Solar/photovoltaic renewable energy industry, 205–206, 206f
- Special additives, 195–196
 - electrically conductive fillers, 195
 - flame retardants, 195
 - heat stabilizers, 195
 - thermally conductive fillers, 195–196
- Specialty epoxy resins, 13
- Split Hopkinson pressure bars (SHPB), 563–565, 564f
- Stabilizers, 123
- Standard determining organizations, 461
- Standard test methods
 - adhesive bonding, 468–469
 - adhesive design, strength and fracture energy in, 466–480, 466f
 - adhesive joint measurements, 463–466, 464f

- Standard test methods (*Continued*)
- Army Research Laboratory (ARL), 482
 - case studies, 469–473*b*, 479–480*b*
 - driving performance gains with, 482–483, 483*f*
 - fracture mechanics, 468–469
 - future opportunities, 481–484
 - industry-specific standards, 462
 - infrastructure of, 460–463
 - joint failure, addressing plasticity in, 469–480
 - large datasets, 483–484
 - machine learning, advent of, 483–484
 - material improvements exceed standard
 - assumptions, 481–482
 - metrology standards, 460–461
 - open data, 483–484
 - opportunities, 462–463
 - production-level testing, cautions on, 468
 - standard determining organizations, 461
 - standards, driving performance gains with, 482–483, 483*f*
 - strengths, 462–463, 466–467
 - structural bonding, expanding roles in, 459–460
 - weakness, 462–463
- Stepped-lap geometry, 1084–1085, 1085*f*
- Strain-based models, 502–503
- Strain energy release rate (SERR), 586–587, 586*f*
- Strain fields, acquisition and applications of, 1044–1046
- adhesive layer strains, 1044–1046
 - analytical and numerical model predictions, 1044, 1045*f*
 - back face deformations, 1044–1046
 - design optimization, 1046
 - nondestructive inspection and damage tracking, 1046
- Strain rate effects, 512
- Strength approaches, 466–467
- Strength/stiffness wearout, 651–653
- stiffness wearout approach, 653
 - strength wearout approach, 651–653, 652*f*
- Strength wearout approach, 651–653, 652*f*
- Stress and strain concepts, 494–495, 494*f*
- Stress-based models, 502
- Stress durability, 811–814, 812–813*f*
- Stress-life approach, 647–649, 648*f*
- Stress/strain-life approaches, 647–651
- damage initiation and crack growth phases, 649
 - fatigue limit, 650–651
 - fatigue limitvariable amplitude fatigue, 649–650, 650*f*
 - stress-life approach, 647–649, 648*f*
 - variable amplitude fatigue, 649–650, 650*f*
- Structural adhesive chemistries and innovations
- digital tools, 242–244
 - digital performance datasets, industry standardization of, 242–243, 243*f*
 - engineering modeling packages, incorporation into, 244
- functionality beyond structural reinforcement, 239–241
- formulation additives for debonding, 239–240
 - intrinsically debondable structural adhesives, 240–241, 241*f*
 - reversible or debondable structural adhesives, 239–241
- property ranges, 221
- rethinking design rules, 222–224, 223–224*f*
- structural adhesives innovations, 225–238
- digital image correlation (DIC), 225–226
 - dynamic fatigue resistance, 229
 - fundamental structure-property-performance tradeoffs, 231–235, 232–234*f*
 - mechanical performance attributes, 225–231
 - overload failure, high probability of, 225–231
 - ring-opening metathesis polymerization (ROMP), 235–238, 236–237*f*, 239*f*
 - single-lap joint performance, 227
- Structural adhesives, 715–718
- Structural bonding, expanding roles in, 459–460
- Structural fillers, 121–122
- Structural health monitoring (SHM), 910, 914–924, 915*f*
- algorithms and machine learning, 919–924
 - artificial neural networks (ANN), 923–924
 - electromechanical impedance spectroscopy, 918–919, 919*f*
 - gradient boosting, 922, 922–923*f*
 - k-nearest neighbors (kNN), 920–921
 - lamb waves, 916–918, 917*f*
 - Naive Bayes classifier, 921–922
 - random forest, 922–924
- Structural polyurethane adhesives, 124–127
- application equipment, 126–127, 127*f*
 - industrial use, 124–126, 124–126*f*
- Structural sealant glazing (SSG), 201
- Structural silicone adhesives
- applications of, 196–206
 - automotive, 197–200, 197*f*
 - aviation and aerospace, 200–201
 - construction, 201–204
 - domestic appliances, 204
 - electronics, 204–205
 - solar/photovoltaic renewable energy industry, 205–206, 206*f*
 - structural sealant glazing (SSG), 201
 - total vision system (TVS), 201
- catalysts, 192–193
- addition-cure catalysts, 193

- adhesion promoters, 193–194
- condensation-cure catalysts, 192–193
- fillers, 194–195
- crosslinkers, 191–192
 - RTV condensation-cure, 191–192, 192*t*
 - RTV/LTV addition cure, 192
- cure chemistry, 181–189
 - addition cure chemistry, 187–189
 - condensation cure chemistry (RTV), 181–187
 - electron-beam and photo-cure induced
 - addition chemistry, 189
 - hydrolysis reactions, 181–182
 - RTV cure, physics of, 182–187, 183*f*, 185*f*
- design techniques, 206–211, 207*f*
 - analytical analysis, 208
 - durability/failure analysis, 210–211
 - finite element analysis, 208–211
 - model simplification, 209
 - model validation, 210, 210*f*
- dual cure chemistry, 196
- polymers, 190
 - plasticizer (trimethylsiloxy-terminated PDMS polymer), 190–191
 - silanol-terminated PDMS polymer, 190
 - vinyltrimethylsiloxy-terminated PDMS polymer, 190
- product forms, 181–189
- properties of, 179–181
- silicone adhesive formulations, 190–196
- special additives, 195–196
 - electrically conductive fillers, 195
 - flame retardants, 195
 - heat stabilizers, 195
 - thermally conductive fillers, 195–196
- Structural verification
 - civil engineering practice, 833–834
 - designing bonded joints, 834
 - suggestion, 834–835
- Structural wood composite products, 420–424, 421*t*, 424–425*t*
- Structural wood products adhesive bonding
 - adhesive bond durability, 442–445
 - cross-laminated wood products, adhesive effects in, 443–445, 444*f*
 - bondline stiffness, 445–446
 - fracture testing, 438–442
 - direct fracture energy methods, 440–442, 441*f*
 - modified fracture mechanics methods, 438–440
 - structural wood composite products, 420–424, 421*t*, 424–425*t*
 - substrate considerations, 418–420, 419*f*
 - wood adhesives, new developments of, 425–434
 - adhesive/wood interactions, 422*f*, 434–436, 435*f*
 - amino resins, 428
 - bio-based adhesives, 430–433
 - formaldehyde emissions, 433–434
 - phenolics, 425–427, 431*t*
 - polymeric isocyanate, 428–429
 - polyurethane, 429–430
 - quality control methods, 437–438
 - strength characterization, 437–438
 - wood-adhesive bondline characterization, 436–437
- Substrate considerations, 418–420, 419*f*
- Substrate materials, 785
- Substrates and adhesives, bonding formation between, 330–332
- Substrates and dies, 758
- Super glue, 877
- Supply-chain uncertainty, 98
- Surface-active agents, 122–123
- Surface cleaning and treatment technologies, 306–308
 - chemical treatments, 307–308
 - physical treatments, 307
 - processes out of control, 308–322
 - surface tolerant adhesive systems, 308
- Surface contact-wetting/spreading, 328–329, 329*t*
- Surface energy
 - solubility parameters, 332–334, 333*t*
 - wetting, temperature on, 334
- Surface preparation, critical concepts for, 305–306
 - low energy surfaces, 306
 - oxide layers, 306
 - surface contaminants, 305–306
- Surface properties, mold temperature on, 367–370, 368–370*f*
- Surface protection, 855–856
- Surfaces and interfaces, 295–303, 296*f*, 298–300*f*, 302*f*
- Surface science, bonding processes
 - adhesion measuring, 292–303
 - bonded and coated structures, adhesion failure in, 304
 - compound annual growth rate (CAGR), 290–291
 - failure analysis, 292–295, 304–305
 - mysterious bond reliability issues, 291
 - plastics, 290
 - sheet molding compound (SMC), 289
 - surface cleaning and treatment technologies, 306–308
 - chemical treatments, 307–308
 - physical treatments, 307

Surface science, bonding processes (*Continued*)
 processes out of control, 308–322
 surface tolerant adhesive systems, 308
 surface preparation, critical concepts for,
 305–306
 low energy surfaces, 306
 oxide layers, 306
 surface contaminants, 305–306
 surfaces and interfaces, 295–303, 296*f*, 298–300*f*,
 302*f*
 unexplainable failures, 289–290
 Surface treatment, 399–401, 406
 joint preparation, 394, 394*f*
 techniques, 390–391
 Sustainability credentials, 171–175
 methyl methacrylate (MMA), 171–172, 172*f*
 overview, 171, 171*f*
 renewable sources, oligomers from, 172–175,
 173*f*, 174*t*
 Sustainable adhesives
 biodegradable and compostable adhesives,
 961–966, 963–965*f*, 966*t*
 bio-derived materials, 958
 biological systems, controlled adhesion in,
 953–957
 lignin and lignin derivatives, 958–961
 multifunctional materials in nature, 953–957
 photo-debondable adhesives, 971–973
 chemically triggered debondable adhesives,
 973
 covalent and supramolecular, 972–973
 crosslinkages, photodegradation of, 972–973
 photoinduced overcuring, 971–972
 triggered debondable adhesives, 974
 self-healing adhesives, 974–978
 autonomic intrinsic self-healing, 976
 autonomic self-healing, 974–976
 microcapsules or microvascular/fiber network
 systems, 974–976
 nonautonomic healing-thermal/light trigger,
 976–978
 smart adhesives for recyclability, 967–974
 thermally debondable adhesives, 969–971
 additive approaches, 971
 debonding features, chemical modification
 with, 969–970
 dynamic covalent networks and vitrimers,
 970–971
 reversible adhesion, 970–971
 underwater adhesion, 954–957, 957*f*
 universal adhesion, 954, 956*f*
 Swelling stresses, 497–498
 Synthetically complex mechanophores, commercial
 availability of, 1135

T

Temperature effects, 514
 Tensile stress, 495
 Thermal conductivity and thermal expansion,
 1022–1023
 Thermally conductive fillers, 195–196
 Thermal modeling, 362–364
 Thermal shock, 84
 Thermal stresses, 497
 Thermomechanical and stability testing, 128
 Thermomechanical properties, 109–111
 Thermoplastic composites (TPCs)
 future work, 411–412
 joint preparation, 399–401, 406
 lap shear strength, 394–395, 395*t*, 401–403, 401*t*,
 402*f*
 metals, 399–406
 mode I and mode II fracture behavior, 395–399,
 396–399*f*, 403–406
 adhesive joints, failure mode of, 403–404, 403*f*
 adhesive joints, fracture energies of, 404–406,
 405*f*, 406*t*
 mode I fracture behavior, 409–411, 409–410*f*
 polyether ether ketone (PEEK), 389–390
 surface treatment, 399–401, 406
 surface treatment and joint preparation, 394, 394*f*
 surface treatment techniques, 390–391
 UV irradiation, 391–394, 392*t*
 Thermo-reversible PUR/debonding effects,
 129–130
 Thiols, 24–30, 25–29*t*
 Threadlocking, 164–165, 164*f*
 Thread sealing, 165, 165*f*
 Time-temperature superposition principle (TTSP),
 695–699
 physical aging on, 696–697, 697*f*
 physical aging reversing effects, 697–699, 698*f*
 Tissue adhesives, 891
 adhesive families, 888*t*
 bone adhesives, 890–891
 case studies, 892, 892–893*t*
 clinical application of, 888–892
 dental adhesives, 890
 drug delivery patches, 891
 general surgery, 888–889
 laparoscopic surgery, 890
 medical tapes, 891
 skin closure and cosmetic surgery, 889
 vascular surgery, 889–890
 Total vision system (TVS), 201
 Toughened MMA-based acrylic adhesive, 70
 Toughened THFMA-based acrylic adhesive,
 70–71, 71*t*

- Tougheners, 41, 52–53
flexibilizers, 37
- Toughening
adhesive bond gap thickness, 274–275, 275*f*
bulk epoxy polymers, 252–260
 block copolymers, 255–256
 chemical modification, 252
 hybrid toughening, 259–260
 inorganic rigid particles, 256–257
 organic rigid particles, 257–259
 rubber toughening (*see* Rubber toughening)
 thermoplastic toughening, 255
cohesive and interfacial failure, 275, 276*f*
fiber and platelet-type reinforcements, 272–274
 bridging, 272–273, 273*f*
 pull-out, 273–274, 273*f*
finite element modeling, 267–269, 268*f*
future trends, 276–277
Huang-Kinloch model, 264–267
 plastic void growth, 266–267
 plastic zone radius, 264–265
 rubber bridging, 267
 shear band yielding, 265–266
prediction of effectiveness, 260–274
principles, embodiments of, 1111–1120
rigid secondary phases, 269–272
 crack deflection, 270–271, 270–271*f*
 crack pinning, 269, 270*f*
 debonding and plastic void growth, 271–272, 272*f*
soft secondary phases, 260–264
 plastic void growth, 262–263, 262*f*
 rubber bridging, 263–264
 shear band yielding, 260–261, 261–262*f*
- Traction-separation laws, 1059–1064
 cohesive zone models, 1060
 extraction, 1060–1062
 rate-dependent traction-separation laws, 1062–1063, 1063*f*
- Triggered debondable adhesives, 974
- Two-component cyanoacrylate adhesives, 146–149, 147*f*
- Typical form factors and packaging of, 38–39
- U**
- Unexplainable failures, 289–290
- Untoughened MMA-based acrylic adhesive, 70
- UV irradiation, 391–394, 392*f*
- V**
- Variable amplitude, 660
 fatigue, 649–650, 650*f*
- Vibration, 715
- Vehicle crash worthiness, 97
- W**
- Wavy-lap geometry, 1083, 1083*f*
- Williams' global partitioning approach, 587–588
- Wood adhesives, 425–434
 adhesive/wood interactions, 422*f*, 434–436, 435*f*
 amino resins, 428
 bio-based adhesives, 430–433
 bondline characterization, 436–437
 formaldehyde emissions, 433–434
 phenolics, 425–427, 431*t*
 polymeric isocyanate, 428–429
 polyurethane, 429–430
 quality control methods, 437–438
 strength characterization, 437–438

This page intentionally left blank

WOODHEAD PUBLISHING SERIES IN MATERIALS

This second edition of *Advances in Structural Adhesive Bonding* reviews the latest developments in adhesive bonding for a range of advanced structural engineering applications. This new edition has been fully revised and expanded to include the latest advances in materials, testing, and modeling methods; life cycle considerations; industrial implementation; and emerging areas of research.

The first section of the book reviews advances in the most commonly used groups of structural adhesives, with chapters covering epoxy, acrylic, polyurethane, cyanoacrylate, anaerobic, and silicone adhesives as well as toughening strategies and emerging chemistries. The second set of chapters opens with a problem-solving chapter on resolving adhesive failures, then covers various types of adherends and pretreatment methods for structural materials, including plastics, composites, and wood. The third part of the book focuses on joint design, testing, and durability considerations, discussing topics such as fracture mechanics, life prediction techniques, and advancements in testing methods. This is followed by two new sections in the book, the first of which examines the application of adhesives across specific key industrial areas, covering specification, quality control, and risk mitigation for each sector. The final section then introduces several emerging modeling, testing, characterization, and green formulation concepts and techniques that offer special promise for adhesive applications.

This second edition is a valuable guide for those working with structural adhesives, including, in an industrial setting, adhesive specialists, structural engineers, design engineers, research and development professionals, and scientists as well as academic researchers and advanced students in adhesives, joining technology, materials science, and mechanical, aerospace, and civil engineering.

Key features

- Provides detailed coverage of the main adhesive groups, including epoxy, acrylic, polyurethane, cyanoacrylate, anaerobic, silicone, and emerging adhesives.
- Includes the latest developments across adherends, pretreatment methods, joint design and testing, durability, and life cycle-related issues.
- Addresses loading and environmental challenges, adhesive specification, quality control, and risk mitigation for specific industrial application areas.
- Offers perspectives in emerging areas including sustainable chemistries, processing and modeling, and experimental characterization methods.

About the editor

David A. Dillard is the Adhesive and Sealant Science Professor in the Biomedical Engineering and Mechanics Department at Virginia Polytechnic Institute and State University in the United States. He has worked extensively in the field of adhesive bonding, having experience in structural adhesives for aerospace, automotive, and infrastructure applications; adhesives and coatings for microelectronic applications; pressure-sensitive adhesives; elastomeric adhesives and sealants; and polymeric membranes. Dillard has authored or coauthored more than 200 refereed publications. He regularly teaches courses in adhesion science, polymer viscoelasticity, and sustainable energy solutions. His research involves developing test methods and predictive models for understanding and estimating the performance and durability of polymeric materials, adhesives, and bonded joints using the principles of fracture mechanics and viscoelasticity. Dillard has received several awards in recognition of his research.

Cover image: Robotic dispensing of an adhesive on a formed structural member. Photo courtesy of Atlas Copco Industrial Assembly Solutions, Auburn Hills, Michigan



WP
WOODHEAD
PUBLISHING

An imprint of Elsevier
elsevier.com/books-and-journals

ISBN 978-0-323-91214-3



9 780323 912143